



Claudio Margottini
Paolo Canuti · Kyoji Sassa
Editors

Landslide Science and Practice

Volume 3
Spatial Analysis and Modelling



 Springer

Landslide Science and Practice

Claudio Margottini • Paolo Canuti • Kyoji Sassa
Editors

Landslide Science and Practice

Volume 3: Spatial Analysis and Modelling



Editors

Claudio Margottini
ISPRA - Italian Institute for
Environmental Protection and Research
Geological Survey of Italy
Rome, Italy

Paolo Canuti
ICL - International Consortium on Landslides
Florence, Italy

Kyoji Sassa
UNITWIN Headquarters Building
Kyoto University Uji Campus
Uji, Kyoto, Japan

Associate Editors

Filippo Catani
Department of Earth Sciences
University of Florence
Firenze, Italy

Alessandro Trigila
ISPRA - Italian Institute for
Environmental Protection and Research
Geological Survey of Italy
Rome, Italy

Additional material to Volume 1 can be downloaded from <http://extras.springer.com>

ISBN 978-3-642-31309-7 ISBN 978-3-642-31310-3 (eBook)
DOI 10.1007/978-3-642-31310-3
Springer Heidelberg New York Dordrecht London

Library of Congress Control Number: 2013932640

© Springer-Verlag Berlin Heidelberg 2013

This work is subject to copyright. All rights are reserved by the Publisher, whether the whole or part of the material is concerned, specifically the rights of translation, reprinting, reuse of illustrations, recitation, broadcasting, reproduction on microfilms or in any other physical way, and transmission or information storage and retrieval, electronic adaptation, computer software, or by similar or dissimilar methodology now known or hereafter developed. Exempted from this legal reservation are brief excerpts in connection with reviews or scholarly analysis or material supplied specifically for the purpose of being entered and executed on a computer system, for exclusive use by the purchaser of the work. Duplication of this publication or parts thereof is permitted only under the provisions of the Copyright Law of the Publisher's location, in its current version, and permission for use must always be obtained from Springer. Permissions for use may be obtained through RightsLink at the Copyright Clearance Center. Violations are liable to prosecution under the respective Copyright Law.

The use of general descriptive names, registered names, trademarks, service marks, etc. in this publication does not imply, even in the absence of a specific statement, that such names are exempt from the relevant protective laws and regulations and therefore free for general use.

While the advice and information in this book are believed to be true and accurate at the date of publication, neither the authors nor the editors nor the publisher can accept any legal responsibility for any errors or omissions that may be made. The publisher makes no warranty, express or implied, with respect to the material contained herein.

Printed on acid-free paper

Springer is part of Springer Science+Business Media (www.springer.com)

Preface

Landslide Science and Practice

Proceedings of the Second World Landslide Forum

The Second World Landslide Forum (**WLF**) was organized at the headquarters of the Food and Agriculture Organization of the United Nations (FAO), Rome, Italy, on 3–9 October 2011. WLF is a triennial mainstream conference of the International Programme on Landslides (**IPL**) which is jointly managed by the IPL Global Promotion Committee consisting of the International Consortium on Landslides (**ICL**), the United Nations Educational, Scientific and Cultural Organization (UNESCO), the World Meteorological Organization (WMO), the Food and Agriculture Organization of the United Nations (FAO), the United Nations International Strategy for Disaster Risk Reduction (UNISDR), the United Nations University (UNU), the International Council for Science (ICSU), and the World Federation of Engineering Organizations (WFEO).

Background to the World Landslide Forums

The International Consortium on Landslides (ICL) was established by the 2002 Kyoto Declaration “Establishment of an International Consortium on Landslides,” with the Statutes adopted in January 2002. The Statutes defined the **General Assembly** of ICL: In order to report and disseminate the activities and achievements of the consortium, a General Assembly shall be convened every 3 years by inviting Members of the International Consortium on Landslides, individual members within those organizations, and all levels of cooperating organizations and individual researchers, engineers, and administrators. The General Assembly will receive reports on Consortium activities and provide a forum for open discussion and new initiatives from all participants.

The First General Assembly 2005 to the First World Landslide Forum 2008

The First General Assembly was organized at the Keck Center of the National Academy of Sciences in Washington D.C., USA, on 12–14 October 2005. At this Assembly, the first full-color book reporting consortium activities for the initial 3 years, 2002–2005, was published as “Landslides-Risk analysis and sustainable disaster management” through Springer. The 2006 Tokyo Round-Table Discussion – “Strengthening Research and Learning on Earth System Risk Analysis and Sustainable Disaster Management within UN-ISDR as Regards Landslides” – toward a dynamic global network of the International Programme on Landslides (IPL) was held at the United Nations University, Tokyo, on 18–20 January 2006. **The 2006 Tokyo**

Action Plan – Strengthening research and learning on landslides and related earth system disasters for global risk preparedness – was adopted. The Tokyo Action Plan established a new global International Programme on Landslides (IPL) including holding World Landslide Forums. Accordingly, the Second General Assembly 2008 was replaced by the **First World Landslide Forum** and held at the United Nations University, Tokyo, Japan, on 18–21 November 2008.

Report of the Second World Landslide Forum

The Second World Landslide Forum – *Putting Science into Practice* – was organized at the Headquarters of the Food and Agriculture Organization of the United Nations (FAO) on 3–9 October 2011. It was jointly organized by the IPL Global Promotion Committee (ICL, UNESCO, WMO, FAO, UNISDR, UNU, ICSU, WFEO) and two ICL members in Italy: the Italian Institute for Environmental Protection and Research (ISPRA) and the Earth Science Department of the University of Florence with support from the Government of Italy and many Italian landslide-related organizations.

- 864 people from 63 countries participated. Attendance was larger than expected, and twice the attendance at the First World Landslide Forum 2008 in Tokyo (430 participants: 175 from Japan and 255 from abroad).
- 25 technical sessions were held, and 465 full papers were submitted. All accepted papers were edited in 7 volumes including this volume:
 1. Landslide Inventory and Susceptibility and Hazard Zoning
 2. Early Warning, Instrumentation and Monitoring
 3. **Spatial Analysis and Modeling – this volume**
 4. Global Environmental Change
 5. Complex Environment
 6. Risk Assessment, Management and Mitigation
 7. Social and Economic Impact and Policies

Requests of Cooperation for Further Development of ICL and IPL

ICL and IPL are global multidisciplinary and cross-sectoral initiatives to promote landslide science and capacity-development to reduce landslide disasters. The core activities of ICL and IPL are *Landslides: Journal of International Consortium on Landslides*, World Landslide Forum, and IPL projects. Thanks to worldwide support of the journal, the Impact Factor of *Landslides* was 2.216 for 2011 which is the highest within 30 ISI journals in category of Engineering, Geological. The journal will develop from a quarterly journal to a bimonthly journal from Vol. 10 in 2013. The Third World Landslide Forum – Landslide risk mitigation toward a safer geo-environment – at the China National Convention Center, Beijing, China, on 2–6 June (conference) and 7–11 June (Field Trip) 2014. The ICL entered into the second decade of its activities and organized a 10th anniversary Conference on 17–20 January 2012, in Kyoto, Japan. ICL adopted the ICL Strategic Plan 2012–2021, *To create a safer geo-environment-* as an outcome of this conference.

ICL is an international nongovernmental and nonprofit scientific organization promoting landslide research and capacity-building for the benefit of society and the environment, and is

the thematic landslides platform in the UNISDR Global Platform for Disaster Risk Reduction. ICL activities are supported by voluntary efforts of ICL members and supporting organizations. All people involving in landslide research and landslide disaster mitigation activities are requested to cooperate for the development of this initiative through its second decade 2012–2021. (<http://www.iplhq.org/> and <http://icl.iplhq.org/>).

We are deeply appreciative of all the Second World Landslide Forum participants and of the contributions from our UNESCO, WMO, FAO, UNISDR, UNU, ICSU, WFEQ partners and all of our colleagues in ICL for the development of IPL up to now. Finally we address our sincere thanks to Filippo Catani and Alessandro Trigila (the associate editors) for their extensive efforts covering the technical sessions, and reviewing and editing the papers.

Claudio Margottini
Forum Chair



Paolo Canuti
President of ICL



Kyoji Sassa
Executive Director of ICL



ICL and IPL Secretariat

IPL office: UNITWIN headquarters Buildings, Kyoto University Uji Campus,
Uji, Kyoto 611-0011, Japan

ICL office: The Association for Disaster Prevention Research,
138-1 Tanaka Asukai-cho, Sakyo-ku, Kyoto 606-8226, Japan

Email: secretariat@iclhq.org

URL: <http://www.iplhq.org/> and <http://icl.iplhq.org/>

Organizational Structure of the Second World Landslide Forum

Organizers

IPL Global Promotion Committee including:

- International Consortium on Landslides (ICL) *
 - United Nations Educational, Scientific and Cultural Organization (UNESCO)
 - World Meteorological Organization (WMO)
 - Food and Agriculture Organization of the United Nations (FAO)
 - United Nations International Strategy for Disaster Risk Reduction (UNISDR)
 - United Nations University (UNU)
 - International Council for Science (ICSU)
 - World Federation of Engineering Organizations (WFEO)
 - Italian Institute for Environmental Protection and Research (ISPRA)
- (* Members are listed in the last page of this book)

Co-sponsors

- International Union of Geological Sciences (IUGS)
- International Union of Geodesy and Geophysics (IUGG)
- International Geographical Union (IGU)
- International Flood Initiative (IFI)

Under the Auspices of

- International Association for Engineering Geology and the Environment, Italian Section (IAEG)
- Italian Association of Engineering Geologists (AIGA)
- Italian Association of Geotechnique (AGI)
- Italian Association for Mining Engineers, Environment and Territory (ANIM)
- Italian Georesources and Environment Association (GEAM)

International Organizing Board

Honorary Chairpersons

- Irina BOKOVA (UNESCO Director-General)
- Catherine BRECHIGNAC (ICSU President)
- Jacques DIOUF (FAO Director-General)

- Michel JARRAUD (WMO Secretary-General)
- Maria P. LAFFARGUE (WFEO President)
- Konrad OSTERWALDER (UNU Rector)
- Bernardo DE BERNARDINIS (ISPRA President)
- UNISDR Director

Chairpersons

- Claudio MARGOTTINI (ISPRA, Forum Chair)
- Paolo CANUTI (ICL President)
- Kyoji SASSA (ICL Executive-Director)

Deputy Chairpersons

- Peter BOBROWSKY (IUGS Secretary General)
- Deliang CHEN (ICSU Executive Director)
- Peter LYTTLE (ICL Vice President, US Geological Survey)
- Eduardo ROJAS-BRIALES (Assistant Director General of FAO)
- Badaoui ROUHBAN (Director of UNESCO's Section for Disaster Reduction)
- Yueping YIN (ICL Vice President, China Geological Survey)

Scientific Advisory Board

Representing Organisation

- Irasema ALCANTARA-AYALA (Vice President of International Geographical Union - IGU)
- Walter AMMAN (President Davos Forum)
- Michael CROZIER (President of International Association of Geomorphologists - IAG)
- Carlos DELGADO (President of International Association of Engineering Geology - IAEG)
- Luca DEMICHELII (Secretary General of EuroGeoSurveys)
- John HARDING (United Nations Secretariat to International Strategy for Disaster Reduction - UNISDR)
- Srikantha HERATH (Senior Academic Programme Officer of the United Nations University - UNU)
- Thomas HOFER (Forestry officer, Food and Agriculture Organization of the United Nations - FAO)
- Yumio ISHII (Chair of the Committee on Disaster Risk Management of The World Federation of Engineering Organizations WFEO)
- Derek MARTIN (Vice President for North America of International Society for Rock Mechanics - ISRM)
- Howard MOORE (Senior Advisor, International Council for Science - ICSU)
- Pedro SECO E PINTO (Past President of International Society for Soil Mechanics and Geotechnical Engineering - ISSMGE)
- Luciano PICARELLI (Chairperson of the Joint Technical Committee on Landslides and Engineered slopes - JTC1 of ISSMGE, ISRM, IAEG)
- Kaoru TAKARA (Vice chairperson of the Intergovernmental Council of the International Hydrological Programme of UNESCO - IHP)
- Kuniyoshi TAKEUCHI (President of GeoRisk Commission of International Union of Geodesy and Geophysics - IUGG)

Landslide Experts

- Giovanni BARLA (Politecnico di Torino, Italy)
- R.K. BHANDARI (Consultant, India)
- Christophe BONNARD (Swiss Federal Institute of Technology, Lausanne, Switzerland)
- Nicola CASAGLI (University of Florence, Italy)
- Leonardo CASCINI (University of Salerno, Italy)
- Giovanni CROSTA (University of Milano Bicocca, Milano, Italy)
- Jordi COROMINAS (Technical University of Catalonia, Barcelona, Spain)
- Dave CRUDEN (University of Alberta, Edmonton, Alberta, Canada)
- Thomas GLADE (University of Vienna, Austria)
- Jerome DE GRAFF (United States Department of Agriculture , Fresno - Ca - USA)
- Michel HERMELIN (Universidad EAFIT, Medellin, Colombia)
- Ken HO (Hong Kong Geotechnical office, Hong Kong, China)
- Jurgen KROPP (Potsdam Institute for Climate Change - PIK, Potsdam, Germany)
- Richard M. IVERSON (United States Geological Survey - Vancouver, WA , USA)
- C. F. LEE (Hong Kong University, China)
- Jacques LOCAT (University of Laval, Canada)
- Paul MARINOS (University of Athens, Greece)
- Hideaki MARUI (Niigata University, Japan)
- Hormoz MODARESSI (BRGM, Orléans, France)
- Farrouk NADIM (Norwegian Geotechnical Institute - NGI, Oslo, Norway)
- Gabriele SCARASCIA MUGNOZZA (University of Rome, Italy)
- Wang SIJING (Tsinghua University, China)
- Vern SINGHROY (Canada Centre for Remote Sensing, Ottawa, Canada)
- Alexander STROM (Institute of Geospheres Dynamics, RAS, Moscow, Russia)
- Ikuo TOWHATA (University of Tokyo, Japan)
- Keith TURNER (Emeritus Professor, Colorado School of Mines, Denver, Colorado USA)
- Keizo UGAI (Gunma University, Kiryu, Gunma, Japan)
- Roger URGELES (Institut de Ciències del Mar - CSIC, Barcelona, Spain)
- Yasser el SHAYEB (Cairo University, Egypt)
- Sergio SEPULVEDA (University of Chile, Santiago)
- Mauro SOLDATI (University of Modena and Reggio Emilia, Italy)
- Pasquale VERSACE (Calabria University, Cosenza, Italy)
- Cees van WESTEN (ITC, Enschede, Netherlands)
- Kifle WOLDEAREGAY (University of Mekelle, Ethiopia)

Local Organizing Board

Forum Chairs

- Paolo CANUTI (ICL President - WLF2 Chairperson)
- Claudio MARGOTTINI (ISPRA - WLF2 Chairperson)
- Kyoji SASSA (ICL Secretary General - WLF2 Chairperson)

Scientific Programme Committee

- Luciano PICARELLI (Second University of Napoli)
- Marco AMANTI (ISPRA)
- Filippo CATANI (University of Firenze)
- Fausto GUZZETTI (CNR-IRPI)
- Javier HERVAS (JRC)

- Thomas HOFER (FAO)
- Carla IADANZA (ISPRA)
- Claudio MARGOTTINI (ISPRA - WLF2 Chairperson)
- Paolo TOMMASI (CNR-IGAG)
- Alessandro TRIGILA (ISPRA)

Editorial Committee

- Filippo CATANI (University of Firenze)
- Riccardo FANTI (University of Firenze)
- Fausto GUZZETTI (CNR-IRPI)
- Javier HERVAS (JRC)
- Irene RISCHIA (ISPRA)
- Gabriele SCARASCIA MUGNOZZA (Università di Roma "La Sapienza")
- Alessandro TRIGILA (ISPRA)

Logistic Committee

- Thomas HOFER (FAO)
- Claudio MARGOTTINI (ISPRA - WLF2 Chairperson)
- Orlando PANDOLFI (ECN)
- Luna GUBINELLI

Field Trips

- Gabriele SCARASCIA MUGNOZZA (University of Roma "La Sapienza")
- Giuseppe DELMONACO (ISPRA)
- Riccardo FANTI (University of Firenze)
- Irene RISCHIA (ISPRA)
- Daniele SPIZZICHINO (ISPRA)
- Paolo TOMMASI (CNR-IGAG)

Fund Raising and Exhibition

- Claudio MARGOTTINI (ISPRA - WLF2 Chairperson)
- Paolo FARINA (IDS SpA)
- Giorgio LOLLINO (CNR-IRPI)

Secretariat

ISPRA, Italian Institute for Environmental Protection and Research
Dept. Geological Survey of Italy, Via Vitaliano Brancati, 48-00144 Rome, Italy.

Logistics and Administration

Orlando PANDOLFI - ECN yourLIFE Foundation

Contents

Part I Advances in Slope Stability Modelling	
Introduction by Ken Ho, Filippo Catani, Giulio Iovine, and Alberto Ledesma	
Geomechanical Basis of Landslide Classification and Modelling of Triggering	3
Gianfrancesco Rocchi and Giovanni Vaciago	
Study of Shock Landslide-Type Geomechanical Model Test for Consequent Rock Slope	11
Xu Xiangning, Chen Yuliang, and Li Shengwen	
Landslide Processes in the Urbanized Moscow Area	17
Valentina Svalova	
Landslide Hazard Assessment Based on FS_{3D} Combined with an Infiltration Model	21
Aline Silva and Lázaro Zuquette	
Modelling the Motion of Mobile Debris Flows in Hong Kong	29
J.S.H. Kwan, T.H.H. Hui, and K.K.S. Ho	
Modeling Potential Shallow Landslides over Large Areas with SliDisp⁺	37
Daniel Tobler, Rachel Riner, and Robert Pfeifer	
Three Dimensional Stability Analysis of the Grohovo Landslide in Croatia	47
Chunxiang Wang, Željko Arbanas, Snježana Mihalić, and Hideaki Marui	
Mass Movement Classification Using Morphometric Parameters (Puebla, Mexico)	53
Veronica Ochoa-Tejeda, Parrot Jean-François, and Fort Monique	
The 2010 Muddy-Debris Flow of Anganguero (Mexico): Modelling and Simulation	61
Jean-François Parrot and Veronica Ochoa-Tejeda	
A Rock Fall Analysis Study in Parnassos Area, Central Greece	67
George Papathanassiou, Vasilis Marinos, Dimitris Vogiatzis, and Sotiris Valkaniotis	
<i>CM</i>SAKe: A Hydrological Model to Forecasting Landslide Activations	73
Oreste G. Terranova, Pasquale Iaquina, Stefano L. Gariano, Roberto Greco, and Giulio G.R. Iovine	
Shallow-Landslide Susceptibility in the Costa Viola Mountain Ridge (Italia)	81
Giulio G.R. Iovine, Roberto Greco, Stefano L. Gariano, Pasquale Iaquina, Annamaria Pellegrino, and Oreste G. Terranova	

Extraction of Rock Mass Structural Data from High Resolution Laser Scanning Products	89
Giovanni Gigli and Nicola Casagli	
Geological and Geophysical Tests to Model a Small Landslide in the Langhe Hills	95
Sabrina Bonetto, Cesare Comina, Andrea Giuliani, and Giuseppe Mandrone	
Regional Distribution of Ash-Fall Pyroclastic Soils for Landslide Susceptibility Assessment	103
Pantaleone De Vita and Michele Nappi	
Geotechnical Features of the Volcanic Rocks Related to the Arteara Rock Avalanche in Gran Canaria (Canary Islands, Spain)	111
Martín Jesús Rodríguez-Peces, Jorge Yepes Temiño, and Esther Martín-Nicolau	
Effects of Parameters in Landslide Simulation Model LS-RAPID on the Dynamic Behaviour of Earthquake-Induced Rapid Landslides	119
Bin He, Kyoji Sassa, Maja Ostric, Kaoru Takara, and Yosuke Yamashiki	
Different Methods to Produce Distributed Soil Thickness Maps and Their Impact on the Reliability of Shallow Landslide Modeling at Catchment Scale	127
Samuele Segoni, Gianluca Martelloni, and Filippo Catani	
Simulating Infiltration Processes into Fractured and Swelling Soils as Triggering Factors of Landslides	135
Annalisa Galeandro, Jirka Šimůnek, and Vincenzo Simeone	
Dimensionless Numerical Approach to Perched Waters in 2D Gradually Layered Soils	143
Stefano Barontini, Marco Peli, Thom A. Bogaard, and Roberto Ranzi	
Landslide Motion Forecasting by a Dynamic Visco-Plastic Model	151
Marco M. Secondi, Giovanni Crosta, Claudio di Prisco, Gabriele Frigerio, Paolo Frattini, and Federico Agliardi	
Intelligent Analysis of Landslide Data Using Machine Learning Algorithms . . .	161
Natan Micheletti, Mikhail Kanevski, Shibiao Bai, Jian Wang, and Ting Hong	
Challenging Calibration in 3D Rockfall Modelling	169
Paolo Frattini, Giovanni B. Crosta, Federico Agliardi, and Silvia Imposimato	
A Simple Model for Passive Failure Compression Structure at the Toe of Landslide	177
Angelo Doglioni, Annalisa Galeandro, and Vincenzo Simeone	
Recovery of Strength Along Shear Surfaces in Clay Soils	183
Angelo Doglioni and Vincenzo Simeone	
Protection from High Energy Impacts Using Reinforced Soil Embankments: Design and Experiences	189
Alberto Grimod and Giorgio Giacchetti	
Quantitative Evaluation of Roughness with a 2D Digital Instrument	197
Fabrizio Mazza, Davide Brambilla, Laura Longoni, Paolo Mazzoleni, Monica Papini, and Emanuele Zappa	
Use of SAR Interferometry for Landslide Analysis in the Arno River Basin . . .	203
Marcello Brugini, Bernardo Mazzanti, Giovanni Montini, and Lorenzo Sulli	

Experimental Approach for Stability Evaluations of Carrara Marble Basins	211
Domenico Gulli, Maura Pellegrini, and Alessandro Cortopassi	
Part II Rapid Runout Analysis	
Introduction by Marina Pirulli and Claudio Scavia	
Runout Prediction of Debris Flows and Similar Mass Movements	221
Christian Scheidl, Dieter Rickenmann, and Brian W. McArdell	
A Ready to Use GRASS GIS Workbench for Rockfall Analysis	231
Andrea Filipello and Giuseppe Mandrone	
Runout Modelling of Shallow Landslides Over Large Areas with SliDepot . . .	239
Daniel Tobler, Rachel Riner, and Robert Pfeifer	
DEM and FEM/DEM Modelling of Granular Flows to Investigate Large Debris Avalanche Propagation	247
Irene Manzella, Herbert H. Einstein, and Giovanni Grasselli	
Assessment of Discrete Element Modelling Parameters for Rock Mass Propagation	255
Guilhem Mollon, Vincent Richefeu, Pascal Villard, and Dominique Daudon	
On Controls of Flow-Like Landslide Evolution by an Erodible Layer	263
Giovanni B. Crosta, Silvia Imposimato, Dennis Roddeman, and Paolo Frattini	
Influence of Bed Curvature on the Numerical Modelling of Unconstrained Granular Materials	271
Gabriele Pisani, Marina Pirulli, Vincent Labiouse, and Claudio Scavia	
Single or Two-Phase Modelling of Debris-Flow? A Systematic Comparison of the Two Approaches Applied to a Real Debris Flow in Giampileri Village (Italy)	277
Laura Maria Stancanelli, Giorgio Rosatti, Lorenzo Begnudelli Aronne Armanini, and Enrico Foti	
Runout Prediction of Rock Avalanches in Volcanic and Glacial Terrains	285
Rosanna Sosio, Giovanni B. Crosta, Johanna H. Chen, and Oldrich Hungr	
Physical Modelling of the Propagation of Rock Avalanches: Recent Developments and Results	293
Claire Sauthier and Vincent Labiouse	
Debris Flow Analysis: From Lithological Classification of the Basin to Deposition	301
Chiara Deangeli, Erika Paltrinieri, and Davide Tiranti	
Stability Conditions and Evaluation of the Runout of a Potential Landslide at the Northern Flank of La Fossa Active Volcano, Italy	309
Maria Marsella, Aurora Salino, Silvia Scifoni, Alberico Sonnessa, and Paolo Tommasi	
Analysis and Uncertainty Quantification of Dynamic Run-Out Model Parameters for Landslides	315
B. Quan Luna, J. Cepeda, A. Stumpf, C.J. van Westen, A. Remaître, J.-P. Malet, and T.W.J. van Asch	
Effects of Grain-Size Composition Examined in Laboratory and Numerical Tests on Artificial Mud-Flows	319
Simonetta Cola, Nancy Calabrò, Paolo Simonini, and Manuel Pastor	

Slope Instabilities in High-Mountain Rock Walls. Recent Events on the Monte Rosa East Face (Macugnaga, NW Italy)	327
Andrea Tamburini, Fabio Villa, Luzia Fischer, Oldrich Hungr Marta Chiarle, and Giovanni Mortara	
New Approach to Rapid Risk Evaluation in Disasters Related to Landslides-Brazil	333
Renato Eugenio Lima	
Part III GIS Application Developments	
Introduction by Serafino Angelini, Esther Jensen, and Raffaele De Amicis	
Different Approaches of Rockfall Susceptibility Maps in Lower Austria	341
Herwig Proske, Christian Bauer, and Klaus Granica	
Mathematical and GIS-Modeling of Landslides in Kharkiv Region of Ukraine	347
Oleksandr Trofymchuk, Yuriy Kalyukh, and Hanna Hlebchuk	
Evaluation and Zonation of Landslide Hazard of Northern Tehran District	353
Ali Uromeihy and Mahsa Sharif	
Three-Dimensional Modelling of Rotational Slope Failures with GRASS GIS	359
Martin Mergili and Wolfgang Fellin	
A GRASS GIS Implementation of the Savage-Hutter Avalanche Model and Its Application to the 1987 Val Pola Event	367
Martin Mergili, Katharina Schratz, Alexander Ostermann, and Wolfgang Fellin	
Proposed Landslide Susceptibility Map of Canada Based on GIS	375
María José Domínguez-Cuesta and Peter T. Bobrowsky	
Statistic Versus Deterministic Method for Landslide Susceptibility Mapping	383
Iuliana Armas, Florica Stroia, and Laura Giurgea	
Two Integrated Models Simulating Dynamic Process of Landslide Using GIS	389
Chunxiang Wang, Hideaki Marui, Gen Furuya, and Naoki Watanabe	
Using the Information System and Multi-Criteria Analysis in the Geological Risk Management in São Paulo	397
Eliene Coelho and Luciana Pascarelli	
Maps of Landslide Areas with Technical G.I.S.: The Use of High Resolution DTM	403
Mauro Palombella	
A New Digital Catalogue of Harmful Landslides and Floods in Italy	409
Paola Salvati, Ivan Marchesini, Vinicio Balducci, Cinzia Bianchi, and Fausto Guzzetti	
Application of the Computerised Cartography to the Territory Management: The Geomorphological Map of Palaeolandslides in the Velino River Valley (Central Apennines, Italy)	415
Serafino Angelini, Piero Farabollini, Riccardo Massimiliano Menotti, Fabrizio Millesimi, and Marco Petitta	

Database of Unstable Rock Slopes of Norway	423
Halvor Bunkholt, Bobo Nordahl, Reginald L. Hermanns, Thierry Oppikofer, Luzia Fischer, Lars Harald Blikra, Einar Anda, Halgeir Dahle, and Stine Sætre	
Landslides and Spatio-Temporal Processing of Geographical Information . . .	429
Raffaele De Amicis, Federico Prandi, Giuseppe Conti, Diego Taglioni, Stefano Piffer, Marco Calderan, and Alberto Debiasi	
Lahar, Floods and Debris Flows Resulting from the 2010 Eruption of Eyjafjallajökull: Observations, Mapping, and Modelling	435
Esther H. Jensen, Jon Kr. Helgason, Sigurjón Einarsson, Gudrun Sverrisdottir, Armann Höskuldsson, and Björn Oddsson	

Advances in Slope Stability Modelling

Introduction by Ken Ho¹, Filippo Catani², Giulio Iovine³, and Alberto Ledesma⁴

1) Hong Kong Geotechnical office, Hong Kong, China

2) Dipartimento di Scienze della Terra, Università degli Studi di Firenze,
Florence, Italy

3) CNR-IRPI – U.O.S. of Cosenza, Rende, Cosenza, Italy

4) University of Catalonia, UPC, Barcelona, Spain

Slope modelling traditionally refers to the analysis of detail-scale slope stability under known specific boundary conditions. Many methods have been proposed and used in the last 30 years to cope with the related problems and, lately, new numerical solutions have been developed to improve our ability to model the behaviour of a given slope, both in two and three dimensions. However, even more recently, new advances in constitutive models and computational methods, software engineering, field and laboratory instrumentation, quantitative geomorphology and hydrology seem to have set the stage for a new breakthrough in slope modelling, making it possible to positively face the challenge of going from slope-specific to basin-scale analysis and from limited time frames (single event approach) to continuous, real-time applications. Recent advances in slope modelling are not confined to analysis concerning the conditions prior to the onset of landslides or complete detachment of ground mass, but also the simulation of post-failure dynamics. Numerical models have evolved to assess the runout of landslide debris, which have practical applications in hazard and risk assessment.

In this context, this chapter addresses a wide range of case studies and methodological applications on landslide modelling offering an overview of actual issues worldwide.

Slope stability modelling issues are reported under both seismic (China, Japan) and pore water pressure stresses (Brazil, Switzerland, Italy). Run-out modelling is also treated, with examples in China for rock slides, Hong Kong and Italy for debris flows and Mexico for mud flows. Some interesting case studies on landslide behaviour are also included, in Russia, Croatia, Greece, Italy and Spain.

Besides, more theoretical studies are devoted to the hydrological and geotechnical modelling for landslide stability, to the data retrieval on important slope stability parameters using new methods (using TLS for rock falls, modelling for soil depth, specific new devices for roughness), to rock fall modelling in Italy (Alps and the Carrara marble basins). A final case on mitigation measures to cope with slope instability in Italy concludes the chapter.

Geomechanical Basis of Landslide Classification and Modelling of Triggering

Gianfrancesco Rocchi and Giovanni Vaciano

Abstract

A proposal to supplement existing landslide classifications with a more detailed description of the geomechanical characteristics of the materials to include the effects of “structure”, stress history and initial state has been developed as part of the EC sponsored SafeLand project. This approach provides a valuable insight into and a rational basis for the modelling of the physical mechanisms that govern landslide triggering and subsequent development. The classification, behaviour and modelling of saturated clays and sands is summarized here. The use of advanced strain hardening plasticity models which, where necessary, include progressive damage to the “structure” of the material helps to replicate mechanical weathering, delayed failure and the triggering of flows or slides, depending on the type of material. A numerical example is presented, illustrating the different response of sensitive clays and mechanically overconsolidated clays to rapid erosion or excavation. More details of the proposed geotechnical classification and other numerical examples may be found in Deliverable 1.1 of the SafeLand project.

Keywords

Classification • Clay • Sand • Modelling

Introduction

Early classifications of landslides (Varnes 1978) were based on geomorphological aspects, describing the types of movement in great detail, but typically relating them to broad categories of geomaterials (“rock”, “debris”, “earth”). These classifications have been progressively supplemented with additional details on the geotechnical characteristics of the geomaterials involved. This focused initially on (Carson 1976; Hutchinson 1988):

- The control exerted by liquidity index on whether instability in clays occurs by flow or sliding;
- “Soil fabric conditions”, distinguishing between first time slides and slides on pre-existing shear surfaces;

- Pore water pressure, distinguishing between undrained, drained and intermediate conditions.

A more comprehensive classification has been developed in the 1990s, resulting in a 3D matrix (Fig. 1) which classifies landslides in terms of slope movement (geomorphological classifications), movement stage (pre-failure, failure, post-failure, reactivation) and materials, as described in Fig. 2.

Figure 2 presents fairly broad categories of materials. Soils are described mainly on the basis of their grain size distribution and degree of saturation, with only an ill-defined distinction between “soft” and “stiff” clays and no attention paid to the density of coarse grained soils.

To refine the classification of materials and to provide further insight into the factors which influence the triggering and subsequent development of landslides, Rocchi et al. (2010) considered in greater detail the case of saturated soils from the viewpoint of their mechanical characterization and constitutive modelling, taking into account the “structure” of the material, its stress history and its initial state in terms of

G. Rocchi (✉) • G. Vaciano
Studio Geotecnico Italiano, via G. Ripamonti 89, Milan 20141, Italy
e-mail: g.vaciano@studiogeotecnico.it

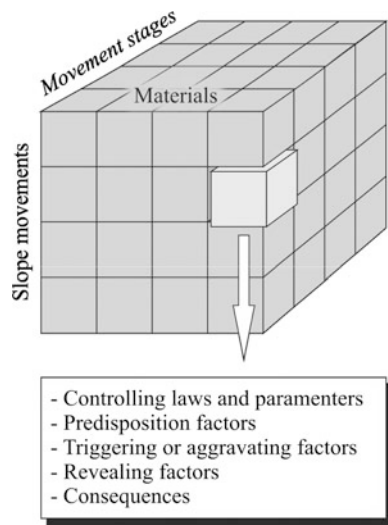


Fig. 1 Schematic characterization of slope movements (Leroueil et al. 1996)

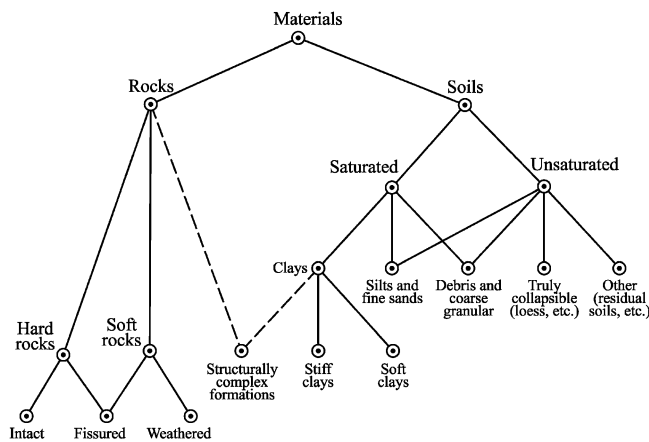


Fig. 2 Material types considered in the geotechnical characterization of slope movements (Leroueil 2001)

void ratio and effective geostatic stresses. They also addressed rocks and complex formations, but these materials are not considered here due to space limitations.

In association with the use of advanced strain hardening plasticity models, which include, where necessary, progressive damage to the “structure” of the material, this approach provides a rational basis for finite element (FEM) analyses of landslide triggering which correctly predict mechanical weathering, delayed failure and whether landslides will take the form of flows or slides, depending on the type of material. Whilst this approach may involve some idealization compared to the complexity and heterogeneity of landslides, it is certainly a powerful tool, which overcomes the gross simplification inherent in limit equilibrium (LEM) methods of analysis.

Proposed Amendment to the Classification of Materials

It is widely recognized that the mechanical behaviour of saturated clays and sands is controlled by:

- The combination of void ratio and effective stresses, which define the “condition” of the material relative to a “reference line”, i.e. the intrinsic compression line (ICL, Burland 1990) for clays and the initial dividing line (IDL, Ishihara 1993) for sands;
- The microstructure of the material.

Compared to the classification shown in Fig. 2, for saturated sands and clays Rocchi et al. (2010) propose to distinguish between *clays* (C) and *sands* (S) *above* (A), *on* (O) or *below* (B) the “reference line”, as shown in Fig. 3, where further distinctions are made between uncemented (1) and cemented (2) and between fissured (F) and intact (I) materials. Select cases are described below, using also the terminology proposed by Nagaraj and Miura (2001).

CA: Clays with Initial States Above the ICL: Naturally Cemented Clays

With reference to the framework proposed by Jardine et al. (1991), these materials have the following characteristics (Fig. 4):

- Limit State Surfaces (LSS) for natural and reconstituted materials. The LSS representing the “gross yield” of the natural material, is outside that of reconstituted material and is strain rate dependent.
- Zones around the point representing the initial effective stress state within which the behaviour is linear elastic (Zone 1) and non-linear elastic (Zone 2).
- Outside Zone 2, even within the LSS of the natural material, generation of destruction processes with associated irreversible visco-plastic strains and strain rate dependent behaviour. The outer boundary of Zone 2 represents the “true yield” of the natural material. The volumetric component of the visco-plastic strains for states outside the LSS of the reconstituted material results in contractant behaviour (i.e. reduction in void ratio or development of positive excess pore pressure in drained or undrained conditions respectively).
- Destruction process and associated visco-plastic strains take place in the pre-failure stage up to failure. Additional remoulding energy is delivered to the material in the post-failure (propagation) stage. As a result, the LSS of the natural material shrinks, leading to conditions which may be governed by the behaviour of the reconstituted

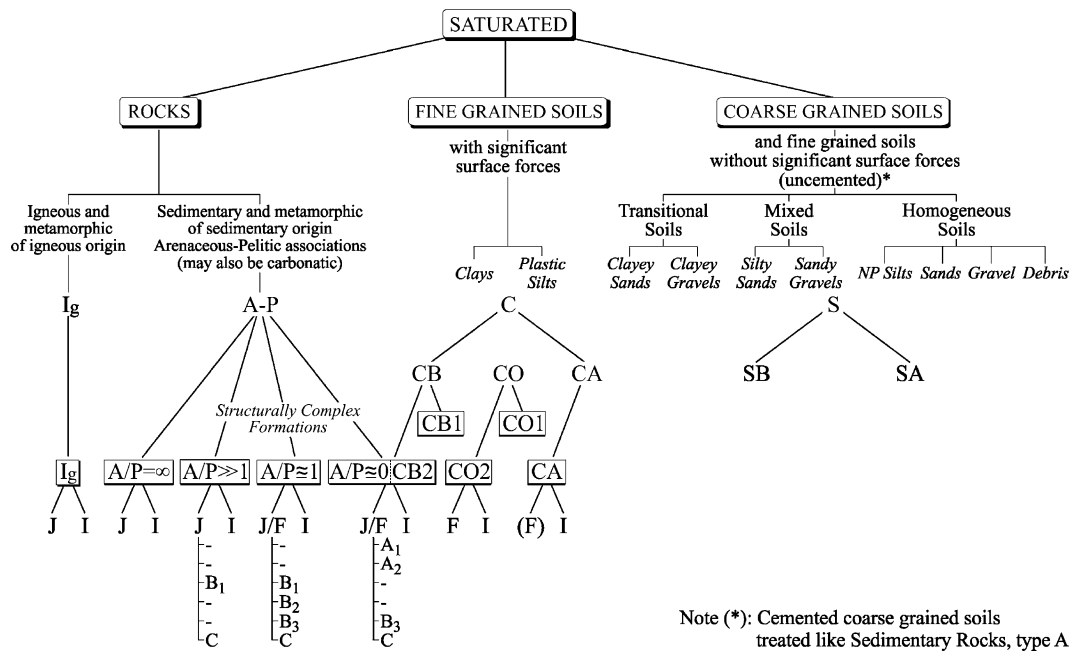


Fig. 3 Revised classification of material types for the geotechnical characterization of slope movements (Rocchi et al. 2010)

material where all the microstructure has been removed. In undrained conditions, the destruction processes may lead to a substantial reduction of undrained shear strengths. In the extreme case represented by “quick clays”, the remoulded material may behave as a fluid, making these clays particularly susceptible to dramatic failure (Tavenas et al. 1971). Considering typical failure and post-failure conditions and mechanisms, residual effective strength envelopes are of secondary significance in these materials.

In oedometric conditions the preconsolidation pressure σ'_{vp} is due primarily, if not exclusively, to bonding, rather than mechanical preconsolidation. It is thus better referred to as “apparent” preconsolidation pressure. It is strain rate dependent and does not reflect the “true yield” σ'_{vy} of the natural material, which is significantly lower than σ'_{vp} (Fig. 4, Bjerrum 1967; Larsson et al. 1977). At extremely slow strain rates, for “ideal” truly undisturbed samples σ'_{vp} reduces to σ'_{vy} .

The behaviour of these materials can be reproduced realistically only by means of elasto-viscoplastic constitutive models which simulate appropriately in the time domain the effects of progressive destruction of the microstructure (see for example Adachi et al. 1996; Rocchi et al. 2003; Hinchberger and Qu 2009).

In relation to the overburden and degree of bonding, these clays may appear either as ‘soft clays’ or as ‘stiff/hard clays’ as defined by common classifications. The use of this terminology in the classification of Fig. 2 does not convey

sufficient information to distinguish this type of clays and their associated behaviour from other types of clays.

For this reason these clays need to be classified also in terms of “sensitivity”, commonly defined as the ratio of the undisturbed to the remoulded undrained shear strength, as determined for example by in situ vane tests.

CB: Clays with Initial States Below the ICL: Mechanically Overconsolidated Clays

Clays with initial states below the ICL can be either without (type CB1) or with (type CB2) bonding; their microstructure is stable at the initial stress state in situ irrespective of the presence of bonding. In their natural state type CB1 materials have the following characteristics (Fig. 5):

- LSS practically coincident with that characteristic of the reconstituted material.
- Zones around the point representing the initial effective stress state within which the behaviour is linear elastic (Zone 1) and non-linear elastic (Zone 2).
- Outside zone 2 up to and on the LSS, mainly plastic behaviour. For all practical purposes visco-plastic strains and strain rate dependency can be considered negligible. The volumetric component of the plastic strains result in a moderately contractive or dilatant behaviour depending on the distance of the current state from the ICL. The behaviour becomes progressively more dilatant as this distance increases, implying a greater development of

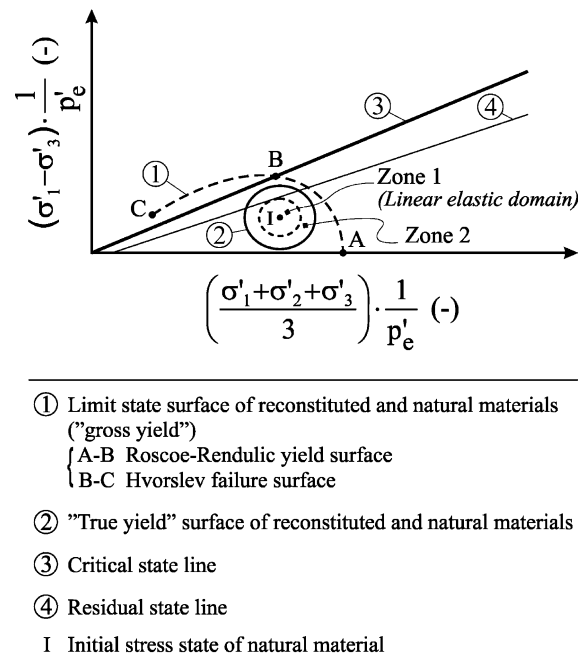
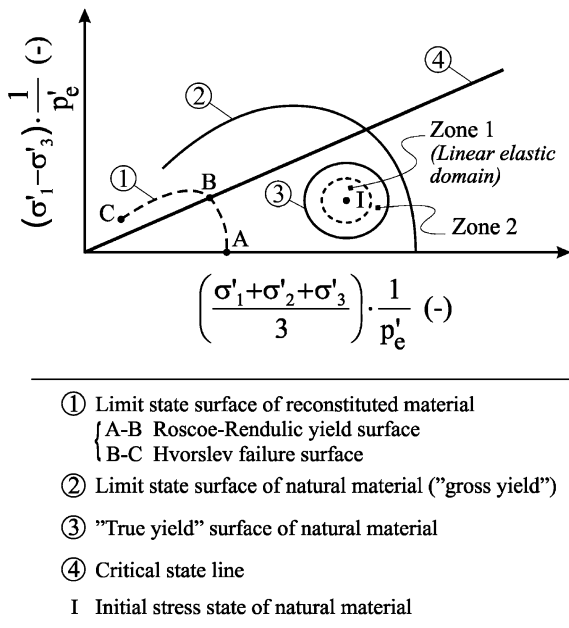
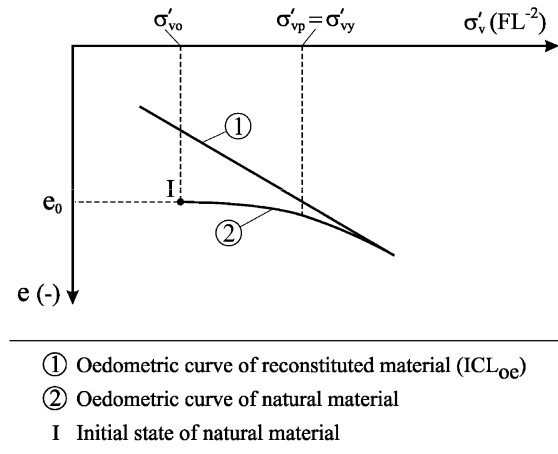
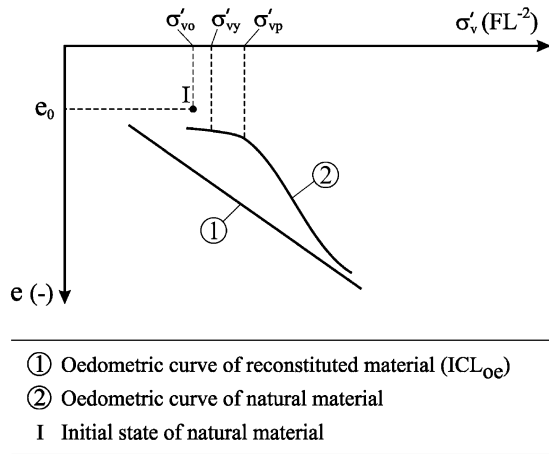


Fig. 4 Basic elements of clay behaviour – Material type CA (Rocchi et al. 2010)

Fig. 5 Basic elements of clay behaviour – Material type CB1 (Rocchi et al. 2010)

negative excess pore pressures or a greater drop in resistance from peak to critical state in undrained and drained conditions respectively. Under certain circumstances, governed essentially by clay content, activity, water chemistry and effective confining pressure, a significant reduction of the effective strength envelope may occur from critical state to ‘residual’ in the more highly sheared zones (Skempton 1985).

Conventional vertical preconsolidation pressure σ'_{vp} as typically determined from oedometer tests is practically linked only to mechanical pre-compression; in heavily mechanically overconsolidated clays, σ'_{vp} is not necessarily equal to the maximum vertical effective stress σ'_{vmax} experienced by the deposit; plastic strains during drained unloading may cause a partial loss of “memory” (Calabresi and Scarpelli 1985).

The behaviour of these materials can be replicated by elasto-plastic constitutive models with volumetric and kinematic hardening capable of reproducing non-linearity also inside the LSS (see for example Al-Tabbaa and Wood 1989; Stallebrass and Taylor 1997).

SA and SB: Sands Above and Below the Initial Dividing Line

A summary of the extensive technical literature describing the essential aspects of the behaviour of sands is presented by Rocchi et al. (2010) with reference to the meaning of Steady State (SS), Compression Lines, Phase Transformation (PT), Quasi Steady State (QSS) Initial Dividing Line

(IDL) and Collapse or Instability Surface (CS or IS), as relevant for the behaviour of these materials in landslides.

From conventional undrained triaxial tests carried out on specimens prepared at different void ratios (e_c) with different mean effective consolidation pressures (p'_c) it is possible to distinguish between two classes of initial states (e_c ; p'_c) where a temporary drop in shear stresses can or cannot occur (Ishihara 1993).

The IDL can be drawn through the data points separating the initial states with and without the occurrence of minimum strength. By definition, only the materials with initial states located above the IDL may be susceptible to initiation of flow instability. These materials are identified as type SA, while those whose initial states are located below the IDL and are thus not susceptible to flow are identified as SB.

The proposed classification focuses on the susceptibility to flow because this is the most significant aspect of the behaviour of sands in the context of landslides.

The simulation of the main aspects of the behaviour of sands, including non linear behaviour, shear-induced plastic volumetric strains (dilation/contraction), strain softening/hardening, etc., may be attempted by adopting advanced plasticity models consistent with the framework of Critical State Soil Mechanics (Wood 1990), including also:

- Non-associative flow rules;
- The state parameter as an essential variable to describe the current state of the material compared to the SS or other characteristic states (Li and Dafalias 2000; Jefferies and Been 2006).

Numerical Example: CA Versus CB1 Clays

A numerical example is presented here to illustrate the potential of the proposed geotechnical classification of materials in explaining the fundamentally different behaviour of sensitive clays compared to mechanically overconsolidated clays. More details on this and other examples replicating mechanical weathering, delayed failure and formation of “badlands” in mechanically overconsolidated clays and flow failures in loose sands are discussed by Rocchi et al. (2010).

Let us consider two 10 m high slopes inclined 1 (vertical): 3 (horizontal), one excavated in clayey materials CB1 (mechanically overconsolidated, unbonded) and the other in clayey materials CA (metastable microstructure, bonded) with a 3 m “crust” of CB1 material.

The behaviour of the CB1 clay is simulated by an elasto-plastic constitutive model of the CAM-CLAY family, modified to include both generalized plasticity within the Intrinsic State Boundary Surface and variation of the strength parameter M with the Lode angle (θ).

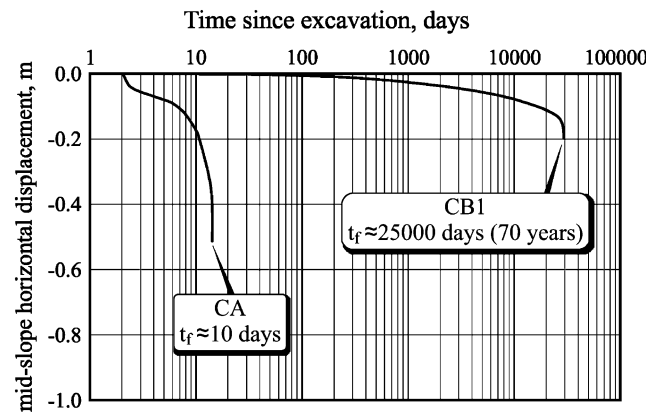


Fig. 6 Numerically simulated mid-slope horizontal displacements as a function of time since excavation of a 1(v): 3(h), 10 m high slope for CA and CB1 clays (Rocchi et al. 2010)

The clay materials CA below the clayey “crust” have been simulated by the elasto-viscoplastic model initially developed by Rocchi et al. (2003) as updated by Rocchi et al. (2006).

Figure 6 shows the mid-slope horizontal displacement for the two cases considered as a function of time. Failure conditions are reached at considerably different times, i.e. 10 days for CA clays and approximately 70 years for CB1 clays. While in CB1 materials shear plastic strains tend to localize in a unique, relatively narrow shear band, in CA materials multiple shear bands and/or diffused failure conditions are observed which reach greater depths than in CB1 materials.

Figure 7 compares the excess pore pressures (suction positive, as per definitions in the computer code) at 10 days after excavation, corresponding to failure conditions for materials type CA. The excess pore pressure distributions in the two cases are very different; while in CB1 materials they correspond essentially to the distribution of negative excess pore pressures induced by undrained unloading, in CA materials the excess pore pressures are generally low, appearing to correspond to complete dissipation to the steady state conditions. In fact, localized positive excess pore pressures near the multiple shear bands confirm that shear induced positive excess pore pressures have compensated and locally exceeded the negative excess pore pressures induced by the reduction of mean total stress by undrained unloading, and that this mechanism prevails, rather than consolidation.

In the simpler case represented by rapid cuts or basal erosion the time necessary to reach pore pressure equilibrium is strictly related to:

- Deformability characteristics of the clay which govern both the amount and sign of the excess pore pressure and the overall behaviour in the pre-failure and possibly failure stages;

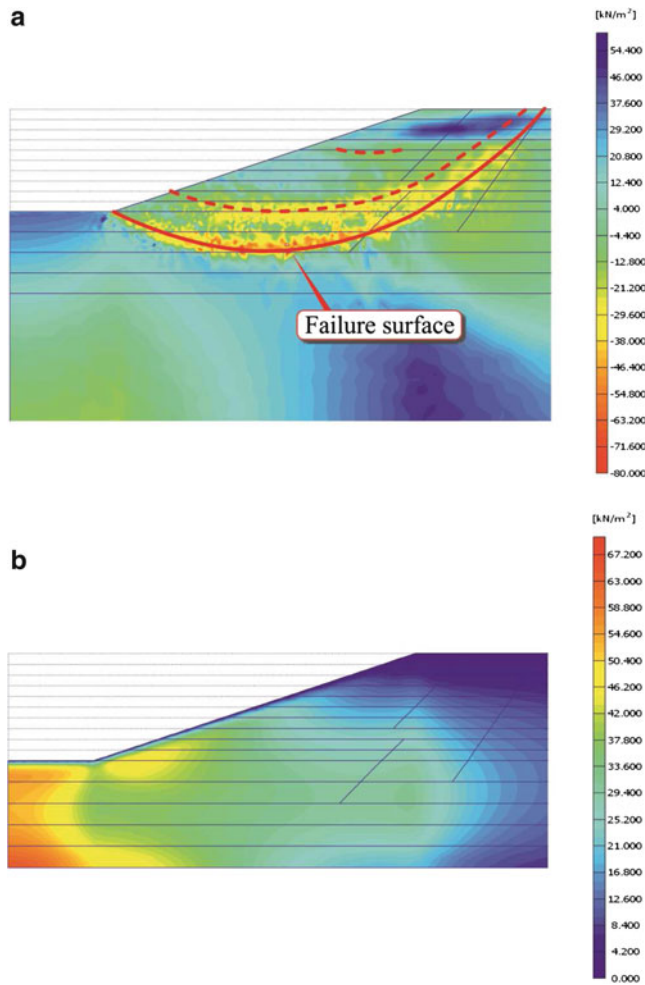


Fig. 7 Numerically simulated distributions of excess pore pressures for a 1(v): 3(h), 10 m high slope at 10 days in (a) CA clays ($K_o = 0.6$) and (b) CB1 clays ($K_o = 1$) (Rocchi et al. 2010)

- Permeability characteristics of the clay which may vary with time as a consequence of variation of void ratio;
- Geometry of the slope (height and inclination).

The very short time necessary to reach pore pressure equilibrium observed in material type CA compared to that necessary to reach similar conditions in material type CB1 can be well understood in the light of the general behaviour described above for the different materials and of the following relationship proposed by Henkel (1960) for determining initial excess pore pressure (Δu) as a function of stress changes:

$$\Delta u = \beta \cdot \left(\frac{\Delta \sigma_1 + \Delta \sigma_2 + \Delta \sigma_3}{3} \right) + \alpha \cdot \sqrt{(\Delta \sigma_1 - \Delta \sigma_2)^2 + (\Delta \sigma_2 - \Delta \sigma_3)^2 + (\Delta \sigma_3 - \Delta \sigma_1)^2}$$

where

$\Delta \sigma_i$ = changes of total principal stress

α, β = excess pore pressure parameters

In rapid excavation (artificial or natural), there is a decrease in pore pressure (development of negative excess pore pressure) associated with a reduction in mean total stresses (Leroueil 2001).

In heavily overconsolidated clays of the type CB, the parameter α is negative and the shear stresses generate additional negative excess pore pressure in such a way that the difference in pore pressure between the end of excavation and the steady state condition is significant.

On the other hand, in clays of the type CA the parameter α is positive and the shear stresses generate positive excess pore pressure, compensating to some extent the negative excess pore pressure due to the change in mean total stresses. In these conditions, the resulting overall changes in pore pressure due to excavation can be quite small and dissipate quickly.

Back analyses of the pore pressure variation with time such as those reported in Laflamme and Leroueil (1999), where the excavation at Saint Hilaire has been simulated by finite element analyses assuming linear elasticity ($\alpha = 0$), result in the need to assign unnecessarily high values of stiffness to the soil to match the observed rapid equilibration of excess pore pressures.

This example shows how the use of appropriate constitutive models in numerical FEM analyses is sufficient to replicate realistically the overall behaviour of the two clays, including the pore pressure responses.

Conclusions

The classification of materials described here, based on relating the combination of void ratio and effective geostatic stresses of saturated soils to “reference conditions”, provides a rational basis for refining landslide predictions, associating the type of movement that can be expected to the classification of the soils involved.

In association with advanced constitutive and numerical modelling, for the given boundary conditions, this approach can provide quantitative predictions of the triggering and subsequent development of landslides, overcoming the limitations of LEM methods of analysis.

Acknowledgments The work summarized here was carried out as part of the SafeLand project, funded by the EC 7th Framework Programme (Grant Agreement No. 226479). The Authors are grateful to colleagues and partners in the Project for valuable discussion. The numerical models were developed with the assistance of Ing. Maurizio Fontana of Autosoft, whose contribution is gratefully acknowledged.

References

- Adachi T, Oka F, Mimura M (1996) Modelling aspects associated with time dependent behaviour of soils. Sheahan TC, Kallakin VN (eds) Geotechnical Special Publication no 61, on measuring and modelling time dependent soil behavior, sponsored by Geo-Institute of ASCE, in conjunction with ASCE Convention in Washington, DC
- Al-Tabbaa A, Wood MD (1989) An experimentally based bubble model for clay. In: Pande GN, Pietruszek S (eds) Proceedings of numerical models in geomechanics. NUMOG III, Elsevier, London, pp 91–98
- Bjerrum L (1967) Engineering geology of Norwegian normally consolidated marine clays as related to settlements of buildings. *Géotechnique* 17(2):81–118
- Burland JB (1990) On the compressibility and shear strength of natural clays. *Géotechnique* 40(3):329–378
- Calabresi G, Scarpelli G (1985) Effects of swelling caused by unloading in overconsolidated clays. In: Proceedings of 11th ICSMFE, vol 2. San Francisco, pp 411–414
- Carson MA (1976) Mass-wasting, slope development and climate. In: Derbyshire E (ed) *Geomorphology and climate*. Wiley, London, pp 101–136
- Henkel DJ (1960) The shear strength of saturated remolded clays. In: Proceedings of the ASCE Research conference on shear strength of cohesive soils, Boulder, pp 533–554
- Hinchberger SD, Qu G (2009) Viscoplastic constitutive approach for rate-sensitive structured clays. *Can Geotech J* 46:609–626
- Hutchinson JN (1988) Morphology and geotechnical parameters of landslides in relation to geology and hydrogeology. In: Proceedings 5th international symposium on landslides, Lausanne 1, Balkema, pp 3–35
- Ishihara K (1993) Liquefaction and flow failure during earthquakes. *Géotechnique* 43(3):351–415
- Jardine RS, St John ND, Hight DW, Potts DM (1991) Some practical applications of a non-linear ground model. In: Proceedings of 10th ECSMFE, vol 1. Florence, pp 223–228
- Jefferies M, Been K (2006) *Soil liquefaction – a critical state approach*. Taylor & Francis, London, 479p
- Lafamme JF, Leroueil S (1999) Analyse des pressions interstitielles mesurées aux sites d'excavation de Saint-Hilaire et de Rivière-Vachon, Quebec. Report GCT-99-10 prepared for the Ministère des Transports du Quebec, Université Laval
- Larsson R, Bengtsson PE, Eriksson L (1997) Prediction of settlements of embankments on soft, fine-grained soils- calculation of settlements and their course with time. Information 13E, Swedish Geotechnical Institute, Linköping
- Leroueil S (2001) Natural slopes and cuts: movement and failure mechanism. *Géotechnique* 51(3):197–243
- Leroueil S, Vaunat J, Picarelli L, Locat J, Faure R, Lee H (1996) A geotechnical characterization of slope movements. In: Seneset K (ed) Proceedings of 7th international symposium on landslides. Trondheim 1, Balkema, pp 53–74
- Li XS, Dafalias YF (2000) Dilatancy for cohesionless soils. *Géotechnique* 50(4):449–460
- Nagaraj TS, Miura N (2001) *Soft clay behaviour: analysis and assessment*. Balkema, Rotterdam
- Rocchi G, Fontana M, Da Prat M (2003) Modelling of natural soft clay destruction processes using viscoplasticity theory. *Géotechnique* 53(8):729–745
- Rocchi G, Vaciago G, Fontana M, Plebani F (2006) Enhanced prediction of settlement in structured clays with examples from Osaka Bay. *Geomech Geoen Int J* 1(3), Taylor and Francis, pp 217–237
- Rocchi G, Vaciago G, Callerio A, Fontana M, Previtali R (2010) Chapters 2 and 4 in: *SafeLand – living with landslide risk in Europe: assessment, effects and global change, and risk management strategies*. Crosta GB, Agliardi F, Frattini P, Sosio R (eds) Deliverable 1.1: landslide triggering mechanisms in Europe – overview and state of the Art, Rev. 1 – final, pp 11–81
- Skempton AW (1985) Residual strength of clays in landslides, folded strata and the laboratory. *Géotechnique* 35(1):3–18
- Stallebrass SE, Taylor RN (1997) The development and evaluation of a constitutive model for the prediction of ground movements in overconsolidated clay. *Géotechnique* 47(2):235–253
- Tavenas F, Chagnon JY, La Rochelle P (1971) The Saint-Jean-Vianney landslide: observations and eyewitness accounts. *Can Geotech J* 8:463–478
- Varnes DJ (1978) Slope movement types and processes. In: Schuster RL, Krizek RJ (eds) *Landslide analysis and control special report 176*, Transportation research Board, N.R.C., National Academy of Sciences, Washington, DC, vol 2, pp 11–33
- Wood MD (1990) *Soil behaviour and critical state soil mechanics*. Cambridge University Press, Cambridge



Study of Shock Landslide-Type Geomechanical Model Test for Consequent Rock Slope

Xu Xiangning, Chen Yuliang, and Li Shengwen

Abstract

Mountain deformation and fracture as a result of earthquakes is a complicated evolution process. We need to take advantage of geomechanical simulation and shock effects to reproduce the mountain deformation process based on the understanding and conceptual model through geological analysis, in order to verify and disclose the facts. The author has chosen a certain typical landslide-type geomechanical model of consequent rock slope under earthquake effect, and carried out the simulation testing study for the geomechanical mechanism under the vibration conditions. This paper introduces the methods of model preparation, the test plan design and testing methods, and studies the testing results, from the vibration trace and deformation and fracture evolution process, deformation and fracture evolutionary process and vibration acceleration time-history changes, vibration intensity and deformation and fracture evolution of different geological structures, so some useful results and new knowledge are reported.

Keywords

Vibration test • Geomechanical simulation mechanism • Shock landslide-type geomechanical model for rock slopes dip toward excavation • Deformation and fracture evolution of mountains

Introduction

Destabilization is likely to happen to the gently titled external stratified slope, medium titled external or consequent slope with changeable angle, with the deformation and fracture mechanical mechanism generally as sliding-rip type and sliding-bending type, and destruction instability mode generally as consequent slope, consequent-tangential slope or rotating landslide, such as the typical front edge of rock slope

dip toward excavation of Diexi Jiaochang of Diexi Seismic Area in Sichuan in 1933, Yiwanshui Landslide in Longling Seismic Area in Yunnan in 1976, some consequent slope at Jueta Mountain of Caoling and Kandou Mountain of Niufen'er Mountain after the Taiwan jiji Earthquake in 1999, as well as landslide in Jiazi Village of Baishui, Hetaoyuan Landslide in Hudiaoxia, Bendiwan Landslide and Wenziping Landslide in Lijiang Seismic Area in Yunnan in 1996, etc. (Wang Lansheng et al. 2000; Wang Sijing 1987). In the Wenchuan Earthquake in Sichuan on May 12, 2008, such series of landslides occurred at the seismic zones, such as Daguangbao Massive Landslide in Anxian County (see Fig. 1), Tangjiashan Landslide in Beichuan, Donghekou Landslide in Qingchuan, Magongwoqian Landslide, Shibangou Landslide, Niujuangou Landslide in Yingxiu of Wenchuan, Hongchungou H5 Landslide, Shaofanggou Landslide, Wenjiagou Landslide in Mianzhu, etc.

X. Xiangning (✉) • L. Shengwen
Chengdu Center of Hydrogeology and Engineering Geology of Sichuan Provincial Geology and Mineral Resources Bureau, Chengdu, Sichuan 610081, China
e-mail: xuxiangning@263.net

C. Yuliang
Institute of Geological Surveying of Sichuan Provincial, Chengdu, Sichuan 610081, China

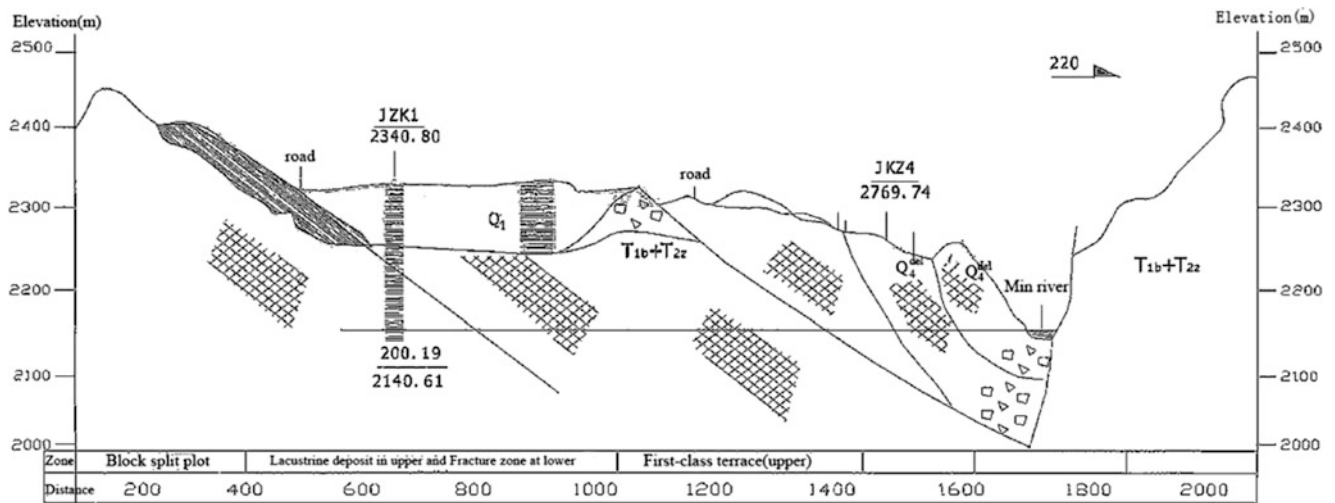


Fig. 1 Profile of Diexi Jiaochang landslide induced in 1933s earthquake

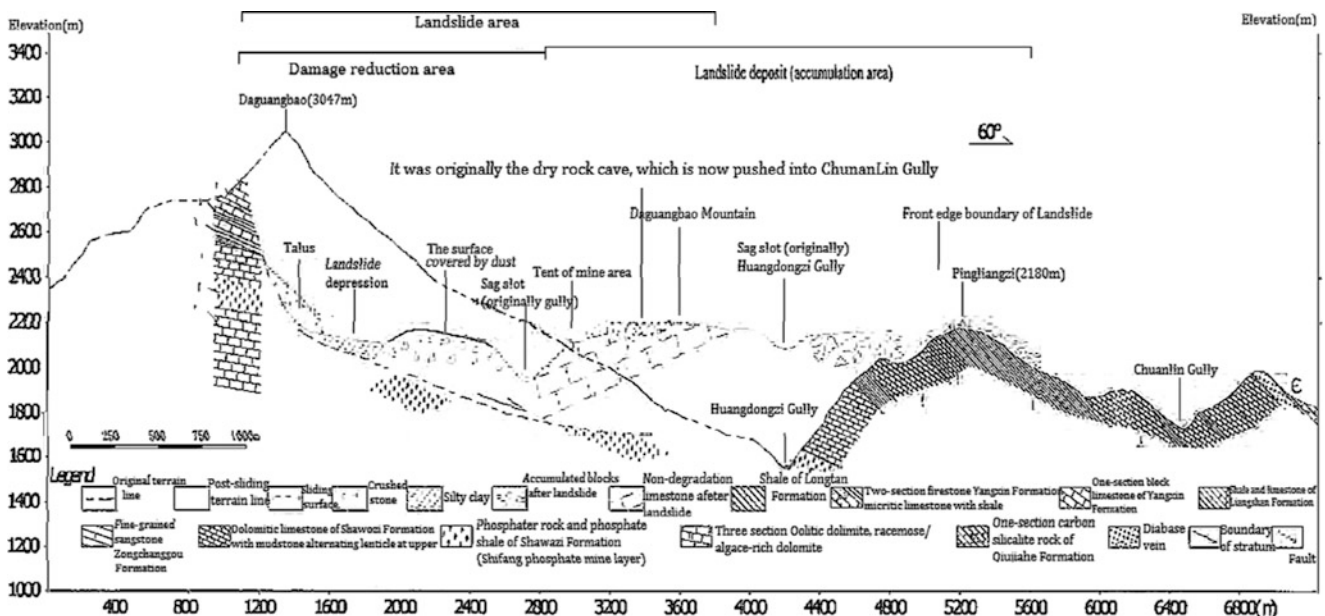


Fig. 2 Profile of Daguangbao landslide induced in 2008s earthquake

Test Model and Test Plan

Model Preparation

Diexi Jiaochang Landslide and Daguangbao Consequent Slope in Anxian are taken as the reference (Figs. 1 and 2). Based on the similarity theory, the geometric similarities between the model and reference, distribution of hard and soft rock mass, difference of parameters are factored into the model.

The model shall be staked by 5 cm long, 5 cm wide and 5 cm thick sandstone blocks at an angle of 10–40° of the stratum for different testing plans. The rock blocks shall be

bonded by clay, with gradient of 50–60° (see Pictures 1 and 2). The unit weight, modulus of elasticity, modulus of deformation, Poisson ratio, shearing strength and other physical and mechanical indexes of the blocks basically meet the requirements. See Table 1 for the model parameters. The base is a 10–40° slope of barite powder.

The model is 45 cm long, 38 cm high and 40 cm wide in size, with scale of 1:1,000. The weight of the model shall be controlled between 230 and 250 kg.

The model is directly made within the model cabinet of the vibrating table, with one model of the same size on the left and right sides and one 10 cm wide channel in the middle (see Pictures 1 and 2).



Picture 1 Model of block structure of bonding by the clay



Picture 2 Model of slop dip toward excavation

Test Purpose and Plan

In the testing design, the geological background, the rock mass medium characteristics and structure characteristics of the reference model is analyzed in order to study the forms and characteristics of seismic force deformation and destruction of mountains with synthetic structure. The specific test purpose and plan are as follows:

1. The mode, process and regularity of the deformation and fracture of stratified rock mass under the earthquake effects shall be observed and understood throughout the whole process, particularly the deformation and destruction extent, and earthquake acceleration, vibration frequency, the rock mass structure surface distribution features, bonding force between layers and relativity of slope dip.

Table 1 Model material parameter table

Sandstone		Clay		
Density (g/cm ³)	Deformation modulus (10 ⁴ MPa)	Density (g/cm ³)	C (kpa)	φ(°)
2.68	0.95	2.7	40~60	6~13

2. The vibration amplitude, trace, dip of stratum, gradient of slope surface, bonding strength as well as initial vibration direction are changed, and the fracture process shall be observed and recorded. The digital camera and video camera shall be used for recording before, during and after each vibration, respectively.

Analysis of Testing Results

Analysis of Vibration Trace and Deformation and Fracture Evolution Process

According to the images collected by the video camera during the test, the motion trace of the vibrating table shall be drawn (as shown in Fig. 3a), and the relationship between the appearance, evolution and vibration trace status shall be observed during the vibration (as shown in Fig. 3a, b). Moreover, the displacement curves of a certain deformation and fracture characteristic point of the model shall be drawn (as shown in Fig. 3c).

Take the consequent slope model vibration instability evolution process with the stratum dip of 30° and gradient of 60° as an example. The amplitude is 5 cm, and the elliptic vibration trace is shown in the chart. The points A1–A3 are deformation and fracture deflection points, the corresponding deformation and fracture status is shown in Fig. 3b, and the movement displacement curve of the corresponding deformation fracture point is shown in Fig. 3c.

Figure 3 shows that the deformation and fracture of the mountain generally appeared at the deflection point of the vibration movement trace, i.e. deflection point of changing the movement direction. As seen from the trace image and deformation sign, when the motion direction of the vibrating table changes to the rightward movement from leftward, the inertia force of the model movement is generally identical with the free surface direction as it is opposite the model movement direction, which may trigger the sliding-rupture deformation and fracture. And when the movement acceleration direction is changed from upward to downward movement, the vertical restricted strength of the rock masses is reduced under the reduced gravity, which facilitates the tension of structural surface and rock mass displacement, so that the rock blocks with smaller strength will be likely to

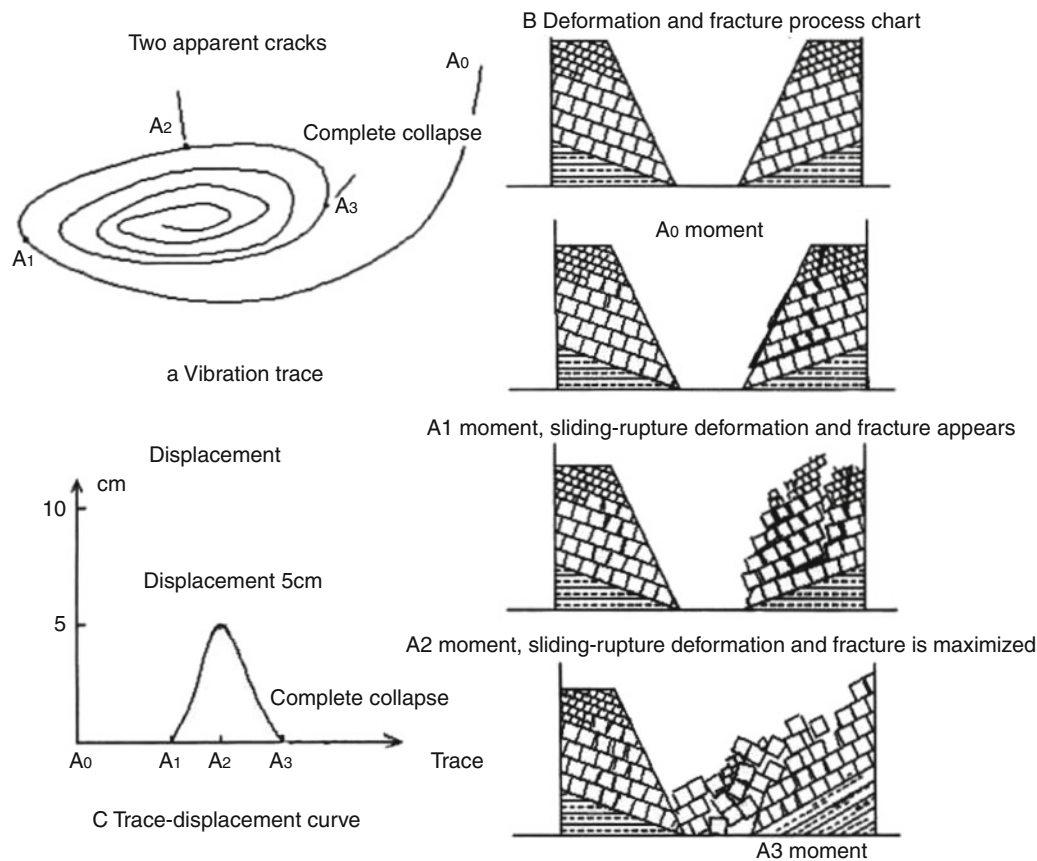


Fig. 3 Contrast diagram of shock instability evolution process for consequent slope model

separate from the intact mass, and sliding-rupture deformation, fracture or instability will be caused, and trigger effects will come out. When the displacement is accumulated to a certain critical value, a certain through face will be formed, and landslide will be caused.

The test also shows that the vibration of the elliptic orbit has greatest impact on the slope deformation and fracture, followed by horizontal vibration trace and inclined vibration trace. The vertical vibration trace has no obvious deformation or fracture. Generally, the damage and instability appears in the 2nd or 3rd recycle movement, and that is to say, the damage and instability movement of the first deflection point after the first peak acceleration and a circulation direction changes will stop after the 4th to 6th movement cycle trace.

Analysis of Deformation and Fracture Evolutionary Process and Vibration Acceleration Time-History Variance

Comparing the deformation and fracture process and vibration trace with acceleration time-history, the results show that when the vibration level acceleration is less than 0.4 g,

the stratum structure rocky slope produces only overall vibration, without noticeable damages. For the consequent slope, when the vibration level acceleration is greater than 0.4 g (equivalent to the design basic earthquake acceleration value at the seismic intensity of Magnitude 9), deformation and fracture will begin to appear and the extent of damage is associated with amplitude, the initial motion direction, vibration trace, rock structural strength and other factors. The damage extent deteriorates gradually with the increase in the vibration acceleration. As the vibration level acceleration is close to 0.8 g (equivalent to the design basic earthquake acceleration value at the seismic intensity of Magnitude 10), the consequent slope will show the extensive overall instability. The shear-tension and pull-tension will further extend to a deep extent, and the layers become staggered and displaced obviously, which is mainly represented by sliding-rupture deformation and cracking, and the slope with low structural strength will cause landslide (see Picture 3). The slope with strong rock mass structure strength will be subject to milder damages, but it will cause deep shear-tension and pull-tension fractures (see Picture 4) and some interlayer displacement or sliding.

The deformation and fracture process also shows that when rock structure of the model has certain bonding



Picture 3 Third level sliding face destabilization occurs on the consequent slope



Picture 5 Polished surface and scrapes cinch marks clearly shown on the top slickenside



Picture 4 Tension crack and sinking zone occur at the trailing edge of the consequent slope



Picture 6 Gliding or tension crack and fracture of consequent slope

strength, only deformation fracture accumulated displacement is produced in the 1st peak acceleration of the vibration acceleration time-history process, and pull-tension and shear-tension cracks (see Picture 4) will appear. When the displacement is accumulated to a certain level, once again, the direction of the acceleration changes from up to down and instability damage will be generated.

In a vibration, deformation and fracture extent of the mountain is proportional to vibration duration. The accumulated displacement of the mountain deformation and fracture displacement is also proportional to the vibration duration, i.e. the longer the vibration is, the larger the generated displacement will be, and thus sliding damage will be likely to occur to the rock masses of the slope.

Analysis of Vibration Intensity and Deformation and Fracture Evolution of Different Geological Structures of the Mountain

The above test results show that:

1. Relationship with amplitude, the pull-tension cracks occur in the slope and back edge at the horizontal amplitude of 2.5 cm. When the horizontal level is 3.5 cm, obviously pull-tension and shear-tension cracks will occur (see Picture 4), and apparent tension cracks and settlement zones occur at the back (see Picture 5). When the horizontal amplitude is 5 cm, shear-tension and pull-tension cracks extend to the deep extent, the layers become staggered and displaced obviously, and sliding-rupture deformation and cracking will occur (see Picture 6). The slopes with small structural strength will be causing the landslide.

2. Compared with the relationship of initial motion orientation, both in consequent slope and countertendency slope, the indication and extent of deformation and fracture in right side slope are singly than left side (see Picture 3). Generally, the right side slope becomes unstable while the left slope is only subject to slope deformation and fracture.
3. The deformation and fracture of the inclined external stratified slope is controlled by the structural surface, which will cause serious shear-tension and pull-tension cracks at the moment of vibration starting and gradually extend to the deep extent (see Picture 4). Meanwhile, layers become staggered and cause accumulated displacement, which shows obvious sliding-rupture fracture and becomes unstable as a result of landslides.
4. The steeper the outward tilted dip of the stratum, the more obvious sliding-rupture deformation and fracture will be, and the starting acceleration will be small.

References

- Wang Lansheng, Li Tianbin et al (2000) Landslide and environmental protection of Diexi Jiaochang earthquake for Minjiang river in Sichuan. *Geol Hazard Environ Prot* 11(3)
- Wang Sijing (1987) Dynamic stability study for slope rock masses. Institute of Geology and Geophysics, Chinese Academy of Sciences. *Geomechanical issues of rock engineering*, vol 2. Science Publishing House, Beijing



Landslide Processes in the Urbanized Moscow Area

Valentina Svalova

Abstract

Landslides process is one of the most widespread and dangerous processes in the urbanized territories. In Moscow the landslips occupy about 3 % of the most valuable territory of the city. In Russia many towns are located near rivers on high coastal sides. There are many churches and historical buildings on high costs of Volga River and Moscow River. The organization of monitoring is necessary for maintenance of normal functioning of city infrastructure in a coastal zone and duly realization of effective protective actions. Last years the landslide process activation took place in Moscow.

Keywords

Landslides • Activization • Monitoring

Introduction

Landslide motions is extremely actual and difficult problem which decision is necessary for preservation of valuable historical monuments and modern city constructions. There are near 15 places of deep landslides and many shallow landslides in Moscow (Fig. 1).

One of landslide sites is on Vorob'yovy mountains, on a high slope of the right coast of the river Moscow. Within the limits of a considered site there is a historical monument of federal value – “Andreevsky monastery”, based in 1648 (Figs. 2, 3, and 4).

Also there the complex of buildings of Presidium of the Russian Academy of Sciences, constructed in 70–80th years of twentieth century (Fig. 4), bridge with station of underground “Vorob'yovy mountains” and a sports complex are located. Landslide slope (Fig. 5) is in an active condition. In June 2007 a rather big landslide took place there near ski-jump (Fig. 6).

Another landslide site is in a southeast part of Moscow near museum – reserve “Kolomenskoye”(Figs. 7, 8, and 9). Last serious activation of a landslide has taken place there in 2002.

Catastrophic activation of the deep blockglide landslide in the area of Khoroshevo on the left-hand shore of the Moskva River at Karamyshevskaya embankment took place in 2006–2007.

Deep landslide activation was in Moskvorechye area in September 2009.

Such complicated situation demands development of new investigations of landslide prone zones (Osipov et al. 2002; Kutepov et al. 2002; Postoev and Svalova 2005; Svalova and Postoev 2008).

Conclusions

Landslides process is one of the most widespread and dangerous processes in the urbanized territories. The landslide process activation took place in Moscow last years. Such complicated situation demands development of new investigations of landslide prone zones.

V. Svalova (✉)
Institute of Environmental Geoscience RAS, Ulansky per., 13, Moscow
101000, Russia
e-mail: inter@geoenv.ru

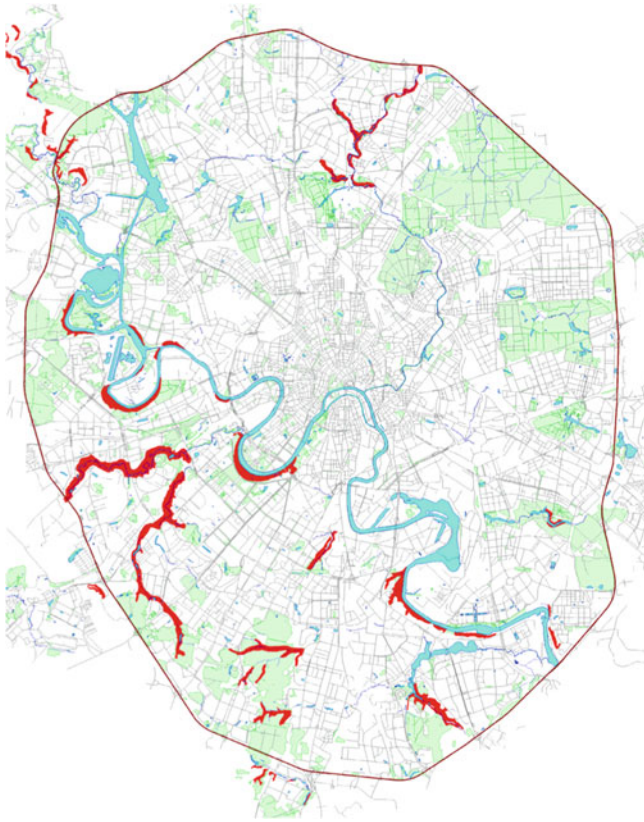


Fig. 1 Landslides danger places in Moscow (in red)



Fig. 3 Andreevsky monastery and new buildings on landslide slope



Fig. 2 Vorob'yovy mountains. Landslide slope



Fig. 4 Presidium of RAS, Andreevsky monastery and new buildings on landslide slope

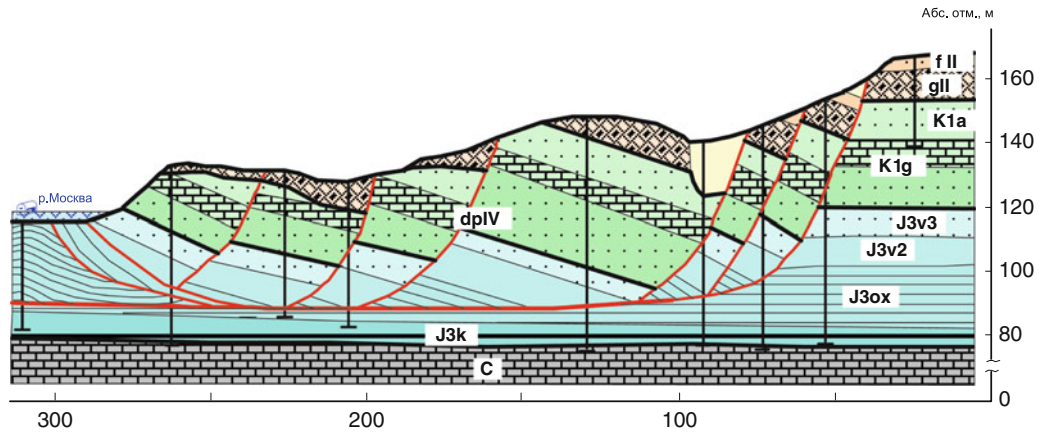


Fig. 5 Schematic cross-section of landslide slope at Vorob'yovy mountains



Fig. 6 Place of landslide activation near ski jump



Fig. 7 Museum – reserve “Kolomenskoye”. Common view. Landslide slope



Fig. 8 Museum – reserve “Kolomenskoye”. The church of beheading of the honest head of Iowan Predecessor

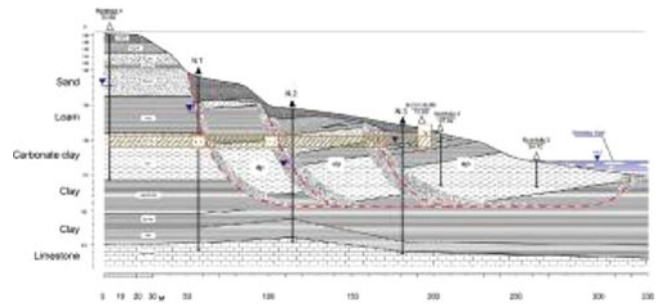


Fig. 9 Deep blockglide landslide. Moscow, Kolomenskoye. N.1, N.2, N.3 – extensometers, inclinometers

References

- Kutepov VM, Sheko AI, Anisimova NG, Burova VN, Victorov AS et al (2002) Natural hazards in Russia. Exogenous geological hazards. KRUK, Moscow, 345p
- Osipov VI, Shojgu SK, Vladimirov VA, Vorobjev Yu L, Avdod'in VP et al (2002) Natural hazards in Russia. Natural hazards and society. KRUK, Moscow, 245p
- Postoev GP, Svalova VB (2005) Landslides risk reduction and monitoring for urban territories in Russia. In: Proceedings of the first general assembly of ICL (International Consortium on Landslides) “Landslides: risk analysis and sustainable disaster management”. Springer, Washington, DC, pp 297–303
- Svalova V, Postoev G (2008) Landslide process activation on sites of cultural heritage in Moscow, Russia. In: Proceedings of the first world landslide forum 2008. United Nations University, Tokyo, 4p



Landslide Hazard Assessment Based on FS_{3D} Combined with an Infiltration Model

Aline Silva and Lázaro Zuquette

Abstract

Studies assessing landslide hazards have become increasingly common in recent years. They provide information that guides decision-making and the adoption of preventive and mitigation measures for control and protection. The aim of this study was to develop a set of procedures for the prediction of landslides from the results of geotechnical mapping at scales larger than 1:10,000. A methodology based on geotechnical parameters using the calculation of three-dimensional (3D) safety factor combined with an infiltration model it was developed. This set of procedures was applied to pre-defined areas in the city of Campos do Jordão, SP, Brazil. These areas were chosen based on geomorphic variability of geological materials and size criteria. The results from these areas are very promising and reflect the geological, geotechnical and hydrogeological conditions in each area.

Keywords

Landslide • Hazard • Three-dimensional safety factor • Infiltration model • Campos do Jordão • Brazil

Introduction

Natural and human-induced geological processes have increased in frequency and magnitude over recent decades around the world, with a concomitant exponential increase in forecast studies (e.g., Varnes 1984; Hutchinson 1992; Aleotti and Chowdhury 1999; Chacón et al. 2006). Even with these advances, the hazard or risk maps available at most scales in Brazil show just a content of susceptibility. There are different levels of studies for the classification and evaluation of natural processes such as landslides, ranging from inventory studies of the process to management of the risk. Hazard assessment represents an intermediate level of study. According to Varnes (1984) hazard is the probability of a potentially damaging phenomenon occurring in a given area in a given period of time, which means that a landslide hazard assessment includes

necessary information about the susceptibility (where), the probability (when) and the intensity (how big) of the event.

In this study, a methodology based on geotechnical parameters using the calculation of three-dimensional (3D) safety factor combined with an infiltration model it was developed. This study is justified by the scientific attempt to establish a set of procedures that enable the prediction of landslides using geotechnical maps at scales greater than 1:10,000. The set of procedures combines a column-based 3D slope-stability analysis model with the infiltration conditions that are induced by a particular rainfall event considering the intensity and duration of the rainfall. The probability of occurrence was calculated for each rainfall event studied for the next 1, 5 and 10 years.

Methodology

The first procedure is the basic characterization of the area, the consolidation of necessary information, such as a topographic map (with 1-m contour lines), a slope map, an aspect

A. Silva (✉) • L. Zuquette
School of Engineering of São Carlos, University of São Paulo,
Av. Trabalhador São-Carlense, 400, São Carlos, Brazil
e-mail: alinefreitassilva@uol.com.br

map and the basic characterization of unconsolidated material, including a map of unconsolidated material, the index of physical data, hydrological characterization and the resistance parameters for each material.

With this information, the potential rupture surfaces are defined mainly based on the geomorphic features of the area (type of slope, declivity and direction of the strands), the variability of unconsolidated material and the size of the area.

An analysis of the rainfall data is carried out independently. The quality of pluviometric data is also crucial because, in addition to the duration and amount of total precipitation of the rain events, information regarding the behaviour of rain throughout the event is necessary. The chosen pluviometric events are used as input data in the infiltration model in the next step, and the likelihood of similar event(s) occurring over time is calculated. The probability distribution used is the Poisson distribution with T_1 representing the time of recurrence of the desired event, as expressed by the following equation:

$$F_{T_1}(t) = P(T_1 \leq t) = 1 - e^{-vt} \quad (1)$$

Where, t = time; v = average rate of occurrence; and e = Neperian base. The average rate of occurrence is simply the ratio between the number of events and the time frame considered.

Once information about selected rain events is gathered, the infiltration model can be initiated. The influence of rain on landslides is known and has been observed in numerous studies (e.g., Gasmo et al. 2000; Wilkinson et al. 2002). Studies on shallow landslides show that they are the result of water infiltration into the geological material. Thus, in predicting slope stability, conceptual and physical models must be considered that simulate the hydro-geological and the geotechnical transients responsible for their stability. The infiltration model in this study aims to determine volumetric moisture: the average volumetric moisture (θ_M) of the soil profile and the desired volumetric moisture at a specific depth ($\theta(z)$), after a rain event. To meet these objectives, the HYDRUS 1D version 3.0 program was used (Simunek et al. 2005).

The HYDRUS 1D model is a finite-element numerical model for the unidirectional simulation of water, heat and multiple solutes flowing in a saturated or unsaturated condition. The program numerically solves the Richards equation for the variable flow of water in soil and the advection and the dispersion equations for heat and the transport of solutes.

Based on the average volumetric moisture data, θ_M , obtained in the previous step and the dry unit weight (γ_d) and specific weight of water (γ_w) for each unconsolidated material, the corresponding average specific weight is obtained from correlations of the physical indices to calculate the 3D safety factor.

The 3D safety factor is calculated based on the cohesion and the friction angle of the rupture surface depth. We determined the correlation between the maximum and minimum values of these parameters in relation to the degree of saturation (S_r) of the point in question (the desired depth). With the volumetric moisture value at depth $z - \theta(z)$ and with the porosity (n) of the respective unconsolidated material, we obtained the saturation at a given depth with correlations among the physical indices.

The last step before calculating the FS_{3D} is the definition of grid sizes for the selected areas. Because the initial 3D safety factor analysis is conducted by columns, the area must be divided into regular grids to complete the calculation. Based on the area size, the volume of necessary information and the feasibility of the calculation, it was determined that the grid should be 10 m wide or 100 m² in surface area.

The three-dimensional analysis model of slope stability adopted in this work is that proposed by Hovland (1977), modified by Xie et al. (2003) and again adapted by Silva (2009). Equation 2 shows the calculation of the FS_{3D} by Silva (2009) used in this work.

$$FS_{3D} = \frac{\sum_I \sum_J cA + [\gamma_i(Z_{ij} - z_{ij}) + (\gamma_M - \gamma_i)(Z_{ij} - z_{ij})] a^2 \cos \alpha \tan \phi}{\sum_I \sum_J [\gamma_i(Z_{ij} - z_{ij}) + (\gamma_M - \gamma_i)(Z_{ij} - z_{ij})] a^2 \sin \alpha_P} \quad (2)$$

where FS_{3D} = 3D Safety Factor; c = total cohesion (kN/m²); A = area of the rupture surface (m²); Z_{ji} = ground surface elevation (m); z_{ji} = elevation of the rupture surface (m); γ_M = average specific weight of the soil (kN/m³); γ_i = initial specific weight of the soil (kN/m³); a = grid size (m); α = dip angle of the rupture surface (°); ϕ = angle of total friction (°); α_P = dip angle of the main landslide direction (°); and J and I = the total rows and columns in the interval of the rupture area, respectively.

Application in Campos do Jordão, SP, Brazil

In Brazil, the increasing incidence of natural disasters, especially shallow landslides and floods, is considered to be due to the intense urbanization processes occurring in the country in recent decades, with the unplanned growth of cities in areas unsuitable for occupancy because of unfavourable geological and geomorphological characteristics. The city of Campos do Jordão in the state of São Paulo is located in Serra da Mantiqueira. This area was selected for the present study because of the history of landslide incidents and the need for data from an engineering geological map at a 1:2,000 scale (Ahrendt 2005) (Fig. 1). The area ranges across UTM 23 K coordinates 438.010/438.330 W and 7.485.390/7.485.110 S and covers approximately 90,000 m². The results for four

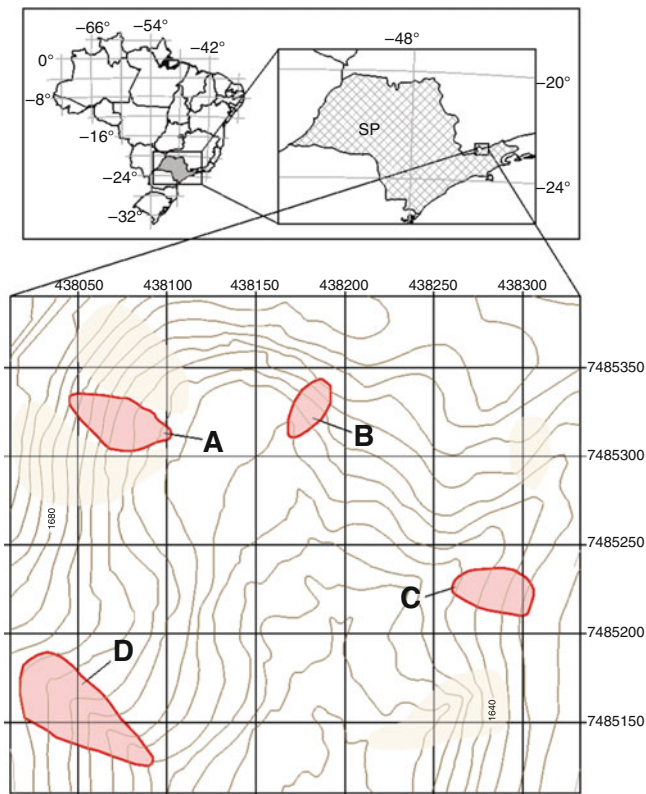


Fig. 1 Location of the study areas in the city of Campos do Jordão, SP, Brazil

of the slopes that were studied are presented as areas A, B, C and D.

Area A has a surface of 1,202 m² with a main dip direction of 109° and an average slope angle of 27° (minimum 15°, maximum 42°). This slope can be considered linear-linear (LL) and covers two geological units: U4 and U8 (the characteristics of each geologic unit will be described below). Area B is the smallest slope selected, with a surface of only 665 m²; although the area is not extensive, it includes three geological units (U2, U4 and U10). This slope can be considered linear-linear (LL), with a main dip direction of 221° and an average slope angle of 36° (minimum 24°, maximum 48°). Area C has a surface of approximately 1,011 m² and covers two geological units (U4 and U8), with a dip direction of 287° and an average slope angle of 21°. It is an area that has generally lower declivity values, with a minimum of 10° and a maximum of 28°; this slope can be considered to have a linear-linear (LL) shape. Area D is the largest of the slopes, with a surface of 2,654 m² covering several geological units. It contains a valley, resulting in a large variability in the direction of the aspect and the slope angle values. The geological units covered by this area are U4, U6, U6a and U9, and the main dip direction is 128°. The upstream part has a slope angle of approximately 20° (minimum 14°), whereas the downstream part

has slope angles of approximately 30° with a maximum of 42° because of the narrow valley; the average slope angle of this area is 25°. This area can be classified as linear-concave (LC).

In these four areas, there are seven different types of unconsolidated material differentiated according to their origin and composition, with each type possessing particular characteristics. Information regarding these unconsolidated materials and their spatial distributions was published by Ahrendt (2005). The unconsolidated residual materials were classified as residuals of alteration (IR and II-R) and saprolites (III-S, IV-S and V-S). Two main types of unconsolidated landfill materials, known as VI-A and VII-A, and one type of alluvial material (VIII-T) were defined. From the stratigraphic arrangement of the unconsolidated material, typical profiles were established that are common to the area. Data on physical indices, strength parameters, the Van Genuchten parameters referring to each unconsolidated material, and the map of unconsolidated material units were compiled from the data published by Ahrendt (2005). The data used in this study are shown in Table 1.

The pluviometric data used in this study are from 1975 to 2001, including records with up to 5 min intervals. In this study, we selected three rainfall events. One event is of long duration with low intensity, and the other two are short events, one with moderate and one with high intensity.

The first event occurred on October 13–14 of 1995, lasted 27 h and had a total rainfall of 149.7 mm. The second event occurred on January 25 of 2000, with 23 mm of precipitation in 20 min. The last rainfall event studied resulted in 85 mm of precipitation in 20 min and occurred on February 5 of 2001. The 2001 event is unique in the entire series analyzed, and the Poisson distribution was used to calculate the probability of occurrence of a similar event in the future. The probability of occurrence of an event similar to the 2001 event was calculated for 1-, 5- and 10-year projections, with results of 4 %, 18 % and 34 %, respectively. For the 2000 event, the likelihoods of occurrence of a similar event were 19 %, 66 % and 88 % over 1-, 5- and 10-year projections, respectively. For the 1995 event, the likelihoods of occurrence of a similar event over 1, 5 or 10 years were 29 %, 82 % and 97 %, respectively.

For all rainfall events and each unconsolidated material unit, a simulation in the HYDRUS-1D infiltration model was completed at a depth of up to 5 m. Table 2 presents the volumetric moisture values at depth *z*, with average volumetric moisture, average specific weight, total cohesion and total friction angle for 120 min (for the 2000 and 2001 events) and 48 h (for the 1995 event) used in the calculation of the 3D safety factor.

The FS_{3D} was calculated for four different scenarios to consider each rainfall event. Two levels of potential rupture surfaces were defined. The first (SP1) was more superficial,

Table 1 Physical indices, thickness, strength parameters and Van Genuchten parameters of unconsolidated material existing in the study areas

Unit	Materials	Thickness (cm)	γ_s (kN/m ³)	γ_d (kN/m ³)	n_{Med}	θ_{cc}	K_{sat} (cm/min)	c (kN/m ²)	c_s (kN/m ²)	φ (°)	φ_s (°)	θ_r	θ_s	α (cm ⁻¹)	n
U2	I-R	50	26.71	13.5	0.55	0.15	5.56E-01	9.8	1.68	28.5	29.5	0.035	0.550	0.115	1.474
	II-R	100	27.89	14.3	0.48	0.25	2.11E-01	20.0	0.20	26.0	30.0	0.109	0.485	0.034	1.168
	III-S	—	27.51	12.8	0.49	0.30	6.00E-04	30.0	0.20	30.0	35.0	0.075	0.490	0.039	1.194
U4	I-R	50	26.71	13.5	0.55	0.15	4.67E-01	10.0	0.40	26.0	33.5	0.035	0.550	0.115	1.474
	II-R	50	27.89	14.3	0.48	0.25	5.89E-01	20.0	0.20	26.0	30.0	0.109	0.485	0.034	1.168
	V-S	—	27.70	12.5	0.52	0.10	6.00E-05	50.0	0.20	35.0	40.0	0.020	0.520	0.138	1.592
U6	VI-A	20	27.50	11.6	0.55	0.15	9.12E-01	20.0	0.61	26.0	31.3	0.020	0.550	0.138	1.592
	I-R	20	26.71	13.5	0.55	0.15	3.38E-01	10.0	0.40	26.0	33.0	0.035	0.550	0.115	1.474
	II-R	10	27.89	14.3	0.48	0.25	5.89E-01	20.0	0.20	26.0	30.0	0.109	0.485	0.034	1.168
U6a	V-S	—	27.70	12.5	0.52	0.10	6.00E-05	50.0	0.20	35.0	40.0	0.020	0.520	0.138	1.592
	VI-A	20	27.50	11.6	0.55	0.15	6.00E-02	20.0	0.61	26.0	31.3	0.020	0.550	0.138	1.592
	I-R	20	26.71	13.5	0.55	0.15	5.56E-01	10.0	0.40	26.0	33.0	0.035	0.550	0.115	1.474
U8	V-S	—	27.70	12.5	0.52	0.10	6.00E-05	50.0	0.20	35.0	40.0	0.020	0.520	0.138	1.592
	VII-A	100	28.00	11.8	0.54	0.20	1.26E + 00	10.0	0.60	26.0	31.0	0.028	0.540	0.130	1.700
	V-S	—	27.70	12.5	0.52	0.10	6.00E-05	50.0	0.20	35.0	40.0	0.020	0.520	0.138	1.592
U9	V-S	200	27.70	12.5	0.52	0.10	6.00E-04	50.0	0.20	35.0	40.0	0.020	0.520	0.138	1.592
	VIII-T	100	31.04	11.0	0.50	0.20	6.00E-02	10.0	0.40	26.0	33.0	0.078	0.500	0.036	1.500

γ_s specific weight of solid particles (kN/m³), γ_d dry unit weight of the soil (kN/m³), n_{Med} average porosity, θ_{cc} field volumetric moisture capacity, K_{sat} saturated hydraulic conductivity (cm/min), c total cohesion (kN/m²), c_s saturated total cohesion (kN/m²), φ angle of total friction (°), φ_s angle of saturated total friction (°), θ_r residual volumetric moisture, θ_s saturated volumetric moisture, α inverse value of the air-entry (cm⁻¹), n a shape form

Table 2 Volumetric moisture values at depth z , degree of saturation at depth z , average volumetric moisture, average specific weight, total cohesion and total friction angle for 120 min (for the 2000 and 2001 events) and 48 h (for the 1995 event)

Unit	z (cm)	1995 event						2000 event						2001 event					
		θ_z	Sr(z) (%)	θ_{Ave}	γ_M (kN/m ³)	c (kN/m ²)	ϕ (°)	θ_z	Sr(z) (%)	θ_{Ave}	γ_M (kN/m ³)	c (kN/m ²)	ϕ (°)	θ_z	Sr(z) (%)	θ_{Ave}	γ_M (kN/m ³)	c (kN/m ²)	ϕ (°)
U2	50	0.4424	80.44	0.2978	16.478	3.27	29.30	0.2905	52.82	0.1977	15.477	5.51	29.03	0.2904	52.80	0.3172	16.672	5.51	29.03
	150	0.2714	55.96	0.3163	17.463	8.92	28.24	0.2547	52.52	0.2321	16.621	9.60	28.10	0.2547	52.52	0.2733	17.033	9.60	28.10
U4	50	0.4201	76.38	0.2988	16.488	2.67	31.73	0.2863	52.05	0.1975	15.475	5.00	29.90	0.2863	52.05	0.3170	16.670	5.00	29.90
	150	0.3723	76.76	0.3487	17.787	4.80	29.07	0.1003	20.68	0.1826	16.126	15.91	26.83	0.2554	52.66	0.2849	17.149	9.57	28.11
U6	20	0.4568	83.05	0.3170	14.770	3.90	30.4	0.1855	33.73	0.2565	14.165	13.46	27.79	0.4425	80.45	0.3443	15.043	4.40	30.26
	40	0.5500	100.00	0.4176	17.676	0.40	33.00	0.2082	37.85	0.2842	16.342	6.37	28.65	0.2843	51.69	0.3559	17.059	5.04	29.62
U6a	50	0.5200	100.00	0.4325	18.625	0.40	33.00	0.2553	49.10	0.2162	16.462	9.58	28.11	0.2554	49.12	0.3379	17.679	9.57	28.11
	20	0.5500	100.00	0.4106	15.706	0.61	31.30	0.1661	30.20	0.2360	13.960	14.14	27.60	0.1661	30.20	0.2511	14.111	14.14	27.6
U8	40	0.5500	100.00	0.4752	18.252	0.40	33.00	0.2291	41.65	0.1956	15.456	6.00	28.92	0.3195	58.09	0.2046	15.546	4.42	30.07
	50	0.2611	48.35	0.2109	13.909	5.45	28.42	0.201	37.22	0.2448	14.248	6.50	27.86	0.3569	66.09	0.3198	14.998	3.79	29.30
U9	100	0.5400	100.00	0.3336	15.136	0.60	31.00	0.213	39.44	0.2227	14.027	6.29	27.97	0.2006	37.15	0.2842	14.642	6.51	27.86
	50	0.1003	19.29	0.1405	13.905	40.39	35.96	0.1003	19.29	0.1035	13.535	40.39	35.96	0.1003	19.29	0.1115	13.615	40.39	35.96
U10	100	0.1003	19.29	0.1206	13.706	40.39	35.96	0.1003	19.29	0.1019	13.519	40.39	35.96	0.1003	19.29	0.1060	13.560	40.39	35.96
	50	0.3871	77.42	0.3730	14.730	2.57	31.42	0.2001	40.02	0.2359	13.359	6.16	28.80	0.2005	40.10	0.2526	13.526	6.15	28.81
	100	0.2005	40.10	0.3480	14.480	6.15	28.81	0.2001	40.02	0.2182	13.182	6.16	28.80	0.2005	40.10	0.2268	13.268	6.15	28.81

z depth (cm), θ_z volumetric moisture at a specific depth z (–), Sr(z) degree of saturation at depth z (%), θ_{Ave} average volumetric moisture (–), γ_M average specific weight (kN/m³), c total cohesion (kN/m²), ϕ total friction angle (°)

Table 3 FS_{3D} of areas A, B, C and D

Area	1995 event				2000 event				2001 event			
	Natural cohesion		Minimum cohesion		Natural cohesion		Minimum cohesion		Natural cohesion		Minimum cohesion	
	SP1	SP2	SP1	SP2	SP1	SP2	SP1	SP2	SP1	SP2	SP1	SP2
A	2.03	1.70	1.25	1.15	2.64	3.12	1.18	1.05	2.48	2.30	1.19	1.09
B	1.28	1.20	0.84	0.75	1.81	1.33	0.79	0.74	1.77	1.27	0.79	0.75
C	2.52	1.90	1.59	1.50	3.12	2.95	1.48	1.36	2.89	2.37	1.50	1.42
D	3.36	1.74	1.54	1.60	7.88	3.29	1.40	1.35	3.65	2.66	1.50	1.42

SP1 first potential rupture surface (more superficial), SP2 second potential rupture surface (deeper)

representing the first geotechnical discontinuity of each unconsolidated material unit. The second level of rupture (SP2) was defined for the second geotechnical discontinuity, somewhat deeper. The FS_{3D} was calculated using a cohesion value determined from the volumetric moisture at the depth of the rupture level in consideration (called the natural cohesion in Table 3). Additionally, the FS_{3D} was calculated using a minimum cohesion value (0.1). For the 2000 and 2001 events, the security factor was calculated for a period of 120 min, and for the 1995 event, it was calculated for a period of 48 h. Table 3 shows the 3D security factor values obtained in areas A, B, C and D under the four conditions tested.

Analyses

Choosing and delimiting areas for the FS_{3D} calculation is a fundamental step because the size, geomorphic features and geological materials involved all directly affect the final result. The method presented here is most effective when the bounded area is part of a hillside with a small surface area. When large areas are chosen, two kinds of problems can occur: the presence of valleys, which implies the presence of grids with very low slope, and the presence of grids with dip directions (direction of slope) that are very different from the general inclination of the slope. Both of these situations contribute to increases in the general security factor of an area.

The chosen rupture surfaces represent geotechnical discontinuities between the different types of unconsolidated materials. By using volumetric moisture and depth graphics obtained by HYDRUS-1D, it is possible to observe that, where these contacts occur, especially in materials with saturated hydraulic conductivities with different orders of magnitude, there is an increase in the volumetric moisture because of this natural hydraulic barrier.

Regarding the moistening front in the unconsolidated material profiles after pluviometric events (obtained from the HYDRUS-1D program), there was a significant difference in the results because of the difference in the selected rainfall events, with two short-duration and high-intensity events and one low-intensity and long-duration event.

With regards to the most extreme events studied (of highest and lowest intensity), there is a low annual probability of

events similar to the 2001 event occurring (approximately 4 %); on the other hand, there is a nearly a 30 % probability of occurrence of an event similar to the 1995 event over the course of a year. Over 10 years, this value approaches 100 %.

An analysis of the FS_{3D} values observed in the study areas results between the first and second rupture surfaces reveals a decrease of approximately 17 %, 30 %, 25 % and 48 % in areas A, B, C and D, respectively. In terms of the findings based on the minimum values of cohesion (0.1 kN/m²), when compared to the first scenario (natural cohesion), there was a decrease of approximately 53 %, 56 %, 49 % and 59 % in areas A, B, C and D, respectively, thus validating the influence of cohesion in the calculation of the safety factor. However, despite its great influence, this parameter is not solely responsible for the process, because there were cases in which the FS_{3D} did not approach a 1.0 value. This is justified in areas that have grids with a low slope and/or a high standard deviation in relation to the dip direction of the slopes.

Conclusion

Existing methodologies can analyze the stability of slopes, forecast the occurrence of shallow landslides and consider conditions of rainfall and infiltration. One of the highlights of the methodology presented here is that the steps are closely related and the determination of any parameter depends on the other parameters; no parameter is considered as a fixed or constant value in calculating the safety factor. By incorporating this type of infiltration analysis, including variation of soil moisture with depth, the portion of increased soil weight caused by the amount of infiltrated water after the rainfall event and the shear strength parameters considered in the calculation of the FS_{3D} for the potential rupture surface are directly related to the degree of saturation, these changes represent an improvement in the field of landslide prediction. The final FS_{3D} results were consistent with the geological, hydro-geological and geotechnical settings considered, and they suggest a promising future for the study.

Acknowledgments The authors thank all those who contributed to this work in any way and those who work for the advancement of science.

References

- Ahrendt A (2005) Movimentos de massa gravitacionais – Proposta de um sistema de previsão: aplicação na área urbana de Campos do Jordão – SP. São Carlos, Ph.D. thesis, São Carlos School of Engineering, São Paulo University, São Carlos, 360p
- Aleotti P, Chowdhury R (1999) Landslide hazard assessment: summary review and new perspectives. *Bull Eng Geol Environ* 58:21–44
- Chacón J, Irigaray C, Fernández T, El Hamdouni R (2006) Engineering geology maps: landslides and geographical information systems. *Bull Eng Geol Environ* 65:341–411
- Gasmo JM, Rahardjo H, Leong EC (2000) Infiltration effects on stability of a residual soil slope. *Comput Geotech* 26:145–165
- Hovland HJ (1977) Three-dimensional slope stability analysis method. *J Geotech Eng Div GT9:971–986*
- Hutchinson JN (1992) Landslide hazard assessment. In: *Proceedings of 6th international symposium on landslides*, vol 1. Christchurch, pp 1805–1841
- Silva AF (2009) Estudo de previsão de escorregamento a partir do fator de segurança 3D: Campos do Jordão-SP. Masters dissertation, São Carlos School of Engineering, São Paulo University, São Carlos, 353p
- Simunek J, Van Genuchten MTh, Sejna M (2005) The Hydrus-1D soft. pack. for simulating the 1D movement of water, heat, and multiple solutes in variably-saturated media. V.3.0, HYDRUS software series 1. Department of Environmental Sciences, University of California, Riverside, 270p
- Varnes DJ (1984) Landslide hazard zonation: a review of principles and practice. Commission on landslides of the IAEG, vol 3, Natural hazards. UNESCO, Paris, 61p
- Wilkinson PL, Anderson MG, Lloyd DM (2002) An integrated hydrological model for rain-induced landslide prediction. *Earth Surf Proc Landf* 27:1285–1297
- Xie M, Esaki T, Zhou G (2003) Three-dimensional stability evaluation of landslides and a sliding process simulation using a new geographic information systems component. *Environ Geol* 43: 503–512



Modelling the Motion of Mobile Debris Flows in Hong Kong

J.S.H. Kwan, T.H.H. Hui, and K.K.S. Ho

Abstract

Lantau Island is located at the south-western part of Hong Kong. Over 75 % of its areas are natural hillsides and approximately one third of the hillsides are sloping at 30° or above. The geology comprises tuff and granite. On 7 June 2008, a severe rainfall with a return period of 1,100 years occurred over the western part of Lantau Island. This triggered over 2,400 landslides, about 900 of which were debris flows. Some of these were sizeable and mobile, involving active debris volumes and travel distances in excess of 10,000 m³ and 1,700 m respectively. This paper examines the runout characteristics of selected mobile debris flows. Two-dimensional and three-dimensional dynamic models developed by the Geotechnical Engineering Office (GEO), Civil Engineering and Development Department were used to back analyse the long-runout debris flows, taking into account the complicated geometry of the runout paths. The findings and their engineering implications are presented in the paper.

Keywords

Landslide • Debris flow • Numerical modelling

Introduction

Rain-induced landslide is a common form of natural hazards in Hong Kong. The landslide debris is liable to develop into a channelized debris flow (CDF) after the debris mass enters the natural drainage line. Those CDFs have long runout and are disastrous. The assessment of debris motion would require mobility analysis to establish the runout distance, extent of affected areas and other important parameters, such as debris velocity and depth. Nowadays, numerical models have been developed and are increasingly used to simulate landslide debris motion for mobility analysis. With appropriate rheological parameters as input to continuum models, numerical analyses can produce reasonable estimates of the debris

runout characteristics. Hung et al. (2007) summarised details of various numerical models which were used in a debris mobility benchmarking exercise held in Hong Kong in 2007.

On 7 June 2008, a severe rainstorm with a statistical return period of 1,100 years occurred over the western part of Lantau Island, Hong Kong. The rainfall caused over 2,400 natural terrain landslides, about 900 of which developed into CDFs. Some of these CDFs affected facilities within developed area, e.g. residential buildings and the expressway linking the city centre and the airport as well as some sole vehicular accesses.

A study of the runout of the more mobile CDFs has been carried out. The study included field mapping, statistical analysis of the mobility data and back analysis using both two-dimensional and three-dimensional numerical models (i.e. using the 2dDMM and 3dDMM programmes), developed in-house by the GEO. The observations made by the study are presented in this paper.

J.S.H.Kwan (✉) • T.H.H.Hui • K.K.S.Ho
Geotechnical Engineering Office, Civil Engineering and Development
Department, The Government of the Hong Kong Special Administrative
Region, Hong Kong, China
e-mail: juliankwan@cedd.gov.hk

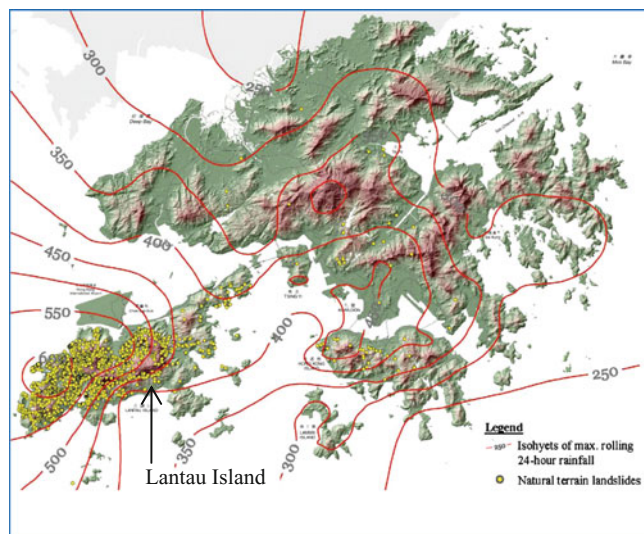


Fig. 1 Maximum 24-h rainfall contours of the 7 June 2008 rainfall and locations of natural terrain landslides

Rainfall Event on 7 June 2008

Previous study on the rainfall-landslide correlation in Hong Kong observed that the occurrence of natural terrain landslides was closely related to both 4-h and 24-h rainfall (Ko 2005). Rainfall data collected from the three raingauges on Lantau have been analysed. The maximum 4-h (384 mm) and 24-h (623 mm) rainfall depths correspond to return period of about 1,100 years and 200 years respectively. The June 2008 rainstorm was more severe than that experienced previously in the recent history of Hong Kong. Figure 1 shows the maximum 24-h rainfall contours of the 7 June 2008 rainfall event as well as the locations of natural terrain landslides.

Mobility of Landslides

Over the years, the GEO has continued with the updating of the Enhanced Natural Terrain Landslide Inventory based on aerial photography interpretation (API), which contains records of more than 110,000 historical landslides.

The GEO has completed mapping of the June 2008 natural terrain landslides in Lantau Island using satellite images as well as vertical and oblique aerial photographs, from which about 2,400 landslides were identified and mapped. Detailed field mapping has also been carried out for the more mobile CDFs (i.e. runout distance >200 m) and landslide clusters. In total, more than 130 landslides were mapped in the field.

The June 2008 landslides predominantly involved shallow failures (typically within 1–2 m of the surface mantle),

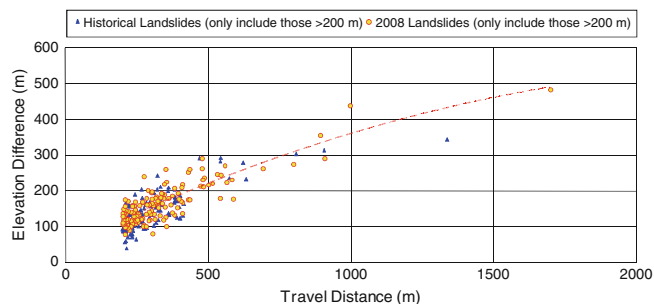


Fig. 2 Runout distance of June 2008 CDFs and historical landslides

whereas deep failures rarely occurred. Over 90 % of the landslides have source volumes less than 100 m^3 . However, severe entrainment (with entrainment ratio up to 10 or higher) was noted in many of the long runout CDFs.

Landslide debris mobility was found to have increased with rainfall intensity. Figure 2 shows that the June 2008 CDFs have considerably higher mobility than that of historical landslides. It is noted that 15 CDFs in the June 2008 rainstorm had runout distances exceeding 500 m, while there are only eight historical landslides including one case in Lantau Island, over the last several decades. Results of field mapping revealed that many of these CDFs involved watery debris (i.e. very wet debris mass) of high mobility.

Modelling of Long-Runout, Large-Scale Debris Flows

Back analyses of selected June 2008 CDFs of high mobility were carried out using the 2dDMM program (Kwan and Sun 2006), as well as 3dDMM program (Kwan and Sun 2007). Amongst them, CDFs at Yu Tung Road and Shek Mun Kap as well as two CDFs at Shek Pik were relatively sizable and mobile (see Table 1).

2dDMM and 3dDMM

Both 2dDMM and 3dDMM consider debris flow as a continuum material, and the dynamic characteristics are assumed to be governed by modified shallow water equations. The major modifications involve (1) inclusion of the base friction as determined using either a frictional or Voellmy rheology, and (2) incorporation of the Savage-Hutter theory to calculate the internal pressure within the debris mass.

2dDMM is an enhanced version of the DAN model proposed by Hungr (1995). It solves the shallow water equation using a Lagrangian framework and is capable of simulating debris flows travelling along a pre-set runout path with trapezoid cross-sections. Details of the formulation of the 2dDMM are presented by Kwan and Sun (2006).

Table 1 Mobile debris flows selected for back analyses

Debris flow	Source volume (m ³)	Maximum active volume (m ³)	Runout distance (m)	Catchment area (m ²)
Yu Tung Road	~2,350	~3,300	>590	1,02,000
Shek Mun Kap	~220	>1,700	>980	1,21,000
Shek Pik 'A'	~1,000	>8,500	>910	1,65,000
Shek Pik 'B'	~150	>5,000	>1,700	6,72,000

3dDMM is developed using a numerical strategy called Particle-in-cell and can evaluate the dynamics of debris travelling over a three-dimensional terrain. In the algorithm, the debris mass is represented by a number of imaginary mass points, and the terrain is divided into arrays of cells. The debris mass and debris height at a particular cell are determined based on the number of mass points located within the cell. It had been used to analyse the dynamics of landslides and debris flows that occurred in Hong Kong and other countries including Italy and Canada. Kwan and Sun (2007) described the modelling techniques and the simulation results.

The effects of entrainment can be simulated by both 2dDMM and 3dDMM. The calculation procedure proposed by McDougall and Hungr (2005) has been incorporated in 3dDMM. The procedure assumes that the amount of entrainment is directly proportional to the debris velocity and the overburden pressure of the debris acting on the ground. 2dDMM calculates the amount of entrainment based on a different algorithm which assumes that the total volume of debris increases in accordance with a specified rate. In the back analyses, the entrainment rate or coefficient was back-calculated to match the estimated active debris volume as inferred from the field mapping results.

Digital Elevation Map (DEM) and the volume of the detached ground mass at the landslide source are the basic input parameters required for debris mobility analyses. In the analyses carried out in this study, except for the Yu Tung Road CDF, the DEM provided by the Survey and Mapping Office, Lands Department of the Hong Kong SAR Government had been adopted. For Yu Tung Road CDF, the results of a post-landslide topography survey were used to develop the DEM. In all the cases, the landslide volume was established based on field measurements.

Yu Tung Road Debris Flow

A landslide occurred at the source area at about 8:30 a.m. on 7 June 2008. Figure 3 shows the debris trail. The whole debris flow process was captured by a video, which provides valuable information for the understanding of debris motion and the subsequent back analyses.

About 2,350 m³ of debris was detached in one go from a 32° steep terrain, which was discharged as a debris avalanche down the open hillslope below the source area.

**Fig. 3** Layout plan of the Yu Tung Road CDF

Rock outcrop was observed at the landslide crown during the field mapping. On the rupture surface, completely and highly decomposed fine ash tuff was observed. The crown is about 30 m above an incised drainage line. The width of the landslide scrap is 32 m and the maximum thickness of the detached ground mass is about 3 m.

The debris entered the drainage line at CH65, where the active volume was about 2,450 m³, then mobilized into a fast-moving pulse that travelled downslope as a CDF. From CH65 to CH330, the drainage line was predominantly incised and moderately steep. The active volume increased to a maximum of about 3,300 m³ near CH330. Virtually all the perched materials (including boulders) on the drainage line were entrained. Between CH330 and CH510, the drainage line broadened and became more gently sloping, with intermittent parts of the channel bed comprising steep rock faces. The debris flow was travelling at a high speed along this section, with an average velocity of about 10 m/s. Debris super-elevation data were also recorded to provide estimates of debris flow velocities at various locations along the flow path (see the dots in Fig. 4). The debris was discharged at the drainage line outlet principally in one large pulse that lasted for about 20 s. The debris runout distance was about 550 m and the corresponding travel angle was about 17°. The debris flow process was simulated using both 2dDMM and 3dDMM with Voellmy rheology. The entrainment coefficient and rheological parameters have been back-calculated

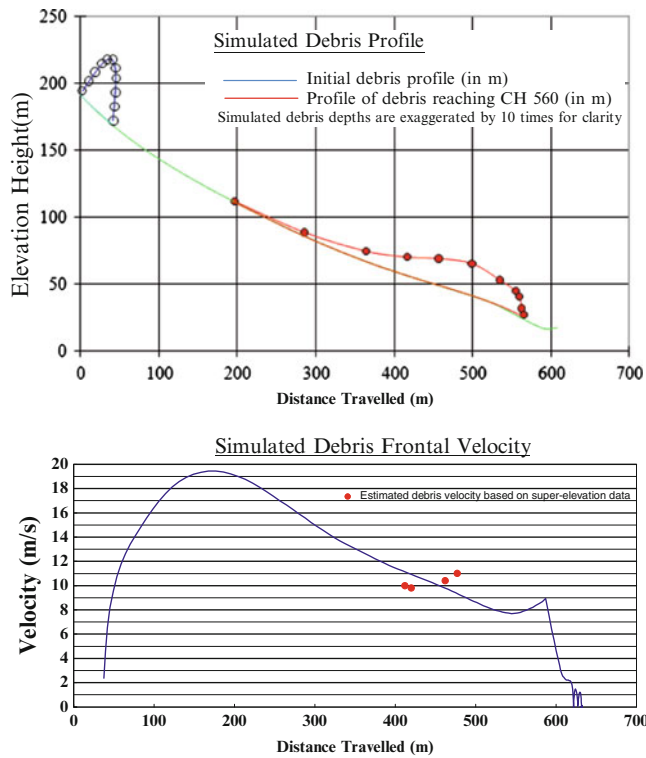


Fig. 4 2dDMM results: debris profile and debris frontal velocity

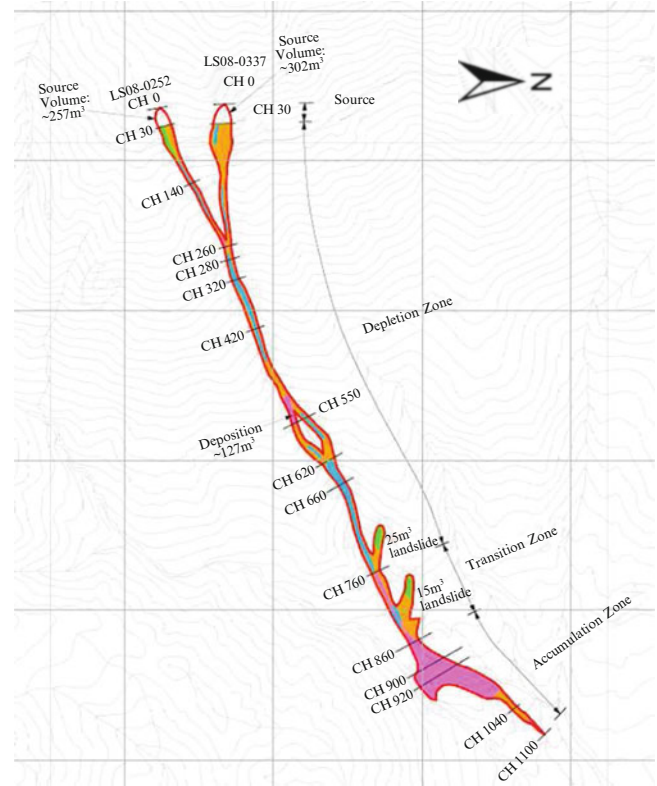


Fig. 6 Layout plan of Shek Mun Kap debris flow

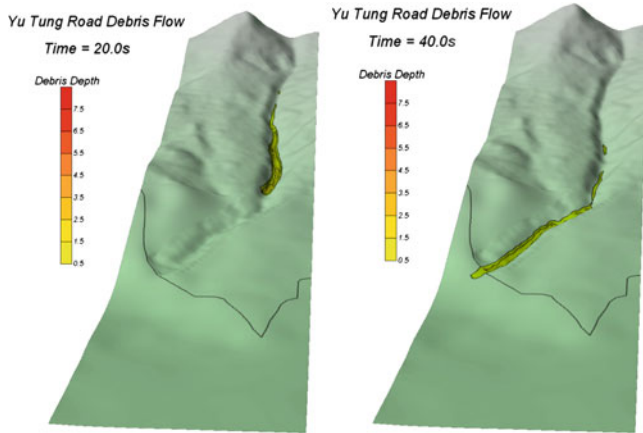


Fig. 5 Debris thickness profiles produced by 3dDMM at 20 and 40 s after onset of landslide

based on the super-elevation data, time of travel revealed by the video and the amount of entrainment as estimated during field mapping.

Both 2dDMM and 3dDMM provide reasonable simulation results based on an apparent basal friction angle of 8° with the Voellmy coefficient equal to 500 m/s^2 . The entrainment coefficients adopted in 2dDMM and 3dDMM are $36 \text{ m}^3/\text{s}$ and 0.0011 m^{-1} respectively. Figures 4 and 5 show some of the simulation results given by 2dDMM and 3dDMM.

Shek Mun Kap Debris Flow

Figure 6 shows an overview of the debris flow at Shek Mun Kap. The debris was sourced from two open hillslope landslides. The exact times of the failures were not reported. Field mapping established that the volumes of the two landslides are about 250 and 300 m^3 respectively. The two debris trails merge at about CH260, at which debris was fed into a narrow local depression. From the layering sequence of the debris deposition observed at the confluence of the two debris trails, the southern landslide probably occurred first. The debris of this landslide travelled on a relatively planar slope in the form of a debris avalanche. Most of the debris of this first failure deposited close to CH260. The deposition was then activated by the debris from the northern landslide which occurred at a later stage. A total of 500 m^3 active debris entered into the local depression downstream. The local depression is about 15 m wide and 2 m deep, with a gradient of about 32° . This gradient remains essentially unchanged for some 500 m downstream. Signs of considerable erosion along the depression were evident. It is estimated that the maximum active debris flow volume could be up to $1,500 \text{ m}^3$.

The debris flow diverged upon reaching a hump-like topographic feature at CH550. At the end of the hump, the debris flow paths merged. An abrupt change in the gradient of the runout trail was observed at CH760, where the

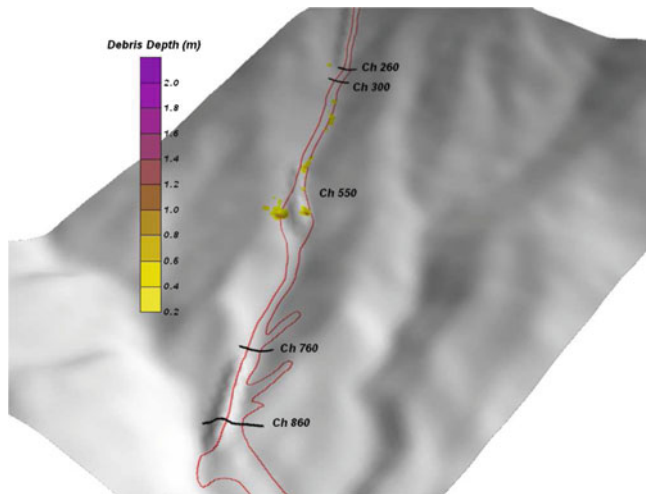


Fig. 7 Output of 3dDMM showing the debris flow diverged at CH550

gradient is less than 20° . Deposition of debris started at this chainage. The deposition zone extended for some 200 m to CH1000. The debris runout distance was about 980 m and the corresponding travel angle was about 24° .

Numerical simulations of the Shek Mun Kap debris flow have been conducted based on some simplifications. A single open hillslope failure with a volume of 300 m^3 is assumed. An appropriate value of entrainment coefficient is then applied to the region between the landslide and the local depression at CH260 to obtain an active debris volume of 500 m^3 at the head of the local depression.

Another simplification has been made in the 2dDMM analysis. As 2dDMM does not consider the three-dimensional topography of the runout path, between CH550 and CH760 where the debris flow diverged and travelled in two separated runout paths, the simulation was carried out as if the debris travelled on a single runout trail.

The Voellmy rheology has been adopted in the dynamic analyses. Apparent basal friction angle of 8° and a Voellmy coefficient of 500 m/s^2 have been used in the 3dDMM analysis, while a slightly higher apparent basal friction angle of 9° with the same value of Voellmy coefficient has been adopted in the 2dDMM analysis.

The bifurcation of the debris flow at CH550 has been simulated by the 3dDMM analysis (see Fig. 7). The simulated debris depth at this location is about 1 m, which is consistent with the site observation.

Shek Pik 'A' Debris Flow

The landslide which initiated Shek Pik 'A' debris flow was located at a steep slope of about 40° below a rock cliff of about 35 m high. The hillside of concern is some 350 m above the Shek Pik Reservoir. An aerial photograph

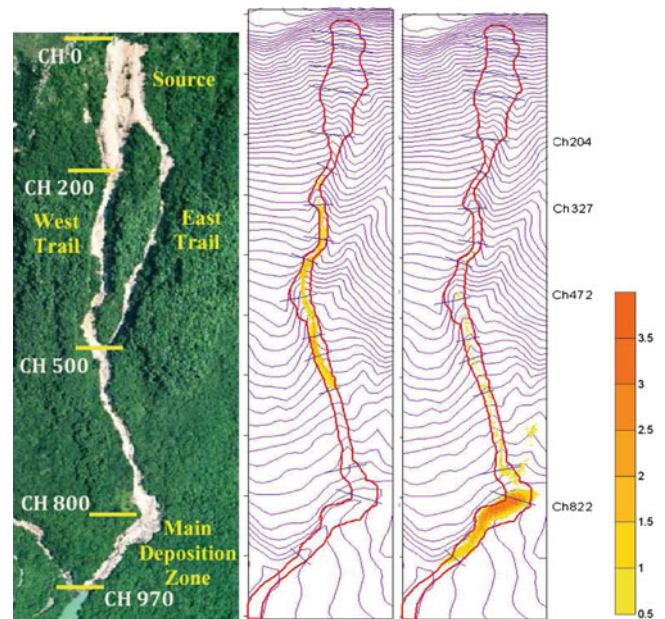


Fig. 8 (Left) Layout plan of Shek Pik 'A' debris flow (middle and right) 3dDMM results showing the Shek Pik 'A' debris flow at run-time 30 and 60 s after the onset of landslide

interpretation study revealed that two major landslides at this location had occurred in 1993 and 1995 previously.

Figure 8 shows the layout of the Shek Pik 'A' CDF in 2008. The source area of Shek Pik 'A' was about 60 m wide and 1.2 m deep and the total volume was about $1,000 \text{ m}^3$. Materials involved were mainly talluvium and colluvium. The majority of the landslide debris followed the west trail (see Fig. 8) and entered an incised drainage line at CH200. The debris mixed with a stream of concentrated surface runoff within the drainage line and developed into a CDF. Erosion of the side slope was observed along the debris trail. It is estimated that the volume of the CDF increased to about $4,000 \text{ m}^3$ at CH530.

The loose debris of 1993 and 1995 landslides deposited between CH500 and CH800 probably provided an addition source of entrainable material. Field mapping revealed that significant erosion of the loose materials had occurred. Materials with a depth of up to 3 m had been scoured and entrained as part of the CDF. The maximum active volume of the debris flow was estimated to be greater than $8,500 \text{ m}^3$ at CH790.

The slope gradient gradually reduced along the runout trail. At CH820, the debris flow entered into a deposition zone where the gradient is less than 10° and the width of the drainage line broadens to over 20 m. Due to the hydraulic action of the surface runoff, some of the debris mass had been washed down into the Shek Pik Reservoir at CH900. The total runout distance of the CDF on land is about 910 m and the corresponding travel angle is about 18° . Based on

super-elevation data, the flow velocities at CH470 and CH750 were estimated to be about 12 and 6 m/s respectively.

2dDMM and 3dDMM analyses have been carried out. The east trail (see Fig. 8) has not been considered in the analyses, since the amount of debris travelling within this trail is considerably less than that of the west trail. The analyses show that Voellmy rheology with apparent basal friction angle of 8° with Voellmy coefficient equal to 500 m/s^2 can describe the dynamics of the CDF well.

Shek Pik 'B' Debris Flow

An oblique aerial photograph showing the trail of the debris flow is presented in Fig. 9. The main source of Shek Pik 'B' was located on a steep slope of about 37° below a rock cliff of about 15 m in height. It was a shallow failure (depth about 0.75 m). The total volume of the landslide at source was about 150 m^3 . The failure developed into a CDF upon entering the existing drainage line at CH100.

Significant entrainment of perched materials and erosion of the side slopes were observed between CH100 and CH1000, and the total active volume was estimated to be greater than $5,000 \text{ m}^3$. No significant change in active volume was observed between CH1000 and CH1500, indicating that effects of erosion and deposition might have been balanced out within this section.

Between CH1500 and CH1700, deposition of debris was observed. The maximum width of the drainage channel was about 50 m. Boulder levees along both sides of the drainage line had a total volume of about $3,300 \text{ m}^3$, which comprised sorted debris up to 2 m in height. Some of the debris mass had travelled further downslope and was deposited in the Shek Pik Reservoir below CH1700. The runout distance on land is about 1,700 m and the corresponding travel angle is about 16° .

The runout distance of this Shek Pik 'B' debris flow is the longest amongst the four CDFs presented in this paper whilst its landslide volume at source is the least. This may be related to its distinct geomorphological setting of the Shek Pik 'B' catchment. The size of Shek Pik 'B' catchment is large (about $672,000 \text{ m}^2$ in area) and there are many tributaries feeding water into the major drainage line (see Fig. 9). Each of these tributaries probably fed concentrated, powerful stream of surface runoff to the trail of the debris flow and might have provided an additional driving force to the CDF. In any event, the surface runoff fed by these tributaries increased the water content of the debris flow, thus reducing the flow resistance.

Dynamic mobility modelling on the Shek Pik 'B' CDF has been carried out. The most appropriate parameters derived using the 3dDMM were apparent basal friction angle of 8° and Voellmy coefficient of 500 m/s^2 , while a



Fig. 9 Many tributaries feeding water into the major drainage line of Shek Pik 'B'

slightly lower apparent basal friction angle of 7° was established by the 2dDMM.

Discussion

The Voellmy rheology has been adopted in the 2dDMM and 3dDMM simulations of the above four mobile debris flows in Hong Kong. The parameters involved, i.e. basal apparent friction angle and Voellmy coefficient, as well as the entrainment coefficient, have been adjusted to best fit the estimated debris flow velocity and volume profile. The most appropriate parameters for these four long-runout CDFs are 7° to 9° for the basal apparent friction angle and 500 m/s^2 for the Voellmy coefficient (Table 2).

Lo (2000) reviewed the Voellmy parameters applicable to the simulation of debris flows in Hong Kong based on the back-analyses of previous debris flows in Hong Kong using DAN. It was recommended that for landslide volume exceeding 400 m^3 , the apparent basal friction angle and Voellmy coefficient could be taken as 11° and 500 m/s^2 respectively. However, for the sizeable, watery debris flows, like the ones analysed in the present study, mobility analyses adopting the above recommended parameters would have under-estimated the debris runout distance.

Both the video of the Yu Tung Road debris flow and site observations made shortly after the events confirmed that the four debris flows covered in this study involved watery debris. The watery nature of these torrents is likely to be attributed to the extreme and prolonged rainfall in June 2008 as well as the large catchment size of the drainage lines concerned (see Table 1).

On the basis of the above, it is considered prudent to adopt an apparent basal friction angle of 8° , together with a

Table 2 Results of back analyses based on 2dDMM and 3dDMM

Debris flow	Back analyses (2dDMM)		Back analyses (3dDMM)	
	ϕ_a	ζ (m/s ²)	ϕ_a (°)	ζ (m/s ²)
Yu Tung Road	8	500	8	500
Shek Mun Kap	9	500	8	500
Shek Pik 'A'	8	500	8	500
Shek Pik 'B'	7	500	8	500

Voellmy coefficient of 500 m/s², for the prediction of runout characteristics of sizeable CDFs under the following adverse site settings as diagnosed by Wong (2009):

- Sizeable debris flow at a major drainage line e.g. sites with a large catchment and a long flow path where a large amount of surface runoff and entrainable materials may be available for mixing with the landslide debris.
- Sizeable debris flow along a major drainage line into which many tributaries are feeding, i.e. possible sudden increase in the water content of the moving debris whenever the debris passes through a confluence point.
- Discharge of debris to a pool of water on the drainage line or debris from a small drainage line onto a major drainage line where there is potential for a large amount of running storm water.

Conclusions

This paper presents the natural terrain landslides, including four sizeable, long-runout debris flows, triggered by a severe rainstorm in Hong Kong on 7 June 2008.

Two dimensional and three dimensional analyses of the debris flows have been carried out using the 2dDMM and 3dDMM programmes developed by the GEO. The above long-runout CDFs were more mobile than the predicted using the prevailing recommendations on rheological parameters for mobility analyses. Based on the field mapping and back analyses, the rheological parameters for such mobile CDFs involving watery debris have been updated. The corresponding site settings that

are potentially conducive to give rise to such mobile CDFs are also given.

Acknowledgements This paper is published with the permission of the Head of the Geotechnical Engineering Office and the Director of Civil Engineering and Development, Government of the Hong Kong Special Administrative Region.

References

- Hungr O (1995) A model for the runout analysis of rapid flow slides, debris flows and avalanches. *Can Geotech J* 32:610–623
- Hungr O, Morgenstern NR, Wong HN (2007) Review of benchmarking exercise on landslide debris runout and mobility modelling. In: *Proceedings of the international forum on landslide disaster management*, vol 2, Hong Kong, pp 945–966
- Ko FWY (2005) Correlation between rainfall and natural terrain landslide occurrence in Hong Kong, GEO Report No. 168. Geotechnical Engineering Office, Hong Kong, 77p
- Kwan JSH, Sun HW (2006) An improved landslide mobility model. *Can Geotech J* 43:531–539
- Kwan JSH, Sun HW (2007) Benchmarking exercise on landslide mobility modelling – runout analyses using 3dDMM. In: *Proceedings of the international forum on landslide disaster management*, vol 2, Hong Kong, pp 945–966
- Lo DOK (2000) Review of natural terrain landslide debris-resisting barrier design, GEO Report No. 104. Geotechnical Engineering Office, Hong Kong, 91p
- McDougall S, Hungr O (2005) Dynamic modelling of entrainment in rapid landslides. *Can Geotech J* 42:1437–1448
- Wong HN (2009) Rising to the challenges of natural terrain landslides. In: *Proceedings of the HKIE Geotechnical Division annual seminar on natural hillsides: study and risk management measures*. Hong Kong Institution of Engineers, Hong Kong, pp 15–53



Modeling Potential Shallow Landslides over Large Areas with SliDisp⁺

Daniel Tobler, Rachel Riner, and Robert Pfeifer

Abstract

The deterministic model SliDisp⁺ calculates the potential detachment zones of shallow landslides. It is a grid-based model using an infinite slope analysis to calculate the safety factors F (ratio of retaining and driving forces) for each cell.

The input data consists of the slope topography, soil strength parameters, depths and shapes of potential shear planes, and the hydraulic behavior. The variables are derived from a digital elevation model (DEM), geological, geotechnical, and pedological documents, or field investigations. From this data the soil is classified over large areas. For each cell, the critical slope angle as well as the soil cohesion is determined.

Studies in several test areas showed that pedological aspects as well as joint water-input from underlying rock must be taken into account. Combined with the run-out model SliDepot, SliDisp⁺ calculates the extent of potential landslides over large areas and thus can be applied for spatial planning and optimized positioning of protection measures.

Keywords

Shallow landslide modeling • SliDisp⁺ • SliDepot

Introduction

In mountain regions many residential areas as well as important lifelines are generally exposed to potential shallow landslide events (Griffiths et al. 2002). Spatial planning is one of the major key elements in protection against natural hazards and requires a comprehensive assessment of landslide processes (Glade et al. 2005; Sidle and Ochiai 2006). By applying process models, the extent of potential landslides can be calculated over large areas (Guzzetti et al. 2006; Zolfaghari and Heath 2008; Dai and Lee 2002). The resulting maps

provide a quick identification of endangered areas with conflicts between hazards and land use. It is the base on which to set priorities for a more accurate hazard assessment.

Since 2000, the authors have applied the process model SliDisp to indicate hazard zones within large administrative areas. Within the same period, the model and the assessment method to gather input-data have been redesigned and improved.

Model SliDisp/SliDisp⁺

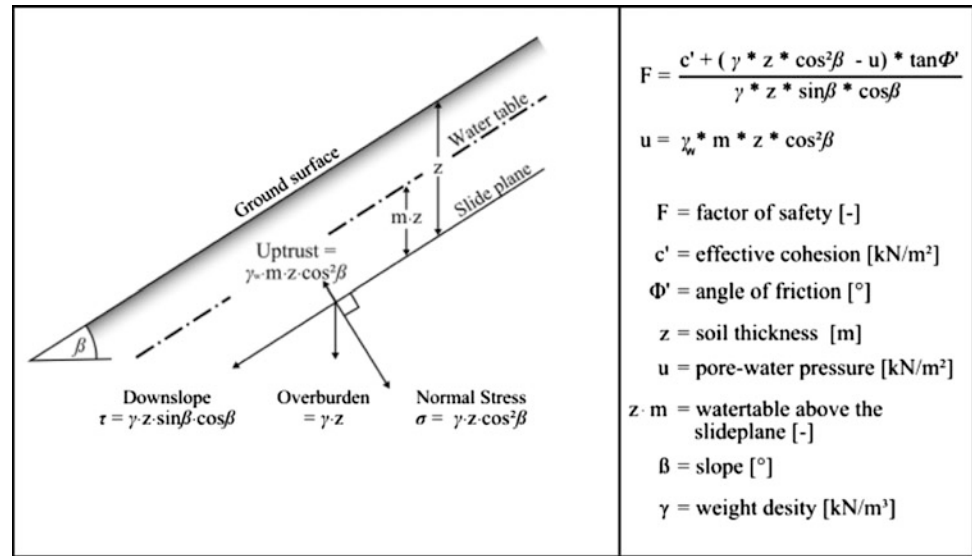
The original model SliDisp was developed by Liener (2000) at the University of Berne. Studies in several test areas showed that the assessment of detachment zones for potential shallow landslides must inevitably take pedological aspects as well as joint water-input from the underlying bedrock into account (Guimarães et al. 2003; Rickli and Bucher 2003; Dahal 2008; Paulin and Bursik 2009). During the last 5 years various modifications were made and the program advanced to SliDisp⁺ (Riner 2009).

D. Tobler (✉)
Institute of Geography, University of Berne, Hallerstrasse 12, Berne
CH-3012, Switzerland

GEOTEST AG, Birkenstrasse 15, Zollikofen CH-3052, Switzerland
e-mail: daniel.tobler@geotest.ch; info@geotest.ch

R. Riner • R. Pfeifer
GEOTEST AG, Birkenstrasse 15, Zollikofen CH-3052, Switzerland
e-mail: info@geotest.ch; info@geotest.ch

Fig. 1 Principle for the calculation of the factor of safety F for every raster cell (Selby 1993). Indication of all parameters needed for the calculation, except the root cohesion (WK, see Formula 1)



Stability Calculation in SliDisp

SliDisp is a deterministic model which calculates the landslide susceptibility of slopes. The calculation of stability is based on the formula of Selby (1993), whereas the characteristic soil-physics, the thickness of subsoil, the ground water level, the slope, and the force of roots are taken as determining parameters (Fig. 1, Formula 1).

For the model calculation a term for root cohesion (WK) has been added to the original formula of the factor of safety F (Formula 1). This empirical adjusted parameter takes the roots-retaining forces of the vegetation layer into account (Schmidt et al. 2001; Chok et al. 2004; Hales et al. 2009).

$$F = \frac{WK + c' + (\gamma \cdot z \cdot \cos^2\beta - \gamma_w \cdot m \cdot z \cdot \cos^2\beta) \cdot \tan\varphi'}{\gamma \cdot z \cdot \sin\beta \cdot \cos\beta} \quad (1)$$

The safety factor F is calculated for each cell of the grid, based on the data from the digital elevation model (DEM). If $F < 1$, the cell is potentially unstable, and the material can be set into motion by triggering factors. The total of all instable grid elements equals the maximum detachment area (= landslide susceptibility).

The normal variation of shearing parameters is acknowledged by a Monte-Carlo simulation (Kalos and Whitlock 1986). By applying this method, 100 random values are chosen from the deviation of the shearing parameters to calculate the factor of safety (F). With this random combination of parameters, the factor of safety is calculated 100 times for each cell. We assume that both the cohesion and the friction angle show a normal distribution and do not correlate with each other (Lacasse and Nadim 1996).

Areas with more than 60 % of the parameter combination showing a safety factor $F < 1$ are indicated as potential

sources. If more than 90 % of the F -values are < 1 , a medium to large chance of a potential landslide is expected. The data preparation as well as its visualization is carried out by means of a geographic information system (GIS). The calculation of the stability factors is implemented by a C-application and then integrated into the GIS.

Model-Parameter SliDisp

Deterministic models based on the infinite slope analysis (cf. Formula 1) call for strongly simplified model parameters (Dahal 2008). Concretely these are: soil thickness, slope angle, ground water level, shear strength, cohesion, and root strength. The parameters are derived from the variable morphology, the geology, and the geotechnical characteristics of the loose rock and vegetation cover (Guzzetti et al. 2006; cf. Fig. 1). The different parameters and their determination are described in the following sections.

Therefore the three main data sources are the digital elevation model (DEM), geological and geotechnical information (maps, laboratory data, results from field investigations) and pedological datasets (type of soil). Figure 2 demonstrates the relationship or derivation of the different datasets used in SliDisp/SliDisp⁺.

Morphological Variables

Digital elevation models (DEM) are of central significance as database to assess morphological variables. They serve as basic information to calculate the slope angle and the topographically induced water saturation potential of each grid cell (topographic-index, Beven et al. 1995; Liener et al. 1996). The topographic index corresponds to the natural logarithm of the ratio of drained area of the cell to slope angle β of the cell (cf. Formula 2, Fig. 3). The hydrologically

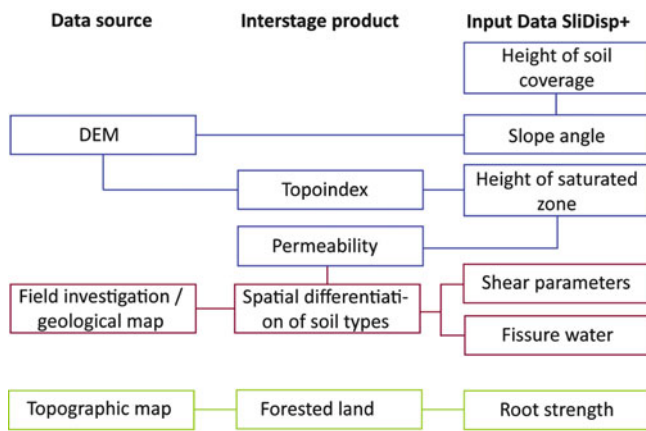


Fig. 2 Derivation of the model-parameters (input data) for the infinite slope model SliDisp/SliDisp⁺ (Riner 2009)

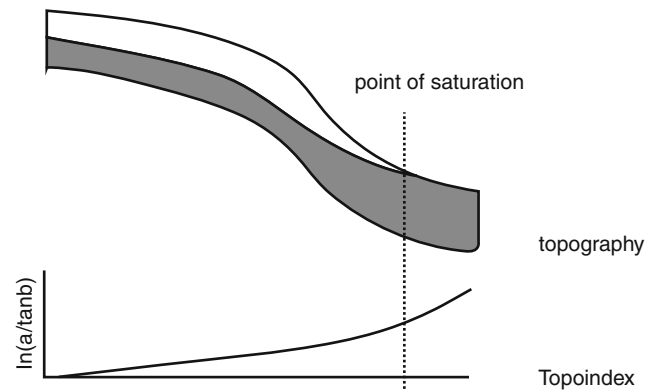


Fig. 3 Relationship between the topography and the topographic index (After Quinn et al. 1995, slightly modified)

relevant morphologies (ridge, flank, basin/dell, channels) are derived from the topo-index values. In a further step, these values serve as a basis to calculate ground water levels.

$$\text{topographic-index} = \ln(a/\tan \beta) \quad (2)$$

Soil Thickness

There are different ways to gain data about the thickness of the soil coverage: from existing datasets (boreholes, soundings, field mapping), from field investigations, and from model calculations (Godt et al. 2008). Today, different models exist – but all are based on the derivation from the slope gradient (Seconi and Catani 2008).

Therefore, according to DeRose (1996) and Salciarini et al. (2006), the correlation between the soil thickness z and the slope angle β (Formula 3) is given as an exponential function, where

$$z = 7.72 \times e^{-0.04\beta}. \quad (3)$$

Table 1 Soil thickness classes according to specified slope angle ranges in the case study Lauterbrunnen, Switzerland (GEOTEST AG 2011)

Slope angle [°]	Soil thickness [m]
<20°	3.0
20°–25°	2.5
25°–30°	2.0
30°–35°	1.5
35°–40°	1.0
40°–45°	0.75

The model SliDisp uses a similar approach. Here six different slope angle classes with their corresponding depth of bedrock interface are specified (Table 1). The better the knowledge about local conditions, the more precisely the soil thickness can be defined.

AGN (2004) as well as the results of different field campaigns (Liniger 2006; GEOTEST AG 2011) show that especially slopes with angles from 20° to 45° are susceptible to shallow landslides. Generally, with such steep slopes the soil thickness varies between 0.2 and 0.5 m on topographic ridges, and reaches 3.0 m in hollows (Riner 2009).

Geotechnical Parameters

Depending on the local geology and the subsoil type, the geotechnical characteristics (such as permeability, angle of internal friction, cohesion) and the spatial pattern of loose rock are specified. Geological and geotechnical maps, bore-hole data, and soil maps can also serve as database for this task. Additionally, field mapping and geotechnical analysis of the subsurface can be realized if necessary.

For simulation purposes, areas with the same geotechnical characteristics (subsoil classes) are merged into polygons. The mean values for permeability, angle of internal friction ϕ' , and cohesion c' are referred to all assigned polygons. The geotechnical characteristics of the subsoil are assumed to be uniform within a single polygon and homogeneously distributed (Liu and Wu 2008).

Permeability

According to Hölting and Enke (1996), the permeability of loose rock can be estimated approximately, depending on the distribution of the grain size. Six different permeability ranges are generally considered, from gravel to mid-size sand to clay (Table 2).

The classification adopted in SliDisp considers six classes (according to VSS 1999 and Wittke 1984). For each class, a permeability number from 1 to 6 is designated. Within the model, this number is translated into a coefficient ($m = 0.15\text{--}0.9$) and is taken as the basis for calculating the groundwater level.

Areas with different grain sizes and different permeability may constitute hydraulic barriers and are more common

Table 2 Derivation of the permeability coefficient “m” from different grain sizes (VSS 1999; Riner 2009). Example from Lauterbrunnen case study, Switzerland (GEOTEST AG 2011)

Class	Respective grain size	Permeability (k-values)	Permeability coefficient m
1	Pure gravel	$<10^{-8}$	0.15
2	Sand	10^{-7} bis 10^{-8}	0.30
3	Fine sand	10^{-6} bis 10^{-7}	0.45
4	Silty sand	10^{-4} bis 10^{-6}	0.60
5	Clayey silt	10^{-2} bis 10^{-4}	0.75
6	Clay	$>10^{-2}$	0.90

in heterogeneous soils. The probability for increasing positive pore pressures is higher at such locations (Lourenco et al. 2006). Therefore soils identified as heterogeneous are ranked one class lower (Riner 2009). For example, heterogeneous silty sand will not achieve the permeability number 3, but 2.

Angle of Internal Friction (ϕ')

The characteristic value of the internal friction angle (ϕ') of the subsoil was determined by shear experiments or derived from existing tables with indicated soil parameters for different underground types (VSS 1999). If no laboratory datasets from shear experiments are available the definition of the parameters follows the instructions of Liener (2000) and Riner (2009). The determination of ϕ' , c' and permeability is based on the weathering product of the different geological units (bedrock). By defining the grain size distribution and potential of erosion of the weathering product of the bedrock it will be possible to determine ϕ' , c' by the standard USCS classification categorized in VSS (1999). An example is given in Fig. 4 for a limestone bedrock. Its weathering product is classified according to the USCS classification as SC with the characteristic geotechnical parameters.

Cohesion (c')

Very often the spatial distribution of the cohesion c' is an unknown parameter. Furthermore cohesion varies depending on the natural moisture content and may disappear altogether with total saturation of the subsoil. Due to these uncertainties, several model approaches minimize the influence of cohesion (Guimarães et al. 2003) or ignore it (Rickli 2001; Rickli and Bucher 2003). The experiences made with SliDisp show that cohesion can be considered in the model (Liener 2000; Tobler and Krummenacher 2004; Riner 2009).

Root Cohesion WK

Vegetation plays an important role in the stability of slopes. Among experts, it is disputed whether the root strength should be acknowledged in the stability formula or not. Quantitative performed measurements prove that the root

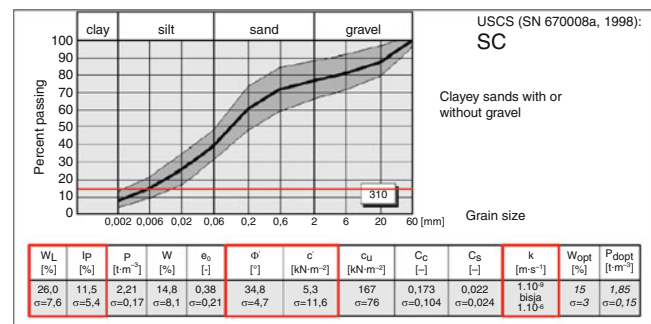


Fig. 4 Soil-parameters of clayey sands with or without gravel (SC) and grain-size distribution. The red line marks the 15 % passing line which defines the characteristic parameters wL and IP, the permeability (k-value) and shearing parameters ϕ' and c' (VSS 1999)

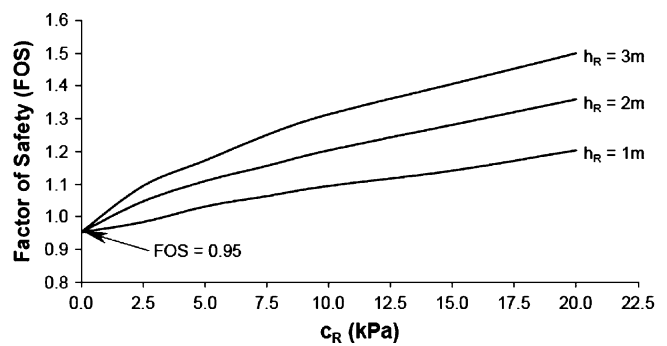


Fig. 5 Variation of factor of safety with different depths of root zones (h_R) applying the root cohesion (c_R) where $c' = 0$ and vegetation extends entirely over the ground surface, including the upper slope, slope surface, and slope toe (Chok et al. 2004)

system may serve as reinforcement, and therefore may strengthen the stability of the soil (Schmidt et al. 2001). The calculation of stability acknowledged the root strength (WK) as additional cohesion force (Meisina and Scarabelli 2007). Chok et al. (2004) describe the influence of root cohesion on the factor of safety F for different depths of root zones (Fig. 5). F increases as the apparent root cohesion c_R increases. It is noted that, when the entire slope is protected by vegetation, the effects on F are significant. For example, when $h_R = 1$ F is increased by 26 % for $c_R = 20$ kPa. The increase is even more significant with a deeper root zone (higher h_R).

Hales et al. (2009) describe the spatial variability of root cohesion in landslide-prone forests. Root tensile forces were consistent among most of the tree species measured. They postulate higher mean root cohesive strength on noses (~10 kPa) than in slopes and hollows (5.5 kPa). It is obvious that the variation in root cohesion between different vegetation communities must be significant. But after Schmidt et al. (2001) the variation is quantifiable.

In the model SliDisp⁺ the root cohesion is taken into account as a semi-empiric value between 2 and 7 kN/m²,

depending on the relevant soil thickness and characteristics of vegetation (such as condition, age, and type of the forest (Riner 2009)). Actual investigations focus on this aspect.

Calculation of the Ground Water Level ($m \cdot z$)

One of the most difficult issues in landslide susceptibility modeling is to determine the average height of totally saturated subsoil or soil. Statistical ground water models are very often used to calculate the slope stability. These models do not consider the influence of external aspects (such as precipitation, snow melt) on the temporal changes in ground water levels. As for other models, SliDisp assumes a statistical ground water level running parallel to the sliding surface.

The ground water level is the product of soil thickness z and a permeability controlled coefficient m (cf. Fig. 6, Table 2). According to Sidle and Ochiai (2006), this calculation helps to achieve an improved estimation of the stability. To consider the influence of the topographical convergence at hollows and noses the ground water level is modified by an index “ t ”. Cox and Davies (2002) as well as Yang et al. (2005) describe the relationship between the permeability and the topographic index (TI, cf. Formula 2) by the soil-topographic index, which is a modified TI that includes a soils component (soil depth and saturated permeability data). Both indexes are part of the topmodel concept (Quinn et al. 1995). Based on Agnew et al. (2006) and Riner (2009) the semi-empiric parameter t has a range of -0.1 – 0.0 on noses and 0.1 – 0.25 in hollows (Table 3).

Thus, the ground water level implemented in the model SliDisp⁺ is calculated by:

$$\text{Depth of saturated zone} = (m + t) \cdot z \quad (4)$$

where z = soil thickness, m = permeability coefficient, and t = empiric index for topographic influence. There is a hydrological condition for m : $0 < m \leq 1.0$. Negative values will be corrected to 0, values >1 to 1.0 (complete saturation).

Upgrade from SliDisp to SliDisp⁺

The process model SliDisp has been upgraded with two important new features. The approach to calculate the ground water level in the subsoil or in debris has been changed and the impact of joint water (KW) has been considered by implementing a correction value to the stability formula (Formula 5, red circles for new features). Both features are described in the following two sections.

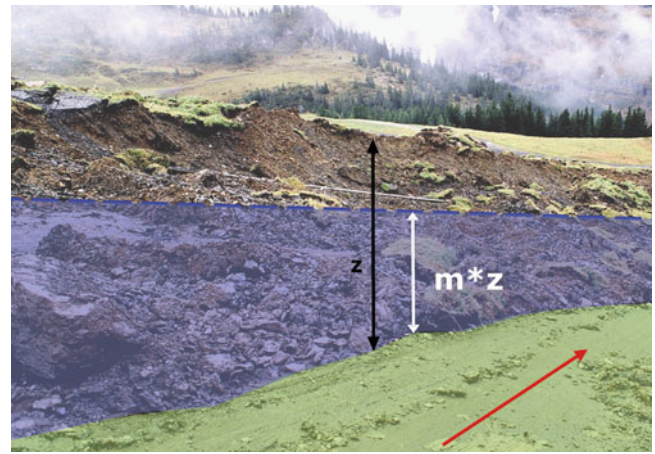


Fig. 6 Visualization of the saturated zone $m \cdot z$ on an open landslide scarf, with z = soil thickness and m = permeability coefficient. Red arrow slip surface and slip direction

Table 3 Topographic-Index classes with indication of “ t ” value for the case study Lauterbrunnen, Switzerland (GEOTEST AG 2011)

Class	Topo-index range	Description	Index “ t ” [–]
1	<3.0	Nose	–0.1
2	3.0–5.7	Slope	0
3	5.7–8.1	Hollows	0.1
4	>8.1	Channels	0.25

$$F = \frac{WK + c' + (\gamma \cdot z \cdot \cos^2 \beta - \gamma_w \cdot gw \cdot \cos^2 \beta) \cdot \tan \varphi' - KW}{\gamma \cdot z \cdot \sin \beta \cdot \cos \beta} \quad (5)$$

Calculation of the Saturated Zone (gw) According to SliDisp⁺

According to the calculation of the saturated zone in SliDisp, the ground water level is proportional to the soil thickness (Lineback Gritzner et al. 2001). Therefore the proportion of saturated material $(m + t) \cdot z$ (Formula 4) referring to the total thickness of subsoil z remains constant. This is formally not correct. Then shallow layers may show a proportionally higher ground water level than thicker soils (Sidle and Ochiai 2006).

With SliDisp⁺ the ground water level $(m + t) \cdot z$ is adjusted by using an empirically determined height, which varies depending on the thickness of the soil. Following this calculation, the water saturated zone may be enlarged in shallow soils (thickness of 0.3–1 m) by maximally 20 cm; it may be lowered by maximally 70 cm in deep soils of 1–3 m. The corrected ground water level is implemented as a parameter called “ gw ” in the stability formula (Formula 5).

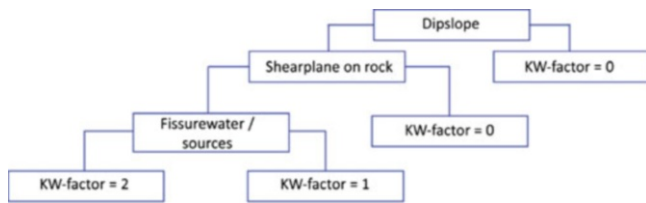


Fig. 7 Flow chart for the definition of KW-coefficient (Riner 2009)

Fissure Water Coefficient (KW)

At locations where joints and cracks crop out beneath the covering soil layer, enormous pore water pressures may develop. The joint water infiltrates into the potential slip surface and may therefore support the triggering of shallow landslides.

The model SliDisp⁺ implements the susceptibility of joint water as a qualitative correction value KW into the stability analysis (Fig. 7). KW may have the value 0 (small influence) or 2 (large influence); it is taken into account as a “negative” cohesion in the stability formula (Formula 5).

The parameter KW has to be determined by field investigations. Therefore the orientation of the bedrock is essential. Following the decision tree in Fig. 7, the KW parameter is easy to define.

Case Study Lauterbrunnen, Switzerland

In 2010 model calculations with SliDisp⁺/SliDepot (runout) were carried out within the settlements (approx. 30 km²) of the community of Lauterbrunnen during a review of the existing hazard map (GEOTEST AG 2003).

Lauterbrunnen is situated in central Switzerland at an altitude of 800–1,500 m a.s.l. (Fig. 8). The bedrock consists mainly of schist and sandstones of the Aalenian and the Bajocian (Dogger), sandstones of the Oxfordian and Callovian, as well as compact Malm lime and sediments from the Tertiary (Günzler-Seiffert 1962). The rock is folded in a large scale and disrupted by several steep tectonic displacements. The weathering-resistant lime and the sandstones form striking steep rock walls falling towards the valley bottom (Fig. 9). The schists of the Aalenian are very susceptible to landslides (GEOTEST AG 2003, 2007).

On both sides of the valley the rock is covered by silty moraines, dislocated slope debris and historic deposit from rock falls. The bottom of the valley consists of fine-grained



Fig. 8 Investigation area for the review of the hazard map in Lauterbrunnen, central Switzerland (Swissmap 2011)



Fig. 9 View from the South through the Lauterbrunnen valley with the steep cliffs of limestone and landslide-susceptible deposits in the valley bottom

flood sedimentation from the river and shows a heterogeneous layering of material.

Model Input

A detailed geological map is available for the investigation area (1:25,000) as well as numerous event documentations. Furthermore, field studies were made for the review of the hazard map (GEOTEST AG 2011). Eighteen different sub-soil types were identified in total. They were classified according to USCS (Table 4) and the described method in previous chapters. The relevant geotechnical parameters

Table 4 Classified underground with input parameters for SliDisp⁺ (GEOTEST AG 2011)

Type of loose rock/soil	USCS-classification	Φ' [°]	C'	PC
Aalenian schist	CL–ML	32.7	0.4	2
Alluvion	GP	38	0	5
Marl	CL	30.7	4.2	2
Moraine	SC	34.8	5.3	2
Tertiary	ML >30 %	28.8	11.7	2
Triassic	ML	33.9	6.5	2
Slope debris	SP–SM	34.4	0	3

PC indicates permeability class number (cf. Table 2)

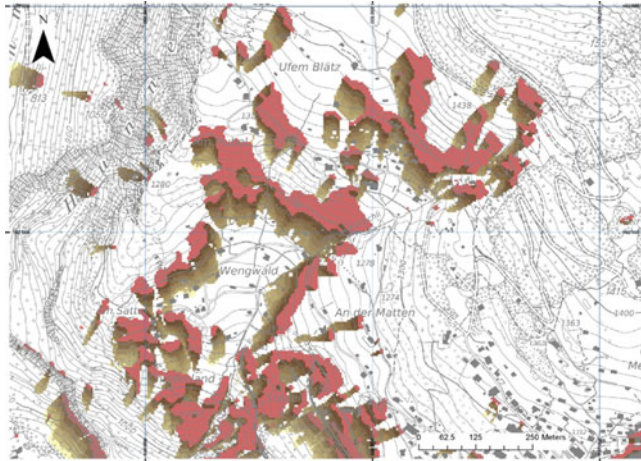


Fig. 10 Section of the calculated shallow landslide areas in Lauterbrunnen (*red* = source modeled with SliDisp⁺; *brown-yellow* = runout modeled with SliDepot; GEOTEST AG 2011)

(ϕ' , c' and permeability DL) were derived from laboratory tests on four representing samples (Wakatsuki and Matsukura 2008).

Results

Figure 10 shows the source areas (detachment zones of shallow landslides in red) calculated with SliDisp⁺ as well as the runout areas (brown-yellow) calculated with SliDepot (Tobler et al. 2011; GEOTEST AG 2011). SliDepot is an absolute GIS modeling. Starting with the data from the defined source zones the distribution of material in a downhill flow direction is calculated. The model focuses on the amount of water within the shallow landslide that will be reduced during the natural process. Finally the lack of process water will determine the point where the distribution of material stops (Tobler et al. 2011).

Starting from the dark red areas in Fig. 10 (calculated source locations for shallow landslides) the runout areas are modeled by stepwise reducing the original water content

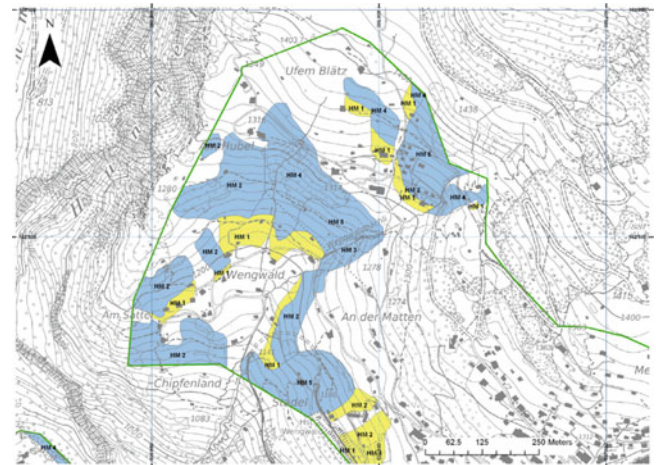


Fig. 11 Section of the actual hazard map for shallow landslide processes of Lauterbrunnen with hazard levels (*blue and yellow areas*; *green* = investigation area; GEOTEST AG 2011). The numbers indicate the field in the intensity-probability diagram (AGN 2004)

through max. eight discharge steps, each of 20 m. For Lauterbrunnen an excellent event register exists. So the final number of necessary discharge steps and therefore the maximal runout range has been calibrated with silent witnesses from events in 1999 and the event register (GEOTEST AG 2007). The average angle of reach of all shallow landslides is 27° and lies within the range postulated by Dai and Lee (2002).

The model results indicate the landslide-prone areas. For creating a hazard map process intensities have to be added. Therefore the additional field investigations focused (a) on the verification of modeled areas (detachment zones as well as runout) and (b) on the definition of the process intensities. AGN (2004) defines the different process intensities in hazard mapping. The actual hazard map is shown in Fig. 11. Comparing the calculated areas with the hazard map it is obvious that nearly all hazard zones have a smaller extension than the modeled process areas. The model results suit for hazard indication maps, but are not precise enough to derive directly hazard maps.

Conclusion

Many uncertainties are not considered in the calculation of the detachment zones for shallow landslides. These uncertainties underlying the model may include the type of material, mechanism of failure, ground water, the volume of failure and the geology. The parameters obtained are applicable to predict the shallow landslide susceptibility on regional scales. By employing a GIS, the analysis helps to identify conflict zones between damage potentials and process areas, which again enables efficient spatial planning or the definition of measurements to protect human lives and the infrastructure (Casadei et al. 2003).

The quality of the results correlates directly to the quality of the input parameters (e.g. knowledge of the underground, of the hydrogeological system, and of the soil cover). With the implementation of soil parameters, joint water (pressure) and a corrected, quasi-realistic ground water level, the model may soon be used directly for hazard mapping. The focus for future investigations has to be on the determination of subsurface water flows. Especially in shallow seated areas, macro pores like mouse channels may have an important influence on the stability of slopes. Observations during heavy rainfall events in the Lauterbrunnen valley lead to the assumption that slopes with high macro pore rates are better drained than others.

Acknowledgments We would like to thank Karen Bennett and Nigel Hulbert to improve the manuscript.

References

- AGN (2004) Gefahreinstufung Rutschungen i.w.S. Permanente Rutschungen, spontane Rutschungen und Hangmuren. Entwurf, Bern
- Agnew JA, Lyon S, Marchant PG, Collins VB, Lembo AJ, Steenhuis TS, Walter MT (2006) Identifying hydrologically sensitive areas: bridging the gap between science and application. *J Environ Manage* 76:63–76
- Beven KJ, Quinn P, Romanowicz R, Freer J, Fisher J, Lamb R (1995) TOPMODEL and GRIDATB, a user guide to the distribution versions (95.02). CRES Technical Report 110 (2nd edn). Lancaster University
- Casadei M, Dietrich WE, Miller NL (2003) Testing a model for predicting the timing and location of shallow landslide initiation in soil-mantled landscapes. *Earth Surf Process Landf* 28:925–950
- Chok YH, Kagwa WS, Jaksa MB, Griffiths DV (2004) Modelling the effects of vegetation on stability of slopes. In: Proceedings of the 9th Australia New Zealand conference on geomechanics, Auckland, vol 1, pp 391–397
- Cox JW, Davies PJ (2002) The duration of soil saturation: point measurements versus a catchment-scale method. In: McVicar TR, Li R, Walker JI, Fitzpatrick RW, Chanming L (eds) Regional water and soil assessment for managing sustainable agriculture in China and Australia. ACIAR monograph 84, pp 224–230
- Dahal RK (2008) Predictive modelling of rainfall-induced landslide hazard in the lesser Himalaya of Nepal based on weights-of-evidence. *Geomorphology* 102:496–510
- Dai FC, Lee CF (2002) Landslide characteristics and slope instability modeling using GIS, Lantau Island, Hong Kong. *Geomorphology* 42:213–228
- DeRose RC (1996) Relationships between slope morphology, regolith depth, and the incidence of shallow landslides in eastern Taranaki hill country. *Z Geomorphol Suppl. Bd.* 105:49–60
- GEOTEST AG (2003) Technischer Bericht zur Gefahrenkarte Lauterbrunnen, Nr. 00063.5, Zollikofen (unpublished)
- GEOTEST AG (2007) Lauterbrunnen, Rutschung Gryfenbach, Synthese und Prognosen, Report Nr. 94152.26, Zollikofen (unpublished)
- GEOTEST AG (2011) Lauterbrunnen, Naturgefahren, Bericht zur Teilrevision Gefahrenkarte, Nr. 10151.01, Zollikofen (unpublished)
- Glade T, Anderson M, Crozier MJ (2005) Landslide hazard and risk. Wiley, Chichester, 824 p
- Godt JW, Baum RL, Savage WZ, Salciarini D, Schulz WH, Harp EL (2008) Transient deterministic shallow landslide modelling: requirements for susceptibility and hazard assessments in a GIS framework. *Eng Geol* 102(3–4):214–226
- Griffiths J, Mather AE, Hart AB (2002) Landslide susceptibility in the Rio Aguas catchment, SE Spain. *Q J Eng Geol Hydrogeol* 35:9–18
- Guimarães RF, Montgomery DR, Greenberg HM, Fernandes NF, Gomes RA (2003) Parameterization of soil properties for a model of topographic controls on shallow landsliding: application to Rio de Janeiro. *Eng Geol* 69:99–108
- Günzler-Seiffert H (1962) Geologischer Atlas der Schweiz 1:25,000, Blatt 6 Lauterbrunnen. Schweizerische Geologische Kommission
- Guzzetti F, Reichenbach P, Ardizzone F, Cardinali M, Galli M (2006) Estimating the quality of landslide susceptibility models. *Geomorphology* 81:166–184
- Hales TC, Ford CR, Hwang T, Vose JM, Band LE (2009) Topographic and ecologic controls on root reinforcement. *J Geophys Res* 114: F03013. doi:10.1029/2008JF001168
- Hölting B, Enke F (1996) Einführung in die Allgemeine und Angewandte Hydrogeologie, 5th edn. Stuttgart Verlag, Stuttgart
- Kalos MH, Whitlock PA (1986) Monte Carlo methods, vol 1, Basics. Wiley, New York
- LaCasse S, Nadim F (1996) Uncertainties in characterising soil properties. Geotechnical Special Publication No. 58, vol 1, pp 49–75
- Liener S (2000) Zur Feststofflieferung in Wildbaechen. Dissertation, Geographica Bernensia, Bern
- Liener S, Kienholz H, Liniger M, Krummenacher B (1996) SDLISP – a procedure to locate landslide prone areas. In: Senneneset K (ed) Landslides. Balkema, Rotterdam, pp 279–284
- Lineback Gritzner M, Marcus WA, Aspinall R, Custer SG (2001) Assessing landslide potential using GIS, soil wetness modeling and topographic attributes, Payette River, Idaho. *Geomorphology* 37:149–165
- Liniger M (2006) Die Herausforderung der Gefahrenprognose bei Massenbewegungen: Rutsch- und Sturzprozesse. *Bull Angew Geol* 11(2):75–88
- Liu CN, Wu CC (2008) Integrating GIS and stress transfer mechanism in mapping rainfall-triggered landslide susceptibility. *Eng Geol* 101:60–74
- Lourenco SDN, Sassa K, Fukuoka H (2006) Failure process and hydrologic response of a two layer physical model: implications for rainfall-induced landslides. *Geomorphology* 73:115–130
- Meisina C, Scarabelli S (2007) A comparative analysis of terrain stability models for predicting shallow landslides in colluvial soils. *Geomorphology* 87:207–223
- Paulin GL, Bursik M (2009) Assessment of landslides susceptibility – LOGISNET: a tool for multimethod, multilayer slope stability analysis. VDM Verlag Dr. Müller, Saarbrücken
- Quinn PF, Beven KJ, Lamb R (1995) The $\ln(a/\tan b)$ index: how to calculate it and how to use it within the topmodel framework. *Hydrol Process* 9:161–182
- Rickli Ch (2001) Vegetationswirkungen und Rutschungen. Untersuchung zum Einfluss der Vegetation auf oberflächennahe Rutschprozesse anhand der Unwetterereignisse Sachseln am 15.8.1997. Eidg. Forschungsanstalt (WSL), Birmensdorf, 97p
- Rickli C, Bucher H, (2003) Oberflächennahe Rutschungen, ausgelöst durch die Unwetter vom 15.–16.7.2002 im Napfgebiet und vom 31.8.–1.9.2002 im Gebiet Appenzell. Eidg. Forschungsanstalt (WSL) und Bundesamt für Wasser und Geologie (BWG), 75p
- Riner R, (2009) Geotechnische Analysen von Lockergesteinen zur Modellierung von Rutschdispositionen im Untersuchungsgebiet Niesen. Masterarbeit Philosophisch-Naturwissenschaftliche Fakultät Universität Bern, 103 p (unpublished)

- Salciarini D, Godt JW, Savage WZ, Conversini R, Baum RL, Michael JA (2006) Modeling regional initiation of rainfall-induced shallow landslides in the eastern Umbria Region of central Italy. *Landslides* 3:181–194
- Schmidt KM, Roering JJ, Stock JD, Dietrich WE, Montgomery DR, Schaub T (2001) The variability of root cohesion as an influence on shallow landslide susceptibility in the Oregon Coast Range. *Can Geotech J* 38:995–1024
- Seconi S, Catani F (2008) Modeling soil thickness to enhance slope stability analysis at catchment scale. In: Abstract 33rd international geological congress, Oslo. <http://www.cprm.gov.br/33IGC/1345585.html>
- Selby MH (1993) *Hillslope materials and processes*. Oxford University Press, Oxford
- Sidele RC, Ochiai H (2006) *Landslides: processes, prediction, and land use*. Water resource monograph 18. American Geophysical Union, Washington, DC
- Swissmap (2011) Topographic map Lauterbrunnen, Blatt 1228. www.swisstopo.ch
- Tobler D, Krummenacher B (2004) Modellierung von Anrissgebieten für flachgründige Rutschungen und Hangmuren. In: Proceedings of the 2nd Swiss geoscience meeting, Lausanne
- Tobler D, Riner R, Pfeifer R (2011) Runout modeling of shallow landslides over large areas with SliDepot. In: Proceedings of the second world landslide forum, Rome
- VSS (1999) SN 670 010b. Bodenkennziffern, Zürich
- Wakatsuki T, Matsukura Y (2008) Lithological effects in soil formation and soil slips on weathering-limited slopes underlain by granitic bedrocks in Japan, Catena. *Trans Jpn Geomorphol Union* 72:153–168
- Wittke W (1984) *Felsmechanik – Grundlagen für wirtschaftliches Bauen im Fels*. Springer, Berlin/Heidelberg, 1050 p
- Yang X, Chapman GA, Young MA, Gray JM (2005) Using compound topographic index to delineate soil landscape facets from digital elevation models for comprehensive coastal assessment. In: “MODSIM” conference, Melbourne, 12–15 Dec 2005
- Zolfaghari A, Heath AC (2008) A GIS application for assessing landslide hazard over a large area. *Comput Geotech* 35:278–285



Three Dimensional Stability Analysis of the Grohovo Landslide in Croatia

Chunxiang Wang, Željko Arbanas, Snježana Mihalić, and Hideaki Marui

Abstract

The Grohovo Landslide, situated on the north-eastern slope in the central part of the Rječina River valley, is the largest active landslide along the Croatian part of the Adriatic Sea coast. The Grohovo Landslide is also a key pilot area for implementation of the monitoring activities of the Japanese-Croatian joint research project on “Risk identification and land-use planning for disaster mitigation of landslides and floods in Croatia”. This complex retrogressive landslide was reactivated in December 1996. It is considered that the basal failure surface is positioned at the contact between the slope deposits and the flysch bedrock. Based on the data from boreholes, geological mapping, geophysical surveys and the geological cross-section of the slope, the three dimensional shape and the position of the sliding surface were simulated using the inverse distance weighted interpolation. Using 3D extended Janbu’s simplified method, global stability of the Grohovo Landslide and stability of 12 separate landslide bodies were analyzed.

Keywords

Grohovo landslide • Slip surface • Interpolation • 3D stability analysis

Introduction

The Grohovo Landslide is located on the northeastern slope in the central part of the Rječina River valley near the City of Rijeka, Croatia. It is the largest active landslide along the Croatian part of the Adriatic Sea coast. Just upstream of this landslide, the Valići reservoir with the 35 m high concrete gravity dam is situated (Fig. 1).

Numerous historical data, figures and maps, which document landslides in the Rječina River valley, have found in the Croatian State Archive in Rijeka. These documents provide evidence of the landslides occurrence in the Rječina River valley near the Grohovo village. Slidings were first time recorded in 1767, when numerous landslides and rockfalls in the Rječina River valley were caused by the 1750 earthquake, which had an epicenter in the City of Rijeka. Many landslides triggered by rainfall were noticed along river banks near the Grohovo village at the end of nineteenth century. A large landslide occurred in 1893 on the northeastern slope of the Rječina River valley, and the Rječina River channel was shifted to the south for approximately 50 m (Mihalić and Arbanas 2013).

The most recent large displacement was observed on 5 December 1996 (Benac et al. 2002). The reactivated landslide has a volume of approximately $3.0 \times 10^6 \text{ m}^3$, and it consist of 13 different landslide bodies, including movements of the carbonate mega-blocks at the top of the slope. During the reactivation, sliding mass completely

C. Wang (✉) • H. Marui
Research Institute for Natural Hazards and Disaster Recovery, Niigata University, Nishi-ku, Ikarashi ni-no-cho 8050, Niigata City 950-2181, Japan
e-mail: chunxiangwang@hotmail.com

Ž. Arbanas
Faculty of Civil Engineering, University of Rijeka, Viktora Cara Emina St. 5, Rijeka 51000, Croatia

S. Mihalić
Faculty of Mining, Geology and Petroleum Engineering, University of Zagreb, Pierottijeva 6, Zagreb 10000, Croatia

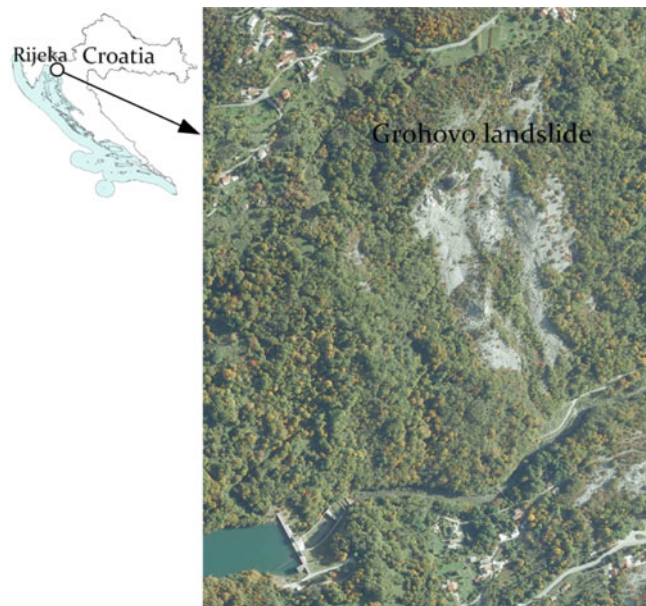


Fig. 1 Location of the Grohovo Landslide

buried the Rječina River channel, and a landslide foot formed a dam and a lake. After sliding, this landslide mass was removed immediately from the river channel, eliminating the risk of dam collapse and the resulting flood that could have caused serious damage to the City of Rijeka (Benac et al. 2002, 2005).

The hazard and risk of possible sliding on the flysch slopes of the Rječina Valley remain the same 15 years after the last large landslides occurred. Landslide occurrence is very probable during unfavorable hydrogeological conditions. Recently, Croatian researchers have been conducting field investigation, monitoring and basic research. In order to determine the hazard and risk of possible future landslide occurrences using the collected data, it was necessary to perform 3D landslide stability analyses. On the north-eastern slope, slope deposits are mostly a mixture of clayey silt that was formed by weathering of flysch bedrock and fragments to blocks of limestone originating from the cliffs placed on the top of the slope. It is considered that the basal failure surface is positioned at the contact between the slope deposits and the flysch bedrock. Based on the data from boreholes, geological mapping, geophysical surveys and reconstruction of the geological cross-sections through the slope, the three dimensional shape and the position of the sliding surface were simulated using a revised inverse distance weighted interpolation method. The whole Grohovo Landslide and twelve

separate landslide bodies, which have the unique three dimensional slip surface, were analyzed using a 3D extended Janbu's simplified method.

3D Stability Analysis Methods

The Interpolated 3D Slip Surface

The shape and location of slip surface are important in determining the stability of a slope. There are various methods to determine this surface. These can be classified into two main categories. One group assumes a slip surface to have a particular shape, for example, a straight or curve line, a circular arc, a log spiral surface (Giger and Krizerk 1975), a part of sphere or ellipsoidal surface (Zhang 1988), or a surface determined by finite element analysis, and the other group is for an arbitrary shape slip surface. A method of random generation of 3D slip surface was recommended by Thomaz and Lovell (1988) and Yamagami and Jiang (1997). A practical way in using NURBS (Non-Uniform Rational B-Splines) surface and ellipsoidal surface to simulate a three dimensional sliding surface was introduced by Cheng et al. (2005). In this study, based on the boreholes data, geological mapping, geophysical surveys and adopted geological cross-sections of the slope, the three dimensional shape and the position of the sliding surface are simulated using a revised inverse distance weighted interpolation method (Zhang 1995).

The three dimensional curved surface functions are classified to monodrome function and multivalued function. $Z = f(x,y)$ is the monodrome function. It corresponds to only one z , such as the surface of terrain, underground water surface, and so on. $W = f(x,y,z)$ is the multivalued function. When two random variables in (x,y,z) coordinates are given, the third variable may have one or more values. This curved surface is the spatial hypersurface, such as the underground temperature field. With the continuous changing of the variable W , the related hypersurface is changed with the ladderlike form. Therefore, $W = f(x,y,z)$ is used to be the fitting function of the strata surface. Before the strata surfaces are fitted, the surfaces should be numbered top-down. If there are L surfaces, then the number of strata is $k_i = 1, 2, 3, \dots, L$. In each surface, all the discrete data of $x_i, y_i, z_i, k_i, N_i, \alpha_i, \beta_i$ ($i = 1, 2, \dots, N$) are necessary, where x_i, y_i, z_i are the control spatial coordinates, k_i is the number of the stratum; N_i is the symbol of the dip or the dip direction of one column base surface (slip surface). If $N_i = 0$, there is no inclination or tendency. When the surface is fitted, the



Fig. 2 Grohovo Landslide map with positions of vertical cross sections

strata surface of k_i must be through this sample point. When $N_i = 2$, there are the dip angle α_i and the dip direction angle β_i . Not only k_i surface must be passed through this sample point, but also the k_i surface has the same α_i and β_i as the tangent plane passed through this point. N is the total number of sample points. The following equation is the fitting function:

$$\begin{aligned}
 W(x, y, z) = & \sum_{i=1}^{M_1} A_i \left(\frac{r_i^2}{R^2} \ln \frac{r_i^2}{R^2} + 1 - \frac{r_i^2}{R^2} \right) + \\
 & \sum_{i=M_1}^{M_1+M_2} \left[(A_i + B_i + C_i) \left(\frac{r_i^2}{R^2} \ln \frac{r_i^2}{R^2} + 1 - \frac{r_i^2}{R^2} \right) + \right. \\
 & \left. (B_i \times S_i \times C_i \times T_i) \left(\frac{r_i^2}{R^2} \ln \frac{r_i^2}{R^2} + 1 - \frac{r_i^2}{R^2} \right) \right]
 \end{aligned} \quad (1)$$

where M_1 is the number of sample points when there is no dip or dip direction; M_2 is the number of sample points when there are dip and dip direction; $M_1 + M_2 = N$; A_i , B_i and C_i are coefficients; R is the max search radius in the calculated spatial region; $r_i^2 = (x - x_i)^2 + (y - y_i)^2 + (z - z_i)^2$; r_i is

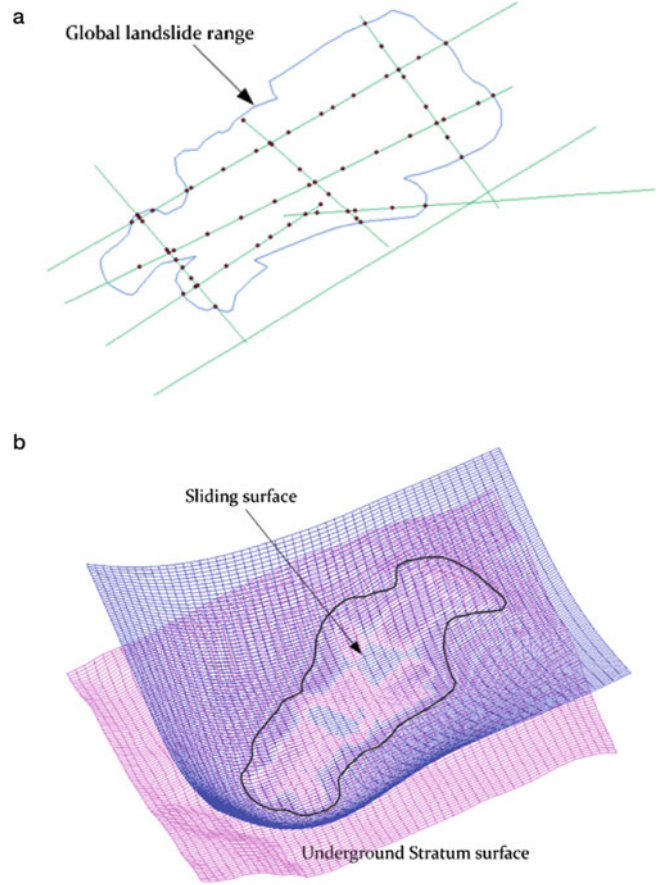


Fig. 3 The interpolated sliding surface by control points

the search radius of No. i point; S_i and T_i are used to describe the position of the tangent plane.

In the model of the Grohovo Landslide, it is considered that the basal failure surface is at the contact between the slope deposits and the flysch bedrock. The thickness of the displaced sliding mass was estimated and the position of slip surfaces was determined on the basis of the geological mapping and geophysical surveys. Locations of the cross sections in the Grohovo Landslide are shown in Fig. 2.

Figure 3a shows the control points along the cross sections. Figure 3b shows the interpolated slip surface derived using the revised inverse distance weighted interpolation method, on the basis of the control points in the vertical cross sections located within the Grohovo Landslide and the elevation points of the ground surface.

3D Extended Janbu's Simplified Method

Three dimensional limit equilibrium approaches are widely used for three dimensional slope stability analyses. Duncan (1996) and Chang (2002) reviewed the main aspects of

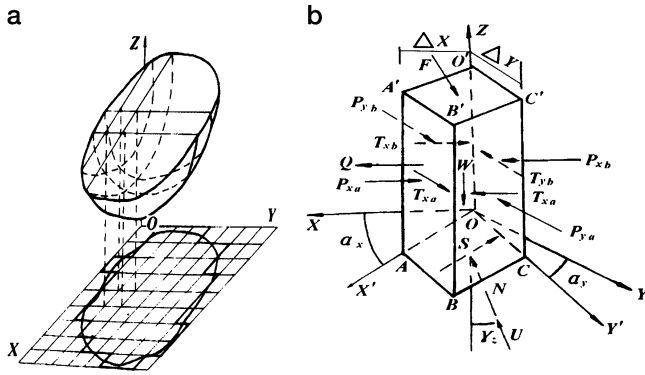


Fig. 4 3D sliding body and forces acting on a column

publications dealing with 3D limit equilibrium approaches. Many researchers have developed different limit equilibrium methods. The majority of 3D methods proposed in these studies are simply based on extensions of Bishop's simplified, Spencer's, or Morgenstern and Price's original 2D limit equilibrium slice methods. Differences between each study arise due to the arbitrary assumptions made regarding inter-column forces. The sliding mass is divided into a number of columns with vertical interfaces. The conditions for static equilibrium are used to find the factor of safety after making assumptions about the forces on adjacent columns (Fig. 4).

Feng et al. (1999) and Jiang et al. (2003) presented a simple and practicable 3D equivalent of Janbu's simplified method. With reference to Fig. 4, the equation of the 3D safety factor is as follows:

$$SF_{3D} = \frac{\sum \{C_{ij}A_{ij} \cos \beta_{zij} + [(W_{ij} + F_{zij}) - U_{ij} \cos \beta_{zij}]f_{ij}\}}{\sum (Q_{ij} - F_{xij}) + \sum (W_{ij} + F_{zij}) \tan \alpha_{xij}} \times \frac{\sec \alpha_{xij}}{\cos \beta_{zij} + \frac{f_{ij}}{SF_{3D}} \sin \alpha_{xij}} \quad (2)$$

where, ij is the number of a column; C_{ij} is the cohesion; f_{ij} is the frictional coefficient; A_{ij} is the base area of slip surface; Q_{ij} is the total force of the water pressure acting in the sides of $A'ABB'$ and $O'OCC'$; W_{ij} is the weight of a column; F_{xij} and F_{zij} are the x and y component of water pressure which acts on the slope surface; if the slope elevation is greater than the ground water, $F_{xij} = F_{zij} = 0$. α_{xij} is the dip direction to the x -axis; β_{zij} is the dip angle.

3D Stability Analysis of the Grohovo Landslide

The complex Grohovo Landslide consists of 13 individual landslide bodies; those are shown in Fig. 5 and identified as follows (Benac et al. 2002, 2005): initial landslide (1),



Fig. 5 Grohovo Landslide: 12 separate landslide bodies

landslides in talus material (2), lateral landslides in soil material (3), reactivated landslides (4) and sliding of separated limestone blocks (5). The geometry of the complex landslide is described in the Table 1, following the WP/WLI suggested nomenclature for landslides (Benac et al. 2005; Arbanas et al. 2010).

Landslide occurrence started with sliding of initial landslide body (No. 7) and developed during the time laterally (landslide bodies No. 12, 6, 5) and then retrogressively (landslide bodies No. 11, 2, 4, 1, 10, 9, 3) as shown in Fig. 5 (Arbanas et al. 2010). Borders between different landslide bodies are clearly expressed on the site. According to the boreholes data and geological cross-sections, 12 sliding bodies have unique slip surface at the contact between the slope deposits and the flysch bedrock. The landslide bodies No. 1, 3, 4, 8, 9, 10, and 11 are located in the upper part of the slope. The landslide bodies No. 2, 5, 6, 7, and 12 are located in the lower part of the slope. Inclinations of the bedrock surface differ in the lower and upper parts of the slope. The physical and geotechnical parameters obtained by laboratory test and back analyses of 2D slope stability calculations are listed in Table 2 (Benac et al. 2005). In 3D analysis, the sliding directions are determined as the angle between the possible movement direction and direction of x -axis.

The groundwater pressure is also considered in this analysis. The groundwater flow in the bedrock varies from very rapid to slow depending on the nature of the deposits. The quantity of water in the zone of superficial deposit fluctuates depending on rainfall conditions, such that it may be surface flow after periods of intense precipitation. There is evidence of water flow at the contact between the bedrock and overlying disturbed material of the rupture zone (Benac et al. 2002, 2005). The data about groundwater levels in the lower part of the slope were taken from the water levels measured in piezometers. In the upper part of the slope, there were no piezometers and the groundwater level was assumed

Table 1 Geometry of the complex Grohovo Landslide

Landslide geometry elements	Dimension
Total length	L = 425 m
Length of the displaced mass	Ld = 420 m
Length of the slip surface	Lr = 405 m
Width of the displaced mass	Wd = 200 m
Width of the slip surface	Wr = 200 m
Depth of the displaced mass	Dd = 6–20 m
Depth of the slip surface	Dr = 6–9 (20) m
Total height (the height from the crown to the tip of the toe)	DH = 165 m

Table 2 Physical and geotechnical parameters

	ρ (kN/m ³)	C (kN/m ²)	ϕ (°)
Upper part	20	7.5	25
Lower part	20	16	16
Bedrock	21	25	32

to be 1~3 m above the contact between the bedrock and the overlying disturbed materials.

Using the adopted parameters, the 3D slope global safety factor of the complex landslide and 12 separate local landslide bodies were calculated (Table 3). The calculations indicate that No. 3 landslide body, located at the upper part of the slope, has the lowest factor of safety. It is a key unsafe block, such that in this part of the slope new displacements can be expected in the future, e.g. triggered by heavy rainfall and unfavorable hydrogeological conditions or strong earthquake. The 3D safety factor of No. 10 landslide body, located at the middle of the landslide, is greater than 2.1 due to gently inclined base slip surface. The global safety factor of the complex landslide is 1.35, which is greater than that obtained by the 2D slope stability analysis (Benac et al. 2005).

The distinction in results between 2D and 3D analyses is not unexpected; it seems very clear that the safety factor for 3D analyses is greater than the safety factor for 2D analyses (Hungry et al. 1989; Duncan 1996). Other reasons for greater 3D safety factors are: using of the soil strength parameters obtained from 2D back analyses; and using geometry of landslide obtained from present landslide topography, i.e., landslide reached stable position after sliding. There is also present a lack of groundwater level data that can be crucial for calculation of the present state of the slope stability.

Conclusions

The Grohovo Landslide on the north-eastern slope of the Rječina River valley is the largest active landslide along the Croatian part of the Adriatic Sea coast. Recently, field investigation, monitoring and basic research were conducted by the Croatian researchers. Many individual movements indicated that there are 13 separate landslide bodies. Among them, 12 landslides bodies have the

Table 3 3D safety factors of the global landslide and 12 separate landslide bodies

Landslide body	Sliding direction (°)	SF _{3D}
Slide_global	-52	1.35
Slide_1	-60	1.38
Slide_2	-60	1.54
Slide_3	-30	1.02
Slide_4	-25	1.36
Slide_5	-30	1.12
Slide_6	-30	1.37
Slide_7	-52	1.40
Slide_8	-52	1.11
Slide_9	-45	1.56
Slide_10	-45	2.11
Slide_11	-45	1.70
Slide_12	-45	1.35

unique base slip surface. It is considered that the basal failure surface is at the contact between the slope deposits and the flysch bedrock. In order to determine the hazard and risk of possible future landslide occurrences, 3D landslide stability analyzes were performed.

In the past, location of critical 3D slip surface is mainly confined to spherical and ellipsoidal shape and random failure surface is seldom considered. Based on the borholes data, geological mapping, geophysical surveys and adopted geological cross-sections of the slope, the three dimensional shape and the position of the slip surface are simulated using a revised inverse distance weighted interpolation method. Using the 3D extended Janbu's simplified method, the global 3D factor of safety of the complex landslide and factors of safety of 12 separate landslide bodies were analyzed. The stability analysis indicates that No. 3 landslide body, located at the upper part of the slope, is a block with the lowest safety factor, such that in this part of the slope new displacements can be occurred in the future, especially triggered by heavy rainfall and unfavorable hydrogeological conditions or strong earthquake.

As a part of the joint research activities in the Japanese-Croatian scientific project on "Risk identification and land-use planning for disaster mitigation of

landslides and floods in Croatia” which was launched in 2008, a comprehensive integrated real-time monitoring system will be installed in the Grohovo landslide. The monitoring system will consist of geodetic and geotechnical monitoring. More attention should be given to the movements of the upper part of the Grohovo Landslide. A part of the geotechnical monitoring will be permanent measuring of pore pressures in the slope that will provide better understanding of groundwater variations in the slope and enable more accurate slope stability analyses.

Acknowledgments This research was performed as a part of Japanese-Croatian joint research project on “Risk Identification and Land-Use Planning for Disaster Mitigation of Landslides and Floods in Croatia”, which was funded by JST-JICA Science and Technology Research Partnership for Sustainable Development Project (SATREPS).

References

- Arbanas Ž, Benac Č, Dugonjić S (2010) Dynamic and prediction of future behavior of the Grohovo landslide. In: Proceedings of the 1st workshop of the project risk identification and land-use planning for disaster mitigation of landslides and floods in Croatia, Dubrovnik, Nov 2010
- Benac Č, Arbanas Ž, Jardas B, Jurak V, Kovačević SM (2002) Complex landslide in the Rječina River valley (Croatia): results and monitoring. In: Landslides, Proceedings of the 1st European conference on landslides, Prague, June 2002. A. A. Balkema, Lisse/Abingdon/Exton/Tokyo, pp 487–492
- Benac Č, Arbanas Ž, Jurak V, Oštrić M, Ožanić N (2005) Complex landslide in the Rječina River valley (Croatia): origin and sliding mechanism. *Bull Eng Geol Environ* 64(4):361–371
- Chang M (2002) A 3D slope stability analysis method assuming parallel lines of intersection and differential straining of block contacts. *Can Geotech J* 39:799–811
- Cheng YM, Liu HT, Wei WB, Au SK (2005) Location of critical three-dimensional non-spherical failure surface by NURBS functions and ellipsoid with applications to highway slopes. *Comput Geotech* 32:387–399
- Duncan JM (1996) State of the art: limit equilibrium and finite-element analysis of slopes. *ASCE J Geotech Eng* 129(2):577–596
- Feng S, Feng D, Ge X, Gu X (1999) 3D limit equilibrium method for slope stability and its application. *Chin J Geotech Eng* 21(6):657–661
- Giger MW, Krizerk RJ (1975) Stability analysis of vertical cut with variable corner angle. *Soils Foundat* 15(2):63–71
- Hungr O, Salgado FM, Byrne PM (1989) Evaluation of a three-dimensional method of slope-stability analysis. *Can Geotech J* 26:679–686
- Jiang Q, Wang X, Feng D, Feng S (2003) A three-dimensional limit equilibrium method analysis software for slope stability and its application. *Chin J Rock Mech Eng* 22(7):1121–1125
- Mihalić S, Arbanas Ž (2013) The Croatian–Japanese joint research project on landslides: activities and public benefits. In: Sassa K, Rouhban B, Rouhban S, McSaveney M, He B (eds) *Landslides: global risk preparedness*. Springer-Verlag, Berlin/Heidelberg, pp 333–349
- Thomaz JE, Lovell CW (1988) Three-dimensional slope stability analysis with random generation of surfaces. In: Proceedings of the 5th international symposium on landslides, Lausanne, July 1988, vol 1. A.A. Balkema, Rotterdam, pp 777–781
- Yamagami T, Jiang JC (1997) A search for the critical slip surface in three-dimensional slope stability analysis. *Soils Foundat* 37(3):1–16
- Zhang X (1988) Three-dimensional slope stability analysis of concave slopes in plan view. *ASCE J Geotech Eng* 114(6):658–671
- Zhang JM (1995) Design and display of three-dimensional geological model. *Advancement of Chinese mathematical geology*. Press of Geology, Beijing, pp 158–167



Mass Movement Classification Using Morphometric Parameters (Puebla, Mexico)

Veronica Ochoa-Tejeda, Parrot Jean-François, and Fort Monique

Abstract

The Sierra Norte de Puebla (Mexico) is a tropical mountain frequently affected by torrential rains induced by depressions and hurricanes. In October 1999 and 2005, intense precipitation triggered hundreds of landslides and caused heavy human losses and material damages. All the landslides surveyed in the field and their traces extracted from the satellite images have been analyzed by using morphometric parameters in order to characterize and to classify them. The spatial distribution of observed landslides types is not random but responds to both regional structural features and material nature involved in the movement. It is particularly important to establish these close relationships in order to assess landslide hazards by using different factors and methods and the approach proposed in this paper seems to be very useful to do that.

Keywords

Morphometric parameters • Landslide classification • Sierra Norte de Puebla (Mexico)

Introduction

Landslide hazard assessment is based on a landslide susceptibility evaluation, that is to say the research of the location of potential landslides that can occur in a given region and remobilize specific terrain material (Guinau et al. 2007). It is commonly assumed that the future landslides triggering obey to the same conditioning parameters than those observed in the past and the present (Varnes 1984; Carrara et al. 1995; Jadda et al. 2009). Such an analysis requires estimating the terrain failure susceptibility and the behavior of the remobilized material (Glade et al. 2005; Hürlimann et al. 2006) as well as the land cover changes particularly

when studying the shallow landslides (Collinson et al. 1995; Fannin et al. 1996; García-Ruiz et al. 2010).

Independently of the classifications established by different authors (i.e. Hutchinson 1988; Cruden and Varnes 1996), we assume that the predominant types of landslides are essentially related to the nature of the material involved in the process (soils, colluvial deposits, talus deposits and talus breccias, uncovered rock zones). In the case of rock sliding and rock avalanches, eventually coarse debris flows, the structural geologic factor plays a predominant role (Ochoa-Tejeda 2004), since the presence of faults, fractures, as well as planes of weakness (schistosity, joints, etc.), work like zones that supply the gravitational movements.

The purpose of this paper is to analyze, in a context of dense vegetation, all the landslides surveyed in the field as well as their traces extracted from satellite images. This analysis is mainly based on morphometric parameters, and has been developed in order to characterize and to classify the mass movements. High resolution satellite images and high resolution Digital Elevation Model (DEM) generated by a multidirectional interpolation (Parrot and Ochoa-Tejeda 2005) have been used with such a goal. Actually IKONOS

V. Ochoa-Tejeda (✉) • F. Monique
Université Paris Diderot, Sorbonne-Paris-Cité, UMR PRODIG
8586 – CNRS, Paris cedex 13, France
e-mail: veronikot@yahoo.com.mx; beronik@hotmail.com

P. Jean-François
LAGE, Instituto de Geografía, UNAM, Mexico City, Mexico
e-mail: parrot@igg.unam.mx

images give not only information about land cover, presence of bare and water surfaces, influence and extent of human settlements, vegetation cover and area of fragmentation, but can also be used to identify the different types of landslides that occurred in the study region by means of photo interpretation (Nichol et al. 2006) or using the semi-automated method developed by Ochoa-Tejeda and Parrot (2007).

We assume that it is possible to define geographical unstable zones in a simple way and then to characterize the type of events susceptible to be expected in a more or less short time according to the type of geological formation that would be involved in the mass movement.

Studied Area

The Sierra Norte de Puebla (Mexico) is a tropical mountain frequently affected by torrential rains inducing regularly hundreds of landslides that affect steep hillslopes mainly formed by intensively folded and fractured metamorphic rocks and weathered sedimentary formations both covered by slope deposits of variable thickness.

This mountain is situated in the province of Puebla located within the transition of the Trans-Mexican Volcanic Belt (TMVB) and the Sierra Madre Oriental mountains mainly formed by Mesozoic sedimentary rocks. The TMVB consists of Late Tertiary and Quaternary volcanic formations essentially of calc-alkaline type (Alva-Valdivia et al. 2000).

The studied sub-scene is centered on the 135 km² region of La Soledad Lake (Fig. 1), where 98 landslides recorded by the Regional Civil Protection Unit of Puebla, actually 144 observed on the satellite image, have been triggered by torrential rainfalls in October 1999.

In this zone located between 19°53' and 20°00' (North latitudes) and 97°25' and 97°30' (W longitudes), the main geological units are ranging from Palaeozoic to Quaternary ages (Angeles-Moreno and Sánchez-Martínez 2002).

The Palaeozoic formations are represented by mylonites and strongly deformed phyllonites originally defined as Xucayucan schists. Mesozoic folded sedimentary rocks overlay discordantly the Palaeozoic deposits and comprise limestones, sandstones, lutites, limolites and conglomerates. Tertiary deposits from the Pliocene are formed by andesitic lava flows up to 300 m thick intercalated with volcanic tuffs. Quaternary materials are composed of dacitic and rhyolitic pyroclastic deposits derived from the activity of the Los Hornos caldera, which is situated 35 km southwards of the studied area. These materials overlay both Mesozoic and Tertiary deposits.

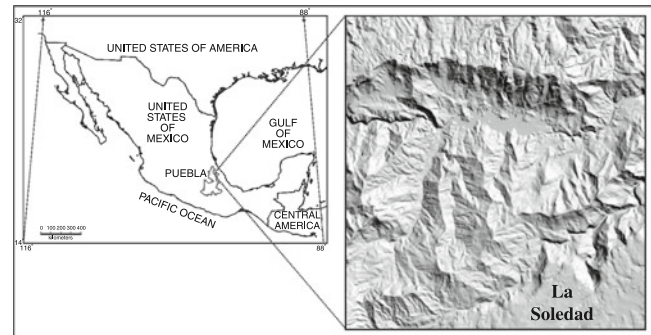


Fig. 1 Localization of the studied zone

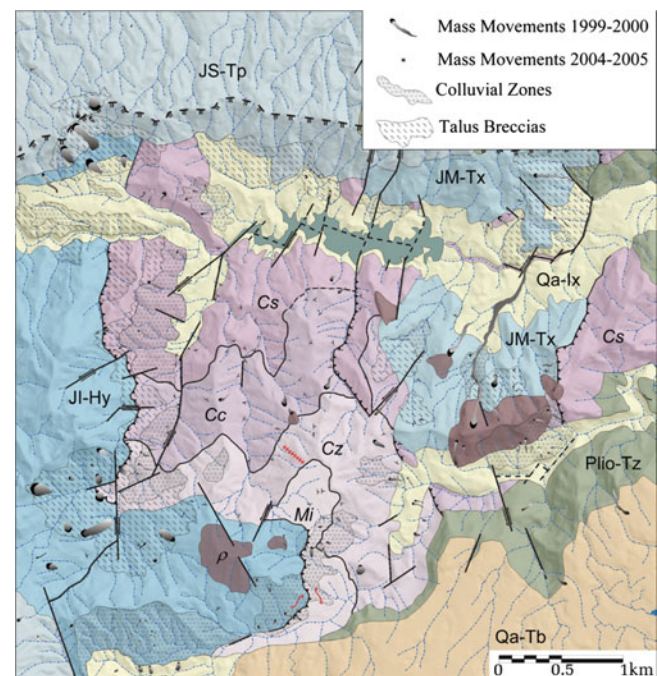


Fig. 2 Geological map of the study zone. *Qa-Ix* Xaltipan formation (Quaternary Ignimbrites), *Qa-Tb* Quaternary andesitic tuffs; *Plio-Tz* Teziutlan formation (andesitic flows and tuffs), *JS-Tp* Taman-Pimienta formation (marls and limestone), *JM-Tx* Tenexcate formation (sandstones and conglomerates), *JI-Hy* Huayacocotla formation (sandstones and shale), Xucayucan mylonitic complex: *Mi* El Mirador (metamorphosed basaltic rocks); *Cz* Cozolexco (metabasalts); *Cc* Chicuco (schist); La Soledad mylonitic complex [*Cs*] = gneisses; ρ intrusive rhyolites

Moreover, this zone is characterized by the development of different superficial formations (regolith, old landslide deposits) that are easily remobilized by the frequent torrential rains affecting this tropical region. The behavior of different types of material can therefore be studied in this very limited zone.

The reinterpreted geologic map (Ochoa-Tejeda 2009, 2010) takes into account field observation and the information provided by INEGI (1994), Mooser (2000) and Angeles-Moreno and Sanchez-Martinez (2002). We reported (Fig. 2)

landslide locations as the traces extracted from the Ikonos image for the 1999 event, and as points for the more recent mass movements.

Methodological Approach

All the landslides surveyed in the field and their traces extracted as previously described from the satellite images, have been analyzed by using morphometric parameters in order to characterize and to classify them. Some parameters are directly related with the shape of studied landslides: for instance, the surface S , the perimeter P , the ratio between these two parameters, as well as the presence of holes that allows defining a porosity index.

The simplest method used to measure the surface consists to calculate the total number of pixels N_{bp} belonging to the connected component; but according to Pratt (1978), another approach consists to consider the surface as $S = \sum P_s + \sum P_p/2$, where P_s are the pixels that strictly belong to the surface and P_p the pixels describing the perimeter. The surface in m^2 or km^2 is obtained by multiplying S by the value of the pixel surface. There are some more accurate methods that take into account the configuration of P_p and the neighboring pixels in order to know exactly the portion of the pixel P_p that belongs to the surface (Parrot 2007). The perimeter P corresponds either to the total number of pixels (N_p) describing the perimeter or to the length (L_p) of this perimeter measured by using the length of the segment linking two successive pixel centers.

Taking into account the values of the former parameters, it is possible to define various ratios such as for example the ratio perimeter/surface [in pixels] $\rho = (N_p/N_{bp}) \times 100$, the ratio perimeter versus surface [in meters and square meters] $\theta = (L_p/S) \times 100$ or the circularity index $\varpi = (P^2/S) \times 100$.

The notion of porosity characterizes topographically heterogeneous ensembles as encountered in some landslides, especially in the case of rotational landslides (graben-like structures). The calculation is as follow:

$$\xi = \left[\frac{\sum P_h}{\left(\sum P_h + \sum P_s + \sum \frac{P_p}{2} \right)} \right] \times 100$$

where P_s and P_p are all the pixels describing the shape (surface and perimeter) and P_h the pixels corresponding to the holes.

Another way to describe the shape is to compare this shape and some plain shapes such as the rectangle, the circle or the smaller convex zone that circumscribes the studied item. It is then possible to measure the length and the width of the

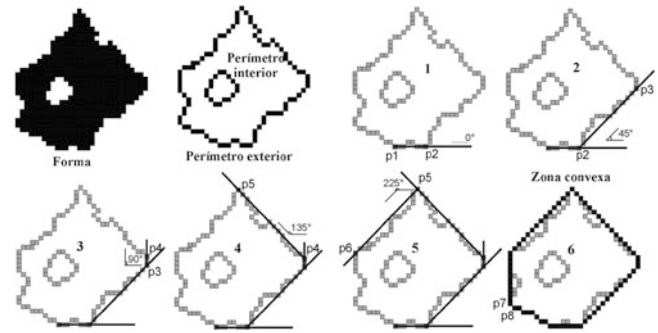


Fig. 3 The Jarvis's march procedure

studied shape, to define the relation existing between these two values, etc. This approach requires to research the gravity center (GC) and to define the principal axis (PA) passing through the gravity center. The gravity center GC with coordinates X_c , Y_c and the second order moments μ_{xx} , μ_{yy} and μ_{xy} are equal to:

$$X_c = \frac{1}{N_{bp}} \sum_{i=1}^{N_{bp}} X_i \quad Y_c = \frac{1}{N_{bp}} \sum_{i=1}^{N_{bp}} Y_i$$

$$\mu_{xx} = \sum_{i=1}^{N_{bp}} (X_i - X_c)^2 \quad \mu_{yy} = \sum_{i=1}^{N_{bp}} (Y_i - Y_c)^2$$

$$\mu_{xy} = \sum_{i=1}^{N_{bp}} (X_i - X_c)(Y_i - Y_c)$$

N_{bp} is the total number of pixels and X_i Y_i the coordinates of a pixel i .

The principal axis PA that passes through GC is equal to: $tg(2\alpha) = 2\mu_{xy}/(\mu_{yy} - \mu_{xx})$ if $(\mu_{yy} - \mu_{xx}) \neq 0$. When the difference between μ_{xx} and μ_{yy} is equal to 0, the connected component does not present any orientation. Otherwise, the PA orientation is calculated clockwise in degrees (from 0° to 180° , 0° corresponding to the north). It is also possible to compute all the distances between GC and all the perimeter pixels; in this case, PA corresponds to the perpendicular to the straight line that links GC and the closest pixel belonging to the perimeter. It is then possible to measure the length and width of the rectangle circumscribing the studied landslide surface and calculate its ratio. As the principal axis PA intersects the shape perimeter in two points (D_1 and D_2), the direction D of the landslide can be computed (Ochoa-Tejeda and Parrot 2007). The relative hypsometric values of D_1 and D_2 permit to define a minimum (A_{min}) and a maximum (A_{max}). The direction D of the landslide corresponds to the straight line that links GC and A_{min} . The measurement of the direction, especially in the case of shallow (hypersaturated) debris slides allows defining zones that present an uniform slope gradient related to the triggering of such superficial mass movements.

There are many different procedures that allow defining a convex zone. Among them, the Jarvis's march such as it is described by Akl and Toussaint (1978) is a simple algorithm that efficiently draws a convex contour (Fig. 3).

The surface of the convex zone S_c (or the total number of pixels N_{tc} of this zone) and its perimeter P_c calculated in pixels or in meters allows calculating several parameters: the ratio S/S_c or the relation N_{bp}/N_{tc} that both correspond to two convexity indices based on the surface, the ratio P_c/P_p (perimeter convexity or external roughness index) or P_n/N_{tc} (porosity inside the convex zone).

Results

The morphometric parameters as well as the relationships between each other allow defining accurately the characteristics of the different extracted traces produced in the landscape by slope movements. Only two diagrams are reported here in order to illustrate some of the characteristics of these traces. The graph width versus length (Fig. 4a) reveals that, except for two items, small landslides essentially form a dense group of linear type; the relation width/length ranges from 0.2 to 0.8 with an average of 0.55; 40 % of the traces display a relation equal or inferior to 0.5 % and 24 % of them are inferior or equal to 0.4.

Two bigger landslides are present. The first one (symbol A in the Fig. 6) corresponds to a rotational landslide in the region of San Jose Chagchaltzin; it has an almost circular form (relation width/length of 0.82) with a width size of 238 m and a length of 289 m. The second landslide (symbol B in the Fig. 6) is located northwards the El Dos village; its length is equal to 480 m and the width to 90 m; the ratio width/length of this linear structure is equal to 0.18.

Figure 4b establishes the existing relation between the external roughness index P_c/P_p and the surface S . The more the index value decreases, the more irregular will be the studied shape. The majority of the studied landslides are grouped in the zone corresponding to small landslides having an almost regular form; the external roughness index of the cluster gravity center is equal to 75. Even if the large debris flow B is more elongated, it has the same P_c/P_p value. For the large rotational landslide A, even if it is almost circular, the great irregularity of its contour related to the heterogeneous topography during the rotational sliding implies a low value of the external roughness index. It should be noted that the porosity parameter of this item is the highest obtained in the studied zone.

All the possible combinations between the various parameters calculated in such a way have been tested; finally, because these indices present a weak correlation creating the strongest dispersion of all the points, the graph between the perimeter convexity index P_c/P_p and the ratio perimeter

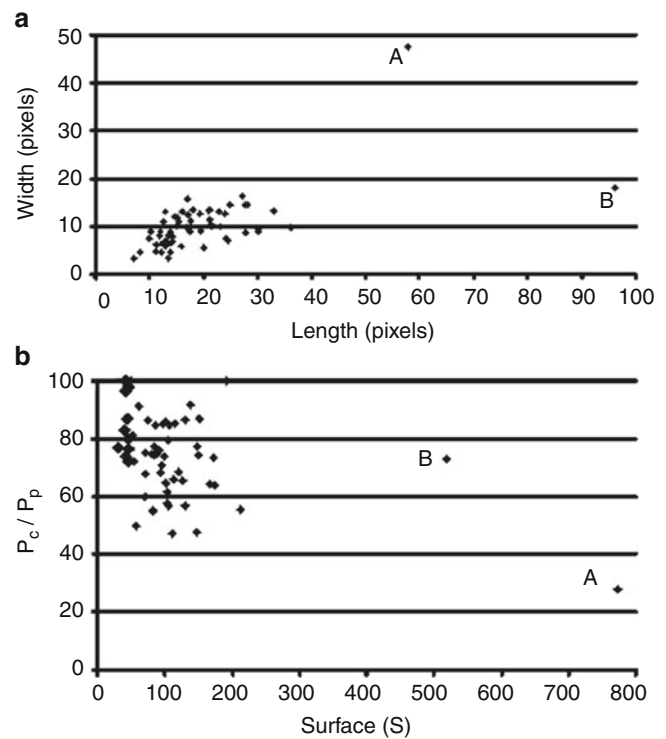


Fig. 4 Two examples of parameters correlation

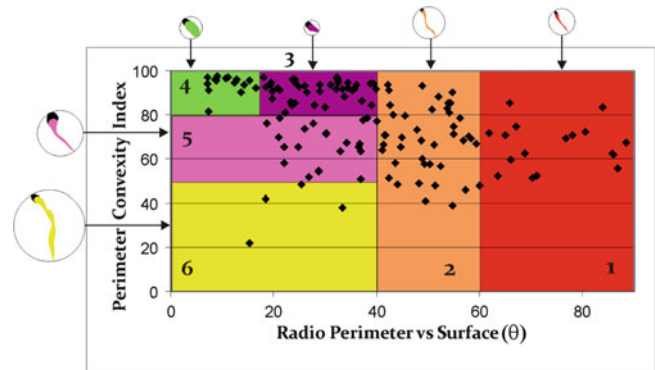


Fig. 5 Landslide classification using the diagram perimeter convexity P_c/P_p versus the ratio perimeter/surface $\theta = (L_p/S) \times 100$

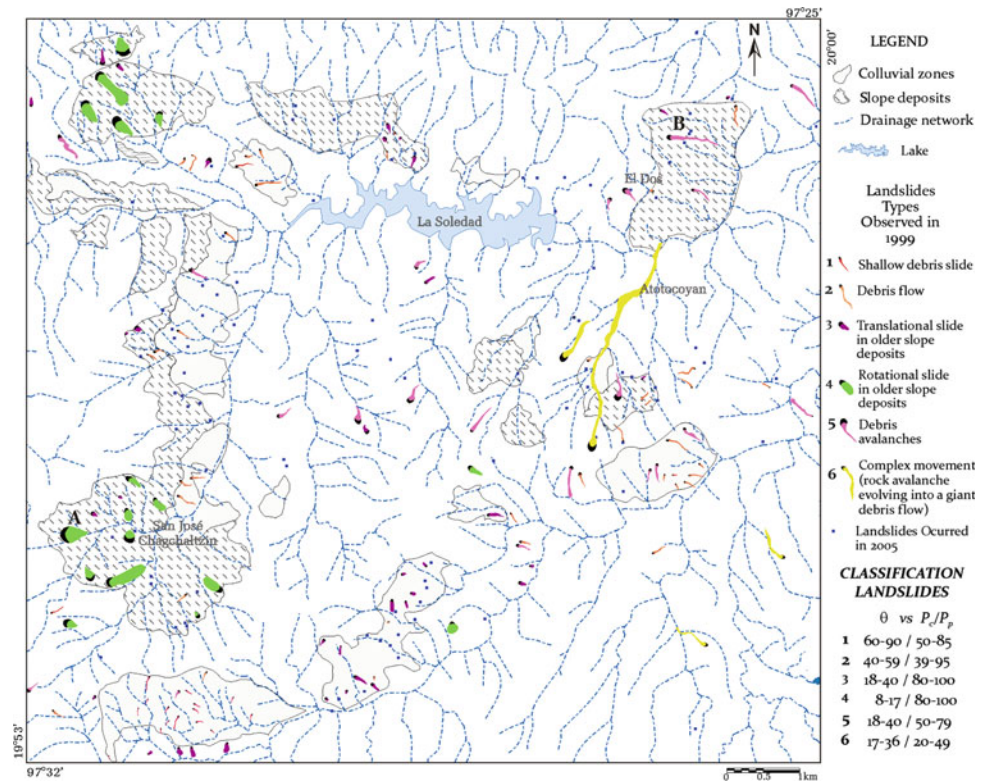
versus surface θ allows classifying better the different traces extracted from the Ikonos satellite image (see Fig. 5).

It is then possible to define six classes taking into account ranges of common values of these two parameters.

The parameter θ in fact reflects the globularity of a shape. Regardless of its length a line has a θ value equal to 100. This value decreases when this line thickens. Thus for a circle the size of which is greater than 150 pixels, the value θ is lower or equal to 10 and this value decreases when the circle is growing.

Dividing the θ axis in three groups, high, medium and low values, it may be noted that shallow debris slides correspond to θ values >60 , debris flow developed in slope deposits

Fig. 6 Repartition of the mass movement families in the studied region



have θ values comprised between 40 and 60, and many other features have a value <40 . Among these latter, a few items (large debris flows and complex movements) have a perimeter convexity index value <50 .

The last mentioned group corresponds to a very thick line, reason why its θ value is lower than 40, and the low value of the perimeter convexity index P_c/P_p indicates that the shape corresponds to a broken line (constrained by thalweg).

The following group (P_c/P_p between 50 and 80) corresponds to thick lines which present a slightly curved contour; all the debris avalanches are comprised in this group.

Finally convex forms have a P_c/P_p value greater than 80. Actually, according to field observations, it is possible to introduce a division in this last group.

We obtain then a class where are located the entirely convex shape of high globularity ($\theta > 18$) and another one where convex shape not so globular ($18 > \theta > 40$); this distinction allows to sort out rotational from translational landslides.

A label and a color are attributed to the different traces according to the landslide class they belong to. As shown by the Fig. 6, the six classes are not randomly distributed and different groups are perfectly distinguishable.

As presented in this figure, the shallow debris slides (1) are located on thin colluviums that especially cover the metamorphic rocks, and the debris slides (2) occur on thicker colluviums that correspond to a mixture of soils and broken metamorphic and sedimentary elements. The translational and rotational landslides (respectively 3 and 4) are essentially

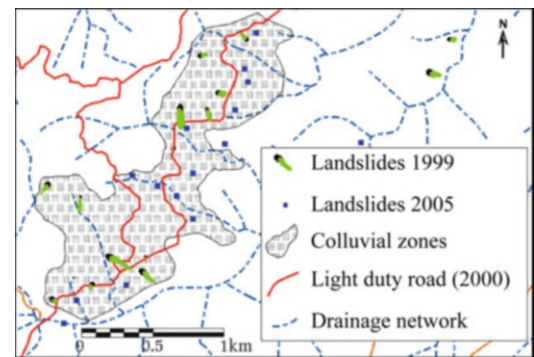


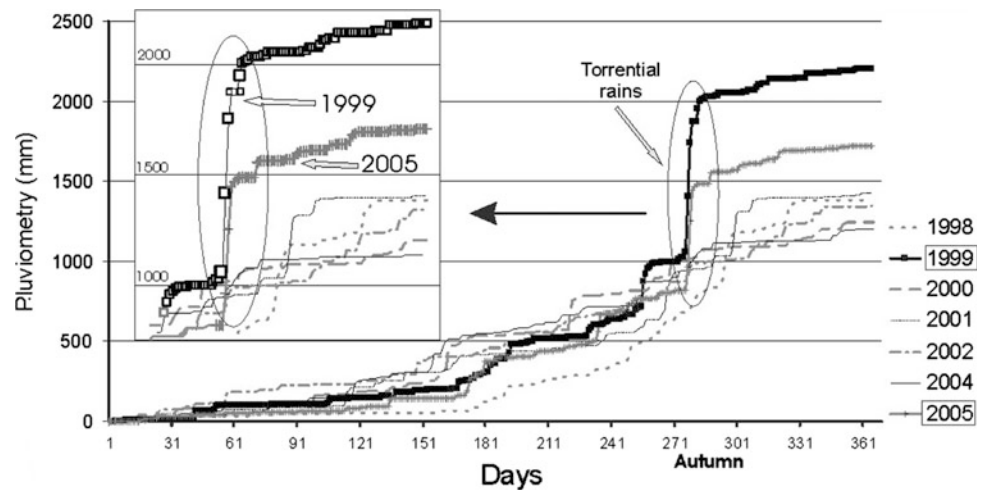
Fig. 7 Position of the October 1999 mass movements (extracted from the satellite image) and the landslides detected at the end of 2005

related to older slope deposits. Debris avalanches (5) are mainly observed in the folded and fractured metamorphic formations and the complex movements (6) are related to uncovered rock zones.

Discussion

According to the classification provided by using morphometric parameters, it is obvious that the distribution of the different mass movement types is not random, but corresponds to the material that can be involved in the movement. This is particularly clear for the linear traces remobilizing slope deposits. Thus it was possible to define geographical unstable

Fig. 8 Cumulative pluviometric curves during 7 years (1998 until 2005)



zones in a simple way and to characterize the type of events susceptible to be expected in a more or less short time according to the type of material that would be involved in the mass movement. For instance, on the main road linking Tlatlauquitepec and Atotocoyan (Fig. 7), shallow slides and superficial debris flows triggered by 2005 rainfall took place exactly at the location considered after the 1999 event as an unstable hillslope covered by thick unconsolidated colluviums.

The soil behaviour depends on its texture, porosity and mineralogical composition. In the present case, the colluvial formation reported in Fig. 7 comes from weathering, erosion and degradation of the upper part of the metamorphic formation. It is a very heterometric, easily broken material with a high porosity, and it can be rapidly saturated as it was the case in 1999 and 2005.

Parrot and Ochoa-Tejeda (2009) and Ochoa-Tejeda and Fort (2011) have recently shown the relationship existing between heavy rain periods (tropical hurricane) and the hillslope behaviour, hence mass movement types. For instance, as it occurred in 1999 (see Fig. 8), when a sequence of 3 days of intense rainfall was followed by a pause of 2–3 days, then by another short period of intense showers, the material remobilized by the mass movements affected not only the superficial slope deposits, but also uncovered rock zones. When the rainfall interruption is shorter as it occurred in 2005, the landslides affect mainly superficial formations, and may reactivate previous landslide zones.

The method presented in this paper appears quite efficient when extracting and characterizing shallow slides, debris flows and even debris avalanches, i.e. more or less linear structures. In contrast the sorting out of “globular”, compact and convex shapes appears more difficult and claims a perfect understanding of parameters significance. In a tropical mountainous area with relatively dense vegetation cover these traces are easier to extract than linear structures yet are

more difficult to classify. Even if the method needs some improvements in the definition of adaptive parameters to avoid this weakness, the algorithm is easy to implement and the output is obtained rapidly enough so that it can directly be used and implemented in crisis management by the authorities when infrastructures and populations are severely impacted by landslides occurrences.

Conclusion

We propose here a new method for extracting landslide traces from satellite images. The study area is a tropical mountain frequently subjected to torrential rains, and characterized by relatively dense vegetation cover and a variety of geological and superficial formations. The landslide traces were analyzed in using a set of morphometric parameters, including perimeter, surface, convexity, porosity, and defining some specific ratios. The method developed here allows characterizing and classifying easily different landslide types. It appears quite robust for identifying linear landslide types such as shallow debris slides, triggered by intense hurricane rains and causing most damages to the population and infrastructure. This method appears as fairly simple and rapid to implement, and its results are robust enough, so that it can be applied in other tropical regions as a useful tool in crisis management following landslide occurrences in areas of difficult access.

References

- Akl SG, Toussaint G (1978) Efficient convex hull algorithms for pattern recognition applications. In: Proceedings of the 4th international joint conference on pattern recognition, Kyoto, pp 483–487
- Alva-Valdivia LM, Goguitchaichvili A, Urrutia-Fucugauchi J, Ferrari L, Rosas-Elguera J, Zamorano-Orozco JJ (2000) Paleomagnetic data from the Trans-Mexican volcanic belt: implications for tectonics and volcanic stratigraphy. *Earth Planets Space* 52(7):467–478
- Angeles-Moreno E, Sánchez-Martínez S (2002) Geología, geoquímica y geología estructural de las rocas del basamento del macizo de

- Teziutlan, estado de Puebla. Professional thesis, Facultad de Ingenieria, UNAM, México, 105 p
- Carrara A, Cardinali M, Guzzetti F, Reichenbach P (1995) GIS technology in mapping landslide hazard. In: Carrara A, Guzzetti F (eds) *Geographical information systems in assessing natural hazards*. Academic, Dordrecht, 360p
- Collinson AJC, Anderson MG, Lloyd DM (1995) Impact of vegetation on slope stability in a humid tropical environment: a modeling approach. In: *Proceedings of the Institute Civil Engineers, Water Maritime and Energy*, vol 112. 168–175
- Cruden DM, Varnes DJ (1996) Landslides types and processes. In: Turner AK, Schuster RL (eds) *Landslides: investigation and mitigation*, vol 247, Special report: transportation research board., pp 36–75
- Fannin RJ, Wise MP, Wilkinson JMT, Rollerson TP (1996) Landslide initiation and runoff on clearcut hillslopes. In: *Proceedings of the 7th international symposium on landslides*, Trondheim, pp 195–199
- García-Ruiz JM, Beguería S, Alatorre LC, Puigdefábregas J (2010) Land cover changes and shallow landsliding in the flysch sector of the Spanish Pyrenees. *Geomorphology* 124:250–259
- Glade T, Anderson M, Crozier MJ (eds) (2005) *Landslide hazard and risk*. Wiley, Chichester, 803p
- Guinau M, Vilajosana I, Vilaplana JM (2007) GIS-based debris flow source and runoff susceptibility assessment from DEM data – a case study in NW Nicaragua. *Nat Hazards Earth Syst Sci* 7:703–716
- Hürlimann M, Copons R, Altimir J (2006) Detailed debris flow hazard assessment in Andorra: a multidisciplinary approach. *Geomorphology* 78:359–372
- Hutchinson JN (1988) General report morphological and geotechnical parameters of landslides in relation to geology and hydrology. In: Bornnard C (ed) *Proceedings of the fifth international symposium on landslides*, vol 1. A. A. Balkema, Rotterdam, pp 3–35
- INEGI (1994) *Carta Geologica de Poza Rica*. Esc: 1:250,000. Mexico
- Jadda M, Shafri HZM, Mansor SB, Sharifikia M, Pirasteh S (2009) Landslide susceptibility evaluation and factor effect. Analysis using probabilistic-frequency ratio model. *Eur J Sci Res* 33(4):654–668
- Mooser F (2000) *Mapa geológico de Laguna Verde*. Comision Federal de Electricidad, Mexico
- Nichol J, Shaker A, Wong M-S (2006) Application of high-resolution stereo satellite images to detailed landslide hazard assessment. *Geomorphology* 76:68–75
- Ochoa-Tejeda V (2004) *Propuesta metodologica para el estudio de inestabilidad a partir de los MDT y la Percepción Remota*. Master's thesis, UNAM, 213p
- Ochoa-Tejeda V (2009) *Control estructural de la inestabilidad de laderas: Modelación tridimensional de los rasgos geológicos. Aplicación al estudio de los procesos de remoción en masa de La Soledad, Sierra Norte de Puebla, México* (2009). Ph.D. thesis, Earth Sciences, Geophysical Institute, UNAM, 217p
- Ochoa-Tejeda V (2010) *Etude des facteurs favorables au déclenchement des glissements de terrain dans les formations superficielles et les affleurements rocheux de la Sierra Norte de Puebla (Mexique)*. Ph.D. thesis, Université Paris 7 Denis Diderot, Paris, France. 215p
- Ochoa-Tejeda V, Fort M (2011) Relation entre la pluviométrie et le déclenchement des glissements de terrain dans La Soledad, Sierra Norte de Puebla, Mexique. *Bull de l'Assoc des Géographes Français* 1:27–34
- Ochoa-Tejeda V, Parrot J-F (2007) Extracción automatizada de trazas de los deslizamientos utilizando un modelo digital de terreno e imágenes de satélite de alta resolución. Ejemplo de aplicación: La Soledad, Sierra Norte, Puebla, México. *Revista Mexicana de Ciencias Geológicas* 24(3):354–367
- Parrot J-F (2007) Tri-dimensional parameterization: an automated treatment to study the evolution of volcanic cones. *Géomorphologie* 3:37–47
- Parrot J-F, Ochoa-Tejeda V (2005) Generación de Modelos Digitales de Terreno Raster. Método de digitalización. *Geografía para el Siglo XXI*. UNAM, 31p
- Parrot J-F, Ochoa-Tejeda V (2009) Auto-related fractal analysis of triggering factors and landslide assessment. An example from the Sierra Norte de Puebla, Mexico. In: 6th annual meeting AOGS. Singapore, 11–15 Aug 2009
- Pratt WK (1978) *Digital image processing*. Wiley, New York, 750p
- Varnes DJ (1984) *Landslide hazard zonation: a review of principles and practice*. IAEG commission on landslides and other mass-movements. UNESCO Press, Paris, 63p



The 2010 Muddy-Debris Flow of Anganguero (Mexico): Modelling and Simulation

Jean-François Parrot and Veronica Ochoa-Tejeda

Abstract

In tropical mountainous regions, heavy rainfalls often induce landslides and mudflows. Mexico is continually subjected to natural hazards. In February 2010 the town of Anganguero in the state of Michoacán was devastated by a huge muddy debris flow. Use of morphological and climatic parameters of the affected areas can be incorporated into a model that simulates the extension of this natural disaster. It appears that zones whose slope aspect is against the flow direction represent the most vulnerable zones. The model described herein can easily and rapidly be applied to any other tropical region to reliably prevent such catastrophic phenomena. Because in many areas the colluvial slope deposits register multiple cracks and active scars, an assessment of the risk related to slope movements in Mexico is essential.

Keywords

Mudflow • Modeling and simulation • Anganguero • Michoacán state (Mexico)

Introduction

Observations of climatic change at a local scale are consistent with those obtained at a global scale. Unusual variation of precipitation can include torrential rains that, in a single event, can reach 150 mm on the plain and 250 mm in mountainous regions. Heavy and persistent rainfalls in mountainous areas can erode and modify the hill slope profiles and induce mudflows that are able to move stones, boulders and even trees (Mei et al. 2001). These heavy rainfalls and subsequent high levels of ground water flowing through cracked bedrock may trigger movement of sediment or soil when the slope material becomes saturated.

The movement of debris flows either in a thalweg or on the hill slopes depends on the erosive power of the water

flowing onto the sedimentary layers (Tognacca et al. 2000; Berti and Simoni 2005; Griffiths et al. 2004; Coe et al. 2008; Gregoretti and Dalla Fontana 2008; Fanti et al. 2010); a debris flow occurs when the runoff in a thalweg is greater than a critical value calculated empirically.

Muddy-debris flows often arise from slope-related factors. Shallow landslides that dam up riverbeds frequently result in temporary water blockage; this can markedly increase the volume of the flowing mass subsequently released, which in turn takes up the debris in the stream channel. The resulting solid-liquid mixture can reach densities up to 2 tons/m and velocities up to 14 m/s (Chiarle and Luino 1998; Arattano 2003).

Some broad mudflows are viscous and therefore slow (some m/s). Others begin very quickly and end like an avalanche. They are composed of at least 50 % silty and clayey material and up to 30 % water. Models that predict mudflow and debris flow velocities have been tested with 350 field and laboratory measurements (Julien and Paris 2010).

Ground movements are generated by two sets of factors: on one hand, natural conditions that control slope stability

J.-F. Parrot (✉)
LAGE, Instituto de Geografía, UNAM, Mexico City, Mexico
e-mail: parrot@igg.unam.mx

V. Ochoa-Tejeda
Université Paris Diderot, Sorbonne-Paris 7, UMR PRODIG
8586 – CNRS, France

and on the other hand, factors of climatic or anthropogenic origin (Dikau et al. 1996; Lang et al. 1999; Dai et al. 2002; Glade and Crozier 2005). Despite recent significant progress, the respective contribution of each factor to the mass movement or its reactivation is still not well understood (Guzzetti et al. 1999; Van Asch et al. 2007).

Mexico is subjected to various natural hazards such as earthquakes, floods and mass movements. Landslides newly generated by intense precipitations caused by hurricanes or tropical depressions constitute the most frequent hazard regularly affecting this country. Each year sees a drastic increase in the damage and number of casualties.

Between 2 and 5 February 2010, continuous rains were recorded in the town of Angangueo (State of Michoacán) with a peak of more than 200 mm on 4 February. The town was devastated by a huge muddy debris flow causing considerable loss and damage (33 fatalities, 61 disappearances, 5,000 people moved from their homes and 40 % of the urban structures destroyed or damaged). The behaviour of soil saturation has been shaped by the pluviometry, especially with four consecutive rainy days are observed (Parrot and Ochoa-Tejeda 2009; Ochoa-Tejeda and Fort 2011),

Landsliding is not limited to the spread of the rock mass on the slopes, but may also affect the valley bottoms. For instance, landslides can cause partial or total obstruction of the thalwegs leading to inflection of the river path or upstream flooding. The sudden rupture of this temporary dam can provoke disastrous floods carrying huge amounts of sediment that destroy infrastructure, roads and homes in the valley bottom where the rare flat spaces correspond to alluvial terraces.

Area Studied

Angangueo is a mining city in Michoacán state (Fig. 1). The city stretches along the Puerco river, a narrow and deep valley between the Chincua Sierra and the Sierra Rancho Grande where the Monarca butterfly sanctuaries are located. From upstream to downstream, there are three Lead Zinc mines (El Ventilador, Catingon and San Luis).

The ubiquity of landslides in the Angangueo area is mainly related with: (a) the Pleistocene volcanic material that forms the basement and its geo-structural characteristics; (b) frequent earthquakes in the neighboring regions of Tlalpujahua and Zitácuaro; (c) extraordinary and intense rainfalls inducing severe soil saturation and consequently the loss of cohesion and local failures; (d) slope disturbance in relation with animal activity and slope excavations; (e) the rapid development of road networks carried out with minimal

technical means, without prior understanding of the morphoclimatic and hydrological dynamics prevailing in these subtropical mountains.

The area mainly affected in February 2010 lies between the two blue points (Fig. 2a, b), where there was considerable damage (Fig. 3) and the Catingon mine at the confluence between Puerco river and Charco river (red point) was destroyed (Fig. 4).

The material mobilized by the landslides corresponds to colluvial deposits resulting from alteration and fragmentation of the volcanic formation. These colluvial deposits vary in particle size, ranging from clay layers containing centimetric fragments up to clusters of boulders of metric size (Fig. 5).

Many slopes still show dislodgement of these colluviums, and multiple cracks and active scars, foreshadowing future mass movements. Recent accumulation areas were observed on the river banks upstream of Angangueo. We assume that landslides are consecutive to saturation of colluvial deposits through a temporary retention of water, an event followed by a sudden discharge of mud flows. The first step in the following simulation is based on this observation.

Method

A simulation was used to analyze the 2010 disaster, to define the total amount of mobilized material and to assess local vulnerability inside the narrow valley where the town lies. The modeling takes into account the following considerations based on field observations: (1) mass movements are not confined to the spread of the rock mass slopes, but may also affect the valley bottom; (2) landslides occurring upstream of the city created a temporary dam that retained a part of the water flux coming from mountainsides; (3) the pressure of water flows breached the temporary dam and generated a large mudflow composed of a mixture of water and soils derived from slope colluviums; (4) during its displacement, the mudflow dislodged debris and boulders on its passage; and (5) the mudflow volume increased with contributions from the tributary streams.

Following this scenario, taking into account the total volume available and doing successive approximations of the mudflow thickness, we could estimate the extension of the mud and debris flow and localize the affected zones.

In assessing the risk related to muddy-debris flows in the study area, the research takes into account the following three axes:

- **Identification of potential hazards and dangerous areas.** Field study is essential to accomplish this goal.

Fig. 1 Location of the studied zone

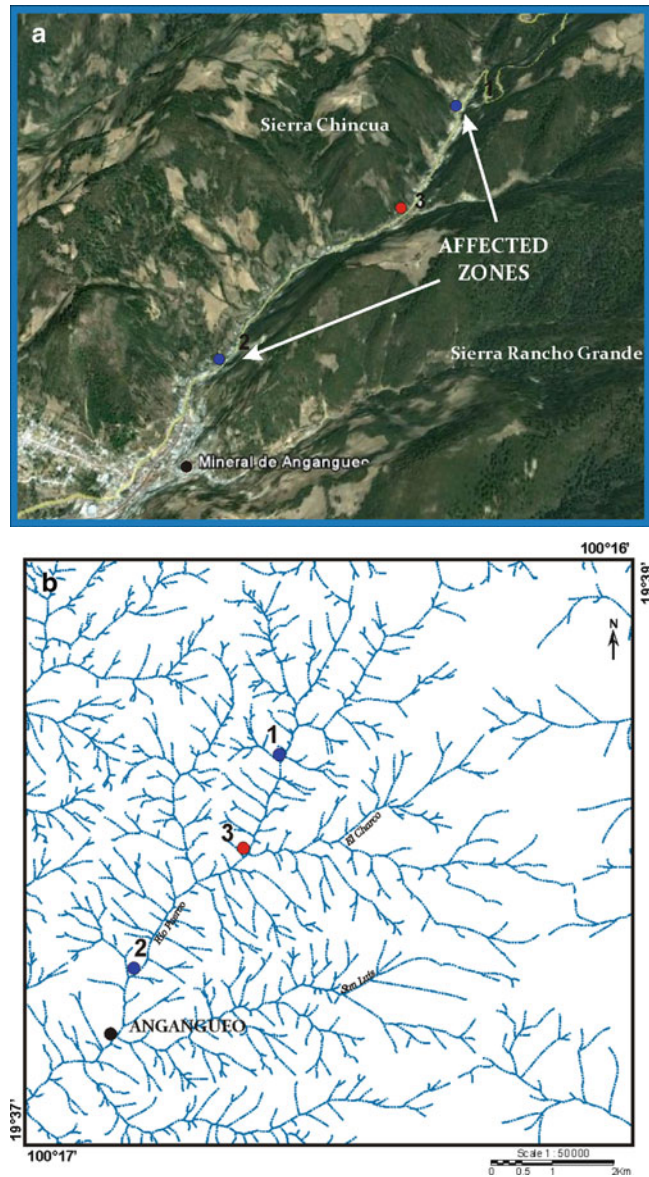
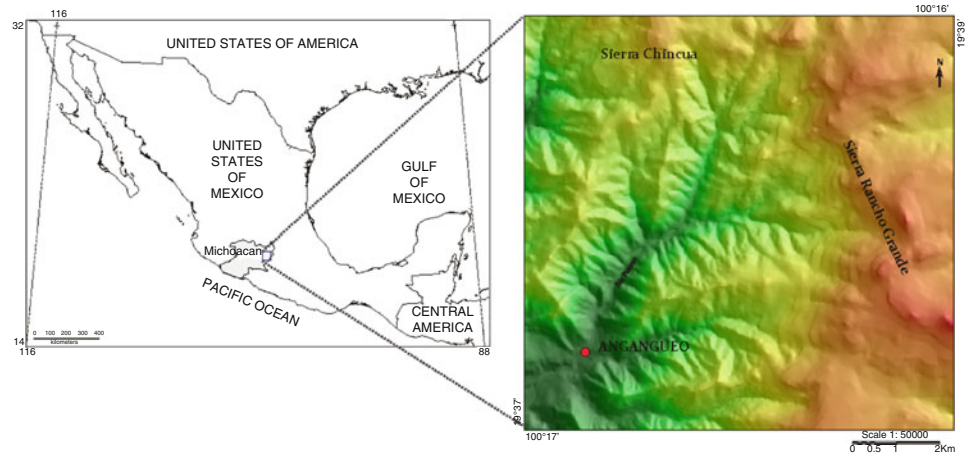


Fig. 2 (a) Affected zones reported on a 3D Google earth image. (b) Drainage network.. *Points 1 and 2*: upper and lower limits of the area affected by debris flow, February 2010. *Point 3*: confluence of the Puerco and Charco rivers



Fig. 3 Examples of damaged zones along the river bed and the intervention of the Michoacán State Civil Protection Authority during the disaster

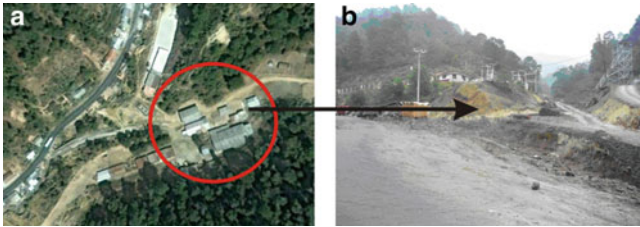


Fig. 4 Lead zinc Catingon mine. (a) Google earth image acquired September 3, 2006. (b) Mine destruction from February 2010 (Photograph, June 2010)

In particular we need to distinguish the “favorable” factors that promote a priori slope instability (type of material and faults), the triggering factors (precipitation), the predisposing factors (fluvial erosion on the slopes) and the aggravating factors (road construction, slope modification related to human activity).

- **Characterization of the mud flows.** Mud flows must be studied with the help of topographic documents, diachronic satellite images and high-resolution Digital Elevation Model (DEM) to link frequency and magnitude.
- **Vulnerability evaluation.** Vulnerability is estimated at several levels and dynamically according to the existing interactions between the active elements of the physical environment and of human activities.

The method is based on field data and on a high-resolution DEM derived from a multidirectional interpolation (Parrot and Ochoa-Tejeda 2005) applied on 1:50,000 contour lines. Despite a few inherent artifacts related to this

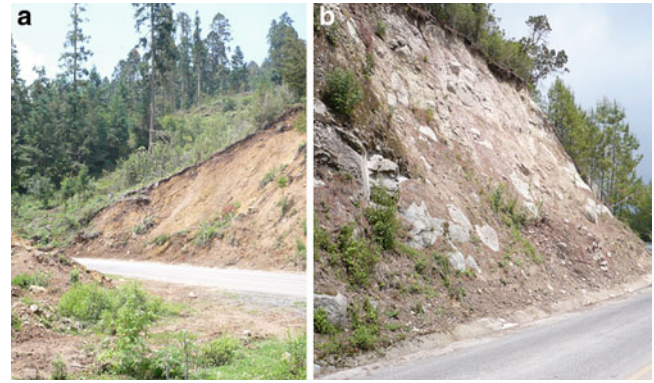


Fig. 5 Types of material involved in the process. (a) Clay layers containing rocky fragments. (b) Clusters of boulders of metric size

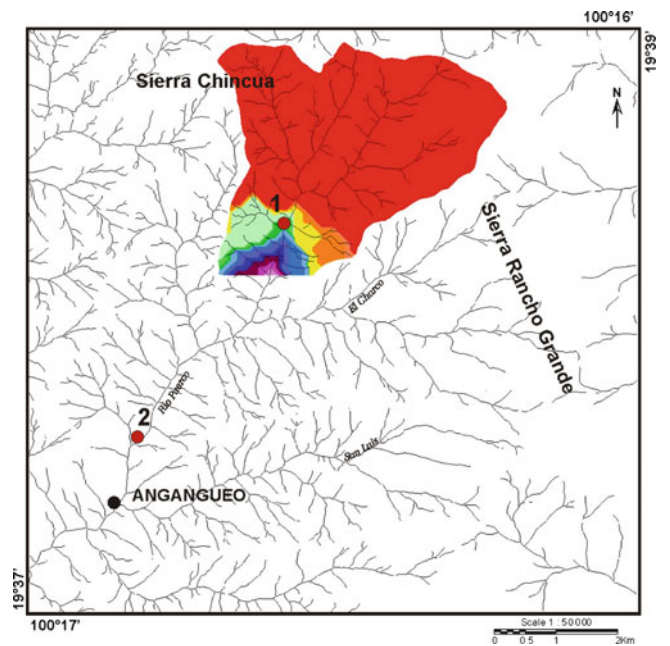


Fig. 6 Example of volumetric calculation in a catchment area taking into account the lateral contributions as shown in Fig. 7. In red the whole catchment area above 2,837 m

data type, it is possible to obtain a DEM good enough to realize the simulation. The pixel resolution is 5 m and the vertical scale is centimeters.

Results

The modeling involves the following steps:

- (a) Calculation of the available fluid volume at the triggering point of the mass movement; this calculation is based

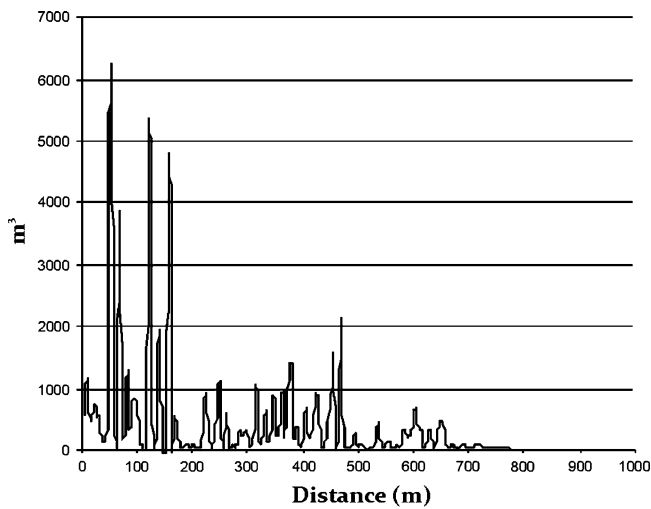


Fig. 7 Example of lateral inputs between 2,836 and 2,737 m a.s.l., calculated every 5 m (DEM resolution)

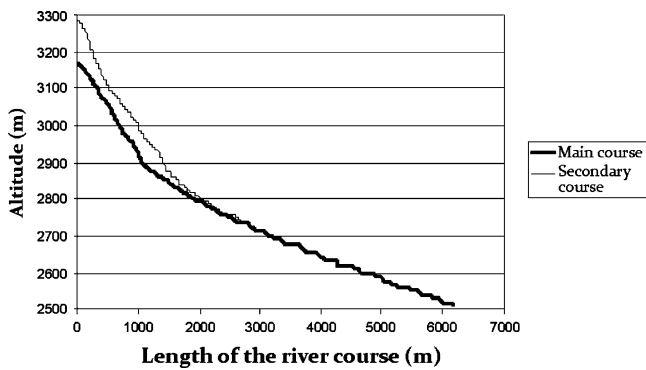


Fig. 8 Puerco and Charco profiles

on the rainfall rate and the surface area of the catchment (Fig. 6). This step also includes an estimation of the volume of the mobilized material to determine the viscosity of the mudslide since the viscosity is, with the slope, one of the factors that define the velocity of the movement.

It is also necessary to calculate all the inputs received laterally along the river course (Fig. 7). The calculated volume depends on the local catchment configuration (Fig. 8). For instance, at the confluence between the Puerco and Charco rivers (2,735 m a.s.l.), the volume of the water collected in the two catchment areas is, respectively, 3,54,687.5 and 3,82,972.5 m³ for a 100 mm rainfall.

- (b) Calculation of the maximum height reached by the flooding according to the volumes of water available at the starting point (Fig. 9); according to this, for a given volume of water (in this case 250,000 m³) derived from

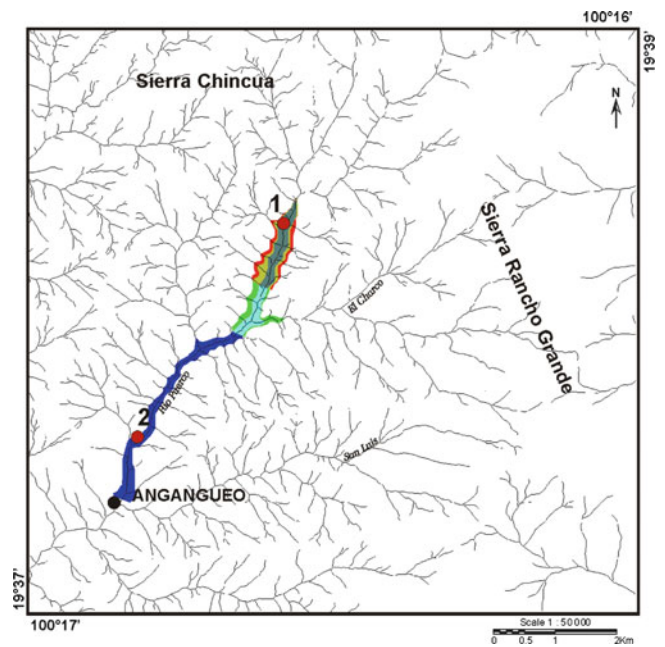


Fig. 9 Simulation of the flow extension according to the thickness of the flux

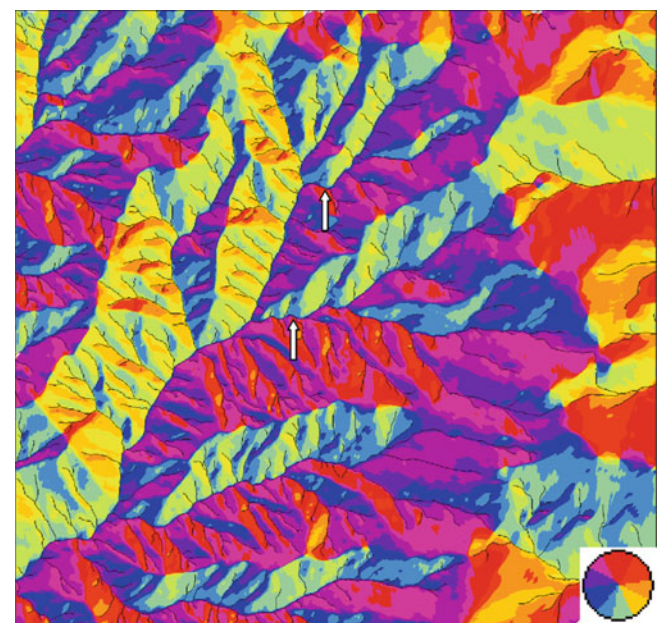


Fig. 10 Example of an area where slope aspect is against the flow direction. Circle in the bottom right corner: palette progressing from 0° to 360°. Arrows: slope aspect is against the flow direction decomposed in vectors

the initial catchment area and lateral inputs, the maximum thickness of the mud flow reaches 1.80 m. The balance is negative for 2 m (in red in the figure) and positive for a value of 1.5 m (in green in the figure) or

1 m (in blue in the figure). In the last case, the flow even reaches the city lying 5 km from the starting point.

- (c) Research of the more vulnerable points within the thalweg, presumed to correspond to zones whose slope aspect is against the flow direction (Fig. 10).

The aspect is calculated and reported in an image that does not present any rupture as generally observed in this kind of document. The painter palette permits a progression from red corresponding to the North (0°) to yellow (120°) passing through orange tones, and then from yellow to blue (240°) passing through green tones and finally coming back to the red passing through violet tones.

Zones where the slope aspect is against the flow direction decomposed in vectors are considered as particularly vulnerable regions (see white arrows).

Conclusion

Simulations allowed assessment of the extension of the mud and debris flow observed in Anganguero according to different scenarios. Such an approach permits objective definition of the vulnerability of each point along the river in order to take measures to prevent or alleviate disaster effects.

The method requires a modeling that takes into account the landscape configuration, the type of material involved in the movement, the pluviometric rate and a realistic scenario. It is then possible to assess the muddy debris flow extension and localize the affected zones. Among them, zones whose slope aspect is against the flow direction seem to be the most vulnerable zones. Results obtained easily and rapidly by this method can be applied in other tropical regions in order to allow crisis management by the authorities. Presently, in many areas upstream of Anganguero, the colluvial slope deposits register multiple cracks and active scars that presage future mass movements. An assessment of the risk related to slope movements in Mexico appears essential.

References

- Arattano M (2003) Monitoring the presence of the debris-flow front and its velocity through ground vibration detectors. In: Rickenmann D, Wieczorek GF (eds) Debris-flow hazards mitigation: mechanics, prediction, and assessment. Proceedings of the 3rd international conference, Davos, Switzerland, 10–12 Sept 2003. Mill Press, Rotterdam
- Berti M, Simoni A (2005) Experimental evidences and numerical modelling of debris flow initiated by channel runoff. *Landslides* 2(3):171–182
- Chiarle M, Luino F (1998) Colate detritiche torrentizie innescate dal nubifragio dell'8 luglio 1996 sul M. Mottarone (VB-Piemonte). *Convegno Internazionale: "La prevenzione delle catastrofi idrogeologiche: il contributo della ricerca scientifica"*, Alba, CN, 5–7 novembre 1996. vol II, pp 231–245
- Coe JA, Cannon SH, Santi PM (2008) Introduction to the special issue on debris flows initiated by runoff, erosion, and sediment entrainment in western North America. *Geomorphology* 96:247–249
- Dai FC, Lee CF, Ngai YY (2002) Landslide risk assessment and management: an overview. *Eng Geol* 64:65–87
- Dikau R, Brunsden D, Schrott L, Ibsen ML (1996) *Landslide recognition: identification, movement and causes*. Wiley, Chichester/Royaume Uni, 274p
- Fanti R, Gigli G, Morelli S, Arreygue Rocha E (2010) The catastrophic debris-flow of Minatitlan (Colima, Mexico): description and modeling. In: *Proceedings of mountain risks: bringing science to society*, Firenze, 24–26 Nov 2010, pp 243–248
- Glade T, Crozier MJ (2005) The nature of landslide hazard and impact. In: Glade T, Anderson MG, Crozier MJ (eds) *Landslide hazard and risk*. Wiley, London, pp 43–74
- Gregoretti C, Dalla Fontana G (2008) The triggering of debris flow due to channel-bed failure in some alpine headwater basins of the Dolomites: analyses of critical runoff. *Hydrol Process* 22:2248–2263
- Griffiths PG, Webb RH, Melis TS (2004) Frequency and initiation of debris flows in Grand Canyon, Arizona. *J Geophys Res* 109 (F04002):1–14
- Guzzetti F, Carrara A, Cardinali M, Reichenbach P (1999) Landslide hazard evaluation: a review of current techniques and their application in a multi-scale study, central Italy. *Geomorphology* 31:181–216
- Julien PY, Paris A (2010) Flow velocities for mudflows and debris flows. *J Hydraul Eng* 136(9):676–679
- Lang A, Moya J, Coromina S, Schrott L, Dikau R (1999) Classic and new dating methods for assessing the temporal occurrence of mass movements. *Geomorphology* 30:33–52
- Mei CC, Liu KF, Yuhi M (2001) Mud flow – slow and fast. In: Provencale A, Balmforth N (eds) *Geomorphological fluid mechanics*, vol 582, Lecture notes in physics. Springer, Berlin/New York, pp 548–577
- Ochoa-Tejeda V, Fort M (2011) Relation entre la pluviométrie et le déclenchement des glissements de terrain dans La Soledad, Sierra Norte de Puebla, Mexique. *Bull Assoc Géogr Fr* 1:27–34
- Parrot J-F, Ochoa-Tejeda V (2005) Generación de Modelos Digitales de Terreno Raster. Método de digitalización. *Geografía para el Siglo XXI*, UNAM, 31p
- Parrot J-F, Ochoa-Tejeda V (2009) Auto-related fractal analysis of triggering factors and landslide assessment. An example from the Sierra Norte de Puebla, Mexico. In: 6th annual meeting AOGS, Singapore, 11–15 Aug 2009
- Tognacca C, Bezzola GR, Minor HE (2000) Threshold criterion for debris-flow initiation due to channel-bed failure. In: Wieczorek GF, Naeser ND (eds) *Debris-flow hazards mitigation: mechanics, prediction and assessment*. A. A. Balkema, Rotterdam, pp 89–97
- Van Asch TWJ, Malet JP, Van Beek LPH, Amitrano D (2007) Techniques, issues and advances in numerical modelling of landslide hazard. *Bull Soc Géol Fr* 178(2):65–88



A Rock Fall Analysis Study in Parnassos Area, Central Greece

George Papathanassiou, Vasilis Marinos, Dimitris Vogiatzis, and Sotiris Valkaniotis

Abstract

The paper presents the kinematics of rock instability of a high promontory, where Tithorea village is situated, in the Central Greece peninsula. The instability phenomena pose a significant threat on the town situated immediately down slope. Rock fall episodes occurred in the past, as it has been noted by local authorities and published reports. A more recent rockfall is investigated in this paper, which caused considerable damages to two village houses. The detailed rock fall path was mapped obtaining more than 15 hit points and rolled on different scree and vegetation material till it stopped and crushed upon the house roofs. The predominant types of kinematic instability are of planar or wedge failure and toppling of large blocks. In order to investigate the existing stability conditions and decide upon the protection measures, rockfall analysis was carried out. Such an analysis can be compared in detail with the actual situation, since the geometrical data of the recent rockfall incident are very accurate. On the other hand, other parameters of rockfall hazard such as the run-out distance of the boulders was examined.

Keywords

Rockfall • Hazard • Limestone • Protection measures • Run-out distance • Tithorea • Greece

Introduction

A rock fall is a fragment of rock detached by sliding, toppling or falling that falls along a vertical or sub-vertical cliff, proceeds down slope by bouncing and flying along ballistic trajectories or by rolling on talus or debris slopes (Varnes 1978). Very occasionally, rockfall initiates catastrophic debris streams, which are even more dangerous (Hsu 1975). Distinct evidences of rockfall are talus slope deposits at the foot of steep cliff faces, but also on slopes covered with vegetation where evidence is less distinct. Minor rockfalls can be met in almost all the rock slopes, whereas large size ones such as cliff falls and rock avalanches, affect only great rock slopes

with geological conditions favourable to instability (Rouiller et al. 1998).

The detachment of rock from bedrock slope is triggered by several factors such as weathering, earthquake and human activities while the fall of a rock is determined by factors like the slope morphology and the properties of the direct surrounding of the potential falling rock (Dorren 2003). The generation of a rockfall is a rapid phenomenon and represents a continuous hazard in mountain areas worldwide. There are numerous examples of infrastructure destroyed or people killed by rockfall. To protect endangered residential areas and infrastructure, it is necessary to assess the risk posed by rockfall.

On December 19, 2010, a rockfall event took place at the mountainous area of Parnassos inducing structural damages at the village of Tithorea. According to the examination of the slope and to eyewitnesses, the source area of the rockfall was located at the elevation of 770 m (Fig. 1).

G. Papathanassiou (✉) • V. Marinos • D. Vogiatzis • S. Valkaniotis
Department of Geology, Aristotle University of Thessaloniki,
Thessaloniki, Greece
e-mail: gpapatha@auth.gr

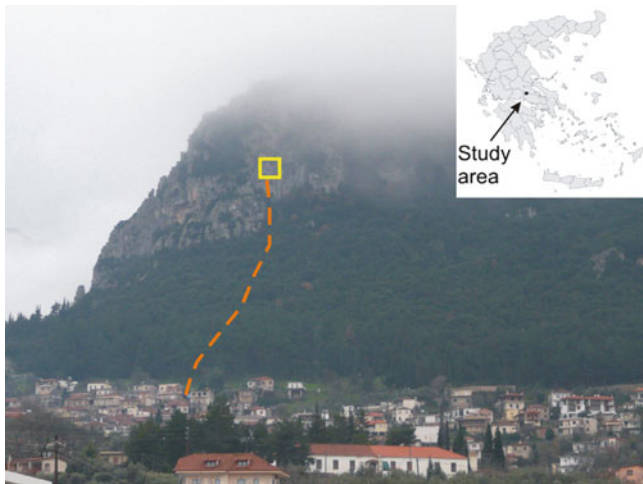


Fig. 1 The Tithorea rockfall in Parnassos area



Fig. 2 Barrier constructed in order to reduce the rockfall hazard and in only a part of the slope

Similar events were reported, in 1957 and 1999 and induced structural damages at houses. These events were located few meters away from the damaged by the 2010 event one. In order to reduce the rockfall hazard and to avoid future structural damages, local authorities constructed a barrier at the foot hill of the mountain (Fig. 2). However, as it was indicated by the 2010 event, further measures should be designed and constructed.

An in site-investigation was done mapping the detailed rock fall path and obtaining more than 15 hit points, since the remnants were fresh and clear. The hit-points involved trees, low vegetation, scree material (soft soil cover or limestone boulders).

The goal of this study is to assess basic parameters of the rockfall trajectory of the December 19, 2010 failure and evaluate the rockfall hazard in the area of Tithorea village. The rockfall analysis was done using the software Rocfall of

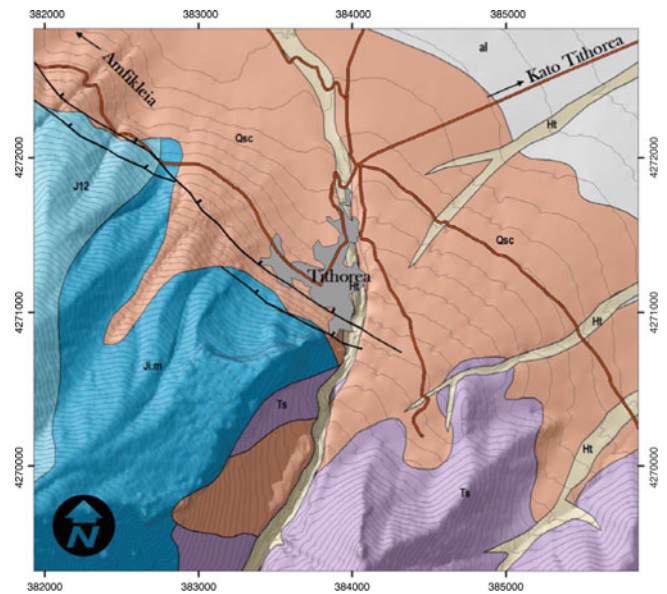


Fig. 3 Geological map of the Parnassos area. *Ht* Holocene stream bed loose deposits (sand and gravel), *al* recent alluvial and floodplain deposits, *Qsc* colluvial deposits, slope fan debris and conglomerates (quaternary), *J12* thick-bedded, dark limestones (upper Jurassic), *Ji-m* dark-coloured bituminous limestones (middle-lower Jurassic), *Ts* crystalline dolomites (upper Triassic)

the Rocscience Inc. and the estimation of the rockfall hazard as the run-out distance of boulders was done using the methodology of shadow angles.

Geological Setting

The area under study is part of the Parnassos-Gkiona geotectonic Zone, according to Renz (1940). This is comprised mainly of alpine neritic carbonate rocks (i.e. dolomite, limestone and oolite limestone) and a Palaeocene-Eocene flysch, whereas the pre-alpine basement does not outcrop and any igneous bodies are absent (Fig. 3). At the base of the nearly vertical rock, scree material are evident consisted mainly by boulders covered by soft clayey eroded geomaterial. River deposits are met in lower altitudes, at the end of the Tithorea village.

As far as the tectonic regime is concerned, Tithorea is situated in the southern rim of the Kifissos Basin, along the Tithorea – Amfiklia Fault Zone (Valkaniotis 2009). Tithorea – Amfiklia Normal Fault Zone consists of two fault segments, part of the Kifissos Basin Fault System, showing propable recent (Late Pleistocene – Holocene) activity (Philip 1974; Mercier et al. 1979; Ganas and White 1996; Valkaniotis 2009). Parallel fault scarps are found across the slope, from the fault scarp bounding limestone bedrock and talus south of the Tithorea village, to the area north of the village. Dense faulting and fracturing in the bedrock is the main factor



Fig. 4 Damaged house and the boulder of the 19 December 2010

controlling steep topography and rock instability, leading to numerous rock falls.

Tithorea Rockfall Event on 19 December 2010

At 20:45 on 19 December 2010, a rockfall occurred from the Parnassos mountain. A boulder of approximately 10 m^3 in volume detached from the source area and caused significant damages on two houses of the village Tithorea, without any casualties (Fig. 4). Regarding the triggering mechanism, it is believed that a combination of meteorological and lithological conditions generated the rockfall. The week before the event, heavy rainfall was dropped and low temperatures during the night were recorded. Thus, taking into account the heavily jointed nature of the rock and the low drainage due to heavy rainfall and low temperatures, which froze the water, it is believed that the water pressure was increased and generated the rockfall.

Few days after the rockfall event, a field survey took place in order to map and study the fall track of the boulder. A total of 15 impact-points, reported as craters, and silent witnesses such as broken trees (Fig. 5) were mapped and recorded using GPS instrument.

The collected data have been introduced into GIS software, ArcGIS, and the longitudinal profile of the fall track was compiled. As it is shown in Fig. 6, the detachment area of the rockfall is at the elevation of 770 m and the lowest recorded crater, at the end of pine forest, is at the elevation of 470 m. Based on our observation, the initial volume of the boulder was larger since at the first impact-point we have mapped traces of a split. Regarding the vegetation the rock



Fig. 5 Silent witnesses of the fall track

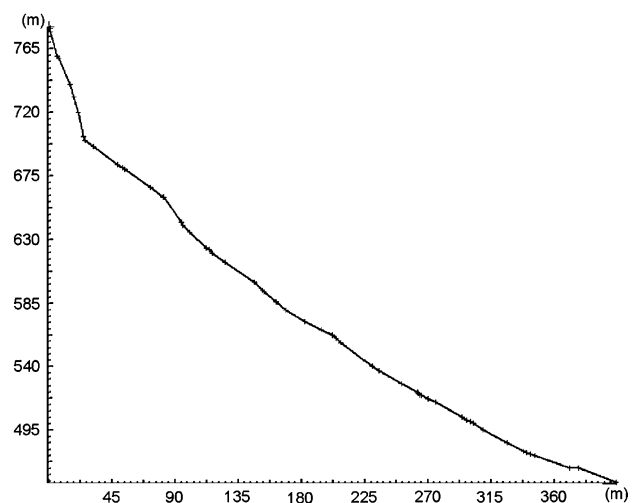


Fig. 6 The longitudinal profile

rolled on, two zones have been mapped; the first one, located at the upper part of the fall track, is characterized by low-vegetation, while the second zone, toward the village, is an artificial pine forest.

Evaluating Rockfall Hazard

The goal of our study was twofold; the assessment of the bounce height and the kinetic energy of the boulder that caused structural damages on two houses in the village of Tithorea and the estimation of the run-out distances of rock-fall events. These goals were achieved by applying empirical methods and computer-based models concerning the landslide hazard mapping in regional scale and using software in order to simulate the fall of a boulder down a slope and to define the fall tracks.

Simulating the Rockfall Trajectory

The fall track of the rockfall was simulated using the Rocfall software, which is a robust, easy to use computer program that is available from Rocscience and performs a probabilistic simulation of rockfalls and can be used to design remedial measures and test their effectiveness.

As it was shown in several applications of this methodology, the runout of a rockfall is influenced by the geological characteristics of the slope materials and the roughness of slope. The former influence the loss of energy during impacts and the latter the type of rockfalling. Although the fact that in our study we simulate the fall track of a large size boulder, we took into consideration the slope roughness by employing a value of 5 in the relative field of Rocfall software.

Moreover, one of the most important and difficult issues for the simulation of a fall track is the reliability of the employed material properties. Typical values for the coefficient of normal (R_n) and tangential (R_t) restitution used in rockfall analyses range from 0.3 to 0.5 and from 0.8 to 0.95, respectively (Stevens 1998). In this study, the values of R_n and R_t that were used for the areas characterized as talus cover, talus with vegetation, soil with vegetation, asphalt was taken as proposed by Rocfall software while the relative employed parameters for the limestone (clean hard bedrock) were based on the suggestions by Robotham et al. (1995). The initial point in the model has been reported during the field survey and was defined as a single point in Rocfall software.

It should be noted that the output of the simulation, regarding the horizontal location of the craters is in agreement with the observed fall track, validating our scenario.

Having validated the basic parameters of the fall track, we proceeded to the estimation of the kinetic energy and the bounce height of the boulders using a collector of data that is located at the boundary between the forested and the urban area (Fig. 7)

As an outcome of the simulation of the fall track, we concluded that there is 20 % possibility for a boulder to

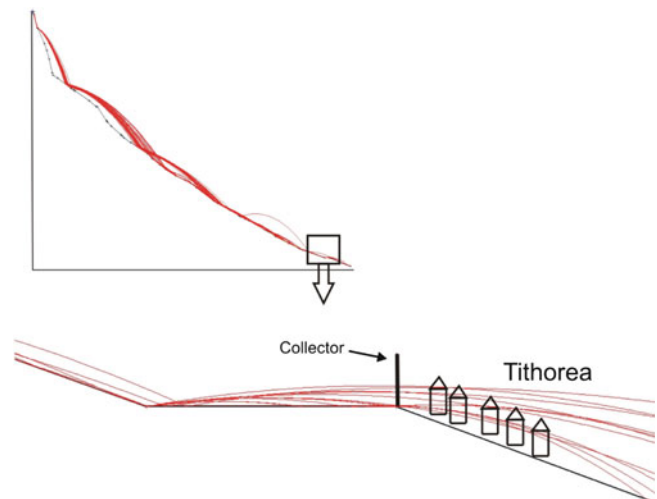


Fig. 7 Data collector located between the urban area of Tithorea and the artificial pine forest

reach the urban area of Tithorea; 11 of 50 rock blocks that were used as sample in our study went beyond the data collector point. In addition, the total kinetic energy that was recorded at collector varies from 8,000 to 27,000 kJ and the bounce height of the boulders was lower than 0.5 m (Fig. 8a–c). Thus, in case of design and construction of remedial measures in this point, the estimated values provided by this study could be used in order to avoid future structural damages.

Rockfall Hazard Assessment

The rockfall hazard for the Tithorea area is examined here by estimating the run-out distance of the boulders. Empirical rockfall models are generally based on relationships between topographical factors and the length of the run-out zone (Dorren 2003). Usually, the parameters to describe the rockfall runout zones can be the angle or the horizontal distance (Petje et al. 2005). In general, two methods are mainly applied for the estimation of the maximum distance that a boulder can reach. The first model, Fahrboschung angle, was suggested by Heim (1932) and predicts the run out zone using the angle that is defined by the horizontal plane and the line from the top of a rockfall source scar to the stopping point for any given rockfall. The second method is the model known as minimum shadow angle proposed by Evans and Hungr (1993), which were based on Lied (1977). According to them, the area beyond the base of a talus slope that is reached by large size boulders is termed the rockfall shadow and the equivalent shadow angle is defined as the angle between the outer margin of the shadow and the apex of talus slope. The distal part of the shadow often contains only very few boulders, which are sparsely distributed on the surface (Evans and Hungr 1993).

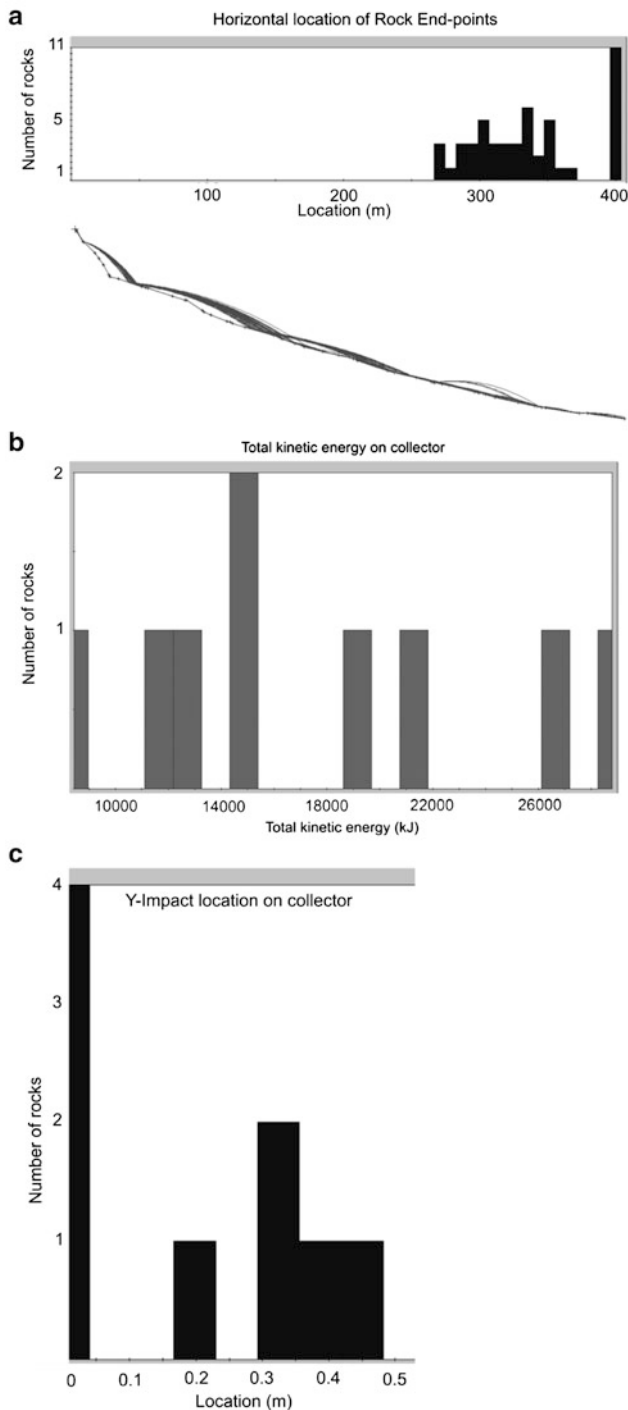


Fig. 8 (a) End-points of the sample of rocks introduced to the simulated fall track on Rocfall, (b) total kinetic energy of the boulders as it was recorded by the data collector, (c) bounce height of the boulders as it was recorded by the data collector

Evans and Hungr (1993), having investigated 16 talus slopes in British Columbia, suggested that a minimum shadow angle of 27.5° is adequate for a preliminary estimation of a rockfall runout distance while Dorren (2003) having compared the

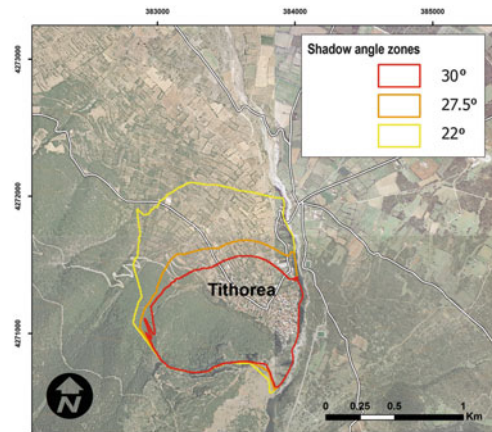


Fig. 9 Map showing the delineated shadow angle zones of 30° , 27.5° and 22°

outcomes of several studies, concluded that the angle lies between 22° and 30° .

In our study, the shadow angle method was taken into account because shows acceptable reliability at a large scale (Meibl 2001; Copons and Vilaplana 2008) and due to the fact that is more suitable comparing to Fahrboschung angle model which predicts an excessively long travel distance (Evans and Hungr 1993; Wiczorek et al. 1999). Taking into consideration the proposed values of shadow angle, 22° , 27.5° and 30° , relevant zones of run-out distances were compiled (Fig. 9).

As it is shown in Fig. 9, part of the village of Tithorea is situated within the area that is delineated by the shadow angles of 30° and 27.5° . Moreover, taking into account the most conservative scenario, the whole area of Tithorea is included within the shadow angle of 22° zone. Thus, the landslide hazard both for the houses at Tithorea and the road network can be characterized as high and protection measures should be constructed in order to avoid rockfall-induced damages.

References

- Copons R, Vilaplana JM (2008) Rockfall susceptibility zoning at a larger scale: from geomorphological inventory to preliminary land use planning. *Eng Geol* 102:142–151
- Dorren L (2003) A review of rockfall mechanics and modelling approaches. *Prog Phys Geogr* 27:69–87
- Evans SG, Hungr O (1993) The assessment of rockfall hazard at the base talus. *Can Geotech J* 30:620–636
- Ganas A, White K (1996) Neotectonic fault segments and footwall geomorphology in Eastern Central Greece from Landsat TM data. *Geol Soc Greece Spec Publ* 6:169–175
- Heim A (1932) Bergsturz und menschenleben. *Beiblatt zur Vierteljahrsschrift der Naturforschenden Gesellschaft in Zurich* 77:218
- Hsu KJ (1975) Catastrophic debris streams generated by rockfalls. *Geol Soc Am* 86:129–140
- Lied K (1977) Rockfall problems in Norway, Bergamo publication, vol 90. Instituto Sperimentale Modelli e Strutture, Bergamo, pp 51–53

- Meibl G (2001) Modeling the runout distances of rockfalls using a geographic information system. *Z Geomorphol* 125:129–137
- Mercier JL, Delibassis N, Gauthier A, Jarrige JJ, Lemeille F, Philip H, Sebrier M, Sorel D (1979) La néotectonique de l'Arc Égéén. *Rev Geol Dyn Geogr Phys* 21(1):67–92
- Petje U, Ribicic M, Mikos M (2005) Computer simulation of stone falls and rockfalls. *Acta Geographica Slovenica* 45(2): 93–120
- Philip H (1974) Etude néotectonique des rivages égéens en Locride et Eubée nordoccidentale (Grèce). Thèse doc. sp., Acad. de Montpellier, 86p
- Renz C (1940) Die tektonik der griechischen Gebirge. *Pragm Akad Athino* 8:171s
- Robotham ME, Wang H, Walton G (1995) Assessment of risk from rockfall from active and abandoned quarry slopes. *Trans Inst Min Metal Sect A* 104:A25–A33
- Rouiller JD, Jaboyedoff M, Marro Ch, Philipposian F, Mamin M (1998) Pentes instables dans le Pennique valaisan. Rapport final du programme national de Recherche PNR 31/CREALP, vol 98, 239p
- Stevens W (1998) Rocfall: a tool for probabilistic analysis, design of remedial measures and prediction of rockfalls. M.A.Sc. thesis, Department of Civil Engineering, University of Toronto, Ontario, 105p
- Valkaniotis S (2009) Correlation between neotectonic structures and seismicity in the broader area of Gulf of Corinth (Central Greece). Unpublished Ph.D. thesis, Aristotle University of Thessaloniki, 247p
- Varnes DJ (1978) Slope movements types and processes. In: Schuster RL, Krizek RJ (eds) *Landslide analysis and control*, vol 176, Transportation research board, special report. Transportation Research Board, Washington, DC, pp 11–33
- Wieczorek GF, Morrissy MM, Iovine G, Godt J (1999) Rock-fall potential in the Yosemite Valley, California, vol 99–578, USGS Open file report. U.S. Geological Survey, Reston



^{CM}SAKE: A Hydrological Model to Forecasting Landslide Activations

Oreste G. Terranova, Pasquale Iaquina, Stefano L. Gariano, Roberto Greco, and Giulio G.R. Iovine

Abstract

Worldwide, most landslides are generally triggered by rainfalls. In this paper, the hydrological model ^{CM}SAKE to forecast the timing of activation of slope movements is described.

Model calibration can be performed through an iterative algorithm (named “Cluster”): in this way, optimal kernels can be refined from an initial tentative solution. At each iteration, shape and base time of the tentative kernels are optimized by means of a discretized, self-adapting approach; the fitness is computed for all the examined solutions, and new individuals are generated starting from the best kernel obtained at the previous step.

The initial shape of the kernel can be selected among a set of standard basic types: (1) rectangular; (2) decreasing triangular; (3) any other geometrical shape which may sound reasonable on the base of the physical knowledge of the phenomenon. Alternatively, the kernel can be automatically optimized based on antecedent rainfalls with respect to a given date of landslide activation.

In this paper, a first example of application of the model to a large debris slide threatening a village in Northern Calabria is discussed, together with the results of a preliminary sensitivity analysis aimed at investigating the role of the main parameters.

Keywords

Hydrological model • Rain threshold • Landslide

Introduction

In Italy, a recent nationwide investigation has identified more than 1.6 landslides per km² (Guzzetti et al. 2008). In the Country, most of the landslides are usually triggered by rainfalls: slope instability conditions are in fact influenced by the water that, thanks to infiltration, affects groundwater dynamics. Generally, groundwater may reach a specific location within the slope by surface flow, direct infiltration from the surface, throughflow and seepage from the bedrock toward the overlying colluvium. The length of

the different paths may be quite different, and characterized by distinct velocities: as a consequence, aliquots of the same rainfall event may reach a given site at different times, variously combining with other groundwater amounts, thus resulting in complex dynamics.

In this study, the hydrological model ^{CM}SAKE (i.e. the release “cluster model” of the *Self Adaptive Kernel*) to forecast the triggering of slope movements is synthetically described. Aiming at model calibration, the dates of activation of a given phenomenon (or of a set of similar phenomena in a homogeneous study area), and the series of rainfalls are needed. Through an iterative cluster modification algorithm, optimal kernels can be refined from initial tentative discretized solutions. Once properly calibrated, the model can be used to predict the activation of either shallow or deep-seated landslides.

O.G. Terranova • P. Iaquina • S.L. Gariano • R. Greco • G.G.R.Iovine (✉)
CNR-IRPI – U.O.S. of Cosenza, Via Cavour 6, Rende, Cosenza, Italy
e-mail: g.iovine@irpi.cnr.it

An application of the model to a landslide threatening the village of San Benedetto Ullano (“SBU”, in Northern Calabria-Italia) is also discussed, together with the preliminary results of a sensitivity analysis aimed at investigating the role of the main parameters.

Background

Slope instability can occur when the soil shear strength gets lower than a given threshold, e.g. when rain infiltration leads to an increase in pore water pressure. To model the relationships between rainfall and landslide occurrence, two distinct approaches are generally adopted in literature: (1) “physically-based” (firstly developed by Montgomery and Dietrich 1994), and (2) hydrological (cf. e.g. Campbell 1975; Caine 1980; Sirangelo and Versace 1996; Terranova et al. 2007).

The hydrological approach (adopted in the present study) is based on a statistical-probabilistic analysis of the rainfall series and of the dates of occurrence of landslide activation. With respect to shallow landslides, the dynamics of deep-seated slope movements generally shows more complex relationships with rains: their activation commonly requires greater rainfall amounts, spanned over longer periods (from ca. 30 days to some rainy seasons).

Different hydrological mechanisms may play a significant role in landslide activation. In some cases, a combination of diverse mechanisms must be assumed. Therefore, efforts aimed at generalizing the triggering thresholds – e.g. the combination of intensity and duration of rains able to activate a given (type of) slope movement in a specific area – appear to be a quite complex issue (Marques et al. 2008).

Generally, a slope can be seen as a dynamic system for which the following reference values can be defined: (1) a minimum threshold (z_{\min}), below which the slope is always stable, and (2) a maximum threshold (z_{\max}), above which the slope is always unstable (Crozier 1997). Intermediate conditions occur for values between z_{\max} and z_{\min} , which may be expressed by a probability function:

$$G[z(t)] \in]0, 1[\quad (1)$$

In other terms:

$$\begin{aligned} P(E_i) &= 0 && \text{for } z(t) < z_{\min} \\ P(E_i) &= 1 && \text{for } z(t) > z_{\max} \\ P(E_i) &= G[z(t)] && \text{for } z_{\min} \leq z(t) \leq z_{\max} \end{aligned} \quad (2)$$

in which: P is the probability of occurrence; E_i is the succession of the events in time (t); $z(t)$ is the “mobility function”, i.e. the value assumed by the variable that expresses the condition of instability.

Hydrological models may employ “filter functions” (kernels) to express the influence of rainfalls on runoff and groundwater dynamics. With reference to this last aspect, the “base time”, t_b , defines the length of time during which rainfalls can effectively affect groundwater dynamics. Aiming at modelling slope stability, both the shape and the base time of the kernel must be properly selected by considering, on one side, type and dimension of the investigated phenomena, and, on the other, the geo-structural and hydro-geological characteristics of the affected slopes (cf. Capparelli et al. 2010). Unfortunately, in many real cases, simple, analytical functions do not allow to properly capture the observed complexity of groundwater dynamics. In this respect, the adoption of discretized kernels may offer effective solutions to relate landslide activations to rainfalls.

The Model ^{CM}SAKe

SAKe is a new hydrological model – inspired from Sirangelo and Versace (1996) – for predicting the activation of slope movements. The kernel of the model is discretized, as it is made of a set of elements, h_i , defined per each time interval (i). A linear, steady scheme is adopted: $z(t)$ can be described by means of an integral of convolution between the kernel, $h(t)$, and the rainfall, $p(t)$. The mobility function of the model is defined as:

$$z(t) = \int_0^t h(t - \tau)p(\tau)d\tau = \int_0^t h(\tau)p(t - \tau)d\tau \quad (3)$$

$$h(t) = \int_0^{+\infty} h(\tau)d\tau = 1, \quad h(t) \geq 0, \quad \forall t \quad (4)$$

In practical applications, the lower boundary of (4) is set to zero (i.e. the initial time), while the upper boundary is equal to the base time.

In classic hydrological problems, $z(t)$ represents the discharge at the time t , and the kernel can be determined through calibration, by relating discharge measurements to rains. Unfortunately, in slope-stability modelling only few dates of activation are commonly available, and the values of $z(t)$ are unknown. Such a problem can be mathematically handled only by assuming that the timing of the maxima of $z(t)$ corresponds to the dates of landslide activation; as a consequence, the shape of the kernel may turn out highly indeterminate.

In ^{CM}*SAKe*, an approach based on the adoption of discretized kernels, automatically calibrated through iterative computational techniques, was adopted. At the beginning of any calibration experiment, the rainfall series and a coherent

Table 1 Model parameters

Parameter	Description	Value
t_{b-max}	Maximum base time	60 days
w_s^0	Initial width of the cluster	6 days
dh_{max}	Maximum variation of h_i	40.0 %
dh_{min}	Minimum variation of h_i	0.5 %

set of dates of landslide occurrence must be given as input to the model. Dates may either refer to a number of historical re-activations of a given slope movement, or to geo-hydrological events characterized by widespread activations of numerous landslides of the same type/dimension within a geologically homogeneous area. The initial shape and maximum base time, t_{b-max} , of the kernel must also be specified, as well as other operational parameters (cf. Table 1).

The fitness function is defined as follows:

- The N available dates of landslide activation are sorted, in chronological order, in the vector $S = \{S_1, S_2, \dots, S_i, \dots, S_N\}$;
- The vector of the relative maxima of the mobility function $Z = \{z_1, z_2, \dots, z_k, \dots, z_M\}$, where M is the number and k is the rank of the relative maxima, is sorted in decreasing order;
- The vector of the partial fitness values is defined as $\varphi = \{\varphi_1, \varphi_2, \dots, \varphi_i, \dots, \varphi_N\}$.

The following cases can occur:

- $\varphi_i = 1$ if the date of the i -th activation, S_i , matches, within a pre-fixed tolerance (Δ , in days), the date of a k -th relative maximum of the mobility function, z_k , with $k \leq N$;
- $\varphi_i = (k-N+1)^{-1}$ – i.e. it is inversely proportional to the rank of z_k in Z – if the date of the i -th activation, S_i , matches, within a pre-fixed tolerance (Δ , in days), the date of a k -th relative maximum of the mobility function, z_k , with $k > N$;
- $\varphi_i = 0$ if the date of the i -th activation, S_i , does not match any date of the relative maxima in Z .

Consequently, the fitness of a generic kernel is:

$$\Phi = \frac{1}{N} \sum_{i=1}^N \varphi_i \quad (5)$$

Furthermore, let's define z_{k-min} as the smallest of the peaks of the mobility function in correspondence of one of the dates of activation. The “critical threshold” (z_{cr}) is defined as the value of the mobility function at the highest peak just below z_{k-min} .

In *CM-SAKe*, the optimizing tool designed to maximize the value of the fitness is named “Cluster”. During a given calibration experiment, the value of t_b is allowed to change in the range $[1, t_{b-max}]$, i.e. from few minutes to some weeks for shallow landslides, up to several months for deep-seated gravitational phenomena.

The initial shape of the kernel can be selected among a set of standard basic types: (1) rectangular, if the oldest precipitations are assumed to have the same weight as the most recent; (2) decreasing triangular, if the oldest precipitations have a progressively smaller weight compared to the most recent; (3) increasing triangular, if the oldest precipitations have a progressively greater weight than the most recent; (4) any other geometrical shape which may sound reasonable on the base of the physical knowledge of the phenomenon (like the functions: Power, Beta, Gamma, Nash, etc.).

Alternatively, the initial shape of the kernel can be selected according to the following “rain-driven” procedure. If only one date of landslide activation is available (e.g. in case of a “first-time” landslide), a high fitness can be obtained by simply initializing the kernel h^0 by considering the series of antecedent rains of length t_{b-max} , taken backward from the activation date, and by normalizing the values of h_i with respect to their cumulative value. On the other hand, if N dates of activation are available (e.g. re-activations of a given phenomenon), a set of different kernels, h^{0j} (with $j = 1, \dots, N$) are obtained per each date: the initial kernel is therefore computed as the average of the N kernels. As a rule, the generic ordinate of any initial kernel at the time i is given by:

$$h^0_i = \frac{\sum_{j=1}^N h^{0j}_i}{N} \quad (6)$$

Note that, when adopting the above mentioned rain-driven procedure, the fitness, Φ , related to the initial kernel may not be attain the maximum value; though, high values (i.e. relative maxima) of the mobility function can be obtained in correspondence with the dates of landslide activation.

During model calibration, shape and base time of the kernel are iteratively refined by means of a discretized, self-adapting approach. For each iteration, the fitness is computed for all the examined solutions, and new individuals are generated starting from the best kernel obtained at the previous step. More in detail, once the input data are given, the initial kernel selected, and the model parameters initialized, the fitness of the first individual can be computed. Aiming at finding better solutions, the kernel is therefore subdivided into N_c consecutive, not overlapping, clusters; these latter are made of a number of elements, so that

$$t_b = \sum_{s=1}^{N_c} w_s \quad (7)$$

where N_c is the number of clusters, and w_s is the width (i.e. the temporal extent) of the s -th cluster. At the beginning of the procedure, the initial width of the cluster is given by w_s^0 (cf. Table 1).

At each step, the iterative calibration procedure modifies the elements of a given cluster (e.g. increases their values by an amount dh , expressed in percentage of the maximum value of h_i of the whole kernel), and simultaneously modifies (e.g. decreases) the elements of the remaining clusters, by assuring that their overall sum remains unitary (note that, at the first iteration, the initial value of dh is given by dh_{max} – cf. Table 1). The fitness of the obtained solution is therefore computed. The same procedure is successively applied to another cluster, until all the available clusters are considered.

At this point, only the best solution is maintained, and another level of iteration can start, by halving the width, w_s (and therefore increasing the number, N_c) of the clusters, until the condition $w_s = 1$ is reached. Again, by maintaining only the best solution, another level of iteration can start, by halving the value of dh (until the condition dh_{min} is reached). At the end of each level of iteration, when two or more kernels show equivalent values of fitness, Φ , the one characterized by the greatest $\Delta z_{cr} = (z_{k-min} - z_{cr})/z_{k-min}$ is selected.

The above described calibration procedure may fail at the first iteration, if all the examined solutions have null fitness. In such a case, a new phase of calibration can be attempted by selecting a different initial shape of the kernel.

The procedure may result quite time-consuming (and even fail) if the considered set of dates of occurrence of slope movements do actually refer to different types of phenomena: in this case, a kernel only partly consistent with the physical processes under investigation is in fact obtained.

Finally, once the best solution is determined at the end of a given iteration, the procedure can be re-launched (cf. option “continue”), aiming at searching for further solutions characterized by greater fitness and/or Δz_{cr} . In this latter case, the solution shows a shorter response to rainfall, and therefore allows for activating early-warning procedures with a greater advance (which may turn out useful for Civil Protection purposes).

An Example of Application

The landslide here considered (Fig. 1 – cf. Iovine et al. 2009) developed at SBU, along the left flank of the Crati Graben. The village lies at the base of the Coastal Chain, in a sector marked by a N-S trending normal fault, belonging to the

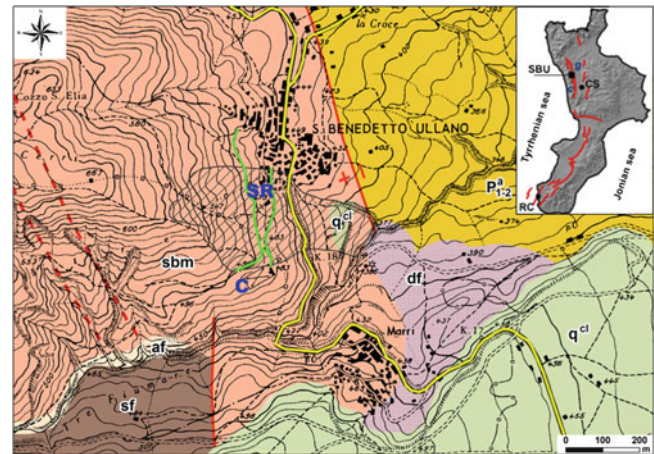


Fig. 1 Top-right: location of the study area. Key: SBU San Benedetto Ullano, CS Cosenza, RC Reggio Calabria, *c* coastal chain; *g* Crati Graben, in red the main tectonic structures belonging to the Calabrian-Sicilian Rift Zone. Main figure: geological map. Key: *af* alluvial sediments (Holocene), *df* landslide debris (Holocene), *q^{cl}* loose conglomerate (Pleistocene), *P^a₁₋₂* grey-blue silty clay (Middle-Late Pliocene), *sbm* gneiss and biotitic schist (Palaeozoic), *sf* grey phyllitic schist (Palaeozoic). The black hatched area delimits the sector threatened by the landslide. The roads (in green) to the cemetery (C), the church of S. Rocco (SR), and the provincial road to Marri (SP.31, in yellow) are also shown

Calabrian-Sicilian Rift Zone (Monaco and Tortorici 2000), which extends for ca. 30 km. Along this fault, the metamorphic rocks of the Chain, to the West, give place to the Pliocene-Quaternary sediments of the Graben, to the East (CASMEZ 1967).

In Calabria, average yearly rainfalls vary between 1,000 and 2,000 mm/year in mountainous and internal areas, with a mean regional value of about 1,150 mm/year. In Table 2, the average rains recorded at Montalto Uffugo (the closest rain gauge to the study case) are shown.

After a period of exceptional rainfalls, on 28 January 2009 the landslide started mobilizing, threatening the southern border of SBU and its cemetery. During the 2 and 3-months antecedent to this mobilization, cumulated rains approached the first two critical cases ever recorded since 1921. Thanks to a basic monitoring system (made of datum points plus extensometers) – implemented in the early stages of activation to support the Authority of Civil Protection for risk mitigation purposes – a peak of ca. 10 cm/day of superficial velocity was recorded on 30 January 2009. On 31 January, superficial velocities of ca. 7 cm/day were

Table 2 Rainfalls (mm) recorded at the Montalto Uffugo gauge (468 m a.s.l.) during the 2008/2009 and 2009/2010 hydrologic years. Mean values of the 1921–2006 period are also shown (in bold, values greater than averages)

	Sep	Oct	Nov	Dec	Jan	Feb	Mar	Apr	May	Jun	Jul	Aug	Year
2008/2009	174.8	89.0	216.6	524.4	647.8	335.6	417.0	142.5	26.4	77.8	0.4	0.0	2,652.3
2009/2010	141.0	247.6	129.6	350.2	575.2	592.2	130.4	90.6	126.0	139.8	5.4	1.4	2,529.4
Average	70.4	125.1	187.9	220.8	198.1	160.3	132.8	98.9	64.6	27.8	18.3	28.6	1,333.6

measured at several sites. Significant velocities were still observed in the following days, in coincidence with notable rains. In the late Spring 2009, velocities gradually decreased down to few mm/month. Geomorphologic evidences and kinematic observations suggested a confined type of distribution of activity. The local road to the cemetery and the provincial road (SP.31) to Marri were the most damaged by the landslide activation, while only minor damage was recorded along the southern margin of the village and in the cemetery.

During Autumn-Winter 2009/10, exceptional rains were recorded again. Between 31 January and 1 February 2010, a new phase of mobilization began. On 10–11 February, 295 mm of rain caused a new paroxysmal phase. Starting from the end of March 2010, the landslide activity gradually reduced to few mm/month in the late Spring. As a whole, the 2009/2010 mobilization caused by far greater damage with respect to the 2008/2009 one: the local roads and the SP.31 were completely destroyed, great part of the slope affected by the landslide was devastated, and notable damage was recorded in the cemetery and along the margin of the village.

Aiming at refining the cited monitoring system, information gathered through five boreholes, drilled in Spring 2009 (equipped with one open-pipe piezometer and four inclinometers) were employed to perform a parametric stability analysis (Iovine et al. 2010); moreover, a preliminary hydrological analysis was carried out by adopting the *FLaiR* approach (Capparelli et al. 2010).

The model *CM*SAKe was therefore applied to the case study of SBU, by taking into account a period of over 30 years (from 1 January 1970 to 30 September 2010). In the considered period (as well as in previous years), no other reports of landslide damage could be found in the consulted archives for the study area. Therefore, for the considered landslide, the only available dates of activation were: 31 January 2009, and 1 February 2010.

Results

Based on both geomorphologic evidence and on hydrological knowledge on the 2008/2009 and 2009/2010 wet seasons (in which the considered landslide activations occurred), a parametric analysis was performed (Fig. 2) by assuming $t_{b-max} = 60$ days, and initializing the remaining model parameters as in Table 1.

As for the initial shape of the kernel, the following types were considered: (1) “rain-driven” (RD), (2) rectangular (RE), (3) decreasing triangular (DT), and (4) increasing triangular (IT). The calibration experiments were performed on a standard PC platform (CPU 3 GHz, RAM 4 GB,

standalone system SQL and application process); each experiment lasted less than 30 min.

The fitness reached the maximum in all the calibration experiments after only few iterations. In particular, the maximum of Φ was reached at the first step of computation when initializing the shape of the kernel by the RD approach; five steps were needed when adopting the DT; seven steps for the RE; and eight steps for the IT (Fig. 2). In the same experiments, after reaching the maximum of Φ , further iterations allowed to refine the results by increasing the value of Δz_{cr} . The final values of Δz_{cr} attained the values of 36.2 %, 30.5 %, 26.1 % and 16.6 % for the RD, IT, RE, and DT, respectively.

Furthermore, it can be noticed that, if the four final kernels are concerned, the elements h_i exceed the average value (i.e. $1/t_{b-max} = 0.01\bar{6}$ – cf. height of the RE) in correspondence with three main temporal windows, and approximately between: 1–6, 22–24, and 47–48 days. This result is independent from the initial shape of the kernel, and suggests a quite complex scheme of groundwater dynamics for the SBU case study, which seems to be affected by distinct water contributions: a “short-term” response combines with a “middle-term” response, and with an older contribution.

Conclusions

The calibration experiments of *CM*SAKe were performed by adopting $t_{b-max} = 60$ days and 4 types of initial shape of the kernel (RD, RE, DT, IT). The fitness reached the maximum in all the calibration experiments after few iterations (the fastest was the RD, the slowest the IT). The final values obtained for Δz_{cr} ranged from a maximum (RD) to a minimum (DT). Further improvements could still be obtained by further re-launching the model. Due to the limited number of known dates of activation, validation could not be performed for this specific case study.

Obtained results could usefully be applied for early warning purposes. In general, in such type of application, in case two or more kernels show equivalent values of fitness, the one characterized by the smallest t_b , the greatest Δz_{cr} and/or the lowest momentum of the first order with respect to the time origin should be employed (as it refers to a faster response of the slope to rainfalls).

The model is self-adaptive, but computation times can be reduced by properly initializing t_{b-max} and the shape of the kernel, based on landslide characteristics. The kernels obtained by calibration constitute a family of optimal solutions, characterized by the highest values of fitness. In case the quality of input data is improved, and/or the number of activations increases (e.g. in case of either new activations or discovery of further historical dates), the family of solutions tends to be less numerous, and its significance increases.

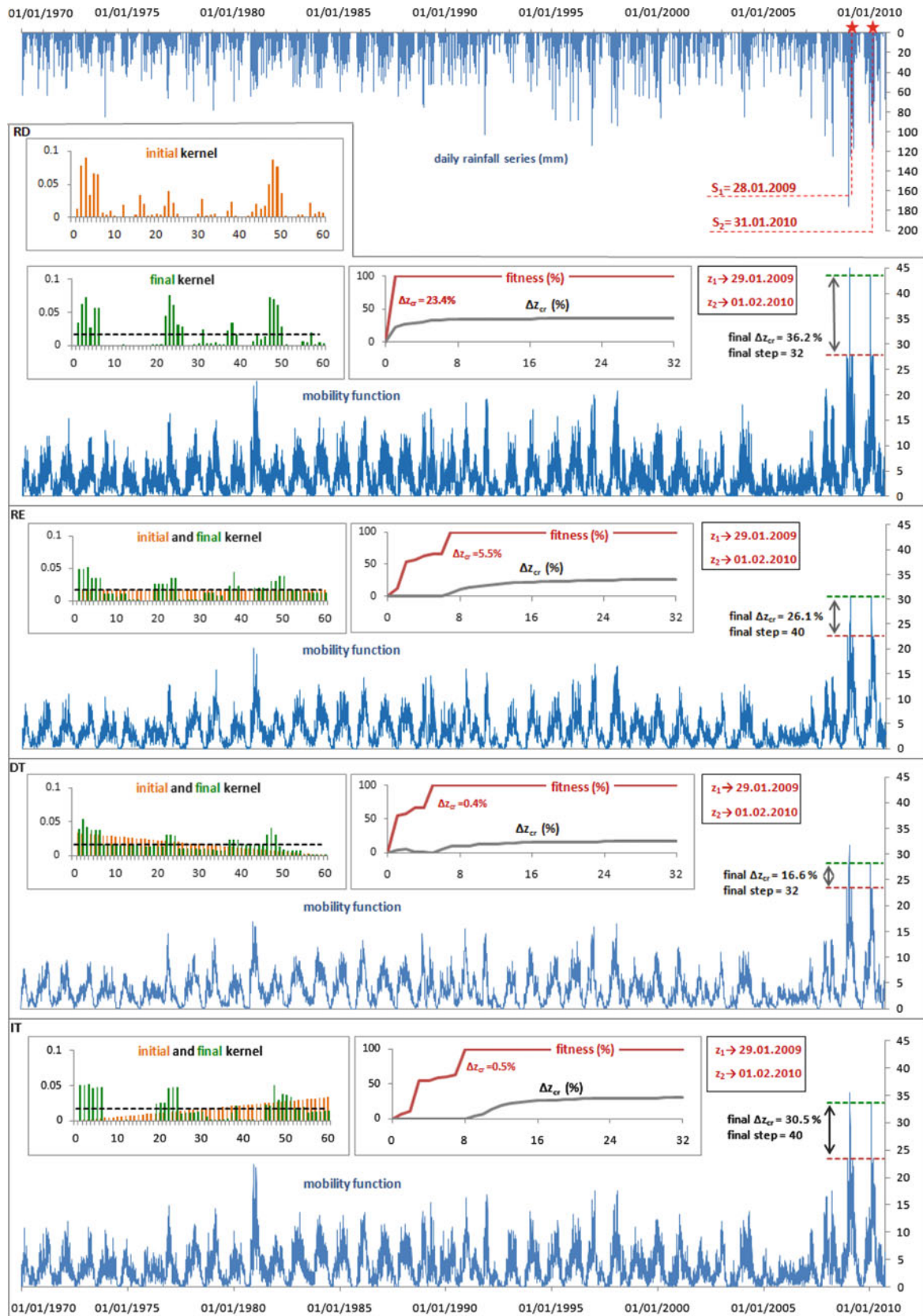


Fig. 2 Example of output of CM SAKe. On top, the series of daily rainfalls (from 1 January 1970 to 30 September 2010) is shown. Two red stars mark the timing of landslide activations (S_1 and S_2). Below, the kernels (initial in orange and final in green; the dashed black line

represents the average) for each of the four different shapes considered (RD, RE, DT, IT), and related mobility functions plus final values of Δz_{cr} are also shown. Per each calibration experiment, evolution graphs of Φ and Δz_{cr} are shown in red and grey, respectively

CM SAKe allows to identifying distinct behaviours of groundwater dynamics, related to complex interactions among the different infiltrated aliquots of rain affecting slope stability. In the case of SBU, three main groundwater contributions could be identified from the analysis of the final kernels, which may never be captured by adopting a single analytical function (e.g. when simple mathematical functions are adopted).

Nevertheless, as the indeterminateness above cited remains, it is rather preferable to consider – instead of a single solution – a set of optimal kernels that, based of available information, allows to satisfactorily simulating the response of the considered slope to rainfalls.

An automated technique of calibration (based on Genetic Algorithms) and a detailed sensitivity analysis are presently being performed against a set of case studies (of different types), characterized by a greater number of activation dates (thus also allowing for model validation).

References

- Caine N (1980) The rainfall intensity-duration control of shallow landslides and debris flows. *Geogr Ann* 62A(1–2):23–27
- Campbell RH (1975) Debris flow originating from soil slip during rainstorm in southern California. *Q J Eng Geol* 7:377–384
- Capparelli G, Iaquina P, Iovine GGR, Terranova OG, Versace P (2010) Modelling the rainfall-induced mobilization of a large slope movement in northern Calabria. *Nat Hazards*. doi:[10.1007/s11069-010-9651-1](https://doi.org/10.1007/s11069-010-9651-1)
- CASMEZ (1967) Carta Geologica della Calabria, F.229-III-NE “Lattarico” (in scale 1/25000). Poligrafica & CarteValori, Ercolano
- Crozier MJ (1997) The climate-landslide couple: a southern hemisphere perspective. In: Matthews JA, Brunsten D, Frenzel B, Gläser B, Weiß MM (eds) *Rapid mass movement as a source of climatic evidence for the Holocene*, vol 19. Gustav Fischer, Stuttgart, pp 333–354
- Guzzetti F, Peruccacci S, Rossi M, Stark CP (2008) The rainfall intensity-duration control of shallow landslides and debris flow: an update. *Landslides* 5:3–17
- Iovine GGR, Iaquina P, Terranova OG (2009) Emergency management of landslide risk during Autumn-Winter 2008/2009 in Calabria (Italy). The example of San Benedetto Ullano. In: Anderssen RS, Braddock RD, Newham LTH (eds) *Proceedings of the 18th World IMACS congress and MODSIM09 international congress on modelling and simulation*, Cairns, pp 2686–2693. ISBN 978-0-9758400-7-8
- Iovine GGR, Lollino P, Gariano SL, Terranova OG (2010) Coupling limit equilibrium analyses and real-time monitoring to refine a landslide surveillance system in Calabria (Southern Italy). *Nat Hazards Earth Syst Sci (NHES)* 10:2341–2354
- Marques R, Zêzere J, Trigo R, Gaspar J, Trigo I (2008) Rainfall patterns and critical values associated with landslides in Povoação County (São Miguel Island, Azores): relationships with the North Atlantic Oscillation. *Hydrol Process* 22:478–494
- Monaco C, Tortorici L (2000) Active faulting in the Calabrian arc and eastern Sicily. *J Geodyn* 29:407–424
- Montgomery DR, Dietrich WE (1994) A physically-based model for the topographic control on shallow landsliding. *Water Resour Res* 30:1153–1171
- Sirangelo B, Versace P (1996) A real time forecasting for landslides triggered by rainfall. *Meccanica* 31:1–13
- Terranova O, Antronico L, Gullà G (2007) Landslide triggering scenarios in homogeneous geological contexts: the area surrounding Acri (Calabria, Italy). *Geomorphology* 87:250–267



Shallow-Landslide Susceptibility in the Costa Viola Mountain Ridge (Italia)

Giulio G.R. Iovine, Roberto Greco, Stefano L. Gariano, Pasquale Iaquinata, Annamaria Pellegrino, and Oreste G. Terranova

Abstract

The “Costa Viola” mountain ridge (Calabria) is exposed to severe geo-hydrological risk conditions, especially in the sector between Bagnara Calabria and Scilla. This sector has repeatedly been affected by slope instability events in the past, mainly related to debris slides, rock falls and debris flows.

An attempt of shallow-landslide susceptibility mapping has been performed for the mentioned coastal sector through a logistic regression (LR) approach. LR is a multivariate type of analysis that allows estimating the presence/absence of a phenomenon in terms of probability (ranging between 0 and 1), on the basis of linear statistical relationships with a set of independent territorial variables.

The adopted LR procedure consists of four steps: (1) variable parameterization, (2) sampling, (3) fitting, and (4) application. Obtained results can be considered acceptable, as 85.6 % of cells are correctly classified.

Keywords

Shallow-landslide • Susceptibility • Logistic regression

Introduction

In Calabria, a region characterized by rough morphology and landslide-prone outcrops, mass movements are a significant natural hazard (Carrara et al. 1982; Sorriso-Valvo 1993; Pellegrino and Borrelli 2007). Due to their high kinetic energy and long paths, shallow landslides (like debris slides and debris flows) are commonly the most destructive and dangerous type of slope movements for people and infrastructures.

Evaluation of landslide susceptibility (i.e. the spatial probability of occurrence of mass movements) is the first step when dealing with regional hazard management. This

aim can be achieved by means of several, different approaches (Aleotti and Chowdhury 1999; Guzzetti et al. 1999), including multivariate statistical analyses (Carrara et al. 1977, 1982, 1991; Reger 1979; Carrara 1983; Carrara and Guzzetti 1995; Chung et al. 1995; Guzzetti et al. 1999; Baeza and Corominas 2001; Gullà et al. 2008).

Logistic Regression is a type of multivariate analysis widely utilized (cf. e.g. among the most recent studies: Greco et al. 2007; Nefeslioglu et al. 2008; Mathew et al. 2009; Sorriso-Valvo et al. 2009; Rossi et al. 2010; Van Den Eeckhaut et al. 2010), that allows estimating the presence/absence of a phenomenon, represented by the dependent variable y , in terms of probability $P(y)$, whose value ranges between 0 (no occurrence) and 1 (occurrence) on the basis of linear statistical relationships with a set of independent variables. Note that, in case of independent variables which are correlated with each other (e.g. those derived from a given DEM), the evaluation ability of LR remains unaffected.

G.G.R. Iovine (✉) • R. Greco • S.L. Gariano • P. Iaquinata • O.G. Terranova
CNR-IRPI – U.O.S. of Cosenza, Via Cavour 6, Rende, Cosenza, Italy
e-mail: g.iovine@irpi.cnr.it

A. Pellegrino
ABR Calabria, Via Crispi 33, Catanzaro, Italy

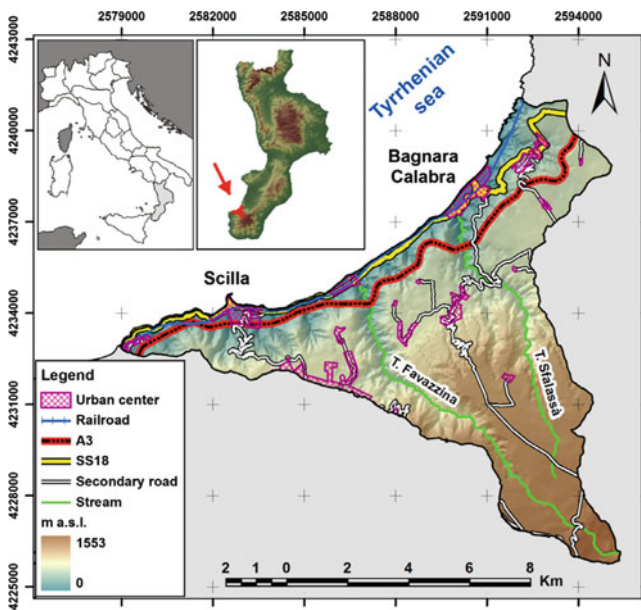


Fig. 1 Location, altimetry and main infrastructures of the study area

In the present study, the shallow-landslide susceptibility of a sector of the “Costa Viola” mountain ridge (Calabria), frequently struck by geo-hydrological events, was analyzed by means of LR. The main results of the analysis are summarized below.

Study Area

The study area, extended approximately 82.2 km², is located in a sector of the “Costa Viola” mountain ridge, between Bagnara Calabria and Scilla (Fig. 1). It is characterized by Palaeozoic metamorphic and crystalline bedrocks, strongly tectonized, and deeply weathered, covered by Upper Miocene to Holocene sedimentary deposits (Fig. 2). At the base of the mountain ridge, a NE-SW trending fault, belonging to the Calabrian-Sicilian Rift Zone (Tortorici et al. 1995), marks the transition between the basement and the overlying sedimentary terrains of the coastal plan.

From a morphological point of view, the area is characterized by steep and uneven slopes, cut by deep canyons; a set of marine terraces can be recognized between 100 and 600 m a.s.l. Along the coast, short high-gradient torrents (the longest thereof are T. Favazzina and T. Sfalassà – cf. Fig. 1) drain the western slope of the ridge. In this area, cold winter air fronts commonly approach from NW, originating intense storms.

The study area is crossed by the railway, the highway A3 (“Salerno-Reggio di Calabria”), and the southern Tyrrhenian state road (SS.18) (cf. Fig. 1). The narrow and discontinuous

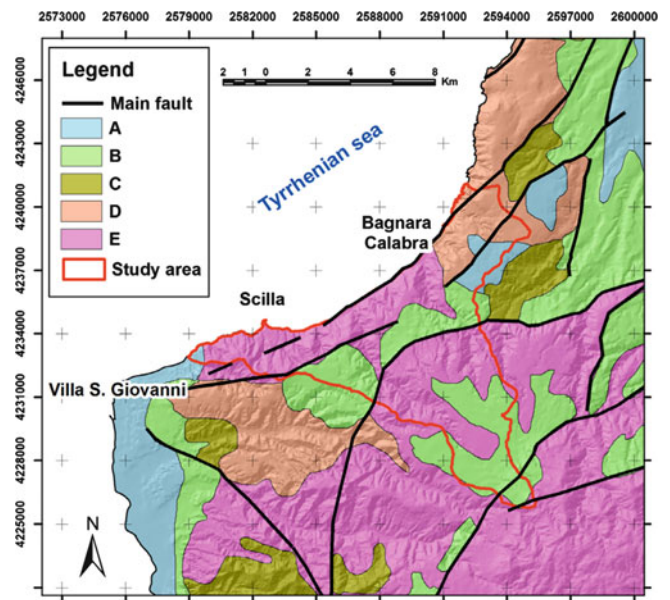


Fig. 2 Geological sketch of the study area (After modified Tortorici 1982). Key: (A) gravel, sand, silt and clay (upper Pleistocene-Holocene), (B) terraced sand, pebble (middle Pliocene-middle Pleistocene), (C) conglomerate, arenite, clay, and marl, with subordinate evaporite (upper Miocene-middle Pliocene), (D) acid intrusive rocks (Paleozoic), (E) middle-high grade metamorphic rocks (Paleozoic)

strip of land between the coastline and the base of the ridge is densely urbanized.

This sector has repeatedly been affected by slope instability events in the past, mainly related to debris slides, rock falls and debris flows. In the last decade, the frequency of the damaging events increased (the last one occurred in Winter 2010/2011): in 2001 and in 2005, a couple of events severely hit the main transportation infrastructures, also causing the derailment of a train, and the urbanized areas (Bonavina et al. 2005).

Method

The methodology used to evaluate the susceptibility to shallow landslide in the considered sector of the Costa Viola mountain ridge is based on Logistic Regression. In LR, the presence/absence of a landslide can be expressed in terms of a dichotomic dependent variable, whose probability of being true is determined on the basis of linear statistical relationships with a set of independent territorial variables. The probability of occurrence of the dependent variable, $P_{(y)}$, can be calculated as follows:

$$P_{(y)} = \frac{1}{1 + e^{-a_0 - \sum^n a_i x_i}} \quad (1)$$

in which a_i and X_i are the regression coefficients (i.e., the weights related to the variables), and the independent variables, respectively.

The adopted LR procedure, first proposed by Greco et al. (2007) for evaluating landslide susceptibility in the Aspromonte Massif (southern Calabria), consists of four steps: (1) variable parameterisation, (2) sampling, (3) model fitting and (4) model application, as summarized below.

LR Procedure

LR analysis can be developed by using both parametric and non-parametric variables. Previous studies demonstrated that if non-parametric variables are ranked or transformed into parametric variables (e.g. ordering their classes on the basis of landslide incidence in each class) results may be improved (Sorriso-Valvo et al. 2009). In this study, the parameterisation was performed by considering landslide incidence in given portions of the study area, named the “sampling zones”.

In sampling, the values of the independent variables are obtained from selected zones. This phase can be performed in different ways: data from the whole study area can be used to generate the fitting data set (Ohlmacher and Davis 2003; Ayalew and Yamagishi 2005); alternatively, data from a limited portion of the study area, with either equal proportions of 1 and 0 pixel (Dai and Lee 2002) or unequal proportions (Atkinson and Massari 1998), can be used. In this study, sampling zones were obtained in the GIS environment by generating a buffer around each landslide. Each cell of the data base is characterized by an id-index, cell coordinates, and parameterized values of dependent and independent variables.

During model fitting, LR is iteratively performed by testing all the possible values for the weights of the independent variables, until the root mean square residuals are minimized. The adopted software (Arc-Info, version 9.3) provides regression weights (a_i), RMSE (Root Mean Square Error) and Chi-square. Results can be considered good when RMSE is minimized and Chi-square maximized. The forecast capability can be evaluated, at this step, by means of the ROC analysis (Receiver Operating Characteristics Analysis, Hosmer and Lemeshow 1989).

In model application, the logistic function obtained in the previous step of the procedure is applied to the remaining

part of study area (i.e. where only independent variables are known). A grid of values, ranging between 0 and 1, is obtained as output.

The Dependent Variable

Presence or absence of shallow landslides in the study area was chosen as the dependent variable for susceptibility classification. The territorial distribution of the phenomena was obtained from a multi-temporal landslide inventory map (1:10,000 scale) obtained by interpreting two sets of aerial photographs, taken in 1994–1995 and in 1990–1991, respectively (Fig. 3). In Fig. 3a, the 181 landslides employed as training set during the phase of calibration are shown; in Fig. 3b, the 81 landslides employed as validation set are shown.

Independent Variables

Independent variable maps were obtained from available published maps (e.g. lithology from Burton 1971; land use from European Environment Agency 2007; pedological units from ARSSA 2003) or by processing other variables (derived from the DEM).

The data set of independent variables includes the nine causal factors (LU, LUS, ST, ELEV, SLO, ASP, ACUR, DCUR, TWI) described below.

- Lithology: obtained by grouping, on the basis of similarity in compositional and mechanical properties, the formations of the Geological Map of Calabria (1:25,000 scale) (Burton 1971). In Fig. 4a, the territorial frequency of the eight lithological units (LU) outcropping in study area is shown.
- Land use: obtained from the digital map of the Corine-Land Cover project (European Environment Agency 2007). From the layer of highest detail, the 15 land use categories (LUS) used for the analysis were extracted. In Fig. 4b, LUS frequency is shown.
- Soil type (ST): obtained from a vector map at 1:25,000 nominal scale, supplied by the Regional Agency for Agriculture Development and Services (ARSSA). In this map, soil types are classified into 155 pedological units, (ARSSA 2003). In Fig. 4c, the frequency of the 13 pedological units outcropping in the area of interest is shown.

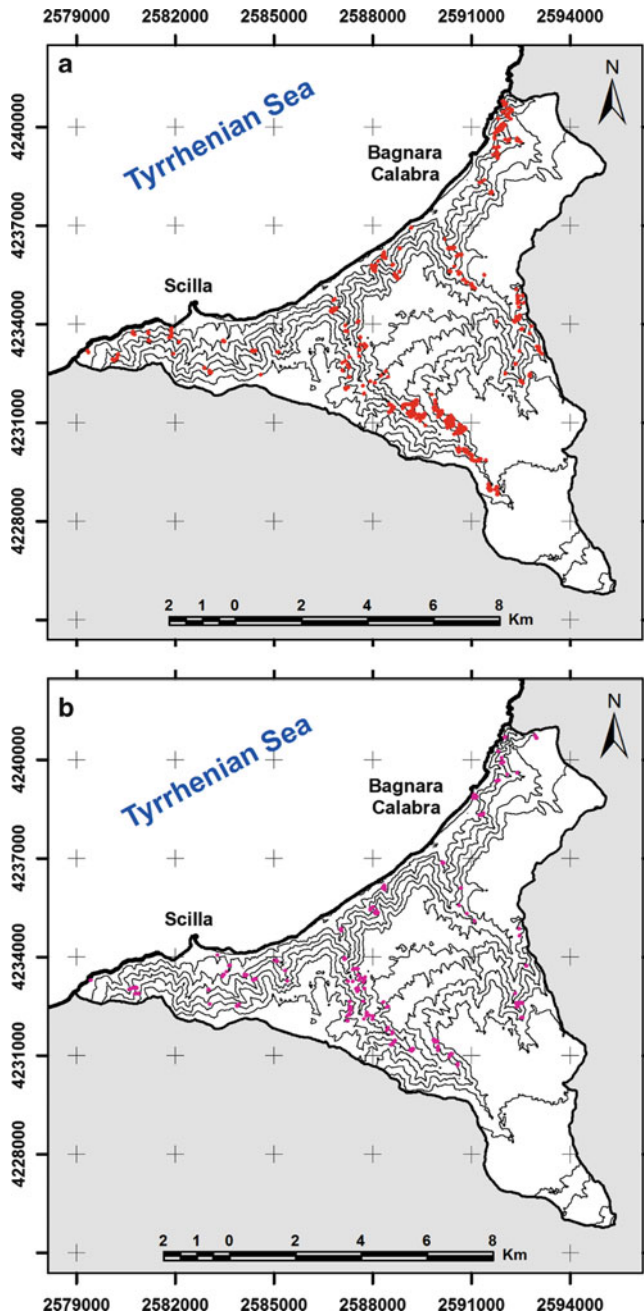


Fig. 3 Landslide inventory maps of the study area: (a) training set; (b) validation set

- Elevation (ELEV): obtained from a 20-m square-grid DEM, it was classified into elevation classes 100 m wide (Fig. 4d);
- Slope angle (SLO): derived by DEM, it was classified into seven classes (10° wide) (Fig. 4e);
- Aspect (ASP): derived from DEM, it was classified into eight classes (Fig. 4f);

- Curvatures: derived from DEM by mathematical intersection of the ground surface with (1) a vertical plane set along the direction of maximum slope (ACUR), and (2) with a horizontal plane set orthogonally to the direction of maximum slope (DCUR) (Fig. 4g);
- Topographic wetness index (TWI) (Moore et al. 1991): derived from the DEM, it expresses the potential surface runoff inflow to any given cell; its value is obtained from:

$$TWI = \ln(A_s / \tan \beta) \quad (2)$$

in which A_s is the specific flow-accumulation area (i.e. for each cell, the total area of up-hill cells delivering overland flow), and β is the slope angle (in degrees). In Fig. 4h, the frequency of TWI in the study area is shown.

Results

As mentioned above, the susceptibility to shallow landslide was evaluated by considering the following nine variables: lithology (LU), land use (LUS), pedological units (ST); elevation (ELEV), slope gradient (SLO), aspect (ASP), cross slope curvature (ACUR), down slope curvature (DCUR) and topographic wetness index (TWI). In Table 1, regression weights of each independent variable, and RMSE and Chi-square values obtained in the phase of model fitting are shown.

In addition, ROC analysis was performed to check the performance of the LR models obtained by fitting. The obtained ROC-curve is shown in Fig. 5. Through the logistic function (1), the probability of existence $P_{(y)}$ was evaluated for the whole study area (Fig. 6a).

Finally, the probability map was reclassified into five susceptibility classes (Fig. 6b): Null ($P_{(y)} \leq 5\%$); Low ($5\% < P_{(y)} \leq 25\%$); Medium ($25\% < P_{(y)} \leq 55\%$); High ($50\% < P_{(y)} \leq 75\%$); Very high ($P_{(y)} > 75\%$).

Conclusion

Shallow-landslide susceptibility of a sector of the “Costa Viola” was evaluated by means of Logistic Regression by employing nine territorial variables, considered as main causal factors. In the adopted sampling procedure, weights of LR models were computed by considering only a portion of the study area (the sampling zone).

The regression values of $P_{(y)}$ range from 0% to 78% (Fig. 6a), allowing for the susceptibility classification shown in Fig. 6b. In terms of susceptibility, the sectors most threatened by shallow-landslides are located by the Tyrrhenian coast, as a consequence of the local structural

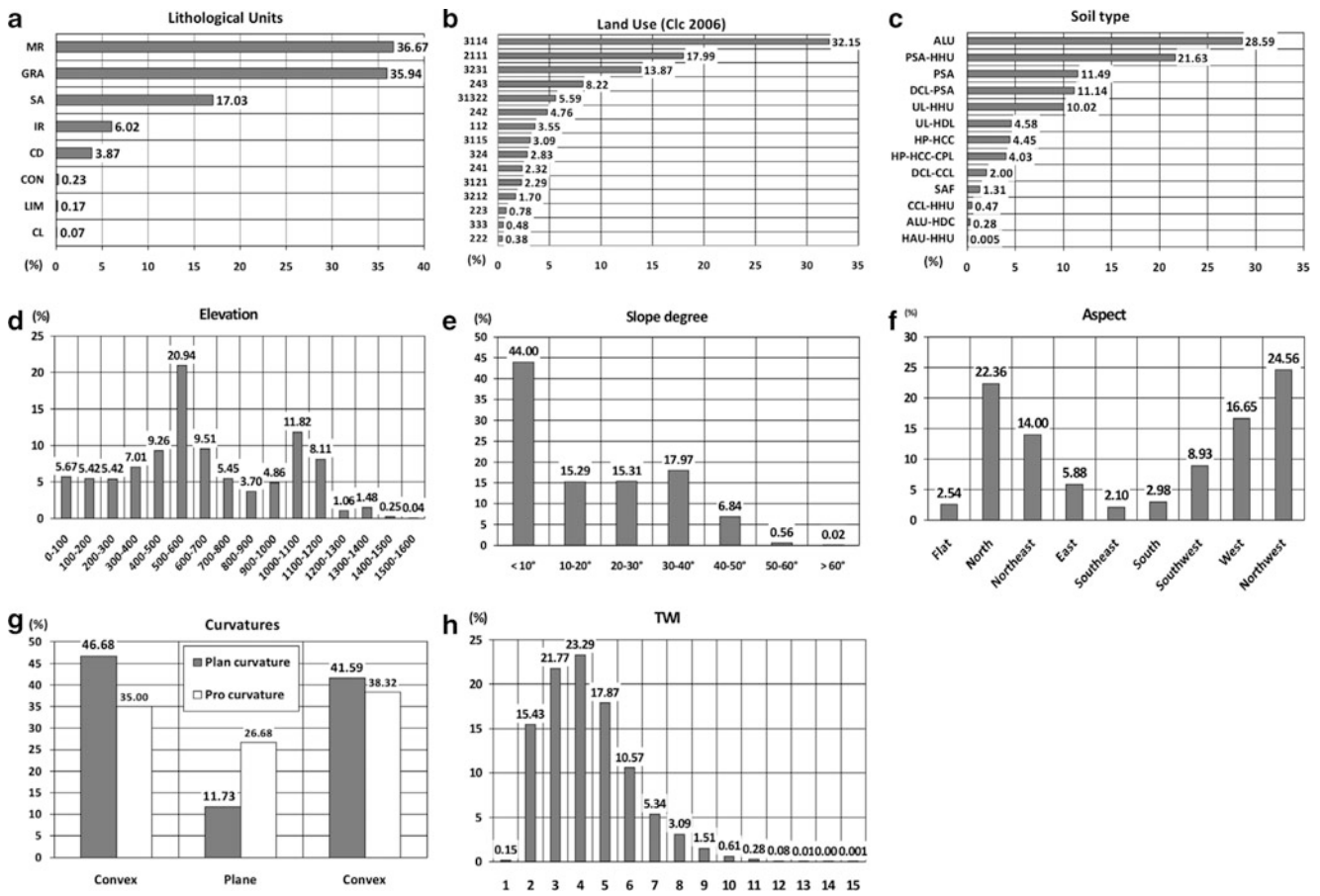


Fig. 4 Distribution of independent territorial variables for the study area: Keys: (a) Lithological units: *CL* clay, *LIM* limestone, *CON* conglomerate, *CD* colluviums and debris, *IR* igneous rock, *SA* sand, *GRA* gravel, *MR* metamorphic rock; (b) Land use categories: *112* discontinuous urban fabric, *2111* intensive cultivations, *222* fruit trees and berries plantations, *223* olive groves, *241* annual crops associated with permanent crops, *242* complex cultivation patterns, *243* land principally occupied by agriculture, with significant areas of natural vegetation, *3114* chestnut forest, *3115* beech forest, *3121* coniferous

forest, *31322* mixed forest, *3212* discontinuous grassland, *3231* high “Macchia”, *324* transitional woodland-shrub, *333* sparsely vegetated areas; (c) Soil type: *ALU* Artenic-Leptic Ubrisol, *CCL* Cutanic Chromic Luvisols, *CPL* Chromi Profondic Luvisols, *DCL* Dystri-Cutanic Luvisol, *HAU* Humi-Arenic Umbrisols, *HCC* Haspli-Calcaric Cambisols, *HDC* Hapli-Dyctic Cambisols, *HDL* Hapli-Dystric Leptosols, *HHU* Hapli-Humic Umbrisols, *HP* Haplic Phaeozems, *PSA* Pachi-Silic Andosols, *SAF* Skeletic-Arenic Fluvisols, *UL* Umbrihumic Leptosols

setting (cf. Fig. 2), and along the steep flanks of the major streams (T. Sfalassà and T. Favazzina). Notable values of susceptibility are also to be found in the middle portion of the study area, again in correspondence of a major fault belonging to the Calabrian-Sicilian Rift Zone.

Obtained weights (Table 1) suggest that down-slope curvature, topographic wetness index, aspect and lithology play a primary role in favouring slope instability. Differently from previous applications of the method (Greco et al. 2007; Sorriso-Valvo et al. 2009), pedological unit doesn't seem to play any significant role. This may be due to an even distribution of the training set among the different types of soil considered. Further investigation is needed to better understand this specific result.

ROC analysis indicates a percentage of 85.6 % of correctly classified cells; this is by far the best result

among those obtained in previous applications of the method in Calabria. In addition, the overlay between the landslide validation set (Fig. 3b) and the susceptibility map (Fig. 6b) shows that 44 % of cases fall in the Medium Susceptibility class, and 56 % in the High Susceptibility class, thus confirming the goodness of classification for the “Costa Viola” study area, where the LR sampling procedure satisfactorily described the probability of presence of mass movements.

In the study area, the zones most exposed to risk from shallow-landslides are quite urbanized and/or are crossed by relevant transportation infrastructures. The potential sources were identified in the present study, in terms of susceptibility, through LR. The next step, presently in progress, is the evaluation of the expected intensity (related to the triggering rainfalls) and potential path of

Table 1 Regression weights, and values of RMSE and Chi-square, as obtained through regression

Coefficient	Variable	Value
a_0	Intercept	-11.552
a_1	LU	0.028
a_2	LUS	0.013
a_3	ST	0.000
a_4	ELEV	0.018
a_5	SLO	0.025
a_6	ASP	0.032
a_7	ACUR	0.027
a_8	DCUR	0.043
a_9	TWI	0.037
RMSE		0.485
Chi-square		475.990

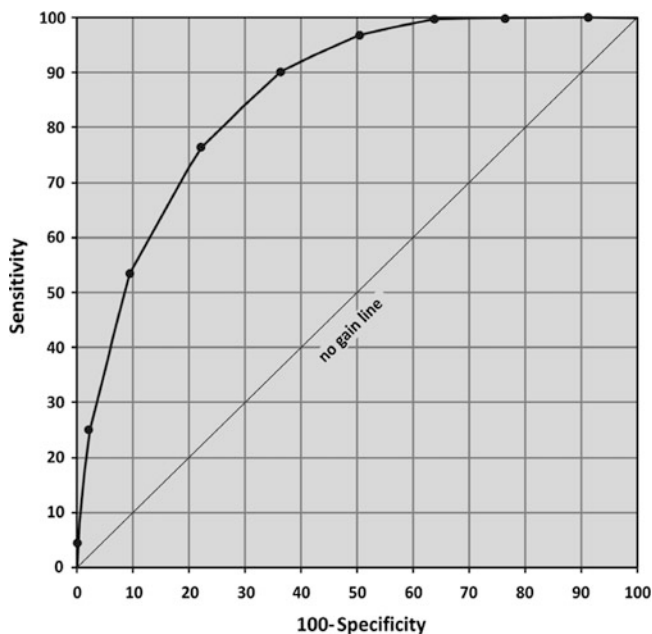


Fig. 5 Obtained ROC curve

the debris flows which may originate by fluidization of the shallow landslides, and propagate towards the coastline (Iovine 2008; Iovine and Mangraviti 2009) – as frequently occurred in the past.

References

- Aleotti P, Chowdhury R (1999) Landslide hazard assessment: summary review and new perspectives. *Bull Eng Geol Environ* 58:21–44
- Atkinson PM, Massari R (1998) Generalised linear modelling of susceptibility to landsliding in the Central Apennines, Italy. *Comput Geosci* 24(4):371–383
- Ayalew L, Yamagishi H (2005) The application GIS-based logistic regression for landslide susceptibility mapping in the Kakuda-Yahiko Mountains, central Japan. *Geomorphology* 65:15–31
- Baeza C, Corominas J (2001) Assessment of shallow landslide susceptibility by means of multivariate statistical techniques. *Earth Surf Process Landf* 26:1251–1263
- Bonavina M, Bozzano F, Martino S, Pellegrino A, Prestininzi A, Scandurra R (2005) Mud and debris flows along the coastal slope between Bagnara Calabria and Scilla (Reggio Calabria): susceptibility evaluations (in Italian). *Giornale di Geologia Applicata* 2:65–74
- Burton AN (1971) *Carta Geologica della Calabria (1:25,000). Relazione Generale*. Cassa per Opere Straordinarie di Pubblico Interesse nell'Italia Meridionale (Cassa per il Mezzogiorno). 120p

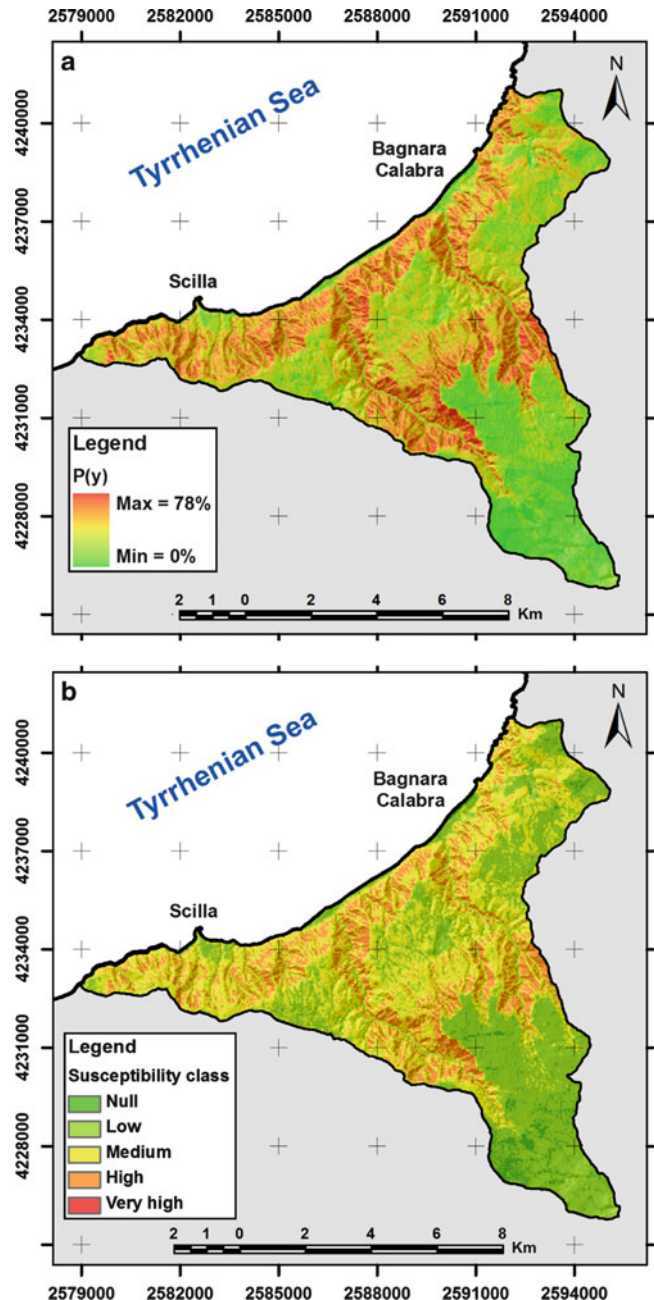


Fig. 6 Probability map (a) and susceptibility map (b)

- Carrara A (1983) Multivariate models for landslide hazard evaluation. *Math Geol* 15(3):403–426
- Carrara A, Guzzetti F (eds) (1995) Geographical information systems in assessing natural hazard. Kluwer, Dordrecht, 342p
- Carrara A, Pugliese Caratelli E, Merenda L (1977) Computer-based data bank and statistical analysis of slope instability phenomena. *Z Geomorph N F* 21(2):187–222
- Carrara A, Sorriso-Valvo M, Reali C (1982) Analysis of landslide form and incidence by statistical techniques, Southern Italy. *Catena* 9:35–62
- Carrara A, Cardinali M, Detti R, Guzzetti F, Pasqui V, Reichenbach P (1991) GIS techniques and statistical models in evaluating landslide hazard. *Earth Surf Process Landf* 16(5):427–445
- Chung C, Fabbri A, Van Westen CJ (1995) Multivariate regression analysis for landslide hazard zonation. In: Carrara A, Guzzetti F (eds) Geographical information systems in assessing natural hazard. Kluwer, Dordrecht, pp 107–142
- Dai FC, Lee CF (2002) Landslide characteristics and slope instability modeling using GIS, Lantau Island, Hong Kong. *Geomorphology* 42:213–228
- European Environment Agency (2007) CORINE Land Cover CLC2006 technical guidelines. EEA technical report 17/2007, 70p. ISBN 978-92-9167-968-3
- Greco R, Sorriso-Valvo GM, Catalano E (2007) Logistic regression analysis in the evaluation of mass-movement susceptibility: the Aspromonte case study, Calabria, Italy. *Eng Geol* 89:47–66
- Gullà G, Antronico L, Iaquinata P, Terranova O (2008) Susceptibility and triggering scenarios at a regional scale for shallow landslides. *Geomorphology* 99:39–58
- Guzzetti F, Carrara A, Cardinali M, Reichenbach P (1999) Landslide hazard evaluation: a review of current techniques and their application in a multi-scale study, Central Italy. *Geomorphology* 31:181–216
- Hosmer DW, Lemeshow S (1989) Applied regression analysis. Wiley, New York, 307p
- Iovine G (2008) Mud-flow and lava-flow susceptibility and hazard mapping through numerical modelling, GIS techniques, historical and geo-environmental analyses. In: Sánchez-Marrè M, Béjar J, Comas J, Rizzoli A, Guariso G (eds) Proceedings of 4th biennial meeting of iEMSs, Barcelona, pp 1447–1460
- Iovine G, Mangraviti P, (2009) The CA-model FLOW-S* for flow-type landslides: an introductory account. In: Anderssen RS, Braddock RD, Newham LTH (eds) Proceedings of 18th World IMACS/ MODSIM congress, Cairns, 13–17 July 2009, pp 2679–2685
- Mathew J, Jha VK, Rawat GS (2009) Landslide susceptibility zonation mapping and its validation in part of Garhwal Lesser Himalaya, India, using binary logistic regression analysis and receiver operating characteristic curve method. *Landslides* 6:17–26
- Moore ID, Grayson RB, Ladson AR (1991) Digital terrain modeling: a review of hydrological, geomorphological, and biological application. *Hydrol Process* 5:3–30
- Nefeslioglu HA, Gokceoglu C, Sonmez H (2008) An assessment on the use of logistic regression and artificial neural networks with different sampling strategies for the preparation of landslide susceptibility maps. *Eng Geol* 97:171–191
- Ohlmacher GC, Davis JC (2003) Using multiple logistic regression and GIS technology to predict landslide hazard in northeast Kansas, USA. *Eng Geol* 69:331–343
- Pellegrino A, Borrelli S, (2007) Analisi del dissesto da frana in Calabria. In: Trigila A (ed) Rapporto sulle frane in Italia. Il progetto IFFI – Metodologia, risultati e rapporti regionali. Rapporti 78/2007. APAT, Roma (978-88-448-0310-0), 681 p
- Reger JP (1979) Discriminant analysis as possible tool in landslide investigations. *Earth Surf Process Landf* 4:267–273
- ARSSA – Regione Calabria (2003) I Suoli della Calabria (Carta in scala 1:250.000). Monografia divulgativa. 387p
- Rossi M, Guzzetti F, Reichenbach P, Mondini AC, Peruccacci S (2010) Optimal landslide susceptibility zonation based on multiple forecast. *Geomorphology* 114:129–142
- Sorriso-Valvo M (1993) The geomorphology of Calabria, a sketch. *Geografia Fisica e Dinamica Quaternaria* 16:75–80
- Sorriso-Valvo M, Greco G, Catalano E (2009) Spatial prediction of regional scale mass movement using the logistic regression analysis and GIS – Calabria, Italy. *Isr J Earth Sci* 57:263–280
- Tortorici L (1982) Lineamenti geologico-strutturali dell'Arco Calabro-Peloritano. *Rendiconti della Società Italiana di Mineralogia e Petrologia* 38:927–940
- Tortorici L, Monaco C, Tansi C, Cocina O (1995) Recent and active tectonics in the Calabrian Arc (Southern Italy). *Tectonophysics* 243:37–55
- Van Den Eeckhaut M, Marre A, Poesen J (2010) Comparison of two landslide susceptibility assessments in the Champagne-Ardenne region (France). *Geomorphology* 115:141–155



Extraction of Rock Mass Structural Data from High Resolution Laser Scanning Products

Giovanni Gigli and Nicola Casagli

Abstract

With the aim of extracting 3D structural information of rock masses from high resolution remote sensing data, a Matlab tool, called DiAna (Discontinuity Analysis) has been compiled.

In particular, the proposed approach is able to semi-automatically retrieve some relevant rock mass parameters, namely orientation, number of sets, spacing/frequency, persistence, block size and scale dependent roughness, by analyzing high resolution point clouds acquired from terrestrial or aerial laser scanners.

The proposed method has been applied to different case studies, and the obtained properties have been compared with the results from traditional geomechanical surveys.

These applications demonstrated DiAna's ability to investigate rock masses characterized by irregular block shapes, and suggest applications in the field of engineering geology and emergency management, when it is often advisable to minimize survey time in dangerous environments and, in the same time, it is necessary to gather all the required information as fast as possible.

Keywords

Laser scanner • Point cloud • Geomechanical survey • Discontinuity • DiAna

Introduction

Traditional geomechanical surveys are performed in situ, either in one dimension (scanline method) or two dimensions (window method), and require direct access to the rock face for the collection of the relevant parameters.

ISRM (1978) selected the following ten parameters for the quantitative description of discontinuities in rock masses: orientation, spacing, persistence, roughness, wall strength, aperture, filling, seepage, number of sets, block size.

For practical and safety reasons, traditional geomechanical surveys are often carried out on limited sectors

of the rock mass, and usually they do not provide data for a complete reconstruction of the full variability of a rock mass.

The advantage of employing remote and high resolution surveying techniques for geomechanical purposes is based on the capability of performing both large scale (Oppikofer et al. 2008) and small scale (Lombardi et al. 2006) analyses and to rapidly obtain information on inaccessible rock exposures.

The main product of a long range laser scanning survey is a high resolution point cloud, obtained by measuring with high accuracy (millimetric or centimetric) the distance of a mesh of points on the object, following a regular pattern with polar coordinates.

During the last years many authors have been working on the extraction of 3D rock mass properties from remotely acquired high resolution data, mainly digital photogrammetry and LIDAR (Slob et al. 2005; Jaboyedoff et al. 2007; Ferrero et al. 2009; Lato et al. 2009; Sturzenegger and Stead 2009).

G. Gigli (✉) • N. Casagli
Department of Earth Sciences, University of Florence, Via La Pira 4,
Florence, Italy
e-mail: giovanni.gigli@unifi.it



Fig. 1 The investigated rock wall next to Triponzo village

Description of the Algorithm

Rock faces with rugged shape can be investigated by inspecting the discontinuity surfaces exposed on the slope. Such 3D approach requires the extraction of clusters of points belonging to the same discontinuity plane from the point cloud; subsequently, a spatial analysis for the quantitative description of discontinuities within the rock mass has to be performed.

The proposed approach is described in detail in Gigli and Casagli (2011), and is based on the definition of least squares fitting planes on clusters of points extracted by moving a sampling cube on the point cloud. If the associated standard deviation is below a defined threshold, the cluster is considered valid. By applying geometric criteria it is possible to join all the clusters lying on the same surface; in this way discontinuity planes can be reconstructed, and rock mass geometrical properties are calculated.

The advantage of using this procedure lies in its capability to investigate all the geomechanical parameters that do not require direct access to the rock mass, thus, making this a more complete analysis with respect to the existing methods. The output ISRM (1978) parameters are: orientation, number of sets, spacing/frequency (and derived RQD), persistence, block size and scale dependent roughness.

Field Applications

Triponzo (Umbria Region, Central Italy)

Due to its morphology, seismicity and geomechanical features of rock masses, the valley formed by the Nera river (Valnerina) is characterized by high rock fall risk especially in the villages and along the main roads. Rock

falls were abundant near the Triponzo village, where during the last most relevant seismic shock (September and October 1997) many events seriously damaged the main roads (ss209, ss320) and the Village itself (Marzorati et al. 2002; Guzzetti and Reichembach 2004).

The tool described in this paper was employed within a semi-automatic procedure for the complete definition of risk scenarios associated with rockfalls using laser scanning technologies.

Geomechanical surveys were executed using traditional methodology and laser scanning technique on the main rock wall, near the village of Triponzo, where the Maiolica Formation (micritic limestones) outcrops (Fig. 1).

A total of more than 400 discontinuity planes were extracted from the high resolution point cloud of the rock wall (Fig. 2), and their orientation was employed as input parameter for the kinematic analysis together with the high resolution DEM obtained by processing laser scanning data. In this way a wider portion of the rock mass has been investigated, with respect to traditional surveying methods, with a consequent higher significance from a statistical point of view.

In particular, for the definition of the main source areas, a spatial kinematic analysis has been performed by using discontinuity orientation data extracted from the point cloud by Diana.

This kind of analysis is able to establish where a particular instability mechanism is kinematically feasible, given the geometry of the slope and the orientation of discontinuities (Goodman and Bray 1976; Hoek and Bray 1981; Matheson 1983; Hudson and Harrison 1997).

The main instability mechanisms investigated with this approach are: *plane failure*; *wedge failure*; *block toppling*; *flexural toppling*.

Casagli and Pini (1993) introduced a kinematic hazard index for each instability mechanism. These values are calculated by counting poles and discontinuities falling in critical areas.

A spatial kinematic analysis was performed on each unit triangle of the surface model by applying the method proposed by Lombardi (2007), which extends the validity of kinematic analysis concepts to overhanging slopes.

From the kinematic analysis results (Fig. 3) it follows that the slope next to the village of Triponzo is subject to instability related to plane failure, wedge failures and flexural toppling, and the main source areas, useful for runout simulations, were extracted.

Chiessi (Elba Island, Tuscany)

In the western sector of Elba Island, the monzogranitic body of Mt. Capanne, and its associated thermo-metamorphic aureole outcrop (Barberi and Innocenti 1966; Dini et al. 2002).

Fig. 2 Point cloud coloured based on the different joint sets (*red: Jn1; blue: Jn2; yellow: BG*) and polygons bounding the extracted discontinuities (*left*). Stereographic projection of discontinuity pole density, and modal planes (*right*)

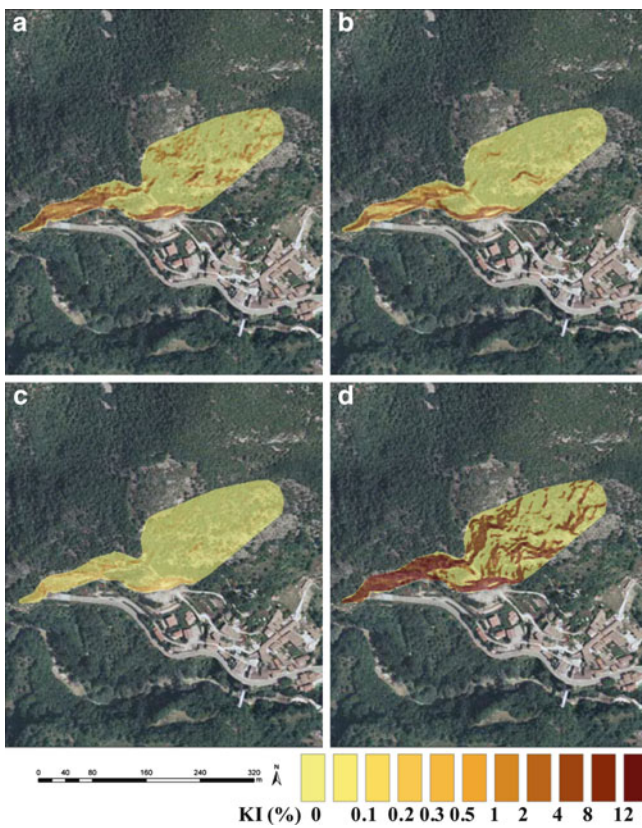
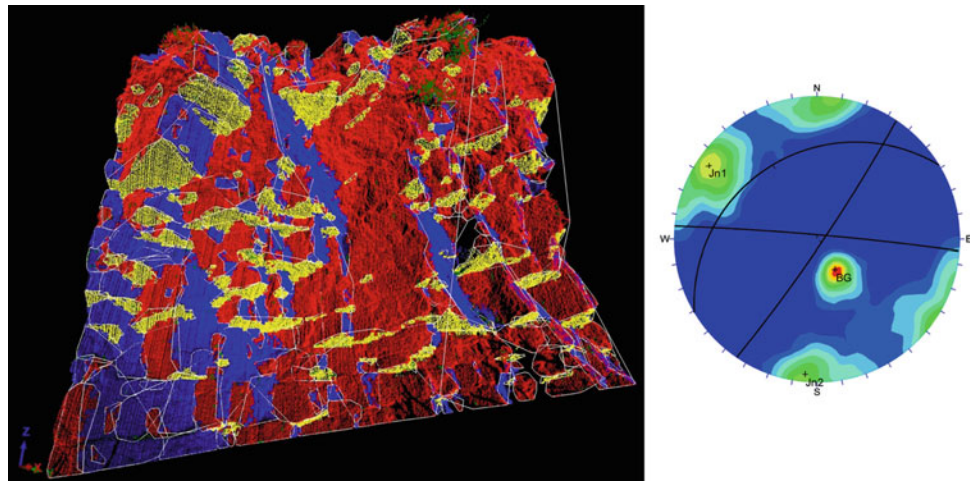


Fig. 3 Kinematic analysis results: (a) Planar failure; (b) wedge failure; (c) block toppling; (d) flexural toppling

From a geomorphologic point of view the investigated area is characterized by extremely steep rock slopes (Fig. 4), which, due to their high fracturing and to the occurrence of an important slope dipping joint set, often experience the detachment of rock blocks of various dimensions. The most credible scenario is thus associated to the plane or wedge failure of large portions of rock mass. These blocks threaten



Fig. 4 The investigated rock mass

the beautiful panoramic route of the Provincial Road n. 25 that is located on the hillside.

In order to investigate these phenomena, an accurate geomechanical survey has been carried out by using traditional methods as well as advanced semi-automatic remote sensing applications (Gigli and Casagli 2011).

Figure 5a reports the stereographic projection of poles and density contour lines of the traditionally surveyed discontinuities, where five different joint sets can be recognized.

A laser scanning survey of the whole investigated area has been carried out with the following purposes:

- To build a detailed 3D model;
- To accurately define the risk scenarios by extracting the shape of the main blocks and calculating their volume;
- To integrate the traditional geomechanical survey in inaccessible areas by applying the DiAna tool.

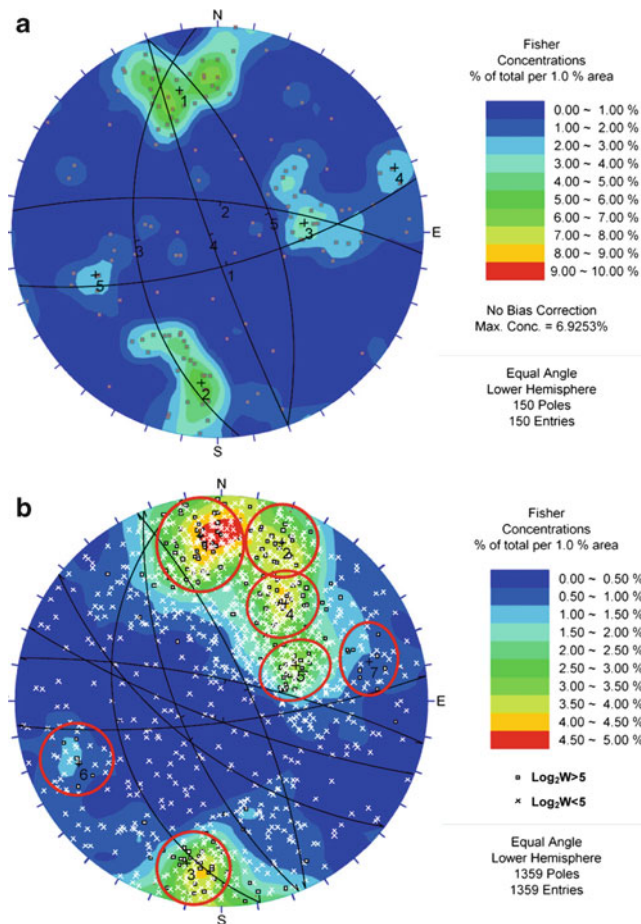


Fig. 5 Stereographic projection of discontinuity poles and modal planes from the field survey (a) and from the semi-automatic analysis (b)

Figure 5b reports the poles of the semi-automatically extracted discontinuities. A total of 1,359 planes have been recognized and their density contour lines are very similar to those obtained by means of traditional surveys. With the aim of identifying the main discontinuity sets, each plane has been assigned a weight (W) based on the product between its surface area and the number of points constituting it; the poles have been consequently drawn with different symbols based on the $\log_{10} W$.

By observing Fig. 5b the poles with higher weight are clustered according to seven different discontinuity sets, reported in Fig. 6.

Thus the high resolution of the point cloud allowed the semi-automatic method to analyzed a higher number of poles and to distinguish even those discontinuity sets separated by low dihedral angles.

The presence of an important discontinuity set with high persistence dipping with slope due to rock foliation (FO) (Jn3 in Fig. 5a; Jn5 in Fig. 5b; Fig. 6e), is responsible for the

occurrence of slipping planes which are able to isolate very large portion of rock mass (Figs. 4 and 7).

Should this kind of event happen, the defense barrier would be destroyed and the road plane would be covered by a huge amount of rock debris.

For this reason a detailed stability analysis of the main overhanging masses has been carried out. The most important parameter for this analysis is the frictional resistance acting on the basal plane, which, in turn, depends on the uniaxial compressive strength of the discontinuity walls and on the surface roughness (Patton 1966; Barton 1973, 1976). The most practical method for estimating the roughness of a discontinuity plane is by visual comparison of sampled roughness profiles with standard profiles published by Barton and Choubey (1977). Moreover, it has been observed that discontinuity roughness is characterized by a very marked scale effect (Barton and Bandis 1982).

To overcome this problem a 3D approach can be pursued, as suggested by ISRM (1978), by sampling the local surface orientation with a compass and disc clinometers with different diameters. This procedure requires however direct accessibility to the discontinuity plane and is quite time consuming, as a minimum number of 250 measures is suggested for the operation to be valid. The proposed algorithm fits in well with these concepts and allows us to rapidly perform quantitative measures of the roughness of the main discontinuity surfaces at various scales.

A searching cube with different dimensions (0.1, 0.2, 0.4, 1, 2 m and maximum surface persistence) is moved along the point cloud representing the selected discontinuity. If the number of points within the cube exceeds a prescribed threshold (to make sure the selection is centred on the surface) the best fitting plane dip and dip direction are obtained, and associated points are extracted from the surface. By plotting the orientation values on a stereoplot, the discontinuity roughness angles at various scales can be measured.

It is worth stressing that the reliability of this procedure depends mainly on the accuracy of the point cloud data; if it is too low, this could lead to an overestimation of surface roughness (Rahman et al. 2006), especially for small scale analyses (0.1, 0.2 m), or low resolution point clouds.

Figure 8 reports the stereographic projection of the roughness characteristics for different reference dimensions, calculated for the basal plane represented in Fig. 7. We can observe how the pole scattering decreases with increasing reference cube dimension, while the very high scattering associated to small reference cube dimension are probably due to the relative low accuracy of the laser scanning measurements.

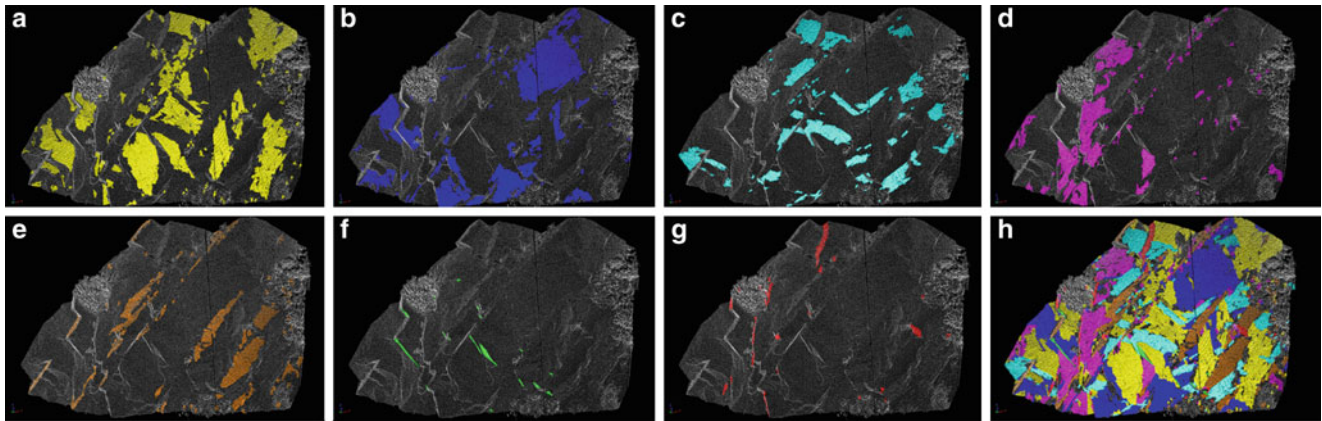


Fig. 6 Main joint sets extracted from the point cloud. (a) Jn1; (b) Jn2; (c) Jn3; (d) Jn 4; (e) Jn5 (FO); (f) Jn6; (g) Jn7; (h) all



Fig. 7 Plane failure surface along high persistence discontinuity

For the stability analyses, the frictional resistance associated to large scale roughness (reference cube dimensions: 1, 2 m) was calculated, and the resulting Factor of safety of the investigated rock masses are quite low, ranging from 1.14 to 1.27. For this reason a real time monitoring system equipped with meteo-station and crack gauges has been installed.

Conclusions

With the aim of extracting 3D structural information from high resolution point clouds, a Matlab tool, called DiAna (Discontinuity Analysis) has been compiled.

Six of the ten parameters suggested by ISRM for the quantitative description of discontinuities (orientation, spacing, persistence, roughness, number of sets, block size) can be semi-automatically calculated with the proposed method.

The remaining four parameters (aperture, seepage, wall strength and filling) cannot be assessed from conventional high resolution point clouds, as their estimation requires direct access to the rock face.

The presented method allows us to investigate larger portions of the rock mass related to field surveys, and all output parameters are quantitatively measured.

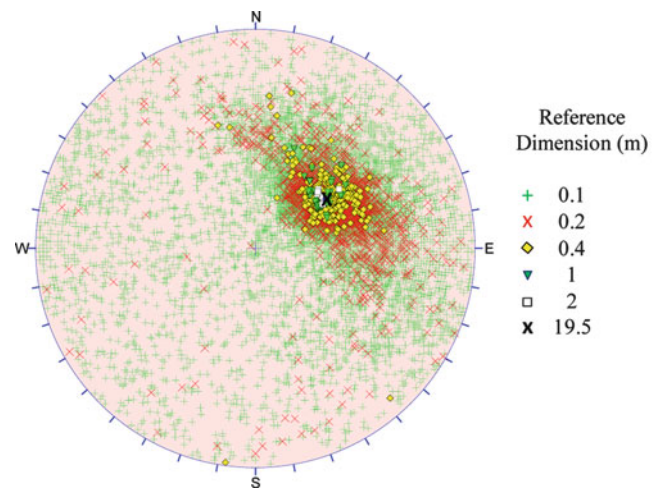


Fig. 8 Surface roughness represented by pole scattering calculated by varying the reference cube dimension

The presented applications show how the proposed method can be useful to improve and integrate data acquired by means of traditional field surveys.

References

- Barberi F, Innocenti F (1966) I fenomeni di metamorfismo termico nelle rocce peridotitico-serpentinose dell'aureola del Monte Capanne (Isola d'Elba). *Period Mineral* 25:735–768
- Barton NR (1973) Review of a new shear strength criterion for rock joints. *Eng Geol* 7:287–332
- Barton NR (1976) The shear strength of rock and rock joints. *Int J Rock Mech Min Sci Geomech Abstr* 13:1–24
- Barton NR, Bandis S (1982) Effects of block size on the shear behavior of jointed rock. In: *Proceedings of the 23rd U.S. symposium on rock mechanics, Berkeley*. Keynote lecture, pp 739–760
- Barton NR, Choubey V (1977) The shear strength of rock joints in theory and practice. *Rock Mech* 10:1–54
- Casagli N, Pini G (1993) Analisi cinematica della stabilit  in versanti naturali e fronti di scavo in roccia. In: *Proceedings 3^o Convegno Nazionale dei Giovani Ricercatori in Geologia Applicata, Potenza* (in Italian)

- Dini A, Innocenti F, Rocchi S, Tonarini S, Westerman DS (2002) The magmatic evolution of the late Miocene laccolith-pluton-dyke granitic complex of Elba Island, Italy. *Geol Mag* 139:257–279
- Ferrero AM, Forlani G, Roncella R, Voyat HI (2009) Advanced geostructural survey methods applied to rock mass characterization. *Rock Mech Rock Eng* 42:631–665
- Gigli G, Casagli N (2011) Semi-automatic extraction of rock mass structural data from high resolution LIDAR point clouds. *Int J Rock Mech Min Sci* 48(2):187–198
- Goodman RE, Bray JW (1976) Toppling of rock slopes. In: *Proceedings of the special conference on rock engineering for foundations and slopes*, vol 2. ASCE, Boulder, pp 201–234
- Guzzetti F, Reichenbach P (2004) Rockfall hazard and risk assessment along a transportation corridor in the Nera Valley, central Italy. *Environ Manage* 34(2):191–208
- Hoek E, Bray JW (1981) *Rock slope engineering*, revised 3rd edn. Institution of Mining and Metallurgy, London
- Hudson JA, Harrison JP (1997) *Engineering rock mechanics*. Pergamon, Oxford
- ISRM (1978) Suggested methods for the quantitative description of discontinuities in rock masses. *Int J Rock Mech Min Sci Geomech Abstr* 15:319–368
- Jaboyedoff M, Metzger R, Oppikofer T, Couture R, Derron MH, Locat J, Turmel D (2007) New insight techniques to analyze rock-slope relief using DEM and 3D-imaging cloud points: COLTOP-3D software. In: *Proceedings of 1st Canada – U.S. rock mechanics symposium*, Vancouver, 27–31 May 2007, pp 61–68
- Lato M, Diederichs MS, Hutchinson DJ, Harrap R (2009) Optimization of LiDAR scanning and processing for automated structural evaluation of discontinuities in rockmasses. *Int J Rock Mech Min Sci* 46:194–199
- Lombardi L (2007) *Nuove tecnologie di rilevamento e di analisi di dati geomeccanici per la valutazione della sicurezza*. Ph.D. thesis, Università degli studi di Firenze, in Italian
- Lombardi L, Casagli N, Gigli G, Nocentini M (2006) Verifica delle condizioni di sicurezza della S.P. Lodovica in seguito ai fenomeni di crollo nella cava di Sesto di Moriano (Lucca). *Giornale di Geologia Applicata* 3:249–256, in Italian
- Marzorati S, Luzi L, De Amicis M (2002) Rockfalls induced by earthquakes: a statistical approach. *Soil Dyn Earthq Eng* 22:565–577
- Matheson GD (1983) *Rock stability assessment in preliminary site investigations – graphical methods*. Transport and Road Research Laboratory Report 1039
- Oppikofer T, Jaboyedoff M, Keusen HR (2008) Collapse at the eastern Eiger flank in the Swiss Alps. *Nat Geosci* 1:531–535
- Patton FD (1966) Multiple modes of shear failure in rock. In: *Proceedings of the 1st congress of the international society of rock mechanics*, vol 1, Lisbon, pp 509–513
- Rahman Z, Slob S, Hack R (2006) Deriving roughness characteristics of rock mass discontinuities from terrestrial laser scan data. In: *Proceedings of the 10th IAEG congress, “Engineering geology for tomorrow’s cities”*, 6–10 Sept 2006, Nottingham, UK, Geological Society of London, paper 437, 12p
- Slob S, Hack R, Van Knapen B, Turner K, Kemeny J (2005) A method for automated discontinuity analysis of rock slopes with 3D laser scanning. *Transport Res Rec* 1913:187–208
- Sturzenegger M, Stead D (2009) Quantifying discontinuity orientation and persistence on high mountain rock slopes and large landslides using terrestrial remote sensing techniques. *Nat Hazard Earth Syst Sci* 9:267–287



Geological and Geophysical Tests to Model a Small Landslide in the Langhe Hills

Sabrina Bonetto, Cesare Comina, Andrea Giuliani, and Giuseppe Mandrone

Abstract

In April 2009, North-West Italy was interested by heavy rainfalls that triggered several landslides, especially of shallow type, and caused relevant rise of water level in many rivers, in some cases even beyond the alert level. Particularly in the hills near Alba (NW Italy), many landslides occurred, most of them belonging to the debris flow or soil slip types. In this area, a small but interesting landslide involved a local road and a high quality, recently planted, vineyard. The present study shows the use of different disciplinary approaches focused to understand the behaviour of this landslide: in particular, besides geological and geomorphologic studies, detailed topographic and geophysical surveys together with an in situ geotechnical/geomechanic characterization were applied. The combined interpretation of the different techniques and of field observations allowed to define a geological and technical model of the landslide, both in surface than in depth, that clarified the triggering mechanism of the landslide and allowed to perform a back analysis on both strength and pore pressure parameters.

Keywords

Heavy rainfall • Heterogeneous rock masses • Geophysical tests • Landslide • Langhe • NW-Italy

Introduction

The study area is located in the southern Piedmont's hilly territory (Langhe), near Alba (Fig. 1a). The geology is represented by sedimentary units mainly composed of terrigenous successions of interbedded layers of sandstone, marls and siltstone which are shaped with a typical "cuestas" morphology.

In this zone, between 26th and 28th April 2009 heavy rainfall, substantially exceeding the monthly values, were recorded (among 150 and 200 mm, which corresponds to about 25 % of average annual rainfalls). Moreover, this event was anticipated by a particular rainy period: April

2009 was, in fact, the third rainiest month in the last century, and it followed a particular rainy and a very snowy winter too. For these reasons, a remarkable rise of water level in most of the rivers (especially Tanaro and Po Rivers) and the triggering of many landslides were observed. In this respect, Langhe hills are well known for their tendency to slide, especially with planar type movements (Cruden and Varnes 1996), that mainly occurred on the gently dipping slope, and are very interesting for the very low angle of the sliding surfaces (Mandrone 2004). On the contrary, steep slopes are mainly interested by surface phenomena connected to the movement of the covers, such as earth flows or rotational earth slides.

As it can be observed in Fig. 1b, the study area is characterized by many recent landslides related to the mentioned rain event. The present study is focalized on a small failure, about 100 m long \times 50 m wide, involving a road and a recently planted vineyard (Fig. 1b). A multidisciplinary

S. Bonetto (✉) • C. Comina • A. Giuliani • G. Mandrone
Dipartimento di Scienze della Terra, Università degli Studi di Torino,
Via Valperga Caluso 35, Torino, Italy
e-mail: sabrina.bonetto@unito.it

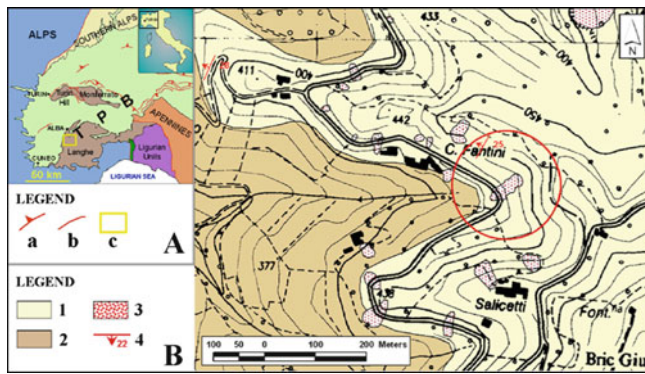


Fig. 1 Location map and geological setting of the study area. (a) Geological sketch map of Tertiary Piedmont Basin (TPB): (a) thrust fault, (b) fault, (c) study area; (b) geological setting of the study area: (1) Diano d'Alba Sandstones F., (2) Sant'Agata Fossili Marls F., (3) recent landslides occurred in April 2009, (4) strike and dip of beds. The studied area is marked by a red circle

integrated approach (Chelli et al. 2006) has been adopted: topographic surveys, geophysical surveys and geotechnical characterization were combined to obtain a geological and technical model of the slope.

A common task in slope stability studies is to retrieve the internal structure and the mechanical properties of the soil characterizing the slope together with the groundwater circulation. It is indeed of major importance to determine the geometry of slope instability, particularly the position of the sliding surface, in order to facilitate reliable analyses and mitigation (Bruno and Marillier 2000).

In many cases, the information on the depth and lateral continuity of the sliding surface cannot be obtained through boreholes (due to the cost of drilling) or geological investigations, as well as the identification of water distribution inside the slope. Geophysical techniques can be profitably used for this purpose. Satisfactory results in the investigation of landslides by means of a combination of geophysical and geotechnical techniques are reported by many authors (e.g. Mauritsch et al. 2000). Moreover, when shallow and small landslides are concerned, as in the present study, geophysical tests can be strongly cost effective in respect to other invasive methods. Best practice suggests that various (direct and indirect, surface and subsurface) methods should be used and cross checked to obtain more realistic results and best data to plan monitoring systems and mitigation.

In respect to geophysical techniques, water circulation paths or infiltration zones may successfully be delineated by electric resistivity methods (Bogoslovsky and Ogilvy 1977; McCann and Forster 1990; Hack 2000). Moreover the limit between unstable weathered material and underlying stable bedrock is possible where they have different porosities and thus different resistivity values. The imaging of the electrical properties of the subsoil can thus provide

information about the overburden thickness, the geometry of the sliding surface and the groundwater pathways (Godio and Bottino 2001; Suzuki and Higashi 2001). On the other hand, seismic methods can be used to infer the mechanical structure of the sliding body. Seismic refraction is particularly useful to detect discontinuities in the subsoil where strong contrast of seismic velocity have occurred between near surface degraded materials and stable bedrock. However, the low sensitivity to the solid skeleton properties in saturated soils, due to the influence of water on the P wave velocity, and the lack of resolution of surface refraction tomography affects the reliability of the P-waves analysis. In this respect, a combined acquisition of S-wave velocities will help in delineating a more complete framework (e.g. Jongmans et al. 2000).

Geophysical tests usually are not completely adequate alone, so the combined use with other geotechnical surveys (e.g. drillings or penetration tests, as in this study) will strongly help in confirming the uncertainties deriving from their evidence.

Geological and Morphological Setting

The studied area (Fig. 1a) belongs to the Tertiary Piedmont Basin (Gelati and Falletti 1996). This sequence forms a gentle NW dipping uplifting structure, characterized by “cuestas” morphogenesis carried out by fluvial erosion. Indeed, the hills of the Langhe are characterized by asymmetrical slopes that range from 25° to 40° towards SW and from 10° to 25° towards NW.

This geological sequence is intersected by a series of faults mainly NE-SW and NW-SE trending. In some areas, these faults produced joints, sometimes very pervasive in surface. Most of the discontinuities are weathered due to water circulation; as an evidence of the high jointing level producing a surface water reservoir, the presence of many perpetual springs and shallow wells is noted (Mandrone 2004). The drainage pattern is mainly controlled by morphology: main rivers cut deeply the landscape, according NE-SW faults trending, while most of the second-order streams mainly follow others geological structures in NW-SE direction.

Two geological formations characterize in detail the studied area (Fig. 1b): the Diano d'Alba Sandstones Formation at the top of the hill, and the S. Agata Fossili Marls Formation, in the lower part of the slope. The former is represented by sand and sandstones dark-grey or yellowish coloured, some metres thick, interbedded to clayey-sandy marls, some decimetres thick. The latter is characterized by marls and clayey-marls, blue-grey coloured. These formations are usually considered as impermeable, but a remarkable water circulation takes place during heavy or prolonged rainfalls

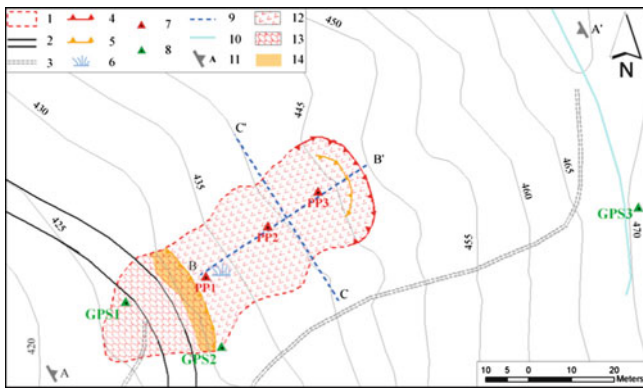


Fig. 2 Details of the landslide and of the field investigations: (1) landslide borders, (2) road, (3) track, (4) main scarp, (5) minor scarp, (6) water impoundments, (7) dynamic penetration test sites, (8) GPS ground control point and total station bases, (9) geophysical arrays, (10) trace of geological section, (11) slide, (12) flow, (13) man-made slope

within the coarser levels and/or within the less cemented ones. The bedrock coverage is usually very thin (less than half meter) and characterized by silts and fine sands.

These geological structures are responsible for the tendency of the area to slide: last widespread events were during the flooding of November 1994 (Bottino et al. 2000). Furthermore, the landslides themselves create typical landforms that play an important role in their further development and reactivation.

Field Surveys

Topography and Morphometry of the Landslide

The landslide involved a concave slope dipping SW of about 20° which is cut by a road just at the bottom (Figs. 2 and 3). After the event, a field survey was carried out on the area: preliminary surface observations pointed out two scarps, at the top of the landslide area, with height of about 1 m each. Using a total station, a more detailed topographic survey investigated the landslide and a significant area around it, allowing to define the morphometry after the failure. Georeferentiation was obtained using information from accurate location of ground control points during post-processing elaborations. These points (three stations) were collected through a GPS device (dual frequency, dual-constellation RTK GPS, 24 GPS + 11 GLONASS Satellites with fully integrated receiver/antenna). Data elaboration was carried out by a GIS system to relate the collected data with the following digital thematic cartographies.

Water must have played an important role, as humidity traces were clearly visible for many days after the event in different parts of the landslide body, in particular in the central and in the lower part of the slide. Particular attention

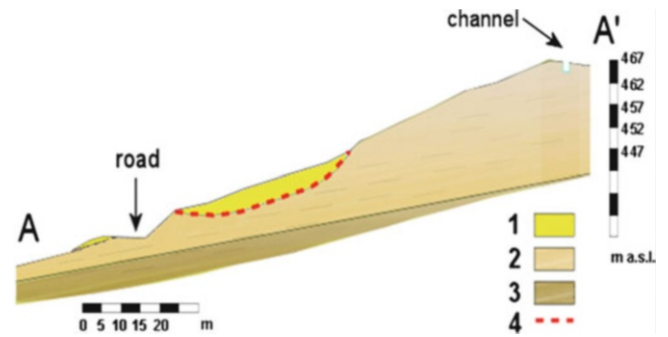


Fig. 3 Longitudinal section of landslide (for location see Fig. 2): (1) displaced material, (2) Diano d'Alba Sandstones F., (3) Sant'Agata Fossili Marls F., (4) sliding surface

was paid to a wet area observed in the lower part of the slide, where evidence of liquefaction of the sandy levels was widespread.

The foot of the landslide over passed the road: it is represented by a debris flow of the displaced material. Luckily, a rural house located just a few meters below the road wasn't affected by the landslide; all dismembered material lying on the road was immediately taken away to permit local traffic.

Just on the other side of the hill, a man made trench was observed (Fig. 3). This trench acts as agricultural channel and collects water from houses and fields located to the E of the study area; due to the abundant rainfalls of the days immediately before the sliding, it should be almost full when the slope failed.

Geological/Geomechanic Characterization

The outcropping geological formations are characterized by alternations of sands (differently cemented) and clays or claystones. They are generally subjected to quick meteoric weathering when outcropping. According to the mechanical classification proposed by Marinis and Hoek (2001), the Arenarie di Diano d'Alba Formation represents a heterogeneous rock mass, belonging to the C type, with a GSI (Hoek and Brown 1997) equal to 35. Furthermore, this complex shows low-quality geomechanical properties, with the uniaxial compressive strength of the intact rock elements (σ_{ci}) of about 5 MPa and m_i (constant defining the frictional characteristics of mineral components in the rock elements) of 10 (Mandrone 2006).

The Marne di S. Agata Fossili Formation outcrops in a lower position: mostly made up of silts and clayey-silts belonging to Flysch type G (undisturbed silty or clayey shale with or without few very thin sandstone layers), and can be also reference as weak, heterogeneous rock masses (WH type; $\sigma_{ci} = 2$ MPa, $m_i = 7$). This formation is deeply

influenced by degree of saturation, showing a brittle to ductile transition at low lithostatic pressure. In respect to water circulation, this formation may be considered almost impermeable.

From an hydrogeological point of view, a remarkable water circulation takes place within the coarser levels and/or within those less cemented, or along the more open joints of faults.

Geotechnical Characterization

Geotechnical surveys were done some days after the landslide event. For in situ surveys, a light dynamic penetrometer was used with 30 kg weight hammer falling from a height of 20 cm. Three tests (PP₁, PP₂ and PP₃) were carried out in the central part of the main body of the landslide, along a line also used for geophysical surveys (Fig. 2), in order to verify the state of the subsoil (according to the mechanical resistance) and to obtain approximate location of the sliding surface.

The results of the three surveys are reported in Fig. 4. All tests revealed a general increase in soil density with depth. First change is evident at 0.8–1 m of depth, probably in correspondence of the soil-subsoil transition. However, at this depth, a still low subsoil resistance is noted; an abrupt change in penetration resistance can be instead observed at about 3–3.5 m of depth, where the bedrock was probably reached.

Since a non-standard penetrometer was used, no relations are attempted of the N-value with specific soil properties, and only qualitative profiles referred to penetration resistance of the soil and subsoil were used, particularly to integrate and validate the results of geophysical tests. The grain-size distribution curve of samples of dismembered material collected within the main landslide body was also obtained, corresponding to weakly silty-clayey sand.

Geophysical Surveys

Two different geophysical methods were applied: respectively, electric and seismic tomography (concerning both P and S waves velocities) along the major and minor axis of the ellipse drawn by the border of the landslide (for location, see Fig. 2).

Electric tomographies were acquired with two different spreads of 32 electrodes with 1.5 m electrode spacing deployed along the B-B' and C-C' lines, to provide an image of the slope in both directions. The acquisition used a PASI tomograph and a Wenner-Schlumberger measuring

sequence; with such a sequence, it is indeed possible to obtain a good compromise between both vertical and lateral resolution. Due to the relatively shallow expected sliding surface, reduced arrays length were used allowing for an investigation depth of about 10 m. Acquired data were inverted by the commercial inversion code Res2Dinv® (Loke and Barker 1996).

Seismic tomographies were performed only along the maximum slope line (B-B' line) but, in order to retrieve both S and P wave velocities, different sources and sensors were used. For P waves, an array of 24 vertical 4.5 Hz geophones with 2 m spacing and a vertical hammer source were used; for S waves, an array of 24 swyphones™ (Sambuelli and Deidda 1999) with 2 m spacing and an appropriate SH source were adopted. Different shot positions were used along the survey line in order to have adequate data for tomographic interpretation. Both arrays were acquired with a Geometrics Geode Seismograph and interpreted for tomography with the commercial code Rayfract®. The use of swyphones™ allowed a reduced time acquisition since no inversion of the source was necessary. The measuring techniques for S wave velocities usually require a more complex acquisition, which are particularly difficult to be attained – especially in complicated logistical conditions such as the ones that commonly characterize landslide sites.

The results of the two electric tomographies are shown in Fig. 5. A very shallow (1–1.5 m) dry layer overlying a zone of reduced resistivity can be noticed. This zone is located inside the sliding body and is probably related to porous wet material. At the bottom of this high-conductivity zone, evidence of an increase in resistivity can be related to the contact between the landslide body and the bedrock. A very good coherence in the results of the two surveys can be observed, particularly in the overlapping central zone where both images underline a decrease in resistivity in the central part of the slope. This can be explained by the presence of preferential flow path that can have favoured the sliding movement. Indeed, field evidence underlined the presence of a significant amount of water in this area right after landslide activation.

With respect to seismic tomographies, in Fig. 6 the results of P and S wave tests are shown. From both images, a clear evidence of the contact between the displaced material and the stable rock can be evidenced, helping to delineate the sliding surface. The P wave tomography seems to identify the presence of a low water table (around 15 m depth for P wave velocities of 1,500 m/s). This is coherent with previous data in the area since the tests were executed some times after the rainfall events, and a reequilibration of the water level probably occurred. In this respect, the results of the electric tomographies can be reinterpreted by excluding the

Fig. 4 Technical profiles of the dynamic penetrometer tests

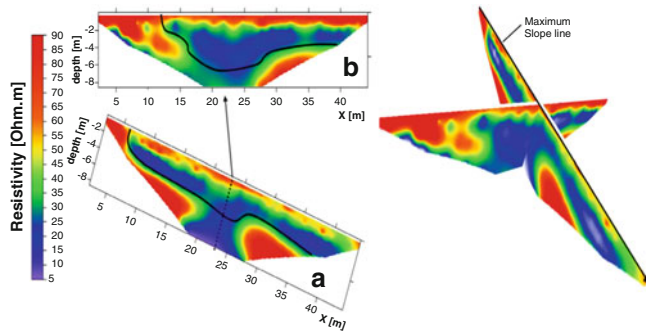
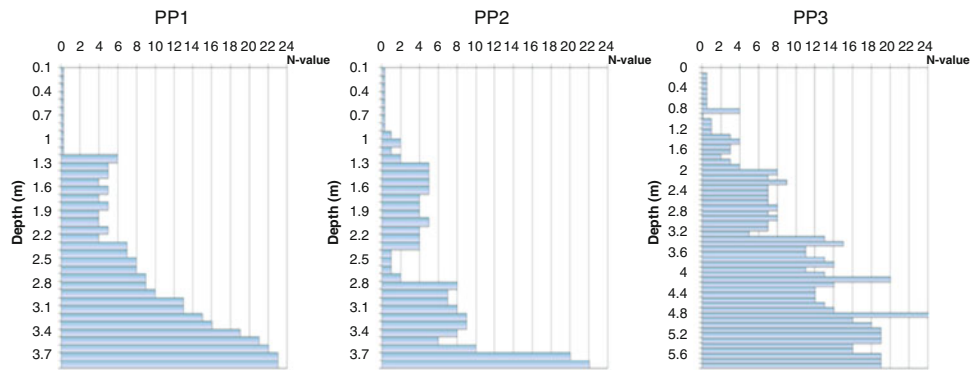


Fig. 5 Electric topographies, executed (a) longitudinal (B'-B) and (b) transversal (C'-C) to the slope, and probable position of the sliding surface (thick black line). On the right, a combined view of the two sections

presence of saturated material near the surface, and by attributing the decrease in resistivity to wet material with some clay content (cf. grain size distribution curves). Due to the increased sensitivity of shear waves to the soil skeleton properties, the S wave tomography is instead more able to delineate the variations in the structure of the soil near the slope. Indeed, the presence of a reduced velocity zone just in the middle of the slope is highlighted. The position of this zone is very coherent with the reduced resistivity of the central portion of the slope body, and can be related to loose material which favoured the water flow in the slope.

Discussion

Very often, small landslides are overlooked in term of geotechnical parameters by scientific research because risk associated with them are usually – but not always – negligible. In particular, small landslides are mostly considered from a statistical point of view, identifying – for example – threshold of rainfall to predict further failures (Aleotti 2004; Campus et al. 2000; Crosta 1998). Of course, detailed studies on many small landslide are too expensive in term of cost/benefits, especially if they do not represent a serious risk for society. However, even small phenomena can pose risk to people, lifelines and productive activities.

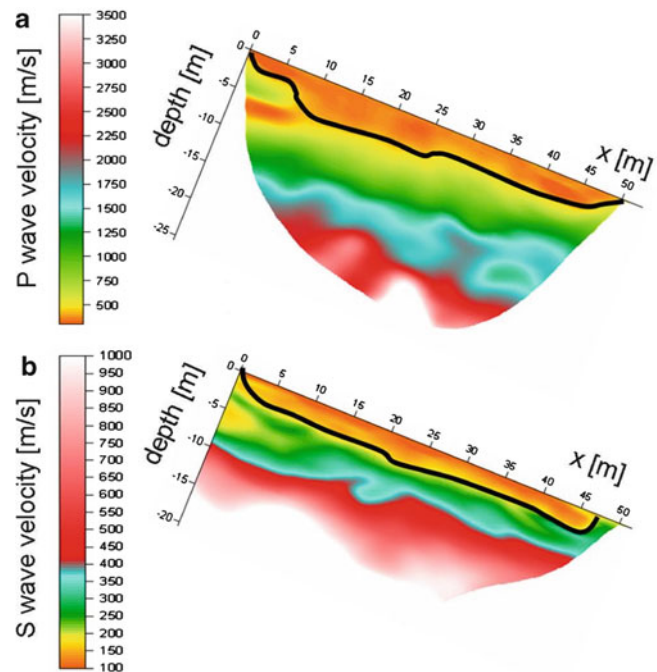


Fig. 6 Seismic P wave tomography and seismic S wave tomography executed longitudinal (B'-B) to the slope with probable position of the sliding surface (thick black line)

Instead, if the aim is to understand complex systems (like most landslides), by investigating a small phenomenon may allow to limit the unknowns and point out its peculiarities. In this case, the small size of the studied landslide (both in area and depth) allowed the application of relatively standard methodologies. The integration of these simple techniques suggests new approaches and solutions which can be applied also to more complex geological situations.

In particular, the applications of multidisciplinary approach allowed to: (1) identify the shape of the sliding surface, (2) characterize the geological materials from a technical point of view and (3) give suggestions about the role of groundwater. Only at this point of the research a numerical modelling, to better understand the triggering of the phenomenon, including the definition of shear strength resistance parameters and pore pressures acting at the time of sliding, is possible.

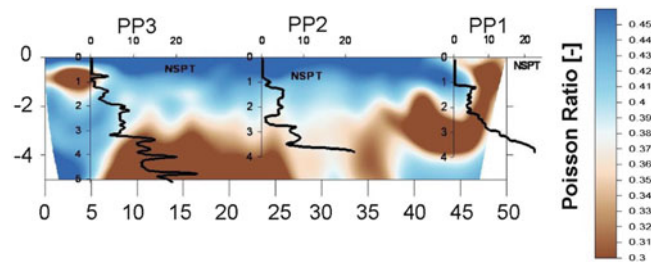
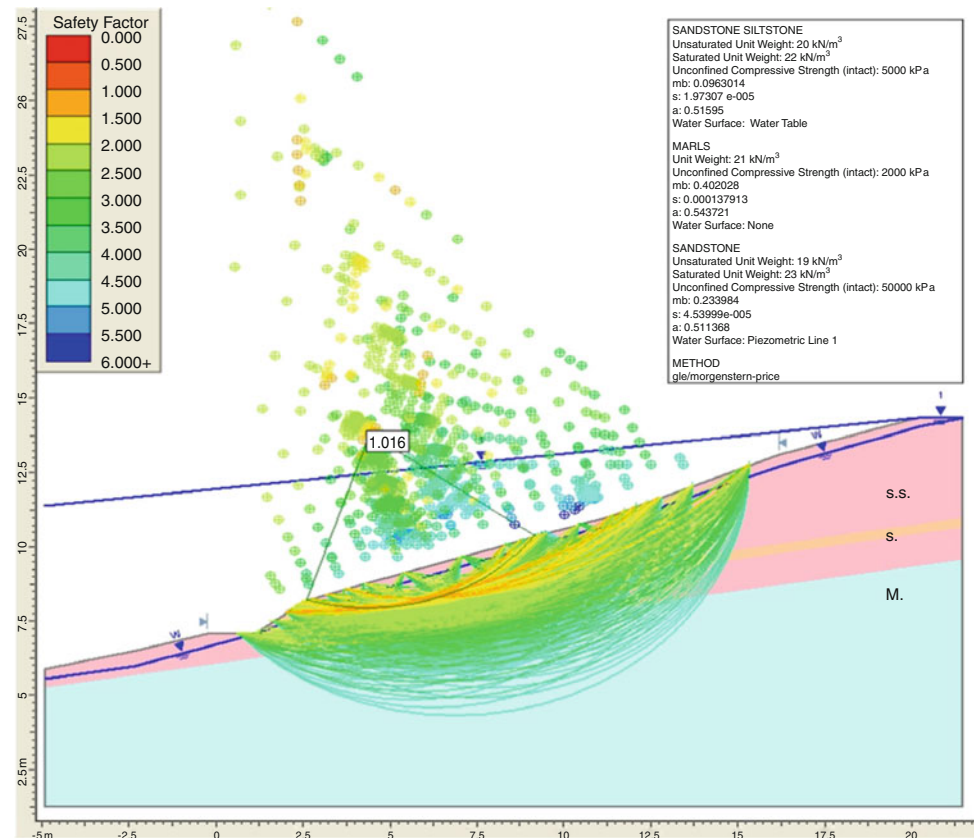


Fig. 7 Poisson ratio map in relation to of penetrometer tests along the major axis of the landslide

Fig. 8 Slope stability analysis with minor safety factor value coherent with measured sliding surface. Keys: S.S. sandstone and siltstone, S. sandy level, M. marl, w water table in S.S., l pressured water table in S.



Field observations and geophysical investigations highlighted that the landslide probably involved also the bedrock, and that the landslide body was composed by silty-sand about 3–4 m thick. Coherently with field observations and dynamic penetrometer tests, the sliding surface extracted from geophysical tests seemed to have a compound shape (rotational and translational). In this respect, in Fig. 7 a representation based on the poisson ratio extracted from the P and S wave velocity values is used to relate the results of both seismic and penetrometer tests. A very good correspondence is observed between the two results: particularly, the decrease in poisson ratio from typical values of shallow unconsolidated soils to the ones of more consistent and compacted bedrock is observed with a high correspondence with the increase in penetration

resistance. Moreover, a remarkable difference is observed between the different locations of penetrometer tests. In particular, near the PP₂ test, a reduced resistance zone was found.

Different conceptual models were supposed in the preliminary stage of the study, and numerical simulations aided to select the most realistic one.

In particular, we were successful to reconstruct the observed sliding surface introducing the following characteristics: (1) a high permeable sandy level below the landslide, where the wet level is located, implemented the simple geology of the slope; this level is probably connected to the channel at the top of the hill thanks to the jointing of the rock mass in that area, (2) a free water table in the Diano d'Alba formation close to the surface (“w” in Fig. 8), (3)

a pressured fast water circulation in the sandy level (“1” in Fig. 8) fed by waters in the channel at the top of the hill.

As a matter of fact, the main triggering mechanisms for this small landslide had both natural and man made origin. According to field evidence and using this conceptual model, back analysis allowed to obtain a good correspondence in terms of sliding surface.

Conclusions

The multidisciplinary approach used for this small landslide allowed to reconstruct a detailed geological model. Figures 3 and 8 show the conceptual model of the slope according to geological surveys, which was confirmed by the subsurface investigations. The landslide involved a flysch-type bedrock; it moved – at the top – as a rotational slide, and – in the middle part – as a translational one. The mobilized material turned into a debris flow that swept the road and part of the slope below.

The triggering of the landslide can be attributed mainly to the consistent groundwater incoming along a permeable sandy layer located 3–4 m in depth beneath the landslide. The water incoming was highlighted by surface evidence and confirmed by geophysical surveys which allowed to identify a permeable level just below the wetlands observed at surface. This should have substantially increased pore pressures and made the slope unstable, so that the “engine” of the phenomenon would be under the central part of the landslide body.

At moment, we have no groundwater direct measurements to demonstrate this theory but many evidences agree with our assumption: (1) very wet area at the base of the landslide was still present several days after the slide (notable ground water flow is necessary), (2) the location of this wet area can not be referred to direct rainfall, but is coherent with flows coming along sandstone levels at depth, (3) the recharge area of this permeable level can be placed near divide (probably just on the other slope), through NW-SE open joints and/or faults, and (4) numerical model confirmed this configuration.

The recognition of the influence of the man made channel near the divide as the main predisposing factor for this landslide allowed to design effective countermeasures for the safety of the slope (e.g. hydraulic insulation of the channel boundaries).

In conclusion, this small landslide was a good test site to cross-check data from various sources (geology, geomorphology, topography, geotechnics and geophysics), to collect them in a unique model verified by a numerical simulation that confirmed all the supposed conditions.

Acknowledgments We are glad to two students in Geology at Turin Faculty of Science (Miss Antonietti and Poti) that helped in collecting row data and to Dr. Sara Castagna who helped in a preliminary edition of the paper. Many thanks also to Giorgio Carbotta and Luigi Perotti for

technical support in the field measurements. We are indebted with Politecnico di Torino for the permission of using geophysical instrumentations.

References

- Aleotti P (2004) A warning system for rainfall-induced shallow failures. *Eng Geol* 73:247–265
- Bogoslovsky VA, Ogilvy AA (1977) Geophysical methods for the investigation of landslides. *Geophysics* 42:562–571
- Bottino G, Mandrone G, Torta D, Vigna B (2000) Recent morphological evolution and slope instability in a hilly area of piedmont (North Italy). In: Proceedings of the international symposium on engineering, geology, hydrogeology and natural disasters, Katmandù, Nepal. *J Nepal Geol Soc*, vol 22, pp 67–76
- Bruno F, Marillier F (2000) Test of high-resolution seismic reflection and other geophysical techniques on the Boup landslide in the Swiss Alps. *Surv Geophys* 21:333–348
- Campus S, Forlati F, Scavia C (2000) Preliminary study for landslides hazard assessments: GIS technique and multivariate statistical approach. In: Proceedings of the 8th international symposium on landslide, Cardiff, 26–30 June, vol 1, pp 215–220
- Chelli A, Mandrone G, Truffelli G (2006) Field investigations and monitoring as tools for modelling the Rossena castle landslide (northern Apennines – Italy). *Landslides* 3:252–259
- Crosta G (1998) Regionalization of rainfall thresholds: an aid to landslide hazard evaluation. *Environ Geol* 35:131–145
- Cruden DM, Varnes DJ (1996) Landslide types and processes. In: Turner AK, Schuster RL (eds) *Landslides: investigation and mitigation*. Transportation Research Board, Special report no. 247, National Research Council, Washington, DC, pp 36–75
- Gelati R, Falletti P (1996) The piedmont tertiary Basin. *Giorn Geol* 58:11–18
- Godio A, Bottino G (2001) Electrical and electromagnetic investigation for landslide characterisation. *Phys Chem Earth* 26:705–710
- Hack R (2000) Geophysics for slope stability. *Surv Geophys* 21:423–448
- Hoek E, Brown ET (1997) Practical estimates of rock mass strength. *Int J Rock Mech Min Sci Geomech Abstr* 34(8):1165–1186
- Jongmans D, Hemroulle P, Demanet D, Renardy F, Vanbrabant Y (2000) Application of 2-D electrical and seismic tomography techniques for investigating landslides. *Eur J Environ Eng Geophys* 5:75–89
- Loke MH, Barker RD (1996) Rapid least-squares inversion of apparent resistivity pseudosections using a quasi-Newton method. *Geophys Prospect* 44:131–152
- Mandrone G (2004) Il ruolo dell’acqua nell’insacco di frane planari negli ammassi rocciosi eterogeneo delle Langhe (Italia nord-occidentale). *GEAM* 112:83–92
- Mandrone G (2006) Engineering geological mapping of heterogeneous rock masses in the North Apennines: an example from the Parma Valley (Italy). *Bull Eng Geol Environ* 65:245–252
- Marinos P, Hoek E (2001) Estimating the geotechnical properties of heterogeneous rock masses such as Flysch. *Bull Eng Geol Environ* 60:85–92
- Mauritsch HJ, Seiberl W, Arndt R, Römer A, Schneiderbauer K, Sendlhofer GP (2000) Geophysical investigations of large landslides in the Carnic region of southern Austria. *Eng Geol* 56:373–388
- McCann DM, Forster A (1990) Reconnaissance geophysical methods in landslide investigations. *Eng Geol* 29:59–78
- Sambuelli L, Deidda GP (1999) Swyphonetm: a new seismic sensor with increased response to SH-waves. In: Proceedings of the 5th meeting of environmental and engineering geophysical society, Budapest
- Suzuki K, Higashi S (2001) Groundwater flow after heavy rain in landslide–slope area from 2-D inversion of resistivity monitoring data. *Geophysics* 66:733–743



Regional Distribution of Ash-Fall Pyroclastic Soils for Landslide Susceptibility Assessment

Pantaleone De Vita and Michele Nappi

Abstract

Debris flows involving ash-fall pyroclastic soils, which mantle slopes in the mountain ranges around the Somma-Vesuvius, represent a relevant societal risk. In the last years, many methods were applied to evaluate susceptibility and mobility of these landslides, considering at least two fundamental parameters: the slope angle and the thickness of the pyroclastic mantle. Despite this understanding, the assessment of soil thickness along slopes is still a challenging issue due to its high spatial variability and the steep morphological conditions that limit the use of traditional exploration methods. To overcome this problem, heuristic geomorphological methods were mostly applied up to now. In this paper, a regional-scale model of the ash-fall pyroclastic soils distribution along slopes is proposed, considering the isopach maps of each principal eruption. By means of field surveys, the model was validated and an inverse relationship between thickness and slope angle was found.

Keywords

Debris flows susceptibility • Debris flows runout • Ash-fall pyroclastic soil thickness

Introduction

The areas that surround volcanoes are worldwide recognised as characterised by a high economic value but prone to risks, directly and indirectly related to the volcanic activity. Besides lahars following eruptions, landslides, due to the instability of ash-fall pyroclastic deposits that mantle slopes of the surrounding mountain ranges, are the most important among the secondary risks. A unique case of this kind of landslide risk is represented in that part of the Campania region (southern Italy) that includes and surrounds the volcanic centers of the Somma-Vesuvius, the Phlegrean Fields and the Ischia Island. Owing to the high loss of human lives and the diffused damages suffered by buildings and infrastructures in the last century, Campania is one of the regions of Italy most threatened by landslides. The greatest

part of damages and loss of human lives due to landslides occurred at the feet of the mountainous chain that surround the Somma-Vesuvius volcano, where the ash-fall pyroclastic overburdens are still prone to become unstable in consequence of heavy and prolonged rainfall, events generating very rapid debris flows.

Field observations and slope stability modelling led to the understanding that this kind of flow-like landslides are triggered by initial small landslides (Jakob and Hungr 2005), occurring within the pyroclastic mantle, which subsequently evolve as debris avalanche on open slopes (Hungr et al. 2001) and becoming debris flows after channelling in the hydrographic network (Hungr et al. 2001).

The occurrence of a great number of deadly landslides is known from the chronicles of the last century and of recent years. Among these events, that occurred between 5 and 6 May 1998 in the Sarno mountain range was a high magnitude one because of the initiation of several tens of shallow landslides, the activation of many debris flows and the loss of 162 lives. After this major landslide event, national laws regarding the assessment of landslide risk were issued and

P. De Vita (✉) • M. Nappi
Department of Earth Sciences, University of Naples "Federico II",
Via Mezzocannone, 8, Naples 80132, Italy
e-mail: padevita@unina.it

many researches were carried out in order to assess landslide susceptibility and mobility. The studies based on geomorphological and heuristic approaches demonstrated that the slope morphological conditions and the ash-fall pyroclastic thickness along slopes were the fundamental factors controlling the instability. In detail, morphological factors, namely morphological discontinuities along slopes and the slope angle itself were recognised as key factors for the assessment of the landslide susceptibility as well as for the slope stability modelling (Celico and Guadagno 1998; Crosta and Dal Negro 2003; Di Crescenzo and Santo 2005; Guadagno et al. 2005; Cascini et al. 2008; Perriello Zampelli et al. 2011). Moreover, different scenarios of debris flows runout (Corominas 1996; Budetta and de Riso 2004) were issued considering both the relative altitude of the landslide and estimations of the potential debris volumes. The latter were inferred by both variable scenarios of areas detached by shallow landslides and of pyroclastic mantle thickness along slopes. The same scenarios were considered in designing of passive defence works constructed at the footslopes. Therefore, the distribution along slopes of ash-fall pyroclastic soils was considered as a fundamental factor to be assessed. Different attempts of estimating pyroclastic soil thickness along slopes were carried out applying geophysical surveys in some of the initiation areas of the 5 and 6 May 1998 landslides and applying geomorphological heuristic methods constrained by field measurements (Cascini et al. 2000).

In this paper, we propose a new approach for the assessment of the thickness of the pyroclastic mantle based on the regional distribution of ash-fall pyroclastic deposits and of their draping deposition along slopes (Fisher 1985). We considered previous results (De Vita et al. 2005, 2006, 2012), obtained in three sample areas of the Sarno and Lattari mountain ranges, which demonstrated the existence of an inverse relationship between the ash-fall pyroclastic soil thickness and the slope angle for values greater than 30° , up to the bedrock outcropping for values greater than 50° . According with these results, in the slope angle range lower than 30° , complete volcanoclastic series and thicknesses of the pyroclastic mantle, correspondent to the total ash-fall deposits fallen in the area, were observed.

Geologic Setting

The geology of the mountainous area that surrounds the volcanic centers of Campania is characterised by a carbonate platform pre-orogenic sedimentary series, deposited from the Mesozoic to the Cenozoic, which was involved in the Apennine orogenesis during the Miocene and constitute a thrust tectonic unit. This unit outcrops in Campania forming

the mountain ranges of Avella, Sarno, Lattari, Picentini and Salerno. Due to the Miocene and Pliocene tectonic phases, the carbonate series formed mountains and were faulted in monocline structures with structural slopes controlled by the recession of fault line scarps. The last extensional tectonic phase determined the sinking of the carbonate tectonic unit toward the Tyrrhenian Sea and the formation of a semi-graben structure at whose centre the volcanic activity began in the late Quaternary. The structural depression was filled by pyroclastic and alluvial deposits mainly erupted from the Phlegrean Fields and the Somma-Vesuvius, volcanoes forming the Campanian Plain. The explosive volcanic activity determined a number of Plinian and sub-Plinian eruptions whose ash-fall products were irregularly distributed within the Campanian Plain and on the surrounding mountain ranges, in accordance with the different orientation of the dispersal axes. Considering the principal explosive eruptions, the most important part of the ash-fall volcanoclastic series was outlined as follows (Rolandi et al. 2000).

The older volcanic deposits are mainly represented by the Campanian Ignimbrite (39 k-years), erupted from the Phlegrean Fields, for which an ash-fall phase was recognised, besides of the prevalent ash-flow one. These deposits were named "Ancient Pyroclastic Complex" (APC) (Rolandi et al. 2000), whose distal ash-fall tephra distribution involved a wide area of the European continent (Perrotta and Scarpati 2003). The younger pyroclastic products, named "Recent Pyroclastic Complex" (RPC) (Rolandi et al. 2000), were erupted by the Somma-Vesuvius constituting the prevalent deposit that cover slopes of the mountain ranges surrounding the Campania Plain. The most important eruptions constituting the RPC were: the Codola eruption, 25 k-years B.P. (Rolandi et al. 2000); the Sarno eruption, 17 k-years B.P. (Rolandi et al. 2000); the Ottaviano eruption, 8.0 k-years B.P. (Rolandi et al. 1993a); the Avellino eruption, 3.6 k-years B.P. (Rolandi et al. 1993b); the Pompei eruption, A.D. 79 (Lirer et al. 1973); the A.D. 472 (Rolandi et al. 1998) and the A.D. 1631 eruption (Rosi et al. 1993). The abovementioned eruptions have had dispersal axes mainly oriented eastward and oriented southward only in the case of the Pompei eruption (A.D. 79).

The complete volcanoclastic series, constituted by both the APC and the RPC, were observed in many natural and artificial outcrops as well as boreholes in the Campania Plain. Stratigraphic correlations carried out in the alluvial plain area showed different spatial distribution of the pyroclastic deposits due to the orientation of the dispersal axes of each eruptions and the erosional action of the drainage network. Despite the gradually variable stratigraphic setting that characterises the flat areas, the volcanoclastic series were identified as stratigraphically incomplete and reduced along the slopes due to denudational processes started since the

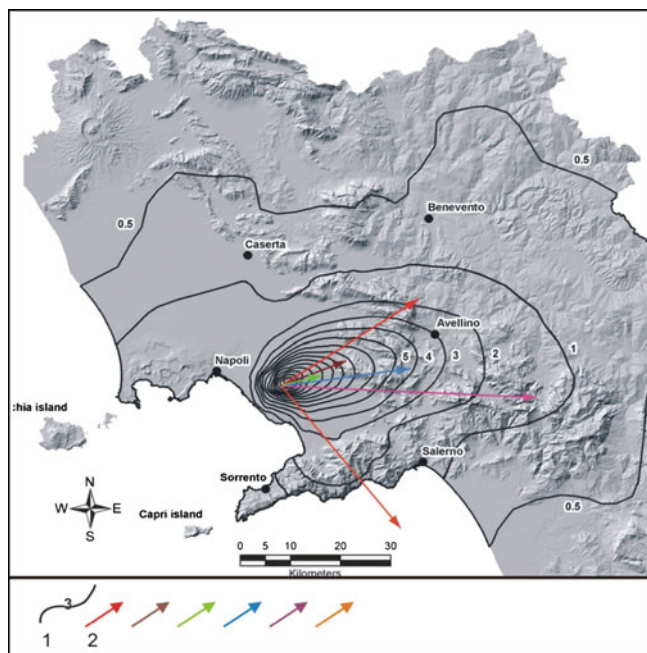


Fig. 1 Isopach map of ash-fall deposits obtained by summing the contribution of APC and RPC. Symbols: (1) total ash-fall isopachous lines; (2) dispersal axes of the main eruptions of the Somma-Vesuvius constituting the RPC (see text)

deposition, as it is clearly demonstrated by ancient debris flows deposited after or during the eruptions themselves.

Data and Methods

In order to assess the distribution of ash-fall pyroclastic soils along slopes, we updated previous results (De Vita et al. 2005) reconstructing the regional distribution of the ash-fall tephra by means of the isopach maps known from the volcanological literature. The sum of the ash-fall isopach maps of all the considered eruptions was carried out by means of the respective georeferentiation, conversion in numeric grids and algebraic sum in a GIS system (Fig. 1). The new estimation of the total ash-fall deposits resulted slightly different from the preceding one because of the additional implementation of the ash-fall phase of the APC (Perrotta and Scarpati 2003), besides of the RPC deposits. As previously observed (De Vita et al. 2005), the distribution of total ash-fall deposits can be recognised as inhomogeneous at the regional scale because it is characterised by two main dispersal axes, the principal oriented eastward and the secondary southward (Fig. 1).

Since the thicknesses of ash-fall deposits of each eruption were estimated in outcrops or boreholes mainly located

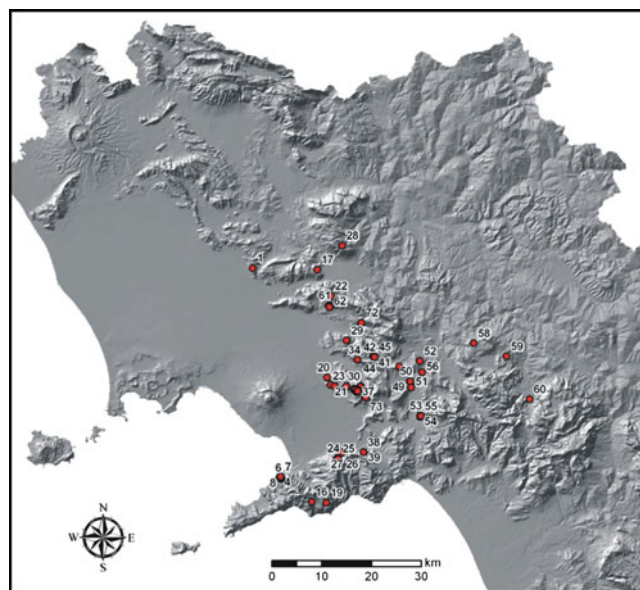


Fig. 2 Location of test sites

within the Campanian Plain or at the base of the surrounding mountains, we considered as fundamental the comparison of stratigraphic setting and thicknesses of volcanoclastic series along the slopes with those derived from the regional distribution model. With this purpose, we applied field methods consisted in test pits and light dynamic penetrometric tests, carrying out 73 field investigations distributed along slopes of the Avella, Sarno, Lattari, Picentini and Salerno mountain ranges (Fig. 2).

Test pits were dug by means of hand tools in favourable morphological conditions, reaching always the carbonate bedrock for thicknesses lower than 4 m. For greater thicknesses, the stratigraphic setting and the total thickness of the pyroclastic mantle were assessed by means of light dynamic penetrometric tests that were executed down to the bedrock.

According to previous results (De Vita et al. 2005, 2006), we oriented field investigations prevalingly in slope sectors with slope angle values lower than 30° with the purpose to verify the correspondence with the regional distribution model (Fig. 1).

Field data of thicknesses collected along the slopes were elaborated considering real values, namely stratigraphic thickness, estimated as the projection of the apparent thickness, measured along the vertical, in the plane normal to the slope. Thus, the real thickness values (z) were verified respect to a theoretical distribution model along slopes, based on the total thickness fallen in the area (z_0), derived from the regional distribution model (Fig. 1), and the slope angle (α) (1).

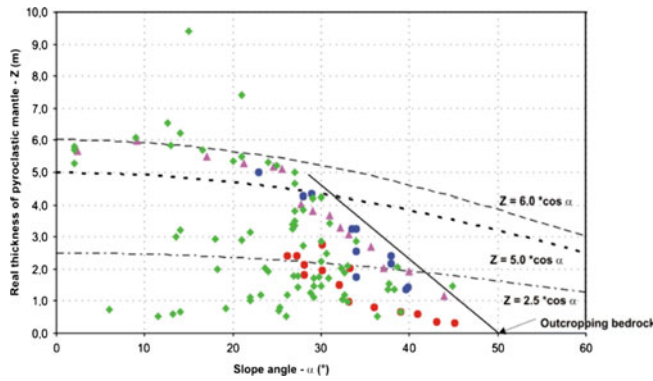


Fig. 3 Comparison between real thicknesses of the pyroclastic mantle measured along the slopes (*dots*) and theoretical distribution of ash-fall pyroclastic soils (*dashed curves*). The theoretical distributions of three sample areas, characterised by different z_0 values, are shown: 6 and 5 m, respectively for the southwestern and northeastern slopes of the Sarno mountain range, and 2.5 m for the northeastern slopes of the Lattari mountain range. The *continuous black line* represents the upper envelope

$$z = z_0 \times \cos \alpha \quad (1)$$

Results

The approach based on the validation of the ash-fall distribution model at the regional scale through the comparison with stratigraphic settings and thicknesses of volcanoclastic series allowed the reconstruction of a regional distribution model of the ash-fall pyroclastic deposits within the mountains that surround the Somma-Vesuvius. The obtained results concerned different aspects which were considered relevant for the assessment of landslide susceptibility and mobility as well as for the slope stability modelling. Among these aspects, both the modelling of ash-fall pyroclastic deposits distribution and the stratigraphic settings of the volcanoclastic series along the slopes were considered.

Distribution of Pyroclastic Soils Along Slopes

Considering the thickness data collected in a wide range of the mountain areas that surround the Somma-Vesuvius volcano (Fig. 2), the maximum values measured in each test site were observed not to exceed the theoretical value fallen in that area (Fig. 3), as calculated by the previous formula (1). In detail, for slope angle values lower than 28° , the ash-fall pyroclastic total thickness was observed as correspondent to that theoretically fallen in the area. Differently, for

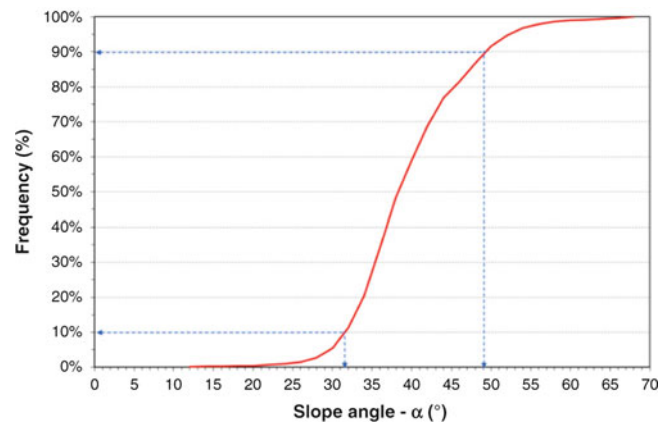


Fig. 4 Frequency analysis of the slope angle in the initiation areas of debris flows occurred on 5 and 6 May 1998 in the Sarno mountain range

slope angle values greater than 28° the ash-fall pyroclastic total thickness was found lower than that theoretically fallen in the same area. Field data confirmed the discontinuity and the negligible thickness of the pyroclastic mantle for slope angle values greater than 50° .

The abovementioned model of distribution was considered as the effect of the denudational processes, including landsliding, which reached a dynamic equilibrium, between resisting and driving forces, leading to slope instability, in which vegetation and rainfall triggering events play a spatially and temporally variable role.

This model was found in good agreement with the frequency of the slope angle values analysed in the initiation areas of debris flows occurred on 5 and 6 May 1998. From this comparison, it was observed that the 80 % of the landslide initiated in the slope angle ranging between 32° and 49° (Fig. 4).

A further analysis based on the comparison of field thicknesses data, limited to values measured in morphological conditions with slope angle values lower than 28° , and the theoretical thickness (Fig. 1) showed also a good correlation (Fig. 5), which validated the distribution model and allowed its extension at the regional scale.

Regional Distribution Model of Ash-Fall Pyroclastic Deposits

The previously discussed results allowed the implementation of a regional distribution model of ash-fall pyroclastic deposits along slopes by means of a raster GIS environment. The model was based on the combined application of the ash-fall distribution model derived from the sum of the isopach maps (Fig. 1) and the constraints due to the

Fig. 5 Correlation between the theoretical and the actual thickness of the pyroclastic mantle, derived from field thickness data. Values are in real terms

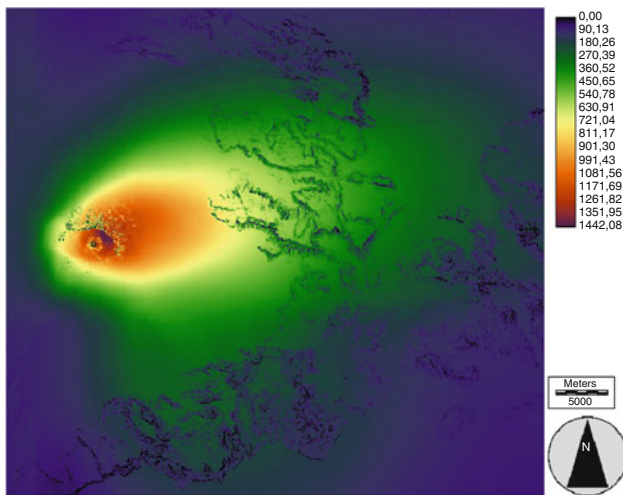
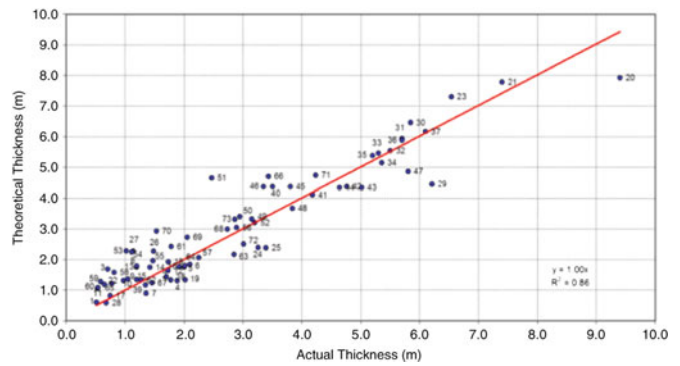


Fig. 6 Regional distribution model of ash-fall pyroclastic deposits in the area surrounding the Somma-Vesuvius volcano. The thickness values are in centimetres and expressed in real terms

observations that the thickness of the pyroclastic mantle decreases for slope angle values greater than 28° up to the annulment for values greater than 50° (Fig. 6).

Based on such a model, a total volume of about $73 \times 10^6 \text{ m}^3$ was estimated for ash-fall pyroclastic deposits existing in the critical slope angle range between 28° and 50°.

Stratigraphic Setting of the Volcaniclastic Series Along Slopes

Test pits carried out in different sites allowed reconstructing the stratigraphic setting of the volcaniclastic series. In order to describe the stratigraphy, considering also the pedogenetic horizons formed during the periods following each eruptions, we adopted a criterion based on the recognition of the principal pedogenetic horizons (USDA 2010; Terribile et al. 2000) combined with the litostratigraphic

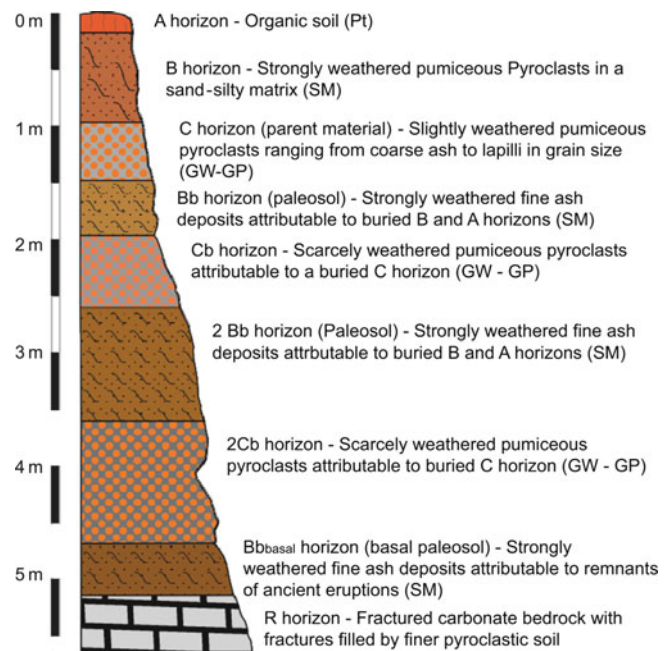


Fig. 7 Representative volcaniclastic series found in conservative areas of the Sarno Mountain range

and technical classification of horizons by means of the USCS system (De Vita et al. 2006).

Complete volcaniclastic series were found in morphological conservative areas (with slope angle lower than 28°) of the Avella, Sarno, Lattari, Salerno and Picientini mountain ranges. Due to the different orientation of dispersal axes of each eruption, different complete stratigraphic settings were found. In the conservative areas of the Sarno mountain range, complete volcaniclastic series were observed as constituted by (Figs. 7 and 8): (1) A horizon, classified as an organic soil (Pt); (2) B horizon, consisting of strongly weathered and pedogenised fine and coarse pumiceous ashes, corresponding to a slightly plastic sand with silt (SM); (3) C horizon, namely “parent material”, consisting of scarcely weathered pumiceous gravels, ranging from coarse ash to lapilli in grain size, classified as clean gravel

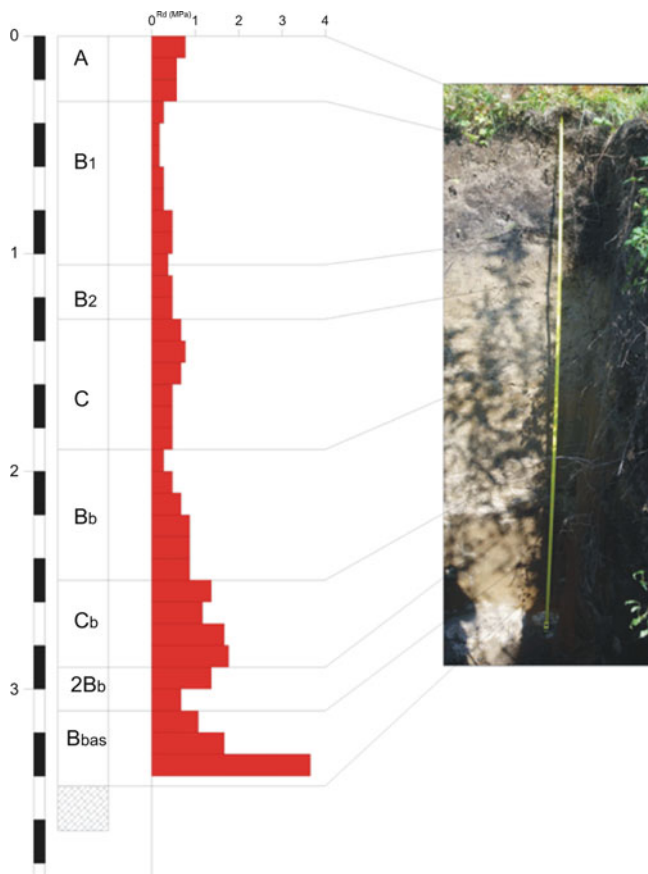


Fig. 8 Comparison between the two types of surveys applied in the field: test pit and light dynamic penetrometer test. The logs of dynamic resistance were used to reconstruct the thickness of the pyroclastic mantle and the stratigraphic setting in the cases of total thickness greater than 4 m

and sand from well to poor graded (GW and GP), ascribed to the A.D. 472 eruption; (4) Bb horizon, consisting of strongly weathered fine ash deposits, representing buried B, and subordinately A, horizons, (paleosol), classified as sand with silt (SM); (5) Cb horizon, consisting of buried and scarcely weathered pumiceous pyroclasts, classified similarly to C horizon, attributed to the Avellino eruption (3.6 k-years); (6) 2Bb horizon, consisting of strongly weathered fine ash deposits, representing buried B horizon (paleosol), classified as sand with silt (SM); (7) 2Cb horizon, consisting of buried and scarcely weathered pumiceous pyroclasts, classified similarly to C horizon, ascribed to the Ottaviano eruption (8.0 k-years); (8) Bb_{basal} horizon, consisting of strongly weathered and pedogenised fine ashes wrapping the bedrock interface (basal paleosol); (9) R horizon, consisting of fractured carbonate bedrock with fractures filled by the Bb_{basal} paleosol.

Complete volcanoclastic series were found on the Lattari mountain range as similarly characterized by paleosols, but with a unique C horizon ascribed to the deposits of the A.D.

79 eruption. Also in this case, a basal paleosol wrapping the carbonate bedrock was found. The basal paleosol was attributed to the remnants of deposits of the APC.

The reduction of the thickness of the pyroclastic soil mantle for slope angle greater than 28°, up to its annulment for slope angle values greater than 50°, was observed to have a strong influence on the stratigraphic settings of the volcanoclastic series along the slopes (De Vita et al. 2006). The reduction of the total thickness was found to determine the downstream pinch out of the pyroclastic horizons, both C and Bb horizons, up to the direct overlying of the B horizon on the Bb_{basal} horizon.

Conclusions

The results discussed in this paper can be considered a further, but not ultimate, step to link the assessment of landslide susceptibility at the regional scale to a distribution model of ash-fall pyroclastic soils in the areas surrounding the volcanic centers of the Campania region.

The modeling of the ash-fall distribution, considering both the thickness and the stratigraphic settings of the pyroclastic mantle, was considered an advance for the understanding of slope instability in volcanoclastic soil mantled slopes. In fact the pyroclastic soil thickness evaluation and mapping was commonly recognized as a fundamental achievement for the assessment of landslide susceptibility, from the preliminary to the advanced zoning levels (Fell et al. 2008). Regarding the zoning of susceptibility at the regional scale, the discussed approach would allow identifying those slope sectors covered by ash-fall pyroclastic soils and with slope angle values ranging from 28° to 50° as potentially unstable. Moreover, about the zoning at the site specific or detailed scale, the model would permit to recognise the higher landslide susceptibility conditions as corresponding with the pinch out of the pyroclastic horizons were pore pressure enhances during heavy rainstorms (De Vita et al. 2006).

The same approach could be applied in other perivolcanic areas of the world, whereas ash-fall deposits distributed along slopes are prone to instability due to rainfall-triggered shallow landslides.

Acknowledgments This research was supported by the PRIN Project (2007) “Analysis and susceptibility and hazard zoning for landslides triggered by extreme events (rainfall and earthquake)” funded by the Ministry for Education, University and Research (MIUR-Italy).

References

- Budetta P, de Riso R (2004) The mobility of some debris flows in pyroclastic deposits of the northwestern Campanian region (southern Italy). *Bull Eng Geol Environ* 63:293–302

- Cascini L, Guida D, Nocera N, Romanzi G, Sorbino G (2000) A preliminary model for the landslides of May 1998 in Campania Region. In: Proceedings of the 2nd international symposium on geotechnics of hard soil-soft rocks, Balkema, Napoli, vol 3, pp 1623–1649
- Cascini L, Cuomo S, Guida D (2008) Typical source areas of May 1998 flow-like mass movements in the Campania region, Southern Italy. *Eng Geol* 96:107–125
- Celico P, Guadagno FM (1998) L'instabilità delle coltri piroclastiche delle dorsali carbonatiche in Campania: attuali conoscenze. *Quaderni di Geologia Applicata (in Italian)* 5(1):75–133
- Corominas J (1996) The angle of reach as a mobility index for small and large landslides. *Can Geotech J* 33:260–271
- Crosta G, Dal Negro P (2003) Observations and modeling of soil slip-debris flow initiation processes in pyroclastic deposits: the Sarno 1998 event. *Nat Hazards Earth Syst Sci* 3:53–69
- De Vita P, Agrello D, Ambrosino F (2005) Landslide susceptibility assessment in ash-fall pyroclastic deposits surrounding Mount Somma-Vesuvius: Application of geophysical surveys for soil thickness mapping. *J Appl Geophys* 59(1):126–139. doi:10.1016/j.jappgeo.2005.09.001
- De Vita P, Celico P, Siniscalchi M, Panza R (2006) Distribution, hydrogeological features and landslide hazard of pyroclastic soils on carbonate slopes in the area surrounding Mount Somma-Vesuvius. *Ital J Eng Geol Environ* 1:75–98
- De Vita P, Napolitano E, Godt JW, Baum RL (2012) Deterministic estimation of hydrological thresholds for shallow landslide initiation and slope stability models: case study from the Somma-Vesuvius area of Southern Italy. *Landslides* 1–16. ISSN:1612–5118, doi:10.1007/s10346-012-0348-2
- Di Crescenzo G, Santo A (2005) Debris slides—rapid earth flows in the carbonate massifs of the Campania region (Southern Italy): morphological and morphometric data for evaluating triggering susceptibility. *Geomorphology* 66:255–276
- Fell R, Corominas J, Bonnard C, Cascini L, Leroi E, Savage WZ (2008) Guidelines for landslide susceptibility, hazard and risk zoning for land use planning. *Eng Geol* 102:85–98
- Fisher RV (1985) *Pyroclastic rocks*. Springer, Berlin, 472p. ISBN 3-540-12756-9
- Guadagno FM, Forte R, Revellino P, Fiorillo F, Focareta M (2005) Some aspects of the initiation of debris avalanches in the Campania Region: the role of morphological slope discontinuities and the development of failure. *Geomorphology* 66:237–254
- Hungro O, Evans SG, Bovis MJ, Huctinson JN (2001) A review of the classification of landslides of flow type. *Environ Eng Geosci* 7(3):221–238
- Jakob M, Hungro O (2005) *Debris-flow hazards and related phenomena*. Springer, Berlin, 739p. ISBN 3-540-20726-0
- Lirer L, Pescatore T, Booth B, Walker JPL (1973) Two plinian pumice-fall deposits from Somma-Vesuvius. *Geol Soc Am Bull* 84:759–772
- Perriello Zampelli S, Bellucci Sessa E, Cavallaro M (2011) Application of a GIS-aided method for the assessment of volcanoclastic soil sliding susceptibility to sample areas of Campania (Southern Italy). *Nat Hazards*. doi:10.1007/s11069-011-9807-7
- Perrotta A, Scarpati C (2003) Volume partition between the plinian and co-ignimbrite air fall deposits of the Campanian Ignimbrite eruption. *Mineral Petrol* 79:67–78
- Rolandi G, Maraffi S, Petrosino P, Lirer L (1993a) The Ottaviano eruption of Somma-Vesuvio (8000 y B.P.): a magmatic alternating fall and flow forming eruption. *J Volcanol Geotherm Res* 58:43–65
- Rolandi G, Mastrolorenzo G, Barrella AM, Borrelli A (1993b) The Avellino plinian eruption of Somma-Vesuvius (3760 y B.P.): the progressive evolution from magmatic to hydromagmatic style. *J Volcanol Geotherm Res* 58:67–88
- Rolandi G, Petrosino P, Mc Geehin J (1998) The interplinian activity at Somma-Vesuvius in the last 3,500 years. *J Volcanol Geotherm Res* 82:19–52
- Rolandi G, Bartolini F, Cozzolino G, Esposito N, Sannino D (2000) Sull'origine delle coltri piroclastiche presenti sul versante occidentale del Pizzo d'Alvano. *Quaderni di Geologia Applicata* 7(1):213–235
- Rosi M, Principe C, Vecchi R (1993) The 1631 Vesuvius eruption. A reconstruction based on historical and stratigraphical data. *J Volcanol Geotherm Res* 58:151–182
- Terribile F, Di Gennaro A, Arrone G, Basile A, Buonanno M, Mele G, Vingiani S (2000) I suoli delle aree di crisi di Quindici e Sarno: aspetti pedofeografici in relazione ai fenomeni franosi del 1998. *Quaderni di Geologia Applicata* 7(1):81–95, in Italian
- USDA (2010) *Keys to soil taxonomy- 11th edition*. USDA, Natural Resources Conservation Service, Washington, DC, 338p



Geotechnical Features of the Volcanic Rocks Related to the Arteara Rock Avalanche in Gran Canaria (Canary Islands, Spain)

Martín Jesús Rodríguez-Peces, Jorge Yepes Temiño, and Esther Martín-Nicolau

Abstract

The Arteara rock avalanche is developed in the Fataga Group which is related to the first volcanic stage in the Gran Canaria Island (8.6–13.3 Ma). The materials of the avalanche are mainly phonolitic ignimbrites and lava flows. We have investigated the geotechnical quality of the five lithotypes distinguished in the area: (a) phonolitic lava, (b) phonolitic agglomerate breccia, (c) reddish non-welded ignimbrite, (d) welded fiamme-bearing ignimbrite, and (e) pumice tuff with lithics. The weak geotechnical properties of the reddish non-welded ignimbrite, the pumice tuff with lithics and the agglomerate breccia, and their location at the middle of the slope suggest that these lithotypes can be regarded as potential sliding surfaces of the avalanche. The geomechanical features of the volcanic rocks found in this study could be very useful for future studies concerning the modelling of the mechanism of failure and run out of the Arteara rock avalanche.

Keywords

Canary Islands • Geotechnical parameter • Gran Canaria • Point load test • Rock avalanche • Rock mechanics • Schmidt hammer

Introduction

The Arteara rock avalanche is located on the Fataga ravine (Fig. 1), in the south of Gran Canaria (Canary Islands, Spain). This slope instability is a significant case since it is the first rock avalanche described in the Canary Islands (Yepes and Lomoschitz 2008, 2009, 2010). The rock avalanche was developed in the Fataga Group, which is related to the first volcanic stage of the Gran Canaria evolution. This stage is divided in the Mogán and Fataga formations, which are dated between 8.6 and 13.3 Ma (McDougall and

Schmincke 1976; Bogaard and Schmincke 1998; Schmincke and Sumita 2010). The Fataga Group comprises lavas flows, ignimbrites (welded and non-welded) and fall-out tephtras, all of them with a trachyphonolitic to phonolitic composition. The ignimbrites and lavas are interbedded forming a large sub-horizontal succession of around 600 m thick. In general, the phonolitic lavas have the highest thickness and columnar jointing, while the ignimbrites have more convex profiles.

In this paper, the geomechanical features of the main volcanic rocks involved in the Arteara rock avalanche have been analysed by means of in situ and laboratory tests and different empirical correlations. These geotechnical parameters could be very useful for future particular studies concerning about the modelling of the mechanisms of failure and run out of the slope instabilities developed in the Fataga ravine, in particular, the Arteara rock avalanche.

M.J. Rodríguez-Peces (✉) • E. Martín-Nicolau
Department of Geodynamics, University Complutense of Madrid.
Ciudad Universitaria, s/n. 28040 Madrid, Spain
e-mail: martinjr@geo.ucm.es

J.Y. Temiño
Department of Civil Engineering, University of Las Palmas de Gran
Canaria, Las Palmas 35017, Spain
e-mail: jyepes@dic.ulpgc.es

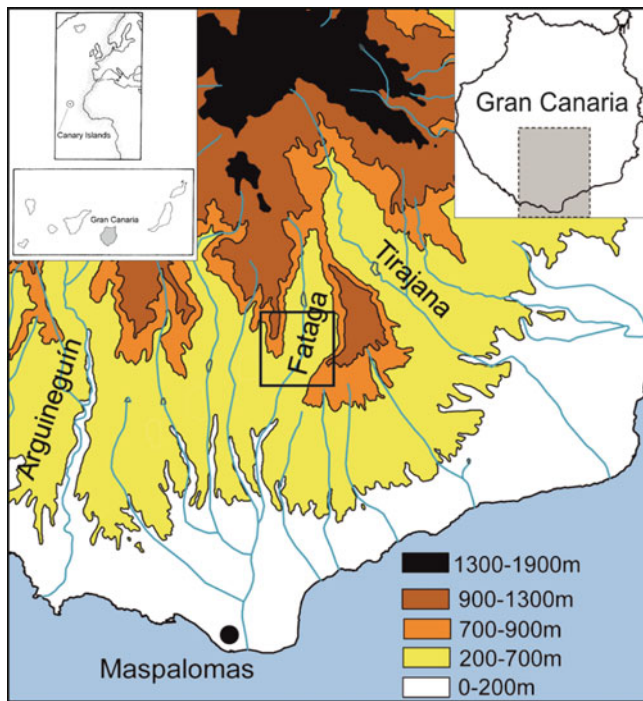


Fig. 1 Location of the Arteara rock avalanche (see the *black square*) on the Fataga ravine at the south of Gran Canaria (Canary Islands, Spain)

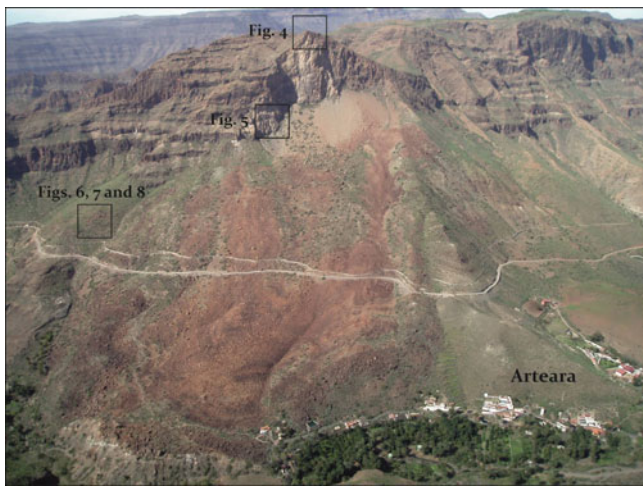


Fig. 2 Panoramic view of the Arteara rock avalanche, which comprises a superficial deposit of reddish blocks that cover the right slope of the Fataga ravine over a prior rock slide. The location of the Arteara village and the detailed views of the main lithotypes are depicted

Arteara Rock Avalanche

The Arteara rock avalanche is a superficial accumulation (1–15 m thick) of large blocks of reddish-brown colour that cover the right slope of the Fataga ravine (Fig. 2).

The surface area of the deposit is 0.5 km^2 and the estimated volume is 3.96 hm^3 . A more detailed geomorphologic description of the Arteara rock avalanche can be found in Yepes and Lomoschitz (2009). The age of the rock avalanche was estimated as Holocene since it is well preserved and it is located over a rock-slide deposit of Pliocene age. Moreover, a pre-Hispanic necropolis (fifteenth century) exists on the distal area that uses the fallen blocks for building tombs. This slope instability was caused by the collapse of a large block of the rock mass of about 300 m high, with an estimated volume of 2.83 hm^3 . The energy of impact triggered the fragmentation of the block and immediately afterward the resulting granular flow of the blocks in dry conditions.

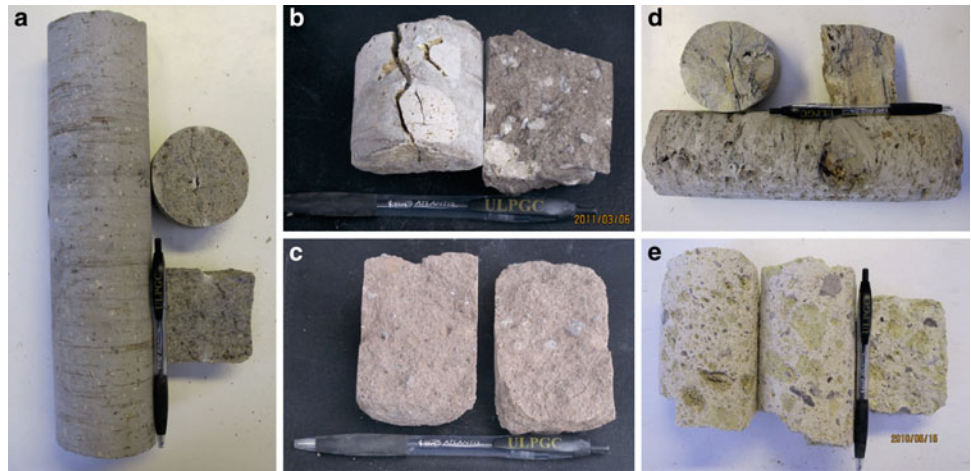
The avalanche deposit comprises volcanic rocks related to the substratum (Fataga Group), mainly phonolitic ignimbrites and lavas. In general, these rocks have a reddish-brown colour due to weathering or hydrothermal alteration. In this study, we have distinguished five lithotypes related to the Arteara rock avalanche: (a) massive phonolitic lava, (b) phonolitic agglomerate breccia, (c) reddish non-welded ignimbrite, (d) welded fiamme-bearing ignimbrite, and (e) pumice tuff with lithics (Fig. 3).

Geotechnical Investigations

The characterisation of the mechanical behaviour of the volcanic rocks involved in the Arteara rock avalanche has been approached through the study of the strength and deformability of intact and weathered rock samples (Fig. 3). These geotechnical parameters should be ideally tested in uniaxial compression under laboratory conditions in which the axial strain, strain rate and load can be controlled and measured, and the uniaxial compressive strength, Young's modulus and Poisson's ratio can be estimated directly. However, a number of borehole cores are needed to carry out this test and extracting and carrying such samples from remote areas across volcanic terrain is very difficult, expensive and time consuming. For these reasons, alternative indirect testing methods are often used to estimate the mechanical behaviour of rocks.

Measurements of rock strength were made by means of several in situ tests using a L-type Schmidt hammer, and the point load test in laboratory conditions. The Schmidt hammer rebound (R_L) was obtained following the most recent procedure suggested by the International Society for Rock Mechanics (Aydin 2009), while the point load test (PLT) was performed following the ASTM (2000). The PLT was expressed in the form of PLT index $I_{s(50)}$. The results of both geotechnical tests were correlated with uniaxial compressive strength (UCS), indirect tensile strength and Young's modulus following a number of empirical correlations (D'Andrea

Fig. 3 Main lithotypes related to the Arteara rock avalanche. (a) massive phonolitic lava, (b) phonolitic agglomerate breccia, (c) reddish non-welded ignimbrite, (d) welded fiamme-bearing ignimbrite, (e) pumice tuff with lithics



et al. 1964; Broch and Franklin 1972; Beverly et al. 1979; Read et al. 1980; ISRM 1985; Xu et al. 1990; Aggitalis et al. 1996; Chau and Wong 1996; Quane and Russel 2003; Dinçer et al. 2004; Yasar and Erdogan 2004; Aydın and Basu 2005; Fener et al. 2005; Kahraman et al. 2005; Kiliç and Teymen 2008; Kahraman and Gunaydin 2009). In addition, a number of available borehole samples were used to obtain the basic friction angle by means of the tilt test (Barton 1981). Unit weight and absorption of the rock samples were estimated using a hydrostatic balance (AENOR 1994). Finally, our results have been compared with the geotechnical properties suggested by other authors for the main lithotypes of volcanic rocks in the Canary Islands (Rodríguez-Losada et al. 2007, 2009; González de Vallejo et al. 2008; del Potro and Hürlimann 2008, 2009). We have completed the geotechnical characterisation of the materials involved in the Arteara rock avalanche with additional parameters (e.g. Poisson's ratio and friction angle) in the case that our investigations agree with the results of these prior works.

Massive Phonolitic Lava

The phonolitic lavas are mainly located at the top of the Fataga Group, being the most frequent lithology in the area. These lavas flows are forming a very thick unit of 200–500 m with variable individual thickness between 5 and 25 m. The intact rocks have the typical greenish-gray colour of the phonolites, while the weathered rocks have a significant patina of an intense reddish-brown colour. Compositionally, the unit has both porphyritic and aphanitic textures (Fig. 3a). The rock massif has a very strong sub-vertical jointing, typical of this type of volcanic rocks (Fig. 4). In general, the phonolitic lavas show a weathered condition, which seems to be related to the rainfall infiltration through the sub-vertical joints.

The unit weight of this material ranges between 19.5 and 21.3 kN/m³. These values are close to the lower bound of unit weight (19–29 kN/m³) suggested by other researchers (Rodríguez-Losada et al. 2009). The average Schmidt hammer rebound (R_L) is 43 (± 9) and the PLT index $I_{s(50)}$ is 4.1 (± 2.3) MPa. The $I_{s(50)}$ value agrees with the range of 0.6–9.4 MPa found by Rodríguez-Losada et al. (2009). Considering these data, the uniaxial compressive strength (UCS) of the intact rock is estimated between 62 and 108 MPa, very similar to the results (30–114 MPa) found in previous works (Rodríguez-Losada et al. 2009). However, the UCS of weathered rock is significantly lower (6–28 MPa), very similar to the value of 32.8 MPa estimated by del Potro and Hürlimann (2008) for weathered lavas. The UCS of weathered rock is very close to the tensile strength value (9–14 MPa), which is slightly lower than the suggested value of 19–83 MPa (Rodríguez-Losada et al. 2009). The basic friction angle ranges between 38° and 41°, being inside the range of 36–54° proposed by Rodríguez-Losada et al. (2009). The estimated Young's modulus is between 12 and 24 GPa, which is in agreement with the values (15–30 GPa) suggested by González de Vallejo et al. (2008). Due to the good correlation between our results and the values proposed by Rodríguez-Losada et al. (2009), we have assumed a Poisson's ratio of 0.29 (± 0.11) from these authors.

Phonolitic Agglomerate Breccia

The agglomerate breccias are related to thin (1–6 m) and isolated volcanic deposits which are intercalated between the main succession of phonolitic lavas and ignimbrites. This lithology is mainly composed by rounded and large fragments of phonolitic composition with a greenish-gray colour, typical of phonolites (Fig. 3b). In general, the weathered rocks have a brownish colour, which seems to be related to the rainfall infiltration. The size of the fragments is very



Fig. 4 Detailed view of the massive phonolitic lava, showing the sub-vertical jointing. See Fig. 2 for site location



Fig. 5 Detailed view of phonolitic agglomerate breccia, showing the high heterogeneity of the size of the fragments. See Fig. 2 for site location

variable from 2 cm to 1 m, being very large in several cases ($\phi > 2$ m). They do not have grain selection and internal organization, but are embedded in a sandy or clayey matrix (Figs. 3b and 5).

The unit weight ranges between 18.65 and 21.05 kN/m³, which agrees with the range of 12–28 kN/m³ suggested by González de Vallejo et al. (2008). The average R_L is 16 (± 4) and the PLT index $I_{s(50)}$ is 2.7 (± 1.7) MPa. Considering these data, the UCS for intact rock is between 24 and 73 MPa. The lower bound of our results is similar to the

upper bound of the range (0.5–30 MPa) found by other authors (Rodríguez-Losada et al. 2007; González de Vallejo et al. 2008). The estimated tensile strength is between 1 and 11 MPa, which agrees with the value of 2.5 MPa proposed by del Potro and Hürlimann (2008). The estimated Young's modulus is between 0.7 and 4.6 GPa, which is in agreement with the values (0.1–4.7 GPa) suggested by previous studies (del Potro and Hürlimann 2008; González de Vallejo et al. 2008). Considering that our results are in good agreement with the values proposed by others authors, we have assumed an internal friction angle of 25–42° (González de Vallejo et al. 2008).

Reddish Non-welded Ignimbrite

The non-welded ignimbrites are located at the top of the Mogán Group (trachytic-rhyolitic composition), being the contact with the bottom of the Fataga Group. The individual thicknesses of the rhyolitic to trachytic ignimbrites are between 1.5 and 6 m. The most significant feature of this unit of ignimbrites is that presents a reddish-gray colour due to an intensive hydrothermal alteration of volcanic origin (Figs. 3c and 6). In addition, these rocks are very weathered by the rainfall infiltration, showing, in some cases, a most typical behaviour of a soil than a rock.

The unit weight of this rock ranges between 14.76 and 15.25 kN/m³. These values are in agreement with the unit weight (9–23 kN/m³) suggested by other researchers (Rodríguez-Losada et al. 2009; González de Vallejo et al. 2008). The obtained R_L is 10 (± 6) and the PLT index $I_{s(50)}$ is 0.4 (± 0.2) MPa. The $I_{s(50)}$ value agrees with the range of 0.2–6.2 MPa found by Rodríguez-Losada et al. (2009) for non welded ignimbrites. Considering these data, the UCS of the intact rock is between 5 and 12 MPa, which is similar with the range (2–5 MPa) proposed by González de Vallejo et al. (2008) and close to the lower bound of the ranges of 4–34 MPa and 2.5–58 MPa found by Rodríguez-Losada et al. (2007, 2009), respectively. The UCS corresponding to a saturated sample is slightly lower (2–4 MPa), very close to the estimated tensile strength (1 MPa) which can be related to the lower bound of the range (1–50 MPa) suggested by Rodríguez-Losada et al. (2009). The Young's modulus is between 1.7 and 3.1 GPa, which is slightly lower than the values (4–12 GPa) found by Rodríguez-Losada et al. (2009) and del Potro and Hürlimann (2008). In this case, our results are also in agreement with the values suggested by other researchers, so we have assumed a friction angle between 25° and 38° (Rodríguez-Losada et al. 2009; González de Vallejo et al. 2008) and a Poisson's ratio of 0.28 (± 0.13) from Rodríguez-Losada et al. (2009).



Fig. 6 Detailed view of the reddish non-welded ignimbrite. See Fig. 2 for site location



Fig. 7 Detailed view of the welded ignimbrite, showing a large number of fiammes. See Fig. 2 for site location

Welded Fiamme-Bearing Ignimbrite

The welded ignimbrites are mainly located at the bottom of the Fataga Group. The most significant feature of this unit of phonolitic ignimbrites is that it presents a large number of fiammes (Figs. 3d and 7). The intact rocks have the typical greenish-gray colour of the phonolites (Fig. 3d), while the weathered rocks have a yellowish-brownish colour (Fig. 7).

The unit weight of this ignimbrite ranges between 17.92 and 18.50 kN/m³, which agrees with the range of 13–29 kN/m³ suggested by Rodríguez-Losada et al. (2009)

and González de Vallejo et al. (2008). The average R_L is 26 (± 8) and the PLT index $I_{s(50)}$ is 1.6 (± 1.2) MPa. The $I_{s(50)}$ value agrees with the range of 0.2–10 MPa found by Rodríguez-Losada et al. (2007, 2009) for welded ignimbrites. Considering these data, the estimated UCS of the intact rock is between 22 and 47 MPa, which agrees with the ranges of 15–70 MPa and 22–92 MPa found by González de Vallejo et al. (2008) and Rodríguez-Losada et al. (2007, 2009), respectively. However, the UCS considering a sample with abundant fiammes is slightly lower (6–28 MPa), whose lower limit is very close to the estimated tensile strength (3–6 MPa). This value of tensile strength is very close to the lower limit of the range (3.5–51 MPa) suggested by Rodríguez-Losada et al. (2007, 2009). The obtained basic friction angle ranges between 36° and 39°, which is inside the range of 30–40° proposed by Rodríguez-Losada et al. (2009). The estimated Young's modulus is between 4 and 10 GPa., which is significant lower than the range (30–50 GPa) proposed by others authors (Rodríguez-Losada et al. 2009; González de Vallejo et al. 2008) for welded ignimbrites. This relatively low value of Young's modulus could be related to the large number of fiammes. Nevertheless, a Poisson's ratio of 0.20 (± 0.17) can be assumed considering the proposal of Rodríguez-Losada et al. (2009).

Pumice Tuff with Lithics

The pumice tuffs are related to very thin (0.25–2 m) and isolated “block and pumice” and “ash and pumice” deposits, which are intercalated between the main units of ignimbrites. This lithotype have a yellowish-whitish colour and is mainly composed of pumice fragments of variable sizes ($2 \text{ mm} < \phi < 10 \text{ cm}$) and lithics which comprise fragments of phonolitic lavas ($\phi < 6 \text{ cm}$) and feldspar crystals (Figs. 3e and 8).

The unit weight of this material ranges between 10.62 and 14.57 kN/m³, which is in agreement with the range of 8–18 kN/m³ suggested by González de Vallejo et al. (2008). The estimated R_L is 9 (± 5) and the PLT index $I_{s(50)}$ is 1.0 (± 0.5) MPa. Considering these data, the average uniaxial compressive strength of the intact rock is between 8 and 24 MPa, which agrees with the range (1–50 MPa) found by González de Vallejo et al. (2008) for volcanic tuffs. The UCS obtained considering a saturated sample (13–23 MPa) is similar to the UCS of the intact rock. In the saturated case, González de Vallejo et al. (2008) proposed UCS values lower than 10 MPa. The estimated tensile strength is very low (1–2 MPa). The basic friction angle ranges between 37° and 42°, which is in agreement with the values (25–42°)



Fig. 8 Detailed view of the pumice tuff with lithics. See Fig. 2 for site location

suggested by González de Vallejo et al. (2008). However, a lower value of friction angle of 12–30° can be assumed for weathered tuffs (González de Vallejo et al. 2008). The estimated Young's modulus is between 1.5 and 2.9 GPa, which is inside the range of 0.1–22 GPa suggested by González de Vallejo et al. (2008).

Discussion and Conclusions

The volcanic rocks with the weakest geotechnical features are the reddish non-welded ignimbrite and the pumice tuff with lithics. The uniaxial compressive strength of the intact rock found for these materials is very low, being significantly lower considering a complete saturation of the rock. This condition could be possible taking into account that the volcanic rocks seem to be altered by water of hydrothermal and rainfall origin. Since these two lithotypes are mainly located at the middle of the Arteara slope, very close to the location of the base of the fallen rock mass, they could be regarded as potential sliding surfaces of the Arteara rock avalanche.

The deposit of the Arteara rock avalanche comprises mainly sharp blocks of the massive phonolitic lava, which is the material with the best geotechnical quality. The uniaxial compressive strength of these lavas is very large, comparing with the values found for the rest of lithotypes. The second most frequent lithology present in the avalanche deposit is the phonolitic agglomerate breccia. In this case, the uniaxial compressive strength is about half of the strength found in the phonolitic lavas.

The large size (8–27 m³) of the boulders of phonolitic lava and agglomerate breccia located at the most distal zone of the avalanche could be explained considering the relatively high strength of these materials, which allows going further. However, the blocks of lava described above have

open cracks, broken faces, indented edges and faceted corners (Yepes and Lomoschitz 2008, 2009, 2010). This fact seems to be related to very strong sub-vertical jointing and the low tensile strength of the lavas, which could contribute to the effective fragmentation of the rock mass during the avalanche movement. These geotechnical observations confirm the hypothesis that the Arteara rock avalanche was developed by means of a dry granular flow in which the blocks of rock were transported by bouncing with a number of impacts between them (Yepes and Lomoschitz 2008, 2009, 2010).

The geomechanical parameters of the five lithotypes described in this paper could be very useful for future particular studies concerning the modelling of the most likely mechanism of failure and run out of the Arteara rock avalanche, and also of other slope instabilities developed in the slopes of the Fataga ravine.

References

- AENOR (1994) UNE 103-301/94. Determination of a soil density. Method of the hydrostatic balance. Asociación Española de Normalización y Certificación, Madrid, 2p
- Aggastalis G, Alivizatos A, Stamoulis D, Stournaras G (1996) Correlating uniaxial compressive strength with Schmidt hammer rebound number, point load index, Young's modulus, and mineralogy of gabbros and basalts (Northern Greece). *Bull Eng Geol* 54:3–11
- ASTM (2000) Standard test method for determination of the point load strength index of rock. American Society for Testing and Materials. ASTM 04.08, D5731-02
- Aydin A (2009) ISRM suggested method for determination of the Schmidt hammer rebound hardness: revised version. *Int J Rock Mech Min* 46:627–634
- Aydin A, Basu A (2005) The Schmidt hammer in rock material characterization. *Eng Geol* 81:1–14
- Barton N (1981) Shear strength investigations for surface mining. In: Bowner CO (ed) *Stability in surface mining*, vol 3. In: Third international conference, Vancouver, pp 171–192
- Beverly BE, Schoenwolf DA, Brierly GS (1979) Correlations of rock index values with engineering properties and the classification of intact rock. Brierley Associates, Washington, DC
- Bogaard P van den, Schmincke H-U (1998) Chronostratigraphy of Gran Canaria. In: Weaver PPE, Schmincke H-U, Firth JV, Duffield W (eds) *Proceedings of the ODP, Sci results*, College Station, TX (Ocean drilling program), vol 157, pp 127–140
- Broch E, Franklin JA (1972) Point-load strength test. *Int J Rock Mech Min Sci* 9(6):669–697
- Chau KT, Wong RHC (1996) Uniaxial compressive strength and point load strength. *Int J Rock Mech Min Sci* 33:183–188
- D'Andrea DV, Fisher RL, Fogelson DE (1964) Prediction of compression strength from other rock properties. *Colo Sch Mines Q* 59:623–640
- del Potro R, Hürlimann M (2008) Geotechnical classification and characterisation of materials for stability analyses of large volcanic slopes. *Eng Geol* 98:1–17
- del Potro R, Hürlimann M (2009) A comparison of different indirect techniques to evaluate volcanic intact rock strength. *Rock Mech Rock Eng* 42:931–938

- Dinger I, Acar A, Çobanoğlu I, Uras Y (2004) Correlation between Schmidt hardness, uniaxial compressive strength and Young's modulus for andesites, basalts and tuffs. *Bull Eng Geol Environ* 63:141–148
- Fener M, Kahraman S, Bilgil A, Gunaydin O (2005) A comparative evaluation of indirect methods to estimate the compressive strength of rocks. *Rock Mech Rock Eng* 38(4):329–343
- González de Vallejo LI, Hijazo T, Ferrer M (2008) Engineering geological properties of the volcanic rocks and soils of the Canary Islands. *Soils Rocks* 31(1):3–13
- ISRM (1985) ISRM suggested methods. Suggested method for determining point-load strength. *Int J Rock Mech Min Sci* 22:53–60
- Kahraman S, Gunaydin O (2009) The effect of rock classes on the relation between uniaxial compressive strength and point load index. *Bull Eng Geol Environ* 68:345–353
- Kahraman S, Gunaydin O, Fener M (2005) The effect of porosity on the relation between uniaxial compressive strength and point load index. *Int J Rock Mech Min Sci* 42(4):584–589
- Kiliç A, Teymen A (2008) Determination of mechanical properties of rocks using simple methods. *Bull Eng Geol Environ* 67:237–244
- McDougall I, Schmincke HU (1976) Geochronology of Gran Canaria (Canary Islands): age of shield building volcanism and other magmatic phases. *Bull Volcanol* 40(1):57–77
- Quane SL, Russel JK (2003) Rock strength as a metric of welding intensity in pyroclastic deposits. *Eur J Mineral* 15:855–864
- Read JRL, Thornto PN, Regan WM (1980) A rational approach to the point load test. In: *Proceedings of 3rd Australian-New Zealand geomechanics conference*, vol 2. New Zealand Institution of Engineers, Wellington, pp 35–39
- Rodríguez-Losada JA, Hernández-Gutiérrez LE, Lomoschitz Mora-Figueroa A (2007) Geotechnical features of the welded ignimbrites of the Canary Islands. In: Malheiro AM, Nunes JC (eds) *Volcanic rocks*. Taylor & Francis, London, pp 29–33. ISBN 978-0-415-45140-6
- Rodríguez-Losada JA, Hernández-Gutiérrez LE, Olalla C, Perucho A, Serrano A, Eff-Darwich A (2009) Geomechanical parameters of intact rocks and rock masses from the Canary Islands: implications on their flank stability. *J Volcanol Geotherm Res* 182:67–75
- Schmincke HU, Sumita M (2010) *Geological evolution of the Canary Islands*. Görres Verlag, Koblenz, 188 pp
- Xu S, Grasso P, Mahtab A (1990) Use of Schmidt hammer for estimating mechanical properties of weak rock. In: 6th international IAEG congress. Balkema, Rotterdam, pp 511–519
- Yasar E, Erdogan Y (2004) Estimation of rock physicommechanical properties using hardness methods. *Eng Geol* 71:281–288
- Yepes J, Lomoschitz A (2008) Los depósitos de ladera del barranco de Fataga (Gran Canaria). *Geo-Temas* 10:767–770
- Yepes J, Lomoschitz A (2009) Caracterización geomorfológica del alud de rocas de Arteara, Gran Canaria. In: *Proceedings of VII Simposio Nacional sobre Taludes y Laderas Inestables*, 27–30 Oct 2009. Barcelona, 13pp
- Yepes J, Lomoschitz A (2010) Geomorphology of the Arteara Holocene rock-avalanche deposit, Gran Canaria Island, vol 12, *Geophysical research abstracts*. EGU General Assembly 2010, Vienna, pp 12017–12018



Effects of Parameters in Landslide Simulation Model LS-RAPID on the Dynamic Behaviour of Earthquake-Induced Rapid Landslides

Bin He, Kyoji Sassa, Maja Ostric, Kaoru Takara, and Yosuke Yamashiki

Abstract

In this study, the effects of parameters in landslide simulation model (LS-RAPID) on the dynamic behaviour of earthquake-induced rapid landslides were examined to demonstrate the importance of each parameter. It was applied to a case study in Suruga Bay, Shizuoka Prefecture in Japan. The topographic data of the slope surface and sliding surface was generated from digital elevation model (DEM). Three different real seismic records were used as the inputs of earthquake i.e. 2008 Iwate-Miyagi Nairiku Inland Earthquake, 2009 Suruga Bay Earthquake, and the latest 2011 Tohoku Earthquake. Results show that landslides can be triggered by strong seismic loading using 2011 Tohoku real seismic records under a certain pore water pressure within LS-RAPID. The key parameters, including shear resistance at the steady state with physical meaning were found to have significant effect on the dynamic behaviour of these earthquake-induced rapid landslides.

Keywords

Earthquake-induced landslides • Parameter • Simulation model • Dynamic behaviour

B. He (✉)

Educational Unit for Adaptation and Resilience for a Sustainable Society, Center for Promotion of Interdisciplinary Education and Research, Kyoto University, Gokasho, Uji, Kyoto 611-0011, Japan

Disaster Prevention Research Institute (DPRI), Kyoto University, Gokasho, Uji, Kyoto 611-0011, Japan
e-mail: hebin@flood.dpri.kyoto-u.ac.jp

K. Sassa

International Consortium on Landslides, Gokasho, Uji, Kyoto 611-0011, Japan

M. Ostric

Department of Environmental Engineering, Graduate School of Engineering, Kyoto University, Gokasho, Uji, Kyoto 611-0011, Japan

K. Takara • Y. Yamashiki

Disaster Prevention Research Institute (DPRI), Kyoto University, Gokasho, Uji, Kyoto 611-0011, Japan

Introduction

Growing population and expansion of settlements and life-lines over hillside areas have largely increased the numbers of deaths, injuries, and economic losses due to landslides both in industrialized and developing countries. Therefore, regional prediction of landslide is urgent, especially in mountainous areas, where variations in topography, geology, human activities are quite large. However, the mechanism of landslide is complex since it is related to many geo-environmental factors such as geomorphology, lithology, land cover, and bedrock geology. Based on the nonlinear relationship between landslides and the various factors causing landslides, various qualitative and quantitative models have been postulated. The current available landslide simulation models are classified as two categories i.e. lumped mass models idealizing the landslide motion as a single point (Perla et al. 1980; Hutchinson 1986), and models based on continuum mechanics (Sassa 1988; Wang and Sassa 2010).

Sassa (1988) proposed a geotechnical model for landslide motion based on the kinematic principle of block motion and

the continuity principle of the behaviour of material during landslide motion process. Due to the contribution of IPL-M101 APERITIF Project – Arial Prediction of Earthquake and Rain-Induced Rapid and Long Travelling Flow Phenomena – by the Special Coordinating Fund for Promoting Science and Technology of the Government of Japan (Representative: K. Sassa), the simulation program was professionally improved. The program is written in C++ language. Its interface is very similar to MS-Word and is user-friendly. It can be easily operated in a Windows system. It was further improved in 2004 (Sassa et al. 2004a) and new knowledge obtained from a dynamic loading ring shear apparatus (Sassa et al. 2003, 2004b). The new development is to simulate the initiation process of landslide from the local failure to the post-failure landslide motion through the progressive failure. So far, the initiation of landslides has been analyzed by limit-equilibrium slope stability analysis assuming that the whole sliding mass fails at once, while existing landslide run-out models deal only with post-failure motion. This model is the first to integrate the initiation process and the post-failure motion. The integrated simulation model LS-RAPID has been applied in many areas, including subaerial and submarine megaslides, to assess the initiation and motion of landslides triggered by earthquakes, rainfalls or the combined effects of rainfalls and earthquakes (Sassa et al. 2004a, 2011).

As the important input of this model, the mechanical parameters of the sliding zone and sliding mass have effect on the dynamic behaviour of landslides, especially earthquake-induced rapid landslides. Most of the mechanical parameters can be decided using ring shear test on samples. This paper will investigate the effects of the mechanical parameters in landslide simulation model LS-RAPID on the dynamic behaviour of earthquake-induced rapid landslides. It will be presented by the inclusion of a parametric study, together with the presentation of a case study of a submarine landslide in Suruga Bay. Different frequencies, periods, amplitudes of earthquake records were compared for a potential submarine landslide and their responses in their respective simulations by LS-RAPID will be analyzed.

Methodology

Landslide Simulation Model

Basic concept of the landslide simulation model is shown in Fig. 1 (Sassa et al. 2004a). A vertical imaginary column is considered within a moving landslide mass. The forces acting on the column are (1) self-weight of column (W),

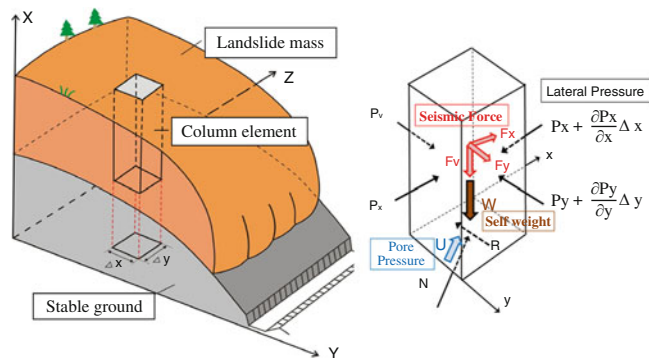


Fig. 1 Geotechnical model for landslide motion (left) and forces acting on a sliding mass column (right). The mesh size at x-y plane is $\Delta x \times \Delta y$. The forces include gravity W , supporting force N , shear resisting force R , and earth pressures P_x and P_y

(2) lateral pressure acting on the side walls (P), (3) shear resistance acting on the bottom in the upward direction of the maximum slope line (before motion) or in the opposite direction of landslide movement (during motion) (R), and (4) the normal stress acting on the bottom (N) given from the stable ground as a reaction of normal component of the self-weight (W_n). The sum of three forces of (1) (2) (3) will cause the motion of landslides, namely the component of the self-weight parallel to the slope (W_p), and the sum of the balance of lateral pressures in the directions of X and Y and Shear resistance (R). The landslide mass (m) will be accelerated by an acceleration (a) given by the sum of these three forces.

$$am = W_p + \left(\frac{\partial P_x}{\partial x} \cdot \Delta x + \frac{\partial P_y}{\partial y} \cdot \Delta y \right) + R \quad (1)$$

$$W_p = W + F_v + F_x + F_y$$

where, W : self weight, F_v, F_x, F_y : seismic force.

The angle of slope is different in the position of column within landslide mass. All stresses and displacements are projected to the horizontal plane and calculated on the horizontal plane.

This simulation model can express the landslide initiation by the combined effects of pore water pressure and seismic shaking and post-failure motion until the deposition. Landslides can be triggered by seismic loading either using real seismic records or simple cyclic waves under a certain pore water pressure (pore pressure ratio) within LS-RAPID. The effect of seismic force is much affected by frequency of shear wave and the wave form. It is quite different in the case of static, low frequency, high frequency and the magnitude of peak acceleration.

Setting of Seismic Loading

In LS-RAPID, the seismic loading force can be set as an inducement of the landslide. We can set a constant seismic load or a fluctuating seismic load over time by choosing one of the following seismic operation methods i.e. Static, Cyclic, and Seismic. In the Static method, the seismic coefficient varies linearly. In the Cyclic method, the seismic coefficient varies as a sine wave while the value of the amplitude changes linearly. In the Seismic method, the seismic coefficient varies based on the actual seismic wave form data.

Parameters

As for the parameters necessary for the computer simulation, most of soil parameters can be decided by the test on drilled sample by undrained cyclic loading ring shear test, namely the steady state shear resistance, the friction angle at peak, and the friction angle during motion, the shear displacement at the start of strength reduction (DL), the shear displacement at the end of strength reduction (DU). Cohesion is regarded to be small (10 kPa) assuming the shear surface was formed in a not over-consolidated sand layer like the drilled core.

Some parameters such as the lateral pressure ratio and parameters for non-frictional energy consumption are not decided by the ring shear tests. Those are decided from the following examinations. Lateral Pressure ratio ($k = \sigma_h/\sigma_v$) is one of important factors. K value is expressed by the Jaky's equation as the equation.

$$k = 1 - \sin \phi_{ia} \quad (2)$$

where, $\tan \phi_{ia} = (c + (\sigma - u) \tan \phi_i)/\sigma$; $\tan \phi_{ia}$: Apparent friction coefficient within the landslide mass; $\tan \phi_i$: Effective friction within the landslide mass, which is not always the same as the effective friction during motion on the sliding surface ϕ_m .

In the liquefied state, $\sigma = u$, $c = 0$, then, $\sin \phi_{ia} = 0$, and $k = 1.0$. In the rigid state, c is big enough, then $\sin \phi_{ia}$ is close to 1.0, then k is close to 0.

As for the sand layer in the Suruga Bay, it should have been almost fully saturated because it is a submarine slope. Accordingly we used 0.99 as the pore pressure generation rate (Bss). A high pore pressure would have been generated within the fully saturated sand layer during the motion of landslides. In case of no pore pressure generation and the friction angle within the soil mass $\phi_i = 30^\circ$, $k = 0.5$. If the sand layer is completely liquefied and becomes a true liquid, it will be 1.0. We used the in-between value of 0.8. In this

case, the apparent friction angle inside mass (ϕ_{ia}) is calculated to be 11.5° because $\sin \phi_{ia} = 0.2$.

Earthquake Records

On 11 March 2011, the Tohoku Earthquake occurred off-shore the Tohoku region of Japan. Some hundreds to a few thousands gal of acceleration were recorded at monitoring stations in the Tohoku Region. The greatest earthquake acceleration was recorded along the NS Component (2,699 gal) at station MYG004 in the Miyagi Prefecture.

The effect of seismic loading on landslide initiation differs by frequency, length of period as well as the acceleration of shaking. A great earthquake possibly triggered the landslide in Senoumi was not the same with the Tohoku earthquake. However, we used the record at MYG004 (Fig. 2) for this computer simulation as the most practical reference record in Japan. It has two main shocks resulting from two major ruptures in the subduction plane. A strong and possibly long seismic shaking induced by the combined activation of Tokai (Suruga Bay area), Tonankai and Nankai segments of the Nankai megathrust are assumed to occur in Japan. In this case, two or three main shocks are possible to occur and it may give a long and strong shaking which should have a great impact to trigger landslides.

As a comparison, the previous records of earthquakes in Iwate-Miyagi (14 June, 2008) and Suruga Bay (11 Aug., 2009) were also input to LS-RAPID as seismic records. The effects of parameters in landslide simulation model LS-RAPID on the dynamic behaviour of earthquake-induced rapid landslides will be analyzed for Suruga Bay (Fig. 3) using these three actual earthquake records.

Results and Discussion

Model Application in Suruga Bay

In this study, we use the full mode simulation of LS-RAPID model (Initiation + Motion + Expansion). The simulation will reduce the friction coefficient and the cohesion from their peak values to the normal motion time values within the source area in the determined distribution of the unstable mass (reducing from " \tan_{ϕ_p} " to " \tan_{ϕ_m} " and from " C_p " to " C_m "). When the travel length becomes DL (mm), the reduction will be started. Once the travel length reaches DU (mm), the reduction will be completed and then normal motion simulation will start. In this study, most of the mechanical parameters, including DL, DU, \tan_{ϕ_p} , and \tan_{ϕ_m} , were decided by the test on drilled sample by undrained cyclic loading ring shear test (Sassa et al. 2011). Firstly, we simulated the potential landslide initiation and

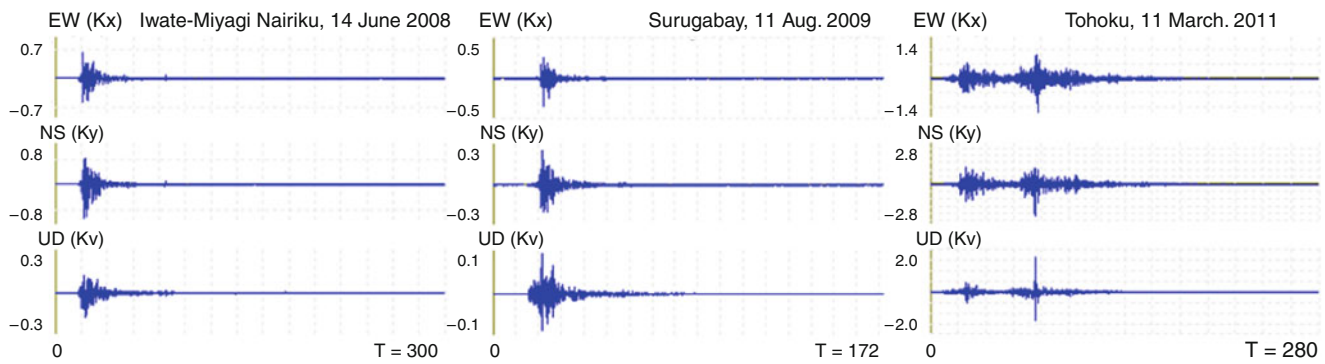
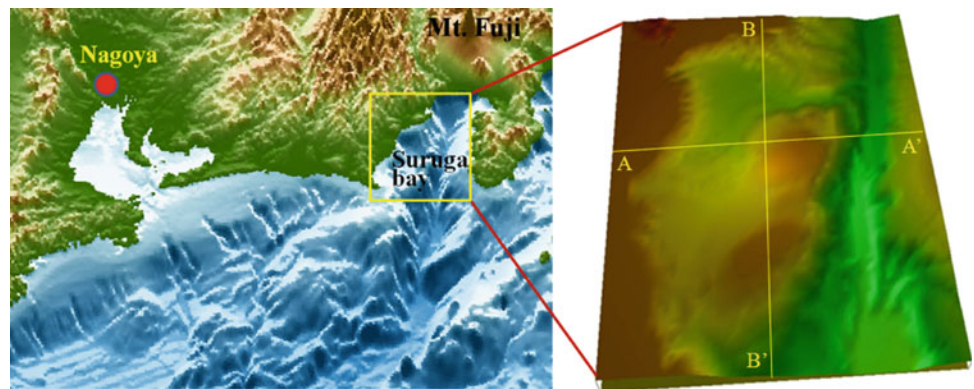


Fig. 2 Strong ground motion record of the 2008 Iwate-Miyagi Nairiku Earthquake (IMNE), 2009 Suruga Bay Earthquake (SBE), 2011 Tohoku Earthquake (TE) monitored at MYG 004. (X axis unit: second; Y axis Unit: 1,000 gal)

Fig. 3 Location of investigation area in Suruga Bay and 3D imagery of LS-RAPID simulation area



motion by using three actual earthquake records. Then the key parameters of LS-RAPID were evaluated to test their effects on the dynamics of earthquake-induced rapid landslides.

Simulation of Landslide Motion

Firstly, the landslide initiation and motion was simulated by using 1.0 times acceleration of 2008 Iwate-Miyagi Nairiku Earthquake (IMNE), 2009 Suruga Bay Earthquake (SBE), and 2011 Tohoku Earthquake (TE). As results, only TE can trigger large landslide in Suruga Bay. Then, we tested stronger acceleration of IMNE and SBE, i.e. 2.0 and 4.0 times of IMNE and SBE. As for TE, we tested for smaller seismic acceleration by using 0.3, 0.5, and 0.7 times of TE. Figure 4 presents the motion of soil mass triggered by these scenarios earthquake accelerations. It shows that the landslide motions triggered by 1.0 and 2.0 times SBE are all smaller than those triggered by IMNE, which has only landslide motion in the northern part of simulation area and has no initiation of mass movement in the southern part of simulation area. When 4.0 times acceleration of SBE and IMNE were used, the significant landslide motion has occurred in both cases, however,

the landslide motion in IMNE is larger than that in SBE since IMNE acceleration is stronger than SBE.

As for the Tohoku Earthquake (TE), the peak acceleration was 2,699 gal. We simulated landslide motion by 0.1, 0.2, 0.3, 0.5, 0.7 and 1.0 times of monitored acceleration record for Suruga Bay, respectively. Here, 30 s and 80 s is around 10 s after the first main shock and the second main shock respectively, when the effects of main shocks clearly appeared. Results show that, two cases of 0.1 and 0.2 did not cause any motion in Senoumi area (Northern part of Suruga Bay). But, 0.3 times of acceleration, namely 809 gal at peak triggered local failures in steep parts of slopes (Fig. 5). Thereafter, the local failures are spread to other areas in the progressive failure process due to strength reduction at failed areas. It formed a landslide mass and transported the mass into the deep sea of Suruga Bay along which the mass moved downward to the Pacific Ocean. 0.5 times of acceleration, can also trigger local failures in steep parts of slopes, which is slightly bigger than that triggered by 0.3 times of acceleration. Moreover, 0.7 times of acceleration (1,889 gal at peak) triggered a landslide mass at the first main shock, and thereafter, the landslide mass moved. But the landslide area was not expanded until termination. 1.0 times of acceleration of Tohoku Earthquake triggered the

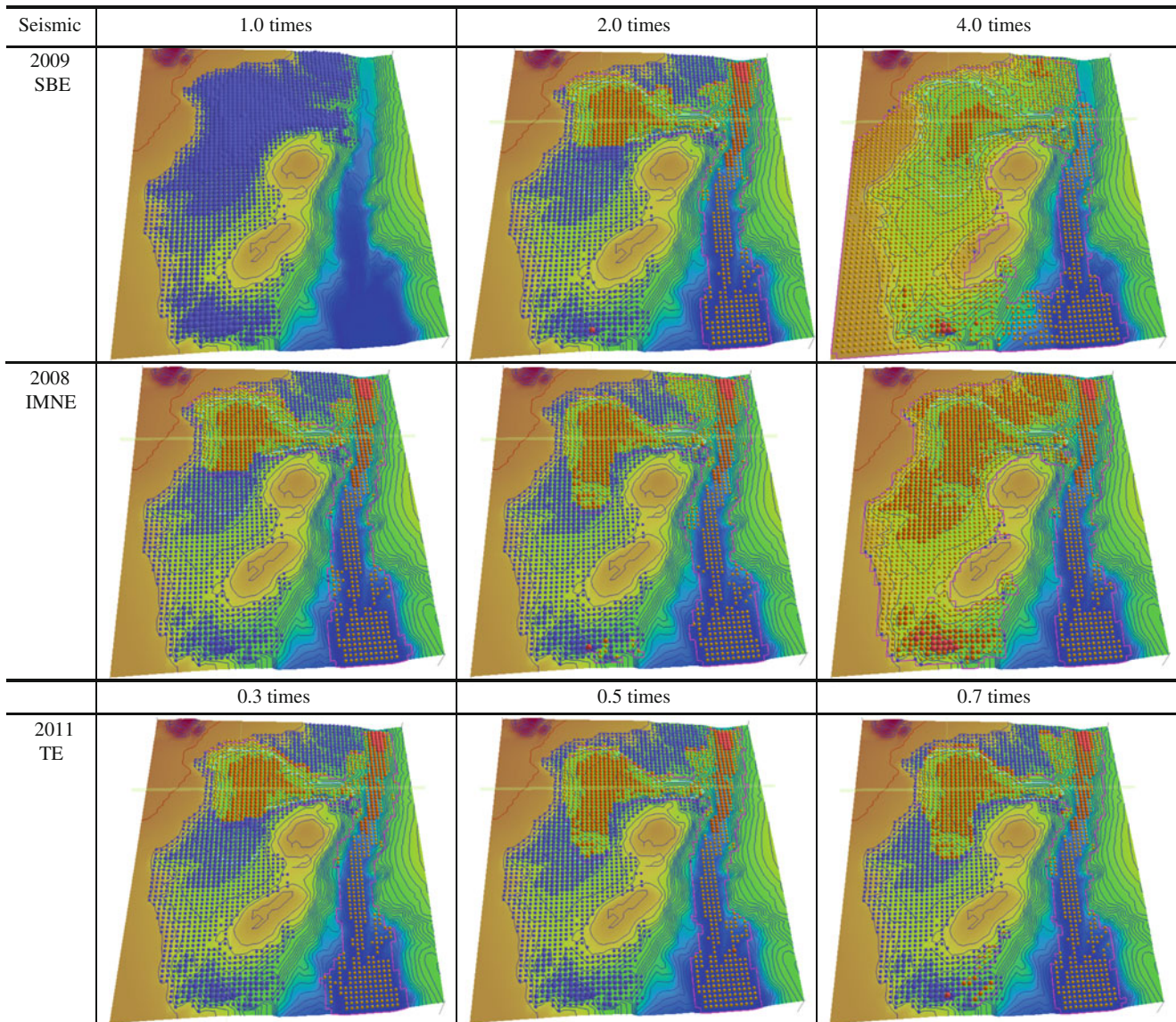


Fig. 4 Simulation results of 1.0 times, 2.0 times and 4.0 times acceleration of the 2008 Iwate-Miyagi Nairiku Earthquake (IMNE) and 2009 Suruga Bay Earthquake (SBE); and the simulation results of 0.3 times, 0.5 times and 0.7 times acceleration of 2011 Tohoku Earthquake (TE). The cell of mass is depicted as a ball with different colour. The

critical velocity to change ball colour is set as 0.5 m/s which means the stable mass will change to the moving mass if the mass's velocity is bigger than this velocity. The *blue ball* stands for the stable mass and the moving mass is depicted from orange (small velocity) to brown (big velocity)

Fig. 5 Simulation results of 1.0 times acceleration of the 2011 Tohoku Earthquake. 30 s and 80 s is around 10 s after the first main shock and the second main shock respectively

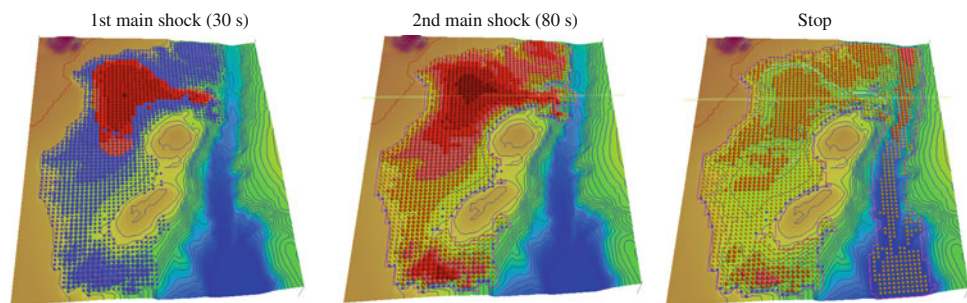
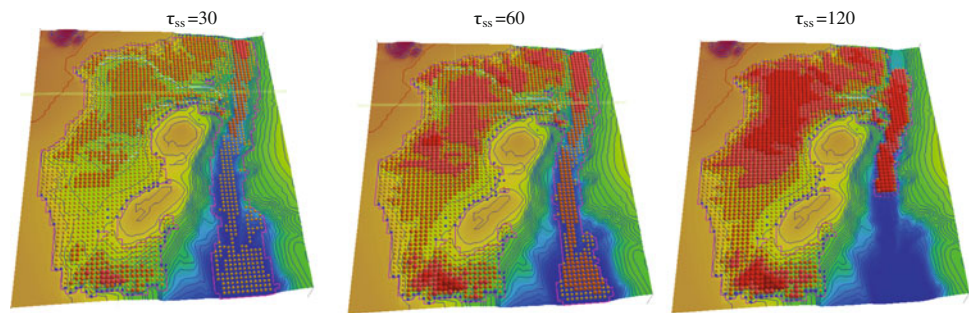


Fig. 6 Simulation results of 1.0 times acceleration of the 2011 Tohoku Earthquake using $\tau_{ss} = 30$, $\tau_{ss} = 60$ and $\tau_{ss} = 120$, respectively. Here, lateral pressure ratio $k = 0.8$, peak friction coefficient angle at sliding surface $\varphi_p = 36.9^\circ$



same size of landslide at the first main shock with the case of 0.7 times. However, the second main shock triggered a great landslide involving the whole Senoumi area. The moved landslide mass gradually flowed out through the narrow exit and went down along the Suruga Trough. The termination of simulated motion in the case of 0.3, 0.7, 1.0 was 6,021 s, 5,959 s and 6,254 s respectively. Namely the simulated soil mass movement continued for around 1.7 h. The toe of landslide mass is out of this simulation area.

Thus, from the simulation results, 0.7 times and 1.0 times TE records can trigger very big landslide motion in Suruga Bay. As an example, Fig. 5 presents the simulated landslide motion of Senoumi soil mass in Suruga Bay which was potentially triggered by the 2011 Tohoku Earthquake. In addition, the crossing sections A-A' and B-B' after termination of motion in the case of 1.0 times of acceleration of 2011 Tohoku earthquake demonstrated that the elevation of the sea floor after the landslide is higher than the current sea floor. Further downward movement of sea floor was possibly caused by other than landslides, such as submarine erosion process by the water flow provided by the Oi river which has formed the alluvial fan in the Senoumi area.

Effect of Parameters on Landslide Dynamics

Based on the above simulation, we changed the values of several key parameters of LS-RAPID. As an example, Fig. 6 shows the results of landslide motion by changing the values of τ_{ss} (steady state shear resistance at sliding surface) under the condition of 1.0 times 2011 TE. When τ_{ss} changed from 30 (obtained from ring shear test) to 60, the large landslide motion can occur but most of the mass still remains in the Senoumi area and the mass transported to the sea floor is less than that under the condition of $\tau_{ss} = 30$. When $\tau_{ss} = 120$, the mass in the Senoumi area is harder to move. The motion of landslide is terminated very soon. The mass transported from Senoumi to sea floor is small. Therefore, the effect of τ_{ss} on the motion of landslide is significant. But, it has no significant effect on the initiation of landslide since in all the

three cases ($\tau_{ss} = 30$, 60, and 120) the motion of landslide is apparent.

Conclusion

From the above simulation results, the conditions to cause landslides by earthquake can be summarized as:

1. 2008 Iwate-Miyagi Nairiku Earthquake can initiate the motion of landslides in 1.0 times of earthquake wave. However, 2009 Suruga Bay Earthquake cannot trigger landslides in the same conditions.
2. 2009 Suruga Bay Earthquake can cause small landslides in 2.0 times of earthquake wave, and large landslide in 4.0 times of earthquake wave.
3. As for 2011 Tohoku Earthquake, it can cause large landslide in Suruga Bay in 1.0 times of earthquake wave.
4. The effect of τ_{ss} on the motion of potential landslide is significant in Suruga Bay area.

Summarily, the simulation results in this study visualized that it was possible for the Senoumi topography in Suruga Bay to be created by the strong ground motion record of the 2011 Tohoku Earthquake or another similar or even greater earthquake which possibly occurred in this area in the past.

Acknowledgments The ring shear apparatus was developed by the International Programme on Landslides (IPL) and the Science and Technology Research Partnership for Sustainable Development Programme (SATREPS) of Japan Science and Technology Agency (JST) and Japan International Cooperation Agency (JICA). We are also grateful for the support by the Kyoto University GCOE program "Sustainability/Survivability Science for a Resilient Society Adaptable to Extreme Weather Conditions" and JSPS Grant-in-Aid for Young Scientists (B) (90569724).

References

- Hutchinson JN (1986) A sliding-consolidation model for flow slides. *Can Geotech J* 23(2):115–126
- Perla R, Cheng TT, McCling DM (1980) A two-parameter model of snow avalanche motion. *J Glaciol* 26:197–207
- Sassa K (1988) Special lecture: the geotechnical model for the motion of landslides. In: *Proceedings of the 5th international symposium on landslides, Lausanne, vol 1, pp 33–52*

- Sassa K, Wang G, Fukuoka H (2003) Performing undrained shear tests on saturated sands in a new intelligent type of ring-shear apparatus. *Geotech Test J* 26(3):257–265
- Sassa K, Wang G, Fukuoka H, Wang FW, Ochiai T, Sugiyama M, Sekiguchi T (2004a) Landslide risk evaluation and hazard zoning for rapid and long-travel landslide in urban development areas. *Landslides* 1(3):221–235
- Sassa K, Fukuoka H, Wang G, Ishikawa N (2004b) Undrained dynamic-loading ring-shear apparatus and its application to landslide dynamics. *Landslides* 1(1):7–19
- Sassa K, He B, Miyagi T, Ostric M, Baba T, Nagai O, Furumura T, Konagai K, Kaneda Y, Yamashiki Y (2011) A possible submarine megaslide in Suruga bay in Japan – an interpretation of Senoumi (Stony flower sea) bathymetric feature. *Landslides* (in submission)
- Wang F, Sassa K (2010) Landslide simulation by a geotechnical model combined with a model for apparent friction change. *Phys Chem Earth* 35:149–161



Different Methods to Produce Distributed Soil Thickness Maps and Their Impact on the Reliability of Shallow Landslide Modeling at Catchment Scale

Samuele Segoni, Gianluca Martelloni, and Filippo Catani

Abstract

In this paper we made a comparison between various methods to enter soil thickness as a spatial variable in a deterministic basin scale slope stability simulator. We used a slope stability model that couples a simplified solution of Richards infiltration equation and an infinite slope model with soil suction effect. Soil thickness was entered in the stability modelling using spatially variable maps obtained with four state-of-art methods: linear correlation with elevation; linear correlation with slope gradient; exponential correlation with slope gradient; a more complex geomorphologically indexed model (GIST model). Soil thickness maps and the derivate Factor of Safety (FS) maps were validated. Results confirmed that FS is very sensitive to soil thickness and showed that the same slope stability model can be highly sensitive or highly specific depending on the input soil thickness data. The uncertainty in the FS calculation can be reduced by applying more precise soil thickness input data: mean error of soil thickness maps is closely related to the sensitivity or specificity of the FS computation, while the overall performance of the stability simulation depends on mean absolute error and skewness of the frequency distribution of the errors of soil thickness maps. Despite the fact that slope-based methods are the most used in literature to derive soil thickness, in our application they returned poor results. Conversely, the use of the GIST model improved the performance of the stability model.

Keywords

Soil thickness • Soil depth • Shallow landslide • Factor of safety • Validation • Sensitivity • Infinite slope

Introduction

Soil thickness is considered as one of the most important factors controlling shallow landsliding (Johnson and Sitar 1990; Wu and Sidle 1995; Van Asch et al. 1999). Notwithstanding, to enter soil thickness in basin scale models, many authors rely on straightforward and simplistic solutions such as: considering a spatially constant value (Khazai and Sitar 2000; Savage et al. 2004), using soil thickness classes

(Revellino et al. 2008), assigning a reference value for each geological formation (Savage et al. 2004), or deriving a distributed soil thickness map from a single known topographic attribute such as the elevation (Saulnier et al. 1997) or the slope gradient (De Rose 1996; Salciarini et al. 2006). More complex methods that make use of multivariate statistical analyses (Gessler et al. 2000; Tesfa et al. 2009) or that employ process-based models (Casadei et al. 2003; Pelletier and Rasmussen 2009) are less frequently used as input data in large scale slope stability analyses because they are very site-specific and require some effort to be correctly applied and calibrated over large areas.

In this paper a slope stability model was applied on a pixel-by-pixel basis using four different distributed soil

S. Segoni (✉) • G. Martelloni • F. Catani
Dipartimento di Scienze della Terra, Università degli Studi di Firenze,
via La Pira 4, Florence 52021, Italy
e-mail: samuele.segoni@unifi.it

thickness maps, each obtained using a distinct method. The outcomes were compared in order to: (1) evaluate which soil thickness model is more effective when used in conjunction with basin scale slope stability models; (2) understand the sensitivity of slope stability analysis to soil thickness; (3) discuss if (and how) the errors in soil thickness mapping are correlated with errors in slope stability assessment.

Material and Methods

Test Site

The test site is the Armea Creek basin (Fig. 1), a mountain catchment located in the Western Alps (Liguria, Northern Italy). The area is about 37 km² and it is dominated by Cretaceous Flysch (limestone and sandstone) with a complex structural setting characterised by faults, thrusts, a tectonic window, recumbent folds and polyphase folds (Sagri 1984; Menardi-Noguera 1988; Merizzi and Seno 1991). The steep slopes and the high energy of relief make the area very prone to shallow landsliding. The Armea valley is mainly occupied by forests and small olive groves, and the population concentrates in the village of Ceriana.

Slope Stability Model

The model used in the analysis couples a hydrological model (which calculates the spatial pressure head distribution as a function of time and depth, and which is based on a reduced form of Richards' equation) with an infinite slope stability analysis in which suction effects in unsaturated soils are also taken into account (Segoni et al. 2011). The slope stability simulator used during this study is suitable for complex storms characterised by different and alternating intensities in both space and time. The stability simulator is implemented in a computer code designed to be applied in operational forecasting systems in near real time (Mercogliano et al. 2010, 2011), but in this work it was used for back analysis, simulating the ground effects of a historical rainfall event. As every other model based on infinite slope theory, it is designed to be applied to shallow landslides wherever soil coverage, compared to the underlying bedrock, exhibits a marked change in hydraulic properties.

The model works on a pixel by pixel basis: for every pixel, it calculates the factor of safety at increasing depths, allocating the lower FS value found. The computation is automatically repeated at different time steps.

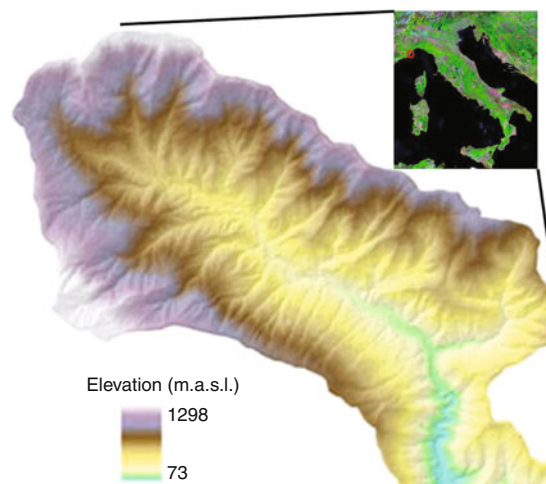


Fig. 1 Location and morphology of the Armea basin (Italy)

Soil Thickness Maps

To feed in the slope stability model with respect to soil thickness, we used four different soil thickness maps, obtained with the following methods.

- GIST model. The “geomorphologically indexed soil thickness” (GIST) is an empirical model that combines morphometric attributes with geomorphological and geological factors (Segoni 2008; Catani et al. 2010; Segoni and Catani under review). The model is based on three factors (C, P and S), whose values range from 0 to 1, and indicate a tendency to have a thicker soil. At every pixel, the value assumed by each factor depends on the local value of the corresponding morphometric attribute (curvature, for factor C; position along the hillslope profile, for factor P; slope gradient, for factor S), but the relationship linking the morphometric attribute with the corresponding factor is not constant over the entire test area. Factor C values were basically assumed inversely proportional to curvature values, except where geomorphologic survey highlighted a direct proportionality (e.g. in footslopes characterised by accumulation of loose material); the relationship linking factor P and hillslope position was calibrated according to the toposequences characterising the hillslopes; factor S reduces soil thickness values when the local gradient exceeds a threshold which is differentiated on a lithological basis. The product of the three factors is then translated into a soil thickness measure by means of calibration functions defined using a few in situ soil thickness measurements. For further details on this model, see Catani et al. (2010) and Segoni and Catani (under review).

- Z model assumes that soil thickness values are inversely proportional to the elevation, since in higher locations erosion usually prevails over deposition, producing shallower soils, whilst at lower elevations the predominance of deposition usually determines thicker colluvial and alluvial soils. The soil thickness – elevation relationship can be established according to a linear law derived from a few calibration measures (Saulnier et al. 1997).
- S model assumes that soil thickness values are inversely proportional to the slope gradient, since on steeper slopes more intense erosive processes produce shallower soils, whilst thicker colluvial and alluvial soils can be usually found on flat surfaces where erosion is less intense. The slope gradient – soil thickness relationship can be established according to a linear law derived from a few calibration measures (Saulnier et al. 1997; Blesius and Weirich 2009).
- Sexp model. This model is a more advanced version of the previous one: the slope gradient – soil thickness relationship is established by an exponential law (thus soil thickness is assumed to decrease more rapidly with increasing slope gradient values). A similar approach has been used in shallow landslide assessments by De Rose (1996), Salciarini et al. (2006) and Godt et al. (2008).

These four methods were applied to the test site on a pixel-by-pixel basis by means of a GIS system and four very different soil thickness maps were obtained (Fig. 2).

Slope- and elevation-dependent soil thickness maps exhibit a spatial variability identical to that of the attribute used for its derivation. Despite that, the two gradient-based models returned very different results as the exponential relationships (Sexp model) depicted shallower soils than the linear one (S model). The GIST model-derived soil thickness pattern, in turn, is evidently influenced by the relative position along the hillslope profile.

Other Input Data and Slope Stability Simulation

We performed four stability simulations, holding all the input parameters constant excepted soil thickness, which was entered using the four aforementioned maps.

The values of the geotechnical and hydraulic parameters were differentiated for each geological formation encountered in the study area (Table 1) and were obtained from previous works on the same test site (Segoni et al. 2009).

Slope gradient was derived from a 5 m grid DEM.

The rainfall event considered in the simulation is related to the 8th of December 2006, when intense precipitations triggered 141 shallow landslides (mainly debris flows and soil slips). Their sliding area was generally very small (one half were smaller than 100 m²) and only a few phenomena

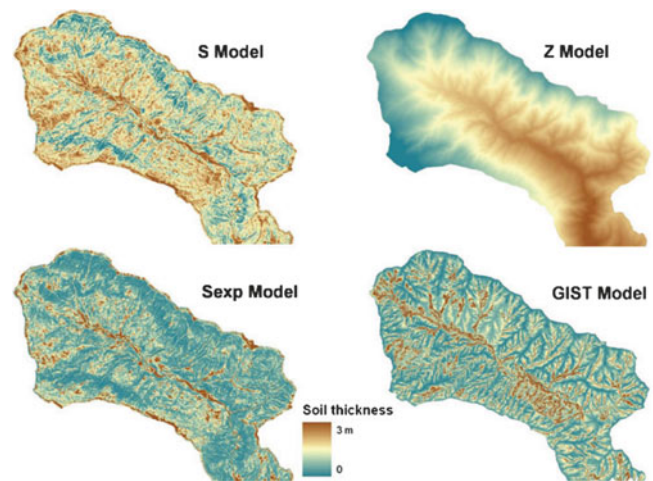


Fig. 2 Soil thickness maps

with relevant magnitude occurred (Segoni et al. 2009). Despite that, the event had a relevant destructive impact on properties, roads, assets and population (Segoni et al. 2009).

The evolution of the slope stability was computed through 24 hourly time steps making use of distributed radar rainfall maps downscaled to a 1.75 km spatial resolution (Segoni et al. 2009).

Results

Factor of Safety (FS) Maps

The stability model was applied four times (using the mentioned four soil thickness maps) on a pixel-by-pixel basis at hourly time steps; for each of them, a FS map was produced with a 5 m spatial resolution.

For each simulation, a summarising FS map of the event was produced assigning to every pixel the lowest FS value assumed during the analysed period (Fig. 3). Pixels with FS values higher and lower than 1 (limit equilibrium) were interpreted as stable and unstable (respectively).

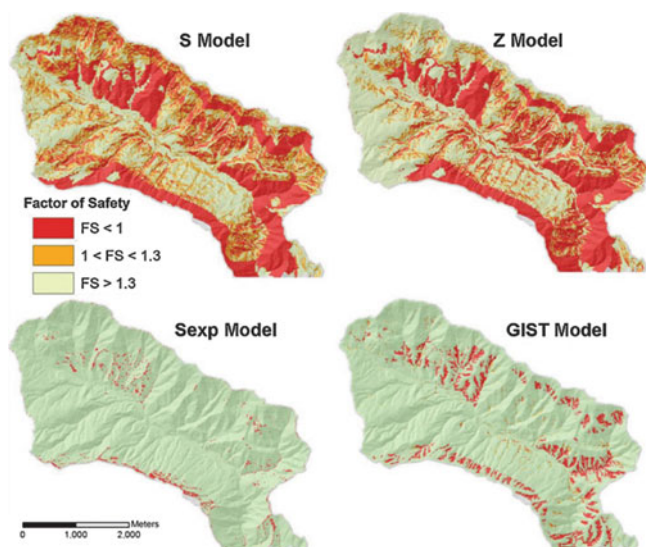
When Z and S models were used as input, a generalised instability affected the studied area. On the other hand, the Sexp model depicted a diametrically opposite scenario, in which the Armea basin was considered stable almost everywhere. With the GIST model, an intermediate result was obtained between these two very extreme conditions.

Validation of FS Maps

A validation was carried out comparing the summarising maps with an inventory of the triggered landslides (Segoni et al. 2009).

Table 1 Geotechnical and hydraulic parameters

Geological formation	C (KPa)	Φ ($^{\circ}$)	γ (N/m ³)	K (m/s)
Colluvial and eluvial deposits	4	28	20	$1 \cdot 10^{-3}$
Alluvial deposits	3	27	20	$2 \cdot 10^{-3}$
Ventimiglia Flysch (massive sandstones)	5	27	24	$2 \cdot 10^{-4}$
Ventimiglia Flysch (pelites and sandstones)	12	18	23	$3 \cdot 10^{-6}$
Sanremo Flysch (marlstones and mudstones)	11	21	24	$3 \cdot 10^{-5}$
Sanremo Flysch (mudstones and marlstones)	10	22	24	$2 \cdot 10^{-5}$
Bordighera sandstone (distal facies)	7	29	24	$8 \cdot 10^{-4}$

**Fig. 3** Summarising factor of safety maps. Differences depends solely on the soil thickness map used as input parameter

To quantify correct predictions and errors committed by each simulation, for every simulation we determined true positives (TP; area of the correctly predicted landslides); true negatives (TN; total area of stable pixels located outside landslide polygons); false positives (FP; total area of unstable pixels located outside landslide polygons); and false negatives (FN; area of the unpredicted landslides). These statistics were combined to derive quantitative indexes assessing the effectiveness of the four simulations (Table 2).

In general, the use of the S and Z model led to overestimate instability: a high percentage of landslides was correctly identified with the drawback of producing also many false alarms (high sensitivity and low specificity). Conversely, using the Sexp model the area was considered stable almost everywhere: in this case, even if the false alarms were less frequent, only a few landslides were correctly predicted (low sensitivity and high specificity). When the GIST model was taken into account, the derivate FS map was more balanced between those two extremes, producing the highest likelihood ratio. Likelihood ratio can be considered as the best statistics to summarise the behaviour of the models since it is less influenced by the

Table 2 Validation statistics of the four FS maps, as defined by Begueria 2006 (likelihood ratio, sensitivity, specificity, efficiency, misclassification rate, positive predictive power, negative predictive power)

	GIST	Sexp	S	Z
Likel. ratio	4.50	1.99	2.20	2.09
Sensitivity	0.40	0.05	0.87	0.81
Specificity	0.91	0.97	0.60	0.61
Efficiency	0.91	0.97	0.61	0.61
Misclass. rate	0.09	0.03	0.39	0.39
Pos. pred. pow.	0.0085	0.0038	0.0042	0.0040
Neg. pred. pow.	0.0013	0.0019	0.0004	0.0006

large bias of the statistical sample (unstable areas represent only a very small portion of the whole test area) (Begueria 2006).

Validation of Soil Thickness Maps

The four soil thickness maps were validated using a number of soil thickness measures which ranges from 91 to 154, depending on the number of measures required for the calibration of each model (Table 3 and Fig. 4).

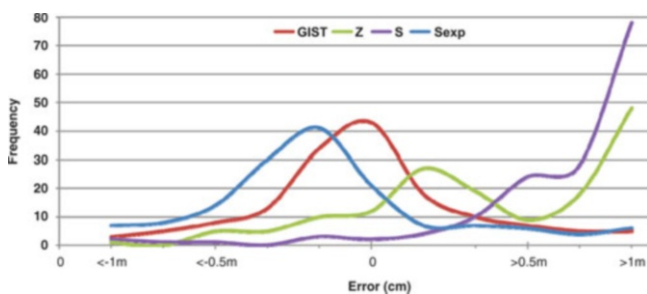
The Z and S models had the worst performance, with high mean absolute error, high frequency of large residuals and a pronounced tendency to overestimate soil thickness. The Sexp model returned quite good results (45 cm mean absolute error), but the frequency distribution of the residuals showed a proneness to underestimation. The soil thickness map obtained with the GIST model was more reliable than the others: mean absolute error was lower (23 cm), very large residuals were less frequent and no marked tendency to overestimation or underestimation was revealed by the frequency distribution of the residuals.

Discussion and Conclusions

Validation results confirmed that that slope stability models based on the infinite slope theory are very sensitive to soil thickness (Johnson and Sitar 1990; Wu and Sidle 1995; Van

Table 3 Validation statistics of the four soil thickness maps. Values are expressed in meters

	Z-model	S-model	Sexp-model	GIST model
Maximum underestimation	-1.18	-1.16	-2.04	-1.30
Maximum overestimation	1.61	2.01	1.70	1.91
Mean absolute error	0.68	1.03	0.45	0.33
Mean error	0.57	0.97	-0.18	-0.01
Standard deviation	0.48	0.56	0.57	0.48
Skewness	-0.18	-1.05	0.27	0.94
Kurtosis	-0.77	2.29	2.3	3.20

**Fig. 4** Frequency distribution of the errors committed by the four soil thickness models applied in the Armea basin

Asch et al. 1999; Segoni et al. 2009): the choice of the model to be used to obtain a distributed soil thickness map greatly influences the derived FS maps and, in general, a more reliable soil thickness map, combined with infinite slope based models, improves spatial distribution of FS values at basin scale. Therefore, in process-based approaches the uncertainty in slope stability assessments can be reduced by applying more accurate input data (i.e. soil thickness).

Furthermore, results pointed out that the same stability model can be more sensitive or more specific depending on quality of input data. When a soil thickness model which generally overestimate soil thickness (e.g. S and Z models) was used to feed the slope stability simulator, highly sensitive and lowly specific results were obtained (many true positives but also many false positives). Conversely, the use of a soil thickness model which generally underestimated soil thickness (e.g. Sexp model) led to low sensitive but high specific results (few false positives but many false negatives).

This outcome also put in the right perspective the belief that infinite slope-based approaches overestimate instability related to shallow landsliding: our simulations show that an important contribution to overestimation can be provided by the errors made by feeding the slope stability model with inaccurate soil thickness maps.

In order to quantify how much FS validation statistics can be influenced by soil thickness uncertainties, we calculated the correlation coefficient between each validation statistic of the FS maps (Table 2) and each validation statistic of the soil thickness maps (Table 3). Resulting linear correlation coefficients are summarized in Table 4. A correlation

coefficient of 1 (-1) means that the two variables are perfectly directly (inversely) correlated, while if the correlation coefficient approaches zero, the relationship between the two variables is less robust and other factors influence it.

As can be seen from Table 4, mean error of the input soil thickness map is highly related to most of the validation statistics quantifying the accuracy of FS maps (only likelihood ratio and positive predictive power show a low correlation coefficient). It could be inferred that, in general, the higher the mean error in the input soil thickness data, the higher the sensitivity of the FS model (i.e. the capability of predicting landslides) and, at the same time, the lower the specificity of the FS model (i.e. the capability of predicting stable areas). Therefore, although highly related to the performance of the stability model, mean error cannot be directly used to assess the overall performance of the stability model.

Compared to absolute error, the mean absolute error has a correlation coefficient which is higher with the likelihood ratio, but lower with almost all the other FS validation indexes.

Skewness is the only parameter that shows a moderate correlation with all the FS validation indexes. In particular, likelihood ratio is the index most commonly associated to the overall performance of a model (as it combines both sensitivity and specificity), and it results mostly correlated with the skewness (and, to a lesser extent, to mean absolute error).

Standard deviation and kurtosis of the soil thickness errors are scarcely related to any index used to measure FS maps reliability. The errors characterized by extreme values (max overestimation and max underestimation of soil thickness) exhibit the lowest correlation coefficients, highlighting that the overall performance of the stability model is scarcely influenced by the extreme values of the errors in soil thickness maps as long as overestimations compensate underestimations.

To sum up, the overall performance of the slope stability model resulted correlated to the absolute mean and the skewness of the errors committed in considering the input soil thickness map, but this correlation cannot be considered strong. Mean error is more strictly related to the reliability of the slope stability modelling (measured in terms of

Table 4 Linear correlation coefficients between the validation statistics of FS and soil thickness maps (for abbreviations please refer to Tables 2 and 3)

	Max und.	Max ov.	Mean abs err	Mean error	St. dev.	Skew	Kur
Likel. ratio	0.25	0.42	-0.58	-0.37	-0.58	0.71	0.56
Sensitivity	0.91	0.24	0.78	0.94	-0.29	-0.69	-0.49
Specificity	-0.78	-0.09	-0.85	-0.96	0.15	0.80	0.62
Efficiency	-0.78	-0.09	-0.85	-0.96	0.14	0.80	0.62
Misclass. rate	0.78	0.09	0.85	0.96	-0.14	-0.80	-0.62
Pos. pred. power	0.25	0.42	-0.58	-0.37	-0.58	0.71	0.56
Neg. pred. power	-0.91	-0.29	-0.80	-0.95	0.25	0.71	0.45

sensitivity and specificity), as it better takes into account the general tendency of the model to overestimate or underestimate soil thickness.

Therefore, it can be concluded that for the calculation of reliable FS maps, the absence of systematic errors in soil thickness input maps is more important than any other validation statistic. In our case study, Sexp-derived FS map depicted an almost uniformly stable scenario, while Z and S models identified a high percentage of landslides only because they predicted a diffused instability over the whole area. Despite slope-based methods are the most used in literature to derive soil thickness (De Rose 1996; Salciarini et al. 2006; Godt et al. 2008), a linear correlation scheme between slope gradient and soil thickness returned poor results. Moreover, the use of an exponential (rather than a linear) relationship in our case study even worsened the results. A substantial improvement was obtained when FS was derived from a soil thickness model based on geomorphological criteria (GIST model – Catani et al. 2010; Segoni and Catani under review).

References

- Beguieria S (2006) Validation and evaluation of predictive models in hazard assessment and risk management. *Nat Hazards* 37:315–329
- Blesius L, Weirich F (2009) The use of high-resolution satellite imagery for deriving geotechnical parameters applied to landslide susceptibility. *ISPRS Hannover Workshop 2009*, Hannover, 2–5 June 2009
- Casadei M, Dietrich WE, Miller NL (2003) Testing a model for predicting the timing and location of shallow landslide initiation in soil-mantled landscapes. *Earth Surf Proc Land* 28(9):925–950
- Catani F, Segoni S, Falorni G (2010) An empirical geomorphology-based approach to the spatial prediction of soil thickness at catchment scale. *Water Resour Res* 46:W05508. doi:10.1029/2008WR007450
- De Rose RC (1996) Relationships between slope morphology, regolith depth, and the incidence of shallow landslides in eastern Taranaki hill country. *Zeitschrift fur Geomorphologie Supplementband* 105:49–60
- Gessler PE, Chadwick OA, Chamran F, Althouse L, Holmes K (2000) Modeling soil-landscape and ecosystem properties using terrain attributes. *Soil Sci Soc Am J* 64:2046–2056
- Godt JW, Baum RL, Savage WZ, Salciarini D, Schulz WH, Harp EL (2008) Transient deterministic shallow landslide modeling: requirements for susceptibility and hazard assessments in a GIS framework. *Eng Geol* 102(3–4):214–226
- Johnson KA, Sitar N (1990) Hydrologic conditions leading to debris-flow initiation. *Can Geotech J* 27:789–801
- Khazai B, Sitar N (2000) Assessment of seismic slope stability using GIS modeling. *Geogr Inform Sci* 6(2):121–128
- Menardi-Noguera A (1988) Structural evolution of a Briançonnais cover nappe, the Caprauna-Armetta unit (Ligurian Alps, Italy). *J Struct Geol* 10:625–637
- Mercogliano P, Schiano P, Picarelli L, Olivares L, Catani F, Tofani V, Segoni S, Rossi G (2010) Short term weather forecasting for shallow landslides prediction. In: *Proceedings of the “Mountain risks: bringing science to society” final conference*, Florence, 24–26 Nov 2010
- Mercogliano P, Schiano P, Sikorski B, Tofani V, Catani F, Segoni S, Casagli N, Rossi G, Damiano E, Picarelli L, Olivares L, Comegna L (2011) Short term weather forecasting for prediction of shallow landslides. In: *Proceedings of the 2nd world landslide forum*, Rome, 3–9 Oct 2011
- Merizzi G, Seno S (1991) Deformation and gravity-driven translation of the S. Remo-M. Saccarello nappe (helminthoid flysch, Ligurian Alps). *Boll Soc Geol Ital* 110:757–770
- Pelletier JD, Rasmussen C (2009) Geomorphically based predictive mapping of soil thickness in upland watersheds. *Water Resour Res* 45:W09417. doi:10.1029/2008WR007319
- Revellino P, Guadagno FM, Hungr O (2008) Morphological methods and dynamic modelling in landslide hazard assessment of the Campania Apennine carbonate slope. *Landslides* 5:59–70
- Sagri M (1984) *Litologia, stratimetria e sedimentologia delle torbiditi di piana di bacino del flysch di San Remo (cretaceo superiore, Liguria occidentale)*. *Mem Soc Geol Ital* 28:577–586
- Salciarini D, Godt JW, Savage WZ, Conversini R, Baum RL, Michael JA (2006) Modelling regional initiation of rainfall-induced shallow landslides in the eastern Umbria Region of central Italy. *Landslides* 3:181–194
- Saulnier GM, Beven K, Obed C (1997) Including spatially variable effective soil depths in TOPMODEL. *J Hydrol* 202:158–172
- Savage WZ, Godt JW, Baum RL (2004) Modelling time-dependent areal slope stability. In: *Lacerda WA, Erlich M, Fontoura SAB, Sayao ASF (eds) Landslides: evaluation and stabilisation*. *Proceedings of the 9th international symposium on landslides*. A.A. Balkema, London, pp 23–36
- Segoni S (2008) *Elaborazione ed applicazioni di un modello per la previsione dello spessore delle coperture superficiali*. Unpublished Ph.D. thesis. Università degli Studi di Firenze, Department of Earth Sciences, Florence
- Segoni S, Catani F (submitted 2011) General definition and site specific applications of the Geomorphologically Indexed Soil Thickness (GIST) model. *Geomorphology*
- Segoni S, Leoni L, Benedetti AI, Catani F, Righini G, Falorni G, Gabellani S, Rudari R, Silvestro F, Rebora N (2009) Towards a definition of a real-time forecasting network for rainfall induced shallow landslides. *Nat Hazards Earth Syst Sci* 9:2119–2133

- Segoni S, Rossi G, Catani F (2011) Improving basin scale shallow landslide modelling using reliable soil thickness maps. *Nat Hazards*. doi:[10.1007/s11069-011-9770-3](https://doi.org/10.1007/s11069-011-9770-3)
- Tesfa TK, Tarboton DG, Chandler DG, McNamara JP (2009) Modelling soil depth from topographic and land cover attributes. *Water Resour Res* 45:W10438. doi:[10.1029/2008WR007474](https://doi.org/10.1029/2008WR007474)
- Van Asch TWJ, Buma J, Van Beek LPH (1999) A view on some hydrological triggering systems in landslides. *Geomorphology* 30(1):25–32
- Wu W, Sidle RC (1995) A distributed slope stability model for steep forested basins. *Water Resour Res* 31(8):2097–2110



Simulating Infiltration Processes into Fractured and Swelling Soils as Triggering Factors of Landslides

Annalisa Galeandro, Jirka Šimůnek, and Vincenzo Simeone

Abstract

The influence of rainfall in triggering landslides is a widely discussed topic in scientific literature. The slope stability of fractured surface soils is often influenced by the soil suction. Rainfall, infiltrating into soil fractures, causes the decrease in soil suction and shear strength, which can trigger the collapse of surface soil horizons. Water flow through fractured soils can also be affected by soil swelling and by capillary barrier effects in the case of low permeable soil overlying a more permeable one.

These conditions are rarely investigated by the existing models, especially from the point of view of rainfall triggering surface landslides. For this purpose, we have developed a dual-porosity model that simulates water flow through fractured swelling soils overlying a more permeable soil. The model has been applied to a soil profile consisting of a thin layer of fractured loamy soil above a coarse sand layer, in order to investigate the influence of different rainfall intensities on the infiltration process, and on the distribution of the pore pressure that affects slope stability.

Keywords

Infiltration • Rainfall threshold • Shallow landslides

Introduction

Rainfall-induced landslides are an important topic in the scientific literature. There is mainly an interest in evaluating the rainfall threshold that triggers the slope failure (e.g. Frattini et al. 2009; Guzzetti et al. 2008; Picarelli et al. 2009; Pagano et al. 2010; Doglioni et al. 2011). The complexity of hydrologic and mechanic processes involved in rainfall-triggered landslides makes it difficult to develop a

reliable physical slope model to be used to evaluate the thresholds, especially for stratigraphically complex situations.

There is empirical evidence that a long low-intensity rainfall can sometimes be more dangerous than a short and intense one (Cotecchia and Simeone 1996), and that the singularity of an event is sometimes more relevant than its exceptionality. It is therefore important to analyse infiltration processes in detail, in order to better understand how rainfall events can affect the pore pressure in the soil and how they can trigger a landslide.

In particular, the stability of the surface unsaturated soil layer along a slope is often related to the soil suction. In unsaturated soils, rainfall infiltration induces significant changes in the pressure head distribution, causing a decrease in suction and shear strength, eventually triggering slope instability.

The presence of fractures in the topsoil accelerates infiltration and influences pore pressure variations, depending on rainfall intensity and soil properties (Beven and Germann

A. Galeandro (✉) • V. Simeone
Engineering Faculty of Taranto, Technical University of Bari,
viale del Turismo 8, Taranto, Italy
e-mail: annalisa.galeandro@poliba.it

J. Šimůnek
Department of Environmental Sciences, University of California
Riverside, Riverside, CA 92521, USA

1982; Jarvis et al. 1991). Additionally, soil swelling can cause a progressive closure of cracks and can also significantly influence water flow (Vogel et al. 2005). The mechanisms acting in surface fine-grained unsaturated soils overlying more permeable material could also be significantly affected by capillary barrier phenomena (Mancarella and Simeone 2007; Mancarella et al. 2012; Mancarella and Simeone 2012). Combined effects of cracks, swelling, and capillary barriers can thus seriously influence the pressure head distribution, and therefore slope stability of unsaturated soils.

Existing models commonly do not consider all these conditions. A reliable study of rainfall-induced landslides and infiltration by means of empirical or theoretical models should not ignore such relevant processes, which affect the soil behaviour under unsaturated conditions and the pressure head distribution. A study of the infiltration mechanisms which considered all these conditioning factors could be useful for better understanding the influence of rainfall in triggering landslides and for reliably defining hydrological risks.

During the last few decades various empirical hydrological models have been proposed (Caine 1980; Brunetti et al. 2009; and others; see a recent review by Guzzetti et al. 2008) that relate precipitation and landslides using empirical relationships. Commonly, these models do not take into account a number of physical phenomena affecting soils (Picarelli and Vinale 2007). In particular, they do not consider how hydrologic processes affect location, timing, and rates of landslides, and how land use and climate can influence slope stability (Iverson 2000).

Recently, several theoretical models evaluating landslide phenomena (Tsai and Yang 2006; Pagano et al. 2010; and others) have been developed, based on topographic, geologic, and hydrologic variables, and on changes in land use. In addition, there is also a large number of models, such as the HYDRUS codes (Šimůnek et al. 2008), which simulate infiltration processes.

In this paper we propose a dual-porosity model (Šimůnek et al. 2003), in which fractures become progressively narrower during infiltration due to the increase in water content in the swelling matrix. The presence of a coarse grained soil underlying the fine fractured layer, which creates a capillary barrier effect at the contact between the two types of soils (Galeandro and Simeone 2010) is also considered.

The model is applied to a soil profile consisting of a fractured loamy soil overlying a coarse sand layer. Results show how the infiltration process and the water content

distribution can be strongly affected by rainfall intensity, swelling phenomena and the presence of the underlying capillary barrier, subsequently affecting the overall slope stability.

The Model

The model simulates water flow in swelling fractured soils, which are considered to be dual-porosity systems. In the model, fractures represent the macroporous domain, and the soil matrix between them the microporous domain. The rainfall intensity is assumed to be constant. The soil is considered to consist of a homogeneous porous medium with vertical fractures (Fig. 1), which become progressively narrower during the infiltration process as a result of swelling of the matrix (Fig. 1a).

The model assumes that there is no vertical flow in the matrix and that all rainfall infiltrates into the fractures. Water flows into the cracks; then, it can laterally infiltrate by diffusion into the matrix through the fracture-matrix interface (Fig. 1).

The unsaturated soil hydraulic properties are described by using the van Genuchten (1980) and Mualem (1976) relationships. Water transfer through the fractures-matrix interface is modelled by the mass balance equation, which assumes that the matrix-fracture interactions are proportional to the pressure head gradient between the fractures and the matrix (Gerke and van Genuchten 1993). Water flow in the matrix is described by the Richards equation for horizontal flow and the flow rate (cm^3/s) in the fractures is obtained as the difference between the fracture inflow rate and the amount of water laterally adsorbed by the matrix (Fig. 1).

Matrix swelling is evaluated by a linear relationship between the matrix volumetric water content and the soil volume (Novak et al. 2002), assuming that the maximum swelling at full saturation is 2 % of the initial volume.

The coarse soil underlying the fractured fine-textured surface soil layer acts as a capillary barrier. Water accumulates in cracks and at the interface between the two soil layers up to a maximum capillary height (Fig. 1b). In the matrix, water is stored until the pressure head at the interface between the layers reaches a critical value, assumed to be the water-entry pressure head of the lower coarse layer (Shackelford et al. 1994; Stormont and Anderson 1999).

The parameters needed to parameterize the model are:

- Rainfall intensity i and its duration T ;

Fig. 1 Schematic representation of a soil system and a flow model

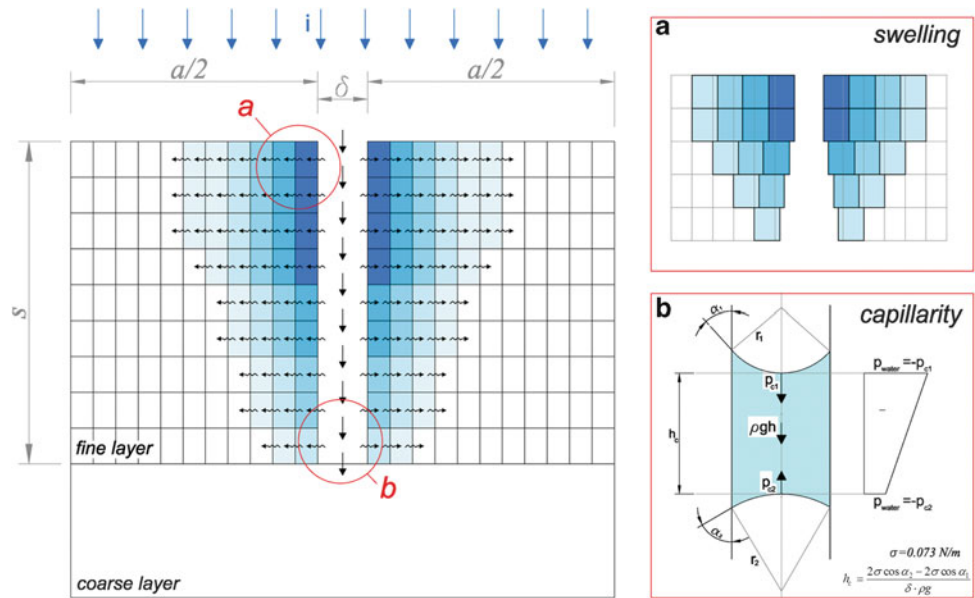


Table 1 Parameters describing the fractures

Fractures	
Saturated hydraulic conductivity K_{fs} (m/s)	1.00×10^{-3}
Spacing a (m)	0.50
Opening δ (m)	0.01
Thickness (m)	2

- Geometry of the fracture system (depth s , opening δ , and fracture spacing a);
- Hydraulic properties and material status characteristics (saturated hydraulic conductivity of fractures K_{fs} ; matrix initial water content θ_{mit} , residual water content θ_{res} , saturated water content θ_{sat} , saturated hydraulic conductivity K_{ms} , and van Genuchten parameters α and n ; maximum swelling percentage, and parameters relating swelling to water content).

In order to solve the flow equations, the system needs to be spatially discretized into elements of small dimensions in the x - z plane: the third dimension (in the direction of fractures) is assumed to be equal to 1 cm. The calculations are repeated at regular intervals.

Application of the Model: Results and Observations

The Case Study

The model has been applied to a soil system involving a loamy fractured soil layer overlying a coarse sand. The fine-textured soil has been assumed to be 2 m thick, with a fracture interspacing of 0.5 m and a fracture opening of

0.01 m. Parameters describing the fracture network are summarized in Table 1. Soil hydraulic parameters of the soil matrix (the upper soil layer) are summarized in Table 2. The initial water content of the upper soil layer has been assumed to be $0.1 \text{ (m}^3 \text{ m}^{-3}\text{)}$; i.e., close to the residual water content. A water-entry pressure head at the interface between the two layers has been assumed to be equal to 200 mm (Stormont and Morris 1998).

The model has been used to simulate two rainfall events with intensities of 2 and 20 mm/h (Table 3) and durations of 10 and 1 h (denoted below as events A and B), respectively, i.e., with the same amount of rainfall per event of 20 mm. A time step equal to 10 s has been used.

Simulations Results and Discussion

The behaviour of the system has been analysed in terms of water content and pressure head distributions, crack closure dynamics, and the capillary barrier breakthrough process during the two events (Figs. 2, 3, and 4). Results allow us to make several observations with regards to the simulated evolution of water contents in the soil.

Water Content and Pressure Head Distribution Dynamics

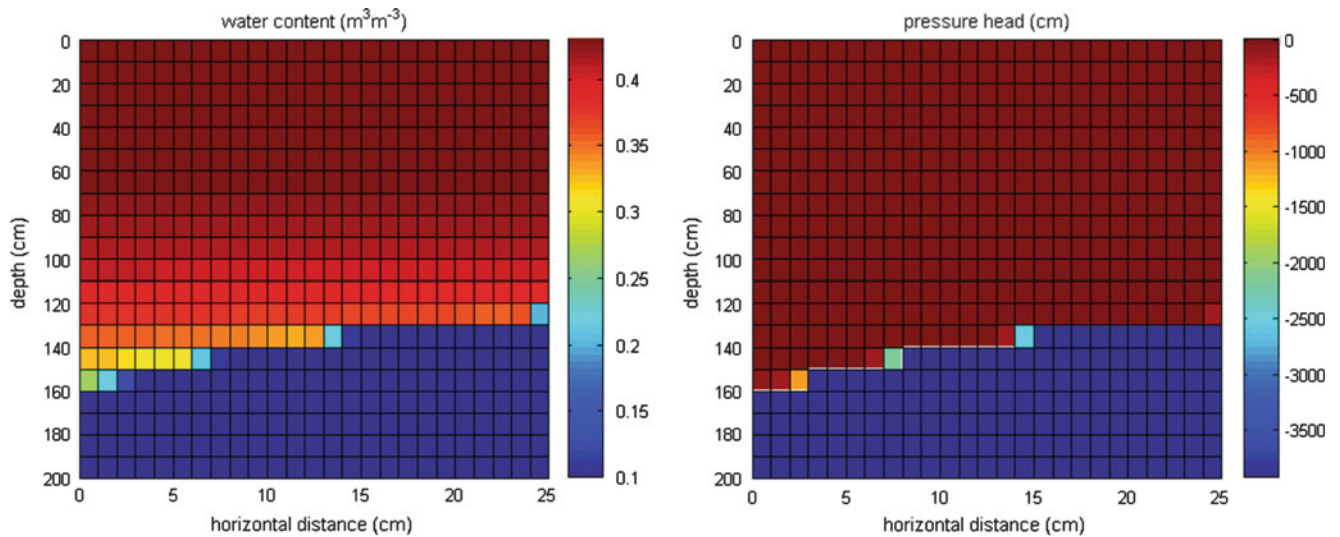
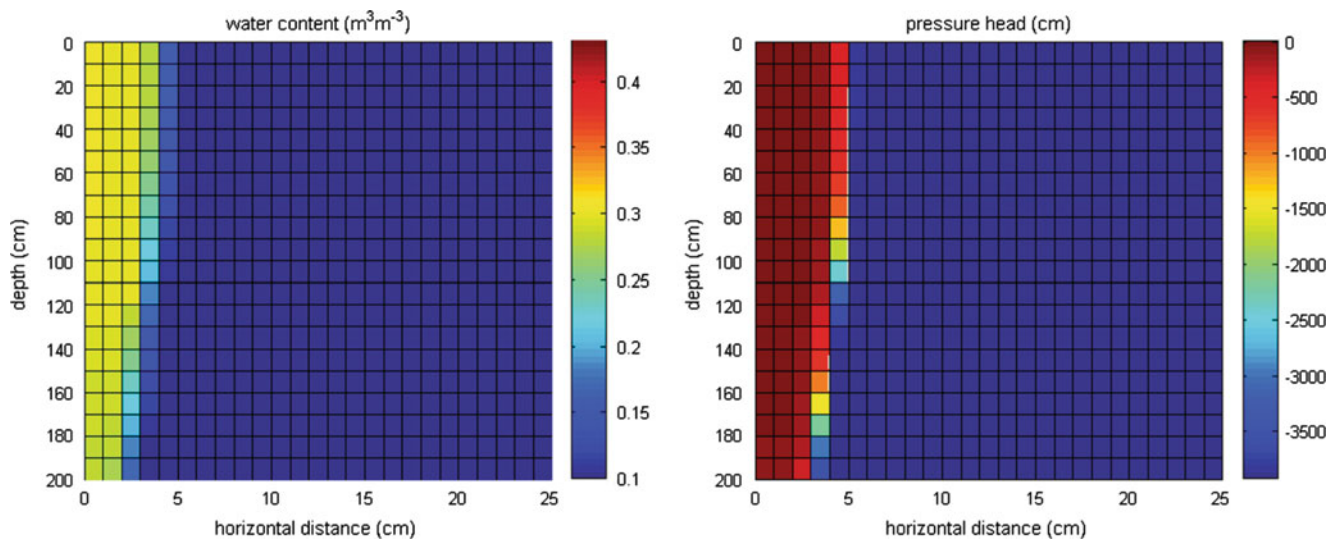
The presence of fractures in soils and the water flow through them produce water content and pressure head dynamics, along with corresponding shear strengths, in response to the rainfall intensity that is different than in homogeneous soils. Fractures significantly accelerate water flow and affect the dynamics of the water content distribution. The storage of water in the fractures and the matrix depends on the rainfall

Table 2 Soil hydraulic parameters for the soil matrix (Data from Carsel and Parrish 1988)

Upper layer (loamy soil)	
Saturated hydraulic conductivity K_{ms} (m/s)	2.89×10^{-6}
Saturated water content θ_{sat} ($m^3 m^{-3}$)	0.43
Residual water content θ_{res} ($m^3 m^{-3}$)	0.078
α (van Genuchten 1980) (m^{-1})	3.6
n (van Genuchten 1980)	1.56
l (Mualem 1976)	0.5

Table 3 Parameters of two rainfall events and inflow rates into fractures

Rainfall event	Rainfall intensity (mm/h)	Duration (h)	Inflow rate in fracture (cm^3/s)
A	2	10	0.0014
B	20	1	0.0139

**Fig. 2** Water content and pressure head distributions at the end of the rainfall (event A: 2 mm/h, 10 h)**Fig. 3** Water content and pressure head distributions at the end of the rainfall (event B: 20 mm/h, 1 h)

duration, crack opening, and functioning of the capillary barrier.

Initially, lateral adsorption of water into the soil matrix involves only a few centimetres of the soil near the matrix-

fracture interface. Later, flow into the matrix depends on the flow in the fractures, on the rainfall intensity, and on the swelling process, which could close fractures and interrupt flow in both domains.

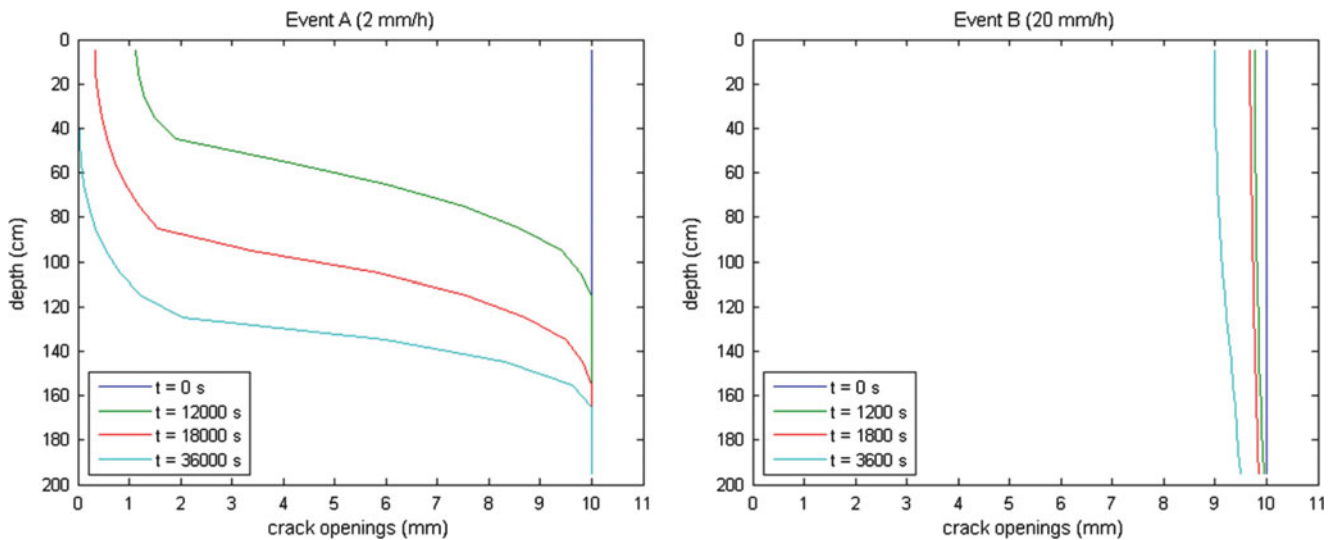


Fig. 4 Crack closure dynamics

During low intensity rains (i.e., 2 mm/h, event A), water flows slowly into the fractures. Infiltrated water needs several hours to reach the maximum depth of the fractures, enabling the storage of water in the fractures and lateral inflow into the matrix. At the end of rainfall event A, there is significant absorption into the soil matrix involving the entire upper soil layer, where the soil suction becomes zero (Fig. 2).

For shorter and more intense precipitations (i.e., 20 mm/h, event B), water flows fast through fractures, reaching the bottom of the surface layer quite quickly (in about 20 min) and continuing to flow downwards. At the end of event B, horizontal water absorption involves only a thin portion of the upper soil (only about 5 cm) close to the fracture surface (Fig. 3).

According to the performed simulations, different water absorption into the matrix seems to depend on rainfall intensity and on the interactions between water in the fractures and the matrix. Different rainfall intensities produced different water content distributions at the end of the simulated rainfall events. Water tends to be more uniformly distributed in the soil matrix for slow-intensity and longer events than for shorter and high-intensity precipitation. The average water content in the first 80 cm of the upper soil layer is close to saturation ($0.428 \text{ m}^3 \text{ m}^{-3}$) for the low-intensity rainfall, while for the high-intensity precipitation the average water content is only about $0.136 \text{ m}^3 \text{ m}^{-3}$, with the maximum value of about $0.30 \text{ m}^3 \text{ m}^{-3}$.

Accordingly, water content distributions, and corresponding pressure head distributions, resulted more critical for triggering surface landslide for low-intensity rains than for high-intensity precipitations.

Cracks Closure Dynamics

The process of crack closing starts at the soil surface and then propagates downwards toward the bottom of the surface soil layer. Simulation results show how crack closing is controlled by the rainfall intensity and duration. Crack closing is quite irregular for low-intensity rains (event A, Fig. 4a). Horizontal water absorption is quite significant in the topsoil, inducing substantial swelling and causing the closure of surface cracks after several hours. Deeper parts of the loamy soil are not reached by infiltrating water and the cracks opening at the bottom of the surface soil layer remains equal to the initial value (1 cm). Closed cracks hold infiltrating water and prevent it from moving downward, producing pressure heads in the soil matrix near the surface, close to saturation (Fig. 2). For high-intensity precipitations (event B), the swelling process is quite uniform along the entire depth of the fractures. Also the closure of the fracture is almost uniform and much less significant (about 1 mm) (Fig. 4b).

Capillary Barrier

There is no capillary barrier breakthrough for event A either in the matrix or the fracture because of the crack closures after about 7 h. Water cannot reach the coarse layer and break through the capillary barrier. The pressure head regime does not change at the interface between the two layers and the eventual stability failure could involve only the upper fine-textured layer.

The breakthrough of the capillary barrier below the fracture is quite a fast process in the case of event B when rain

water can quickly flow down towards groundwater. The breakthrough occurs already after 2 min (corresponding to the rainfall of 0.61 mm). The breakthrough of the capillary barrier allows water to flow quickly through the fine layer towards the coarse one. While water flows quickly towards groundwater and can cause stability problems in deeper soil layers, it is less harmful for surface layers.

Conclusion

A new dual-porosity model is proposed, which simulates water infiltration into unsaturated fractured swelling soils, while considering matrix swelling and fracture closures as well as the presence of a highly permeable soil underlying a less permeable one. The model enables to better simulate the dynamics of the pore-water pressure in fractured swelling soils.

The model has been used to simulate infiltration into a loamy soil characterized by shrinking cracks for different rainfall intensities. Results show that water flow in the fractures and the matrix depends on rainfall intensities. For low-intensity precipitations, lateral water absorption is an important process, which may produce saturation of the entire soil matrix close to the soil surface. This results in significant variations in the pressure head distribution in the surface layer, which may be more critical for low-intensity rains than for high-intensity precipitations. Long-duration, low-intensity rain could thus potentially trigger surface landslides. Our calculations confirm that, sometimes, prolonged low-intensity rainfalls can be more critical than short high-intensity rainfalls in triggering soil landslides in the surface horizons. The application of the model showed that intense rainfall can cause capillary barrier breakthrough below the fractures in a very short time, since this depth can be reached quickly by infiltrating water.

The simulation results underlined the influence of rainfall intensity and dynamics, of swelling, and capillary barrier effects on water content and pore pressure dynamics affecting the stability of surface layers. The ongoing research will involve the use of these types of models for evaluating rainfall thresholds in fractured swelling soils. The implementation of such infiltration model can contribute to the development of more reliable approaches to landslide risk analysis, by relating landslide susceptibility to rainfall amount, intensity and distribution over time.

References

- Beven K, Germann P (1982) Macropores and water flow in soils. *Water Resour Res* 18:1311–1325
- Brunetti MT, Peruccacci S, Rossi M, Guzzetti F, Reichenbach P, Ardizzone F, Cardinali M, Mondini A, Salvati P, Tonelli G, Valigi D, Lucani S (2009) A prototype system to forecast rainfall-induced landslides in Italy. In: Picarelli L, Tommasi P, Urciuoli G, Versace P (eds) *Proceedings of 1st Italian workshop on landslides, rainfall-induced landslides: mechanisms, monitoring techniques and nowcasting models for early warning systems*, vol 1, Naples, 8–10 June 2009, pp 157–161
- Caine N (1980) The rainfall intensity–duration control of shallow landslides and debris flows. *Geografiska Annaler Ser A Phys Geogr* 62:23–27
- Carsel RF, Parrish RS (1988) Developing joint probability distributions of soil water retention characteristics. *Water Resour Res* 24:755–769
- Cotecchia V, Simeone V (1996) Studio dell'incidenza degli eventi di pioggia sulla grande frana di Ancona del 13.12.82. – Convegno Internazionale su “La prevenzione delle catastrofi idrogeologiche: il contributo della ricerca scientifica”, vol I. Alba (CN) 5–7 Nov 1996, pp 19–29
- Dogliani A, Fiorillo F, Guadagno FM, Simeone V (2011) Evolutionary polynomial regression to alert rainfall-triggered landslide reactivation alert. *Landslides*, Springer. ISSN: 1612-510X (print version) ISSN: 1612-5118 (electronic version). doi:10.1007/s10346-011-0274-8
- Fratini P, Crosta G, Sosio R (2009) Approaches for defining thresholds and return periods for rainfall-triggered shallow landslides. *Hydrol Process* 23(10):1444–1460
- Galeandro A, Simeone V (2010) A dual porosity model for infiltration processes in fractured porous swelling soils. In: *Proceedings of the 11th IAEG Congress, geologically active*, Auckland, 5–10 Sept 2010, pp 683–689
- Gerke HH, van Genuchten MT (1993) Evaluation of a first-order water transfer term for variably saturated dual-porosity flow models. *Water Resour Res* 29:1225–1238
- Guzzetti F, Peruccacci S, Rossi M, Stark CP (2008) The rainfall intensity-duration control of shallow landslides and debris flows: an update. *Landslides* 5(1):3–17
- Iverson RM (2000) Landslide triggering by rain infiltration. *Water Resour Res* 36:1897–1910
- Jarvis NJ, Bergstrom L, Dik PE (1991) Modeling water and solute transport in macroporous soil. II. Chloride breakthrough under nonsteady flow. *J Soil Sci* 42:71–81
- Mancarella D, Simeone V (2007) Analysis of capillary barrier effects in the activation of debris avalanches in pyroclastic cover. In: *Proceedings of the fourth international conference on debris-flow hazards mitigation: mechanics, prediction, and assessment*, Chengdu, China, 10–13 Sept 2007. Chen C-L, Major JJ (eds), pp 45–54, 2008, Millpress, Rotterdam. ISBN:978-90-5966-059-5
- Mancarella D, Dogliani A, Simeone V (2012) On capillary barrier effects and debris slide triggering in unsaturated layered covers. *Eng Geol*, Elsevier. ISSN:013-7952, vol 147–148, 12 Oct 2012, pp 14–27. doi:10.1016/j.enggeo.2012.07.003
- Mancarella D, Simeone V (2012) Capillary barrier effects in unsaturated layered soils with special reference to the pyroclastic veneer of the Pizzo d'Alvano, Campania, Italy. *Bull Eng Geol Environ* 71:791–801. doi:10.1007/s10064-012-0419-6
- Mualem Y (1976) A new model for predicting the hydraulic conductivity of unsaturated porous media. *Water Resour Res* 12:513–515
- Novak V, Šimůnek J, van Genuchten MT (2002) Infiltration into a swelling cracked clay soil. *J Hydrol Hydromech* 50(1):3–19
- Pagano L, Picarelli L, Rianna G, Urciuoli G (2010) A simple numerical procedure for timely prediction of precipitation-induced landslides in unsaturated pyroclastic soils. *Landslides* 7:273–289
- Picarelli L, Vinale F (2007). Analysis of the bibliography (1 July 2007). CMCC research paper no. 21. Available at SSRN: <http://ssrn.com/abstract=1392137>
- Picarelli L, Tommasi P, Urciuoli G, Versace P (eds) (2009) *Rainfall-induced landslides: mechanisms, monitoring techniques and nowcasting models for early warning systems*. In: *Proceedings of*

- IWL the first Italian workshop on landslides, vol 1, Naples, 8–10 June 2009, pp 249. ISBN: 978-88-89972-12-0
- Shackelford CD, Chang C-K, Chiu T-F (1994) The capillary barrier effect in unsaturated flow through soil barriers. In: Proceedings of 1st international congress on environmental geotechnics, Edmonton, 10–15 July 1994, pp 789–793
- Šimůnek J, Köhne JM, Kodešová R, Šejna M (2008) Simulating non-equilibrium movement of water, solutes, and particles using HYDRUS: a review of recent applications. *Soil Water Res* 3(special issue 1):S42–S51
- Šimůnek J, Jarvis NJ, van Genuchten MT, Gardena A (2003) Review and comparison of models for describing non-equilibrium and preferential flow and transport in the vadose zone. *J Hydrol* 272:14–35
- Stormont JC, Anderson CE (1999) Capillary barrier effect from underlying coarser soil layer. *J Geotech Geoenviron Eng* 125(8):641–648
- Stormont JC, Morris CE (1998) Method to estimate water storage capacity of capillary barriers. *J Geotech Geoenviron Eng* 124:297–302
- Tsai T-L, Yang J-C (2006) Modeling of rainfall-triggered shallow landslide. *Environ Geol* 50:525–534
- van Genuchten MT (1980) A closed form equation for predicting the hydraulic conductivity of unsaturated soils. *Soil Sci Soc Am J* 44:892–898
- Vogel HJ, Hoffmann H, Roth K (2005) Studies of crack dynamics in clay soil. I. Experimental methods, results and morphological quantification. *Geoderma* 125:203–211



Dimensionless Numerical Approach to Perched Waters in 2D Gradually Layered Soils

Stefano Barontini, Marco Peli, Thom A. Bogaard, and Roberto Ranzi

Abstract

Aiming at better understanding the processes involved in perched water tables onset and in their development, the case of a soil slope characterised by gradually decreasing hydraulic conductivity at saturation with depth was numerically investigated. Different anisotropy factors and steepness values were accounted for. The problem was led to a dimensionless form on the basis of the Buckingham π -theorem. Coherently with a theoretical solution of the 2D sloping case, the simulations evidenced (a) non-monotonic transverse profiles of the pressure head within the perched water, (b) slightly lower infiltration thresholds for perched water onset and for soil waterlogging, with respect to the 1D case. If the slope is long enough, an almost uniform flux can be observed in a branch of its central part.

Keywords

Perched water table • Soil slope stability • 2D modelling

Introduction

The formation of perched water tables in the upper soil layers, during an infiltration process at low infiltration rate, is an important shallow-landslide triggering mechanism. In fact, when the soil approaches the saturation of the upper layers, the apparent cohesion reduces and, when the saturation is reached, also the effective strengths reduce. Soil failures can therefore be triggered not only by a positive pore pressure, but also by the presence of soil layers close to saturated conditions (e.g. van Asch et al. 2009). An accurate description of the subsurface soil-water dynamics, also accounting for the effect of the unhomogeneities of the soil hydraulic properties, can therefore lead to important information on soil safety. In this paper we will focus on the effect of the layering of the hydraulic conductivity at

saturation on the soil-water dynamics. As a consequence of the genetic layering, in fact, the conductivity at saturation tends to decrease across the upper soil horizons, being higher in the A horizons, rich in macropores, and – due to intrasolum leakage – lower in the B ones (Kirkby 1969). On mountains, where strong erosive processes act and the mass movement is a key soil forming factor, the soil horization cannot fully develop and a smooth decrease of the conductivity at saturation typically occurs in the upper soil layers. Two limit cases can then describe the soil characteristics below the upper soil layers: one can find either an impervious bedrock, or a highly permeable layer of regolith or fractured and fissured rock. During our field measurement campaigns in two Alpine catchments, a gradual decrease, on average, was observed for the vertical conductivity at saturation through the upper soil layers (Barontini et al. 2005). Consistent with literature data (e.g. Beven 1984), the pattern was found to be reasonably approximated by an exponential decay. By means of an analytical solution of the 1D Richards equation in a layered soil, Barontini et al. (2007) proved that, during an imbibition at constant water content at the soil surface, a gradual decrease of the hydraulic conductivity can lead to

S. Barontini (✉) • M. Peli • R. Ranzi
DICATA University of Brescia, Via Branze 43, Brescia, Italy
e-mail: barontin@ing.unibs.it

T.A. Bogaard
CiTG, Delft University of Technology, Delft, The Netherlands

non-monotonic profiles of water content. The profiles show a peak which onsets at the soil surface. It is then enveloped as the position of the maximum moves downward and its magnitude increases. Therefore, after some time since the beginning of the imbibition, a subsurface layer is characterized by a closer to saturation water content than the surface one. As the soil saturation is reached at one point, there a perched water table is expected to onset.

With the aim of better understanding these phenomena the case of infiltration at constant rate in a 2D sloping soil layer of finite thickness, with exponentially decreasing hydraulic conductivity at saturation with depth, was numerically investigated by means of Hydrus-2D/3D (Simunek et al. 1999) and the results are here presented. In order to extend the validity of the analyses to different soils and to guide further investigations, the problem was led to a dimensionless form based on an application of the Buckingham π -theorem and the results were compared with theoretical ones for the 1D (Barontini and Ranzi 2010) and 2D case (Barontini et al. 2011). Since a description of the pressure field in case of a perched water table formation is provided, the obtained results can contribute to better define the hydrological loads of hillslope stability analyses, particularly in the framework of the undefined-length slope. After a theoretical recall, the adopted dimensionless approach is presented. Then the set up of the numerical simulations and the results are introduced and discussed.

Theory

Perched Water Tables Formation and Properties

In a classical work, Zaslavsky (1964) stated that, in case of a horizontal pervious soil with conductivity $K_{s,1}$ laying on an impervious one with conductivity $K_{s,2} < K_{s,1}$, the condition for a perched water table to onset in the upper layer is that the Darcian flux downward q , due to infiltration from the soil surface, is $q > K_{s,2}$. When a steady condition is reached in this case, the flux in the upper soil layer takes place in the direction of the increasing tensiometer-pressure potential, whose maximum is reached at the bottom of the saturated layer, at the interface with the impervious horizon. In a sharply layered soil, therefore, a perched water will onset within a layer (the layer 1 in the example) due to external causes, viz the conductivity reduction at the interface between the layer 1 and the underlying layer 2.

Barontini and Ranzi (2010) recently showed that in a horizontal and gradually layered soil, with decreasing hydraulic conductivity at saturation with depth $K_s(x^*)$,

being x^* the vertical coordinate positive downward, a perched water table can onset also due to internal causes to the soil layer. Let us consider, in fact, a soil layer with finite thickness x_f^* characterized by monotonically decreasing $K_s(x^*)$:

$$K_s(x^*) = K_{s,o} f(x^*), \quad (1)$$

in which $K_{s,o}$ is the conductivity at saturation at the soil surface $x^* = 0$ and $f(x^*)$ is a monotonically decreasing function such that $f(0) = 1$. Let us assume besides that the underlying soil layer is characterized by higher conductivity $K_{s,2} > K_s(x_f^*)$ and it is not able to exercise any retention. For the sake of continuity of the total hydraulic head $\Phi = \eta - x^*$, the tensiometer-pressure potential η of the soil at x_f^* should be null. We recall that the tensiometer-pressure potential is defined as $\eta = \psi$, i.e. the matric potential, if it is non-positive, while $\eta = h$, i.e. the pressure potential, if it is positive. A perched water table onsets if at x_f^* , being $\eta = 0$, the gradient of η is negative, i.e.:

$$\left. \frac{d\eta}{dx^*} \right|_{x_f^*} < 0. \quad (2)$$

The infiltration threshold i_f above which a perched water table onsets in the upper layer is given by:

$$i_f = K_s(x_f^*), \quad (3)$$

i.e. the value of $K_s(x_f^*)$ is the upper boundary for the infiltration rate in order not to onset a perched water table. At i_f , in fact, the downward flux in x_f^* , expressed by the Darcy law, is sustained by a purely gravitational gradient. With the same hypotheses the infiltration rate i^* leading the soil layer to waterlogging is given by the value of the equivalent hydraulic conductivity at saturation over the interval $[0, x_f^*]$, i.e.:

$$i^* = K_{s,eq}^{[0,x_f^*]} \equiv K_{s,o} \frac{x_f^*}{\int_0^{x_f^*} \frac{dx^*}{f(x^*)}}. \quad (4)$$

As the perched water table is bounded by two surfaces at $\eta = 0$, it is also characterized by a maximum of η inside, in the position x_{\max}^* such that:

$$i = K_s(x_{\max}^*) \quad , \quad i_f < i \leq i^*. \quad (5)$$

The corresponding $\eta_{\max} = h_{\max}$ is directly given by an integration of the Darcy law within the saturated layer:

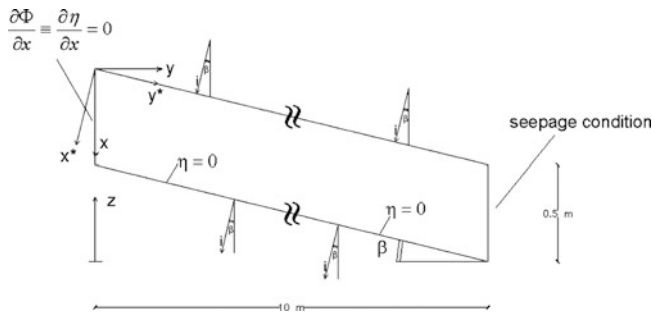


Fig. 1 Sketch of the investigated soil domain with details on the boundary conditions

$$h_{\max} = -\left(x_f^* - x_{\max}^*\right) + \int_{x_{\max}^*}^{x_f^*} \frac{i}{K_x(x')} dx'. \quad (6)$$

Let us consider now a finite thickness soil layer laying on a hillslope, tilted of an angle β with the horizontal as represented in Fig. 1. Let x^* be the transverse coordinate, such that $x^* = 0$ at the soil surface and x^* is positive as entering within the soil. Conversely let x be a vertical coordinate, with same origin as x^* , positive downward. From Fig. 1 one gets that:

$$x^* = x \cos \beta. \quad (7)$$

Let the soil conductivity be eventually anisotropic, with principal directions x^* and y^* . The ratio r between the lateral and transverse conductivity at saturation is usually higher than 1. Now let i be the rainfall component normal to the soil surface. With the same condition at the lower boundary, i.e. $\eta(x_f^*) = 0$, but accounting for the 2D domain, a perched water is now considered to onset if:

$$\left. \frac{\partial \eta}{\partial x^*} \right|_{x_f^*} < 0. \quad (8)$$

Consistent conditions at the lateral boundary at the domain are a no flux entering the domain at the upstream boundary, as for the presence of a watershed, and a seepage condition at the downstream boundary.

Barontini et al. (2011) showed that, under the hypothesis of undefined length of the slope, the infiltration threshold for condition (8) to hold is given by:

$$i_f(\beta) = K_s(x_f^*) \cos \beta, \quad (9)$$

which is less than the case of horizontal soil given by (3). This is due to the fact that the gravitational gradient sustaining the flux transversely to the soil layer is less effective as

the slope increases. Therefore, the maximum infiltration, which can be sustained without gaining any negative pressure gradient at the lower soil interface, will be reduced accordingly. In the case of the soil of Fig. 1, one can also get the infiltration rate leading to waterlogging by means of the following equation:

$$i^*(\beta) = K_{s,eq}^{[0;x_f^*]} \cos(\beta), \quad (10)$$

which substitutes (4). The authors proved also that the position x_{\max}^* , of the maximum pressure head within the perched water table, given by (5) does not depend, at fixed thickness of the perched water table, on the soil slope β . The value of the maximum h at waterlogging is given, from (6), by:

$$h_{\max}(\beta) = h_{\max} \cos \beta. \quad (11)$$

In the investigated case the conductivity at saturation was assumed to exponentially decrease with depth with a scale of exponential decrease L . Equation 1 takes the form:

$$K_s(x^*) = K_{s,o} e^{-\frac{x^*}{L}}. \quad (12)$$

If referred to x , (12) takes the form:

$$K_s(x) = K_{s,o} e^{-\frac{x}{L'}} \quad , \quad L' = \frac{L}{\cos \beta}. \quad (13)$$

Equations 12 and 13 allow to determine the numerical values given by (3, 4, 5 and 6) and (9, 10 and 11) for a horizontal and a sloping soil, respectively.

Dimensionless Approach

According to Corey et al. (1965) the firsts to describe the displacement of immiscible fluids in a porous medium by means of a dimensionless approach were Leverett and Coauthors in their 1942 paper (Leverett et al. 1942). Since then various approaches were attempted in this direction, both at the microscale, typically in view of petrologic applications, and at a continuum scale, for hydraulic and hydrological applications. A dimensionless approach can prove to be very powerful both in order to design hydraulic models and in order to lead the parameters choices for numerical applications. One of the key aspects of a dimensionless approach to the flow of immiscible fluids in a porous medium is the capability of properly representing, in dynamically coherent dimensionless form, the interfacial pressure of the fluids, viz the capillary curve in the case of

the water flow in a granular porous medium. Leverett et al. (1942) suggested that, if expressed in a particular dimensionless form, the capillary curves of unconsolidated sands coalesce on a single curve, the so called j function. In the case, instead, of an organic soil, for which the relationship between the water content and its energetic state should account also for the effect of the organic matter content, the coalescence of the retention relationship on the same curve is much more difficult. Corey et al. (1965) therefore stated that a model of flow in an unsaturated soil will be effective only if the soil-water constitutive laws have the same structure and the same values for some parameters.

In this work we propose a parameters choice, based on an application of the Buckingham π -theorem in the framework of a continuum approach, in order to describe the effect of the soil anisotropy and steepness on the following steady properties of the perched water tables: (a) the infiltration threshold for a perched water table to onset, (b) the infiltration rate to lead the soil to waterlogging, (c) the position and magnitude of the maximum positive pressure head at waterlogging. Even if the problem is characterized by a transition from unsaturated to saturated soil, the proposed dimensionless approach is focused on steady and saturated flow conditions, which are not sensitively affected by the soil-water retention relationship. The obtained results can be therefore reliable also for different soils with different soil-water constitutive laws.

Considering the case of a steady infiltration in an exponentially K_s -decreasing soil, inferiorly bounded by a surface at $\psi(x_f^*) = \psi(x_f) = 0$ and for defined initial conditions, we can write, for any generic state property S of the soil, the formal dependency:

$$S = f(\phi, \theta_s, \theta_r, \psi_1, m, n, \ell, K_{s,o}, L', r, x_f, y_v, \beta, i). \quad (14)$$

In (14), besides the parameters already introduced, ϕ , θ_s , θ_r [–] are respectively the porosity, the volumetric water content at saturation, and the volumetric residual water content; ψ_1 [L], m [–], n [–] are the parameters of the soil-water retention relationship described by van Genuchten's function, with the usual constraint that $m = 1 - 1/n$; ℓ is the relative-conductivity function parameter, according to Mualem's framework; y_v is the horizontal projection of the slope length.

Before analysing (14) three important remarks need to be added. Firstly, as a continuum approach was chosen, the dependency on the water mechanical properties, viz its density, its dynamic viscosity and its capillary tension at the air–water interface, are not explicitly represented but they are implicitly accounted for in the definition of the hydraulic conductivity at saturation and of the soil–water retention relationship parameters. Then, focusing on the description of

the soil–water dynamics, it is not needed to explicit any dependency of S on soil mechanical properties, e.g. the soil particle density, its cohesion or its angle of internal friction. Finally as the unique mass force involved in the problem is the gravitational field, it is not explicitly represented in the formulation but it is implicitly included in the definition of the hydraulic conductivity at saturation.

In (14) there are on the whole 14 parameters which can be roughly grouped as in the followings. The parameters ϕ , θ_s , θ_r , ψ_1 , m , n , ℓ , $K_{s,o}$ (8 parameters) describe the soil–water constitutive laws. Among these, the porosity ϕ does not play here an important role as the control role on the soil capacity of storing water is played by the effective porosity $\theta_s - \theta_r$; ϕ will be therefore neglected in the further analysis. Moreover Mualem's parameter is usually set at 0.5. Its dependency in the dimensional analysis will be neglected as well. The characterising parameters of the soil-water constitutive laws are therefore reduced to the 6 parameters of the van Genuchten-Mualem framework. L' and r (2 parameters) describe the conductivity unhomogeneity and anisotropy (L' being introduced in [13]); x_f , y_v , β (3 parameters) describe the problem geometry. Finally i , only 1 parameter, describes the boundary conditions as the other boundary conditions are structural for the problem and will not be explicitly introduced in the dimensional analysis. By a dimensional point of view the parameters can be grouped into three groups. ϕ , θ_s , θ_r , m , n , ℓ , r , β (8 parameters) are dimensionless and are presented in their basic form, i.e. they have not been normalized yet; ψ_1 , L' , x_f , y_v (4 parameters) are lengths [L]; $K_{s,o}$, i (2 parameters) are velocities [LT⁻¹].

As observed e.g. by Corey et al. (1965, p.7), the effective soil porosity $\theta_s - \theta_r$ characterises the non-steady soil dynamics. Here, as steady conditions are focused on, it is dropped from the dimensional analysis. Moreover as it appears from (5, 9, 10 and 11), which hold for a sloping soil, also the other parameters characterizing the unsaturated soil flow, i.e. m , n , and ψ_1 , do not explicitly emerge from the theoretical framework. This fact is mainly due to the focus on properties of saturated conditions flow. Therefore also these parameters are dropped from the dimensional analysis. Equation 14 is rewritten as:

$$S = f(K_{s,o}, L', r, x_f, y_v, \beta, i). \quad (15)$$

According to the Buckingham π -theorem, only two dimensional scales are required in this case to fully express the problem in a dimensionless form. The set of dimensional variables we propose is given by a scaling-length $L_s = x_f$ and a scaling-velocity $U_s = K_{s,o}$. In dimensionless form, and with the usual symbol π for the dimensionless variables, (15) is rewritten as:

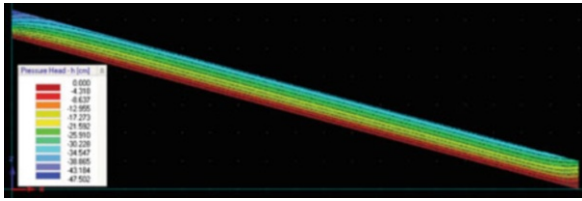


Fig. 2 Initial conditions of the flow domain after 12 h infiltration at low infiltration rate, $\beta = 15^\circ$, $r = 5$

$$\pi_S = F(\pi_{L'}, \pi_y, \pi_i, r, \beta). \quad (16)$$

The effect of π_i , r , β on the formation, the thickness and the maximum pressure head of a perched water table will be explored. The theoretical values previously presented are rewritten in dimensionless form. One gets for i_f :

$$\pi_{i_f} = e^{-\frac{1}{\pi_{L'}}} \cos \beta, \quad (17)$$

and for i^* :

$$\pi_{i^*} = \frac{1}{\pi_{L'} \left(e^{\frac{1}{\pi_{L'}}} - 1 \right)} \cos \beta. \quad (18)$$

Numerical Experiments

The numerical experiments were designed in order to simulate a steady process at constant infiltration rate by means of the software Hydrus-2D/3D, which numerically solves the Richards equation. The dimensions of the mesh are given in Fig. 1. In order to represent a gradually decreasing conductivity with depth, the 0.5 m-thick soil layer was subdivided into five layers of 0.1 m, each of them with uniform conductivity at saturation, equivalent to that of the gradually varying layer over the same thickness (e.g. Barontini et al. 2007). $K_{s,o}$ was assumed to be 8.14E-04 m/s and $L' = 0.19$ m. A coupled van Genuchten-Mualem constitutive laws model applied to describe the unsaturated soil-water properties. $\psi_1 = 0.16$ m, $m = 0.34$, $n = 1.51$, measured for a sand, were chosen as retention curve parameters. As initial conditions were required in order to perform the simulations, aiming at defining steady and almost uniform conditions along the slope, a 12 h preliminary simulation at low infiltration rate (1.4E-06 m/s) was performed. The obtained initial conditions are represented in Fig. 2. Referring to (16) two dimensionless parameters were fixed ($\pi_{L'} = 0.38$, $\pi_y = 20$); the maximum value of π_i was chosen bigger than π_{i^*} , enough to observe waterlogging; r was chosen equal to 1, 5, 10, and β spanning from 5° to 30° each 5° .

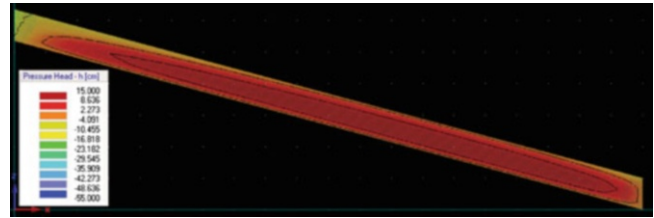


Fig. 3 Steady state conditions after 6 h simulation with soil at waterlogging, $\beta = 15^\circ$, $r = 5$

As an example of the results, in Fig. 3 the pressure potential field of a 15° sloping soil with anisotropy factor $r = 5$ is represented for i^* . As it can be seen an area of positive pressure head, up to a pressure potential of 0.15 m, is observed in the central part of the mesh. This area is above and below bounded by surfaces at null or negative matric potential ψ and, even if there is a long central branch at almost uniform characteristics, upstream and downstream boundary effects are observed. The length of the branches affected by boundary effects increases as the anisotropy factor increases, so that at $r = 10$ it was not recognizable, for the investigated slope, a central branch with uniform-flow pattern. On the other hand, at $r = 1$, i.e. in the absence of anisotropy, the central branch with almost uniform pressure distribution is much longer and there the hypothesis of uniform flow is realistic.

Discussion

In Figs. 4 and 5 the steady profiles of ψ and h in the middle section of the mesh are plotted, as a function of β and at $r = 5$, for the two limit cases of infiltration rate i_f and i^* . In the unsaturated range a flow takes place in the direction of the increasing ψ . The ψ -profiles are weakly sensitive to β and close to saturation, thus playing an important role for the soil stability. At the bottom an almost vertical slope of the profile is observed. The corresponding dimensionless $i_f(\beta)$ given by (17) are represented in Fig. 6. It can be seen that $i_f(\beta)$ is less than that estimated for the case of $\beta = 0^\circ$, coherently with the theory. It is moreover well interpreted by the theoretical model both for the magnitude and for the independence on the soil anisotropy.

In Fig. 5 the pressure profiles at waterlogging are represented for the same case at $r = 5$. The non-monotonic patterns of h are observed. Moreover the maximum of h is reached almost in the same position for all the curves, accordingly with the theoretical analyses, and it is quite sensitive at β , since it decreases as β increases. The corresponding dimensionless $i^*(\beta)$ given by (18) are represented in Fig. 6 and compared with the theoretical 1D and 2D estimate. Also in this case $i^*(\beta)$ is less than that

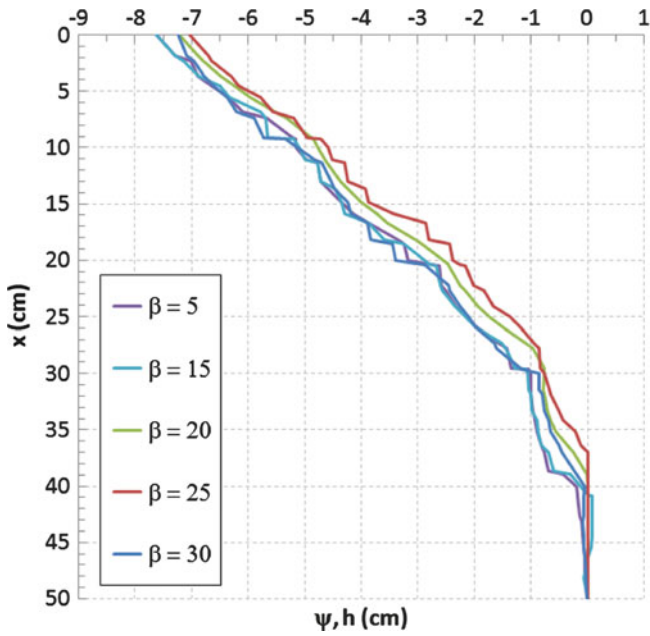


Fig. 4 Tensiometer-pressure profiles in the middle section of the flow domain, in steady conditions, at $i = i_f$

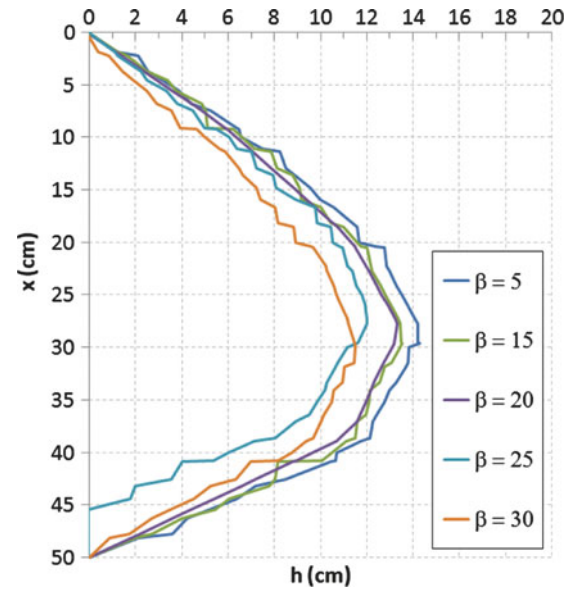


Fig. 5 Pressure profiles in the middle section of the flow domain, in steady conditions, at $i = i^*$

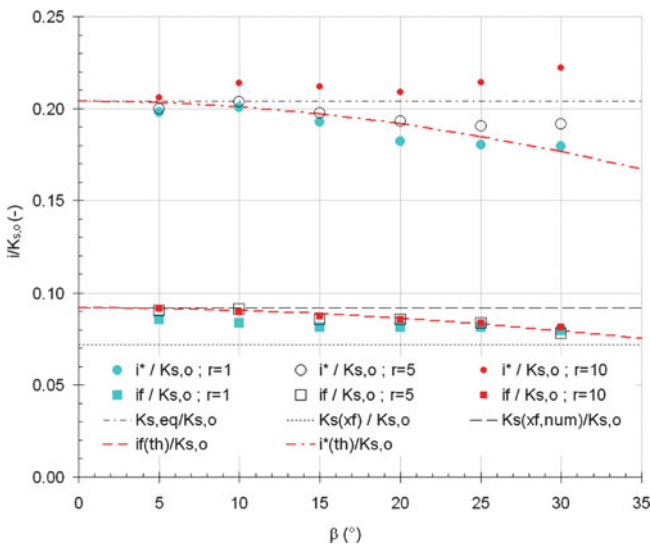


Fig. 6 Dimensionless infiltration rates $\pi_{if} = i_f/K_{s,o}$ and $\pi_{i^*} = i^*/K_{s,o}$ as a function of the slope β and of the anisotropy factor r , compared with the corresponding estimates for the 1D case (dashed black lines) and for the 2D case (dashed red lines)

estimated for the case of $\beta = 0^\circ$ and it is sensitive to the soil slope. The agreement with theoretical values is worse than for $i_f(\beta)$ as the anisotropy factor r increases. This behavior is attributed to the fact that, at increasing r the branch, where an almost uniform flux takes place, reduces and the boundary effects gain importance.

The maximum pressure head $\pi_{h,max} = h_{max}/x_f$ is represented in Fig. 7 depending on β and r and compared

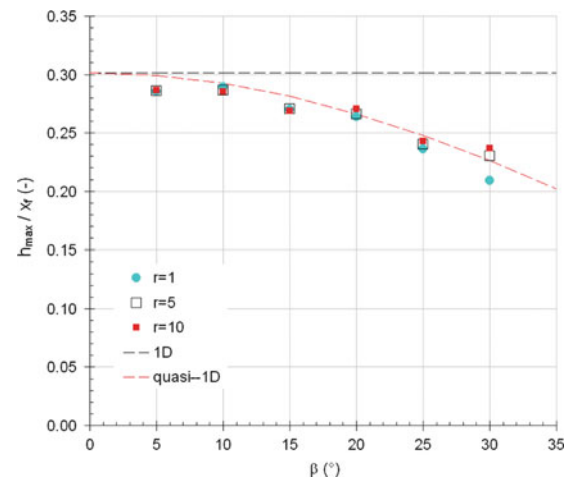


Fig. 7 Dimensionless maximum pressure head $\pi_{h,max} = h_{max}/x_f$ in the middle section at waterlogging infiltration rate as a function of the slope β and of the anisotropy factor r , compared with the corresponding estimates for the 1D case (dashed black line) and for the 2D case ("quasi-1D", dashed red line)

with theoretical 1D and 2D estimates (the latter is reported as quasi-1D in the Figure). It is not sensitively dependent on r and the agreement between the 2D theoretical and numerical results is fair.

Conclusions

The conditions for perched water table formation and for waterlogging were numerically investigated for a sloping soil layer characterized by exponentially decreasing conductivity with depth. The numerical results were

compared with theoretical analyses. In order to lead the numerical experiments and to define a methodology to generalize the results, a preliminary dimensional analysis was performed. The vertical soil depth x_f and the upper soil hydraulic conductivity at saturation $K_{s,o}$ were proposed as a set of independent variables in order to transform the problem in dimensionless form. Five dimensionless groups, including the anisotropy coefficient r and the soil slope β , were addressed to describe the steady properties of the perched water table. The numerical results and the theoretical 2D analyses provided by Barontini et al. (2011) were found to be in good agreement for the infiltration rate at the perched water table onset, for the maximum pressure head at waterlogging, and for the infiltration rate at waterlogging for low values of the anisotropy factor. The agreement is worse as the anisotropy factor increases because the uniform flow hypotheses underlying to the theoretical framework require longer slopes in order to properly apply.

Acknowledgments The work was partly founded in the framework of European FP7 Project KULTURisk (Grant Agreement n.265280).

References

- Barontini S, Ranzi R (2010) Su alcune caratteristiche delle falde pensili in suoli gradualmente vari. In: Proceedings of 32nd congress of hydraulics and hydraulic structures, Palermo, 14–17 Sept 2010, pp 10
- Barontini S, Clerici A, Ranzi R, Bacchi B (2005) Saturated hydraulic conductivity and water retention relationships for Alpine mountain soils. In: De Jong C, Collins D, Ranzi R (eds) Climate and hydrology of mountain areas. Wiley, Chichester, pp 101–122
- Barontini S, Ranzi R, Bacchi B (2007) Water dynamics in a gradually non-homogeneous soil described by the linearized Richards equation. *Water Resour Res* 43. ISSN: 0043-1397
- Barontini S, Peli M, Bakker M, Bogaard TA, Ranzi R (2011) Perched waters in 1D and sloping 2D gradually layered soils. First numerical results. Submitted to the XXth Congress of AIMETA, Bologna
- Beven KJ (1984) Infiltration into a class of vertically non-uniform soils. *Hydrol Sci J – Journal des Science Hydrologique Bulletin* 24:43–69
- Corey GL, Corey AT, Brooks RH (1965) Similitude for non-steady drainage of partially saturated soils. Hydrology papers. Colorado State University, Fort Collins, 39p
- Kirkby M (1969) Infiltration, throughflow and overland flow. In: Chorley R (ed) *Water, Earth and man*. Taylor & Francis, Kirkby, pp 215–227
- Leverett MC, Lewis WB, True ME (1942) Dimensional-model studies of oil-field behavior. *Trans Am Inst Min Met Eng Petroleum Div* 146:175–193
- Simunek J, Sejna M, van Genuchten MT (1999) The Hydrus-2D software package for simulating two-dimensional movement of water, heat, and multiple solutes in variably saturated media. Version 2.0. IGWMC – TPS – 53. International Ground Water Modeling Center, Colorado School of Mines. Golden, 251p
- Van Asch Th WJ, Van Beek LPH, Bogaard TA (2009) The diversity in hydrological triggering systems of landslides. In: Picarelli L, Tommasi P, Urciuoli G, Versace P (eds) *Rainfall-induced landslides. Mechanisms, monitoring techniques and nowcasting models for early warning systems*. Proceedings of the 1st Italian workshop on landslides, vol 1, Napoli
- Zaslavsky D (1964) Theory of unsaturated flow into a non-uniform soil profile. *Soil Sci* 97(6):400–410



Landslide Motion Forecasting by a Dynamic Visco-Plastic Model

Marco M. Secondi, Giovanni Crosta, Claudio di Prisco, Gabriele Frigerio, Paolo Frattini, and Federico Agliardi

Abstract

To model the evolution with time of the Bindo-Cortenova translational landslide (Italian Prealps, Lombardy, Italy), a 1D pseudo-dynamic visco-plastic approach, based on Perzyna's theory, has been conceived. The viscous nucleus has been assumed to be bi-linear: in one case, irreversible deformations develop uniquely for positive yield function values; in a more general case, visco-plastic deformations develop even for negative values. The model has been calibrated and subsequently validated on a long temporal series of monitoring data and it seems quite reliable in simulating the in situ data.

Keywords

Visco-plasticity • Delayed plasticity • Dynamic model • Landslide • Movement prediction

Introduction

A challenging issue in geological and geotechnical problems associated with slope stability concerns the analysis of sliding masses subject to continuous slow movements and intermittent stages of slowing and accelerating motion.

Many translational or roto-translational landslides occurring in Northern Italy (Crosta et al. 2006) are characterized by velocities on the order of few centimetres per year. Usually, this behaviour does not originate sudden and unexpected failures, nevertheless it is critical for infrastructures (roads, tunnels, etc.) and civil buildings. The need of defining deformation thresholds in order to prevent damage is a major issue for civil protection actions.

Displacements are usually triggered by hydrologic factors and many authors (Angeli et al. 1996; Corominas et al. 2005; Gottardi and Butterfield 2001; Ranalli et al. 2010) observed a

direct correlation between groundwater level oscillations (usually induced by rainfall) and slope movements. Therefore, the slope movements are characterised by a seasonal trend, with periods of rest and acceleration. This dynamic behaviour is not instantaneous but shows a delay between perturbation (increase in water table) and system reaction. It can be correlated with a typical viscous response, associated with creep phenomena, inducing a permanent – and time delayed – deformation of the soil mass.

A simple static limit equilibrium analysis is not suitable for modelling and correctly reproducing this type of slope kinematics. A dynamic, or at least pseudo-dynamic, analysis should be adopted, and a delayed-plastic constitutive approach must be employed. The first issue can be addressed by evaluating the inertial effects on the soil mass by using a pseudo-dynamic approach, as that introduced by Newmark (1965) for dams under seismic actions, whereas, viscous components can be described by employing the visco-plasticity theory introduced by Perzyna (1963). According to this theory, the standard plastic flow rule is modified and the consistency condition abolished. Therefore, the visco-plastic strain rate tensor $\dot{\epsilon}_{ij}^{vp}$ is defined as follows:

$$\dot{\epsilon}_{ij}^{vp} = \gamma \cdot \phi(f) \cdot \frac{\partial g}{\partial \sigma_{ij}} \quad (1)$$

M.M. Secondi (✉) • G. Crosta • P. Frattini • F. Agliardi
Dipartimento di Scienze Geologiche e Geotecnologie, Università di Milano-Bicocca, P.za della Scienza 4, Milan, Italy
e-mail: marco.secondi@unimib.it

C. di Prisco • G. Frigerio
Dipartimento di Ingegneria Strutturale, Politecnico di Milano, Milan, Italy

where f is the yield function, g the plastic potential, γ a constitutive parameter, σ'_{ij} the effective stress tensor and $\phi(f)$ the viscous nucleus. To evaluate the rate of viscoplastic deformations and, hence, the displacements, many different analytic expressions for the viscous nucleus can be naturally introduced.

In order to reproduce the monitored deformations of a translational landslide, we present hereafter a 1D viscoplastic pseudo-dynamic model based on the Perzyna's constitutive relationship (Secondi et al. 2011). In addition, the results obtained are compared with other approaches in which the evaluation of the viscous parameter is based on simplified analytical formulations (Corominas et al. 2005).

The Bindo-Cortenova Landslide

The Bindo-Cortenova landslide is a 1.2 km² wide translational landslide located in Valsassina (Lecco province, Lombardy, Italy). The site is characterized by a large and active slope failure occurring in a Permian conglomerate formation. The sliding material is formed by very large conglomeratic rock blocks, up to 100 m in size, immersed in a gravely sand matrix. Various small landslide activations (on June 1987, November 2000, and May 2001), involving few hundred or thousand of cubic metres of material, took place at the slope toe. The toe of the slope underwent a catastrophic failure in December 2002 (volume ca $1.2 \cdot 10^6$ m³) after a period of extremely heavy rainfall (up to 850 mm in 14 days with respect to an annual rainfall of 1,500–2,000 mm/year). On May 2004, a second event caused a new collapse ($0.2 \cdot 10^6$ m³) which stepped over the 2002 deposit and affected part of the installed monitoring network.

Slow sliding movements (about 200 mm/year on average) are still affecting the slope (about 1 km in length, from the 2004 event crown to the main scarp at 1,250 a.s.l., Le Gronde in Fig. 1; mean slope angle $\alpha = 28^\circ$), on a 30–50 m deep slip surface. Laboratory tests, carried out on samples recovered at the failure surface, provided the following geomechanical parameters: saturated unit weight $\gamma_{sat} = 19.01$ kN/m³, cohesion $c' = 0$ kPa, residual and peak friction angles $\phi'_{res} = 33.9^\circ$ and $\phi' = 36^\circ$. Friction angle values were obtained by means of load and displacement controlled triaxial creep tests. Rheometer tests were also carried out to investigate the viscous mechanical behaviour of the material involved at different water contents.

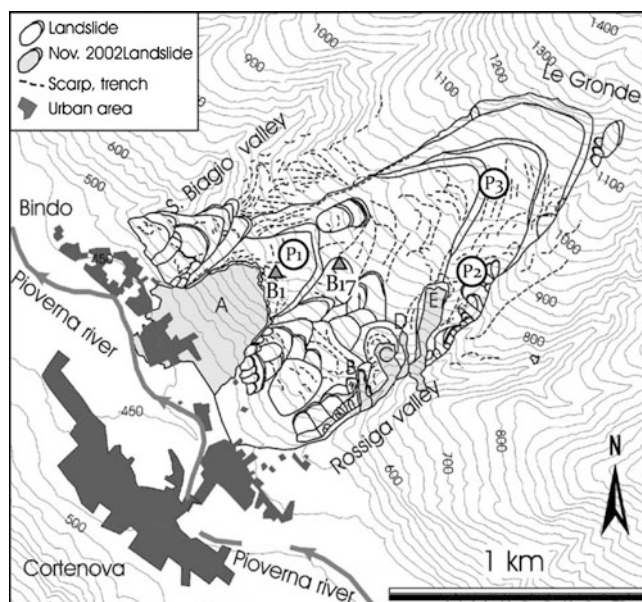


Fig. 1 Bindo-Cortenova failure (2004 event, Zone A) and unstable area (black lines, up to Le Gronde). Piezometers are specified by the points P1, P2, P3 while the two considered optic devices by B1 and B17

In Situ Monitoring System

An in situ monitoring system is operating since May 2003 at the site. Figure 1 shows the location of the instruments, consisting of a series of optical targets, monitored every 2 h through two total stations, three inclinometers and TDR cables, and three open-pipe piezometers instrumented with pressure transducers. Inclinometric records have been considered to determine the depth and thickness of the sliding surface (on average 38 and 0.3 m, respectively). In the following we will consider only piezometric data and optical target displacements for model calibration. In particular, optical targets B1 and B17 (Fig. 1) were used to calibrate and validate the model presented, since they are located close to piezometer P1 and thus their data can be directly correlated to water table level data.

The used dataset consists of 6–12 daily readings on a 5 years' time span (from January 2005 to December 2009) for which both groundwater level and displacements are available. Daily rainfall data are available from two rain gauge stations sited at the toe of the slope and 10 km to the SE. Figure 2 shows the entire dataset, in order to underline the correlation between water table level and induced displacements. Figure 3 illustrates a typical event where it is possible to verify both the dynamic-inertial effects and the highly viscous mechanical response of the slope. The slope motion starts after 6 days from the increase in water table

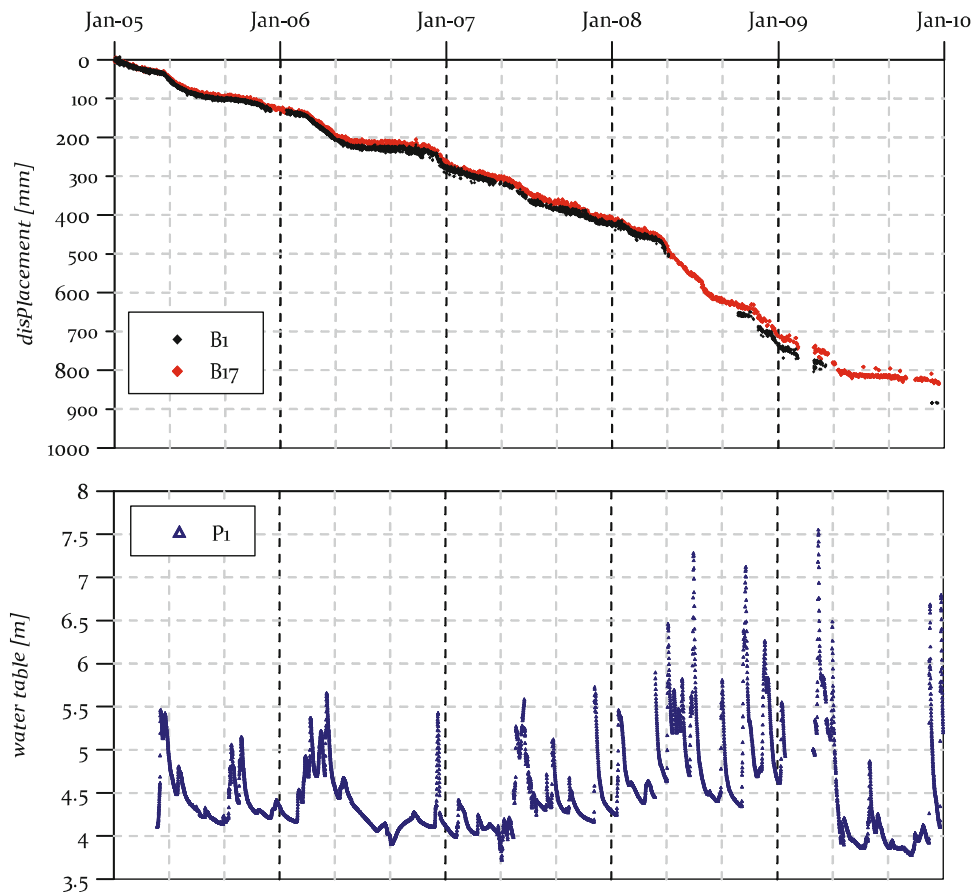
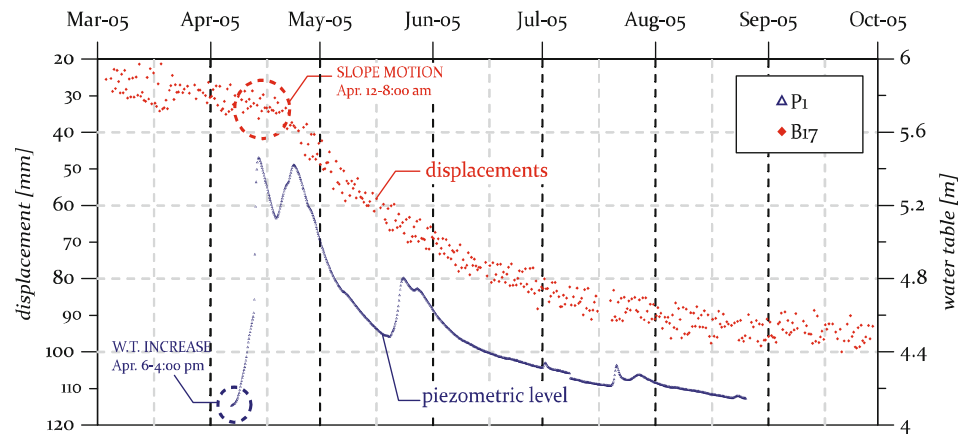


Fig. 2 Displacements at B1 and B17 and groundwater level oscillation at P1 (see Fig. 1), from Jan 2005 to Dec 2009

Fig. 3 The landslide (red) starts accelerating 6 days after the water table rise (blue), and the slope motion continues after the piezometric level has reached the asymptotic level



elevation and the system continues to accelerate also after the peak in water level. This suggests that the deformative reaction is delayed in time and it is not instantaneous.

The Visco-Plastic Model

Usually, the mechanical behavior of granular materials is assumed as time-independent. Nevertheless, experimental evidence (di Prisco and Imposimato 1996; di Prisco and Zambelli 2003)

shows that their mechanical response is very rapid but not instantaneous. The propagation of a stress wave due to a load increment (such as the oscillation of the water table) induces a time-dependent evolution in the soil micro-structure strictly linked to the mechanical properties of the continuum.

Hence, the stress distribution evolves, carrying to a new non-equilibrated stress configuration. The time interval needed to reach a final equilibrium state can be interpreted as the time period during which plastic deformations occur (in contrast, the elastic deformation can be assumed as

instantaneous). As in standard elastoplasticity, the total strain rate tensor $\dot{\epsilon}_{ij}$ can be assumed to be the sum of the elastic $\dot{\epsilon}_{ij}^{el}$ and the irreversible $\dot{\epsilon}_{ij}^{vp}$ strain rate tensors:

$$\dot{\epsilon}_{ij} = \dot{\epsilon}_{ij}^{el} + \dot{\epsilon}_{ij}^{vp} \quad (2)$$

Since the elastic deformation can be neglected for the Bindo-Cortanova landslide, and a rate in angular deformation $\dot{\gamma}$ (a 1D problem is considered) is assumed to be sufficient for describing the slope mechanical behaviour, (2) can be simplified as follows:

$$\dot{\gamma} = \dot{\gamma}^{vp} \quad (3)$$

As a residual strength condition is considered for the slope (the shear band is assumed at a steady state) dilatancy is neglected. Hence, no displacements normal to the sliding surface have to be taken into account and the system can be modelled as 1D. Equation (1) becomes:

$$\dot{\gamma}_{ij}^{vp} = \frac{\tilde{\gamma}}{p'} \cdot \phi(f) \quad (4)$$

where $\tilde{\gamma}$ is a viscous constitutive parameter (calibrated on experimental data or by means of back analyses), $\dot{\gamma}$ a function of the axial deformation rate \dot{x} and of the shear band thickness Δs , and p' the isotropic pressure:

$$\dot{\gamma} = \frac{\dot{x}}{\Delta s}; p' = \frac{\sigma'_v + 2\sigma'_h}{3} \quad (5)$$

The $\phi(f)$ function directly governs the modulus of $\dot{\gamma}^{vp}$, thus no consistency law is needed and the stress state can violate condition $f \leq 0$. Irreversible deformations can evolve for any value of the f function. As described by (4), visco-plastic deformations can occur even without any load increment. The $\tilde{\gamma}$ constitutive parameter represents the velocity through which the system evolves and reaches the asymptotic value of deformation.

In (4) hardening or softening are neglected. Either the shape or the dimension of the yield surface are constant during the irreversible visco-plastic deformation.

The Viscous Nucleus

To evaluate the rate of visco-plastic deformations and, hence, of the slope displacements, an analytic expression for the viscous nucleus $\phi(f)$ has to be assigned. The $\phi(f)$ function describes the evolution of visco-plastic deformation; it always satisfies the following condition:

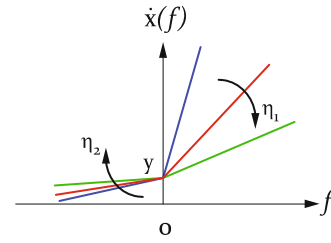


Fig. 4 Rate of axial deformation as a function of the parameters of viscosity η_1 and η_2

$$\frac{d\phi}{df} \geq 0 \quad (5)$$

A simple formulation for the viscous nucleus is the bi-linear: the deformative behaviour of the slope is different if the stress state lies inside or outside the plastic surface (Fig. 4). Two parameters $\tilde{\gamma}_1$ ($f > 0$) and $\tilde{\gamma}_2$ ($f \leq 0$) must be introduced:

$$\begin{aligned} \dot{\gamma}_{ij}^{vp} &= y' + \frac{\tilde{\gamma}_1}{p'} \cdot f \text{ if } f > 0 \\ \dot{\gamma}_{ij}^{vp} &= y' + \frac{\tilde{\gamma}_2}{p'} \cdot f \text{ if } f \leq 0 \end{aligned} \quad (6)$$

where the $\tilde{\gamma}_1$ replaces $\tilde{\gamma}$ of Eq. (4) and y' is a new constant parameter. The latter identifies the velocity value in x-direction when $f = 0$.

The f function can be put in an explicit form:

$$f = \tau - \tau_{res} \quad (7)$$

where τ represents the effective shear stress and τ_{res} the yield threshold (depending on the failure criterion adopted). As dynamic and inertial effects must be taken into account, the effective shear stress is composed both by the static term τ_{stat} (weight of the masses acting on the system), and a dynamic one (depending on the acceleration in the x-direction and on the masses per unit area m^*):

$$\tau = \tau_{stat} - m^* \ddot{x} \quad (8)$$

By substituting (5), (7) and (8) into (6) and by introducing the parameters in (9):

$$\begin{cases} y = y' \cdot \Delta s \\ \eta_i = \frac{p'}{\Delta s \cdot \gamma_i} \quad i = 1, 2 \end{cases} \quad (9)$$

the following expression for x-acceleration can be obtained (where $i = 1$ if $f > 0$, or $i = 2$ if $f \leq 0$):

$$10^{-3} \cdot m^* \ddot{x} + \eta_I \dot{x} = \eta_I y + (\tau_{stat} - \tau_{res}) \quad (10)$$

As is shown in Fig. 4, when the stress state lies outside the plastic surface ($f > 0$), an increase in η_I brings to a decrease in the visco-plastic deformations. The opposite occurs when $f \leq 0$.

The Newmark Approach

The limit equilibrium approaches usually suppose a rigid-perfectly plastic behaviour for the slope. This leads to the conclusion that the deformations start only after the failure condition is reached. If the failure criterion is satisfied, the shear resistance can be considered as constant and not depending on the accumulated displacements. Then, in a limit equilibrium condition, the resistance on the shear band is not influenced by the slope movements and can be considered as constant (and equal to shear resistance).

Within the same framework, in order to introduce a dependence on the time factor, the Newmark pseudo-dynamic approach (Newmark 1965) can be used. This model allows to introduce the acceleration term as shown in (8). By means of a finite difference method, (10) can be solved in terms of both velocity and displacements for the landslide considered. The slope is still considered as a non-deformable mass subjected to a translational motion on a stable-rigid layer. In contrast with a classical limit equilibrium approach, the acting forces can be either higher or smaller than the constant resisting forces, depending on the magnitude of load increment (e.g. water table oscillations). The higher is the difference between acting and resisting forces, the higher is the velocity of the system.

As a pseudo-ductile mechanical behaviour is introduced when the limit equilibrium conditions are reached, irreversible deformations can always occur.

In the present study, the Newmark approach and the Perzyna's theory have been coupled to model the Bindo-CortenoVA landslide. The Newmark approach considers the slope as a rigid block placed in the centre of mass. As the available monitoring system data are referred to the toe of the Bindo-CortenoVA site (zone A, Fig. 1), the equations of the model must be modified and an active force S_A (divided by the total contact area) must be added.

$$\tau_{stat} = W'[h(t)] \cdot \sin \alpha + J + S_A \quad (11)$$

where W' is the immersed weight divided by the total contact area, J the seepage force divided by the total contact area, and $h(t)$ the water table level (as a function of time t).

In order to solve (10), a Mohr-Coulomb failure criterion is introduced. As the slope considered is characterised by

Table 1 Geomechanical and geometrical parameters (cohesion c' is neglected) of the sliding material

Geo-mechanical parameters		Geometrical parameters	
Stress state			
Res. friction angle ϕ'_{res} [°]	33.9	Mean slope angle α [°]	28
Dry unit weight γ_d [kN/m ³]	15.8	Slide thickness H_{un} [m]	38
Sat. unit weight γ_{sat} [kN/m ³]	19.0	Shear band thick. Δs [m]	0.3
Mean isotr. press. p' [kPa]	380	Sliding length L_{un} [m]	100

slow movements inducing irreversible deformations due to post-failure conditions, a residual friction angle ϕ'_{res} is used:

$$\tau_{res} = N'^* \tan \phi'_{res} \quad (12)$$

where N'^* is the effective force normal to the sliding plane divided by the total contact area.

By substituting (11) and (12) into (10), and by means of a classical finite difference integration scheme (both for $f > 0$ and $f \leq 0$), it is possible to simulate the displacements for the slope.

Numerical Simulations

In order to numerically simulate the slow motion acting during the 2005–2009 period on the Bindo-CortenoVA slope, it is necessary to calibrate, by means of back analysis, the set of viscous constitutive parameters (η_1 , η_2 and y) using the previously described displacements (B1 and B17) and groundwater (P1) datasets. Employed mechanical, geotechnical and geometric parameters, together with stress state (isotropic pressure p'), are listed in Table 1. The pressure p' , acting at the depth of the sliding surface (38 m), has been evaluated considering a value of the mean piezometric level of 4.47 m (2005–2009 period) above the failure surface.

The Calibration Procedure

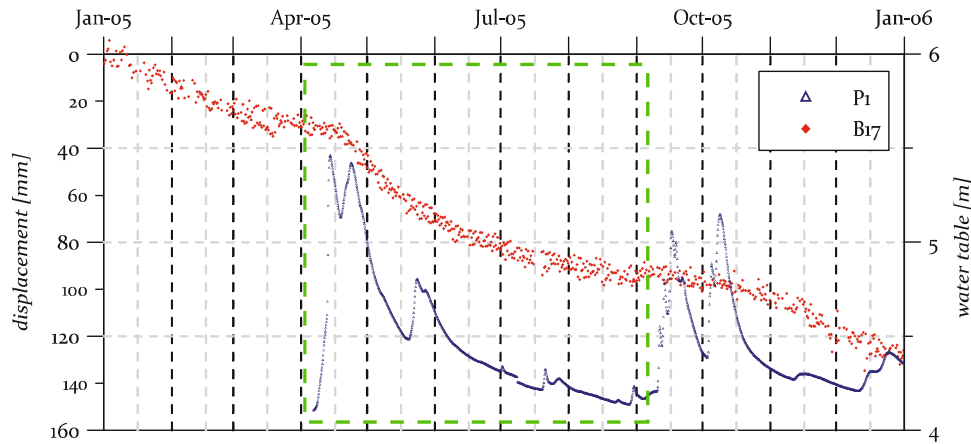
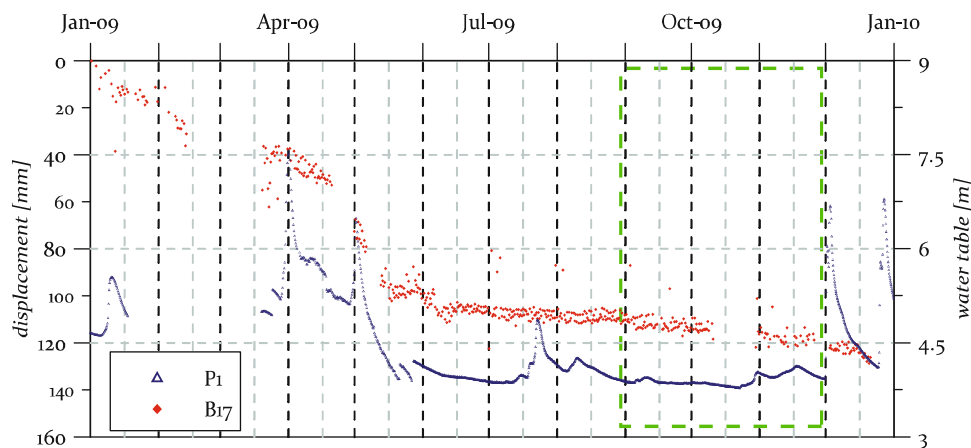
Various calibrations of the viscous parameters (y , η_1 and η_2), based on different yearly datasets, have been compared. Here we present the best results in terms of modelled displacements.

The slope behaviour must be defined under three different mechanical conditions (stress state outside, $f > 0$, inside $f < 0$, or on the f surface, $f = 0$), leading to the necessity for three different calibrations.

The same event has been used also to calibrate the η_2 parameter (Table 2).

Table 2 Viscous nucleus parameters

Calibrated viscous nucleus parameters			
y [m/s]	$1.44 \cdot 10^{-9}$	y' [1/s]	$7.79 \cdot 10^{-9}$
η_1 [kPa.s/m]	$5.06 \cdot 10^8$	$\tilde{\gamma}_1$ [1/s]	$2.05 \cdot 10^{-6}$
η_2 [kPa.s/m]	$4.00 \cdot 10^9$	$\tilde{\gamma}_2$ [1/s]	$3.17 \cdot 10^{-7}$

**Fig. 5** 2005 dataset and (green rectangle) 6/04–10/09 event, used to calibrate η_1 parameter**Fig. 6** 2009 dataset and (green rectangle) 27/08–30/11 event, used to calibrate y parameter

Anyway, as the displacement velocity $\dot{x}(f)$ is always linear (Fig. 4), it is not necessary to define how much the stress state exceeds condition $f = 0$. The η_1 ($f > 0$) parameter has been evaluated using the data available between April and September 2005. During this time period an extremely regular oscillation in water table has been observed (Fig. 5, green rectangle). The piezometric level always exceeds its equilibrium level (4.47 m). Hence τ always exceeds τ_{res} and then $f > 0$.

The y parameter (corresponding to the velocity in a limit equilibrium condition, $f = 0$) has been calibrated by means of the event illustrated in Fig. 6 (green dashed box), characterised by a piezometric level equal to the equilibrium

level. The value of the rate of displacement in this condition corresponds to the y parameter.

The Simulated Landslide Displacements

Figure 7 illustrates a comparison between predicted and measured displacements at point B17, using the pseudo-linear viscous nucleus. The model predictions fit quite well the monitored data. Note that the adopted residual friction angle was not calibrated by means of back analysis, but measured by means of standard triaxial compression tests. The viscosity parameters were calibrated on small scale rheometer tests

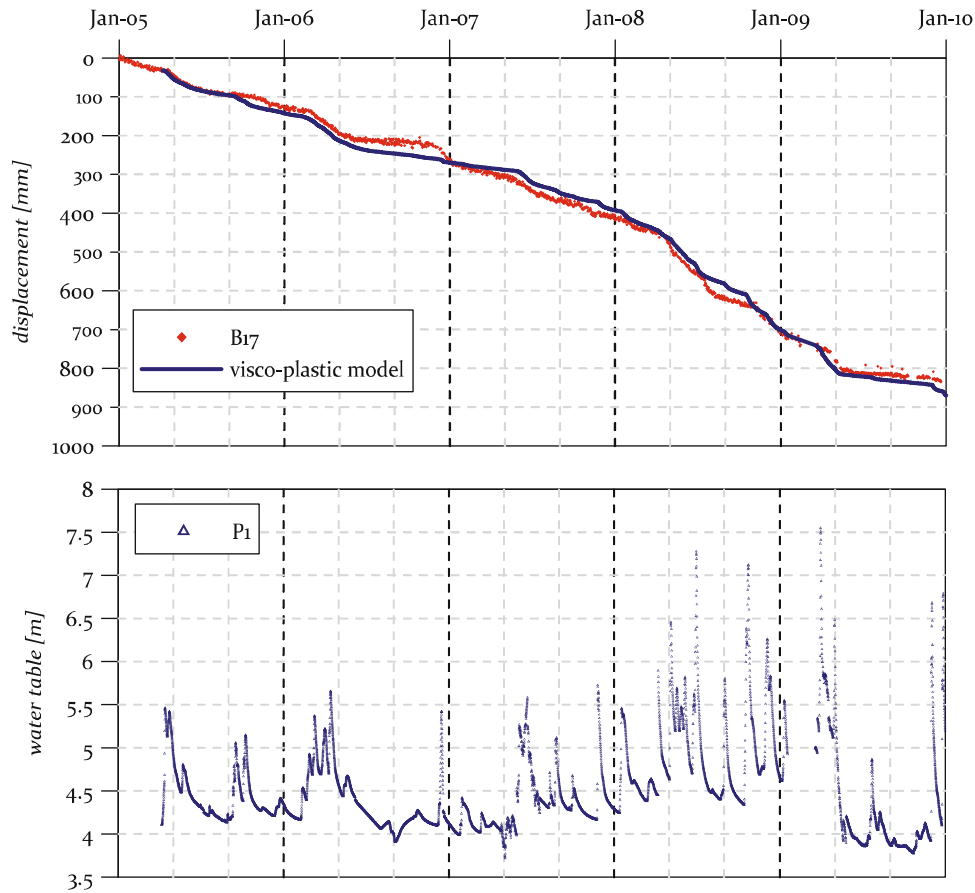


Fig. 7 Measured and predicted displacements obtained by using the previously discussed approach

(Frigerio 2010) and only the shear band thickness (0.3 m) was derived by back analysis.

Numerical Simulations on the Vallcebre Landslide

Many authors (Butterfield 2000; Gottardi and Butterfield 2001; Corominas et al. 2005) adopted a typical viscous fluid type approach (Bingham model) or analytical laws (Ranalli et al. 2010) to model slow slope displacements. In order to test the capability of the previously discussed constitutive approach to evaluate the deformations of a different landslide, the Vallcebre case study (Corominas et al. 2005) is here presented.

In this case, the viscous nucleus formulation has been simplified and the parameters η_2 and γ are imposed to be null: the visco-plastic deformations only develop if the stress state lies outside the f surface. When an instantaneous load increment is applied, the f function and the rate of irreversible deformation are set as positive.

By means of the same procedure described for (10) and by introducing the η viscous constant, the following expression for x-acceleration can be obtained

$$10^{-3} \cdot m^* \ddot{x} + \eta \dot{x} = \langle \tau_{stat} - \tau_{res} \rangle \quad (13)$$

Calibration based on the entire displacement dataset available for the Vallcebre landslide (Corominas et al. 2005) allowed to obtain both the viscous η parameter ($\eta = 6.66 \cdot 10^7$ kPa · s/m) and the residual friction angle ($\phi'_{res} = 11.12^\circ$). The latter was compared to the experimental friction angle ($\phi'_{res} = 11.8^\circ$, Corominas et al. 2005) in order to test the capability of the proposed model to provide also a calibration of geomechanical parameters, when not available. Figure 8 shows a very good agreement between simulated and measured displacements.

Conclusions

In order to numerically reproduce the slow motion of slides, a visco-plastic constitutive modelling approach has been adopted and coupled to a pseudo-dynamic Newmark model, to take into account the inertial effects. A pseudo-linear formulation for the viscous nucleus has been adopted. The proposed model is capable of reproducing quite satisfactorily the dataset of displacements concerning the Bindo-Cortenova case study over a long period of time (about 5 years). The same constitutive approach was also

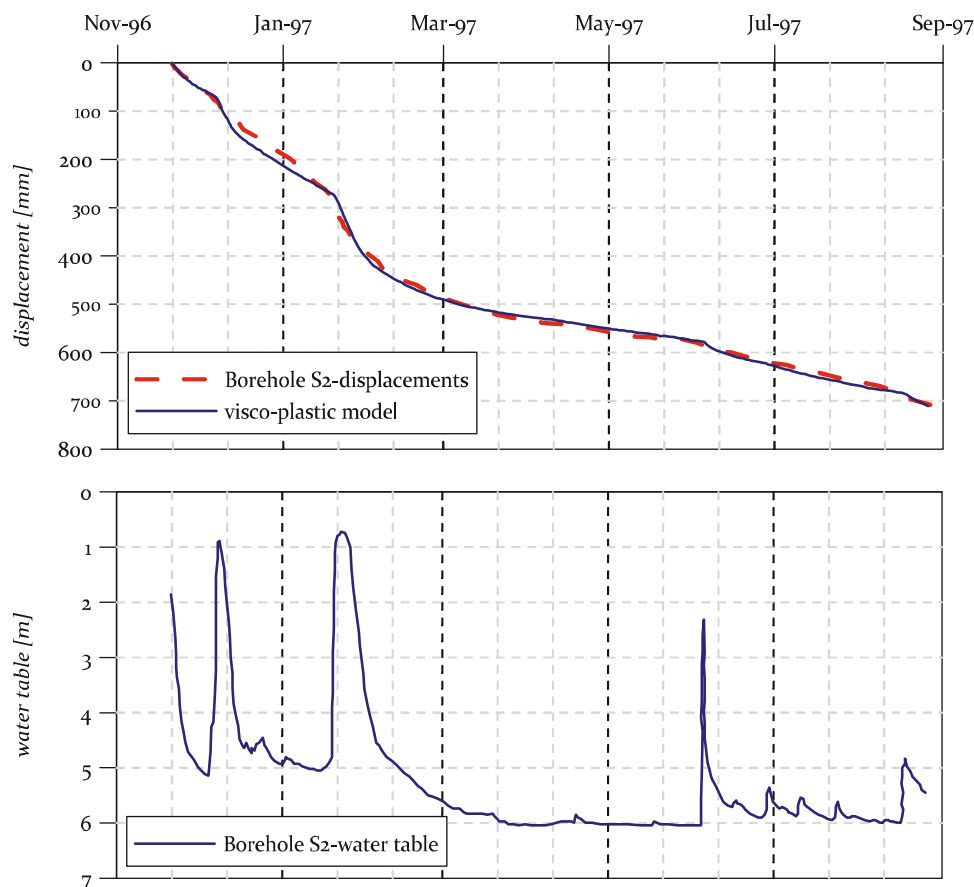


Fig. 8 Measured and predicted displacements for the Vallcebre landslide

tested on a different slow movement (Vallcebre, Spain), in terms of dimensions, geometries and materials.

Future efforts are directed at developing the method to include the effects of multiple sliding blocks to simulate the progressive acceleration and/or deceleration of different landslide sectors as influenced by groundwater pressures changing along the slope, or their inertial effects. The development of a simplified hydrological model to simulate the groundwater response to rainfall or snow melting events could be implemented for improving the forecasting capabilities and the use for civil protection and emergency actions.

Finally, an evolution of the model would be the possibility to include elements to simulate the collapse of the entire mass.

Acknowledgments This work was partially funded by the MORFEO-Italian Space Agency (ASI) project, within the Natural and Human Related Activities Induced Risks Program. The authors are also grateful to the Administration of the Municipality of Cortenova and of the Comunità Montana della Valsassina, Valvarrone, d'Esino e Riviera.

References

- Angeli MG, Gasparetto P, Menotti RM, Pasuto A, Silvano S (1996) A visco-plastic model for slope analysis applied to a mudslide in Cortina d'Ampezzo, Italy. *Q J Eng Geol* 29:233–240
- Butterfield R (2000) A dynamic model of shallow slope motion driven by fluctuating groundwater levels. In: *Proceedings of the 8th international symposium on landslides*, vol 1. Thomas Telford, London, pp 203–208
- Corominas J, Moya J, Ledesma A, Lloret A, Gili JA (2005) Prediction of ground displacements and velocities from groundwater level changes at the Vallcebre landslide (Eastern Pyrenees, Spain). *Landslides* 2:83–96
- Crosta GB, Chen H, Frattini P (2006) Forecasting hazard scenarios and implications for the evaluation of countermeasure efficiency for large debris avalanches. *Eng Geol* 83(1–3):236–253
- di Prisco C, Imposimato S (1996) Time dependent mechanical behaviour of loose sands. *Mech Cohes Frict Mater* 1(1):45–73
- di Prisco C, Zambelli C (2003) Cyclic and dynamic mechanical behaviour of granular soils: experimental evidence and constitutive modelling. *Rev Franç de Genie Civil* 7(7–8):881–910
- Frigerio G (2010) Evoluzione di movimenti franosi lenti: interpretazione dei dati mediante modellazione numerica semplificata. Master thesis (in Italian), Politecnico di Milano

- Gottardi G, Butterfield R (2001) Modelling ten years of downhill creep data. In: Proceedings of the 15th international conference on soil mechanics and geotechnical engineering, Istanbul, 27–31 Aug 2001, pp 1–3
- Newmark NM (1965) Effects of earthquakes on dams and embankments. *Geotechnique* 15(2):139–160
- Perzyna P (1963) The constitutive equations for rate sensitive plastic materials. *Q Appl Math* 20:321–332
- Ranalli M, Gottardi G, Medina-Cetina Z, Nadim F (2010) Uncertainty quantification in the calibration of a dynamic viscoplastic model of slow slope movements. *Landslides* 7:31–41
- Secondi M, Crosta GB, di Prisco C, Frigerio G, Frattini P, Agliardi F (2011) Forecasting landslide motion by a dynamic elasto-visco-plastic model. Geophysical research abstract 13, EGU2011-13850, European Hazards Session NH3.8, Wien, 3–8 Apr 2011



Intelligent Analysis of Landslide Data Using Machine Learning Algorithms

Natan Micheletti, Mikhail Kanevski, Shibiao Bai, Jian Wang, and Ting Hong

Abstract

Landslide susceptibility maps are useful tools for natural hazards assessments. The present research concentrates on an application of machine learning algorithms for the treatment and understanding of input/feature space for landslide data to identify sliding zones and to formulate suggestions for susceptibility mapping. The whole problem can be formulated as a supervised classification learning task. Support Vector Machines (SVM), a very attractive approach developing nonlinear and robust models in high dimensional data, is adopted for the analysis. Two real data case studies based on Swiss and Chinese data are considered. The differences of complexity and causalities in patterns of different regions are unveiled. The research shows promising results for some regions, denoted by good performances of classification.

Keywords

Landslide susceptibility mapping • Machine learning • Support vector machines

Introduction

Over the last decade, landslide hazard and risk have been one of the major research fields at the international level. The increasing of economic costs for the insurance companies resulting for landslide events and other natural hazards introduce the need of better knowledge and tools to treat and to study this phenomenon. Because of landslide susceptibility (LS) maps are useful tools for natural hazards assessment, a lot of research was carried out to find the efficient and precise methods for LS mapping. The use of statistical classification models instead of physical approaches is justified by the fact that the link between

landslide events and predisposing and triggering factors is complex or even not well-known.

During last years, the number of studies about slope stability and susceptibility to landslides using machine learning algorithms increased considerably. Examples of publications about this subject are Yao et al. (2008) and Brenning (2005). For more information, a state-of-the-art about this topic is presented in Micheletti (2011). The most widely used methods include artificial neural networks (ANN), kernel methods (i.e. support vector machines, SVM) and logistic regression (LR).

Generally, landslide susceptibility analysis by using machine learning is formulated as a supervised classification learning problem. Despite of the increasing number of publications on this topic, many open questions still remain. The main challenges consist in choosing a suitable sampling technique, formulating the input-output spaces properly and selecting the relevant features for the learning task.

In this research we introduce a complete analysis, starting from raw data to landslide susceptibility mapping, using Support Vector Machines as a modelling tool using real datasets from different regions.

N. Micheletti (✉) • M. Kanevski
Institute of Geomatics and Risk Analysis, University of Lausanne,
Lausanne, Switzerland
e-mail: Natan.Micheletti@unil.ch

S. Bai • J. Wang • T. Hong
Key Laboratory of Virtual Geographic Environments, Nanjing Normal
University, Nanjing, China

Methodology

Supervised Learning

In a supervised learning task, the output is known for every observation. Hence, the learning task is to model the unknown dependence between input and output. To model landslide susceptibility a supervised classification task is formulated. In this case, estimation of the class of an unseen sample using a model constructed on examples provided by the user is aimed.

Support Vector Machines

Support Vector Machines, the workhorse of Statistical Learning Theory (Vapnik 1998), is a very attractive approach developing robust and stable models using high dimensional datasets. SVM can be adapted to different supervised classification learning task. In the present research, two-class SVM is applied. SVM is using Structural Risk Minimization principle of inference trying to minimize classification error and controlling the complexity of the model. Details about this approach and its application to environmental studies are presented in Cherkassky and Mulier (2007) and Kanevski et al. (2009).

The simplest case is a separable linear problem. Considering labelled samples provided by the user, SVM aims the separation of the classes in the input space by a hyperplane (linear model) of the form

$$f(\mathbf{x}) = \langle \mathbf{w}, \mathbf{x} \rangle + b \quad (1)$$

where \mathbf{x} is a vector describing position of data in high dimensional input space, \mathbf{w} and b are the constants obtained after the solution of SVM optimization problem (Vapnik 1998).

The correct location of the classification samples in relation to the hyperplane is controlled by corresponding constraints. Further, the margin between the two classes is maximized to ensure a classification model with good generalization ability. In most cases the solution of the optimization problem is sparse and only support vectors (SV) – the samples located on margin borders – contribute to the solution with non-zero weights.

For the non-separable case (noisy data) the SVM was extended by allowing some misclassifications and keeping solution simple - linear. This is done by introducing the slack variables ξ . A hyper-parameter C balances the trade-off between margin maximization and classification error (empirical risk). The optimization problem can be formulated as follows:

$$\begin{cases} \min & \frac{1}{2} \|\mathbf{w}\|^2 + C \sum_{i=1}^L \xi_i \\ \text{Subject to} & y_i(\langle \mathbf{w}, \mathbf{x} \rangle + b) \geq 1 - \xi_i \end{cases} \quad (2)$$

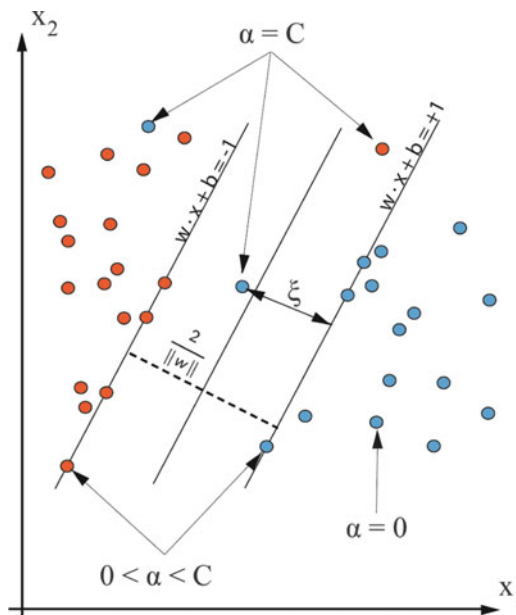


Fig. 1 Support vector machine scheme

The optimization problem (minimization with constraints) is solved in a classical way by introducing the Lagrange multipliers α . Figure 1 presents a two dimensional illustration of the two-class (red and blue dots) classification problem. Well classified points ($\alpha = 0$) do not contribute to the solution. “Normal” support vectors correspond to $0 < \alpha < C$ and “atypical” or noisy SV to $\alpha = C$.

The prediction for a sample \mathbf{x} is formulated as follows:

$$\text{Sign}(f(\mathbf{x})) = \text{sign}\left(\sum_{i=1}^L y_i \alpha_i \langle \mathbf{x}_i, \mathbf{x} \rangle + b\right) \quad (3)$$

where $y_i = \{+1, -1\}$ for two-class problem (e.g. $+1 = \text{red}$ and $-1 = \text{blue}$) and only points with $\alpha_i \neq 0$ contribute to the solution.

To solve non-linear problems, a kernel function $K(x_i, x)$ can be introduced. The latter replaces the dot product $\langle x_i, x \rangle$ and maps data into a higher dimensional feature space, where a linear decision boundary can be constructed. The most commonly used is the Gaussian RBF kernel, which introduces another hyper-parameter, the so-called kernel bandwidth σ :

$$K(\mathbf{x}_i, \mathbf{x}) = e^{-\frac{(\mathbf{x}_i - \mathbf{x})^2}{2\sigma^2}} \quad (4)$$

The goal of SVM training is to select the optimal values for the regularization parameter C and the kernel bandwidth σ . There are many algorithms to do it but the most usual procedure is to split data into training, validation and testing subsets and to use the validation data with a grid search. The optimal parameters minimize validation error (see Kanevski et al. 2009).

Landslide Susceptibility Mapping Using SVM in Vaud, Switzerland

Vaud Region

The Swiss case study of this research is canton Vaud, Switzerland. The location of Vaud in the Swiss territory is illustrated in Fig. 2.

The three main geological regions of Vaud (Prealpes, Plateau and Jura) were selected as separate study zones. This is done because of triggering factors and landslide nature differ considerably between these zones. Hence, the patterns of these regions which we want to reproduce probably also differ significantly. Figure 3 shows the canton Vaud and its three main geological and morphological sectors.

The Plateau zone is located in the middle part of canton Vaud. Its rock tender lithology is easily affected by surface processes as hydrological action and wind erosion. Plateau features countless moraine formations, generated during last ice age. After the glaciers melting, hydrological processes influenced the surface morphology. Today the region is characterized by gentle hills and an articulated hydrographical network. Landslide phenomena in Plateau are linked to fluvial erosion and thus they are mainly located along the rivers. Generally, these surface sliding zones are strictly influenced by local hydrological conditions, as preferential flow channels, presence of aquifers, soil infiltration, etc.

On the North-West side of canton Vaud we can find the Jura zone. Its structure is characterized by a large scale folded tectonic, featuring folds of more than a hundred kilometres length. This structure follows a NE-SW orientation. Valleys and local morphology are strictly controlled by these folds, following their direction. Jura's landslides are mainly associated to tender rocks and quaternary forms. The karst nature of Jura hydrogeology prevents the development of large landslide phenomena, unless extreme rainfalls occur.

Prealpes are located in the South-East of Vaud. This mountainous zone features a complex morphology with steep slopes. The geological context is characterized by tablecloths juxtaposed during the Alps formation. The Prealpes slope stability is strictly correlated to its lithology and tectonic adduction. Moreover, glacial and hydrological influences remodelled the surface, resulting in an even more complex situation. Prealpes feature many huge landslides. Even if some triggering factors are well known, tectonic and geological complexity make predictions in this zone really difficult.

Data and Feature Extraction

To compute SVM classification, an input space including relevant features for the task must be constructed. The Vaud lithotype database derived from a geological map has been

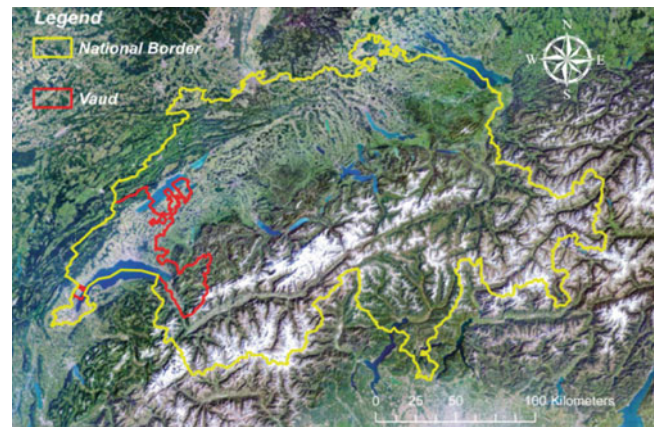


Fig. 2 Vaud location

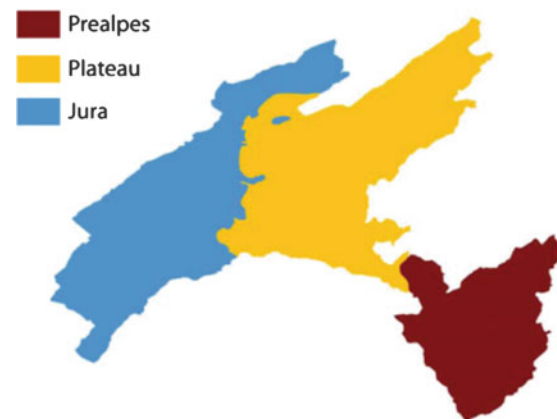


Fig. 3 Main geological regions of Vaud

used. To introduce this categorical information, a binary formulation is necessary, indicating with 1 the presence of a given lithology.

A digital elevation model (DEM) of 25×25 m resolution allowed the extraction of different topographic features. Firstly, the most used features for slope analysis were created. The latter are aspect, slope, plan curvature, profile curvature, topographic wetness index (TWI) and surface curvature. Then the hypothesis that some variables could be important not only at small spatial scale, but also at a larger spatial scale has been formulated. The efficiency of this approach was demonstrated in other environmental study concerning modelling of wind fields in complex topography (Foresti et al. 2011). Therefore, some Gaussian filters were applied to some commonly useful features describing soil curvatures. We chose two filter of different size: 21 and 101 pixels. Finally, the continuous features in the input space are: aspect, slope, DEM height, slope filtered with Gaussian filter 101 pixels-sized (G. 101), topographic wetness index, plan curvature, profile curvature, plan curvature G. 21, plan curvature G. 101, profile curvature G. 21, profile curvature G. 101, surface curvature, surface curvature G. 21.

Finally, the Vaud landslide database is used to extract the target labels. The output has a binary formulation, -1 indicating an alleged stable sample and $+1$ indicating a sliding one.

Sampling and Experimental Setup

Both linear and non-linear SVM analyses were carried out. Linear SVM needs only tuning of the C hyper-parameter, while non-linear SVM requires the selection of C as well as of σ . For both algorithms, three subsets are needed to perform the analysis. Firstly, a training set to build the classifier (SVM training) is necessary. Then, a validation set is used to select the best pair of hyper-parameters. Here a grid search (scanning of different C and σ values and looking for a minimum on a validation surface error) was applied. We allowed four values for C (1, 10, 100 and 1,000) and we looked for the best σ between 1 and 10. Finally, a test set allows the evaluation of the model (model assessment or the estimation of generalization error).

In addition, two-class SVM needs samples of the two classes to be performed. Usually, alleged stable examples can be randomly selected from the region of study. On the other hand, the sampling of positive sample is more complicated. Many questions arise from this task: the heterogeneity of landslides zones (where to sample?) and the non-independence of training, validation and test set in the case of random sampling, just to mention two of them.

We proposed an object-based sampling strategy. All landslides have been labelled, and then divided into three groups: a training one, a validation one and a testing one. A random sampling is performed from these groups, achieving landslides independence in geographical space.

Different sizes of training and validation datasets have been created, featuring 10 subsets for each size to compute empirical confidence intervals of the results. A single set of 10,000 points is kept as test set. The performance measure used for model selection assessment is the Area Under the ROC Curve (AUC).

SVM-Performances

Five hundred and two thousand sized datasets are used to analyse SVM performances. Five hundred sized datasets are a benchmark for their good quality/computational time ratio, while 2,000-sized sets generally ensure a solid classification.

A first analysis of SVM performances considers the percentage of support vectors in the training set, presented in Table 1. This percentage is a good indicator of the level of overfitting of the model. The latter is very satisfactory for our case, since percentages are very low for such a complex task.

Table 1 Percentage of support vector in the training set for Gaussian SVM (with standard deviation)

Points	Plateau
500	43.72 % (5.63 %)
2,000	36.60 % (3.28 %)

Table 2 SVM performances: mean test AUC (with standard deviation)

Model	Points	Plateau
Gaussian SVM	500	0.87 (0.010)
Gaussian SVM	2,000	0.88 (0.011)
Linear SVM	500	0.84 (0.020)
Linear SVM	2,000	0.88 (0.015)

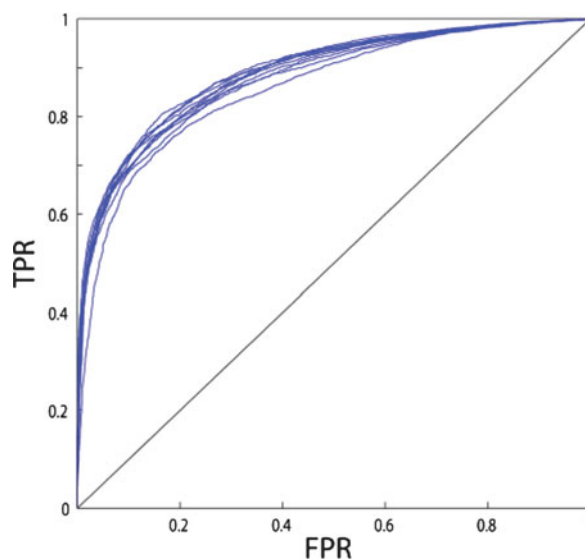


Fig. 4 ROC curves for 10 experiments with 2,000 samples (Gaussian SVM)

Table 2 summarizes the performances of linear and non-linear SVM algorithms. The evaluation of models is performed by using the test set. Mean and standard deviation on 10 models created with the same training and validation number of data provide a solid estimation of the performance efficiencies and their uncertainties. Very good results are found for Plateau sub-region, motivating the application of similar approach for other zones.

It is interesting to note how linear SVM has very similar performances to the Gaussian one for Plateau. The same is proven true for Jura. The hypothesis that, including enough training samples, the two-classes are linearly separable in these sub-regions can be advanced.

Finally, ROC curves for 2,000-sized datasets models are given in Fig. 4.

Performances analyses indicate that Plateau is an easy case study. The two classes are discriminated very well, resulting in a mean test AUC of 0.88 using 2,000 samples. Empirical observations underline that landslides are almost

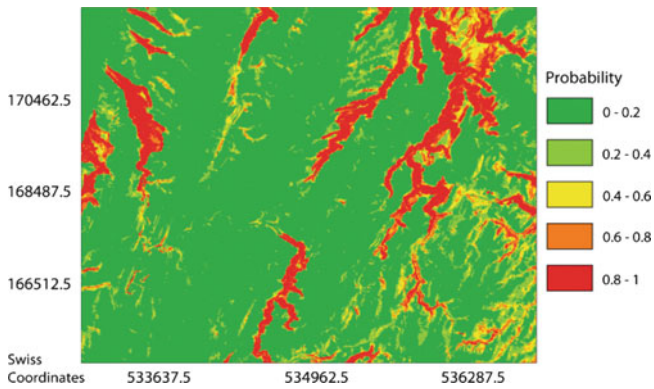


Fig. 5 Plateau ROI, landslide susceptibility mapping using two-class Gaussian SVM with 2,000 points, split n° 5

only present on riverside slopes in this sub-region, thus the model can detect them easily. A trustful and accurate landslide susceptibility mapping can be advanced.

In next section, landslide susceptibility mapping in Vaud's Plateau provides a visual explanation of these considerations.

Landslide Susceptibility Mapping

The SVM decision function is continuous and unbounded. Therefore, a probabilistic mapping can be more accessible to readers and most importantly to stakeholders, who are the biggest users of such maps. Some regions of interest (ROI) have been chosen for predictions, in order to have a more suitable visualization of quality of the results. In addition, a visualization of labels in the same ROI can be useful to visually estimate the quality of predictions.

Landslide probabilistic maps for a Plateau ROI provide outstanding results (Fig. 5). A very strong discrimination between landslide susceptibility zones and stables ones can be observed which can be confirmed by comparing the predictions with the known landslide locations (Fig. 6). Very high confidence in uncertainties illustrates how the model's performances are solid and trustful.

Introduction to Landslide Data Analysis in Gansu Province, China

Baiyhue Catchment Area in Gansu

The Baiyhue catchment area in China's north-western province Gansu is the subject of a work-in-progress landslide analysis and modelling using SVM. The goal of this study is to assist regional planning and risk management.

The lithology of the mountainous 432 km² large study area comprises loess deposits, mudstones and other weak formation. These soil property, associated to the steepness of

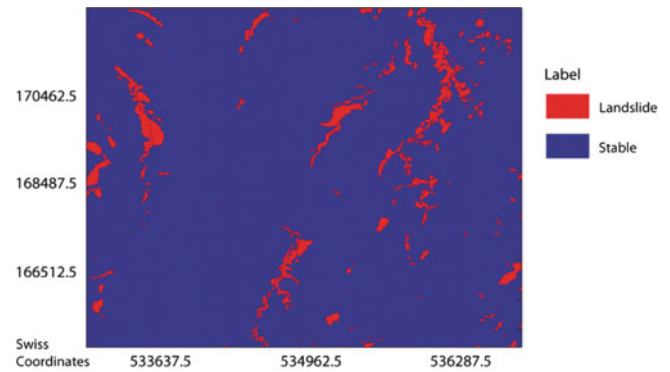


Fig. 6 Plateau region of interest: known landslides

regional valleys and heavy rainfall events, causes strong soil erosion, landslides and viscous debris and mud flows on slopes. The large volume of material delivered to the valley also causes problems.

Data and Feature Extraction

Data for SVM classification for Baiyhue catchment area has three different sources.

Twelve geological formations were derived from geological maps and used to define fine lithological units, grouping rock types that present similar compositional and mechanical characteristics.

A digital elevation model was generated from a triangulated irregular network model. The DEM was used to produce continuous variables such as elevation, slope angle, aspect, terrain roughness, shape of the slope parameters, plan curvature and profile curvature.

Land cover information is interpreted from TM 5 (Path 127/Row 39, dated 7/2000) satellite imagery using various image processing and enhancement techniques. The interpreted images were digitally processed to further modify the boundaries by a supervision classification task. The accuracy of the land-use interpretation was checked in the field. Eleven vegetation types were recognized.

Finally, drainages, roads and faults digitized from topographic maps have been used. Distances from these objects are included as features.

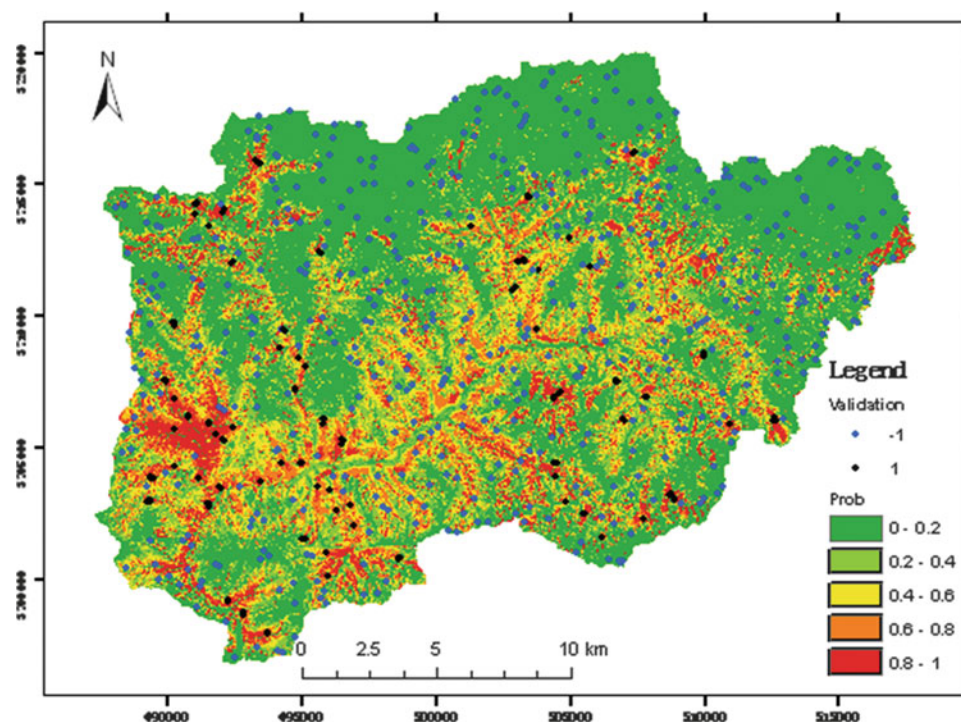
A detailed landslide-inventory map of the study area was constructed by interpretation of aerial photographs. Extensive field studies were used to check the size and shape of landslides.

SVM-Analyses

Like for Swiss case study, SVM algorithm is used to perform a supervised classification for landslide susceptibility mapping.

Data was divided in three subsets for model construction, selection and assessment. Training dataset includes 1,820

Fig. 7 Landslide susceptibility mapping using two-class Gaussian SVM, Baiyue catchment area, Gansu, China



samples, while validation and test sets include 636 examples each. In the datasets the number of landslide and alleged stable point is the same. After the first analysis by applying SVM, an accuracy of 80.04 % is found on independent data.

A probabilistic map of landslide in Baiyue area is presented in Fig. 7. Independent data used to assess the model is added to the map (+1 for landslide samples, -1 for stable ones).

In general, results are satisfactory, identifying well the valley slopes known as landslide susceptible. However, more efforts to assess the model are still in progress, as additional data and a more detailed analysis of results.

Conclusions

In conclusion, SVM analysis in Plateau, Vaud, Switzerland confirms prior knowledge acquired by empirical observations. Good performances achieved illustrate how Support Vector Machines could be useful for landslide susceptibility mapping. The other Vaud sub-regions can be analysed with the same methodology. The interested reader can find insight about this case study in Micheletti (2011). An important question in landslide susceptibility mapping is the feature space construction and feature selection, especially because different regions can be feature specific. The first results in this direction are quite promising and can be found in Micheletti (2011).

Besides being a work-in-progress, SVM analysis in the Baiyue catchment area of Gansu, China already produced interesting new results, as illustrated by solid performances and a trustful landslide susceptibility mapping.

In general, results show that SVMs can be successfully adopted in landslide susceptibility mapping. Future perspective for such approach include, besides feature selection, analysis of different regions and application of other machine learning algorithms (artificial neural network, random forest, self-organizing maps, general regression neural networks, etc.) for comparison and decision-oriented mapping.

Acknowledgments This research was partly supported by Sino-Swiss cooperation project EG 42-032010, Swiss National Science Foundation, project “GeoKernels: kernel-based methods for geo- and environmental sciences, Phase II: 200020-121835/1” and National Natural Science Foundation of China (Nos. 40801212).

We would like to thank A. Pedrazzini and M. Jaboyedoff for their important contribution in data gathering and the indispensable knowledge in the field of landslides they provided to the current research. We also are grateful to L. Foresti, G. Matasci and M. Volpi for all interesting discussion and valuable help.

References

- Brenning A (2005) Spatial prediction models for landslide hazards: review comparison and evaluation. *Nat Hazard Earth Syst Sci* 5:835–862
- Cherkassky V, Mulier F (2007) *Learning from data: concepts, theory and methods*. John Wiley & Sons, Inc., Hoboken, New Jersey
- Foresti L, Tuia D, Kanevski M, Pozdnoukhov A (2011) Learning wind fields with multiple kernels. *Stoch Environ Res Risk Assess* 25(1):55–66
- Kanevski M, Pozdnoukhov A, Timonin V (2009) *Machine learning for spatial environmental data: theory, applications and software*. EPFL Press, Lausanne

- Micheletti N (2011) Landslide susceptibility mapping using adaptive support vector machines and feature selection, M.S. thesis, University of Lausanne, Switzerland
- Vapnik V (1998) Statistical learning theory. Wiley, New York
- Yao X, Tham LG, Dai FC (2008) Landslide susceptibility mapping based on support vector machines: a case study on natural slopes of Hong Kong, China. *Geomorphology* 101:572–582



Challenging Calibration in 3D Rockfall Modelling

Paolo Frattini, Giovanni B. Crosta, Federico Agliardi, and Silvia Imposimato

Abstract

Rock fall hazard assessment is a very demanding problem because of the complexity of the involved physics and its intrinsic stochasticity. New powerful tools, developed in the last few years, are characterized by different degrees of completeness, models, and algorithms. In the following, the modelling approach developed through the years within the code Hy_Stone is presented. Some issues related to the sensitivity to 3D topographic descriptions, the effects of stochasticity on model results and the calibration of 3D rockfall simulation are presented.

Keywords

Rockfall modelling • DEM ruggedness • DEM resolution • Stochasticity • Calibration

Introduction

The increasing availability of advanced data-collection techniques and powerful computers allowed a substantial step forward in simulating and understanding the physics of rockfall processes. Useful tools to assess rockfall hazard, and to improve the reliability of countermeasure design, are now available. In this respect, the development of 3D modelling techniques provides advanced tools to assess rockfall hazard either over large areas or at the local scale.

Nevertheless, not all the models are able to take into account the different aspects of the rockfall physics, including impact and related controls, 3D effects (e.g. lateral dispersion), impact against structures, effects of vegetation, and block fragmentation. Accounting for all this phenomena in a reasonably simple way is important to reliably predict block trajectories, frequency and energy for susceptibility, hazard and risk analysis, and for countermeasure design.

Nevertheless, modular semi-empirical algorithms, which give generally consistent results, but may fail to provide a physically-sound simulation of complex phenomena, are sometimes adopted. For example, pseudo-hydrologic approaches adopted in the trajectory simulation and forcing the simulated blocks to follow curved fall paths can be misleading. On the other hand, introduction of many simplified empirical relationships could give a false sense of comprehension of the phenomenon, suggesting consequently an unrealistic level of refinement that could hamper a correct interpretation of the results and of the obtained derived maps.

Here some modelling approaches implemented in the 3D rockfall simulator Hy_Stone are presented, with special focus on the sensitivity to 3D topographic descriptions, the effect of stochasticity on model results and the calibration of 3D rockfall simulation.

The core module of Hy_Stone (Crosta et al. 2004; Frattini et al. 2008; Agliardi et al. 2009; Frattini et al. 2012) is a hybrid algorithm based on modifications of Pfeiffer and Bowen (1989) and Azzoni et al. (1995), which exploits high resolution 3D descriptions of topography (e.g. LIDAR) up to sub-metrical scale. The algorithm allows to simulate free fall, impact and rolling with different damping relationships available. Topography is described by a DEM, and all the relevant parameters are spatially distributed. Stochasticity of rockfall

P. Frattini (✉) • G.B. Crosta • F. Agliardi
Dipartimento di Scienze Geologiche e Geotecnologie, Università di
Milano-Bicocca, P.za della Scienza 4, Milan, Italy
e-mail: paolo.frattini@unimib.it

S. Imposimato
FEAT, Finite Element Application Technology, Heerlen,
The Netherlands

processes and parameters is accounted for by slope ruggedness, and by random sampling of most parameters.

Specific model components have been implemented allowing to explicitly, albeit simply account for the interactions between blocks and countermeasures or structures. A new elasto-viscoplastic (VPL) constitutive model (Di Prisco and Vecchiotti 2006) has been implemented into Hy_Stone as a damping model to simulate the response of homogeneous granular layers of any inclination subjected to the impact of spherical rigid boulders. The module accounts for the time dependence of the mechanical response of soil layers due to material fabric rearrangement induced by block penetration, using coupled visco-plastic and Coulomb friction mechanisms.

A specific module explicitly accounts for the geometric and dynamic effects of vegetation (Crosta et al. 2005, 2006), with different types of simulated impacts depending on the relative position of the block with respect to the obstacle, and a stochastic approach implemented to account for uncertainty. Finally, a specific fragmentation model has been developed and included in Hy_Stone. The model detects fragmentation conditions based on a fracture energy criterion. At each fragmentation point, the fragment grain size distribution and the kinetic energy of each generated particle are determined according to user-defined constraints. The stochastic nature of this process is also accounted for and the model allows for a complete traceability of the primary and secondary trajectories.

Here the model performance is tested through the back analysis of real, well characterised events and experimental data, and the potential of this kind of modelling for local-scale hazard assessment and countermeasure evaluation and design is discussed. Analyses have been performed in a complex area located in the Italian Alps (Venezia Friuli Venezia Giulia) that has been interested by two main earthquakes occurred in May and September 1976. These earthquakes triggered hundreds of rockfalls that have been mapped soon after the event (Comunità Montana del Gemonese 1977; Govi 1977; Onofri and Candian 1979).

Rockfall Modelling Approaches

Available modelling tools can be differentiated on the basis of the basic assumptions, considered spatial dimensions, physical soundness, data analysis/exchange capabilities, and computational efficiency. It is therefore important to be aware of the differences among the proposed approaches and to evaluate correctly their appropriateness for the planned scopes. Furthermore, the difficulty in parameterization and calibration of more recent models, and the consequences on the results in terms of susceptibility, hazard

and risk zonation and interpretation should be accurately considered.

Two-dimensional modelling tools have been developed on the basis of lumped mass, hybrid or rigid-body approaches to simulate rockfall along “subjectively” predefined slope profiles following the most probable fall paths. They are reliable tools to which a high degree of subjectivity and uncertainty can be associated. Three-dimensional effects resulting from slope ruggedness, vegetation, topographic irregularities, block geometry, natural or artificial obstacles and barriers cannot be considered.

Three-dimensional models (Guzzetti et al. 2002; Agliardi and Crosta 2003; Crosta et al. 2004; Dorren et al. 2006; Lan et al. 2007; Agliardi et al. 2009) can take advantage of the Digital Elevation Models available at different resolutions. The quality of the results depends on the type of adopted approach, the number of trajectories, the cell resolution, the dynamic description of the motion and impact, the prevalence of physics-based or empirically-based laws, the possibility to introduce a probabilistic approach. In the following, possible approaches, problems and results are discussed by performing simulations by the Hy_Stone code.

Energy Loss Modelling

Apart from the geometrical constraints, the block impact and rebound are the most complex and influent processes in rock fall propagation. Different modelling approaches have been proposed (Falcetta 1985; Bozzolo and Pamini 1986; Pfeiffer and Bowen 1989; Jones et al 2000; Di Prisco and Vecchiotti 2006; Bourrier et al. 2008) and require different data about the material at the, or proximal to the surface.

Contact functions make use of restitution and friction coefficients for which empirical values are often presented and tabulated (Paronuzzi 1989; Pfeiffer and Bowen 1989; Azzoni et al. 1992; Azzoni and De Freitas 1995; Ushiro et al. 2000; Wong et al 2000; Chau et al. 2002; Labiouse and Heidenreich 2009) but that can be influenced by many variables and that cannot be unique and deterministically defined.

More sophisticated numerical approaches based on either finite element (FEM) or discrete element (DEM) methods have been employed to simulate the impact process.

To improve the Hy_Stone model performance and to accomplish a more reliable countermeasure design the BIMPAM constitutive model (Di Prisco and Vecchiotti 2006) has been implemented in the code. The impact model assumes a spherical rigid boulder; it neglects block spin rate and fragmentation, and considers a cohesionless soil and a constant local value for the slope. The required input data are the local slope gradient, block size and impact velocity, and values of the physical mechanical soil properties. The model

can simulate impacts on any slope surface, with inclination lower than the internal friction angle of the material, by using a visco-plastic and a coupled Coulomb friction mechanism. This last occurs in case of trajectories inclined with respect to the normal to the impact surface. The Hy_Stone numerical iterative explicit solution of the non-linear differential equation system provides the block displacement and the exit velocity vector, dynamic load on the soil, and depth of penetration.

Effects of Topographic Model Resolution and Ruggedness

Contact functions are frequently used for energy loss modelling due to the simplicity to incorporate this approach into the model. Such functions are expressed as restitution and friction coefficients, whose values have been derived through experimental or empirical observations of scale or in situ rock fall tests. However, these values can be very different since the coefficients include the effects of different characteristics of both the slope and the block (e.g., type of substrate and surface material, block mass, block shape, block material, geometry of the block to surface contact).

Here, the influence of DEM resolution and surface ruggedness on model rockfall restitution and friction coefficients is investigated. This is of interest since LIDAR and terrestrial laser scanning (TLS) DEMs have been recently made available, allowing for a very accurate surface description resulting in a generally rougher surface with respect to other techniques adopted for DEM generation. For the study area of Venzona (Friuli, Northern Italy), 3D simulations have been performed with DEMs generated with different tools and algorithms (LiDAR DEM, TOPOGRID DEM and TIN-to-RASTER DEM), at different resolution (from 1 to 20 m grid) for a total of nine models.

Using the same parameter sets with different DEMs, large differences in the results can be observed, with longer runout simulated for coarser DEMs and shorter runout with more resolute DEMs (Fig. 1).

This effect can be attributed to different ruggedness of DEMs as a function of cell size (Crosta and Agliardi 2004).

In order to obtain, with different DEMs and by back analysis of real events, a consistent pattern of impact marks, runout, 3D dispersion pattern (e.g. different curvature of trajectory), and type of motion (e.g. bouncing, rolling) it is therefore necessary to adopt a different set of input restitution and friction coefficients. In particular, parameter values were adjusted in percentage with respect to the values calibrated using the 1 × 1 m LiDAR DEM, and the variation of parameters plotted as a function of DEM resolution (Fig. 2).

The comparison of the different models allows to recognize variations of required restitution and friction

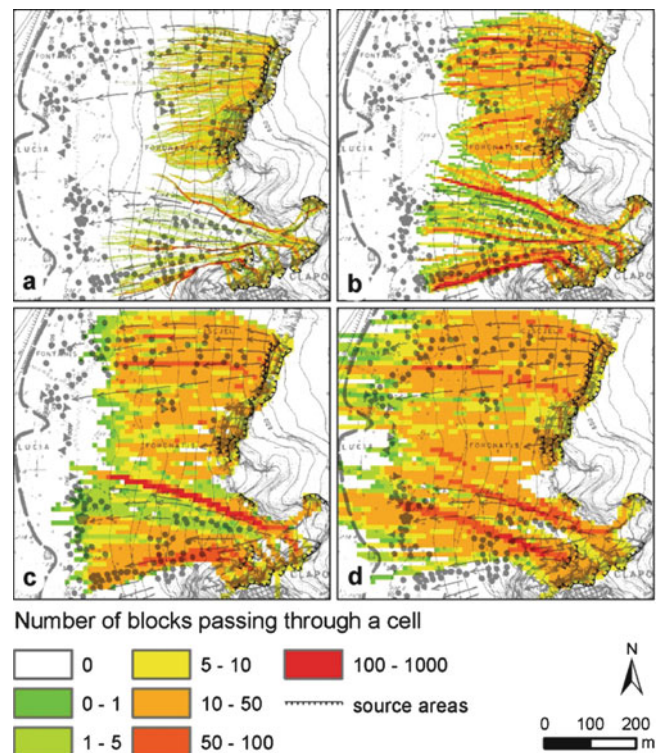


Fig. 1 Modelling results obtained by using DEMs generated with different algorithms and resolutions: (a) 1 m gridded LiDAR DEM, (b) 5 m gridded DEM by resampling of 1 m LiDAR, (c) 10 m gridded DEM by resampling of 1 m LiDAR, (d) 10 m gridded interpolated DEM from TOPOGRID algorithm. All models have been simulated using a single parameter set (correctly calibrated for 10 m gridded DEM by resampling of 1 m LiDAR, b). The background map shows the approximate trajectories and the arrest position for block fallen during the 1976 Friuli earthquakes (Comunità Montana del Gemonese (1977))

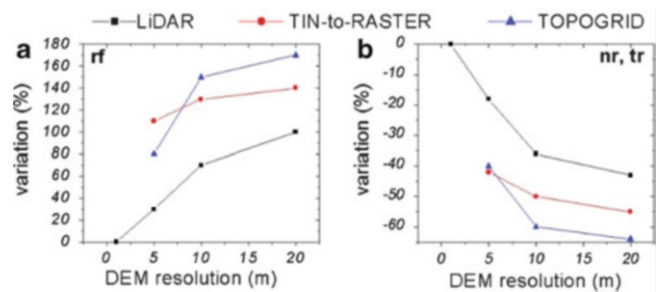


Fig. 2 Variation (in percentage with respect to calibrated values of the coefficients for a 1 m gridded LiDAR DEM) of (a) rolling friction (*rf*) and (b) restitution coefficients (normal and tangential, *nr* and *tr*) required to calibrate the rockfall models as a function of DEM resolution

coefficients up to 170 %. Although the effect of DEM resolution is evident, it can be observed that DEMs generated with different algorithms needed different parameter sets for the same cell size. Hence, it is not possible to derive a general law that simply scales the parameter values as a function of DEM resolution.

In order to explicitly investigate the dependence of coefficients on surface ruggedness, the Vector Ruggedness Measure, VRM (Fig. 3), based on a geomorphological method for measuring the dispersion of vectors normal to each grid cell (Sappington et al. 2007), has been computed for each DEM. This measure has been proved to be less correlated with slope than other approaches (Sappington et al. 2007).

By plotting the variation of coefficients needed to calibrate the models as a function of ruggedness (Fig. 4), a trend which can be interpolated by different functions (e.g. linear, along the entire data interval or for a partial range; sigmoidal) can be outlined. Plots suggest that VRM parameter is suitable to describe the control of ruggedness on friction and restitution coefficients.

Hence, it could be possible to use this relationship as a general-purpose law for scaling the coefficients according to DEM ruggedness. This can be a fundamental tool when performing simulations and calibrating models in areas where field observations and high resolution DEM are not available.

Effects of Stochasticity on Model Results and Calibration

The stochastic approach adopted in the Hy_Stone code allows to take into account for a series of possible influencing factors as the block/scree size ratio, the block size, the block trapping, the block irregular geometry as well as the slope ruggedness at a scale lower than the DEM resolution. All these processes, in fact, affect the propagation of blocks, resulting in a wide range of behaviour and runout distances reached by single blocks moving along the slope.

Stochasticity of rockfall processes and parameters is accounted for by random sampling of most parameters. The model allows for the selection of different distributions (e.g. uniform, gaussian or exponential) and for the setting of parameters that controls the dispersion about the nominal value, and the truncation of the distribution for lower and upper limits.

For example, Gaussian distributions can be used for restitution and friction coefficients. Spatially distributed mean values are assigned to each grid-cell of the area using raster files. The dispersion is attributed in terms of a stochastic range. This value is a percentage which multiplies a random variate distributed as a standard normal distribution, (i.e., mean = 0, standard deviation = 1). In other words, for each impact, the restitution and friction coefficients are assigned as:

$$coeff = coeff_{raster} + p^*stochR \quad (1)$$

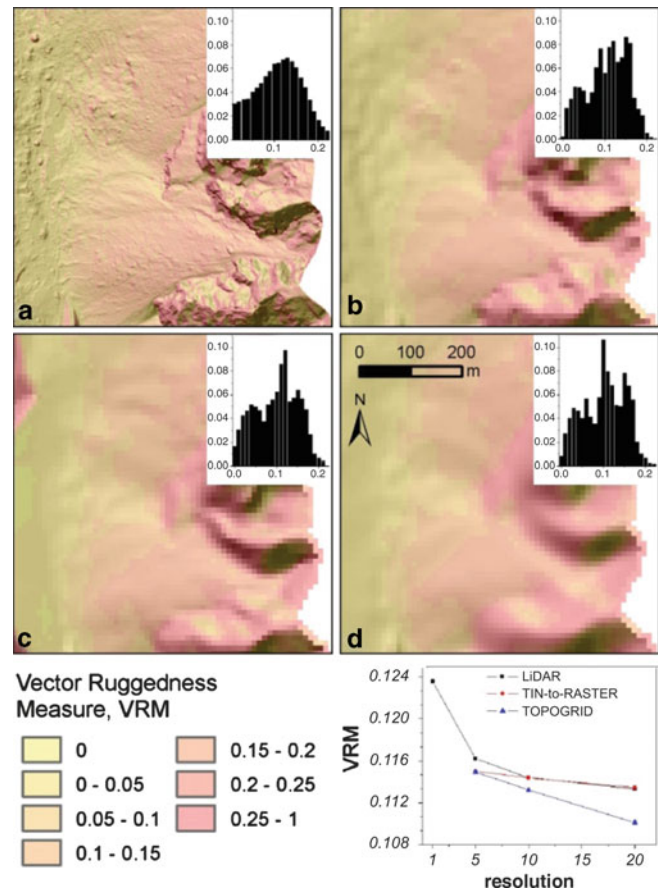


Fig. 3 Examples of Vector Ruggedness Measure (VRM) for DEMs with different resolution and generation algorithms: (a) 1 m gridded LiDAR; (b) 10 m gridded DEM by resampling of 1 m LiDAR; (c) 10 m gridded DEM generated by TOPOGRID algorithm; (d) 10 m gridded DEM generated by TIN model. The relative frequency histogram of VRM values for each map is reported. The lower-right plot shows the relationship between VRM and DEM resolution

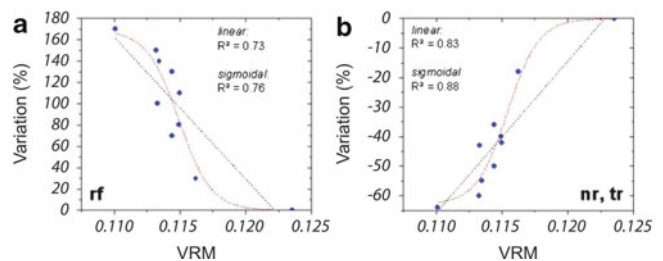


Fig. 4 Variation (in percentage with respect to calibrated values) of the coefficients for a 1 m gridded LiDAR DEM of (a) rolling friction (*rf*) and (b) restitution coefficients (normal and tangential, *nr*, *tr*), required to calibrate the rockfall models as a function of ruggedness (VRM). Linear and sigmoidal fittings are shown

where $coeff_{raster}$ is the nominal value given by the operator for each grid cell of the area, p is the random normally distributed variate and $stochR$ is the stochastic range, in percentage (Fig. 5).

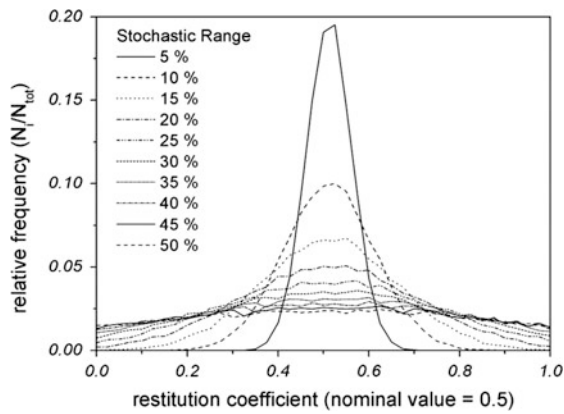


Fig. 5 Examples of stochastic distribution of restitution coefficients starting from a nominal value of 0.5. Relative frequency refers to the number of samples in each bin, N_i , (bin width = 0.025) divided by the total number of samples, N_{tot} (here, $N_{tot} = 30,000$)

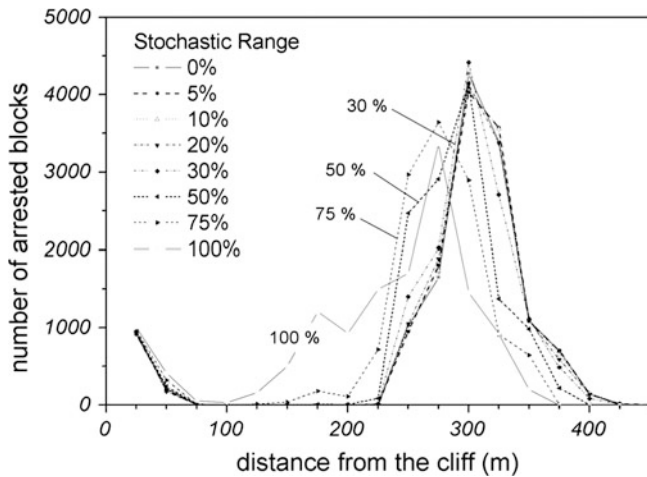


Fig. 6 Distribution of simulated arrest points along the slope as a function of the distance from the cliff, for different stochastic range values

In order to avoid meaningless values, the coefficient distribution can be truncated between significant minimum and maximum values (e.g., for restitution coefficients 0–1).

Here, the Venzone study area has been considered to investigate the influence of stochasticity on rockfall modelling. Back analyses of real events with different values of the stochastic range have been performed.

For a stochastic range of 0 % (no stochasticity), the distribution of arrested blocks along the cliff is narrow with a maximum frequency located approximately 300 m from the cliffs (Fig. 6).

The maximum distance reached by blocks is 425 m. Similar results can be observed for values of stochastic range lower than 30 %. Increasing the stochastic range above 30 %, a larger number of blocks arrested along the

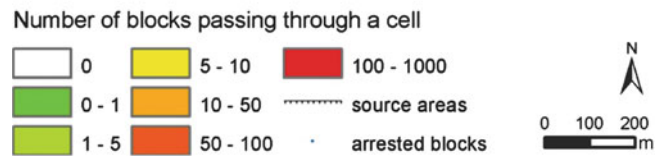
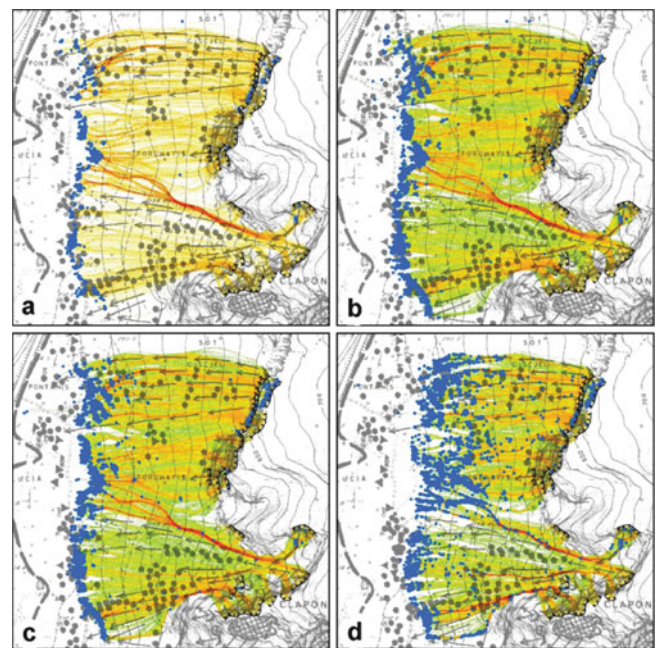


Fig. 7 Maps of transits and arrest points obtained by adopting different values of stochastic range for the 1 m LiDAR-DEM models: (a) 0 %, (b) 30 %, (c) 50 %, (d) 100 %. Ten blocks have been launched from each source cell. For the model with 0 % of stochastic range, all blocks simulated from a given cell follow exactly the same trajectory, i.e., the minimum number of blocks passing through a cell is 10. Background map as in Fig. 1

debris talus, and a progressive decrease of the maximum runout, are observed.

With a stochastic range of 100 %, the maximum frequency is observed at 275 m, with maximum runout at 375 m. Hence, the distribution of blocks along the talus is strongly controlled by the degree of stochasticity of restitution and friction coefficients (Fig. 7).

Using a high degree of stochasticity it is possible to simulate a more realistic population of blocks along the slope (e.g., Fig. 7d). Some blocks stop along the upper sector of the talus due to the random extraction of very low values for the restitution coefficients. This stochastic process mimics the effect of block trapping, and slope ruggedness at a scale lower than the DEM resolution, and for example the abundance of very small particles in proximity of the talus apex. However, the maximum runout is underestimated because the effect of randomly selecting lower values (e.g., restitution close to 0) is stronger than the selection of high values (e.g., restitution close to 1): once the energy is lost

due to a low restitution value it cannot be retrieved by successive selection of high restitution values.

Using a low degree of stochasticity, it is possible to accurately calibrate the model with respect to the maximum observed runout, because the distribution is narrow, and most of the blocks tend to reach the same distance. However, the distribution of blocks along the slope is unrealistic with respect to the debris talus and its formation.

Discussion

The choice of the mean value and of the stochastic range strongly control the final result of modelling. Model calibration can be carried out in a conservative or more design-oriented approach or in an evolutionary-oriented approach.

The former methodology implies that the operator tries to fit the maximum runout events because those stopping along the talus are of no interest or even go undetected. In this case, the restitution coefficients must be larger (opposite for the friction coefficient) and characterized by a smaller dispersion (i.e., small stochasticity).

On the contrary, the calibration of a model oriented to the simulation of rockfalls during the formation and development of a talus slope, requires in general lower values of the mean and a larger dispersion (i.e., large stochasticity). The choice of the frequency distribution could also control the final result. As a consequence, the person involved in hazard and risk assessment activities should carefully consider how he has accomplished calibration and how he takes into account the block transit and arrest frequency.

Furthermore, it is clear that a non unique set of parameters exists for a material because of the inherent variability of local conditions (block shape and irregularities, water and ice content, vegetation cover, debris geometry and debris to block size ratio) and of the adopted descriptors or topographic reconstruction. Modern DEM (LiDAR and TLS) resolutions make slope ruggedness a sort of obsolete descriptor unless when working with low resolution models.

On the other hand, lower resolution DEMs influences directly the local slope gradient. As a consequence, the same roughness values introduced in DEMs with different resolutions will result in different local slopes and runout.

Finally, the interpretation of 3D models for hazard and risk assessment is more complicated. The effects of convergence/divergence and of the different spatial distribution of the controlling factors make the probability of arrest a difficult property to be evaluated and interpreted. As a consequence, a different approach in hazard zonation is required.

Conclusions

Calibration of rockfall models is a tricky and painstaking task. Physical and topographic constraints make it difficult: as a consequence, the results can be misinterpreted. Calibration of 2D models is easier and the interpretation of the results is more straightforward. On the contrary, 3D models allow a much more significative zonation and the inclusion of multiple controlling factors.

The adoption of more physically-based impact models, such as BIMPAM (di Prisco and Vecchiotti 2006), allows a more sound simulation. For the description of the materials, this type of approach introduces different mechanical parameters that can be surveyed in the field.

Acknowledgments This work has been partially carried out within the MASSMOVE Interreg II project. Emanuela Barbanti and Francesca Colucci from the University of Milano – Bicocca performed part of the modelling.

References

- Agliardi F, Crosta G (2003) High resolution three-dimensional numerical modelling of rockfalls. *Int J Rock Mech Min Sci* 40(4):455–471
- Agliardi F, Crosta GB, Frattini P (2009) Integrating rockfall risk assessment and countermeasure design by 3D modelling techniques. *Nat Hazard Earth Syst Sci* 9(4):1059–1073
- Azzoni A, De Freitas MH (1995) Experimentally gained parameters, decisive for rock fall analysis. *Rock Mech Rock Eng* 28(2):111–124
- Azzoni A, Rossi PP, Drigo E, Giani GP, Zaninetti A (1992) In situ observations of rockfalls analysis parameters. In: *Proceedings of the sixth international symposium of landslides*. Balkema, Rotterdam, pp 307–314
- Azzoni A, La Barbera G, Zaninetti A (1995) Analysis and prediction of rock falls using a mathematical model. *Int J Rock Mech Min Sci Geomech Abstr* 32(7):709–724
- Bourrier F, Nicot F, Darve F (2008) Physical processes within a 2D granular layer during an impact. *Granul Matter* 10(6):415–437
- Bozzolo D, Pamini R (1986) Simulation of rock falls down a valley side. *Acta Mech* 63:113–130
- Chau KT, Wong RHC, Wu JJ (2002) Coefficient of restitution and rotational motions of rockfall impacts. *Int J Rock Mech Min Sci* 39:69–77
- Crosta GB, Agliardi F (2004) Parametric evaluation of 3D dispersion of rockfall trajectories. *Nat Hazard Earth Syst Sci* 4:583–598
- Crosta GB, Agliardi F, Frattini P, Imposimato S (2004) A three-dimensional hybrid numerical model for rockfall simulation. *Geophys Res Abstr* 6:04502
- Crosta GB, Agliardi F, Frattini P (2005) Modelling rockfall impact on structures. *Geophysical Research Abstracts*, EGU05-A-08555; H3.01-1WE4P-0110
- Crosta GB, Frattini P, Imposimato S, Agliardi F (2006) Modeling vegetation and fragmentation effects on rockfalls. *Geophys Res Abstr* 8:07694
- Comunità Montana del Gemonese (1977) *Carta geostatica del Comune di Venzone*. Direzione Nazionale dei Lavori Pubblici, Servizio delle Calamità Naturali, Regione Friuli Venezia Giulia
- Di Prisco C, Vecchiotti M (2006) A rheological model for the description of boulder impacts on granular strata. *Geotechnique* 56:469–482

- Dorren LKA, Berger F, Putters US (2006) Real size experiments and 3D simulation of rockfall on forested and non-forested slopes. *Nat Hazard Earth Syst Sci* 6:145–153
- Falcetta JL (1985) Un nouveau modele de calcul de trajectoires de blocs rocheux. *Revue Francaise de Geotechnique* 30:11–17, in French
- Fratini P, Crosta G, Carrara A, Agliardi F (2008) Assessment of rockfall susceptibility by integrating statistical and physically-based approaches. *Geomorphology* 94(3–4):419–437
- Fratini P, Crosta GB, Agliardi F (2012) Rockfall characterization and modeling. In: Clague JJ, Stead (eds) *Landslides types, mechanisms and modeling*. Cambridge University Press, pp 267–281. ISBN:978-1-107-00206-7
- Govi M (1977) Carta delle frane prodotte dal terremoto (Map showing the landslides triggered by the earthquake). *Rivista Italiana di Paleontologia e Stratigrafia* 83, Plate 1
- Guzzetti F, Crosta G, Detti R, Agliardi F (2002) STONE: a computer program for the three-dimensional simulation of rock-falls. *Comput Geosci* 28(9):1081–1095
- Jones CL, Higgins JD, Andrew RD (2000) Colorado rock fall simulation Program version 4.0. Colorado Department of Transportation, Colorado Geological Survey, 127p
- Labrousse V, Heidenreich B (2009) Half-scale experimental study of rockfall impacts on sandy slopes. *Nat Hazard Earth Syst Sci* 9:1981–1993
- Lan H, Martin CD, Lim CH (2007) RockFall analyst: a GIS extension for three dimensional and spatially distributed rockfall hazard modeling. *Comput Geosci* 33:262–279
- Onofri R, Candian C (1979) Indagine sui limiti di massima invasione dei blocchi rocciosi franati durante il sisma del Friuli del 1976. Regione Autonoma Friuli-Venezia-Giulia: CLUET, 42pp
- Paronuzzi P (1989) Probabilistic approach for design optimization of rockfall protective barriers. *Q J Eng Geol Hydrogeol* 22: 175–183
- Pfeiffer TJ, Bowen TD (1989) Computer simulations of rockfalls. *Bull Assoc Eng Geol* 26:135–146
- Sappington JM, Longshore KM, Thompson DB (2007) Quantifying landscape ruggedness for animal habitat analysis: a case study using Bighorn sheep in the Mojave Desert. *J Wildl Manage* 71(5):1419–1426
- Ushiro T, Shinohara S, Tanida K, Yagi N (2000) A study on the motion of rockfalls on slopes. In: *Proceedings of the 5th symposium on impact problems in civil engineering*. Japan Society of Civil Engineers, Tokio, Japan, pp 91–96
- Wong RH, Ho KW, Chau KT (2000) Shape and mechanical properties of slope material effects on the coefficient of restitution on rockfall study. In: *Proceedings of the 4th North American rock mechanics symposium NARMS 2000*, Seattle, pp 507–514



A Simple Model for Passive Failure Compression Structure at the Toe of Landslide

Angelo Doglioni, Annalisa Galeandro, and Vincenzo Simeone

Abstract

The toe of landslides is subject to compression stresses induced by the upward sliding masses and often characterized by a compression structure. These structures can evolve in passive toe thrust, which bias the geomorphologic evolution of the toe zone, particularly for prevailing longitudinal dimension landslide. This work presents a simple analytic model of the passive thrust at the toe of landslide based on the infinite slope approach to stability analysis. It is based on the analysis of the state of stresses according to Mohr circle representation and can be implemented also into a spreadsheet and making it possible to evaluate the form of failure surface at the toe of the landslide and the shear strength contribution to the factor of safety of a landslide.

Keywords

Landslide toe • Passive failure • Toe landslide compression structure • Passive toe thrust • Infinite slope

Introduction

At the toe of landslide, ground surface is often upward concave and is characterized by a compressive state of stress (Savage and Smith 1986) that may originate compressive plastic flow and compression structure that can evolve in passive failure thrust (Sdao and Simeone 1997) (Fig. 1).

Savage and Smith (1986) model landslides in Mohr-Coulomb plastic soil showing how compressive, extending or plug flow happen in different zone of the landslide masses. They predict tensile longitudinal stresses at the upper part of the landslide and compression stresses and listric thrust faults and thrust fault scarps at the surface in compressive flow at the toe of instable masses.

Sdao and Simeone (1996, 1997) proposed a geomorphic model for the lobes at the toe of main longitudinal dimension

landslide as earth-flow based on a sequence of passive toe thrust. The sliding materials arrive at the accumulation zone, loading the toe of the slope. When the compression stresses of the sliding soil exceed the passive shear strength at the toe, a thrust due to passive failure surface is created. Therefore, when the landslide is subject to several reactivations, its toe is constituted by different overlapped retrogressive lobes, due to different passive failure surfaces, each one referred to different activation stages of the landslide.

Urciuoli (2002) analysed the state of stress of an infinite slope according to Mohr plane circle representation. He showed how the position of the pole in Mohr plane representation is related to the ratio of stresses, between the stress component parallel and normal to the slope. This plays a crucial role in defining the thickness of the shear zone and in strains and displacement before failure.

Savage and Wasowski (2006) used the Savage and Smith (1986) model to analyse scarp and toe failure surface for the Acquara-Vadoncello landslide in Senerchia, Southern Italy. The modelled failure surface was really close to that reconstructed from a detailed in situ survey.

A. Doglioni (✉) • A. Galeandro • V. Simeone
Engineering Faculty of Taranto, Technical University of Bari, viale del
Turismo 8, Taranto, Italy
e-mail: a.doglioni@poliba.it

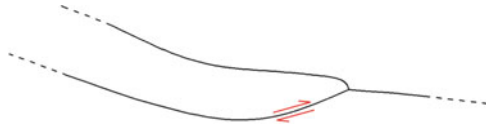


Fig. 1 Schematic representation of the failure surface at the accumulation zone

Simeone and Sdao (2002) presented a first step analytical formulation of the proposed passive failure mechanism applied to a case study of a huge earth-flow slide in Southern Apennine.

Starting from that formulation, this work yields a simple analytic model of the passive thrust at the toe of a landslide based on Mohr plane circle representation of the state of stress in an infinite slope. The model allows for theoretically evaluating the inclination and the form of the backward passive failure surfaces and the contribution of the toe strength to the safety factor of the slope. The work presents the model and the results of the passive toe thrust failure surface obtained in different cases. To validate the results, the model is applied to the case study of Acquara-Vadoncello landslide (Savage and Wasowski 2006). The obtained passive thrust failure surface is compared with the slip surfaces reconstructed and predicted by Savage and Wasowski (2006).

The Model

The proposed model allows for a simple and theoretically correct evaluation of the shape of the backward passive failure surfaces at the toe of an infinite slope landslide channel, using Mohr-Coulomb failure criterion. The approach is based on Mohr circle plane representation of the state of stresses. Moreover, it is also possible to evaluate the contribution of the toe strength to the stability of the upward masses.

The landslide flow channel is modelled as an infinite slope with an inclination β and a shear surface at depth z and unit weight of the soil γ (Fig. 2).

According to the classical analytical expression for the state of stress along the slip surface, the state of stress at a point S along the slip surface in the toe zone can be evaluated (Fig. 2) as:

$$\sigma_S = \gamma z \cos^2 \beta \quad (1)$$

$$\tau_S = \gamma z \cos \beta \sin \beta \quad (2)$$

where $\gamma z = W$.

Then, in a Mohr plane representation, the point representing the state of stress along the sliding surface of the infinite slope, is on a straight line starting from the origin and β sloping. At the compression zone, like the toe, according to Mohr plane circle representation of the state of stress, the point S , i.e. the state of stress along the sliding surface, is on the

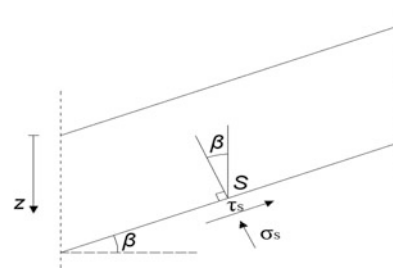


Fig. 2 Infinite slope model

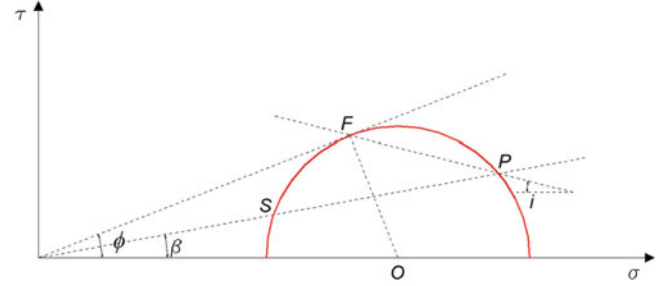


Fig. 3 Mohr circle of the state of stress at the toe of the landslide flow channel (cohesion = 0)

left side of the centre of Mohr circle (Fig. 3). Pole P according also to Urciuoli (2002) and Lancellotta (2004) is on the right side of Mohr circle centre. Toward the toe of the landslide, the sliding masses increase the compression stress and then the diameter of Mohr circle, until the circle is tangent to the failure criterion in F (Fig. 3). Therefore, there is a passive failure of the sliding masses according to a failure surface that has an inclination i (Fig. 3).

Using a Mohr-Coulomb failure criterion where the cohesion equals zero (Fig. 3), the analytical coordinates of pole P are:

$$\sigma_P = \sigma_0 [1 + (\sin^2 \phi - \cos^2 \phi \tan^2 \beta)^{0.5}] / (1 + \tan^2 \beta) \quad (3)$$

$$\tau_P = \sigma_P \tan \beta \quad (4)$$

where the state of stress of the centre of Mohr circle σ_0 is:

$$\sigma_0 = (\sigma_s / \cos^2 \phi) [1 + (\cos^2 \phi / \cos^2 \beta)^{0.5}] \quad (5)$$

The state of stress along the passive failure surface (point F , Fig. 3) is:

$$\sigma_F = \sigma_0 \cos^2 \phi \quad (6)$$

$$\tau_F = \sigma_0 \sin \phi \cos \phi \quad (7)$$

Then, it is possible to evaluate the inclination of the passive failure surface i , which is evaluated as:

$$i = \tan^{-1} [(\tau_F - \tau_P) / (\sigma_P - \sigma_F)] \quad (8)$$

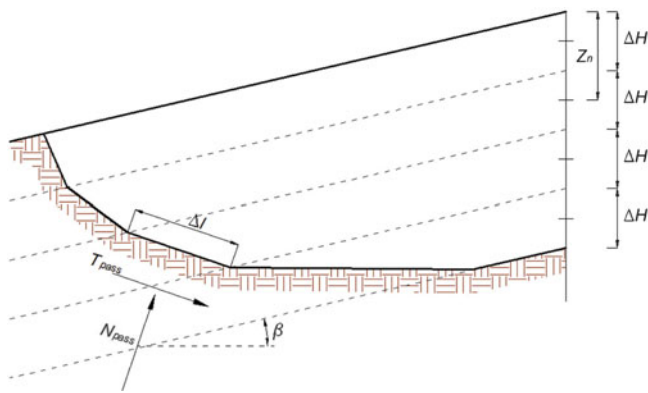


Fig. 6 Passive thrust failure surface when cohesion $\neq 0$

where

$$R_n = \sqrt{\sigma_{o,n} \sin^2 \phi + c^2 \cos^2 \phi + 2\sigma_{o,n} c \sin \phi \cos \phi} \quad (18)$$

Then, the inclination of the passive failure surface could be evaluated for each layer as:

$$i_n = \tan^{-1}[(\tau_{F,n} - \tau_{P,n})/(\sigma_{P,n} - \sigma_{F,n})] \quad (19)$$

Similarly, the passive strength at the toe of the landslide can be derived by the (9, 10, 11, and 12) to each layer, as shown by Fig. 6 and making a vector sum of the forces evaluated for each layer.

Application of the Model

The described procedure is used to calculate the shape of the passive failure surface for different values of shear strength parameters (cohesion and friction angle, Figs. 7 and 8) and slope in a sort of sensitivity analysis.

Figure 7 shows the passive toe thrust shear surface for a slope of 5° , a unit weight of 21 kN/m^3 , a friction angle of 5° and cohesion values growing from 2 to 50 kPa. The shape of the failure surface is really sensitive to the variations of cohesion. In particular the lowest is the cohesion value the longer and bow shaped is the slip surface at the toe.

For the same slope, Fig. 8 shows the same slope whereas a constant cohesion value of 5 kPa and different values of friction angle from 5° to 15° are assumed.

The results show that the passive failure surface is really long and bow shaped for low values of friction angle. Then, the form of the passive failure surface is really sensitive to low values of friction angle.

Looking at shear strength parameters, the general result is that high values of shear strength parameters return shorter and steeper surfaces.

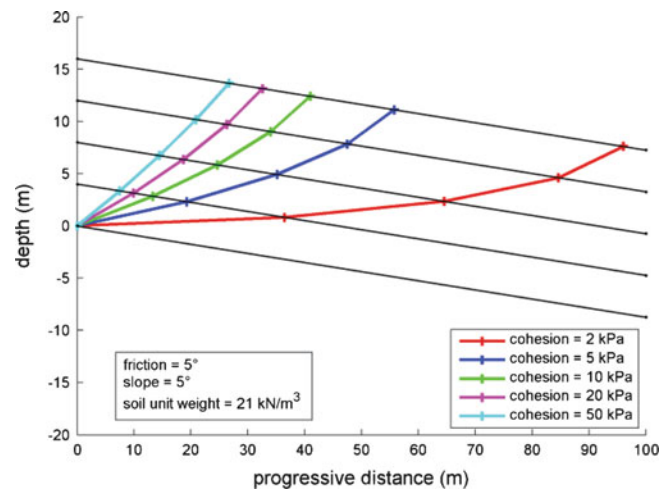


Fig. 7 Passive thrust failure surface as function of cohesion

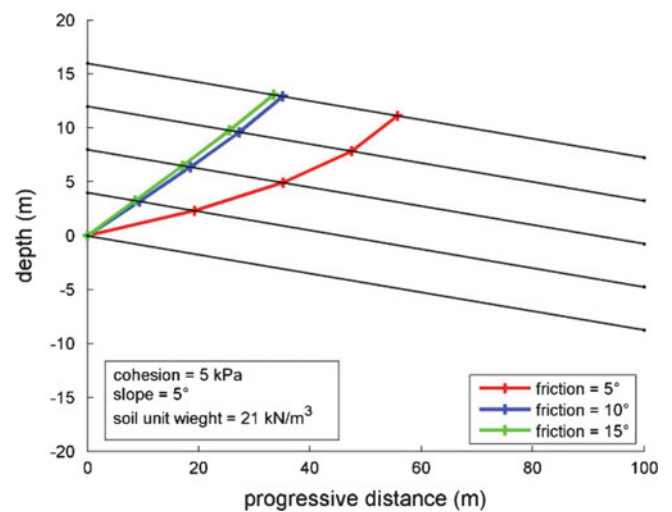
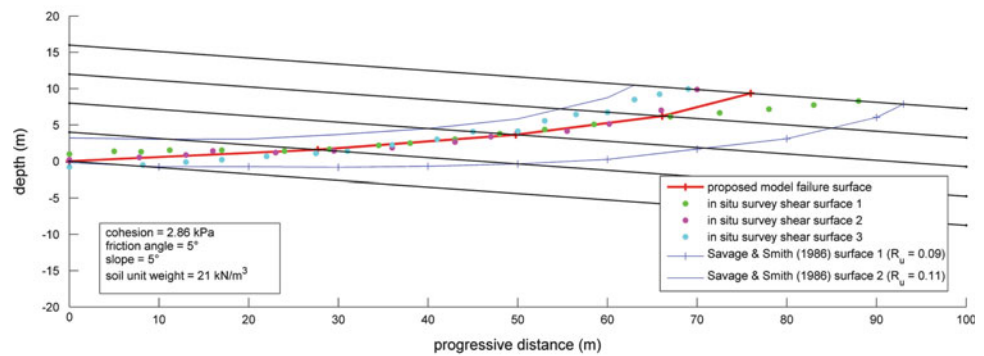


Fig. 8 Passive thrust failure surface as function of friction angle

Acquara Vadoncello Case Study

Model validation is done on the case study of Acquara Vadoncello landslide in Southern Italy. Here passive failure thrust surface at the toe of a landslide was identified and reconstructed in details by a large campaign of in situ surveys by Savage and Wasowski (2006). In particular, they reconstructed three different compression thrust failure surfaces at the toe of the landslide. They interpreted that passive thrust failure surfaces by the flow plastic model of Savage and Smith (1986). For their calculation, they assumed a unit weight of 21 kN/m^3 , a cohesion of 2.86 kPa, a friction angle of 5° , a slope angle of 5° and values of the pore pressure parameters $R_u = 0.1 \pm 0.01$. The assumed values can be considered quite reliable, since consistent with the results if in situ survey and laboratory tests (Savage and Wasowski 2006).

Fig. 9 Failure surface calculated according to the proposed model (red line) compared with the results of in situ survey (dots) and with the surface calculated according to the model of Savage and Smith (1986)



The proposed model was applied to this case history using the values suggested by Savage and Wasowski (2006). The results obtained by the proposed model are here compared with the results, obtained from in situ survey and on the base of Savage and Smith model as reported in Savage and Wasowski (2006) (Fig. 9). It is noteworthy that the calculated failure surface fits quite well the surface deriving from in situ surveys as well as that by Savage and Wasowski.

Conclusions

A simple analytical model for the evaluation of the compressive passive failure surface at the toe of landslide modelled by infinite slope method is here presented. The mechanical behaviour of soil is modelled according to a Mohr Coulomb failure criterion.

The model is theoretically based but quite simple, then it can be implemented into a spread-sheet and it is a useful support to understand the complex subsurface geometry of the toe passive thrust observed in landslides and to calculate the shear strength at the toe of the landslide. The model shows that the shape of the passive thrust failure surface is really sensitive to shear strength parameters.

It can be a useful tool to understand landslide behaviours and mechanisms and also to estimate the stress state at landslide toe, besides the contribution of the toe to the safety of prevailing longitudinal dimension landslide.

To validate the model, it was used to interpret the results obtained in a case study, where passive failure surface at the toe of the landslide have been reconstructed on the base of a detailed in situ survey, returning really

interesting results highly fitting to the results of in situ surveys.

The result obtained by the presented model agrees with that obtained by Savage and Smith (1986) model, but using a completely different and simpler approach. Differently from Savage and Smith model, the proposed approach can be implemented on a simple spreadsheet without a finite element approach, immediately returning the results. The proposed model made it also possible to evaluate the contribution of the passive toe thrust to the stability of the instable masses.

References

- Lancellotta R (2004) Geotecnica. Zanichelli Ed, Bologna, 496p. ISBN 8808076539
- Savage WZ, Smith WK (1986) A model for the plastic flow of landslides: U.S. Geological Survey professional paper 1385
- Savage W, Wasowski J (2006) A plastic flow model for the Acquara-Valdoncello landslide in Senerchia, Southern Italy. Eng Geol 83:4–21
- Sdao F, Simeone V (1996) Fasi di attivazione e maturità geomorfologica di due frane tipo colata nei pressi di Campomaggiore vecchio (Basilicata). Geol Appl e Idrogeol 21:153–168
- Sdao F, Simeone V (1997) Activation phases and geomorphic maturity of two earth-flow slides in Southern Italy. Landslide News 10:25–27
- Simeone V, Sdao F (2002) Modelling of the geomorphic characteristics of the toe accumulation zone of earth-flow landslides. In: Proceedings of 9th congress of the international association for engineering geology and environment (IAEG 2002), Durban, 16–20 Sept 2002, pp 1360–1367
- Urciuoli G (2002) Strains preceding failure in infinite slopes. Int J Geomech 2(1):93–112



Recovery of Strength Along Shear Surfaces in Clay Soils

Angelo Doglioni and Vincenzo Simeone

Abstract

The residual shear strength as operative strength along the shear surface is commonly used for analyzing the stability of reactivated landslides. On this base, it is not possible to have brittle failure or progressive failure mechanisms. In fact, these kinds of phenomena claim for a recovery of strength along the shear surface, which is due to ageing effects during the quiescence time. Several tests on clay samples were performed using Bromhead ring shear apparatus to verify the presence of shear strength recovery. Tests showed that recovery of strength are present along the shear surface. Moreover, they proved the stress-strain behavior is characterized by a brittle failure after that the strength, along the shear surface, falls again to the residual value.

Keywords

Residual strength • Ageing • Recovery of strength • Shear surface • Quiescent landslide • Clayey soils • Thixotropy

Introduction

The study of stability of reactivated landslides is usually based on the assumption that along the failure surface the operative strength is the residual one or a near value. In fact, during previous landslide movements, the strength along the shear surface falls down from the peak value to the residual one (Skempton 1964, 1985).

According to this assumption, the reactivation of quiescent landslides does not allow for progressive failures, since the minimum shear strength shows along the whole shear surface. So it is not possible that reactivation of quiescent landslides can occur with brittle failure and progressive failure mechanisms. In fact, along all the shearing surfaces the minimum strength has just been reached. It is thus necessary to assume a recovery of strength along the shear

surface of landslide during the quiescence time to explain how reactivation can occur with brittle or progressive failure. Then, it is possible also to explain how landslide close to limit equilibrium conditions can be stable for long periods, without being subject to continuous reactivation (Simeone 1993a, b).

Recovery of strength along shear surface also contributes to explain the observed delay (D'Elia et al. 1985; Cotecchia 1986) during the reactivation of old landslide in clayey materials after seismic shocks. In fact the delay can be considered as the time necessary to the development of progressive failure.

It is well known that remolded clay left quiescent is subject to an increment of stiffness and shear strength with time (Skempton and Northey 1952). This also happens if clay material is not subject to variation of volume or water content.

When residual strength conditions occur, clayey particles assume an iso-oriented texture, corresponding to the lower value of shear strength (Skempton 1964, 1985; Lupini et al. 1981). Therefore, it is necessary to suppose a structural rearrangement during the quiescence period, to get recovery

A. Doglioni (✉) • V. Simeone
Engineering Faculty of Taranto, Technical University of Bari, viale del
Turismo 8, Taranto, Italy
+390994733204
e-mail: a.doglioni@poliba.it

of strength along shear surfaces where residual strength has been reached.

Along a shear surface in clay soils, when the landslide movement stops, clay particles can flocculate into a more stable different texture with a low energy level. Flocculating clay particles evolve into a different structure, which can have a higher value of shear strength. This allows for a recovery of strength along the shear surface. During the quiescence period arrangements of clay particles evolve toward the minimum energy texture, which can be different with respect to the minimum strength texture, as function of the clay mineralogy and of the chemistry of pore water.

The phenomenon of shear strength and stiffness increasing with time is broadly defined as thixotropy by modern scientific literature. However, the word “age hardening” should be strictly used (Mitchell 1961; Schmertmann 1992) to describe this phenomenon. This is typical of many soils, when they have been reworked and then left resting.

During their experimental study on thixotropic phenomena, Osipov et al. (1984) observed recovery of strength at constant volume and water content conditions in diluted suspensions of clay; comparing the value with the lowest strength measured when the system undergoes vibrations.

Simeone (1993a, b, 2007) and Guerricchio et al. (1996) using a Bromhead ring shear apparatus observed recovery along shear surface in clayey soil for different clays from South Italy. Also Gibo et al. (2002), Angeli and Gasparetto (2003), Angeli et al. (2004), and Carrubba and Del Fabbro (2006) got similar behaviours in clayey samples.

Aim of this work is to better evaluate this phenomenon by mean of laboratory tests as well as its main variables.

Testing Procedure

Several tests on clay samples were performed using Bromhead ring shear apparatus (1979) at the Engineering Geology laboratory of the Engineering Faculty of Taranto of the Technical University of Bari (Italy). The choice of this apparatus is related to the possibility of quite well simulating what happens, along the shear surface of a landslide, during a quiescence period, where the stresses are constant and there is no movement. This simulation scenario is arranged by not releasing the dynamometrical rings during the break in the shear processes, and then leaving the sample in a stress state close to that, which it finds by itself during the shear processes.

Tests were undergone, using Italian marine blue clay samples of medium plasticity (LL = 45 %; FC = 42 %). Moreover, different values of the normal stress were assumed, a long leaching process varied pore water chemistry.

Samples were prepared using remolded clay mixed with water, till the complete destruction of the original texture, to obtain a slurry with a consistency index of about 0.5. This consistency is a good compromise between the workable exigencies of samples and the problem of avoiding excessive extrusion of material from the apparatus during the loading phase. The normal load was gradually increased to reach the chosen value. The sample is kept under vertical load for 2 or 3 days. Either during its consolidation and during its shearing, the sample should always be completely saturated and covered with water to avoid its drying. The rotation is started with the lowest velocity enabled by the apparatus (0.024 mm/min in all the tests) and the sample has a thickness of 5 mm and is drained at the top and at the bottom, so that the test can be considered fully drained and “rate effects” can be avoided. After a sufficient shear movement to assure (under drained conditions) the reaching of a quite constant strength (residual strength or a near value) the test is stopped and the sample left in the shearing apparatus.

During this phase, the loading rings were not unloaded, so that the sample kept a stress status closer to that in which it finds itself during the shearing phase. This is a procedure, which simulates what happens along the shear surface of a landslide movement when the movement ends. In this particular scenario, the normal stress remains as uniform as the shear stress. After quiescence time of different durations, the test is restarted without modifying the frequency of measuring the strength along the shearing surface, to evaluate the stress–strain behavior of clay. The test is continued until a steady value of the shearing strength is reached again. Then, the shear movement is stopped again for a different time and the test is repeated with the same approach. Then, it is possible to evaluate the recovery of strength, related to different periods of shear movement stop.

Test Result

The test showed that recoveries of strength are present along the shear surface and that the stress–strain behavior is characterized by a brittle failure, after that the strength along the shear surface falls again to the residual value until there is movement along the shear surface (Fig. 1). The recovery of strength is formulated as a ratio between the residual shear strength and the increase of strength obtained during the quiescence time, Fig. 2. The amount of shear strength recovery is function of the quiescence time and it linearly grows up with the logarithm of the quiescence time according to the previous results by Simeone (1993a, b, 2007).

It is noteworthy that during the stop phases, for all the tests, no relevant settlements have been measured. It means

Fig. 1 Recovery of strength measured for a sample of blue clay

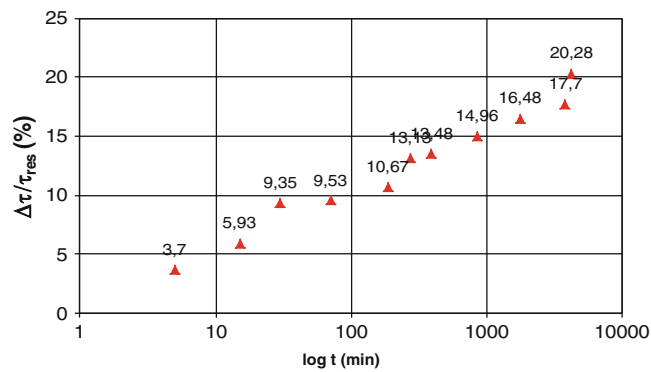
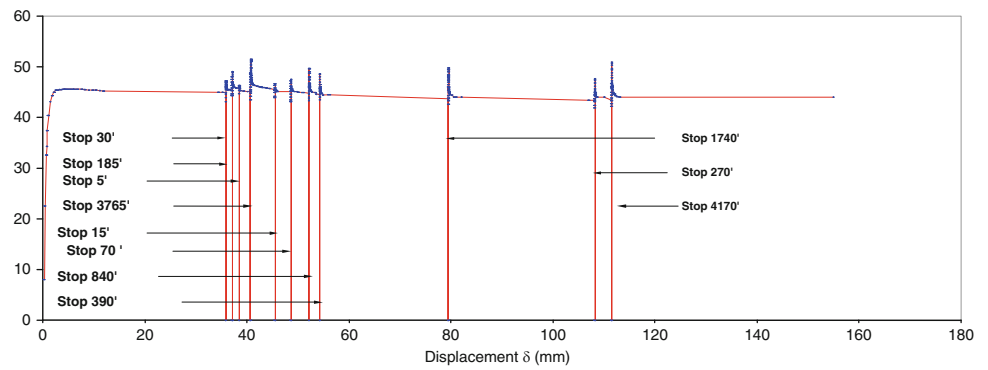


Fig. 2 Increase of the percentage strength recovery measured

that it is not possible to depute the obtained recovery of strength to volume changes of the sample. It is not assumable to attribute the obtained recovery of strength to density increases or to particle arrangements, due to spacing reduction among the particles and related to secondary compression (i.e. the solid skeleton distortion under a constant effective stress). This confirms the thixotropic-ageing nature of the phenomenon. Significant recovery of strength was obtained even after very short stop times (order of minutes) of the shear.

Different specific aspects of the recovery of strength were analyzed with different tests. At first, the influence of the normal stresses was analyzed, to consider the influence of normal stress on the amount of the recovery of strength (Fig. 3).

The blue clay was tested with three different value of the normal stress. Three values of the normal stress were assumed, corresponding to surficial medium and deep-seated landslides: 30, 100 and 750 kPa. The amount of the recovery of strength is expressed as a function the normal stress. Test results show that the amount of strength recovery is much more severe for low normal stress, while it is quite low when the normal stress is high.

This is probably due to the fact that recovery of strength is related to the rearrangement of the particles. This is less easy at high normal stress and then the system of the particles is

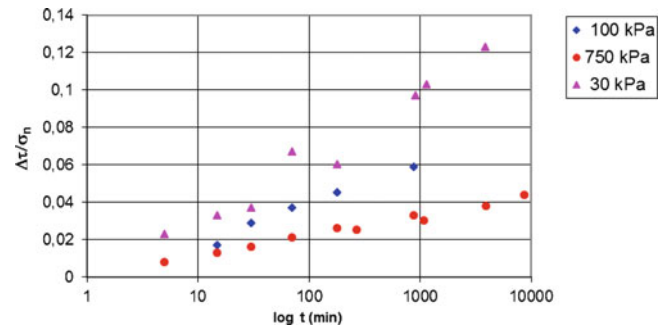


Fig. 3 Recovery of strength for a blue clay for different values of the normal stress

strongly conditioned. Moreover, the influence of the electrochemical forces, that made it possible the particles rearrangements, has a lower influence.

It was also investigated the stress–strain behavior after each stop to obtain information on the brittleness and the stiffness of the material along the shear surface. The tests returned that for low normal stress (30 kPa) the stress–strain behavior is characterized by high brittleness and stiffness (Fig. 4).

For high normal stress (750 kPa) both brittleness and the stiffness are lower (Fig. 5).

The duration of the quiescence period does not relevantly affect stiffness and the stress–strain behaviour. Figure 6 shows a comparison of the stress–strain behavior after a stop of about 900 min for different values of the normal stress. Stiffness and brittleness are conditioned by the same factors. For low normal stress, the stiffness and the brittleness are higher. When normal stress increase there is a decrease of stiffness and of brittleness.

Finally the effect of the chemistry of pore water fluid is investigated. The clay used for the tests is a marine clay with a high content of salt and carbonates. The clay sample experienced prolonged leaching procedure, to remove part of the salt and of carbonate that can relevantly affect the residual shear strength (Di Maio 1996; Hawkins and Mc Donald 1992). The stress–strain behavior of the normal clay sample was compared with the behavior of leached clay

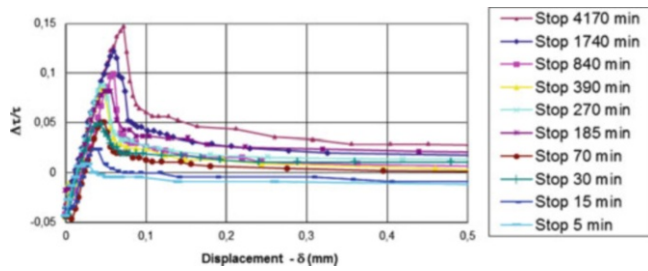


Fig. 4 Stress-strain behaviour for different stop period for a normal stress of 30 kPa

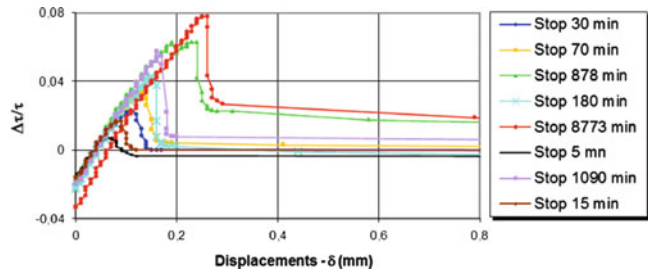


Fig. 5 Stress-strain behaviour for different stop periods for a normal stress of 750 kPa

sample (Fig. 7). The leaching procedure seems to have a really small influence on the amount of strength recovery and on the stiffness of the material after the stop, even if causing a relevant decrease of brittleness.

The final investigated aspect is the influence of plasticity of the involved clay. A sample of bentonitic clay (LL = 192) is accounted, which was tested according to the aforementioned procedure. The percentage of recovery of strength obtained is higher than that obtained for the blue clay of medium plasticity. Figure 8 shows a comparison between the percentage of shear strength recovery of blue and bentonitic clay, obtained at the same normal stress (750 kPa).

It confirms the assumption of high percentage of shear strength recovery for a high plasticity clay.

Conclusion

The presented study is aimed at verifying the existence of recovery of strength along shear surface in clayey soils and to analyse some variables affecting this phenomena and the brittleness consequence of these recovery of strength. On this premise, it is possible to justify the reason why often reactivation happens according a brittle or progressive failure, which cannot normally occur if along the whole failure surface the only available strength is the residual one.

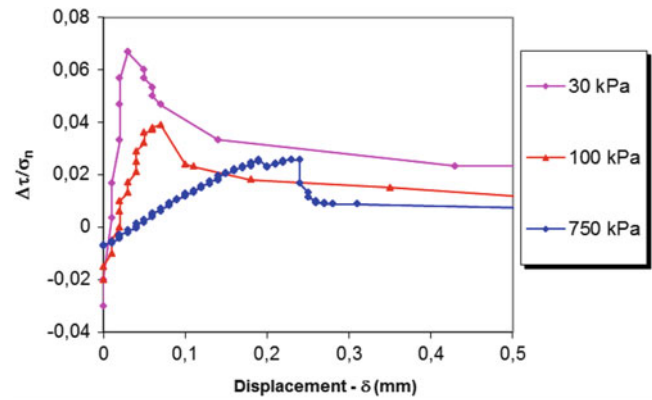


Fig. 6 Effects of normal load on stiffness and brittleness behaviour for a blue clay. Quiescence period is 900 min for each test

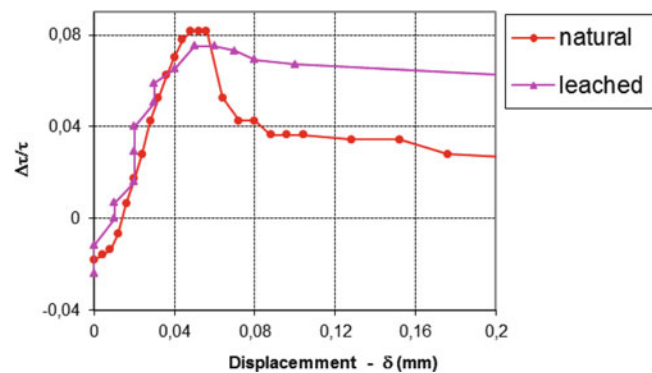


Fig. 7 Effects of leaching processes on shear strength recovery and on stiffness and brittleness

Tests results proved the amount of recovery of strength in percentage increases with the time of quiescence according to a linear relation. The amount of the recovery of strength is strongly related to the normal stress. The higher is the normal stress the lower is the recovery of strength. The amount of the strength recovery increases with the plasticity of clay and in some way also with the salt content in pore water. These kind of behaviour are likely due to the fact that this kind of phenomenon is related to the electrochemical forces between clay particles and pore water. When electrochemical forces have a more relevant role than mechanical forces (low normal stress; high plasticity clay) for the interaction between clay particles, there is higher recovery of strength. In fact, clay particles have a higher possibility in the rearrangements of their texture of obtaining stiffer structures. When the mechanical forces between clay particles are higher than electrochemical one (high normal stresses, leached clays, low plasticity clay) it is difficult to have good clay particle rearrangements and recovery of strength are less relevant.

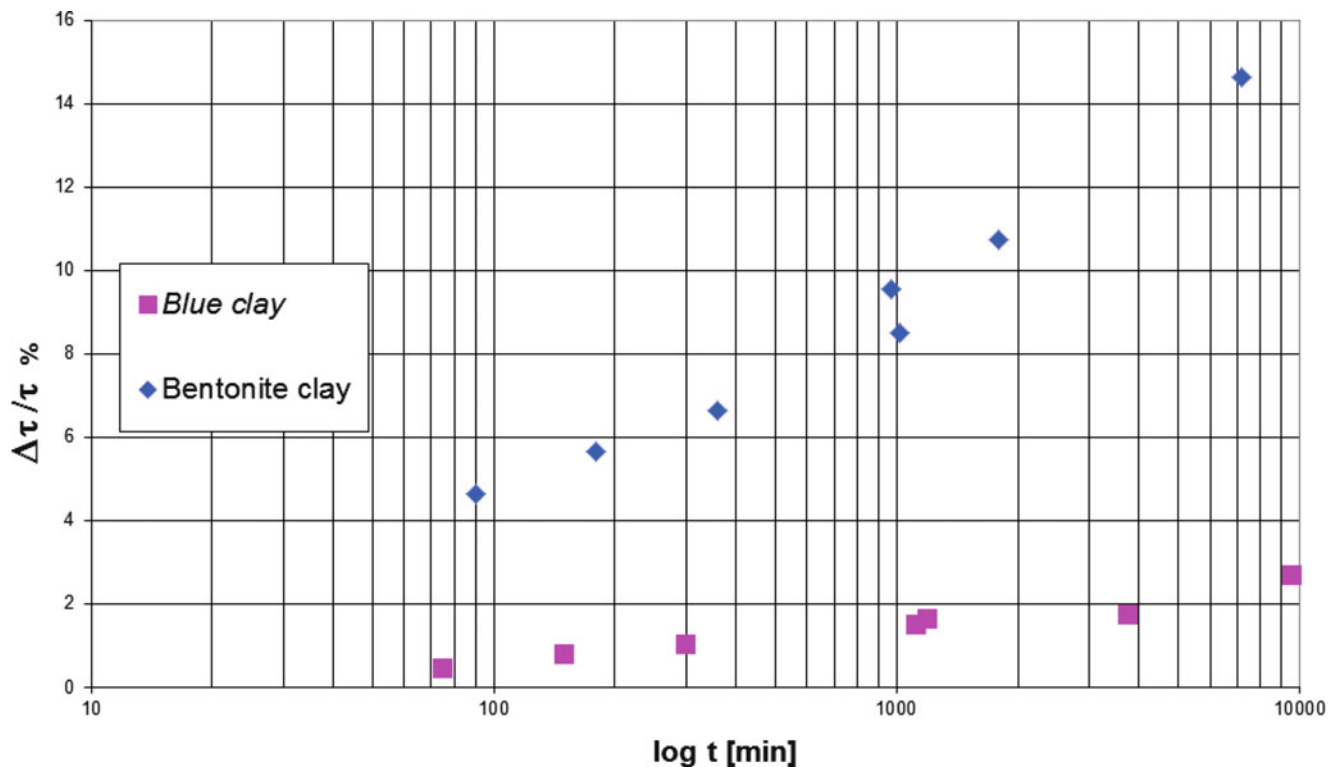


Fig. 8 Recovery of strength along the shear surface for soil with different plasticity for a normal stress of 750 kPa

Analysing stress–strain behaviour after the recovery of strength, stiffness and brittleness are conditioned by the same variables. For low normal stress the stiffness and the brittleness are higher. When normal stress increase there is a decrease of stiffness and of brittleness. The duration of the quiescence period does not significantly affect stiffness and brittleness.

Acknowledgments We wish to thank Mr. Valerio Del Prete and Mr. Emanuele Fontana, who during their master Thesis work at the Engineering Faculty of Taranto, cooperated to arrange the tests presented by this work.

References

- Angeli MG, Gasparetto P (2003) Simple mechanisms for strength regain on the slip surface of stop-start mudslides. IC-FSM2003, vol 2, Sorrento, 11–13 May 2003, pp 151–158
- Angeli MG, Gasparetto P, Bromhead EN (2004) Strength-regain mechanisms in intermittently moving slides. In: Proceedings of the 9th international symposium on landslides, vol 1, Rio de Janeiro, Brasile, June 2004, pp 689–696
- Bromhead EN (1979) A simple ring shear apparatus. *Ground Eng* 12(5):40–44
- Carrubba P, Del Fabbro M (2006) Resistenza residua alla riattivazione del flysch di Corrons. *Rivista Italiana di Geotecnica* 1:28–51
- Cotecchia V (1986) Ground deformations and slope instability produced by the earthquake of 23 November 1980 in Campania and Basilicata. In: Proceedings of the international symposium on engineering geology problems in seismic srea, vol 5, Bari, pp 31–100
- D’Elia B, Esu F, Pellegrino A, Pescatore TS (1985) Some effects on natural slope stability induced by the 1980 Italian earthquake. In: Proceedings of the 11th international conference on soil mechanics and foundation engineering, vol 4, San Francisco, pp 1943–1950
- Di Maio C (1996) The influence of pore fluid composition on the residual shear strength of some natural clayey soils. In: Proceedings of the 7th international symposium on landslides, vol 2. Balkema, Trondheim, pp 1189–1194
- Gibo S, Egashira K, Ohtsubo M, Nakamura S (2002) Strength recovery from residual state in reactivated landslide. *Geotechnique* 52(9):683–686
- Guerricchio A, Melidoro G, Simeone V (1996) Le grandi frane di Petacciato sul versante costiero adriatico (Molise). *Mem Soc Geol Ital* 51:607–632
- Hawkins AB, Mc Donald C (1992) Decalcification and residual shear strength reduction in Fuller’s Earth clay. *Geotechnique* 42(3):453–464
- Lupini JF, Skinner AE, Vaughan PR (1981) The drained residual strength of cohesive soils. *Geotechnique* 31(2):181–213
- Mitchell JK (1961) Fundamental aspects of thixotropy in soils. *J Soil Mech Found Div Proc ASCE* 126(1):1586–1620
- Osipov VI, Nikolaeva SK, Sokolov VN (1984) Microstructural changes associated with thixotropic phenomena in clay soils. *Geotechnique* 34(2):293–303
- Schmertmann JH (1992) The mechanical aging of soils. *J Geotech Eng* 117(9):1288–1330
- Simeone V (1993a) Recovery of strength along shear surface in clay soils, where residual strength has been reached as a consequence of previous movements. In: 7th young geotechnical engineer’s conference, Böblingen, 7–11 Sept 1993, pp 1.34–1.36
- Simeone V (1993b) Recupero di resistenza lungo superfici di taglio in terreni argillosi, Gruppo Nazionale di Coordinamento per gli Studi

-
- di Ingegneria del C.N.R.- Attività di ricerca 1992–1993, pp 153–156
- Simeone V (2007) Recovery of strength along shear surface in clay soils. Geophysical Research Abstract, vol 9. 2007 EGU General Assembly 2007
- Skempton AW (1964) The long-term stability of clay slopes. *Geotechnique* 14(2):75–102
- Skempton AW (1985) Residual strength of clay in landslide, folded data and the laboratory. *Geotechnique* 35(1):3–18
- Skempton AW, Northey RD (1952) The sensitivity of clays. *Geotechnique* 14(2):77–101



Protection from High Energy Impacts Using Reinforced Soil Embankments: Design and Experiences

Alberto Grimod and Giorgio Giacchetti

Abstract

It is nowadays evident the remarkable increase of natural events such as landslides and rock falls. This paper describes and shows how the ground reinforced soil embankments represent an efficient solution for the mitigation of the rockfall related damage. The advantages of these types of construction are that they can resist multiple impacts and their downslope deformation is negligible. This means they can safely be placed close to infrastructure and moreover, they are environmental friendly. In the last few years the Polytechnic of Turin and Officine Maccaferri S.p.A. has developed a new approach to design reinforced soil embankments used for rockfall applications. This approach is based on FEM modelling, full-scale tests results and real experiences utilized to validate the numerical analysis and modelling.

Keywords

Rockfall • Rockfall embankment • High energy impact

Preliminary Remarks

Rockfall embankments are commonly used to stop high energy rockfall phenomena which could damage infrastructures, buildings, inhabited areas, etc.

The embankments built all around the world are made in different ways: by the simple compaction of soil, from gabions, from huge stones, but by far the most effective and reliable method is using reinforced soil, which represent a very good solution from both technical and economical point of view.

In spite of the large amount of installations already made, only in the last few years a new approach has been established to design these reinforced soil embankments using the ultimate limit state and the serviceability limit state philosophy.

This paper will analyse this new design method in order to define the most suitable geometry for a reinforced soil structure based on the energy and the trajectory parameters of the falling rocks.

Reinforced Soil Embankments

The rockfall embankments are made as ordinary reinforced soil structures (RSS).


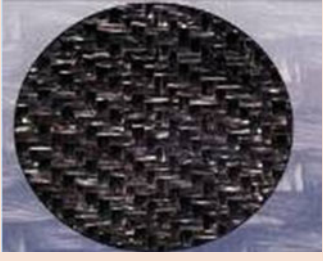

From a geotechnical point of view RSSs are composed of soil and reinforcing elements which help to distribute tensile stresses. These reinforcements are normally located horizontally during the installation phases, and they are wrapped at the edges of the structure to enclose layers of soil. The soil is compacted in layers of nominal 300–350 mm thickness.

In this way, the stresses on the RSS, due to the increasing of loads, are absorbed by the tensile strength of the reinforcements which are mobilized through the friction with the soil. At the same time, the compacted soil can resist to the compression stresses linked the vertical loads. Rockfall

A. Grimod (✉)
Alpigeo Consultant, Via Barozzi 45, Belluno, Italy
e-mail: alberto.grimod@maccaferri.com

G. Giacchetti
Maccaferri Technical Department, Bologna, Italy

Table 1 Type of reinforces used on the RSS

Reinforce name	Typical tensile strength	Picture
Geogrid	Up to 1,300 kN/m	
Geotextile	Up to 250 kN/m	
Double twist wire mesh	Up to 60 kN/m	

embankments are bi-facial reinforced soil structures with a vegetative or a gabion external facing (Table 1).

The most important advantages associated with reinforced soil embankments, are listed below:

1. The foundation surface is reduced because the facade inclination increases from 30°–40° to 65°–90° (Fig. 1);
2. The amount of soil necessary to build the reinforced embankment is around 2–2.5 times less than the volume used for normal soil embankment;
3. The risk that a boulder overcomes the embankment after the impact is reduced because of the high inclination of the mountain side facing, as shown in Fig. 2

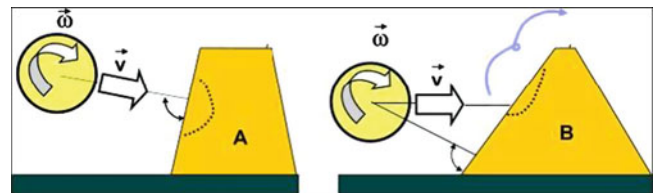


Fig. 1 The block has not enough rotational energy to overcome the embankment because reinforced embankments have 65°–90° mountain side face inclination

The Researches

Polytechnic of Turin, supported by Officine Maccaferri S.p.A., has developed a simple design procedure to size the geometry of the rockfall embankments.

This method is based on a research that, by utilizing full-scale tests, numerical modelling using the Finite Element

Method (FEM), and real case histories, is able to give a tool that can be easily used by the designer of these structures as a guide line.

The full-scale tests were carried out by crashing concrete blocks, with variable mass (from 5,000 to 8,700 kg) and a speed, measured at the impact time, of 31 m/s, against embankments built by sand and gravel and reinforced with polymeric geogrids.

The dimensions of the tested ground reinforced embankments were: height = 4.2 m, base foundation = 5.0 m,



Fig. 2 Effect on downslope side of the reinforced embankment impacted during full-scale tests

facing inclination = 67° and geogrids vertical distance = 0.60 m.

These tests have shown that the impact of a block produces two main effects on the structure: the creation of a hole in the upslope side, and the sliding on the downslope side of the strata, defined by the geogrids located close to the impact point. Table 2 shows the summary of the results of the full-scale tests:

The numerical analyses are used to know and to predict the behaviour of the impacted embankments in a more economical way compared to the full-scale tests.

They have been done, by the Polytechnic of Turin, with a commercial code (ABACUS/Explicit), which use a 3D Finite Element Method (F.E.M.) based on the “central difference method” algorithm. With this tool all the dynamics aspects of the rock impact and their consequence on structures have been considered.

The models consider embankments composed of sand and gravel reinforced by a metallic double twist wire mesh, which is the typical reinforcement used on the Maccaferri Embankment System, called Terramesh (Fig. 3 and 4).

During simulation the compacted soil was considered as a perfect elasto-plastic material characterised by: density 21 kN/m^3 , Young’s modulus $110,000 \text{ kPa}$, Poisson’s ratio 0.25 , drained friction angle 34° , drained cohesion 0 kPa , flow stress ratio (ratio of the yield stress in triaxial tension to the yield stress in triaxial compression) 0.78 , dilatation angle 0° and yield stress 540 kPa . The presence of water was neglected. The different layers enclosed by the metallic reinforcements have been modelled as single elements, and their contacts have been identified with frictional characteristics and a friction coefficient equal to 0.44 (soil friction angle tangent reduced by 0.65 , which is a reduction coefficient suggested in the Officine Maccaferri technical notes-2005). Moreover, the friction interaction between the soil and the block surface is characterized by a tangential

friction coefficient equal to 0.40 (soil friction angle tangent reduced in a parametric way).

The simulations consider an embankment (height = 6 m , foundation width = 6.30 m , facing inclination = $67^\circ\text{--}70^\circ$, distance between the reinforcements = 75 cm) impacted by a cubic mass which develops $5,400 \text{ kJ}$ kinetic energy (mass = $12,000 \text{ kg}$; speed = 30 m/s) at 1.20 m from the toe of the structure (Fig. 5).

F.E.M. modelling results show that the impact consequences are limited only on the layers directly involved in the impact, as already observed in the full-scale tests.

The internal embankment area influenced by the block impact is defined by the type of reinforcement. A truncated cone shape is observable and it is planimetrically constituted by an inclination angle ψ of around 45° (Fig. 6).

Moreover, it is possible to note that at the impact time the kinetic energy of the block is dissipated in three different ways:

1. $80\text{--}85 \%$ of this energy is dissipated because of the creation of the hole in the mountain side: plastic dissipation;
2. $15\text{--}20 \%$ of the kinetic energy is dissipated because of the sliding on the downslope side of the layers involved in the impact: friction dissipation;
3. Around 1% is dissipated because of the settlement of the grains of the soil in the impacted surface: elastic dissipation.

It is possible to define the relationship between the impact energy and the volume of the crater made by the block during its crash (Fig. 7). This connection is tightly linked to the type of reinforcement used, which defines a linear coefficient (k) (Fig. 8)

$$A_b \cdot d = k \cdot E_{correct} \quad (1)$$

where:

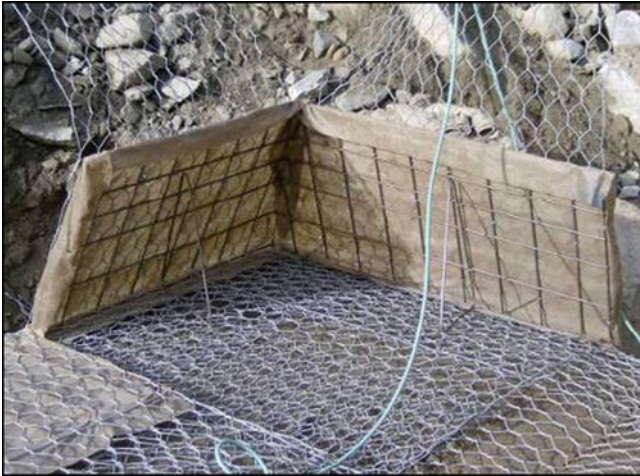
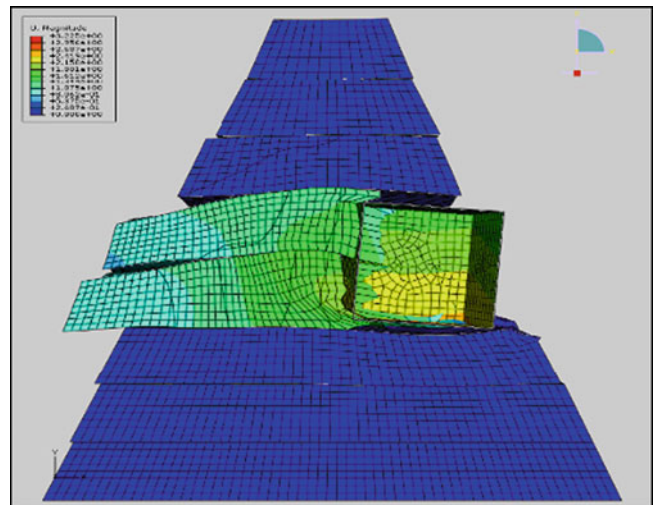
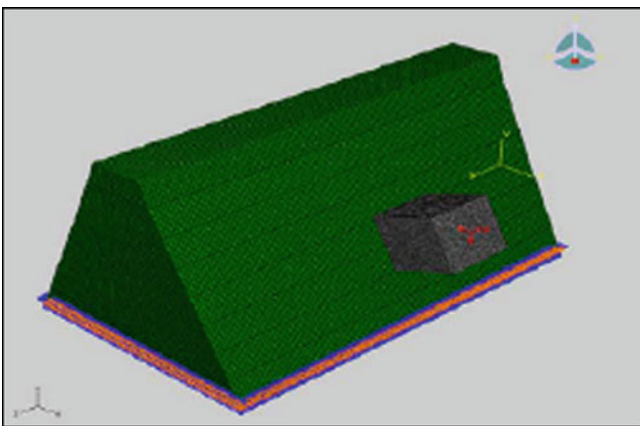
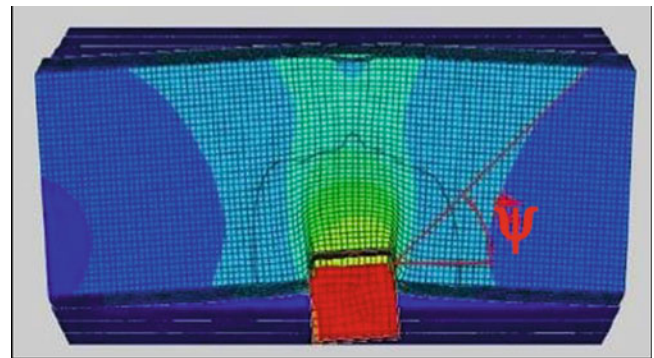
- A_b = block area [m^2];
- d = displacement of the block into the embankment [m];
- k = coefficient function of the reinforcement: inclination of the curve shown in Fig. 9;
- $E_{correct}$ = block kinetic energy corrected taking into account the plastic dissipation [kJ].

Finally, numerical analyses have confirmed that the blocks are not able to pass over the embankment, the only critical situation is when the impact is at the top of the embankment.

To validate the numerical analyses described above a back analysis on a real case history has been done. The embankment taken into account was built in Cogne (Aosta Valley-Italy) with Maccaferri Green Terramesh (GTM) and geogrids placed every 2.19 m (every 3 GTM layers), it is composed of 14 layers 0.73 cm height at 65° ; its total height

Table 2 Full-scale test results

Test	Impact energy	Number of impacts	Upslope max displacement	Downslope max displacement
Test 1	2,500 kJ	1	0.60 m	0.17 m
Test 2	4,500 kJ	3	0.95 m	0.80 m
			1.30 m	1.20 m
			Collapse	–

**Fig. 3** Maccaferri Green Terramesh used to build a rockfall embankment. The reinforcement is a double twist wire mesh**Fig. 5** Contours plot of the numerical analysis made on a Green Terramesh embankment (Oggeri et al. 2009)**Fig. 4** Model of the impact against the rockfall embankment made with double twist wire mesh reinforcements (Oggeri et al. 2009)**Fig. 6** Contour plot of the embankment area involved in the impact (plan view) (Oggeri et al. 2009)

is 10.22 m, the base width is 13.33 m and the top width is 3.81 m.

The soil used belongs to A1, A2, A3, A2-4, A2-5 classes, without elements with a diameter higher than 15 cm (CNR UNI 10006:1963; UNI EN ISO 14688-1:2003), and every compacted 30 cm layers had a compaction grade no lower than 90 % of the Proctor Test (ASTM D 1557:2007).

During the modelling the soil has been analyzed considering the Drucker-Prager law, because it was easier to define it, knowing the Mohr-Coulomb friction angle and cohesion (Table 3).

This rockfall embankment was impacted by a prismatic block (volume = 6 m³; total mass = 15 tons; velocity = 20 m/s; kinetic energy = 3,000 kJ) which penetrated into the embankment by around 70 cm (Fig. 10).

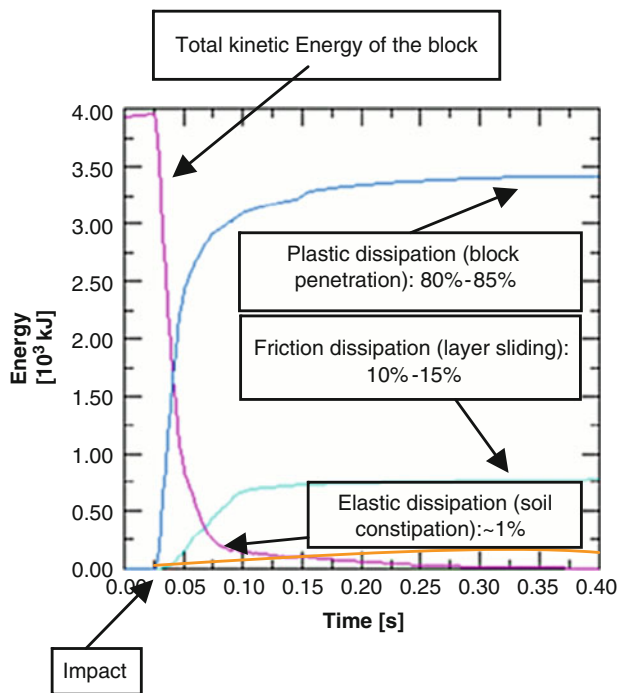


Fig. 7 Representation of the kinetic energy dissipation of the block after the impact

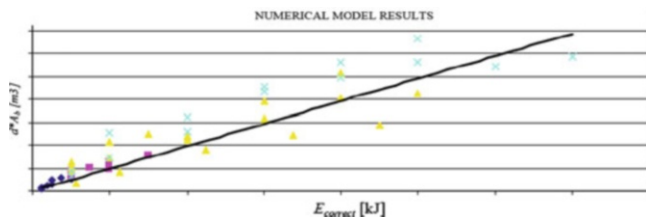


Fig. 8 Linear relationship between energy and crater volume

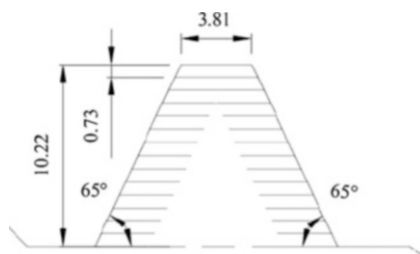


Fig. 9 Typical cross section of the rockfall embankment build in Cogne (Aosta Valley-Ita) which is used for the back analysis

From the analysis of this impact it was possible to define, in terms of the Young’s modulus, the penetration of the block into the structure and the sliding of the impacted reinforced layers on the downslope side (Table 4).

As shown in the table above, the downslope sliding does not depend on the Young’s modulus of the soil. On the

Table 3 Parameters values of the embankment soil used in the back analysis. The Young’s modulus is variable because there were no tests during the embankment construction (Oggeri et al. 2009)

Geotechnical parameter	Value
Density [kg/m ³]	1,900
Young’s modulus [kPa]	75,000; 90,000; 110,000
Poisson’s ratio [–]	0.30
Mohr-Coulomb friction angle	35°
Mohr-Coulomb drained cohesion [kPa]	0
Drucker-Prager friction angle	55°
Flow stress ratio [–]	0.78
Yield stress [kPa]	540



Fig. 10 Block impacted against the GTM embankment and used on the back analysis

Table 4 Maximum values of penetration and downslope sliding for the 3 different values of Young’s modulus considered (Oggeri et al. 2009)

Young’s modulus [kPa]	Upslope penetration [m]	Downslope sliding [m]
75,000	0.74	0.17
90,000	0.71	0.07
110,000	0.62	0.17

contrary, this parameter influences the dimension and the shape of the crater on the upslope side: the penetration can be reduced by improving the soil settlement of the structure.

In any case, it is important to highlight that this parameter is only conventional, because the phenomena during the

impact are neither elastic or linear. Moreover, the values ranges are limited both for the mountain side penetration (from 0.62 to 0.74 m) and the valley side sliding (from 0.07 to 0.17 m).

These results reflect the reality: the analysis method is technically-effective.

The Rockfall Embankment Design Method

The design of any rockfall embankment requires the following checks and analyses:

1. Definition of the rock falling data;
2. Definition of the geometry of the embankment;
3. Structural stability checks.

The parameters of blocks during the falls can be found with commercial software that are able to simulate their trajectories along the slope.

These tools give the possibility to find the dynamic parameter, by knowing the type of soil and the topography of the slope, the mass of the unstable rocks and their positions. Kinetic energy, velocity and height of the block during its falling motion can be calculated at every point of the analyzed slope, also where the embankment will be built (Fig. 11).

By using these parameters it is possible to size the embankment through the design guideline published by the Polytechnic of Turin and Officine Maccaferri S.p.A., according to the researches described in the previous chapter.

The stability checks during the design rock impact have to guarantee that the structure does not collapse because of the effects of the block penetration on the upslope side and/or because of the sliding on the downslope side of the reinforced layers involved in the impact.

The design can be done at Ultimate Limit State (ULS) or at Serviceability Limit State (SLS) to define the geometry of the structure able to stop the design rock masses.

The maximum impact energy absorbed by the embankment ($E_{embankment}$), without any collapse, can be calculated taking into account the downslope sliding of the impacted layers (ξ) and the penetration of the block into the structure (δ) (Fig. 12).

$$E_d - \frac{E_e}{\gamma_e} \leq 0 \quad (2)$$

where:

- E_d = design energy, calculated with the trajectory evaluation;
- E_e = energy level that can be dissipated by the embankment;
- γ_e = safety factor (>1.0).

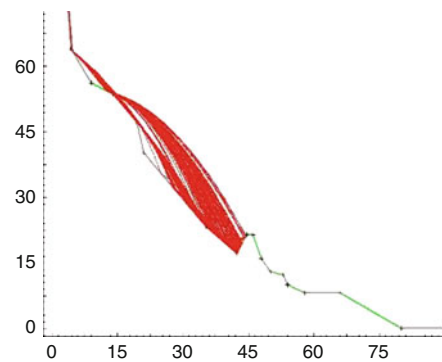


Fig. 11 Example of a rockfall simulation (software RocFall, RocScience Inc.)

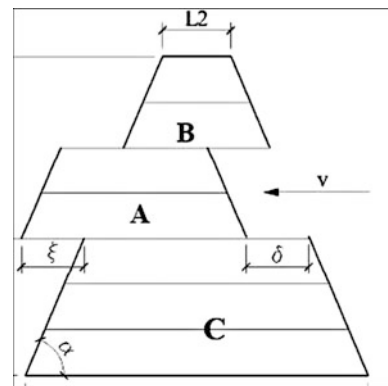


Fig. 12 Simplified cross section of the embankment geometry after the block impact

ULS is determined by evaluating the static stability of the structure after the deformation, by simple equilibrium evaluation: the projection of Block A (see Fig. 13) centre of mass has to be inside the front support of Block C (see Fig. 13), or the projection of the Block B (see Fig. 13) centre of mass has to stay in equilibrium with Block A. The design at Ultimate Limit State does not allow the embankment to stop other blocks with the designed energy level.

SLS conditions have to permit an easy maintenance of the structure, the mountain side penetration and the valley side displacement have to be imposed. In this way, the embankment will be able to stop multiple design blocks impacts. Generally, the parameters mentioned above should not exceed the following values:

- Upslope penetration: lower than 20 % of the embankment thickness at the impact height and not higher than 50–70 cm. For larger displacement it is difficult to repair the structure.
- Downslope sliding: lower than 30–40 cm.

Finally, the height of the embankment has to be defined considering that, as discussed in the previous chapter, blocks can overpass the structure only if they impact at the top of the embankment; this problem can be solved by introducing an adequate safety factor:

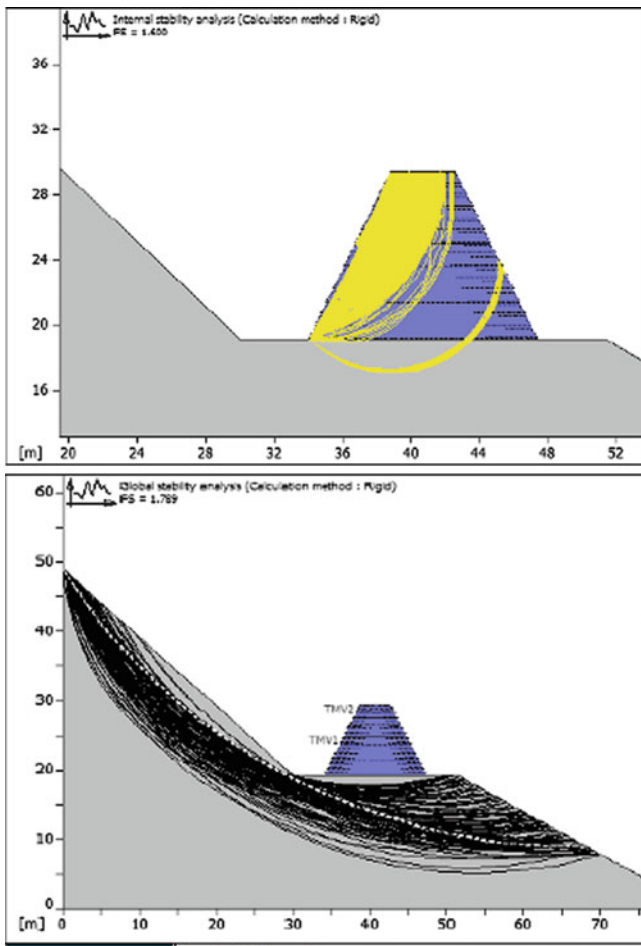


Fig. 13 Internal and global stability check of the embankment (software MacStaRS W, Maccaferri)

$$h_d - \frac{h_i}{\gamma_h} \leq 0 \quad (3)$$

where:

- h_d = design height, calculated with the trajectory evaluation;
- h_i = embankment interception height;
- γ_i = safety factor (>1.0).

Finally, the last step of the embankment design considers the analysis of the embankment from a statical point of view: the global and the internal stability checks have to be done.

These analyses are realized utilizing specific software generally used for the design of Reinforced Soil Structure (RSS) and able to define the type of reinforcement according to the size of the structure and the type of filling ground. For embankments designed with Green Terramesh, it is appropriate to use designed parameters developed by Maccaferri.



Fig. 14 Embankments built along the SR 47 (291 m and 50 m long)



Fig. 15 Embankments built along the SR 47 (291 m and 50 m long) and fill with stones, debris and trees

These checks verify, both in the static and seismic conditions, that the designed structure is stable (Fig. 14) and it does not provoke negative effects on the global stability of the entire slope (Fig. 15) which is overloaded by a new load.

Experience: Cogne Case History

The 5th June 2007 large blocks (larger than 30 m³) impacted on the regional road Aymavilles-Cogne (SR 47) in locality Pont Laval. The road was closed, and the town of Cogne was isolated for few days.

Aosta Valley municipality has decided to build two rock-fall embankments above the SR 47 road, with Maccaferri Terramesh method. The height of both structures is 10.22 m and their lengths are respectively 291 and 50 m.

After a few months from the end of the construction, the smallest embankment was impacted by a landslide with the

collapse of large blocks. One of these blocks was used by the Polytechnic of Turin for the back analysis described in the previous chapter “The researches” (see Fig. 11).

In these last 4 years other rock falls, landslides and avalanches have completely fill the 50 m long embankment on the mountain side with stones, soil, debris and tree trunks. These events have given the possibility to understand that these structures are able to protect structures and infrastructures not only from the high energy rock fall impacts but also from soil landslides, avalanches and debris flows.

Reference

Oggeri C, Peila D, Ronco C (2009) *Analisi numerica del comportamento di rilevati paramassi in terra rinforzata. Relazione finale*



Quantitative Evaluation of Roughness with a 2D Digital Instrument

Fabrizio Mazza, Davide Brambilla, Laura Longoni, Paolo Mazzoleni, Monica Papini, and Emanuele Zappa

Abstract

Roughness of discontinuities, when clean and unfilled, has a significant impact on rock joint mechanical behaviour and, as a consequence, of rock masses. The need to solve ambitious rock mechanics problems encouraged research to study shear mechanism acting at the joint level and to produce sound models to reproduce it. In this framework, roughness measurement allows to gather information about shear strength of rock joints at an acceptable cost.

A brief summary of published approaches and parameters for quantitative roughness evaluation is presented. Then, measures taken on rock samples extracted in a test site placed in the nearby of Esino Lario, 60 km north of Milan, are shown and discussed. The device used on-site to obtain digital replicas of profiles is a laser-camera profilometer, developed in the Department of Mechanical Engineering of the Politecnico di Milano. This device, combining a digital camera and a laser source, uses the principle of laser triangulation to extract a maximum of 746 points/profile. Numerical coordinates obtained by rock joint profiles are submitted to a Matlab® script which computes geometric parameters.

Statistical analysis of gathered data was used to define a minimum number of measures that have to be used to determine roughness of a joint set.

Keywords

Roughness • Shear strength • Joints • Rock mass

Introduction

Rock mass is a complex natural material in which discontinuities of different geological nature disconnect portions of intact rock. A full understanding of its hydro-mechanical behavior is strategic for many engineering applications like stability assessment of rock slopes,

tunnelling, mining, design of dam foundations and nuclear waste disposal facilities. The high complexity of mechanical interactions acting on the two surfaces of joints, and the coupled effects with temperature, water circulation and chemical attack makes joint behaviour almost impossible to be reproducible by numerical or physical models. As a consequence, since the beginning of intense research activity in this field empirical models have been the main target. However such models are not exactly black boxes in which input data are somehow transformed into the output, but rely on simplification of actual physical mechanisms. The simplest roughness model is the famous Mohr-Coulomb law, in which shear strength is provided by cohesion, c , normal load acting on the discontinuity, σ_n , and basic shear angle, ϕ_b :

F. Mazza (✉) • D. Brambilla • L. Longoni • M. Papini
Department of Environmental Hydraulical, Infrastructural and
Surveying Engineering, Politecnico di Milano, P.zza L. Da Vinci 32,
Milan, Italy
e-mail: fabrizio.mazza@polimi.it

P. Mazzoleni • E. Zappa
Department of Mechanical Engineering, Politecnico di Milano,
Via la Masa 1, Milan, Italy

$$\tau_p = c + \sigma_n \cdot \tan(\phi_b) \quad (1)$$

Patton criterion (Patton 1966), specifically developed for rock joints, was the first model that could take into account roughness of discontinuities. The two relations describing shear resistance (2 and 3), are similar to Mohr-Coulomb law, with additional terms representing the inclination angle of asperities, i , the residual friction angle, ϕ_r , and the apparent joint cohesion, c_j . Patton model in fact reproduces the shear resistance of an idealized rock joint in which all the asperities have the same inclination angle. The model is bilinear: for low normal loads (2) the shear resistance is provided by both basic friction angle, ϕ_b , and inclination of asperities, i , then, for high confinement (3), asperities are supposed to break up and only residual friction angle, ϕ_r , and apparent joint cohesion, c_j , provide further resistance. Obviously this model is too coarse to describe accurately the complex behaviour of real rock joints, which is determined by the presence of asperities with different shapes and inclinations.

$$\tau_p = \sigma_n \cdot \tan(\phi_b + i) \quad (2)$$

$$\tau_r = c_j + \sigma_n \cdot \tan(\phi_r) \quad (3)$$

In Barton-Bandis model ([4], Barton 1973; Barton and Choubey 1978) roughness of discontinuities is described by the joint roughness coefficient (JRC), while the ratio between joint compressive strength (JCS) and applied normal stress measures the intensity of applied stresses on the joint walls. JRC is the roughness parameter that has undergone the greatest diffusion among practitioners and it constitutes the base of the ISRM suggested method for roughness quantification (ISRM 1978). It can be obtained by back analysis from shear tests or, more easily, by geometric features of the surface. In this second approach, that is the most interesting for the aim of this work, JRC parameter can be computed in two different manners: (1) by comparing sketch of profiles of the surface with reference ones; (2) by measuring the maximum difference in height from a rigid rod to the rock joint surface, and then analyzing the maximum measured distance with the aid of an abacus. The interesting feature of Barton method is that it can take somehow in consideration complex features of rock surface with a really simple method. On the other hand it is very subjective, especially for the visual comparison approach, and has some intrinsic problems (JRC should be a fully geometric parameter, but in fact it changes if computed with back analysis for different rocks with the same surface shape).

$$\tau_p = \sigma_n \cdot \tan\left(\phi_b + JRC \cdot \text{Log}_{10} \frac{JCS}{\sigma_n}\right) \quad (4)$$

With the development of rock mechanics a method to characterize rock joint roughness with quantitative measures was becoming more and more needed. Digital instruments were found to be an opportunity to measure roughness in a quantitative manner. At the beginning these instruments were used to compute JRC quantitatively. A lot of parameters and relations have been proposed to assure this task, then empirical relations were developed to compute JRC starting from these parameters (Tse and Cruden 1979; Hong et al. 2008). Some of these relations have been developed by regression analysis on the ten reference profiles published by Barton (1973) and, in the authors' opinion, their validity is questionable for two reasons: (1) standard profiles represent "typical" profiles of rock samples for which JRC was computed in back analysis, but there's no way to know how well they represent roughness features of the surfaces; (2) ten profiles are a very little database to calibrate regression curves that should be used to compute JRC for very different situations (different rocks, different applied stresses, etc.). Another huge problem, that affects both relation calibrated on reference profiles and those obtained after test campaigns, is that usually configurations of the measuring systems have not been specified, despite the great sensitivity parameters exhibit to variations of resolution and base length. Some of the parameters proposed over the years to assign a value to roughness are: root-mean square (RMS), RMS of the first derivative (Z2), RMS of the second derivative (Z3), roughness profile index (RP), fractal dimension (D), range and sill of the semivariogram, threshold deep angle (θ^*). A detailed description of these quantities can be found in Hong et al. (2008) and in Kulatilake et al. (2006). Among quantitative roughness evaluation methods it is mandatory to make a distinction between 3D and 2D approaches: while the former guarantees a complete description of joint wall geometry, the latter has the advantage of relying on easy low-cost measuring systems and simple data processing.

Qualitative measures, because of their nature, are prone to be biased and imprecise (Beer et al. 2002); on the other hand even quantitative parameters can provide variable results because: (1) the choice of measuring system configuration (resolution and base length) influences the results; (2) roughness is subjected to spatial and directional variability. Despite these open problems, if properly used quantitative methods are able to provide measures featuring a higher degree of reliability with respect to qualitative ones.

In the last ten years the object of research has moved from objective JRC evaluation accomplished through quantitative measure to the development of new joint models relying on morphological parameters showing an evident correlation with shear strength of discontinuities (Lanaro and Stephansson 2003; Lopez et al. 2003). Lopez et al. measured roughness of fracture surface replicas before the execution of experimental shear tests and then, by means of a multivariate

statistical regression analysis, identified the roughness parameter exhibiting the greater ability in describing joint shear behaviour. Among tested roughness parameter Z_4 , a direction dependent estimator, was the one containing the greatest level of information.

A complete study of shearing mechanisms acting at rock joints allowed Grasselli (Grasselli 2006) to observe that damage was localized in those areas of the surface characterized by the steepest inclination and oriented against the direction of application of the shear stress. On the basis of these observations Grasselli developed a new roughness parameter, r , which is able to catch differences in roughness along different directions. This parameter was then used as a base on which a new shear strength criterion for rock joints was developed. Grasselli's criterion has been subjected to some reviews that lead to its actual form (7).

Roughness parameter, r , is obtained as the ratio between the maximum inclination angle of asperities opposing shear direction, θ^*_{max} , and the quantity $(C + 1)$:

$$r = \frac{\vartheta^*_{max}}{c + 1} \quad (5)$$

The parameter C is obtained by non-linear regression on (6), where A_0 is the percentage of area of the surface opposed to shear direction and A_{θ^*} is the percentage of area opposed to shear direction featuring steepness greater than θ^* . In Grasselli's model (7) peak shear strength is computed taking into account rock tensile strength, σ_t , and an empirical constant, $B = 1.15$. According to Tatone (Tatone and Grasselli 2010), Grasselli's roughness parameter can also be computed on 2D profiles by substituting areas with lengths in the algorithm.

$$L_{\vartheta^*} = L_0 \left(\frac{\vartheta^*_{max} - \vartheta^*}{\vartheta^*_{max}} \right)^c \quad (6)$$

$$\tau_p = \left[1 + e^{-\left(\frac{r \sigma_n}{9A_0 \sigma_t} \right)} \right] \sigma_n \tan(\phi_b + r^B) \quad (7)$$

Materials and Methods

Laser-Camera Profilometer

The goal of the laser-camera profilometer is to obtain the shape of the surface of the rock along linear profiles. The profilometer was designed to obtain a measuring range of about 200 mm and a resolution of 0.1 mm, in order to guarantee at least the same measuring range and accuracy of a traditional Barton comb. The hardware of the profilometer is

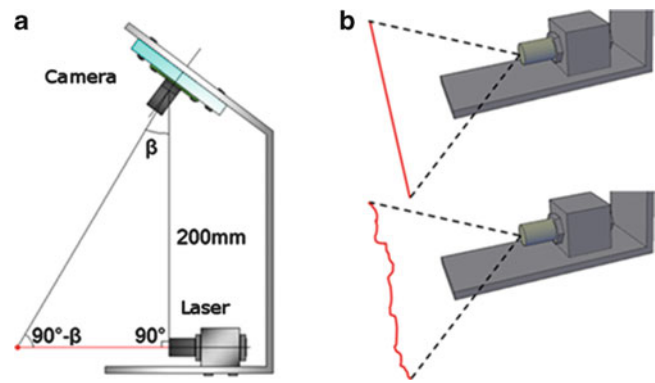


Fig. 1 Laser profilometer: (a) main geometric features; (b) examples of projected laser traces



Fig. 2 A measurement stage: the profile is instantaneously printed on the netbook screen

composed by a camera, a laser source and a support structure (Fig. 1a). The laser has a wavelength of 635 nm (red), a power of 10 mW (class II-M) and a fan angle of 90° . We choose a grayscale USB camera, equipped with a $1/3''$ CMOS sensor (resolution 744×480 pixels) and 6 mm focal length optics. A CMOS sensor has been preferred to a CCD one, because of its better behavior in acquiring the scenes characterized by important brightness variations and because of lower cost. The USB connection between the camera and the PC allows a fast data transmission and a direct connection to the control PC; in this work an Asus EEE netbook was used.

Figure 1b shows the profilometer working principle: the laser source projects a linear pattern on the rock surface to be measured, while the camera acquires the scene. On acquired images the laser line appears as a bright stripe on dark background.

Analyzing the trend of the laser line on the image it is possible, after proper calibration, to measure the shape of the object section illuminated by the laser. In this way the profilometer measures the position in space of each point

of the intersection between the laser and the rock surface (Fig. 2).

Choice of a Roughness Parameter

The output provided by the profilometer is a collection of (x,y) coordinates of points belonging to a scanned profile. These data have to be submitted to a process of analysis to produce values of roughness. Among all different roughness parameters, the choice fell on Tatone's one (Tatone and Grasselli 2010), which takes into account features of the geometry that should be closely related to roughness behaviour, it is direction dependent and it doesn't require heavy computations to be extracted. Tatone proposed also a formula for the computation of JRC values, but actually this formula was developed with a regression analysis on the base of the ten Barton standard profiles and, as it was outlined in the Introduction, such kind of relations are not fully reliable. Despite this, JRC obtained with Tatone's relation can be used as reference values for people usual with this quantity just to get a first idea of the degree of roughness.

Roughness Measurement

Roughness of rock surfaces is a variable quantity with values that can be subjected to conspicuous oscillations from a region to an adjacent one, and this is more evident with 2D measurement techniques. In fact, in case of a non-homogenous surface, profiles are prone to exhibit more differences from one to another with respect to surfaces, because they may intersect or not some particular features of the region of the joint wall under investigation. The direct consequence is that one has to collect a minimum number of profiles to obtain reliable roughness estimation. One of the aims of our work is to define a strategy to compute the minimum number of measures that are needed to obtain reliable roughness estimation.

Eleven samples of Perledo-Varenna formation have been collected on two outcrops placed along the S.P. 65 road which links the towns of Esino and Parlasco, in the province of Lecco, about 50 km North of Milan. Perledo-Varenna is a calcareous formation dated back to the Ladinic stage of Triassic period; in the zone where samples have been gathered it consists of a greyish to blackish mudstone-wackeston in parallel strata featuring a thickness ranging from 10 to 30 cm. The two chosen sites present different structural conditions: samples marked with letter A have been extracted from a zone where strata dip against the slope and, since they were just below the surface, water was allowed to infiltrate and circulate in joints. In the other zone, where dip direction of the strata is almost parallel to the slope, we took samples just

below the surface (marked with letter C) and some metres below the surface (marked with letter B). Along each rock surface specimen we measured roughness on parallel profiles spaced with a constant offset of about 3 mm.

Sufficient Number of Measurements

The opportunity of taking quantitative measures of roughness has highlighted a new problem: spatial variability of roughness. Even on an apparently homogenous natural rock surface, values of roughness can exhibit oscillations from one region to another. It is then straightforward to collect a certain number of measures and to use a central value estimator, like the mean, to give a value to the roughness of the whole surface. To make this estimation accurate enough, a minimum number of measurements have to be used: but how to know if the measurement is accurate enough? A first possible approach consists in setting the minimum number of measurements in correspondence of that number of measures for which the cumulative mean of roughness (7) enters the confidence intervals of the global mean to remain inside there. However this approach can be used only after the execution of a number of measures greater than necessary, otherwise there's no way to a compute a good estimator of the global mean.

$$\hat{Y}_n = \frac{1}{n} \sum_{i=1}^{n \leq N} y_n \quad (8)$$

We then chose to proceed following the approach developed by Hoad (2010). This method consists of computing the confidence intervals on the cumulative mean and to evaluate the precision of the measurement as the ratio between the amplitude of the interval and the cumulative mean:

$$\hat{Y}_n \pm t_{(\alpha/2, n-1)} \sqrt{\frac{S^2(n)}{n}} \quad (8)$$

where α is the desiderate confidence level (5 % in this study), $s^2(n)$ is the unbiased variance estimator of the first n measurement and $t_{(\alpha/2, n-1)}$ is the inverse Student distribution of $\alpha/2$ with $(n-1)$ degrees of freedom. When data are not independent this equation loses validity since both \hat{Y}_n and $s^2(n)$ become biased. To take into account dependence of data, the equivalent number of independent measures is computed according to Malavasi (Malavasi and Blois 2007). Confidence intervals are still computed by (8) after substituting n with n_e :

$$n_e = n \cdot [1 + (n-1)\lambda_c]^{-1} \quad (9)$$

where λ_c is the average correlation of data.

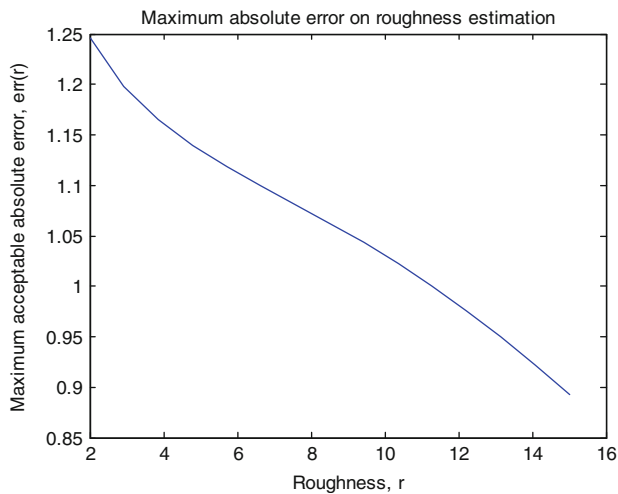


Fig. 3 Upper bound of the absolute error on r

Considering that confidence intervals can increase or decrease in amplitude with increasing the number of measurements, according to the trend of variance, the procedure imposes to continue collecting at least five measurements after the target precision has been reached; this precaution allows to check if precision is still good or if it is necessary to gather other profiles.

During a geological survey it is usual to gather roughness measurements of more than on joint set of the same discontinuity family. In this case the approach that has been shown to compute the roughness of a single surface can be used to compute the average roughness of the joint set with a minimum number of measurements. In cases in which one is interested also to the variation of roughness among surfaces of the same family, that could be the case if results of measurements should be used in numerical models with random sampling of roughness values, one should use the procedure proposed for each surface of the family he/she wants to characterize.

The minimum target precision for the chosen roughness parameter has to be fixed according to the required precision on the shear strength estimation. Considering the moderate degree of approximation of shear models, it can be agreed that a $\pm 5\%$ error on shear strength estimation would be lower than the bias due to restrictive hypothesis and simplifications. If we accept this error on the shear strength we can compute the correspondent maximum error on the roughness parameter. The procedure we used to obtain the maximum acceptable level of approximation on roughness estimation is the following: we fixed three levels of applied normal stress ($\sigma_{n1} = 10$ KPa), ($\sigma_{n2} = 100$ KPa), ($\sigma_{n3} = 1$ MPa), a reasonable value of tensile strength of the rock ($\sigma_t = 10$ MPa) and of the basic friction angle ($\phi_b = 31^\circ$). With these data we computed three $\sigma_n - \tau$ curves. We then obtained their correspondent $\pm 5\%$ error bands and, by inverting (7), an upper

and lower limiting curve of the roughness parameter r for each considered normal stress level. Finally, for each value of r belonging to the range 0–15, we extracted the maximum allowable absolute error as half the difference from the upper and lower acceptable values of r . Results shown in Fig. 3 lead us to fix the maximum absolute error on r at 0.9. Roughness measurements with at least this precision should allow obtaining good shear strength estimations in the considered range of normal stresses and degree of roughness.

Anisotropy of Rock Joint Surface

Previous studies (Grasselli 2006; Tatone and Grasselli 2010; Kulatilake et al. 2006) put in evidence the existence of a certain degree of anisotropy of rock joint surfaces, causing roughness to assume different values depending on the measurement direction. While processing 3D measurements it is possible to extract automatically roughness values for different directions, with a 2D measurement device like the laser-camera profilometer measurement must be done by scanning the rock surface along a minimum number of 4–6 directions that, thanks to the directional sensibility of the chosen roughness parameter, correspond to 8–12 points on the polar plot (Grasselli 2006). This clearly raises the amount of work that should be done to measure a surface with the laser-camera profilometer but, thanks to the rapidity of measurement that is practically immediate, our instrument remains competitive with 3D measurement techniques.

Results and Discussion

The program controlling the profilometer saves coordinates on points belonging to the laser trace in two columns text file. These files are opened in a Matlab® script written on purpose that process them in order to extract roughness values. Before computing parameters, this script allows the user to select the region of the profile that has to be analyzed, since sometimes laser trace is projected onto other objects in the field of view of the camera not belonging to the surface of interest. The program allows comparing results obtained from parallel profiles collected on the same surface to put in evidence the degree of dispersion of measures. Table 1 collects roughness values measured for each samples in the two directions parallel to dip direction of the slope. In Fig. 4 data of sample A1 (direction 0°) are shown together with their cumulative and total means. Roughness values are similar inside each of the considered zones. Samples taken in proximity of rock mass external surfaces show greater roughness values, which have to be ascribed to surface damaging caused by external agents.

Table 1 Comparison between the global mean of measured roughness values and the cumulative mean of the minimum number of measures; the last column shows values of the relative error (assuming global mean as the true value)

Sample	N	\hat{Y}_N	n^*	\hat{Y}_{n^*}	ε
A1	25	8.66	10	8.56	-1.23 %
A2	29	8.60	16	8.97	4.28 %
A3	26	8.66	10	8.04	-7.24 %
A4	26	8.15	10	8.52	4.51 %
B1	48	5.47	8	5.79	5.78 %
B2	55	4.95	10	5.37	8.48 %
B3	30	4.85	10	4.77	-1.60 %
B4	46	4.47	8	4.52	0.99 %
C1	52	10.69	10	9.80	-8.36 %
C2	42	9.37	8	9.26	-1.16 %
C3	38	8.73	8	8.72	-0.05 %

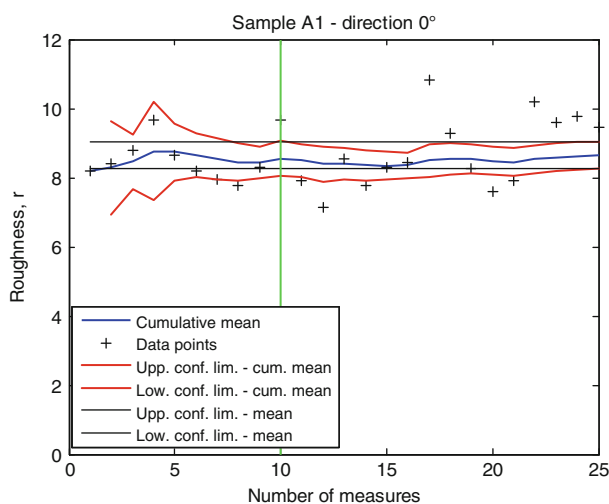


Fig. 4 Sample A1: comparison between measured data points, global mean and cumulative mean. Target precision is reached in correspondence of the vertical bar

One of the objectives of this work was to answer the question “how many measurements do I need to be confident with roughness estimation?” The last three columns of Table 1 show the minimum number of measurements, n^* , computed following the approach introduced in the previous chapter, the corresponding roughness values, \hat{Y}_{n^*} , and the relative differences between these value and those computed using the total number of measurements. It is possible to observe that sufficient precision is reached always with less than 10 measurements, and that relative errors are always less than 9 %.

Conclusions

Rock joint surface specimens have been measured with a 2D laser-camera profilometer developed by the Department of Mechanical Engineering of the Politecnico di Milano. Data points have been processed with a Matlab®

script that allowed to extract roughness parameters r . The minimum number of profiles to be measured was computed following the approach of Hoad et al. (2010), consisting of a continue gathering of profiles until a target precision is reached.

Thanks to the simplicity of this procedure, it will be included in the profilometer control program to make the user constantly informed about precision reached by the measurement. Currently profilometer acquisition is governed by a button that the user pushes to scan a profile. To make measurement more rapid the acquisition software will be modified to let the profilometer gather a set of profiles while the user moves it over the surface with a previously set velocity. This will allow to substantially increase the productivity of the laser-camera profilometer.

References

- Barton N (1973) Review of a new shear-strength criterion for rock joints. *Eng Geol* 7(4):287–332
- Barton N, Choubey V (1978) The shear strength of rock joints in theory and practice. *Rock Mech Felsmechanik Mécanique des Roches* 10(1–2):1–54
- Beer AJ, Stead D, Coggan JS (2002) Estimation of the Joint Roughness Coefficient (JRC) by visual comparison. *Rock Mech Rock Eng* 35(1):65–74
- Grasselli G (2006) Manuel Rocha medal recipient shear strength of rock joints based on quantified surface description. *Rock Mech Rock Eng* 39(4):295–314
- Hoad K (2010) Automated selection of the number of replications for a discrete-event simulation. *J Operat Res Soc* 61(11):1632–1644
- Hong E, Lee J, Lee I (2008) Underestimation of roughness in rough rock joints. *Int J Numer Anal Methods Geomech* 32(11):1385–1403
- ISRM Commission on Standardization of Laboratory and Field Tests (1978) Suggested methods for the quantitative description of discontinuities in rock masses. *Int J Rock Mech Min Sci & Geomech Abstr* 15(6):319–368
- Kulatilake PHSW, Balasingam P, Park J, Morgan R (2006) Natural rock joint roughness quantification through fractal techniques. *Geotech Geol Eng* 24(5):1181–1202
- Lanaro F, Stephansson O (2003) A unified model for characterisation and mechanical behaviour of rock fractures. *Pure Appl Geophys* 160(5–6):989–998
- Lopez P, Riss J, Archambault G (2003) An experimental method to link morphological properties of rock fracture surfaces to their mechanical properties. *Int J Rock Mech Min Sci* 40(6):947–954
- Malavasi S, Blois G (2007) Influence of the free surface on the flow pattern around a rectangular cylinder. In: 9th international symposium on fluid control measurement and visualization 2007, FLUCOME 2007, Tallahassee, 17–19 Sept 2007, p 1140
- Patton FD (1966) Multiple modes of shear failure in rock. In: *Proceedings of the 1st congress of international society of rock mechanics*, Lisbon, pp 509–513
- Tatone BSA, Grasselli G (2010) A new 2D discontinuity roughness parameter and its correlation with JRC. *Int J Rock Mech Min Sci* 47(8):1391–1400
- Tse R, Cruden DM (1979) Estimating joint roughness coefficients. *Int J Rock Mech Min Sci & Geomech Abstr* 16(5):303–307



Use of SAR Interferometry for Landslide Analysis in the Arno River Basin

Marcello Brugioni, Bernardo Mazzanti, Giovanni Montini, and Lorenzo Sulli

Abstract

Deformation data obtained by differential interferometric analysis of radar images acquired by the satellite platform were used as a useful support in the definition of geometry and state of activity of landslides for identifying areas at risk and defining priorities for action. The interferometric data derived from radar images acquired by the ERS, RADARSAT and ENVISAT satellites were processed and used for the implementation of the database of landslides in the Arno basin (Tuscany, Italy). This database identifies some 25,500 landslide sites, of which about 10 % have risk elements, such as buildings, infrastructures and so. Of these, over 90 % present information about the movements that have permitted to perform statistical analysis of the velocity values recorded by satellites, reconstruct the displacement vector in the EWZN plane and obtain important information concerning the activity of landslides. The results were organized into a web-GIS project that represents a very important tool for river basin planning.

Keywords

SAR interferometry • Persistent scatterers • Landslides • Natural hazards • GIS analysis

Introduction

The advent of advanced interferometric techniques, developed since the 1990s, led to a rapid evolution of the potential of multitemporal analysis of radar images acquired by satellite platform for the examination of the phenomena of deformation of the ground (Ferretti et al. 2001, 2007; Colesanti et al. 2002; Ferretti and Hanssen 2002; Colombo et al. 2003a; Costantini et al. 2008, 2009).

The nature of the Permanent Scatterers (PS) and the characteristics of the satellite acquisition system provide useful information in the analysis of slow movements, which do not deviate too much from the EW directive and are located in relatively populated areas (Hilley et al. 2004; Strozzi et al. 2005; Meisina et al. 2007; MINAMB 2009).

Algorithms that allow to significantly increase the information in homogeneous areas of low reflectivity have been recently developed (Ferretti et al. 2011).

The use of such techniques for ground deformation analysis has proven particularly useful as an aid in determining the status of landslide risk (Catani et al. 2006; Colesanti and Wasowski 2006; Notti et al. 2009; Poggi and Riccelli 2009; Righini and Casagli 2009; Notti 2010), in particular the detection of instability in areas subject to deep-seated gravitational slope deformations (DGPV) that, following the considerable depths of the sliding surface, are difficult to monitor using traditional tools (Ambrosi and Crosta 2005; Crosta et al. 2009).

A very important feature of the system of satellite acquisition is the fact that the particular combination of satellite orbits, with approximately NS direction, and motion of the Earth's rotation causes the same area is illuminated using two different viewpoints, that is to say from West to East when the satellite moves in its orbit from South to North (ascending geometry) and from East to West when instead the satellite

M. Brugioni (✉) • B. Mazzanti • G. Montini • L. Sulli
Arno River Basin Authority, Via dei Servi 15, Florence, Italy
e-mail: m.brugioni@adbarno.it

moves in its orbit from North to South (descending geometry). The possibility of observing the same scene from two different points of view allows to better define the phenomenon through the reconstruction of the displacement vector in the plane EWZN (MINAMB 2009). Finally, comparison of speed values recorded in the same area in different time periods shows important assessments about the state of activity of the observed phenomena, providing an objective evaluation basis of considerable support for analysis at regional scale.

Interferometric Data Used

The PS data used for landslide analysis in the Arno river basin (Tuscany, Italy) are derived from processing of SAR images acquired from the European Space Agency satellites ERS 1/2 in the period 1992–2000 and ENVISAT in the period 2003–2008, and from the Canadian Space Agency satellite RADARSAT 1 in the period 2003–2006. In particular, the ERS and ENVISAT data were developed under the Extraordinary Plan for Environmental Remote Sensing (Lot 2) made by the Italian Ministry for the Environment, Land and Sea (Article 27 of Law 179 of July 31, 2002), obtained by application of PSInSAR (Ferretti et al. 1999, 2001; Colesanti et al. 2003) and PSP-DIFSAR (Costantini et al. 2008, 2009) methods. The RADARSAT data were processed using the technique PSInSAR and collected directly by the Basin Authority as part of a study on ground deformation at basin scale.

The ERS 1 satellite acquired data from July 1991 to March 2000, while ERS 2 has been operational since summer 1995. The SAR sensor (Synthetic Aperture Radar) is characterized by a frequency of 5.3 GHz or a wavelength equal to 5.66 cm (C-band). For both ERS satellites the review period is 35 days.

The ENVISAT satellite was launched in November 2002 and replaced and expanded the functions of the satellites ERS 1 and ERS 2. It is equipped with a sensor ASAR (Advanced Synthetic Aperture Radar) that uses multiple antennas with different polarizations and angles of incidence. Also in this case, the instrument acquires data in C-band (frequency of 5.331 GHz and a wavelength of 5.63 cm) and the satellite has a revisiting time of 35 days.

The RADARSAT satellite is instead a commercial satellite, which captures images on a commission basis and therefore, although in operation since November 1995, the Italian territory has been covered only since March 2003.

The sensor mounted on the satellite RADARSAT 1 is a sensor ASAR operating in C-band, with a multibeam acquisition mode and resolution from 100 to 8 m, with coverings of single cell capture from 500 km cells up to 50 km cells. The regularity of the acquisition of RADARSAT 1 and the time of review, amounting to 24 days instead of the 35 of

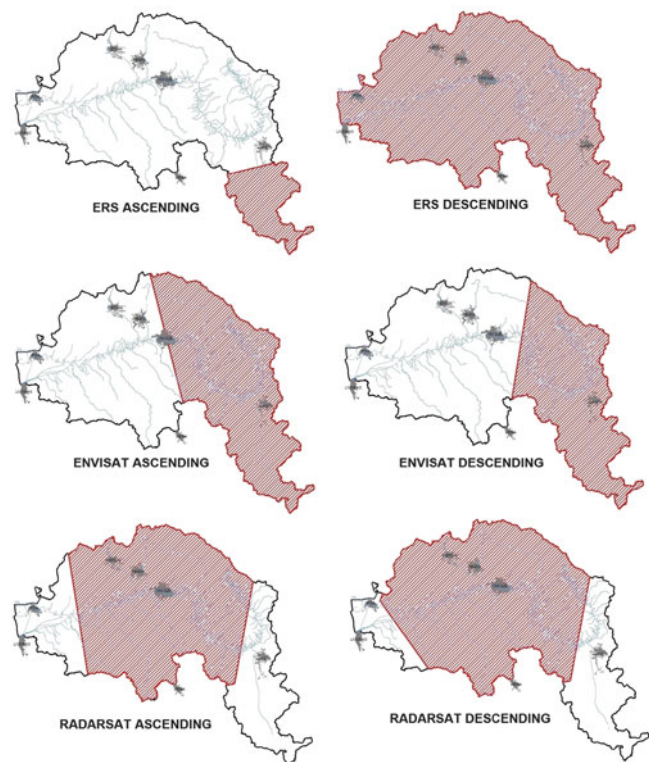


Fig. 1 Coverage of the ascending and descending datasets from ERS, ENVISAT and RADARSAT satellites in the catchment of the River Arno

satellites ERS and ENVISAT, make this datum particularly suitable for monitoring projects in individual areas.

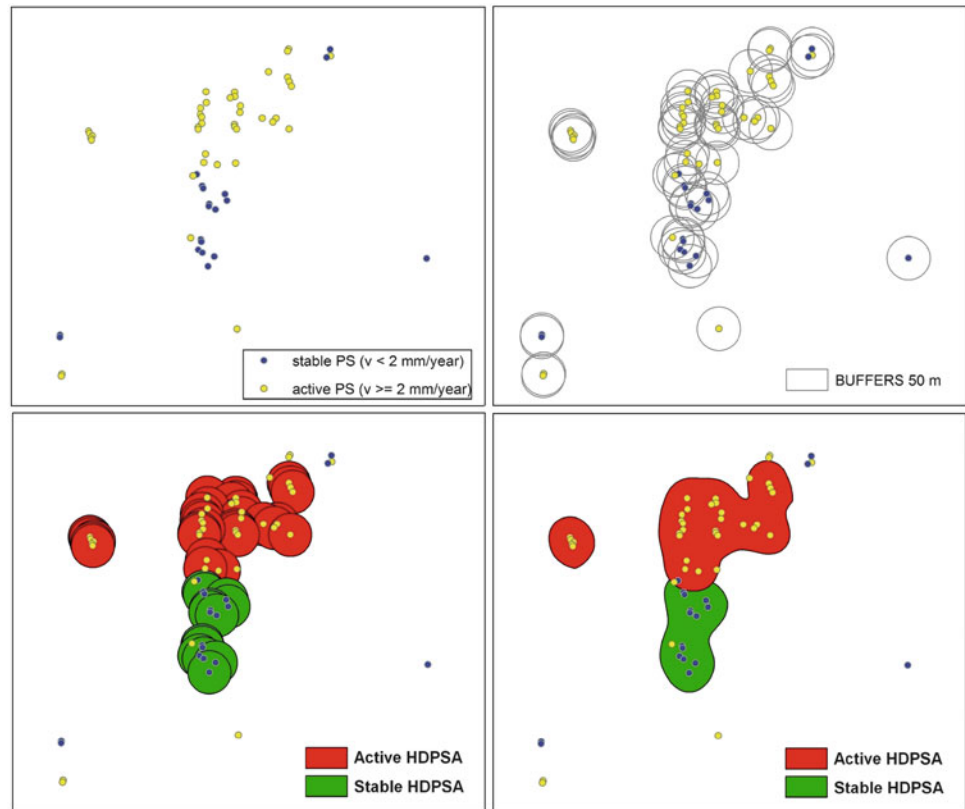
Figure 1 shows the distribution of ascending and descending covers of ERS, ENVISAT and RADARSAT satellites in the catchment of the river Arno. As we can see the covers of the three satellites are not uniform throughout the territory and, even for the same satellite, there are differences, still important (ERS), between the two geometries of acquisition.

Methods

The Arno River Basin Authority, as part of its planning and monitoring tasks, has used for some years the ground deformation data obtained by differential interferometric analysis of radar images acquired by the satellite platform (Brugioni et al. 2003, 2008a, b; Colombo et al. 2003b; Catani et al. 2006; Farina et al. 2006; Montini et al. 2007).

Within the various PS data processing performed by the Arno River Basin, three reference products have been identified, useful for the characterization of the phenomena of deformation and of their status of activities, as well as for the delimitation of the most affected by landslides areas.

Fig. 2 Procedure for the identification of active HDPSA and stable HDPSA



Delimitation of Areas of PS High Density (HDPSA)

It is often very difficult, if not through detailed surveys and field inspections, to understand whether the state of deformation of the PS provided by the satellite analysis is to be put in relation to the nature of the reflective element or to a phenomenon of generalized movement of the land on which that element insists. The analysis of the distribution of PS velocities of displacement also allows to discriminate areas where the movements are evenly distributed in space, and therefore more easily attributable to generalized deformations of the ground, from those areas where it is not possible to identify a prevailing trend of the deformation with the presence of PS clouds of different behaviour. In the latter case it is more likely to be that outliers of deformation could be related to the nature of the radar target (structural problems, the phenomena of bedding, etc.), rather than to the presence of generalized deformations of the ground (gravitational instability, areas in subsidence, etc.).

To discriminate this different behaviour in the distribution of deformation and, in particular, in determining the areas most likely affected by gravitational instability, it was decided to resample the PS data using a spatial density criterion which takes into account both the concentration and the activity state of radar targets considered (Fig. 2).

First, all PS have been classified as active or stable depending on whether, respectively, contained average annual rate higher or lower than the instrumental error (± 2 mm/year). For each of them was therefore found the around circle with a radius of 50 m and was determined the number of active and stable PS falling inside. The buffers obtained were then classified as areas with high density of PS (HDPSA) “active” or “stable” according to the criteria shown in Table 1. These criteria were defined on the basis of comparisons between the actual distribution of the deformations observed on the ground and the processing obtained by setting different values of buffers distance, number and nature of the PS.

The classified buffers were extracted, geometrically reshaped to better approximate the distribution of PS, and finally put into a single file by requiring overlapping of active buffers on the stable ones. The polygons obtained from this first processing were finally used to calculate the main statistical parameters of PS velocity values falling within. This procedure was repeated both for ascending (asc) and descending (desc) datasets, to then merge the two pieces of information into a single file and classify polygons resulting as follows:

1. Active areas: polygons where at least one dataset (asc or desc) identifies active HDPSA;
2. Stable areas: polygons where both datasets (asc and desc) identify stable HDPSA;

Table 1 Criteria for definition of HDPSA

Type	Center point	PS number and type	PS %
Active HDPSA	Active PS	Active PS ≥ 3	Active PS ≥ 75
Stable HDPSA	Stable PS	Stable PS ≥ 3	Stable PS ≥ 75

3. Stable/uncertain areas with evidence of instability: polygons where only a dataset (asc or desc) identifies stable HDPSA and the other dataset (desc or asc) presents PS within the polygon with average speeds greater than instrumental error (± 2 mm/year);
4. Stable/uncertain areas with evidence of stability: polygons where only a dataset (asc or desc) identifies stable HDPSA and the other dataset (desc or asc) presents PS within the polygon with average speeds less than instrumental error (± 2 mm/year);
5. Stable/uncertain areas: polygons where a dataset (asc or desc) identifies stable HDPSA, while the other dataset (desc or asc) does not have PS inside.

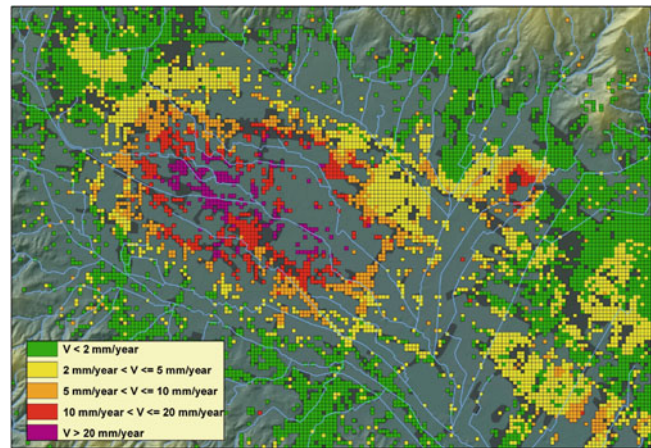
The procedure set out above has been applied both to the PS data obtained from processing of radar images acquired by ERS in the period 1992–2000, and to those obtained from processing of radar images acquired by RADARSAT satellite during the period 2003–2006 and ENVISAT satellite in the period 2003–2008. Of course the information obtained are closely related to the range of observation time of each satellite.

This procedure made it possible to identify those areas which in the last 20 years (the period covered by the observations of the three satellites) have been affected by phenomena of deformation stress.

Reconstruction of the Displacement Vector in the Plane EWZN

The possibility to analyse the same phenomenon from two different viewpoints offered by the two geometries for the acquisition of satellite data (ascending and descending), allows to reconstruct the component of the displacement vector in the plane EWZN in order to better understand the nature of the phenomenon that we are analysing (MINAMB 2009).

This type of processing needs to resample, throughout the basin, the punctual deformation data acquired in the two geometries in order to make them comparable with each other for the reconstruction of the resulting vector. The Arno basin has been divided into square cells with sides of 100 m (Fig. 3) and the main statistical parameters of the PS average annual rate of displacement recorded by satellites, both for ascending and descending dataset, for each of the

**Fig. 3** Resampling of ascending-descending data on regular cells with 100 m mesh

three satellites considered, have been calculated within each cell.

For each cell that showed PS data in both geometries of acquisition, the respective values of average speed were given and then proceeded to the reconstruction of the displacement vector so that its projection along the two directions of acquisition (ascending and descending) surrendered the observed values.

This operation was carried out by simplifying the geometry of the acquisition system, assuming that the direction of movement of the satellites corresponds to the NS directive (EW acquisition direction) for both geometries. In reality this condition is not fulfilled and therefore the results obtained should be interpreted as an indication of a behaviour and not exhaustive for quantitative analysis. The definition of the displacement vector in the plane EWZN thus obtained was then identified by the value of its modulus, corresponding to the speed of movement in the plane EWZN expressed in millimetres per year, and the value of the angle formed by the vector as compared to the zenith, in order to specify direction and orientation.

Comparison of Average Speeds Recorded in Separate Time Periods

This type of processing was performed to compare the values of speed recorded by satellites in separate time periods in order to assess, where possible, the degree of activity of observed phenomena (MINAMB 2009).

The comparison between the speed values observed by the different satellites has been made keeping separate the two datasets, comparing ascending with ascending and descending with descending.

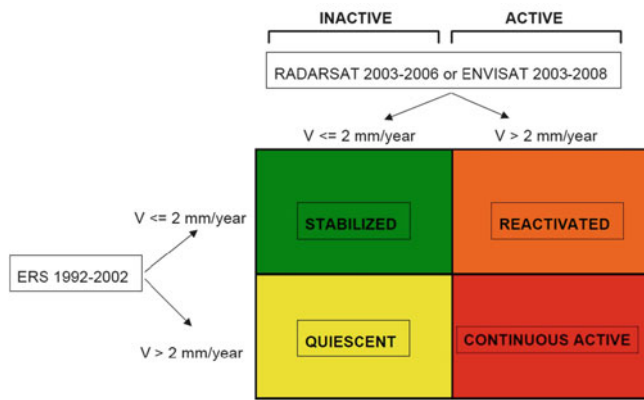


Fig. 4 Classification of the activities on the basis of a comparison of speed values recorded in different time periods (MINAMB 2009, amended)

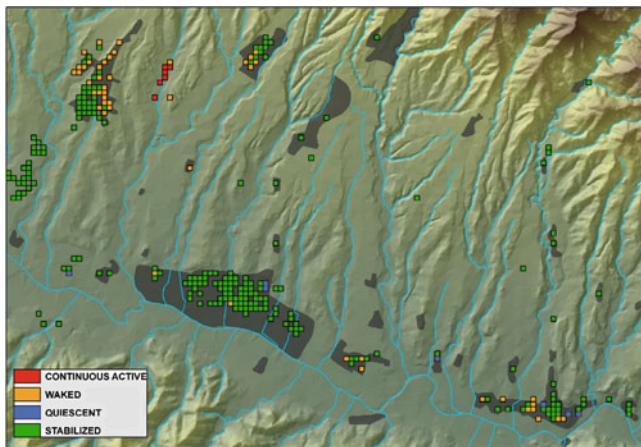


Fig. 5 Example of the classification of reference cells by comparing the average velocity recorded in separate time periods

Again the original PS data were resampled using a grid with a pitch of 100 m, to then proceed to the comparison of the average velocity values obtained.

Unfortunately, the coverages of satellite data on the Arno basin for the three satellites considered are very uneven (Fig. 1), and therefore it was possible to compare the average speeds only for the descending dataset. In particular, the descending dataset of the ERS satellite (1992–2000), with almost complete coverage for the entire Arno Basin, was compared with that of the ENVISAT satellite (2003–2008) for the area Casentino-Val di Chiana-upper Valdarno, and that of the RADARSAT satellite (2003–2006) for the remainder of the river basin.

Thank to this analysis it is possible to define the degree of activity of the selected cells according to the schedule of Fig. 4. Figure 5 shows an example of the comparison between different time periods following the classification of the activity of the cells with at least three PS for both satellites.

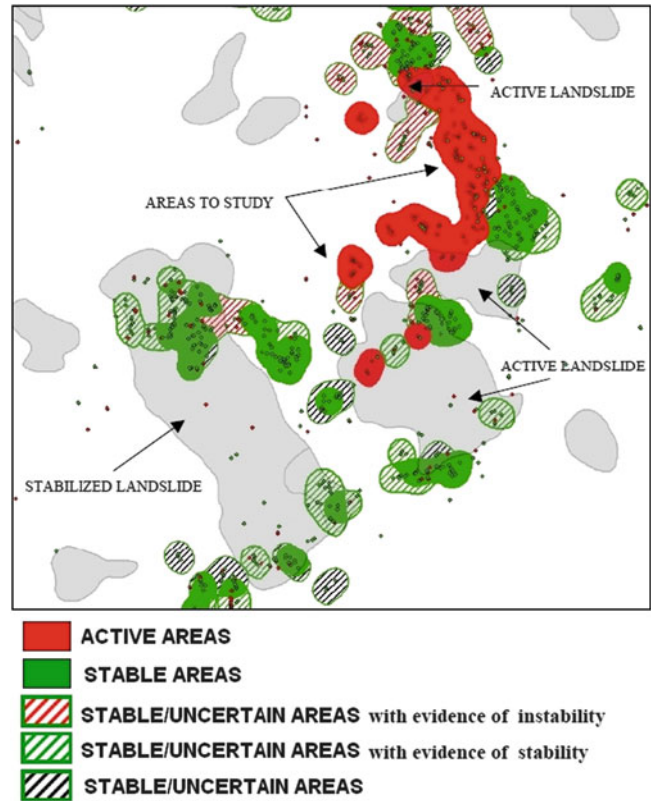


Fig. 6 Application of HDPSA processing to IFFI database

Results

The deformation data of PS and the products derived from their processing have been used to enrich the information in the database of the landslide hazard areas in the basin of the river Arno, realised according to IFFI (Italian Landslides Inventory) standard (updated December 2010) and delivered to ISPRA (Superior Institute for the Protection and Environmental Research) for the implementation in the national database.

The results were organized into a web-GIS project in order to display both the actual spatial distribution of punctual data of deformation within the landslide areas and the different information due to the possible presence of HDPSA. Furthermore it is possible to reconstruct the evolution of the displacement vector in the plane EWZN or to make punctual estimations on the state of activity of the observed phenomenon. The web-GIS project can be viewed on the web site dedicated to the IFFI project in Arno river basin <http://www.adbarno.it/iffi/>.

The census database of landslides in the Arno basin, updated in December 2010, identifies some 25,500 landslide hazard areas throughout the basin, of which about 10 % are significant anthropogenic elements for an assessment of the

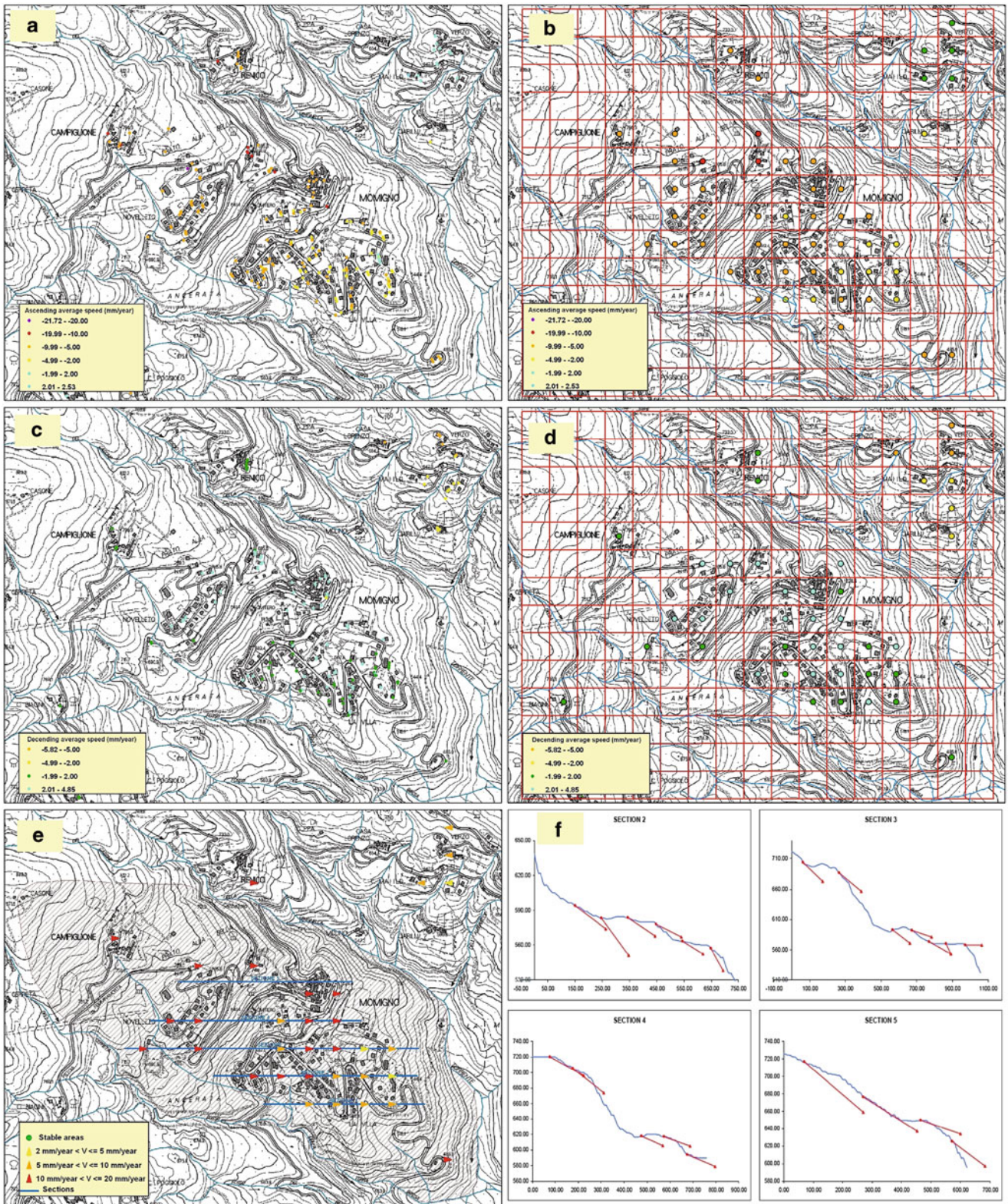


Fig. 7 Example of resampling ascending-descending with reconstruction of the displacement vector in the plane EWZN. (a) Display of average speeds of the PS ascending dataset; (b) resampling on the common grid for the PS ascending dataset; (c) display of average

speeds of the PS descending dataset; (d) resampling on the common grid for the PS descending dataset; (e, f) reconstruction of the displacement vector in the plane EWZN

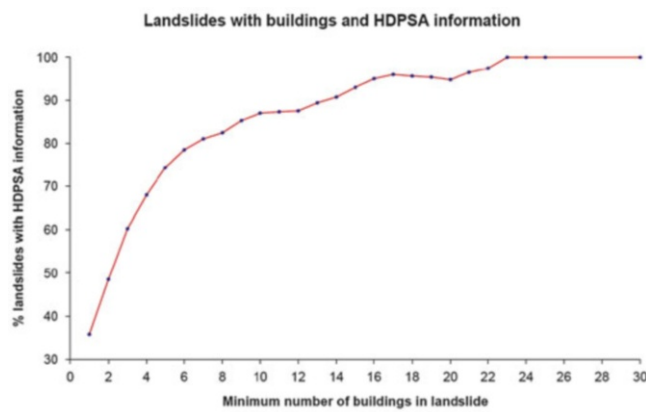


Fig. 8 The relationship between the minimum number of buildings located in landslides and the presence of HDPSA

risk status. Of these, over 90 % are affected by the presence of PS.

The identification of HDPSA (Fig. 6) has resulted in the discrimination, within the landslide hazard areas, of zones affected by important deformation stress in the last 20 years from those where the processing carried out identifies the presence of a substantial state of stability.

The results from this analysis showed a substantial coherence between the state of activity attributed on the basis on bibliographic data and the distribution of deformation stress. The distribution of HDPSA on the territory has also highlighted the need to proceed, in some cases, to a review of the geometry of the landslide hazard areas and, in other cases, to an in-depth study to identify new areas originally escaped the census.

The landslides with HDPSA information are about 6 % (1,443 cases of instability) of the total.

Although this percentage figure may seem rather modest, such landslides are those that affect areas with high presence of human activities and therefore of greater importance for risk estimation. In fact, as shown in graph of Fig. 8, the percentage of landslides with HDPSA information is highly dependent from the concentration of buildings in the area. In particular, while HDPSA can provide useful information to the characterization of the damages only for about 60 % of landslide areas with a number of buildings less than or equal to 3, the same information can instead be used for about 93 % of the landslides with at least 15 buildings within them, up to cover all landslides with at least 23 buildings.

The landslide areas with information about the reconstruction of the displacement vector in the plane EWZN were about 5 % (1,276 landslides). If we consider, as a selection criterion to increase the reliability of the data, the presence, in each cell reference, of at least 3 PS for both acquisition geometries, the percentage of landslides analysed falls to 1.6 % (297 landslides), but areas affected are the most relevant for estimating the risk.

Assuming that the movements recorded by PS are indicative of what happens along the sliding surface, that information can be very useful to get information on the type of landslide: (1) rotational slip, with directions of displacement tending to horizontalisation moving from head to foot of the landslide, or (2) translational phenomenon, with directions of movement approximately parallel to the topographic surface. An example of resampling on square cells of 100 m mesh and determination of the displacement vector in the plane EWZN aimed at the reconstruction of areas subject to greater deformation in a deep gravitational slope deformation (DGPV) is shown in Fig. 7.

To complete the information on the movements recorded by satellites, the database has been implemented with the data for the comparison among the values of average speed recorded by the three satellites. This information layer, very useful for assessments about the state of activity of the landslides recorded, for the reasons previously seen, has a limited coverage and still refers only to descending datasets. For this reason, the landslides affected by this type of information were approximately only 2.2 % (550 landslides) of the total.

The results show that the majority (93.7 %) of cells that contain at least 3 PS for both satellites have differences between the average velocity values with deviations below instrumental error (± 2 mm/year), showing a substantial consistency of the values recorded by the two satellites (ERS/Envisat and ERS/RADARSAT). The 4.7 % of the cells instead has highlighted an increase in average speed, from one stable state to an active state, while 1.6 % suffered a movement to stop, moving from an active state to absolute values of speeds of up to 2 mm/year.

The comparison between the average speeds in the three sub-time periods used was also made between data obtained from the combination of the two geometries seen previously. In this case, in particular, to optimize the coverage of the final result, the comparison was made between ERS (1992–2000) and ENVISAT (2003–2008) and between RADARSAT (2003–2006) and ENVISAT (2003–2008). Landslides affected by this type of information are about 1.8 % (456 landslides) of the total. Given the very limited extension of coverage of information, this percentage represents a good result.

Conclusions

The use of information on displacement provided by PS data is particularly useful for the characterization of the areas in gravitational slope instability phenomena and, in particular, the definition of the state of risk. For a correct interpretation of the phenomena it is very effective to make, where possible, a joint examination of the ascending and descending datasets. The data carried out in this work provide a number of very useful tools for identifying areas

at greatest risk and defining the state of activity and type of motion observed. Obviously, this information may provide an important support to classical geomorphological-geological analysis, but can not replace it.

The use of these data has also proved particularly effective in identifying areas subject to very slow movements of relatively deep nature, as in the case of DGPV, which are difficult to examine by traditional monitoring tools.

References

- Ambrosi C, Crosta GB (2005) Large sackung along major tectonic features in the Central Italian Alps. *Eng Geol* 83:183–200
- Brugioni M, Casagli N, Colombo D, Defflorio AM, Farina P, Ferretti A, Gontier E, Graf K, Haerberle J, Latentin O, Manunta P, Meloni E, Mayoraz R, Montini G, Moretti S, Pagnini M, Palazzo F, Spina D, Sulli L, Strozzi T (2003) Slam, a service for landslide monitoring based on EO-data. In: *Proceedings of Fringe 2003*, Frascati, 1–5 Dec 2003
- Brugioni M, Menduni G, Montini G (2008a) Lo studio del bacino dell'Arno con interferometria satellitare PSInSAR™. *Special supplement ARPA Rivista Regione Emilia Romagna* 1:26–28
- Brugioni M, Menduni G, Montini G (2008b) Analisi dei fenomeni di subsidenza nel bacino del fiume Arno tramite l'utilizzo dell'interferometria radar differenziale da piattaforma satellitare. In: *Proceedings of Stato del territorio e delle risorse naturali in Toscana*, Ordine dei Geologi della Toscana, Florence, 23–25 Oct 2008
- Catani F, Colombo D, Farina P, Fumagalli A, Kukavicic M, Marks F, Menduni G, Moretti S (2006) Utilizzo di dati telerilevati nella mappatura e nel monitoraggio dei fenomeni franosi e nell'analisi della suscettibilità da frana. *Giornale di Geologia Applicata* 3:173–180
- Colesanti C, Wasowski J (2006) Investigating landslides with spaceborne Synthetic Aperture Radar (SAR) interferometry. *Eng Geol* 88:173–199
- Colesanti C, Locatelli R, Novali F (2002) Ground deformation monitoring exploiting SAR Permanent Scatterers. In: *Proceedings of the IEEE international geoscience and remote sensing symposium*, vol 2, Toronto, 24–28 June 2002, pp 1219–1221
- Colesanti C, Ferretti A, Novali F, Prati C, Rocca F (2003) SAR monitoring of progressive and seasonal ground deformation using the Permanent Scatterers technique. *IEEE Trans Geosci Remote Sens* 41:1685–1700
- Colombo D, Ferretti A, Prati C, Rocca F (2003a) Monitoring landslides and tectonic motions with the Permanent Scatterers technique. *Eng Geol* 68:3–14
- Colombo D, Farina P, Moretti S, Nico G, Prati C (2003b) Land subsidence in the Firenze-Prato-Pistoia basin measured by means of spaceborne SAR interferometry. In: *Proceedings of IGARSS 2003*, Toulouse
- Costantini M, Falco S, Malvarosa F, Minati F (2008) A new method for identification and analysis of persistent scatterers in series of SAR images. In: *Proceedings of international geoscience and remote sensing symposium*, Boston, 7–11 July 2008, pp 449–452
- Costantini M, Falco S, Malvarosa F, Minati F, Trill F (2009) Method of Persistent Scatterers Pairs (PSP) and high resolution SAR interferometry. In: *Proceedings of international geoscience and remote sensing symposium*, Cape Town, 12–17 July 2009
- Crosta G, Agliardi F, Frattini P, Allievi J (2009) Analisi di DGPV tramite integrazione di monitoraggio tradizionale, PS-InSAR e modellazione numerica. *Rendiconti online Società Geologica Italiana* 6:186–187
- Farina P, Colombo D, Fumagalli A, Marks F, Moretti S (2006) Permanent Scatterers for landslide investigations: outcomes from the ESA-SLAM project. *Eng Geol* 88:200–217
- Ferretti A, Hanssen R (2002) Deformation monitoring by satellite radar interferometry. *GIM Int Worldwide Mag Geomat* 16(9):52–57
- Ferretti A, Prati C, Rocca F (1999) Multibaseline InSAR DEM reconstruction: the wavelet approach. *IEEE Trans Geosci Remote Sens* 37(2):705–715
- Ferretti A, Prati C, Rocca F (2001) Permanent Scatterers in SAR interferometry. *IEEE Trans Geosci Remote Sens* 39(1)
- Ferretti A, Savio G, Barzaghi R, Borghi A, Musazzi S, Novali F, Prati C, Rocca F (2007) Sub-millimeter accuracy of InSAR time series: experimental validation. *IEEE Trans Geosci Remote Sens* 45(5):1142–1153
- Ferretti A, Fumagalli A, Novali F, Prati C, Rocca F, Rucci A (2011) A new algorithm for processing interferometric data-stacks: SqueeSAR™. *IEEE Trans Geosci Remote Sens* 49(9):3460–3470
- Hilleg G, Burgmann R, Ferretti A, Novali F, Rocca F (2004) Dynamics of slow-moving landslides from Permanent Scatterer Analysis. *Science* 304:1952–1955
- Meisina C, Zucca F, Conconi F, Verri F, Fossati D, Ceriani M, Allievi J (2007) Use of Permanent Scatterers technique for large-scale mass movement investigation. *Quatern Int* 171–172:90–107
- MINAMB (2009) Linee guida per l'analisi di dati interferometrici satellitari in aree soggette a dissesti idrogeologici. *Progetto Persistent Scatterers Interferometry*. http://www.pcn.minambiente.it/GN/progetto_psi.php?lan=it#
- Montini G, Benvenuti L, Menduni G (2007) Analisi dei fenomeni di subsidenza nel bacino del fiume Arno. In: *Proceedings of 10° Conferenza Italiana utenti ESRI*, Rome, 18–19 Apr 2007
- Notti D (2010) Landslides mapping and analysis by means of Persistent Scatterers SAR data: approaches at different scales. *Scientifica Acta* 4(1):3–8
- Notti D, Meisina C, Zucca F (2009) Analysis of PSInSAR™ data for landslide studies from regional to local scale. In: *Proceedings of Fringe workshop*, Frascati, 30 Nov–4 Dec 2009
- Poggi F, Riccelli G (2009) PSI technique for slow landslides analysis: a useful tool to handle with care. *Rendiconti online Società Geologica Italiana* 6:380–381
- Righini G, Casagli N (2009) Contribution of remote sensing to landslide analysis for civil protection applications: outcomes from FP6 PREVIEW project. *Rendiconti online Società Geologica Italiana* 6:397–398
- Strozzi T, Farina P, Corsini A, Ambrosi C, Thüring M, Zilger J, Wiesmann A, Wegmüller U, Werner C (2005) Survey and monitoring of landslide displacements by means of L-band satellite SAR interferometry. *Landslides* 2(3):193–201



Experimental Approach for Stability Evaluations of Carrara Marble Basins

Domenico Gulli, Maura Pellegrini, and Alessandro Cortopassi

Abstract

Because of the modern exploitation technologies for marble extraction, the open pit and underground quarries can quickly reach impressive sizes. Moreover the selection of exploited material or the geostructural conditions of the site can produce excavation with unusual and irregular shapes. Also for these reasons the appropriate design of the excavations, for quarrying activities, should require the knowledge of mechanical behaviour of the rock mass, of geo-structural conditions and of in situ stress. The main purpose of the quarry project should be to prevent instability of the rock mass, in every step of the foreseen exploitation. The lack of this specific technical evaluation contributed in the past to the development of large rock slide. The paper presents an applied approach for enhancing stability assessment and safety controls of marble quarries.

Keywords

Safety • Stability analysis • In situ stress • Brittle structures • Numerical models

Introduction

The presented approach was developed in particular for the study of underground quarries, allowing to underline the fundamental importance of experimental measurements and of monitoring for calibration of numerical models and for the assessment of quarries stability conditions. The same approach is now applied also for the study of the Monte Torrione site, a relief located in prominent position at the center of Fantiscritti Valley, that is exploited at different levels from underground and open pit quarries (Fig. 1).

The applied methodology is based on large scale geo-structural study, in situ stress measurements, laboratory characterization of intact rock and calibration of numerical models. In particular the study consists of (1) the determination of the site geometry and morphology, (2) a geological study for the determination of rock mass geo-structural

characteristics – at different scales – and tectonic stress orientation from brittle structures analysis, (3) the in situ stress measurements through different methods and the monitoring of stress and displacements changes, (4) the determination of the mechanical behaviour of rock by means of in situ and laboratory tests, (5) the calibration of numerical models of rock mass using continuous and discontinuous approaches.

A part from the case of local cinematic slides, for the global stability of a quarry site it must be noted that the tectonic genesis of marble, the topographic gradients of Apuane Alps ridge, the geo-structural assessment of marble deposits and the excavation geometries play an important role on the development of failures within the rock mass.

For stability analysis of open pit or large underground excavation, in particular in situ stress is recognized as one of the most important factors, especially where high non lithostatic stresses can be encountered such as in most cases during exploitation of Carrara marble, even in presence of low overburden rock.

D. Gulli (✉) • M. Pellegrini • A. Cortopassi
Operative Unit of Mining Engineering (U.O.I.M.) AUSL 1, Regione
Toscana, Carrara, Italy
e-mail: d.gulli@usl1.toscana.it

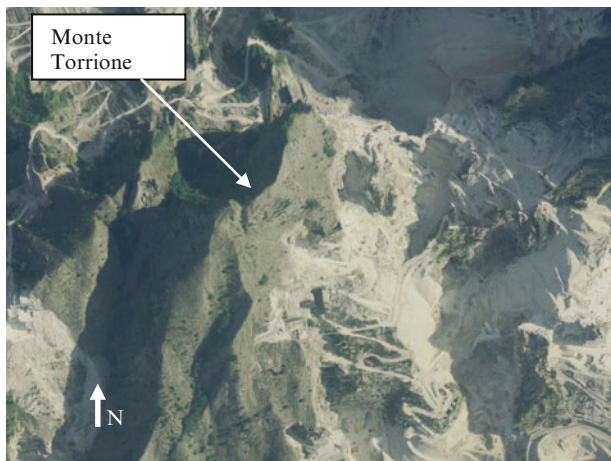


Fig. 1 Monte Torrione site, interested by underground and open pit quarries

In general stress state evaluation is needed in underground quarries in order to prevent static collapse of support structures. In surface quarries, stresses orientations and intensities, together with the cinematic structure of the rock mass, dominate the possibility of major induced displacements due to the deepening of the excavation and to the consequent stress re-distribution from the base to the top of the slope.

Geological Overview of Apuan Alps

The Apuan Alps (NW Tuscany) are the geometrically lowest outcropping part of the Northern Apennine structural stacking. Their formation resulted from the originally sedimentary, then tectonic evolution of a sector of continental crust, pertaining to the Adria Plate, involved in an accretional/collisional system during the Upper Oligocene-Lower Miocene. The Apuan Unit (Fig. 2) formed by a Hercynian basement and by a Permian-Triassic to Oligocene metasedimentary sequence. The structural evolution of the Apuan Unit includes two main tectono-metamorphic events (Carmignani and Kligfield 1990). During the D1 main event the major structuration takes place within the metamorphic units.

This is confirmed by penetrative axial plane schistosity (S1) of isoclinal folds that can be observed at the kilometeric scale as well as at the microscopic scale. The peak metamorphic conditions have been estimated in approx. 450 °C of maximum temperature and 0.5–0.6 GPa of pressure. The most recent stages of the D2 deformation, which are of a specific interest in this study, are connected to a polyphase deformation that caused the development of brittle structures (fault and fracture systems). The Apuan Alps have a history of brittle deformation which makes them a homogeneous

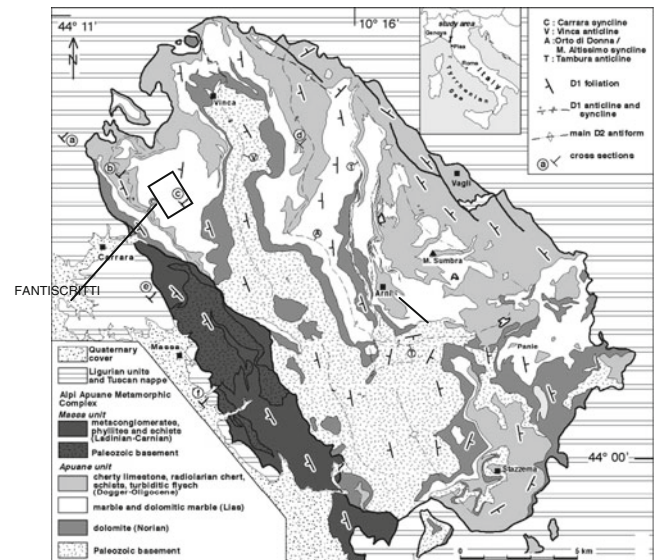


Fig. 2 Schematic geological-structural map of the Apuan Alps with indication of quarry site investigated through the application of the presented approach (Carmignani and Kligfield 1990)

domain of “low strain”, surrounded by main faults (border faults) to the East and West, (Otrria and Molli 2000). This structural frame is characterized by a not quite evolved organization of the fault systems within the massif which show a very low degree of interconnection between the single structures.

Description of Applied Approach

In order to apply an observational design method, the combined contribution of laboratory tests, in situ measurements and surveys, rock mass monitoring, geological observation, and numerical models has been considered. Laboratory tests were performed in order to evaluate static and dynamic elastic constants, uniaxial compressive strength, biaxial strength and indirect tensile strength. The laboratory characterization allowed, for the intact rock, to define well fitted Mohr-Coulomb and Hoek & Brown envelopes. The Hoek & Brown empirical strength envelope for the rock mass have been calibrated through laboratory tests and geostructural scanlines: in the Monte Torrione site this criterion well simulated the strength behavior observed in situ for rock mass, giving reasons for superficial extension failures in some exploited underground rooms, where measured stress intensities are closer to the failure envelope due to the low confinement.

The rock stress was measured using commonly applied methods, such as Hydraulic fracturing (HF), Biaxial C.S.I.R. (Doorstopper) and triaxial thin Hollow Inclusion CSIRO-type Cell (3D HI-Cell). HI Cells were used for the 3D

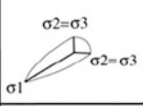
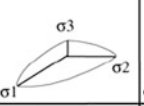
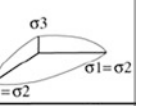
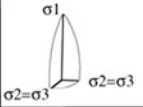
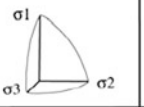

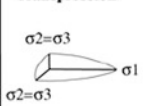
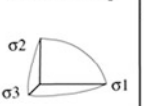

σ vertical	$R = 0$ $\sigma_2 = \sigma_3$	$0.33 < R < 0.66$ $\sigma_1 > \sigma_2 > \sigma_3$	$R = 1$ $\sigma_1 = \sigma_2$
σ_3	Transpression 	Pure Compression 	Radial Compression 
σ_1	Radial Extension 	Pure Extension 	Transension 
σ_2	Transpression 	Pure Strike-slip 	Transension 

Fig. 3 Classification of tectonic stress tensors represented by their stress ellipsoid shape

local stress measurements. The 12-gauge cells used were equipped with two axial, five tangential and five $\pm 45^\circ$ inclined strain gauges, plus a thermistor. For the overcoring of the 38 mm diameter pilot hole a 128 mm overcoring diameter were used. As for the other used methods, the in situ stress calculations have been based on the assumptions that the rock was linear-elastic, isotropic and subjected to a homogeneous stress. During the biaxial tests, needed for the direct determination of the elastic parameters of rock core, the isotropic and linear-elastic behavior of the rock has been verified through the responses of differently oriented strain gauges during the loading-unloading tests (pressures ranging between 0 and 15–20 MPa with steps of 2–5 MPa). The work suggests that, among the other adopted methods, 3D Hi-Cell represents the most reliable method for investigating 3D local stresses in underground marble quarries. Apart from the possibility of a 3D evaluation of local stresses with a single measurement (without previous knowledge of principal stress directions), it offers many advantages as (1) the acquisition of all sensors curves before, during and after overcoring, enhancing the possibility of quality controls for each test and (2) the estimation of elastic constants of rock within the same overcored volume using the same testing apparatus, during biaxial tests. The choice of using a stress relief technique in underground marble quarries is also in accordance with the method used for the exploitation, that is mainly performed using chain or diamond wire cutters causing less rock destressing than with blasting.

The paleostress fields were obtained by means of the “Tensor” software (Delvaux 1993). The results include the orientation of the principal stresses and the tensor shape, identified as the ratio between the principal stress intensities differences, $R = (\sigma_2 - \sigma_3) / (\sigma_1 - \sigma_3)$.

This ratio provides the qualitative definition of the stress ellipsoid (Fig. 3). The detected brittle structures were: (1) first order faults (dislocation surfaces, associated to cataclastic zones, with surfaces showing visible movement indicators); (2) minor faults with movement indicators; (3) fractures s.l. (joints s.s., and fractures with no evidence of movement); (4) systems of conjugated fractures.

Both differential and integral methods were used for the numerical simulations, with the setting up of 2D and 3D, BEM, DEM and FEM, numerical models. The numerical models have been set up and calibrated – at different scale – for extending the field of stress measurements, evaluating the general stability conditions of investigated sites and simulating the rock mass response to the future planning excavations.

Finally, for the monitoring of the stress–strain behavior of rock mass during excavation, stressmeters (both rigid and soft inclusion type) and multipoint borehole extensometers (with vibrating wire transducers) have been used. Useful information for the choice of measuring devices and their positioning has been obtained by means of preliminary simple models of the expected stress and deformation induced by excavations. For the cinematic analysis of possible unstable rock blocks simple limit equilibrium models have been used.

Fantiscritti Marble Basin

The Fantiscritti marble basin is located on the northeastern normal limb of the Carrara syncline. In this area (1) the main axial plane foliation has a monoclinial setting plunging towards SW with increased inclination from NE to SW, (2) a mineral and extensive lineation is associated with the main foliation, trending NE-SW on average, (3) the analysis of the existing fracture and fault systems shows a deformation framework typical of a polyphase brittle tectonic evolution.

The tectonic framework of Fantiscritti Valley, shows the consistency of the faults distribution with an approx. N10 oriented sub-horizontal maximum compression stress (σ_1). In this context, the N30-45 trending sinistral strike-slip master faults develop, associated with the subordinate approx. N160 trending dextral strike-slip faults. Cross-cutting relations obtained by means of fracture systems and kinematic indicators allowed the determination of a first brittle deformation phase – generated by a paleostress field with subhorizontal σ_1 direction – in which the strike-slip fault systems originate. A subsequent deformation phase, generated by a paleostress field with vertical σ_1 direction

Fig. 4 Plan view of the Monte Torrione – Fantiscritti site

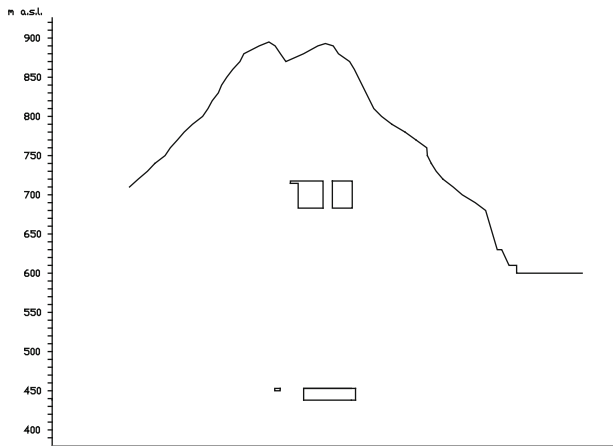
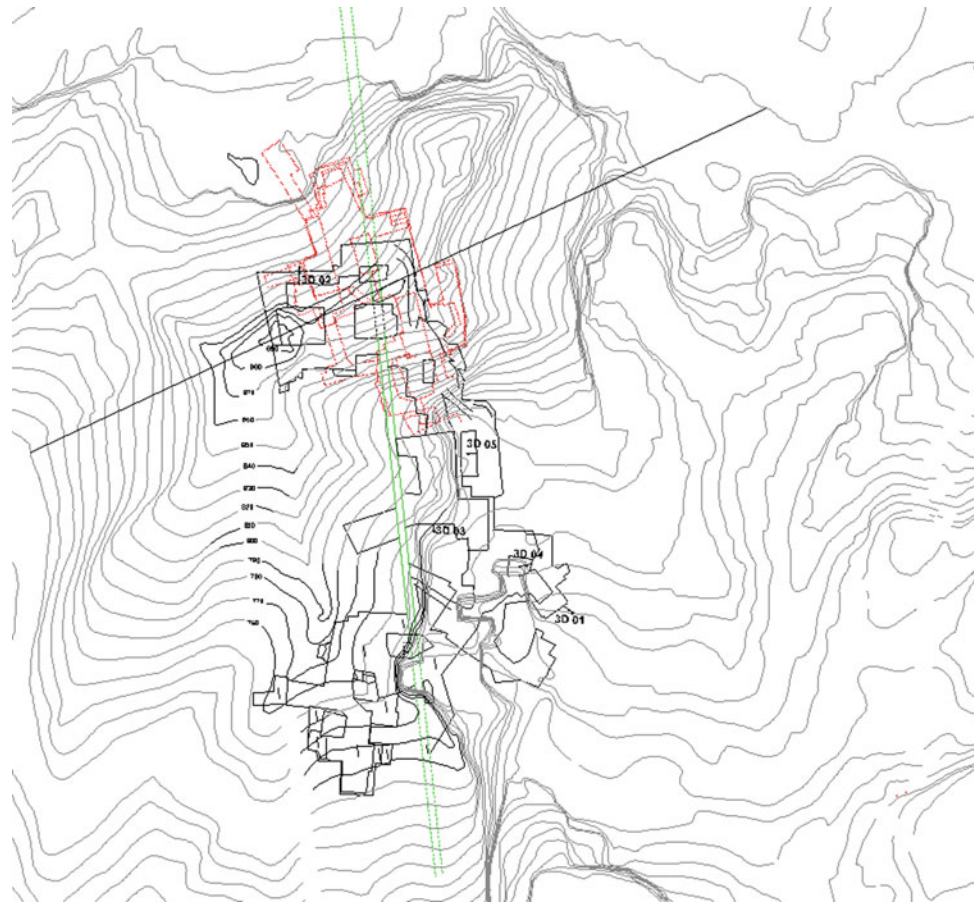


Fig. 5 NE-SW section of the Monte Torrione – Fantiscritti site

allowed the development of normal fault systems. An average RMR_{89} of 63 has been evaluated for the investigated site.

Main Results of Experimental Approach

The proposed approach has been applied in three underground quarries located below Mt. Torrione (two of them are located along the tunnel connecting the Fantiscritti valley to the Torano valley at a depth of about 450 m and one is more superficial having a rock cover of about 100 m) and in the external East slope of the mountain (Figs. 4 and 5).

The estimation of induced state of stress around the quarries of Fantiscritti was attained using three different testing methods: HF (11 boreholes for a total of 52 tests), Doorstopper (5 boreholes for a total of 13 tests) and 3D Hi-Cell (6 measurement stations for a total of 12 tests). The results allowed for the estimation of an extensive stress regime characterized by a subvertical maximum compression component σ_1 , and a minimum and intermediate compression components poorly constrained on the horizontal plane (Fig. 6).

In the two deeper quarries (having an average rock cover of 450 m) an average far field stress can be assumed of about $\sigma_1 = 15.8$ MPa 70/175; $\sigma_2 = 3.5$ MPa 07/220, $\sigma_3 = 3.3$ MPa 06/305. Actually a stress variations has been

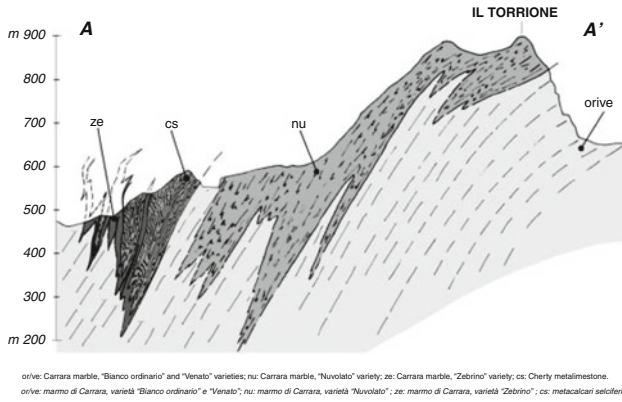


Fig. 6 NE-SW geological section of the Monte Torrione – Fantiscritti site

observed within the site. A deeper investigation of the stress conditions has been carried out particularly in the North area (just below the mountain peaks) where rock walls and pillars are locally subjected to mining induced fractures and superficial damages (particularly evident in N and W sides). In this area an average of $\sigma_1 = 16.5$ MPa 83/291; $\sigma_2 = 1.7$ MPa 05/095, $\sigma_3 = 0.5$ MPa 02/186 have been measured: therefore the induced stress tends to be more anisotropic – when compared to the average condition of the entire site – with a high unconfined vertical stress acting on slim, unconfined, rock structures. The Hoek & Brown empirical strength envelope, calibrated through laboratory tests and geostructural scanlines, well simulated the strength behavior observed in situ for rock mass, giving reasons for possible failures in these rooms, where measured stress intensities are closer to the failure envelope due to the low confinement.

In this area an attempt to compare the results of the three test methods has also been made. The HF and 3D Hi-Cell showed a good fitting for the σ_1 but HF does not advert the low horizontal confinement which was assessed by means of the 3D stress relief tests. The Doorstopper tests showed very scattered results with evidences of horizontal tensile stresses.

Comparing the data from the stress measurements and from the tectonic regime analysis it is possible to underline that the conjugated fractures system and the normal faults are consistent with a radial extensive paleostress characterized by a subvertical maximum compression component σ_1 , and a minimum and intermediate compression components poorly constrained on the horizontal plane (Fig. 7).

Recently more stress measurements, performed by UOIM inside a third, more superficial, underground quarry located just below the Monte Torrione peaks and by external quarries consultants, in the East external slope, confirmed

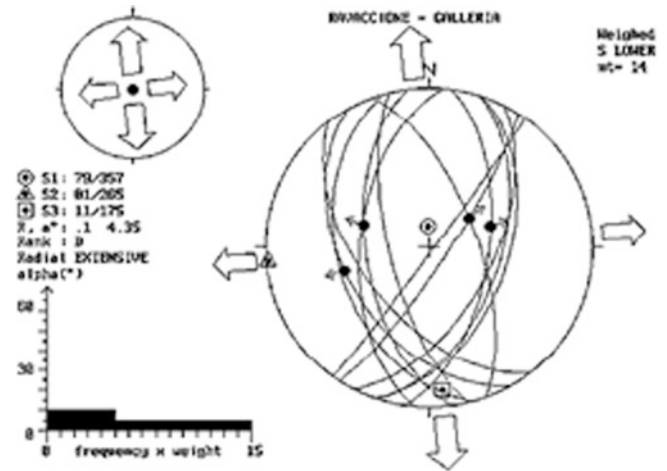


Fig. 7 Fantiscritti Northern rooms – Stereonet (Schmidt, lower hemisphere): faults and fractures are represented

the previously indicated stress regime. Also in this case the three more 3D Hi-Cell stress measurements showed a good reliability and confirmed the presence of horizontal tensile stresses (average stress of with $\sigma_1 = 5$ MPa 63/254; $\sigma_2 = 1$ MPa 19/195, $\sigma_3 = -2$ MPa 16/100); also in this case the Doorstopper tests (made in the external slope) showed scattered results with qualitative indication of horizontal tensile stresses.

The experimental results were used to set up and calibrate numerical models by means of BEM, DEM and FEM approach. Numerical analysis were performed at different scale in order to evaluate global stability conditions of the site and local problems such as the behavior of the rock mass during the realization of a support pillar. Generally, the BEM allows a first evaluation of the rock mass areas mostly subjected to stress concentrations due to a given stress orientation as regards to the quarry layout. This method allows to take in account of the entire scale of the site but it is not able to simulate the presence of rock discontinuities.

However, the BEM showed good qualitative correlations simulating the above mentioned average condition of far field stress: the numerical values are in good agreement particularly with the stress measurements results. Thus BEM method turned out to be useful for a first preliminary analysis. In order to study specific problems – such as the best orientation of the excavation or the definition of pillar size and shape for given stress state and geological settings – the work showed that the DEM and FEM methods can represent a most useful tool, taking into account the presence of the faults and allowing the assessment of the possible stress concentrations and re-orientations, due also to the excavation shape and direction (Fig. 8).

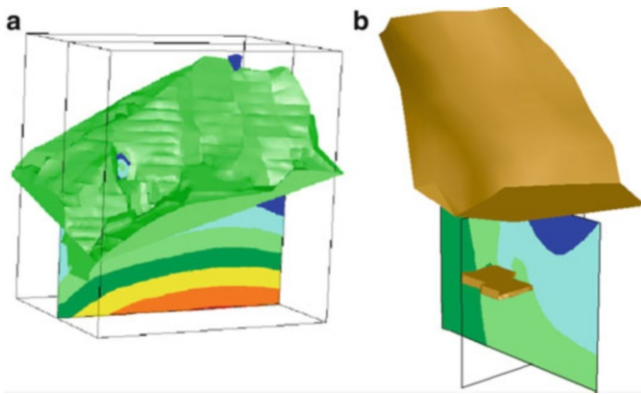


Fig. 8 Representation of large scale 3D model of the site (a) and small scale analysis for the evaluation of pillar performance during his realization (b)

Some numerical 2D analyses, performed with Finite Element Methods (FEM), enabled the simulation of simple plane problems also taking into account the presence of some discontinuities. For these simple models mechanical properties of rock discontinuities have been analysed in parametric form.

For the external slope one important rule is to evaluate initial stress state have simulated the excavation of the natural slope preceding the current geometry.

For a best calibration of model a monitoring system has been installed in one of the underground quarries while a new monitoring system will continuously measure induced displacements during external excavations of the Monte Torrione East side.

In the East slope of the Monte Torrione, apart from the extension of the stress evaluation performed for the underground, the setting up of 2D e 3D models and the monitoring systems, a deep investigation of geo-structural assessment was performed with the collaboration of the CNR-IGG (National Research Council, Geo-Science Inst. of Pisa) and of the CGT-University of Siena. This in-depth examination allowed the accurate definition (orientations and main characteristics) of the brittle structures and a photogrammetric survey of the external walls finalized to rock block stability analysis.

The detection of the main brittle structures allowed the definition of possible rigid blocks that can influence the large scale stability of the slope (Fig. 9) while the data from photogrammetric survey were organized in a relational geo-database in order to perform for every rock block a cinematic analysis – at small scale – and to identify the main geometrical mechanism of possible instability (Fig. 10)

This comprehensive analysis of the site allowed for the re-definition of parameters used for the quarry project leading to a knowledge of the acting stress, in order to properly design underground support elements, and of geo-structural

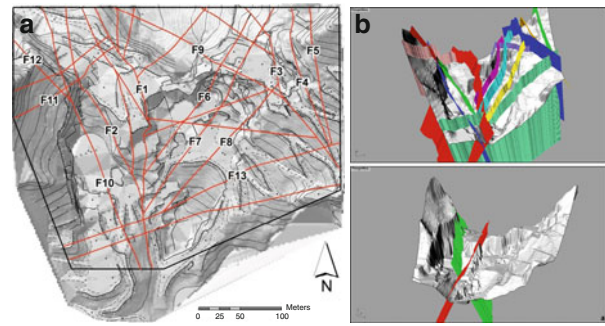


Fig. 9 Identification of the main brittle structures (a) and study of large scale rock blocks (b)

main features, in order to define open pit quarry geometry that can minimize the possibility of cinematic failures. In particular for the open pit quarries at the East side of the Monte Torrione this analysis led to a re-definition of the pit slope geometry with properly defined orientation and average dip of 65° instead of 82° , previously defined.

Conclusions

The work confirmed that in most cases, for rock of meta-morphic origin, such as for the Carrara marble, the stress regime cannot be explained by referring only to the lithostatic hypothesis: thus in situ measurements and observations are needed.

The stress state has been experimentally evaluated using three different testing methods, however the work suggests that particularly Hi-Cell represents a reliable method for investigating 3D local stresses for the tested material for which an isotropic and linear-elastic behavior has been verified at the rock core scale.

The comparison between the measured and tectonic stress showed encouraging correlations and highlighted the possibility of predicting stress shape (Fig. 3) through a preliminary brittle structures analysis. However geo-structural investigation of the site is of fundamental importance in order to evaluate the rock volumes that, at every scale, can produce induced displacements or failures: the exploitation of the quarries, in particular of open pit, have to take in account the presence of large scale blocks of which removability must be avoided.

The application of the presented approach allowed the definition of an extensional stress regime that can be correlated to most recent stages (tectono-metamorphic D2 deformation) of the structural evolution of the Apuan Unit. The work underlined the fundamental importance of calibrating numerical models also if those tools are, in some cases, unable to reproduce the local stress variations shown by the measurements. However BEM models have shown to be useful for an average, qualitative, analysis of the rock mass behavior while

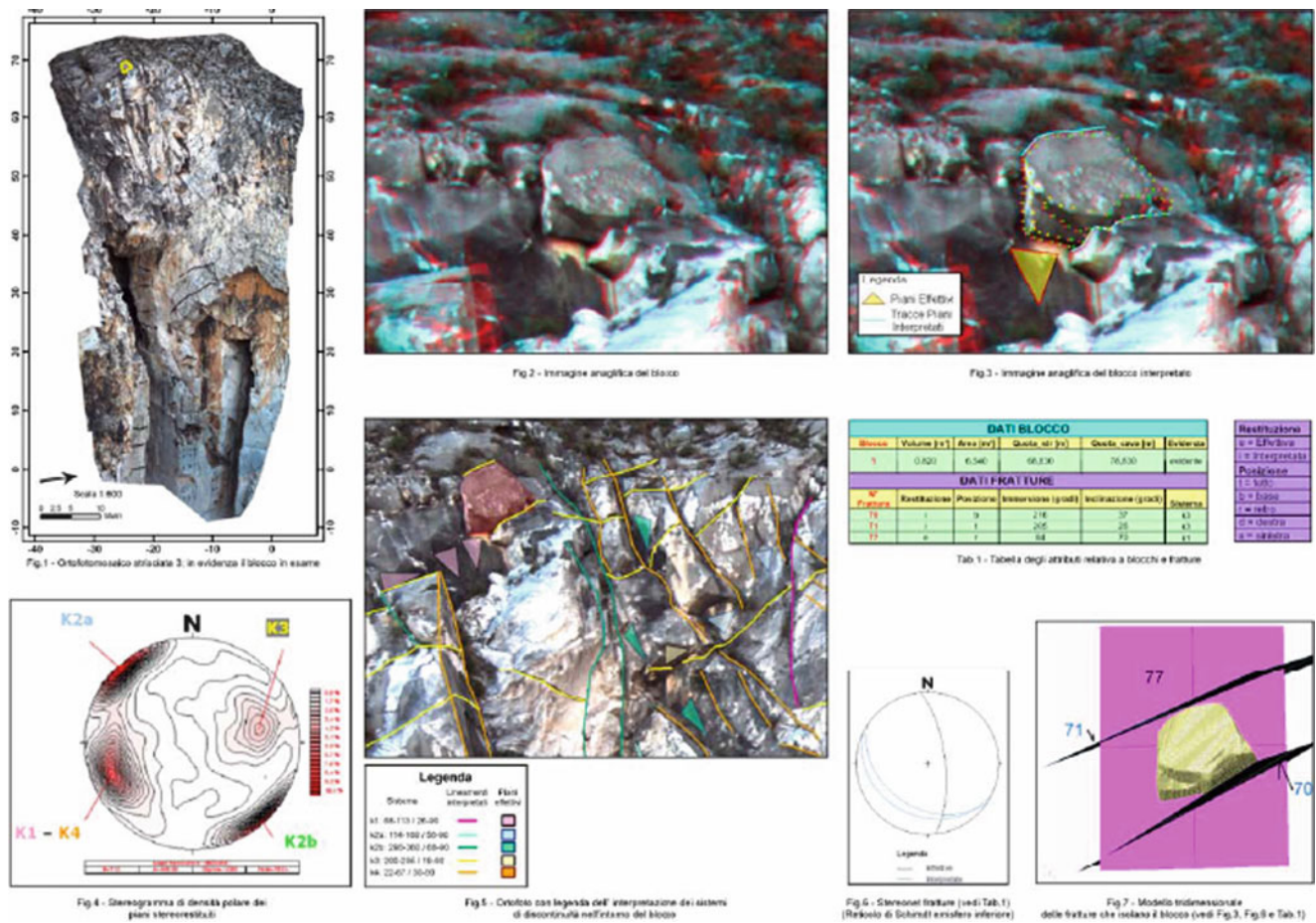


Fig. 10 Identification of a 3D solid: geometry, orientation of discontinuity surfaces with evaluation of his stability

DEM while FEM methods can represent a useful tool for the study of most specific problems, taking into account the presence of rock discontinuities.

Acknowledgments The Region of Tuscany (Italy) supported this work. The research has been performed with the contribution of the CNR-IGAG (Geo-Eng. Inst. of Turin), the CNR-IGG (Geo-Science Inst. of Pisa), the DCE-UNIPA (Civ. Eng. Dep. of University of Parma) and the CGT (University of Siena). We acknowledge the cooperation of owners and workers of investigated quarries.

References

Carmignani L, Kligfield R (1990) Crustal extension in the Northern Apennines: the transition from compression to extension in the Alpi Apuane Core Complex. *Tectonics* 9:1275–1303

Delvaux D (1993) The TENSOR program for reconstruction: examples from the east Africa and the Baikal rift system. *Terra Abstr Suppl Terra Nova* 5:216–224

Ortria G, Molli G (2000) Superimposed brittle structures in the late orogenic extension of the Northern Apennine: results from Carrara area. *Terra Nova* 12(2):1–8

Part II

Rapid Runout Analysis

Introduction by Marina Pirulli and Claudio Scavia

Politecnico di Torino, Department of Structural, Geotechnical and Building Engineering,
Torino, Italy

Landslides may damage any human structure and may even cause the loss of lives when they occur in a catastrophic way. In order to supply improved means of mitigation and planning to the Organisms working in land management for landslide prevention and hazard mitigation, the main goals of landslide runout analysis should be the assessment of future landslide activity with a range of potential scenarios. In particular, when a potential source of instability is identified, hazard mapping through runout analyses may contribute to define which areas could be threatened by landslide propagation.

Two main approaches to runout analysis can be identified: qualitative and quantitative. Numerical models are part of the latter approach and, in recent years, have particularly emerged as a useful tool for landslide runout analysis and risk assessment. With increasing attention and advances in computational capabilities, a large number of models have been developed or are currently in development. Several of these models have included innovations that have significantly advanced both the ability to simulate real events and the fundamental understanding of rapid landslide processes. Contributions have been made by a number of researchers with a wide variety of perspectives and goals, making this topic truly multidisciplinary. Still, some significant challenges remain as we move towards more accurate and objective runout prediction using numerical models. Accordingly to this scenario, a large number of the contributions that are part of this Chapter focus on numerical modeling.

The simplest qualitative method, which mainly consists in estimating the distal limit of motion, the distribution of intensity within the impact area and the potential direction of motion on a topographic map by following the direction of steepest descent from the source area (subjectively accounting for spreading, superelevation and possible avulsion in channel bends), is here proposed only by Lima who describes a methodology called “Relative Rapid Landslides Analysis” for rapid evaluation of risk. This methodology is based on five different indicators of risk. Each of these indicators is estimated based on experience, judgment and the observation of similar landslides. The sum of these values results in an index of relative landslide risk of the area.

Quantitative runout analysis methods are less subjective and can be broadly classified as either empirical or analytical. In regard to the analytical class, discontinuum and continuum methods have advanced incrementally over the past three decades to the point where, when used in combination with careful engineering and geological judgment, first-order runout prediction appears to be possible. However, there is still room considerable for improvement.

In defining the characteristics of mathematical and numerical models for the simulation of rapid landslides, it is important that all the key aspects that control the dynamics of a moving mass are taken into account. As to this, Crosta et al. investigate the important role of processes as entrainment of material located along the landslide path in changing the runout configuration. Before moving to the application to real site problems, they interpret this phenomenon referring to laboratory experiments. Similarly, Pisani et al. evidence that the rheological parameter calibration can result altered, even in simulating laboratory experiments, if some important factors as the centripetal acceleration are neglected in the numerical

implementation. In this regard, it is proved that the consequence of including the centripetal effect in the set of governing equations is a significant lowering of the dynamic basal friction angle necessary to back-calculate some simulated experiments, this makes the value of the friction angle much closer to the real one than if the centripetal acceleration term is neglected.

A major problem in applying numerical modeling to the study of real events is the definition of constitutive laws and the calibration of their rheological parameters, which cannot be measured directly and which are crucial for a realistic simulation of a landslide behavior. Both Deangeli et al. and Quan Luna et al. focus their papers on this aspect. In particular, Deangeli et al. analyze debris-flows and propose that the constitutive law is selected as a function of the lithology existing in the investigated basin. They evidence that, among others, the content of fine fraction in the flowing mass contributes in the distinction from collisional to viscoplastic regimes. Validation of the approach is made through the application of a Cellular Automata Model to cases of debris-flows at basins having different lithological characteristics in North-western Alps. Quan Luna et al. aim to quantify the uncertainties in resistance parameters and release volumes through the definition of probability distributions to be used as input for runout modeling probabilistic methodologies.

With regard to rheological problems, laboratory experiments can give an interesting contribution in investigating landslide dynamics from a physical point of view, in validating a numerical model and in identifying the more appropriate rheology for an analysed event. In particular, Cola et al. perform laboratory experiments to study the interrelations between the grain-size composition of mud-flows and the rheological properties at different solid concentrations. Guilhem et al. analyse in laboratory a single-particle impacts to assess parameters to be used in the contact law adopted in a numerical model based on the discrete element method. Once calibrated, the model allows the study of the influence of several parameters on the propagation of a granular mass.

On the other side, Manzella et al. and Sauthier and Labiouse use laboratory experiments specifically to study the influence of different parameters (e.g. volume, falling height, slope angle) on the characteristics of the final deposit (e.g. runout and extension). In particular, Manzella et al. investigate the motion of large masses with the aim of determine the reasons of the mass high mobility, which results much greater than could be predicted using frictional models. The same aspect is treated by Sosio et al. who replicate the motion of historical rock/debris avalanches using a Frictional and a Voellmy models and define a range of values for the parameters of each rheology, which best replicate the propagation.

With reference to site analysis, Marsella et al. discuss the implication of parameter choice on maximum runout and invasion of inhabited areas in case of some pyroclastic debris-avalanches. Similarly, Mortara et al. calibrate the input parameters for the rheological model assumed to numerically simulate a well-documented case of ice-rock avalanche. In site applications, Tobler et al. and Filipello and Mandrone propose the approach to runout modeling with GIS-based models with reference to shallow landslides and rockfall, respectively.

An interesting discussion on the possible advantages of using a two-phase model respect to the above mono-phase model, to simulate debris-flow propagation, is open by Stancanelli et al. They underline that the calibration of a two-phase model could be easier, since parameters have a more specific physical meaning respect to the empirical tuning of the parameters used in a mono-phase model.

From a detailed analysis of the all the here described contributions, it emerges that numerical models for landslide runout simulations are of wide interest given the high importance of the results they can give in respect to the territory management, however the major problem that concerns all the approaches is the difficulty in calibrating the parameters necessary to reproduce the real behavior of the complex type of investigated phenomena.

A consensus on the best method of determining the input resistance parameter values for predictive runs has not yet emerged.



Runout Prediction of Debris Flows and Similar Mass Movements

Christian Scheidl, Dieter Rickenmann, and Brian W. McArdell

Abstract

All around the world, people meet a challenge to find a balance between the risk of natural hazards and the need for spatial developments. Densely populated hillside regions in humid, subtropical or tropical climatic zones are often prone to various types of landslides. The complex flow behaviour of such gravitationally driven mass movements is reflected by inconsistent terminologies and ambiguous definitions of various landslide types in literature (Varnes 1978; Hutchinson 1988; Hungr et al. 2001). In this paper we focus on a discussion of on runout prediction methods of flow like mass movements, particularly on debris flows, where all transported material is generally in suspension and fluid and solid particles of all sizes typically travel with the same velocity. The term runout refers to the depositional part of a landslide or debris-flow event, providing information on the areas potentially covered by the transported solid material.

Keywords

Runout • Debris flows • Mass movements • Deposition • Simulation • Hazard assessment

Introduction

All around the world, people meet a challenge to find a balance between the risk of natural hazards and the need for spatial developments. Densely populated hillside regions in humid, subtropical or tropical climatic zones are often prone to various types of landslides. The complex flow behaviour of such gravitationally driven mass movements is reflected by inconsistent terminologies and ambiguous definitions of various landslide types in literature (Varnes 1978; Hutchinson 1988; Hungr et al. 2001). In this paper we focus on a discussion of on runout prediction methods of flow like mass movements, particularly on debris flows,

where all transported material is generally in suspension and fluid and solid particles of all sizes typically travel with the same velocity. The term runout refers to the depositional part of a landslide or debris-flow event, providing information on the areas potentially covered by the transported solid material.

In Alpine regions, debris flows are often observed in small catchments with steep channels endangering human settlements and infrastructures. After several decades of active mitigation measurements against slope instabilities and channel erosion, passive protection methods were established and the concept of risk management was introduced (Fuchs et al. 2008). In Alpine countries hazard assessment methods were introduced (Heinimann et al. 1988; Länger 2003) and qualitative and semi-qualitative risk analysis methods conceptually applied (Guzzetti 2000; Kappes et al. 2011). Starting in the middle of the last century hazard maps were established, delineating endangered areas based on the magnitude and the intensity of the examined process. The quantitative estimation of principal landslide parameters, such as event magnitude, runout length, and

C. Scheidl (✉)
University of Natural Resources and Life Sciences, Vienna A-1190,
Austria
e-mail: christian.scheidl@boku.ac.at

D. Rickenmann • B.W. McArdell
Swiss Federal Research Institute WSL, Birmensdorf CH-8903,
Switzerland

deposition area are therefore an important task for an effective hazard assessment.

For flow like mass movements, the magnitude of an event is often characterized by the potential landslide volume. Several approaches were developed during the last years, to simulate deposition and runout behaviour of mass movements. However, the practical application, respectively the selection of adequate runout prediction models, is mainly based on their availability and on the requirements of local hazard assessments (Scheidl and Rickenmann 2011).

In this paper a brief overview of runout prediction methods is given for flow like mass movements and especially for debris flows. Furthermore, examples of 2D runout predictions for debris-flow events are presented, applying an empirically based simulation model (TopRunDF) and a dynamic numerical simulation model (RAMMS). Finally input parameters necessary for both simulation models are discussed.

Runout Prediction Methods

Griswold (2004) listed four basic principles for the development of runout prediction methods. Such methods are based either on (1) the use of historic and geologic evidence of past flows to estimate inundation limits of future flows, (2) the use of physically based models that invoke conservation of mass, momentum, and energy to calculate prospective inundation limits, (3) the use of statistically calibrated empirical equations derived from analysis of inundation data, or (4) the use of statistically calibrated inundation equations that are constrained by physical scaling arguments. Chen and Lee (2004) identified empirical, physical scale and dynamical approaches to model kinematic parameters and hazard zones. Rickenmann (2005) distinguished between empirical-statistical and dynamical runout prediction methods for debris flows. Many empirical-statistical methods for runout prediction require only a few input parameters and are easy to use. However, such empirical methods should only be applied to conditions similar to those on which their development is based (Rickenmann 2005). In contrast, dynamical models are independent from local conditions, since such models implement physical principles like the conservation of mass, momentum and energy of bulk mixtures. Dynamical models are often continuum based and solved with numerical methods, allowing the simulation of flow and deposition behaviour over a complex three-dimensional topography. However, the challenge with these models is the selection of an appropriate flow rheology or of the constitutive equations of the material behaviour and the estimation or calibration of the key model parameters (e.g. O'Brien et al. 1993; Iverson and Denlinger 2001; McDougall and Hungr 2005; Medina et al. 2008; Pirulli 2005; Beguería et al. 2009).

Empirical-Statistical Methods

Empirically based one dimensional runout prediction methods for rock- and dense snow- avalanches and other flow like mass movements were first applied and further developed in the context of landslide hazard assessment (Heim 1932; Scheidegger 1973; Körner 1976), and were later adapted to debris flows (Corominas 1996; Rickenmann 1999; Legros 2002; Toyos et al. 2008). One of the most simple empirical model estimates the total travel distance as a function of the potential event volume and the angle of reach, using or the longitudinal profile of the expected flow path. Applying such a model to 140 debris flows from the Swiss Alps and 51 large landslides/rock avalanches, comparatively shorter travel distances are observed for landslides/rock avalanches than for debris flows or lahars or mud flows (Rickenmann 2005). Hence, for a given volume, debris flows usually show a larger mobility, or lower travel angles, than landslides and rock falls. However, Rickenmann and Scheidl (2010) showed that the uncertainties of the estimated runout distance on the fan (the depositional part of a debris-flow event) can be high, according to the predicted angle of reach or total travel distance. Prochaska et al. (2008) proposed a similar empirical method, estimating the runout for non-volcanic debris flows (ACS-model), but this method uses solely topographical parameters and does not account for a changing event volume. Scheidl and Rickenmann (2010) applied the ACS model to a subset of observed debris-flow events and found that the ratio of predicted to observed runout lengths has a tendency for a systematic under-prediction of runout lengths with increasing event volumes. Cannon (1993) as well as Fannin and Wise (2001) estimated the total travel distance based on a sediment budget along the flow path. A more detailed discussion of volume-balance approaches can be found in Rickenmann (2005).

However, for a more detailed delineation of potentially endangered areas, the runout pattern or the surface area on the debris-flow fan should be known, i.e. the two-dimensional aspect of the deposition pattern should be considered as well. A simple empirical model for this purpose was first developed for lahars by Iverson et al. (1998). Based on the assumption of geometric similarity they proposed a semi-theoretical relationship between the planimetric deposition area, the cross sectional flow area and the total event volume. This approach was implemented in the program LAHARZ, a GIS-based simulation model (Schilling 1998). Subsequently, more comprehensive observations on debris flows were used to test or modify the original approach of Iverson et al. (1998) in studies by Crosta and Agliardi (2003), Griswold (2004), Berti and Simoni (2007), and Griswold and Iverson (2008). Scheidl and Rickenmann (2010) developed the GIS-based simulation tool TopRunDF

to predict deposition area as well as deposition height of a debris-flow event on the fan. The model combines the geometric similarity criterion between the planimetric deposition area and the total event volume with a random walk method for the flow path estimation, first proposed by Hürlimann et al. (2008). An example application of TopRunDF to a debris-flow event in Italy is presented below.

The geometric similarity relationship between surface area and debris-flow volume shows a tendency for varying mobility coefficients (reflecting varying mean deposition heights) as a function of process type. For a given event volume, Scheidl and Rickenmann (2010) found smaller planimetric deposition areas for granular debris flow processes than for debris-floods or mudflows; this smaller mobility of the former process type may also be reflected by steeper fan slopes. Crosta et al. (2003) proposed that the variations of the mobility coefficient indicate that non volcanic debris-flows move less fluidly and form thicker deposits than most lahars. Several studies describe granular debris flows, debris avalanches or rock avalanches as less mobile than debris-floods, mudflows or lahars, which show a higher concentration of finer material and/or water, implying a more viscous or muddy interstitial fluid (Crosta et al. 2003; Hungr et al. 2001; Iverson 1997).

Dynamical Methods

Kinematic flow parameters like flow velocities or dynamic impact forces are often needed for a more detailed hazard assessment. This typically requires to apply numerical simulation models, which represent a more physically based description of the flow behaviour of gravitational mass movements of solid-water mixtures. The kinematic flow characteristics of a debris flow depend for example on the topographical and surface friction conditions, the water content, the sediment size and sorting and on the dynamic interaction between the solid and fluid phases of the debris-flow mixture (Iverson 1997). Therefore, dynamical models are sometimes difficult to apply and generally require a “calibration” of rheologic or friction parameters by back-calculation of past events (Naef et al. 2006; Rickenmann et al. 2006; Tecca et al. 2007; Hürlimann et al. 2008; Pirulli and Sorbino 2008; Hochschwarzer 2009).

A simpler dynamical approach determines the kinematic parameters of a single phase bulk mixture represented by a mass-point (often referred to as mass-point model). A one-dimensional, analytical mass-point model for debris flows was first proposed by Takahashi and Yoshida (1979), Hungr et al. (1984) and Takahashi (1991). This one-dimensional model assumes that (1) discharge from upstream is constant, and (2) deposition starts at the place where the channel

abruptly levels out; it is therefore also denoted as leading-edge or constant discharge model (VanDine 1996; Prochaska et al. 2008). For a constant flow-width, the linear runout distance on the fan can analytically be estimated under consideration of mass and momentum conservation. The constant discharge model can only yield plausible results (positive runout distances), if the friction slope (S_{fric}) exceeds the average channel gradient of the fan (S_f). Studies of Jackson et al. (1987), Marchi and Tecca (1995), Chau et al. (2000) and Rickenmann (2005) imply that granular flow behaviour will lead to a higher roughness and friction during depositional flow, resulting in steeper fan slopes on average and in a smaller mobility. A more viscous or muddy flow behaviour, on the other hand, shows higher mobility and results in smoother and flatter fans. Based on five Canadian debris-flow events, Hungr et al. (1984) found reasonable agreement between observed runouts on the fan and those predicted by the constant discharge model by assuming a constant friction slope ($S_{fric} = \tan 10^\circ = 0.176$). Based on 14 debris-flow events at the Kamikamihori valley in Japan (Okuda and Suwa 1984), Rickenmann (2005) reported better runout predictions with $S_{fric} = 1.12 S_f$. He further found reasonable predictions of runout length for 12 Swiss debris-flow events of 1987 with $S_{fric} = 1.08 S_f$. D’Agostino et al. (2010) found $S_{fric} = 1.072 S_f$, based on investigations of six debris-flow events in the Dolomites (Eastern Italian Alps). Based on 63 observed debris-flow runout distances in Northern Italy (South Tyrol) and Switzerland, Rickenmann and Scheidl (2010) proposed a friction slope of $S_{fric} = 1.29 S_f$.

The two parameter mass-point model of Voellmy (1955), originally developed for snow avalanches (Körner 1980; Perla et al. 1980), has been widely used to simulate the runout of debris flows (Rickenmann 1990; Zimmermann et al. 1997; Gamma 2000; Hürlimann et al. 2003; Bertolo and Wieckzorek 2005; McDougall 2006; Naef et al. 2006; Evans et al. 2007; Scheuner 2007; Revellino et al. 2008; Hochschwarzer 2009; Stricker 2010). This model has also been applied to rock avalanches (Körner 1980; Sosio et al. 2008; Hungr and Evans 1996; McKinnon et al. 2008) and ice-rock avalanches (Knobel 2007; Allen et al. 2009). Applications of the Voellmy approach to estimate the runout of snow avalanches can be found in Barbolini et al. (2000) and Christen et al. (2010). The Voellmy “fluid” characterises the total resistance to flow by a basal friction coefficient (Coulomb-friction) and a turbulence friction coefficient. The basal frictional term relates the shear stress to the normal stress through the friction coefficient μ . The turbulent term summarises all velocity-dependent factors of flow resistance, and is expressed by either a Chezy coefficient C (used in hydraulics) or a turbulence coefficient $\xi = C^2$ (ξ is often used in snow avalanche modelling). Figure 1 illustrates the range of best fit parameters C and μ obtained from back-calculation in different studies, typically optimizing

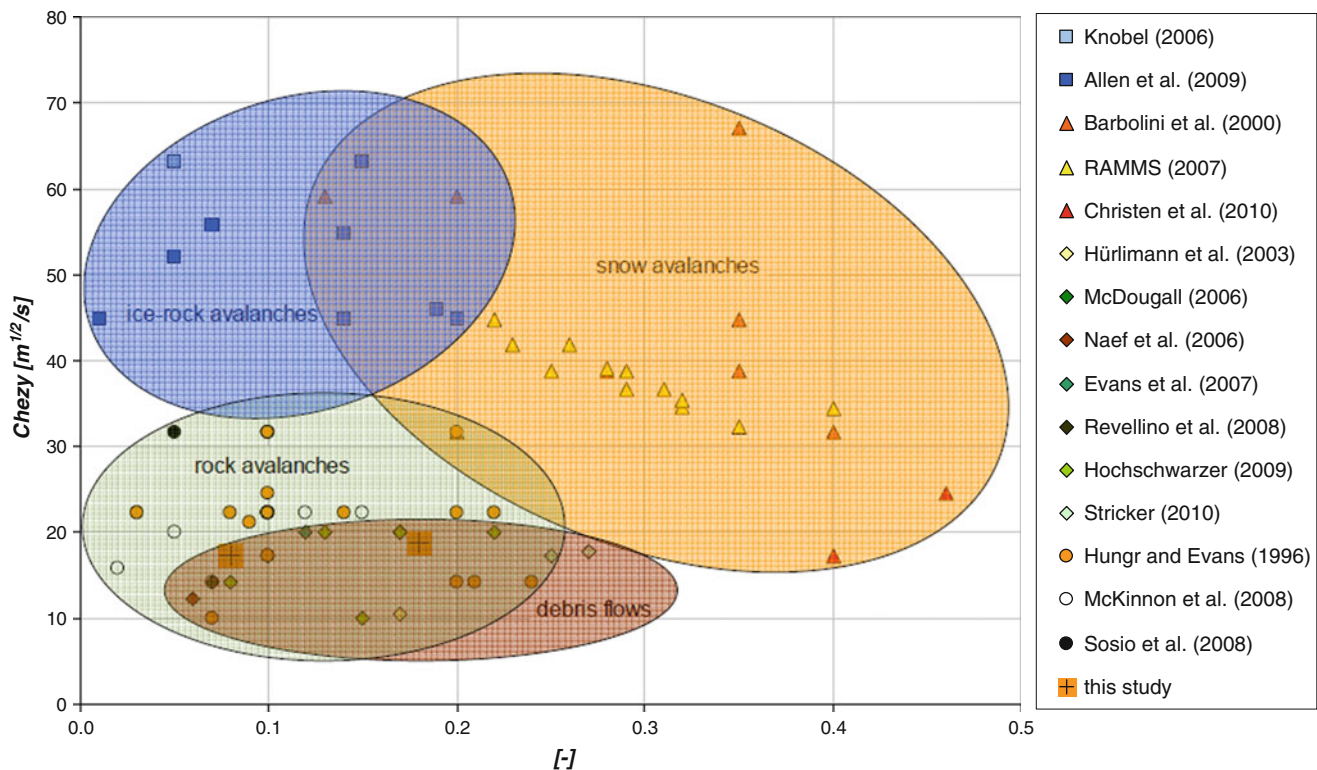


Fig. 1 Turbulent and coulomb friction best-fit parameters for back-calculations of observed events with a continuum model for flow simulations based on a Voellmy “fluid”, as obtained in selected studies.

The parameter domains delineated by ellipsoidal surfaces represent a rough grouping according to process type

predicted and observed depositional area and/or flow velocities along the flow path. A grouping of gravitational flow-like mass movements is illustrated in Fig. 1, based on the compiled ranges of the best fit parameters C and μ . However, this grouping shows a large variability of the parameter domain for a given process type.

The Voellmy fluid approach is implemented in several runout simulation tools such as DAN (Hungr 1995), FlatModel (Medina et al. 2008), RAMMS-avalanche (Bartelt et al. 1999; Christen et al. 2010; RAMMS 2010), MassMov2D (Beguiría et al. 2009) or RASH3D (Pirulli and Sorbino 2008). An example application of a runout simulation using the RAMMSmodel for a debris-flow event in Italy is presented below.

A continuum based simulation model with a viscoplastic flow rheology considers a debris flow as a single phase Bingham – or Herschel-Bulkley – fluid for which the normal and shear stresses vary either linearly or as a power function with shear rate (Johnson and Rodine 1984; Coussot 1997; Coussot et al. 1998; Kaitna and Rickenmann 2007). The viscoplastic model has been implemented for example in the simulation tools DAN, FlatModel and MassMov2D.

Another rheological approach, referred to as the “quadratic rheology” model, combines the Bagnold grain shearing model accounting for dispersive shear stress, the Bingham model accounting for viscous stress, and a Manning coefficient accounting for turbulent stress. This rheological model is implemented in Flo2D (O’Brien et al. 1993), a widely used flood routing simulation tool for assessing mud- and debris flow behavior.

Another model proposed for debris flows accounts for the interaction of solid particles and the fluid within the simulated mass flux. Based on the work of Bagnold (1954), the inertial grain flow model considers interaction of grains suspended in a fluid. Takahashi (1991) developed both one- and two-dimensional continuum models based on the Bagnold theory. A similar model for the two-dimensional simulation of grain-inertia debris flows in erodible channels was proposed by Armanini et al. (2009). The fluid–solid momentum transport model or mixture theory incorporates both fluid-particle and particle-particle interactions and was proposed by Iverson (1997). Kowalski (2008) enhanced the mixture theory by taking into account a varying, vertical distribution of mass based on possible slip between the bulk flow components.

Table 1 Upper part: input parameters and back-calculated best-fit parameters for the study site. Lower part: input and back-calculated values are related to the used simulation models in this study. A *sign denotes fixed input parameters whereas a (*)sign denotes variable parameters for back-calculation

	V_{obs} [m ³]	B_{obs} [m ²]	S_{fan} [-]	k_{Bobs} [-]	μ [-]	ζ [m/s ²]
Arundakopfbach	15,000	35,505	0.19	58	0.08	300
Seefeldbach	70,000	62,266	0.26	37	0.18	350
TopRunDF	*			*		
RAMMS-av.	*				(*)	(*)

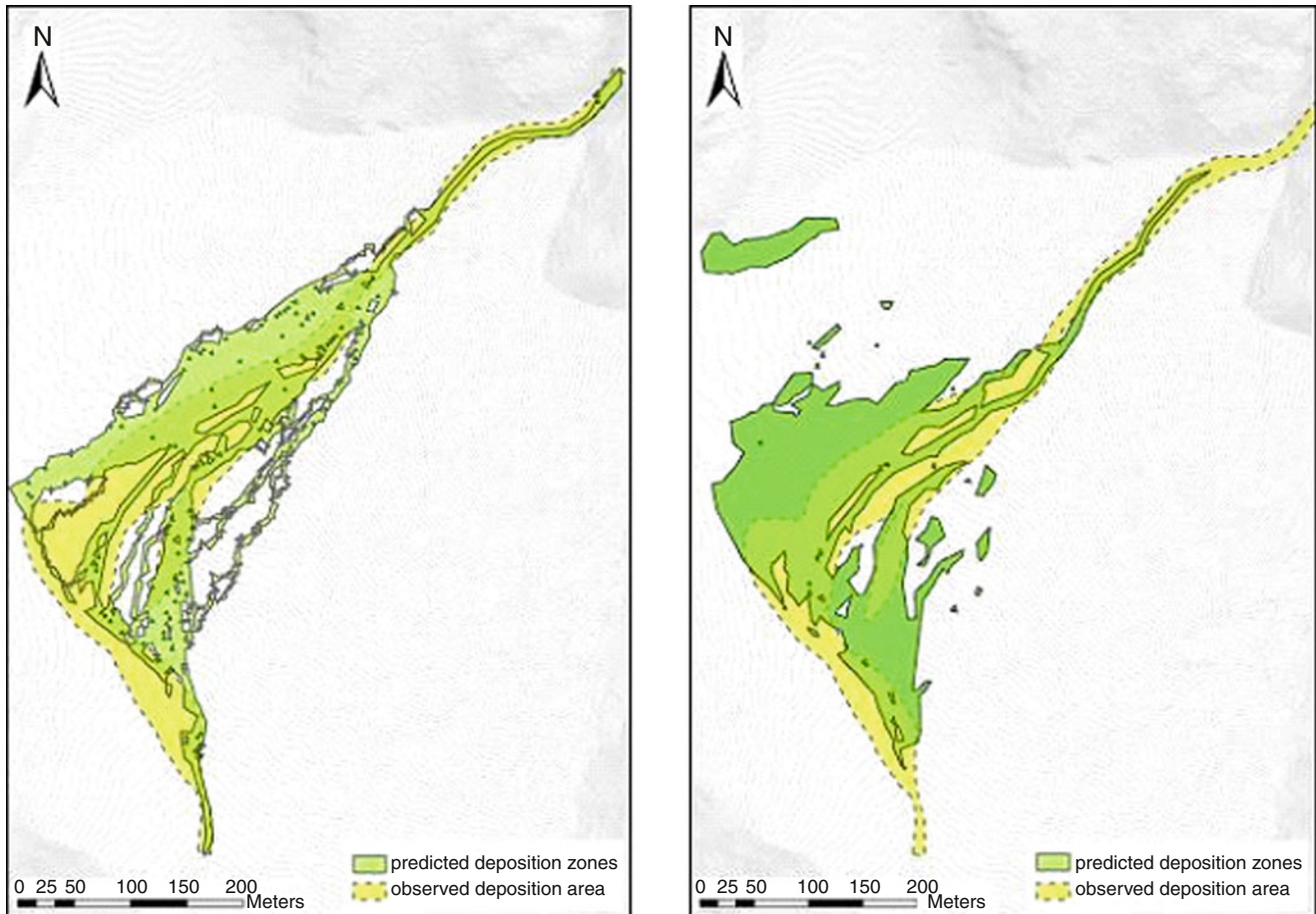


Fig. 2 (Left): Best-fit simulation results of the debris-flow event at the Arundakopfbach (IT), using TopRunDF. (Right): Best-fit simulation results of the Arundakopfbach debris-flow event using RAMMS-avalanche

Comparison of Two Debris-Flow Runout Simulation Models

Here we apply two debris-flow runout simulation models to the debris-flow events in June 2002 at the Arundakopfbach and at the Seefeldbach, both located in South Tyrol (Italy). For this event a back-calculation was performed to determine the best-fit simulation, using the empirically based runout model TopRunDF and the continuum based dynamical model RAMMS-avalanche with the Voellmy fluid “rheology”. The best-fit simulation is obtained for a

minimum difference between the simulated deposition zones and the observed deposition area. A more detailed comparison of simulated and observed deposition areas and volumes was made for lahar inundation zones by Carranza and Castro (2006) and for debris-flow runout patterns by Scheidl and Rickenmann (2010).

Using TopRunDF, the best-fit simulation is directly related to the observed debris-flow deposition area B_{obs} for a given event volume V_{obs} , characterised by the individual mobility coefficient $k_{Bobs} = B_{obs}V_{obs}^{-2/3}$. Apart from the starting point of deposition and the choice of the mobility coefficient k_{Bobs} , no further parameter selection is needed.

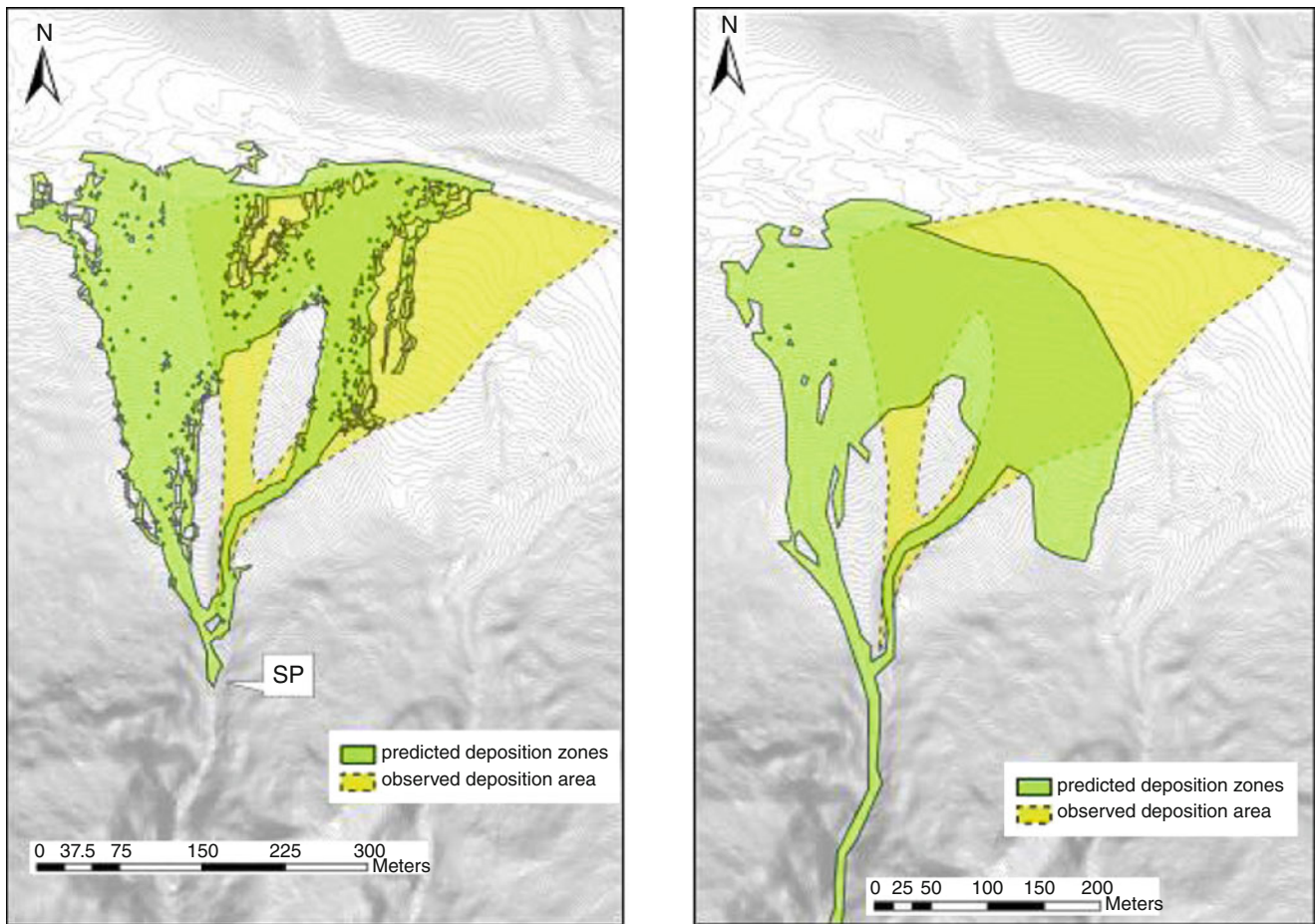


Fig. 3 (Left): Best-fit simulation results of the debris-flow event at the Seefeldbach (IT), using TopRunDF. (Right): Best-fit simulation results of the Seefeldbach debris-flow event using RAMMS-avalanche

In RAMMS-avalanche the “Voellmy” model is applied, resulting in two variable parameters, μ and ζ , which required a study of multiple parameter-comparisons to obtain the best-fit simulations for the test-site. Table 1 gives an overview of the used parameters for both simulations. The upper part refers to the documented (with S_{fan} the average fan slope) and “best-fit” back-calculated input values for the case study events. The lower part in Table 1 shows which general input parameters of the used simulation models remained fixed and which rheological parameters needed to be adapted for the back-calculation analysis.

Figure 2 shows the best-fit results of the debris-flow event at the Arundakopfbach, simulated with TopRunDF and RAMMS-avalanche. For TopRunDF the average deposition height of 0.43 m is given as input by the ratio of observed event volume to observed deposition area. The average deposition height predicted with RAMMS-avalanche is 0.33 m. Since the same input volume was used for the simulations with the two models, this implies a larger simulated total deposition area obtained with RAMMS than with TopRunDF. However, for this TopRunDF

simulation the size of the observed deposition area (but not its location) is used as input parameter. If TopRunDF is used for predictions, an estimated size of the deposition area is used for the simulation of its location. The deposition area of the RAMMS simulation in Fig. 2 is related to the “final” simulation time step of 300 s. This time step was defined for the condition that 95 % of the total volume remained immobile or that the average velocity at the front reached a value less of than 0.5 m/s.

Generally the runout prediction of both simulation models for the debris-flow event at the Arundakopfbach show plausible results as compared to the observed deposition zones. For TopRunDF the starting point of the simulation was chosen near the upmost region of the observed deposition area on the fan. The simulation results are only influenced by the topography on the fan and the flow path routing algorithm. Since the RAMMS model does not allow to run with an input-hydrograph (including debris material), the input-volume was applied within a freely defined release area in the transition zone. Assuming constant friction parameters μ and ζ , Hochschwarzer (2009) showed that the shape and location of

the selected release area does not result in variable dynamic parameters as long as the release zone is far enough from the starting point of the observed deposition area. However, the results of the RAMMS simulation may be influenced by the topography near the starting point of the observed deposition area, which appears to be sensitive with regard to the determination of the best-fit friction parameters. As shown for the Arundakopfbach (Fig. 2, right), a certain amount of deposited material lies outside the expected region, mainly because of a deflection of the flowing mass above the start point of the observed deposition area. The overall runout distances predicted with RAMMS are very similar to the results of TopRunDF which might be partly due to the deflection of the flow by the hill slope at the bottom of the fan.

The best-fit results for the simulation of the debris-flow event at the Seefeldbach with TopRunDF and RAMMS are shown in Fig. 3. For TopRunDF the average deposition height of 1.11 m is given as input by the ratio of observed event volume to observed deposition area. The average deposition height predicted with RAMMS-avalanche is 0.99 m. The deposition area of the RAMMS simulation in Fig. 3 is related to the “final” simulation time step of 260 s. Both applied simulation models predict large parts of the deposition outside the observed deposition area. However, the similar runout patterns predicted by both models reflect the important influence of the topography of the fan near the apex. The stopping criterion for the RAMMS simulation was the same as for the simulation of the Arundakopfbach debris-flow event.

Concluding Remarks

A variety of runout prediction models based on different approaches were proposed for gravitationally driven flow-like mass movements. Most approaches are essentially of empirical nature and better predictions may be expected for situations which are similar to the underlying data. Some simple and GIS based simulation tools, such as LAHARZ and TopRunDF, combine empirical equations with topographical information, and may be used to predict potential hazard zones. The relative success of such models is due to the fact that topography governs runout flow and deposition pattern in many situations to a large extent. However, such models are not able to estimate flow depth and mean velocity which are often required for a more detailed hazard assessment.

The most complete characterisation of debris-flow processes is provided by continuum based dynamic runout methods. In many case studies, the two parameter model representing a Voellmy “fluid” was applied successfully to different gravitational mass movements. This approach appears to be quite robust. In most cases, the two governing

friction parameters were held constant during the simulation. Further research is needed to improve the “rheological” models describing the flow process and to guide the selection of an appropriate model “rheology” for practical applications of continuum based simulation models of gravitational mass movements.

References

- Allen KS, Schneider D, Owens IF (2009) First approaches towards modelling glacial hazards in the Mount Cook region of New Zealand's Southern Alps. *Nat Hazards Earth Syst Sci* 9:481–499
- Armanini A, Fraccarollo L, Rosatti G (2009) Two-dimensional simulation of debris flows in erodible channels. *Comput Geosci* 35:993–1006
- Bagnold RA (1954) Experiments on a gravity-free dispersion of large solid spheres in a Newtonian fluid under shear. *Proc Roy Soc Lond* 225:49–63
- Barbolini M, Gubler U, Keylock CJ, Naaim M, Savi F (2000) Application of statistical and hydraulic-continuum dense-snow avalanche models to five real European sites. *Cold Reg Sci Technol* 31:133–149
- Bartelt P, Salm B, Gruber U (1999) Calculating dense-snow avalanche runout using a Voellmyfluid model with active/passive longitudinal straining. *J Glaciol* 45:212–254
- Beguéría S, Asch TWJV, Malet J-P, Gröndahl S (2009) A GIS-based numerical model for simulating the kinematics of mud and debris flows over complex terrain. *Nat Hazards Earth Syst Sci* 9:1897–1909
- Berti M, Simoni A (2007) Prediction of debris flow inundation areas using empirical mobility relationships. *Geomorphology* 90:144–161
- Bertolo P, Wieczorek GF (2005) Calibration of numerical models for small debris flow in Yosemite Valley, California, USA. *Nat Hazard Earth Syst Sci* 5:993–1001
- Cannon SH (1993) An empirical model for the volume-change behavior of debris flows. In: Shen HW, Su ST, Wen F (eds) *Hydraulic engineering 93*, vol 2. American Society of Civil Engineers, New York, pp 1768–1773
- Carranza EJM, Castro OT (2006) Predicting Lahar-inundation zones: case study in west Mount Pinatubo, Philippines. *Nat Hazards* 37:331–372
- Chau KT, Chan LC, Wai WH (2000) Shape of deposition fan and runout distance of debris-flow: effects of granular and contents. In: Wieczorek GF, Naeser ND (eds) *Debris-flow hazards mitigation: mechanics, prediction, and assessment*. A.A. Balkema, Rotterdam/Brookfield, pp 387–395
- Chen H, Lee CF (2004) Geohazards of slope mass movement and its prevention in Hong Kong. *Eng Geol* 76:3–25
- Christen M, Kowalski J, Bartelt P (2010) RAMMS: numerical simulation of dense snow avalanches in three-dimensional terrain. *Cold Reg Sci Technol* 63:1–14
- Corominas J (1996) The angle of reach as a mobility index for small and large landslides. *Can Geotech J* 33:260–271
- Coussot P (1997) *Mudflow rheology and dynamics*, IAHR monograph series. Balkema, Rotterdam
- Coussot P, Laigle D, Arattano M, Deganutti A, Marchi L (1998) Direct determination of rheological characteristics of debris flow. *J Hydraul Eng* 124:865–868
- Crosta G, Agliardi F (2003) A methodology for physically-based rock-fall hazard assessment. *Nat Hazards Earth Syst Sci* 3:407–422

- Crosta G, Cucchiario S, Frattini P (2003) Validation of semi-empirical relationships for the definition of debris-flow behavior in granular materials. In: Rickenmann D, Chen C-I (eds) Debris-flow hazards mitigation: mechanics, prediction, and assessment. Millpress, Rotterdam
- D'Agostino V, Cesca M, Marchi L (2010) Field and laboratory investigations of runout distances of debris flows in the Dolomites (Eastern Italian Alps). *Geomorphology* 115:294–304
- Evans S, Guthrie RH, Robert N, Bishop N (2007) The disastrous 17 February 2006 rockslide-debris avalanche on Leyte Island, Philippines: a catastrophic landslide in tropical mountain terrain. *Nat Hazards Earth Syst Sci* 7:89–101
- Fannin RJ, Wise MP (2001) An empirical-statistical model for debris flow travel distance. *Can Geotech J* 38:982–994
- Fuchs S, Kaitna R, Scheidl C, Hübl J (2008) The application of the risk concept to debris flow hazards. *Geomechanik und Tunnelbau* 2:120–129
- Gamma P (2000) dfwalk – Ein Murgang-Simulationsprogramm zur Gefahrenzonierung, vol G66, Geographica Bernensia. Geographisches Institut der Universität Bern, Bern, p 144
- Griswold JP (2004) Mobility statistics and hazard mapping for non-volcanic debris flows and rock avalanches. Master's thesis, Portland State University, pp 200
- Griswold JP, Iverson RM (2008) Mobility statistics and automated hazard mapping for debris flows and rock avalanches, vol 5276, Scientific investigations report. U.S. Geological Survey, Reston
- Guzzetti F (2000) Landslide fatalities and the evaluation of landslide risk in Italy. *Eng Geol* 58:89–107
- Heim A (1932) Bergsturz und Menschenleben. Fretz & Wasmuth, Zürich
- Heinimann H, Hollenstein K, Kienholz H, Krummenacher B, Mani P (1988) Methoden zur Analyse und Bewertung von Naturgefahren Umwelt Materialien. Bundesamt für Umwelt, Wald und Landschaft, Bern, p 248
- Hochschwarzer M (2009) Vergleich von Simulationsmodellen zur Reichweitenabschätzung alpiner Murgänge am Beispiel Südtiroler Ereignisse. Master's thesis, University of Applied Life Sciences and Natural Resources, p 135
- Hungr O (1995) A model for the runout analysis of rapid flow slides, debris flows, and avalanches. *Can Geotech J* 32:610–623
- Hungr O, Evans S (1996) Rock avalanche run out prediction using a dynamic model. In: Senneker K (ed) Landslides. A.A. Balkema, Rotterdam, pp 233–238
- Hungr O, Morgan G, Kellerhals R (1984) Quantitative analysis of debris torrent hazards for design of remedial measures. *Can Geotech J* 21:663–677
- Hungr O, Evans S, Bovis MJ, Hutchinson JN (2001) A review of the classification of landslides of the flow type. *Environ Eng Geosci* 7:221–238
- Hürlimann M, Rickenmann D, Graf C (2003) Field and monitoring data of debris-flow events in the Swiss Alps. *Can Geotech J* 40:161–175
- Hürlimann M, Rickenmann D, Medina V, Bateman A (2008) Evaluation of approaches to calculate debris-flow parameters for hazard assessment. *Eng Geol* 102:152–163
- Hutchinson JN (1988) General report: morphological and geotechnical parameters of landslides in relation to geology and hydrogeology. In: Bonnard C (ed) Fifth international symposium on landslides, vol 1. A.A. Balkema, Rotterdam/Brookfield, pp 3–136
- Iverson RM (1997) The physics of debris flows. *Rev Geop* 35(3):245–296
- Iverson RM, Denlinger RP (2001) Flow of variably fluidized granular masses across three-dimensional terrain. *J Geophys Res* 106:537–552
- Iverson RM, Schilling SP, Vallance JW (1998) Objective delineation of lahar-inundation hazard zones. *Geol Soc Am Bull* 110:972–984
- Jackson L, Kostaschuk R, McDonald G (1987) Identification of debris flow hazard on alluvial fans in the Canadian Rocky Mountains. *Geol Soc Am Rev Eng Geol* 7:115–124
- Johnson AM, Rodine JR (1984) Debris flow. In: Brunson D, Prior DB (eds) Slope instability. Wiley, Chichester, p 257
- Kaitna R, Rickenmann D (2007) A new experimental facility for laboratory debris flow investigation. *J Hydraul Res* 45:797–810
- Kappes MS, Malet J-P, Rematre A, Horton P, Jaboyedoff M, Bell R (2011) Assessment of debris-flow susceptibility at medium-scale in the Barcelonnette Basin, France. *Nat Hazards Earth Syst Sci* 11:627–641
- Knobel R (2007) Modellierung von Murgängen und Eislawinen in Nordostetien mit Hilfe des RAMMS-Modells und systematischen Testens von Satellitenbildern. Master-thesis at the University of Zürich
- Körner HJ (1976) Reichweite und Geschwindigkeit von Bergstürzen und Fliesslawinen. *Rock Mec* 8:225–256
- Körner HJ (1980) Modelle zur Berechnung der Bergsturz- und Lawinenberechnung. In: Internationales symposium "Interpraevent", vol 2. Klagenfurt, Austria, pp 15–55
- Kowalski J (2008) Two-phase modelling of debris flows. Ph.D. thesis, ETH Zürich, Dissertation, ETH No. 17827, p 135
- Länger E (2003) Der Forsttechnische Dienst für Wildbach- und Lawinenverbauung in Österreich und seine Tätigkeit seit der Gründung im Jahre 1884. Ph.D. thesis, University of Natural Resources and Life Sciences, Vienna
- Legros F (2002) The mobility of long-runout landslides. *Eng Geol* 63:301–331
- Marchi L, Tecca P (1995) Alluvial fans of the eastern Italian alps: morphology and depositional processes. *Geodinamica Acta* 8:20–27
- McDougall S (2006) A new continuum dynamic model for the analyses of extremely rapid landslide motion across complex 3D terrain. Dissertation at the University of British Columbia, Canada
- McDougall S, Hungr O (2005) Dynamic modelling of entrainment in rapid landslides. *Can Geotech J* 42:1437–1448
- McKinnon M, Hungr O, McDougall S (2008) Dynamic analysis of Canadian landslides. In: Locat J, Perret D, Turmel D, Demers D, Leroueil S (eds) Proceedings of the 4th Canadian conference on Geohazards: from causes to management, Presse de l'Université Laval, Québec, 8p
- Medina V, Hürlimann M, Bateman A (2008) Application of FLATModel, a 2D finite volume code, to debris flows in the north-eastern part of the Iberian Peninsula. *Landslides* 5:127–142
- Naef D, Rickenmann D, Rutschmann P, McArdell BW (2006) Comparison of flow resistance relations for debris flows using a one-dimensional finite element simulation model. *Nat Hazards Earth Syst Sci* 6:155–165
- O'Brien JS, Julien PY, Fullerton W (1993) Two-dimensional water flood and mudflood simulation. *J Hydraul Eng* 119:244–260
- Okuda S, Suwa H (1984) Some relationships between debris flow motion and microtopography for the kamikamihori fan, north Japan Alps. In: Burt TP, Walling DE (eds) Catchment experiments in fluvial geomorphology. GeoBooks, Norwich, pp 447–464
- Perla R, Cheng T, McClung D (1980) A two parameter model of snow avalanche motion. *J Glaciol* 26:197–208
- Pirulli M (2005) Numerical modelling of landslide runout, a continuum mechanics approach. Dissertation, Politecnico di Torino, Torino
- Pirulli M, Sorbino G (2008) Assessing potential debris flow runout: a comparison of two simulation models. *Nat Hazards Earth Syst Sci* 8:961–971
- Prochaska AB, Santi PM, Higgins J, Cannon SH (2008) Debris-flow runout predictions based on the average channel slope (ACS). *Eng Geol* 98:29–40

- RAMMS (2010) RAMMS 1.3.0 rapid mass movements, a modelling system for snow-avalanches in research and practice. User Manual v 1.01, WSL, Institute for Snow and Avalanche Research SLF, pp 109
- Revellino P, Guadagno FM, Hungr O (2008) Morphological methods and dynamic modelling in landslide hazard assessment of the Campania Apennine carbonate slope. *Landslides* 5:59–70
- Rickenmann D (1990) Debris flows 1987 in Switzerland: modelling and fluvial sediment transport. Hydrology in mountainous regions II – artificial reservoirs, water and slopes. IAHS Publication no 194, Lausanne, pp 371–378
- Rickenmann D (1999) Empirical relationships for debris flows. *Nat Hazards* 19:47–77
- Rickenmann D (2005) Runout prediction methods. In: Jakob M, Hungr O (eds) *Debris-flow hazards and related phenomena, praxis*. Springer, Berlin/Heidelberg, pp 305–324
- Rickenmann D, Scheidl C (2010) Modelle zur Abschätzung des Ablagerungsverhaltens von Murgängen. *Wasser Energie Luft* 102:17–26
- Rickenmann D, Laigle D, McArdeell BW, Hübl J (2006) Comparison of 2D debris-flow simulation models with field events. *Computat Geosci* 10:241–264
- Scheidegger AE (1973) On the prediction of the reach and velocity of catastrophic landslides. *Rock Mech* 5:231–236
- Scheidl C, Rickenmann D (2010) Empirical prediction of debris-flow mobility and deposition on fans. *Earth Surf Proc Land* 35:157–173
- Scheidl C, Rickenmann D (2011) TopFlowDf – a simple GIS based model to simulate debris-flow runout on the fan. In: Genevois R, Hamilton D, Prestininzi A (eds) *Proceedings of the 5th international conference on debris-flow hazards: mitigation, mechanics, prediction and assessment*. Italian journal of engineering geology and environment-book, Padua, pp 253–262
- Scheuner T (2007) Modellierung von Murgangereignissen mit RAMMS und Vergleich durch GIS-basiertes Fliessmodell. Master thesis at the University of Zürich, p 106
- Schilling SP (1998) GIS programs for automated mapping of lahar-inundation hazard zones. U.S. Geological Survey Open-File Report, U.S. Geological Survey, Vancouver, p 98
- Sosio R, Crosta GB, Hungr O (2008) Complete dynamic modeling calibration for the Thurwieser rock avalanche (Italian Central Alps). *Eng Geol* 100:11–26
- Stricker B (2010) Murgänge im Torrente Riascio (TI): Ereignisanalyse, Auslösefaktoren und Simulation von Ereignissen mit RAMMS. Master thesis at the University of Zürich, p 104
- Takahashi T (1991) Debris flow. A.A. Balkema, Rotterdam/Brookfield
- Takahashi T, Yoshida H (1979) Study on the deposition of debris flows, part I-Deposition due to abrupt change of bed slope. *Annuals, Disaster Prevention Research Institute, Kyoto University*, p 22
- Tecca P, Genevois R, Deganutti A, Armento M (2007) Numerical modelling of two debris flows in the Dolomites (Northeastern Italian Alps). In: Chen-lung C, Major JJ (eds) *Fourth international conference on debris-flow hazards mitigation: mechanics, prediction, and assessment*, Millpress-Rotterdam, Chengdu
- Toyos G, Gunasekera R, Zanchetta G, Oppenheimer C, Sulpizio R, Favalli M, Pareschi MT (2008) GIS-assisted modelling for debris flow hazard assessment based on the events of May 1998 in the area of Sarno, Southern Italy: II. Velocity and dynamic pressure. *Earth Surf Proc Land* 33:1693–1708
- VanDine DF (1996) Debris flow control structures for forest engineering. Working paper, Ministry of Forest Research Program, Victoria, British Columbia, pp 75
- Varnes DJ (1978) Slope movement types and processes. In: Schuster RL, Krizek RJ (eds) *Landslides, analysis and control*, vol 176, Transportation research board, Special report. National Academy of Sciences, Washington, DC, pp 11–33
- Voellmy A (1955) Über die Zerstörungskraft von Lawinen. *Schweizerische Bauzeitung* 73(12):159–162, (15), pp. 212–217, (17), pp. 246–249, (19), pp. 280–285
- Zimmermann M, Mani P, Gamma P, Gsteiger P, Heiniger O, Hunziker G (1997) Murgangefahr und Klimaänderung: ein GIS-basierter Ansatz. (Schlussbericht NFP 31, p 161), ETH, Zurich



A Ready to Use GRASS GIS Workbench for Rockfall Analysis

Andrea Filipello and Giuseppe Mandrone

Abstract

Open Source software is of great interest to many users and developers. One of the main advantages is that users can develop and adapt it to suit their purposes. This work shows modules developed into GRASS GIS for rockfall analysis. Modules examine both the potential failure detection (rockfall susceptibility) and the area of potential propagation. The study investigate three different mechanisms of failure: planar sliding, wedge sliding and toppling. The modules for rockfall susceptibility are called r.SMR, r.SSPC, r.fsplanar, r.wedgeSMR and r.wedgeSSPC according to the method of analysis adopted, while r.droka is the name of the module developed for the propagation of the landslide. Input data are both numbers and raster maps. GIS modules have been tested with good results in Ossola Valley and, in general, they should be applied in geological settings where the failure mechanism is mainly governed by discontinuity sets.

Keywords

Rockfall susceptibility • GIS • Open source • Rock mass classification • Laser scanner

Introduction

Rock falling and, more generally, fast moving slope processes are very common in the Alps and serious threat to roads, houses, industries and mining activities. High hazard conditions are related not only to the velocity of landslides but also to their high energy and mobility. For these reasons, their hazard analysis and evaluation are two main goals for scientists and institutions that, for various reasons, deal with land use planning. Our test sites are located in Ossola Valley, one of the main N-S trending valley of western Alps, wide-spread affected by rock falling and debris flow (Fig. 1).

In this work we always assess relative hazard (Harlen and Viberg 1988) not considering the time because of the difficulty in defining the triggering factors and, therefore, the evaluation of a returning time.

Since the 1990s, geographic information systems (GIS) took an increasingly important role in the analysis and modeling hazard and susceptibility to landslide, as testified by hundreds of papers produced over the past 20 years from researchers all over the world (Chacón et al. 2006). The use of GIS has some advantages, such as the opportunity to adopt techniques of analysis that would not otherwise be used due to the ability to easily perform calculations of a large number of parameters and to the possibility of overlapping and cross correlating spatial data (map overlay). GIS also offers the possibility to verify results and correct the incoming data.

It is important to emphasize that methods for hazard analysis are not necessarily related to the use of a GIS. For example, slope stability analysis based on physical equations has a long tradition. On the other hand, the development of many statistical approaches, that need to manage and analyze huge quantity of environmental data, is strongly connected with the increasing use of GIS. In this study, GRASS (Geographic Resources Analysis Support System) is the software used to develop modules dedicated to solve

A. Filipello (✉) • G. Mandrone
Dipartimento di Scienze della Terra, Università degli Studi di Torino,
Via Valperga Caluso 35, Torino, Italy
e-mail: andrea.filipello@gmail.com



Fig. 1 Example of typical landslide that can be found in the study area. The photos show the same area before and after a landslide occurred near Formazza during the heavy rainfall of the 19.04.2009

fast moving landslide (especially rock falling). GRASS is a free and open source code that has been developed since the mid-1980s and that knows some diffusions in the Earth Sciences, especially with regard to hydrologic modeling, geomorphology and remote sensing.

Tools and Methods

The main data required for the use of our modules are physical parameters of rock masses and digital elevation model of terrain. Both these data were acquired by traditional analysis, according to specific and well-established techniques of acquisition (as further described) and using innovative techniques based on remote sensing. In particular, the use of terrestrial laser scanning for engineering geology studies is a crucial aspect of this research.

Our study enriches the examples, in strong growth, of applications of terrestrial laser scanning to geological issues, without neglecting the importance of the traditional topographic modeling, field surveys and interpretation of morpho-structural evidences.

Digital Elevation Data

Generation of terrain digital model is needed to extract morphometric characteristics of slopes (slope and aspect), parameters used to analyze geometric conditions that govern the stability of the slope and propagation of gravitational phenomena. Source of elevation data, essential to generate the Digital Terrain Model (DTM), is quite varied and is closely related to the scale and objectives of the study. In summary, sources or techniques used for the acquisition of topographical data, are:

1. Existing base maps;
2. Topographic surveys using total station and GPS;
3. Photogrammetric restitution of aerial photos;
4. Laser scanner surveys;
5. Field radar measurements (GB-InSAR);

In most cases studied, DTM are the interpolation of contour lines and elevation points derived from existing topographic maps (AA.VV 2006).

Geomechanic Parameters

Geomechanic characterization mainly consist in the definition of variables that influence the strength along a discontinuity (dip and dip direction, persistence, spacing, roughness, wall strength, opening, filling, presence of water and number of systems). The methods for the detection and the techniques of analysis, processing and representation of the data are based on the procedures proposed by ISRM (1978) and PRIEST (1993).

Table 1 Modules developed in GRASS for the analysis of the susceptibility to failure for rock instability and to estimate the propagation of landslides

Code	Kinematic	Methodology
r.SMR85	Planar sliding	Romana (1985)
r.SMR07	Wedge sliding	Tomás et al. (2007)
	Toppling	
r.SSPC	Planar sliding	Hack (1998), Hack et al. (2003)
	Wedge sliding	
	Toppling	
r.fsplanar	Planar sliding	Hoek and Bray (1981)
r.droka	Rockfall	Evans and Hungr (1993)

When the logistic is complicated usually due to the steepness of the slope, laser scanner represents the technique for remote analysis of discontinuities that in recent years has seen a growing number of applications and software procedures (Hack et al. 2007). The techniques of processing point cloud for the determination of geomechanics data can be automatic or semi-automatic. The approach in this study is the semi-automatic one and is based on a product derived from data supplied by the laser scanner: the solid image. This product consists in a classic digital image (RGB) added with a matrix containing the distance values obtained from DDSM (Dense Digital Surface Model). Solid image is widely used, especially in geology and architecture. Main applications are referred to the possibility to do a variety of measures (angles, lines, surfaces, distances) in a georeferenced three-dimensional space. Within geological applications, it has a particular meaning due to the ability to extract the equation of the mean plane of any point cloud, simply by selecting the area on the solid image: this feature can be used to identify orientation of discontinuities.

In this study, we used a software called Sirio (Bornaz 2005) that permits to identify planes on solid image using three different procedures:

1. Choosing only three points;
2. Selecting a set of points used to calculate the equation of a best fit plane;
3. Drawing a polygon that bounds the surface of the discontinuity and the code selects all points that fall within the polygon calculating the equation of the plan that best fits this spatial position.

Developed GIS Modules

Table 1 summarizes the modules developed in GRASS for this study. The suffix “r” indicates that are modules based on operations of raster calculation. The first four modules allow analysis of susceptibility to failure, while the latter is focused on a empirical study of propagation of displaced material.

A preliminary phase of the work consisted in the logical and mathematical validation of the modules. This phase, which differs from the analysis of the predictive ability of the method, consisted in the use of the modules in order to ascertain the presence of errors. The procedure followed involved the creation of a synthetic DTM, that is characterized by a very simple geometry, but able to play all the possible geometric situations of the slope. At this point, a series of test were performed, checking the same operations both with modules and with commercial softwares (StereoNett, RocFall by rocscience inc.) or using specific spreadsheet. Cross-checking of results allowed us to test and validate the modules and to identify and correct any errors.

r.SMR

It allows the evaluation of spatial distribution of susceptibility to failure of a rock mass according to the SMR geomechanic classification (Slope Mass Rating). The calculation of correction factors is done with the equations of Romana (1985) in the SMR85 module or with continuous functions (Tomás et al. 2007) in the SMR07 module.

Parameters required are (Fig. 2): DTM, dip and dip direction of discontinuity, the F4 index (which takes into account the method of excavation) and BRMR index (Basic Rock Mass Rating). The BRMR index of Bieniawski (1989) is the score that is obtained assigning a numerical value to each of the above five parameters that characterize the rock mass, without any correction for the relationship between design and discontinuities. Regarding the BRMR index, the user can enter a unique numeric value or a raster map. We suggest to use numeric value when the study area is homogeneous in terms of geology and morphology. On the contrary, the use of a raster map for the RMRb index allows consideration on spatial variation of rock mass quality.

r.SSPC

This module allows the evaluation of spatial distribution of the susceptibility to failure on the basis of the Slope Stability Probability Classification (SSPC). It is a geomechanic classification introduced by Hack (1998) with the aim to consider, on the basis of statistical processing, the stability of natural and artificial slopes. Stability is estimated using orientation dependent stability and orientation independent stability.

The module uses the equations suggested for the orientation-dependent stability. The parameters that determine the failure are (Fig. 2): discontinuity and slope orientation and shear strength of joints. This empirical parameter is

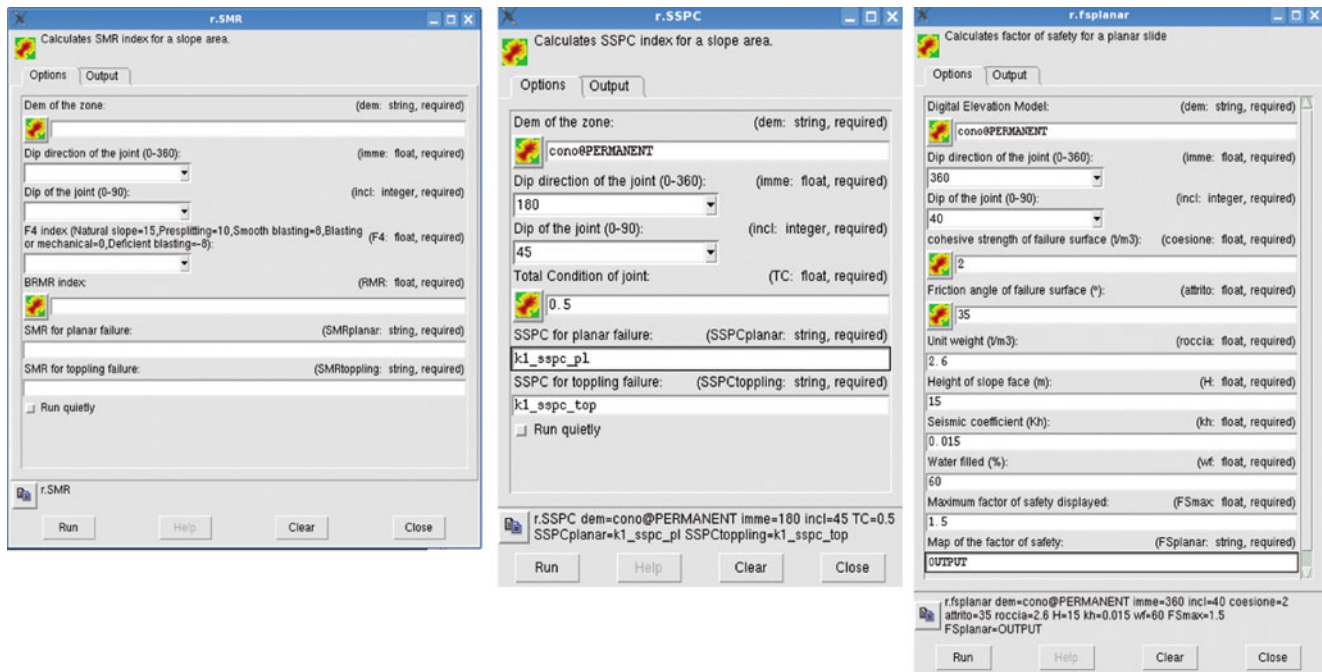


Fig. 2 Print screens of the proposed modules. From *left to right*, r.SMR, r. SSPC e r.fsplanar

provided by the TC (Total Condition), obtained multiplying the values that describe shape (R1), roughness (Es), degree of alteration (Al), type of filling (Im) and presence of karst.

The result of the processing for each discontinuity system consists of two raster maps: one referred to planar slide and one to toppling.

r.fsplanar

It allows to evaluate spatial distribution of safety factor calculated for planar slide and is based on the use of the analytical method proposed by Hoek and Bray (1981).

Input parameters are (Fig. 2): DTM, dip and dip direction, cohesion and friction angle on the discontinuity surfaces, bulk density of rock mass, height of the slope, earthquake coefficient, percentage of water saturation of the joints, maximum safety factor to display and the name for the output.

The result is a raster map showing the distribution of values of safety factor that allows an indication of the degree of the overall stability of the slope. If the module is systematically applied, it is possible to compare objectively areas characterized by different geological and geomorphologic situations. Results of the modules have not to be seen in

terms of safety factor, but they should be considered as stability indexes useful to select areas at different degree of stability.

r.droka

It evaluates area of propagation, velocity and kinetic energy associated with rock falling according to empirical methods suggested by Evans and Hungr (1993) and Corominas (1996). Recent examples of similar applications in GIS can be found in Cannata and Molinari (2008) and Jaboyedoff and Labiouse (2003).

The intersection between topographic profile and the line that starts from the point of detachment at a defined angle to the horizontal defines the point of maximum propagation. This angle of inclination (φ_p) and the line of propagation are, respectively, defined zenith angle (also called travel angle, Cruden and Varnes 1996) and shadow cone. φ_p values can be obtained using back analysis in cases where it is possible to recognize detachment area and accumulation zone, or by reference to bibliography values for similar geomorphologic contexts and land use.

Input parameters are (Fig. 3): DTM, coordinates of detachment point (East, North, Quote), zenith angle (φ_p), correction factor (fv) that takes into account kinetic energy

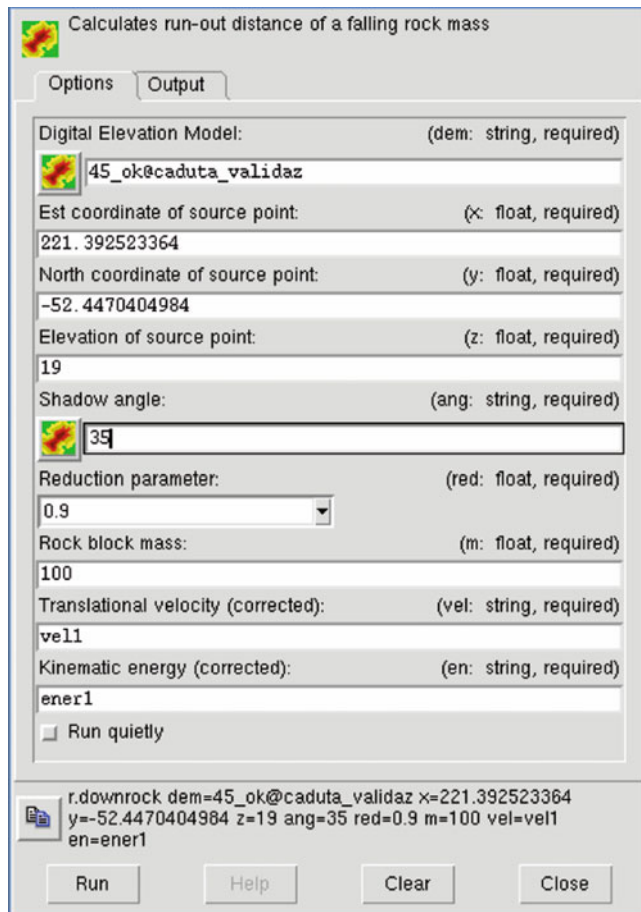


Fig. 3 Printscreen from r.droka module

dispersion, mass of the falling block and name of the outputs. The module returns two raster maps showing velocity and energy variations (each pixel is associated at the value of the velocity in m/s and at the value of the kinetic energy in kJ).

Application to Real Cases

Methods, traditional or using remote sensing, for the determination of input data and GIS modules for the evaluation of the susceptibility to landslide have been used and applied appropriately in some test site in the north-western Alps (Ossola valley).

From a geological point of view, Ossola valley is one of the most interesting sections of exposed continental crust (Boriani and Giobbi 2004) and, moreover, contains a complete section of the Sesia-Lanzo Zone (Austroalpino). The geomorphologic and geologic-structural complexity that differentiates the study areas permit to test GIS modules in different contexts. The selected cases (a mining area and a

landslide) also differ in the extent of investigated area, in quality of topographic bases and in the possible effects coming from the application of the results.

A Mining Area Problem

The Province of the VCO is one of the most important mining districts in Italy for dimensional stone, both for production and variety of extracted rock types. Knowledge of the susceptibility to landslide for a slope interested by quarries assumes an important meaning in terms of mining safety and economic profitability.

Modules were tested in two different contexts (Fig. 4): a portion of the slope of about 130 ha in which there are eight different production units (a) and a single area of 1 ha quarry (b). Both cases are characterized by gneisses, respectively, from the Falda Antigorio and from the Falda of Monte Leone, both belonging to Alpine Domain (Bigioggero et al. 1977).

The geomechanic characterization identified the main families of discontinuities and allowed to classify the quality of the rock mass. In case (a) was made a map of the distribution of the BRMB index, while in case (b) a unique value for the whole area was used. The case studies also differ for the dimension of the cells used in the DTM, 10×10 m in (a) and 2×2 m in (b). In the (b) case, two different DTM were used related to the evolution of exploitation after 5 and 10 years.

Modules r.SMR, r.SSPC and r.fsplanar were used to evaluate the susceptibility to landslide. The maps obtained were used to design the technical pattern of exploitation and to identify possible critical situations due to the presence of many quarry in a small area.

A Land Planning Problem

In this case the maps obtained from GIS modules allow to identify technical and management solutions for safety and mitigation of landslide risk.

The first case study concerns the left side of the Diveria creek, at the Swiss-Italian border, where it creates a narrow valley with very steep slopes. The main buildings are overlooking the road for the famous Simplon Pass. Data on discontinuity families were derived using traditional geomechanic surveys, carried out both at the base of the slope and from the solid image obtained by laser scanner survey. The solid image analysis allowed the identification of five families of discontinuity, two more than those identified in the field surveys. This is due to the possibility

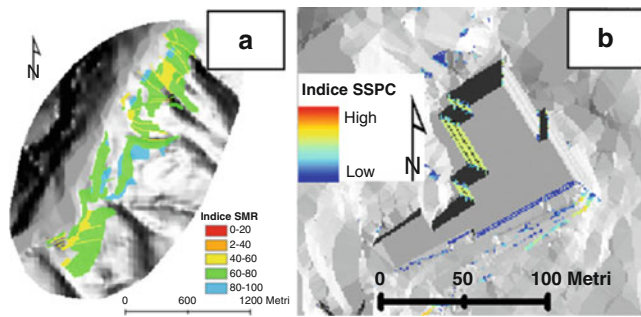


Fig. 4 Results for the for the (a) test site (eight exploitation units) and for the (b) test site (single quarry)

to study a larger portion of the slope, rather than only limited periferical areas and in difficult conditions.

From the laser point cloud a DTM was generated with cells of 1×1 m in an area of about 5.5 ha.

GIS modules were applied to all systems of discontinuity analyzing planar slide, wedge slide and toppling. Maps obtained for each discontinuity and for any kinematism have been overlapped (a function in r.series), in order to obtain a new map in which each cell was assigned the most critical value for stability. Spatial forecasts provided by modules were verified and supplemented by direct analysis represented by new field surveys, visual inspections by helicopter and analysis of laser-solid images. The empirical module r.droka was applied for the five source areas of failure that the modules r.SMR r.SSPC indicated at higher instability. A value of 35° for ϕ_p and a reduction factor of 0.9 fv was used in modeling.

The results of the r.droka module were compared with two-dimensional simulation of rockfalls (RocFall by Rocscience). The comparison showed good consistency in terms of kinetic energy and velocity for the rock falling (Fig. 5).

The second study area is located on the eastern slope of Monte Camoscio, near major historical granite quarries, active since 1500. The bedrock consist in Granito dei Laghi, belonging to the Hercynian plutonic body of Mottarone, Sudalpino Domain (Boriani et al. 1992).

The DTM used for the analysis has 2×2 m cells and was derived from contour lines and spot elevations returned from a low altitude aerial photo.

The modeling of the rockfall was done using HY-STONE (Crosta et al. 2004), based on kinematic equations. The results were compared with maps obtained with the module r.droka. This, using an angle of ϕ_p of 35° , provides results more precautionary than the ones from HY-STONE and indicates a more extensive area of propagation.

The values of kinetic energy and velocity obtained with the two methods are fully comparable. Blocks can reach

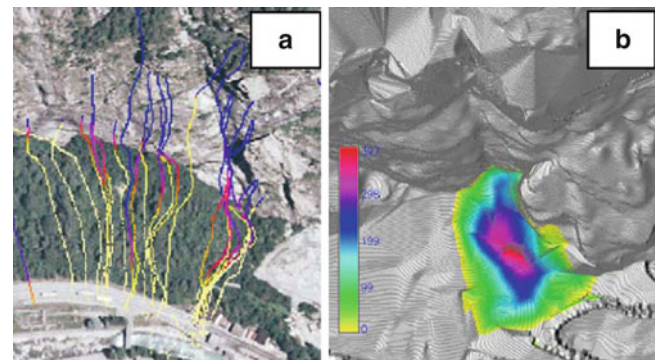


Fig. 5 Comparison between the classic simulation of rock falling trajectories (a) and the result of the r.droka module (b). Colors express kinetic energy (kJ): in (a) red lines show higher kinetic energy (about 5,000 kJ) and in yellow lower value, in (b) color bar is in 10 kJ

velocities above 20 m/s and kinetic energies greater than 100 kJ.

Back Analysis

The study area is at Valdo (1,220 m) in the Municipality of Formazza, famous summer and winter tourist resort along Toce river. At the base of the slope, Antigorio orthogneiss outcrops; they are overlapped by Mesozoic metasediments. At the top of the sequence there are conglomeratic schist of Monte Giove.

In 2009 a landslide hit the left side of the river Toce basin (Fig. 1). Volume of the landslide was estimated, by visual comparison between the images before and after the event, in about $350,000 \text{ m}^3$ that partially covered a pre-existing alluvial fan. This case study was chosen to test and verify the reliability of the r.droka module applying to a recent phenomenon of which there is a direct and recent knowledge. The cells of the DTM were 10×10 m. The value of the zenith angle (ϕ_p), estimated from the volumes involved, was chosen in 26° .

Despite the uncertainties related to the topographic base and real volumes of the landslide, it was obtained a good correspondence between module predictions and field observations especially for the main debris accumulation, the one characterized by the higher destructive power (Fig. 6).

The module did not, however, predicted the projections of small fragments (decimeters in size), which reached the village and generated the highest levels of risk.

Conclusions

The study shows the development of the application of GIS modules for the evaluation of relative hazard,

Fig. 6 The r.droka module applied to the Valdo case study. *Red dots* show larger boulders identified by field surveys

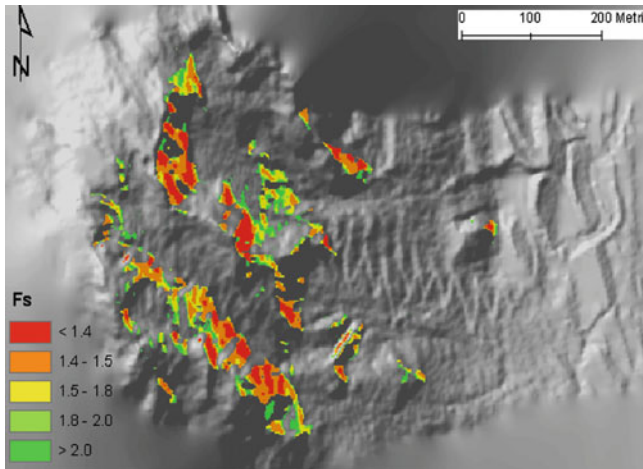
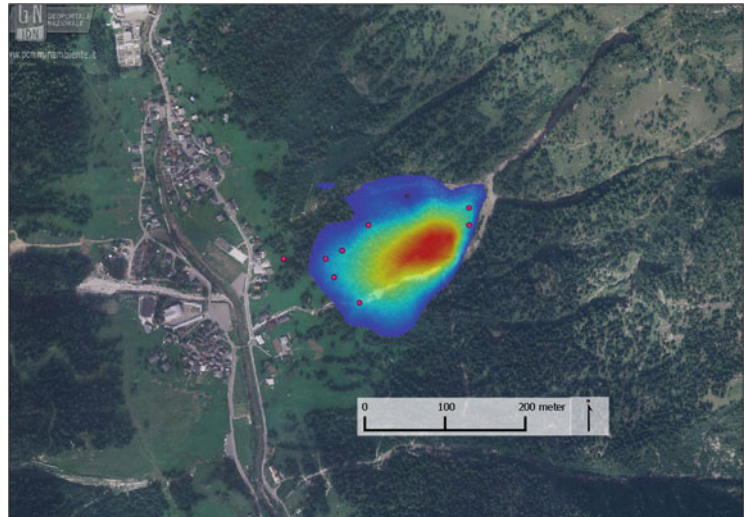


Fig. 7 An example of stability map from r.fsplanar module: *red areas* are characterized by higher instability

without any temporal connotation. The modules are based on different methodological principles:

- r.SMR89 and r.SMR07 have been developed according to the criteria defined by the geomechanics classification of Romana (1985);
- r.SSPC is based on the geomechanic classification of Hack (1998), Hack et al. (2003)
- r.fsplanar (an example is shown in Fig. 7) is used to calculate the distribution of the safety factor according to the Hoek and Bray (1981) equations.

The first three modules (r.SMR89, r.SMR07 and r.SSPC) analyze the kinematics of planar sliding, toppling and wedge sliding while r.fsplanar is aimed to analyze planar slide. The r.droka module was developed to assess area of propagation, velocity and kinetic energy associated with rock falling and are based on empirical methods suggested by Evans and Hungr (1993).

The modules are equipped with a graphical user interface (GUI) for entering data and have been developed to minimize errors during data uploading. All modules are freeware and can be downloaded at the web page of the Dept of Earth Science of Turin University:

http://www.unito.it/unitoWAR/page/dipartimento2/D011/D011_la_ricerca2?id=1464012

Moreover, a customized version of Linux operating system, based on Slax, has been developed to promote the use of modules for beginners. It uses self configuration functionality to be used directly from a CD, without hard disk installation. The CD Live allow users to try out fully-operational version of GRASS and it also contains a demo data set. Users can run analysis with their own data and save results on hard disk.

Acknowledgments The authors are grateful to the Provincia del Verbano Cusio Ossola Geologic Service for providing data and laser scanner survey and to support the study.

References

- AA.VV (2006) Progetto Interreg IIIa 2000–2006 Itineracharta. Elaborati numerici e cartografici
- Bieniawski ZT (1989) Engineering rock mass classifications. Wiley, New York, 251p
- Bigioggero B, Boriani A, Giobbi ME (1977) Microstructure and mineralogy of an orthogneiss (Antigorio Gneiss – Lepontine Alps). Rend Soc It Mineral Petrol 33:99–108
- Boriani A, Giobbi E (2004) Does the basement of western Alps display a tilted section through the continental crust? A review and discussion. Periodica Mineral 73(special issue 2):5–22
- Boriani A, Caironi V, Giobbi OE, Vannucci R (1992) The Permian intrusive rocks of Serie dei Laghi (Western Southern Alps). Acta Vulcanol 2:73–86
- Bornaz L (2005) LSR 2004 software. A solution to manage terrestrial laser scanner point clouds and solid images. In: International workshop on recording, modeling and visualization of cultural heritage.

- Centro S. Franscini Monte Verità Ascona (Suisse). 22–27 maggio 2005, pp 479–484, ISBN/ISSN: 041539208X
- Cannata M, Molinari M (2008) Natural hazards and risk assessment: the FOSS4G capabilities. In: Proceedings of the academic track of the 2008 Free and Open Source Software for Geospatial (FOSS4G) conference, incorporating the GISSA 2008 conference, Cape Town, 29 Sept–3 Oct 2008, pp 172–181, ISBN 978-0-620-42117-1
- Chacón J, Irigaray C, Fernández T, El HR (2006) Engineering geology maps: landslides and geographical information systems. *Bull Eng Geol Environ* 65:344–411
- Corominas J (1996) The angle of reach as a mobility index for small and large landslides. *Can Geotech J* 33:260–271
- Crosta GB, Agliardi F, Frattini P, Imposimato S (2004) A three-dimensional hybrid numerical model for rockfall simulation. *Geophys Res Abstr* 6, n. 0450
- Cruden DM, Varnes DJ (1996) Landslide types and processes. In: Turner AK, Schuster RL (eds) *Landslides: investigation and mitigation*, vol 247, Transportation research board, special report. National Research Council, Washington, DC, pp 36–75
- Evans SG, Hungr O (1993) The assessment of rock fall hazard at the base of the talus slope. *Can Geotech J* 30:620–636
- Hack HRGK (1998) Slope stability probability classification. ITC publication no 43, Enschede, Netherlands, ISBN: 90 6164 125 X, 258 p
- Hack HRGK, Price D, Rengers N (2003) A new approach to rock slope stability – a probability classification (SSPC). *Bull Eng Geol Environ*. Springer, vol 62: article: DOI: [10.1007/s10064-002-0155-4](https://doi.org/10.1007/s10064-002-0155-4), pp 167–184 & erratum: DOI: [10.1007/s10064-002-0171-4](https://doi.org/10.1007/s10064-002-0171-4), pp 185–185
- Hack HRGK, Slob S, Feng Q, Röshoff K, Turner AK (2007) Fracture mapping using 3D laser scanning techniques. In: e Sousa LR, Rossmann CON (eds) 11th congress of ISRM, Lisbon, Portugal, 9–13 July, 2007. Taylor & Francis/Balkema, Leiden. Specialised session 9; S09 – 3D laser scanning applied to geotechnical problems, vol 1, 9–13 July 2007, pp 299–302
- Harlen J, Viberg L (1988) General report: evaluation of landslide hazard. In: Bonnard C (ed) *Proceedings of the 5th international symposium on landslides*, vol 2. Lausanne, pp 1037–1058
- Hoek E, Bray JW (1981) *Rock slope engineering*, 3rd edn. Taylor & Francis, London, 358p
- ISRM (1978) Suggested methods for the quantitative description of discontinuities in rock masses. *Int J Rock Mech Min Sci Geomech Abstr* 15(6):319–368
- Jaboyedoff M., Labiouse V (2003) CONEFALL: a program for the quick preliminary estimation of the rock-fall potential of propagation zones. (<http://www.quanterra.com>) (3 Dec 2012)
- Priest SD (1993) *Discontinuity analysis for rock engineering*. Chapman & Hall, London, 473p
- Romana M (1985) New adjustment ratings for application of Bieniawski classification to slopes. In: *International symposium on the role of rock mechanics*, Zacatecas, pp 49–53
- Tomás JR, Delgado MJ, Serón GJB (2007) Modification of slope mass rating (SMR) by continuous functions. *Int J Rock Mech Min Sci* 44(7):1062–1069



Runout Modelling of Shallow Landslides Over Large Areas with SliDepot

Daniel Tobler, Rachel Riner, and Robert Pfeifer

Abstract

The GIS-based model SliDepot simulates the runout zones of landslide prone areas. It was developed by GEOTEST AG and applied during the last 10 years for numerous projects. In combination with the SliDisp+ software (modelling of slope instabilities, cf. Tobler and Krummenacher (Modellierung von Anrissgebieten für flachgründige Rutschungen und Hangmuren. In: Proceedings of the 2nd Swiss geoscience meeting, Lausanne, 2004); Tobler et al. (Modeling potential shallow landslides over large areas with SliDisp+. In: Proceedings of the second World landslide forum, Rome, 2011) SliDepot allows to calculate decisive parameters for the dimensioning and optimized positioning of protection measures.

In contrast to other GIS-based models “Casadei et al. (Earth Surf Process Landf 28:925–950, 2003); Godt et al. (Eng Geol 102(3–4):214–226, 2008)”, SliDepot does not rely on a single-flow approach, which calculates the flow direction by direct neighbourhood relationship. The software is capable of analysing multiple cells in a 20°-sector above a potential runout area up to the extent of four cells. The potential runout cell will only be connected to the runout area if the mentioned 20°-sector contains an instable cell or if the necessary initial volumes of mobilised mass are guaranteed. Furthermore the program also considers geomorphologic phenomena like convex topography. With this approach the runout direction is simulated fairly realistic.

The runout is based on the degradational water content of the sliding mass during its downslope movement which finally leads to the break-off. Results from a case study in Switzerland will be presented.

Keywords

Shallow landslide modelling • Runout modelling • Protection measures • Case study • SliDepot model

D. Tobler (✉)
Institute of Geography, University of Berne, Hallerstrasse 12, CH-3012
Bern, Switzerland

GEOTEST AG, Birkenstrasse 15, CH-3052 Zollikofen, Switzerland
e-mail: daniel.tobler@geotest.ch; info@geotest.ch

R. Riner • R. Pfeifer
GEOTEST AG, Birkenstrasse 15, CH-3052 Zollikofen, Switzerland
e-mail: info@geotest.ch; info@geotest.ch

Introduction

In mountain regions many residential areas as well as important lifelines are generally exposed to potential shallow landslide events. Spatial planning is one of the major key elements in protection against natural hazards and requires a comprehensive assessment of landslide processes (Glade et al 2005; Sidle and Ochiai 2006). By applying process models, the extent of potential landslides can be calculated over large areas (Guzzetti et al. 2006; Zolfaghari and Heath 2008).

The resulting maps provide a quick identification of endangered areas with conflicts between hazards and land use. It is the base to set priorities for a more accurate hazard assessment. Moreover, due to the importance of cost efficiency the planning of protection measures calls for (more) detailed information about the intensity and probability of expected landslide incidents for a given area. The model SliDepot calculates the runout of shallow landslides (the distance downslope that the shallow landslide will affect).

Travel distance of a debris flow once it reaches a low-gradient surface is a function of its volume and viscosity (Wakatsuki and Matsukura 2008; DeRose 1996). The solid volume of a debris slide or flow deposit is a function of soil depth, distance traveled down the hillslope, and the gradient of the traveled path. The proportion of water is the main control on viscosity. Several studies have suggested a relationship between runout distance and the angle of internal friction of shallow landslides (Corominas 1996; Griffiths et al. 2002). Others predict a simple volumina-depending relationship of the maximal runout distance. Hayashi and Self (1992) or Legros (2002) for example postulate:

$$L_{\max} = 15.6V^{0.36}, \quad (1)$$

where L_{\max} is runout distance and V is the volume of the landslide. Clearly this relationship is sufficiently strong to form the basis of a runout distance calculation, but it requires that a landslide volume be derived. This is problematic as it requires a calculation of both the surface area of the landslide and its depth, neither of which are easy. Intensive field investigations are necessary to determine the required parameters (Salciarini et al. 2006).

The model SliDepot calculates runout distances of shallow landslides within a given area efficient and fairly realistic. The above mentioned relationships between runout distance and volume, viscosity of the subsoil, roughness of subsoil, vegetation and slope gradient are summarized in an empirical parameter. With this simplification an implementation of the complex thematic in a GIS is possible – modeling of runout distances from potential landslide detachment zone of large investigation areas are easy to handle.

Shallow Landslide Modeling

General Remarks

The process of shallow landslides has to be divided into two sub processes – the detachment- and the runout process (Lourenco et al. 2006; Rickli 2001). Both processes can be modeled with different approaches.

Detachment (Source) Zones: Model SliDisp+

SliDisp is a deterministic numerical model which calculates the landslide susceptibility of slopes (Liener et al. 1996). The original model was developed by Liener (2000) at the University of Bern. Studies in several test areas showed that the assessment of detachment zones for potential shallow landslides must inevitably take pedological aspects as well as joint water-input from the underlying bedrock into account (Guimarães et al. 2003; Rickli and Bucher 2003; Dahal 2008). During the last 5 years different alterations were carried out and the program advanced to SliDisp+ (Riner 2009).

The model SliDisp+ determines the stability of the slope for each cell within the grid by applying the Infinite-Slope-Analysis, using the simplified safety factor F (Selby 1993, see Fig. 1). F will be calculated to describe the ratio of retentive and impulsive forces. Fundamental basic data are the slope angle, derived from the DEM (cf. Legorreta Paulin and Bursik 2009) from which the thickness of soil will be deduced and the geology which allows to determine friction angle and cohesion (VSS 1998) as geotechnical parameters (Meisina and Scarabelli 2007). To consider the high natural variability of the sheering parameters these values are not described as single values per geological class but as normal distribution, calculated with randomly chosen values.

For the model calculation a term for root cohesion (WK) has been added the original formula of the factor of safety F . This empirical adjusted parameter takes the roots retaining forces of vegetation layer into account (Schmidt et al. 2001; Chok et al. 2004; Hales et al. 2009; see formula [2]).

$$F = \frac{WK + c' + (\gamma \cdot z \cdot \cos^2 \beta - \gamma_w \cdot m \cdot z \cdot \cos^2 \beta) \cdot \tan \varphi'}{\gamma \cdot z \cdot \sin \beta \cdot \cos \beta} \quad (2)$$

WK: Root cohesion [kN/m²]

c' : cohesion [kN/m²]

γ : specific bulk density [kN/m³]

z : soil thickness [m]

β : slope angle [°]

γ_w : specific bulk density of the saturated zone [kN/m³]

$m^* z$: height of the water table [m]

φ' : friction angle [°]

The safety factor F is calculated for each cell of the grid, based on the data from the digital elevation model (DEM). If $F < 1$, the cell is potentially unstable, and the material can be set into motion by triggering factors. The total of all instable grid elements equals the maximum detachment area (= landslide susceptibility).

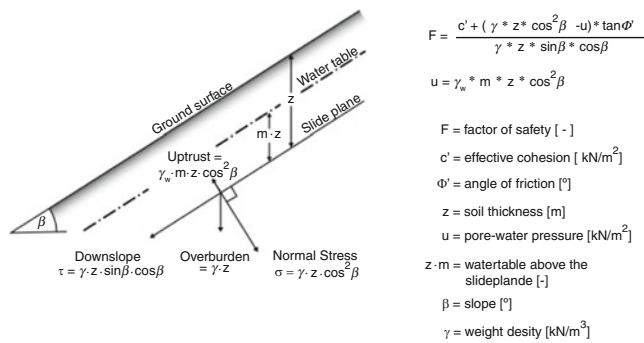


Fig. 1 Principle for the calculation of the factor of safety F for every raster cell (Selby 1993). Indication of all parameters needed for the calculation, except the root cohesion (WK, see formula [2])

The normal variation of shearing parameters is acknowledged by a Monte-Carlo-Simulation. By applying this method, 100 random values are chosen from the deviation of the shearing parameters to calculate the factor of safety (F). With this random combination of parameters, the factor of safety is calculated 100 times for each cell. We assume that both – the cohesion and the friction angle – show a normal distribution and do not correlate with each other (Lacasse and Nadim 1996).

Areas with more than 60 % of the parameter combination showing a safety factor $F < 1$ are indicated as potential sources. If there are more than 90 % of the F -values < 1 , a medium to large chance of a potential landslide is expected. The data preparation as well as its visualisation is carried out by means of a geographic information system (Liu and Wu 2008). The calculation of the stability factors is implemented by a C-application and then integrated in to the GIS.

If there are only fragmentary or rough digital input data available (geology, underground data) the model output will be insufficient. In that case the source zones should be defined from a simple slop-analysis. The slop-analysis should be based on the nationwide available event statistic (AGN 2004) for a certain underground. For such cases it is recommended to let field experts map the detachment zones. On that base the run out zones of shallow landslides can be calculated with SliDepot.

The quality of the results correlates directly with the quality of the input parameters in SliDisp+. The better the knowledge of the underground, the hydrogeological system and the soil cover, the better the results for the detachment zones will be.

Runout: Model SliDepot

SliDepot is an absolute GIS modeling. Starting with the data from the defined source zones the distribution of material in downhill flow direction is calculated. The model focuses on the amount of water within the shallow landslide that will be

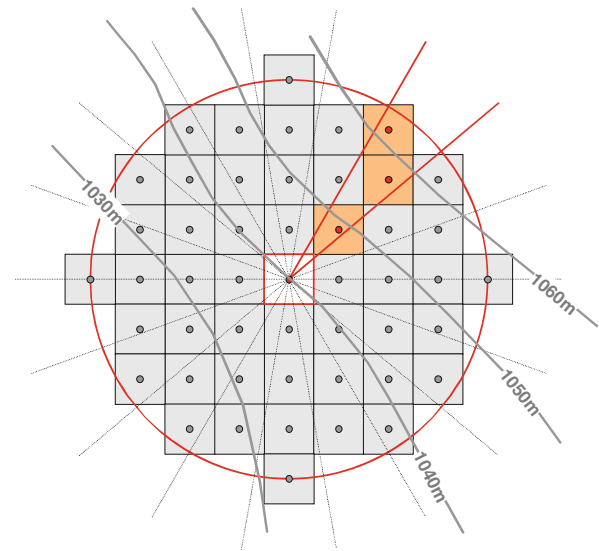


Fig. 2 Three analyzed grid cells of the sector for cell exposition from 210° to 230° (example: 5 m cell → radius of red circle = 20 m)

reduced during the natural process. Finally the lack of process water will determine the point where the distribution of material stops. In contrary to many other GIS applications for runout calculations (Lineback Gritzner et al. 2001; Zolfaghari and Heath 2008), the model does not use a “single-flow” approach to calculate the flow direction. This model bases on a complicate, advanced nearest neighbor analysis.

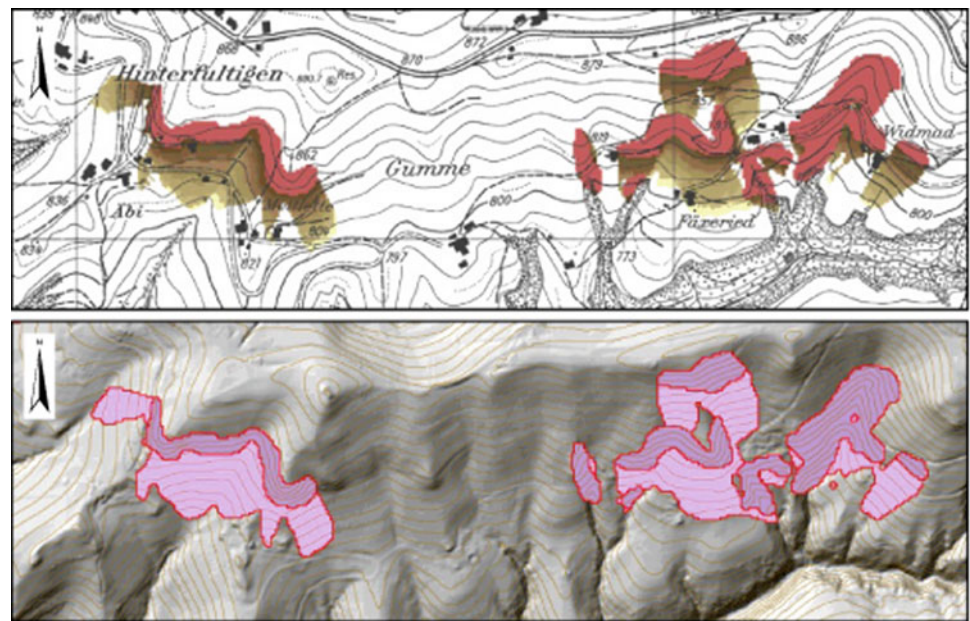
For the modeling, the runout movement of a shallow landslide has to be divided in two different parts: the calculation of the flow direction and the calculation of the maximal flow distance. For the flow direction, several cells within a 20°-section above (inverse direction to the cell exposition) a potential distribution cell and up to an extension of four grid cells are analyzed (Fig. 2). For the focused grid cell the distribution will be calculated if (a) there is a detachment cell respectively a cell with sufficient water saturation and (b) when the topography of the section is strongly convex. The SliDepot approach allows a far better prediction of the distribution direction than the ‘single-flow’ approach.

For the calculation of the maximal runout distance the water content of the sliding mass is the most important parameter (Hölting and Enke 1996). With every distribution step the neighboring cells up to a distance of 20 m (for grid cells of 5 × 5 m) will be analyzed. By using a local reduction parameter the quantity of starting water (i.e. 1.0) respectively the remaining actual amount of water is reduced. This parameter is mostly determined by the local slope gradient, the type of underground as well as the vegetation (e.g. forest). The term underground summarizes the soil type, the terrain roughness and the topography itself. The availability of accurate data finally determines the reducing parameters. Hungr (1995) as well as Hancox and Wright

Table 1 Possible reduction factors for the runout calculations with SliDepot. Note influence of slope gradient and vegetation (grassland, forest, cf. Hancox and Wright 2005)

Slope gradient	Reduction parameters according to distribution step number				
	(Maximal runout distance)				
g: grass		1	2	3	4
f: forest	Original starting value	(20 m)	(40 m)	(60 m)	(120 m)
>25° (g)	1.0	0.85	0.72	0.61	...
>25° (f)	1.0	0.60	0.36	0.22	
17–25° (g)	1.0	0.75	0.56	0.42	...
17–25° (f)	1.0	0.50	0.25	0.13	
10–17° (g)	1.0	0.65	0.42	0.27	
10–17° (f)	1.0	0.40	0.16		
<10° (g)	1.0	0.45	0.20		
<10° (f)	1.0	0.20			

Fig. 3 Calculated source and runout zones of possible shallow landslides in the Bernese Prealps (Switzerland); reddish-brown = detachment zone; brown = calculated runout with SliDepot (above). Generalized view for the presentation on the hazard maps; dark lila: detachment zone; light lila: runout zone



(2005) describe a possible way of the implementation of a reduction parameter. The distribution stops if either a pre-defined number of distribution steps (i.e. 8) achieved or if the calculated water amount drops below a pre-defined threshold (i.e. 0.1). As an example Table 1 shows a typical reducing parameter and the maximum range of a hypothetical distribution under stable conditions (slope angle, forest).

With the above mentioned parameters the average angle of reach lies between 25° and 30° in grassland areas. In the forest the average angle is around 20°. These values correlate with the AGN recommendations (2004) as well as the investigation of Dai and Lee (2002).

Combined Results SliDisp+ and SliDepot

Figure 3 shows the results of a runout calculation from shallow landslides. Starting at the dark red areas (calculated

source locations for shallow landslides with SliDisp+, cf. Tobler and Krummenacher 2004; Tobler et al. 2011) the run out zones are calculated. The starting amount of water is reduced within eight steps each of 20 m. Usually the final number of necessary discharge steps and therefore the maximal distribution range is calibrated with the event register or silent witnesses.

Case Study, Lauterbrunnen, Switzerland

Investigation Area

In 2010 model calculations with SliDisp+/SliDepot (runout) have been carried out within the settlements (approx. 30 km²) of the community of Lauterbrunnen during a review of the existing hazard map (GEOTEST AG 2003).



Fig. 4 Investigation area for the review of the hazard map in Lauterbrunnen, central Switzerland (Swissmap 2011)



Fig. 5 View from the South through the Lauterbrunnen valley with the steep cliffs of limestone and landslide susceptible deposits in the valley bottom

Lauterbrunnen is situated in central Switzerland at an altitude of 800–1,500 m a.s.l (Fig. 4). The bedrock consists mainly of schist and sandstones of the Aalenien and the Bajocien (Dogger), sandstones of the Oxfordien and Callovien, as well as compact Malm lime and sediments from the Tertiary (Günzler-Seiffert 1962). The rock is folded in a large scale and disrupted by several steep tectonically displacements. The weathering resistant lime and the sandstones form striking steep rock walls falling towards the valley bottom (Fig. 5). The schists of the Aalenien are very susceptible to landslides (GEOTEST AG 2007)

On both sides of the valley the rock is covered by silty moraines, dislocated slope debris and historic deposit from rock falls. The bottom of the valley consists of fine-grained flood sedimentation from the river and shows a heterogeneous layering of material.

Results

Figure 6 shows the source areas (detachment zones of shallow landslides in red) calculated with SliDisp+ as well as the runout areas (brown-yellow) calculated with SliDepot (GEOTEST AG 2011). Starting from the dark red areas (calculated source locations for shallow landslides) the runout areas are modeled by stepwise reducing the original water content through max. eight discharge steps, each of 20 m. For Lauterbrunnen an excellent event register exists. So the final number of necessary discharge steps and therefore the maximal runout range has been calibrated with silent witnesses from events in 1999 and the event register (GEOTEST AG 2007). The average angle of reach of all shallow landslides is 27° and lies within the range postulated by Dai and Lee (2002).

The model results (SliDisp+ and SliDepot) indicate the landslide prone areas within the investigation perimeter. For creating a hazard map process intensities have to be added to the susceptibility map. Therefore additional field investigations focused (a) on the verification of modeled areas and (b) on the definition of the process intensities. AGN (2004) defines the different process intensities in hazard mapping. The actual hazard map is shown in Fig. 7. Comparing the calculated areas (Fig. 6) with the hazard map it is obvious, that nearly all hazard zones have a smaller extension than the modeled process areas. The model results suit for hazard indication map, but still not for hazard maps.

Conclusion

There are a lot of uncertainties not considered in the study of calculating the runout areas. These uncertainties underlying the model may include the type of material, mechanism of failure, groundwater, the volume of failure and the geology. The parameters obtained are applicable to predict the travel distance on regional scales, and provide an effective means for the assessment of runout distance of landslide mass when incorporated into a map showing slope instability and the digital elevation model (DEM) within GIS.

With a sophisticated GIS approach it is possible to produce innovative runout maps. The comparison with silent witnesses and the event register indicate that the model is useful and suitable for the scale adopted in this study (hazard indication map) For a hazard map additional field investigations have to be done.

With SliDepot it is possible to calculate and indicate slopes with a higher disposition for shallow landslides over large-scale areas (several km^2). The calculation helps to identify conflict zones between damage potentials and process areas, which again enables efficient spatial

Fig. 6 Section of the calculated shallow landslide areas in Lauterbrunnen (*red* = source modeled with SliDisp+; *brown-yellow* = runout modeled with SliDepot)

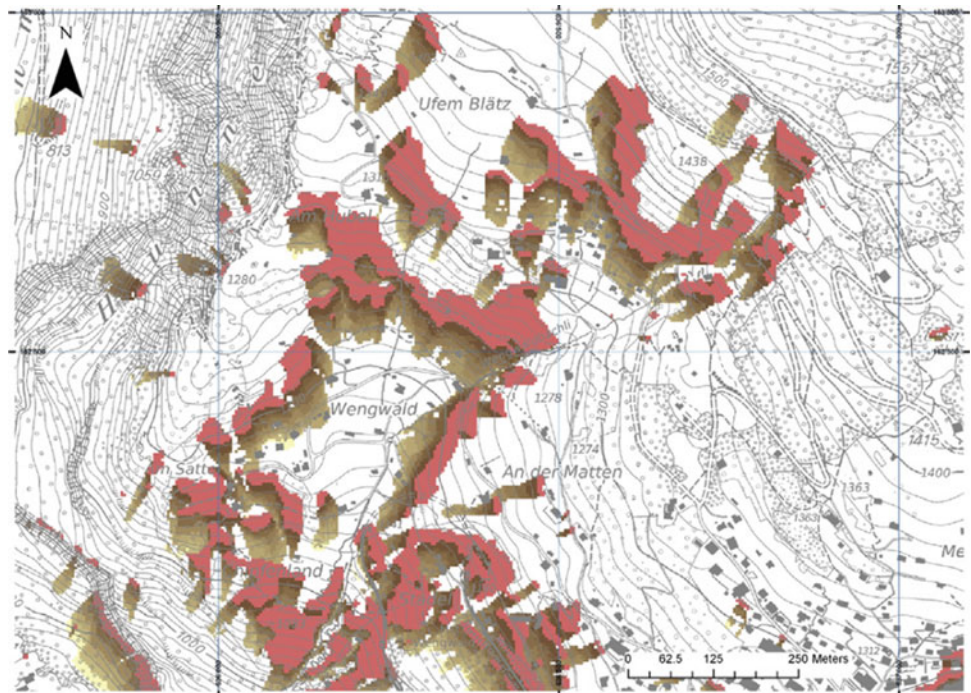
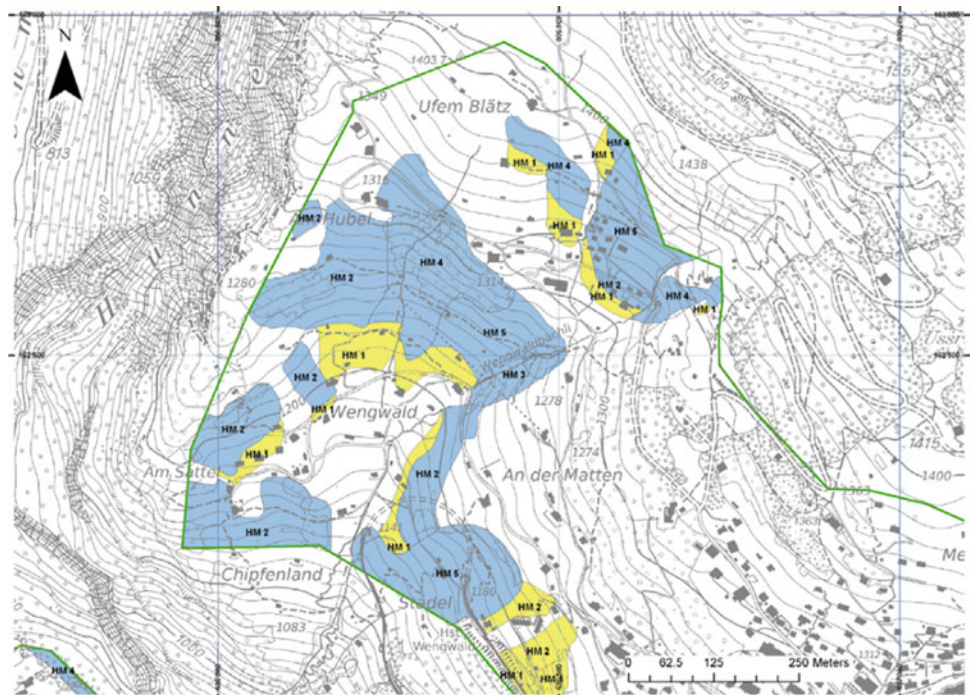


Fig. 7 Section of the actual hazard map for shallow landslide processes of Lauterbrunnen with hazard levels (*blue* and *yellow* areas; *green* = investigation area, GEOTEST AG 2011). The *numbers* indicate the field in the intensity-probability diagram (AGN 2004)



planning or the definition of measurements to protect human lives and the infrastructures.

In future it will be a challenge to implement water content of the sliding mass and detailed underground conditions into the reduction parameter of the runout model. At the actual state the model SliDepot may

be used for hazard indication maps. With additional field investigation hazard map quality will be achieved.

Acknowledgments We would like to thank GEOTEST AG for supporting the development of the model. Thanks also to all persons involved in the technical discussions.

References

- AGN (2004) Gefahreinstufung Rutschungen i.w.S. Permanente Rutschungen, spontane Rutschungen und Hangmuren. Entwurf, Bern
- Chok YH, Kaggwa WS, Jaksa MB, Griffiths DV (2004) Modelling the effects of vegetation on stability of slopes. In: Proceedings of the 9th Australia New Zealand conference on geomechanics, vol 1. Auckland, pp 391–397
- Corominas J (1996) The angle of reach as a mobility index for small and large landslides. *Can Geotech J* 33:260–271
- Dahal RK (2008) Predictive modelling of rainfall-induced landslide hazard in the Lesser Himalaya of Nepal based on weights-of-evidence. *Geomorphology* 102:496–510
- Dai FC, Lee CF (2002) Landslide characteristics and slope instability modeling using GIS, Lantau Island, Hong Kong. *Geomorphology* 42:213–228
- DeRose RC (1996) Relationships between slope morphology, regolith depth, and the incidence of shallow landslides in eastern Taranaki hill country. *Z Geomorphol Suppl Bd* 105:49–60
- GEOTEST AG (2003) Technischer Bericht zur Gefahrenkarte Lauterbrunnen, Nr. 00063.5, Zollikofen (unpublished)
- GEOTEST AG (2007) Lauterbrunnen, Rutschung Gryfenbach, Synthese und Prognosen, Report Nr. 94152.26, Zollikofen (unpublished)
- GEOTEST AG (2011) Lauterbrunnen, Naturgefahren, Bericht zur Teilrevision Gefahrenkarte, Nr. 10151.01, Zollikofen (unpublished)
- Glade T, Anderson M, Crozier MJ (2005) *Landslide hazard and risk*. Wiley, Chichester, 824p
- Griffiths J, Mather AE, Hart AB (2002) Landslide susceptibility in the Rio Aguas catchment, SE Spain. *Q J Eng Geol Hydrogeol* 35:9–18
- Guimarães RF, Montgomery DR, Greenberg HM, Fernandes NF, Gomes RA (2003) Parameterization of soil properties for a model of topographic controls on shallow landsliding: application to Rio de Janeiro. *Eng Geol* 69:99–108
- Günzler-Seiffert H (1962) *Geologischer Atlas der Schweiz* 1:25,000, Blatt 6 Lauterbrunnen. Schweizerische Geologische Kommission
- Guzzetti F, Reichenbach P, Ardizzone F, Cardinali M, Galli M (2006) Estimating the quality of landslide susceptibility models. *Geomorphology* 81:166–184
- Hales TC, Ford CR, Hwang T, Vose JM, Band LE (2009) Topographic and ecologic controls on root reinforcement. *J Geophys Res* 114: F03013. doi:10.1029/2008JF001168
- Hancox GT, Wright K (2005) Analysis of landsliding caused by the 15–17 February 2004 rainstorm in the Wanganui-Manawatu hill country, southern North Island, New Zealand. Institute of Geological & Nuclear Sciences. Science report 2005/11, 64p
- Hayashi JN, Self S (1992) A comparison of pyroclastic flow and landslide mobility. *J Geophys Res* 97:9063–9071
- Hölting B, Enke F (1996) *Einführung in die Allgemeine und Angewandte Hydrogeologie*, 5th edn. Stuttgart Verlag, Stuttgart
- Hungr O (1995) A model for the runout analysis of rapid flow slides, debris flows, and avalanches. *Can Geotech J* 32:610–623
- LaCasse S, Nadim F (1996) Uncertainties in characterising soil properties. Geotechnical special publication no. 58, vol 1, pp 49–75
- Legorreta Paulin GL, Bursik MI (2009) Assessment of landslides susceptibility – Logisnet: a tool for multimethod, multiple soil layers slope stability analysis. *Comput Geosci* 35(5):1007–1016
- Legros F (2002) The mobility of long-runout landslides. *Eng Geol* 63:301–331
- Liener S (2000) Zur Feststofflieferung in Wildbaeichen. Dissertation, Geographica Bernensia, Bern
- Liener S, Kienholz H, Liniger M, Krummenacher B (1996) SDLISP – a procedure to locate landslide prone areas. In: Senneneset K (ed) *Landslides*. Balkema, Rotterdam, pp 279–284
- Lineback Gritzner M, Marcus WA, Aspinall R, Custer SG (2001) Assessing landslide potential using GIS, soil wetness modeling and topographic attributes, Payette River, Idaho. *Geomorphology* 37:149–165
- Liu CN, Wu CC (2008) Integrating GIS and stress transfer mechanism in mapping rainfall-triggered landslide susceptibility. *Eng Geol* 101:60–74
- Lourenco SDN, Sassa K, Fukuoka H (2006) Failure process and hydrologic response of a two layer physical model: Implications for rainfall-induced landslides. *Geomorphology* 73:115–130
- Meisina C, Scarabelli S (2007) A comparative analysis of terrain stability models for predicting shallow landslides in colluvial soils. *Geomorphology* 87:207–223
- Rickli Ch (2001) Vegetationswirkungen und Rutschungen. Untersuchung zum Einfluss der Vegetation auf oberflächennahe Rutschprozesse anhand der Unwetterereignisse Sachseln am 15.8.1997. Eidg. Forschungsanstalt (WSL), Birmensdorf, 97p
- Rickli C, Bucher H (2003) Oberflächennahe Rutschungen, ausgelöst durch die Unwetter vom 15.–16.7.2002 im Napfgebiet und vom 31.8.–1.9.2002 im Gebiet Appenzell. Eidg. Forschungsanstalt (WSL) und Bundesamt für Wasser und Geologie (BWG), 75p
- Riner R (2009) Geotechnische Analysen von Lockergesteinen zur Modellierung von Rutschdispositionen im Untersuchungsgebiet Niesen. Masterarbeit Philosophisch-Naturwissenschaftliche Fakultät Universität Bern, 103p (unpublished)
- Salciarini D, Godt JW, Savage WZ, Conversini R, Baum RL, Michael JA (2006) Modeling regional initiation of rainfall-induced shallow landslides in the eastern Umbria Region of central Italy. *Landslides* 3:181–194
- Schmidt KM, Roering JJ, Stock JD, Dietrich WE, Montgomery DR, Schaub T (2001) The variability of root cohesion as an influence on shallow landslide susceptibility in the Oregon Coast Range. *Can Geotech J* 38:995–1024
- Selby MH (1993) *Hillslope materials and processes*. Oxford University Press, Oxford
- Sidle RC, Ochiai H (2006) *Landslides: processes, prediction, and land use*. Water Resource Monograph 18, American Geophysical Union, Washington, DC
- Swissmap (2011) Topographic map Lauterbrunnen, Blatt 1228. www.swisstopo.ch
- Tobler D, Krummenacher B (2004) Modellierung von Anrissgebieten für flachgründige Rutschungen und Hangmuren. In: Proceedings of the 2nd Swiss geoscience meeting, Lausanne
- Tobler D, Riner R, Pfeifer R (2011) Modeling potential shallow landslides over large areas with SliDisp+. In: Proceedings of the second World landslide forum, Rome
- VSS (1998) SN 670 010b. Bodenkennziffern, Zürich
- Wakatsuki T, Matsukura Y (2008) Lithological effects in soil formation and soil slips on weathering-limited slopes underlain by granitic bedrocks in Japan, Catena. *Trans Jpn Geomorphol Union* 72:153–168
- Zolfaghari A, Heath AC (2008) A GIS application for assessing landslide hazard over a large area. *Comput Geotech* 35:278–285



DEM and FEM/DEM Modelling of Granular Flows to Investigate Large Debris Avalanche Propagation

Irene Manzella, Herbert H. Einstein, and Giovanni Grasselli

Abstract

Large debris avalanches are characterized by extremely rapid, flow-like motion of large masses and they travel extremely long distances showing much greater mobility than could be predicted using frictional models. In order to investigate the mechanisms involved and the reasons for the large propagation of these phenomena a discrete element model (DEM) and a combined finite and discrete element one (FEM/DEM) are used to simulate small-scale laboratory experiments carried out by Manzella “Manzella and Labiouse (Rock Mech Rock Eng 41(1):133–151, 2008, Eng Geol 109(1–2):146–158, 2009, Landslides, 2011 submitted); Manzella (Dry rock avalanche propagation: unconstrained flow experiments with granular materials and blocks at small scale. Ph.D. n 4032, Ecole Polytechnique Fédérale de Lausanne, Lausanne, CH, 2008)”. The combined use of different models produces a more complete study of the phenomena since each model can fill certain gaps of the other; they also help in a better understanding of some mechanisms and factors, which are important in the longitudinal propagation of granular and block flows, such as the progressive failure, the initial block packing and the topographical characteristics of the slope break.

Keywords

Large debris avalanches • Granular flows • Block flows • Runout • DEM • FEM/DEM

Introduction

Volcanic debris avalanches (i.e. block and ash flows caused by volcanic sector collapses) and rock avalanches (i.e. flows of fragmented rock derived from a bed-rock failure) are both examples of what are here called large debris avalanches. They represent one of the most lethal and destructive

phenomenon among all geophysical gravitational flows: they can travel for several kilometers along slopes and valleys, their speed usually exceeds 100 km/h and their volume is greater than a million cubic meters (Hungar et al. 2001; Kelfoun et al. 2008). The large quantity of mass in movement can develop a considerable energy, greater than the one developed by an earthquake of magnitude 6. This enormous energy developed in a short time has tremendous power of destruction that can cause irreparable damage, changes in the landscape and a large number of fatalities. In 1949 the Khait debris avalanche (Tajikistan), destroyed the entire town of Khait with the loss of more than 7,000 people (Evans et al. 2009).

At present, the mechanisms involved in these phenomena are still for most part unknown. The reasons for their high mobility are not completely understood and even if several theories have been proposed and some mechanisms could play an important role for some specific cases, it is difficult

I. Manzella (✉)

Section de Sciences de la Terre et de l'environnement, University of Geneva, rue des Maraîchers 13, 1205 Genève, Switzerland
e-mail: irene.manzella@unige.ch

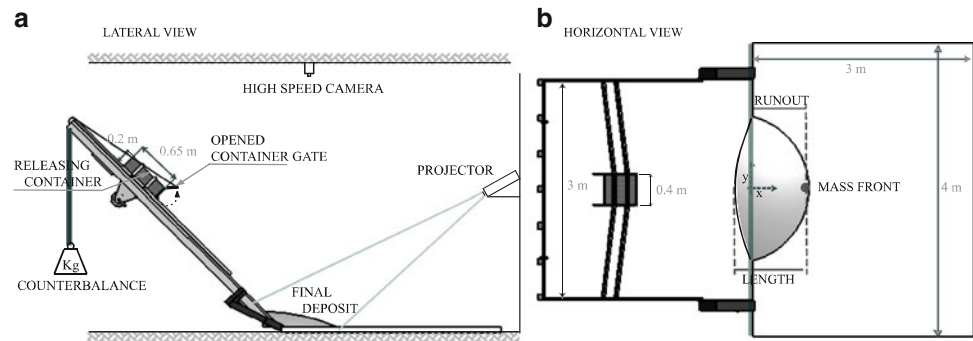
H.H. Einstein

Department of Civil and Environmental Engineering, Massachusetts Institute of Technology, Cambridge, MA, USA

G. Grasselli

Geomechanics Group, Department of Civil Engineering, University of Toronto, Toronto, ON, Canada

Fig. 1 Experimental set-up: lateral (a) and top view (b) (From Manzella and Labiouse 2009)



to decide, which is the most significant one and how it controls the dynamics of the flow. Because of the complex behaviour of these geophysical flows, it is important to derive an empirical understanding of the effects of material and topographic characteristics on mobility and granular flow mechanisms.

In this framework experiments and numerical simulations are of great importance because conditions are known and consistent and accurate measurements can be performed.

Models of this type of phenomenon exist, which consider the mass of the debris avalanche as concentrated in a point and the dynamic of its propagation as governed by frictional law, and energy dissipation at the sliding surface. These are called sled block models and they are often used in literature to understand the basic processes, e.g. (Heim 1932; Hsü 1975; Davies 1982; Van Gassen and Cruden 1989). When the mass is not considered as a unique body but as composed of several particles and the dynamics is considered as governed by friction and interaction not only with the sliding surface but also between the particles, we talk about discrete element models; e.g. (Bagnold 1954; Drake 1990, 1991). Because of the flow-like behaviour of large debris avalanches, continuum mechanics models are also often used to model their propagation, e.g. (Pirulli and Mangeney 2008; Manzella et al. 2008; Naaim et al. 1997; Hungr 2009).

In the present article, laboratory unconstrained granular and block flows (see Manzella and Labiouse 2008, 2009, 2011) are simulated with different models, i.e. a discrete element model (DEM) and a combined discrete and finite element one (FEM/DEM), which combines discontinuum and continuum mechanics analysing discontinuum behaviour by discrete elements while continuum behaviour is modelled through finite elements. This allows one to highlight the characteristics of each of these numerical approaches and how they can be useful in the simulation of the propagation of real events.

Experimental Framework

Manzella (2008) carried out several small-scale granular and block flow experiments at the Rock Mechanics Laboratory of the Ecole Polytechnique Fédérale de Lausanne varying

parameters such as avalanche volume, number of consecutive releases, initial arrangement of the blocks, fall height, slope, basal friction and topographical features. In the present article some of these tests, which gave particularly interesting results are considered for numerical simulations. Tests consisted of triggering an unconstrained granular flow on a slope ending with a slope break and a horizontal accumulation zone (see Fig. 1). The characteristics of the tests considered here are the following:

- Constant slope: 45° and fall height: 100 cm
- Materials: gravel of $D_{90} = 0.4$ cm (Gr, see Fig. 2a) and blocks (Br), i.e. terracotta bricks of 1.5 cm \times 3.1 cm \times 0.8 cm.
- Arrangement of the blocks: initially randomly poured into the releasing container (BrR) or piled orderly one on top of the other (BrP) as shown in Fig. 2b, c respectively
- Number of consecutive releases: $40,000$ cm³ in one or in two pulses of $20,000 + 20,000$ cm³
- Slope break: sharp or curved (see Fig. 3), i.e. the sharp angular slope break between the two panels has been replaced by a smooth curve. The radius of the arc is approximately 0.5 m.

The runout, i.e. the distance travelled by the front of the mass on the horizontal accumulation zone (see Fig. 1), of the tests considered here is reported in Table 1. The values reported are an average of three different tests with the same initial conditions.

In the progressive failure experiments considered here (series B in Table 1) one first volume of $20,000$ cm³ is released and, only after it has come to a complete stop, the next one of $20,000$ cm³ is also released. As shown in Table 1, when $40,000$ cm³ are released at once (series A) they reach longer runout than when released in two pulses (series B). In the latter case, it is the first release that determines how far the entire volume will travel, i.e. the runout does not change from $20,000$ cm³ (series C) to $20,000 + 20,000$ cm³ (series B).

When the mass is initially packed and structured (Piled Bricks, series E) it reaches longer runout than if it is loose (Gravel and Random Bricks, series A and D respectively). Even longer runout are reached when the mass is structured (Piled bricks) and the slope break is curved, (series F).

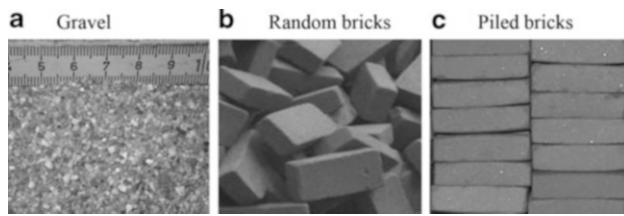


Fig. 2 Used materials: (a) gravel, *Gr*; (b) bricks randomly poured into the container, *BrR*; (c) bricks piled orderly into the container, *BrP* (From Manzella and Labiouse 2009)

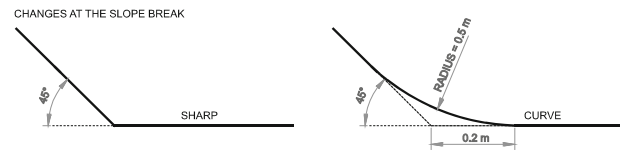


Fig. 3 Changes at the slope break (From Manzella and Labiouse 2011)

Table 1 Characteristics and average values of runout on the horizontal accumulation zone of the tests considered in the present article

Series	Total volume (cm ³)	Release number (1 or 2)	Material (Gr, BrR, BrP)	Slope break (sharp or curved)	Runout (cm)
A	40,000	1	Gr	Sharp	85
B	40,000	2	Gr	Sharp	73
C	20,000	1	Gr	Sharp	73
D	40,000	1	BrR	Sharp	85
E	40,000	1	BrP	Sharp	115
F	40,000	1	BrP	Curved	180

Numerical Simulations

The laboratory experiments highlighted the importance of three factors:

- Progressive failure
- Initial block packing
- Regularity of the pathway

Numerical simulations are used here to better highlight how these parameters influence the runout and the propagation mechanisms.

Discrete Element Model

A discrete element model simulates a granular mass as an assembly of elements (spheres or superquads) that can interact with each other but are free to move. The numerical discrete element code WinMimes (Williams and O'Connor 1995, 1999) developed at the Massachusetts Institute of Technology (MIT) has been used to simulate the flow dynamics of progressive failure granular flow tests (series A, B, C in Table 1). The 40,000 cm³ experiment has been simulated with an assembly of 7,060 elements (superquads) of 0.4 “simulation units” diameter corresponding to the 0.4 cm diameter of gravel particles. The geometry has been determined proportionally in “simulation units” (i.e. 100 simulation unit fall height, 45° slope, followed by a horizontal accumulation plane as shown in Fig. 4). The number of elements can vary slightly depending on the assembly construction.

The laboratory test in which the total volume released at once is considered with numerical simulation with a first

pulse of 0 % of the total assembly of around 7,064 and a second pulse of 100 %. In order to simulate the progressive failure and to see the extent of the effect of the first pulse on the total travel distance, the first pulse has been increased gradually by 1/8th of the total assembly, while at the same time the second one has been decreased by the same quantity in order to keep the same total amount of elements. As a consequence runs have been done according to the following percentages:

- First pulse: 0 %; second pulse: 100 %
- First pulse: 12.5 %; second pulse: 87.5 %
- First pulse: 25 %; second pulse: 75 %
- First pulse: 37.5 %; second pulse: 62.5 %
- First pulse: 50 %; second pulse: 50 %

Observing Fig. 5, where the y axis has been magnified for a better visualization, it is possible to see the evolution into a conical shape of the deposit along with the increasing of the importance of the first pulse. In addition it is possible to observe how the ratio between the first pulse and the second pulse is a very important factor in determining the runout, i.e. as the first pulse increases, the shorter the runout. Even when the first pulse is small compared to the second one (12.5–87.5 %), the first one has still an influence on the runout which is shorter than in the case of a 100 % release at once. However, observing the velocity snapshot of the experiments in Fig. 6a it is possible to see how for simulation with a first pulse of 12.5 % of the total assembly the elements of the second pulse are only slightly decelerated when they impact on the deposit formed at the base. In the case of an equal partition between the two pulses (see Fig. 6b), the deposit at the base works as a barrier for the elements of the second pulse and their impact with the deposit influences only the elements of the first pulse in the rear part; the

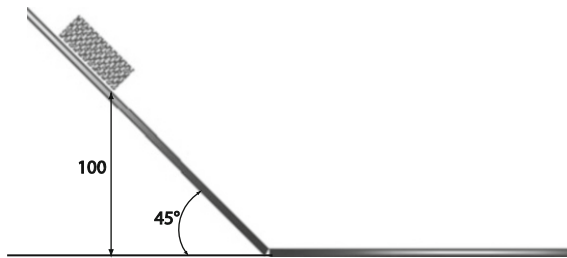


Fig. 4 Discrete element simulation geometry

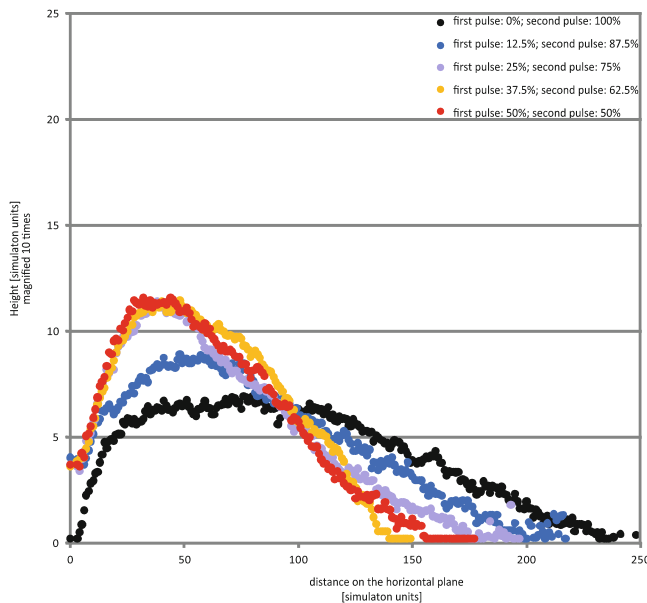


Fig. 5 Discrete element simulation results of progressive failure

elements in the front are not affected by the second failure and they do not move.

Finite/Discrete Element Model

In order to simulate experiments carried out with parallelepiped terracotta bricks a Finite Element-Discrete Element Method (FEM/DEM) has been preferred to the simple discrete element one since it can better describe the shape of the blocks and, as a consequence, the interactions between them.

The code used here has been developed by the Geomechanics Group at the University of Toronto and it is based on the Y-Code of (Munjiza 2004) who developed the combined finite-discrete element method (FEM/DEM) numerical technique (Munjiza et al. 1995). In the FEM/DEM method the Discrete Element Method (DEM) algorithms are used to model the interaction between different solid elements, while the Finite Element Method (FEM) principles are used to analyze their deformability. A penalty function method (Munjiza and Andrews 2000), is used for

the interaction algorithm and a Coulomb type friction law is employed in the code to calculate shear interaction forces (Mahabadi et al. 2010b). Material properties and boundary conditions are assigned using the Y-GUI program (Mahabadi et al. 2010a).

Three different numerical set-ups were built corresponding to the series with bricks D, E and F in Table 1. Also in this case the geometry has been built following the laboratory test conditions as shown in Fig. 7. The slope was meshed with three elements to simulate the slope with a sharp slope break and with 5,280 elements created with the software CUBIT to simulate the smooth slope break. Each brick consisted of a discrete element made from four triangular finite elements but no brick fracturing was allowed to occur. Rectangular elements have been piled one on top of the other or distributed randomly before opening the gate. The latter configuration has been obtained letting the 5,280 piled elements free to fall under the effect of gravity from 1 m above the gate in a kind of funnel (see Fig. 7a); in this way the elements distribute themselves randomly under their own weight against the gate (Manzella et al. 2011).

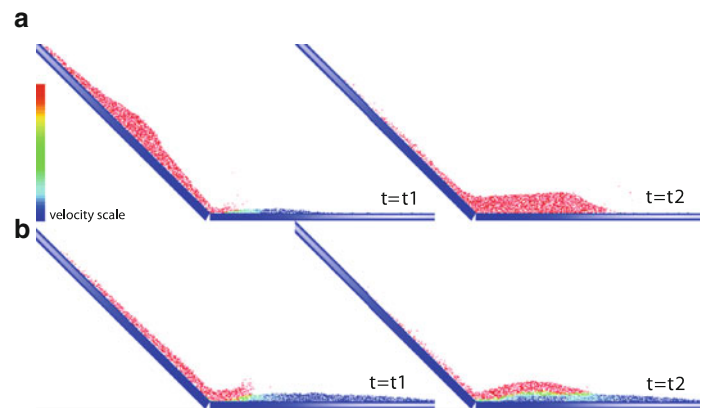
The numerical simulations show that the longest runouts are obtained with piled bricks and a curved slope break. By observing the snapshots here, it is possible to understand the mechanisms likely to happen within the block flow.

When the mass is initially packed in a structured way (piled elements and sharp slope break, Fig. 8b), at the moment of the impact with the sharp slope break its structure and the initial packing are lost. This is different from the case where an initially unstructured mass impacts the slope break (random elements and sharp slope break, Fig. 8a), where the mass behaves as a loose material before and after the impact. It is also different from the case of an initially packed mass and a smooth slope break (piled elements and curved slope break, Fig. 8c) where the packing is preserved and the shattering of the mass at the impact with the horizontal is reduced.

Discussion

Eberhardt et al. (2004) affirmed that for cases where the slide mass does not fail as a singular event, the total travel distance and the characteristics of the final deposit do not depend on the entire failed volume but on the individual episodic events of smaller volumes. These considerations are based on observations of the Randa event in the Matter Valley (1991, Swiss Alps). As a matter of fact the Randa event involved the progressive failure of $30 \times 10^6 \text{ m}^3$ of massive crystalline rock (Eberhardt et al. 2004) and it has a characteristic steep conical deposit. It is the result of two main events which took place on the 18th of April and the 9th of May 1991, both occurred over several hours

Fig. 6 Discrete element simulation of progressive failure (a) First pulse: 12.5 % ; second pulse: 87.5 %. (b) First pulse: 50 %; second pulse: 50 %; at $t = t_1$ where the elements of the second pulse impact with the deposit formed by the first one and at $t = t_2$ where in (a) the elements of the first pulse are involved in the flow and in (b) the elements of the second pulse are stopped by the first ones deposited



(Schindler et al. 1993). It is the largest rock avalanche in Switzerland since the Goldau event in 1806 but because of the fact that the volume has not failed at once but progressively, divided into two main events, the runout distance was significantly shorter than the one observed for other large rockslides of comparable volume. This is in agreement with what was observed in granular flow experiments by Manzella and Labiouse (2008): if the mass falls all at once it reaches longer runout than if it is released at different times and equal quantities. Present Discrete Element Simulations highlighted that even if the first pulse is much smaller than the second one there is an influence on the total final runout because even if the small deposit cannot stop the particles approaching, it decelerates them. The first deposit at the base constitutes an irregularity on the pathway of the granular mass of the second pulse. This irregularity is composed by particles of the same size as the ones approaching which partly or totally mobilize the deposit at the base. This process is energy consuming and as a consequence can decelerate or completely stop the granular flow mass of the second pulse.

The irregularity of the pathway affects energy loss within the mass flowing and as a consequence shorter runout results compared to flows on more regular pathways. This has been pointed out by Heim (1932) and (Friedmann et al. 2006) and by the experiments with a curved slope break by Manzella and Labiouse (2011). These experiments are particularly interesting since the effect of the regularity of the pathway is combined with the initial packing of the material. FEM/DEM simulations allowed us to observe the behaviour of the structure before and after the impact with the slope break confirming the intuitive considerations made by Manzella and Labiouse (2009), i.e. blocks randomly poured into the box behave as a loose material and energy is dissipated from the beginning through both friction and collision at the base and within the mass. When blocks are initially structured, they remain packed together on the inclined slope where energy dissipation takes place mainly through friction at the base. Only after the impact with the horizontal panel,

do they lose their structure and energy is then mainly dissipated through friction/collisions between the blocks. When the slope break is smoother, the structure is maintained and less energy is dissipated at the impact with the horizontal.

Both simulation types put into evidence the combined effect of the structure of the mass flowing relative to the regularity of the pathway, i.e. if the mass is composed by loose material, such as in the case of DEM granular flow and FEM/DEM random blocks, it is the size of the single element compared to the size of the irregularities that it is important in the mobility of the flow, i.e. irregularities, even if small compared to the total mass, but of size comparable to the one of the grains, affect the mobility leading to shorter runout. On the other hand, if the mass is structured it is not the size of the single blocks that has to be taken into account, but the size of the internal structures formed by packed blocks within the flowing mass compared to the size of the irregularities. In this case packed elements work as a single block of larger size compared to the one of the irregularities and as a consequence the mobility of the mass is less or not affected. This puts into evidence how the actual combination of the size of the topographic irregularities of the pathway and of the size of the internal structure of the flowing mass influences the mobility of the flow. If the material is loose, i.e. no major internal structure are formed within the mass, the size of the structure is reduced to the size of a single block, which becomes important.

Conclusions

The reasons of the high mobility of large debris avalanches are not completely understood. In order to investigate the mechanisms involved and the reasons of the large propagation of these phenomena, a discrete element code and a combined finite and discrete element one are used to simulate small-scale laboratory experiments (Manzella and Labiouse 2008, 2009, 2011).

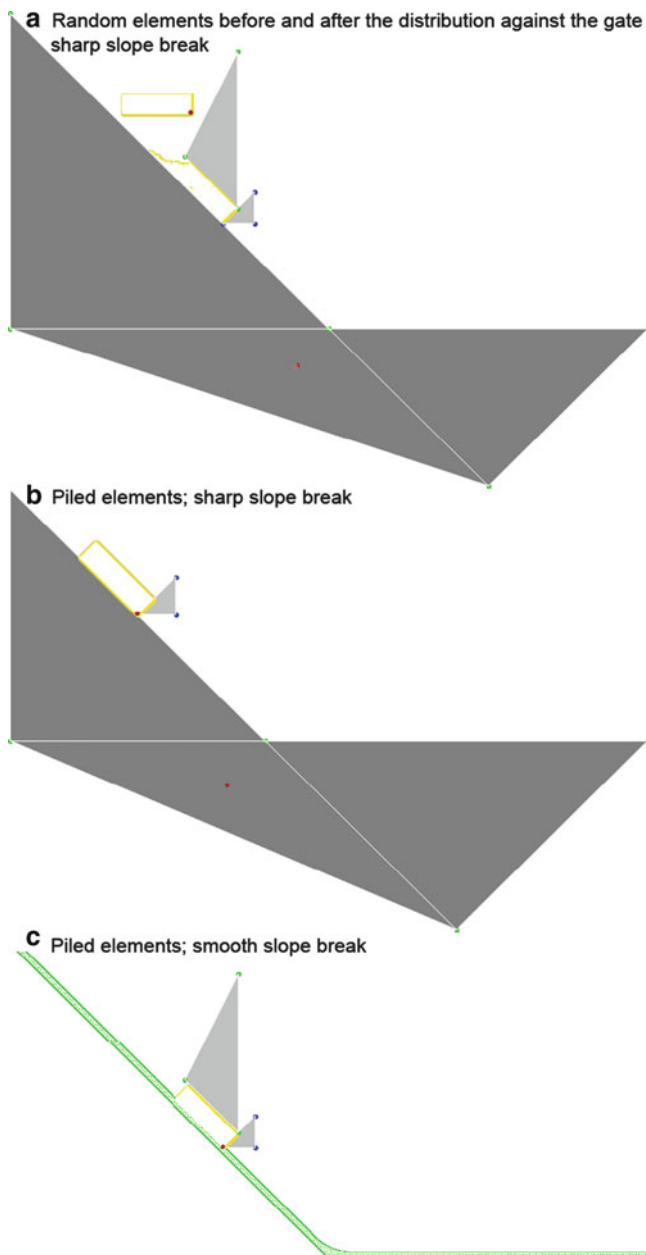


Fig. 7 Numerical set-ups: (a) random elements before and after the distribution against the gate, sharp slope break; (b) piled elements, sharp slope break; (c) piled elements, smooth slope break. Yellow lines define groups of 5,280 elements either piled on top of the other (rectangle in a, b and c) or randomly distributed (irregular shape in a). Light grey triangles confine the elements at start; they are removed when the simulation is triggered (From Manzella et al. 2011)

Tests considered here consist of triggering an unconstrained granular flow on a 45° slope ending with a slope break and a horizontal accumulation zone. The discrete element code WinMimes (Williams and O'Connor 1999) developed at the Massachusetts Institute of Technology (MIT) has been used to study the effect of progressive failure on mobility of granular flows. Even though the

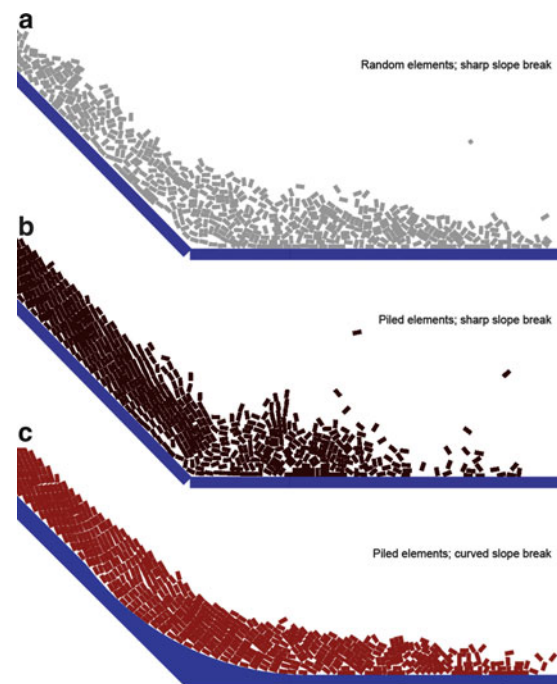


Fig. 8 Difference in shattering with (a) loose elements (*BrR*) and a sharp slope break; (b) piled elements (*BrP*) and a sharp slope break; (c) piled elements (*BrP*) and a smooth curved slope break. In (a) the material is de-structured before and after the slope break, in (b) the structures of the piled elements are broken at the impact with the horizontal; in (c) the elements simply slide on the curve (From Manzella et al. 2011)

two-dimensional nature of the code does not allow one to reproduce the actual geometrical dimensions, simulations confirmed the effects of volume and periodic pulses on the final deposit characteristics (Einstein et al. 2010) detected in the experiments. The discrete element model allows us to establish a relationship between the difference in volume between the first and the second pulse and the difference in the final runoff.

In order to simulate experiments carried out with parallelepiped terracotta bricks a Finite Element-Discrete Element Method (FEMDEM) has been preferred to the simple discrete element one since it can better describe the shape of the blocks and, as a consequence, the interactions between them. Also in this case the two-dimensional nature of the code prevents a quantitative match. Simulations, though, can satisfactorily reproduce the influence of the parameters varied during the experiments, such as the initial packing of the blocks and the regularity of the pathway and they allowed us to detect to which extent the initial packing is preserved in the final deposit (Manzella et al. 2011).

As a conclusion, it can be seen how a combined use of different models produces a more complete study of the

phenomena since each one can highlight different aspects of the same process. Specifically, it is possible to take into account the interactions between blocks and between blocks and topography; simulations highlighted the importance of the relative size of the topographic irregularities of the pathway compared to the one of the internal structure of the mass flowing and pointed out how this is likely to affect the mobility of debris avalanches.

Acknowledgments Dr. Manzella would like to thank “Fondation Ernst and Lucie Schmidheiny” for funding and Professor John Williams and Professor Costanza Bonadonna for fruitful discussions. Dr. Grasselli’s work has been supported by the National Science and Engineering Research Council of Canada in the form of Discovery Grant No. 341275.

References

- Bagnold RA (1954) Experiments on a gravity free dispersion of large solid spheres in Newtonian fluid under shear. *Proc R Soc Lond Ser A Math Phys Sci* 225:49–63
- Davies TRH (1982) Spreading of rock avalanche debris by mechanical fluidization. *Rock Mech Felsmechanik Mécanique des Roches* 15(1):9–24
- Drake TG (1990) Structural features in granular flows. *J Geophys Res* 95(B6):8681–8696
- Drake TG (1991) Granular flow – physical experiments and their implications for microstructural theories. *J Fluid Mech* 225:121–152
- Eberhardt E, Stead D, Coggan JS (2004) Numerical analysis of initiation and progressive failure in natural rock slopes – the 1991 Randa rockslide. *Int J Rock Mech Min Sci* 41(1):69–87
- Einstein HH, Sousa RL, Karam K, Manzella I, Kveltsvik V (2010) Rock slopes from mechanics to decision making. In: Zhao J, Labiouse V, Dudt J-P, Mathier J-F (eds) *Rock mechanics in civil and environmental engineering*. CRC Press/Taylor & Francis, Boca Raton
- Evans SG, Roberts NJ, Ischuk A, Delaney KB, Morozova GS, Tutubalina O (2009) Landslides triggered by the 1949 Khatit earthquake, Tajikistan, and associated loss of life. *Eng Geol* 109(3–4):195–212. doi:10.1016/j.enggeo.2009.08.007
- Friedmann SJ, Taberlet N, Losert W (2006) Rock-avalanche dynamics: insights from granular physics experiments. *Int J Earth Sci* 95:911–919. doi:10.1007/s00531-006-0067-9
- Heim A (1932) *Bergsturz und menschenleben*. Frets und Wasmuth, Zurich, 218p
- Hsü KJ (1975) Catastrophic debris streams generated by rockfalls. *Geol Soc Am Bull* 86(1):129–140
- Hungr O (2009) Numerical modelling of the motion of rapid, flow-like landslides for hazard assessment. *KSCE J Civil Eng* 13(4):281–287
- Hungr O, Evans SG, Bovis MJ, Hutchinson JN (2001) A review of the classification of landslides of the flow type. *Environ Eng Geosci* 7(3):221–238
- Kelfoun K, Druitt T, van Wyk de Vries B, Guilbaud M-N (2008) Topographic reflection of the Socompa debris avalanche, Chile. *Bull Volcanol* 70:1169–1187. doi:10.1007/s00445-008-0201-6
- Mahabadi OK, Grasselli G, Munjiza A (2010a) Y-GUI: a graphical user interface and pre-processor for the combined finite-discrete element code, Y2D, incorporating material heterogeneity. *Comput Geosci* 36(2):241–252. doi:10.1016/j.cageo.2009.05.010
- Mahabadi OK, Lisjak A, Grasselli G, Lukas T, Munjiza A (2010b) Numerical modelling of a triaxial test of homogeneous rocks using the combined finite-discrete element method. In: Zhao J, Labiouse V, Dudt J-P, Mathier J-F (eds) *Rock mechanics in civil and environmental engineering*. CRC Press/Taylor & Francis, Boca Raton
- Manzella I (2008) Dry rock avalanche propagation: unconstrained flow experiments with granular materials and blocks at small scale. Ph.D n°4032, Ecole Polytechnique Fédérale de Lausanne, Lausanne, CH
- Manzella I, Labiouse V (2008) Qualitative analysis of rock avalanches propagation by means of physical modelling of non-constrained gravel flows. *Rock Mech Rock Eng* 41(1):133–151
- Manzella I, Labiouse V (2009) Flow experiments with gravel and blocks at small scale to investigate parameters and mechanisms involved in rock avalanches. *Eng Geol* 109(1–2):146–158. doi:10.1016/j.enggeo.2008.11.006
- Manzella I, Labiouse V (2011) Empirical and analytical analyses of laboratory granular flows to investigate rock avalanche propagation. *Landslides* (submitted)
- Manzella I, Pirulli M, Naaim M, Serratrice JF, Labiouse V (2008) Numerical modelling of a rock avalanche laboratory experiment in the framework of the “Rockslidetec” alpine project. In: *Proceedings of the symposium on landslides and engineered slopes: from the past to the future*, vol 1. Xi’an, China. CRC Press/Taylor & Francis, Boca Raton, pp 835–841
- Manzella I, Lisjak A, Mahabadi OK, Grasselli G (2011) Influence of initial block packing on rock avalanche flow and emplacement mechanisms through FEM/DEM simulations. Paper presented at the 2011 PanAm-CGS geotechnical conference, Toronto, 2–6 Oct 2011
- Munjiza A (2004) *The combined finite-discrete element method*. Wiley. doi:10.1002/0470020180.333 p
- Munjiza A, Andrews KRF (2000) Penalty function method for combined finite-discrete element systems comprising large number of separate bodies. *Int J Numer Methods Eng* 49(11):1377–1396
- Munjiza A, Owen DRJ, Bicanic N (1995) A combined finite-discrete element method in transient dynamics of fracturing solids. *Eng Comput* 12(2):145–174
- Naaim M, Vial S, Couture R (1997) Saint Venant approach for rock avalanches modelling. In: *Multiple scale analyses and coupled physical systems: Saint Venant symposium*. Presses de l’École Nationale des Ponts et chaussées, Paris
- Pirulli M, Mangeney A (2008) Results of back-analysis of the propagation of rock avalanches as a function of the assumed rheology. *Rock Mech Rock Eng* 41(1):59–84. doi:10.1007/s00603-007-0143-x
- Schindler C, Cuenod Y, Eisenlohr T, Joris CL (1993) The events of Randa, April 18th and May 19th 1991 – an uncommon type of rockfall. *Die Ereignisse vom 18. April und 9. Mai 1991 bei Randa (VS) – ein atypischer Bergsturz in Raten Eclogae Geologicae Helveticae* 86(3):643–665
- Van Gassen W, Cruden DM (1989) Momentum transfer and friction in the debris of rock avalanches. *Can Geotech J* 26(4):623–628. doi:10.1139/t89-075
- Williams JR, O’connor R (1995) A linear complexity intersection algorithm for discrete element simulation of arbitrary geometries. *Eng Comput* 12(2):185–201
- Williams JR, O’Connor R (1999) Discrete element simulation and the contact problem. *Arch Comput Methods Eng* 6(4):279–304



Assessment of Discrete Element Modelling Parameters for Rock Mass Propagation

Guilhem Mollon, Vincent Richefeu, Pascal Villard, and Dominique Daudon

Abstract

The efficiency of a numerical model depends on both the realism of the assumptions it is based on, and on the way its parameters are assessed. We propose a numerical model based on the discrete element method which makes possible, thanks to the definition of an appropriate contact law, to simulate the mechanisms of energy dissipations by friction and shocks during the propagation of an avalanche of granular material on a slope. The parameters of the contact model are obtained from laboratory experiments of single impacts. A particular attention was paid to the values of the run-out, the morphology of the deposit, the proportions of energy dissipations by impacts or friction, and the kinetic energies of translation and rotation. The results of this numerical study provide valuable information on the relevance of some usual assumptions of granular flow continuous models.

Keywords

Discrete element method • Rock avalanches • Dissipative contact law • Parameter identification • Experimental validation

Introduction

Understanding and prediction of rock avalanches are key elements for the risk management in the development of mountain areas. Due to the complexity of the involved mechanisms, numerical models such as continuous models (McDougal and Hungr 2004; Mangeney-Castelnau et al. 2003; Tommasi et al. 2008) based on fluid mechanics or discrete element models (Cundall and Strack 1979) are needed to estimate the morphology of the deposit or the propagation distance of a rock mass.

Compared with continuous models, discrete models allow more accurate modelling of the propagation phenomenon, without the need of accounting for all existing mechanisms of interaction. At the scale of an actual event, rather simple contact laws can be used without any loss of accuracy.

The model proposed here is based (1) on realistic block shapes and (2) on the definition of simple interaction laws that hold physical parameters easily assessable. These laws incorporate the mechanisms of energy dissipation in a global way.

To validate this approach, which is extremely difficult to carry out in the case of rock avalanches, we replicated laboratory experiments conducted under idealized test conditions (Manzella and Labiouse 2009). Model parameters, optimized through tests conducted on single brick release, were used to simulate the collective behavior of a set of bricks on a slope.

The advantage of the numerical model is that it gives access to quantities difficult to assess experimentally at any point of the granular mass: velocity and rotation of bodies, energy dissipated by friction or shocks with the slope or within the mass movement, nature of flow and geometry of the final deposit.

After the validation, the numerical model is used to evaluate the quality of some usual assumptions of continuous models of granular flows (i.e. assumptions of no-dilatancy and of velocity uniformity in a cross-section of

G. Mollon (✉) • V. Richefeu • P. Villard • D. Daudon
UJF-Grenoble 1, Grenoble-INP, CNRS UMR 5521, 3SR Lab,
Grenoble F-38041, France
e-mail: guilhem.mollon@gmail.com

the flow), and the relevance of some parameters by studying the different modes of energy dissipation along the slope and inside the flow.

Numerical Model

Discrete models have the advantage to model the deterministic movements of a set of interacting particles. We present in this section the numerical model implemented within the C++ toolkit DEMbox (www.cgp-gateway.org). The movement of each block, governed by the fundamental principle of dynamics, is integrated by means of the velocity-Verlet scheme (Allen and Tildesley 1989) which is a good compromise between accuracy of the block velocities (for both translations and rotations) and memory saving.

Rock avalanches are far from being treated as a quasi-static evolution of block movements. For this reason, the so-called local non-viscous damping (Cundall et al. 1982) – which affects the block movements, can not be used since it would lead to unphysical behavior. Indeed, this artefact of calculation dissipates energy in an arbitrary manner. It affects both the kinematics of free bodies and bodies that interact with each other.

Another solution to introduce dissipative behaviour is to account for a local viscous damping at the contact level (Cleary and Prakash 2003). This solution has also been set aside because it introduces a viscosity parameter which can not be connected to a well-defined dissipation rate in the case where multiple contacts occur at the same time. More precisely, the effective mass involved in the critical viscosity is not well-defined and should depend on the positions of the contact points and their amount.

In fact, the energy loss may result from very complex physical mechanisms (heat production, wave propagation. . .) that are beyond our understanding in the case of collective behavior. For the contact-force laws, we wanted a simple formulation while incorporating the energy dissipation due to block impacts. We opted for minimalist laws where friction and normal damping coefficients are required to dissipate the kinetic energy of the blocks. We will see in the sequel that the simple laws proposed here are sufficient to satisfactorily describe the main rebound patterns even if our model is obviously not able to reproduce more complex behaviors like e.g. rocking block (Bourgeot et al. 2006).

Block Shapes

In the rock avalanche problematic, the shape of the blocks is of primary importance and it must be taken into account explicitly in the model. Different strategies are possible (e.g. polyhedra, clumps) but we chosed spheropolyhedra

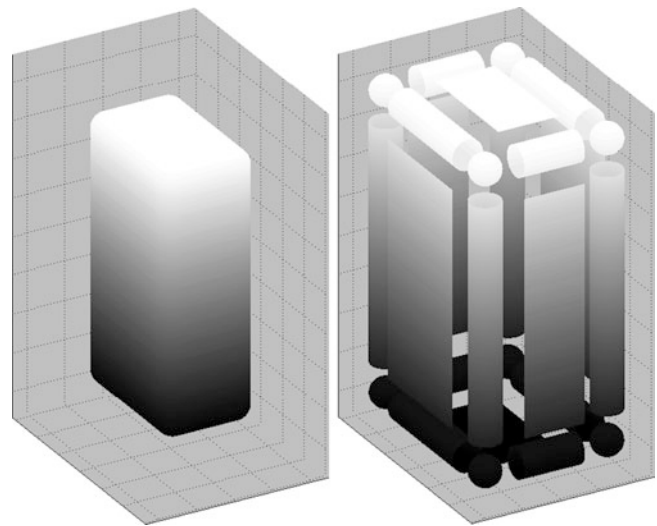


Fig. 1 Layout of a brick modelled by spheropolyhedron

which has several advantages including a highly simplified contact detection (Alonso-Marroquin 2008). The block shape is defined by a set of vertices interconnected by edges (lines) and faces (Fig. 1). The rounded shape is then defined by sweeping a sphere of radius r along each point of its edges and faces. From a mathematical viewpoint, our block shapes can be seen as the Minkowsky sum of a polyhedron with a sphere (Van Den Bergen 2003).

In practice, the contact position, the overlap and the local frame are determined by considering a few basic geometric computations based on the distances between points, lines and planes. This geometric trick allows the contact area between spheropolyhedra to be defined by a set of contact points resulting from elementary intersection tests involving the swept sphere radii: (1) vertex-vertex, (2) vertex-edge, (3) edge-edge, and (4) vertex-face. One can better appreciate the benefit of this method when considering for example face-face intersection test: it is simply replaced by a set of edge-edge and vertex-face tests. The spheropolyhedra method has many other benefits such as the ability to define concave and/or hollow shapes. Also, the normal vectors at contacts are well defined.

Contact Force Laws

The interaction model integrates the energy dissipation related to friction and to normal damping between solids in contact. The most minimalist formulation we found for the normal force is a linear elastic law with two different stiffnesses in case of loading or unloading (Banton et al. 2009). This way, the rate of non-restored work of the normal force (i.e. the normal restitution parameter e_n^2) after an impact is the ratio between the unloading and the loading

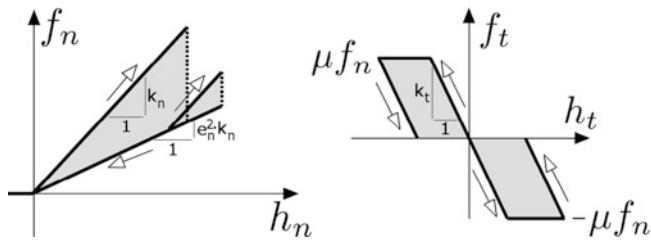


Fig. 2 Normal and tangential Force-displacement relations with: h_n = normal interpenetration of the two solids, f_n = normal repulsive force, h_t tangential relative displacement between the two solids, f_t = tangential force. Energy dissipations are represented in grey

stiffnesses. As described in Fig. 2, the other parameters of the contact law are the Coulomb friction coefficient (μ) and the normal and tangential stiffnesses of the contact (k_n and k_t respectively). The number of parameters of a given contact is therefore equal to four.

Assessment of the Contact Parameters

As an attempt to give the proposed model a predictive character, the physical parameters of the contact law were assessed from additional experiments of the impact of a single brick on a support (clay brick and plastic support called “forex”, identical to the ones used by the Manzella and Labiouse 2009). The brick was filmed at 1,000 images per second by two high-speed cameras positioned along orthogonal directions.

After synchronization (impact time is set as the time origin) and scaling (pixel sizes for each camera), the 2D trajectories of four vertex points for each camera were obtained by means of digital image correlation and made possible the 3D trajectory reconstruction. The parameters involved in the theoretical trajectory (in particular the velocities before and after the impact) were then optimized by means of an error function that gives a distance measure between the identified trajectory and the theoretical one (that obey Newton’s second law). Four Brick/Support impacts and two Brick/Brick impacts were analysed, and the contact parameters were identified for each kind of contact so as to optimize the trajectories of all the studied impacts. The resulting parameters are stored in Table 1. Figure 3 proposes more visual results, and describes from left to right the different steps of the parameters assessment: (1) experimentation and shooting of the impact, (2) mathematical identification of the trajectory before and after impact, and (3) numerical identification of the parameters (stored in Table 1) allowing to optimize the simulation of all the experimental impacts. Figure 3a and b correspond to the two cameras with perpendicular axes used for the shooting.

Table 1 Optimal parameters obtained by minimizing an error function

	e_n^2	μ	k_n	k_t/k_n
Brick/support	0.53	0.46	10^5	0.42
Brick/brick	0.13	0.86	10^5	0.27

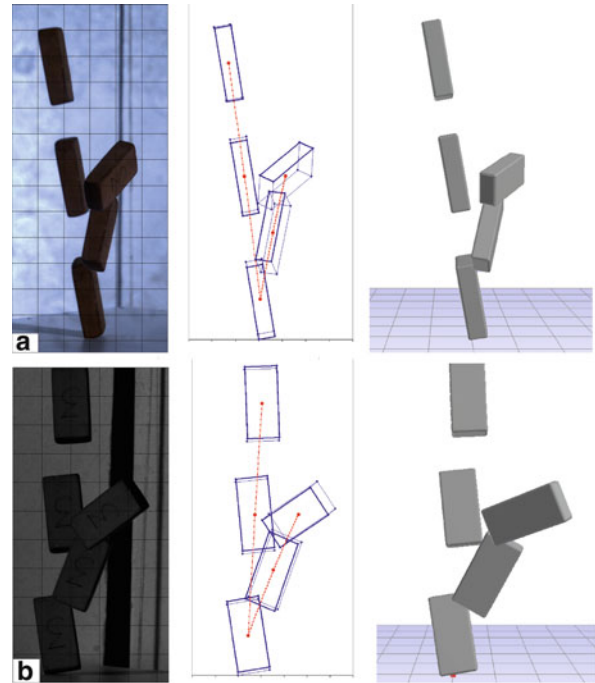


Fig. 3 Example of successive steps for the identification of the contacts parameters (time interval of 20 ms); (a) Camera 1; (b) Camera 2

Validation of the Model on a Small-Scale Experiment

The contact laws and model parameters have been proved as consistent in the case of a single impact, but a validation is needed to make sure that it is able to predict accurately the behaviour of a granular flow involving a large number of particles. This validation is performed using the experimental results by Manzella and Labiouse (2009). These authors realized a series of launches of a large number of bricks on a device composed by two rectangular boards (3 m*4 m) of forex (kind of plastic) linked by a hinge. The first board was fixed and horizontal while the second was inclined by a user-defined angle. A rectangular box (height 20 cm, width 40 cm, depth 60 cm) was filled with a given amount of material, and positioned at a determined height on the inclined plane. A trap was open to release the material, which propagated on the slope until it eventually deposited on the horizontal plane. The validation proposed here focuses on one specific experimentation involving 40 l of randomly poured bricks (size of 3.1 cm*1.5 cm*0.8 cm,

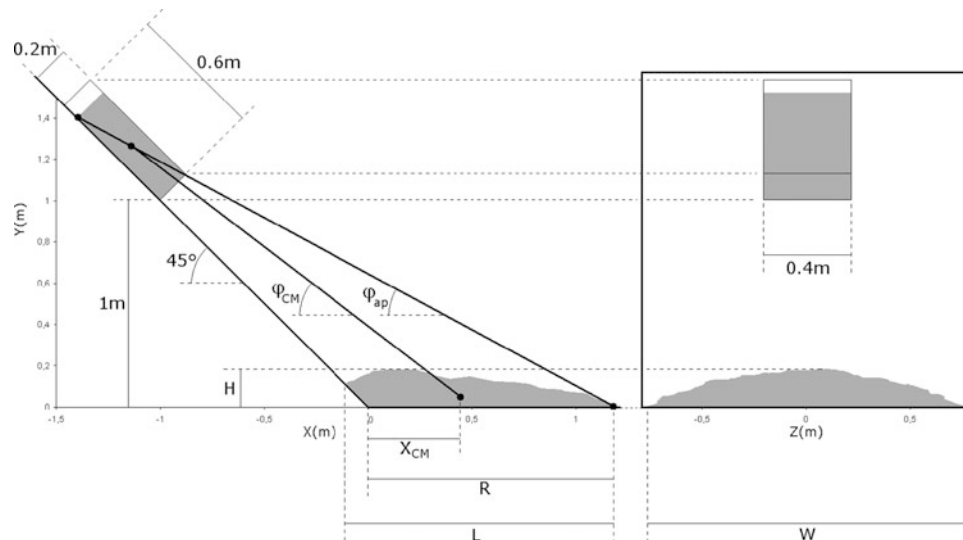


Fig. 4 Layout of the experimental device used in Manzella and Labiouse (2009)

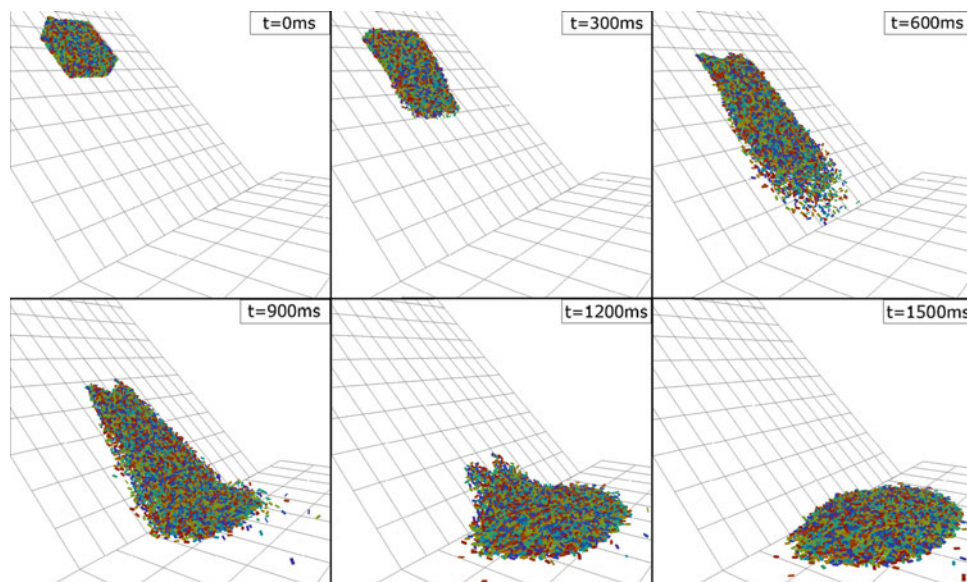


Fig. 5 Perspective view of the avalanche predicted by the numerical model

material density of 17kN/m^3 , apparent density of 10kN/m^3), launched on a 45° slope from a height of 1 m. The bricks and support were identical to the ones used for the identification of the contact parameters in the previous section. The layout of the experiment is represented in Fig. 4, as well as some of the measurements performed on the material deposit : length L , runout R , width W , height H , travel angle ϕ_{CM} (related to the centre of mass before and after the flow), and Fahrböschung ϕ_{ap} (related to the extremity of the deposit as defined by Heim 1932).

This experiment is reproduced numerically with 6,300 bricks randomly poured in the starting box. This number of

bricks corresponds to a rough estimate of the one used in the actual experiment. The simulation starts when the lower face of the box is deleted. Figure 5 shows several stages of the simulated avalanche with a time step of 300 ms. The results of the simulation are compared with the experimental ones in Fig. 6. In Fig. 6a, the shapes of the numerical and experimental deposits are compared in terms of their contour in a horizontal and a vertical plane. A very satisfying correspondence appears for the horizontal contour and this correspondence is a bit less accurate for the vertical contour, the numerical deposit having a larger height than the experimental one.

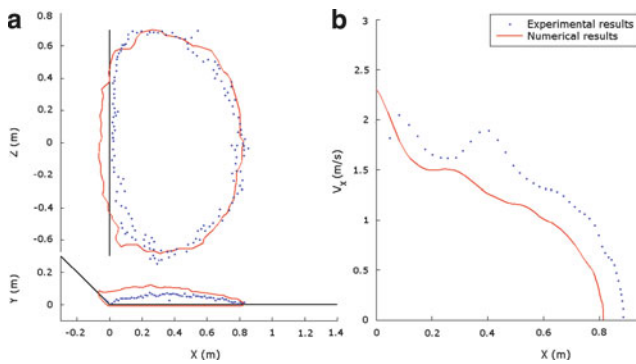


Fig. 6 Comparison between the experimental and numerical results; (a) Horizontal and vertical contours of the deposit; (b) Velocity of the avalanche front on the horizontal plane

Figure 6b presents the evolution of the mass front velocity on the horizontal plane with respect to the position of this front, as provided by the experimental and numerical results. The two curves show a good qualitative correspondence. The observed quantitative differences may be linked to the inaccuracy of the concept of “mass front”, which has no rigorous and objective definition and was determined by different methods in the experimental and numerical frameworks. Qualitatively, this curve provides some interesting information about the kinematics of the deposit. We first observe a strong reduction of the velocity corresponding to the first impact of the avalanche on the horizontal plane (from $x = 0$ m to $x = 0.2$ m), then a zone for which the velocity does not decrease a lot, corresponding to the accumulation of the material on the plane (between 0.2 m and 0.6 m), and finally an important stage of deceleration until the end of the motion (between 0.6 m and 0.8 m). Table 2 presents a quantitative comparison between the dimensions of the deposit provided by the experiment and by the simulation, and shows a very good correspondence except for the deposit height. This result emphasizes the predictive ability of the proposed numerical model, since this correspondence was achieved by fitting the contact parameters of single-impact experiments instead of running a back-analysis on the full-scale experiment. It shows that it is possible to assess the collective behaviour of a large number of particles if the individual behaviour of each particle is well-defined.

Numerical Study of the Kinematics of the Granular Flow

In order to assess the validity of some usual assumptions adopted for continuous modelling of granular flows, the velocity field, angular velocity field, and stress field inside the flow are computed using spatial interpolation techniques. Figure 7 provides in shades of grey the velocity magnitude

Table 2 Quantitative comparison between the experimental and numerical deposits

	L (cm)	R (cm)	W (cm)	H (cm)	ϕ_{CM} (°)	ϕ_{ap} (°)
Experiment	93	84	140	7.5	40	32
Simulation	88.2	82.4	138.3	12.0	40.1	32.2

(in m/s), the angular velocity magnitude (in °/s) of the bricks, and the average stress (in Pa) in the plane of symmetry of the flow, at different stages of the simulation. Figure 7a shows that the velocity magnitude of the particles composing the flow increases regularly while the avalanche develops, and decreases suddenly when the flow reaches the transition between the two planes. The velocity profile in a vertical direction appears to be uniform at any abscise of the flow, and there is no pronounced vertical velocity gradient. It may be seen on Fig. 7b and c that the magnitudes of the angular velocity of the bricks and of the average stress are much more important around the angle between the two planes than in the slope and in the deposit. It seems therefore that the zone of transition between the two planes induces a brutal reduction of the velocity magnitude, but also triggers an important perturbation of the flow by increasing the rotation of the particles and the stress level. Moreover, the angular velocity of the bricks accumulating on the horizontal plane after the transition is very low, while their velocity is uniform on the deposit and decreases along time until the end of the motion (at $t = 1.4$ s). The particles belonging to the accumulated deposit seem therefore to have a slow motion of decelerating translation. This motion is induced by the fact that the particles still falling on the slope transfer their kinetic energy by “pushing” the deposit in the transition zone, inducing the stress peak observed in this area. The displacement of the deposit ends when this transfer of kinetic energy stops, i.e. when there is no more flow on the slope. This assumption is in good agreement with the experimental and numerical estimation of the velocity of the avalanche front (Fig. 6).

Energy Considerations

The analysis of the modes of energy dissipation during the flow is a relevant investigation tool to determine the relative importance of each of the parameters of the contact law. Figure 8 depicts the evolution along time of the repartition of the different kinds of energies (potential energy, kinetic energy, dissipated energy) inside the system. At $t = 0$, there is no motion and the system only has potential energy (in white in Fig. 8). When the flow develops along the inclined plane (from $t = 0$ to $t = 0.64$ s), the part of potential energy decreases and a kinetic energy (shades of grey in the upper part of the figure) appears, due to the velocity of the particles composing the flow. This kinetic energy

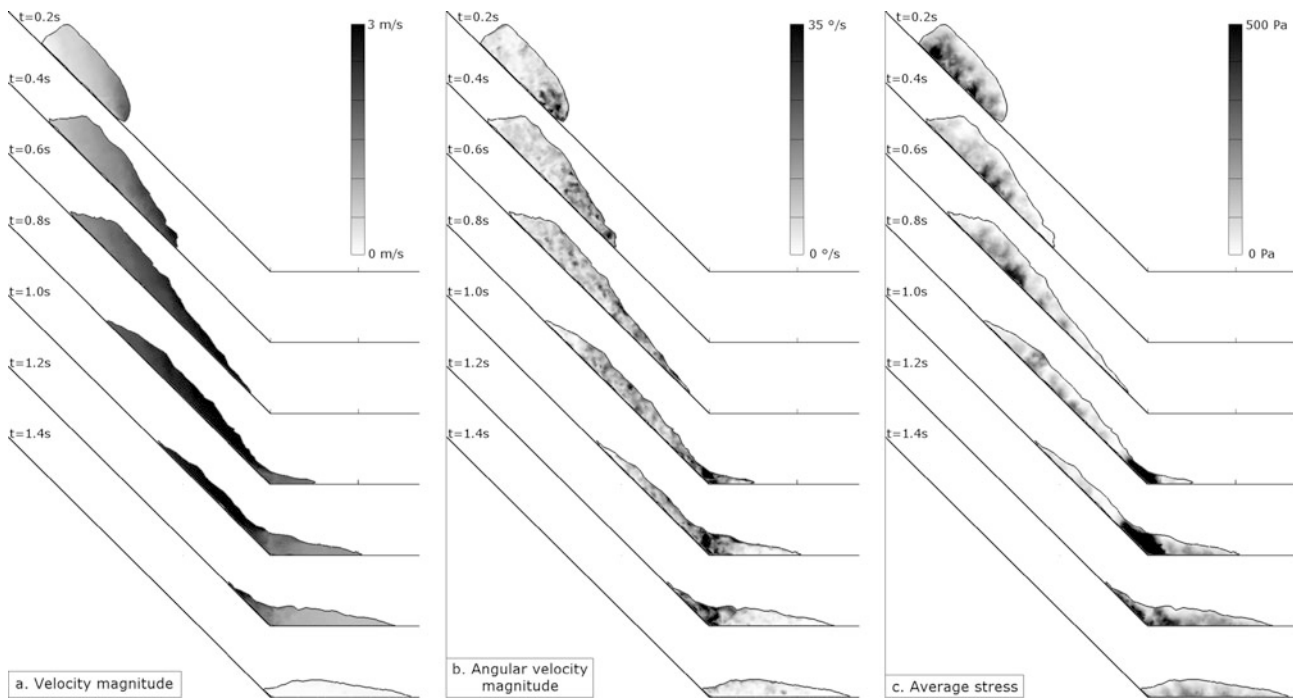


Fig. 7 Interpolated fields inside the flow; (a) Velocity magnitude; (b) Angular velocity magnitude; (c) Average stress

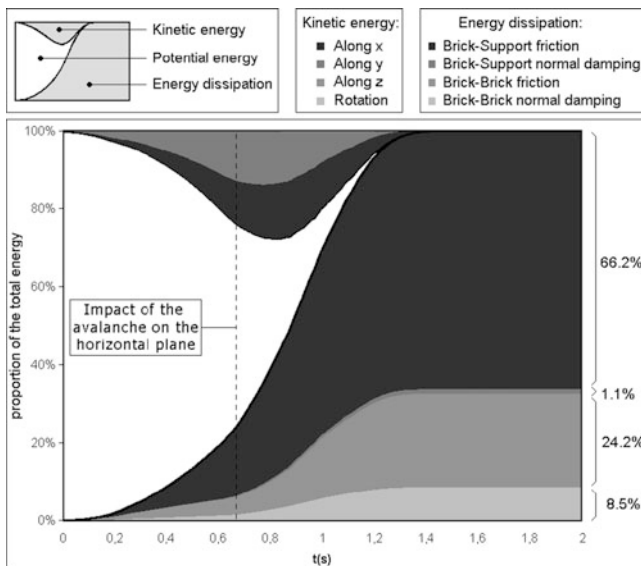


Fig. 8 Evolution of the energy repartition inside the system

may be decomposed in its components along the axes x , y , and z , and in rotational energy. Figure 8 shows that only the components along x and y have a significant value, and that the energies along z (lateral spreading of the granular mass) and in rotation are negligible.

Besides, the sum of the kinetic and potential energies during the flow is not equal to the initial potential energy because of the energy dissipations (shades of grey in the lower part of the figure). These dissipations are related to the contact law depicted in a previous section, and may be

decomposed in four categories: Brick-Support frictional dissipation, Brick-Support normal dissipation, Brick-Brick frictional dissipation, and Brick-Brick normal dissipation.

After the impact of the avalanche on the horizontal plane, the kinetic energy reaches a peak and decreases until the end of the motion, at $t = 1.4$ s. Meanwhile, there is an increase of the total rate of energy dissipation (i.e. of the slope of the envelope of the total energy dissipation), probably because of the phenomena occurring in the transition zone and pointed out in the previous section. The dissipated energy increases until the motion stops, which corresponds to a dissipation of 100 % of the initial potential energy. The proportions of the different kinds of energy dissipations are provided in Fig. 8, and clearly show that, over the entire event, most of the energy is dissipated by friction between the support and the bricks (66.2 %), and by friction between bricks (24.2 %). The dissipations by normal damping are much less significant.

The localizations of the different sources of energy dissipation may be found in Fig. 9. To plot this figure, the system was divided in several horizontal slices along the x -axis, each slice having a width of 0.1 m. The energy dissipations occurring in each slice were monitored during the simulation, and the figure provides the cumulated dissipated energies of each kind and in each slice during the entire flow.

In the two planes of the system (i.e. everywhere except in the transition zone around $x = 0$), the Fig. 9 clearly shows that the energy mostly dissipates by friction between the bricks and the support (around 90 % of the total energy dissipated). On the inclined plane, the repartition

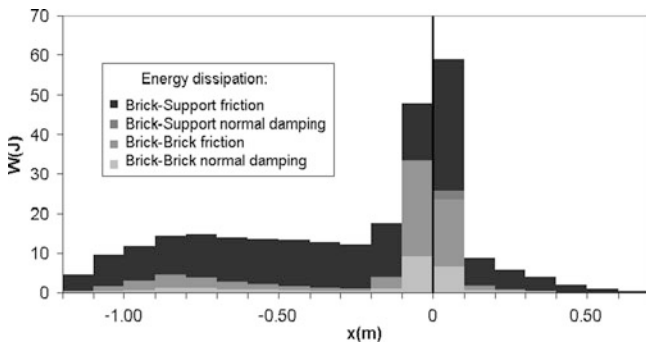


Fig. 9 Localisation along the x-axis of the four sources of energy dissipation

of this dissipation is roughly uniform, and the dissipation level remains quite low. On the contrary, the transition zone between the two planes exhibits much higher levels and different modes of dissipation. The larger amount of dissipation by contacts between bricks (either by friction or by normal damping) might be related to the phenomena depicted in the previous section (Fig. 7), i.e. to the apparition of important rotations of the particles and to high stress levels because of the flow perturbation induced by the transition between the two planes. This observation probably means that the important proportion of Brick-Support frictional dissipation observed in Fig. 8 is only relevant because of the perfect regularity of the slope, and that a granular flow on a slope with important roughness would probably induce a different repartition of the energy dissipations.

Conclusion

The mechanisms of propagation of a granular mass were investigated using the discrete element method. The numerical model, calibrated from the elementary rebounds of a single particle, demonstrated the ability to describe accurately the collective movement of a granular flow along a slope. The model was validated from experimental results found in the literature and involving a large number of particles. This model makes possible to assess the position and geometry of the deposit, as well as the kinematics of the whole flow. It also gives access to several quantities (i.e. particle kinematics or energy dissipations) which are out-of-reach of the experimental devices. It was for example demonstrated that, along the slope, most of the energy is dissipated by basal friction between the bricks and the support. The velocity field being rather homogeneous, it induces a small number and intensity of the impacts inside the flow, which leads to a limited dissipation related to these impacts in this zone of the flow. On the contrary, the slope transition constitutes an obstacle to the flow which is therefore strongly perturbed. The contacts between bricks are

much more numerous and intense, which leads to the apparition of energy dissipations by friction and normal damping between bricks. The downstream part of the flow (located on the horizontal plane) is slowed down by the absence of slope, and its motion is only triggered by the transfer of kinetic energy from the upstream part of the flow. For the complete event, the proportions of the different modes of energy dissipation are 66.2 % by Brick-Support friction, 24.2 % by Brick-Brick friction, and respectively 8.5 % and 1.1 % by Brick-Brick and Brick-Support normal damping.

The proposed model was applied to laboratory experiments with simple and controlled geometric parameters, and must be confronted to more complicated topographies and block shapes. It is likely that a lack of regularity of the slope may considerably change the characteristics of the flow. The procedure of determination of the model parameters, which proved relevant for laboratory tests, has also to be tested on in-situ block impacts. Only when this procedure is validated will it be possible to obtain predictive results for real granular flow events such as rock avalanches.

Acknowledgments This study was performed as a part of the European project ALCOTRA-MASSA, with financial support from the European Funds For Regional Development (FEDER).

References

- Allen MP, Tildesley DJ (1989) Computer simulation of liquids. Clarendon, New York
- Alonso-Marroquin F (2008) Spheropolygons: a new method to simulate conservative and dissipative interactions between 2d complex-shaped rigid bodies. *EPL (Europhysics Letters)* 83(1):14001
- Banton J, Villard P, Jongmans D, and Scavia C (2009) Two-dimensional discrete element models of debris avalanches: parameterization and the reproductibility of experimental results. *J Geophys Res Earth Surf* 114: F04013, 15p.
- Bourgeot J-M, Canudas-de Wit C, Brogliato B (2006) Rocking block to the biped robot impact shaping for double support walk: From the. In: Tokhi MO, Virk GS, Hossain MA (eds) *Climbing and walking robots*. Springer, Berlin/Heidelberg, pp 509–516
- Cleary PW, Prakash M (2003) Discrete-element modelling and smoothed particle hydrodynamics: potential in the environmental sciences. *Philos Trans R Soc A Math Phys Eng Sci* 362 (1822):2003–2030
- Cundall PA, Strack ODL (1979) A discrete numerical-model for granular assemblies. *Geotechnique* 29(1):47–65
- Cundall PA, Drescher A, Strack ODL (1982) IUTAM conference on deformation and failure of granular materials, Delft
- Heim A (1932) *Bergsturz und Menschenleben*. Fretz und Wasmuth Verlag, Zürich
- Mangeney-Castelnau A, Vilotte JP, Bristeau MO, Perthame B, Bouchut F, Simeoni C, Yerneni S (2003) Numerical modeling of avalanches based on saint venant equations using a kinetic scheme. *J Geophys Res-Solid Earth* 108:2527–2542

- Manzella I, Labiouse V (2009) Flow experiments with gravels and blocks at small scale to investigate parameters and mechanisms involved in rock avalanches. *Eng Geol* 109:146–158
- McDougall S, Hungr O (2004) A model for the analysis of rapid landslide motion across three-dimensional terrain. *Can Geotech J* 41:1084–1097
- Tommasi P, Campedel P, Consorti C, Ribacchi R (2008) A discontinuous approach to the numerical modelling of rock avalanches. *Rock Mech Rock Eng* 41(1):37–58
- Van Den Bergen G (2003) Collision detection in interactive 3D environments (The Morgan Kaufmann series in interactive 3D technology). Morgan Kaufmann, San Francisco



On Controls of Flow-Like Landslide Evolution by an Erodible Layer

Giovanni B. Crosta, Silvia Imposimato, Dennis Roddeman, and Paolo Frattini

Abstract

The role played by the presence of erodible material along the path of flow-like landslides is analyzed. The effects of type and physical mechanical properties of materials, thickness and slope geometry on the runout and the deposit geometry are investigated. Fully 2D and 3D numerical simulations have been performed representing small scale laboratory experiments and large scale field examples. The properties adopted for the erodible material strongly control the evolution of the landslide and the type of occurring mechanisms. These aspects have a major influence on the results and on the hazard zonation and should be taken into account.

Keywords

Rock avalanches • Erosion • Entrapment • Modeling • FEM • 3D • Granular flow

Introduction

Flow-like landslides (e.g. debris flow, debris avalanches, flow-slides and rock avalanches) are characterized by high velocity and mobility, extremely variable properties and, frequently, an extreme erosion capability. The result of such an erosive power that has been most frequently reported is the increase in volume. Nevertheless, on the basis of field and experimental observations, the role of material located along the landslide path (substrate material) or temporarily above the topographic surface (e.g. snow, ice or water) in controlling the dynamics of rock- or debris-avalanches has been suggested (Hung and Evans 2004; Crosta 1992; Crosta et al. 2006, 2009; Dufresne et al. 2010; Mangeney et al. 2010). The influence on simulation results has been suggested by various authors (Pitman et al. 2003; Crosta et al. 2006, 2009; Chen et al. 2006; Mangeney et al. 2010).

Crosta et al. (2006) show this features and behavior by some illustrative numerical models evidencing the occurrence of shallow erosion, local deposition and ploughing of impacted structures and/or obstacles.

The material (e.g. soil partially or fully saturated, rock, ice) forming the surface over which the rock/debris avalanche moves can influence the emplacement mechanisms and the observed runout distances. The material can be characterized by different thickness (up to tens or hundreds of meters), physical mechanical properties (e.g. frictional, cohesive, with constant or variable strength, high or low permeability), and characterized by different mechanical behaviour (e.g. collapsible, liquefiable, dilatant). These physical mechanical parameters control, together with those of the moving mass, if the basal material can be entrained, dragged, sheared, ploughed, bulldozed or remain unaffected by the landslide motion.

Field evidence has been presented for rock and debris avalanches under different geological and environmental conditions, and entrained volumes have been quantified (e.g. McDougall 2006: shallow flows/debris avalanches in pyroclastic deposits, erosion rate of $0.01-0.1 \text{ m}^{-1}$; Nomash river rock slide, erosion rate $1.9 * 10^{-3} \text{ m}^{-1}$; Zymoetz River: $500,000 \text{ m}^3$ at an erosion rate of $3.3 * 10^{-4} \text{ m}^{-1}$;

G.B. Crosta (✉) • P. Frattini
Dipartimento di Scienze Geologiche e Geotecnologie, Università
degli Studi di Milano-Bicocca, Milan, Italy
e-mail: giovannibattista.crosta@unimib.it

S. Imposimato • D. Roddeman
FEAT, Maaierhof 27, 6418 JL Heerlen, The Netherlands

Hungr and Evans 2004, suggest total entrainment values up to 10 times the original failure volume; Crosta et al. 2004, for the Val Pola rock avalanche report an entrainment of about 8 Mm^3 or 20 % of the initial volume; Chen et al. 2006 estimate an increase in volume of more than 10 times for shallow debris avalanches along alpine slopes). Rock slide/avalanche processes along steep rocky cliffs have been observed to trigger large slumping/entrainment within the talus slopes. Crosta (1992) observed a $0.15 * 10^6 \text{ m}^3$ rock slide/avalanche which entrained $0.25 * 10^6 \text{ m}^3$ of prevalently dry material while moving along a 35° inclined scree slope deposit. Similar processes have been observed for snow avalanches

We studied the influence of these controlling characteristics by running a series of fully 2D and 3D simulations to get a more complete understanding of the processes and local effects on material spreading and redistribution. Laboratory scale experimental tests with granular columns on erodible layers and a real case study have been simulated to calibrate and validate the finite element modeling code.

Materials and Methods

Laboratory Experiments

The collapse of a granular column has been recognized as a phenomenon useful for studying transient granular flow conditions at the laboratory scale. This process is similar to the well known dam break problem but involves a granular material. Well detailed experiments performed by releasing different types of granular materials on inclined channels/slopes, and adopting different geometries have been described in the literature (Lajeunesse et al. 2005; Lube et al. 2004, 2005, 2007; Balmforth and Kerswell 2005; Mangeney-Castelnau et al. 2007). The results of these tests have been compared both with qualitative and theoretical models, aimed at finding general scaling laws or at testing depth averaged shallow water and particle mechanics models.

To generalize the adopted approach and test its validity for real case studies it is necessary to consider the presence of an erodible layer along the spreading surface. Few tests of this type, performed at different scales and under different conditions, have been published (Mangeney-Castelnau et al. 2007; Crosta et al. 2008a, b, 2009; Mangeney et al. 2010; Iverson et al. 2011).

Experimental results demonstrate the effect of an erodible basal layer in reducing generally the material runout. Measured runout distances (Crosta et al. 2009) are always shorter than for the case of smooth basal surface and shorter also for the case of a rough channel base, this last case being characterized by a strong agitation, bouncing and projection of the particles at the front. Particle velocimetry (PIV, Crosta

et al. 2009) demonstrates that dragging occurs at the base of the moving material and that no real mixing between the two materials occurs along the contact surface.

Numerical Models

To validate the model and to extend the analysis to materials with different shear strength, we modelled the collapse of a granular column with variable aspect ratio (height/width, 0.6–20) and variable friction angle and thickness of the erodible layer. The internal friction angle of the basal erodible layer was varied (from 10° to 30°), as well as thickness (0.2–0.5 m) and initial column height (0.6 m). We use a particular combination of Eulerian–Lagrangian methods (Roddeman 2008; Crosta et al. 2003, 2005, 2009) which does not distort the FE mesh and guarantees accurate calculation results. The code can describe the large deformations and sliding of landslide material, filled or not filled with groundwater. We neglect nonlinear soil behaviour, cracking phenomena and partial groundwater saturation.

The numerical model uses isoparametric finite elements for space discretisation. We typically apply three-noded triangles in 2D, and eight-noded hexahedrals in 3D. For the 2D calculations we used 40.000 to 150.000 triangular three-node elements to discretize the 2D space with a mean element size ranging between 0.004 m and 0.01 m. An implicit Euler time stepping, with automatic time step adjustment is adopted. The initial equilibrium stress state is reached through quasi-static time stepping. The initial movement is triggered by either lowering cohesion in time or imposing an external perturbation, or deleting a lateral constrain (as for the granular column). A predefined failure surface (as for the Arvel case study) is not always required. We assume an elasto-plastic material and a Mohr-Coulomb yield rule.

In the case of an erodible layer characterized by a low internal friction angle (10°) the front of the advancing material is thinner than for the case of spreading on a hard smooth frictional surface.

Initially, the collapsing material sinks within the erodible bed, without evident differences for the different layer thicknesses (20 or 50 cm), and successively it slightly runs up and over the material removed from the erodible layer and pushed at the flow front.

Sinking and ploughing tend to disappear with increasing internal friction angle values. For a 30° material no sinking and erosion are observed and no material is pushed in the front (Fig. 1). No migration of the interface between static and flowing material is observed for the case of a basal layer with low values of internal friction angle. On the contrary, the migration of the interface is observed when no scouring and ploughing occurs along a layer characterized by higher

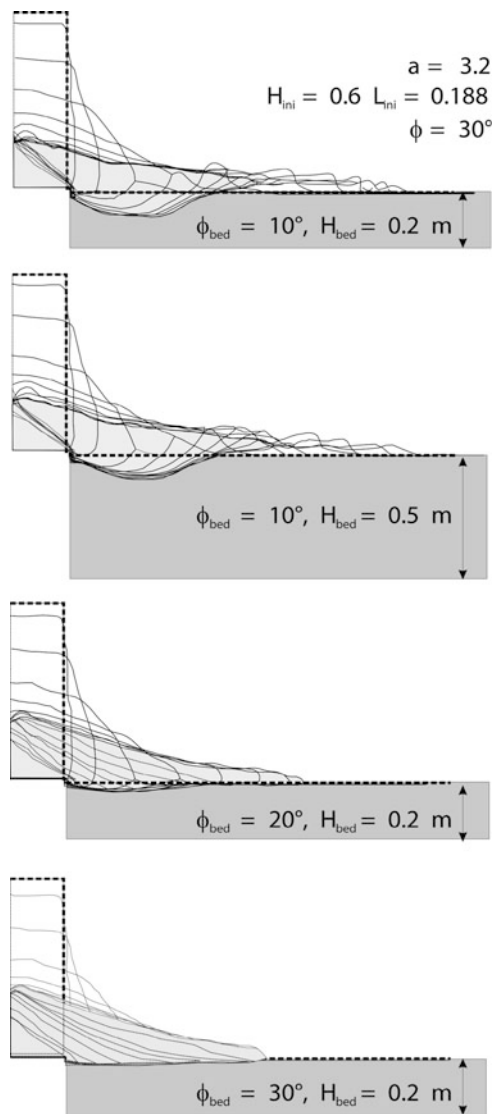


Fig. 1 Numerical results for 2D granular column (initial height, H_{ini} , initial width, L_{ini} , ϕ = internal friction angle of column material) collapse simulations. The free surface and the basal interface, separating static and flowing material, at different time steps are drawn. Effects of basal layer properties and geometry on the runout and erosion are shown

friction angles. This demonstrate a major difference in flow behaviour that is worth to be modelled and that is not easily implemented in shallow water approaches. The maximum velocity is higher for the case of higher internal friction angle even if the motion stops earlier than for the cases with lower friction.

This is probably the result of the minimized or null sinking, entrainment and material plowing by the moving mass. On the contrary, we observe that the increase in the internal friction angle of the erodible layer causes a decrease in the final runout, and the formation of a slightly thicker toe of the deposit.

Simulations have been run along both horizontal and inclined (at 10° , 16° and 22°) channels. The material has been modelled as a Mohr-Coulomb material characterized by a friction angle of 26° and a very low cohesion variable between 0 and 24 Pa for channels inclined from 0 up to 22° .

In any case this value is quite low when considered for example against the initial vertical stress at the base of the column (e.g. for the case of an horizontal plane equals 1,300 Pa). One more series of simulations has been run by considering the presence of a 4.6 mm thick erodible layer placed directly on a smooth channel surface. Channel inclination affects both the maximum velocity and the duration of the flow. Maximum runout distance increases by 5 times passing from a 0° to 22° inclination, while maximum velocity increases of about 30 % and total duration doubles. By comparing the numerical results with those from these sets of experiments an almost perfect coincidence occurs with the dataset by Mangeney et al. (2010), whereas some differences are evident with Lube et al. (2005) dataset.

The case of a channel covered by a thin erodible layer and inclined at an angle close to the repose angle of the granular material could simulate some natural condition for a flow over a previously deposited thin layer of material. We observe that the erosion depth is close to the layer thickness at the beginning but decreases progressively toward the front as this moves forward. This decrease together with the dragging of the eroded material along the interface between the falling mass and the erodible layer, generates along the interface a wave-like feature which slowly moves forward.

Much more difficult is the simulation of the runout along an erodible layer in metastable conditions as experienced in the laboratory by Mangeney et al. (2010). This is still a research subject under development.

Arvel Case Study

The Arvel landslide (ca 0.6 Mm^3 ; March 14, 1922, Switzerland, Choffat 1929; Jaboyedoff 2003; Crosta et al. 2008a, b; Figs. 2 and 3) affected a 120 m high steep rocky cliff of a limestone quarry. The rockfall/rock-avalanche was characterized by a simple geometry, a steep source and a flat propagation, erosion and deposition areas, occupied by alluvial deposits with a water table located few metres below the surface. The maximum horizontal distance, from the top of the main scarp to the extreme tip of the deposit, and the total maximum drop height were about 337 and 240 m, respectively (35.5° fahrboschung). The deposit thickness ranged between 6 and 24 m. As a consequence of the deposition, the alluvial deposits were affected by faulting, thrusting and folding over an area of about 8 ha and up to 340 m beyond the front of the landslide deposit (total fahrboschung 19.5°).

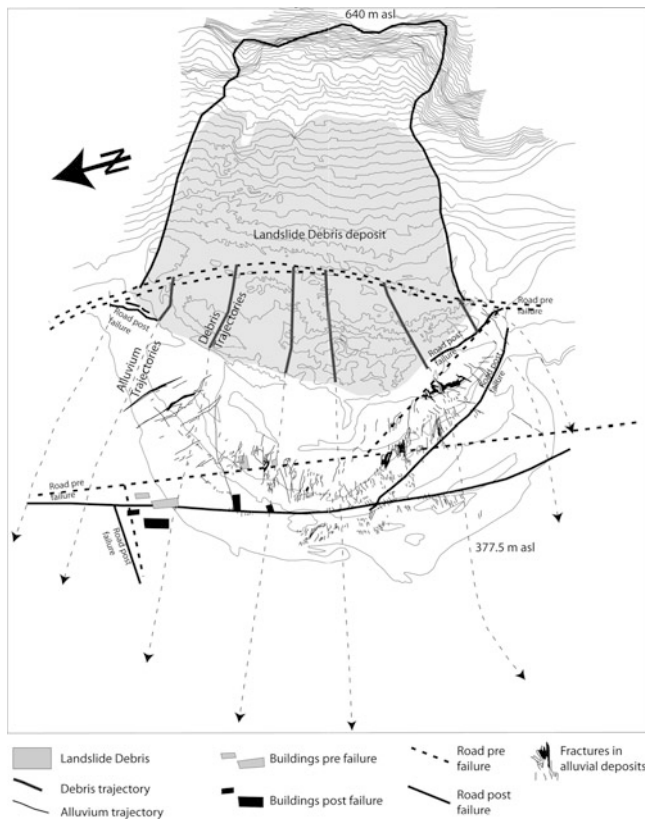


Fig. 2 Arvel rockfall/rock avalanche. Landslide debris and the sector of the alluvial deposits affected by the thrusting and ploughing action of the landslide are shown. Pre- and post-failure positions of roads and buildings, and fracturing within the alluvial deposits are presented

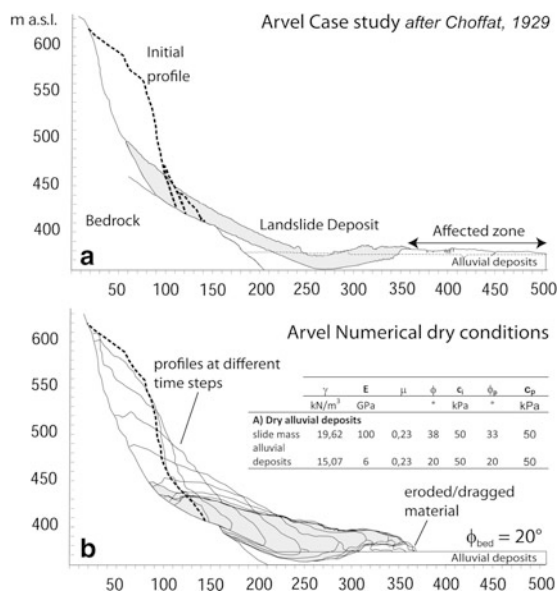


Fig. 3 Map of the Arvel rockfall/rock avalanche. Landslide debris and the sector of the alluvial deposits affected by the thrusting and ploughing action of the landslide are shown. Pre- and post-failure positions of roads and buildings, and fracturing within the alluvial deposits are presented. Table summarises the properties values adopted for the analyses

This general setting resembles that of the collapse of a granular step, with an aspect ratio of 3.2, spreading along a flat horizontal surface covered by an erodible material.

To verify the similarities between the small scale and large scale collapse behaviours, and the capabilities of the approach for hazard assessment, we ran 2D simulations along a longitudinal profile used by Choffat (1929, Fig. 3) to represent field observations. We assumed a maximum thickness of 30 m for the alluvial deposits and the adopted properties are summarized within Fig. 3. The role of the presence of water within the alluvial deposits and of the excess pore pressures induced by the impact of the rock fall have been examined in Crosta et al. (2008b) and are summarized in the following. The upper scarp is narrower than the rest of the detachment zone and the deposit has a fan like geometry. This geometry introduces a certain 3D effect in material redistribution.

2D: Numerical Results

The landslide mass moves along the failure surface with minimal erosion along the talus slope located immediately below the rocky cliff. Erosion starts when the dry alluvial deposit is encountered (Fig. 3). The thin layer of eroded alluvial material is pushed with an almost vertical front, and it is subsequently folded over and overcome by the landslide debris (Fig. 3). A rapid decrease in the velocity of the landslide mass is observed at the impact against the alluvial material and this causes an evident slowing down of the rear part of the mass. Finally, the slide debris moves on the ploughed alluvial material with a sub-horizontal contact, 30–40 m long, while a slight rotational instability occurs at the front. Velocity distribution within the landslide and eroded materials has been analyzed in more detail both for dry and saturated conditions by Crosta et al. (2008a). The motion lasts for about 20 s. The main differences that can be recognized with respect to Choffat’s profile (Fig. 3) consist in the rear limit along the slope and in the thickness of the final deposit. Both these features can be controlled by the three dimensional effects or out of plane spreading of the real landslide deposit (Fig. 2) that is not considered in the 2D simulations. Eventually, the back of the final deposit passes the rear limit mapped by Choffat suggesting a too high energy of the material in this sector when the front comes to rest. This could be partly the result of lack of third dimension in the model.

By comparing the final geometries resulting from simulations considering dry and saturated alluvial deposits with the geometry observed by Choffat we note that for:

- Dry materials: the landslide mass remains compact with a surface characterized by a regular slope. The tail reaches the lowest elevation and the front the shortest distance.

The maximum erosion depth is the lowest among the values from the different models.

- Saturated materials (Crosta et al. 2008b): the deposit is thick but the upper surface is concave. The model is in good agreement with field observations in terms of erosion, maximum debris distance and longer alluvial deposit remobilization.

The maximum velocities (from 24 to 26 m s⁻¹) are computed for all the simulations at the toe of the rocky cliff and along the initial part of the alluvial deposits. In all the simulations we observe a rapid freezing of the moving mass and a final pattern of the velocities showing a sub-circular front instability. This seems comparable with field observations of secondary slope instabilities within the landslide deposit. The analysis of the velocity distribution within the landslide and alluvial materials shows that the moving mass is sheared at its interior and that in the later stages tends to move “rigidly” shearing at the contact with the alluvial mattress.

3D: Numerical Results

As stated above, the 3D constrains can strongly control the landslide behaviour altering the final geometry. The Arvel case study evidences this 3D dependency and Choffat’s detailed observations can be used to verify the model performance as well as to analyse the influence of the main controlling factors, both physical and geometrical.

We prepared a series of 3D models to carry out fully 3D numerical analyses, by using 330.000 hexahedrons, 8 m × 8 m and 2 m in thickness. The mechanical properties have been modified in the simulations to model alluvial deposits as a Mohr-Coulomb material ranging from almost purely frictional ($\rho = 16 \text{ kN/m}^3$; $\nu = 0.23$, $\phi = 20^\circ\text{--}14^\circ$, $c = 100\text{--}5 \text{ kPa}$) to almost purely cohesive ($\rho = 16 \text{ kN/m}^3$; $\nu = 0.4$, $c = 50 \text{ kPa}$), and to simulate a drained to an almost completely undrained behaviour. Properties of the landslide material have been maintained constant ($\rho = 20 \text{ kN/m}^3$; $\nu = 0.23$, $\phi = 38^\circ$ to 33° , $c = 50 \text{ kPa}$). Model geometry has been modified by introducing different thicknesses for the alluvial material covering the valley bottom.

Three main thickness values have been adopted: 10, 25 and 100 m. We adopted this wide range of values to simulate: the general control played by the layer thickness on internal structures and material spreading; the presence of strong layers acting as hard non erodible materials, able to limit the maximum sinking and excavation of the landslide; the influence on the type of mechanism which characterises the landslide propagation and deformation of the alluvial deposits.

In general, the results show that:

- The thickness of the alluvial layer is inversely related to landslide runout; for the 100 m thick layer most of the landslide material stops at the slope toe;
- The deposit area increases for decreasing thickness of the erodible layer;
- The maximum deposit thickness does not depend on the alluvial layer thickness (e.g. for the 10, 25 and 100 m layers, the maximum thickness values are 36, 34 and 36 m respectively);
- The deformation is more spread within thicker and more frictional materials, resulting in smaller changes in elevation of the initially flat valley surface;
- The radial pattern of deformation is well developed through all the models;
- The maximum elevation is observed, for the cohesive model, before the final arrest of the landslide mass and subsequent readjustments at the propagating front control the final topography.

Discussion

From the performed simulations we observe that:

- The characteristics and conditions of materials that can be entrained strongly control the evolution of rock and debris avalanches; in fact, both the initial impact and the temporary, and final geometry of the landslide debris/alluvial deposit contact surface, change with material properties (or assumed conditions);
- Undrained loading plays a relevant role but it is not limited at the debris-alluvial deposits interface and its effect on mobility is counteracted by the erodibility of the alluvial deposits;
- Both velocity and thickness of the entrained/pushed materials increase with saturation (Crosta et al. 2008b);
- Different behaviours should be expected as a function of depth of alluvial/erodible deposits, volume of the rock avalanche, degree of saturation, mechanical and hydraulic properties;
- Different modes of material entrainment have been observed in the field and have been replicated by simulation (Figs. 4 and 5); in fact, the formation of both wedges, limited by sharp shear zones, and folds of alluvial debris by the bulldozing effect at the front of the rock avalanche material, the basal dragging, and a partial mixing at the front have been simulated. Mixing can induce further changes in behaviour.
- In presence of saturated sediments the erosive process is more intense, the runout is longer and the deformation of

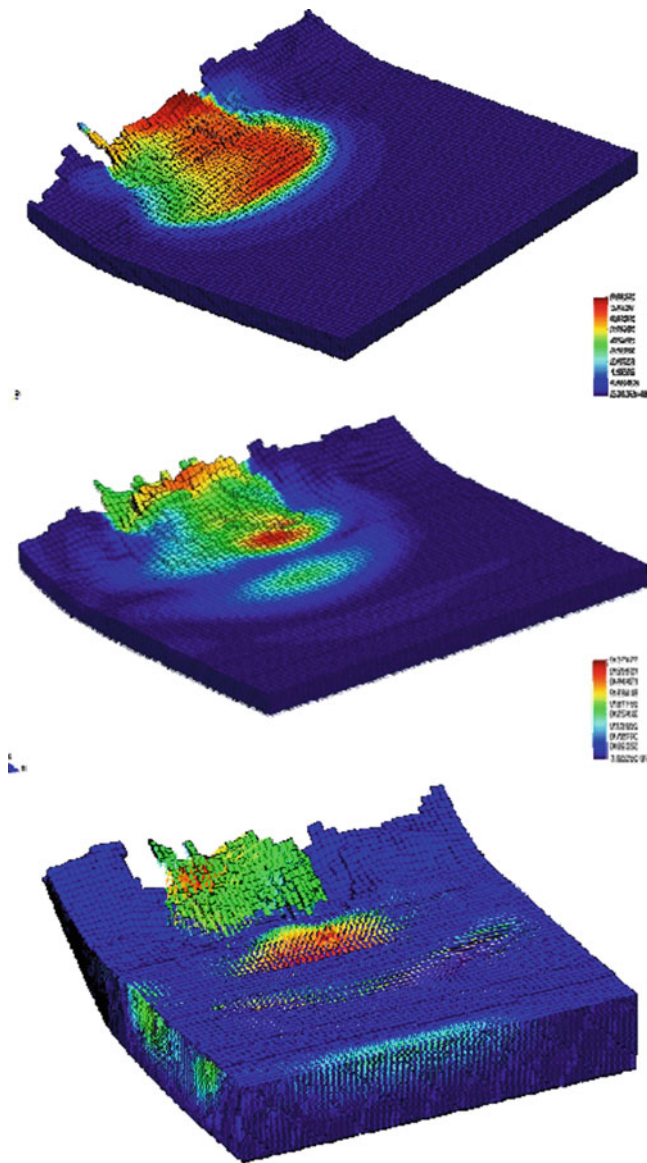


Fig. 4 Velocity field (m s^{-1}) for three models considering different thickness of the alluvial layer: 25 m cohesive, 25 m frictional and 100 m frictional (from *top to bottom*). Radial propagation of the deformation within the alluvial material is evident. A sort of wedge is raised in front of the landslide for the first case of thinner layer. A more spread and wavy pattern is observed for more frictional and thicker layers

alluvial deposits moves farther to the front of the rock-fall-avalanche debris (Crosta et al. 2008b).

The excess pore pressures generated within the alluvial deposits, and computed by considering volumetric compression, moves rapidly at the front of the moving landslide mass.

Observed differences between 2D and field evidences can result by neglecting the role of 3D effects and the local variability of alluvial properties. This 3D variability is suggested by data presented by Choffat, which shows spatial variability of deposit thickness, shape and deformation.

Results of the presented 3D simulations (see 3D in Fig. 4 and for a longitudinal cross section along the landslide axis, in Fig. 5) reveal that:

- Stronger basal layers are associated to smaller erosion, ploughing and other interaction features (Fig. 1) but this should be tested for a wider spectrum of slope and slide geometries and material properties;
- Spreading along thin basal layers sloping downhill causes basal dragging of the material with wave-like features and capturing of the basal material along reverse-like faults;
- A decrease in the thickness of the erodible horizontal layer increases the total runout in the performed simulations; this can result from the sinking of the landslide mass within the thicker basal material;
- Maximum deposit thickness remains grossly constant even when changing basal layer thickness and the computed values are very close to the measured ones, demonstrating the role of 3D effects;
- The invasion area increases for decreasing basal layer thickness; this seems related to the reduced sinking of the landslide mass at the slope toe;
- For a 10 m basal layer the landslide deposit elongates in flow direction;
- Internal deformation of the basal layer is recorded in the form of folding for a thick frictional material but with minimum displacements for the property values adopted in this series of simulations;
- A cohesive undrained-like behaviour favours the formation of wedges and bulging in the alluvial deposit at the front of the landslide material.

Conclusions

Fully 3D simulation of the avalanche and basal layer interaction is an innovative and open research topic. The same approach can be applied to estimate the spreading of an expected rock avalanche for hazard zoning. The advantages of the proposed approach consist in: the capability to directly simulate internal deformation, the interaction with structures and other materials, the use of standard and advanced geomechanical models and parameters. This is an interesting step forward in numerical modelling of such phenomena, where depth averaged models adopt entrainment models based on empirical and semi-empirical laws without directly considering physical and mechanical properties and the modes of interaction between flowing and static materials.

The success at modelling granular flows has been demonstrated (see also Crosta et al. 2009). This is particularly clear when considering for example that the flow following the collapse of a granular column has been simulated directly using the material properties without

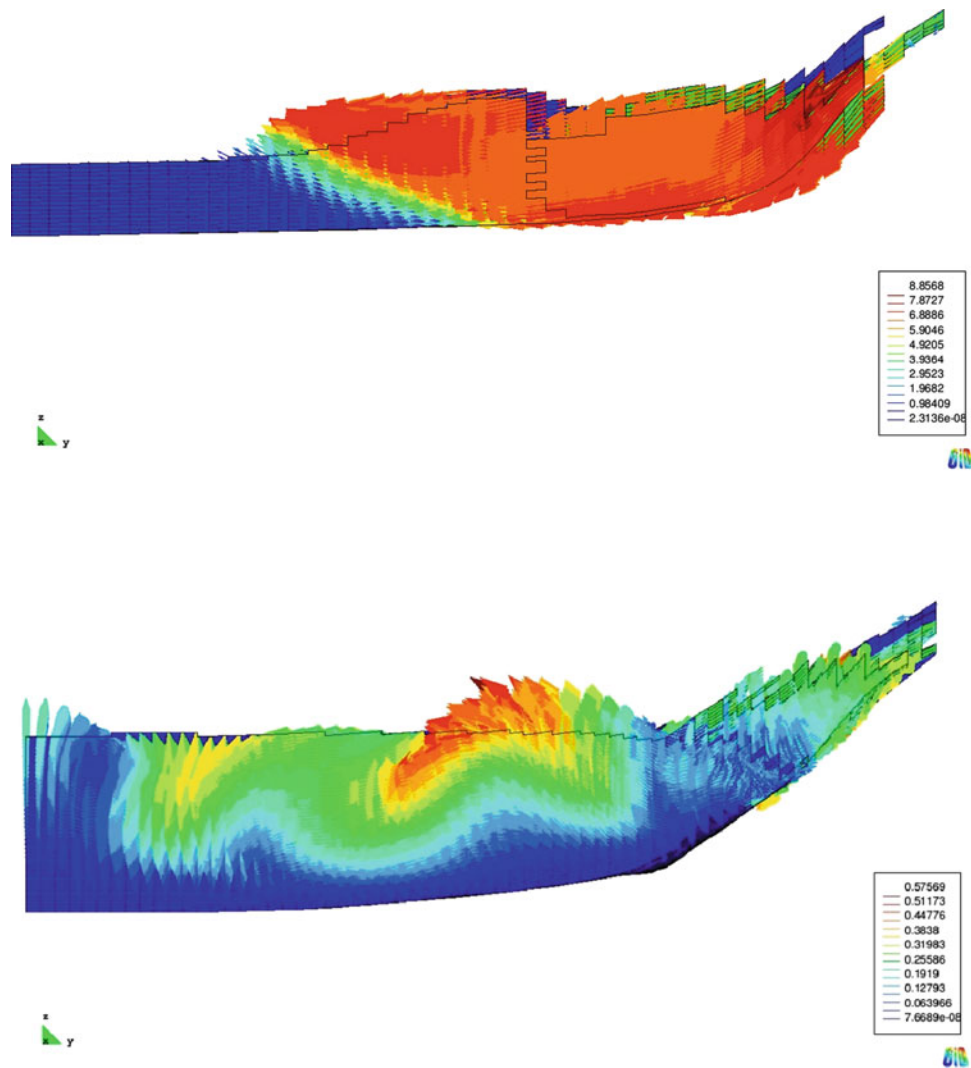


Fig. 5 Velocity field (m s^{-1}) for 2 models considering different thickness and mechanical properties of the alluvial layer: (top) 25 m, only cohesive (bottom) 100 m, frictional. The first model puts in evidence the thrusting action played by the landslide mass on the

alluvial material and the consequent formation of a frontal bulge/wedge. The second model demonstrates the possible folding of the alluvial material and the deformation distributed within the entire layer

calibration as often requested by particle flow or shallow water equation codes.

Present and future efforts are directed at simulating the role of collapsible or meta-stable materials/layers, the effects of changes in the slope inclination along the transport/propagation zone, the combination of features forming at varying the physical mechanical properties (hydraulic diffusivity, friction and cohesion, etc.)

Acknowledgments This study has been partially funded by the EC Safeland Project, GA No.: 226479, Living with landslide risk in Europe: Assessment, effects of global change, and risk management strategies.

References

- Balmforth NJ, Kerswell RR (2005) Granular collapse in two dimensions. *J Fluid Mech* 538:399
- Chen H, Crosta GB, Lee CF (2006) Erosional effects on runout of fast landslides, debris flows and avalanches: a numerical investigation. *Geotechnique* 56(5):305–322
- Choffat P (1929) L'écroulement d'Arvel (Villeneuve) de 1922. *Bull Soc Vaudoise Sci Nat* 57(1):5–28
- Crosta G (1992) An example of unusual complex landslide: from a rockfall to a dry granula flow. *Geol Romana* 30:175–184
- Crosta GB, Imposimato S, Roddeman DG (2003) Numerical modelling of large landslides stability and runout. *Nat Hazards Earth Syst Sci* 3(6):523–538

- Crosta GB, Chen H, Lee CF (2004) Replay of the 1987 Val Pola Landslide, Italian Alps. *Geomorphology* 60(1–2):127–146
- Crosta GB, Imposimato S, Roddeman D, Chiesa S, Moia F (2005) Small fast moving flow-like landslides in volcanic deposits: the 2001 Las Colinas Landslide (El Salvador). *Eng Geol* 79(3–4):185–214
- Crosta GB, Imposimato S, Roddeman DG (2006) Continuum numerical modelling of flow-like landslides. In: Evans SG, Scarascia Mugnozza G, Strom A, Hermanns R (eds) NATO ARW, landslides from massive rock slope failure, vol 49, NATO science series, earth and environmental sciences. Springer, Dordrecht, pp 211–232
- Crosta GB, Imposimato S, Roddeman DG (2008a) Approach to numerical modelling of long runout landslides. In: Proceeding International forum on landslide disaster management, landslide runout analysis benchmarking exercise, GCO, Hong Kong, Dec 2007, 20p
- Crosta GB, Imposimato S, Roddeman DG (2008b) Numerical modelling of entrainment/deposition in rock and debris-avalanches. *Eng Geol* 109(1–2):135–145
- Crosta GB, Imposimato S, Roddeman D (2009) Numerical modeling of 2-D granular step collapse on erodible and nonerodible surface. *J Geophys Res* 114:F03020
- Dufresne A, Davies TR, McSaveney MJ (2010) Influence of runout-path material on emplacement of the round top rock avalanche New Zealand. *Earth Surf Proc Land* 35:190–201
- Hungr O, Evans SG (2004) Entrainment of debris in rock avalanches; an analysis of a long run-out mechanism. *Geol Soc Am Bull* 116 (9–10):1240–1252
- Iverson RM, Reid ME, Logan M, LaHusen RG, Godt JW, Griswold JP (2011) Positive feedback and momentum growth during debris-flow entrainment of wet bed sediment. *Nat Geosci* 4:116–121
- Jaboyedoff M (2003) The rockslide of Arvel caused by human activity (Villeneuve, Switzerland): Summary, partial reinterpretation and comments of the work of Choffat, Ph. (1929): L'écroulement d'Arvel (Villeneuve) de 1922. *Bull. SVSN* 57, 5–28. Quanterra OPEN-FILE REPORT3
- Lajeunesse E, Monnier JB, Homsy GM (2005) Granular slumping on a horizontal surface. *Phys Fluids* 17:103302
- Lube G, Huppert H, Sparks S, Hallworth M (2004) Axisymmetric collapse of granular columns. *J Fluid Mech* 508:175–199
- Lube G, Huppert H, Sparks S, Freundt A (2005) Collapses of two-dimensional granular columns. *Phys Rev E* 72:041301
- Lube G, Huppert H, Sparks S, Freundt A (2007) Static and flowing regions in granular collapses down channels. *Phys Fluids* 19:043301
- Mangeney A, Roche O, Hungr O, Mangold N, Faccanoni G, Lucas A (2010) Erosion and mobility in granular collapse over sloping beds. *J Geophys Res – Earth Surface* 115:F03040
- Mangeney-Castelnau A, Tsimring LS, Volfson D, Aranson IS, Bouchut B (2007) Avalanche mobility induced by the presence of an erodible bed and associated entrainment. *Geophys Res Lett* 34:L22401
- McDougall S (2006) A new continuum dynamic model for the analysis of extremely rapid landslide motion across complex 3D terrain. Ph.D. thesis, The University of British Columbia, 253p
- Pitman EB, Nichita CC, Patra AK, Bauer AC, Bursik M, Webb A (2003) A numerical study of granular flows on erodible surfaces. *Discrete Contin Dyn Syst Ser B* 3:589–599
- Roddeman DG (2008) TOCHNOG user's manual. FEAT, 255p, www.feat.nl/manuals/user/user.html

Influence of Bed Curvature on the Numerical Modelling of Unconstrained Granular Materials

Gabriele Pisani, Marina Pirulli, Vincent Labiouse, and Claudio Scavia

Abstract

This paper deals with the theoretical-numerical and experimental analysis of dry rock avalanches moving down a chute.

Depth-averaged field equations of balance of mass and momentum as prescribed by Savage and Hutter (1991) are implemented in the RASH^{3D} code. They describe the temporal evolution of the depth averaged velocity and the distribution of the avalanche depth. A Coulomb-type mechanical behavior of the mass is assumed. To incorporate the curvature effects of the bed, the centripetal acceleration term has been here implemented in the code.

Carried out experiments consist in the release of granular material on an inclined plane that is connected to a horizontal run-out zone through a sharp transition. Comparison of the experimental findings with the computational results proved that neglecting the centripetal acceleration term can have the effect of leading to errors in the determination of the well fitted friction angle. In particular, an overestimation of the computed dynamic friction angle respect to its measured value is observed.

Keywords

Granular flow • Runout • Numerical modelling • Physical experiments • Centripetal acceleration

Introduction

In the past few years new mathematical descriptions for the motion of rockslides and avalanches have been presented. Several of these models have included innovations that have significantly advanced both our ability to simulate real events and our fundamental understanding of rapid landslide processes.

Some significant challenges still remain as we move towards more accurate and objective runout prediction using continuum dynamic models (e.g. Chen and Lee 2000; McDougall and Hungr 2004; Denlinger and Inverson 2004; Pastor et al. 2004; Pirulli 2005). One of the most important challenges is how to select and calibrate the input rheological parameters.

Without going into detailed rheological assumptions, which would be rather uncertain due to the lack of a physical understanding of the actual forces acting in debris

G. Pisani (✉)

Department of Structural and Geotechnical Engineering, Politecnico di Torino, C.so Duca degli Abruzzi, 24, Torino, Italy

School of Architecture, Civil and Environmental Engineering (ENAC), Laboratory for Rock Mechanics (LMR), École Polytechnique Fédérale de Lausanne (EPFL), Lausanne, Switzerland
e-mail: gabriele.pisani@polito.it

M. Pirulli • C. Scavia

Department of Structural and Geotechnical Engineering, Politecnico di Torino, C.so Duca degli Abruzzi, 24, Torino, Italy

V. Labiouse

School of Architecture, Civil and Environmental Engineering (ENAC), Laboratory for Rock Mechanics (LMR), École Polytechnique Fédérale de Lausanne (EPFL), Lausanne, Switzerland

avalanches, among the characteristics that make such flows quite specific it is here investigated the role that the quite steep and rough topography can play. At this regard, the centripetal acceleration has to be considered and numerically implemented in the balance equations.

At first the experimental set-up used to validate the obtained numerical results is described. Then, the basic equations and conservation laws which govern the evolution of granular avalanches along a realistic topography, when depth averaged Saint Venant equations are used, are presented. Particular attention is devoted to the theoretical formulation necessary for the centripetal acceleration numerical implementation.

A comparison of the theoretical findings with the experiments is finally given to demonstrate which consequences can occur if the centripetal acceleration effect is neglected in rheological parameter calibration.

Description of the Laboratory Experiments

Below a description is given of the small scale laboratory apparatus planned and constructed at the Rock Mechanics Laboratory of EPFL (École Polytechnique Fédérale de Lausanne) to study the runout of dry rock avalanches.

The experimental set-up mainly consists of two rectangular panels joined by either a curved (curvature radius of 50 cm) or a sharp transition to the bottom of the slope (Fig. 1). The first panel is horizontally fixed on a concrete floor slab and the second one can change its inclination.

A wooden box (height \times width \times length = 20 cm \times 40 cm \times 65 cm) is placed on the inclined panel and is used to store the material to be released. The granular material placed in the box is then released by opening the downward box gate in an almost instantaneous way, so allowing the material directly slip on the panel surface.

Each test is filmed by a digital high speed camera placed at a height of about 5 m over the horizontal panel (Manzella and Labiouse 2008).

Final deposit characteristics such as runout R , length L and width W are manually measured with a tape, while the deposit morphology and position of its centre of mass X_{CM} are defined by means of the fringe projection method (Manzella 2008).

In the present paper results obtained releasing aquarium gravel from the above mentioned box, when runout surfaces are covered with forex, and in case of sharp transition between the two panels, are used to numerically investigate the effect of centripetal acceleration in computing energy dissipation.

The gravel static (ϕ_{static}) and dynamic ($\phi_{dynamic}$) basal friction angles, measured through tilting tests, together with physical and mechanical characteristics are summarised in Table 1.

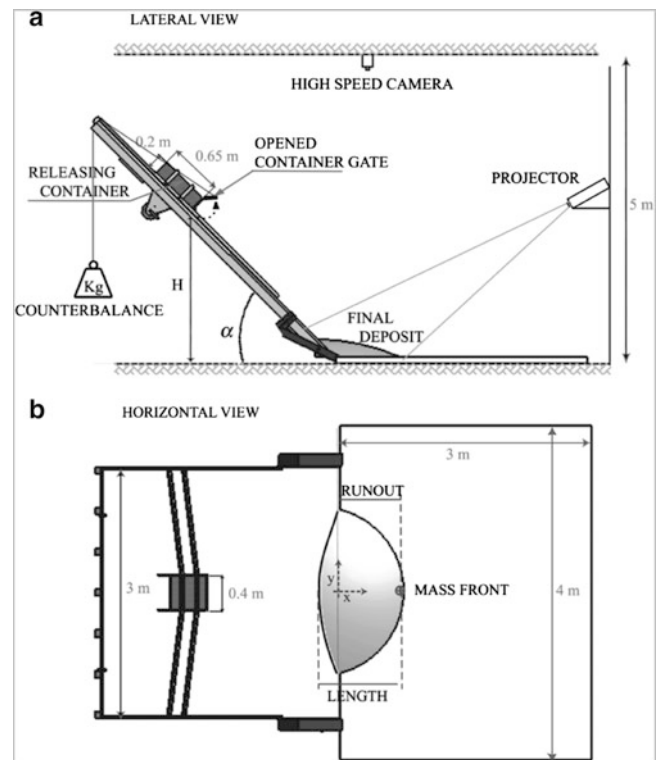


Fig. 1 Lateral (a) and horizontal (b) view of experimental set-up and laboratory measurements (Manzella and Labiouse 2009)

Table 1 Characteristics of released material (Manzella 2008; Manzella and Labiouse 2009). ϕ_i = gravel internal friction angle

d [mm]	D_{90} [mm]	γ [kN/m ³]	ϕ_i [°]	ϕ_{static} [°]	$\phi_{dynamic}$ [°]
0.5–4	2	14.3	34 ± 1	28 ± 1	23.5 ± 0.5

Table 2 Test conditions for analysed experiments (Manzella 2008)

α [°]	H [m]	V [l]	Transition [-]
45.0	1.0	40	sharp

The considered experiment consists in the release of a volume (V) of gravel of 40 l, from a falling height (H) of 1 m on a surface with a slope angle (α) of 45°. As already mentioned, the junction between the inclined and the horizontal planes is sharp. Test conditions are summarised in Table 2.

The RASH^{3D} Code

The RASH^{3D} code (Pirulli 2005) originates from a pre-existing continuum mechanics model (SHWCIN) in which the governing equations are solved in an Eulerian framework on a triangular finite element mesh through a kinetic scheme based on a finite volume approach (Audusse et al. 2000; Bristeau et al. 2001; Mangeny-Castelnau et al. 2003).

The real heterogeneous mass is compared to an incompressible equivalent fluid whose behaviour is described by balance equations of mass and momentum. By assuming that the flow thickness is much smaller than its characteristics length, the code integrates the balance equations in depth obtaining the so-called depth-averaged continuum flow model (Savage and Hutter 1989), and the general system of equations to be solved, written in a reference frame linked to the topography, becomes as follows:

$$\frac{\partial h}{\partial t} + \text{div}(h\bar{v}) = 0 \quad (1)$$

$$\begin{aligned} \rho \left(\frac{\partial(h\bar{v}_x)}{\partial t} + \frac{\partial(h\bar{v}_x^2)}{\partial x} + \frac{\partial(h\bar{v}_x\bar{v}_y)}{\partial y} \right) \\ = -\frac{\partial(h\bar{\sigma}_{xx})}{\partial x} + \tau_{zx} - \rho g_x h \end{aligned} \quad (2)$$

$$\begin{aligned} \rho \left(\frac{\partial(h\bar{v}_y)}{\partial t} + \frac{\partial(h\bar{v}_x\bar{v}_y)}{\partial x} + \frac{\partial(h\bar{v}_y^2)}{\partial y} \right) \\ = -\frac{\partial(h\bar{\sigma}_{yy})}{\partial y} + \tau_{zy} - \rho g_y h \end{aligned} \quad (3)$$

where h is the flow normal depth, ρ is the mass density, $\bar{v}(x, y, z, t) = [\bar{v}_x(x, y, z, t), \bar{v}_y(x, y, z, t)]$ is the depth-averaged flow velocity vector in the reference frame (x, y, z) , $\bar{\sigma}_{xx}(x, y, z, t)$ and $\bar{\sigma}_{yy}(x, y, z, t)$ are the depth-averaged component of the Cauchy stress tensor, g_x and g_y are the projection of the gravity vector along the x and y directions respectively and τ_{zx} and τ_{zy} are the shear resistance stresses in the x and y directions, respectively.

The complex rheology of the granular material is incorporated into a single term which describes the basal shear stress that develops at the interface between the flowing mass and the sliding surface. Among different rheologies, a basal cohesionless Coulomb-type friction law was assumed in the present study:

$$\tau_{zi(i=x,y)} = -\mu \rho g_i h \frac{\bar{v}_i}{\|\bar{v}\|} \quad (4)$$

where the basal shear stress is related to the normal stress through the coefficient of friction $\mu = \tan\phi$, where ϕ is the dynamic basal friction angle.

Centripetal Acceleration Effect

Equation (4) is obtained neglecting the curvature term. But, curvature effects lead to an additional friction force linked to centripetal acceleration. According to McDougall (2006),

the curvature effect has been recently implemented in RASH^{3D} (Pisani et al. in prep.) by adding a term involving the curvature radius of the bed profile R in the momentum equations, that is modifying (4) as follows:

$$\tau_{zi(i=x,y)} = -\mu \rho h (g_z + a_{c,i}) \frac{\bar{v}_i}{\|\bar{v}\|} \quad (5)$$

where $a_{c,i}$ is the centripetal acceleration in the considered i direction.

Due to topographic deflection (i.e., changing in bed slope), the apparent weight of the moving mass increases and the resistance due to basal sliding friction is modified. Where the bed slope decreases (i.e., in the curved transition between the inclined and the horizontal planes), the external reaction force provided by the underlying surface (assumed to be infinitely massive and immobile) increases the bed normal stress by an amount of $(\rho h \bar{v}_i^2)/R_i$, where $\bar{v}_i^2/R_i = a_{c,i}$ (see (5)).

In the analysed experiment (see § Experimental set-up), the local curvature radius in the y direction tends to infinity and the y component of bed curvature consequently tends to zero, i.e. (5) simplifies to (4) in the limits $R_y \rightarrow \infty$ and $a_{c,y} \rightarrow 0$, that is applicable to planar beds.

Numerical Modelling of a Laboratory Experiment

The RASH^{3D} code is here used to numerically simulate the results obtained in laboratory for the experiment whose characteristics are resumed in Table 2.

In particular, the role of centripetal acceleration is investigated running numerical analyses with and without the centripetal acceleration term and comparing obtained results.

Comparison Between Numerical and Laboratory Results

Three steps are necessary to run numerical analyses with RASH^{3D}: (1) implementing the mesh for the topography of the study area, (2) defining the initial volume geometry and (3) selecting the rheology and calibrating its rheological parameters.

In the studied case a mesh with a 2 cm grid spacing was defined. A higher resolution was used at the sharp transition and for the triggering volume definition.

Due to the characteristics of the released material a simple frictional rheology was assumed. This required only the calibration of the dynamic friction angle ϕ .

The first set of analyses was carried out neglecting the centripetal acceleration term, that is (4) is adopted in the resolution of the implemented balance equations.

The best fit results in terms of deposit shape and longitudinal profile was obtained assuming a dynamic friction angle equal to 34.5° .

Obtained results evidence that the model has some problems in fitting the shape of the deposit in plan view even if the position of the rear and of the front are quite respected (Fig. 2a). On the contrary, if the longitudinal profile is analysed a good distribution of the thickness can be observed together with a quite good approximation of the centre of gravity position (Fig. 2b).

Moving to the version of RASH^{3D} in which the centripetal acceleration is implemented, that is (5) is adopted, the above mentioned geometry and mesh characteristics were used. But, in this case the calibration of the dynamic friction angle evidenced that the best fit result is obtained with a value of $\varphi = 23^\circ$.

Obtained results evidence that the model fits quite well the shape of the deposit in plan view (Fig. 2a) but some problems emerge if the longitudinal profile is analysed (Fig. 2b). In fact, the centre of gravity does not coincide with the measured one and the deposit proximal part partially deposits on the inclined surface.

Comparison between numerical results obtained with and without the centripetal acceleration term has evidenced that when the centripetal acceleration term is not taken into account, i.e. when the topography shape does not slow down the granular material, a higher value of the friction angle is necessary to correctly stop the mass.

As a consequence, dropping its effect can lead to unverifiable error in the determination of the well fitted friction angle because the tuned parameter obtained for fitting a runout distance may be dependent on these local effects (Mangeney-Castelnaud et al. 2003).

The present work has particularly evidenced that, using the centripetal acceleration term, the value of the computed friction angle is close to the value of the dynamic friction angle measured in laboratory (Table 1). This physical meaning disappears if centripetal acceleration is neglected (i.e. $\varphi = 34.5^\circ$).

Conclusions

In the present paper the effect of centripetal acceleration in a flow dynamics and consequently in the calibration of the parameter of a selected rheology is investigated.

To this aim the numerical model RASH^{3D} has been used to numerically simulate results obtained in a laboratory test where a granular mass is released on a 45° inclined plane that, in the lower part, is joined to a horizontal surface through a sharp transition.

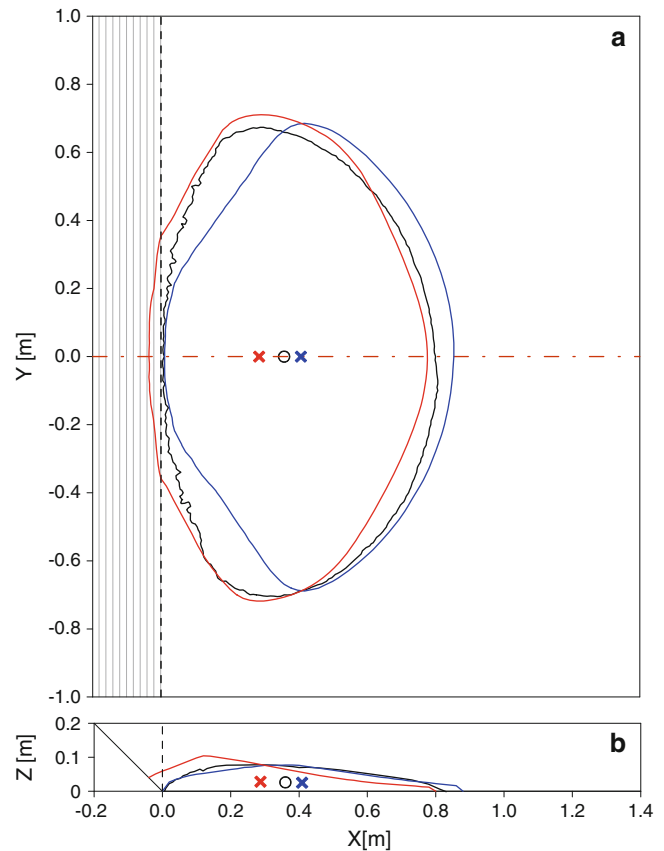


Fig. 2 Comparison between numerical and experimental results. *Black line and black circle*: experimental data; *Blue line and blue symbol*: numerical results obtained with $a_c = 0$, $\varphi = 34.5^\circ$; *Red line and red symbol*: numerical results obtained with $a_c \neq 0$, $\varphi = 23^\circ$

The RASH^{3D} code is based on Savage and Hutter's equations and the moving mass behavior can be described using a Coulomb-type friction law with a constant friction angle, φ .

The comparison between numerical and laboratory results has evidenced that the calibrated friction angle is close to the value of the dynamic friction angle measured in laboratory when the centripetal acceleration term is considered in the implemented equations. On the contrary, if the centripetal acceleration term is neglected, the value of the friction angle necessary to properly stop the mass has to be higher since it has to take also into account the energy dissipation that in reality is due to the above mentioned term.

Based on these observations the current work is intended to extend the application of the numerical model to a larger number of laboratory tests. In particular, it is expected that a change in the laboratory apparatus geometry (i.e. a different volume, falling high or surface slope angle), released material and cover of the runout surface being unchanged, the value of the dynamic friction angle should remain the same.

However, some problems still remain and are evidenced by the impossibility of simulating the deposit profile in a correct way (Fig. 2b). This aspect has to be further investigated and some considerations on the role of the “shock” effect for the particular geometry considered are still necessary.

Acknowledgments The authors wish to thank Anne Mangeney (IPGP, France) and Marie-Odile Bristeau (INRIA, France) for having offered the use of the SHWCIN code and for having helped to solve some fundamental numerical problems.

References

- Audusse E, Bristeau MO, Perthame B, (2000) Kinetic schemes for Saint-Venant equations with source terms on unstructured grids. INRIA report 3989, National Institute for research and computational sciences and control, Le Chesnay
- Bristeau MO, Coussin B, Perthame B (2001) Boundary conditions for the shallow water equations solved by kinetic schemes. INRIA report 4282, National institute for research and computational sciences and control, LeChesnay
- Chen H, Lee CF (2000) Numerical simulation of debris flows. *Can Geotech J* 37:146–160
- Denlinger RP, Inverson RM (2004) Granular avalanches across irregular three-dimensional terrain: 1. Theory and computation. *J Geophys Res* 109: F01014, 14pp, doi:10.1029/2003JF000085
- Mangeney-Castelnau A, Vilotte JP, Bristeau O, Perthame B, Bouchut F, Simeoni C, Yerneni S (2003) Numerical modelling of avalanches based on Saint Venant equations using a kinetic scheme. *J Geophys ResSolid Earth* 108(B11):2527
- Manzella I (2008) Dry rock avalanche propagation: unconstrained flow experiments with granular materials and blocks at small scale. Ph.D. thesis 4032, Ecole Polytechnique Fédérale de Lausanne, Switzerland
- Manzella I, Labiouse V (2008) Qualitative analysis of rock avalanches propagation by means of physical modelling of not constrained gravel flows. *Rock Mech Rock Eng J* 41(1):133–151
- Manzella I, Labiouse V (2009) Flow experiments with gravel and blocks at small scale to investigate parameters and mechanisms involved in rock avalanches. *Eng Geol* 109(1):146–158
- McDougall S (2006) A new continuum dynamic model for the analysis of extremely rapid landslide motion across complex 3D terrain. Ph. D. dissertation, University of British Columbia, Canada
- McDougall S, Hungr O (2004) A model for the analysis of rapid landslide motion across three-dimensional terrain. *Can Geotech J* 41:1084–1097
- Pastor M, Quecedo M, Gonzalez E, Herreros MI, Fernandez Merodo JA, Mira P (2004) Modelling of landslides: (II) propagation, degradations and instabilities in geomaterials. In: Darve, F., Vardoulakis, I (eds) CISM courses and lectures No. 461, Springer
- Pirulli M (2005) Numerical modelling of landslide runout, a continuum mechanics approach. Ph.D. dissertation, Politecnico di Torino, Italy, 204pp
- Pisani G, Pirulli M, Labiouse V, Scavia C (in prep.) The role of the centripetal acceleration on the propagation of flow-like landslides on a complex topography
- Savage SB, Hutter K (1989) The motion of a finite mass of granular material down a rough incline. *J Fluid Mech* 199:177–215
- Savage SB, Hutter K (1991) The dynamics of granular materials from initiation to runout. *Acta Mech* 86:201–223



Single or Two-Phase Modelling of Debris-Flow? A Systematic Comparison of the Two Approaches Applied to a Real Debris Flow in Giampileri Village (Italy)

Laura Maria Stancanelli, Giorgio Rosatti, Lorenzo Begnudelli,
Aronne Armanini, and Enrico Foti

Abstract

A comparison between the performances of two different debris flow models has been carried out. In particular, a mono-phase model (FLO-2D) and a two phase model (TRENT2D) have been considered. In order to highlight the differences between the two codes, the alluvial event of October 1, 2009 in Sicily in the Giampileri village has been simulated. The predicted time variation of several quantities (as the flow depth and the velocity) has been then analyzed in order to investigate the advantages and disadvantages of the two models in reproducing the global dynamic of the event. Both models seem capable of reproducing the depositional pattern on the alluvial fan in a fairly way. Nevertheless, for the FLO-2D model the tuning of the parameters must be done empirically, with no evidence of the physics of the phenomena. On the other hand, for the TRENT2D, which is based on more sophisticated theories, the parameters are physically based and can be estimated from laboratory experiments.

Keywords

Debris flow • Numerical model • FLO-2D • TRENT2D

Introduction

Debris flow models are widely used by engineers for hazard mapping or evaluating the effectiveness of risk mitigation works. However, a systematic comparison of performances of different approaches is still missing. In this framework, a real debris flow event has been analyzed by means of two different models: FLO-2D (O'Brien 1986), which is a widely adopted commercial code, and TRENT2D (Armanini et al. 2009), applied in several advanced researches on debris flows and in the engineering practice. Both models adopt depth-integrated flow equations, but assume different mathematical

descriptions of the phenomenon. The FLO-2D model, which is not fully two-dimensional, is based on a mono-phase approach, modelled through an empirical quadratic rheological relation developed by O'Brien and Julien (1985); TRENT2D is a fully two-dimensional model and its two-phase rheological model is based on the physically grain inertial method of Bagnold-Takahashi. Another important difference is that in FLO-2D the bed is fixed, while in TRENT2D the bed is mobile and completely coupled with the dynamic of the mixture. On the other hand, such a model does not simulate the presence of inerodible zones.

In order to highlight the differences between the two methodologies, the two models have been applied to a real and complex case, namely, the alluvial event of October 1, 2009, which struck the Messina Province (Italy). During the event, in few hours a very intense rainstorm generated more than 600 landslides, which caused 37 fatalities and severe damages to transportation infrastructures as well as to public and private buildings. In particular, in the present work the effects of the mentioned event on the Giampileri village has

L.M. Stancanelli (✉) • E. Foti
Department of Civil and Environmental Engineering,
University of Catania, Catania, Italy
e-mail: lmstanca@dica.unict.it

G. Rosatti • L. Begnudelli • A. Armanini
Department of Civil and Environmental Engineering,
University of Trento, Trento, Italy

been analyzed. Giampilieri has been settled in the Middle Ages and nowadays presents peculiarities in terms of geomorphological and urban configuration. Therefore, the debris flow analysis in this particular type of settings is of particular interest. Regarding the geomorphology, the village is settled on a steep hillslope. Upstream of Giampilieri, three different little basins, with an extension less than 1 km², generated debris flows that propagated across the village and eventually run into the Giampilieri river. Regarding the urban configuration, it is worth to point out that the little village has a population of about 1,800 inhabitants, and it is characterized by high density and narrow streets. This makes the emergency management and the planning of evacuation operations particularly difficult.

Models Description

FLO-2D

FLO-2D is a commercial code worldwide adopted for debris flow phenomena modelling and delineating flood hazards, developed by O'Brien in 1986. The model is two-dimensional in space and adopts depth-integrated flow equations. Hyper concentrated sediment flows are simulated considering a mono-phase approach, based on empirical quadratic rheological relation developed by O'Brien and Julien (1985).

The basic equations implemented in the model consist mainly in the continuity equation:

$$\frac{\partial h}{\partial t} + \frac{\partial(hv_x)}{\partial x} + \frac{\partial(hv_y)}{\partial y} = i \quad (1)$$

and the equation of motion (the dynamic wave momentum equation):

$$S_{fx} = S_{ox} - \frac{\partial h}{\partial t} + \frac{v_x}{g} \frac{\partial v_x}{\partial x} + \frac{v_y}{g} \frac{\partial v_x}{\partial y} - \frac{1}{g} \frac{\partial v_x}{\partial t} \quad (2)$$

where: S_{ox} = the bed slope; h = flow depth; v_x, v_y = depth-averaged velocities; i = excess rainfall intensity (assumed equal to zero in the present application).

Since the model is mono-phase, the bed variation term, i.e.: the bed evolution is not considered.

The total friction slope can be expressed as follows:

$$S_f = \frac{\tau_B}{\rho gh} + \frac{K\mu_B V}{8\rho gh^2} + \frac{n^2 V^2}{h^{4/3}} \quad (3)$$

where τ_B = Bingham yield stress; V = mean flow velocity along the flow direction; ρ = mixture density; K = the laminar

flow resistance coefficient; g = gravitational acceleration; μ_B = Bingham viscosity; n = pseudo-Manning's resistance coefficient which accounts for both turbulent boundary friction and internal collisional stresses. In particular, the yield stress τ_B , the dynamic viscosity μ_B and the resistance coefficient n are influenced by the sediment concentration relationships that can be described by the following equations:

$$\tau_y = \alpha_1 e^{\beta_1 C_v} \quad (4)$$

$$\mu_B = \alpha_2 e^{\beta_2 C_v} \quad (5)$$

$$n = n_t 0.538 e^{6.0896 C_v} \quad (6)$$

where C_v is the volumetric concentration and α_1 , β_1 , α_2 and β_2 are empirical coefficients defined by laboratory experiments (O'Brien and Julien 1988) and n_t is the turbulent n-value (Julien and O'Brien 1998).

To solve the momentum equation FLO-2D considers, for each cell, the eight potential flow directions. Each velocity computation is essentially one-dimensional and solved independently from the other seven directions (FLO-2D User's Manual 2007).

TRENT2D

Trent2D is a numerical code, developed by Armanini et al. (2009), for the simulation of debris flows and hyperconcentrated sediment transport.

Its mathematical model is based on the assumption of a two-phase mixture of sediments and water, with rheological model based on the physically grain inertial method of Bagnold-Takahashi.

Since the reference model is biphasic, the bed is movable (contrary to the FLO-2D model). Moreover, the dynamics of the mixture and the morphological evolution of the bed are solved in a completely coupled way. This is quite important because wave celerities change noticeably from the fixed to the movable bed case.

The depth-averaged PDEs of the model are derived from the conservation balances of mass and momentum (for solid and mixture):

$$\begin{cases} \frac{\partial}{\partial t}(z_B + h) + \frac{\partial}{\partial x}(hv_x) + \frac{\partial}{\partial y}(hv_y) = 0 \\ \frac{\partial}{\partial t}(c_B z_B + ch) + \frac{\partial}{\partial x}(chv_x) + \frac{\partial}{\partial y}(chv_y) = 0 \\ \frac{\partial}{\partial t}[c_\Delta v_x h] + \frac{\partial}{\partial x} \left[c_\Delta \left(v_x^2 h + \frac{gh^2}{2} \right) \right] + \frac{\partial}{\partial y} [c_\Delta v_x v_y h] + c_\Delta gh \frac{\partial z_B}{\partial x} = -Fv_x \\ \frac{\partial}{\partial t}[c_\Delta v_y h] + \frac{\partial}{\partial x} [c_\Delta v_x v_y h] + \frac{\partial}{\partial y} \left[c_\Delta \left(v_y^2 h + \frac{gh^2}{2} \right) \right] + c_\Delta gh \frac{\partial z_B}{\partial y} = -Fv_y \end{cases} \quad (7)$$

where: h = flow depth; v_x, v_y = depth-averaged velocities; z_B = bed elevation; c = solid phase concentration; c_b = solid concentration into the soil; $c_\Delta = (1 + \Delta c)$ where Δ = relative density of solid phase. The friction term $F = F(|v|, h)$ derives from Bagnold's relation modified by Takahashi (1978) on the basis of experimental data:

$$F = 25/4 (1 + \Delta) \sin \varphi \lambda^2 Y^2 \quad (8)$$

where φ is the friction angle and:

$$\lambda = \left[(c_b/c)^{1/3} - 1 \right]^{-1} ; \quad Y = h / (d_{50} \sqrt{a}) \quad (9)$$

where d_{50} is the median grain size and $a = 0.32$ is a constant (Takahashi 1978).

The concentration is computed as a function of the flow variables as:

$$c = \beta c_b (u^2 / gh) \quad (10)$$

where the transport capacity β is a dimensionless parameter.

The numerical scheme, second order accurate both in space and in time, is based on a finite volume, Godunov approach over a Cartesian structured grid. The scheme follows a MUSCL-Hancock explicit time stepping approach. The numerical fluxes at cell interfaces are computed using the LHLL Riemann solver (Fraccarollo et al. 2003), which is able to account for the non conservative terms due to bed discontinuities.

More details on the mathematical scheme and on the numerical model can be found on the Trent2D User's Manual (2011).

Event Description

The comparison of the two models has been carried out by simulating a real complex debris flow event.

During the night of October 1, 2009 a heavy rainfall struck the Messina Province causing fatalities and damages to public and private structures. The event interested an area of more than 50 km², generating over 600 landslides. One of the most damaged villages was Giampilieri, a little village in the Southern Messina Province, located on the left bank side of the Giampilieri river. The town is characterized by a high-density urban area with narrow streets, that during alluvial events become the bed over which the runoff flows.

The soil is composed by metamorphic material, easy to be eroded, also because of the semi-arid climate, which is also characterized by short and very intense rainstorms that occur between October and March.

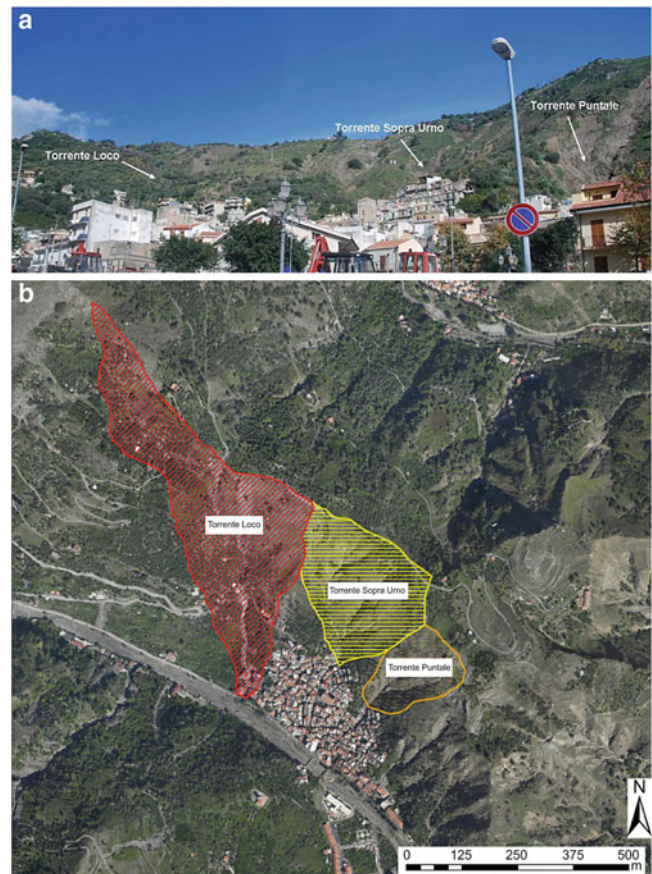


Fig. 1 Images of Giampilieri village, where are indicated: (a) The locations of Loco Creek, Sopra Urno Creek and Puntale Creek; (b) Extensions of Loco, Sopra Urno and Puntale basins

Upstream of the Giampilieri urbanized area, there are three different tributaries named, from West to East, Loco, Sopra Urno and Puntale creeks respectively (Fig. 1).

All of the tributaries are characterized by catchments of small extension, respectively of 1 km² for the Loco basin, 0.7 km² for the Sopra Urno basin and 0.4 km² for the Puntale basin. During the alluvial event of October 1, 2009, all of the three catchments produced debris flows that inundated the village and caused 19 fatalities.

Data Referring to Simulations

In order to model the debris flows, three principal data inputs are needed: Digital Terrain Model (DTM), hydrological data, and rheological properties of sediment water mixture. While the first two inputs are the same for the two models, the rheological properties are completely different because different are the mathematical models they are based upon.

Geometry Data

The geometry input consists in a Digital Terrain Model, based on the surveys taken after the event. The same grid system, with square cells $1.5 \text{ m} \times 1.5 \text{ m}$, has been used in the simulations with the two models.

The presence of buildings inside the flood plain has been considered in both models, thus obtaining the same final configuration, although the implementation of such feature is addressed in FLO-2D and TRENT2D in different ways. In fact, in FLO-2D buildings are by attributing a reduction factor that accounts for the loss of storage and redirection of the flow path, while for TRENT2D the presence of the buildings is implemented by enhancing the elevation of the corresponding computational cells.

Hydrological Inputs

Three hydrological inputs have been considered in this study, relative to the three cited different basins. The input hydrographs have been determined using the data obtained from hydrological analysis, using a 300 years return period rainfall rate. The duration of the hydrographs has been estimated from the concentration time of the three basins.

In order to determinate the discharge rate value of the debris flows for each basin, a simple formula can be derived through a liquid and sediment balance mass, which gives (Armanini 2011, personal communication):

$$Q_{df} = Q_l \frac{c_b}{c_b - c} \quad (11)$$

where Q_{df} is the discharge of debris flow, Q_l is the liquid discharge rate (given by the hydrograph); c and c_b are the concentrations of the solid phase in the debris flow and into the soil, respectively. Assuming that c_{df} cannot exceed $0.9c_b$, when the bed slope is higher than a threshold (that in the present case is equal to 21°), from (11) we get: $Q_{df} = 10 Q_l$. In Fig. 2 the input hydrographs of the different basins are represented.

While for Puntale and Loco only one hydrological input has been considered, for the Sopra Urno basin three inputs have been implemented. Such an assumption relies on the observed event dynamics and from the analysis of the orthophoto gathered after the event, in which it is easy to distinguish the three sub-catchments. Also, it has been assumed that the debris-flows originated from the three sub-catchments did not develop at the same times. Specifically, the debris flow volume has been divided in three different inputs, separated each other by 6 minutes. These hypotheses are supported by the comparison between the volumes calculated from the hydrographs and those resulting from the surveys taken after the event.

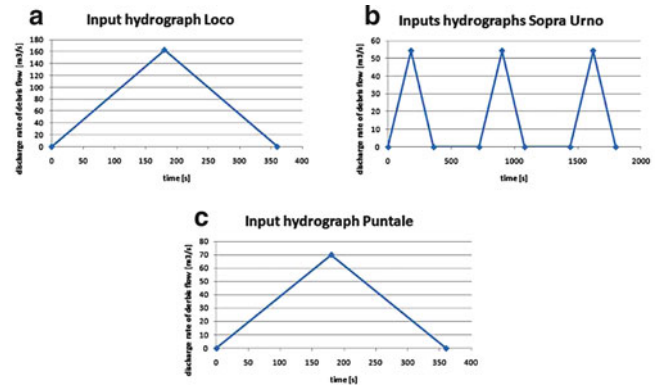


Fig. 2 Debris flow input hydrograph developed respectively for: (a) Loco Basin; (b) Sopra Urno Basin; (c) Puntale Basin

Performed Simulations

FLO-2D

In order to perform the simulations with the FLO-2D model, the coefficients α_1 , β_1 , α_2 and β_2 (4 and 5) need to be estimated. Due to the mono-phase rheology the model is based upon, the parameters cannot be directly evaluated, and must be estimated by means of a back analysis process. In particular the following values have been assumed (Stancanelli et al. 2011):

$$\alpha_1 = 0.006032; \beta_1 = 19.9; \alpha_2 = 0.000707; \beta_2 = 29.8$$

A reconstruction of the inundated area, shown in Fig. 3 by the red line, has been obtained as output of the model. In particular, it is easy to recognize the portion of the urbanized area interested by the debris flow, which fits fairly well with the surveys effected after the event.

The maximum flow depths during the event obtained from the FLO-2D simulation are presented in Fig. 4. The predicted highest flow depths were generated by the Sopra Urno creek, with a maximum value of about 6 m.

Fig. 5 represents the final flow depths, i.e. the debris flow depths after a time of 3 h. Note that, according to the mono-phase approach, there are no bed variations nor settlement of sediments separated from the liquid phase. The whole fluid stops when the bed stress goes under a threshold that depends on the fluid, determining the final deposition. The highest values of the predicted final flow depths are found in the streets perpendicular to the main path followed by the debris flows, with a maximum value of 1.2 m. Finally, the predicted maximum velocities are shown in Fig. 6. It is easy to recognize that the maximum velocities are registered in correspondence of the upper part of the basins, where the slope are the highest, with values ranging from 10 m/s to 20 m/s, while inside the urbanized area the velocities range



Fig. 3 Inundated area as observed for the scenario simulated with the FLO-2D

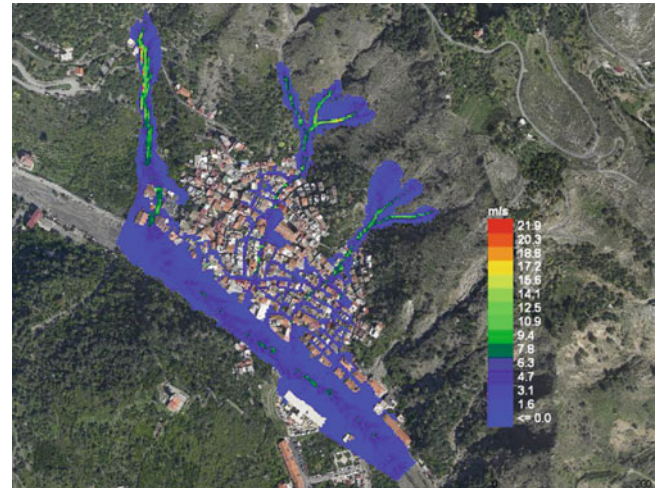


Fig. 6 Maximum velocity as observed for the scenario simulated with the FLO-2D

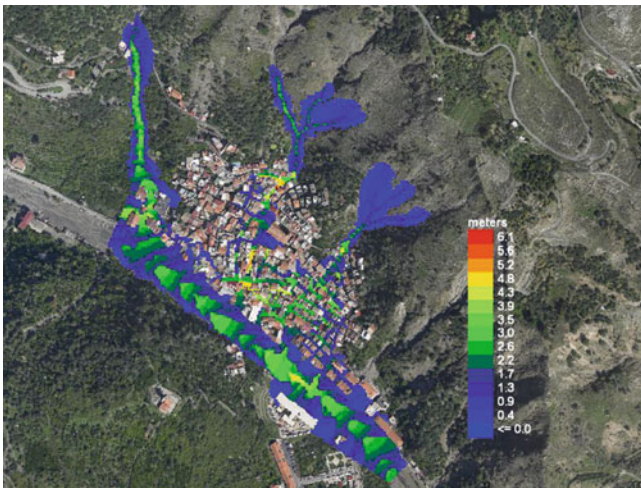


Fig. 4 Maximum flow depth as observed for the scenario simulated with the FLO-2D

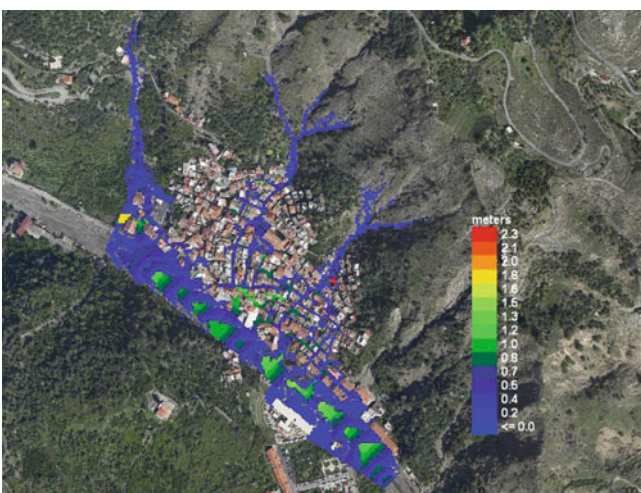


Fig. 5 Final flow depth as observed for the scenario simulated with the FLO-2D

from 1.5 m/s to 5 m/s, although some peaks over 10 m/s are also observed.

TRENT2D

In order to perform the simulations with the TRENT2D model, we need to estimate the parameters φ , Y and β (8, 9, and 10). The friction angle φ should be determined by laboratory test on the soil material of the study site. Here, we have $\varphi = 38^\circ$. As for the parameter Y , it has been set to 10, considering an average value of its expression throughout the flow field (9). Finally, the transport capacity β has been determined as explained in the Trent2D User's Manual (2011), and the value $\beta = 4.28$ has been found.

The maximum flow depths reached during the simulation of the event are shown in Fig. 7. As it can be seen, the values are generally smaller than those predicted by the FLO-2D model for the same event. On the other side, considering the thickness of the final deposition of material (Fig. 8), TRENT2D predicted values are greater than those given by FLO-2D, in particular along the main path followed by the debris flows. Finally, the maximum velocities given by the TRENT2D model are shown in Fig. 9. They are generally smaller than those obtained using the FLO-2D model, with velocities around 2–4 m/s along the main paths and smaller values elsewhere.

Validation Against Field Data

The results of FLO-2D and TRENT2D models have been compared with the data coming from on-site investigations, i.e. videos recorded during the event and measurements of the depth of the sediment deposition. In particular, Fig. 10

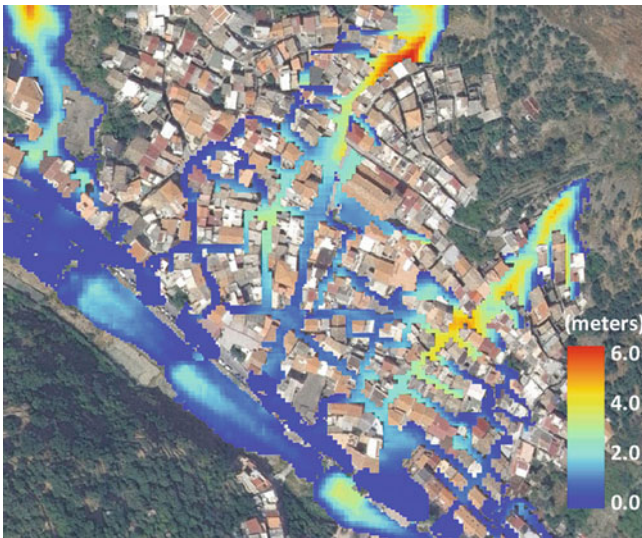


Fig. 7 Maximum flow depth as observed for the scenario simulated with the TRENT2D



Fig. 9 Maximum velocity as observed for the scenario simulated with the TRENT2D

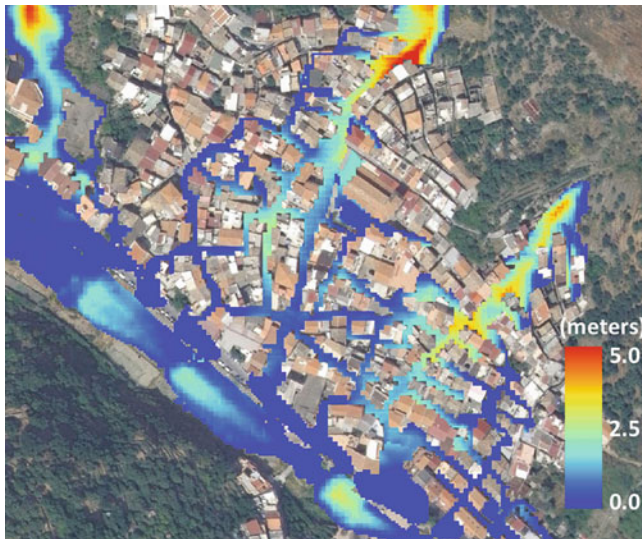


Fig. 8 Depth of the final sediment deposition as observed for the scenario simulated with the TRENT2D



Fig. 10 Orthophoto of Giampileri urban area with positions of data gathered from in site surveys (Ucosich 2009)

shows an orthophoto of the urban area of Giampileri with the positions where measurements have been gathered on purpose for the inherent study.

In particular, two field data are available: the values of the maximum flow depth reached during the event (h_{\max}) and the values of the thickness of the sediment deposit left by the debris flow (dz_b). In Table 1, field data are reported, along with the corresponding predicted data obtained from FLO-2D and TRENT2D. In the table we have reported only the points for which both flow depth and deposit data are available.

Considering maximum flow depths (h_{\max}), FLO-2D predicted values are in general higher than those observed. This can be explained by considering that buildings cannot store debris flow volume and the uncertainty relative of the magnitude event. On the other side, TERNT2D results are slightly smaller than those observed, with more accurate results along the main paths and greater deviations in the smallest streets.

With regard to the deposition depths (dz_b), it must be noted that, given the monophasic approach of FLO-2D the whole fluid stops when the threshold bed stress is reached,

Table 1 Measured and predicted values of maximum flow depths and final sediment deposition for the Giampilieri event

POS.	Survey Data		FLO-2D			TRENT2D		
	h_{\max}	dz_b	h_{\max}	h_{final}	v_{\max}	h_{\max}	dz_b	v_{\max}
[no.]	[m]	[m]	[m]	[m]	[m/s]	[m]	[m]	[m/s]
1	2.4	2	1.41	0.40	3.15	1.8	1.48	1.53
2	1.75	1	2.74	0.78	1.43	1.67	1.46	1.77
3	1.5	1	3.86	0.92	2.39	1.27	0.85	1.02
4	1.7	1.5	4.37	1.12	4.11	1.20	0.98	1.14
5	2	2	4.52	1.12	4.31	1.63	1.44	1.8
6	3.3	2	4.50	1.12	4.43	2.18	1.74	1.29
11	2.83	2	1.76	0.06	5.73	1.50	0.03	1.50
13	2.05	1	1.99	0.69	1.72	1.86	0.85	2.52
15	1.26	2	2.45	0.21	3.15	1.96	1.89	2.13
23	2.04	0.5	2.28	0.46	1.38	1.47	0.34	1.50
24	2.78	0.5	2.13	0.35	0.58	1.91	0.52	0.93
25	2.3	1.2	2.17	0.35	1.21	1.95	1.1	2.34
26	1.93	1.8	2.09	0.05	3.21	2.05	1.98	2.19
27	1.95	1.2	3.98	1.01	1.13	1.80	1.12	1.32
28	5	0.4	2.81	0.10	2.47	1.01	0.24	1.17
30	2	1	1.7	0.68	0.90	1.40	0.57	0.84
Mean errors:			1.17	0.73	–	0.74	0.36	–

determining the final deposition, given by the final flow depth (h_{final}). Predicted values obtained from FLO-2D simulations are smaller than survey data of Ucosich (2009); the reasons can be the value of the viscosity parameter assumed and also the absence of anthropic features in the simulated scenario, such as cars along the streets, which modify the flow to a large extent. Looking at the Trent2D results, predicted final depositions are smaller than those measured. As for the flow heights, results are better in the main streets and less accurate in the lateral narrow ones.

Considering the maximum velocities (v_{\max}), there are no field data available. Using FLO-2D, all values belong to the range from 1.5 m/s to 15 m/s, while using Trent2D velocities are smaller (2–4 m/s along the main paths and smaller values elsewhere). This difference is clearly due to the different rheologies adopted by the two models.

Conclusions

The simulation of the alluvial event of October 1, 2009, in Giampilieri has been reproduced by means of two different debris flow models.

Thanks to the availability of a large amount of data collected after the event, a back analysis has been carried out. For the FLO-2D model, the tuning of the parameters must be done empirically, with no evidence of the physics

of the phenomena. On the other hand, since the parameters of the TRENT2D model have a more specific physical meaning, it is easier to identify the acceptable physical range for the values.

The time variation of several quantities has been analyzed in order to highlight the performances of the two models as well as their differences. The results show that both models seem capable of reproducing the depositional pattern on the alluvial fan. In particular, FLO-2D tends to overestimate the flow depths for the reasons previously explained, while Trent2D slightly underestimates them. As for the final depositions, they are slightly underestimated by both models. Finally, FLO-2D velocities are generally higher than those predicted by Trent 2D, due to the different rheological models.

Acknowledgments All consultants of the OPCM 10th October 2009 n°3815 are greatly acknowledged for the support demonstrated and for the useful information provided.

We would like to thank the Public Civil Engineering Works Office of Messina and the Department of Civil Defence of Sicilian Region for providing important data.

References

- Armanini A, Fraccarollo L, Rosatti G (2009) Two-dimensional simulation of debris flows in erodible channels. *Comput Geosci* 35:993–1006
- Fraccarollo L, Capart H, Zech Y (2003) A Godunov method for the computation of erosional shallow water transient. *Int J Num Meth Fluids* 41(9):951–976
- Julien PY, O'Brien JS (1998) Dispersive and turbulent stresses in hyperconcentrated sediment flows, Unpublished paper
- O'Brien JS (1986) Physical process, rheology and modeling of mudflows. Ph.D. thesis, Colorado State University, Fort Collins, Colorado
- O'Brien JD (2007) FLO-2D user's manual, Version 2007.06, FLO Engineering, Nutrioso
- O'Brien JS, Julien PY (1985) Physical processes of hyperconcentrated sediment flows, Proceeding of the ASCE Specialty Conference on the delineation of landslides, floods, and debris flow Hazards in Utah, Utah Water Research Laboratory, Series UWRL/g-85/03, 260–279
- O'Brien JS, Julien PY (1988) Laboratory analysis of mudflow properties. *J Hyd Eng ASCE* 114(8):877–887
- Stancanelli LM, Bovolin V, Foti E (2011) Application of a dilatant – viscous plastic debris flow model in a real complex situation. *River, Coastal and Estuarine Morphodynamics: RCEM2011*, Beijing
- Takahashi T (1978) Mechanical characteristics of debris flow. *J Hyd Div – ASCE* 104(8):1153–1169
- Trent2D User's Manual (2011) available at: www.simidra.com/pdf/Manuale_Trent2D_versione1.84.pdf
- Ucosich (2009) Map reporting the filling state condition inside the Giampilieri village after to the alluvial event of 1st Oct 2009



Runout Prediction of Rock Avalanches in Volcanic and Glacial Terrains

Rosanna Sosio, Giovanni B. Crosta, Johanna H. Chen, and Oldrich Hungr

Abstract

Among all kinds of landslides, rock avalanches are characterized by exceptional mobility and destructiveness. Their mobility is well larger than explained by the real material properties and it is usually expressed by means of an “apparent” friction angle which is a-priori unpredictable. We replicate the motion of historical rock/debris avalanches evolved in glacial and volcanic environments. The modelled events involved variable volumes (ranging from millions of m^3 to km^3) which are well preserved so that their main features are recognizable from satellite images. Within each class of events, and irrespective of the variety of conditions in which they occurred, the best fitting parameters span in a narrow interval. The bulk basal friction angle ranges within 3° and 7.5° for volcanic debris avalanches, within 6° and 12° for ice-rock avalanches. These values are significantly lower than other rock avalanches which require values as high as 11° to 31° . The consistency of the back-analyzed parameters is encouraging for a possible use of the model in the perspective of hazard mapping while set of calibrated values can help the selection of model input parameter values for prediction and for definition of uncertainty on zonation.

Keywords

Rock avalanche • Numerical modelling • Forward prediction • Rheological parameters

Introduction

When a potential source of instability is identified, hazard mapping through runout analyses may be necessary to define which areas could be threatened by landslide propagation. Nevertheless, due to the sudden evolution of the phenomena, and to the unfeasible use of the measurable material properties

in modelling perspective, a gap remain in the selection of the input values introducing large uncertainty in the modelling prediction. H/L ratio is used as an indicator of the rock/debris avalanche mobility (Fig. 1, Evans and Clague 1988; Hayashi and Self 1992; Siebert 2002), but H/L values obtained for historical events span widely due to variable materials involved and, in particular, topographical constrains which are supposed to have strong influence on the mode of propagation.

The spread between the real material properties and their effective counterpart required by the numerical models is particularly high when the instability involves weak rocks, partially saturated fine materials, such as volcanic debris (Glicken 1996; Voight and Elsworth 1997; Voight et al. 1983) and/or the propagation evolves onto low resistant substrate, such as glacial ice (Evans and Clague 1988). Despite their large magnitude, these events gained little

R. Sosio (✉) • G.B. Crosta

Department of Scienze Geologiche e Geotecnologie, University of Milano Bicocca, Piazza della Scienza, 4, Milan, Italy
e-mail: rosanna.sosio@unimib.it

J.H. Chen

Klohn Crippen Berger, Calgary, Canada

O. Hungr

Department of Earth and Ocean Sciences, The University of British Columbia, Vancouver, Canada

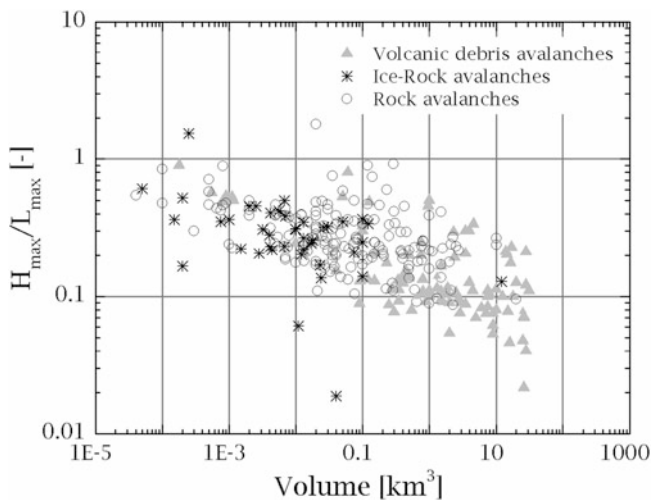


Fig. 1 Bilogarithmic plot of the relative runout (H/L) vs volume (V) of rock and debris avalanches evolved in different settings (Data from Siebert (2002), Evans and Clague (1988), Hayashi and Self (1992))

attentions by scientists, partly because they evolve in remote areas, which are often inaccessible and generally with few element at risk, partly because of the scarcity of data (descriptive and topographic).

This work focuses on the mobility of rock and debris avalanches evolving in glacial and volcanic environments by providing a set of calibrated case histories to be back analysed by two different models. The events developed in a variety of settings and condition and they vary with respect to their morphological constrains, materials, contact surfaces, and styles of failure. The event reconstructions and the back analyses are based on the observations available from the literature (i.e. runout distance, impacted areas, flow velocities). We test the performance of the frictional, Voellmy, and plastic rheologies to define, for each rheology, a range of values for the parameters which best replicate the propagation of selected historical events.

Methods

We selected 19 case histories among the largest and best described rock and debris avalanche events in glacial and volcanic environments worldwide (Table 1). The selected events vary with respect to their magnitude, triggering conditions, involved materials and role of fluids in the propagation. They all have quantitative estimates of the mobilized volumes, well preserved morphological features, and field-data availability. The back analyses of the rheological parameters are performed on the available literature observations which supports also all the assumptions in model reconstruction (i.e. mobilized volumes, entrainment, and event evolution).

Events in volcanic environments evolved as debris avalanches from collapse of the edifice independently of its state activity. Their volume ranges from few km^3 up to tens km^3 . Volcanic debris avalanches are promoted or initiated by different processes; most frequently by rock alteration (i.e. hydrothermal and physical), presence of weak layers in the edifice structure, and seismic or magmatic activity (Voight and Elsworth 1997). Collapse phenomena may occur repeatedly for the same edifice. Events in glacial environments (ice-rock avalanches) are characterized by their interaction with ice/snow either as basal material onto which propagation occurred or as part of the propagating masses. Icy mass can be directly detached at the source or entrained along the path. Their volume ranges from $M \text{ m}^3$ up to tens $M \text{ m}^3$. Common triggers are related to changing thermal conditions (i.e. deglaciation and permafrost degradation) and seismic activity. Seismic shaking, in particular, can seldom trigger clusters of ice-rock avalanches events (e.g. March 27, 1964, Anchorage earthquake and November 3, 2002, Denali Fault earthquake; Post 1967; Jibson et al. 2006).

Topography

Volcanic and glacial events are often difficult to recognize at a local scale and their deposits were often attributed to other origin such as glacial till (Hewitt 1999) and pyroclastic deposits (Crandell et al. 1984). Moreover, areas interested by extreme events are often very remote with difficult access conditions. Therefore, more than field surveys, remotely sensed data, such as satellite imagery, airborne observations, aerial-photographic investigations, and seismic recordings can be fundamental (and in some cases the unique available data) for natural hazard evaluation.

We used satellite data to derive basal topography for the modelling and to support the available maps at delimiting landslide and other geomorphological features (i.e. glacial cover). ASTER-derived satellite grid provides elevations at horizontal resolutions of 1 arc second and cell size DEMs ranging from 22 to 30 m with reference to the considered latitude. In all the cases, the DEMs provided the post-event topography. We reconstructed the pre-failure topography by modifying the original terrain data in the area interested by the detachment and the deposition as outlined by available maps, event descriptions, and morphological evidences. We evaluated the sensitivity to the topographic data by resampling the original ASTER data (30 m grid) to 60 m and 90 m grids.

Numerical Modelling

The debris avalanche motion was modeled using the DAN 3D code (McDougall and Hungre 2004) and the MADFlow code

Table 1 Schematic description of the case studies. Data are collected from available literature and topographic maps. Records in parenthesis indicate the number of events replicated for each location. Question marks indicate inferred data

Collapse event	Location	date	Detached material	Trigger	Evolution	Volume	Erosion	Water presence	References
St Helens	USA	May 18, 1980	Andesite, basalt	Cryptodome intrusion	Debris avalanche	2.1 km ³	Unknown	Ice cap	Glicken 1996
Socompa	Argentina/Chile	6,300–6,400 BP	Dacite, andesite	Gravitational spreading	Debris avalanche	25–26 km ³	Unknown	No evidences	Wadge et al. 1995
Iriga	Philippines	1628 (?)	Basalt, andesite	Unknown	Debris avalanche	1.5 km ³	No evidence	Unknown	Aguila et al. 1986
Shiveluch	Kamchatka	Nov. 12, 1964	Andesite	Magma intrusion	Debris avalanche	1.5 km ³	Unknown	No evidences	Ponomareva et al. 1998
Llullailloco	Argentina/Chile	Late Pleistocene	Dacite, andesite	Gravitational collapse	Debris avalanche	1–2 km ³	Unknown	Ice cap	Richards and Villeneuve 2001
Mombacho El Crater	Nicaragua	Unknown	Basalt, andesite	Hydrothermal weakening	Debris avalanche	1.8 km ³	No evidence	No evidences	van Wyk de Vries and Francis 1997
Pacaya	Guatemala	Unknown	Basalt	Gravitational collapse	Debris avalanche	>0.60 (0.85?) km ³	Pumice	Unknown	Vallance et al. 1995
Bering glacier	Alaska	Nov. 3, 2002	Granite	Denali earthquake	Ice-rock avalanche	11.8 M m ³	Snow/ice	Icy basal material	Jibson et al. 2006
Black Rapids Glacier (2)	Alaska	March 27, 1964		Anchorage earthquake	Ice-rock avalanche	10–14 M m ³	Snow/ice	Icy basal material	Post 1967
Martin River Glacier (4)	Alaska	March 27, 1964		Anchorage earthquake	Ice-rock avalanche	4–18 M m ³	Unknown	Icy basal material	Post 1967
Illiamna, Red Glacier	Alaska	July 25, 2003	Andesite	Intraglacial sliding planes	Ice-rock avalanche	5 M m ³	Snow/ice	Icy basal material	Huggel et al. 2007
Mount Munday	Canada	Unknown	Gneiss	Unknown	Ice-rock avalanche	3 M m ³	Unknown	Icy basal material	Delaney and Evans 2008
Shattered Peak	Alaska	March 27, 1964	Sandstone argillite	Anchorage earthquake	Ice-rock avalanche	10 M m ³	5–30 M m ³ snow/ice	Icy basal material	Shreve 1966
Mount Steller	Alaska	September 14, 2005	Tertiary rock, ice	Permafrost degradation	Ice-rock avalanche	10–20 M m ³	Snow/ice	Icy basal material	Huggel et al. 2008

(Chen and Lee 2000). Both the models assume a fixed frictional internal rheology, which is governed by an internal friction angle, and alternative rheological kernels to describe the basal rheology. The two models differ in the approach used to solve the constitutive equations numerically (i.e. SPH in the DAN-3D model, finite element in the MADflow model).

Debris avalanches evolving from collapse of volcanic edifices were modelled assuming frictional, Voellmy, and plastic basal rheologies. The use of the frictional and Voellmy rheologies is well established for this kind of phenomena and a number of back-analysed historical events are available in the literature. The plastic rheology was first adopted by Kelfoun and Druitt (2005) which successfully replicates the Socompa debris avalanche. Rock avalanches running onto glaciers were modelled assuming frictional and Voellmy basal rheologies.

Internal friction angle is held constant ($\phi_i = 35^\circ$) for all the models. The bulking process is not simulated by the model. To take it into account we increased the detached volume by 20 %, so that the source volumes include the volume increment undergone during propagation by fragmentation.

Entrainment data are only seldom available for ice-rock avalanche events, as an estimation of the total volume admixed to the detached mass. Without more information available (i.e. locally eroded depths, erosion rates), we assumed uniform entrainment rates along the entire ice-covered path as to obtain the final volume estimated for the deposit. Changes in material density due to the presence of amounts of ice and snow do not affect significantly the final results, so they will be not discussed further.

The rheological parameters required for the back analyses (i.e. basal frictional angle, ϕ , for the frictional rheology, frictional, μ , and turbulent, ξ , coefficients for the Voellmy rheology, shear strength for the plastic rheology) were adjusted to match (1) the total runout distance reached by the debris avalanche (i.e. the horizontal distance between the scar highest point to the furthest point of deposit), (2) the aerial extent of the propagation and debris distribution within the deposit, and (3) other information quantitatively available (i.e. flow velocity, deposit thickness, run-up against obstacles, etc.). The parameters are selected by trial and error and adjusted in fixed intervals. In the Voellmy rheology, the frictional coefficient is selected first as to reach the proper distal end of deposition; then, the turbulent coefficient is adjusted which controls the proximal end limit of the deposition, the flow velocity and the overall propagation path.

Modelling Results

Due to the scarcity of data, a complete description of events evolution is often difficult to accomplish. A number of factors are critical for the modelling and could have

influenced the propagation and the final distribution of the deposit. The proper reconstruction of the pre-slide topography in the source and in the deposition area is one of the main elements of uncertainty together with the exact volumes involved during the propagation.

Modelling volcanic debris avalanches requires the removal of large volumes of deposited material and, eventually, of other volcanic products ejected successively to the collapse. In these latter cases, the exact proximal limit of the deposit is either undefined or difficult to recognize from the present topography because of possible post-collapse phenomena (e.g. dome extrusion, effusion of volcanic products), additional sector collapses of the edifice associated to the avalanche (e.g. toreva blocks), or obliteration of the deposit itself. Modelling ice-rock avalanches the local morphology of the glacier strongly influences the propagation due to the low basal resistance. The local micromorphology is only partly captured by the 30 m cell-size grid available.

Volcanic Debris Avalanches

We simulate the propagation of ice-rock avalanches adopting the frictional, Voellmy and plastic rheologies in the DAN 3D code. Several events are modelled with the Madflow model adopting the frictional and Voellmy rheologies (e.g. Figs. 2a and 3a). None of the adopted rheologies completely capture the variety of volcanic debris-avalanches considered and their whole propagation dynamics. The frictional rheology generally provides the best estimates of the deposit extents, with differences within about 9 % with respect to the observed events.

The Voellmy and plastic models fail to replicate the lateral expansion and the initiation of the deposition in many cases, which overestimate deposit areas up to 26 % and 35 %, respectively. Adopting the DAN 3D model, values of $\mu = 0.003\text{--}0.08$ and $\xi = 500\text{--}1,200 \text{ ms}^{-2}$ provide the best results. The friction angle, which is the sole parameter required by the frictional rheology, varies within the range $3^\circ\text{--}7.5^\circ$. The shear strength required by the plastic rheology varies within 45 and 100 kPa (Table 2). The Madflow model requires higher resistance parameters than the DAN 3D code (Table 3).

Ice Rock Avalanches

We simulate the propagation of ice-rock avalanches adopting the frictional and Voellmy rheology in the DAN 3D and Madflow codes (e.g. Figs. 2b and 3b). The models replicate the deposition areas with differences within the 12 % and 9 % for the frictional and Voellmy model, respectively. Modelling the entrainment process is essential at recognizing

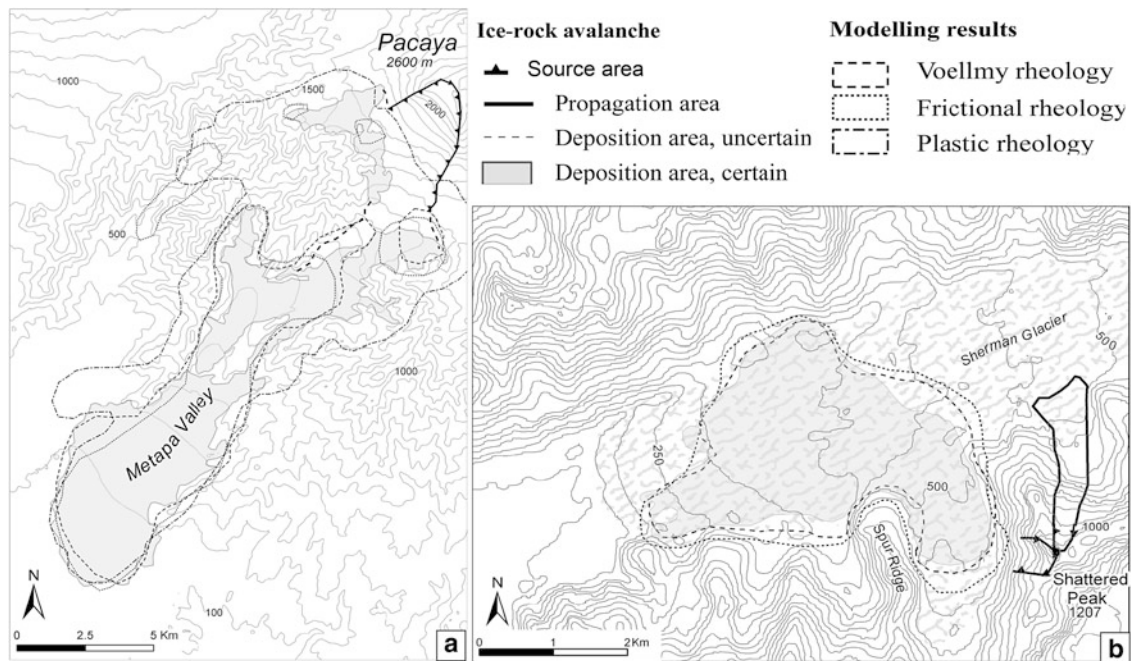


Fig. 2 Examples of application of the DAN 3D numerical model to replicate: (a) the Pacaya debris avalanche event and (b) the Sherman ice-rock avalanche. The deposition extents resulting from different rheologies are superimposed to the observed ones

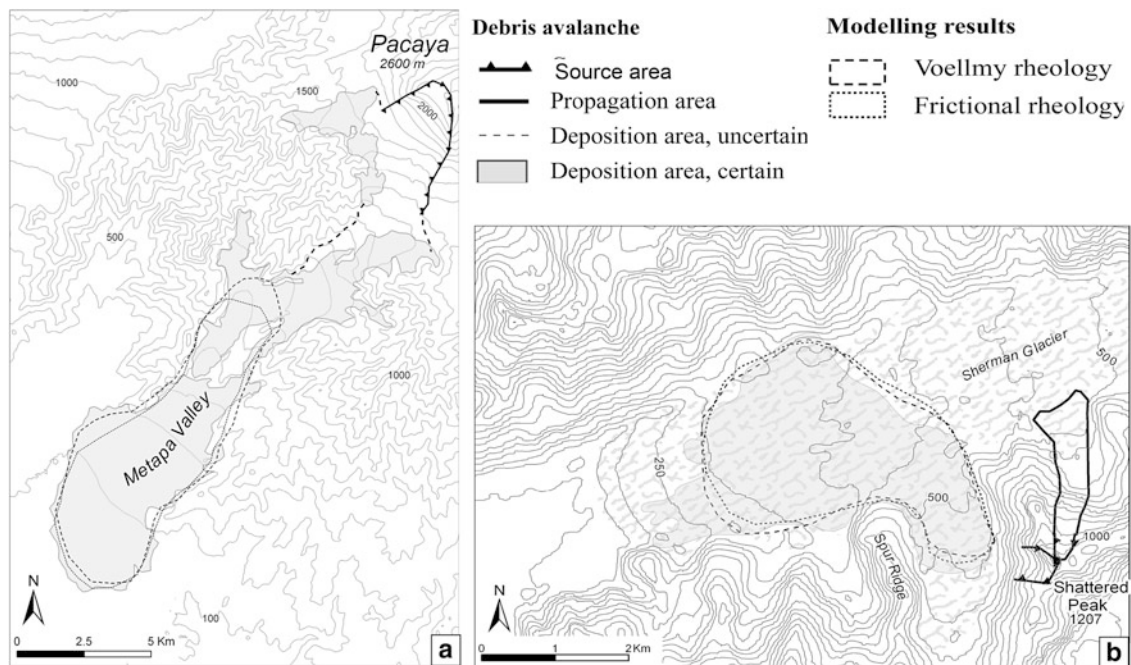


Fig. 3 Examples of application of the MadFlow numerical model to replicate: (a) the Pacaya debris avalanche event and (b) the Sherman ice-rock avalanche. The deposition extents resulting from different rheologies are superimposed to the observed ones

the distribution of the deposit and the areas interested by propagation. Adopting the DAN 3D model, values of $\mu = 0.03\text{--}0.1$ and $\xi = 1,000\text{--}2,000 \text{ ms}^{-2}$ provide the best results. The friction angles vary within the range $5.5^\circ\text{--}10.5^\circ$ (Table 2 and Fig. 4). The Madflow code requires higher resistance parameters and produce thicker deposits than the

DAN 3D code. In both the codes, Voellmy rheology achieves better results than the frictional rheology at recognizing the area involved by the propagation and initiation of the deposition, whereas the frictional rheology better replicates the high flow velocities suggested for some of the modelled cases.

Table 2 Range of the rheological parameters required by the DAN 3D code to replicate rock and debris avalanches in varying environments. Data refers to the presented study and to literature (Hungar and Evans 1996; McDougall 2006)

Type of event	Cases [#]	Basal friction [ϕ , °]	Turbulent coefficient [ξ , ms^{-2}]	Frictional coefficient [η , -]
Rock Av.	8	12–30	300–1,000	0.08–0.25
Volc. debris Av.	18	2.5–7.5	200–1,200	0.003–0.08
Ice-Rock Av.	15	5–11	1,000–2,000	0.03–0.1

Table 3 Range of the rheological parameters required by the Madflow code to replicate rock and debris avalanches in varying environments. Data refers to the presented study and to literature (Chen and Lee 2000)

Type of event	Cases [#]	Basal friction [ϕ , °]	Turbulent coefficient [ξ , ms^{-2}]	Friction angle [η , °]
Rock Av.	6	20–31	200–1,000	6–21
Volc. debris Av.	3	4–11	600–1,200	1.5–3
Ice-Rock Av.	8	7–12.5	800–1,000	2.5–5

Discussion

We applied depth averaged models to simulate the propagation of historic events of long runout rock and debris avalanches evolved in a variety of settings and conditions. The back analyses provide a first database of calibrated volcanic debris avalanches and a range of values for suitable rheological parameters. The uncertainty related to the reconstruction of the pre-event topography as the volume assumed for the collapse mass are some of the factors that mainly affect the quality of the modelling.

Back Analysed Parameters

The DAN 3D model has been extensively applied to a number of calibrated case histories, and the back calculated parameters can be used for comparison (Hungar and Evans 1996; McDougall 2006). The rheological parameters obtained in this study are significantly lower than those commonly used for debris avalanches evolving in different settings. Particularly for the basal friction angle, the sole parameter required by the frictional rheology, values always lower than 10°

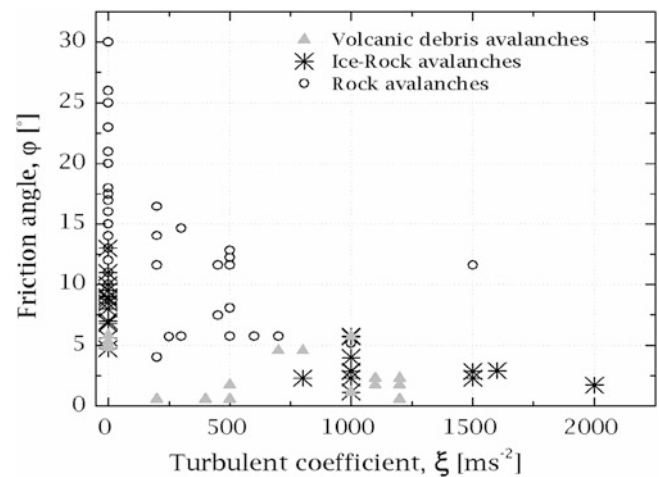


Fig. 4 DAN rheological parameters (Frictional and Voellmy) back analyzed for different rock and debris avalanches (Hungar and Evans 1996; McDougall 2006)

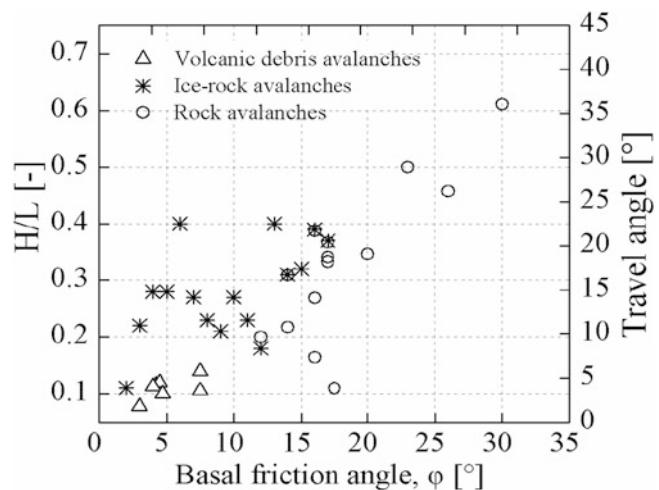


Fig. 5 Basal friction angles resulting from the back analyses of the several case histories compared to the corresponding travel angles

accomplish the best replication of events evolving either in glacial or volcanic settings. These values are well lower than those obtained for other rock avalanches of comparable magnitude which need basal friction angle generally within the range of 11°–31° (McDougall 2006). Intermediate parameters are required for debris avalanches entraining deposits ($8^\circ < \phi < 13^\circ$) or only partly propagating over ice ($10^\circ < \phi < 20^\circ$) (Fig. 5).

The Voellmy model is suggested for replicating the flow motion along the glacial ice, where the resistance has to be reduced to properly enhance the flow mobility (Evans and Clague 1988). Among the selected cases, entrainment of snow and ice along the path is documented only for Shermann and Mt Steller ice-rock avalanches, which more than triplicate their volumes propagating along the glacier.

Dependence on the Input Data

The back analyses of the avalanches performed on different topography data produce final results (deposition area, deposit thickness, lateral extent, and flow velocities) which slightly vary among each others, particularly for unconfined paths. On the other hand, the calibrated parameters vary depending on the origin of the adopted topographic data (i.e. ASTER and SRTM-derived terrain data). Lower values of the rheological parameters are required for modelling on smaller cell sizes. Increasing the cell size from 30 to 90 m grid reduces terrain roughness. The increase in the resistance offered by the material by means of its rheological properties serves to balance the reduced resistance offered by the more even terrain, particularly in the deposition zone.

Conclusions

In this work we demonstrate that, irrespective of the triggering conditions, events evolving in similar environmental conditions (e.g. type of material involved in the detachment, type of basal material, role of fluids, etc.) can be replicated assuming similar values for the flow-resistance parameters. In particular, we propose the range of variability for rheological parameters to be considered for the modelling of debris avalanches evolving from the collapse of volcanic edifices and for ice/rock avalanches propagating onto glaciers. These values are significantly lower than required by rock avalanches propagating in non-glacial, non-volcanic environments, and they can not be inferred from the empirical parameters commonly used to describe the exceptional mobility of granular flows of similar origin.

References

- Aguila LG, Newhall CG, Miller CD, Listanco EL (1986) Reconnaissance geology of a large debris avalanche from Iriga volcano, Philippines. *Philippine J Volcanol* 3:54–72
- Chen H, Lee CF (2000) Numerical simulation of debris flows. *Can Geotech J* 37(1):146–160
- Crandell DR, Miller CD, Glicken HX, Christiansen RL, Newhall CG (1984) Catastrophic debris avalanche from ancestral Mount Shasta volcano, California. *Geology* 12:143–146
- Delaney KB, Evans SG (2008) Application of digital cartographic techniques in the characterization and analysis of catastrophic landslides; The 1997 Mount Munday rock avalanche, British Columbia. In: Locat J, Perret D, Turmel D, Demers D, Leroueil S (eds) Proceedings of the 4th Canadian conference on geohazards: from causes to management. Presse de l'Université Laval, Québec, pp 141–146
- Evans SG, Clague JJ (1988) Catastrophic rock avalanches in glacial environments. *Proc V Int Symp Landslides* 2:1153–1158
- Glicken H (1996) Rockslide-debris Avalanche of May 18, 1980, Mount St. Helens Volcano, Washington. U S Geol Surv Open-File Report, 96–677
- Hayashi JN, Self S (1992) A comparison of pyroclastic flow and debris avalanche mobility. *J Geoph Res* 97:9063–9071
- Hewitt K (1999) Quaternary Moraines vs Catastrophic rock avalanches in the Karakoram Himalaya, Northern Pakistan. *Quaternary Res* 51(3):220–237
- Huggel C, Caplan-Auerbach J, Waythomas CF, Wessels RL (2007) Monitoring and modeling ice-rock avalanches from ice-capped volcanoes: a case study of frequent large avalanches on Iliamna Volcano, Alaska. *J Volc Geoth Res* 168(1–4):114–136
- Huggel C, Schneider D, Julio Miranda P, Delgado Granados H, Käähb A (2008) Evaluation of ASTER and SRTM DEM data for lahar modeling: a case study on lahars from Popocatepetl Volcano, Mexico. *J Volc Geoth Res* 170:99–110
- Hungr O, Evans SG (1996) Rock avalanche runout prediction using a dynamic model. In: Senneset (ed) Proceedings, 7th international symposium on landslides, Trondheim, 1, pp 233–238
- Jibson RW, Harp EL, Schulz W, Keefer DK (2006) Large rock avalanches triggered by the M 7.9 Denali Fault, Alaska, earthquake of 3 November 2002. *Eng Geol* 83:144–160
- Kelfoun K, Druitt TH (2005) Numerical modeling of the emplacement of Socompa rock avalanche, Chile. *J Geophys Res* 110:B12202.1–12202
- McDougall S (2006) A new continuum dynamic model for the analysis of extremely rapid landslide motion across complex 3D terrain. Ph.D. thesis, University of British Columbia, Vancouver
- McDougall S, Hungr O (2004) A model for the analysis of rapid landslide motion across three-dimensional terrain. *Can Geotech J* 41:1084–1097
- Ponomareva VV, Pevzner MM, Melekestsev IV (1998) Large debris avalanches and associated eruptions in the Holocene eruptive history of Shiveluch volcano, Kamchatka, Russia. *Bull Volcanol* 59(7):490–505
- Post A (1967) Effects of the March 1964 Alaska earthquake on glaciers, vol 554-D. U. S. Geological Survey Professional Paper. U.S. Govt. Print. Off, Washington, DC, p 42
- Richards JP, Villeneuve M (2001) The Llullaillaco volcano, northwestern Argentina: construction by Pleistocene volcanism and destruction by edifice collapse. *J Volcanol Geotherm Res* 105:77–105
- Shreve RL (1966) Sherman landslide, Alaska. *Science* 154(3757):1639–1643
- Siebert L (2002) Landslides resulting from structural failure of volcanoes. In: Evans SG, De Graff JV (eds) Catastrophic landslides: effects, occurrence, and mechanisms, vol 15, Geological society of America, reviews in engineering geology. Geological Society of America, Boulder, CO, pp 209–235
- Vallance JW, Siebert L, Rose WI, Giron J, Banks NG (1995) Edifice collapse and related hazards in Guatemala. *J Volcanol Geotherm Res* 66:337–355
- van Wyk de Vries B, Francis PW (1997) Catastrophic collapse at stratovolcanoes induced by gradual volcano spreading. *Nature* 387:387–390
- Voight B, Elsworth D (1997) Failure of volcano slopes. *Géotechnique* 47(1):1–31
- Voight B, Janda RJ, Glicken H, Douglass PM (1983) Nature and mechanics of the Mount St Helens rockslide-avalanche of 18 May 1980. *Geotechnique* 33:224–273
- Wadge G, Francis PW, Ramirez CF (1995) The Socompa collapse and avalanche event. *J Volc Geoth Res* 66:309–336



Physical Modelling of the Propagation of Rock Avalanches: Recent Developments and Results

Claire Sauthier and Vincent Labiouse

Abstract

Rock avalanches are studied at the Laboratory for Rock Mechanics of EPF Lausanne by means of unconstrained flow experiments of dry granular material. Tests aim at studying the influence of different parameters on the propagation and deposition mechanisms as well as on the characteristics of the final deposit. The existing measurement system, based on the fringe projection method, was improved in order to increase the quality and the reliability of the volume measurement and the computation of the centre of mass of the final deposit. The latest developments allow using this method to follow the mass during its motion. Additionally, a new technique that allows tracking the mass front was set up and compared to previous results gathered with the commercial software WINAnalyze. Results of experiments carried out with a gravel supposed to have the same characteristics as the one used in a previous research study Manzella (2008 Dry rock avalanche propagation: unconstrained flow experiments with granular materials and blocks at small scale. Ph.D. thesis 4032, Ecole Polytechnique Fédérale de Lausanne, Switzerland) showed some differences, suggesting that the grading of the material has a certain influence on the runout and the position of the centre of mass of the final deposit. A more significant difference is related to the state of the propagation surface. Recent experiments with a curved transition at the bottom of the slope and a larger volume lead to new results. Contrary to previous observations, for a given falling height of the source base, the distance travelled by the centre of mass on the horizontal panel increases with the volume. This leads to discuss further some conclusions previously drawn.

Keywords

Rock avalanches • Physical modelling • Runout • Fringe projection method • Mass front tracking

Introduction

Rock avalanches are extremely rapid events involving a great amount of materials ($\geq 10^6 \text{ m}^3$). Although they are very infrequent, rock avalanches cause total destruction in

their path and are important in terms of life loss and economic impact (Hungri 1990). The management of this kind of natural hazard requires the identification of potential sources and their monitoring as well as the prediction of runout areas. One way to progress in the understanding of the propagation and energy dissipation mechanisms of such natural hazard is to perform physical modelling, although laboratory similitude requirements are not easy to fulfil.

The Laboratory for Rock Mechanics of EPF Lausanne is performing unconstrained flow experiments on an inclined panel by releasing dry frictional materials. It aims at studying

C. Sauthier (✉) • V. Labiouse
Laboratory for Rock Mechanics (LMR), Ecole Polytechnique Fédérale de Lausanne (EPFL), EPFL-ENAC-LMR, Station 18, CH-1015 Lausanne, Switzerland
e-mail: claire.sauthier@epfl.ch

the influence of several parameters like: the released material, the volume, the falling height, the slope angle, the basal friction angle, the radius of curvature at the bottom of the slope and the number of consecutive releases on the final deposit's characteristics i.e. runout, length, width and centre of mass, as well as on the front propagation (Manzella 2008; Manzella and Labiouse 2009). Among all the conclusions drawn in the framework of the previous research study mentioned above, two of them are very interesting. Firstly, a transfer of momentum between the rear and the front parts of the sliding mass was observed. When the front part reaches the horizontal panel it starts to decelerate, while the rear part on the inclined panel is still accelerating. The rear part pushes the front part, and the rate of deceleration of the latter is reduced. Secondly, the distance travelled by the centre of mass on the horizontal panel does not depend on the volume. This leads to confirm a suggestion made by Davies (1982) and later Davies and McSaveney (1999, 2003). These Authors stated that the centre of mass travels with an angle close to a "normal" friction angle of granular material and that the long runout of rock avalanches is due to the spreading of the mass.

Recently, the range of values of volume, falling height, slope angle and radius of curvature was extended. Improvements and further developments of the measurement system allow assessing the influence of these parameters also on the mass in motion (Sauthier in progress). Related to these modifications, a new technique was developed for the mass front detection and tracking. A series of experiments performed under similar conditions with respect to the previous research study, and with a type of gravel a priori identical to the one used in those tests, showed some different results. The state of the propagation surface and the type of gravel can explain these differences. The geometry of the source leads to difficulties in the interpretation of the results, as the influence of the volume and the initial position of the centre of mass cannot be distinguished. To dispel any uncertainty, two series of tests were performed, and compared; a first one with a constant falling height of the source base and a second one with a constant initial height of the centre of mass. The results obtained lead to discuss further some conclusions drawn so far.

Laboratory Experiments

Experimental Set-up

Unconstrained flow experiments are performed on an inclined panel, which can be positioned at different angles and is connected to a horizontal panel with an adaptive curved

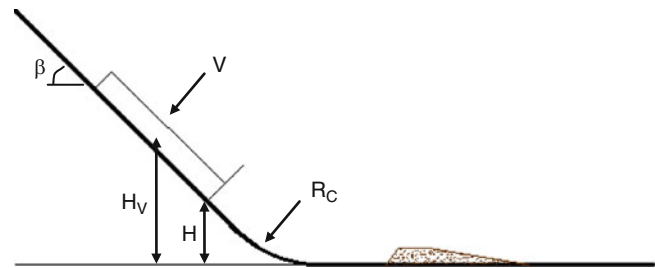


Fig. 1 Experimental set-up

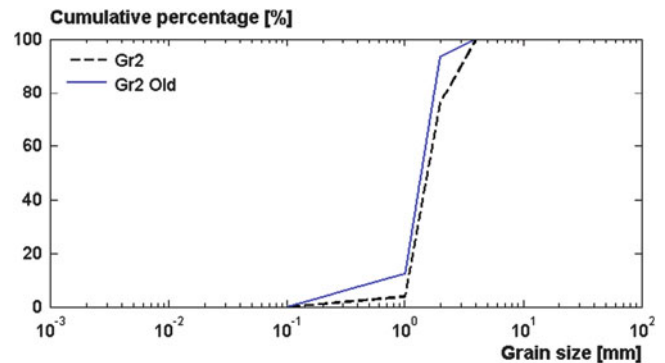


Fig. 2 Grading of the tested materials Gr2 and Gr2_Old (Sauthier in progress)

transition. The radius of curvature can go from about 0.05–1.00 m. The entire surface is currently covered with three connected smooth plastic sheets made up of forex. Up to 100 l of material is released from a box with a height, width and length of 20, 40 and 135 cm respectively. A sketch of the experimental set-up is shown in Fig. 1.

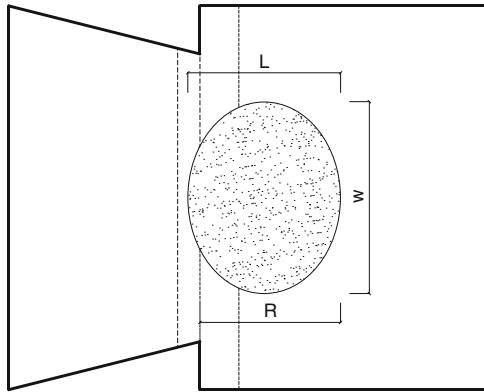
At present the following parameters are studied: the volume V , the falling height of the source base H , the initial height of the centre of mass H_V , the inclination β and the radius of curvature R_C . Their influence is assessed on the final deposit as well as on the mass in motion. Each test is performed three times to check the reproducibility.

Released Material

Experiments were performed with two different type of gravels; Gr2 and Gr2_Old. The latter was used in a previous research study (Manzella 2008; Manzella and Labiouse 2009). The former material contains less fine particles and more coarse grains (Fig. 2). The internal friction angle as well as the static and dynamic basal friction angles on forex were measured with tilting tests (Table 1). In terms of friction angles, the difference between the two gravels is small, even insignificant, as it is within the range of variation of the measurement (1°).

Table 1 Characteristics of the tested materials Gr2 and Gr2_Old (Sauthier in progress)

Friction angles	Gr2	Gr2_Old
Internal friction angle	$37^\circ \pm 1^\circ$	$36^\circ \pm 1^\circ$
Static basal friction angle	$26^\circ \pm 1^\circ$	$27^\circ \pm 1^\circ$
Dynamic basal friction angle	$23^\circ \pm 1^\circ$	$24^\circ \pm 1^\circ$

**Fig. 3** Direct measurements of the final deposit characteristics i.e. runout R , length L and width W

Measurement System

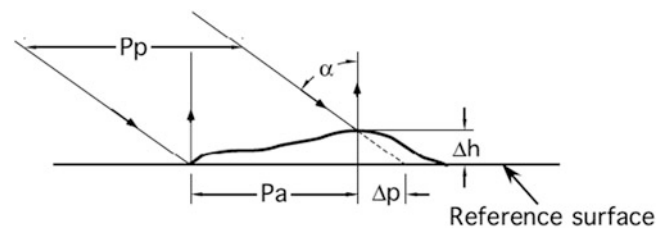
Direct Measurements

After each test, runout R , length L and width W of the final deposit are measured with a ruler. The runout is measured from the intersection between the inclined and the horizontal panels. When the entire mass does not pass the curved transition, the length corresponds to the projection of the final deposit on a horizontal plane (Fig. 3).

Fringe Projection Method

Indirect measurements of the final deposit as well as of the mass in motion are obtained by means of the fringe projection method. This non-destructive measurement technique has already been used in a previous research study for retrieving the morphology of the final deposit and for computing the position of the centre of mass (Manzella and Labiouse 2008). Recent works allowed improving the quality and the reliability of the final deposit measurement and to extend the technique to the measurement of the mass during its motion (Sauthier in progress).

The principle of the technique is to project a fringe pattern with an angle of incidence onto an object. Those fringes appear distorted due to the object topology when seen from a different direction. The measurement of the

**Fig. 4** Projection of parallel lines on an object (Cochard and Ancey 2007)

fringes deformation gives access to the object morphology. To easily explain the relationship between the distortion of the pattern and the object surface height, a couple of parallel lines, projected onto the object of interest, is considered in Fig. 4.

The height difference Δh is given by (1):

$$\Delta h = \frac{\Delta p}{\tan \alpha} = \frac{p_p - p_a}{\tan \alpha} \quad (1)$$

where Δp is the difference between p_p the distance separating the two projected lines and p_a the distance between these two lines as seen by the camera with an angle of incidence α (Cochard and Ancey 2007). This relationship is only valid in a telecentric system. The height information can be retrieved at each line position but is lost in-between. So, to retrieve this lost information, fringes with a cosine profile are preferably projected. Specific algorithms have been designed to retrieve the shape of the object in a Cartesian framework from the images captured with a camera (Cochard and Ancey 2007; Manzella and Labiouse 2008; Sauthier in progress).

Mass Front Detection and Tracking

In a previous research study (Manzella 2008) the mass front was detected and tracked, its velocity and acceleration were computed by means of the commercial image analysis software WINAnalyze. This program mainly works on the contrast to track points. The projection of fringes during the propagation of the mass makes such software useless.

A new technique was developed, using the Empirical Mode Decomposition EMD. The EMD was developed by Huang et al. (1998) to process non-stationary signals by decomposing them into their intrinsic oscillation modes. The standard algorithm is iterative and the final result depends on several parameters and choices leading to a non-unique solution. Recently, Equis and Jacquot (2009) proposed a new implementation of the EMD. If specific experimental conditions are fulfilled, a single iteration produces a zero-mean centred signal, leading then to a straightforward phase

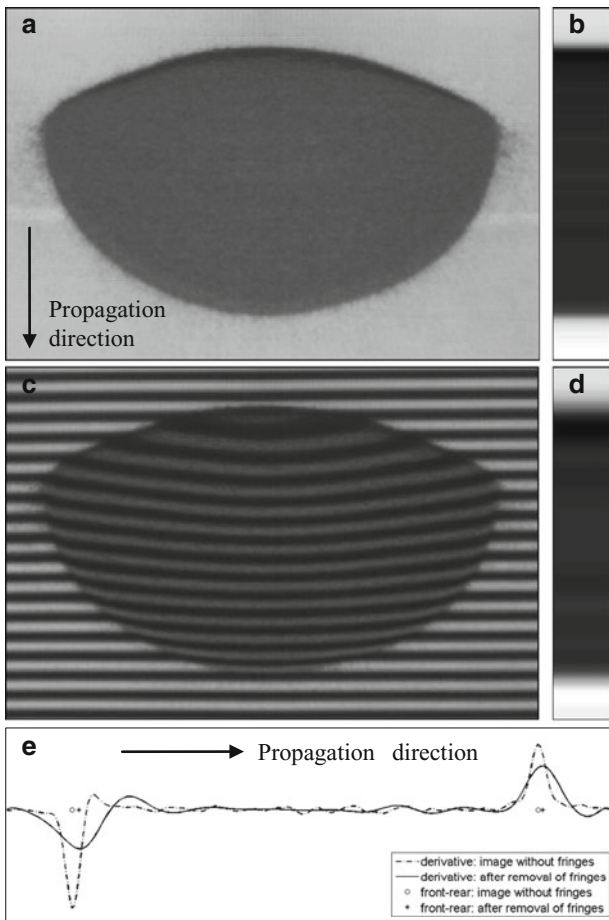


Fig. 5 Detection of the mass front. (a) Final deposit without fringes. (b) Central section of 5 pixels of the final deposit without fringes. (c) Final deposit with fringes. (d) Results of the EMD applied on a section of 5 pixels. (e) Derivative of the mean value of the intensity, front and rear detection on the image of the final deposit without fringes and after removal of the fringes

extraction. This latter version of the EMD was used to compute the mean value of the signal and thus to eliminate the fringes.

This technique is applied on a strip of 5 pixels along the direction of propagation. The result is smoothed with a sine cosine filter (Aebischer and Waldner 1999). The mean value over the 5 pixels is computed and differentiated. The derivative has a positive peak representing the mass front (Fig. 5). The error in the front detection can reach 5 pixels i.e. approximately 2.5 cm. The precision of the new technique is thus similar to the previous one of 2–3 cm (Manzella and Labiouse 2009). In theory, the detection of the rear part is also conceivable, but less accurate due to the unavoidable shadow at the rear part of the mass when it propagates on the horizontal panel. Applying this method on an image sequence allows the automatic detection and tracking of the mass front. After calibration, the distance travelled by the front along the slope is computed. Prior to first and

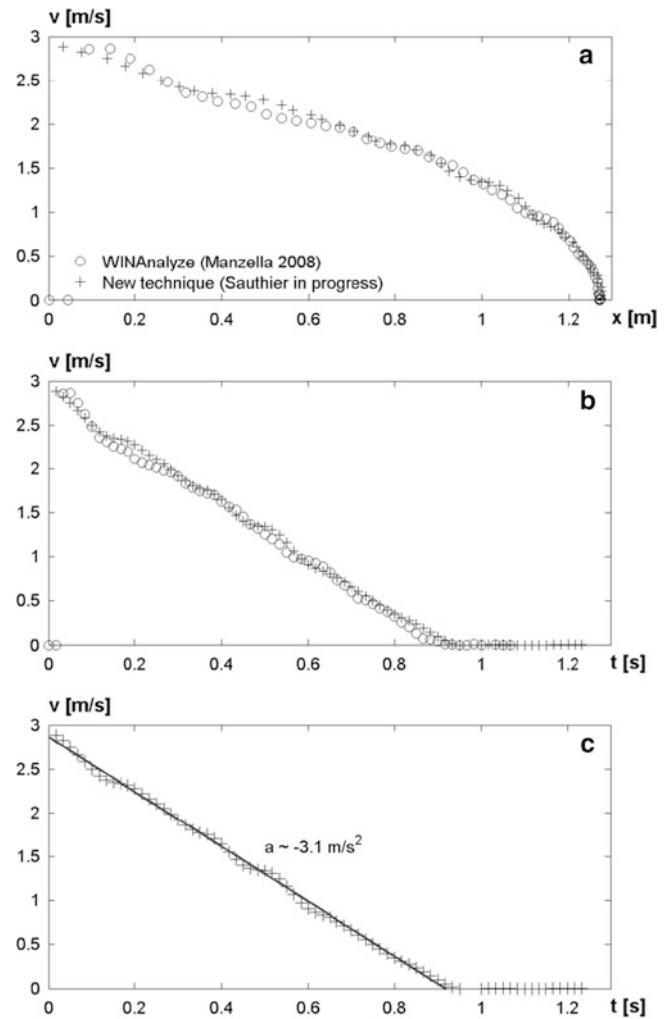


Fig. 6 Comparison between the mass front velocities computed by the commercial software WINAnalyze and the new technique. (a) Mass front velocity over runout. (b) and (c) Front velocity over time. The regression line in (c) points out the deceleration on the horizontal plane, related to the transfer of momentum between the rear and the front parts of the mass

second derivative computations to obtain mass front velocity and acceleration a smoothing step must be carried out. Good results were obtained with the following processing scheme. From the n sets of down sampled by n versions of the raw data, shifted by one between each other, we build n smoothed signals by interpolation with a cubic spline kernel. The last step consists simply in averaging those n samples. This method leads to better results than those obtained with a moving average window of length n .

This method, starting from the front detection, was applied on a series of images without fringes (Manzella 2008) and compared to the result given by the commercial software WINAnalyze (Fig. 6). The results are not strictly identical because of different smoothing techniques and assumptions on the calibration. However, the maximal velocities are

comparable and the trend of the curves leads to draw similar conclusions about a transfer of momentum phenomenon (Manzella and Labiouse 2009). The mean deceleration of -3.1 m/s^2 at the end of the propagation is lower (in absolute value) than the value corresponding to the sliding of a particle, i.e. $-g \cdot \tan \alpha = -4.4 \text{ m/s}^2$. This underlines that there is a driving force pushing the front of the mass ahead. It results from a transfer of momentum between the front part of the mass which is decelerating and rear part which is still on the inclined panel and accelerating.

Results

Comparison Between Previous and Recent Results

For the purpose of comparing results obtained in the framework of two Ph.D. theses (Manzella 2008; Sauthier in progress) and to extend the conclusions obtained so far, a series of experiments was performed again. Volumes of 20 and 40 l of gravel Gr2 were released from 1 m height on a panel covered with forex, inclined at 45° and with a radius of curvature at the bottom of the slope of 0.5 m. Figure 7 presents the obtained results for a volume of 40 l. Firstly, improvements in the delineation of the final deposit can be noticed. Noise was removed and waves, due to harmonics resulting from an imperfect cosine profile of fringes, were smoothed. Secondly, it can be observed that the results are rather different. The experiments performed recently give a longer runout and distance travelled by the centre of mass on the horizontal panel. On the other hand, the length and the width of the final deposit are a bit smaller.

A first reason for explaining such differences is the use of different released materials. To assess the influence of the type of gravel, experiments were performed again with the old gravel Gr2_Old. They confirmed that different gravels provide some differences in terms of runout, and position of the centre of mass. The length and the width of the final deposit are quite similar (Fig. 8). The gravel Gr2_Old contains more fine particles, which can be the source of an artificial cohesion due to electrostatic forces developing when the material is in motion (Iverson et al. 2004).

The second and main reason of the differences observed when comparing previous and recent experiments (Fig. 7) is related to the state of the propagation surface. The inclined panel is covered with forex plates which were replaced before starting the new experiments. The old plates were rather scratched, and this most probably led to an increase of friction at the interface between the basal surface and the sliding material. Moreover, a small gap between two of the three plates was filled up in time with released material creating an obstacle to the gravel flow.

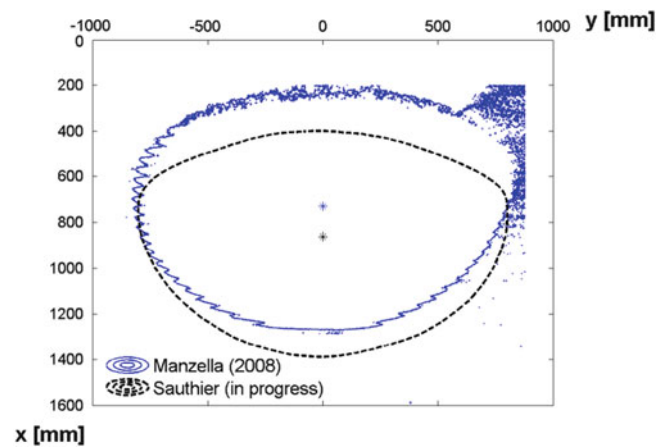


Fig. 7 Comparison between previous and recent results. Tests performed with gravel Gr2_Old (Manzella 2008) and gravel Gr2 (Sauthier in progress). Experimental conditions: $V = 40 \text{ l}$, $H = 1.0 \text{ m}$, $\beta = 45^\circ$, $R_C = 0.5 \text{ m}$, smooth surface

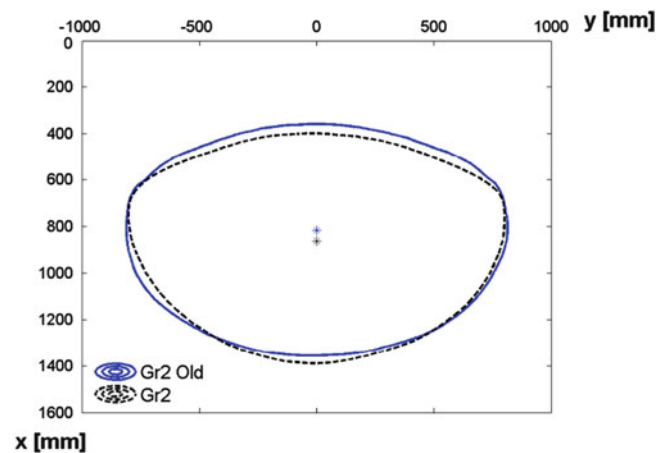


Fig. 8 Comparison between final deposit characteristics of gravel Gr2 and Gr2_Old (Sauthier in progress). Experimental conditions: $V = 40 \text{ l}$, $H = 1.0 \text{ m}$, $\beta = 45^\circ$, $R_C = 0.5 \text{ m}$, smooth surface

Due to these differences in characteristics of the released material and experimental conditions, the results of the two research studies are not strictly comparable from a quantitative point of view. Nevertheless, conclusions drawn from each experimental campaign about the influence of the various parameters on the final deposit characteristics can be compared and discussed.

Influence of the Volume on the Final Position of the Centre of Mass

The increase in volume range tested in the recent experiments leads to discuss further some conclusions drawn in the framework of a previous research study (Manzella 2008; Manzella and Labiouse 2009). Volumes up to 100 l of gravel Gr2 were

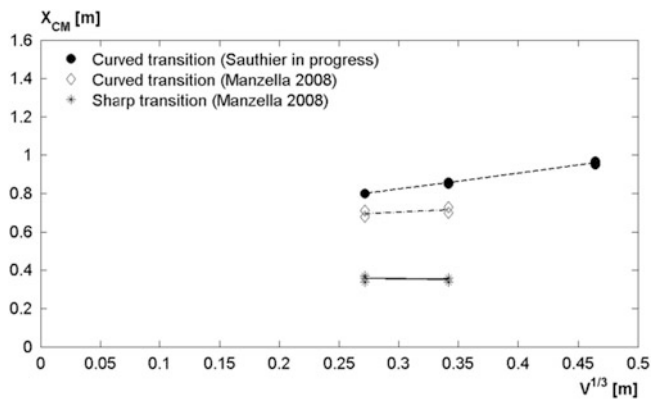


Fig. 9 Influence of the volume on the distance travelled by the centre of mass on the horizontal panel X_{CM} , for a constant falling height of the source base H . Experimental conditions: $V = 40$ l, $H = 1.0$ m, $\beta = 45^\circ$, $R_C = 0.5$ m, smooth surface

released from 1 m height on a panel covered with forex, inclined at 45° and with a radius of curvature at the bottom of the slope of 0.5 m. Contrary to what was stated, for a given falling height of the source base, the volume has some influence on the distance travelled by the centre of mass on the horizontal panel (Fig. 9).

Manzella and Labiouse (2009) draw their conclusion from experiments performed with a sharp transition at the bottom of the slope and extended it to the few experiments carried out with a curved transition. Nevertheless, it is possible that the type of transition plays a role in the propagation of the centre of mass. Moreover, the increase in volume range leads to a straightforward and unambiguous assessment of the influence of this parameter. Indeed, the variation with volume of the final position of the centre of mass is above the range of variation of three experiments performed in the same conditions.

However, this way of analysing the results is too trivial and may mislead. In fact, due to the geometry of the source, an increase of volume leads to a higher position of the initial centre of mass. This raises the following questions: Is the longer distance travelled by the centre of mass on the horizontal panel due to an increase of volume or due to a higher position of the centre of mass of the source? Is there any interaction between these two parameters?

To answer these questions, some experiments were performed, keeping a constant initial position of the centre of mass and using different volumes. An increase of volume from 20 to 40 l leads to a slight and insignificant increase of the distance travelled by the centre of mass on the horizontal panel. Unexpectedly, the distance travelled by the centre of mass is lower for a volume of 100 l than for volumes of 20 and 40 l (Fig. 10). This probably results from the fact that, given the geometry and confinement of the source, a part of the energy is dissipated by friction along the sides of the box.

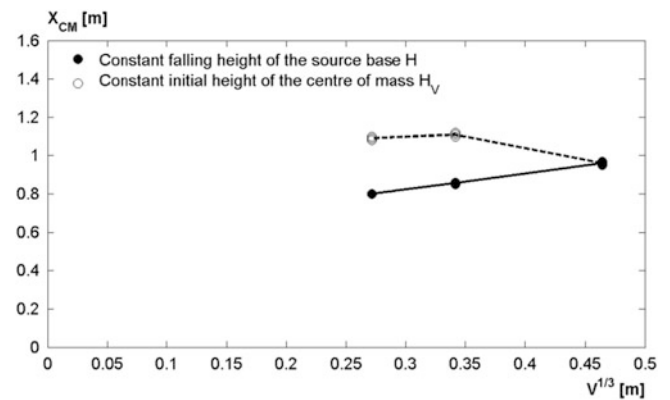


Fig. 10 Influence of the volume on the distance travelled by the centre of mass on the horizontal panel X_{CM} for a constant falling height of the source base H as well as for a constant initial height of the centre of mass H_V . Experimental conditions: $V = 40$ l, $\beta = 45^\circ$, $R_C = 0.5$ m, smooth surface

The travel angle of the centre of mass ϕ_{cm} , i.e. the angle connecting the initial and final positions of the centre of mass, is constant for volumes of 20 and 40 l and slightly increases by 1° for a volume of 100 l.

Conclusions

In order to study rock avalanches, unconstrained flow experiments are performed at the Laboratory for Rock Mechanics at the EPF Lausanne (LMR-EPFL). Those laboratory tests aim at assessing the influence of different parameters and at studying mechanisms of propagation and energy dissipation.

A few years ago, the LMR developed a measurement system, based on the fringe projection method, for retrieving the morphology of the final deposit and computing the position of its centre of mass. The mass front was tracked and its velocity and acceleration were computed using the software WINAnalyze. Recent works allowed improving the quality and the reliability of the final deposit measurement and to extend the technique to the measurement of the mass during its motion. Due to the projection of fringes during the whole experiment, the use of a commercial software to track the mass front is not possible anymore. A new implementation of the empirical mode decomposition EMD was used to remove the fringes and keep the background intensity. This technique is applied on a strip of 5 pixels along the direction of propagation. The signal is then smoothed with a sine cosine filter, averaged over the 5 pixels and derived to detect the mass front. After calibration, the distance travelled by the front along the slope is computed and smoothed by cubic spline interpolation. The first and second derivatives give the mass front velocity and acceleration, respectively.

The results of new experiments were compared to those of a previous research study. The observed differences can be explained by the state of propagation surface and somewhat by the characteristics of the released material, suggesting that the grading may have an influence. Among these two factors, the former has the most significant influence. Although the results are not strictly comparable from a quantitative point of view, the conclusions drawn so far can be extended.

Contrary to previous observations, for a given falling height of the source base, the distance travelled by the centre of mass on the horizontal panel increases with the volume. However, given the source geometry and its influence on the initial position of the centre of mass, it is impossible to claim that this is only due to the volume. A series of experiment performed with a constant initial position of the centre of mass showed that an increase of volume from 20 to 40 l leads to a slight and insignificant increase of the distance travelled by the centre of mass on the horizontal panel. For a volume of 100 l, this distance decreases. The travel angle of the centre of mass ϕ_{cm} is constant for volumes of 20 and 40 l and increases only by 1° for a volume of 100 l. This is probably due to the fact that, for such a volume, a part of the energy is dissipated by friction along the sides of the box.

Acknowledgments The authors thank the Swiss National Science Foundation for funding this research project. Further acknowledgements go to Dr. Equis for his help in the improvement and extension of the measurement system, as well as for his careful review of the third part of this paper. M. Mattheeuws for proofreading this article. Jean-Marc Terraz, Laurent Morier, Michel Teuscher and Laurent Gastaldo for designing and modifying the experimental set-up. Thomas Badoz, Emilie Decrausaz, Mathilde Charrier, Gabriele Pisani, Bastien Ferrot and Laurent Gastaldo for their help during the experimental campaign.

References

- Aebischer HA, Waldner S (1999) Simple and effective method for filtering speckle interferometric phase fringe patterns. *Opt Commun* 162(4–6):205–210
- Cochard S, Ancey C (2007) Tracking the free surface of time-dependant flows: image processing for the dam-break problem. *Exp Fluids* 44(1):59–71
- Davies TRH (1982) Spreading of rock avalanche debris by mechanical fluidization. *Rock Mech* 15(1):9–24
- Davies TRH, McSaveney MJ (1999) Runout of dry granular avalanches. *Can Geotech J* 36(2):313–320
- Davies TRH, McSaveney MJ (2003) Runout of rock avalanches and volcanic debris avalanches. In: *Proceeding of the international conference on fast slope movements*, vol 2. Naples, 11–13 May 2003
- Equis S, Jacquot P (2009) The empirical mode decomposition: a must-have tool in speckle interferometry? *Opt Express* 17(2):611–623
- Huang NE, Shen Z, Long SR, Wu MC, Shih HH, Zheng Q, Yen N-C, Tung CC, Liu HH (1998) The empirical mode decomposition and the Hilbert spectrum for nonlinear and non-stationary time series analysis. *Proc R Soc Lond A* 454:903–995
- Hungr O (1990) Mobility of rock avalanches. National Research Institute for Earth Science and Disaster Prevention, Report 46, Tsukuba, pp 72–93
- Iverson RM, Logan M, Denlinger RP (2004) Granular avalanches across irregular three-dimensional terrain 2. Experimental tests. *J Geophys Res–Earth Surf* 109: F01015, 16pp, doi:10.1029/2003JF000084
- Manzella I (2008) Dry rock avalanche propagation: unconstrained flow experiments with granular materials and blocks at small scale. Ph.D. thesis 4032, Ecole Polytechnique Fédérale de Lausanne, Switzerland
- Manzella I, Labiouse V (2008) Extension of the fringe projection method to measure shape and position of the centre of mass of granular flow deposit. In: *Proceedings of the 12th international conference of international association for computer methods and advances in geomechanics (IACMAG)*, Goa, 1–6 Oct 2008, pp 4547–4554
- Manzella I, Labiouse V (2009) Flow experiments with gravel and blocks at small scale to investigate parameters and mechanisms involved in rock avalanches. *Eng Geol* 109(1):146–158
- Sauthier C. Physical and numerical modelling of the propagation and spreading of dry rock avalanches. Ph.D. thesis in progress, Ecole Polytechnique Fédérale de Lausanne, Switzerland (in progress)



Debris Flow Analysis: From Lithological Classification of the Basin to Deposition

Chiara Deangeli, Erika Paltrinieri, and Davide Tiranti

Abstract

The aim of this study is the development of an integrated approach for definition of scenarios of debris flow deposition. The approach has been applied to basins located in the North-western Alps. Firstly the basins are classified on the basis of the bedrock lithology. Hence the features of debris flows are related to different bedrock lithologies: basin area/fan area ratios, alluvial fan architectures, depositional styles and triggering rainfall characteristics. This method permits to capture the essential features of flow phenomena and to address the choice of proper constitutive laws for the numerical modelling of debris flow propagation and deposition. The numerical model calibration is based on the observed styles of deposition of debris flows and architecture of the alluvial fans (shape, slope, grain-size distribution, etc.). The simulations do not match the deposit of a given past event, but the results are in terms of scenarios and supply a more realistic tool for risk mitigation.

Keywords

Catchment lithology • Sedimentary processes • North-western Alps • Numerical modelling • Cellular Automata

Introduction

Debris flows (DFs) are rapid to very rapid flows of sediment water mixtures, with high solid concentration, mainly composed by irregular and coarse particles. They are among the most dangerous natural processes because of high velocities. Therefore the definition of deposition scenarios is one of the most important aspects for risk mitigation. The definition of scenarios is usually carried out by the numerical simulations of past events. The procedure is generally based on the assessment of the volume of an occurred event, the choice of a suitable constitutive law for the debris flow and the calibration of the

numerical model parameters on the basis of in situ evidences. In this procedure there are two main weakness points: the reliability of the initial volume assessment and the back analysed values of the parameters. It is well known that the estimate of initial debris volumes is a difficult task and the results of two different procedures can be conflicting. Furthermore the parameters calibrated during the process of back analysis can be different, in a given site, for events of low (small initial volume) and high (large initial volume) magnitude. The last matter depends on several aspects but is related to the choice of the constitutive law. First there exists an objective difficulty for determining the rheological behaviour of natural materials because they are composed by irregular and coarse particles over a large range of values, and therefore in the majority of cases rheological properties cannot be measured directly and must be evaluated by historical information or by monitoring field data (run out, flow velocity, etc.). Secondly back analyses supply constitutive parameters by matching the field data. This does not provide evidence that the constitutive equation is appropriate (Ancey 2007).

C. Deangeli (✉) • E. Paltrinieri
Department of Land, Environmental and Geoengineering, Politecnico di Torino, Turin, Italy
e-mail: chiara.deangeli@polito.it

D. Tiranti
Hydrology and Natural Hazards, Department of Forecasting Systems, Environmental Protection Agency of Piemonte, Turin, Italy

The present study seeks to overcome some of the problems previously highlighted and is tested in some pilot sites located in the North-western Alps, in upper Susa Valley (Piemonte, Italy). The basins are classified on the basis of the lithology of the bedrock into three main groups (Tiranti et al. 2008). According to the outcomes of Moscariello et al. (2002) each group corresponds to a peculiar grain-size distribution of the resulting loose material. The three main typologies of catchment lithology are characterized by different basin area/fan area ratios, alluvial fan architectures, debris flow rheologies, depositional styles and triggering rainfall characteristics. The interpretation of in situ evidences supplies also indications about the sedimentary processes occurring in these basins. The depositional styles can therefore supply indications on the predominant type of process (viscous, collisional-frictional) during the runout phase of debris flows.

The results of this geological study have addressed the choice of proper constitutive laws for the propagation phase, simulated by a Cellular Automata model (Segre and Deangeli 1995; Deangeli 2008).

The initial volume of debris material of each simulation does not exactly corresponds to a given past event, but it is just a reasonable value for the investigated basin. The purpose of the numerical models is to reproduce depositional styles and architecture of the alluvial fans for each group. The calibration of the numerical model parameters is hence performed in these terms. The paper reports results obtained by the application of the proposed methodology to three test-basins belonging to the three different groups identified in upper Susa Valley.

Classification of Basins and Related Processes

According to a recent study conducted on several alluvial fans in the Alpine region (Moscariello et al 2002), several North-western Alps basins have been classified by Tiranti et al. (2008) into three main typologies of catchment lithology: (1) massive and/or crudely stratified/foliated carbonate rocks (e.g., dolostones, limestones, marbles); (2) fine-grained sheared finely-foliated metamorphic rocks (e.g., calc-schists, shales, phyllades); (3) massive or coarse-grained crystalline rocks or massive quartzite rocks (e.g., granitoids, gneiss, ultrabasites, meta-qtz-conglomerates).

On the basis of these lithological characteristics, the dominant alluvial fan aggradational processes are related to a cohesive debris flow (CDF) and to a non-cohesive debris flow (N-CDF). The occurrence of the two DF types depends on the amount of clay or clay-like phyllosilicates and clayey silt produced by the different bedrocks. Matrix clay content greater than 5 % characterizes the CDF; matrix clay amount lower than 5 % characterizes N-CDF (Fig. 1).

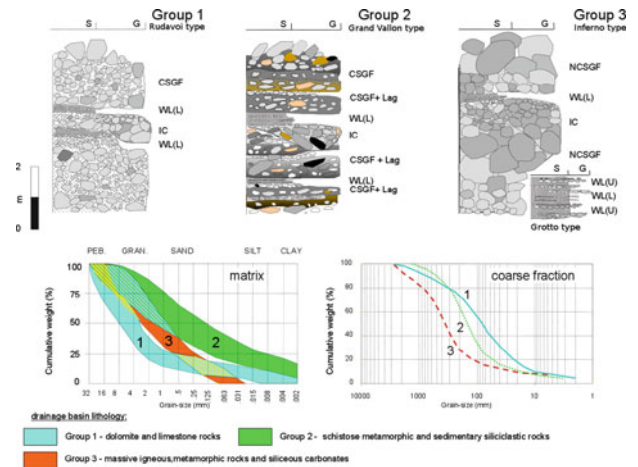


Fig. 1 Sketches of the three depositional styles and relative grain-size curves (*Group 1*: Rudavoi type; *Group 2*: Grand Vallon type; *Group 3*: Inferno and Grotto types). Where: CSGF is cohesive sediment gravity flow; NCSGF is non-cohesive sediment gravity flow; Lag is matrix-free gravels produced by winnowing of debris flow by recessional and/or secondary overland water flows; IC is incised channel facies: massively matrix-poor or-free coarse gravel formed as a result of successive winnowing and erosion of sediment gravity flow deposits by high energy, channelized water flows; WL(U) is waterlaid deposits formed under supercritical flow conditions by sheetflooding; WL(L) is waterlaid deposits formed under subcritical flow conditions (planar stratification) during the waning stage of the flood or secondary overland water flows. Prevailing grain-size: S (sand and silt); G (gravel with matrix) (Modified from Moscariello et al. 2002)

In Table 1 the main features of the three basin types are summarized.

The considerations about the triggering frequency and the triggering seasonality in Table 1 are derived from analysis of historical data from 1728 (first DF triggering historical report in this part of the Western Alps) until today.

The considered average values of critical rainfall intensity (see Table 1) are only indicative of high probability of DF triggering. The characterization of basins is instead based on direct observations of catchments geology, sedimentary features of DF deposits and on the characteristics of alluvial fans (morphology, sedimentology and architecture). In particular, the observed distinctive characteristics for each basin group are summarized as follows.

The G1 basins consist primarily of massive or coarsely stratified carbonate rocks, with average slope of 40°; they are characterized by a good production of clayey silt in loose material and the surficial deposits cover approximately the 30 % of the total area of the basin. The prevalent sedimentary processes are linked to CDF phenomena and to “Rudavoi” type depositional style. The G1 alluvial fans are definitely impressive compared to the feeding basins (fans are about 1/4 of the basins) and are characterized by regular geometry and gentle slope. In non-anthropized alluvial fans it is possible to observe lobes in central and distal areas, and levees in

Table 1 Characteristics of the three catchment lithology groups in the Western Alps (Modified after Tiranti et al. 2008)

Basin group	Fan/basin area (%)	Dominant processes	Main depositional style
1	>20	CDF	Rudavoi
2	5<	CDF	Grand Vallon
3	10<	N-CDF	Inferno – Grotto
Basin group	Triggering recurrence (years)	Minimum triggering rainfall type	Main triggering season
1	4	Storms of high intensity (>30 mm/h)	Late spring
2	1	Storms of moderate intensity (>20 mm/h)	Summer
3	>10	Alluvial events or supercell storms (>50 mm/h)	Autumn and spring (rarely in summer)

**Fig. 2** G1 (e.g. Rio Fosse), G2 (e.g. Rio Saint Draia), G3 (e.g. Rio Secco) alluvial fan geometry plans. The increase of fan slope is shown by the arrow length (Tiranti 2008)

the apex. The transition from levees-rich area to lobes-rich area is underlined by a gradual decrease of the fan slope from apex to toe (Fig. 2).

The G2 basins consist primarily of metamorphic rocks (foliated, fine-grained and phyllosilicates-rich), with average slope of 30°; they are characterized by an excellent production of clay or clay-like minerals in loose material and the surficial deposits cover approximately the 60 % of the total area of the basin. The prevalent sedimentary processes are linked to CDF phenomena and to “Grand Vallon” type depositional style. The G2 alluvial fans are much smaller than the feeding basins (average <5 %) and are characterized by moderate slope and an irregular geometry. In non-anthropized alluvial fans it is possible to observe the occurrence of a higher number of levees than lobes. The former are regularly distributed from apex to toe, near the main channel. As for the G1 alluvial fans, the longitudinal cross-section is regular (Fig. 2). The high cohesion of DF in the G2 is responsible of the small, starved-shape fans. In fact, it has been noted that thick DF deposits are present along and near the main channel at the high and intermediate sections of G2 basins.

The G3 basins consist primarily of massive and coarse-grained metamorphic rocks, with intermediate slope values between G1 and G2 basins (about 35°); cover deposits are smaller than in G2 (about 55 % of basin area). They are characterized by a poor production of clay or clay-like

minerals in loose material. The prevalent sedimentary processes are linked to N-CDF phenomena and to “Inferno” type depositional style with high magnitude, even if, without extreme rainfall, the examined torrents are characterized by prevailing “Grotto” type depositional style (bedload e watersheet deposits). G3 basins, characterized by prevalent Inferno type depositional style, have a relative small alluvial fan lobe-shaped (fan area/basin area <10 %), with high slope particularly in apex zone. A sharp change of debris size is evident from apex to central and distal fan area. Indeed, the larger boulders are concentrated in the apex as lobes and subordinated boulder-trains. From apex to toe, the boulders decrease while the heterogeneity of debris size increases in correspondence to more or less evident morphologic scarps (Fig. 2).

Numerical Modelling of Debris Flows

The propagation and deposition of debris flows in upper Susa Valley are simulated by a 3D numerical code based on Cellular Automata Method (Segre and Deangeli 1995; Deangeli 2008).

The numerical code was originally generated to analyze DFs in the inertial regime (Segre and Deangeli 1995) according to the solution of Takahashi (1978, 1991), based on the dilatant

Bagnold (1954) fluid constitutive law. A detailed description of the mathematical algorithms implemented in the code is reported in the papers of Segre and Deangeli (1995) and Deangeli (2008).

This model was successfully applied to analyse the evolutive behaviour of several actual granular flows, occurred in different settings and contexts (Deangeli and Grasso 1996; Deangeli and Giani 1998; Deangeli 2008).

In the present study the code has been improved and modified by the implementation of a visco-plastic rheology regime, according to the Bingham constitutive law. The choice of the constitutive law is still an open problem.

The behaviour of debris flow depends on many factors and the coexistence for a given event of different regimes during the runout phase has been observed (Deangeli 2008). The simulation of real cases suffers from the lack of direct observations and flow parameters measurements. Insights can be derived from the observations of flume experiments under controlled conditions. However these tests generally refer to idealized conditions.

According to the geological classification we have supposed different rheologies: if CDF are predominant we adopt a visco-plastic rheology, where we consider the mixture to behave as a Bingham fluid; if N-CDF are the main processes we assume the granular material to behave as a dilatant fluid in the grain inertia regime of Bagnold (1954). The initial volumes of loose material do not refer to a particular occurred event, but they have been estimated for each catchment on the basis of several past events, excluding very small phenomena. The values are hence representative of the investigated area and are free from subjective interpretations of an occurred phenomenon. The model parameters are then calibrated on the depositional style and fan architecture.

Results of Debris Flow Simulations by CA Model

The Cellular Automata (CA) model has been used to simulate debris flows in three different basins belonging to the three different groups: Rio Fosse (Bardonecchia)-Group 1, Rio Frejus (Bardonecchia)-Group 2 and Rio Secco (Salbertrand)-Group 3.

Rio Fosse

The Rio Fosse is a small basin extending over about an area of 1.40 km² characterized by a catchment lithology mainly formed by dolostones and limestones and subordinate calc-schists.

Generally debris flows occurring at the Rio Fosse, are initiated when the runoff is able to mobilize the coarser material deposited on the surface bed-sediment layer.

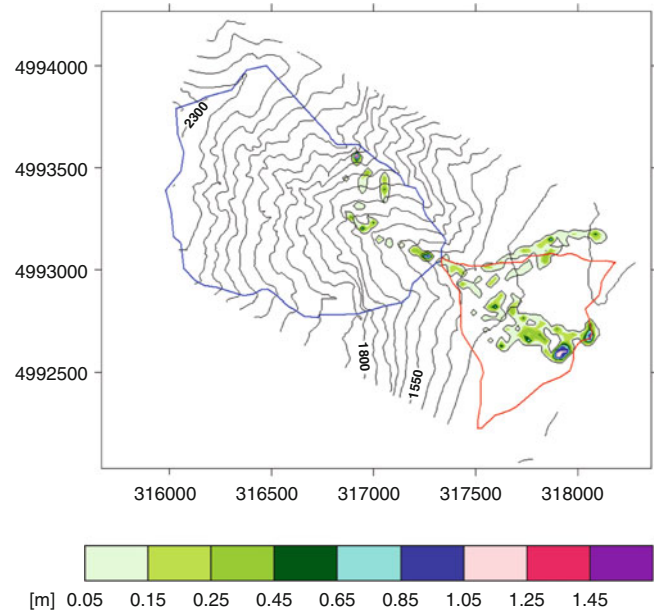


Fig. 3 Results of the numerical analysis of debris flows in the Rio Fosse basin. The *blue line* represents the contour of the watershed; the *red line* represents the contour of the alluvial fan

The surface layer is somehow armoured through the presence of winnowed partially open-work deposit that covers a clast-supported deposit formed by blocks and boulders in a gravel, sand, clayey-silt matrix. The mobilization of coarse sediments in the surface layer triggers the debris flow and the entrainment of underlying deposits is responsible of the cohesive behaviour of debris flows.

The simulations have been performed considering a saturated material and a mixture of mud and water as embedding fluid.

Exclusively for this basin, both the previously introduced rheologies have been adopted in the CA model. As a matter of fact, DFs along Rio Fosse could be characterized by a coexistence of different flow regimes, being the basin intermediate between Group 2 and Group 3 (respectively CDF and N-CDF) (Deangeli et al. 2011).

The results of the two types of simulations seem to indicate that the most appropriate constitutive law is the visco-plastic one as reported in Figs. 3 and 6a. In fact the modelling output shows a good agreement with the depositional style and the geometrical characteristics of alluvial fan typical of the Group 1 basins (wide and regular fan with a gradual decrease of the slope from apex to toe).

Rio Frejus

The Rio Frejus has a basin of about 22 km² and the Bardonecchia town is situated on its alluvial fan.

The Frejus basin is mostly composed by calc-schistes and characterized by an elevated density of active landslides

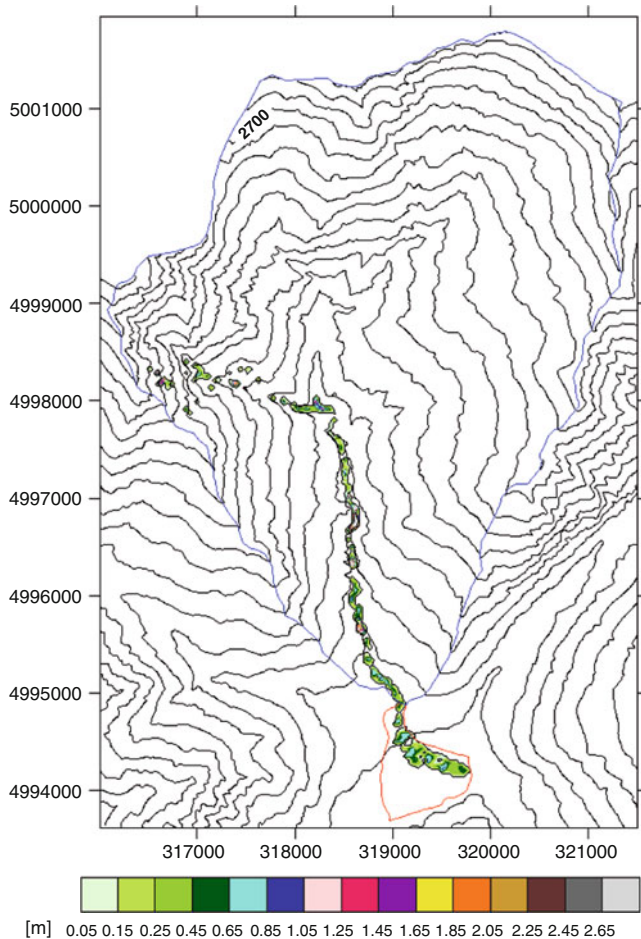


Fig. 4 Results of the numerical analysis of debris flows in the Rio Frejus basin. The *blue line* represents the contour of the watershed; the *red line* represents the contour of the alluvial fan

sometimes involving whole slopes (deep-seated gravitational slope deformations). The high frequency of debris flow phenomena is due to the debris abundance deposited in the stream channels.

The basin of the Rio Frejus is very extended and involves several tributaries in both right and left bank. The numerical modelling has considered only the contribution of Rio Gautier, because, historically, the highest number of DFs was originated along this basin. The watershed between the Rio Merdovine basin and the Rio Gautier basin exhibits large, mixed debris accumulations at the base of cliffs. These cliffs are affected by a high degree of fracturing and alteration. Along less steep slopes there are modest quantities of eluvial-colluvial cover (usually <2 m), where extensive shallow landslides and erosive phenomena can be observed (widespread rill erosion). Even inside the main channel bed there are large quantities of preserved debris flow deposits.

The numerical simulations have considered a saturated material. The basins of Group 2 are characterized by an

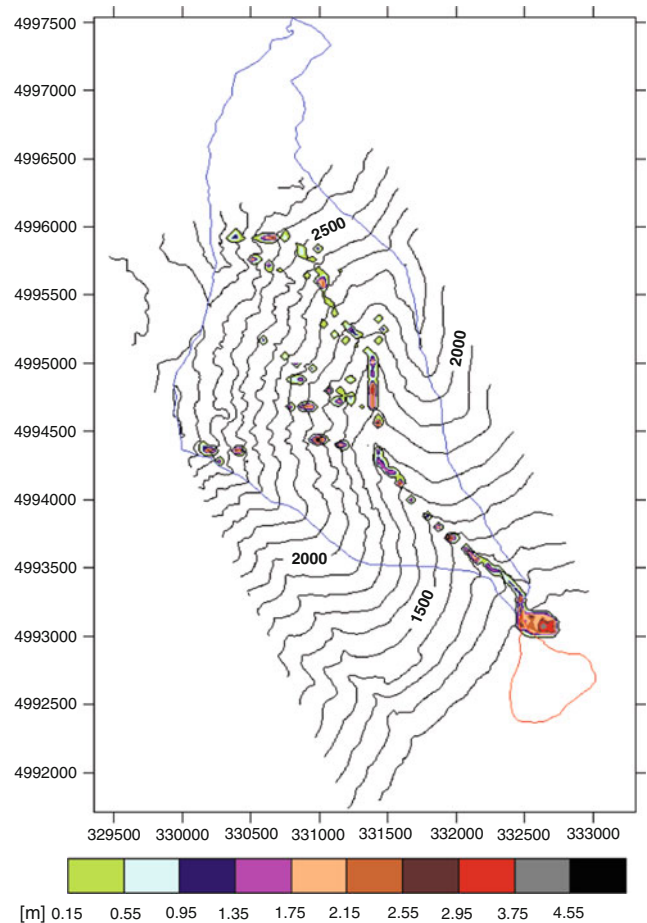


Fig. 5 Results of the numerical analysis of debris flows in the Rio Secco basin. The *blue line* represents the contour of the watershed; the *red line* represents the contour of the alluvial fan

excellent production of clay or clay-like minerals which should give rise to a more “viscous” DF than Group 1 ones.

As for the previous case the modelling results (Figs. 4 and 6b) seems to fulfil the deposition style observed in the geological classification, especially with respect to the alluvial fan geometry and the accumulated debris thickness. A very good agreement between numerical results and in situ observations has been obtained for the strong deposition of debris along the channel.

Rio Secco

The Rio Secco is located in Salbertrand municipality and extends over about an area of 4.85 km².

It is characterized by a catchment lithology mainly formed by gneiss and massive micashists, and, very subordinate dolostones and calc-schists. The source areas were identified with the abundant talus deposits distributed at

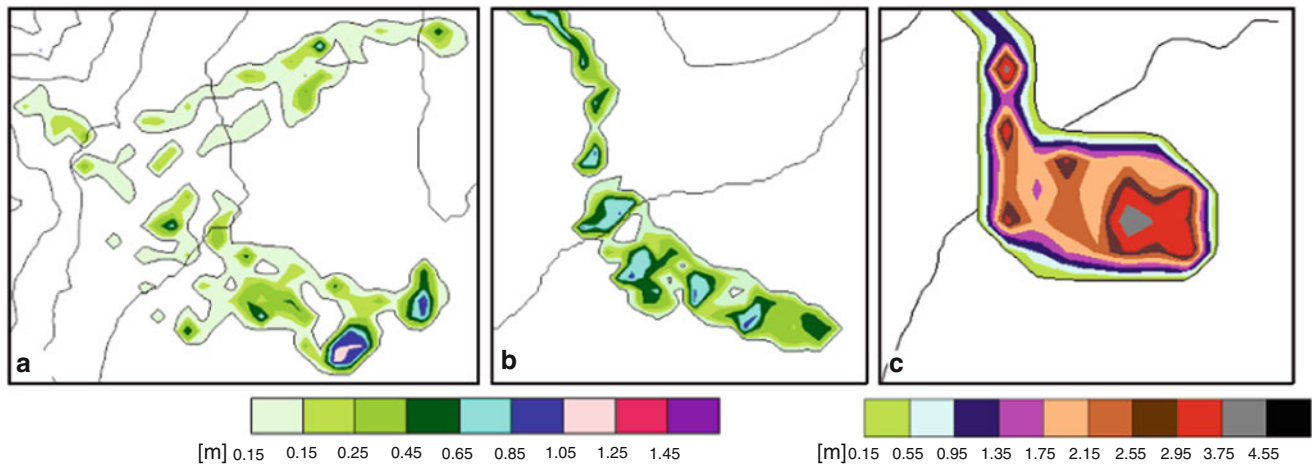


Fig. 6 Fan depositional areas of three test-basins obtained from numerical modelling ((a) Rio Fosse; (b) Rio Frejus; (c) Rio Secco)

basin head. These main source areas are characterized by a high presence of very coarse debris deposits, with open work structure, resting on very steep slopes. The mobilization of coarse sediments is possible only in presence of very extreme rainfalls.

The basins of Group 3 produce less fine fraction compared to Groups 1 and 2. The embedding fluid in this case is clear water. The material is assumed fully saturated.

A value of the friction angle between 30° and 40° has been adopted, being the Group 3 basins characterized by very coarse particles.

The results of the CA modelling (Figs. 5 and 6c) have emphasized again the similarities among the estimates of the geological model, the in situ observations regarding to the depositional style along the channel and the alluvial fan geometry (high slope particularly in apex zone).

Concluding Remarks

The proposed methodology is based on the link between a geological model for characterization of basins (lithology and depositional style) and a routing model. The methodology has been applied to three basins located in the North-western Alps, exhibiting different characteristics according to the geological model.

The paper has reported the results of the application of this comprehensive methodology for the analysis of debris flows, from the lithology of the bedrocks (source rocks) that gives rise to the loose material, to the propagation and deposition.

The choice of proper constitutive laws for the CA modelling has been based on the results of the interpretation of geological observations. The results of the numerical simulations have proved the reliability of the geological model for the investigated test-basins.

The initial volumes of loose material, used in the numerical models, do not refer to a particular occurred event, but they have been estimated for each catchment on the basis of several past events, excluding very small phenomena. The values are hence representative of the investigated area and are free from subjective interpretations of an occurred phenomenon. The model parameters have been then calibrated on the depositional style and fan architecture.

The results show a relatively good agreement with the observed debris flows events. Therefore the attempt of adopting a link between the bedrock lithological characteristics and sedimentary processes of the basins with a propagation model has supplied encouraging outcomes. The proposed methodology seems to be an appropriate tool for the set up of debris flow scenarios devoted to risk mitigation.

Acknowledgments This research was supported by PARAMount project of Alpine Space Programme of European Union (2-2-2-AT) – <http://www.paramount-project.eu/>.

References

- Ancey C (2007) Plasticity and geophysical flows: a review. *J Non-Newton Fluid Mech* 142:4–35
- Bagnold RA (1954) Experiments on a gravity-free dispersion of large solid spheres in a Newtonian fluid under shear. *Proc R Soc Lond A* 225:49–63
- Deangeli C, Grasso P (1996) The evolutive mechanism of debris flows: analysis and protection works. In: *Proceedings of 7th international symposium on landslides*, Balkema, Trondheim/Rotterdam, pp 1183–1188
- Deangeli C, Giani GP (1998) Physical and numerical models to rehabilitate a waste disposal site. In: *Proceedings of 8th international congress IAEG*, Balkema, Vancouver/Rotterdam, pp 1813–1818
- Deangeli C (2008) Laboratory granular flows generated by slope failures. *Rock Mech Rock Eng* 41(1):199–217
- Deangeli C, Gregoretti C, Paltrinieri E, Rabuffetti D, Tiranti D (2011) An integrated approach to simulate channelized debris flows from

- triggering to deposition. In: Proceedings of 5th international conference on debris-flow hazards mitigation: mechanics, prediction and assessment, University of Padua, Italy, 14–17 June 2011, pp 661–668.
- Moscariello A, Marchi L, Maraga F, Mortara G (2002) Alluvial fans in the Alps: sedimentary facies and processes. *Spec Publ Int Assoc Sedimentol* 32:141–166
- Segre E, Deangeli C (1995) Cellular automaton for realistic modelling of landslides. *Nonlinear Processes Geophys* 2(1):1–15
- Takahashi T (1978) Mechanical characteristics of debris flow. *J Hydraul Div* 104(8):1153–1169
- Takahashi T (1991) Debris flow, IAIR monograph. Balkema, Rotterdam
- Tiranti D (2008) The sediment gravity flows triggering mechanisms, evolution and sedimentary processes in Western Italian Alps. Ph.D. thesis, Department of Earth Sciences, University of Torino (Italy) and the Cambridge Quaternary, Department of Geography, University of Cambridge (UK), pp 100
- Tiranti D, Bonetto S, Mandrone G (2008) Quantitative basin characterization to refine debris-flow triggering criteria and processes: an example from the Italian Western Alps. *Landslides* 5(1):45–57



Stability Conditions and Evaluation of the Runout of a Potential Landslide at the Northern Flank of La Fossa Active Volcano, Italy

Maria Marsella, Aurora Salino, Silvia Scifoni, Alberico Sonnessa, and Paolo Tommasi

Abstract

This paper focuses on the quantitative investigations carried out to evaluate stability conditions of the northern flank of the *La Fossa* cone (Vulcano Island) and the consequent runout of the debris avalanche that would be generated by a possible failure. The contribution describes first the geological setting and the typical instability phenomena of the area. Then it illustrates how the global morphology of the flank was reconstructed by combining aerial photogrammetry and high resolution 3D surveying techniques such as terrestrial laser scanner. The resulting digital elevation model (DEM) permitted us to extract and measure structural and morphological elements that drive and influence past and potential instabilities. These elements were used to constrain limit equilibrium analyses (LE) that were used to estimate the volume of soil mass susceptible of failure. Strength parameters at large scale were obtained from laboratory tests, described in previous studies, and back analyses of a past failure whose geometry was reconstructed from the DEM. Finally, results of runout analyses of the debris avalanche are presented and discussed. Analyses were conducted by using DAN-W and DAN-3D codes which allowed an estimate of the maximum runout distance and extension of the accumulation zone with respect to the inhabited area.

Keywords

Active volcano • Landslide • Debris avalanche • Runout

Introduction

Instability phenomena frequently affect the flanks of active volcanic edifices. In many cases inhabited areas have progressively approached active unstable slopes, overlooking that the effects of the runout of the landslide mass on population, infrastructures and buildings can be even more significant than those of volcanic activity. In this respect failures are often missed in the record of event, especially

if the area has been inhabited in recent times or erosion has been so fast and intense to cancel signs of instability.

Major slope failures usually occur at the onset of volcanic phenomena and can be much faster and more unexpected than lava flows. Nevertheless, also during quiescent phases probability of failure is significant, especially when degassing activity increases (unrest periods) and contributes to weaken the volcano flanks. At coastal volcanoes a further risk is related to the tsunami waves that can be generated by the propagation of the landslide mass into the sea.

All these sources of hazard can be found at the active *La Fossa* cone in the northern part of the Island of Vulcano (Fig. 1). The last eruption was in 1899 while at present the activity is essentially hydrothermal with an intense degassing. On the contrary, during the last 30 years, the flanks of the cone were involved in a number of landslides.

M. Marsella (✉) • A. Salino • S. Scifoni • A. Sonnessa
Università di Roma “Sapienza”, Rome, Italy
e-mail: maria.marsella@uniroma1.it

P. Tommasi
Consiglio Nazionale delle Ricerche, Istituto di Geologia Ambientale
e Geingegneria, Rome, Italy

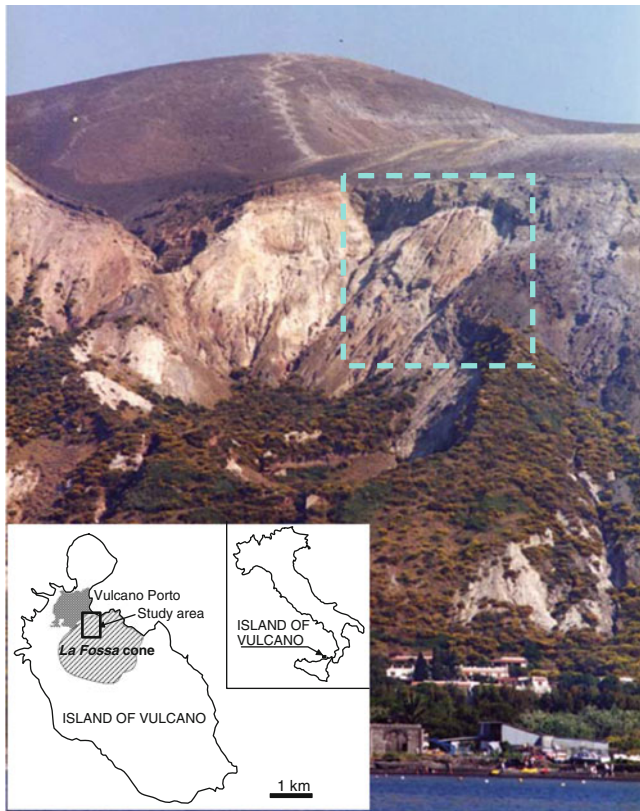


Fig. 1 Front view of the northern flank of the *La Fossa* cone, with the *Forgia Vecchia* crater in the foreground and the main crater in the background; in the box the location of the Vulcano Island with the study area are shown

In particular, on the northern flank the unstable area is delimited by tension cracks where high-temperature volcanic gases flow through. Since the slope overlooks the Vulcano Porto village, where most of resident population and touristic facilities are located, such a failure represents a major concern.

In the following sections, investigations carried out to set up a geotechnical model of the northern flank are described and the results obtained by stability and runout analyses are presented and considerations on risk assessment and alert levels are discussed.

Geology and Morphology

The subaerial part of the *La Fossa* edifice is a 400 m high pyroclastic cone with a base diameter of 1,200 m at sea level. The cone is regular as a whole, with the exception of the *Forgia Vecchia* (FG) parasite crater on the northern slope (Fig. 1). The cone overlies the materials filling the caldera generated by the collapse of the northern part of the island (Keller 1980).

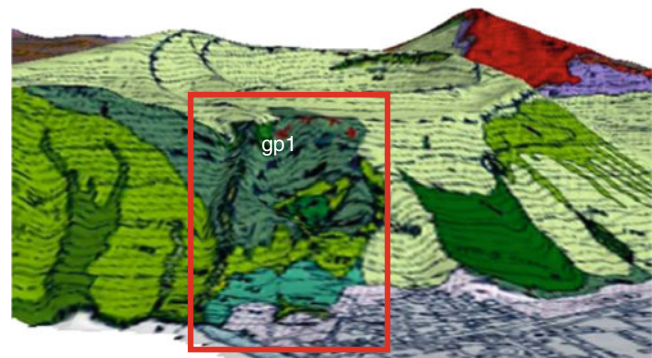


Fig. 2 3D view of the *La Fossa* cone with the geological units proposed by De Astis et al. (2006). Label “gp1” indicates varicoloured pyroclastites forming the FG crater margin

The unstable slope is located at the top of the northern flank, upslope from the *Forgia Vecchia* crater. The sequence of products (Dellino and La Volpe 1997, De Astis et al. 2006) is formed by a “core” consisting of a dry surge deposit (laminated sands) up to 150 m thick overlaid by coarse grained (gravel- to cobble-size) fall products with thin intercalations of sandy layers and by a lava flow closing the eruptive cycle. This sequence is covered up to the ground surface by a blanket of silty-sandy wet-surge varicoloured pyroclastites (gp1 in Fig. 2), up to 20 m thick, which are entirely involved in the instability process. Here the younger products were almost completely eroded (Fig. 2).

Volcanic Activity and Instability Phenomena

In the unstable area, continuous fumarolic activity through fractures has determined a diffuse mineralization, conferring a higher consistency to the pyroclastite which around fractures appears stiff and hard. Degassing, both concentrated along fractures and widespread over relatively large areas, displays recurrent periods of “unrest” characterized by larger vapour release.

Different types of instability were recognized on *La Fossa* cone (Tommasi et al. 2007). Far from paroxysmal phases, the events documented or recognizable by morphological evidences are slides along pyroclastite layers (up to 200,000 m³ in volume), sheet slides over the whole slope of the cone and slumps/topples on the northern flank.

The higher hazard is related to the slides in the pyroclastites in the eastern part of the cone facing the sea and to the failures occurring on the northern flank along the upper rim of the FG crater (Fig. 3). The former can induce tsunami waves propagating towards the harbour area (Porto di Levante) as it occurred in 1988. The latter can generate rock falls and debris avalanches which propagate over the area located just above the Vulcano Porto village.

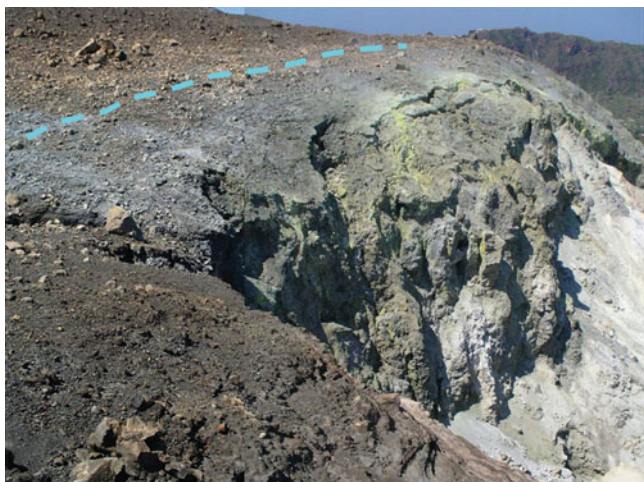


Fig. 3 Summit area of the northern flank of La Fossa Cone overlooking the Forgia Vecchia crater. The *dashed line* indicates a major tension fracture

Occurrence of these events is increased by seismic actions, inflation and pore pressure changes during the intensification of the volcanic activity.

The Forgia Vecchia Crater

Due to its position with respect to the inhabited area, instability phenomena at the upper FG crater rim are analyzed in the following sections.

In this sector of the cone the upper rim of the FG crater coincides with the top of the north-western flank. The uppermost part of the slope is subvertical. Proceeding downslope the gradient progressively decreases down to the lower rim of the crater, where the slope steepen again down to the cone base (Fig. 1).

The bottom of the crater represents an accumulation area of the material detached from the slope top.

The area, located on the western part of the FG crater (Figs. 1 and 3), presents the most apparent signs of active deformation and failures, highlighted by a set of tension cracks that winds parallel to the slope edge (Fig. 3). Two of them are persistent and gaping thus favouring the detachment of thick slices of material.

Available Data

In order to reconstruct the geometry of the slope, aerial photogrammetric data covering the whole island and terrestrial laser scanning data describing the steepest slopes were integrated.

Photogrammetric data were acquired during a GPS-aided survey conducted in 2001 and processed using a digital

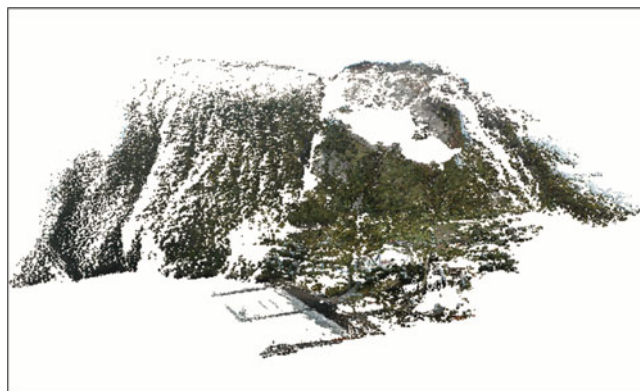


Fig. 4 Point cloud detected by terrestrial laser scanning

photogrammetric workstation. This allowed the generation of a 1 m grid Digital Elevation Model (DEM) and 1:500 scale orthophoto map (Baldi et al. 2000). The slope of an area influence the geomorphology and stability of a mountain flank. Therefore, we jointly analysed the 3D model of the slope overlapped to the most updated geological maps (De Astis et al. 2006) (Fig. 2).

The terrestrial laser scanning data were acquired during a survey conducted in 2009 at *Forgia Vecchia*. The laser points cloud dataset (Fig. 4) was filtered and processed to obtain 0.5 m grid DEM that was integrated with the 2001 DEM (Fig. 5).

In order to detect possible changes in the topography of the area, we analysed the residual map which describes the difference in Z value between the two DEMs (2009 DEM less 2001 DEM). The observed differences were explained by the presence or growth of vegetation, construction of new buildings and in few cases by extremely localized instabilities.

The DEMs were used to reconstruct the global morphology of the flank and to identify structural and morphological elements linked to past and possible future instabilities. Definition of the possible failure geometry was aided by the exact location of fractures formed behind the rim edge (partially visible on the orthophoto) through GPS data collected in 2006 (Fig. 6).

Location and Volume of the Potential Failure

The volume of the potential failure was considered to be equal to that mobilized by a landslide along the critical slip surface estimated through 3D limit equilibrium (LE) analyses. For the estimate of the potential failure, the slip surface was supposed to be the combination of the innermost tension crack and a roughly ellipsoidal surface. The choice of an ellipsoidal surface is supported by the relative homogeneity of the materials.

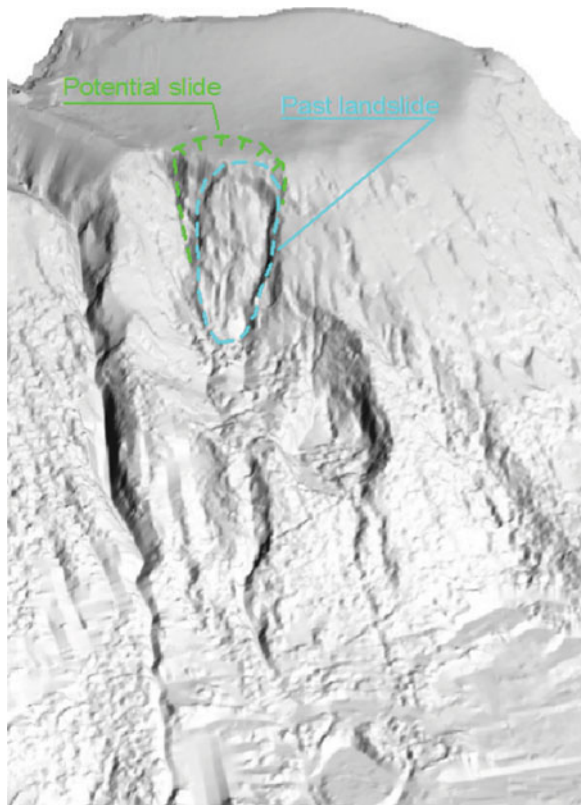


Fig. 5 Shaded relief of Forgia Vecchia zone obtained integrating the 2001 and 2009 DEMs. Area investigated through LE analyses are indicated

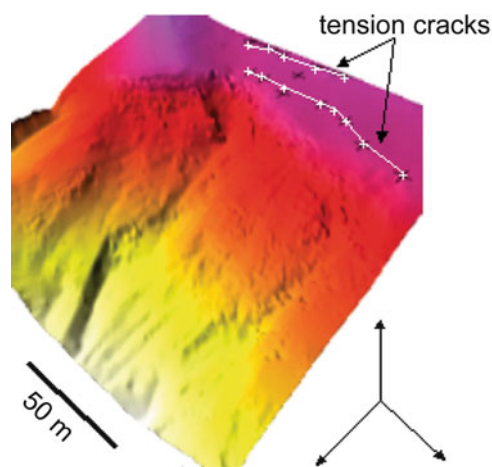


Fig. 6 Shaded relief view of DEM from 2001 photogrammetry survey and GPS points that identify tension fractures

Strength properties of the material introduced in LE analyses for estimating the potential critical failure surface were derived from laboratory tests on the varicoloured pyroclastites and on the basis of a back analysis of an old slump at the FG crater rim recognised by aerial photo interpretation. Its geometry was reconstructed by the

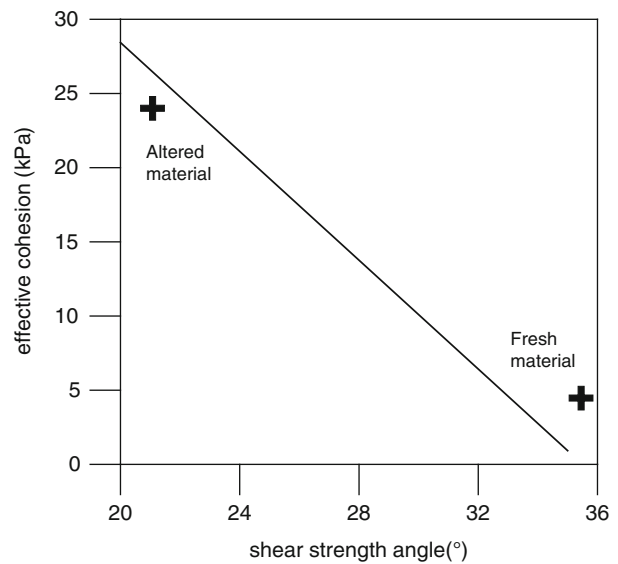


Fig. 7 Couples of c' - φ' data from back analyses and strength parameters obtained from laboratory tests on the varicoloured pyroclastites

high-resolution morphology depicted by the integrated DEM (Fig. 5). Back analyses were conducted through the CLARA-W code using the Bishop simplified method extended to three dimensions (Hungry 1987) in order to account for the particular morphology. Results are reported in Fig. 7: the envelope of the c' and φ' values lies between c' - φ' couples obtained from direct shear tests conducted by Tommasi et al. (2007) on altered (argillified) and fresh varicoloured pyroclastites. Since argillification was not observed at the FG margin, values closer to those of the fresh material were chosen ($c' = 5$ kPa, $\varphi' = 34^\circ$). Null pore pressures were introduced and the unit weight of the material was set equal to that of the samples of the varicoloured pyroclastite in natural conditions.

LE analyses for evaluating the critical failure surface and related slide volume were conducted with the same numerical procedure used for the back analyses. The volume of the slide along the critical slip surface is approximately $25,000 \text{ m}^3$.

Runout Analyses

Once the potential slide volume had been determined, dynamic analyses were carried out to evaluate maximum runout distance and path of the debris avalanche after failure.

Analyses were conducted both in two and three dimensions using the DAN-W and DAN3D codes which assimilate the avalanche mass to a fluid and are based on the integration of the St. Venant equation according to the formulations proposed by Hungry (1995) and McDougall and

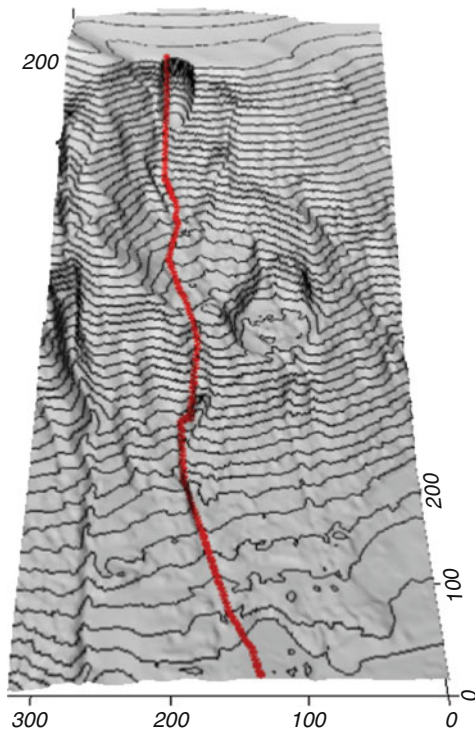


Fig. 8 Path used in 2D runout analyses

Hungr (2004), respectively. The internal dynamic behaviour of the mass is controlled by friction only whilst at the avalanche base both frictional and frictional/turbulent behaviour (Voellmy) rheology are envisaged.

Major uncertainties derived from the choice of the type of rheology and of related parameters because their estimate through back analysis of past avalanche events was not possible. In fact no reliable quantitative information on geometry and location of slope failures and related avalanche deposits was available. A literature research was therefore addressed towards back analyses of debris avalanches or similar phenomena in volcanic formations, possibly in dry conditions. The most similar case was the 2001 Las Colinas landslide which involved volcanic materials with a shear strength angle of 34° overlying a tuff bedrock. McDougall and Hungr (2004) found that the best agreement between calculated and actual path was found using a friction coefficient (μ) of 0.15 and a turbulence coefficient (ξ) equal to $1,000 \text{ m/s}^2$ with a Voellmy rheology, whilst the basal friction angle which best fits field observations was 12° .

Two-dimensional analyses were conducted by means of DAN-W along a conservative profile following the maximum elevation gradient (Fig. 8). In this case frictional rheology provided extremely high velocities and runout

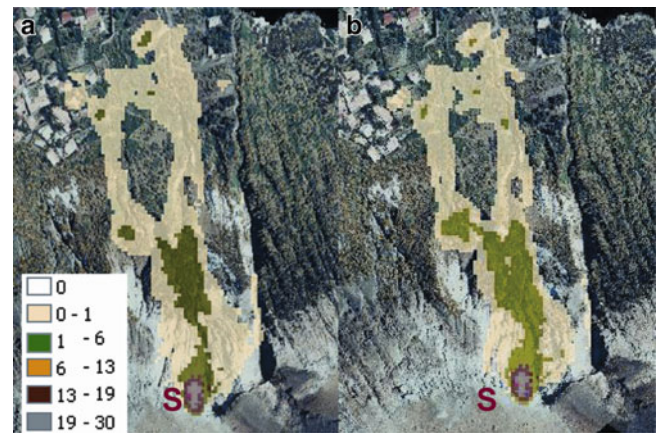


Fig. 9 Area invaded by slide debris using a Voellmy model with (a) $\mu = 0.12$ and $\xi = 500 \text{ m/s}^2$ or (b) $\mu = 0.15$ and $\xi = 1,000 \text{ m/s}^2$. On the left thickness in metres of the final landslide deposit are displayed. The source area is marked with an “S”

distances. Application of Voellmy rheology resulted in more realistic maximum velocities (31 m/s).

Adopting a 3D approach, the influence of the three-dimensional morphology has a marked influence on the runout of a purely frictional slide mass: this is entirely captured by the FG crater which acts as a natural barrier. If a Voellmy rheology is applied, the slide mass overrides the lower FG crater rim and owns sufficient energy to reach the inhabited area. In this case runout distances does not vary significantly when μ and ξ pass from 0.12 to 0.15 and from 1,000 to 500 respectively (Fig. 9). This result could be again explained by the greater influence of the pronounced convex morphology of the FG crater on the frictional component.

The frictional rheology could be more realistic if the sliding mass would remain dry during the path. A Voellmy rheology could better depict the dynamic behaviour of the avalanche if soon after the detachment, wet material, deposited in the crater, would be entrained by the moving mass, especially if the crater shape would channelize the flow (Ayotte and Hungr 2000).

Conclusions

Quantitative assessment of the landslide hazard and consequently of the risk in the northern part of the Island of Vulcano poses a number of problems which can be only partially overcome through investigations and geotechnical analyses. At Vulcano Island consequences of failure are mainly related to the area overlooked by the slope of the La Fossa cone, which has been progressively urbanized during the last 20 years. In fact the slope is neither inhabited nor crossed by footpaths directed to the excursion area at the

top of the main crater. This entails that runout estimate is the main concern.

A major improvement in the quantitative description of the slope surface, to be utilized in stability and runout analysis, has been introduced by increasing the quality of the photogrammetric digital model by merging it with a terrestrial laser scanner survey. This allowed: (1) the recognition and exact location of structural and morphological evidences of past and possible failures (which aided back- and predictive slope stability analyses); (2) a better definition of morphology for runout analyses. In particular the first issue was instrumental in evaluating operative strength of a partially and not homogeneously altered pyroclastic material and in assessing the volume of the potential critical failure at the slope top.

Major uncertainties remain on the evaluation of the maximum runout distance even though DAN3D analyses were conducted with rheological parameters obtained by other Authors from back analyses of avalanche/flows in volcanoclastic materials. In particular the choice of the rheology is determinant for assessing if the avalanche may reach or not the inhabited area. An aid to switch from frictional to Voellmy rheology could come from investigation on thickness and moisture conditions of the debris deposit filling the FG crater.

These considerations deserve further runout analyses with other methods and highlight the importance of a continuous monitoring of the source area in order to detect acceleration of deformations at the slope top in

time for alerting authorities in charge of civil protection procedures.

References

- Ayotte D, Hungr O (2000) Calibration of a runout prediction model for debris-flows and avalanches. In: Wiczorek GF, Naeser ND (eds) Proceedings of the 2nd international conference on debris-flow hazards mitigation, Taipei, pp 505–514
- Baldi P, Bonvalot S, Briole P, Marsella M (2000) Digital photogrammetry and kinematic GPS applied to the monitoring of Vulcano Island, Aeolian Arc, Italy. *Geophys J Int* 142:801–811. doi: [10.1046/j.1365-246x.2000.00194x](https://doi.org/10.1046/j.1365-246x.2000.00194x)
- De Astis G, Dellino P, La Volpe L, Lucchi F, Tranne CA (2006) Carta Geologica dell'Isola di Vulcano 1:10000. De Astis G, La Volpe L (eds) *Litografia Artistica Cartografica*. Firenze
- Dellino P, La Volpe L (1997) Stratigrafia, dinamiche eruttive e deposizionali, scenario eruttivo e valutazioni di pericolosità a La Fossa di Vulcano. In: La Volpe L, Dellino P, Nuccio PM, Privitera E and Sbrana A (eds), *Progetto Vulcano – Risultati delle attività di ricerca 1993–1995*, Felici Editore, Pisa, pp 214–237
- Hungr O (1987) An extension of Bishop's simplified method of slope stability analysis to three dimensions. *Geotechnique* 37:113–117
- Hungr O (1995) A model for the runout analysis of rapid flow slides, debris flows and avalanches. *Can Geotech J* 32(4):610–623
- Keller J (1980) The island of Vulcano. *Rendiconti Società di Mineralogia e Petrologia* 36(1):369–414
- McDougall S, Hungr O (2004) A model for the analysis of rapid landslide motion across three-dimensional terrain. *Can Geotech J* 41(6):1084–1097. doi:[10.1139/t04-052](https://doi.org/10.1139/t04-052)
- Tommasi P, Graziani A, Rotonda T, Bevivino C (2007) Preliminary analysis of instability phenomena at Vulcano Island, Italy. In: Malheiro AM, Nunes JC (eds) *Volcanic rocks*. Taylor & Francis, London. ISBN 978-0-415-45140-6, pp 147–154



Analysis and Uncertainty Quantification of Dynamic Run-Out Model Parameters for Landslides

B. Quan Luna, J. Cepeda, A. Stumpf, C.J. van Westen, A. Remaître, J.-P. Malet, and T.W.J. van Asch

Abstract

The main goals of landslide run-out modeling should be the assessment of future landslide activity with a range of potential scenarios, and the information of the local populations about the hazards in order to enable informed response measures. In recent times, numerical dynamic run-out models have been developed which can assess the velocity and extent of motion of rapid landslides such as debris flows and avalanches, flow slides and rock avalanches. These models are physically-based and solved numerically, simulating the movement of the flow using constitutive laws of fluid mechanics in one or two dimensions. Resistance parameters and release volumes are crucial for a realistic simulation of the landslide behavior, whereas it is generally difficult to measure them directly in the field. Uncertainties in the parameterization of these models yield many uncertainties concerning their frequency values, which must be addressed in a proper risk assessment. Based on the probability density functions of release volumes and friction coefficients of a given landslide model, this work aims to systematically quantify the uncertainties in the run-out modeling. The obtained distributions can be used as an input for a probabilistic methodology where the uncertainties in the release volume and friction coefficients (rheological parameters) inside the dynamic models can be addressed. This will improve the confidence of the dynamic run-out model outputs such as the distribution of deposits in the run-out area, velocities and impact pressures, important components for a risk analysis and regulatory zoning.

Keywords

Run-out • Uncertainty • Landslides

B.Q. Luna (✉) • C.J. van Westen
United Nations University – School for Disaster Geo-information
Management ITC, University of Twente, Enschede, The Netherlands
e-mail: quanluna@itc.nl

J. Cepeda
Norwegian Geotechnical Institute (NGI), Oslo, Norway

A. Stumpf • A. Remaître • J.-P. Malet
School and Observatory of Earth Sciences CNRS, University of
Strasbourg, Strasbourg, France

T.W.J. van Asch
Faculty of Geosciences, Utrecht University, Utrecht, the Netherlands

Introduction

Numerical dynamic models of different complexities have been developed for modeling the behavior and physical properties of fluid-like geomorphological processes. The practical use of these models is mainly to assess the reach and impact forces of the flows for the design of mitigation measures (deflection or catching dams) and the creation of hazard maps. Dynamic models use constitutive laws of solid and fluid mechanics and apply physical laws to calculate the flow run-out in one (1-D) or two (2-D) dimensions in a determined topography array. One dimensional (1-D) models are usually lumped-mass models and can be used in case

of debris flows which are confined in gullies. In this case the 1-D flow path is well known. The 2-D models are able to simulate unconfined debris flows and to predict the 2D extension on alluvial fans. The 2-D models can route the flow over irregular topographic terrains. They need however an accurate and detailed digital elevation model (DEM) (Hürlimann et al. 2007). Most 2-D models are based on a “continuum approach” where the bulk behavior of the simulated flowing mass can approximate to the expected bulk behavior of the real mixture of the solid and fluid phases (Hungr and McDougall 2009). Continuum models solve the conservation equations of mass and momentum and are often applied through a depth-averaged approach that integrates the internal stresses in either vertical or bed-normal directions to obtain a form of Saint-Venant equations (shallow water assumption) (van Asch et al. 2007). The depth-averaged shallow water equation approach using different solvers has been applied commonly for numerical simulations of rapid mass movements over complex topographies (e.g., Iverson and Denlinger 2001; Pitman and Le 2005; Pudasaini and Hutter 2007). Depth averaging allows representing the rheology of the flow as a single term that expresses the frictional forces that interact at the interface between the flow and the bed path. One of the most common type of rheology frequently used in the dynamic models is the frictional-turbulent “Voellmy” resistance proposed initially for snow avalanches (Voellmy 1955) and used for granular cohesionless material with or without the presence of a pore fluid. This model predicts a terminal velocity that scales as the square root of the flow height.

The goal of this study was to analyze the previous work done by other authors regarding the calibration of the Voellmy model according to past events of different types of rapid gravity flows that can hint a range of values of the rheological parameters. This can be defined by probability density functions that can be later used for further stochastic analysis of the models.

The Voellmy Rheology

This model features a velocity-squared resistance term (turbulent coefficient ξ) similar to the Chezy resistance for turbulent water flow in open channels and a Coulomb-like friction (apparent friction coefficient μ). Today, the values of these parameters are still the subject of research. The model assumptions are incompressibility of the flow along the whole path; constant discharge and small variations of flow height along the track; and non-steady quasi-rigid body movement both in the starting and the run-out zone. Voellmy (1955) established this model using a fundamental hydraulic theory with two resistive force contributions, one in which the shear force is proportional to the normal

force (μ) and the other of viscous type, in which the drag is assumed proportional to the velocity squared (ξ). The friction slope for a Voellmy fluid is (1):

$$S_f = \mu \cos \psi + \frac{U^2}{\xi h} \quad (1)$$

where, S_f is the friction slope, μ is the apparent friction coefficient, ϕ the friction angle, U is the flow velocity and ξ is the turbulent coefficient (m/s^2). The parameters μ and ξ are constants whose magnitudes depend, respectively, on the flow properties and the roughness of the flow surface (Christen et al. 2010). Revellino et al. in 2004 gives a thorough explanation of the advantages of using the Voellmy model for analyzing flows. The model treats the liquefied granular material is treated as a frictional fluid with a constant pore-pressure ratio. This assumption produces the first term, the friction constant μ , being the tangent of the dynamic effective friction angle. The second term accounts for an expected increase of the resisting stress as a result of increasing velocity. The velocity value is squared, similar as in a flow which is rheologically similar to a turbulent flow. The use of the turbulent coefficient can be explained by the experimental finding of Bagnold in 1954 where the resisting shear stress in a fully inertial flow of grain dispersion at constant volume varies with the square of velocity.

Various authors have used the Voellmy model to simulate the run-out from extreme avalanches and have calibrated the friction coefficients for past events (Hungr and McDougall 2009; McKinnon et al. 2008; McDougall and Hungr 2005). Their findings shows that the Voellmy model gives better results in terms of velocity distributions and the location and thickness of deposits than other rheologies normally used in modeling flows (i.e. Bingham, Frictional).

Database Compilation and Parametric Analysis of the Voellmy Model

To model and simulate flow behavior and physical characteristics of an event and the different phenomena that happen during the occurrence of an event (i.e. erosion, layering) can be a difficult task. The complexity of the flow processes and its activity are tried to be characterized by a rheological model; that generalizes the flow as a single phase mixture with representative friction parameters. Currently, there is no standard procedure to determine the rheological parameters that can characterize the solid-fluid mixture. Dynamic model friction coefficients can not or are very cumbersome to be measured directly in the field. They are usually determined by back-calibration to reproduce a well documented past event run-out. The resulting modeled velocities and depths can be used to calculate

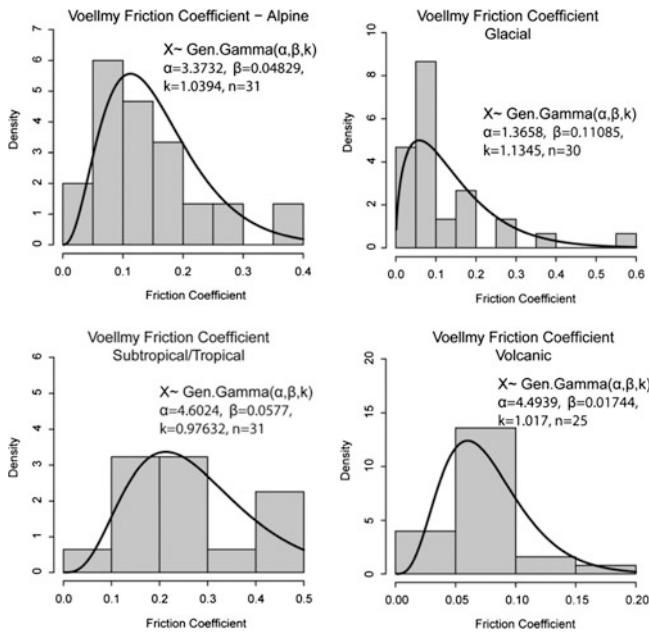


Fig. 1 Best-fitting gamma functions for the friction coefficients of events in the four environmental classes

in detail the impact pressures in the run-out zone. Back-analyses of past-events are the most common practice for estimating friction coefficients. The parameters are iteratively altered until the model results demonstrate a fit with the past field observations. A further source of uncertainties arises from the back analysis itself, whereas existing models use different numerical schemes to approximate a solution of the governing equations. Back-analysis can be problematic in many cases where there is no information on the behavior of the flow, making difficult to define and select the correct rheological parameters. Another approach for estimating friction coefficients can be obtained from modeling flows in similar or close by topography. Uncertainty in the release mass and friction coefficients can be simulated with dynamic models, improving confidence in the runout, impact pressures and return intervals. Also, various scenarios can be modeled to see which yields reliable impact pressures for a given position in the runout zone. This can be the starting point to establish probability-density functions that may provide a starting point to better estimate ranges where the data situation is poor (Brunetti et al. 2010).

As a first step towards a stochastic analysis of ranges and uncertainties of model parameters and their effects on run-out modeling we began with the compilation of a database from past-analyzed events. At present it includes a number of 270 past events, with observations on process types, volumes, run-out behaviors, rock-types, etc. and rheological parameters derived from model back-calibration of past events. The database was compiled from peer-reviewed literature and unpublished material of all collaborators. The database was divided in simulations using the

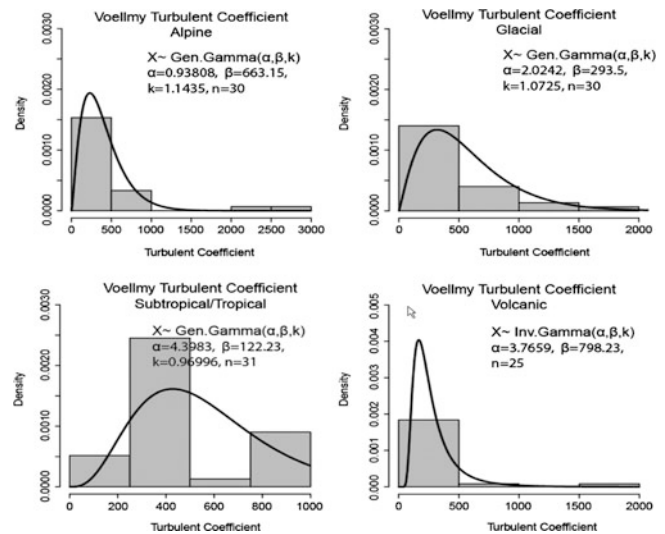


Fig. 2 Best-fitting gamma functions for the turbulent coefficients of events in the four environmental classes

Voellmy model regarding the type of movement (debris flows and rock avalanches) and their environment (alpine, glacial, tropical/subtropical and volcanic).

Probability Density Functions

Numerous studies on the statistical properties of landslide inventories have demonstrated that the probability distribution of landslide areas and volumes can be approximated by heavily-tailed PDFs (e.g. Hovius et al. 1997; Malamud et al 2004; Guzzetti et al. 2002; Antiano and Gosse 2009; Stark and Guzzetti 2009; Brunetti et al. 2010). Power law distributions of those parameters can be observed for historical inventories as well as for event-based inventories mapped directly after regional triggering events.

Assuming that power-law scaling may determine the probability distribution of other physical factors in a similar fashion it was investigated if the turbulent coefficient and the friction coefficient can be approximated with heavily-tailed PDFs. Thirty-three different functions including Weibul, Frechet, Levy, Pareto, Burr and Gamma and other commonly used PDFs were tested approximate probability distributions of the coefficients in the database. The underlying physical model constrains the coefficients to positive values and suggests sharply decreasing probabilities for very small friction and turbulent coefficient approaching zero. All PDFs which were not fulfilling those criteria were disregarded and the remaining solution where compared according to their goodness of fit.

Figures 1, 2, and 3 shows a family of Gamma functions which consistently provided a reasonable approximation of the probability distributions. In most cases the generalized

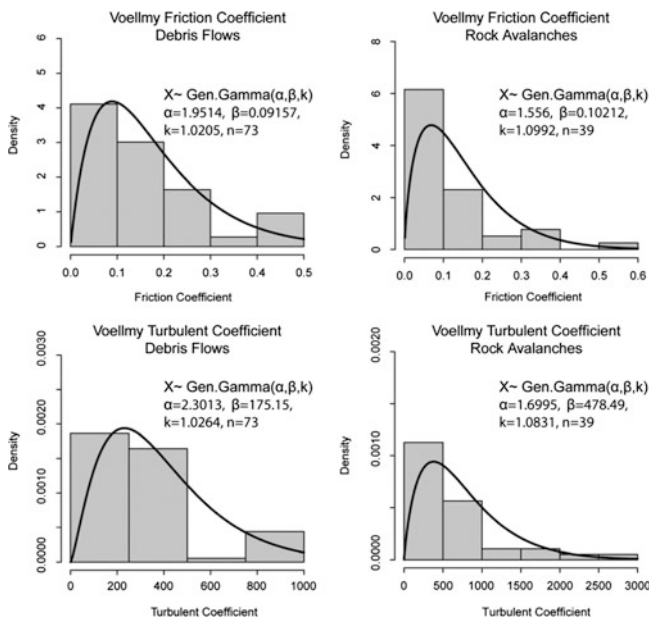


Fig. 3 Comparison between the best-fitting gamma functions for the turbulent coefficients and friction coefficients of debris flows and rock avalanches within the data base

form of the gamma function demonstrated better fit than the closely related Inverse Gamma function, whereas the Inverse Gamma function can be adopted if the generalized form returns non-zero probability densities for coefficient values equal zero (Fig. 2).

Conclusions

Uncertainty in the calculation of run-out estimates from dynamic models are mainly due to simplifications and uncertainty involving equations of flow including depth averaging, and the friction coefficients. Some of the uncertainty can be simulated, increasing the confidence in estimates of extreme runout. The resulting probability density functions obtained can be used as an input for a probabilistic methodology where the uncertainties in the release volume and friction coefficients (rheological parameters) inside the dynamic models can be addressed. This will improve the confidence of the dynamic run-out model outputs such as the distribution of deposits in the run-out area, velocities and impact pressures, important components for a risk analysis and regulatory zoning.

References

- Antiano JL, Gosse J (2009) Large rockslides in the Southern Central Andes of Chile (32–34.5°S): tectonic control and significance for quaternary landscape evolution. *Geomorphology* 104(3–4):117–133
- Bagnold RA (1954) Experiments on a gravity-free dispersion of large solid spheres in a Newtonian fluid under shear. *Proc R Soc Lond Ser A* 255:49–63
- Brunetti MT, Peruccacci S, Rossi M, Luciani S, Valigi D, Guzzetti F (2010) Rainfall thresholds for the possible occurrence of landslides in Italy. *Nat Hazards Earth Syst Sci* 10(3):447–458
- Christen M, Kowalski J, Bartelt P (2010) RAMMS: numerical simulation of dense snow avalanches in three-dimensional terrain. *Cold Reg Sci Technol* 63:1–14
- Guzzetti F, Malamud BD, Turcotte DL, Reichenbach P (2002) Power-law correlations of landslide areas in central Italy. *Earth Planet Sci Lett* 195(3–4):169–183
- Hovius N, Stark CP, Allen PA (1997) Sediment flux from a mountain belt derived by landslide mapping. *Geology* 25(3):231–234
- Hungr O, McDougall S (2009) Two numerical models for landslide dynamic analysis. *Comput Geosci* 35:978–992
- Hürlimann M, Medina V, Bateman A, Copons R, Altimir J (2007) Comparison of different techniques to analyse the mobility of debris flows during hazard assessment-Case study in La Comella catchment, Andorra. In: Chen C-I, Majors JJ (eds) *Debris-flow hazard mitigation: mechanics, prediction and assessment*. Millpress, Netherlands, pp 411–422
- Iverson RM, Denlinger RP (2001) Flow of variably fluidized granular masses across three-dimensional terrain. 1. Coulomb mixture theory. *J Geophys Res* 106:537–552
- Malamud BD, Turcotte DL, Guzzetti F, Reichenbach P (2004) Landslide inventories and their statistical properties. *Earth Surf Proc Land* 29(6):687–711
- McDougall S, Hungr O (2005) Dynamic modelling of entrainment in rapid landslides. *Can Geotech J* 42:1437–1448
- McKinnon M, Hungr O, McDougall S (2008) Dynamic analyses of Canadian landslides. In: Locat J, Perret D, Turmel D, Demers D and Leroueil S (eds) *Proceedings of the 4th Canadian conference on geohazards: from causes to management*, Presse de l'Université Laval, Québec, 594p
- Pitman BE, Le L (2005) A two-fluid model for avalanche and debris flow. *Phil Trans R Soc A* 363:1573–1601
- Pudasaini SP, Hutter K (2007) *Avalanche dynamics – dynamics of rapid flows of dense granular avalanches*. Springer, Berlin
- Revellino P, Hungr O, Guadagno FM, Evans SG (2004) Velocity and runout simulation of destructive debris flows and debris avalanches in pyroclastic deposits, Campania Region, Italy. *Environ Geol* 45:295–311
- Stark CP, Guzzetti F (2009) Landslide rupture and the probability distribution of mobilized debris volumes. *J Geophys Res* 114 (F00A02), doi:[10.1029/2008JF001008](https://doi.org/10.1029/2008JF001008)
- van Asch TWJ, Malet J-P, van Beek LPH, Amitrano D (2007) Techniques, issues and advances in numerical modelling of landslide hazard. *Bull Soc Géol Fr* 178(2):65–88
- Voellmy A (1955) Über die Zerstorungskraft von Lawinen (On breaking force of avalanches). *Schweizerische Bauzeitung* 73:212–285



Effects of Grain-Size Composition Examined in Laboratory and Numerical Tests on Artificial Mud-Flows

Simonetta Cola, Nancy Calabrò, Paolo Simonini, and Manuel Pastor

Abstract

This paper deals with a laboratory and numerical research on mudflows performed in with the aim to study the interrelations between the grain-size composition of the mud and its rheological properties at different solid concentrations. Furthermore, the predicting capability of a new numerical model in reproducing the flow of viscous materials is evaluated.

Keywords

Mudflows • Viscous materials • Run-out model • Grain-size composition

Introduction

Mudflows, or more generally earth-flows, represent a permanent hazard in large part of Italian territory. A clear understanding of these phenomena is required to analyse landslides risk and to optimize slope stabilisation strategies. The risk strictly depends on the run-out, magnitude and displacement rate of mudflows. Particularly, the rate, ranging between some mm/y and some tens of m/s, is the key factor for risk assessment.

The distinctive features of mudflow are related to the slope morphology and the physical and rheological properties of the involved materials, which are responsible for their long travel distances (up to tens of kilometres) and the high velocities they may attain. Among these factors, the most relevant are the geotechnical soil properties (water content, grain size, plasticity properties, etc.).

In the last 20 years, researchers have developed a number of new sophisticated numerical models for the propagation prediction in the framework of the continuum and discrete element mechanics. These models hypothesis that for many

flow-like landslides the average depths are small in comparison with their length or width: in these conditions it is possible to simplify the 3D propagation model by integrating its equations along the vertical axis. The resulting 2D depth-integrated model presents an excellent combination of accuracy and simplicity, providing information about propagation, such as velocity or depth of the flow along the path. For instance, Hutter and his co-workers (Savage and Hutter 1991; Hutter and Koch 1991) or Laigle and Coussot (1997) have successfully used some depth-integrated models to model flow-like landslides.

Recently, Cola et al. (2008) analysed the propagation of Tessina earth-flow (Fig. 1) with a depth-integrated SPH model (Pastor et al. 2008). This model integrates a 2D propagation model with the method of *Smoothed Particle Hydro-dynamics*, SPH, a new integration approach separately proposed by Lucy (1977) and Gingold and Monaghan (1977).

In their work, Cola et al. described the rheological behavior of the soil involved in Tessina earth-flow by means of the Bingham model, with parameters calibrated on tests performed on the soil fine fraction only. They evidenced the important role played by the viscosity on the predicted propagation and the need for rheological parameters calibrated on the behavior of entire soil for a more reliable prediction of real events. At the same time, they showed the importance of checking the numerical

S. Cola (✉) • N. Calabrò • P. Simonini
Università di Padova, Dip. Image, Via Ognissanti 39, 35129 Padova,
Italy
e-mail: simonetta.cola@unipd.it

M. Pastor
Politécnica de Madrid, Madrid, Spain



Fig. 1 View of Tessina landslide and sampling location

model reliability on the base of well-documented flow phenomena, condition seldom if ever verified.

Tests on small-scale physical model represent an alternative powerful tool for investigating the mudflow behaviour in controlled conditions, allowing high precision monitoring of important features, such as the advancing rate of the mud wave or the thickness of the tongue, and, at the same time, permitting to evaluate the influence of soil properties on the propagation process. Finally, the knowledge gained by laboratory tests may be used to validate, improve and calibrate numerical models describing this kind of phenomena.

This paper describes an experimental research carried out at the University of Padova on small artificial mudflows and the following calibration activity for the assessment of the new SPH model.

Testing Program

Experimental tests were performed on three remoulded samples obtained from material collected at the toe of the large Tessina mudflow (Belluno, Italy), along the closing channel near Funes village (Fig. 1).

The in-situ material originates from the alteration of in-situ rocks, mainly Flysch rock composed by alternating layers of hard limestone and weak siltstone. This is evident from the grain-size curve (Fig. 2) showing two distinct portions within the majority of soil gathers: a coarse fraction, constituted by limestone fragments and retained on n.40 ASTM sieve, and the remaining fine fraction, originated from the breaking up of the highest silt content layers. The fine fraction, or matrix, is medium-low plasticity inorganic clay with average liquid and plastic limits equal to 39 and 19 respectively.

The rheological behaviour of the fine fraction was investigated by means of tests with the FANN V-G

rheometer, determining the shear stress in steady state condition at 300 and 600 r/min, and interpreting the readings with the Bingham law. The Bingham viscosity μ_b and the yield strength τ_c were determined for a solid concentration varying from 20 % to 35 % (Fig. 3). According to previous researches (O'Brien and Julien 1988; Major and Pierson 1992; Coussot and Piau 1994), μ_b and τ_c depend on solid concentration by exponential laws, which, in this case, turn out to be as follows:

$$\tau_c = 0.268e^{17.5c_v} \quad (1)$$

$$\mu_b = 5.6 \cdot 10^{-4} e^{12.7c_v} \quad (2)$$

with the solid concentration c_v defined as:

$$c_v = \frac{V_s}{V_T} \cdot 100 = \frac{1}{1 + G_S W} \quad (3)$$

being V_s the solid fraction volume, V_T the total volume of the sample, G_S the specific gravity of the soil particles and W the water content.

In the narrow analyzed range, the yield strength and plastic viscosity vary significantly, rising from 10 to 140 Pa and from 0.002 to 0.08 Pa·s respectively.

Two rectangular metallic planes (50 × 100 cm) laid in series (Fig. 4) constituted the experimental apparatus for reproducing mudflows. The first plane, set up with a 30° dip angle, was roughened by medium-fine sand glued on the surface; the second was smooth and horizontal to halt the flow. A Plexiglas box, having a facing gate and two triangular sides (7 × 14 × 12 cm), spaced out of 15 cm, was fixed on the top of the inclined plane and contained a 636.5 cm³ sample of soil before the test beginning. In order to minimize the material adhesion on the Plexiglas walls, the internal faces were lubricated with Teflon oil.

A digital camera placed above the experimental apparatus, at a 90° angle to the oblique plane, acquired photos of the running mud at a rate of 20 fps and permitted to accurately follow the movements of the soil after the manual lifting of the gate.

To analyze the effect of soil composition on the mudflow run-out three kinds of material were tested, all of them obtained removing or substituting the coarsest particles in the original soil (Fig. 2). According to the aforementioned definition of fine fraction, the compositions of the examined materials were:

- A – 100 % of fine fraction;
- B – 90.5 % of fine fraction and 9.5 % of sandy fraction (portion passing the n.7 ASTM sieve and retained on n.40 ASTM sieve);
- C – 57 % of fine fraction and 43 % of sandy fraction.

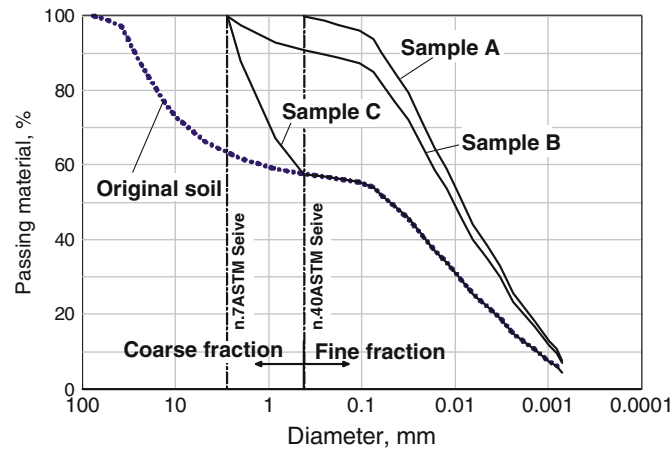


Fig. 2 Grain size distribution of sample collected in Tessina earth-flow and of recomposed samples

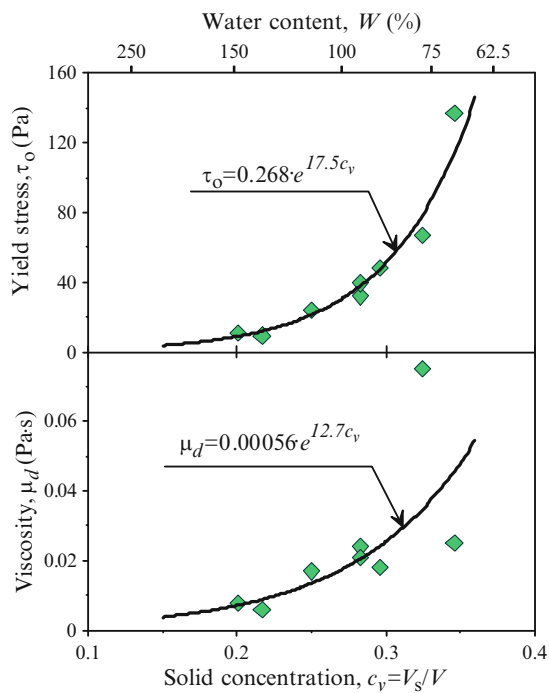


Fig. 3 Bingham yielding stress and viscosity versus solid concentration for the fine fraction of mud (data from two soils)

Since the water content affects both the matrix and global consistences, the samples A, B and C were prepared at a 54–70 % of the fine fraction or matrix water content W_f , defined as:

$$W_f = \frac{P_W}{P_{s,FF}} \cdot 100 \tag{4}$$

where P_W is the water weight and $P_{s,FF}$ the dried weight of the fine fraction.

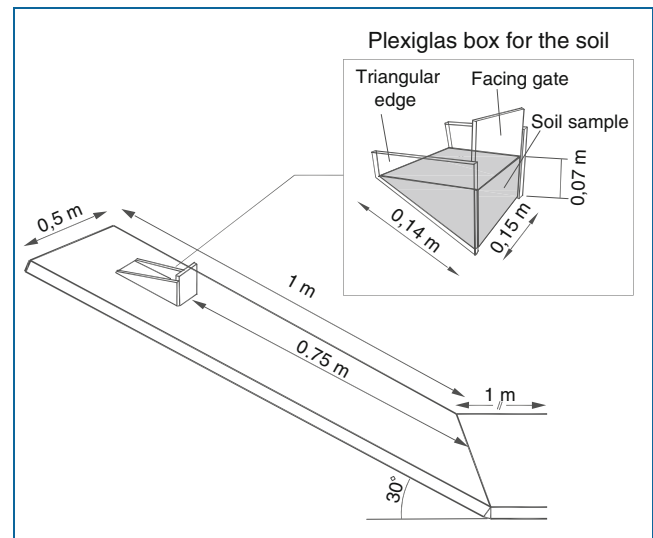


Fig. 4 Set up of equipment for mud-flow test

Experimental Results

The run-out of soil downhill the rough plane was always very rapid: after only 10–30'' the material reduced significantly its displacement rate. The Fig. 5 shows two typical final configurations of the mud tongue. The composition and solid concentration strongly affected the distance covered by the mass, varying from some centimetres to more that 75 cm.

The Fig. 6 shows the evolution of the tip maximum displacement and tongue spreading observed with time during the tests with sample A. Analogous trends were obtained with other mixtures, even if they are not here reported for brevity.

As noticed above, the phenomenon developed very quickly: it came to a halt in about 1 s. We can identify an initial stretch with a parabolic course and constant

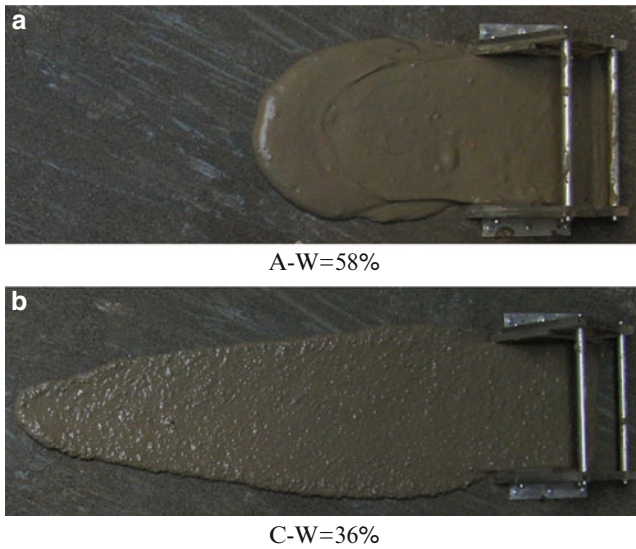


Fig. 5 Mud final configuration in two tests

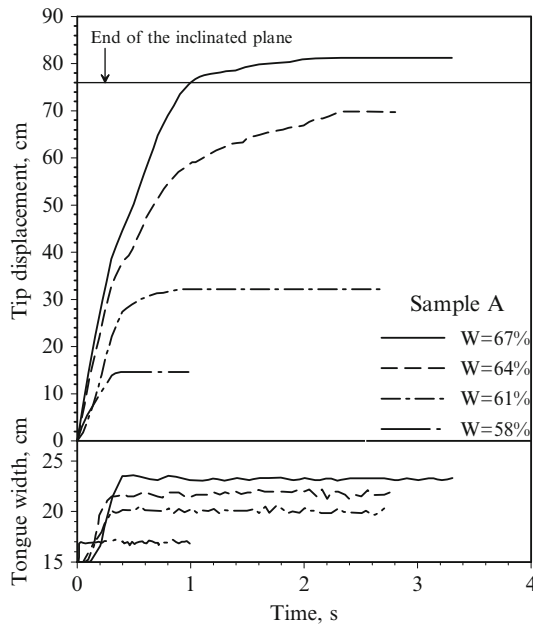


Fig. 6 Tip displacement and tongue width versus time in some tests with sample A

acceleration, then a deceleration phase up to the mass stop. The inflection point of the curve points out the instant (breaking time) at which the velocity is maximum. The lateral spreading showed the same trend, even if its variation is smaller, since the width of the tongue increased from 15 to 24–25 cm only.

Both the total displacement and the tongue width increased consistently with the water content, therefore greater is the water content more deformable is the soil mass. The breaking time also increased with water content.

In Fig. 7a the maximum tip displacements measured in the tests are related to the global water content W . An exponential law, also reported in Fig. 7a, may fit the results of tests for the same sample.

The fitting curve does not accurately interpolate the highest data for sample A, maybe because in this test the flow reached the end of the inclined plane and continued its path on the horizontal plane, as shown in Fig. 6.

Nevertheless, the correlation coefficients are always very good suggesting that the c_v controlled the flow as well as the viscosity parameters. Since this occurred for all the samples, we deduce that, even if the sample C contains a large amount of coarse particles, its flow was still affected by the viscosity of the material.

Supposing that the fitting curve has the same trend also at water contents higher than those tested, the fitting curves of sample C and B would be above the curve of sample A, indicating that, at the same water content, the sample A travels for the shortest distances and, vice versa, the sample C reaches the longest distances.

On the other hand, if we plotted the same data as a function of the fine fraction water content W_f (Fig. 7b), all the points lie in a narrow area. This indicates the key role of fine fraction consistence in determining the mixture behaviour, or, in other words, we may say that only this fraction controls the viscous response of soil. If the sandy fraction is there in small amount, it seems to be a constrain (sample B), but when it increases a lot, it behaves as a dead weight in the mixture, that increases the forces inducing the sliding along the plane without contributing to the viscosity of whole sample.

Unfortunately, it is not possible to draw any conclusions due to the small number of performed tests. Further investigation is required to elucidate the role of the composition of the soil in the behaviour of these processes.

Run-Out Mathematical Model

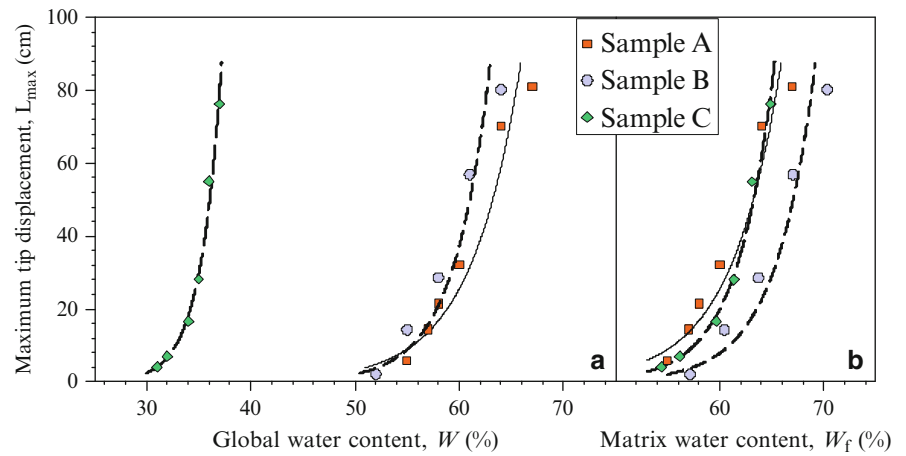
The depth-averaged model derived from the Biot–Zienkiewicz equations for non-linear materials and large deformation problems, i.e. the balance of mass and the balance of linear momentum for the mixture soil skeleton–pore fluid:

$$\frac{D^s \rho}{Dt} + \rho \operatorname{div} \mathbf{v}_s = 0 \quad (5)$$

$$\rho \frac{D^s \mathbf{v}_s}{Dt} = \rho \mathbf{b} + \operatorname{div} \boldsymbol{\sigma} \quad (6)$$

where D_s refers to a material derivative following the soil particles, ρ is the density of the soil and \mathbf{v}_s the velocity of soil

Fig. 7 Maximum tongue elongation in relation to the global water content (a) and the matrix water content (b)



skeleton, b the body forces and σ the Cauchy stress tensor. The integration of the above equations along the vertical axis taking into account the Leibniz's rule in a Lagrangian form is difficult, because the integration is not performed in a material volume. To avoid this difficulty the model refers to an equivalent 2D continuum in which each moving point represents a column of material, extending from the bottom to the free surface and travelling with the depth-averaged velocity.

This is not an exact Lagrangian formulation, because the moving points have no connection with material particles, but it can be denominated either 'quasi-Lagrangian' or arbitrary Lagrangian–Eulerian formulation. Its main advantage is a consistent reduction of the calculation time compared to a standard finite element code based on an Eulerian approach.

The depth-integrated relations derived from (5) and (6) in the quasi-Lagrangian formulation result:

$$\frac{\partial}{\partial x_j}(h\bar{v}_j) + \frac{\partial h}{\partial t} = 0 \quad j = 1, 2 \quad (7)$$

$$\rho \left[\frac{\partial}{\partial t}(h\bar{v}_j) + \frac{\partial}{\partial x_j}(h\bar{v}_i\bar{v}_j) \right] = \frac{\partial}{\partial x_j}(h\bar{\sigma}_{ij}) + t_j^A + t_j^B + \rho b_j h \quad (8)$$

where h is the landslide thickness, \bar{v}_j the depth averaged velocity and the terms t_j^A and t_j^B are the normal stress acting on the surface and bottom respectively.

The above results depend on the chosen rheological model, which, relating the stress tensor to the rate of strain tensor \mathbf{d} and, consequently, to the velocity field \mathbf{v}_s , influences the basal friction and depth integrated stresses $\bar{\sigma}_{ij}$. In the analysis of flow-like landslides the instantaneous flow at a given point may be studied as a uniform steady-state flow. Considering a 1D flow along a channel dip with a constant angle θ , the only non-null velocity component is $v_x = u$ parallel to the base, which varies along the axis

normal to the base. The mobilized shear stress related to a depth z is:

$$\tau = \rho g(h-z) \sin \theta \quad (9)$$

The general rheological law is:

$$\begin{aligned} \tau &= c + \sigma_n \tan \phi + \mu \frac{\partial v_x}{\partial x_3} \\ &= c + \rho g(h-z) \cos \theta \tan \phi + \mu \frac{\partial v_x}{\partial x_3} \end{aligned} \quad (10)$$

where c is the cohesion, σ_n the normal stress and ϕ the friction angle. By combining the three contributions in (10) it is possible to extract different rheological models (Newtonian model, frictional model, and so on).

In this study, we have considered the mud behaving as a Bingham fluid, since the Bingham model is suitable for flows with high water content and clay percentages greater than 10%. The rheological relations become:

$$\begin{aligned} \tau &= c + \mu \frac{\partial v_x}{\partial x_3} \quad \text{for } \frac{\partial v_x}{\partial x_3} \neq 0 \\ \tau &\leq c = \tau_c \quad \text{for } \frac{\partial v_x}{\partial x_3} = 0 \end{aligned} \quad (11)$$

where the second hypothesis implies that for $\tau < \tau_c$ there is no reciprocal motion and the material moves as a rigid block (plug zone).

Finally, (7) and (8) are solved with the method known as Smoothed Particle Hydro-dynamics or SPH, a particle method in which the flow domain is represented by nodal points that move with the flow and are scattered in space with no definable grid structure. Each nodal point carries scalar information, such as density, pressure, velocity components, etc. Interaction between the nodal points and interpolation from a set of N nodes to find the value of a

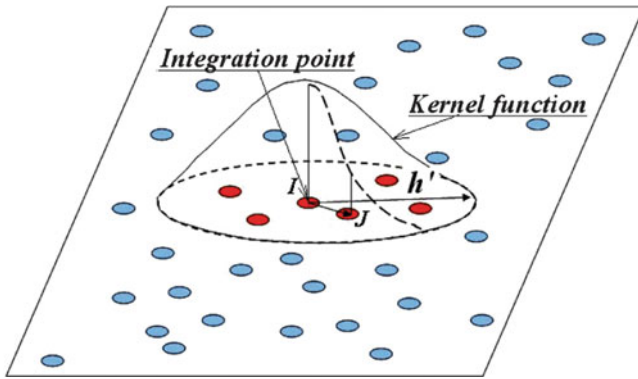


Fig. 8 Kernel function representation

particular quantity at an arbitrary point is obtained with a weighting function, also named the kernel function or smoothing function (Fig. 8).

For more details about the mathematical and numerical formulations, see also Pastor et al. 2008. Here, we remember only that an important numerical parameter of the model is the smoothing length h' , defined as the distance from each node where the weighting function becomes null (Fig. 8). Among the input data for the numerical, one has to assign the parameter h' or the no-size ratio $k = h'/i$, with i the initial spacing of integration point.

Numerical Tests

Figure 9 shows the mesh reproducing the experimental apparatus, formed by a grid with 10,547 nodes spaced of 0.1 m, and the initial position of the mud mass, modelled through 2,601 particles with an initial spacing $i = 0.005$ m.

Two experimental tests, i.e. the tests A–W = 57 % and A–W = 67 %, were simulated adopting viscosity parameters from (1) and (2).

Since the integration scheme is explicit, the time and space steps Δt e Δx have to satisfy the relation:

$$\Delta t \leq \Delta x / \sqrt{gh_{\max}} \quad (12)$$

where h_{\max} is the maximum value of h , equal to 7 cm in the artificial mudflows. Consequently, in addition to the rheological quantities, the parameters controlling the numerical model are the integration steps Δt e Δx and the smoothing length h' . To emphasize the effect of h' , we adopted fixed values for Δt e Δx , 0.006 s and 0.01 m respectively, and calibrated the value of k on the base of test A–W = 67 %.

Figure 10 compares the tip displacement vs. time curves calculated by the model in tests with $k = 0.5$, 2 and 10 with the experimental data. Since the greater is k , and the

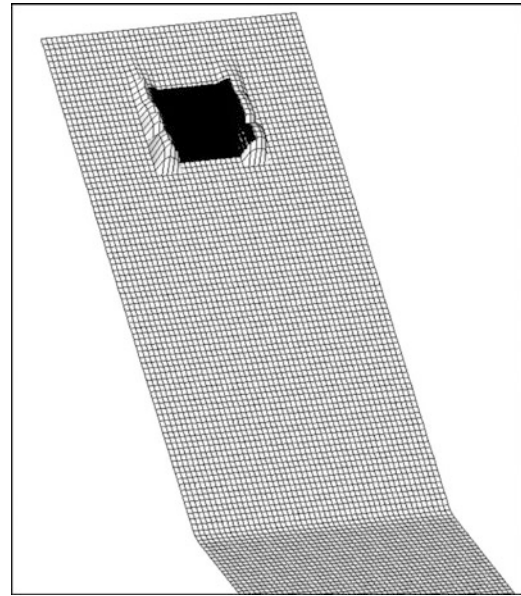


Fig. 9 Initial particles configuration and terrain mesh for the numerical model

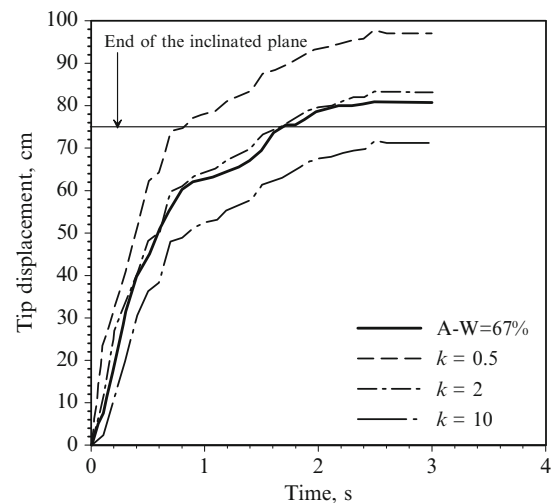


Fig. 10 Effect of the smoothing length on the run-out of mudflows: comparison with data from test A–W = 67 %.

corresponding h' , the greater is the number N of nodes utilized for the interpolation by the kernel function: consequently, with high values of k the nodes result more bonded one to each other and, consequently, the mass resulted more constrained and covered a smaller maximum distance, like it is evident in Fig. 10.

For k equal to 2 we find the best correspondence between experimental and numerical curves: both the curves reach the complete stop in about 2 s and the numerical predicted maximum displacement is 84 cm, against the experimental value of 77.2 cm.

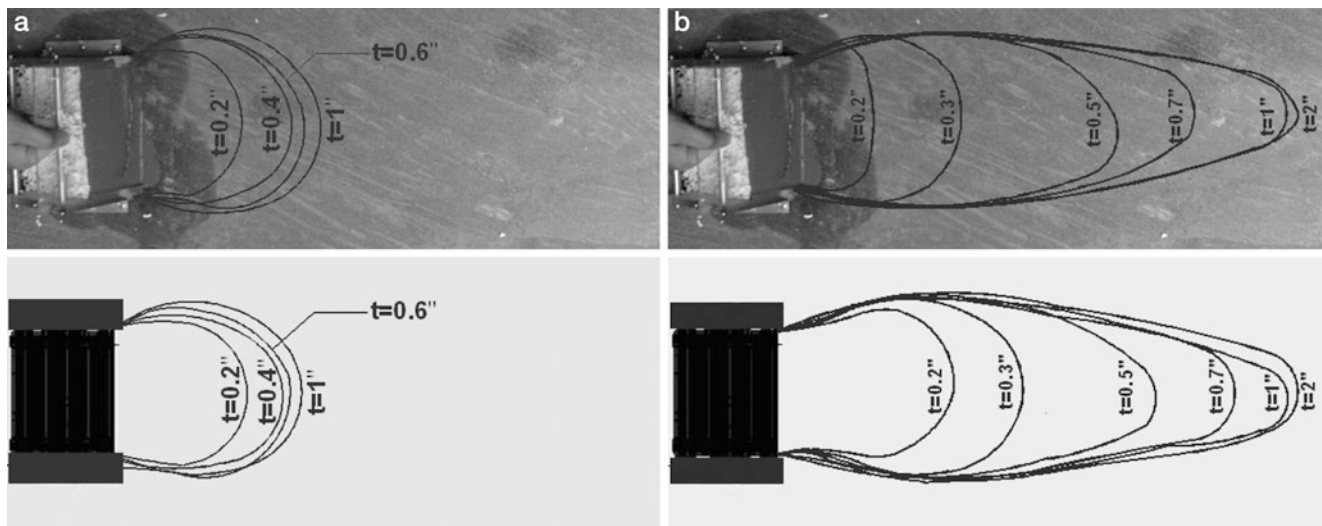


Fig. 11 Tongue configurations in the experimental and numerical tests for (a) A-W = 57 % and (b) A-W = 67 %.

The numerical data deviated from the experimental one only at the beginning of the process when the simulated flow is faster than the experimental one.

Finally, Fig. 11 compares the experimentally observed and numerically predicted configurations of the mudflow at different instants during the reference tests. The phenomenon is properly identified and the mud path and the final tongue form are in agreement with experimental observations.

Conclusion

The paper presents some experimental data on small laboratory mudflow performed with various soil composition and solid concentration: the results highlight the crucial role of fine fraction in controlling the viscosity and the overall behaviour of these phenomena.

The adopted SPH depth-averaged model, which considers the mud as a Bingham fluid, proved to be able to reproduce the observed experimental behaviour as shown by the good agreement between the experimental and numerical run-out distance, lateral spreading and development in time of the process.

Acknowledgements This paper is a part of the research Project MoVeMit financed by the funding of the “Fondazione Cassa di Risparmio di Verona, Vicenza, Belluno e Mantova”. The authors wish thanking also the “Fondazione Angelini” of Belluno and the CNR-IRPI of Padova, which covenant this activity research.

References

- Cola S, Calabrò N, Pastor M (2008) Prediction of the flow-like movements of Tessina landslide by a SPH model. In: Proceedings of the 10th international symposium on landslide and engineering slopes, Xi'an, China, vol. 1. Taylor & Francis, The Netherlands, pp 647–653
- Coussot P, Piau JM (1994) On the behaviour of fine mud suspensions. *Rheol Acta* 33:175–184
- Gingold RA, Monaghan JJ (1977) Smoothed particle hydro-dynamics: theory and application to non-spherical stars. *Mon Not R Astron Soc* 81:375–389
- Hutter K, Koch T (1991) Motion of a granular avalanche in an exponentially curved chute: experiments and theoretical predictions. *Phil Trans R Soc Lond* 334:93–138
- Laigle D, Coussot P (1997) Numerical modeling of mudflows. *J Hydraul Eng, ASCE* 123(7):617–623
- Lucy LB (1977) A numerical approach to testing of fusion process. *Astron J* 82:1013–1024
- Major JJ, Pierson TC (1992) Debris flow rheology: experimental analysis of fine-grained slurries. *Water Resour Res* 28:841–857
- Pastor M, Haddad B, Sorbino G, Cuomo S, Drempetic V (2008) A depth integrated coupled SPH model for flow-like landslides and related phenomena. *Int J Numer Anal Meth Geomech* 33:143–172
- O'Brien JS, Julien PY (1988) Laboratory analysis of mudflow properties. *J Hydraul Eng, ASCE* 110:877–887
- Savage SB, Hutter K (1991) The dynamics of avalanches on granular materials from initiation to runout. Part I: *Anal. Acta Mech* 86, Madrid 2001, pp 201–223



Slope Instabilities in High-Mountain Rock Walls. Recent Events on the Monte Rosa East Face (Macugnaga, NW Italy)

Andrea Tamburini, Fabio Villa, Luzia Fischer, Oldrich Hungr, Marta Chiarle, and Giovanni Mortara

Abstract

The Monte Rosa east face (Macugnaga, Italian Alps) is one of the highest flanks in the Alps. Steep hanging glaciers and permafrost cover large parts of the wall. Since the end of the Little Ice Age (about 1850) the Monte Rosa east face is undergoing a progressive reduction of its ice cover; moreover new instability phenomena related to permafrost degradation and rapid deglaciation have been occurring since over a decade ago. The progressive destabilization of high-mountain faces is a consequence of many factors, such as topography, geological and structural conditions, intense freeze-thaw activity and oversteepened slopes from glacial erosion.

Two major events, an ice avalanche occurred in August 2005 and a rock avalanche occurred in April 2007 are briefly described in this paper. In both cases, the accumulation area was located on the Belvedere Glacier at the foot of the Monte Rosa east face.

A 3D dynamic model (DAN3D) was applied in order to back analyze the runout of the events, enabling the calibration of the input parameters for the assumed rheological models.

Keywords

High mountain rock walls • Permafrost degradation • Rock avalanche • Runout modelling • DAN3D

Introduction

On August 25th, 2005 a huge ice slab of about $1 \times 10^6 \text{ m}^3$, overhanging the Belvedere Glacier, detached from the Monte Rosa east face (NW Italian Alps), at an approximate

elevation of 3,800 m a.s.l. The detached ice slab rapidly fragmented, evolving in an ice-avalanche which flowed down, eroding and entrapping debris and ice along its path. The main volume spread and stopped at the foot of the rock wall (Fig. 1), partially filling the huge depression of the “Lago Effimero”, a supraglacial lake of more than 3 million m^3 formed in summer 2002 and drained in summer 2003, as a consequence of a surge-type evolution of the Belvedere Glacier (Haerberli et al. 2002; Kääh et al. 2004; Tamburini and Mortara. 2005). The avalanche blow reached the Zamboni hut, located more than 3 km downstream, luckily without any casualty or damage.

Surveys carried out immediately after the events allowed to outline the ice-rock avalanche accumulation areas and to describe the morphological and depositional features of both deposits. Seismic and meteorological data recorded during the events provided useful data for a more exhaustive interpretation of their mechanisms. Aerial photos taken before

A. Tamburini (✉) • F. Villa
Imageo S.r.l., via Valperga Caluso 35, Torino, Italy
e-mail: andrea.tamburini@imageosrl.com

L. Fischer
Landslide Department, Geological Survey of Norway (NGU),
Trondheim, Norway

O. Hungr
UBC University of British Columbia, Vancouver, BC, Canada

M. Chiarle
National Research Council (CNR-IRP)I, Torino, Italy

G. Mortara
Comitato Glaciologico Italiano (CGI), Torino, Italy

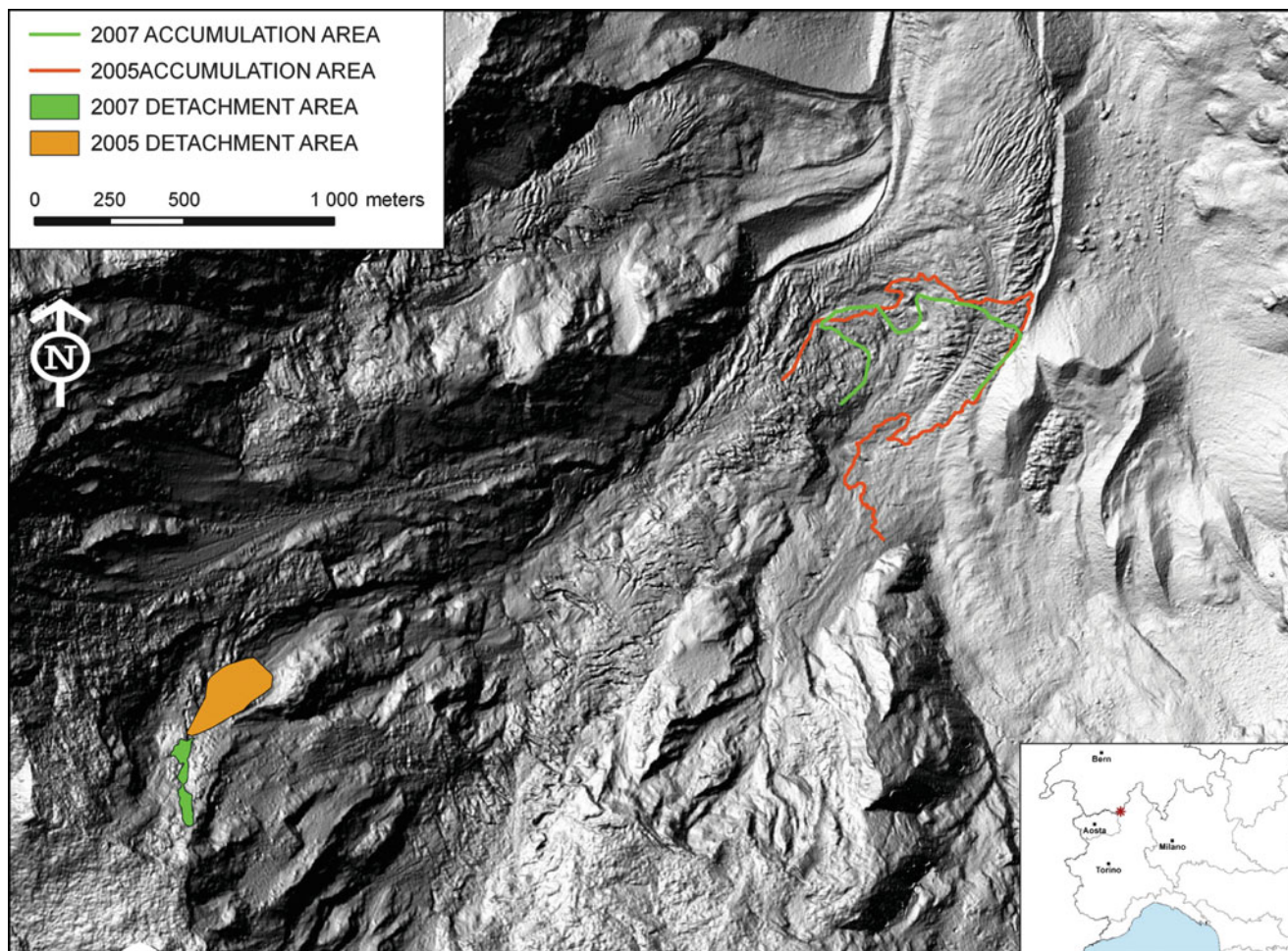


Fig. 1 Detachment and accumulation areas of the August 2005 ice avalanche and April 2007 rock avalanche

and after the events provided detailed maps of the accumulation area.

Two years later, another major event occurred in the same area. In April 2007, a rock avalanche of about 300,000 m³ detached at an elevation of 4,000–4,200 m a.s.l., following the same runout-path with about the same spreading area (Fig. 1). According to the available temperature records, April 2007 was the warmest during the last 150 years in Western Alps.

Helicopter-borne and ground-based lidar surveys helped in calculating the volume of the detachment area and performing a geomechanical characterization of the rock mass by properly processing the laser point cloud, without need to access the rock slope.

These events are particularly significant, as occurred in a glacial basin which is under observation since autumn 2001, because of a distinctive surge-type phenomenon of the Belvedere Glacier, combined with a generalized instability of the Monte Rosa east face due to rapid deglaciation.

A description of the above mentioned events follows. A complete and detailed study of the evolution of the Monte Rosa east face was carried out by Fischer et al. (2011) through the comparison of high-resolution DTMs, providing a quantitative assessment of the topographic changes of the slope over the last 50 years.

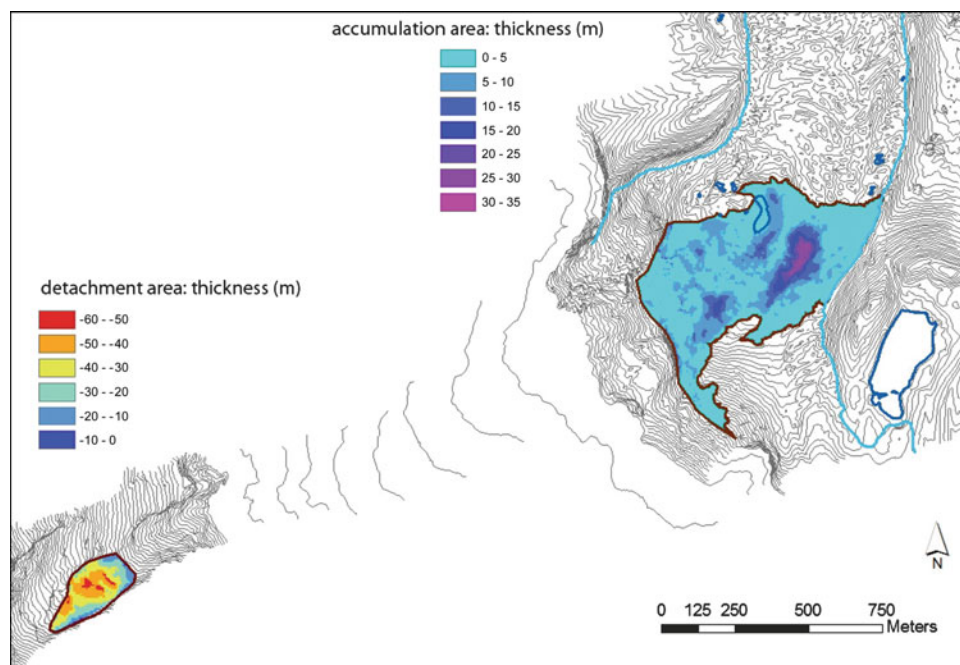
The August 2005 Ice Avalanche

In August 2005 an ice avalanche detached from the Monte Rosa east face at an elevation between 3,580 and 3,820 m a.s.l., involving an ice volume of about 1.1 million m³.

Seismic and meteorological stations next to the area provided useful data for a more exhaustive interpretation of the event.

The event was recorded by the EMSC European Mediterranean Seismological Centre, the Swiss Seismological Service (SED, Schweizerischer Erdbeben dienst) and the

Fig. 2 Thickness map of the detachment and accumulation areas of the August 2005 ice avalanche obtained by subtracting two subsequent DTMs



Italian Seismological Service (INGV, Istituto Nazionale di Geofisica e Vulcanologia). The origin time of the event was assumed as the starting phase of the avalanche: 25th of August 2005 at 02 h 36 m 54 s (GMT).

The seismograms were analyzed as tectonic earthquakes by EMSC and SED and the hypothesis that an earthquake induced the avalanche was taken into account as a first hypothesis. After a more accurate analysis of the recorded signals (Mortara and Tamburini 2009) the possibility that a tectonic earthquake triggered the avalanches was excluded because of the absence of characteristic phases in the seismograms.

An automatic weather station was located close to the right margin of the accumulation area. A peak of 38.7 m/s (140 km/h) was recorded by the anemometer between 2 and 3 a.m. GMT. This peak, which, according to the AWS configuration, represents the highest value recorded within the interval between two subsequent acquisitions, was associated to the blow of the ice avalanche, and confirmed the arrival of the ice avalanche in the spreading area.

The overall runout of the landslide was more than 3 km, the extent of the accumulation area, including the avalanche blow, was estimated in about 110 ha.

Thanks to the availability of multi temporal photogrammetric surveys, it was possible to compute the volume of the ice avalanche by comparing before and after DTMs. Values of 1.1 and 1.4 million m³ were respectively estimated for the detachment and the accumulation area. A thickness map was also performed (Fig. 2). According to literature, the

August 25th 2005 ice avalanche represents one of the major ice fall events documented in the Alps over the past 100 year (Tufnell 1984, <http://www.glacierhazards.ch>; <http://glaciology.ethz.ch/inventar/>).

The April 2007 Rock Avalanche

This event is less documented than the previous one, as it was not possible to obtain seismic data and the AWS station was no longer active when the rock avalanche occurred.

Nevertheless some pictures taken before, during and after the event are available. Before the main event, on April 17th 2007, a skier descending along Canalone Marinelli observed the deposit of a small ice and rockfall probably detached a few days earlier from the same detachment area as the subsequent main event. During the main event, occurred on April 21st at about 10 a.m. a sequence of pictures was taken by an observer (Fig. 3); moreover some pictures taken the day after the event by an alpine guide (Michele Cucchi from Alagna Valsesia) descending along Canalone Marinelli were helpful in delimiting the accumulation area with a good approximation.

The source area is located at an altitude of 4,000–4,200 m a.s.l., not far from the detachment area of the August 2005 ice avalanche (Fig. 4).

This can be considered a quite exceptional event, both for the elevation of the detachment area and the epoch of the year, probably related to the exceptionally high temperatures



Fig. 3 April 2007 rock avalanche (Picture taken during the event)

recorded in April 2007, the warmest recorded in Western Alps over the last 150 years (Mortara and Tamburini 2009).

An helicopter-borne Lidar survey of the Monte Rosa east face was carried out in September 2007 and compared with a previous aerial lidar survey taken in October 2005. The location of the detachment area was clearly identified and a volume of about 150,000 m³ was estimated (Fischer et al 2011; Mortara and Tamburini 2009).

A ground based lidar survey was carried out in August 2010 on the lower part of the Monte Rosa east face, in order to extract data regarding the attitude of geological discontinuities and perform a kinematic slope stability analysis (Goodman 1989). A stereoplot of the main discontinuities identified after the lidar point cloud processing is shown in Fig. 5. According to the local orientation of the slope, most probably a planar sliding along set 1, laterally constrained by subvertical set 3 occurred.

As topographic surveys of the glacier surface were not available, the extent of the accumulation area was estimated by comparing pictures taken from the top of the east face immediately after the event with aerial pictures taken after the August 2005 ice avalanche. Punctual landslide deposit thickness measurements, taken after the event, enabled

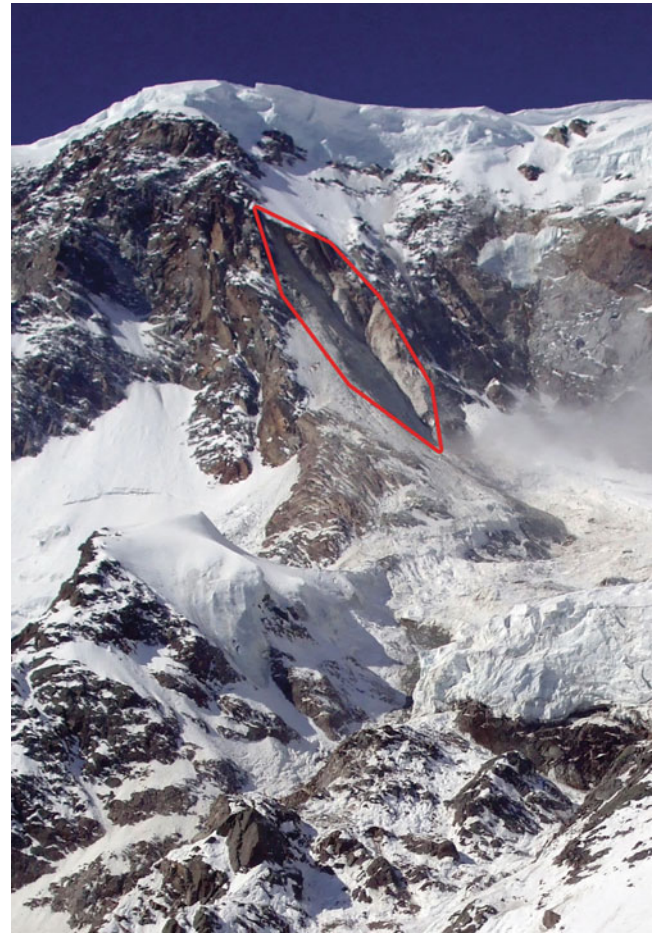


Fig. 4 Detail photograph of the Monte Rosa east face (2007, CNR-IRPI, Turin) showing the detachment area of the April 2007 rock avalanche (*red polygon*)

a rough estimation of the accumulation volume in about 300,000 m³, which seem to be consistent with the initial volume and the entrainment of ice and debris occurred during the runout.

Runout Back-Analyses

A back-analysis of the described events is currently ongoing using DAN3D (McDougall and Hungr 2004), a model based on the “equivalent fluid” approach, as defined by Hungr (1995). DAN3D is a dynamic model, controlled by a small number of adjustable parameters, which enables a simulation of the event in terms of flow distance, velocity and distribution of deposits. Three grid files, describing the initial elevation of the sliding surface, the initial depth of the source failure and the distribution of the different rheologies, has to be provided as input to the model.

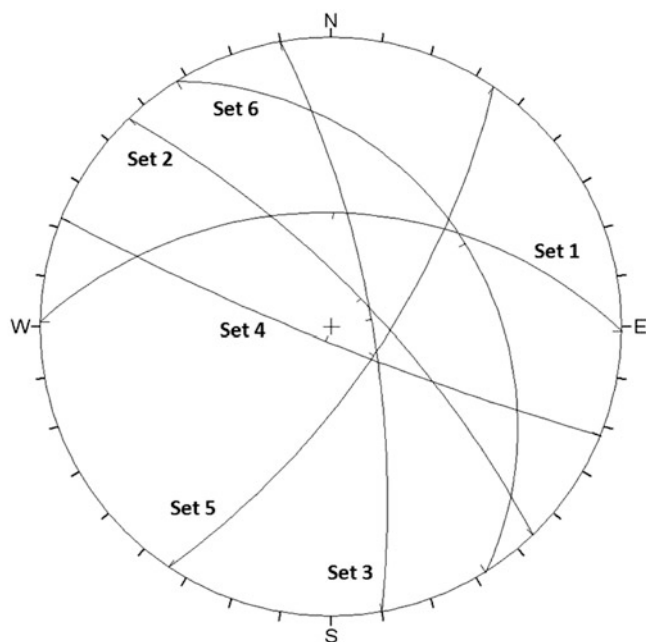


Fig. 5 Stereoplot (Lower hemisphere Schmidt Net Plot) with the great circles of the main discontinuity sets obtained by processing the point cloud provided by a terrestrial lidar survey of the lower part of the Monte Rosa east face

The first results obtained for the April 2007 rock avalanche are presented. The approach adopted in obtaining the surface model and selecting the most appropriate rheologies are briefly discussed.

A first attempt to obtain a reliable topography of the area was made by mosaicing and connecting the most updated available data describing the pre-event situation. For what concerning the detachment area, the already mentioned results obtained by Fischer et al. (2011) were used. The main problem is represented by the topography of the glacier surface, which is still rapidly changing after the end of the surge-type evolution experienced up to the end of 2005 (Mortara and Tamburini 2009). The most recent pre-event topographic survey is relevant to September 2005, and probably does not correctly represent the pre-event morphology of the glacier surface.

Two different rheologies were used, in order to simulate the behaviour of the sliding material on the rock slope and on the snow and ice covered areas.

In accordance with other comparable case studies (Hungri and Evans 1996; McDougall et al. 2006; Sosio et al. 2008;

Deline et al. submitted), a voellmy rheology was used for the ice and snow covered areas, while a frictional rheology was used elsewhere. For the frictional rheology a 25° bulk friction angle was used, while for the Voellmy rheology a friction coefficient ranging from 0.05 to 0.1 and a turbulence coefficient ranging from 700 to 1,000 m/s^2 were set.

According to the adopted evolutionary model, proper erosion rate and a maximum erodible thickness were set, in order to take into account the entrainment of ice and debris during the propagation of the rock avalanche.

The best result obtained with the DAN3D simulation of the April 2007 rock avalanche is presented in Fig. 6. The maximum runout distance and the thickness of the landslide deposit are consistent with field observations and measurements. For what concerning the limit of the accumulation area and the distribution of the deposits the fit between modelled and observed data is less satisfactory. This is undoubtedly due to the topographic model used, which dates back to 2005 and does not correctly represent the morphology of the accumulation area in such a dynamic environment. This is particularly evident in the depression once filled by the Effimero supraglacial lake, where major changes occurred between 2005 and 2007. According to the morphological observations and the surface displacement measurements reported by Mortara and Tamburini (2009), the right side of the Belvedere glacier in 2007 was probably more depressed than the left one, once occupied by the Effimero lake.

Conclusions

The Monte Rosa east face (Macugnaga, Italian Alps) is undergoing a rapid evolution due to deglaciation and permafrost degradation. One of the main consequences is represented by the occurrence of frequent ice- and rockfalls which make the access to the area extremely dangerous. Thanks to the availability of data and observations, a back analysis of two major events, occurred in August 2005 (ice avalanche) and in April 2007 (rock avalanche) respectively, can be carried out. The first results obtained by modelling the April 2007 rock avalanche with DAN3D (McDougall and Hungri 2004) are presented. The results are consistent with reality in terms of maximum runout distance and average deposit thickness. However some problems were encountered in modelling the extent of the accumulation area, due to the

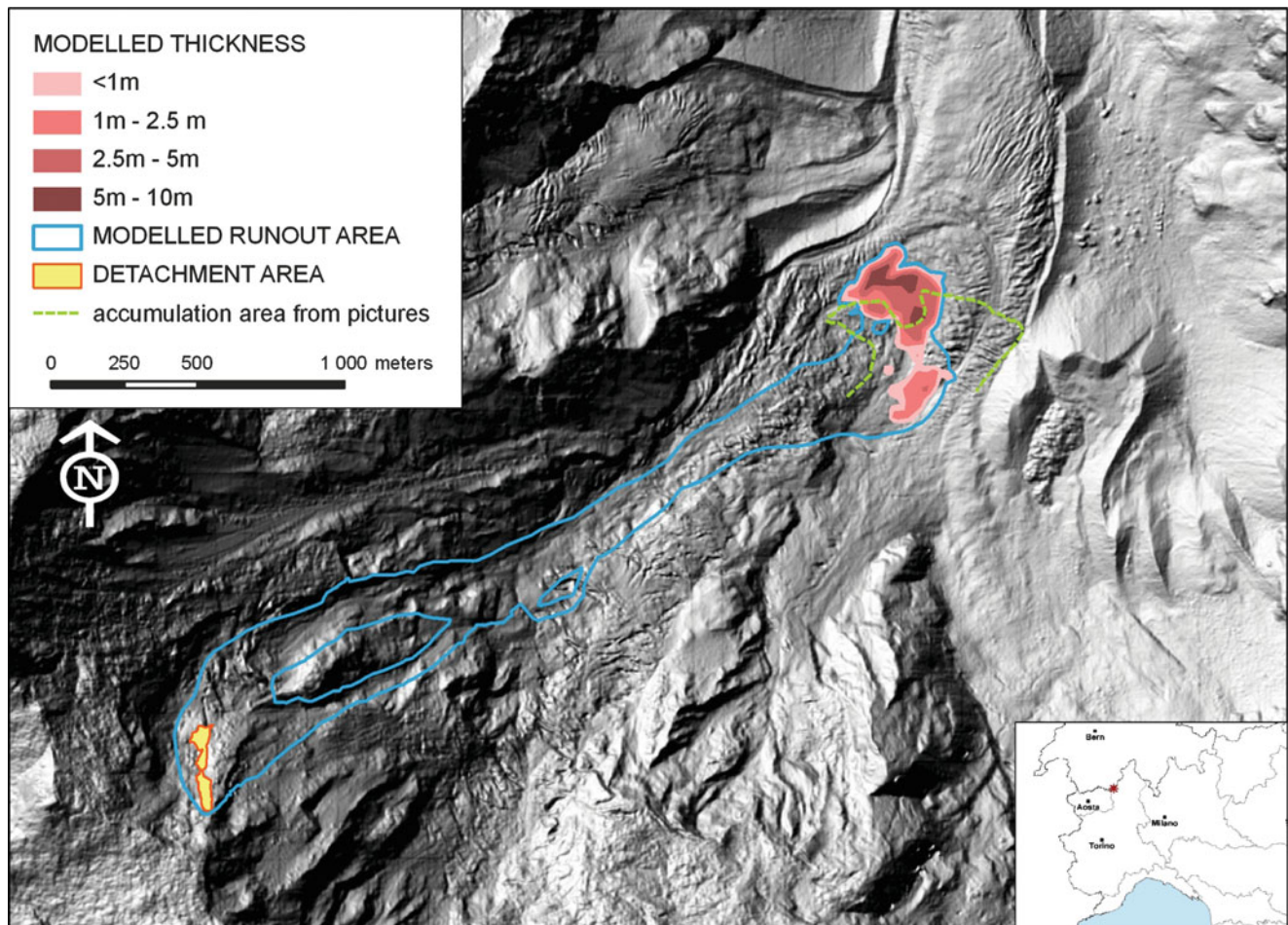


Fig. 6 Back analysis of the April 2007 rock avalanche: the runout distance and the average deposit thickness are consistent with the observed ones, while the spreading area is shifted to the NW, probably due to the lack of an up-to-date DTM of the glacier surface

unavailability of an up-to-date DTM of the glacier surface. The rheological parameters assumed for the back analysis are within the range proposed by literature on similar cases.

References

- Deline P, Alberto W, Broccolato M, Hungr O, Noetzli J, Ravelin L, Tamburini A (submitted to NHESS) The December 2008 Crammont rock avalanche, Mont Blanc massif area, Italy
- Fischer L, Eisenbeiss H, Kääh A, Huggel C, Haerberli W (2011) Monitoring topographic changes in a periglacial high-mountain face using high-resolution DTMs, Monte Rosa East Face, Italian Alps. *Permafrost Periglac Process* 22(2):140–152
- Goodman RE (1989) *Introduction to rock mechanics*. Wiley, New York
- Haerberli W, Kääh A, Paul F, Chiarle M, Mortara G, Mazza A, Deline P, Richardson S (2002) A surge-type movement at Ghiacciaio del Belvedere and a developing slope instability in the east face of Monte Rosa, Macugnaga, Italian Alps. *Nor J Geogr* 56:104–111
- Hungr O (1995) A model for the runout analysis of rapid flow slides, debris flows, and avalanches. *Can Geotech J* 32:610–623
- Hungr O, Evans SG (1996) Rock avalanche runout prediction using a dynamic model. In: Senneset K (ed) *Proceedings of the 7th international symposium on landslides*, vol. 1. Trondheim, pp 233–238
- Kääh A, Huggel C, Barbero S, Chiarle M, Cordola M, Epifani F, Haerberli W, Mortara G, Semino P, Tamburini A, Viazzo G (2004) Glacier hazard at Belvedere Glacier and the Monte Rosa east face, Italian Alps: processes and mitigation. In: *Proceedings of the international symposium interpraevent 2001*, Riva del Garda, Trento, pp 67–78
- McDougall S, Hungr O (2004) A model for the analysis of rapid landslide motion across three-dimensional terrain. *Can Geotech J* 41:1084–1097
- McDougall S, Boulton N, Hungr O, Stead D, Shwab JW (2006) The Zymoetz Rivel landslide, British Columbia, Canada: description and dynamic analysis of a rock slide-debris flow. *Landslides* 3(3):195–204
- Mortara G, Tamburini A, (eds) (2009) *Il ghiacciaio del Belvedere e l'emergenza del lago Effimero*. Ed. Società Meteorologica Subalpina, Castello Borello, Bussoleno. ISBN 978-88-903023-5-0. 191p
- Sosio R, Crosta GB, Hungr O (2008) Complete dynamic model calibration for the Thurwieser rock avalanche (Italian Central Alps). *Eng Geol* 100:11–26
- Tamburini A, Mortara G (2005) The case of the “Effimero” Lake at Monte Rosa (Italian Western Alps): studies, field surveys, monitoring. In: *Proceedings of the 10th ERB conference*, Turin, 13–17 Oct 2004, UNESCO, IHP-VI Technical Documents in Hydrology, 77, 179–184
- Tufnell L (1984) *Glacier hazards*. Longman, London/New York, 97p



New Approach to Rapid Risk Evaluation in Disasters Related to Landslides-Brazil

Renato Eugenio Lima

Abstract

In the last 3 years Brazil was hit by the most important group of accidents related to landslides in the history of the country. The biggest accidents affected the States of Santa Catarina, Rio de Janeiro, Pernambuco, Alagoas and Paraná. We estimated more than 20,000 landslides in these most important disasters and around 2,000 victims dead or disappeared. The effects of these accidents are enormous and in many cases the community will be paying the costs for long time. The group of CENACID-UFPR, Federal University of Paraná, responded to almost all of these accidents and developed a new approach to face the challenge of fast evaluation of risk in these events. This new approach is proposed as a tool to rapid and systematic evaluation of groups of landslides, which we call “landslides systems”. This methodology is called “Relative Rapid Landslides Analysis” and is based in five different indicators of risk.

Keywords

Rapid risk evaluation of landslides • Landslides in Brazil • Landslide indicators

Introduction

The most important natural disasters to Brazil are floods and landslides. Time to time the country is affected by these types of events.

In the last 3 years Brazil was hit by the most important group of accidents related to landslides in the history of the country. The biggest accidents affected the States of Santa Catarina (2008), Rio de Janeiro (2010 and 2011), Pernambuco and Alagoas (2009) and Paraná (2011). The states of Minas Gerais, Rio Grande do Sul, São Paulo and others were also affected by large mass movements

systems. All these hazardous geological processes occurred associated with rain periods and exceptional storms, normally in the summer, which resulted in landslides and floods. We estimated more than 20,000 landslides in these last years disasters and around 2,000 victims dead or disappeared.

The effects of these accidents are enormous and in many cases the community will be paying the costs for long time.

These geological processes resulted in thousands of victims, transformed the landscape regionally and provided a significant quantity of disaster waste and debris which are a problem to deal with.

The proposed methodology aims to provide a tool to very rapid risk analysis in disasters related to gravitational mass movements. Relative Rapid Landslides Analysis (RRLA) is planned to be useful in the absence of previous studies and without other geological information, in the very earlier phase of the disaster response (first 2 or 4 weeks).

R.E. Lima (✉)
Center for Scientific Support in Disasters – CENACID, Federal
University of Paraná (UFPR), Caixa Postal 19023, Curitiba
CEP-81531-990, Brazil
e-mail: renatolima@ufpr.br

Materials and Methods

The study was based in two different approaches. The first was to register the disasters in order to facilitate the understanding about the types, geographic distribution and frequency of the events. As a result we have a data bank with all this information.

The second approach was developed as a field activity related to each disaster situation. Considering that the purpose of the CENACID is to offer scientific knowledge to reduce the suffering and the losses of community in disasters situations, a CENACID team was moved to the disaster areas. The objective is to study, to recognize the dangerous geological process or processes and to evaluate the evolution of the mass movements systems and the possible effects of this evolution, namely, the risk.

Taking into consideration experiences in successive field activities analysing susceptibility to landslides at emergency response and possible effects associated to them, we select five important indicators of the risk.

To choose the indicators we took into consideration the following criteria:

- The significance of the indicator
- The possibility of fast analysis in the field by experienced geologists.
- The absence of necessity for testing or other investigations that could be impossible in the emergency response.

The selected indicators are considered possible of identification during the disaster situation. The Table 1 shows the indicators, the component of the risk analyses related, and the easiness to be evaluated in the field during disasters.

Despite the methodology is easy, fast and with no others requirements to be applied, the results are better if the geologists are experienced and/or have been trained in it.

The methodology was tested in 2008, in the State of Santa Catarina catastrophic landslides and after that was applied in some other landslides events.

Disasters Related to Landslides in Brazil

Landslides are a common accident in Brazil and in many situations caused disasters in different areas of the country. In the last years almost all regions were affected and more than 20,000 landslides could be registered, most of them related to majors disasters.

Most of the disasters affected the South, Southeast and Northeast of the country (Table 2 and Fig. 1), the most populated areas. The total of deaths in natural disasters is superior to thousands of people and the economic losses are not totally estimated.

Table 1 List of selected indicators of risk, risk component, estimation of easiness of evaluation and estimation of required experience of the designed geologist for the study

Indicator	Risk component	Easiness of evaluation	Experience required
Phase of dangerous process	Susceptibility	Medium	High
Possible volume involved	Susceptibility and losses	High	Medium
Velocity and distance	Susceptibility and losses	Low	Medium
Impact probable	Losses	High	Low
Aggravation factors	Vulnerability and both above	Medium	Medium

Table 2 Significant natural disasters by region in 2010, Brazil

Region	S	SE	W	N	NE
Disasters	23	55	14	14	19
Percentage	18.4	44.0	11.2	11.2	15.2

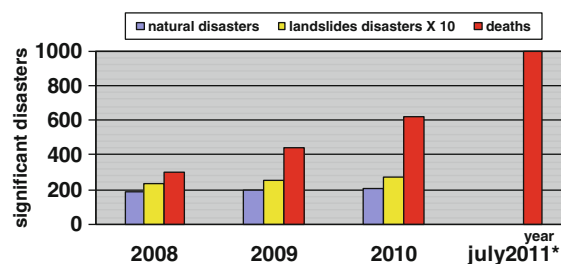


Fig. 1 Evolution of significant natural disasters, disasters related exclusively to landslides and deaths related to natural disasters in Brazil (*preliminary)

Overview of Recent Landslide Disasters in Brazil

Recent Landslide Disasters

Since 2008 Brazil was hit by a series of accidents related with landslides. Most of them were associated with hydrological processes (rain storms and floods). Table 2 indicates the distribution of the more significant accidents in the year 2010.

The number of accidents and victims related to natural disasters in Brazil is growing since 2008 (Fig. 1). Most of the deaths resulted from landslides related accidents. The five more significant disasters related to landslides were located in Santa Catarina, Rio de Janeiro, Paraná, Minas Gerais and Sao Paulo Sates.

Observing the historical series of natural disasters in Brazil (Fig. 1) it is clear that each new year we are having



Fig. 2 System of landslides at Serra do Mar, Paraná, South of Brazil (2011)

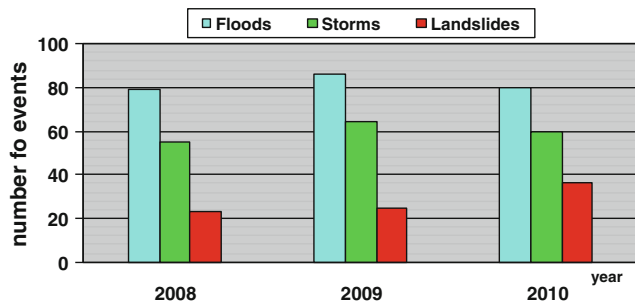


Fig. 3 Comparative evolution of floods, storms and landslides associated with significant disasters in Brazil

more disasters and more deaths. The figures of CENACID indicate that floods and rain storms are the most important in terms of frequency (Fig. 3), but the group landslides causes the growing number of deaths. Also it is clear that disasters related to landslides are growing, and specially the number of deaths related to them is growing faster than the number of accidents. The catastrophic event in the State of Rio de Janeiro (January-2011) results in the exceptional growing of deaths in the first half of this year.

This information from cenacid database (CENACID 2011) indicates that landslides are affecting more populated areas and, probably, the human activity is an additional controller of these dangerous processes.

All this information supports the necessity of development and applying of fast and easy methodologies to analyse risk related to landslides in areas affected by major disasters as presented.

Applying the RRLA Analysis

Preparing

Normally the group will be prepared to the emergency mapping applying RRLA methodology before the accident.

The first action is to prepare the team to apply the methodology. It includes to explain the indicators and the format to be filled in the field. It also includes to prepare the involved people to protect themselves in a disaster area.

Applying the RRLA Analysis in the Field

In the field each geologist or group of geologists goes to the area affected by landslides, evaluate each landslide system (Fig. 2) and provide the relative analysis for the studied area.

During this phase the responsible will analyse the characteristics of the rock and soil, the types of mass movements realized, the occupation of the soil, dangerous facilities and others. These observations will be basic for the RRLA analysis and in this step the previous experience is very important.

During the evaluation the observer will analyze the five selected indicators: (a) phase of the dangerous process (based in Chacon 2008); (b) possible volume of the expected mass movement; (c) velocity and distance to be reached; (d) probable impact; (e) factors of aggravation.

Each one is estimated from one to five following the criteria explained in the form (see Table 3) and based on experience, judgment and the observation of the similar landslides in the system. The sum of these values resulting in the index of relative landslide risk of the area.

It is a risk mapping and it is important to develop the studies searching for a prognosis, not only analyzing the past, but developing a prediction of the geologic process evolution.

The last will be to fill in the RRLA format as a result of the geological analysis in the field.

Registering the Results

During the field and at the end of day, in the office, the geologist will register the results in a map. If necessary this can be done at the same time in the field, in order to make possible to initiate with urgent actions for disaster response (evacuations, etc.).

The plotted results, as a direct result of the methodology will present the affected areas in a relative order of priority of risk. This map showing the analysed areas and relative risk we call “*emergency map of geological risk*”.

This mapping offers to the disasters managers a tool to coordinate the capacity for response with the necessities. The environment of the disaster normally shows the list of necessities bigger than the response possibilities.

Actions like evacuation of people, choosing of safety areas for shelters, priority in clean up of roads can be decided considering the priorities indicated by the RRLA analysis.

Table 3 RRLA form to classification of emergency risk and prioritize actions for disaster response

Rank indicator	Low (1)	Medium (2)	Hight (3)	Dangerous (5)	Result of evaluation
PHASE of the dangerous process	(Advanced or finished) or with no perspectives of evolution	(Preparatory or advanced) Apparent equilibrium or very slow motion (mm-cm/year)	(Development) Indicators of moderate motion (m/year)	(Beginning or development) Indicators of movement and acceleration, possibility of iminency (m/month or >)	
VOLUME probable	~50 m ³ ex. (surface of 10 × 5 m)	~500 m ³ ex. (surface of 10 × 50 m)	~5,000 m ³ ex. (surface of 100 × 50 m)	~50,000 m ³ ex. (surface of 100 × 500 m)	
VELOCITY and DISTANCE anticipated if deflagrated	Velocity moderate and short distance	Velocity moderate and long distance	Fast and short distance	Fast and long distance	
	Moderate: landslides	Fast: falls and flows	Short = up to 50 m	Long = more than 50 m	
IMPACT Soil use at the probable affected area	Natural (woods, etc.)	Edifications for temporary use (roads, walls, etc.)	Low density edification for permanency like houses, etc.	High density edification, people permanency (residential area high density, schools, etc.)	
Aggravation factors (to describe)	Geological or antropic	Ex. water in the masses, favorable foliations, overload, fragile building, etc.		Maximum = 5 (five)	

It is important to provide the most correct information for decision makers like civil defence, mayors, governors and ministers. Also the community needs to receive the information about the immediate risks.

For both it is necessary to make clear that this is an emergency evaluation and there will be necessary to provide complete studies in the next months.

After the Emergency Phase

When the emergency phase is over it is important to re-analyse the results, including new field activities, detailed geological mapping, collect of samples and field and laboratory tests to provide a definitive risk map.

It is also the opportunity to compare the results of RRLA analysis with the immediate evolution (approximately 3 or 4 months) of the geological processes studied.

This final review will permit to the team to improve the capacity to apply the methodology in the next situations.

Santa Catarina Disaster – Example of the Use of RRLA Methodology

The Disaster

In November and December 2008 the State of Santa Catarina in South Brazil was affected by continuous raining with a peak in November-23. This climatic extreme resulted

in 40 municipalities partially destroyed and enormous economic losses. Many municipalities declared “State of Emergency” and 14 declared “State of Calamity”. The number of registered deaths is 135 and 6 disappeared.

Almost all of the deaths were caused by gravitational mass movements and also the economic losses were related to these geological process. We estimate more than 10,000 landslides related processes in this event, including rotational and translational movements, flows and mixed phenomena.

Most of the landslides affected rural areas, but in other cases urban areas were strongly impacted, as Blumenau and region.

RRLA Application in Santa Catarina

CENACID sent three missions to the affected area to support the local authorities with scientific information, especially to provide rapid risk analysis (Lima 2010).

There were more than 40 municipalities affected, probably 1,000/2,000 landslide systems and a lack of previous knowledge about landslide risk in the region.

It was a big challenge to evaluate the risk and offer appropriate information to decision makers in short time as requested in that situation.

To deal with this situation the group of CENACID applied the RRLA approach and performed many emergency maps of geological risk and many others punctual evaluations. This rapid risk analysis supported the various levels of decision in the following actions:



Fig. 4 RRLA emergency map of geological risk (2008) of Blumenau-SC, Brazil (red colour high risk)

- Decision for areas to be evacuated and areas to be monitored. In this event more than one million people were affected by the disaster and it was very difficult to provide the required information for the entire region affected in Santa Catarina State.
- Priority for clean up streets and roads to facilitate the evacuation of people from dangerous areas, choosing the safety routes and considering the communities in highest dangerous situation.
- To evaluate and select appropriate shelter areas to receive the dislocated people.
- To check and authorize the running of important services and community functions in hill sides not affected by visible movements.

Results of the Study in Santa Catarina

CENACID performed hundreds of specific evaluations and 12 emergency maps as the example of Fig. 4 for geological risk.

All these evaluations were produced in very short time and using a common criteria for emergency analysis. The approach RRLA was useful to offer a scale of risk and to permit the production of comparable information within the products of different groups.

Conclusion

In the last 3 years the disasters related to landslides are growing in number and human and economic losses.

The methodology RRLA (Rapid Risk Landslides Analysis) was applied and useful in Santa Catarina State of Brazil where more than 40 municipalities were affected by probably 1,000/2,000 landslide systems.

The RRLA approach was applied in some other major disasters situations in Brazil and provided important information for disaster response.

The essential aspect of the proposed methodology RRLA is to provide a tool to rapid analysis of danger situations, with no need of testing, sampling, detailed mapping, etc.

The proposed methodology includes the terms favourability to the geological process and the term possibility of losses, both composing the risk equation.

This methodology can be useful in reducing the dependency on individual experience and facilitates the comparison with others groups working in the same region.

Acknowledgments The proposed methodology results of many missions to disaster areas with the group of scientists of the Center for Scientific Support in Disasters (CENACID). I would like to acknowledge with gratitude all the CENACID geologists that participated in these missions. It is also important to thank the Federal University of Paraná and Araucaria Foundation for support this initiative.

References

- CENACID (2011) CENACID. <http://www.cenacid.ufpr.br>. Accessed 20 July 2011
- Chacon J (2008) Los conceptos actuales de susceptibilidad, peligrosidad y riesgo, en la prevención de movimientos de ladera, con ejemplos de aplicaciones practicas. In: Proceedings of the XLIV Brazilian geological congress, Special Publication – Roteiro de Excursão Técnica. Curitiba-PR, Brazil, 24–31 Oct 2008, pp 17–60
- Lima RE (2010) Considerações sobre o desastre geoambiental em Santa Catarina –2008. In: Proceedings of the symposium on geotechnical and geoenvironmental cartography, ABGE. Maringa-PR, Brazil, 18–22 Aug 2010, pp 2–10

Part III

GIS Application and Developments

Introduction by Serafino Angelini¹, Esther Jensen², and Raffaele De Amicis³

1) Litografia Artistica Cartografica S.r.l., Florence, Italy

2) Icelandic Meteorological Office, Reykjavik, Iceland

3) Fondazione Graphitech, Trento, Italy

The L.08 session titled “GIS application development” took place within the Second World Landslide Forum from Thursday 10th March p.m. and 11th March a.m. It was introduced by a presentation of the received posters and followed by a series of oral presentations. Session activities were coordinated by Raffaele De Amicis (Fondazione Graphitech), Esther Hliðar Jensen (Icelandic Meteorological Office), Serafino Angelini (Litografia Artistica Cartografica, Florence).

The GIS APPLICATION DEVELOPMENTS session aimed at including research and development work regarding computerised techniques supporting geographic information so as to correctly manage and store data, even historical, and consequently identify new data analysis systems and discuss proposals supporting applied research in these fields.

Fifteen researches have been presented and these entirely fulfilled expectations. Since the subject was transversal, researches ranged in different fields although aspects related to geomatic were central. The last aspects seemed to be the main reason for the speaker to choose this session; after perusal of hundreds of researches presented during the Second World Landslide Forum it appears that the Geographical Information Systems currently involve every aspect of slope instability studies as well as geotechnical geology-engineering. It also appears that many other researches would have had an appropriate place in this session since there is a number of aspects currently related to geomatic.

Geographical information applied to Earth Sciences and thematic Cartography paves a new way in the management of events related to slope instability, landslide risks and mass movements *sensu lato* both in identifying the causes, reducing the risk and managing the consequences even in emergency situations through real time analysis and actions of civil defense.

In this perspective some actions concentrated on criticalities causes and a classification of the events was drawn to be used in the future for comparison and/or analysis; new techniques have also been considered for storing data close to applicative reality; other presentations described a detailed study of these events, based on new models of deterministic type and care was taken in assessing weather theory corresponded to the real development of the specific event; other researches focused on the effects that occur on the territory and its anthropic action when morphological instability occurs.

Some interesting considerations derived from this session; according to the presentations and related observations it appears that:

- Database implementation concerning landslide hazard improves the assessment of the consequence of every factor in the slope instability processes and provides a more objective analysis;
- When planning a dedicated database, the geological and engineering factors must be considerably taken into consideration since these make the theoretical models more complicated;

-
- The majority of slope instability phenomena are in constant development and continuously modify the surrounding conditions: the assessment of new scenarios is essential when modifications occur;
 - Choice of the model type and of the appropriate sliding surface is an essential aspect in every risk analysis; assessment of local conditions must be necessarily a priority followed by the approach type,
 - When assessing the risk, morphodynamical features of a landslide or of a debris flow are extremely important (e.g. expected distance of debris propagation, mass movement speed and depositional area);
 - All efforts must be made so as to compile base geological cartography – which is increasingly accurate and reliable – for identifying potential areas of risk: this cartography is still considered the best tool for a specific analysis;
 - The use of LiDAR technology for producing high resolution DEM and the importance of these supports enable to remarkably accelerate a detailed field survey without influencing data quality;
 - The frequency analysis of landslide phenomena on a regional or national scale through the Land Information Systems is an essential tool for funds allocation aimed at prevention and mitigation actions.



Different Approaches of Rockfall Susceptibility Maps in Lower Austria

Herwig Proske, Christian Bauer, and Klaus Granica

Abstract

Within the frame of the ongoing project MoNOE (Development of Methods for Modelling Natural Hazards in the Province of Lower Austria) the generation of an indicative multi-hazard map to be used as a scientific reference for regional policies of land use management is one of the main objectives. The applicability and reliability of two relatively simple GIS-based approaches have been analysed aiming at the identification of areas which are potentially endangered by rockfall in a fast and cost-effective manner.

Keywords

Rockfall • LiDAR data • Source zone • Runout zone modelling

Introduction

Rockfall hazard zoning for land-use planning is a complex problem, because of the different parameters involved: block size, energy, frequency, characteristics of the vegetation and (micro)topography, uncertainty of all parameters, etc. Rockfall hazard zoning is mostly performed using a relative hazard scale (Van Westen 2004), which does not explicitly take into account the temporal aspect.

With regard to rockfall susceptibility mapping two main aspects have to be taken into account, namely the identification of potential source zones on the one hand and the estimation of the propagation zones on the other hand. Major rockfall events in the past few years were registered

in many parts of Lower Austria affecting railways, roads and residential areas and resulting in complex and expensive remedial actions.

Study Area

The study area in Lower Austria covers approx. 10,200 km² and is located in the east of Austria (Fig. 1). The area is situated at the northern rim of the Alps with peaks reaching approx. 1,900 m asl in the southernmost part.

The geology is characterized by the alpine orogenesis with tectonic units running in west – eastern direction. The Alps are represented by the Northern Calcareous Alps (mainly different carbonates with intercalated clastic sediments), and the Flysch Zone (mainly flyschoid clastic sediments). The clastic sediments of the Molasse Zone, partly overthrust by alpine units, are building the northern foothills of the Alps. North of the river Danube (and in some parts as well cut by the river) the rocks of the Variscan Bohemian massif are forming the crystalline basement (mainly granites

H. Proske (✉) • C. Bauer • K. Granica
Joanneum Research, Institute for Information and Communication
Technologies, Steyregasse 17, Graz, Austria
e-mail: herwig.proske@joanneum.at



Fig. 1 The study area in the eastern part of Austria covering most of the province of Lower Austria

and gneiss). Zones of intense tectonics and high relief energies due to the deeply incised drainage network favour different types of mass movements like landslides, debris flows and rockfalls.

With respect to landcover and landuse the alpine part is mainly covered by forests. In the valley bottoms agricultural land (pastures, grassland) and small settlements can be found whereas alpine pastures and rocky areas dominate the higher parts of the mountains. The larger settlements within the test area are situated in the foothills of the Alps and the floodplain of the river Danube. The Bohemian massiv is mainly covered by forests and grassland.

Data Base

The geographical and geological data base was provided by the Geological Survey and the Department of Spatial Planning and Regional Policy of the federal state government of Lower Austria.

Relevant data include digital geological maps in scales 1:200,000 and 1:50,000, colour aerial fotos (orthofotos), a satellite-based land cover classification, LiDAR data and a mass movement inventory. Especially the analysis of the available high resolution DTM (1×1 m) proved to be of highest potential for the rockfall analysis.

Definition of Potential Source Zones

As most of the minor rockfall events are not registered in the mass movement inventory, statistical approaches for the identification of source areas are leading nowhere. Therefore an empirical approach was selected benefitting a lot from the available 1 m-LiDAR-DTM (Fig. 2). Threshold slope values for potential rockfall release areas were attributed to different lithological units according to field observations and the interpretation of Remote Sensing Data (Orthofotos). Morphometric parameters (e.g. profile curvature) and the specific

tectonic situation (large faults and boundaries of nappes) were taken into account as well. The defined threshold slope angles cover values from 39° in intensely tectonized carbonates up to 48° in massive granites of the Bohemian massive. The area wide modelling resulted in a total of approx. 8.3 km of potential rockfall source areas (0.08 % of the test area), most of it situated in the Calcareous Alps.

Characterisation of Propagation Zones

Assessment of the runout zones from the potential release areas was performed by means of two relatively simple GIS-based approaches, namely the CONEFALL software (Jaboyedoff 2003) and the SAGA module Rock HazardZone (Wichmann 2006).

CONEFALL Method

Maximum rockfall runout zones can be estimated empirically following the cone method (Fahrböschung) (Toppe 1987). This model is based on the idea that an individual falling rock can reach any place in the area situated inside a cone of given aperture. The CONEFALL method (Jaboyedoff 2003) implements the cone method in a GIS environment. It allows the computation of the run-out areas, the number of contributing source pixels, the velocities and kinetic energies. A lateral limitation of the cones is implemented.

Rock HazardZone Method

The SAGA module Rock HazardZone (Wichmann 2006) takes into account the local relief to calculate the magnitude of divergence yielding more realistic results. The mfd (multiple flow directions for debris flows, Gamma (2000)) method is used to calculate potential pathways. The method is implemented as a random walk in conjunction with a Monte Carlo approach and allows for calibrating the amount of modelled divergence by three parameters: (a) a slope threshold, above which no divergence is modelled (i.e. single-flow direction, D8). In case the maximum gradient is lower than the slope threshold, the gradients to all lower neighbouring cells are divided by the threshold to obtain relative slope gradients. Together with (b) a parameter that controls the magnitude of divergence, this ratio is then used as a criterion whether a neighbouring cell exhibits a sufficiently high gradient to be selected as potential pathway. The transition probabilities of all neighbouring cells that meet the criterion are calculated proportional to the sum of their relative slope gradients; (c) a persistence factor that allows to increase the probability of that neighbouring cell, which features the same

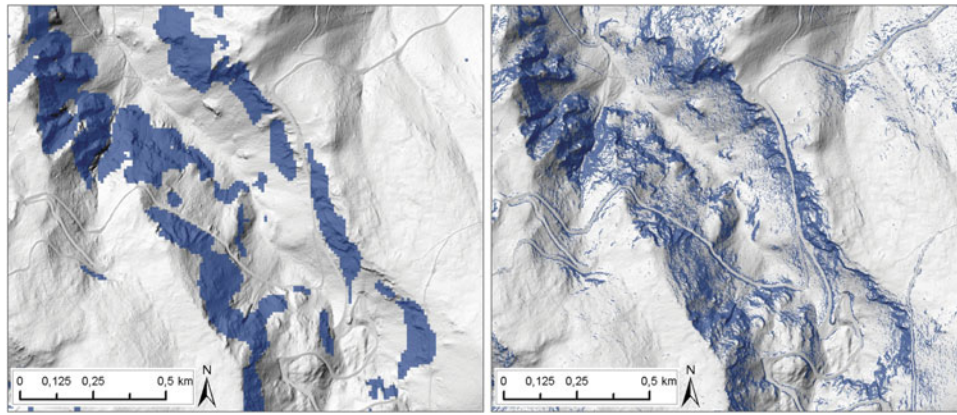


Fig. 2 Rockfall source zones in a forested area in the southern part of the study area: the *left* image displays source zones based on a 10 m Digital Terrain Model (DTM), the *right* image shows source zones

based on the 1 m LiDAR DTM. The same parameters and slope threshold values were used for both maps. The hillshade background is based on the 1 m LiDAR DTM in both images

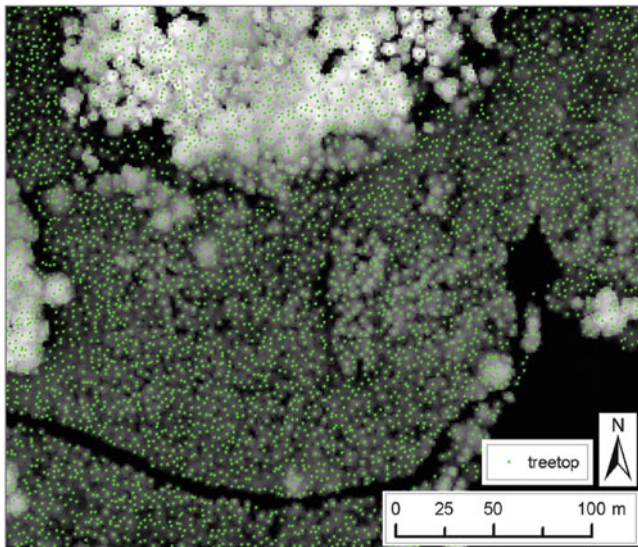


Fig. 3 Identification of tree tops by means of automatic single tree detection from LiDAR DSM data overlaid on Vegetation Height Model (*dark* areas representing low vegetation, *bright* areas representing high vegetation)

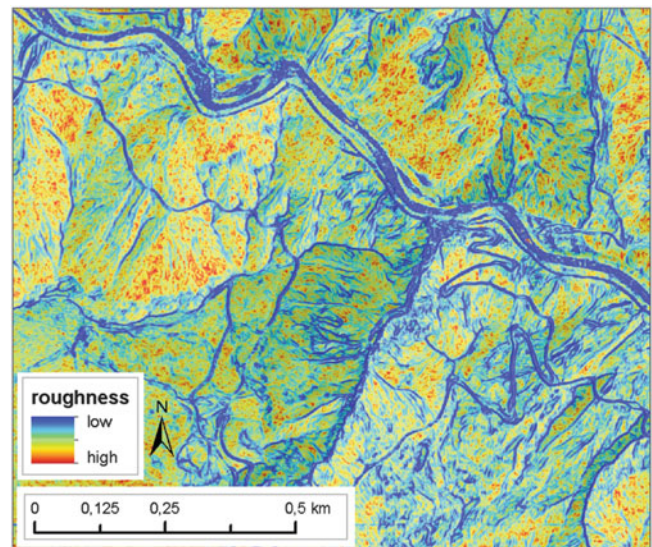


Fig. 4 Surface roughness in a rockfall prone area in the southern part of the study area based on local variability of vector orientations of LiDAR DTM data (window size 5×5 cells, spatial resolution 1 m)

direction like the centre cell was entered (Wichmann and Becht 2006).

The process-based calculation of the runout distance permits the input of a friction coefficient which depends on surface cover characteristics, i.e. material properties, micromorphology and obstacles (vegetation) on the slope. This model therefore allows for the high potential of the LiDAR data.

Forest parameters include vegetation height as well as density of vegetation by means of automatic single tree detection from LiDAR Digital Surface Model (DSM, see Fig. 3).

Surface roughness is calculated by measuring the variability in slope and aspect in local patches of the LiDAR Digital Terrain Model (DTM, see Fig. 4). In this approach, unit vectors are constructed perpendicular to each cell in the DTM. The vectors are defined in three dimensions using polar coordinates by their direction cosines. Local variability of vector orientations is then evaluated statistically (McKean and Roering 2004). Different window sizes (3×3 to 9×9 pixels) and different DTM resolutions were applied to obtain optimum results as compared to field verifications.

Based on these inputs a friction map was compiled displaying five classes of friction.

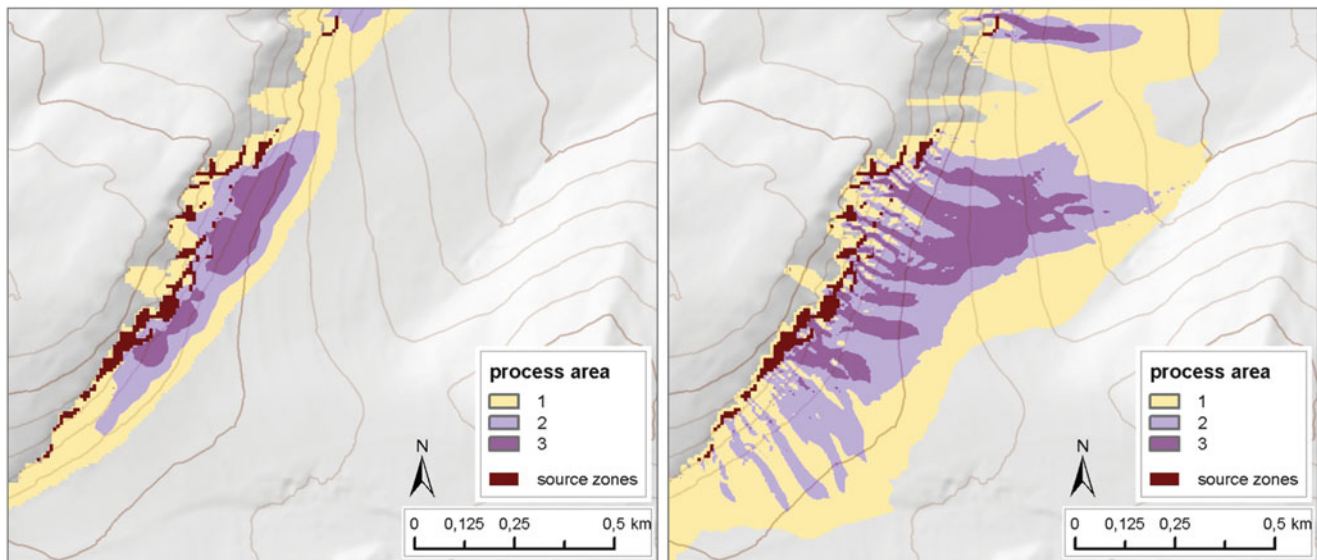


Fig. 5 Modelling of rockfall runout zones by means of the empirical CONEFALL method (*left image*) and the process-based SAGA Rock HazardZone method (*right image*) in a partly forested area in the

eastern part of the study area without considering effects of vegetation and surface roughness (*transparent areas*: no hazard; 1 hazard not to be excluded; 2 hazard to be expected; 3 high hazard to be expected)

Rockfall Runout Zones

CONFALL Modelling Results

The CONEFALL model is applied to each potential rockfall source zone defined previously in order to assess the maximum runout length. The source zones are aggregated to a cell size of 5×5 m.

Aperture angle of the cones is defined empirically by taking into account information from literature (Toppe 1987; Meißl 1998), orthophoto analyses and fieldwork results. Considering the results of several test runs, finally a value of 35° was selected for all tectonic units.

To obtain not only a grid of the potential propagation area but also a rough image of the rock-fall transit density the “Count of contributing source points” – option is activated. As well the energies are estimated. The mean block masses of typical lithological units were classified according to field observations.

An example of the CONEFALL Modelling is presented in Fig. 5. The process area is subdivided in three qualitative classes according to the estimated kinetic energy.

SAGA Rock HazardZone Modelling Results

The SAGA module Rock HazardZone is applied only in selected areas where the number of exposed objects (houses, infrastructure) is high. The input file of the rockfall source zones is the same as for the CONEFALL approach.

The selected modelling method is following the “rockfall velocity” – method (Scheidegger 1975). With regard to the random walk parameters the number of iterations is set to 1,000, the slope threshold is 40° , the exponent controlling the magnitude of lateral divergence is 2 and the persistence factor is 1. The same block masses as for the CONEFALL approach are used.

Examples of the Rock HazardZone Modelling are presented in Figs. 5 and 6. The classification of the process area is adapted to the range of the CONEFALL approach with subdivision in three qualitative classes according to the number of stops. Whereas Fig. 5 displays the modelling result without taking into account any influences of obstacles and surface roughness, Fig. 6 shows the same area under consideration of the classified friction map. As most of the process area is covered by forest considerable differences between the two maps can be detected. As well the influence of forest gaps can be visualized clearly (Fig. 6).

Conclusions

The presented GIS-based methods describe a straightforward and generally applicable approach to develop rockfall susceptibility maps which can be used as indicative hazard maps. The combined use of the two applied methods provide a relatively fast and cost-effective way to overview rockfall prone zones over large areas at a regional scale. Field verifications in selected regions indicated that in most cases the results provided sufficient degree of accuracy. Further investigations and more detailed modelling have to be accomplished in the identified high hazard zones. Compared to previous

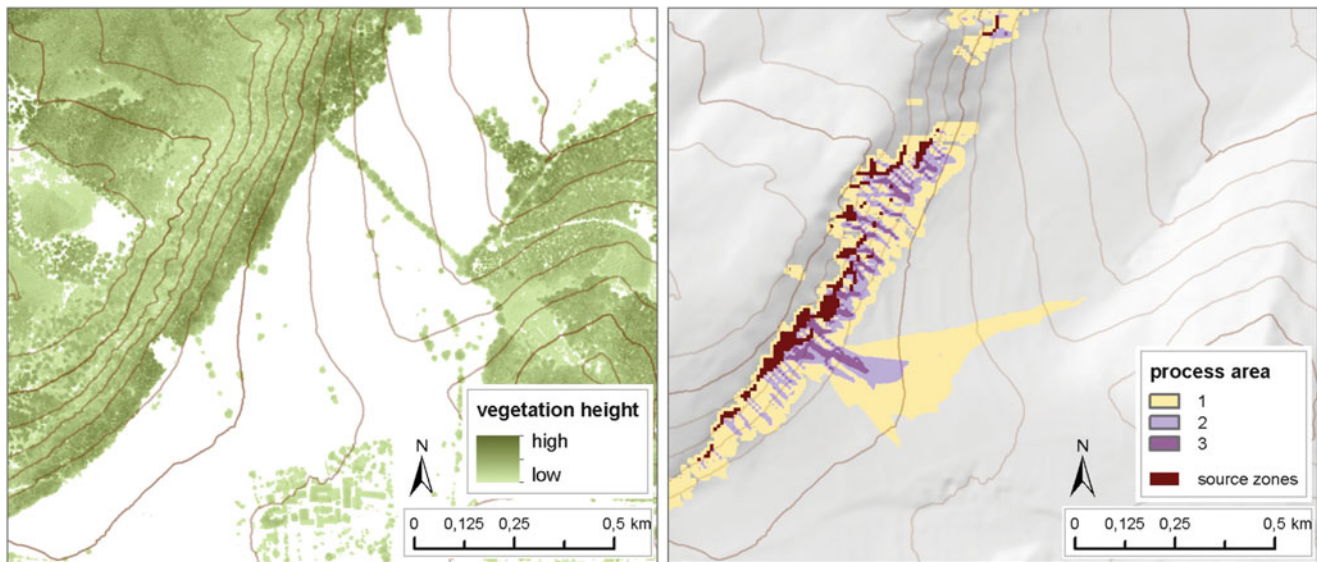


Fig. 6 Modelling of rockfall runout zones by means of the process-based SAGA Rock HazardZone method (*right image*) in a partly forested area in the eastern part of the study area under consideration of effects of vegetation and surface roughness (*transparent areas*: no

hazard; 1 hazard not to be excluded; 2 hazard to be expected; 3 high hazard to be expected). The *left image* displays the LiDAR based vegetation height model clearly showing the consequences of vegetation gaps with regard to the rockfall runout zones

works the results improved significantly using the LiDAR data. However additional efforts have to be made with regard to the generation of more detailed and reliable geological base maps for the identification of potential source areas. This work step has to be attached high importance to, as the whole propagation modelling procedure is based on the results of the source area identification.

The protective functions of forests can be demonstrated by taking into account different forest scenarios, e.g. reduced forest cover in rockfall prone areas.

Acknowledgments The project MoNOE is funded by the Geological Survey and the Department of Spatial Planning and Regional Policy of the federal state government of Lower Austria.

References

Gamma P (2000) dfwalk – Ein Murgang-Simulationsprogramm zur Gefahrenzonierung. *Geographica Bernensia* G66, 144p

- Jaboyedoff M (2003) CONEFALL 1.0: a program to estimate propagation zones of rockfall based on cone method. Quanterra. www.quanterra.ch. Accessed 15 May 2011
- McKean J, Roering J (2004) Objective landslide detection and surface morphology mapping using high-resolution airborne laser altimetry. *Geomorphology* 57:331–351
- Meißl G (1998) Modellierung der Reichweite von Felsstürzen. *Innsbrucker Geographische Studien* 28:249p
- Scheidegger AE (1975) Physical aspects of natural catastrophes. Elsevier Scientific, Amsterdam, 289p
- Toppe R (1987) Terrain models – a tool for natural hazard mapping. In: Salm B, Gubler H (eds) *Avalanche formation, movement and effects*, vol 162, IAHS Publication. IAHS, Wallingford, pp 629–638
- Van Westen CJ (2004) Geo-information tools for landslide risk assessment: an overview of recent developments. In: Lacerda WA, Ehrlich M, Fontoura AB, Sayo A (eds) *Landslides evaluation and stabilization*. Balkema, Leiden, pp 39–56
- Wichmann V (2006) Modellierung geomorphologischer Prozesse in einem alpinen Einzugsgebiet – Abgrenzung und Klassifizierung der Wirkungsräume von Sturzprozessen und Muren mit einem GIS. *Eichstätter Geographische Arbeiten*, 15. Profil Verlag, München/Wien, 231p
- Wichmann V, Becht M (2006) Rockfall modelling: methods and model application in an alpine basin (Reintal, Germany). In: Böhner J, McCloy KR, Strobl J (eds) *SAGA – analysis and modelling applications*, vol 115, Göttinger Geographische Abhandlungen. Goltze, Göttingen, pp 105–116



Mathematical and GIS-Modeling of Landslides in Kharkiv Region of Ukraine

Oleksandr Trofymchuk, Yuriy Kalyukh, and Hanna Hlebchuk

Abstract

In view of the acute need to solve a problem related to a landslide hazard at local and regional levels, the system-based tool, which integrates a mathematical modeling and GIS technologies, has been developed. A mathematical model of landslide process was developed based on the theoretical grounds of statics of granular medium and the most frequently used calculation methods of slope stability coefficient by Maslov-Berer and Shakhunyants and value of landslide pressure by Shakhunyants. Presented model underlies design of software for modeling slopes stress condition given engineering-geological changes (LANDSLIP07). This software is used for analysis of landslide processes. These research activities have been carried out in the framework of the Institute of Telecommunications and Global Information Space of National Academy of Sciences of Ukraine, and the IPL-153 Project “Landslide hazard zonation in Kharkov region of Ukraine using GIS”.

Keywords

Landslide • Landslide slope • Mathematical model • Stability coefficient • Groundwater level • Software LANDSLIP07

Urgency of the Problem

Given the conserved tendency of landslide phenomena activation due to increasing technogenic burden and global natural changes in an environment, forecasting and prevention of dangerous strain processes are the priority state-level problems.

It should be mentioned that change of climate conditions, strongly marked lately, is accompanied by:

- Increase in temperature values and their substantial surges over a day (up to 10 units);
- Increase in precipitation;
- Rise in natural disasters (floods and hurricanes);

- Rise in groundwater levels;
- Seismic activity, which isn't typical for certain areas.

Based on data analysis of the regional groundwater regime in Kharkov region during the 2009 year it can be stated that positions of groundwater level, evaluated in the coefficients of relative position, are near to mark (0.4–0.6), exceeding the average long-term amplitude by 10–30 %.

Finally all of these factors render active (in certain cases render overactive) strain processes in soil, accompanied by displaying of karst, landslide and other phenomena.

In the area of Ukraine there are over 23 thousand of landslides, and 1,615 units are located in Kharkiv region. The landslide affected area is estimated to be 40.3 km² in Kharkiv region, constituting 0.13 % of total. Sixty-seven landslides are located in the built-up area, posing a serious menace for six economic units. Kochetok dam, being a strategic object, is also under the threat of destruction. The number of landslides will vary constantly due to liquidation or joining up certain landslide forms and occurrence of new ones.

O. Trofymchuk (✉) • Y. Kalyukh • H. Hlebchuk
Institute of Telecommunications and Global Information Space,
National Academy of Sciences of Ukraine, 13, Chokolivsky Blvd.,
Kyiv 03186, Ukraine
e-mail: itelua@kv.ukrtel.net; y.kalyukh@ndibk.gov.ua; glebchuk@i.ua

The displaying of landslides in slopes with slope angle equal to 5° was registered in Kupiansk district of Kharkiv region. One of these landslides is situated near the cemetery. This indicates the geo-mechanical degradation of losses as a result of global climate changes. The parts of landslide sites in Kupiansk district are presented at the photos below.

Solving the problems concerning landslide hazard, modification and specialization of existing calculation methods, designing of effective software are essential for making a decision about using ground areas with complex relief and hydrological conditions.



Complex mathematical models in mechanics of deformed medium have been developed by such authors as I. I. Lyashko, V. S. Deyneka, I. V. Sergienko, O. P. Vlasiuk and others.

The principal methods of landslide hazard determination are the methods of slope stability assessment. The methods of landslide hazard calculation have been developed by such authors as N. M. Gersevanov, N. N. Maslov (1949), G. M. Shakhunyants (1953), L. K. Ginzburg (1979), M. N. Golshtein, O. I. Bileush, M. G. Demchishyn.

The main goal of the article is to develop a tool for the landslide hazard forecasting at regional and local levels on the basis of system integration of mathematical modeling and GIS technologies.

Main Part

Meteorological, hydrological and seismic conditions are the fundamental natural driving forces for occurrence and activation of landslides.

The first Project stage included collection of input data including geographical coordinates of a relief, hydrographical network, settlements, road network, seismic zoning of the territory of Kharkov region. Meteorological data for 20 years from meteorological stations of Kharkov region, data on physical-mechanical properties of soils and data on landslide sites were also collected and processed.

These data were obtained with the assistance of the following Ukrainian institutions:

- The Institute of Geological Sciences of National Academy of Sciences of Ukraine;
- The Ukrainian State Leading Research and Industrial Institute of Engineering, Technical and Ecological Researches;
- The Ukrainian Hydrometeorological Institute.

The information obtained was systematized and used subsequently when creating and filling a database.

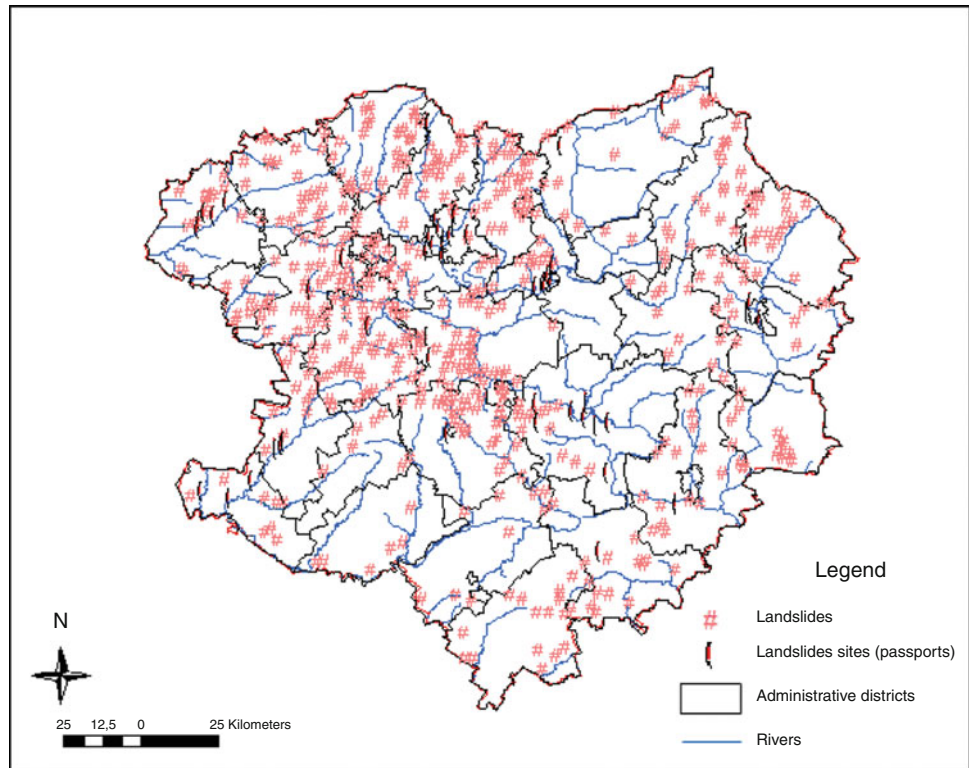
The database has been developed. It includes three main components:

- The first component contains full information on descriptors (passports) of landslide sites;
- The second component contains short-form information on 52 descriptors (passports) of landslide sites;
- The third component contains information on monthly precipitation data from meteorological stations of Kharkov region for 20 years.

The map of distribution of landslides in Kharkiv region is presented bellow (see Fig. 1).

Data on the relief, hydrographic and road networks, settlements, landslide sites, seismic zoning of the territory of Kharkov region have been analyzed, systematized and presented in the form of layers in the developed GIS.

Fig. 1 Map showing distribution of landslides in Kharkiv region



When analyzing the landslide hazard of a slope, methods of mathematical modelling have been used. These methods were based on estimates of coefficient of slopes stability and landslide pressure.

The Maslov-Berer and Shakhunyants calculation methods underlie the developed mathematical model, on which software LANDSLIP07 is based on. They used limit stress state analysis of granular medium in case of plane problem. It can be presented graphically (see Fig. 2).

In general cases the equilibrium equations for linear-strain bodies in stress state can be presented as following:

$$\frac{\partial \sigma_y}{\partial y} + \frac{\partial \tau_{yz}}{\partial z} = 0; \frac{\partial \sigma_z}{\partial z} + \frac{\partial \tau_{yz}}{\partial y} = \gamma \quad (1)$$

There are three unknowns in two equations, that is the problem is statically indeterminate. Adding the condition of limit equilibrium to above equations, we get closed system of three equations for three unknowns, so the problem becomes statically determinate.

$$\frac{(\sigma_z - \sigma_y)^2 + 4\tau_{yz}^2}{(\sigma_z + \sigma_y + 2c \cdot \text{ctg} \varphi)^2} = \sin^2 \varphi \quad (2)$$

Unknowns: σ_y, σ_z – normal stresses,
 τ_{yz} – tangential stresses.

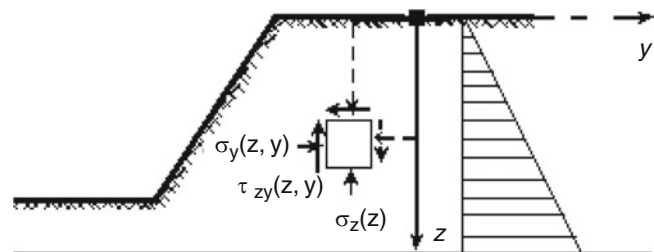


Fig. 2 Limit equilibrium method, plane problem

Constants: c – specific cohesion,
 φ – angle of internal friction;
 γ – soil unit weight.

Boundary conditions:

$$z = 0; \sigma_z(0, y) = 0; \sigma_y(0, y) = 0.$$

The solution of this system of differential equations was presented by V. V. Sokolovskij (1942).

However, in this case an isotropic slope is considered. Generally, landslide slopes are anisotropic, possess a depression curve and sliding surface. Thus, it was decided to apply the Maslov-Berer and Shakhunyants methods, based on calculation of stability coefficient and landslide pressure (see Fig. 3).

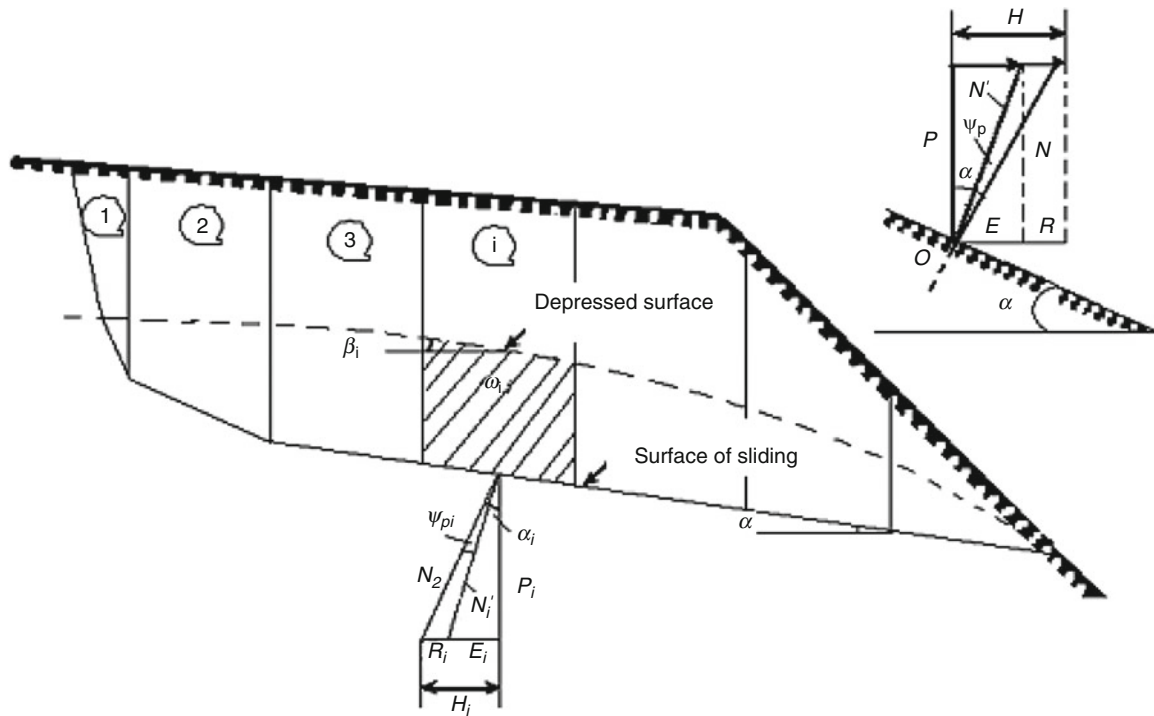


Fig. 3 Maslov-Berer method

Maslov-Berer Method

- N – reaction force on the sliding surface provided $\varphi = 0, c = 0$;
- N' – reaction force (P – weight) provided $\varphi \neq 0, c \neq 0$;
- φ – angle of internal friction;
- ψ_p – angle of shearing resistance;
- H – pressure on a vertical wall below located cell provided $\phi = 0, c = 0$;
- R – pressure on a vertical wall provided $\varphi \neq 0, c \neq 0$;
- E – active pressure.

$$\left. \begin{aligned} H &= P \cdot \operatorname{tg} \alpha \\ E &= P \cdot \operatorname{tg}(\alpha - \psi_p) \\ R &= H - E = P[\operatorname{tg} \alpha - \operatorname{tg}(\alpha - \psi_p)] \end{aligned} \right\} \quad (3)$$

$$\tau_n = \sigma_n \cdot \operatorname{tg} \varphi + c = \sigma_n(\operatorname{tg} \varphi + c/\sigma_n) = \sigma_n \cdot F_p \quad (4)$$

$$F_p = \operatorname{tg} \varphi + c/\sigma_n \quad (5)$$

$$\sigma_{ni} = \frac{P_i \cos \alpha_i}{l_i} \quad (6)$$

$$K_{st} = \frac{\sum R_i}{\sum (\pm H_i)} = \frac{\sum P_i[\operatorname{tg} \alpha_i - \operatorname{tg}(\alpha_i - \psi_{pi})]}{\sum P_i \operatorname{tg} \alpha_i} \quad (7)$$

$$E_{ls} = \sum_{i=1}^n [(K_{st}^3 - 1)P_i \operatorname{tg} \alpha_i + P_i \operatorname{tg}(\alpha_i - \psi_{pi})] \quad (8)$$

However, apart from the physical-mechanical characteristic, the impact of groundwater, saturated soils, seismic forces and weight of building structures were also taken in consideration.

According to these complement:

- **Maslov-Berer formulae:**
 - Subject to seismic forces:

$$K_{st} = \frac{\sum P_i[\operatorname{tg} \alpha_i - \operatorname{tg}(\alpha_i - \psi_{pi})]}{\sum (P_i \cdot \operatorname{tg} \alpha_i + Q_{ci})} \quad (9)$$

$$E_{ls} = \sum [(K_{st}^3 - 1) \cdot P_i \cdot \operatorname{tg} \alpha_i + K_{st}^3 \cdot Q_{ci} + P_i \cdot \operatorname{tg}(\alpha_i - \psi_{pi})] \quad (10)$$

$$Q_c = \mu_c \times P \quad (11)$$

where μ_c – seismic coefficient; P – average soil weight of landslide block.

- Subject to seepage force:

$$K_{st} = \frac{\sum P_i[\operatorname{tg} \alpha_i - \operatorname{tg}(\alpha_i - \psi_{pi})]}{\sum (P_i \cdot \operatorname{tg} \alpha_i + Q_{ci} + j_i \cos \beta_{\Phi_i})} \quad (12)$$

$$E_{ls} = \sum \left[\frac{(K_{st}^3 - 1) \cdot P_i \cdot tg \alpha_i + K_{st}^3 \cdot j_i \cdot \cos \beta_{\Phi_i} +}{+ K_{st}^3 \cdot Q_{ci} + P_i \cdot tg(\alpha_i - \psi_{pi})} \right] \quad (13)$$

$$j_i = \gamma_{\omega} \omega_i \sin \beta_{\Phi_i}, \quad (14)$$

where ω_i – cross-section area of the groundwater stream in i-cell; γ_{ω} – water volume weight; $\sin \beta_{\Phi_i} = i_i$ – gradient (head loss per unit length of water flow).

• **Shakhunyants formulae:**

- Subject to seismic forces:

$$K_{st} = \frac{\sum_{i=1}^n \frac{(P_i \cdot \cos \alpha_i tg \varphi_i + c_{li}) \cos \varphi_i}{\cos(\alpha_i - \varphi_i)}}{\sum_{i=1}^n \frac{(P_i \sin \alpha_i + Q_{ci}) \cos \varphi_i}{\cos(\alpha_i - \varphi_i)}} \quad (15)$$

$$E_{ls} = \sum_{i=1}^n \left[K_{st}^3 (P_i \sin \alpha_i + Q_{ci}) - (P_i \cos \alpha_i tg \varphi_i + c_{li}) \right] \frac{\cos \varphi_i}{\cos(\alpha_i - \varphi_i)} \quad (16)$$

- Subject to seepage force:

$$K_{st} = \frac{\sum_{i=1}^n \frac{(P_{Bi} \cdot \cos \alpha_i tg \varphi_{Bi} + c_{Bi} l_{Bi}) \cos \varphi_{Bi}}{\cos(\alpha_i - \varphi_{Bi})}}{\sum_{i=1}^n \frac{(P_{Bi} \sin \alpha_i + Q_{ci} + j_i) \cos \varphi_{Bi}}{\cos(\alpha_i - \varphi_{Bi})}} \quad (17)$$

$$E_{ls} = \sum_{i=1}^n \left[K_{st}^3 (P_{Bi} \sin \alpha_i + Q_{ci} + j_i) - (P_{Bi} \cos \alpha_i tg \varphi_{Bi} + c_{Bi} l_{Bi}) \right] \times \frac{\cos \varphi_{Bi}}{\cos(\alpha_i - \varphi_{Bi})}$$

Software LANDSLIP07 was developed according to models mentioned above. It helps to automate the process of calculation of stability coefficient and landslide pressure with further construction of landslide pressure diagram. This software completely satisfies the requirements of designers and surveyors and it is easy to use (Trofymchuk et al. 2008a, b, c).

By means of software LANDSLIP07 the assessment of local and overall slope stability was carried out for apartment construction project in Kharkiv (Frontova St, 3).

The assessment of overall slope stability carried out along permissible sliding surface with minimal values of stability coefficient. Local slope stability was estimated along base of banked earth.

Calculations were carried out for two profiles. Shakhunyants method was applied (see Fig. 4). Slope stability was assessed according following schemes: under the assumption of natural water saturated slope, total saturated slope, in the presence of building and total saturation of a slope. For all sliding surfaces of every scheme calculation diagram and landslide pressure diagram are presented.

Summary of calculation results on the slopes stability is presented in Table 1.

Conclusions

Conclusions and recommendations concerning building up of landslide-prone slope:

1. Implementation of the targeted GIS, which contains a number of important layers, makes it possible to assess impact of the above-mentioned factors on a process of landslide formation. It assists local authorities in making effective decisions on prevention of landslides.
2. Engineering-geological conditions are estimated as complicated. There are complicative factors, which should be taken into account when designing, namely the presence of:
 - Sizeable inclination of natural relief and steep slopes;
 - Thickness of banked earth of engineering-geological elements EGE 1 of non-uniform depth, non-homogeneous structure and loose texture (EGE 1 labels banked earth, namely earth deposits of humus loam with inclusion of construction waste up to 20 % and with 0.5 ÷ 8.0 m in depth);
 - Sedimentary soils EGE 2 (EGE 2 are yellow-brown semisolid sedimentary loam with 0.5 ÷ 4.1 m in depth).
3. In the present state total slope stability is guaranteed ($K_{st} = 1.33 > 1.25$). The evolution of landslide process with depth of capture up to 10 m is possible when watering the soils ($K_{st} < 1.0$).
4. Local stability of the slope assembled from banked earth is not ensured ($K_{st} < 1.0$).
5. When executing the construction project, slope stability coefficients exceeds normative values $K_{st} = 1.86$ and $K_{st} = 1.91$ for different sliding surfaces.
6. Local stability of deepened parking (from Frontova St) is reduced ($K_{st} < 1.0$) in the case of watering the soils. It will result in increase of pressure on building units. Recommendations for taking precautions:
 - Construction of intercepting channel (storm water sewer) along Frontova St;
 - Draining of bedding layer.
7. It is recommended to use maximum values of landslide pressure E_{ls} , when calculating retaining constructions for foundation pit walls (for the construction period). They can be computed for the most deepened part of foundation pit by the help of software LANDSLIP07.
8. Foundations of buildings can be realized as plate, driven or bored piles.
9. Planned partial backfilling of gully can be permitted only after arranging storm and melt water outfall and drain. The drain is required for drawing off infiltration water and water falling into the space around pipes because of micro suffosion processes near the building site.

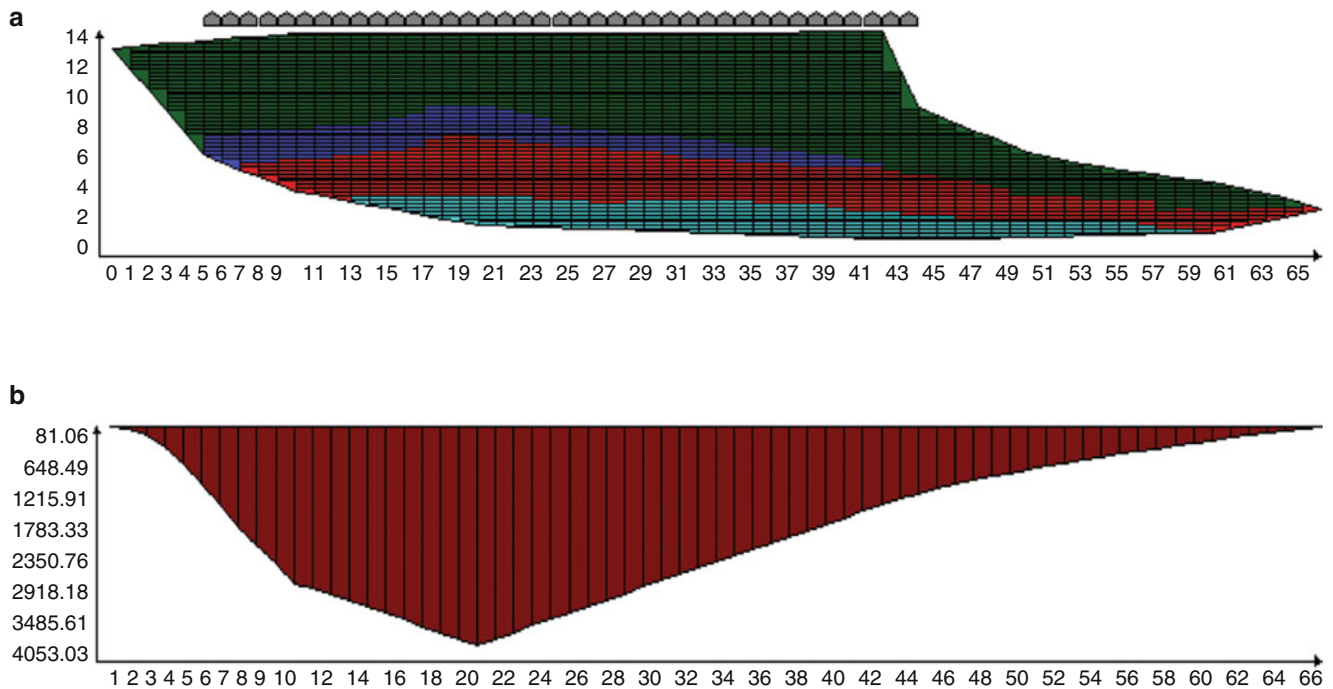


Fig. 4 Sliding surface: (a) landslide calculation diagram with modeling of buildings as tightening weights in the case of total water saturation of soils, LANDSLIP07-assisted. A horizontal axis is an extent of landslide array in a plan (m). A vertical axis is a depth of

landslide array on a vertical line (m). (b) Landslide pressure diagram corresponding to initial slope geometry. A horizontal axis is an extent of landslide array in a plan (m). A vertical axis is a landslide pressure ($\times 10^4 \text{ N}$)

Table 1 Summary of calculation results on the slopes stability

No of calculation profile	Sliding surface	Stability coefficient, K_{st}		
		Initial slope shape		With weight of projected building and total saturation of a slope
		Natural saturated slope	Total saturated slope	
I-I	G0	4.01	1.86	3.07
	B0	2.86	1.33	–
	B1	2.22	1.18	–
	B0	2.06	0.96	–
	A2	0.80	0.32	–

10. Planning work should be carried out by means of layer-by-layer rolling of soils. It prevents from rain and melt water infiltration, evolution of erosive processes and nonuniform self-packing of banked earth.

Acknowledgments The authors would like to thanks the Ukrainian State Leading Research and Industrial Institute of Engineering, Technical and Ecological Researches; Institute of Geological Sciences of National Academy of Sciences of Ukraine.

References

- Ginzburg LK (1979) Landslide-protective and retention constructions. Stroyizdat, Moscow, 80p, in Russian
- Maslov NN (1949) Soil mechanics. Publisher of Ministry of construction of mechanical engineering enterprises, Moscow, 328p, in Russian
- Shakhunyants GM (1953) Roadbed of railways. Tranzheldorizdat, Moscow, 827p, in Russian
- Sokolovsky VV (1942) Statics of loose medium. Academizdat, Moscow, 460p, in Russian
- Trofymchuk OM, Hlebchuk HS, Kalyukh YuI (2008a) Mathematical modeling of change of stressed-deformed condition of landslide mass in presence of building and developing a foundation pit under conditions of underflooding. Building constructions No 71. pp 95–104, in Russian
- Trofymchuk OM, Hlebchuk HS, Polevetsky VV (2008b) On stability of slopes under changes of seismic conditions. Building constructions No 69, pp 304–311, in Russian
- Trofymchuk OM, Kalyukh YuI, Hlebchuk HS (2008c) Mathematical modeling of landslide slope stability under rising the underground waters' level. Ecology and Resources No 18, pp 51–58, in Russian



Evaluation and Zonation of Landslide Hazard of Northern Tehran District

Ali Uromeihy and Mahsa Sharif

Abstract

Tehran is the country's most densely populated district which is located on the southern part of Alborz Mountains. Many sensitive infrastructures such as dams, roads, power lines and housing complexes are located within the area. In this paper the potential of landslide hazard for North Tehran is evaluated and a hazard zonation map based on ARC-GIS method is prepared. Several parameters such as lithology, slope angle, slope direction, distance from faults and seismicity (earthquake deduced acceleration) are considered as main factors. The quality parameters of the defined effecting factors are quantified by the above named software where the data layers are divided into smaller classes. In the next stage, specific weights are assigned to each class and the hazard potential values are determined. Finally they are presented as a landslide hazard zonation map of the area. It was found that slope angle of 16–35°, slope direction from 40° to 140°, lithology of tuffaceous rocks, distance of fewer 2 km from fault and seismicity of over 0.5 g has great effect on the distribution of landslide in the area.

Keywords

Landslide evaluation • Landslide hazard zonation mapping

Introduction

The fast rate of development of Tehran City, involve the build-up of housing complex, highways and other infrastructural construction on the foothills of Alborz Mountains and through it leading to increased incidences of hill slope instability. So there is a requirement for a landslide hazard evaluation technique to be adopted in the planning stage to avoid major problem related to slope instability. In this paper Landslide Zonation Mapping based on ARC-GIS method is implemented as a hazard evaluation technique for application

in planning the expansion of urban settlements in hilly and mountainous terrain of north Tehran districts.

Figure 1 shows the expansion of Tehran City towards the foothills of Alborz Mountains and Fig. 2 shows an example of road construction within the mountainous terrain in north Tehran districts. The high relief of mountain front is the result of tectonic activities which are represented by many east–west oriented thrust faults. The faults usually are surrounded by zones of crushed and weak rocks and alluvium deposits.

An early guideline for landslide hazard zonation was introduced by Varnes (1984), LHZ mapping based on slope facet then reviewed many techniques for multi-scale study for landslide hazard evaluation. Some more recent works in this regard have been done for example; by Ramakrishnan et al. (2002), Anbalagan et al. (2008), Gahgah et al. (2009). In Iran local studies regarding landslide zonation were performed by many researchers, for example: Uromeihy and Mahdaviifar (2000), Ghafoori et al. (2006) and Uromeihy and Fattahi (2011).

A. Uromeihy (✉)
Department of Engineering Geology, Tarbiat Modares University,
Tehran, 14115–175 Iran
e-mail: uromia@yahoo.co.uk

M. Sharif
Northern Tehran Unit, Department of Geology, Islamic Azad
University, Tehran, Iran



Fig. 1 Expansion of Tehran city towards Alborz Mountains



Fig. 2 An example of local road in Alborz Mountains

Tehran General Geology

North region of Tehran is part of Alborz Mountains and consists of a series of stratigraphic units. The units are classified, according to the age of deposition, into four groups as follows:

Unit 1: Consist of a sequence of sedimentary rocks dated from Pre-Cambrian to mid Triassic which includes several geologic Formations and many unconformities indicating land-forming movements.

Unit 2: Contains a series of coal bearing shale and sandstone (Shemshak Formation, mid Jurassic), Marine Carbonate rocks (Dalichie and Lar Formations, mid and upper Jurassic, respectively) and Marl-Carbonate complex (Tizkoh Formation, lower Cretaceous). These units form the highest part of Alborz Mountains in the region.

Unit 3: Comprises sequences of pyroclastic and volcanoclastic (tuffaceous) rocks with several intrusive igneous rocks (Karaj Formation, Eocene). This unit has widest outcrops in the region and covers over 45 % of the land surface area. An example of road cut in this unit is shown on Fig. 3. Rocks younger than Eocene are mainly confined to basic intrusive.

Unit 4: Consists of Quaternary deposits of coarse-grained alluvium deposited by frequent flow of floods and rivers in several alluvial fans and flood plains at the foot hills of Alborz Mountains. The alluvium deposits, regarding their age of deposition, are divided into four zones: A, B, C and D (Rieben 1966). Further studies on Tehran deposits and its seismic history were accomplished by Berberian et al. (1985). The cementation of the alluvium is generally poor but some carbonate materials can be identified as secondary cementation in older deposits (Asghari et al. 2004).

The structural elements of Tehran districts are mainly includes a number of reverse and thrust faults. The two main distinguished faults are identified as North Tehran Fault in the north and Kahrizak Fault in the south. Due to the expansion of the Tehran City towards the north, large area of housing and other development of lifelines project are extended along the location of this fault and the related shear zones. A detailed evaluation of seismic hazard map of Tehran is described by Takada et al. (2004).

Region Data Elevation

Digital elevation model (DEM) is a three dimensional representation of a terrain's surface created from elevation data. A digital elevation model (DEM) of the study area is shown on Fig. 4. The DEM map was built on the base of datasets of aerial photographs using remote sensing techniques in the form of a raster model with a grid of squares of 50 m in dimension. The DEM maps have a wide range applications in earth science studies including landslide hazard map evaluation. In this paper, the DEM map is used as a base map to plot the locations of landslides and to plot the information layers related to the landslide's influencing factors.

Landslide Influencing Factors

Landslide influencing factors in the region are defined on the bases of is expert evaluation and consideration the past history of landslide events in the region.



Fig. 3 Road-cut through Tuffaceous rocks of Karaj formation and development of rock falls

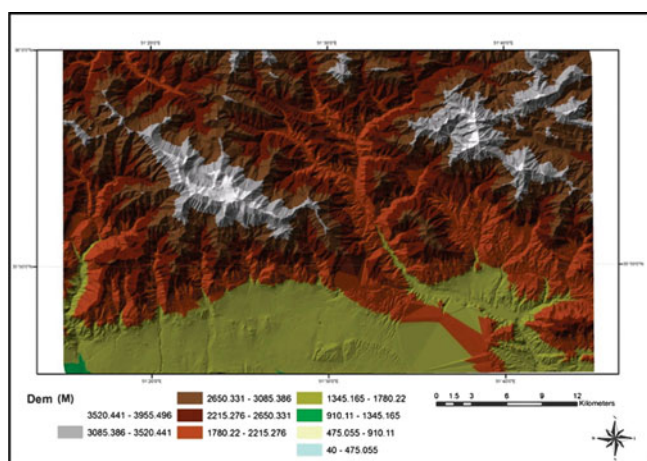


Fig. 4 Digital elevation model map of the region

The influencing factors are identified as lithology, slope angle, slope direction, fault distance and seismicity. Each factor is classified into five categories and by the use of ARC-GIS technique the numerical analysis regarding surface ratio, landslide ratio, the number of pixels involved in landslide and the number of pixels for all area are calculated. The results of these calculations are detailed in Table 2. Details division of each factor is given below:

Lithology: Lithology is an important factor in controlling slope instability. Although various types of rock units and deposits are existed in the region but they are classified into five categories regarding their effect on landsliding (see Table 1). Type 1 includes crystalline rock mainly intrusive igneous and basic volcanic rocks. Type 2 comprises well cemented sedimentary rocks. Type 3 consists of almost soft pyroclastic and volcanoclastic (tuffaceous) rocks. Type 4 contains alluvium deposits

Table 1 Main factor and the calculated

I	Lithology	Surface ratio	Slide ratio	N _{pix} slides	N _{pix} total
1	Volcanic rocks	36.50	14.74	6,049	183,890
2	Sedimentary rocks	04.23	12.70	5,238	21,311
3	Tuffaceous rocks	31.90	37.93	15,567	160,670
4	Alluvium deposits	19.45	25.63	10,518	97,813
5	Recent deposits	07.77	08.90	3,774	39,081
II	Slope angle	Surface ratio	Slide ratio	N _{pix} slides	N _{pix} total
1	00–05	22.30	20.32	8,247	110,969
2	06–15	29.53	30.13	12,228	146,964
3	16–35	17.74	21.24	8,621	88,277
4	36–45	23.18	21.37	8,674	115,359
5	46–90	07.23	06.91	2,805	36,001
III	Slope direction	Surface ratio	Slide ratio	N _{pix} slides	N _{pix} total
1	1–65	20.65	19.51	7,920	102,347
2	66–140	19.98	21.56	8,748	99,040
3	141–212	20.62	20.98	8,516	102,206
4	213–286	19.86	19.97	8,106	98,432
5	287–360	18.86	17.95	7,285	93,456
IV	Fault distance	Surface ratio	Slide ratio	N _{pix} slides	N _{pix} total
1	0–2	32.59	54.81	552	782,321
2	2–4	23.74	15.19	153	569,932
3	4–6	19.03	03.97	40	456,945
4	6–8	14.12	16.68	168	338,938
5	6–10	10.50	09.33	94	252,256
V	Seismicity	Surface ratio	Slide ratio	N _{pix} slides	N _{pix} total
1	0.32–0.38	11.05	02.70	15	851
2	0.38–0.43	18.38	08.30	46	1,416
3	0.43–0.48	22.05	11.19	62	1,698
4	0.48–0.53	20.88	25.00	139	1,608
5	0.53–0.58	27.62	52.70	292	2,127

with poor cementation of early Quaternary deposits. Finally, type 5 consists of un-cemented recent alluvial deposits. Distribution of various types of lithology is shown on Fig. 5. Type 1 and type 3 of lithology cover over 68 % of the land surface.

Slope angle: The morphological feature of the ground surface is presented by a slope angle map. The preparation of the map is based on the classification of slope angle into five divisions as indicated in Table 1. Almost 30 % of the surface area has slope angle between 6 and 15°. The details of slope divisions are also shown on Fig. 6.

Slope direction: In mountainous region of Alborz where the variation of temperatures is high, the slope direction can

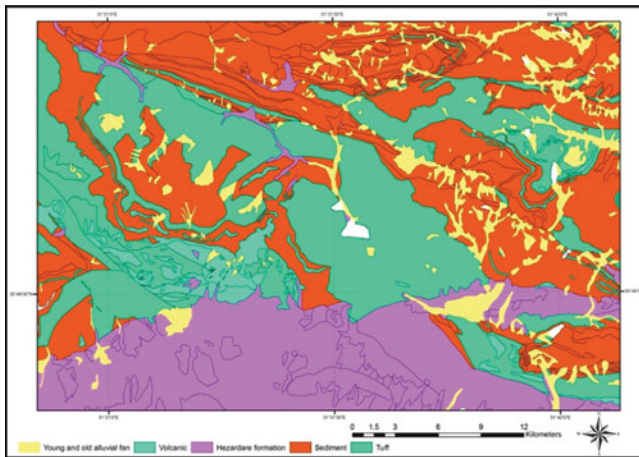


Fig. 5 Lithological division of the study area

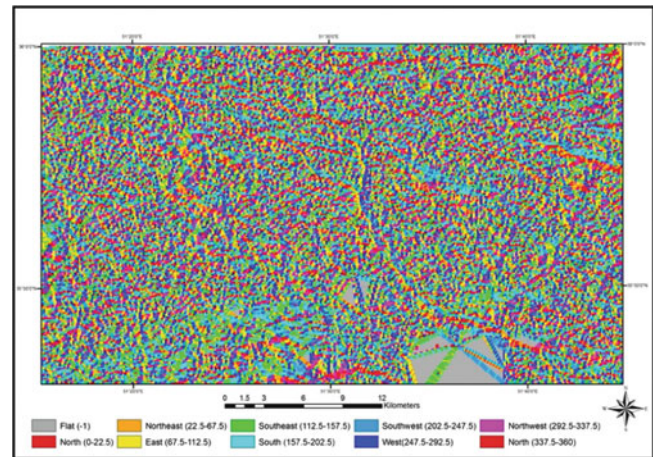


Fig. 7 Slope direction map of the study area

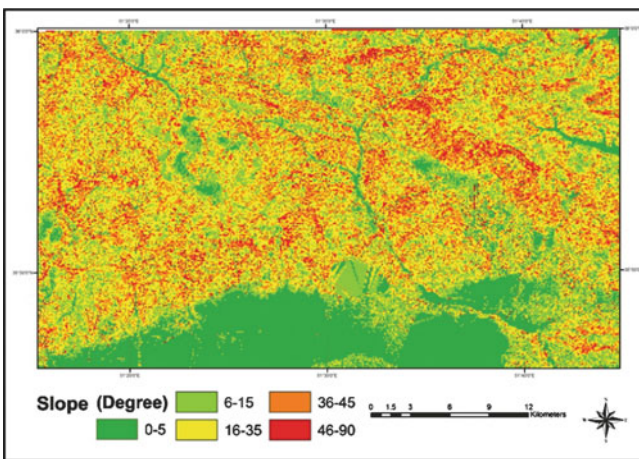


Fig. 6 Slope angle map of the study area

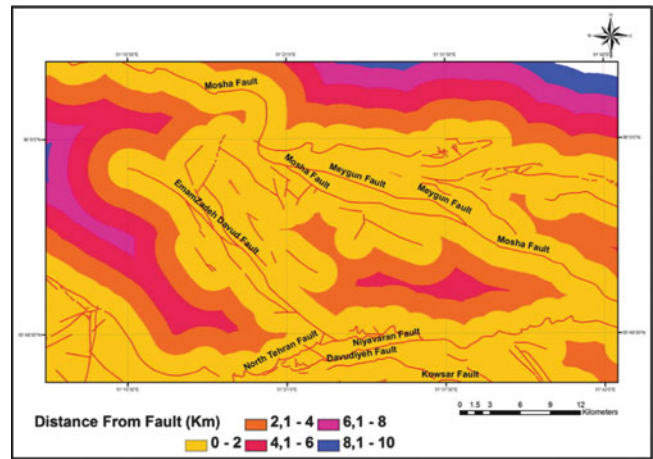


Fig. 8 Buffer zones of fault distance of the region

be accounted as a main influencing factor. Normally the slopes facing the south direction are in more stable condition than those directed towards the north. The slope directions are presented in angle and their orientation are measured from the north position. The details of slope direction divisions are presented in Table 1 and the plot of these data are shown on Fig. 7.

Fault distance: The study area is located in an active tectonic zone which contains numbers of mainly reverse and normal faults. The faults are mainly high-angle with large dip-slip movements. The reserve faults are dominantly oriented in E-W trend (Abbassi and Shabanian 2011). Therefore distance from fault is taken into account as to be one of the main influencing factors. Division of 2,000 m interval, as shown in Table 1, is considered for this factor. Over 55 % of the study area is located within the distance 4 km from the main faults. The buffer zone map regarding the fault distance is presented on Fig. 8.

Seismicity: According to the Iranian Seismic Code (standard no. 2800), Tehran is located in a region with relatively high seismic hazard. Therefore the seismic factor is identified as an essential parameter for developing slope instabilities in the region. According to the rate of the ground acceleration generated by the active faults, Tehran is located between two seismotectonic provinces, i.e., Alborz and Central Iran with acceleration rate of 0.5 and 0.3 g, respectively (see Fig. 9). The effect of seismicity is assisted regarding ground acceleration rate which is divided into five categories are shown in Table 1.

Landslide Hazard Zonation

Landslide hazard zonation mapping is an empirical approach to divide the land surface into zones of varying degree of stability on the bases of their relative hazard vulnerability.

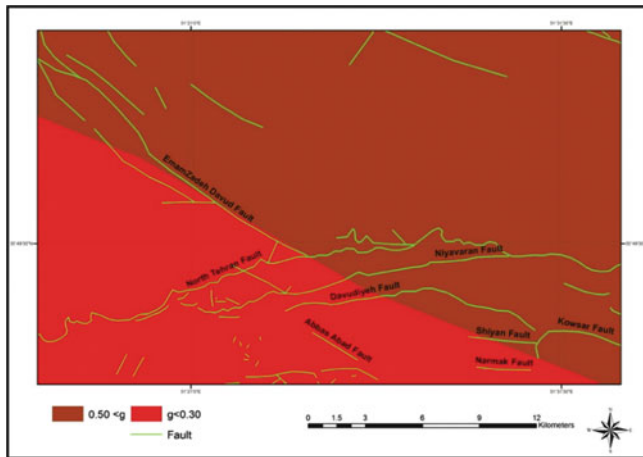


Fig. 9 Map of seismotectonic provinces in Tehran district

Table 2 Values of frequency ratio (Fr) for main factors

Main factors	Classification				
	1	2	3	4	5
Lithology	0.39	1.18	2.00	1.31	1.14
Slope angle	0.91	1.02	1.19	0.92	0.95
Slope direction	0.94	1.07	1.01	1.00	0.95
Fault distance	1.68	0.63	0.20	1.18	0.88
Seismicity	0.23	0.45	0.50	1.19	1.90

Rating the influencing factors of slope instability is based on the calculation a frequency ratio (Fr) for any of the defined factors using the following formula:

$$Fr_i = \left(\frac{N_{pix}(S_i) / \sum_{i=1}^n N_{pix}(S_i)}{N_{pix}(N_i) / \sum_{i=1}^n N_{pix}(N_i)} \right)$$

Where

Fr_i is the frequency factor of each factor
 N_{pix} (S_i) is number of pixels contains landslide
 N_{pix} (N_i) is number of pixels of the defined factor

It is obvious the higher value of frequency ratio (Fr) the higher potential of landslide occurrence for that factor. The values of frequency ratios for all factors in different classes are summarized in Table 2. The plots of these values are also shown on Fig. 10.

It can be noted that sedimentary rocks with high relief have great effect on landslide activities. Slope angle 16–35° affect more on landslide occurrence. Although slope direction variations have little effect on landslide but more landslides can be found on slope with direction 66–140° from the North. Distances from fault have no clear influence on landslide but the nearest distance of less than 2,000 m is more susceptible to landsliding. Finally the seismicity has

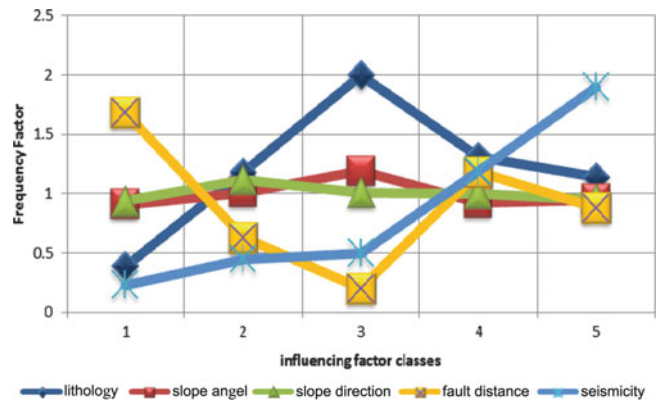


Fig. 10 Variation of frequency factor for different class of influencing factors

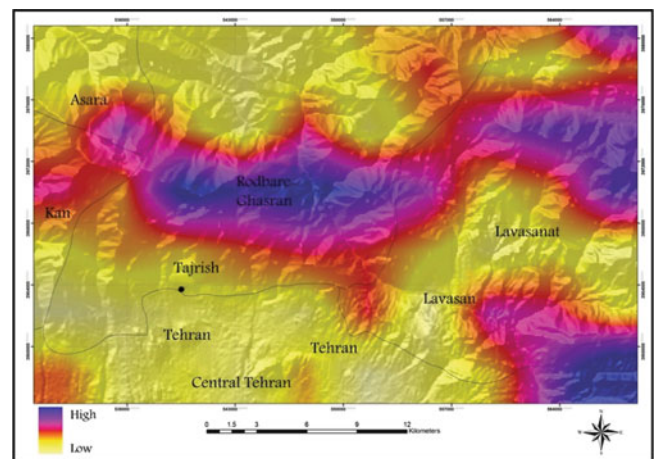


Fig. 11 Landslide hazard zonation (LHZ) map of North Tehran Districts

direct relationship with slope instability. As the level of seismicity increases the potential of landslide occurrences is increased.

The generated landslide zonation map for the region is presented on Fig. 11.

Conclusion

It can be concluded that the slope instabilities in Tehran districts has a wide range of occurrence in the foot hills and within the highest parts of the mountain terrain.

The application of Arch-GIS technique was found to be a useful primary approach for landslide hazard evaluation. The LHZ mapping can be used as a suitable tool to identify relatively safe areas for future construction and development in mountainous districts of north Tehran.

Among the five defined influencing factors, the effect of Lithology is very high and pyroclastic (tuffaceous) rocks of Karaj Formation are more susceptible to landslide than the other units. The effects of slope angel and

slope direction are not too obvious. Slope angel of 16–35° and slope direction between 66° and 140° from the north are more susceptible to landsliding. The effect of the third factor, distance from fault, is not clear but the closest distance shows lager number of landslide events. The rate of seismicity indicates direct effect on landslide occurrences so by the increase of ground acceleration rate the potential of landslide is increasing too.

References

- Abbassi MR, Shabaniyan E (2011) Evaluation of the stress field in Tehran region during the Quaternary. <http://www.iiees.ac.ir>. Accessed 6 Aug 2011
- Anbalagan R, Chakraborty D, Kohli A (2008) Landslide hazard zonation (LHZ) mapping on meso-scale for systematic town planning in mountainous terrain. *J Sci Ind Res* 67:486–497
- Asghari E, Toll DG, Haeri SM (2004) Effect of cementation on the shear strength of Tehran gravelly sand using triaxial tests. *J Sci Islam Repub Iran* 15(1):65–71
- Berberian M, Qorashi M, Arzang-Ravesh B, Mohajer-Ashjaee A (1985) Siesmotectonic and earthquake-fault hazard investigations in Tehran region. Geological Survey of Iran, report no 56 (in Persian), 58p
- Gahgah MM, Akhir JM, Rafek AG, Abdullah I (2009) GIS based assessment on landslide hazard zonation: case study of Cameron highland-Gua Musang road Kelantan, Malaysia. *J Sains Malays* 38 (6):827–833
- Ghafoori M, Sadeghi G, Lashkaripour GR (2006) Landslide hazard zonation using the relative effect method. In: Proceedings of the 10th IAEG international congress, paper no 474, Nottingham, UK, 6–10 Sept 2006
- Ghayomian J, Fatemi Aghida SM, Maleki Z, Shoaee Z (2006) Engineering geology of quaternary deposits of Greater Tehran, Iran. In: Proceedings of the 10th IAEG international congress, paper no. 248, Nottingham, UK, 6–10 Sept 2006
- Guzzetti F, Carrara A, Cardinali M, Reichenbach P (1999) Landslide hazard evaluation: a review of current techniques and their application in multi-scale study, Central Italy. *Geomorphology* 31:181–216
- Ramakrishnan SS, Sanjeevi Kumar M, Zaffar Sadiq M, Venugopal K (2002) Landslide disaster management and planning- a GIS based approach, Indian Cartographer, MFD-05, pp 192–195
- Rieben EH (1966) Geological observations on alluvial deposits in northern Tehran. Geological Survey of Iran, report no 9, 39p
- Takada S, Kuwata Y, Mahdavian A, Rasti R, Imai T (2004) Dislocation and strong ground motion zoning under scenario faults for lifelines. In: Proceedings of the 13th world conference on earthquake, paper no 125, Vancouver, BC, 1–6 Aug 2004
- Uromeihy A, Fattahi M (2011) Landslide hazard zonation of Babolrood watershed, Iran. In: Proceedings of 2nd international conference on environmental sciences and technology (ICEST), vol 2. Singapore, 26–28 Feb 2011, pp 318–321
- Uromeihy A, Mahdaviifar MR (2000) Landslide hazard zonation of the Khoreshrostan area, Iran. *Bull Eng Geol Environ* 58(3):207–213
- Varnes DG (1984) Landslide hazard zonation: a review of principles and practice. UNESCO, France, 63p. ISBN 92-3-101895-7



Three-Dimensional Modelling of Rotational Slope Failures with GRASS GIS

Martin Mergili and Wolfgang Fellin

Abstract

Landslides starting from unstable slopes threaten people, buildings and infrastructures all over the world and are therefore intensively studied. On the one hand, engineers use sophisticated models to identify hazardous slopes, mostly based on longitudinal sections. On the other hand, less sophisticated infinite slope stability models are used in combination with Geographic Information Systems (GIS) in order to cover larger areas. The present paper describes an attempt to combine these two philosophies and to come up with a spatially distributed, three-dimensional model for slope stability going beyond the widely used infinite slope stability concept. Both models are applied to artificial topographies in order to compare the outcomes of different slip surface assumptions and to benchmark the validity of the infinite slope stability model. It was found out that the resulting factor of safety is highly sensitive to the type of model used and to the slip surface geometry. In complex terrain, the performance of the infinite slope stability model strongly depends on the specific situation, particularly on slope curvature and slip surface depth.

Keywords

Slope stability models • Factor of safety • GRASS GIS

Introduction

GIS-supported analyses of slope stability, landslide susceptibility and landslide hazard have become very common with increased computational power in the last decade (e.g. Van Westen 2000; Corominas et al. 2003; Van Westen et al. 2006; Godt et al. 2008). Whilst geostatistical approaches have been applied in some countries (e.g. Italy, Spain, South Korea) in order to get a broad picture of hazardous slopes on the regional or even national scale, deterministic approaches are chosen for more detailed analyses on the

small catchment scale. Infinite slope stability models are most commonly employed for determining the factor of safety FOS_{inf} (e.g. Pack et al. 1998):

$$FOS_{inf} = \frac{c + \cos^2 \alpha [\gamma_s (d_p - d_w) + (\gamma_s - \gamma_w) d_w] \tan \varphi}{d_p \gamma_s \sin \alpha \cos \alpha} \quad (1)$$

where c is the cohesion, α is the slope angle, γ_s and γ_w are the specific weights of regolith and water, d_p is the thickness of regolith above the failure plane, d_w is the thickness of saturated regolith above the failure plane and φ is the angle of internal friction.

Infinite slope stability models are valid for predicting shallow translational slope failures in rather frictional than cohesive regolith on uniform, plane slopes. They are often coupled with hydraulic models (e.g. Wilkinson et al. 2002).

However, this type of model is not necessarily suitable for rotational, deep-seated slope instabilities in cohesive regolith

M. Mergili (✉)
BOKU University of Natural Resources and Life Sciences Vienna,
Peter-Jordan-Strasse 70, 1190 Vienna, Austria
e-mail: martin.mergili@boku.ac.at

W. Fellin
Unit of Geotechnical and Tunnel Engineering, University of Innsbruck,
Innsbruck, Austria

or failures of curved or dissected slopes (which can not be seen as „infinite“). Engineers have based their slope stability calculations on various slip surfaces for many years. Traditionally, 2D models (longitudinal transects in the direction of the steepest descent) are used. An overview is given by Duncan and Wright (2005), Schneider-Muntau and Fellin (2005) provide one of many case studies. The regolith above the slip surface is dissected into a number of columns, and the stabilizing and destabilizing forces or moments are computed for each of them. The summed up values are combined in order to compute the factor of safety. The forces between the columns are unknown in such calculations. There are various assumptions to take them into account. The simplest one is to neglect them (Fellenius approach). This generally leads to the lowest factors of safety (e.g. Kolymbas 2007). The regolith is assumed as rigid body in these approaches. Elliptical – or ellipsoidal – slip surfaces used e.g. in Xie et al. (2003, 2006) are kinematically not possible in such a framework. However, calculations with deformable regolith, like finite element slope stability analyses with the strength reduction technique (e.g. Matsui and San 1992) show various non-circular slip surfaces. For elliptical surfaces, the interslice forces are often neglected, since this simplifies the computation considerably. It may be assumed that this yields too conservative estimates of the factor of safety. Monte-Carlo approaches are frequently used for identifying the most critical slip surface for the area under investigation (Xie et al. 2003, 2006).

Using longitudinal sections means that the width of the potential slope failure and the three-dimensional topography of the slope are not accounted for. Some few attempts are documented to overcome this problem by combining the approach described above with GIS, for example the work of Xie et al. (2003, 2006).

Very few attempts (e.g. Griffiths et al. 2011; Milledge et al. 2011) to compare infinite slope stability models to more advanced models have been published. Instead, infinite slope stability models are sometimes applied without reflection on their validity for the problem to be solved since they are easy to use with GIS. The work presented here is seen as

1. An attempt to integrate a three-dimensional slope stability model based on spherical or ellipsoidal slip surfaces with a raster-based Open Source Geographic Information System (GRASS GIS; GRASS Development Team 1999–2007), in order to allow for the spatially distributed analysis of slope stability going beyond the widely used infinite slope stability concept;

2. An attempt to find out the influence of the slip surface assumption on the factor of safety and to benchmark the validity of the infinite slope stability model. The geometry of the potential landslide body and the type of topography (simple or complex) are taken as criteria. Analytically defined topographies are used for this evaluation.

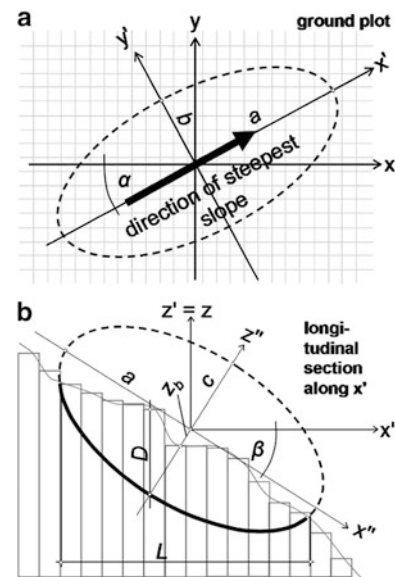


Fig. 1 Ground plot and longitudinal section of the ellipsoidal slip surface

Methods

Model Layout

The three-dimensional model is named *r.rotstab* and works with an ellipsoidal slip surface, defined by the coordinates of the centre, the lengths of the three half axes (a , b and c), horizontal orientation α , and vertical orientation β . The model offers two ways of selecting the parameters:

1. The slope stability computation is run with user-defined parameters for one single slip surface
2. The computation is run for a user-defined number of times, each time using an ellipsoid with randomly determined lengths of a , b , c and offset of the centre over the terrain z_b . α and β are determined in the way that a follows the steepest descent of the slope ζ and c is aligned perpendicular to the terrain surface (Fig. 1). Minimum and maximum lengths of the axes as well as z_b are defined by the user in order to constrain the randomization.

After transforming the ellipsoid into the GIS coordinate system, the depth of the slip surface is determined for each raster cell. The stabilizing and destabilizing forces are then computed for each raster cell, and the factor of safety FOS_{3d} is derived according to the Hovland model (Xie et al. 2003, 2006):

$$FOS_{3d} = \frac{\sum [cA + (W \cos \theta - U) \tan \varphi]}{\sum W \sin \theta_{avr}} \quad (2)$$

where A is the area of the slip surface of the cell, W is the weight of the overlying regolith, U is the pore water force, θ is the angle

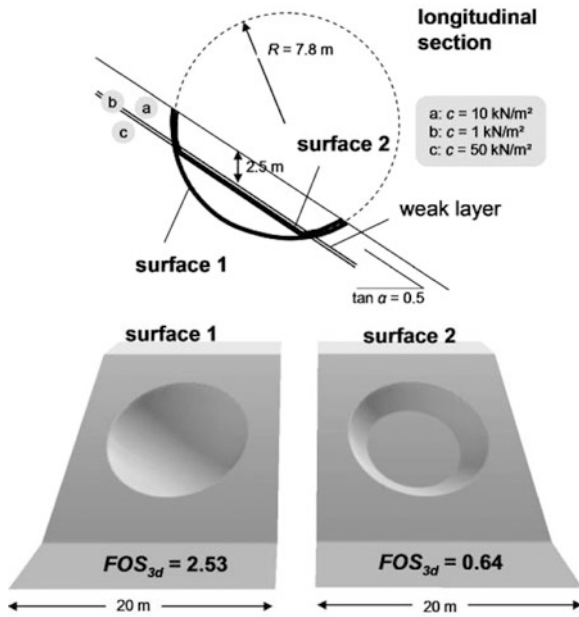


Fig. 2 Influence of the slip surface on the factor of safety

of the slip surface, and θ_{avr} is the average inclination of the slip surface in the main inclination direction of the possible landslide. Additional forces or seismic loads are neglected.

The decisive slip surface is not necessarily the bottom of the ellipsoid: also weak layers within the ellipsoid are considered. Figure 2 shows the tremendous influence of the choice of the slip surface, using a simple arbitrary topography with frictionless regolith and a weak layer at 2.5 m depth, bedded on a resistant layer. The theoretical slip surface (which is a circle in this example) reaches far into the resistant layer, resulting in rather stable conditions ($FOS_{3d} = 2.53$). Allowing the regolith to fail at the bottom of the weak layer leads to unstable conditions ($FOS_{3d} = 0.64$). The model *r.rotstab* includes the option to allow slope failures at the interface between two layers.

Maximum length L , width W and depth D of the potential landslide body are expressed in the coordinate system used in the GIS, with horizontal and vertical axes (see Fig. 1b; W runs perpendicular to L and D and is not shown).

The program requires a digital elevation model, the regolith parameters for each layer (cohesion c , angle of internal friction φ , specific weight γ), the depth of each layer and the groundwater level as input. After repeating the slope stability computation for each randomly determined ellipsoid, the minimum factor of safety from the overlay of all slip surfaces is determined for each raster cell. In addition, a table with the input parameters and the resulting FOS_{3d} for each ellipsoid is generated.

Test Design

Two different sets of tests are performed. The analytically defined slopes used for each test have a size of 500×200 m

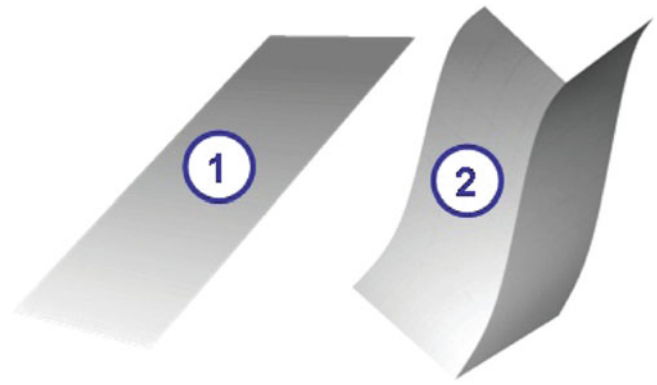


Fig. 3 Hypothetic topographies used for the tests (1) and (2)

and are shown in Fig. 3. Homogeneous and dry regolith with angle of internal friction $\varphi = 30^\circ$, cohesion $c = 10 \text{ kN/m}^2$ and specific weight $\gamma = 20 \text{ kN/m}^3$ is assumed for each test. The regolith overlays unconditionally stable bedrock. The model is run for assumed regolith depths of 2, 5, 10, 20 and 40 m. A raster cell size of 2 m is used.

1. Simple topography: an inclined plane with a slope angle of $\zeta_x = 35^\circ$ in x-direction and $\zeta_y = 0^\circ$ in y-direction is used. Purpose is to explore the influence of the geometry of the slip surface on the factor of safety FOS_{3d} and on the ratio FOS_{3d}/FOS_{inf} . Three types of slip surfaces are tested:

- Spherical slip surface with $a = b = c$;
- Ellipsoidal slip surface with $a \geq b \geq c$.
- Truncated ellipsoidal slip surface, also with $a \geq b \geq c$.

In the case of the truncated ellipsoidal slip surface, the bedrock surface is allowed as slip surface if the ellipsoid reaches into the unconditionally stable bedrock (see Fig. 2). Therefore, this slip surface may actually be the combination of an ellipsoid and a plane.

For each assumed geometry, FOS_{3d} is taken as the minimum factor of safety from 1,000 random slip surfaces. For the Monte Carlo simulation, a , b and c are constrained between 100 and 2 m, z_b is constrained between 0 and c .

In addition, the infinite slope stability model is run, yielding a global FOS_{inf} for each assumed regolith depth. As prescribed for homogeneous and dry cohesive material underlain by stable bedrock, the most critical slip surface is always the bedrock surface.

2. Complex topography: a narrow v-shaped valley with a bell-shaped distribution of the slope in x-direction ζ_x

$$\tan \zeta_x = \frac{3.5}{\pi} e^{-0.5 \left(\frac{x-250}{80} \right)^2} \quad (3)$$

and $\tan \zeta_y = 40^\circ$ is assumed. The purpose of this test is to identify the influence of complex slope curvature on FOS_{3d}/FOS_{inf} of potential slip surfaces. For each assumed

regolith depth, 10,000 truncated ellipsoidal random slip surfaces are tested. The longest axis of the ellipsoid is constrained with 20–100 m, the shortest axis with 2–40 m. The lengths of the three axes and the coordinates of the centre point of the ellipsoid are varied randomly whilst z_b is set to 0. The longest axis of the ellipsoid is always directed along the steepest slope. For each pixel, the lowest factor of safety among the values for all slip surfaces touching the respective pixel is applied as FOS_{3d} . In addition, the infinite slope stability model is applied for each pixel and FOS_{inf} is computed for the bedrock surface.

Results

Simple Topography

In this case of a quasi-infinite slope, assuming spherical or ellipsoidal slip surfaces makes sense for cohesive material only. Technically, such assumptions are also applicable to cohesionless material, but from a physical point of view, rotational failures in slopes with a constant inclination can only occur in cohesive material.

The factor of safety FOS_{3d} yielded for the most critical condition strongly depends on the regolith depth and the geometry of the assumed failure plane. Figure 4 shows longitudinal sections through the slope for all tested cases. In general, FOS_{3d} decreases with increasing regolith depth. However, the decisive slip surface for a regolith depth of 40 m does not reach the bedrock surface, but only a maximum depth <30 m. Support by the underlying slope seems to counterbalance the effect of decreasing stability with increasing slip surface depth, as it is also shown in Fig. 5a. It becomes obvious from Fig. 4 that it makes no big difference in FOS_{3d} whether 20 or 40 m regolith depth is assumed. This means that, whilst the truncated ellipsoidal slip surface yields the most critical factor of safety in shallow regolith, the truncated ellipsoid is not relevant any more when assuming deeper regolith.

For all assumed regolith depths, the most critical factor of safety yielded with the three-dimensional model is very close to FOS_{inf} . This is not surprising for shallow regolith where most of the truncated ellipsoid slip surface is formed by the regolith bottom also relevant for the infinite slope stability model (see Fig. 4). However, it is also true for deeper regolith where the three-dimensional slip surface is much shallower than the regolith bottom.

The safety factors yielded for the different slip surface geometries vary much more for shallow than for deep regolith. The spherical slip surfaces – and for rather shallow regolith also the ellipsoidal slip surfaces – produce significantly higher safety factors than the truncated slip surfaces.

The ratio a/b of the tested ellipsoids has no significant influence on the resulting safety factor. In general, the ellipsoids with the lowest safety factors are those with rather long a axis and short c axis. When reducing the length of the a axis at constant depth, FOS_{3d} increases considerably due to the increased importance of the support by the slope below (Fig. 5b). The small circles and ellipsoids identified as most critical for shallow regolith as shown in Fig. 4 may be the consequence of an insufficient number of tested random ellipsoids and a too coarse spatial resolution. Also the difference between the two ellipsoids identified as most critical for 40 m regolith depth (which should actually be identical) could be eliminated by a much larger number of random simulations.

Complex Topography

Figure 6 illustrates the ratio FOS_{3d}/FOS_{inf} for five different assumptions of regolith depth for the v-shaped valley described above. The general patterns show that in rather plane areas, the ratio is above 1 ($FOS_{3d} > FOS_{inf}$), a phenomenon which was explained in detail in the previous section. In areas with pronounced curvature, the ratio is below 1 ($FOS_{3d} < FOS_{inf}$). Two types of curvatures have to be discussed:

1. Moderate curvature in x direction without change of direction of steepest slope: the curved areas for all five assumptions of regolith depth are characterized by lower FOS_{3d}/FOS_{inf} ratios than the plane portions of the slope – for deep bedrock surfaces, this effect is partly offset, but still clearly visible in principle. The reason for this phenomenon is that for each pixel, the lowest (and therefore relevant) value of FOS_{3d} belongs to an ellipsoid which covers mainly the steeper portion adjacent to the curved area than the flatter one, with a lower factor of safety. FOS_{inf} , in contrast, is only influenced by the slope of the respective pixel and not by its geometric environment.
2. Sharp curvature in y direction with change of direction of steepest slope (valley bottom): except for the pixels directly at the bottom, the influence of the sharp terrain bend is relatively small. The reason for this phenomenon is that the most critical slip surface will hardly touch both sides of the valley (the slope would be smoothed out and FOS_{3d} would be high), but only one side.

However, the ratio FOS_{3d}/FOS_{inf} is higher very close to the valley bottom due to the lower probability of this zone to be included in the most critical slip surface (vicinity of the opposite slope). Similarly, the anomalies at the fringes of the calculation area are caused by the lower number of relevant ellipsoids there. Both effects would probably be removed (or at least reduced) by considerably increasing the number of random simulations.

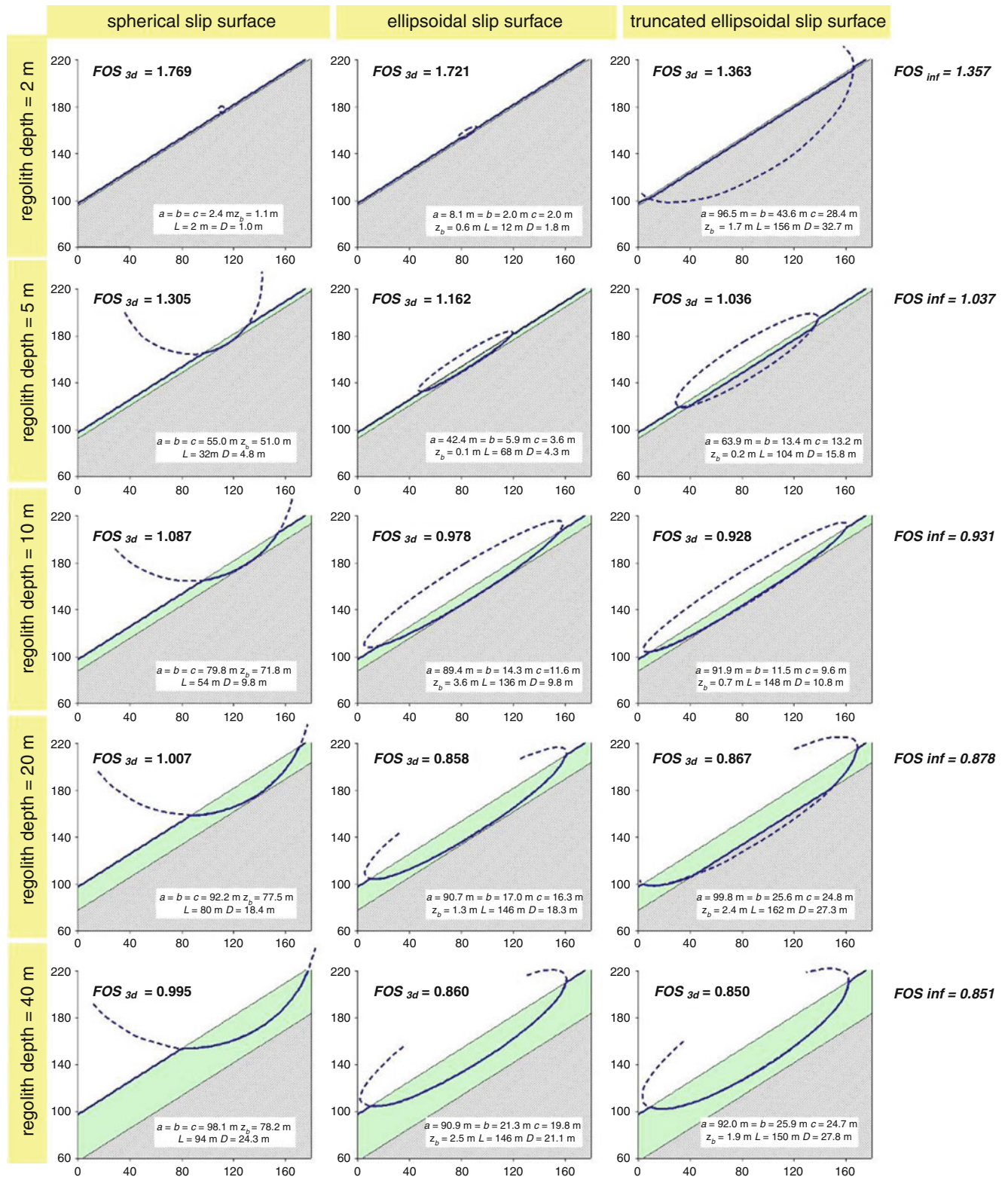


Fig. 4 Longitudinal sections through the most critical slip surfaces for different regolith depths and assumed slip surface geometries. Regolith is shown in green, length units are given in metres

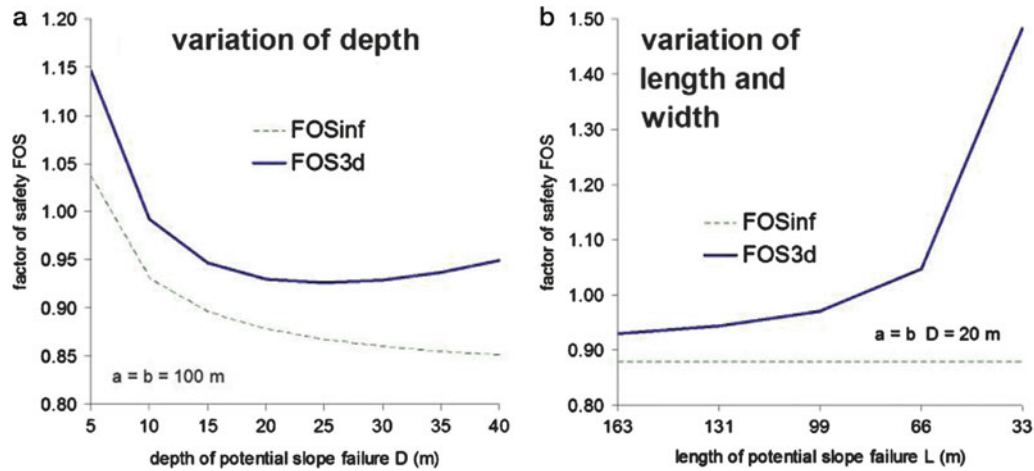
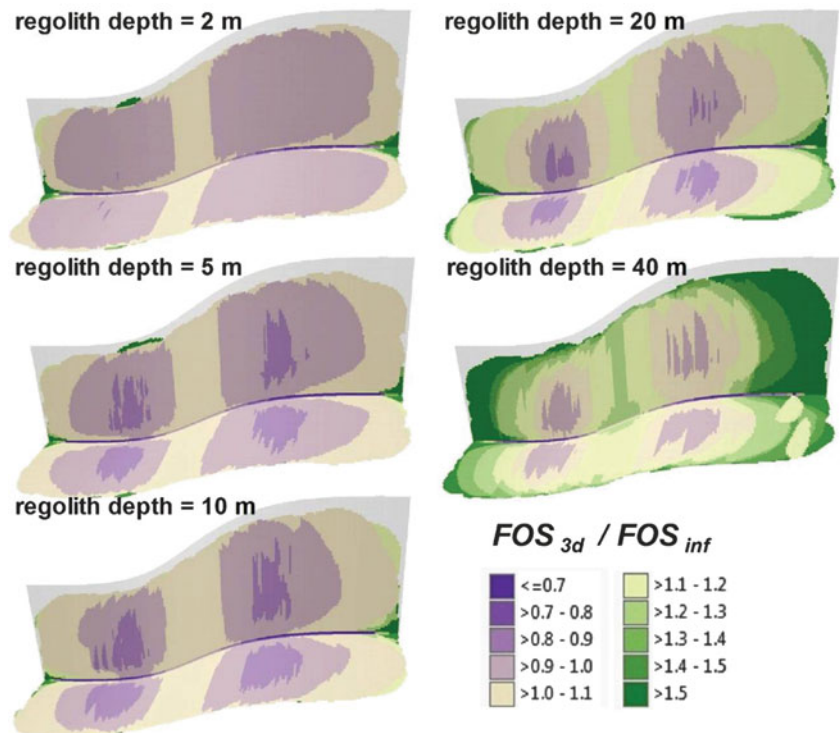


Fig. 5 Variation of FOS_{3d} as a response to slip surface parameters D and L assuming an ellipsoidal potential failure plane, and comparison with FOS_{inf}

Fig. 6 Ratio FOS_{3d}/FOS_{inf} for complex topography with truncated ellipsoidal slip surface and five different assumptions of regolith depth



Conclusions

A GIS-based three-dimensional slope stability model based on spherical or ellipsoidal potential slip surfaces was presented. The factors of safety yielded with different assumptions of slip surface geometry were compared to those derived with the infinite slope stability model for two different analytically defined topographies. The importance of advanced three-dimensional models for slope stability calculations was highlighted and the

influence of slip surface geometry on the predicted factor of safety was worked out.

The choice of an appropriate slip surface is a key for the successful modelling of slope stability. With the assumptions taken in the present study, truncated ellipsoidal slip surfaces generally produce the most conservative results, with safety factors very close to those yielded with the infinite slope stability model. However, the truncation is not relevant for deep homogeneous regolith. The spherical

slip surfaces yield higher safety factors. Particularly for shallow regolith, the critical factor of safety yielded by the infinite slope stability model or the truncated ellipsoidal slip surface differs considerably from the critical factor of safety derived with spherical slip surfaces.

For more complex topographies, the infinite slope stability model does not necessarily provide the most conservative results: particularly in curved areas, the factor of safety yielded with the truncated ellipsoidal slip surface may be significantly lower. More tests with different slip surface geometries and with a variety of terrain geometries are required to get a deeper insight into the problem. The findings presented here are valid only for the assumed conditions. The suitable assumption of sliding surface geometry to be applied to a specific real-world problem strongly depends on the local conditions.

Furthermore, in-depth analyses of the minimum number of random slip surfaces to be tested in order to get reliable results as well as of the suitable raster cell size in relation to the slip surface dimensions are required.

The evaluation of the test results has to consider that the infinite slope stability model and three-dimensional models working with spherical or ellipsoidal slip surfaces are not fully comparable:

1. The infinite slope stability model follows a pixel-based approach, whilst the three-dimensional model works with aggregates of pixels.
2. The depth of the potential slip surface for the three-dimensional model is prescribed by the bottom of the ellipsoid, at least in the case of strictly ellipsoidal slip surfaces. The infinite slope stability model, in contrast, is applied with a plane, slope-parallel slip surface. Whilst the depth of the potential slip surface does not matter for dry and cohesionless regolith, it has a tremendous influence on the stability in cohesive regolith. This hampers the comparison of the two model types. However, Milledge et al. (2011) state that for length to depth ratios >17 , the infinite slope stability model would be unconditionally suitable, whilst lower ratios would also be acceptable under certain conditions, particularly for cohesionless, frictional regolith. Milledge et al. (2011), however, used a two-dimensional model. Also Griffiths et al. (2011) came to similar conclusions: the factor of safety predicted by their finite element analysis approached the factor of safety yielded by the infinite slope stability model for length to depth ratios >16 . However, it has to be emphasized that for predictive studies, the length and depth of slope failures is not a priori known, so that process understanding and knowledge on the local conditions are more important than purely geometric aspects when selecting the suitable model for a specific case study.
3. In general, the infinite slope stability model is rather valid for frictional, cohesionless material, whilst

rotational failures rather occur in cohesive material. The suitability of each model for a given problem therefore also depends on the properties of the rock or debris involved.

The choice of the appropriate model type and the appropriate slip surface geometry is therefore an essential step of each hazard analysis which – in the impression of the authors – is too often governed by the background of the investigator and the software and data available rather than by the so important local conditions. Particularly the relatively easy application of infinite slope stability models with GIS attracts a lot of research. A sensible choice of the appropriate model is essential for the outcome of each slope stability analysis. The work presented here is understood as an attempt to facilitate such a choice and to bring forward GIS-based model development beyond the infinite slope stability concept. However, it has to be emphasized that the results of the present study are only valid for the parameter combinations tested, and more work is required in order to achieve a more comprehensive picture on the suitability of the different methods and geometry assumptions for slope stability calculations.

References

- Corominas J, Copons R, Vilaplana JM, Altamir J, Amigó J (2003) Integrated landslide susceptibility analysis and hazard assessment in the principality of Andorra. *Nat Hazards* 30:421–435
- Duncan JM, Wright SG (2005) *Soil strength and slope stability*. Wiley, Hoboken
- Godt JW, Baum RL, Savage WZ, Salciarini D, Schulz WH, Harp EL (2008) Transient deterministic shallow landslide modeling: requirements for susceptibility and hazard assessments in a GIS framework. *Eng Geol* 102(3–4):214–226
- GRASS Development Team (1999–2007) GRASS GIS reference manual. <http://grass.itc.it/>
- Griffiths DW, Huang J, de Wolfe GF (2011) Numerical and analytical observations on long and infinite slopes. *Int J Numer Anal Method Geomech* 35:569–585
- Kolymbas D (2007) *Geotechnik: Bodenmechanik und Grundbau*. Springer, Berlin/Heidelberg
- Matsui T, San KC (1992) Finite element slope stability analysis by shear strength reduction technique. *Soils Found* 32(1):59–70
- Milledge D, Griffiths V, Warburton J, Lane S (2011) Can we use the infinite slope model within catchment scale landslide models given its landslide length assumption? *Geophys Res Abstr* 13: EGU2011–EGU3127
- Pack RT, Tarboton DG, Goodwin CN (1998) The SINMAP approach to terrain stability mapping. In: *Proceedings of the 8th congress of the international association of engineering geology*, Vancouver, BC.
- Schneider-Muntau B, Fellin W (2005) Fallstudie Mure Nals - Untersuchung des Muranbruchs mittels Standsicherheitsberechnung. *Österreichische Ingenieur- und Architektenzeitschrift* 150:42–45
- Van Westen CJ (2000) The modelling of landslide hazards using GIS. *Surv Geophys* 21:241–255
- Van Westen CJ, Van Asch TWJ, Soeters R (2006) Landslide hazard and risk zonation – why is it still so difficult? *Bull Eng Geol Environ* 65:167–184

- Wilkinson PL, Anderson MG, Lloyd DM (2002) An integrated hydrological model for rain-induced landslide prediction. *Earth Surf Process Landf* 27:1285–1297
- Xie M, Esaki T, Zhou G, Mitani Y (2003) Three-dimensional stability evaluation of landslides and a sliding process simulation using a new geographic information systems component. *Environ Geol* 43:503–512
- Xie M, Esaki T, Qiu C, Wang C (2006) Geographical information system-based computational implementation and application of spatial three-dimensional slope stability analysis. *Comput Geotech* 33:260–274



A GRASS GIS Implementation of the Savage-Hutter Avalanche Model and Its Application to the 1987 Val Pola Event

Martin Mergili, Katharina Schratz, Alexander Ostermann, and Wolfgang Fellin

Abstract

Computer models play an increasing role for the understanding of the dynamics of granular flows (rock avalanches, debris flows, snow avalanches etc.). Simple empirical relationships or semi-deterministic models are often applied in GIS-based modelling environments. However, they are only appropriate for rough overviews at the regional scale. In detail, granular flows are highly complex processes and deterministic models are required for a detailed understanding of such phenomena. One of the most advanced theories for understanding and modelling granular flows is the Savage-Hutter model, a system of differential equations based on the conservation of mass and momentum. The equations have been solved for a number of idealized topographies, but not yet satisfactorily for arbitrary terrain. Not many attempts to integrate the model with GIS were known up to now. The work presented is seen as an initiative to integrate a fully deterministic model for the motion of granular flows, based on the Savage-Hutter theory, with GRASS, an Open Source GIS software package. The potentials of the model are highlighted with the Val Pola rock avalanche as test event. The limitations and the most urging needs for further research are discussed.

Keywords

Granular flows • Physically-based modelling • GRASS GIS • Val Pola rock avalanche

Introduction

Granular flows – including avalanches of snow, mud, debris or even rocks – are highly destructive phenomena putting people, buildings and infrastructures at risk. Delineation of possible impact areas as well as flow velocities and energies is an essential precondition for efficient action towards risk

reduction, e.g. definition of hazard zones, dimensioning of technical structures etc. (Hung et al. 2005).

Since the 1990s, Geographic Information Sciences (GIS) play an increasing role in mapping and prediction of landslide, debris flow, and avalanche hazard and risk. They enable an efficient management of spatial data at all spatial scales, usually in raster or vector format.

Models for the motion of rapid mass movements as granular flows may be classified into empirical-statistical models, point mass models, and physically-based distributed models.

Often, empirical-statistical relationships based on the analysis of historical events are employed for the estimation of key parameters (travel distance, patterns of deposition). Threshold values of slope angles or horizontal and vertical distances (e.g. Vandre 1985; Corominas et al. 2003), related to volume (e.g. Rickenmann 1999 for debris flows) are used as criteria. Empirical-statistical models are often applied in combination with GIS for regional-scale studies.

M. Mergili (✉)
BOKU University of Natural Resources and Life Sciences Vienna,
Peter-Jordan-Strasse 70, 1190 Vienna, Austria
e-mail: martin.mergili@boku.ac.at

K. Schratz • A. Ostermann
Department of Mathematics, University of Innsbruck, Innsbruck,
Austria

W. Fellin
Division of Geotechnical and Tunnel Engineering, University of
Innsbruck, Innsbruck, Austria

Point mass models assume one or more dimensionless starting points of the granular flow being routed downwards separately. Approaches for snow avalanches or debris flows use simple two-parameter friction models (Voellmy 1955; Perla et al. 1980; Gamma 2000). Point mass models are often applied in combination with GIS.

Fully deterministic distributed models are based on the spatial definition of the starting mass (cluster of cells) routed downwards taking into account the interactions between the cells. They are suitable for local-scale studies. Movements are computed based on physical laws, assuming specific flow rheologies (e.g. Savage and Hutter 1989; Hungr 1995; Iverson 1997; McDougall and Hungr 2004, 2005). GIS applications of such models are still rather scarce. Examples exist where numerical models can be coupled with proprietary GIS software, for example FLO-2D (O'Brien 2003) or SAMOS (Sampl and Zwinger 2004), or where numerical models have been used in combination with GIS, like DAN with GRASS GIS (Hungr 1995; Revellino et al. 2008). The RAMMS model (Christen et al. 2010), primarily applied to snow avalanches, uses Voellmy (1955) viscous drag and runs with GRASS GIS in the background. However, the full GIS implementation of more complex models (e.g. Savage and Hutter 1989) remains a challenge. Even though progress on the application of the Savage-Hutter model was recently made on a theoretical basis (e.g. Luca et al. 2009; Pudasaini 2011), no satisfactory solution for arbitrary topography is yet available. Pudasaini (2003) presented a solution for curved and twisted channels, and Wang et al. (2004) devised a numerical scheme applicable to flows over complex terrain on a horizontally straight flow path (Gray et al. 1999). Both solutions rely on non-rectangular coordinate systems. Whilst such are adequate for the problems to be solved, they seem to discourage geoinformation scientists as their application in conventional raster-based GIS environments requires some adaptations.

The present article describes an attempt to implement a fully physically-based model for the motion of granular flows with GIS. The software GRASS GIS was selected for this purpose. As an Open Source GIS package with focus on raster processing, GRASS facilitates model development, distribution and evaluation: the entire scientific community has the chance to contribute to the evaluation of the model and the further development of the program code. Examples of GRASS implementations of mass movement models are provided e.g. by Cannata and Molinari (2008) and Mergili et al. (submitted).

The GRASS module developed was named *r.avalanche*. It builds on the Savage-Hutter model (Savage and Hutter 1989) and a numerical scheme devised by Wang et al. (2004) for simple concave topographies with an only vertically curved flow line (Fig. 1). It is therefore only suitable for flows moving predominantly in downslope direction.

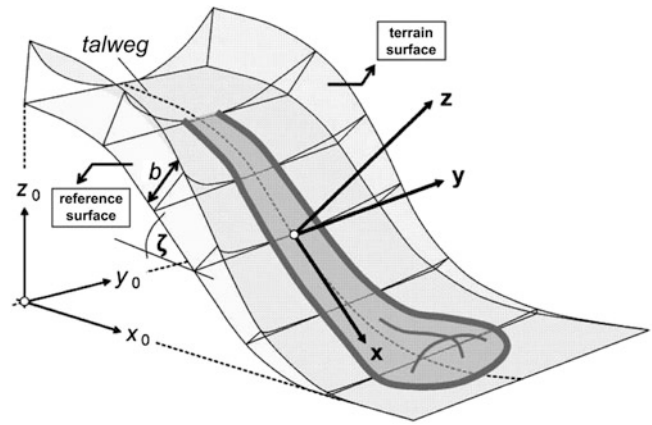


Fig. 1 Idealized topography for the solution of the Savage-Hutter model by Wang et al. (2004), also used for *r.avalanche*

Methods

Model Basics

The Savage-Hutter model (Savage and Hutter 1989) is expressed as a system of differential equations describing the conservation of mass and momentum:

$$\frac{\partial h}{\partial t} + \frac{\partial}{\partial x}(hu) + \frac{\partial}{\partial y}(hv) = 0 \quad (1)$$

$$\frac{\partial}{\partial t}(hu) + \frac{\partial}{\partial x}(hu^2) + \frac{\partial}{\partial y}(huv) = hs_x - \frac{\partial}{\partial x}\left(\frac{\beta_x h^2}{2}\right) \quad (2)$$

$$\frac{\partial}{\partial t}(hv) + \frac{\partial}{\partial x}(huv) + \frac{\partial}{\partial y}(hv^2) = hs_y - \frac{\partial}{\partial y}\left(\frac{\beta_y h^2}{2}\right) \quad (3)$$

where h is the avalanche thickness, and u and v are the depth-averaged downslope and cross-slope velocities. s_x and s_y are the net driving accelerations:

$$s_x = \sin \zeta - \frac{u}{\sqrt{u^2 + v^2}} \tan \delta (\cos \zeta + \lambda \kappa u^2) - \varepsilon \cos \zeta \frac{\partial b}{\partial x}, \quad (4)$$

$$s_y = -\frac{v}{\sqrt{u^2 + v^2}} \tan \delta (\cos \zeta + \lambda \kappa u^2) - \varepsilon \cos \zeta \frac{\partial b}{\partial y}, \quad (5)$$

where ζ is the downslope inclination angle of the reference surface, κ is the local curvature of the reference surface, b is the elevation above the reference surface, and ε and λ are factors. β_x and β_y are defined as

$$\beta_x = \varepsilon \cos \zeta K_x \quad (6)$$

and

$$\beta_y = \varepsilon \cos \zeta K_y. \quad (7)$$

K_x and K_y are the earth pressure coefficients in downslope and cross-slope directions:

$$K_{x,act/pass} = 2 \left(1 \mp \sqrt{1 - \cos^2 \varphi / \cos^2 \delta} \right) \sec^2 \varphi - 1, \quad (8)$$

$$K_{y,act/pass} = \frac{1}{2} \left(K_x + 1 \mp \sqrt{(K_x - 1)^2 + 4 \tan^2 \delta} \right). \quad (9)$$

φ is the angle of internal friction, and δ is the bed friction angle. Active stress rates (subscript *act*) are connected to local elongation of the flowing mass, passive stress rates (subscript *pass*) are connected to local shortening – it depends on acceleration or deceleration of the flow whether active or passive stress rates are applied. Equations 8 and 9 are valid only as long as the flow moves predominantly in downslope direction.

The system of equations described above is only valid for the shallow flow of cohesionless and incompressible granular materials which can be considered as continuum. The curvature of the terrain has to be relatively small. All variables are dimensionless, meaning that the model is scale-invariant and small-scale laboratory tests can be used as reference for large-scale problems in nature.

Numerical Solution of the Equations

Equations 1, 2 and 3 were solved using a Non-Oscillatory Central Differencing (NOC) Scheme, a numerical scheme useful to avoid unphysical numerical oscillations. Cell averages of h , u and v are computed using a staggered grid: the system is moved half of the cell size with every time step, the values at the corners of the cells and in the middle of the cells are computed alternatively. The NOC Scheme devised by Wang et al. (2004) was used for *r.avalanche*. The degree of diffusion of the flow material is governed by using slope limiters, restricting the gradients of flow depth to a certain range. The minmod limiter was already used by Wang et al. (2004) and also for the present work since it is known as the most diffusive one, reducing numerical oscillations.

The simulation is run for a number of time steps until a pre-defined break condition is fulfilled. The time steps have to be kept short enough to fulfil the Courant-Friedrichs-Levy (CFL) condition required for obtaining smooth solutions (see Wang et al. 2004).

Implementation into GRASS GIS

r.avalanche was developed as a raster module for GRASS GIS, using the C programming language. The implementation of the Savage-Hutter model and its solution by Wang et al. (2004) into GIS raises two issues: (1, 2, 3) provide dimensionless values whilst the description of phenomena in nature requires dimensional values, and the solution is valid for a curvilinear reference system only, in contrast to GIS which usually use a rectangular system.

The first issue concerns the non-dimensionalization of the governing parameters. Pudasaini (2003) describes a way to convert the dimensionless variables into dimensional ones, using the typical avalanche length L , the typical avalanche depth H , the typical radius of curvature R and gravitational acceleration g . The implemented model computes the dimensionless variables and converts them to dimensional values according to Pudasaini (2003) for output. The scaling parameters L , H , and R are set to 1 in this paper. The factors $\varepsilon = H/L$ and $\lambda = L/R$ are therefore 1 as well. However, the choice of the scaling parameters does not influence the numerical results since (1), (2), (3), (4), (5), (6), (7), (8) and (9) are scale invariant.

The solution of Wang et al. (2004) is formulated using a curvilinear coordinate system based on a talweg which shall be the predominant flow direction (see Fig. 1). The original rectangular coordinate system of the input raster maps has to be converted into the coordinate system for the simulation: first, the coordinate system is rotated around the z axis so that the direction of the main flow line is aligned with the new x (down-slope) direction. The main flow line is based on two user-defined pairs of coordinates. A reference surface is then created, defined by the given talweg and an inclination of zero in y (cross-slope) direction. Based on this reference surface, the offset b (m) – defined as the distance between terrain surface and reference surface perpendicular to the reference surface – and the initial avalanche thickness h are derived.

After completing the simulation, the entire system is reconverted into the rectangular coordinate system used in the GRASS GIS mapset.

Study Area and Data

The 1987 Val Pola Rock Avalanche

The Val Pola rock avalanche (Valtellina, Lombardy Region, Northern Italy; Fig. 2), like most large mass movements, has been subject of numerous detailed studies. A review with the relevant references is provided by Govi et al. (2002).

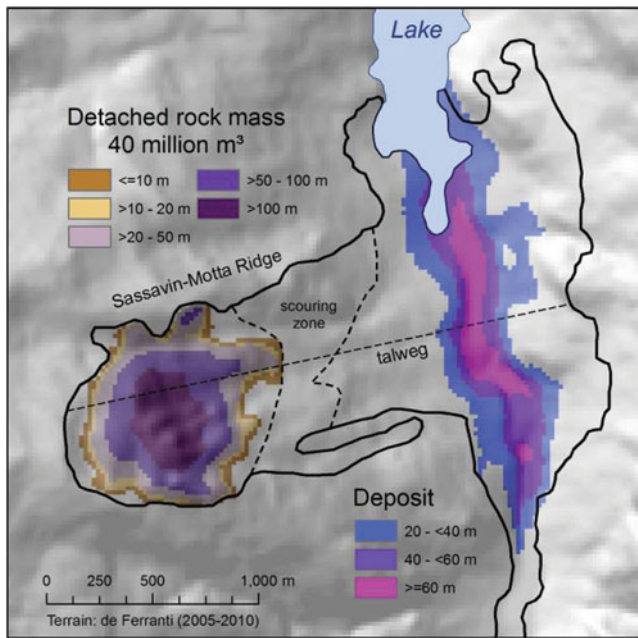


Fig. 2 Val Pola rock avalanche. Distribution of detached and deposited volumes as derived from the DEM change detection, affected area mapped from Landsat TM imagery. DEM source: De Ferranti (2005–2010)

Granular flow modelling was already applied there (e.g. by Crosta et al. 2003, 2004).

The event occurred on July 28, 1987 after a period of heavy and persistent rainfall. Preceded by the opening of a prominent crack, a block of highly fractured and faulted igneous and metamorphic rocks detached and rushed into the valley. The volume of the released mass was estimated to 34–43 million m, the entrainment by the resulting rock avalanche to further 5–8 million m (Crosta et al. 2003), the maximum velocity to 76–108 m/s (see Crosta et al. 2004). Govi et al. (2002) distinguished six phases of the movement, with a duration of the main avalanching phase of 8–12.5 s. The mass moved up 300 m on the opposite slope. In the main valley, it continued 1.5 km downstream and 1.5 km upstream, with a maximum thickness of 90 m. The river Adda was dammed, and an artificial drainage was constructed rapidly in order to avoid an uncontrolled sudden drainage of the rising lake. The event claimed 27 human lives and caused high economic costs (Crosta et al. 2003).

Data

Digital Elevation Models (DEMs) before and after the event, geotechnical parameters of the sliding mass and the sliding surface, and reference information on the distribution of the deposit were obtained. The affected area was mapped from Landsat TM imagery and verified with the Italian Landslide

Table 1 Parameter combinations applied for the simulations

	Cell size (m)	δ (°)	φ (°)
Simulation 1	20	22	35
Simulation 2	40	22	35
Simulation 3	12	22	35
Simulation 4	20	18	35
Simulation 5	20	26	35
Simulation 6	20	22	45
Simulation 7	20	22	55

Inventory (IFFI Project) and a map published by Crosta et al. (2003). Possible inaccuracies are caused by secondary processes, e.g. mud flows downstream blurring the delineation of the impact area down-valley.

r.avalanche was run with different combinations of parameter sets (Table 1), using values applied by Crosta et al. (2004) as a base: angle of internal friction $\varphi = 35^\circ$ and bed friction angle $\delta = 22^\circ$. The standard cell size for the computation was set to 20 m, the same as of the DEM used. The model was also tested with 40 and 12 m cell size.

Results

Simulation with Published Friction Parameters

The model was first run at a cell size of 20 m (according to the DEM resolution) with $\varphi = 35^\circ$ and $\delta = 22^\circ$ (Simulation 1; see Table 1). This simulation can be considered as a blind validation with the parameters used by Crosta et al. (2004). Figure 3 illustrates the distribution of flow depth at selected time intervals from the onset ($t = 0$) to $t = 300$ s, when the flow is assumed having stopped. 86 % of the modelled deposit coincide with the observed area of deposition, and 79 % of the observed deposition area are occupied by the modelled deposit (considering only those areas with depth of deposition > 1 m; Table 2). The travel distance modelled for the central part of the deposit corresponds very well to the observation.

However, the measured maximum depth is approx. 90 m (Govi et al. 2002) and the model yields a maximum depth of 75 m only. Furthermore, some portions of the lateral (N and S) parts of the modelled deposit deviate from the observed deposit. There, the travel distance is rather underestimated. The implementation of the model used for the present study does not allow for a reliable simulation of the very lateral (in this case, N and S) parts of the deposit.

Already shortly after the onset of the flow ($t = 10$ s), the simulation predicts a degree of lateral spreading of the flow beyond the observed extent. As a consequence, part of the material crosses the delineation of the catchment and follows gullies N and S, a behaviour not at all observed in reality.

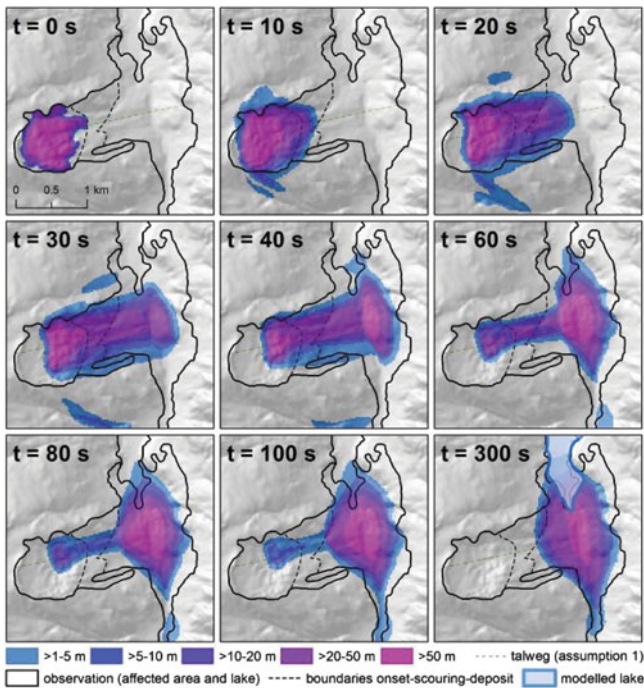


Fig. 3 Time series of flow depth distribution simulated with $\varphi = 35^\circ$ and $\delta = 22^\circ$ at a cell size of 20 m. Only flow depths >1 m are shown

Table 2 Correspondence of observed and modelled rock avalanche deposit and key output parameters for each simulation: c_1 = percentage of surface of modelled deposit with depth >1 m located within the observed deposition area; c_2 = percentage of observed deposition area with modelled deposition of depth >1 m; d_{\max} = maximum depth of modelled deposition (m); v_{\max} = maximum modelled flow velocity (m/s)

	c_1	c_2	d_{\max}	v_{\max}
Simulation 1	86	79	75	94
Simulation 2	73	91	39	86
Simulation 3	93	73	85	96
Simulation 4	85	78	67	107
Simulation 5	74	79	69	80
Simulation 6	84	82	67	97
Simulation 7	82	85	60	99

The lake dammed by the rock avalanche deposit was modelled by filling the sink behind the simulated deposit (see $t = 300$ s in Fig. 3). The modelled lake is slightly larger than the lake observed on September 20, 1987 (see Fig. 2).

Flow velocity is another important characteristic of granular flows. However, it is difficult to verify since direct reference measurements are hardly applicable. The maximum simulated velocity in downslope direction is 94 m/s. This value is well within the estimated range of 76–108 m/s (Crosta et al. 2004), but appears very high, anyway. Very rapid mass movements may reach 100 m/s and more (Scheidegger 1973). However, velocities of rock avalanches comparable to the Val Pola event typically range from 30 to

50 m/s. A two-dimensional model yielded a maximum of 50 m/s for the Val Pola event (Crosta et al. 2003).

Analysis of Parameter Sensitivity

The values used for φ and δ – and their spatial distribution in particular – are uncertain. Therefore, the sensitivity of the model to variations of these governing parameters has to be evaluated. *r.avalanche* is supposed to be sensitive also to the cell size used for the simulation. Table 2 summarizes the key output parameters for each simulation and the correspondence of modelled and observed deposit.

The simulation was first repeated with 40 m (Simulation 2) and 12 m cell size (Simulation 3), respectively, with the remaining parameters left unchanged. The variations of the cell size did not lead to a general shift in the behaviour of the simulated rock avalanche. However, with coarser resolution, spreading of the flow is more pronounced, leading to a larger impact area, but a shallower deposit (see Table 2). This effect is particularly visible when comparing the results for 40 and 20 m and much less pronounced between 20 and 12 m. A maximum flow velocity of 86 m/s was predicted with 40 m cell size, 96 m/s with 12 m cell size. These findings are not surprising as the cell size governs the distance of spreading during each time step of the simulation. Tests with channelized debris flows have shown that *r.avalanche* only works well if the cell size is much smaller than the width of the flow, otherwise lateral spreading is overestimated. A cell size of 40 m is definitely too coarse for the simulation of the Val Pola rock avalanche. The less pronounced difference between the results yielded with 20 and 12 m suggests that these values are close to the cell size ideal for the simulation of this specific event.

The simulation was then repeated with $\delta = 18^\circ$ (Simulation 4) and 26° (Simulation 5; Fig. 4). The expected effects of reduced flow velocity and resulting delayed motion with increasing values of δ were observed. Whilst the simulated maximum travel distance is longer when assuming a lower bed friction ($t = 40$ s and $t = 60$ s in Fig. 4a), the final travel distance at $t = 300$ s is almost the same with $\delta = 18^\circ$ and with $\delta = 22^\circ$ (see Fig. 4b). Also with $\delta = 26^\circ$, the modelled deposit reaches approx. as far E as in the other simulations.

Furthermore, varying the bed friction angle may result in a highly nonlinear response governed by several factors. With $\delta = 18^\circ$, the maximum thickness of the deposit decreases to 67 m (see Table 2), compared to $\delta = 22^\circ$ (75 m), an effect to be attributed primarily to increased lateral spreading (N–S direction). With $\delta = 26^\circ$, part of the flow material would remain in the transit and even onset area. The deposit would therefore assume a much more stretched shape in E–W direction, with a maximum depth of 69 m.

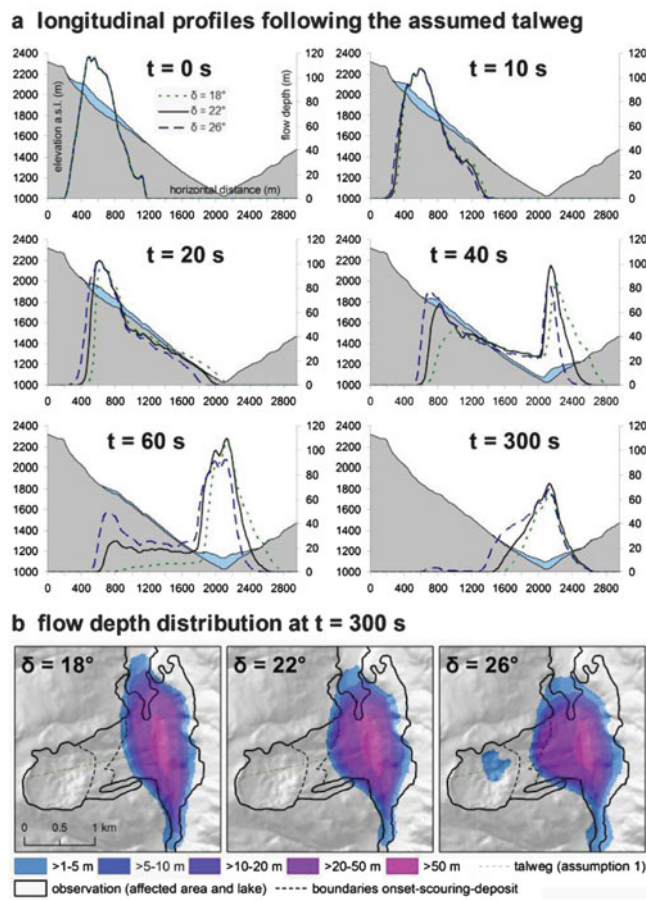


Fig. 4 Longitudinal profiles of the flow at different time steps with $\varphi = 35^\circ$: comparison of the results with $\delta = 18, 22$ and 26° with a cell size of 20 m – the flow depth for $\delta = 18^\circ$ is also shown proportionally to the terrain; (b) flow depth distribution after $t = 300$ s, computed with three different assumptions of δ

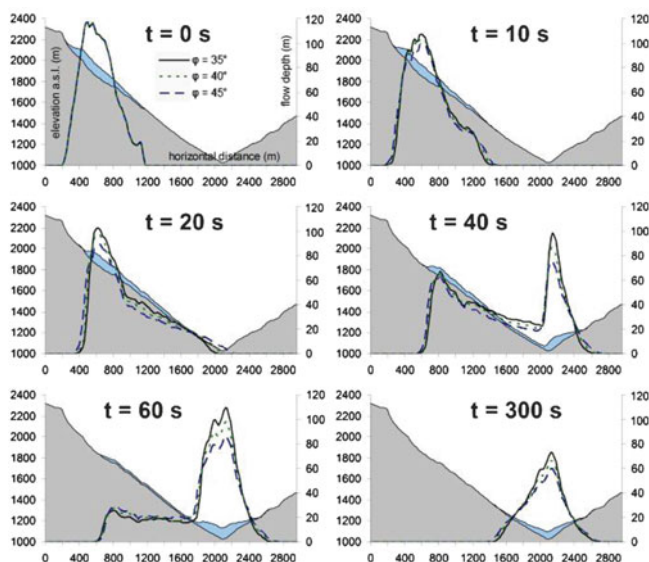


Fig. 5 Longitudinal profiles of the flow at different time steps with $\delta = 22^\circ$: comparison of the results with $\varphi = 35, 40$ and 45° with a cell size of 20 m – the flow depth for $\varphi = 35^\circ$ is also shown proportionally to the terrain

In general, a lower angle of internal friction φ should lead to a thinned deposit due to an increased tendency to spread out, higher values of φ should have the reverse effect. Also here, the situation is more complex in natural terrain, particularly in narrow valleys (Fig. 5): internal friction angles of $\varphi = 40^\circ$ (Simulation 6) and 45° (Simulation 7) were tested against the published value of $\varphi = 35^\circ$. The lowest value of φ causes the model to predict the largest maximum depth of the deposit (75 m).

This actually unexpected outcome is a consequence of the stronger tendency of material with reduced internal friction to level out and therefore fill up the valley bottom. With $\varphi = 0^\circ$, the surface of the deposit would tend to assume a horizontal plane. This case cannot be tested with *r.avalanche* since the Savage-Hutter model is not valid for $\varphi < \delta$. When assuming higher values of φ , there is less of a tendency of the modelled rock avalanche to level out the valley bottom, and the deposit spreads over a larger area, but with a lower maximum depth (67 m for $\varphi = 40^\circ$ and 60 m for $\varphi = 45^\circ$).

Conclusions

r.avalanche represents a first attempt to implement a fully deterministic granular flow model with Open Source GIS. With respect to travel distance and impact areas, the model seems potentially suitable for Class A predictions: the observed patterns were well reconstructed without recalibration of the input parameters. In contrast, the maximum depth of the deposit was rather underestimated. The modelled flow velocity corresponds well to published estimates (Crosta et al. 2004) which, however, appear high when compared to those specified for other rock avalanches. The quality of the results may be limited by uncertainties in the governing parameters and their spatial patterns. However, some drawbacks are also prescribed by the design of the model.

r.avalanche is only applicable to granular flows with approximately straight flow lines, as this was a basic assumption in the derivation of the equations for flows over complex terrain by Gray et al. (1999) on which the here used numerical scheme is based. Pudasaini (2003) has solved the Savage-Hutter model for curved and twisted channels, but this approach is hardly applicable to raster-based GIS.

Furthermore, entrainment of regolith during the flow is disregarded – in the case of the Valpola rock avalanche, entrainment was not extremely significant, but other cases were reported where entrainment has played a major role for the travel distance of granular flows (McDougall and Hungr 2005).

The role of pore water for the motion of the flow is neglected, but many granular flows in nature are a mixture of solid and fluid components and should be considered as such. Another issue is the assumed independence of the bed friction angle δ from earth pressure – a more

realistic account of this relationship could improve the quality of the model.

Attacking the limitations in a comprehensive way will at least require the following steps:

1. To select and adapt a sound method for modelling rapid granular flows over arbitrary topography, using and extending the existing theories. Such an approach would have to build on the latest extensions of the Savage-Hutter model (e.g. Luca et al. 2009; Pudasaini 2011), incorporating particle entrainment and the role of pore fluid;
2. To devise an appropriate numerical scheme (including shock capturing) for solving the differential equations derived in (1). Numerical solutions of the analytical model for arbitrary topography would have to be elaborated, following e.g. Bouchut and Westdickenberg (2004);
3. To perform more tests with well-studied granular flow events.

Since no user-friendly Open Source software for the motion of granular flows fully incorporating the relevant physical processes is available at present, further development of *r.avalanche* in terms of the above points would be highly relevant for reliable process modelling and for the delineation of hazard zones.

Acknowledgments The work was supported by the Tyrolean Science Funds. Special thanks for fruitful discussions go to Kolumban Hutter, Jean F. Schneider and Mechthild Thalhammer.

References

- Bouchut F, Westdickenberg M (2004) Gravity driven shallow water models for arbitrary topography. *Commun Math Sci* 2(3):359–389
- Cannata M, Molinari M (2008) Natural hazards and risk assessment: the FOSS4G capabilities. In: Academic proceedings of the 2008 free and open source software for geospatial (FOSS4G) conference, Cape Town, 29 Sept–3 Oct 2008, pp 172–181
- Christen M, Kowalski J, Bartelt B (2010) RAMMS: Numerical simulation of dense snow avalanches in three-dimensional terrain. *Cold Reg Sci Technol* 63:1–14
- Corominas J, Copons R, Vilaplana JM, Altamir J, Amigó J (2003) Integrated landslide susceptibility analysis and hazard assessment in the principality of Andorra. *Nat Hazards* 30:421–435
- Crosta GB, Imposimato S, Roddeman DG (2003) Numerical modelling of large landslides stability and runout. *Nat Hazard Earth Sys Sci* 3:523–538
- Crosta GB, Chen H, Lee CF (2004) Replay of the 1987 Val Pola landslide, Italian Alps. *Geomorphology* 60:127–146
- De Ferranti J (2005–2010) Digital elevation data. www.viewfinderpa.nopramas.org
- Gamma P (2000) Dfwalk – Murgang-Simulationsmodell zur Gefahrenzonierung. *Geographica Bernensia* G66, 144pp
- Govi M, Gullà G, Nicoletti PG (2002) Val Pola rock avalanche of July 28, 1987, in Valtellina (Central Italian Alps). In: Evans SG, Degraff JV (eds) Catastrophic landslides: effects, occurrence, and mechanism, Geological Society of America reviews in engineering geology. Geological Society of America, Boulder, pp 71–89
- Gray JMNT, Wieland M, Hutter K (1999) Gravity-driven free surface flow of granular avalanches over complex basal topography. *Proc R Soc Lond A* 455:1841–1874
- Hungr O (1995) A model for the runout analysis of rapid flow slides, debris flows, and avalanches. *Can Geotech J* 32:610–623
- Hungr O, Corominas J, Eberhardt E (2005) State of the art paper: estimating landslide motion mechanism, travel distance and velocity. In: Hungr O, Fell R, Couture R, Eberhardt E (eds) Landslide risk management. Proceedings of the international conference on landslide risk management, Vancouver, BC, 31 May–3 June 2005, pp 129–158
- Iverson RM (1997) The physics of debris flows. *Rev Geophys* 35:245–296
- Luca I, Tai YC, Kuo CY (2009) Modelling shallow-gravity driven solid-fluid mixtures over arbitrary topography. *Commun Math Sci* 7:1–36
- McDougall S, Hungr O (2004) A model for the analysis of rapid landslide motion across three-dimensional terrain. *Can Geotech J* 41:1084–1097
- McDougall S, Hungr O (2005) Dynamic modeling of entrainment in rapid landslides. *Can Geotech J* 42:1437–1448
- Mergili M, Fellin W, Moreiras SM, Stötter J. Simulation of debris flows in the Central Andes based on open source GIS: possibilities, limitations, and parameter sensitivity (Submitted to *Natural Hazards*)
- O'Brien, JS (2003) FLO-2D Users' manual version 2003. 06 July 2003. FLO-2D Software Inc., Nutrioso, Arizona, 232pp
- Perla R, Cheng TT, McClung DM (1980) A two-parameter model of snow avalanche motion. *J Glaciol* 26:197–207
- Pudasaini SP (2003) Dynamics of flow avalanches over curved and twisted channels. Theory, numerics and experimental validation. Dissertation, Technical University of Darmstadt, Germany
- Pudasaini SP (2011) A general two-fluid debris flow model. *Geophys Res Abstr* 13:EGU2011-4205-1
- Revellino P, Guadagno FM, Hungr O (2008) Morphological methods and dynamic modelling in landslide hazard assessment of the Campania Apennine carbonate slope. *Landslides* 5(1):59–70
- Rickenmann D (1999) Empirical relationships for debris flows. *Nat Hazards* 19:47–77
- Sampl P, Zwinger T (2004) Avalanche simulation with SAMOS. *Ann Glaciol* 38:393–398
- Savage SB, Hutter K (1989) The motion of a finite mass of granular material down a rough incline. *J Fluid Mech* 199:177–215
- Scheidegger AE (1973) On the prediction of the reach and velocity of catastrophic landslides. *Rock Mech* 5:231–236
- Vandre BC (1985) Rudd creek debris flow. In: Bowles DS (ed) Delineation of landslide, flash flood and debris flow hazards in Utah, Utah Water Research Laboratory, pp 117–131
- Voellmy A (1955) Über die Zerstörungskraft von Lawinen. *Schweizerische Bauzeitung* 73:159–162, 212–217, 246–249, 280–285
- Wang Y, Hutter K, Pudasaini SP (2004) The Savage-Hutter theory: a system of partial differential equations for avalanche flows of snow, debris, and mud. *J Appl Math Mech* 84:507–527



Proposed Landslide Susceptibility Map of Canada Based on GIS

María José Domínguez-Cuesta and Peter T. Bobrowsky

Abstract

Landslides are especially damaging in Canada and despite their extensive occurrence, the exact location of instability is not homogeneous across the country and depends on several factors. Based on clear evidence it is known that there is a wide range in the scale and diversity of landslide environments, especially as they pertain to landslide problems.

A proposed 1:6 million scale landslide susceptibility map of Canada is presented in this study as a first approximation for those individuals interested in pursuing more detailed investigations. The final map has been constructed based primarily on GIS, by considering digital layers of relevant national information including: slope angle, aspect, precipitation, permafrost, surficial geology, vegetation, distance to rivers, distance to coast (lakes and oceans) and bedrock lithology. These variables have been categorized into several classes depending on their greater or lesser favourability to influence slope instabilities. The values assigned to each class are not equal for the whole country and vary depending on the region considered (Canadian Shield, Hudson Bay Lowlands, or the remaining area).

Keywords

Landslide • Susceptibility • Canada • GIS

Introduction

Canada, the second largest country in the world (close to 10 million km²), supports significant environmental diversity and is affected by a great variety of natural hazards. Of all the geophysical hazards, landslides are especially damaging in terms of both mortality and economic costs. According to Evans (1999), during the past 150 years, more individuals have died in Canada from landslides than all other natural hazards combined. Moreover, landslides are known to occur across the country and are estimated to cost Canadians on the

order of \$200 to \$400 million annually (Clague and Bobrowsky 2010).

Landslide research in the country is quite extensive but most studies in Canada deal with site specific occurrences or regional assessments (e.g. Blais-Stevens et al. 2011; Quinn et al. 2010; Jaboyedoff et al. 2009). Only recently has attention been directed towards pan-Canadian inventories and national slope instability issues (Grignon and Bobrowsky 2005; Grignon et al. 2004). Even where detailed studies have been completed, it is clear that the heterogeneity of terrain conditions, relief, precipitation and other factors in the country preclude attempts at simple generalizations.

Although the earthquake hazard in Canada is well documented at a national scale, the absence of such a synthesis for landslide hazards has remained a serious gap in efforts to effectively communicate and educate the broader population on various landslide related issues. In response to this clear need for landslide data relevant at a national scale, the objective of this paper is to introduce a landslide

M.J. Domínguez-Cuesta (✉)
Geology Department, University of Oviedo, C/ Arias de Velasco s/n,
33005 Oviedo, Spain
e-mail: mjdominguez@geol.uniovi.es

P.T. Bobrowsky
Geological Survey of Canada, 601 Booth St., Ottawa ON K1A 0E8,
Canada

susceptibility map of Canada. The map is based on multiple data layers (e.g. geology, relief, etc.) within a GIS platform and tailored by reliance on expert knowledge.

Methodology

The methodology used in this work includes the following several steps: (1) GIS database creation and digital data layers collection, (2) derived Digital Terrain Models creation, (3) relief differentiation of large areas in the country, (4) landscape reclassification, (5) assignment of susceptibility ranking for each data layer based on large areas and variable distribution, and (6) final data information analysis, cross correlation and construction of the susceptibility model.

GIS Database Creation and Digital Data Layers Collection

A digital database was created with a Geographical Information System (GIS) (ArcGIS v. 9.2 ESRI), which allows one to organize information in georeferenced shapes and rasters.

Vector data stored in the database consist of several thematic layers (Fig. 1a–h) comprising precipitation, permafrost distribution, surficial geology, vegetation, bedrock lithology, rivers and coasts (lakes and oceans). These data represent parameters that influence slope stability in Canada to varying degrees. Unfortunately the accuracy, precision and reliability of the data used are not equal, not systematic and cannot be evaluated for reliability. For example, the surficial geology database was published at a large scale with detailed polygonal information and is therefore quite useful. This contrasts for instance to the permafrost layer which is published at a smaller scale and the information contained therein is quite generalized. We were not able to check the integrity of each data layer and simply relied on the efforts of the original data compiler to ensure that the best effort was put forward to release reliable information.

Raster data consisted of a 1 km pixel value Digital Elevation Model (DEM) and other digital derived models. To construct the final susceptibility map it was also necessary to transform the vector layers to raster format (1 km precision). This transformation to raster format facilitated faster data manipulation, analysis and interpretation.

All of the data layers used in this synthesis were obtained from various agencies, departments and ministry websites hosted in Canada. Several of the sources are open to public access, whereas some of the information resides within the data confines of the Geological Survey of Canada.

Derived Digital Terrain Models Creation

The GIS platform allows one to generate other digital models from the DEM by using different mathematic algorithms. For example, a Digital Slope Model (DSM) (Fig. 2a) and a Digital Aspect Model (DAM) (Fig. 2b), have been constructed through GIS based on the original DEM. Both of these derivative maps have the same resolution (1 km² pixel value) as the original DEM upon which they are based.

Relief Differentiation of Large Areas in the Country

Existing knowledge of slope instability type, style and distribution for all of Canada suggests that for this analysis we can distinguish a few large areas by considering regional variations in landslide attributes. For the purposes of this work, four substantially large regions are recognized: (1) the vast territory (> 4 millions km²) occupied by the Canadian Shield (CS), a very stable environment where instability problems are not as abundant as in other areas; (2) an area up to 300,000 km² located in the middle of the country, directly south of the Hudson Bay (Hudson Bay lowlands, HBL). Finally, the remaining terrain has been distinguished between: (3) the areas where the slope is less than 1° as interpreted by 1 km² pixels (low relief areas, L) and (4) those parts of the country where the slope is greater than 1° are considered as high relief areas (H).

Landscape Reclassification

After compiling information for all of the mentioned variables into the GIS, it is possible to classify the Canadian landscape by taking into account the different distribution of terrain elements across the country. For example, when considering **Precipitation**, three classes were established: >3,000, 2,700–3,000 and <2,700 mm annual precipitation (see Table 1).

Five classes were distinguished for **Permafrost**: *Continuous*, *Extensive Discontinuous*, *Sporadic Discontinuous*, *Isolated Patches* and *No Permafrost*.

Surficial Geology is divided into: *Alluvial*, *Colluvial*, *Glacial*, *Glaciers*, *Glaciofluvial*, *Glaciolacustrine* and *lacustrine*, *Glaciomarine* and *marine*, *Lacustrine*, *Marine*, *Rock and Water*. The original detailed landform classification used by the authors was simplified into these categories to facilitate GIS manipulation and generalization.

With respect to **Vegetation** cover data layer, 11 classes have been distinguished: *Broadleaf Forest*, *Coniferous Forest*, *Cropland*, *Forest land/Shrub land*, *Grassland*, *Mixed*

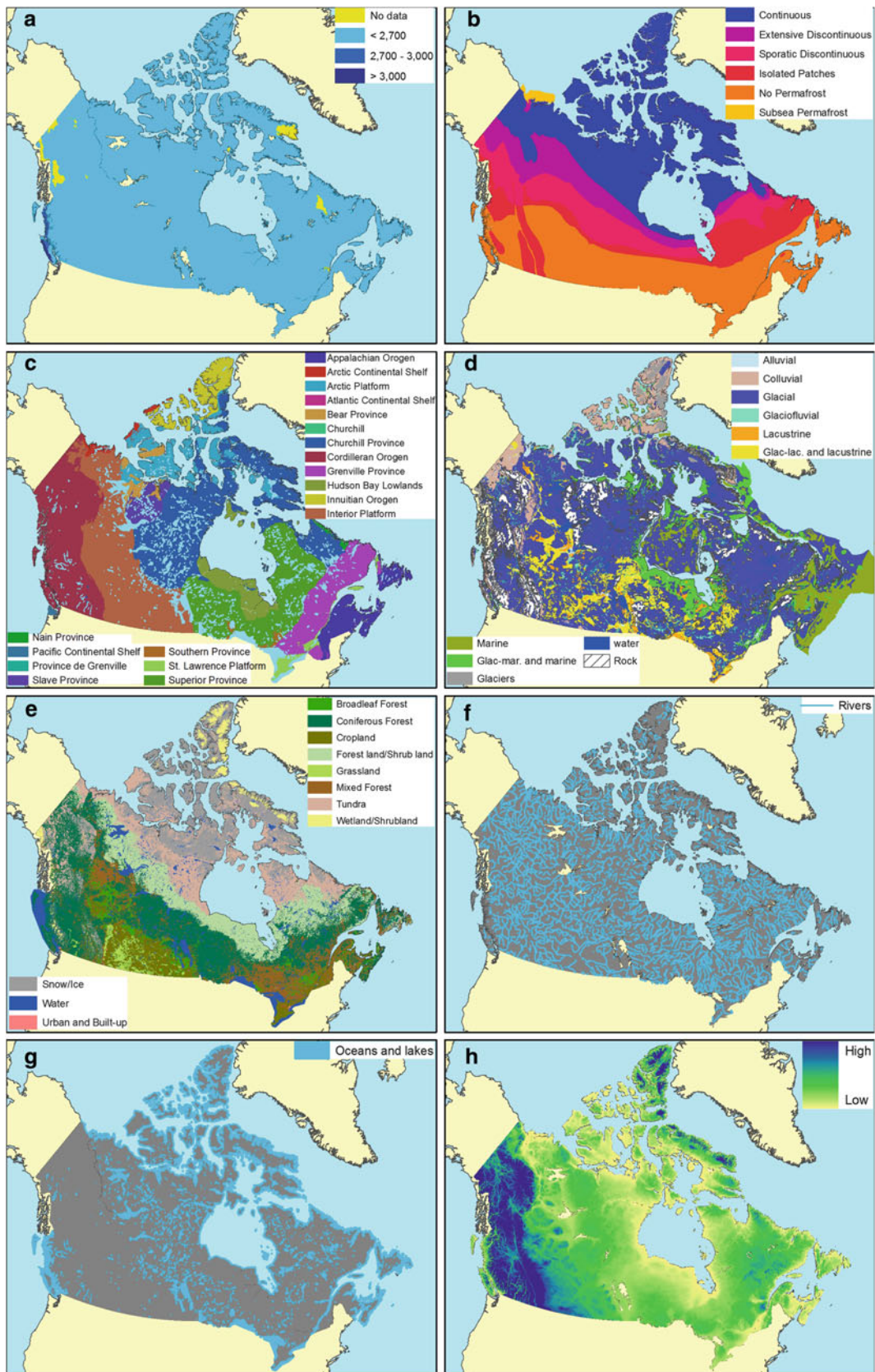


Fig. 1 Layers stored in the GIS database: (a) precipitation, (b) permafrost distribution, (c) bedrock geology, (d) surficial geology, (e) vegetation, (f) rivers, (g) coast (oceans and lakes) and (h) elevation

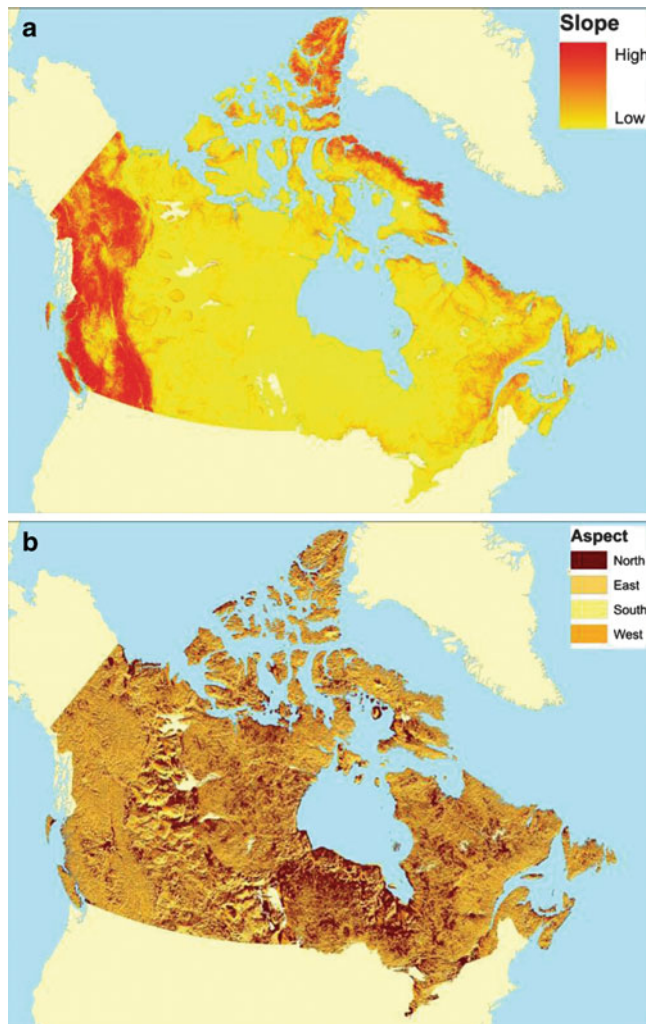


Fig. 2 Derived digital terrain models: (a) slope, (b) aspect

Forest, Snow/Ice, Tundra, Urban and Built-up, Wetland/Shrubland and Water. Vegetation type as well as presence/absence plays an important role regarding root strength, water absorption, etc. in relation to slope stability.

The **Bedrock Geology** data base was also considered, but given the lack of lithology specifics which could prove useful for geotechnical interpretation, we could only recognize two key areas (in the lowland region) where surficial cover is thin and bedrock influences slope hazards: the Canadian Shield and the Hudson Bay Lowlands. For the rest of the country, the drift thickness is more significant and has greater influence for slope instability (this does not apply in the “highlands” regions of Canada).

Distance from Coast (oceans and lakes) has been considered by creating coverage of three classes: <1 , $1-2$ and $2-3$ km from coast. This was based on a 1 km^2 pixel size and the need to take into account tributaries that comprise all drainage basins but are not captured at the scale of resolution used.

The same criterion was applied to create a layer based on **Distance from Rivers** dividing these into three classes: <1 , $1-3$ and $3-5$ km from rivers. The reason for these classes is due to the minimum pixel size of 1 km^2 and the need to include at least some of the tributary valleys in the assessment which lie beyond 1 km in distance from the primary channel.

The **Digital Slope Model** was reclassified into three classes <1 , $1-18$, $18-30$ and $>30^\circ$. The selection of these intervals is based on the commonly observed slope values for triggering different types of instability processes.

And finally, with respect to **Aspect**, this was simplified into three classes: *North*, *South* and *Flat* areas. North includes the areas facing between 270 and 360° as well as $0^\circ-90^\circ$ whereas South are those slopes facing $90-270^\circ$ faced areas. Flat areas are self explanatory. At this scale of DEM it was not possible to divide the aspect into smaller categories.

Assignment of Susceptibility Ranking for Each Data Layer Based on Large Areas and Variables Distribution

To establish the susceptibility ranking of specific data layers, expert opinion was obtained during a workshop at which GSC landslide experts relied on their personal experience and professional knowledge as input to the attribute and parameter relevance regarding landslide hazards.

Attributes within each parameter were assessed and classified (semi-quantitatively) according to six categories of significance (1-low to 6-high).

These categories vary depending on which one of the large areas previously defined was considered: (1) the Canadian Shield, (2) the Hudson Bay Lowlands, and (3) the remaining Canadian territory for Low and High relief terrain (Fig. 3). The H and L relief terrain are not shown on this image given the size of the map representation. As a result three susceptibility ranking tables have been constructed. Susceptibility values shown in Table 1 have been applied to the three areas.

The Hudson Bay Lowlands (HBL) and the Canadian Shield (CS) are recognized as special areas from a landslide susceptibility point of view. These two regions are relatively flat areas, with thin drift cover so that instabilities in these two regions are linked to those conditions where there is some slope, and usually close to rivers or coast. However, distance to water bodies alone was insufficient and the presence of key surficial deposits was also considered (glaciolacustrine and lacustrine, glaciomarine and marine, lacustrine and marine deposits).

Susceptibility classes applied to HBL and CS are shown in Tables 2 and 3. The reason other data attributes are not considered in the HBL and CS areas is because their susceptibility

Table 1 Susceptibility values applied to the Canadian landscape (*H* highlands, *L* lowlands, *CS* Canadian Shield, *HBL* Hudson Bay Lowlands) (see text for explanation of acronyms)

		Susceptibility ranking					
		1	2	3	4	5	6
Slope	<1°	L					
	1°–18°	H					
	18°–30°					H	
	>30°						H
Aspect	North	HL					
	South		HL				
	Flat	HL					
Total annual PPT	>3,000 mm			HL			
	2,700–3,000		HL				
	<2,700	HL					
Permafrost	Continuous	HL					
	Extensive discontinuous			HL			
	Sporadic discontinuous			HL			
	Isolated patches		HL				
	No permafrost	HL					
Surficial geology	Alluvial	HL					
	Colluvial			HL			
	Colluvial deposits			HL			
	Glacial deposits	HL					
	Glaciers						
	Glaciofluvial deposits		HL				
	Glaciolacustrine and lacustrine deposits			CS	HBL	H	L
	Glaciomarine and marine deposits			CS	HBL	H	L
	Lacustrine deposits			CS	HBL	H	L
	Marine deposits			CS	HBL	H	L
	Rock	L				H	
	Water						
	Broadleaf forest		HL				
Coniferous forest		HL					
Vegetation (e.g. Landuse)	Cropland			HL			
	Forest land/Shrub land		HL				
	Grassland			HL			
	Mixed forest		HL				
	Snow/Ice						
	Tundra			HL			
	Urban and built-up			HL			
	Wetland/Shrubland			HL			
	Water						
Distance from rivers	<1 km						HL
	1–3 km					HL	
	3–5 km				HL		
Distance from coast	<1 km						HL
	1–2 km					HL	
	2–3 km				HL		
Distance from lakes	<1 km						HL
	1–2 km					HL	
	2–3 km				HL		

ranking by experts was generally low (for example 2 or less for Aspect, and 3 or less for the other categories). Distance from rivers, coast and lakes was too small to be illustrated at this

scale but was considered. The only other data layer of significance according to the experts was Surficial Geology where HBL and CS would score 3 or greater.

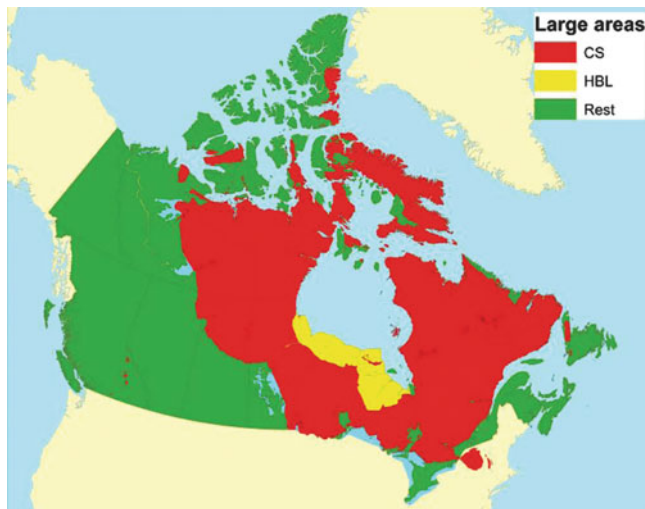


Fig. 3 Large areas distinguished in this study. *CS* Canadian Shield, *HBL* Hudson Bay Lowlands, *Rest* remaining Canadian territory

Table 2 Susceptibility values applied to the Canadian Shield area (*SG1* Alluvial or Colluvial or Glacial or Glaciofluvial deposits or Rocks, *SG2* Glaciolacustrine or Lacustrine or Glaciomarine or Marine deposits)

		SG1	SG2		
Distance from rivers	<1 km	CS			CS
	1–3 km	CS		CS	
	3–5 km	CS	CS		
	>5 km	CS	CS	CS	CS
Distance from coast	<1 km	CS			CS
	1–2 km	CS		CS	
	2–3 km	CS	CS		
	>3 km	CS	CS	CS	CS
Distance from lakes	<1 km	CS			CS
	1–2 km	CS		CS	
	2–3 km	CS	CS		
	>3 km	CS	CS	CS	CS

Final Data Information Analysis, Cross Correlation and Construction of the Susceptibility Model

After classifying all the digital layers as shown in Tables 1, 2, and 3, we applied the designations to the entire Canadian landscape. This procedure leads to the derivation of the final susceptibility map. The result consists of all polygons displaying a susceptibility value varying from 1 to 6. There was no need for a complex weighted algorithm since all layers and parameters were already weighted in their classification. Data layers were simply overlaid and the pixel with the highest score superseded all other scores.

Upon completion of the map, visual inspection of the polygons indicated occasional errors that existed in the original data layers. To minimize propagation of such mistakes

Table 3 Susceptibility values applied to Hudson Bay Lowlands territory (See Table 2 for explanation of acronyms *SG1* and *SG2*)

		SG1	SG2		
Distance from rivers	<1 km	HBL			HBL
	1–3 km	HBL		HBL	
	3–5 km	HBL	HBL		
	>5 km	HBL	HBL	HBL	HBL
Distance from coast	<1 km	HBL			HBL
	1–2 km	HBL		HBL	
	2–3 km	HBL	HBL		
	>3 km	HBL	HBL	HBL	HBL
Distance from lakes	<1 km	HBL			HBL
	1–2 km	HBL		HBL	
	2–3 km	HBL	HBL		
	>3 km	HBL	HBL	HBL	HBL

in the final map, a manual manipulation to the final map results was employed in a few locations where necessary. As an example of one post analysis correction, several lakes in the province Quebec were misclassified as glaciers in the original data layer used in this analysis. This type of input error by the original authors was not recognized by us until after the final map was generated and was corrected manually to reduce further propagation of error.

Results and Discussion

The main result of this work is the completion of the first national scale (1:6 million) landslide susceptibility map for Canada. This map illustrates the significant variability that exists across the country with respect to the likelihood of slope instability (Fig. 4).

The final map provides a “first approximation” characterization of landslide susceptibility for the diverse terrain scattered across Canada by relying on a hot to cold (red to green) legend to illustrate the potential for landslide threat. At this scale of analysis and presentation, the map is most useful in demonstrating regional trends.

In general, the most susceptibility terrains are located in western Canada. That is consistent with the known distribution of high relief and mountainous areas.

The St Lawrence River Valley corridor, in southeastern Canada is another area that displays a greater number of orange and red pixels on the map. Again this is expected given the presence of Leda clays and historic record of instability in the region (Quinn et al. 2010).

The third region of high potential corresponds to the river valleys and glaciolacustrine and lacustrine sediments present in the prairies of west-central Canada.

In general, the rest of the country could be considered to be of lower landslide susceptibility, although local and site specific assessments cannot be reliably extracted from such a national

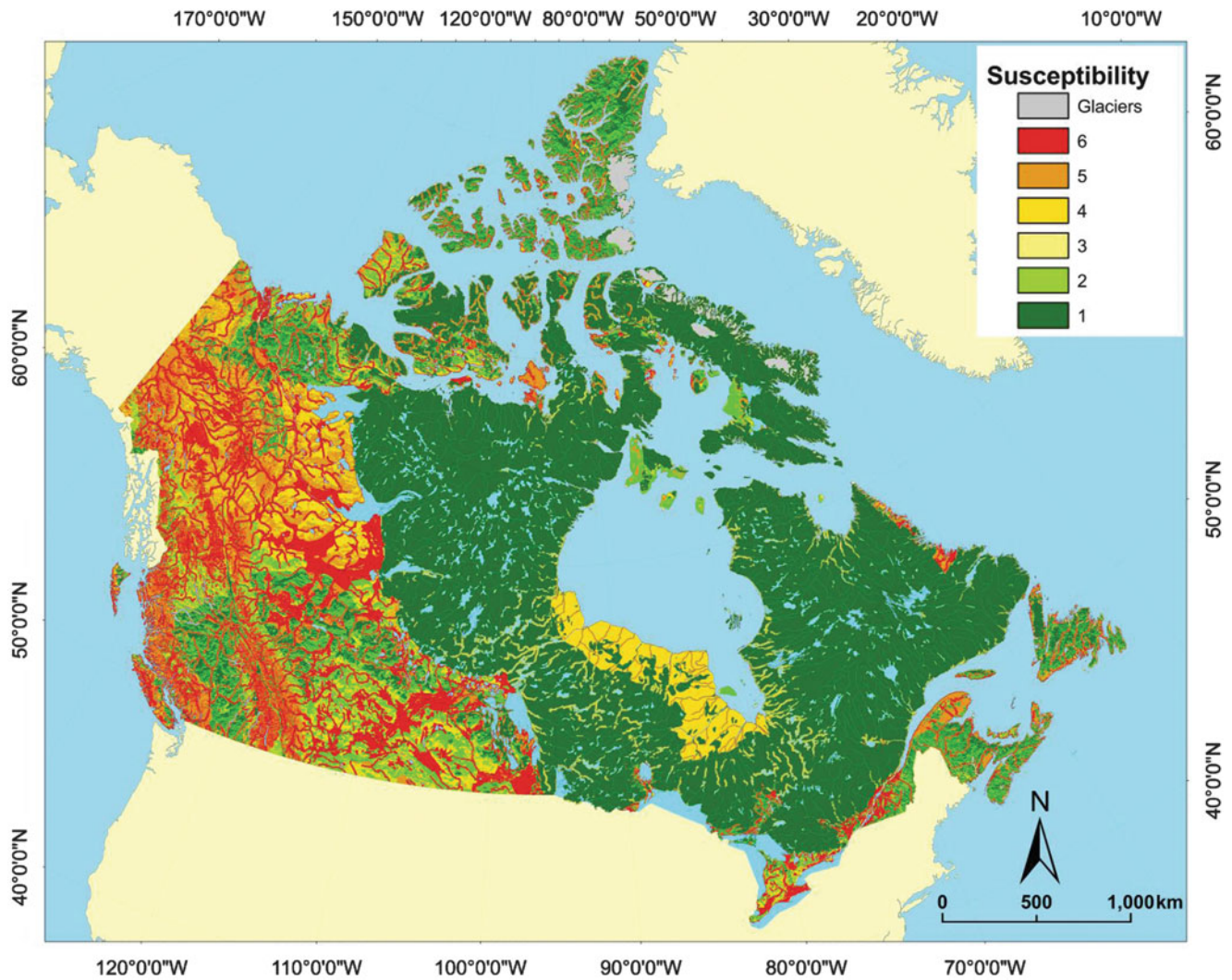


Fig. 4 Landslide susceptibility map of Canada

scale map and therefore more diligent study and interpretation on a case by case basis is advised for detailed needs.

From a methodological point of view, the procedure applied in this work is based considerably on expert knowledge. The quality assessment of collected data is essential in a susceptibility model based on GIS (Trigila et al. 2010). Most of the problems or inconsistencies detected on the final map are due to errors and inaccuracies of the original data layers. For example, the limits of the coast, lakes and rivers are different in each layer. This discrepancy could result in a red susceptibility color appearing in the middle of a lake. The same problem appears related to presence/absence and position of glaciers or water bodies. In the final map several known large glaciers are not shown because they were not part of the original database.

The current landslide inventory of Canada comprises some 22,000 unverified points collected with bias. These data are not statistically representative of the true landslide

inventory of Canada and therefore are not suitable for any model validation efforts. Moreover, most studies employing validation tests are not actually testing the predictability of their models but rather the accuracy of their auto-correlated algorithms.

Conclusions

The methodology and baseline digital data layers (availability, quality, resolution) employed in any susceptibility map strongly influence the final product. Different methods will generate different final maps using the same primary data. With respect to the present susceptibility map it is important to highlight that much of the Cordillera, parts of prairies and the St. Lawrence River valley support the most landslide susceptible terrains. That area corresponding to the Canadian Shield and the Hudson Bay Lowlands supports the lowest landslide susceptibilities.

Acknowledgments The authors are very grateful to the Geological Survey of Canada landslide specialists who participated in the process of classifying the various data layers and Andr e Blais-Stevens for critical review. This activity was supported by the Public Safety Geoscience Program of NRCan. This is GSC Contribution #20110109.

References

- Blais-Stevens A, Hermanns RL, Jermyn C (2011) A ^{36}Cl age determination for Mystery Creek rock avalanche and its implications in the context of hazard assessment, British Columbia, Canada. Landslides. doi:10.1007/s10346-011-0261-0
- Clague JC, Bobrowsky PT (2010) Natural hazards in Canada. *Geosci Can* 37(1):17–37
- Evans S (1999) Landslide disaster in Canada 1840–1998, Geological Survey of Canada, Open File no 3712. Geological Survey of Canada, Ottawa
- Grignon A, Bobrowsky P (2005) Empowering scientists, planners and the public to reduce landslide losses: a simplified web interface to access a national landslide database in Canada. *Geophys Res Abstr* 7:05511, European Geosciences Union
- Grignon A, Bobrowsky P, Coulthick T (2004) Landslide database management philosophy in the Geological Survey of Canada. Ge-engineering for the society and its environment. In: Proceedings of the 57th Canadian geotechnical conference and the 15th joint CGS-IAAH conference, Qu bec, 24–27 Oct 2004
- Jaboyedoff M, Couture R, Locat P (2009) Structural analysis of Turtle Mountain (Alberta) using digital elevation model: toward a progressive failure. *Geomorphology* 103(1):5–16
- Quinn PE, Hutchinson DJ, Diederichs MS, Rowe RK (2010) Regional-scale landslide susceptibility mapping using the weights of evidence method: An example applied to linear infrastructure. *Can J Civil Eng* 37(8):905–927
- Trigila A, Iadanza C, Spizzichino D (2010) Quality assessment of the Italian landslide inventory using GIS processing. *Landslides* 7:455–470



Statistic Versus Deterministic Method for Landslide Susceptibility Mapping

Iuliana Armas, Florica Stroia, and Laura Giurgea

Abstract

The present work aims to assess the landslide susceptibility of a hilly area, using two methods: the weight of evidence statistical method (WOE) that is based on bivariate statistical analysis and the deterministic approach based on the infinite slope model.

To document the efficiency of this quantitative methods, a landslide prone area along Prahova Subcarpathian Valley was chosen, where landslide hazard interacts with human settlement and activities.

The Landslide susceptibility map derived from the WOE method has been compared with that produced from the deterministic method and the results analyzed. The values obtained were also in good agreement with the field observations.

Results show that the main controlling factors in the evolution of landslides are the slope gradient, saturation condition and lithology. Beside these, factors like morphography (slope aspect and flow direction) or human intervention (land use, roads, buildings) can interfere.

Keywords

Landslide susceptibility map • GIS • Weight of evidence statistical method • Infinite slope model • Romanian Subcarpathian area

Introduction

Landslides are related to erosion-prone areas, being common processes in alpine regions with steep, unstable slopes. Most slopes appear stable and static, but they are actually dynamic, evolving systems. The important variables in classifying down slope movements are their mechanisms (movement types), the nature of the displaced material (material type), amount of water present, as well as information on their activity (state, distribution, style), i.e. the rate of

movement over a period of time (Terzaghi 1950; Varnes 1978, 1984; Turner and Schuster 1996; Cruden and Varnes 1996; Thomson and Turk 1997).

In this paper, landslides are understood as a “downslope movement of a soil or rock mass occurring on surface or rupture” (Highland and Bobrowsky 2008).

In the romanian Subcarpathian area, landslides have the biggest impact on human communities and on natural ecosystems (Balteanu et al. 1996; Cioaca 1996; Cioaca et al. 1996; Grecu 1999, 2002; Armaş et al. 2003, 2005; Stroia et al. 2005; Armaş and Damian 2006).

For example, in the study area of Breaza town, in summer 1997 landslides affected 1,100 households, with 8 houses being totally destroyed.

Therefore the first necessary step for landslide risk management and land use planning is to properly demarcate the disaster prone areas through landslide susceptibility mapping (Aleotti and Chowdhury 1999).

I. Armas (✉)
Faculty of Geography, University of Bucharest, 1, Bd. Nicolae
Balcescu, Bucharest, Romania
e-mail: iulia_armas@geounibuc.ro; iuliaarmas@yahoo.com

F. Stroia • L. Giurgea
Faculty of Geology and Geophysics, University of Bucharest, 6, Traian
Vuia, Bucharest, Romania

Susceptibility maps reflect the relative spatial probability of landslide occurrence and do not explicitly incorporate the temporal aspect of movement.

The present work aims to assess the landslide susceptibility of a hilly area, using two methods: the weight of evidence statistical method (WOE) that is based on bivariate statistical analysis and the deterministic approach based on the infinite slope model.

Study Area

To document the efficiency of this quantitative methods, a landslide prone area along Prahova Subcarpathian Valley was chosen, where landslide hazard interacts with human settlement and activities (Fig. 1). The wide span of the Prahova Valley when emerging from the mountain zone, together with the terraced Subcarpathian slopes, are basically involved in the orientation and type of slope dynamics shaped by slope, fragmentation and exposure conditions.

The great number of landslides along the Subcarpathian Prahova Valley mirrors the particular combination of factors that render the slopes unstable. The landslides along the Prahova Valley represent a continuous or occasional reactivation stage, with periods of relative stability being accompanied by creeping on the active steep slopes and by the occurrence of crosswise cracks in the body of the slide or running parallel to the scarps.

The Breaza locality lies on the righthandside of the Prahova River, mainly on the surface of terrace II, which is best preserved.

From a geological point of view, the study area is represented by a large syncline – *the Breaza – Buciumeni syncline* with a west to east orientation.

Miocen-Pliocen-Lower Pleistocen molasses deposits formed the upper part of Breaza-Buciumeni syncline. High vulnerability consist of on stratification and tectonic backgrounds vulnerability. There are a sucesion of sedimentary rocks, marl-clay, sandstone intercalations, sands and gravels. The Breaza terrace scarp develops on marls and clays with intercalations of thin permeable (terrace deposits, sands) and impermeable strata (fat clays) and gypsum horizons.

There are some water springs on slopes. The strata space position is in concordance with the slop surface and has a high degree of instability, undergoing mass movements of rotational type. Mixtures of adverse geological conditions such as weak soil or rock and potential slip planes on steep slopes with torrential rains, heavy snowfall, will continue to produce landslides regardless of human activities.

On the natural factors which lead to instability we can ad high vulnerability due by human activity. A high risk is visible wherever man's actions in the landscape are present

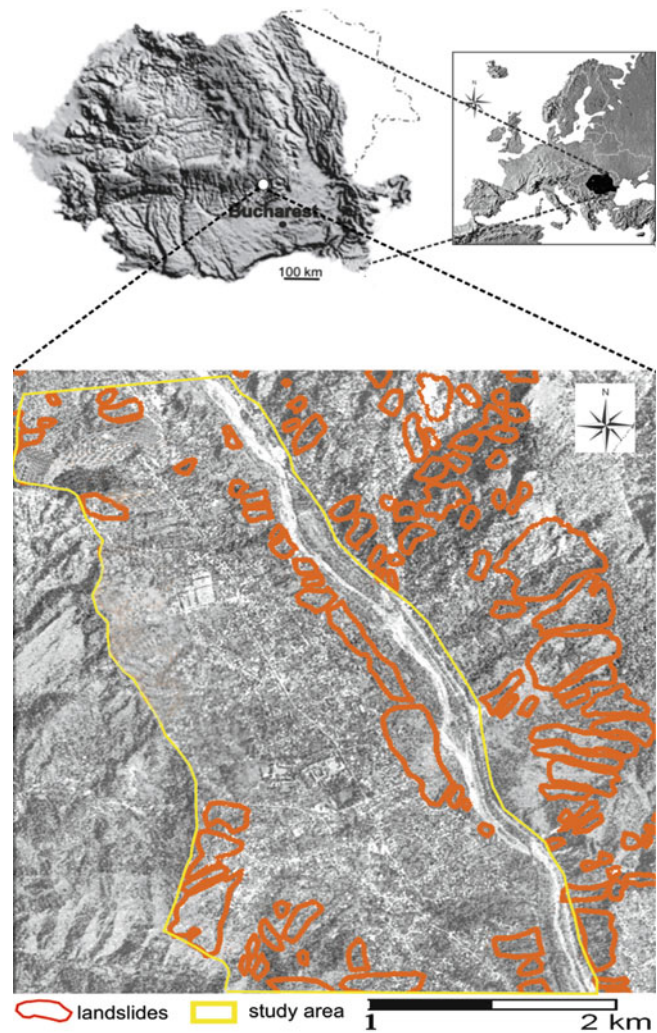


Fig. 1 Study area

(clearing, buildings etc.), landslides affecting households, streets and pasturelands.

Samples taken from outcrops where tested in the geotechnical laboratory. Characteristics like: grain size distribution, plasticity index, consistence index, activity index, share strange parameters – cohesion and internal friction angle (residual and pick values), are established. All this parameters together with the slop topography are useful in slope stability computation.

Method

From the beginning of the 1980s, the enormous potential of statistical tools based on GIS technology have led to a growing interest in the topic of landslide susceptibility assessment and many quantitative approaches have been developed worldwide.

In this research, we applied a quantitative ‘data driven’ method used to combine datasets, known as weight of evidence (WOE) modeling method. This is a statistical approach that compares the spatial distribution of landslides with the predictive variables that are being considered to be important and mutually independent for the occurrences of past events.

In this study, we used the log–linear form of the Bayesian probability model because weights are easier to understand and interpret compared to the probability expression. Relevant thematic maps representing various parameters (e.g., slope, aspect, lithology, groundwater table, soil texture, distances from built environment, land use and geotechnical background) that are related to landslide activity have been generated using GIS techniques. Based on the chi-square test, the selected independent predictive variables were slope gradient, slope aspect and soil thickness. Soil thickness was measured through 36-detailed point measurements uniformly distributed in the research area (Parichi et al. 2006). The WOE method was applied on active, rotational landslides (see Fig. 3).

For a particular landslide susceptibility predictive factor weights were calculated based on:

- The probability of the known predictive factor being present with landslide events
- The probability of the known predictive factor being present without landslide events
- The probability of the known predictive factor being absent with landslide events
- The probability of the known predictive factor being absent without landslide events.

The final susceptibility logit map was obtained by combination of weights of selected conditionally independent predictive factors.

The causes of many landslides and related types of down-slope movement can be examined by studying relations between driving forces and resisting forces.

Deterministic framework involves analyzing specific sites in engineering terms. Slope stability is evaluated by computing a safety factor – named also index of stability, and defined as the ratio of the resisting forces to the driving forces. The index of stability is based on the appropriate geotechnical model. The calculation of the safety factor, F , requires topographical data, data on shear strength parameters (cohesion and angle of internal friction) and information on underground water table. Decisions must be made on whether to use peak shear strength values or residual shear strength values (or values in between) for specific parts of the slip surface (Chowdhury 1976; Chowdhury and Bertoldi 1977).

In this research, the infinite slope model, based on an infinite slope form of the Mohr–Coulomb failure criterion, was integrated with a raster-based GIS (ILWIS) (1). An infinite slope is any line that stays fixed at one constant x -axis coordinate, making the change along the x -axis 0.

$$FS = \frac{c' + (\gamma + m\gamma_w)z \cos^2 \beta \tan \varphi}{\gamma z \sin \beta \cos \beta} \quad (1)$$

where FS is the factor of safety, c' is the effective cohesion (N/m^2), γ is a unit weight of a soil (N/m^3), m is the ratio between the underground water level and the effective soil depth (z_w/z), γ_w is a unit weight of water (N/m^3), z is the soil depth (m), z_w is the underground water level (m), β is the slope surface inclination ($^\circ$), and φ is the effective angle of shearing resistance ($^\circ$).

The outcomes were maps of factor of safety (FS) on a resample 10 m pixel level. Soil properties were represented by soil thickness, unit weight density, and cohesion and friction angle. Adding the depth of the piezometric line and applying the stability model in different scenarios of hydrological conditions extended the analysis.

Figure 2 shows the methodological flowchart of the two methods.

Analysis and Results

Table 1 shows the weights and contrast for the selected variables units included in the WOE approach.

As higher value for W_+ , as stronger is the positive correlation between landslide occurrence and the selected predictive factor. High positive correlations to landslides are obtained for 15–25° slope angle class. This category has also a greater predictive power ($C > 1$). When C is approximately 2, the correlation is very significant (Barbieri and Cambuli 2009). The final weight for each variable was given by the sum of the positive weight and the negative weights of the other classes. In this case, the most susceptible areas are the northern slopes with a 15–25° gradient, and 1 m soil thickness. From a geomorphological point of view, the most susceptible sectors correspond to the scarp of terrace II and the slopes of the upper terraces (Fig. 3).

The landslide susceptibility deterministic approach was tested on two simulated situations: when the ratio between the underground water level and the soil depth was 0 and 1 (e.g., under dry and saturated conditions, see Fig. 4).

As a general aspect, safety factor is decreasing when slope gradient gets higher and when assuming fully saturated soil. The morphological levels act as stability factors.

Fig. 2 Methodological flowchart: (a) The weight of evidence (WOE) method and (b) the deterministic method

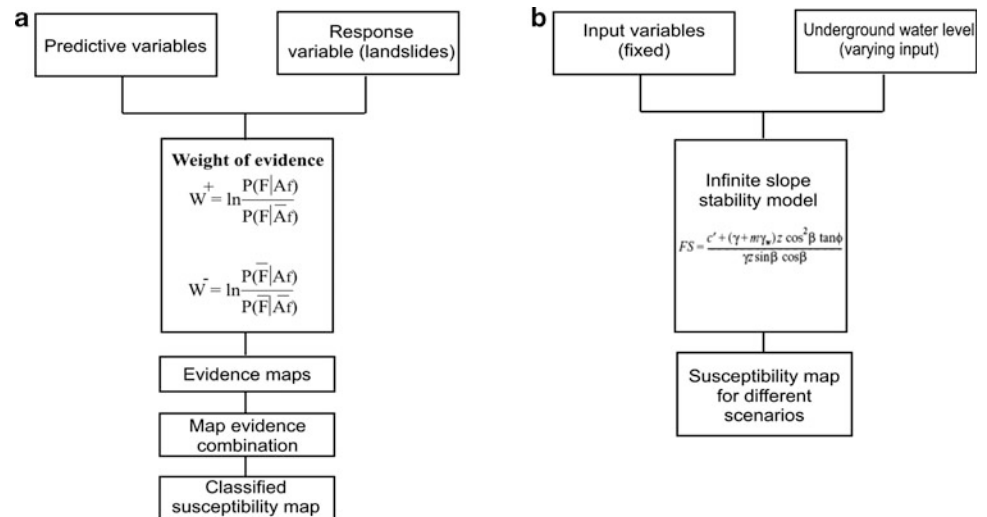


Table 1 The weights and contrast values calculated for the selected predictive factors

Classes of predictive factors	Weight –	Weight +	Contrast value (C)
Slope gradient			
0–3°	0.49	–2.34	–2.83
3–7°	0.13	–0.60	–0.73
7–15°	–0.27	0.58	0.85
15–25°	–0.31	1.42	1.73
25–35°	–0.05	1.22	1.27
35–45°	–0.007	0.82	0.83
45–55°	–0.0001	0.13	0.13
55–65°	0.0001	–2.28	–2.28
65–75°	0.00008	–4.31	–4.31
75–90°	0.00001	–2.77	–2.77
Slope aspect			
NE	–0.16	0.36	0.52
E	–0.08	0.10	0.18
SE	0.06	–0.44	–0.51
S (+flat)	0.09	–1.63	–1.72
SV	0.02	–5.47	–5.49
V	0.01	–1.68	–1.69
NV	–0.006	0.32	0.32
N	–0.01	0.87	0.89
Soil thickness			
0.6 m	0.0003	–0.17	–0.17
1 m	–0.74	0.55	1.29
1.6 m	0.08	–0.22	–0.31
2 m	0.17	–2.19	–2.37
>2.6 m	0.08	–7.65	–7.74

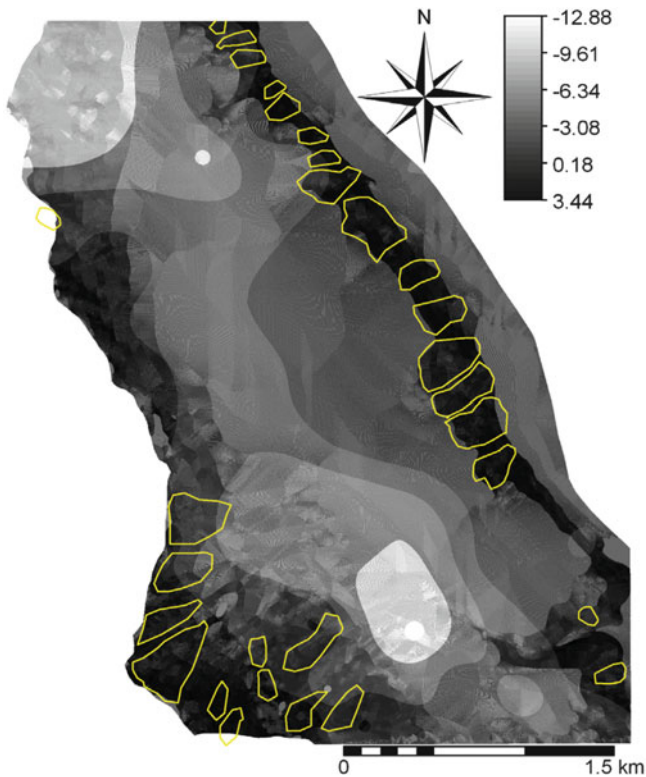


Fig. 3 Combination of weights of selected variables themes in a landslide susceptibility map. In yellow are the active landslides sites

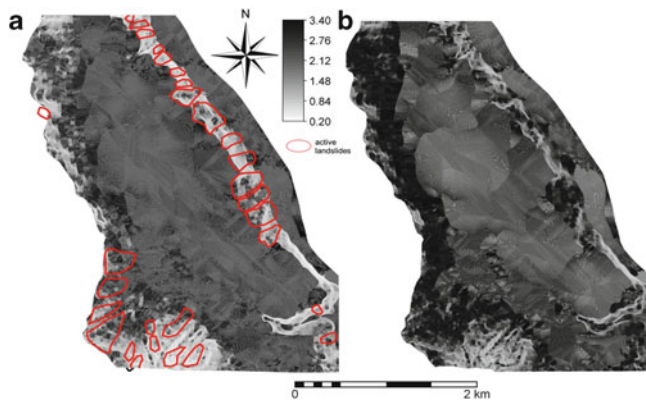


Fig. 4 Unstable areas predicted by the slope instability model under saturated (a) and dry (b) conditions

Conclusions

This paper represents a comparative study of two different approaches of landslide susceptibility mapping, a statistical one and a deterministic approach.

The Landslide susceptibility map derived from the WOE method has been compared with that produced from the deterministic method. Results show that both methods can be successfully applied in landslide

susceptibility mapping. The values obtained were also in good agreement with the field observations.

As a general aspect we can conclude that none of the method is recommended as the most suitable, this depending very much on the quality of the input-data, the how large the study area is and the research objective.

The slope stability model can give more reliable answers, but it is often affected by significant uncertainties associated to the variability of input variables and the uncertainties associated with the mechanisms of failure. Therefore there is difficult to apply it on large areas and this method is more suitable for research data at detailed scales.

In the statistical WOE approach, the major difficulty consists in systematically identifying and assessing the different predictive factors related to landsliding (Carrara 1988). An advantage of this method is that the researcher can validate the importance of each independent predictive variable and decide on the final input maps. Another advantage is that the results can be applied to areas currently free of landslides but where conditions may exist for landslide susceptibility.

References

- Aleotti P, Chowdhury R (1999) Landslide hazard assessment: summary review and new perspectives. *Bull Eng Geol Env* 58:21–44
- Armaş I, Damian R (2006) Evolutive interpretation of the landslides from the Miron Căproiu street scarp (Eternităţii Street– V. Alecsandri Street) – Breaza Town. *Revista de Geomorfologie* 8:65–72
- Armaş I, Damian R, Şandric I, Osaci-Costache G (2003) Vulnerabilitatea versanşilor la alunecări de teren în sectorul subcarpatic al văii Prahova, Ed. Fundaţiei “România de Măine”, Bucureşti
- Armas I, Sandric I, Damian R (2005) Assessing slopes vulnerability to landslides in tectonic active areas using The Bayesian and Dempster-Shafery probability models/Prahova valley/Romania. In: *Proceedings of the European geosciences union, General Assembly, 24–29 Apr 2005, Vienna*
- Balteaun D, Cioaca A, Dinu M, Sandu M (1996) Some case studies of geomorphological risk in the Curvature Carpathians and Subcarpathians, *RRG*, 40
- Barbieri G, Cambuli P (2009) The weight of evidence statistical method in landslide susceptibility mapping of the Rio Pardu Valley (Sardinia, Italy). In: *Proceedings of the 18th world IMACS/ MODSIM congress, Cairns, 13–17 July 2009*. <http://mssanz.org.au/modsim09>
- Carrara A (1988) Landslide hazard mapping by statistical methods: a black box model approach. In: *Proceedings of the workshop on natural disaster in European mediterranean countries*. Perugia, Italy. Consiglio Nazionale delle Ricerche
- Chowdhury RN (1976) Initial stresses in natural slope analysis. In: *Rock engineering for slopes and excavations*. Proceedings 1976, ASCE, Geotechnical Engineering. Specialty conference, Boulder, Colorado
- Chowdhury RN, Bertoldi C (1977) Residual shear tests on soil from two natural slopes. *Aust Geomechanics J* G7:1–9
- Cioaca A (1996) Evaluarea vulnerabilităţii terenurilor afectate de procese geomorfologice actuale, *AUŞMS-Geogr.- Geol.*, V, 1997

- Cioaca A, Balteanu D, Dinu M (1996) Studiul unor cazuri de risc geomorfologic în Carpații de la Curbură, SCGGG - Geogr., XL
- Cruden DM, Varnes DJ (1996) Landslide types and processes, Chapter 3. In: Turner AK, Schuster RL (eds) Landslides-investigation and mitigation, Transportation research board special report 247. National Research Council, Washington, DC, pp 36–75
- Greco F (1999) Potential land uses in the Prahova Subcarpathian area. In: Geography within the context of contemporary development, Cluj University Press, Cluj Napoca, 6–7 June 1997
- Greco F (2002) Risk-prone lands in hilly regions: mapping stages, applied geomorphology: theory and practice. Wiley, London
- Highland LM, Bobrowsky PT (2008) The landslide handbook – a guide to understanding landslides. USGS Circular 1325, 129 p
- Parichi M, Armaș I, Vartolomei F (2006) Evaluari pedologice și morfodinamice pe valea Prahovei subcarpatice. An Spiru Haret 9:103–111
- Stroia F, Armaș I, Damian R (2005) Earth sliding recently revival in Breaza area on Prahova valley. In: Proceedings of international symposium on latest natural disasters-new challenges for engineering geology, geotechnics and civil protection. Organized by Bulgarian National Group of IAEG, Abstract Book, p 93, printed on CD section 20-6-p, Sofia
- Terzaghi K (1950) Mechanism of landslides. In: Paige S (ed) Application of geology to engineering practice. Geol Soc Am 83–123
- Thomson S, Turk T (1997) Introduction to Physical Geology, Landslides and related phenomena, chapter 5, pp 11–126
- Turner AK, Schuster RL (1996) Landslides: investigation and mitigation. Transport Research Board Special Report 247. National Academy of Sciences, Washington, DC, pp 36–75
- Varnes DJ (1978) Slope movements: types and processes. In: Schuster RL, Krizek RJ (eds) Landslides analysis and control, Transportation research board special report 176. National Research Council, Washington, DC, pp 11–33
- Varnes DJ (1984) Landslides hazard zonation: a review of principles and practice. UNESCO, Paris



Two Integrated Models Simulating Dynamic Process of Landslide Using GIS

Chunxiang Wang, Hideaki Marui, Gen Furuya, and Naoki Watanabe

Abstract

Two major movement modes of slope failures: landslides and debris-flows are simulated by two integrated models using GIS to represent the dynamic process across 3D terrains. Landslides occur when earth material moves downhill after failing along a shear zone. Debris flows can be differentiated from landslides by the pervasive, fluid-like deformation of the mobilized material. The formation of debris flows most often occurs as a result of a landslide partially or completely mobilizing into a debris flow. GIS-based revised Hovland's 3D limit equilibrium model is used to simulate the movement and stoppage of a landslide. The 3D factor of safety will be calculated step by step during the sliding process simulation. Stoppage is defined by the factor of safety much greater than one and the velocity equal zero. GIS-based depth-averaged 2D numerical model is used to predict the runout distance and inundated area of a debris flow. The simulation displays the propagation and deposition and deposition of a debris flow across the complex topography. The two GIS-based integrated models are able to provide effective tools for hazard mapping and risk assessment.

Keywords

Landslide • Debris flow • 3D limit equilibrium model • Depth-averaged • GIS • Simulation

Introduction

Slope failures are a wide variety of processes that result in the downward and outward movement of slope-forming materials. The materials may move by sliding, flowing, falling, toppling, or spreading. The various types of slope failures can be differentiated by the kinds of material involved and the mode of movement. A necessary requirement of a quantitative hazard assessment concerned with mobile landslides, is to predict the character and extent of their motion.

In this paper, two common types of slope failures: landslides and debris-flows are simulated by two integrated

models using GIS to represent the dynamic process across three dimensional steep and irregular terrains. Landslides occur when earth material moves downhill after failing along a shear zone. Debris flows can be differentiated from landslides by the pervasive, fluid-like deformation of the mobilized material. The formation of debris flows most often occurs as a result of a landslide partially or completely mobilizing into a debris flow. GIS-based revised Hovland's 3D limit equilibrium model is used to simulate the movement and stoppage of a landslide. In this research, sliding is defined by a slip surface which cuts through the slope, causing the mass of earth to move above it. The factor of safety will be calculated step by step during the sliding process simulation. Stoppage is defined by the factor of safety much greater than one and the velocity equal zero. GIS-based depth-averaged 2D numerical model is used to predict the runout distance and inundated area of a debris flow. As raster grid networks of digital elevation model in GIS can be used as the finite difference mesh, the continuity

C. Wang (✉) • H. Marui • G. Furuya • N. Watanabe
Research Institute for Natural Hazards and Disaster Recovery, Niigata University, Nishi-ku, Ikarashi ni-no-cho 8050, Niigata City 950-2181, Japan
e-mail: chunxiangwang@hotmail.com

and momentum equations are solved numerically using the finite difference method. The simulation displays the propagation and deposition and deposition of a debris flow across the complex topography. The two GIS-based integrated models are able to provide effective tools for hazard mapping and risk assessment.

3D LEM-Based Sliding Process Simulation Using GIS

LEM-Based Sliding Model

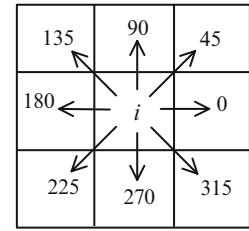
All slope failures have a 3D geometry, which varies in space even along a short distance. For a 3D slope problem, the stability analysis relates to the complicated spatial topographical distribution, strata, shear strength, and/or pore-water pressure conditions. The column-based limit equilibrium methods have been widely used for developing a 3D model of slope stability analysis (Hovland 1977; Hungr 1987; Hungr et al. 1989). GIS represents an ease way and a common platform to manage all of the complicated slope-related information. For a genuine slope failure mass, using the functions of GIS spatial analysis, all input data (such as elevation, inclination, slope, groundwater, strata and slip surface) involved in the 3D safety factor calculation can be available for each grid raster cell, while all slope-related data are in the grid-based form. By inputting these grid data into a deterministic model of slope stability, a value for the safety factor can be calculated. Actually, the 3D grid column, corresponding to each grid cell, is used to represent all the strata data, ground surface and slip surface. GIS-based computational implementation of spatial 3D slope stability analysis has been developed by Xie et al. (2006), in which Hovland's column-based model, 3D extension of the Bishop's model, 3D extension of the Janbu's model and revised Hovland's column-based model have been presented.

In this paper, the revised Hovland's column-based model is used to simulate the sliding process when slope fails. The 3D safety factor can be expressed as (1):

$$SF_{3d} = \frac{\sum_j \sum_i (cA + (h_{ji}\gamma \cos \theta_{ji} - w_{ji}) \tan \phi) \cos \theta_{avr}}{\sum_j \sum_i h_{ji}\gamma \sin \theta_{avr} \cos \theta_{avr}} \quad (1)$$

Where, c is the cohesion, ϕ is the friction angle, γ is the unit weight, w_{ji} is the pore water pressure on the slip surface,

Fig. 1 Possible sliding directions in a cell



and j, i is the number of the row and column of the grid in the range of slope failure. For one grid column, h_{ji} is the height of the sliding body, A is the area of the slip surface, θ_{ji} is the normal angle of slip surface. θ_{avr} is the apparent dip of main inclination direction of landslide.

If 3D safety factor of a landslide is smaller than 1.0, the landslide may be dangerous in the future. Therefore, it is important to evaluate the landslide hazard and to predict the landslide travel distance. When the slope fails, based on the revised Hovland's column-based slope stability analysis model, the sliding process simulation was done by sliding step by step until the 3D factor of safety was larger than 1.0. In a raster-based digital elevation model (DEM) analysis, each cell has eight possible flow directions (left, right, up, down, plus the four diagonals), as show in Fig. 1. The flow direction of a cell is expressed in degrees: left = 0° , up = 90° , right = 180° , down = 270° ; and the diagonals: 45° , 135° , 225° , 315° .

Sliding Simulation of Maoping Landslide

Maoping landslide represents a past slope failure sliding mass located in Qiangjiang Geheyan Hydropower reservoir in China (Fig. 2a). The possible sliding mass was the subject of a detailed investigation through site surveying and its range is illustrated in Fig. 2b. The 3D geological geometry and slip surface are summarized in terms of eight geological engineering sections, of which the plan distribution is also illustrated in Fig. 2b.

The range of sliding mass is represented as a polygon dataset (Fig. 2b), with the digital elevation model dataset of ground surface converted from computer aided design data of scale 1/2,500 and the 3D distribution of slip surface integrated through eight geological engineering sections.

The geomechanical parameters of the upper zones over the slip surface are that the effective cohesion c , the effective frictional angle ϕ , and the unit weight γ are 40 kN/m^2 , 15° ,

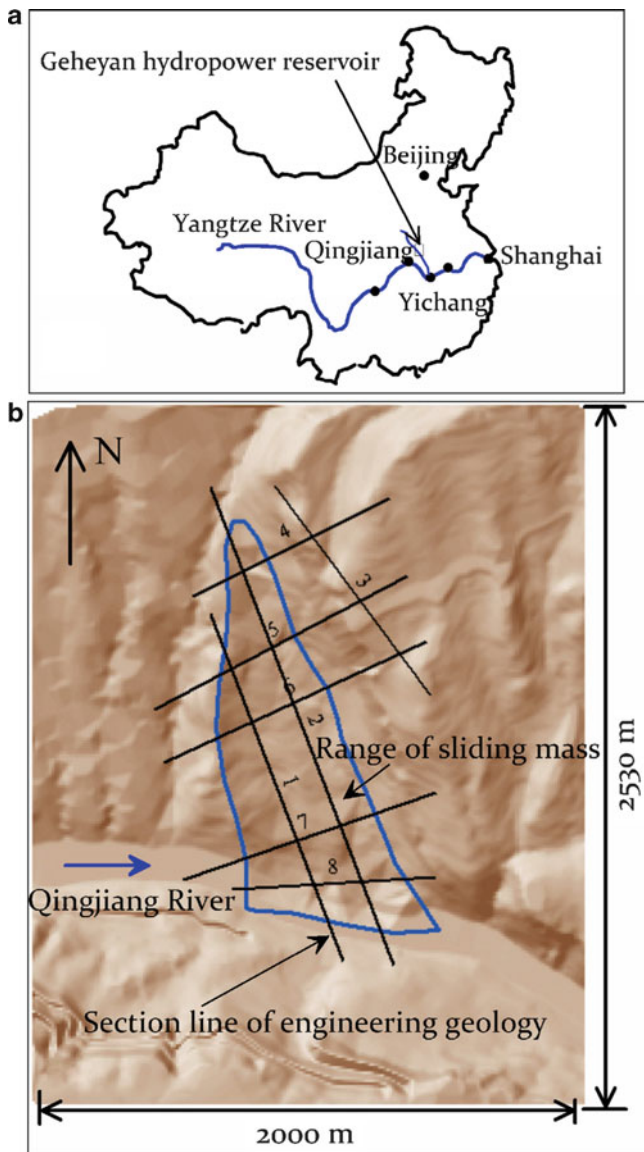


Fig. 2 Maoping landslide: (a) location in China (b) plan schematic

22 kN/m³, respectively. In the sliding simulation, the friction angle of the slip surface is assumed to be unchanged, but the slip surface is assumed to be non-cohesion (cohesion = 0) except in the initial 3D slope safety factor calculating process. The initial 3D slope safety factor is 0.85, after 16 steps sliding (one step = one raster cell size), its 3D factor of safety is 1.02 and the landslide mass becomes

stable. Figure 3 shows the dynamic sliding process and the 3D factor of safety in each step.

2D Depth-Averaged-Model-Based Flowing Simulation Using GIS

2D Depth-Averaged Governing Equations

Debris slides may become extremely rapid debris flows as the displaced masses lose cohesion, gains water and encounters steeper slopes. This type of failure is the most dangerous and destructive of all types of slope failures. Many researchers have developed rheological models for debris flows. These models can be classified as: Newtonian model (Johnson 1970, Trunk et al. 1986, Hunt 1994), Bingham model (Huang and Garcia 1997, Pastor et al. 2004), Herschel-Bulkley model (Laigle and Coussot 1997), generalized viscoplastic model (Chen 1988), dilatant fluid model (Takahashi 1991), and a Coulomb mixture model (Iverson and Denlinger 2001). McDougall and Hungr (2005) developed a depth-averaged model for the simulation of rapid landslide motion across complex 3D terrain. Pudasaini and Hutter (2003) presented a two-dimensional depth-integrated theory for the gravity-driven free-surface flow of a granular avalanche over an arbitrarily but gently curved and twisted topography which is an important extension of the original Savage and Hutter (1989) theory. No single rheological model appears to be valid for all debris flows and debris avalanches.

In this paper, the 2D depth-averaged constitutive equations include the continuity equation paper should start with the title section which has a special single-column formatting (see top of first page).

$$\frac{\partial h}{\partial t} + \frac{\partial M}{\partial x} + \frac{\partial N}{\partial y} = 0 \quad (2)$$

and the 2D equations of motion

$$\begin{aligned} & \frac{\partial M}{\partial t} + \alpha \frac{\partial(MU)}{\partial x} + \alpha \frac{\partial(MV)}{\partial y} = \\ & - \frac{\partial H}{\partial x} gh + v\beta \left(\frac{\partial^2 M}{\partial x^2} + \frac{\partial^2 M}{\partial y^2} \right) - gh \cos \theta_x \tan \zeta \end{aligned} \quad (3)$$

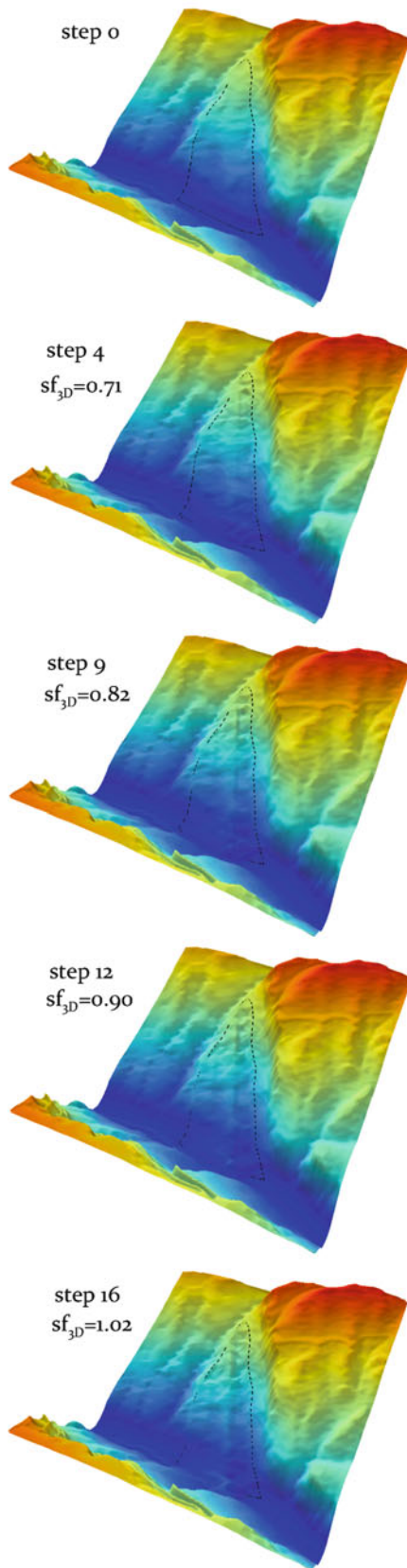


Fig. 3 The dynamic sliding process

240	235	230	240	245
237	232	225	235	240
230	228	220	230	235
228	226	210	220	228
220	218	205	212	215

Fig. 4 Flow direction

$$\frac{\partial N}{\partial t} + \alpha \frac{\partial(NU)}{\partial x} + \alpha \frac{\partial(NV)}{\partial y} = -\frac{\partial H}{\partial y} gh + v\beta \left(\frac{\partial^2 N}{\partial x^2} + \frac{\partial^2 N}{\partial y^2} \right) - gh \cos \theta_y \tan \zeta \quad (4)$$

where $M = Uh$ and $N = Vh$ are the x and y components of the flow flux; U and V are the x and y components of the depth-averaged velocity; H is the height of the free surface; h is the flow depth; θ_x and θ_y are the angle of inclination at the bed along the x and y directions respectively; α and β are the momentum correction factors; $v = \mu/\rho_d$ is kinematic viscosity, ρ_d is the equivalent density of the debris mixture, and $\rho_d = \rho_s v_s + \rho_w v_w$, ρ_s and ρ_w are the densities of solid grains and water, v_s and v_w are the volumetric concentrations of solids particles and water in the mixture; and $\tan \zeta$ is the dynamic friction coefficient.

Numerical Scheme

Numerical models are organized on a grid cell basis. Within a cell overland flow is routed along one flow direction. The flow direction is the maximum downslope direction which is determined from the raster-based DEM (Fig. 4). The numerical solution is achieved using a finite difference formulation based on the DEM grid. The governing equations are approximated using leapfrog time-differencing. A staggered grid approach is followed to evaluate the spatial gradients of (2), (3), and (4). A forward difference scheme is applied to discretize the linear terms, and a central difference scheme is applied to discretize the nonlinear terms. The method of adjusting the time step and mesh size is used to prevent the appearance of numerical instability due to the use of too large a time interval and mesh size.

The model outlined above has been coded into a numerical model of general utility in ArcGIS. The code is written in Visual Basic language and ArcObjects. ArcObjects is the development environment of the desktop ArcGIS applications (ArcMap, ArcCatalog & ArcScene). It is used to customize



Fig. 5 Aerial photograph of the disaster

and extend ArcGIS using Visual Basic. All the input and output data are processed in ArcGIS.

Flowing Simulation of Minamata-Hougawachi Debris Flow

On July 19–20, 2003, a short duration, high intensity rainfall impacted Minamata City, Kumamoto prefecture, Japan. This rainstorm triggered many landslides and debris flows (Nakazawa et al. 2003; Iwao 2003; Taniguchi 2003). The slope failure and resultant debris flow at Hougawachi in Minamata was the largest and most damaging (Fig. 5). The debris flow occurred 4.3 hours after the beginning of the rainstorm, at 4:20 a.m. on July 20, 2003, during the period of highest intensity. A moderately-sized landslide triggered the debris flow about 1.5 km upslope of where the casualties occurred. The maximum depth of the landslide is 9 m. The volume of sediment discharge plunging into the village of Hougawachi-Atsumari district, Minamata City, was estimated to be $68,000 \text{ m}^3$, and the velocity of debris flow was estimated to range from 2.9 to 23.5 m/s (Taniguchi

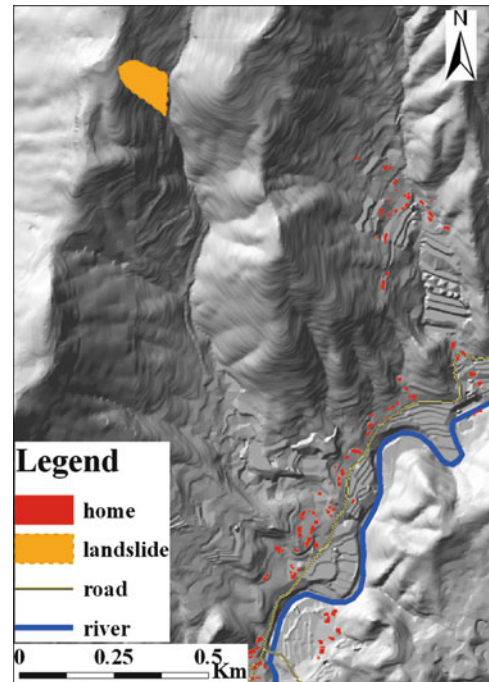


Fig. 6 3D view of the study area with houses and roads

Table 1 Material properties and parameters for simulation

ρ (kg/m^3)	α	β	μ (Pa·s)	g (m/s^2)	$\tan \varphi$
2,200	1.25	1.0	0.11	9.8	0.6

2003). The disaster killed 15 people, and more than 14 houses were either damaged or destroyed.

Based on a 1:2,500 scale topographic map a vector contour line file is generated, with vertical spacing of 2 m. This file is converted to a Triangulated Irregular Network (TIN) and subsequent DEM. The roads and streams are drawn as polylines, and the homes as polygons (Fig. 6).

In the simulation, as the square grid mesh is $\Delta x = \Delta y = 2 \text{ m}$ and the depth-averaged velocities are considered as blunt, therefore, we have set $\alpha = 1$, $\beta = 1$. Before running the simulation, based on field investigation, the inundated area is 0.15 km^2 and the average thickness of deposits is assumed to be 3.5 m. Using these data and through iterative calculations, the best-fit pair of $\tan \zeta = 0.4$ and $\mu = 0.11$ are selected (Table 1).

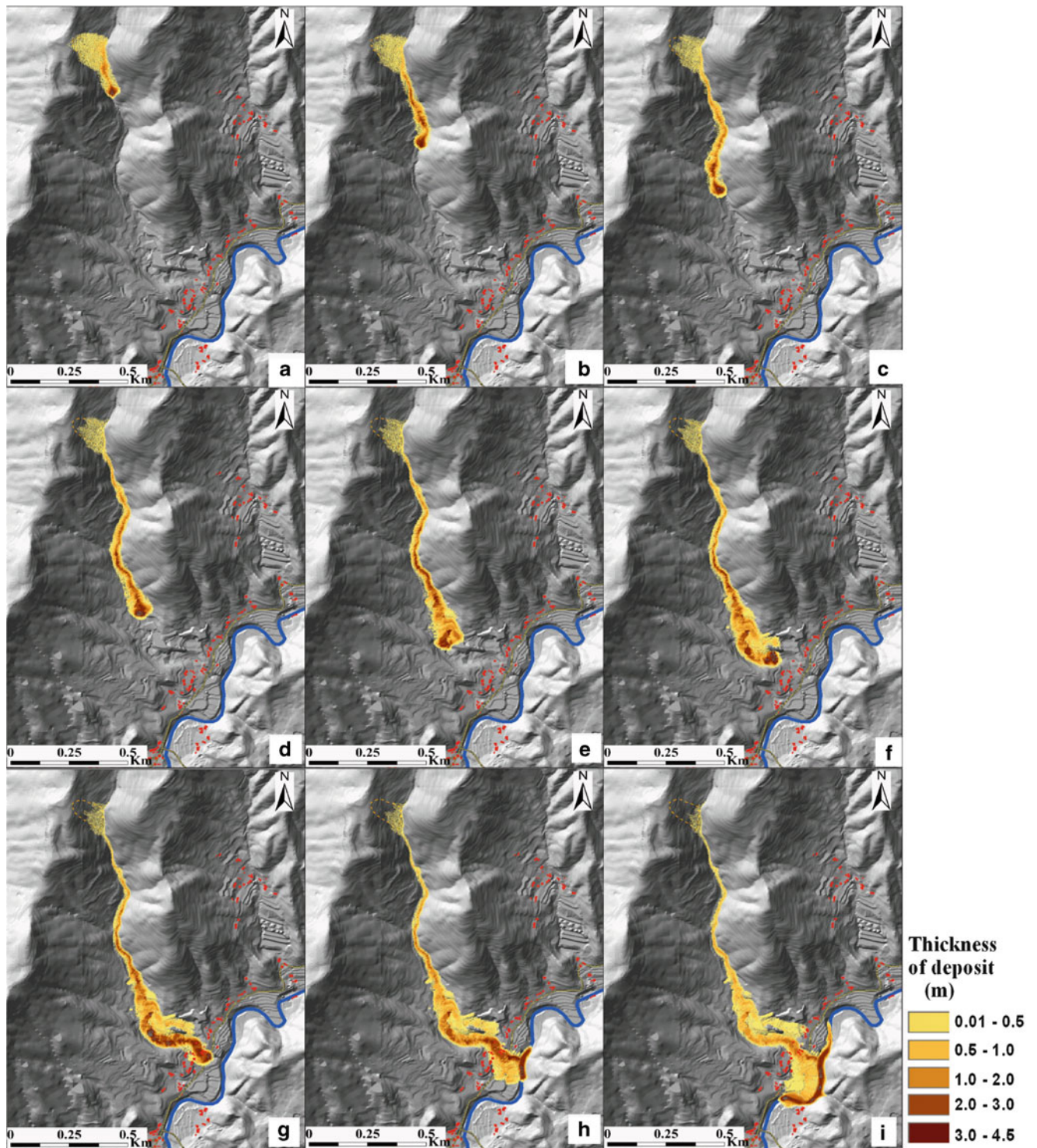


Fig. 7 Debris flow developing and affected regions at different times ((a) 30s; (b) 50s; (c) 90s; (d) 110 s; (e) 150 s; (f) 170 s; (g) 190 s; (h) 210 s; (i) 230 s)

A time-lapse simulation of the dynamic progression and deposition of the debris flow over 3-D terrain is illustrated in Fig. 7. The simulation results show that it took about 170 s for the debris flow to travel 1,500 m along the channel, and the average flow velocity was 8.8 m/s. The affected region can be displayed dynamically at different times. The simulation result is in good agreement with field observation. There are 15 homes inundated in the simulation, which agrees with field observations. This means that the numerical approach proposed here can be used to simulate the debris flows triggered by landslides and rainstorms in the study area.

Conclusions

Combing the GIS grid-based raster data, two main categories of methods have been used for assessing the mobility of landslide debris: a single body model and a continuum model. The single body model idealises the motion of a debris-slide as a single whole-body and have a limitation in being unable to account for internal deformation. The GIS-based revised Hovland's 3D limit equilibrium model is used to simulate the movement and stoppage of the single whole-body landslide named Maoping landslide located in Geheyang Hydropower reservoir, China. The continuum model is more reliable and is associated with distinct rheological formulations. The 2D depth-averaged equations as a continuum model using GIS is a useful tool for simulating the dynamic flowing of debris flow. A debris flow mobilization from rainfall induced landslide occurred in Minamata-Hougawachi, Japan was simulated. This simulation displays the propagation and deposition across the complex topography.

The prediction of the characters of landslides and debris flows, such as the travel distance, the possible propagation extent of the moving debris mass, the velocity of the mass, and the area of deposition is of great importance in landslide risk assessment. The GIS-based integrated models are able to provide an effective tool for risk analysis and hazard mapping. The reliable results, simplified scenario studies and the convenience of data processing will help increase the acceptance of hazard

maps and improve ways for dealing with the risk of landslides.

References

- Chen C (1988) Generalized viscoplastic modeling of debris flow. *J Hydraul Eng* 114(3):237–258
- Hovland HJ (1977) Three-dimensional slope stability analysis method. *J Geotech Eng. Division Proceedings of the American Society of Civil Engineers*. 103(GT9):971–986
- Huang X, Garcia MH (1997) A perturbation solution for Bingham-plastic mudflows. *J Hydraul Eng* 123(11):986–994
- Hungri O (1987) An extension of Bishop's simplified method of slope stability analysis to three dimensions. *Geotechnique* 37(1):113–117
- Hungri O, Salgado FM, Byrne PM (1989) Evaluation of a three-dimensional method of slope stability analysis. *Can Geotech J* 26:679–686
- Hunt B (1994) Newtonian fluid Mechanics treatment of debris flows and avalanches. *J Hydraul Eng* 120:1350–1363
- Iverson RM, Denlinger RP (2001) Flow of variably fluidized granular masses across three-dimensional terrain 1. Coulomb mixture theory. *J Geophys Res* 106:537–552
- Iwao Y (2003) Slope hazard induced by heavy rain in 2003, Minamata city, Kumamoto (in Japanese). *J Jpn Landslide Soc* 40:239–240
- Johnson AM (1970) *Physical processes in geology*. Freeman, San Francisco
- Laigle D, Coussot P (1997) Numerical modeling of mudflows. *J Hydraul Eng* 123:617–623
- McDougall S, Hungri O (2005) Dynamic modelling of entrainment in rapid landslides. *Can Geotech J* 42(5):1437–1448
- Nakazawa T, Saito M, Taguchi Y (2003) Geologic and hydrologic background of slope failure and debris-flow disaster in Atsumari River Basin, Minamata City, Kumamoto Prefecture on July 20, 2003. *Bull Geol Surv Jpn* 55:113–127, in Japanese
- Pastor M, Quecedo M, Gonzalez E, Herreros MI, Fernandez Merodo JA, Mira P (2004) Simple approximation to bottom friction for Bingham fluid depth integrated models. *J Hydraul Eng* 130(2):149–155
- Pudasaini SP, Hutter K (2003) Rapid shear flows of dry granular masses down curved and twisted channels. *J Fluid Mech* 495:193–208
- Savage SB, Hutter K (1989) The motion of a finite mass of granular material down a rough incline. *J Fluid Mech* 199:177–215
- Takahashi T (1991) *Debris flow*. A. A. Balkema, Brookfield
- Taniguchi Y (2003) Debris disaster caused by local heavy rain in Kyushu area on July 20th, 2003 (prompt report), Minamata debris disaster. *J Jpn Soc Eros Control Eng* 56:31–35, in Japanese
- Trunk FJ, Dent JD, Lang TE (1986) Computer modeling of large rock slides. *J Geotech Eng* 112(3):348–360
- Xie M, Esaki T, Qiu C, Wang C (2006) Geographical information system-based computational implementation and application of spatial three-dimensional slope stability analysis. *Comput Geotech* 33(4–5):260–274



Using the Information System and Multi-Criteria Analysis in the Geological Risk Management in São Paulo

Eliene Coelho and Luciana Pascarelli

Abstract

Since 1980s the surveys space could not definitely follow the growth and the density of favelas, and some communities started to trigger the first records of accidents in areas hitherto stable. The mapping made in 2010 is today the largest geological-risk database in the country. Today, all these information are included in the “Habisp”. Habisp is a mapping system of precarious settlements in the city of Sao Paulo, which contains valuable information to face the urban poverty. Poverty which is materialized in Sao Paulo in many ways of informal settlements: slums, irregular settlements, tenement housing, temporary housing and degraded sets. The Habisp stores, organizes, processes and produces high quality geographic information, which serves as support for the technicians of the Housing department in making decisions. The results have been making possible reassessment and adjustment of the low-income intervention projects by the government, prioritizing housing, social-educational infrastructure, and basic-sanitation actions in areas of greatest susceptibility.

Keywords

Mapping • Susceptibility • Geographic information • Priority

The Risk of Landslides in Large Urban Centers

Mass movement processes are natural and a part of the cycle/depositional erosion responsible for determining the scenery of the Earth’s surface. Nevertheless, when as the result of a geological process there is an impact on human beings or their property, what comes to light is the concept of a geological accident, implying that besides the physical process some causes of instability also lead to the consequences observed. The first tales of accidents of this sort in the city of São Paulo relate to urban expansion. More fragile areas, such as slopes and river banks began to

be occupied without the appropriate planning, and the growing number of people affected by the landslides revealed that there was a considerable part and parcel of the population living in risky settlements.

In the city of São Paulo, the first tales of accidents of this nature are directly linked to the urban expansion recorded since the beginning of the 1930s. According to Nogueira (2002), the urban spot in the city grew from 355 to 1.370 km² in approximately five decades. Due to the method adopted by real estate speculation when it came to dividing the land in the city, “urban vacuums” were generated and subsequently occupied by shanty towns and irregular land occupation. Areas of greater environmental fragility, such as slopes and banks of streams also began to be occupied, above all at the end of the 1970s. At the end of the 1980s, there exists a record of the first accidents on slopes and in the mid 1990s, these become ever more frequent and less localized, revealing that a considerable part of the population occupies these areas of risk (Brasil 2007).

E. Coelho (✉)
PMSP, São Paulo City Hall, Habisp, Sao Paulo, Brazil
e-mail: eliene.coe@gmail.com

L. Pascarelli
Consultancy Services and Technical Works Department, Sao Paulo
City Hall, 425, Rua Libero Badaro, Brazil

Table 1 Criteria to rank the degree of risk (simplified from the IPT – 2006)

Degree of probability	Description
R1	Slopes with little inclination (<17°), natural and on stable soils with low probability of having landslides. Absence of indices of instability. This is the least critical condition
R2	Slopes with slight inclination with a medium probability of having a landslide. There is evidence already of incipient instability. If the existing conditions are maintained, there is a slight probability that there will be destructive episodes occurring during intense rainfall
R3	Inclined slopes (>30°) point towards a high potential for developing landslide processes. There is a large amount of evidence regarding instability (cracks on the soils, levels of subsidence of the soil, etc.)
R4	Evidence of instability is expressive (quantity and magnitude). This is the most critical condition. Under such conditions, it is highly probable that there will be destructive events during intense episodes of rainfall

Mapping the Risk Areas in the City of São Paulo

At the end of the 1990s, geotechnical companies carried out an analysis of the risk on the slopes of 240 shanty towns, identifying about 60 % of the situations at risk for landslides. Although such information has been used for the planning and execution of local interventions, activities to control and prevent such risks per se have been negligible for about a decade (1993 to 2001), whilst at the same time the occupation of the hills grew significantly. Cartographic registries and those of occurrences were also rare, making it impossible to carry out any sort of planning with the necessary efficacy.

In 2010, the City Hall of São Paulo, along with the Institute for Technological Research (IPT) came to the conclusion of the need for “Analysis and risk mapping associated to landslides in the areas of slopes and the banks of rivers and streams in shanty towns in the São Paulo municipality” IPT/SMSM (2010). More than a geotechnical survey, the mapping geared its focus on the areas of precarious occupation, where the population’s vulnerability was the steepest. In such sites, any type of event, even the minor ones could entail significant damage for the community, vis-a-vis their low perception of risk and the inability to set forth a speedy response and recovery.

The risk estimates were analyzed quantitatively, based on field observations, integrating the analysis parameters contained on a risk card, with the support of aerial images.

The 407 areas investigated were subdivided into risk sectors, due to the fact that the characteristics of the land and above all of the occupations posed enormous variations within a single shanty town. For each of the sectors, what was evaluated was (1) natural parameters referring to the type of soil topography, natural structures that conditioned land movements, typology of water courses and type and breadth of vegetation and (2) occupational parameters such as the level of interference in the land, the presence of basic infrastructure to supply water, garbage collection and sewage treatment, the condition of public roads and structure of the homes themselves. Additionally to the signs of

instability observed, the parameters assessed ended up in the creation of 1.179 risk sectors, with specific levels of criticality according to Table 1.

More than a geotechnical survey, this broader mapping already carried out in Brazil focused exclusively on settlement areas where the population’s social vulnerability was high. In these sites, any type of event, albeit the smallest ones could cause significant damage to the community, given their low perception of risk and limited ability to respond to the event and recover from it.

In real time, the data collected on the field, which included the perimeters of the areas analyzed, was entered into the Habisp system used the São Paulo City Hall since 2006.

The Habisp System

Habisp is an information system that works through the web, with the ability to store and process alphanumeric and geographic information. The focus is popular housing and the “loci” are the shanty towns, irregular land settlements, tenements or slums and housing enterprises conceived for the population that lives in those areas.

To understand how it operates, it is necessary to explore some conceptual issues regarding the importance of Information and Communication Technology (ICT) in our present day society. It is also necessary to refer to the issue of making decisions, the construction of indicators and their content, objectives and the dynamism relating to the problem of which it is a part: popular housing.

Habisp arose from an initiative to draw up a strategic plan for social housing, within the realm of the project with Alliance with Cities, and throughout the studies, it turned into a proposal to draft a Municipal Housing Plan (MHP) (Prefeitura do Município de São Paulo. Plano Municipal de Habitação PMH 2009–2024). Without the Habisp and the System of Priorities, both planning instruments, the MHP would not have attained its present day level of sophistication and detail. The proposal encompasses goals and objectives to service housing needs until the year 2024,



Fig. 1 Picture of the first page on the Habisp System (Source: (Prefeitura do Município de São Paulo. Plano Municipal de Habitação PMH 2009–2024))

including the cost for urbanization interventions and land ownership regularizing and the construction of new housing units, settlement per settlement (consult the Municipal Housing Plan: document for debate (Prefeitura do Município de São Paulo. Plano Municipal de Habitação PMH 2009–2024), Fig. 1).

Data, information, indicators, knowledge generation, decision making, geographic spaces, popular housing, regularization of land ownership, spatial analysis, maps, registries and population surveys are some of the issues that Habisp relates to. To classify it into a single system modality is not an easy task, these subdivide into categories, in accordance to the activity they support, but Habisp does not fit into a single category, and can be deemed to be a system for managerial information; a transactional processing system or a decision making support tool (BIDGOLI 1989, apud BARBOSA 2003).

As part of this classification set forth by Bidgoli (1989, apud BARBOSA 2003), we can state that Habisp is mostly a management information system, that can be used for planning, control and decision making purposes; condensing or summarizing the information obtained from the transactional data processing systems, with routine and exception reports. The parcel of transactional processing systems in Habisp refers to the housing services part supported by this same system (payment of benefits and issuing land ownership regularization deeds for public areas). Nonetheless, one of its most relevant components, the system to prioritize interventions, brings it closer or even qualifies it as a system that supports the decision making process, although this category so far does not have a broadly accepted definition.



Fig. 2 Picture of the Jaguaré Slum (Archives of the Municipal Housing Secretariat – Sehab. City Hall of the São Paulo Municipality)

The Housing Problem in the Large Urban Centers

Housing, in a very broad sense, is frequently deemed to be key for the problem of poverty; a shanty town or slum is the environment of a poor man according to the operational definition officially adopted at a UN meeting in Nairobi, 2002. It is characterized by an excess of population, precarious or informal housing, inadequate access to drinking water and sanitary conditions and insecurity as part of the ownership of this house.

Throughout the third world, the choice of housing is a complicated calculation of ambiguous considerations. Like the famous phrase of the anarchist architect John Turner. “Housing is a verb”. The urban poor need to resolve a complex equation upon attempting to optimize the cost of housing, guarantee ownership, the quality of the shelter, distance from work and oftentimes their own safety. And for all, the worst situation is a poor and expensive area lacking in public services and without the warranty of ownership (DAVIS 2006, p. 39).

In São Paulo, occupation in precarious settlements – slums, irregular land plots or tenements – has been a part of the urban scenery for quite some time (Fig. 2). The largest city in Latin America has one of the most complex housing problems in the country; and for decades, facing up to this problem has posed a huge challenge for those in government. Concern with the poor, urban poverty and popular housing mixes old and new ideas during each period of history, and successive generations of reformists have struggled for the elimination of slums. The difficulties, in the field of housing management, land market and funding for housing for the low income population become aggravated day after day, thanks to the economic and social problems that exclude the less specialized population from labor markets, evermore demanding and that offer – when they offer – informal employment with an extremely low compensation;

Table 2 Basic objectives of the phases proposed by the characterization, classification, eligibility and prioritization system. Own draft (Coelho and Pérez Machado 2009)

Characterization	Classification	Eligibility	Prioritization
Characterize the precarious settlements in the municipality of São Paulo	Classify these areas into groups that will guide the type of intervention that is needed	Select the areas that will undergo intervention, already establishing at this phase a cut-off for the actions	Prioritize the activities in those areas that fulfil the eligibility criteria

consequently, this means scant opportunities to have access to the formal funding initiatives and their own housing.

Furthermore, the real estate market in São Paulo has attained surreal levels of appreciation. The steep prices are mainly due to the scarcity of supply or land at compatible prices and locations. For those who are poor in São Paulo (families generally with incomes falling below three minimum wages), there are few opportunities, and those that exist at present arise precisely in precarious housing.

What can be observed as a result of this informality, is the greater occupation of areas that are subject to environmental restrictions, areas of risk with steep slopes or subject to flooding, contaminated soils, areas close to sanitary landfills or garbage deposits, among others, besides the concentration of a large number of social problems, especially those linked to unsanitary conditions resulting from the absence of basic infrastructure, aggravated vis-à-vis the vulnerability of its inhabitants, caused by factors relating to informal employment, school abandonment or drop outs, early pregnancy, domestic violence and drug trafficking.

If, for the low income population, there are few alternatives and choosing becomes truly difficult, for public management, this problem is further aggravated, making intervention policies ever more complex. To have an anchor for public policies, what is needed, in the first place, is detailed knowledge of which are the problems that will be faced, in the quest to qualify and quantify the true needs. What does it mean to understand each of these low-income occupations in their totality, but also in terms of their specificities, evaluate the resources that are necessary to invest in each of the housing projects or programs, so as to select those which will make it possible to optimize public investment and attain the greater number of people possible among the destitute population.

For the Sehab, the intervention strategies were clear, since work began to draft the MHP: urbanization and regularization of shanty towns and irregular land plots occupied by low-income populations. However there existed the need to particularize that extensive universe of settlements, to know where to truly begin each of the actions: that is to say, which slums to urbanize in the coming years? In the coming month? With resources available at present? Because of this it was necessary to have surveys and more concrete data, besides using analytical instruments with the ability to offer more precise answers on where and how this housing precariousness manifests itself. The geographical aspect of the problem

benefitted from the use of spatial analytical instruments of proven efficacy, and it became necessary to build a model that could guide decision making, based on the existing data.

The path chosen was to set forth indicators that could be evaluated individually and offer immediate responses, such as: degree of urbanization of a settlement, the population's vulnerability, geological conditions etc., and that could be combined into a single index. Through this procedure, the intention was to attain a goal to set up a decision making model that would take into account the large diversity of variables that existed in the context, and mainly the multiple objectives that had to be reached. Four stages were created to define the priority to service a specific settlement through a specific housing program: characterization, classification, eligibility and prioritization, each with its own objective, as can be observed in Table 2.

The first and foremost stage in the system is that of characterization, as the results found in future stages will be ramifications of the information collected herein. Subsequently the work of updating the data began, as well as the conceptual definition of the types of settlements that would be serviced by the housing policy, described in Table 3 below.

The principle adopted was simple: according to the objective of the action, the SEHAB defined the focus of prioritization. For urbanization projects, the focus of the action was the most precarious areas in all of the issues analyzed. However, for the regularization of shanty towns, as in principle the program cannot regularize precarious situations, the focus shifted to acting upon areas with the best indices (COELHO and PÉREZ MACHADO 2009).

The report "Characterization, Classification, Eligibility and Prioritization System for Interventions in Precarious Settlements in the Municipality of São Paulo/ Brazil (2007)" (Coelho 2007) highlights two principles set forth for the selection of indicators and indices that jointly make up the prioritization index: (1) protection of the population's life and the enhancement of livability conditions to acceptable levels; and (2) protection of the most vulnerable population socially. The same report points out that the first formulations carried out by the Sehab divided the priorities stepwise into three levels: high, medium and low, an approach that proved to be lacking, as the universe of settlements demands a much larger scale, which led to the creation of a "prioritization index", that attributes a score between 0 and 1 to each settlement, being that 0 is the absence of precariousness and 1 maximum precariousness based on a multi-criteria analysis model.

Table 3 Precarious settlements in the city of São Paulo: conceptualization. Own draft (Altered by the City Hall of the Municipality of São Paulo; Alliance of Cities (2008), p 50)

Favelas	Informal occupations, self-built on the fringe of urban legislation, predominantly disorderly and with a highly precarious infrastructure. Occupied by low-income families that are social vulnerable
Irregular settlements	Irregular occupations where the division of land presents a layout that allows for the identification of a plot in comparison to a route of access. These are done mainly on land that is predominantly privately owned and acquired through some sort of marketing and may encompass all of the family income brackets
Tenements	Multi-family collective housing made up of one or more buildings subdivided into several rooms. Sanitary facilities, circulation and precarious infrastructure, and generally overcrowded

The prioritization index is a summarized index that aggregates other indices through a weighted method. Habisp has a logical matrix where the weights are configured to calculate each of the indices that are part of the system, thus allowing the administrator to interact with and validate the process, and also to adapt it to any change in the situations that may have an impact on the decision making process. In Formula (1): (COELHO and PÉREZ MACHADO 2009) we present a mathematical formula to calculate the prioritization index for the urbanization program and for the precarious settlement regularization program.

The indices used arise from several sources or origins. Those of Health and Social Vulnerability were appropriated by the Sehab from other initiatives, which means to say they were not produced exclusively for the prioritization interventions, but serve as a benchmark for sectoral policies in health and social assistance, at the municipal sphere. The Paulista Social Vulnerability Index (PSVI) bases itself on data from the 2000 IBGE Census and the Health Index is based on data from the municipal health system for 2006. The urbanization index is calculated based on the data collected on the field and inserted into Habisp, and updated whenever the field team identifies changes in the situation informed; this falls entirely under Sehab’s responsibility.

$$IP = \frac{[(Y - IF) \times n_f] + (IR \times n_r) + (IV \times n_v) + [(Y - IS) \times n_s]}{(n_f + n_r + n_v + n_s)} \tag{1}$$

Being that:	Being that:
IF = urban infrastructure index	n _f = weight of the urban infrastructure index
IR = index for risks of bank washouts and landslides	n _r = weight of the washout and landslide index
IV = social vulnerability index	n _v = weight of the social vulnerability index
IS = health index	n _s = weight of the health index
Y = priority ordainment factor (of growing order = 1) (if decreasing order = 0)	



Fig. 3 Example of the overlay of the layer with the risk mapping (2010) and the shanty town layer. Santa Madalena Park Slum (Source: www.habisp.inf.br)



Fig. 4 Example of the interface to update data on the risk sectors (2010) (Source: www.habisp.inf.br)

Treatment of the Landslide Risk Index in the Prioritization System

The risk of washouts and landslides is founded on survey carried out by the Foundation for Support to the University of São Paulo (FUSP), through a partnership with the Institute for Technological Research (IPT), under the title of “Mapping the risks associated to washouts and landslides in slope areas and washout of banks in streams in the shanty towns of the municipality of São Paulo, 2003”, in which the Housing Secretariat participated in indicating those areas that should be subject to analysis by the IPT team, along with the technical people (geologists, engineers and

architects) from the sub districts (UNESP/FUSP/IPT 2003/2004).

The Risk Index for the precarious settlements nevertheless was conceived in the context of the prioritization system, and is calculated for each settlement by using overlay operations (Figs. 3 and 4). The Habisp identifies, for each settlement, the percentage of its area (m^2) that lies within each risk area and then, through a calculation formula (2), which attributes a weight to each degree of risk, presenting the risk index for wash outs and landslides for the specific settlement.

Considering that the geological risk is a determinant factor to grant that condition of livability to an area, the use of Habisp as an aid in the new mapping has offered not only the possibility to create a consistent data base on the risks in the city, but has also allowed for the speedy transfer of that knowledge. Nowadays, delimiting the areas surveyed and the main attributes that were part of the evaluation is information that can be accessed by technicians, as well as managers of municipal administration. The location of the risk sectors and the degree of probability that there will be a landslide is also available to universities, research centers, non-government organizations (NGO's) and other stakeholders of this issue, through Habisp.

$$IR = \frac{(P_{rb} \times n_{rb})/100 + (P_{rm} \times n_{rm})/100 + (P_{ra} \times n_{ra})/100 + (P_{rma} \times n_{rma})/100}{n_{rma}} \quad (2)$$

Being that:	Being that:
P_{rb} = % low risk	n_{rb} = weight of low risk
P_{rm} = % medium risk	n_{rm} = weight of medium risk
P_{ra} = % high risk	n_{ra} = weight of high risk
P_{rma} = % very high risk	n_{rma} = weight of very high risk

The result of using HABISP can already be seen in the major of government programs in progress. The main one is the Municipal Housing Plan which can be retrofitted quickly and the interventions, could be reordered according to the risk areas in order to include the elimination of the most serious risks by 2016 (including also the provision of financial resources for such actions). Although the elimination of

risks only in the year 2016 may seem an unpromising scenario, the recognition of this critical situation is optimistic because it drives the municipality in search of more resources and appropriate technical solutions that allow shortening the schedule.

References

- BARBOSA GR (2003) Sistemas de Apoio a Decisão sob o en foque de Profissionais de Tecnologia da Informação e Decisores. Dissertação de Mestrado, PPGEP, UFPE
- Bidgoli H (1989) Decision support systems: principles and practice. West Publishing, St. Paul
- Brasil (2007) Ministério das Cidades/Instituto de Pesquisas Tecnológicas – IPT. Mapeamento de Riscos em Encostas e Margem de Rios. Carvalho CS, Macedo ES, Ogura AT (org). Ministério das Cidades; Instituto de Pesquisas Tecnológicas – IPT, Brasília
- Coelho ECR (2007) Sistema de Caracterização, Classificação Elegibilidade e Priorização de Intervenções em Assentamentos precários no município de São Paulo/ Brasil. Prefeitura do Município de São Paulo. São Paulo, p 181. Disponível em: http://www.habisp.inf.br/theke/documentos/priorizacao/Per_Review_oficial.PDF. Acesso em 20 Jan 2011
- Coelho ECR, Pérez Machado RPO (2009) Sistema de Priorização do Habisp: um estudo de caso. 12 Encontro de geógrafos da América Latina. Montevideo: [s.n.]. p 15. Disponível em: <http://egal2009.easyplanners.info/area>. Acesso em 12 Mar 2011
- Davis M (2006) Planeta Favela. Tradução de Beatriz Medina. Boitempo, São Paulo, 272p. ISBN 85-7559-087-1
- IPT/SMSP (2010) Análise e mapeamento de riscos associados a escorregamentos em áreas de encostas e solapamentos de margens de córregos em favelas do município de São Paulo. Laboratório de Riscos Ambientais (LARA/Cetae/IPT) e Assessoria Técnica de Obras e Serviços (ATOS/SMSP/PMSP)
- Nogueira FR (2002) Gerenciamento de Riscos Ambientais Associados à Escorregamento: Contribuição às Políticas Municipais Para Áreas de Ocupação Subnormal. Rio Claro, São Paulo, 269p. Tese (Doutorado em Geociências) – UNESP
- Prefeitura do Município de São Paulo. Plano Municipal de Habitação PMH 2009–2024: documento para debate público. Disponível em www.habisp.inf.br/doc. Acesso em 06 Jun 2011
- Prefeitura do Município De São Paulo; Cities Alliance (2008) Habitação de interesse social em São Paulo: desafios e novos instrumentos de gestão. Janeiro Projetos Urbanos, São Paulo, 96p
- UNESP/FUSP/IPT (2003/2004) Mapeamento de risco associado a áreas de encosta e margens de córregos nas favelas do Município de São Paulo



Maps of Landslide Areas with Technical G.I.S.: The Use of High Resolution DTM

Mauro Palombella

Abstract

This work describes an organizing of landslides data and proposes to develop research in information technology with the aim to improve the analysis and representation of the landslides areas.

Geological Information System (GIS) techniques were used in a 'test area', by a play of transparency on the layer of orthophotos and of hillshade, to underline physiographic aspects of the area and to map the landslides. Moreover, it is shown that the use of high-resolution DTM in the mapping of landslide hazard, improves the visual interpretation to give a useful contribution to the analysis and photo interpretation.

Keywords

G.I.S. • Landslides • DTM • Hillshade

Introduction

This study proposes the structure of a Geological Information System (GIS) aimed at the implementation of the necessary data to obtain a map of "instability".

It was inspired on the basis of the information given by the document published by the National Geological Survey (SGN) in the 'Miscellanea' series (Amanti et al. 1996) and in the CARG project (CARTografia Geologica) started in 1988, with the purpose to realize geological and geothematic sheets, scale 1:50,000, to cover the entire national territory ISPRA: Progetto CARG (2011); and adapted in order to make it compatible with the format of the census produced for the IFFI project (Inventario dei Fenomeni Franosi in Italia) which provides a detailed overview about the distribution of landslide phenomena on the Italian territory (Amanti et al. 2001; ISPRA: Progetto IFFI 2011).

Moreover, it was proposed a method of mapping aimed at delineating the specific morphology of the places. The

study of the cartographic data storage system was quite complex. The aim was to reconcile the extreme complexity of information in a map of instability, in terms of the graph information content, that the need for modeling, standardization and simplification. Aspects needed to allow further analysis and processing and for the eventual creation of a hazard map.

Study Area

The Apennine thrust belt is part of the W. Mediterranean composite orogeny system, which also includes northern Africa (Maghreb), and represents the suture zone of the continent collision between the European plate and the African plate. It has been built up since Burdigalian time and its direction of tectonic transport or vergence is towards the African foreland (Fig. 1).

The Apennine chain has a characteristic arc shape with convexity towards E direction with a vergence rotating from NNE to S. The overall curvature is determined by a discontinuous deformation largely controlled by transverse grabens.

M. Palombella (✉)
Freelance Geologist, Corso Umberto I n°94, 70056 Molfetta, Ba, Italy
e-mail: geologo_palombella@virgilio.it

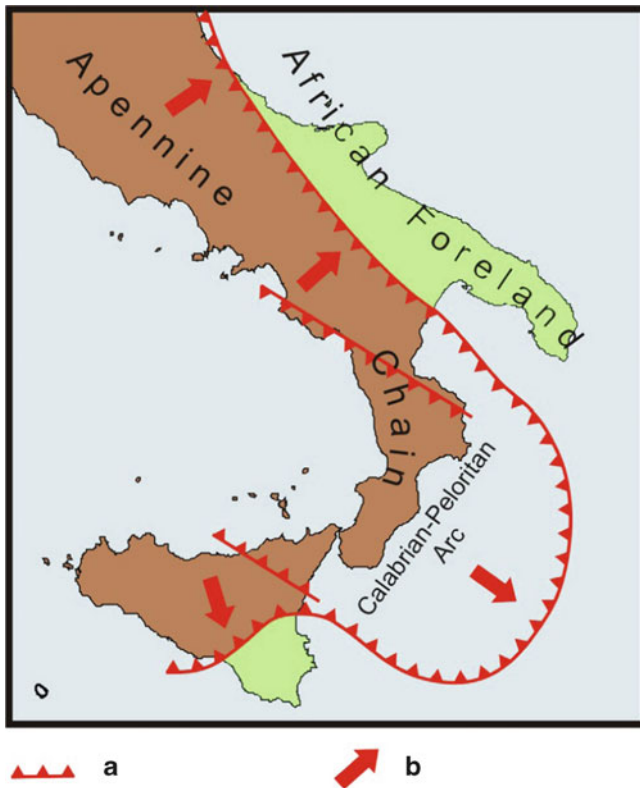


Fig. 1 Schematic structural-geological map of the study area: (a) thrust front; (b) main tectonic stress direction

The present undulations of the Apennine belt are mainly a product of Late Cretaceous to recent deformations, which severely modified the shape of this margin by continental collision and by subsequent development of back-arc features.

Different models have been suggested for the evolution of this area with different shapes of continental margins; the majority infers the impingement of an African promontory, the Adriatic block, into the European continental mass.

The area of study (Fig. 2) is included in the municipality of Alberona, section of “Foglio IGMI at scale 1: 50,000 San Bartolomeo in Galdo” (Pieri et al. 2011).

The spread and extent of landslide areas in the Apennines find their justification in the primary lithology of the outcropping formations but are also determined by the fracturing of the sequences limestone-marly-arenaceous and schistosity of the pelitic sequences; and also to be considered the contribution of the recent uplift of the Apennine chain during the Quaternary.

The technical characteristics of these soils consist of susceptible pelitic sediments to the action of water infiltration makes them particularly susceptible to instability.

On almost all the area there are forms evident of instability of the surface portion of the slope represented by creep, by slow evolving, compatible with agricultural

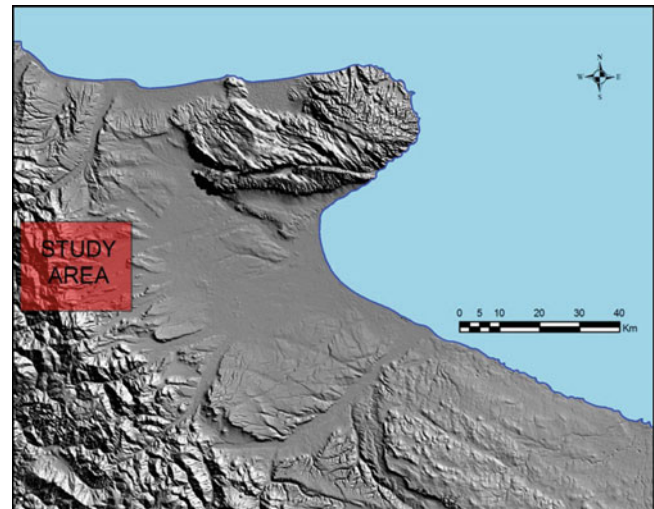


Fig. 2 Study area

activities and with viability and creep rapidly evolving not compatible with human activities.

Landslide Data

Following an analysis of instability phenomena observed in the study area was identified a GIS filing system.

The Geological Information System combines the geometric primitives, points and lines with tables of attributes to describe all the features of graphic data, as follows:

Type of graphic item: points (Tables 1 and 2).

Type of graphic item: lines (Tables 3, 4, 5, 6 and 7).

The polygon objects were distinct, respectively, only for the landslide bodies, and for the common areas of disruption or erosion gullies.

Type of graphic item: polygons.

The body landslide: (Tables 8, 9 and 10).

Areas of surface deformation: (Tables 11 and 12).

The geometric data, such as area, dimensions, coping and nail, are obtained by using appropriate tools and automatic procedures of the DTM.

Maps of Landslide

Once implemented the information system, the instability can be mapped in different ways.

Below we show some ways of mapping that allow you to highlight the phenomenon through GIS processing techniques. As you can see, the use of a high resolution DTM allows you to better highlight the places morphology (Fig. 3).

Table 1 Domain values for the field “type”

Code	type
1	Flow
2	Rock fall
3	Rotational rockslide
4	Translational rockslide
5	Counterslope

Table 2 Domain values for the field “activity”

Code	Type
1	Active
2	Inactive
3	Quiescent

Table 3 Domain values for the field “type”

Code	Type
1	River bed with a tendency to deepening
2	Area of calanque
3	Area affected by surface deformation
4	Area affected by diffuse runoff
5	Potential flood areas
6	Landslide body
7	Edge of escarpment of landslide
8	Edge of the escarpment, locally active for processes different from those that have originated it
9	Furrow erosion concentrated

Table 4 Domain values for the field “activity”

Code	Type
1	Active
2	Inactive
3	Quiescent

Table 5 Domain values for the field “typebody”

Code	Type
1	Of genesis complex, phenomena including mass transit
2	Flow
3	Rock fall
4	Creeping

Table 6 Domain values for the field “movement”

Code	Type
1	Rotational
2	Translational

Table 7 Domain values for the field “edge of the landslide”

code	type
0	No
1	Yes

Table 8 Domain values for the field “type”

Code	Type
1	Of genesis complex, phenomena including mass transit
2	Flow
3	Rock fall
4	Creeping

Table 9 Domain values for the field “movement”

Code	Type
1	Rotational
2	Translational

Table 10 Domain values for the field “activity”

Code	Type
1	Active
2	Inactive
3	Quiescent

Table 11 Domain values for the field “type”

Code	Type
2	Area of bad-lands
3	Area affected by surface deformation
4	Area affected by diffuse runoff

Table 12 Domain values for the field “activity”

Code	Type
1	Active
2	Quiescent

The Geographic Information Systems allow you to perform operations overlay, so you can easily represent the same landslide bodies of a DTM (Fig. 4).

Through a play of transparency on the topographic map, you can view the morphology (Fig. 5).

And, through a play of transparency on the orthophotos, you can view the morphology and land use of the area (Fig. 6).

These geographical analysis tools allow a more immediate visual perception of thematic mapped and help you

understand the phenomenon to decision makers who are often non-experts in the field.

Conclusion

The purpose of this study was to propose a structure of storing GIS geographic data for the types of instability present in the study area. The second purpose was to show different types of mapping, highlighting the usefulness of high resolution DTMs for the visual understanding of the specific phenomenon.

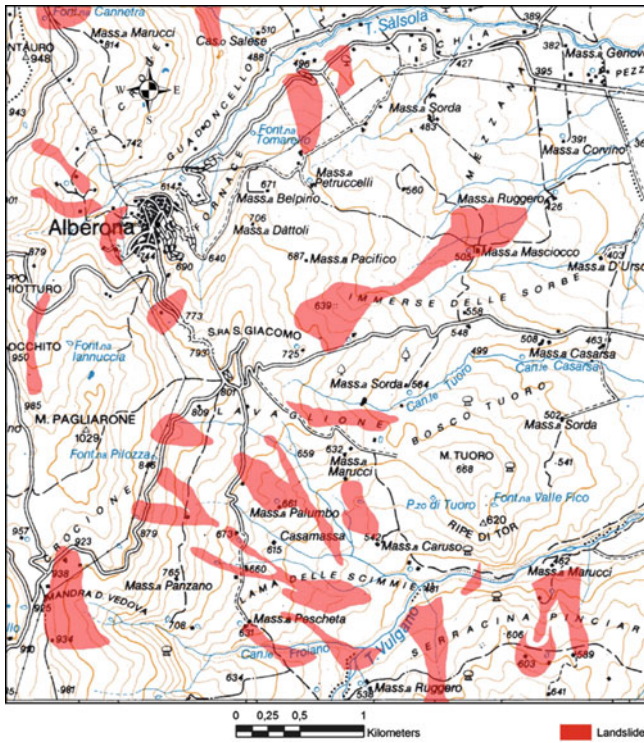


Fig. 3 Topographic map

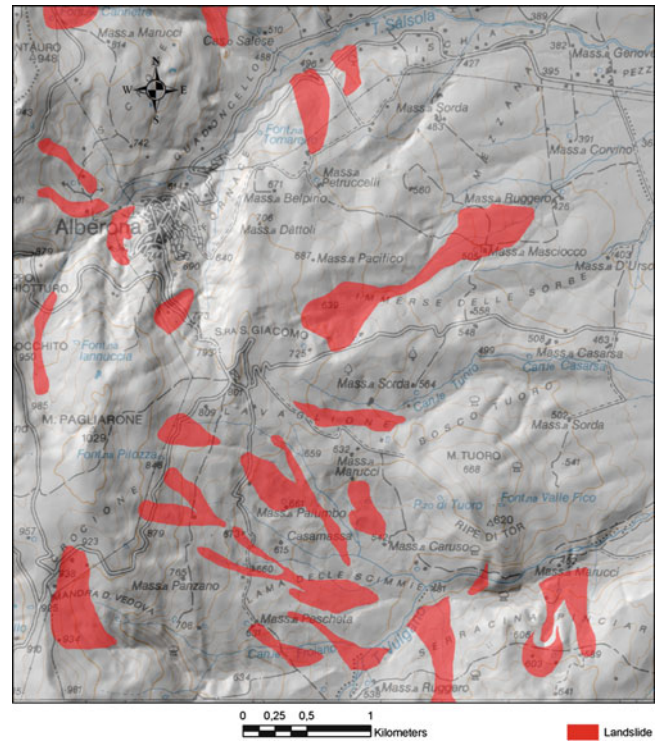


Fig. 5 Overlay of the topographic map on the Hillshade



Fig. 4 Hillshade



Fig. 6 Overlay of orthophotos on the Hillshade

References

- Amanti M, Casagli N, Catani F, D'Orefice M, Motteran G (1996) Guida al censimento dei fenomeni franosi e alla loro archiviazione. In: Miscellanea del Servizio Geologico Nazionale, n° 7, I.P.Z.S., Roma, p 109
- Amanti M, Chiessi V, Bertolini G, Ramasco M, de Nardo MT (2001) Guida alla compilazione della scheda frane IFFI (Inventario Fenomeni Franosi in Italia), Allegato 1 al Progetto IFFI. Servizio Geologico Nazionale, Roma
- ISPRA: Progetto CARG - Cartografia geologica e geotematica. http://www.apat.gov.it/site/it-It/Progetti/Progetto_CARG_-_Cartografia_geologica_e_geotematica/. Accessed 10 Aug 2011
- ISPRA: Progetto IFFI - Inventario dei fenomeni franosi in Italia. http://www.apat.gov.it/site/it-IT/Progetti/IFFI_-_Inventario_dei_fenomeni_franosi_in_Italia/. Accessed 10 Aug 2011
- Pieri P, Gallicchio S, Moretti M (2011) Note illustrative del Foglio 407 "San Bartolomeo in Galdo". ISPRA, Roma



A New Digital Catalogue of Harmful Landslides and Floods in Italy

Paola Salvati, Ivan Marchesini, Vinicio Balducci, Cinzia Bianchi, and Fausto Guzzetti

Abstract

Landslides and floods are widespread and recurrent in Italy, where they cause damage and pose a threat to the population. To estimate geo-hydrological risk in Italy, catalogues of landslide and flood events that have caused damage to the population were compiled from a variety of sources. The catalogues covers the 1,943-year period from 68 A.D. to 2010, and list 3,310 landslide events and 2,624 flood events that have resulted in deaths, missing persons, injured people, and homeless. For each event in the catalogue, different types of information were collected and organized in a database. We describe the Spatial Data Infrastructure (SDI) we have implemented to collect, store, analyze, and disseminate the historical information, and results of the analysis of landslide and flood risk to the population.

Keywords

Landslide • Database • SDI

Introduction

Italy has a long history of climatically induced natural catastrophes (Guzzetti et al. 1994, 2005a, b; Reichenbach et al. 1998; Guzzetti 2000; Salvati et al. 2003, 2010). Inundations and landslides are frequent, and have a significant societal and economic impact. Historical information of landslide or flood events is fundamental to understand the complexities and dynamics of past events, and to predict future events. Beginning in 1998, a collection of digital catalogues of historical, geographical, and bibliographical information on landslide and flood events was assembled and organized in an information system on geo-hydrologic hazards and associated risk in Italy, SICI (Guzzetti and Tonelli 2004, <http://sici.irpi.cnr.it>). Since 2000, specific catalogues of landslides and floods with human consequences were prepared, and used to assess societal and individual landslide and flood risk to the

population of Italy, at the national and the regional scale (Guzzetti et al. 2005a, b; Salvati et al. 2003, 2010).

In the literature, investigators have described criteria to compile historical catalogues of natural events, and methods used for the analysis of the historical information, with emphasis on the quality of the information and the results obtained (Guzzetti et al. 1994; Prestininzi and Romeo 2000; Guzzetti and Tonelli 2004; Petley et al. 2005; Kirschbaum et al. 2009, Rossi et al. 2010, Salvati et al. 2010). Inspection of the literature reveals that investigators rarely describe the data infrastructure, or the spatial data infrastructure (SDI), used to manage (i.e., collect, store, update, analyze, and disseminate) historical information on natural events, including the hardware (HW) and software (SW) components, and their complex interactions (Guzzetti and Tonelli 2004; Salvati et al. 2009). This is surprising, because the logical framework, the system architecture, and the performance of the SDI affect the way the historical data are managed, from the data collection to the dissemination of the results of the analyses. In this work, we present a SDI specifically designed and implemented to collect, store, analyze, and disseminate historical information on landslides and floods with human

P. Salvati (✉) • I. Marchesini • V. Balducci • C. Bianchi • F. Guzzetti
Consiglio Nazionale delle Ricerche, Istituto di Ricerca per la
Protezione Idrogeologica, Via Madonna Alta 126, Perugia, Italy
e-mail: paola.salvati@irpi.cnr.it

consequences to the population of Italy (Guzzetti et al. 1994, 2005a, b, Reichenbach et al. 1998; Salvati et al. 2003, 2010).

Materials and Methods

Catalogues of Harmful Landslides and Floods in Italy

Using multiple sources of information, Guzzetti (2000), Guzzetti et al. (2005a, b), Reichenbach et al. (1998), and Salvati et al. (2003, 2010) have collected systematic and comprehensive information on landslide and flood events with direct consequences to the population of Italy, including deaths, missing persons, injured people, and homeless.

For each event in the historical record, information listed in the catalogues include: (1) the precise or approximate date of the event, (2) the precise or approximate location of the event, including administrative information, (3) the known or inferred trigger, (4) the temporal and spatial evolution of the event, and – most importantly – (5) the exact or approximated number of deaths, missing persons, injured people, and missing and homeless people. The catalogues collectively list 6,186 records, and cover the 1,943-year period from 68 A.D. to 2010. In this period, landslides and floods caused at least 96,030 casualties (16,202 due to landslides and 79,828 to floods). In the recent period 1900–2010, which we consider substantially complete and that we use for statistical analysis, landslides killed or injured at least 8,043 people, an average of 72.5 landslide casualties per year. In the same period, at least 4,890 people died or were injured as a result of flood events, with an average of 44.1 flood casualties per year. Using this detailed historical record, multiple analyses of the risk posed by landslides and floods to the population of Italy are possible (Guzzetti et al. 2005a; Salvati et al. 2010). Figure 1 shows an example of the possible analyses. The figure portrays the density of landslide casualties in the different Italian regions, in the period 1900–2010.

The Spatial Data Infrastructure

A Spatial Data Infrastructure (SDI) facilitates the interoperability of geographical data, and the flow of information between different players, including authors and users of the information and the analyses (Yi Shan-zhen et al. 2001; Marchesini et al. 2010). Interoperability is the ability of a system, or a component of a system, to share information and to manage processes across applications adopting a mechanism of mutual understanding of requests and responses (Groot and McLaughlin 2000; Kralidis 2008). Interoperability is achieved e.g. through web services,

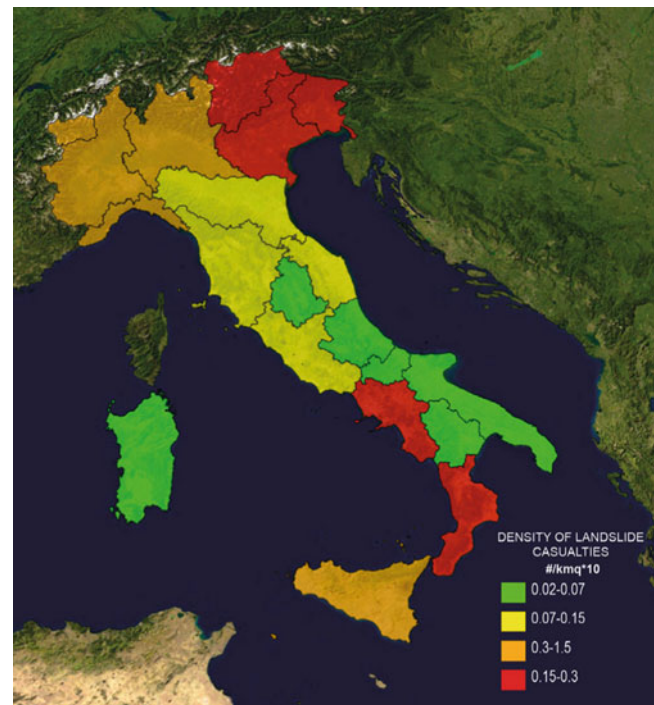


Fig. 1 Density of landslide casualties in the Italian regions, in the period 1900–2010. Density is the number of casualties per 10-km²

standard Internet communication protocols between applications (built on the HTTP protocol), and the XML language (Mitchell 2005).

In the field of mapping and cartography, the Open Geospatial Consortium (OGC) has produced technical specifications for standard communication protocols. Most of the technical specifications were accepted by e.g., the International Organization for Standardization (ISO) in the ISO 19100 series, and were adopted by the European Union INSPIRE, Infrastructure for Spatial Information in Europe Directive. For relational database management systems (RDBMS), interoperability is guaranteed by the compliance to SQL standards ISO/IEC 9075 (1–4,9–11,13,14:2008).

In Fig. 2, we show the logical framework of the SDI we have designed and implemented to manage information on historical landslide and flood events with human consequences in Italy. The SDI was designed towards interoperability, exploits state-of-the-art RDBMS technology, and provides standard web services compliant to OGC technical specifications.

The SDI consists of 14 virtual machines (VMs) operating on two separate physical servers (hosts). For virtualization, VMware ESX 4.1 was installed in the two hosts (HOST A and HOST B in Fig. 2). The VMs run GNU/Linux Ubuntu 10.04 Server – 64 bit OS (S2 to S15 in Fig. 2). Management of the two hosts and of the 14 VMs is performed using VMware VirtualCenter Server, VCS (S1 in Fig. 2) running on a Microsoft Windows 2008 Server OS, and is managed

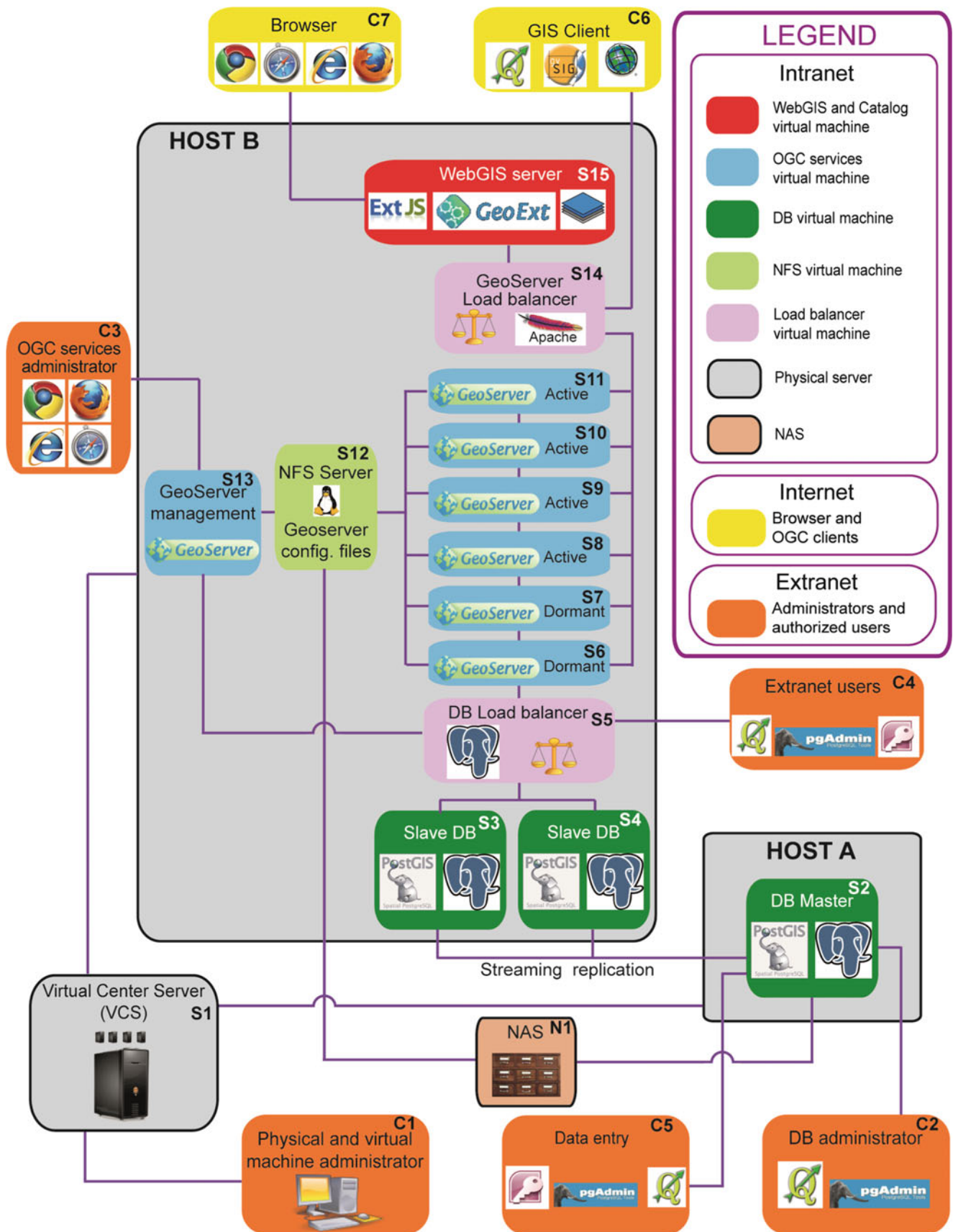


Fig. 2 Logical framework adopted for the Spatial Data Infrastructure used to manage information on historical landslide and flood events with human consequences to the population of Italy

using the client application VMware vSphere Client (C1 in Fig. 2).

A dedicated VM hosts the RDBMS (S2 in HOST A in Fig. 2), which represents the data core of the SDI. In the SDI, the RDBMS software is PostgreSQL 9.0, an open source, licensed, enterprise-class SQL database server that can manage geospatial (vector) information using the spatial extension postGIS 1.5. We exploit the PostgreSQL 9.0 capability of “master-standby” replication that allows designing efficient load balancing systems based on replicated servers. Compliance to the 2008 SQL standard revision guarantees interoperability with others database clients.

In the HOST A (S2 in Fig. 2), the PostgreSQL-PostGIS server runs in a read/write mode, managed by the database administrator (C2 in Fig. 2) using alpha-numeric clients, PgAdmin 1.12.1 SW, and GIS clients, e.g. QGIS 1.6. In the HOST B, two VMs (S3 and S4 in Fig. 2) host “hot-standby” (slave) read-only nodes of a streaming replication system (Riggs 2010) performed by the PostgreSQL RDBMS server in HOST A. Changes made to the master server databases (S2 in Fig. 2) are seamlessly replicated into the two slave servers (S3 and S4 in Fig. 2). A load balancer (a “pooler” implemented with pgpool-II, S5 in Fig. 2) manages the requests and distributes the load between the two slave servers.

Standard OGC services are generated using GeoServer 2.0.2, an open source web application for the publication of geographical information as Web Mapping Services (WMS), Web Feature Services (WFS), and Web Coverage Services (WCS). In the SDI, GeoServer is managed remotely using a web browser. A set of six GeoServer nodes (S6 to S11 in Fig. 2) accesses the data through the pooler. Two of the six nodes are dormant, and become active should a problem arise in one or more of the active nodes. Each GeoServer is installed on an Apache Tomcat 7 servlet container. The six GeoServer nodes share the same configuration files, shared through a dedicated Network File Server (NFS, S12 in Fig. 2).

The OGC services administrator (C3 in Fig. 2) performs changes to the GeoServer nodes configuration files through a dedicated VM (S13 Fig. 2) running GeoServer management SW and sharing the same configuration files. For the changes to become effective, a restart of the six GeoServer nodes is required.

A load balancer (using Apache 2.2.14, S14 in Fig. 2) distributes the external requests to the six GeoServer nodes. External requests are generated by desktop GIS clients (C6 in Fig. 2), and by a specific WebGIS interface (S15 in Fig. 2) written exploiting GeoEXT, OpenLayers, and ExtJS Javascript libraries, and accessed by individual users through a simple web browser (C7 in Fig. 2).

To guarantee the long-term integrity of the data, storage is performed on a Raid 1 disk array, and daily backups are performed on a Network Area Storage system (NAS, N1 in Fig. 2).

Results

The SDI was designed to be efficient and functional for different classes of users, including administrators, users that store, edit and update the information, and users that query the data and visualize maps. For this purpose, the SDI allows for segmenting access to different users, based on user type, network of origin, and user permissions. In Fig. 2, the main virtualization server (S1), the pool of virtual servers (S2 to S15), and the storage and backup systems (N1), are all located in a private network (intranet). Access to the data is provided through specific requests to the OGC services (Internet users, C6-C7 in Fig. 2), and through direct access to the databases (extranet users, C4-C5 in Fig. 2).

External users are granted open access to WMS and WebGIS services. Access to WFS is restricted to a pool of authorized users. Web access to the OGC and the WebGIS (Fig. 3) services is through a dedicated portal (<http://giida.irpi.cnr.it>).

Extranet users can connect remotely to the system through a virtual private network (VPN). Some of the users are authorized to read and/or copy the entire set of data (C4 in Fig. 2). Other users (C5 in Fig. 2) can perform data entry and editing operations. In the databases, landslide and flood sites affected by the damaging events are located (1) entering new point geometries from a GIS client (e.g. Quantum GIS), or (2) manually adding coordinates in specific database tables and fields. To guarantee conformity between geometries and geographical coordinates, specific triggers calculate the correct geometry when the geographical coordinates are inserted or updated. Quantum GIS and pgAdmin III are used to edit geometries and alphanumeric data. Microsoft Access can also interact with the master database via ODBC (Open Database Connectivity). Reuse of preexisting Microsoft Access SQL queries has allowed users to adapt quickly to the new system.

The SDI allows the different classes of users, including internet and extranet users (C6-C7 and C4-C5 in Fig. 2) to have access data that are always updated in the databases. This is a significant advantage that reduces the complexity and unnecessary redundancy in the data, and avoids problems related to the use and exchange of data of different

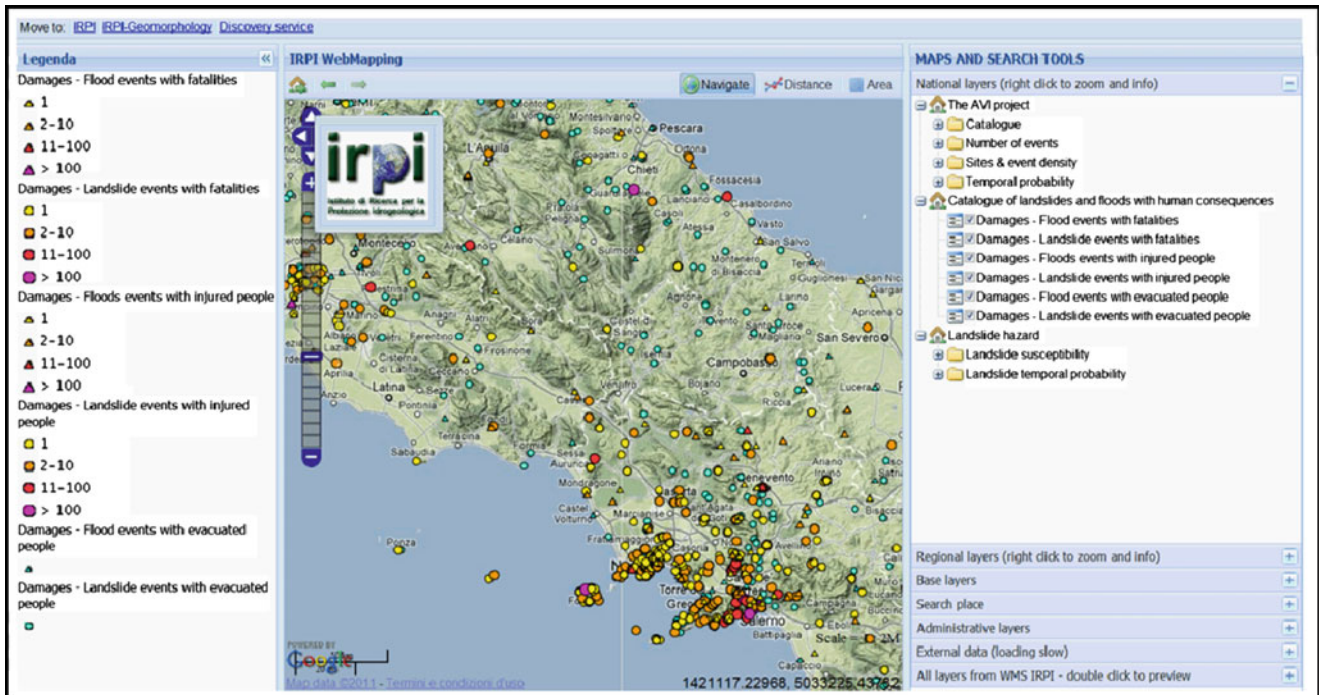


Fig. 3 Screenshot of the IRPI WebGIS

versions, and with different levels of completeness and correctness.

Discussion and Conclusions

To manage the digital catalogues of historical landslide and flood events with human consequences to the population of Italy, we selected a SQL database server. The adopted technology guarantees the necessary independence of the data from the HW and SW infrastructure, and further guarantees proper authentication and authorization policies and management, concurrency control, and semantic and referential integrity. To identify the most appropriate technological solution, we considered the following user and system requirements: (1) ability of the infrastructure to manage geographical (geospatial) information, in vector format, (2) reliability, in terms of data loss and security, (3) improved replication and loading balancing capabilities, (4) the licensing scheme, that should be permissive, (5) the cost of the system, and for its maintenance and update, and (6) the level of compliance with the latest SQL standards. PostgreSQL 9.0, an open source, enterprise-class SQL database server, best matches the listed requirements. With the new replication functionalities PostgreSQL 9.0 allows for: (1) creating redundant systems, greatly limiting the chances of data loss, (2) distributing queries and associated processing

load between the master server (for “insert” and “update” types queries) and the slave servers (for “select” type queries).

The information stored in the databases is geographic, and publication of the information occurs through geographical representations i.e., digital maps showing the information on historical harmful landslides and floods, and related products (Fig. 1). For the purpose, we adopted a technological solution based on a redundant system of multiple GeoServer nodes. The software was selected for the simplicity in the implementation of new services, and the compliance with the latest OGC standards.

The described SDI is complex (Fig. 2), and problems exist for its management and maintenance. The (relatively) large number of VMs (14) requires a constant survey of the individual VMs, and of the necessary connections between the VMS. In case of power failure, network or HW problems, reboot of the SDI requires a specific procedure, including steps to detect and resolve inconsistencies between the replicated database nodes. To implement the SDI we selected SW components that are robust and well tested. Despite, bugs or unresolved problems exist in the SW. As an example, Geoserver does not allow granting access to a specific OGC service on a specific data layer, limiting the functionality of the SDI. Pgpool-II is not trivial to configure, and proves highly sensitive to minor changes in the configuration parameters, with unpredictable consequences to the performance of the cluster of GeoServer nodes.

Acknowledgments We thank G. Tonelli, for many years of management of the databases on historical landslides and floods in Italy, and the GeoSDI team (<http://www.geosdi.org/>) for their strategic and technical support.

References

- Groot R, McLaughlin J (2000) Geospatial data infrastructure: concepts, cases and good practice. Oxford University Press, Oxford
- Guzzetti F (2000) Landslide fatalities and evaluation of landslide risk in Italy. *Eng Geol* 58:89–107
- Guzzetti F, Tonelli G (2004) Information system on hydrological and geomorphological catastrophes in Italy (SICI): a tool for managing landslide and flood hazards. *Nat Hazard Earth Syst Sci* 4:213–232
- Guzzetti F, Cardinali M, Reichenbach P (1994) The AVI project: a bibliographical and archive inventory of landslides and floods in Italy. *Environ Manage* 18:623–633
- Guzzetti F, Salvati P, Stark CP (2005a) Evaluation of risk to the population posed by natural hazards in Italy. In: Hungr O, Fell R, Couture R, Eberhardt E (eds) *Landslide risk management*. Taylor & Francis, London, pp 381–389
- Guzzetti F, Stark CP, Salvati P (2005b) Evaluation of flood and landslide risk to the population of Italy. *Environ Manage* 36(1):15–36
- Kirschbaum DB, Adler R, Hong Y, Hill S, Lerner-Lam A (2009) A global landslide catalog for hazard applications: method, results, and limitations. *Nat Hazard* 52(3):561–575
- Kralidis AT (2008) Geospatial open source and open standards convergences. In: Hall GB, Leahy MG (eds) *Open source approaches in spatial data handling*. Springer, Berlin
- Marchesini I, Balducci V, Tonelli G, Rossi M, Guzzetti F (2010) Geospatial information on landslides and floods in Italy. In: *Proceedings of the international symposium on geo-information for disaster management (Gi4DM)*, Torino, Italy. Geomatics for Crisis Management. ISPRS. ISBN 978-88-903132-3-3, 2–4 Feb 2010
- Mitchell T (2005) *Web Mapping Illustrated*. O'Reilly Sebastopol
- Petley DN, Dunning SA, Rosser NJ (2005) The analysis of global landslide risk through the creation of a database of worldwide landslide fatalities. In: Hungr O, Fell R, Couture R, Eberhardt E (eds) *Landslide risk management*. Taylor & Francis, London, pp 367–374
- Prestininzi A, Romeo R (2000) Earthquake-induced ground failures in Italy. *Eng Geol* 58:387–397
- Reichenbach P, Guzzetti F, Cardinali M (1998) Map of sites historically affected by landslides and floods in Italy, 2nd edn. CNR Gruppo Nazionale per la Difesa dalle Catastrofi Idrogeologiche Publication no. 1782, Scale 1:1,200,000, SystemCart
- Riggs S (2010) *PostgreSQL 9 administration cookbook*. Packt Publishing, Birmingham
- Rossi M, Witt A, Guzzetti F, Malamud B, and Peruccacci, S (2010) Analysis of historical landslide time series in the Emilia-Romagna Region, Northern Italy. *Earth Surf Proc Land* 35(10):1123–1137
- Salvati P, Guzzetti F, Reichenbach P, Cardinali M, Stark CP (2003) Map of landslides and floods with human consequences in Italy. CNR Gruppo Nazionale per la Difesa dalle Catastrofi Idrogeologiche Publication n. 2822, scale 1:1,200,000
- Salvati P, Balducci V, Bianchi C, Guzzetti F, Tonelli G (2009) A WebGIS for the dissemination of information on historical landslides and floods in Umbria, Italy. *Geoinformatica* 13:305–322
- Salvati P, Bianchi C, Rossi M, Guzzetti F (2010) Societal landslide and flood risk in Italy. *Nat Hazard Earth Syst Sci* 10:465–483
- Shan-zhen Y, Li-zhu Z, Ji-cheng C, Qi L (2001) The relation of department components and activity in spatial information infrastructure. *Wuhan Univ J Nat Sci* 6(1–2):460–466



Application of the Computerised Cartography to the Territory Management: The Geomorphological Map of Palaeolandslides in the Velino River Valley (Central Apennines, Italy)

Serafino Angelini, Piero Farabollini, Riccardo Massimiliano Menotti, Fabrizio Millesimi, and Marco Petitta

Abstract

The geomorphological cartography explained in this work is the result of a process of synthesis resulting from detailed geological and geomorphological and hydrogeological researches and from numerous land surveys carried out during the past ten years. The choice of the study area can be explained by the presence of important and complex phenomena involving the upper course of the Velino river, such as palaeo-landslides, mass-movements and debris flows, subsidence phenomena, etc. In particular, these phenomena involve several towns (Posta, Micigliano, Sigillo, Villa Camponeschi), as well as a fundamental route (State Road 4), following the ancient consular road, named Salaria, roman in age.

The informations deriving from the land surveys has been integrated and controlled by photo-interpretation (related at 1982 and 2000 aero-photographs). The result has been implemented by the 2006 cartography, which was obtained from the ortho-rectified images, subject to a “spreading” over the digital model of the terrain that was obtained from the regional topographical cartography at a scale of 1:10,000, promoted by the Lazio Region. Even if they have well-known limits of representation that derive from the approximate restoration of the basic regional maps that were realised in the 1980s, the latter represent a very up-to-date control instrument, depending on a critical analysis of the information.

All the data have been computerised by exploiting the tools made available by the ESRI platform, through the development of an innovative logical pattern for the geomorphology, since the aforesaid data were treated by considering forms, processes and deposits on the basis of the prevailing morphogenetic agent. In this way, the problems deriving from the contiguity and superimposition of several polygonal forms in logical contrast and topological conflict have been overcome.

S. Angelini (✉)

Litografia Artistica Cartografica S.r.l., via del Romito, 11-13R,
50134 Florence, Italy
e-mail: s.angelini@lac-cartografia.it

P. Farabollini

Department of Environmental Sciences, University of Camerino,
Camerino, Italy

R.M. Menotti

IFAC – CNR, Sesto Fiorentino (FI), Italy

F. Millesimi

ARPA – LAZIO, Rieti, Italy

M. Petitta

Earth Sciences Department, University “La Sapienza”, Rome, Italy

Hopefully, several representational limits will be overcome once the set-up valid for the published printing has been made ready, since the instruments currently available have several technical limitations in the raster process and, in spite of the information present is correct, it does not yet respect several qualitative standards typical of Italian graphic representation.

Several graphic improvements typical of the Italian publishing language and cartographic tradition will be the topic of the subsequent phase.

Despite Italian tradition imposes extreme attention on the graphic aspect, it is very important to note that the territorial computer-related systems facilitate an analysis of the coverings, depending on the substrate on which they are imposed, and make it possible to define a model according to which the forms, processes and deposits evolve over time, in fact the whole upper valley of the Velino river is annually subjected to deep changes due to the high energy of relief and extreme weather conditions: knowledge and proper analysis of these phenomena can contribute significantly to the right land management, giving due importance to the prevention and the screening to be daily carried out.

Keywords

Palaeolandslide • Debris flow • Database and geomorphology • Region feature class • Subclasses

Introduction

The complex geological and geomorphological dynamics of the Upper Valley of the Velino River is becoming increasingly interesting although this has been considered mere scientific curiosity for a long time. The new plan for extending and modifying the road sector of the “via Salaria” State Route N° 4 – which runs between Sigillo and Antrodoco – drew the attention to the need for better analysing the actual natural conditions of the Velino Gorges; deep anthropogenic modifications – which are currently active and are acknowledged as extremely invasive in some sectors – must also be considered (Fig. 1). The study-area is bounded by the valley of the Velino River (Central Apennine) between the hamlets of Posta to the north and Antrodoco to the south; this area features outcropping lithotypes of carbonatic platform, hemipelagic marly-clayey sediments and arenaceous-pelitic turbidites (Angelini et al. 2004; Centamore et al. 1991; Centamore and Nisio 1999). The area tectonics has been intensive and complex: this is demonstrated by the occurrence of folds and faults (overthrusts, normal faults as well as faults with complex kinematic anomalies).

Based on the above, there is evidence that a set of data – which are flexible and can be analysed – is absolutely essential so as to investigate possible opportunities; techniques, tools and procedures – which are offered by the Geographic Information Systems as well as by digital cartography – are extremely relevant to this purpose. In particular, the data structure must be highlighted: it has been inspired by the Italian Geological Cartography Plan – which has been published by the Italian Geological Service, CAR.G Project – although in this case it exhibits aspects related to geomorphology.

Area of Interest

Data have been collected over the years basically in the Mt Terminillo massif which is bounded to the east by the Upper Valley of the Velino River. In particular the study area that has been described here belongs to the municipalities of Posta to the north, Antrodoco to the south and comprises the built up areas of Sigillo (hamlet of Posta) and Micigliano. The entire area belongs to the Province of Rieti (region Latium) and is on the boundary of the Province of L’Aquila whose chief town is only 35 km far from it.

From a geological perspective, this area represents the southern edge of the northern Apennine and features the line dubbed “Linea Ancona-Anzio Auct.” (Castellarin et al. 1978; Cantelli et al. 1978); such a line enables the thrust towards ENE of the southern sector of the limestone Umbria-Marche-Sabine Apennine over the Latium-Abruzzo areas with sectors oriented N10+/-10 and sectors oriented N60-80 (Calamita et al. 1987). In particular, between Posta and Antrodoco, the “Ancona-Anzio” line is represented by a huge fold-fault with an overthrust in a few kilometres range oriented NNE-SSW with a dip direction toward SE: this lies Umbrian units of pelagic origin – in transition facies – over Abruzzo units – in shelf facies – partly eliding the Abruzzo threshold facies (Coli 1981; Bigi et al. 1991; Deiana et al. 1995).

This structural setting influences the area morphology which is characterised by steep slopes and high relief energy providing slopes with profiles with a convex trend in the upper sector and a less steep gradient and concave trend close to the valley floor.

From the geomorphological perspective, large slope movements, rockslides and deep gravity-induced deformations

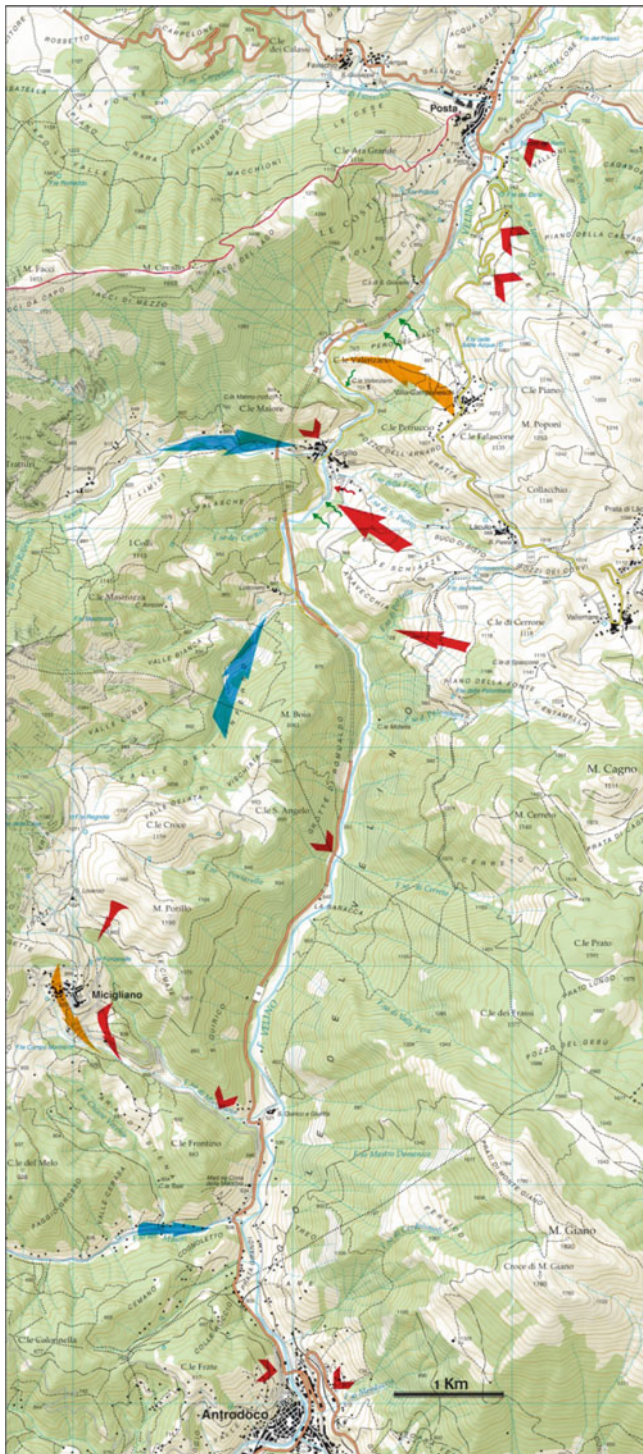


Fig. 1 Location of main phenomena due to gravity, within area of interest; red and orange arrow: earthflow and palaeolandslides; red V: rock falls; light blue arrows: debris flows; little green arrows: soil creep

(Dramis et al. 1994; e Dramis et al. 1995; Genevois et al. 1994; Martino et al. 2004) characterize the high reliefs of the central Apennines, where large-scale slope deformations depend on the high-relief energy, on the intense fracturing of structurally

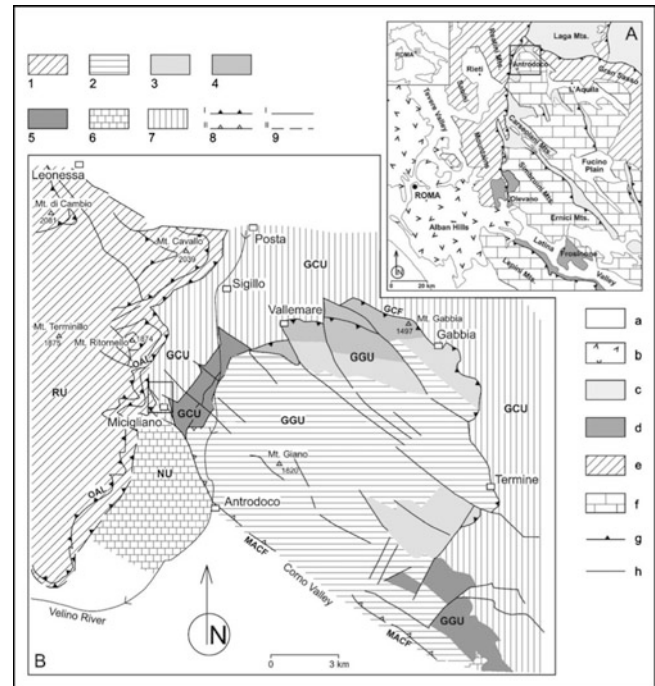


Fig. 2 (A) Tectonic setting of the central Apennines; rectangle indicates the area of B. (B) Close-up of the study area; A: (a) recent alluvial deposits; (b) Pleistocene volcanic deposits; (c) Messinian siliciclastic turbidites; (d) Tortonian siliciclastic turbidites; (e) Meso-Cenozoic calcareous-marly basinal and transitional deposits; (f) Meso-Cenozoic carbonate platform deposits; (g) thrust; (h) fault. B: RU Reatini Mts. unit, GGU Mt. Giano– Mt. Gabbia unit, GCU Gran Sasso-Cittareale unit, NU Mt. Nuria unit, OAL Olevano Antrodoco line, MACF Micigliano–Antrodoco–Corno Valley fault, GCF Mt. Giano–Mt. Cagno thrust fault. (I) calcareous-marly transitional-basinal deposits – RU; (2) carbonate platform deposits s.l. – GGU; (3) carbonate platform margin deposits – GGU; (4) upper slope carbonate facies of the post-Cenomanian drowning – GGU and GCU; (5) upper slope carbonate facies of the pre-Cenomanian drowning – GGU; (6) lower slope carbonate facies of the pre-Cenomanian drowning – NU; (7) slope carbonate facies – GCU; (8) certain (I) and uncertain (II) thrust; (9) certain (I) and uncertain (II) fault

complex lithotypes, on the occurrence of extensive single-layer carbonate aquifers and on the juxtaposition of lithologies with different mechanical and rheologic behaviours, originating specific morphologies (Dramis et al. 1985; Dramis and Sorriso Valvo 1994) (Fig. 2).

In particular, landforms such as trenches, ridge splitting, scarps and reverse slopes, presence of lowered and rotated blocks can be related to tectonic conditions of stress-deformation. The area of interest exhibits intense and extensive mass movements, among which various types of active landslides and deep slope gravitational deformations can be observed (Fig. 3): a rock block slide (Dramis et al. 1985; Menotti et al. 1999) involving the entire southern portion of an ancient deposit of a toppling landslide which can be observed NW of Micigliano; and a huge complex landslide which has been caused by an upstream rotational slide

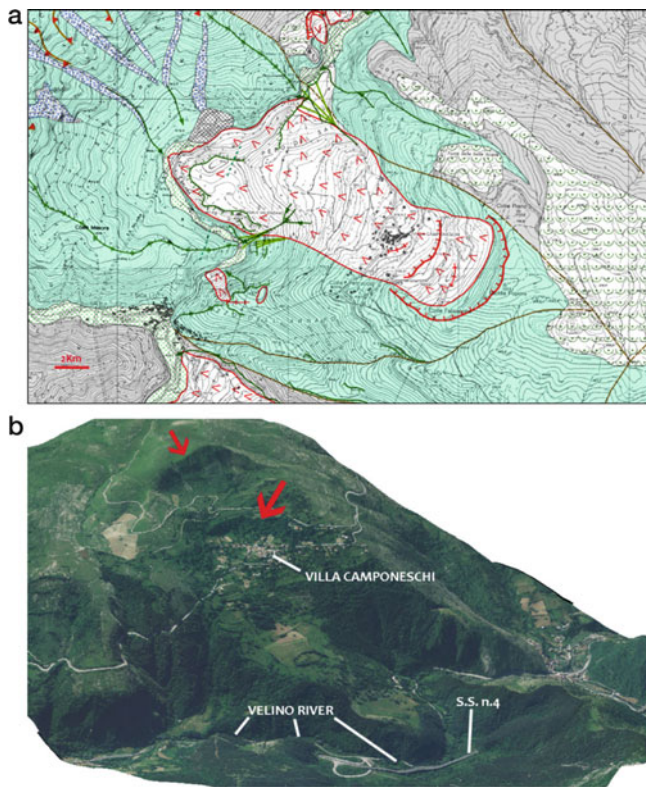


Fig. 3 a,b: Two different representation of Villa Camponeschi palaeo-landslide: (a) geomorphological map 1:10.000 from database, (b) orthorectified image on a digital elevation model (evidenced by red arrows, two main scarps)

developing into an earthflow which partly involved Micigliano itself. The second event that deserves further investigation involves the built up area of Villa Camponeschi: an extensive rock-block-slide involves the entire slope and exhibits an upstream extensive trench bounded by a secondary scarp which is slightly downhill and bounds the final part of the landslide body. This event apparently caused the displacement of the stream axis of the Velino River: this has been displaced by an extensive bending towards the opposite bank and it is demonstrated by sublevel surfaces depending on the terracing of the landslide body during the valley deepening of the river itself.

Data

The Velino River area comprised between Posta and Antrodoco has been investigated by our research team since a long time ago: cartographies, unpublished scientific work regarding geological, geomorphological and hydrogeological aspects have been conducted over the years offering a number of considerations.

Most of the data that have been surveyed over the years have been digitalised and stored in a complex geodatabase



Fig. 4 Overflowing of the external areas of the riverbed of the Scura Valley, alluvial event of the last 1st and the 2nd of December (2010)



Fig. 5 The bank erosion of the Scura Torrent carried out large part of the morphological terrace cancelling out route and temporarily isolating the locality of "Le Casette"

which is currently composed by vector and raster cartographic data (mainly bibliographic), aerial photographs, satellite imagery, attribute tables, external encoded tables, photographs (Figs. 4 and 5), texts and analyses of local type. Data collection dates varies and influences the definition of a picture of the situation at the time data were collected providing further useful elements through change detection operations.

All the cartographic data that have been surveyed are based on raster cartography scale 1:10,000 published by the region Latium in the early Nineties and a cartographic base has recently (2011) been created (copyright owned by the Litografia Artistica Cartografica S.r.l., Florence) scale 1:25,000. I.G.M. data are exclusively available in raster format and date back to '00s.

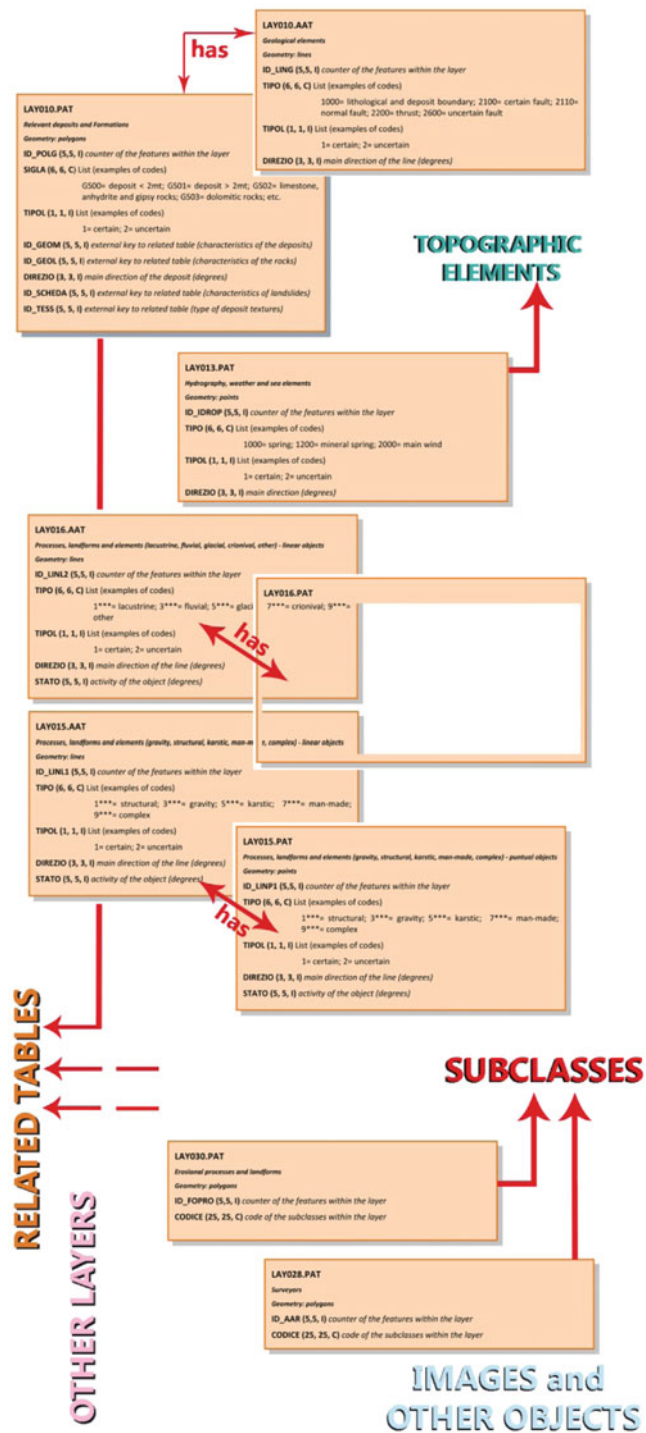


Fig. 6 Extremely simplified logical sketch and its relationships among just main layers of geomorphological information system of reatini mountains; in light pink: main geomorphological levels (data and attributes); in red: main spatial relationships. Metadata aren't included in the sketch

Vectorial data are organized into a relational database ESRI (through the ArcInfo software) which employs entity/relation concepts (Fig. 6) so as to correctly manage geographical (topological) as well as information (attributes)

relations concerning real elements that have been mapped: following this method some information levels are defined (Servizio Geologico d'Italia, 1997, 2008). Geographical features are stored within this levels based on “families” of encoded data; other data can or cannot be related to the analysis that is being conducted according to the aspect that must be highlighted. The cartography that is presented in this paper has the purpose of investigating the geomorphological aspect of the Valley and its relation with the existing infrastructures; for this purpose information concerning geological Formations is generalized following a litho-mechanical logic that is typical of geomorphology: although this is stored in the database, it is considered redundant and is put together with other information.

The information layers that have been used for compiling the geomorphological cartography have been drawn scale 1:10,000 and include punctual, linear polygonal and “region” features; the introduction of the last type of feature is needed as in geomorphology two polygonal shapes belonging to the same “family” of data – thus to the same information level – frequently overlie – partly or entirely – causing a *topological* conflict which is hard to solve if tools are inadequate. For instance, if two avalanches or landslides (possibly with different activity or type of movement) originate from opposite slopes despite the same valley floor.

Trough “regions”, landforms of a level can be easily and correctly managed, despite overlying, as well as coalescent deposits in the suitable main level (Lay010). The use of “regions” is essential when the same information layer has been multi-assigned: choice between the representation of a structural slope or the same slope sculpted by a glacier is no longer needed: these are both erosion types although they belong to different subclasses but are found within the same information layer.

Main information layers that are found in the database are the following:

- Lay010, polygonal information level occupied by the outcrops drawn on the map; by definition it cannot show unlabelled polygons as it identifies a Formation (put together with another because of its lithological aspects) or a relevant deposit; lines of the same level provide information regarding geological and structural elements that are relevant to their scale of representation although they refer to the morphological aspects of a different level (lay 015);
- Lay013: a linear and punctual level which contains information regarding surface hydrography;
- Lay015 and 016: these levels contain information concerning punctual and linear landforms and processes to the representation scale; the main morphogenetic agents are volcanism and structural elements except for tectonic contacts, gravity, karsism, glacialism and crioclastism, wind, sea lakes and swamps;

- Lay028: an information level that enables to easily locate every survey area and people responsible for the survey through the “region” construction;
- Lay030: a “region” information level which contains erosion landforms and processes that have been described in ten subclasses according to the main morphogenetic agent.

Furthermore a few accessory information layers have been added: these contains either “Administrative boundaries” (Lay031) or elements useful for the representation (Lay030) such as “fan branches” or “lines of maximum gradient of areas with glacial flow”. A series of external tables crown the vectorial data outlines which have been used for the cartography described above: these tables have been created for providing details concerning deposits “textures” as well as for describing “depositional environments”.

Topographic elements have been structured in a different list and are exclusively available in the vector version scale 1:25,000.

Considerations

The Italian Geological Service publishes the Italian Geological Map scale 1:50,000 within a national project dubbed CAR.G (Geological Cartography): this project is based on land division of the Italian Map into 652 Sheets following the catalogue of the Italian Military Geographical Institute. Since the Nineties all information collected within this project is stored into a relational database scale 1:25,000; in a number of geographical areas, stored data from field survey are even more detailed (1:10,000).

Despite future publication of geomorphological Sheets, the Project has never provided a specific database for collecting these data and exclusively managed their digitalisation. In particular, the storage of these data involves difficult choices due to their complex origin.

Within this area of interest, information has been heterogeneously collected over the years despite the introduction of well-defined logical outlines that followed the CAR.G Project but involved detailed geomorphology: these outlines enabled easy data cataloguing, extraction, analysis, updating and comparison with similar situations on various geographical areas. Furthermore, as one of the main purposes of this paper is interaction with already structured geological data as well as a wide use of existing data through their reorganization, this work has the ambition to provide reference outlines for normalization of geomorphological data on a national scale.

References

- Angelini S, Fazzini M (2004) Carta di Localizzazione Probabile delle Valanghe del comprensorio di Monte Terminillo. Ed. L.A.C. Firenze
- Angelini S, Farabollini P, Fazzini M, Gaddo M, Gentili B (2003) Analisi meteo climatica e cartografia valanghe: studio per il rilevamento geomorfologico dei Monti Reatini nell'Appennino centrale. AINEVA, Neve e Valanghe, n.43
- Angelini S, Farabollini P, Menotti RM, Millesimi F, Petitta M (2004) Geomorphological-touristic map of Reatini Mountains (Central Apennines, RI). Ed. L.A.C. Firenze
- Arctur D, Zeiler M (2004) Designing geodatabases – case studies in GIS data modeling. ESRI Press, Redlands
- Bigi S, Calamita F, Centamore E, Deiana G, Ridolfi M, Salvucci R (1991) Assetto strutturale e cronologia della deformazione della zona di incontro tra le aree umbro-marchigiana e laziale-abruzzese (marche meridionali e Lazio-Abruzzo settentrionali). Studi Geol Camerti, vol. spec. CROP 11:21–26
- Boni CF, Capelli G, Petitta M (1995) Carta idrogeologica dell'alta e media valle del fiume Velino. Ed. System Cart, Roma
- Burrough PA, McDonnel RA (1998) Principles of geographical information systems. Oxford University press, Oxford
- Calamita F, Deiana G, Invernizzi C, Mastrovincenzo S (1987) Analisi strutturale della “linea Ancona-Anzio” Auct. Tra Cittareale e Micigliano (Rieti). Boll Soc Geol It, 106:365–375
- Cantelli C, Castellarin A, Praturlon A (1978) Tettonismo Giurassico lungo l'Ancona-Anzio nel settore Terminillo-AnTRODoco. Geologica Romana XVII:85–97
- Castellarin A, Colacicchi R, Praturlon A (1978) Fasi distensive, trascorrenze e sovrascorrimenti lungo la linea Ancona-Anzio
- Centamore E, Nisio S (1999) Quaternary geology and morphostructural evolution between the Velino and Salto valleys. Num. Spec. 2002 International workshop Large-scale vertical movements and related gravitational processes
- Centamore E, Civitelli G, Corda L, Mariotti G, Romano A, Capotorti F, Salvucci R (1991) Carta geologica dell'area di M. Giano – M. Gabbia – Gole del Velino- in Studi Geologici Camerti, Volume Speciale n.2 Crop 11
- Coli M (1981) Studio strutturale della linea “Ancona-Anzio” tra Posta e AnTRODoco (Gole del Velino). Boll Soc Geol It 100:171–182
- Damiani AV, Pannuzi L (1976) La glaciazione wurmiana nell'Appennino laziale-abruzzese. Bollettino della oCietà Geologica Italiana XCVII:85–106
- Deiana G, Pasqualini L, Salvucci R, Stroppa P, Tondi E (1995) Il sistema dei sovrascorrimenti nei Monti Reatini: analisi geometrica e cinematica. Studi Geologici Camerti, vol Spec 1995/2:199–206
- Dramis F, Sorriso Valvo M (1994) Deep seated gravitational slope deformations, related landslides and tectonics. Eng Geol 38:231–243
- Dramis F, Maifredi P, Sorriso-Valvo M (1985) Deformazioni gravitative di versante. Aspetti geomorfologici e loro diffusione in Italia. Geol Appl Idrogeol XX(II):377–390
- Dramis F, Gentili B, Pambianchi G (1994) Deep-seated slope deformations and connected large-scale landslides in the Umbria-Marche Regions. Spec. Vol. International Congress IAEG, Lisboa 1994
- Dramis F, Farabollini P, Gentili B, Pambianchi G (1995) Neotectonics and large-scale gravitational phenomena in the Umbria-Marche apennines, Italy. In: Slymaker O (ed) Steepland geomorphology. Wiley, New york
- Genevois R, Prestinzi A, Romagnoli C (1994) Deep seated gravitational slope deformations in Lazio. Spec. vol International Congress IAEG, Lisboa
- Giraudi C (1998) Il glacialismo tardo-pleistocenico del massiccio del Terminillo (Lazio – Appennino centrale). Il Quaternario 11:121–125
- Longley PA, Goodchild MF, Maguire DJ, Rhind DW (2001) Geographic information systems and sciences. Wiley, New York
- Martino S, Moscatelli M, Scarascia Mugnozza G (2004) Quaternary mass movements controlled by a structurally complex setting in the central Apennines (Italy). Eng Geol 72:33–55

- Menotti RM, Millesimi F, Petitta M (1999) Carta dei fenomeni franosi interessanti i centri abitati e la viabilità nella Provincia di Rieti. Ed. SystemCart, Roma
- Servizio Geologico d'Italia (1994) Quaderno 4: Carta geomorfologica d'Italia, Guida al rilevamento, Quaderni del Servizio Geologico d'Italia. Ed. ISPRA
- Servizio Geologico d'Italia (1997) Quaderno 6: linee guida all'informatizzazione e per l'allestimento dalla Banca Dati. Quaderni del Servizio Geologico d'Italia. Ed. ISPRA
- Servizio Geologico d'Italia (2008) Banca dati CARG integrata, Quaderni del Servizio Geologico d'Italia. Ed. ISPRA
- Van Oosterom P, Zlatanova S, Fendel E (2005) Geo-information for disaster management. Ed. Springer



Database of Unstable Rock Slopes of Norway

Halvor Bunkholt, Bobo Nordahl, Reginald L. Hermanns, Thierry Oppikofer, Luzia Fischer, Lars Harald Blikra, Einar Anda, Halgeir Dahle, and Stine Sætre

Abstract

The Geological Survey of Norway is currently developing a database for unstable rock slopes in Norway. The database is intended to serve three main purposes: (1) to serve as a national archive for potential unstable slopes for use in hazard and risk analysis, aerial planning and mitigation work as well as research; (2) to serve as a robust and easy to use database during field mapping of unstable rock slopes; (3) provide a public available database accessible through an online web map service. The database structure contains several feature classes storing both raw and processed data, including structures, lineaments, displacement measurements, run-out areas and other observations. All feature classes are linked to one main point which holds a general summary for each unstable slope.

Keywords

Database structure • Unstable slopes • Online web service • National data archive

Introduction

In Norway large rockslides with fatal consequences have occurred several times in pre-historic and historic times (e.g. Blikra et al. 2005; Furseth 2006). Four times in the last 100 years rock avalanches have hit fjords and lakes, and subsequent tsunami waves have destroyed entire

villages killing in total 188 people (Høst 2006). As the Norwegian Building Act places restrictions on land use of areas that can be affected by rock slope failures and their secondary effects, a national database to store information on potential unstable slopes has been requested by the Norwegian Water and Energy directorate (NVE). NVE has the responsibility of supporting municipalities with landslide mitigation. As a response the Geological Survey of Norway has developed a database for unstable rock slopes since 2008.

H. Bunkholt (✉) • B. Nordahl • R.L. Hermanns • T. Oppikofer • L. Fischer
Geological Survey of Norway, Leiv Eriksons vei 39, Trondheim
NO-7040, Norway
e-mail: halvor.bunkholt@ngu.no

L.H. Blikra
Åknes-Tafjord Beredskapssenter, Stranda, Norway

E. Anda
Møre og Romsdal Fylkeskommune, Molde, Norway

H. Dahle
Geological Survey of Norway, Leiv Eriksons vei 39, Trondheim
NO-7040, Norway

Fylkesmannen i Møre og Romsdal, Molde, Norway

S. Sætre
Fylkesmannen i Møre og Romsdal, Molde, Norway

Current Inventory

Currently, 285 potential unstable slopes have been identified nationwide either from remote sensing data such as interferometric synthetic aperture radar (InSAR) data or orthophotos, or from geological field mapping or knowledge from the local population.

The objects included in the database are commonly larger than 0.1 million m³, and they cluster in specific regions of the country. This clustering reflects both the variation in geology prone to landslide, and also the progress in the

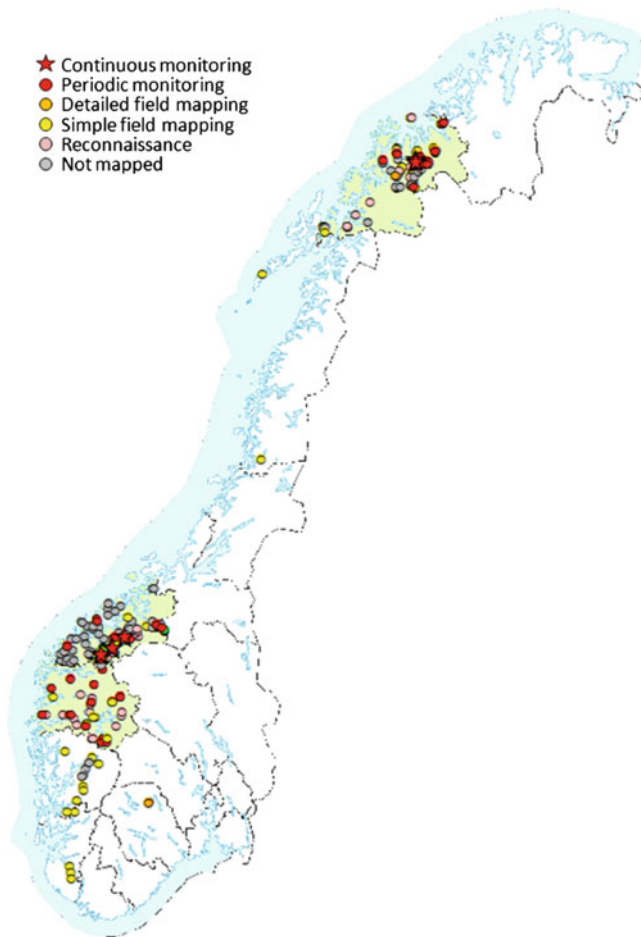


Fig. 1 Current inventory of database: 285 unstable objects

ongoing mapping programme by the Geological Survey of Norway (Fig. 1) (see Hermanns et al. 2011, this volume). In Fig. 1 the unstable objects are visualized according to the level of investigation and monitoring carried out at each site. Currently, 4 unstable slopes are under continuous monitoring and have early-warning systems installed, 55 are monitored periodically, 9 have been mapped in high detail, 60 have been inspected in the field, 42 have been reconnoitred and 95 are yet to be visited or reconnoitred in the field. A classification system based on hazard and risk level is under construction (Hermanns et al. 2011, this volume). The mapping of potential unstable slopes starts by studying remote sensing data such as orthophoto, digital elevation models (DEMs) and InSAR data (Lauknes et al. 2010). Objects identified from these data are classified as “Not mapped.” Next step is to conduct a “simple field mapping.” This involves an on-site investigation of the slope with sufficient sampling of structural data to construct an overall understanding of the slope stability (Henderson and Saintot 2011). If the results after this simple field mapping suggest further follow-up of the potential unstable slope, a detailed field mapping is executed. “Detailed field mapping” includes

comprehensive structural data sampling of discontinuity sets, if necessary using terrestrial laser scanning (TLS) (Oppikofer et al. 2009). The structural data set must be comprehensive enough to allow for construction of kinematic models of the slope and a good understanding of the delimiting structures of the instability (Saintot et al. 2011). Based on simple or detailed mapping, a slope may be put under “Periodic monitoring” by differential GPS systems (dGPS) (e.g. Bunkholt et al. 2011; Hermanns et al. 2011), TLS (Oppikofer et al. 2009), satellite- or ground based InSAR or other data such as extensometers and more. Finally, a few slopes have been classified as representing a high risk for population and/or infrastructure. These are put under “Continuous monitoring” (e.g. Blikra 2008).

Database Structure

Aim and Purpose

The database structure has been optimized to fulfill the following main goals: (1) to serve as a national archive for potential unstable slopes for use in hazard and risk analysis, aerial planning, and mitigation work as well as research; (2) to serve as a robust and easy to use database during field mapping of unstable rock slopes; (3) provide a public available service accessible through the internet. Different user interfaces with varying levels of access both for data entry and data extraction are defined, depending for which of the above goals the user interface is intended for.

Internal Structure

A joint effort between key persons in landslide research in Norway has led to a comprehensive list of Norwegian (and English) terms that are used to describe rockslide features. This list is based on international nomenclature and defines the database structure. Each object in the database is mapped with one main point (“UnstableSlopeMainPoint”) and classified according to the investigation level of the slope. All other data for the object are stored and related to the main point through six feature classes (Fig. 2). All acquired data are classified either as 1st order (field observations, remote sensing data, displacement measurements) or 2nd order data (analysis results)

The “UnstableSlopeMainPoint”

The main point contains a summary of the unstable slope. The attributes are as listed in Table 1, and each attribute is associated with a drop-down list that provides the user with different choices pre-defined from the list of nomenclature. The extensive use of drop-down lists ensures that data are added to the database in a coherent manner, regardless of

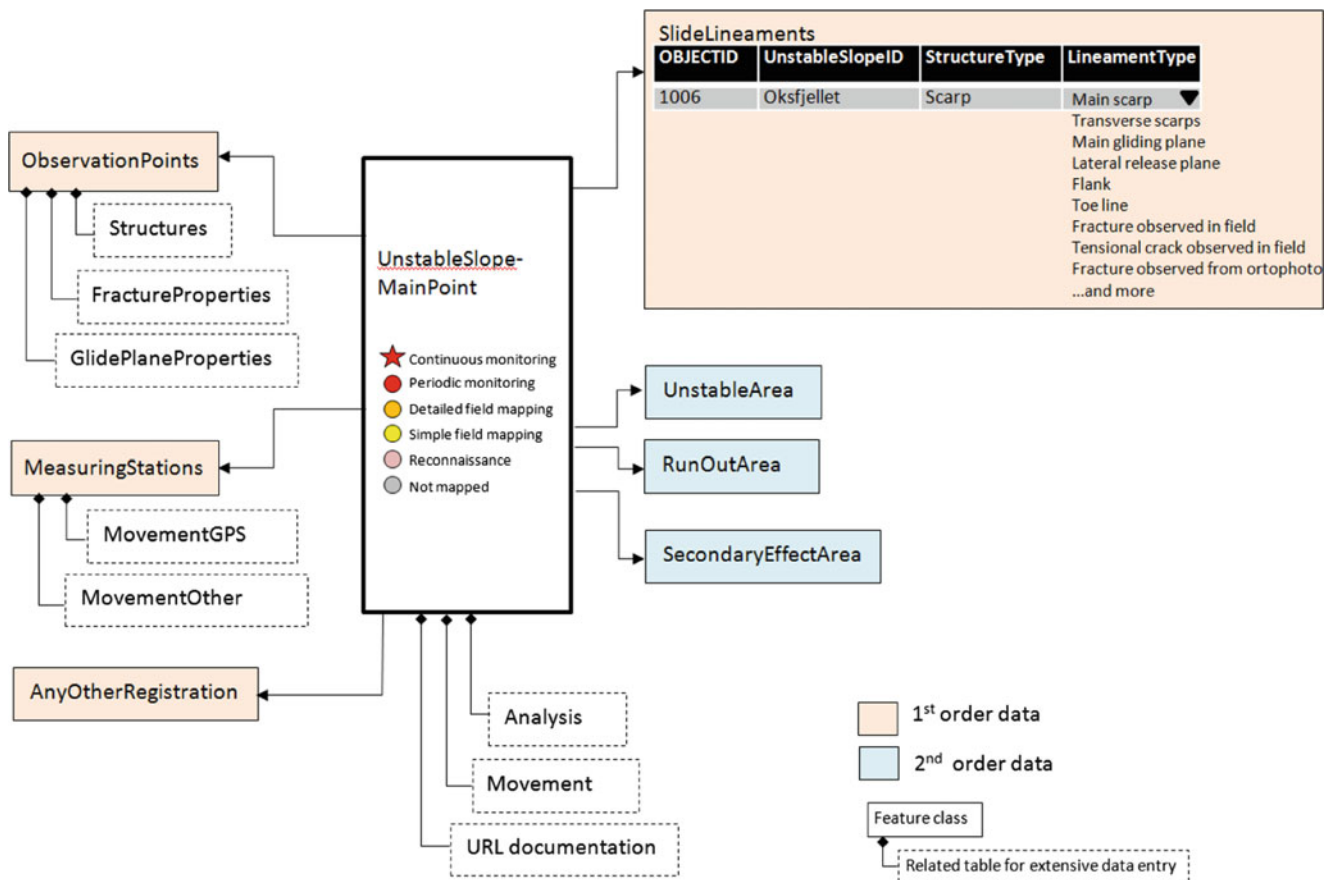


Fig. 2 Structure of the database with feature classes, tables and relations. Feature classes store spatial information with attributes. Tables are used when many-to-one relations are needed for data

entry. Also shown is an example of the feature class “SlideLineaments” with a few of the attributes and the associated drop-down list for the attribute “LineamentType”

user. This strengthens the homogeneity of the database content and the possibilities to execute effective searches. Detailed data are stored in the feature classes for geometric objects, and plain tables for other related information linked to the main point. Additional data such as bathymetry, high resolution DEMs, InSAR data and/or TLS data and more are also stored with links as attributes to the main point object. The three tables linked to the main point (Fig. 2) include data from analysis of the unstable slope in general. Analysis of georadar, seismic surveys, resistivity, hydrological studies and climatic surveys are examples of this. There is also a table for the analysis results of the movement of the unstable slope. The table for URL documentation provides links to additional data, such as geological reports, journal papers, online map services etc.

First Order Data

All data that are collected in the field, from remote sensing or by displacement measurements are regarded as 1st order data. These data are stored in the feature classes “ObservationPoints”, “MeasuringStations”, “SlideLineaments” and

“AnyOtherRegistration”. The feature class “UnstableSlope-MainPoint” also includes some 1st order data.

The feature class “Observation points” contains all observations made in the field (e.g. orientation and displacement measurements on fractures, faults and sliding surfaces, sink holes or any other structural or morphologic point data). Tables such as e.g. “Structures” are used when the collected data need to be stored in a one-to-many relation, such as when measuring numerous orientation data at one specific point in space. Data input for attributes in the tables are also constrained by drop-down lists where found useful. The feature class “Slide lineaments” contains structural or morphological lineaments within the slide area or in its vicinity. The feature class “MeasuringStations” contains data from dGPS measurements, extensometers, TLS data and more. The feature class “AnyOtherRegistration” is intended for storing data temporarily in the field that do not naturally belong in any other feature class. This feature class may be removed in the future, when the current database structure by experience has matured to a final well working structure.

Table 1 Content of the “UnstableSlopeMainPoint” attribute table. The use of drop-down lists ensures a consistent data entry

Attribute	Description
UnstableSlopeID	Manually assigned according to local number system
UnstableSlopeName	Defined by nearest place name from 1:50,000 national map series
MappingLevel	Drop-down list. See legend Fig. 1
CommentField	Any site-specific general comments
MeasuringMethod	Drop-down list. Describe how the object is mapped or digitized
dGPS surveillance	Yes/no
Terrestrial laser scanning surveillance	Yes/no
Terrestrial radar surveillance	Yes/no
Recognizable	Drop-down list. Describes how visible the object is in the field or on aerial photos.
DipDirectionSlope	Drop-down list. N, NE, E, SE, S, SW, W, NW, Varying
DipDirectionLandslide	Drop-down list. N, NE, E, SE, S, SW, W, NW, Varying
SlideRelief	Vertical height from run-out area to back scarp in meters
SlopeDipAvg	Average dip of unstable slope in degrees
SlopeDipMax	Steepest dip of unstable slope
SlopeDipMin	Least dip of unstable slope
CommentSlope	Descriptive comment field
MainRockType	Drop-down list of pre-defined rock types from bedrock database
VolumeMax	Maximum estimated volume of unstable area
VolumeProbable	Probable (mean) estimated volume of unstable area
VolumeMin	Minimum estimated volume of unstable area
MovementType	Drop-down list of different movement types (planar, wedge, toppling, rotation, creep, unknown)
CommentMovement	Comment field to enter additional text for each object if needed.
MovementTypeFailure	Drop-down list of movement types during failure (planar, wedge, toppling, rotation, creep, flow, fall)
CommentMovementTypeFailure	Comment field to enter additional text for each object if needed.
DeformationType	Drop-down list (undulating, stepwise, open cracks, talus)
CommentDeformationType	Comment field to enter additional text for each object if needed.
DeformationAmount	Drop-down list (No deformation, small, medium, large, very large)
CommentDeformationAmount	Comment field to enter additional text for each object if needed.
RunOutMax	Maximum assumed run-out distance (meters)
RunOutMean	Intermediate assumed run-out distance (meters)
RunOutMin	Minimum assumed run-out distance (meters)
SecondaryEffectType	Drop-down list (tsunami, damming, dam breach/flood, none)
ImpactAreaType	Drop-down list (water, land)
HazardDegree	Drop-down list (very high, high, moderate, small, very small, not estimated). According to return period thresholds given in the Norwegian Building Act ranging from <100 years to >10,000 years
Consequence	Drop-down list (Extreme, very high, high, medium, small to none)
CommentConsequence	Comment field to enter additional text for each object if needed.
References	Text field. May be linked to table for multiple references.
Documentation	Text field. May be linked to table for multiple documents.
Illustration	Text field. May be linked to table for multiple documents.
DEM_link	Text field. Hyperlink to map view of unstable slope visualized within www.norgei3d.no digital globe
Date	Date of discovery
County	County where the unstable slope is located
Municipality	Municipality where the unstable slope is located
Geologist	Geologist responsible for detection and mapping of the unstable slope

Second Order Data

Results from analysis of the 1st order data are regarded as 2nd order data. There are three 2nd order feature classes: “UnstableArea,” “RunOutArea” and “Secondary-EffectArea.” Each unstable slope is represented by a polygon “UnstableArea” in addition to the “UnstableSlope-MainPoint.” This polygon is based on the mapped

lineaments “SlideLineaments” and a result of processing and analysis of all available data. If necessary can an unstable area be divided into several sub-areas due to differing kinematic properties, by creating several polygons for each sub-area in the “UnstableArea” feature class.

When a run-out assessment has been carried out, the polygons describing the run-out areas are stored in the

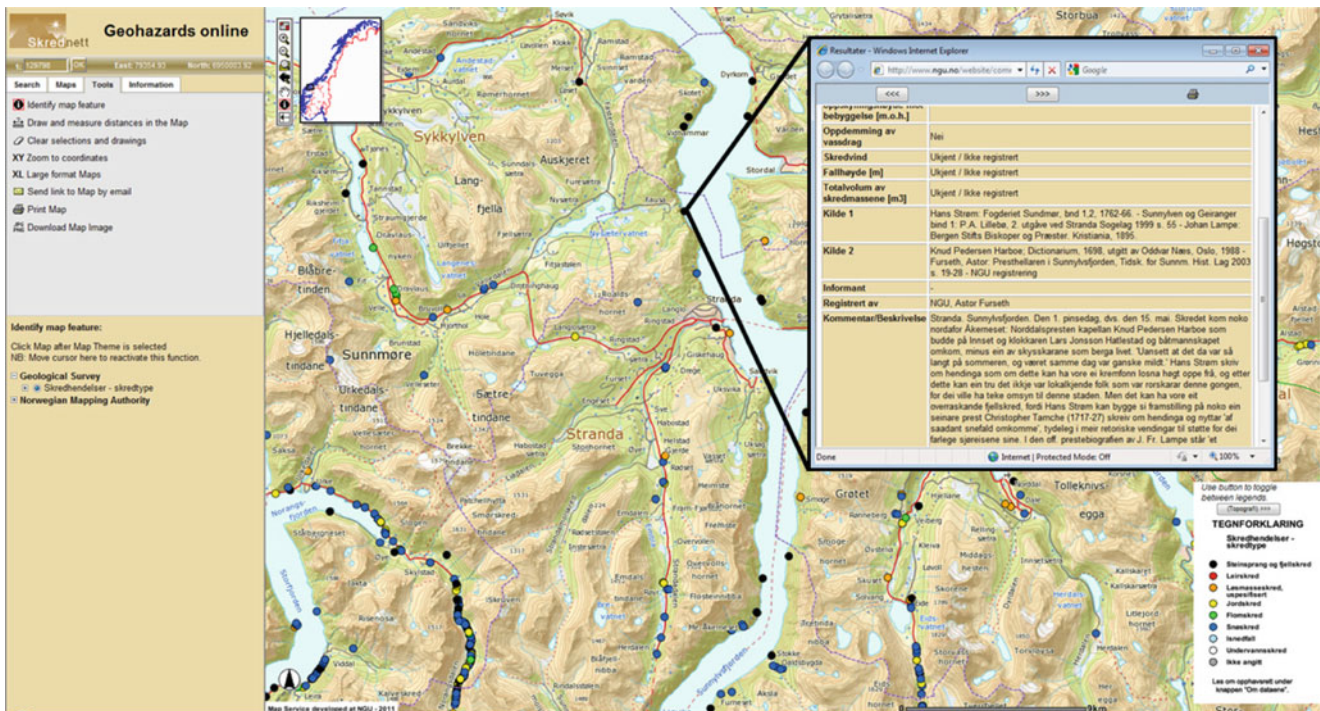


Fig. 3 Screen shot from www.skrednett.no, the national web page for online access to the Norwegian landslide database (Skrednett 2011). The displayed map shows all registered landslides in the selected area subdivided by landslide type. By clicking on the main point, a pop-up

box displays a selection of the content of the attribute tables of the feature classes. The planned online web service for the unstable slopes database will provide similar services

RunOutArea feature class. Information is mainly added by use of pre-defined drop-down lists to ensure consistent data entries. Comment fields are made available to provide space for additional information. Data such as type of area, probability, hazard level, tsunami and damming analysis are added. For areas exposed to threats by secondary effects such as e.g. dam breach, air pressure waves and tsunamis, polygons are created and stored in the SecondaryEffectArea feature class. The main results from the 2nd order feature classes are also included in the attribute table of "UnstableSlopeMainPoint" (Table 1).

Practical Use

National Archive

The database is designed to store a comprehensive dataset from each unstable slope. The input data include all registered field data and all processed data, both 1st and 2nd order data. The content of the database will be public available. The amounts of data that will be presented differ depending on the purpose of the request. For aerial planning, risk and hazard analysis, mitigation work and research

purposes, both 1st and 2nd order data are available. On the online web service that will be made available from the website of the Geological Survey of Norway with the main purpose to serve municipalities and the ordinary citizens, only the feature classes "UnstableSlopeMainPoints" and "UnstableArea" will be available for display on screen.

Field Database

For field mapping purposes a reduced version of the database structure with easy to use drop down menus has been extracted from the structure of the full database. The field database consists of the 1st order data feature classes. Experience has shown that the drop-down lists and attribute tables for each feature class should not be too comprehensive, as very large tables or drop-down lists make the work flow in field less smooth and reduces the effective time spent for measuring and registering of data. To enhance the fieldwork, background information such as e.g. high-detailed orthophoto of the field area, DEMs, bathymetric and seismic fjord data, InSAR data and more are made available in a package with the data model.

Online Web Service

Through the online web service, the feature classes “UnstableMainPoint,” “MeasuringStation” and “UnstableArea” will be selectable for visualization on screen. The content of the attribute tables may be investigated by the user through pop-up information sheets (Fig. 3), and hyperlinks provide access to graphical displays of data such as dGPS measurement results. Hyperlinks are also planned to be used to guide the user to a visualization of the unstable slope on a 3D digital terrain model with draped orthophoto using www.norgei3d.no, or provide direct download of reports related to the selected unstable slope from the web page of the Geological Survey of Norway. Finally, the public part of the data will be downloadable free of charge from the online web service.

Conclusion

The above described database for unstable rock slopes in Norway is planned published on the internet late 2011/early 2012. The database will serve three main purposes: (1) to serve as a national archive for potential unstable slopes for use in hazard and risk analysis, aerial planning and mitigation work as well as research; (2) to serve as a robust and easy to use database during field mapping of unstable rock slopes; (3) provide a public available database accessible through an online web map service. Different user interfaces with varying levels of access both for data entry and data extraction are defined, depending for which of the above goals the user interface is intended for. Extensive use of drop-down menus during ensures consistency of data during data entry. The database interact through hyperlinks with several other web resources such as for example a public available 3-D terrain model, allowing the user to explore the unstable slopes in three dimensions. All access will be free of charge.

Acknowledgments The development of the database of unstable slopes in Norway is through collaboration between the Norwegian Geological Survey (NGU) and the Norwegian Water Resources and Energy Directorate (NVE). The project is fully financed by NVE.

References

- Blikra LH, (2008) The Åknes rockslide; monitoring, threshold values and early-warning. In: Zuyu C, Jian-Min Z, Ken H, Fa-Quan W, Zhong-Kui L (eds). Landslides and engineered slopes. From the past to the future. Proceedings of the 10th international symposium on landslides and engineered slopes, Taylor and Francis, Xi'an, China, June 30–July 4 2008, pp 1089–1094
- Blikra LH, Longva O, Harbitz C, Løvholt F (2005) Quantification of rock-avalanche and tsunami hazard in Storfjorden, Western Norway. In: Senneset K, Flaate K, Larsen JO (eds) Landslides and avalanches: ICFL 2005 Norway. Taylor & Francis, London, pp 57–64
- Bunkholt H, Osmundsen PT, Redfield T, Oppikofer T, Eiken T, L'Heureux J-S, Hermanns R L, Lauknes TR (2011) ROS Fjellskred i Troms: status og analyser etter feltarbeid 2010. NGU rapport 2011.031, p 135
- Furseth A (2006) Skredulykker i Norge. Tun Forlag, Oslo, p 207
- Henderson IHC, Saintot A (2011) Regional spatial variations in rockslide distribution from structural geology ranking: an example from Storfjorden, Western Norway. In: Jaboyedoff M (ed) Slope tectonics, vol 351, Geological society, Special publication. Geological Society, London, pp 79–96
- Hermanns RL, Bunkholt H, Böhme M, Fischer L, Oppikofer T, Rønning JS, Eiken T (2011) Foreløpig fare- og risikovurdering av ustabile fjellparti ved Joasete-Furenkamben-Ramnanosi, Aurland kommune. NGU rapport 2011.025. (ISSN 0800–3416). p 47
- Hermanns RL, Blikra LH, Anda E, Saintot A, Dahle H, Oppikofer T, Fischer L, Bunkholt H, Böhme M, Dehls JF, Lauknes TR, Redfield T, Osmundsen PT, Eiken T (2011). Systematic mapping of large unstable rock slopes in Norway. Proceedings of the second world landslide forum – 3–7 Oct 2011, Rome. This volume
- Høst J (2006) Store fjellskred i Norge. Utredning for Landbruks- og matdepartementet på vegne av 6 departementer. NGU rapport. Geological Survey of Norway, Trondheim. p 87
- Lauknes TR, Piyush Shanker A, Dehls J, Zebker HA, Henderson IHC, Larsen Y (2010) Detailed rockslide mapping in northern Norway with small baseline and persistent scatterer interferometric SAR time series methods. Remote Sens Environ 114:2097–2109
- Oppikofer T, Jaboyedoff M, Blikra LH, Derron M-H (2009) Characterization and monitoring of the Åknes rockslide using terrestrial laser scanning. Natural Hazards Earth Syst Sci 9:1003–1019
- Saintot A, Henderson IHC, Derron M-H (2011) Inheritance of ductile and brittle structures in the development of large rock slope instabilities: examples from Western Norway. In: Jaboyedoff M (ed) Slope tectonics, vol 351, Geological society, special publication. Geological Society, London, pp 27–78
- Skrednett (2011) National online web service for geohazards. <http://www.skrednett.no>. Accessed 10 June 2011



Landslides and Spatio-Temporal Processing of Geographical Information

Raffaele De Amicis, Federico Prandi, Giuseppe Conti, Diego Taglioni, Stefano Piffer, Marco Calderan, and Alberto Debiasi

Abstract

This paper presents the first relevant results of the project BRISEIDE – BRIDging Services, Information and Data for Europe. BRISEIDE aims at providing operators with a time-aware extension of data models and value added services for spatio-temporal data management, authoring, processing, analysis and interactive visualization in several emergency-related scenarios including, most notably, landslides. Within this context a number of WPSs devoted to spatial analysis have been developed and integrated within existing open source frameworks. Spatio-temporal processing services are exposed via the web and are made available through compatible WebGIS applications. Through BRISEIDE, operators can access processing services through an interactive web-based 3D GeoBrowser capable to allow management, authoring, interaction, filtering of existing data. The 3D GeoBrowser allows interactive orchestration of spatio-temporal WPSs providing support to chaining of required processing units. This ensures interactive access to datasets and asynchronous processing at the server side. The project mobilizes a value-chain of stakeholders to validate the pilots from a technical, organizational and legal standpoint.

Keywords

Simulation • Spatio-temporal analysis • GIS • SDI • 3D geobrowser

Introduction

Operators of civil protection agencies and other Public Administrations (PAs) involved in environmental monitoring and management need to access complex spatio-temporal processing features based on Geographic Information (GI). These functionalities should be designed to fit their operational workflow to better support them in terms of decision-making, planning, training as well as in case of emergency. This requires accessing and filtering of GI that refer to a given spatial location through tools capable to match both the temporal coverage of interest as well as the required temporal resolution.

In fact monitoring and mitigation of natural disasters often requires using geospatial technologies typically through client–server infrastructures known as Spatial Data Infrastructures (SDIs). From a technical standpoint, SDIs are often deployed through a federation of interoperable web-services capable to ensure provision of geospatial information through the network, from either a GIS or WebGIS software. However SDIs typically fall short when operators are required to deal with frequently updated repositories and highly dynamic data.

This is typically the case of operators dealing with landslides who need to gain situation awareness and knowledge both in terms of real-time data (from sensor networks and monitoring systems) as well as in terms of previously available information regarding the history of displacements of the site.

It is particularly important for operators to be able access data repositories, usually available through various sources,

R. De Amicis (✉) • F. Prandi • G. Conti • D. Taglioni • S. Piffer • M. Calderan • A. Debiasi
Fondazione Graphitech, Trento, Italy
e-mail: raffaele.de.amicis@graphitech.it

within a single interface and to be able to invoke, in a user-friendly manner, processing functionalities that can help them infer the knowledge required to better understand the phenomena and take the most appropriate decision.

However this requires reconsidering standard data and metadata models, in order to be able to account for time as one of the main variables within a multi-fold representation of all three aspects of the geographical data: thematic, temporal and spatial.

This goal has been at the basis of the project BRISEIDE – BRIDging SErVICES, Information and Data for Europe, a Pilot B project, funded by the ICT Policy Support Programme (ICT PSP). BRISEIDE extends the standard concept of Spatial Data Infrastructure (SDI) to provide operators with more complete and adequate data and processing tools capable to handle the time dimension in several emergency-related scenarios including, most notably, landslides. To do so the project has developed a number of Web Processing Services (WPS) for spatial analysis and it has integrated them within an extended SDI to be used by civil protection operator to better assess risks related to landslides.

State of the Art

Never before has been so much focus and attention on the movements of the Earth and natural hazards these produce. The need to better understand the effects of anthropic activities on the natural environment is nowadays a very urgent matter. In environmental hazard monitoring and risk management this task requires a broad-scale process analysis in order to better understand the phenomena and the related risks. From many years several models for landslide hazard prediction has been developed (Brenning 2005) also considering the GIS analysis (Dai and lee 2002; Xie et al. 2009). In the last years with the spread of the broadband technology and of the SDI the capabilities to allow the access of these analyses is increased (Ambrosanio et al. 2009). These models and infrastructures are in substantially static, in other words they tend to photograph a situation in a specific instant. However many studies and models has been proposed in order to manage the spatio-temporal complexity of the natural phenomena (Peuquet and Duan 1995). The capability to transports these theory models into a services oriented architecture applied to the landslide analysis is the aim of this work.

Spatio Temporal-Management

This research work analysis the three central issues typical of spatio-temporal management. The first concerns the definition of the metadata model describing the temporal properties of the data; with regard to this, an extension of

the current models has been preformed to ensure a complete description of the different types of time properties by extend the INSPIRE metadata profile (for both data and services), considering the elements contained in the ISO 19115 specifications.

The second pivotal issue is related to the process functionalities involving time as dimension. In particular BRISEIDE has developed a number of processing features that can be used to process or relate time with space features. This has required considering both time as a magnitude, for instance the time required to move along a path, and as a temporal series, for instance when considering changes in observations over time. The resulting BRISEIDE infrastructure includes: ingestion services (necessary to automatically populate data repositories, define relevant metadata and ensure proper cataloguing), dissemination and portrayal services (for feature, coverage and raster data access via, respectively WFS – Web Feature Service, WCS – Web Coverage Service and WMS – Web Map Service protocol), sensor enablement services (providing observation and measurements via standard protocol SOS – Sensor Observation Service), and eventually processing service (as WPS – Web Processing Service).

The latter have been divided into processing services providing topological, statistical, change detection, transformation (e.g. re-projection) and raster algebra features.

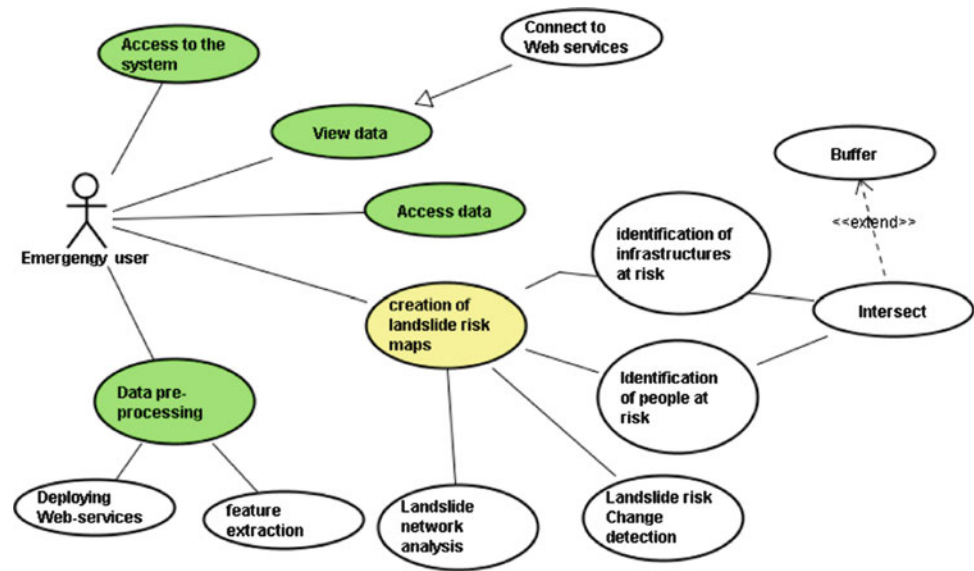
It should be noted that support for time as dimension has required development of specific software components capable to provide support to the features, already included within the WMS, WCS and WFS standards, necessary to manage time and space information.

The last issue regards the visualization of the results. This has required development of a 4D framework capable to provide access to advanced representations of temporal analysis through Geovisual Analytics tools. To do so a double approach has been considered. On the one hand the project has foreseen the deployment of a ready-to-use SDI platform, which could be used to quickly validate and access existing data. On the other hand the project has carried on a comprehensive development activities that has brought to the development of a powerful 3D Client capable to provide access to the aforementioned spatio-temporal services.

Overall Approach Used

The overall approach adopted is based on the concept of federated infrastructure whereby a client, in this case a 3D web-based client, accesses a number of web services over the network. These provide both access to data of various nature (raster, coverage, vector, sensor data etc.) as well as to processing features through interoperable standards.

Fig. 1 An example of UML diagram of the use case addressed



This way the operator can perform complex processing operation by invoking processing functionalities at the server side. This approach, based on Web Process Service (WPS) protocol, ensures maximum flexibility as the processing features are centralised and can be managed consistently at the server level. Being this done in an interoperable manner, any processing functionalities can be accessed by any GIS or Web GIS application complying with the given standard adopted (in this case WPS from OGC – Open Geospatial Consortium).

The Use Case Addressed

The typical actor of the use case analyses is a civil protection operator who needs to be able to access, via interoperable web-services, to a wide range of resources, stored within federated databases, relative to a selected NUTS3 area, and to run a simulation/calculation on top of them.

In particular, as visible in Fig. 1, which shows one of the examples of use cases identified modelled in UML, these regard the assessment of landslide risk through use of geo-processing tools.

This assessment is to be performed on two time scales: short-term assessment, typical of Civil Protection situations, in order to assess and possibly reduce the impact of a landslide (in terms of life claimed, damages created etc.), and long-term assessment, in order to provide information useful for planning purposes, based on data elaboration and analysis. The use case has essentially to goals. The first is to create a landslide risk map through the intersection of areas potentially affected by landslides with the areas where element of risks are located (houses, roads etc.). The second

goal is to identify the portions of the transportation network potentially affected by a landslide and to identify, if any, alternative routing solutions to be adopted by emergency vehicles during a crisis or in the aftermath of a landslide.

Information Used for the Analysis

The data which the operators need to access include: the IFFI dataset (the Italian landslides inventory), the Digital Terrain Model (DTM) at 20 m resolution, the road network (as OpenStreetMap), the railway network, water pipelines, census data as well as several Corine Land Cover (CLC) datasets at different time series (code 1.1.1: Artificial surfaces, Continuous urban fabric; code 1.1.2: Corine Land Cover – Artificial surfaces, Discontinuous urban fabric; code 1.2.1: Corine Land Cover – Artificial surfaces, Industrial, commercial and transport units; code 122: Corine Land Cover – Artificial surfaces, Road and rail networks and associated land).

Data Preparation

After starting a 3D client, the operator selects the area of interest and then visualises the layers containing the information needed. The operators then can adapt existing datasets through the use of specific services for instance to perform format translation, data re-projection etc. Following this the user has to select, in a very interactive manner from a library containing geo-processing functionalities, the simulation and processing tools needed either for tasks in the context of an emergency or to run a simulation.

Identification of Transport Infrastructure at Risk

As soon as the user starts the 3D BRISEIDE client he/she flies to the area of interest (a NUTS3 area). The operator then activates a number of layers corresponding to other resources representing infrastructure potentially subject of risk including main railways and road networks. The user then selects a processing feature responsible for buffering to create a buffer area (e.g. 100 m) surrounding roads and railways. The resulting geometries are again shown as a further layer and stored within the repository.

After activating the layer containing the landslide area, as a further step, the operator selects the processing functionality responsible to calculate geometrical intersections among areas and it connects the simulation component to the landslides areas and the buffer zones. The resulting intersections are the areas potentially subject to risk. The user can eventually pick on the various segments of road or railways, within the areas at risk, and identify the attribute of interest that are shown within a table.

Identification of Urban Area at Risk

The operator then selects the relevant CLC resources at different time series from a table of content (TOC). Through the use of a web-processing service the operator identifies the boundaries of continuous or discontinuous urban areas as well as commercial or industrial areas. This first dataset represents the first element of risk, which are then structured within a new layer and saved to the repository. It should be noted that, in order to improve system performances, the feature extraction process could be performed off-line as pre-processing step. Through the use of the aforementioned intersection operator, the operator can easily identify those urban areas which are subject to risk. These areas are shown within a new layer and then stored within the database.

Identification of People at Risk

The user then selects a web-processing service that calculates the number of people potentially living within the areas at risk starting from census data according to the percentage of census area subject to risk. The final result is shown as chart or table.

Reachability Assessment

The operator finally assesses the connectivity (in terms of road) between any two points within the road network (e.g. two villages) that can be affected by the landslide. To do so,

the operators, after selecting the routing functionality, clicks on two points of the scene corresponding to the two locations. The system calculates the route and shows in on top of the current scene. The user can also connect the areas subject to landslides to the routing algorithm to specify the areas to be avoided during the routing. The final result (if available) is then rendered on top of the scene.

The Front-End System

From a user perspective the operator can use a 3D client which has been developed on top of uDig, which in turns is built over the Eclipse Framework. uDig is an advanced and complete desktop GIS for data access, editing and viewing, integrating advanced GIS capabilities through the well-known Geotools library. uDig provides a user friendly graphical desktop environment to manage GIS data with a web oriented vocation compliant with well-established OGC standards like WMS, WFS, WCS as well as georSS, KML etc. More specifically the client has been developed following a plug-in approach, whereby each is an extension points which define possibilities for functionality contributions (code and non-code) by other plug-ins. Each plug-in has an associated view, in particular a component of the Graphical User Interface. By default the client shows the central area where the 2D and 3D views are available.

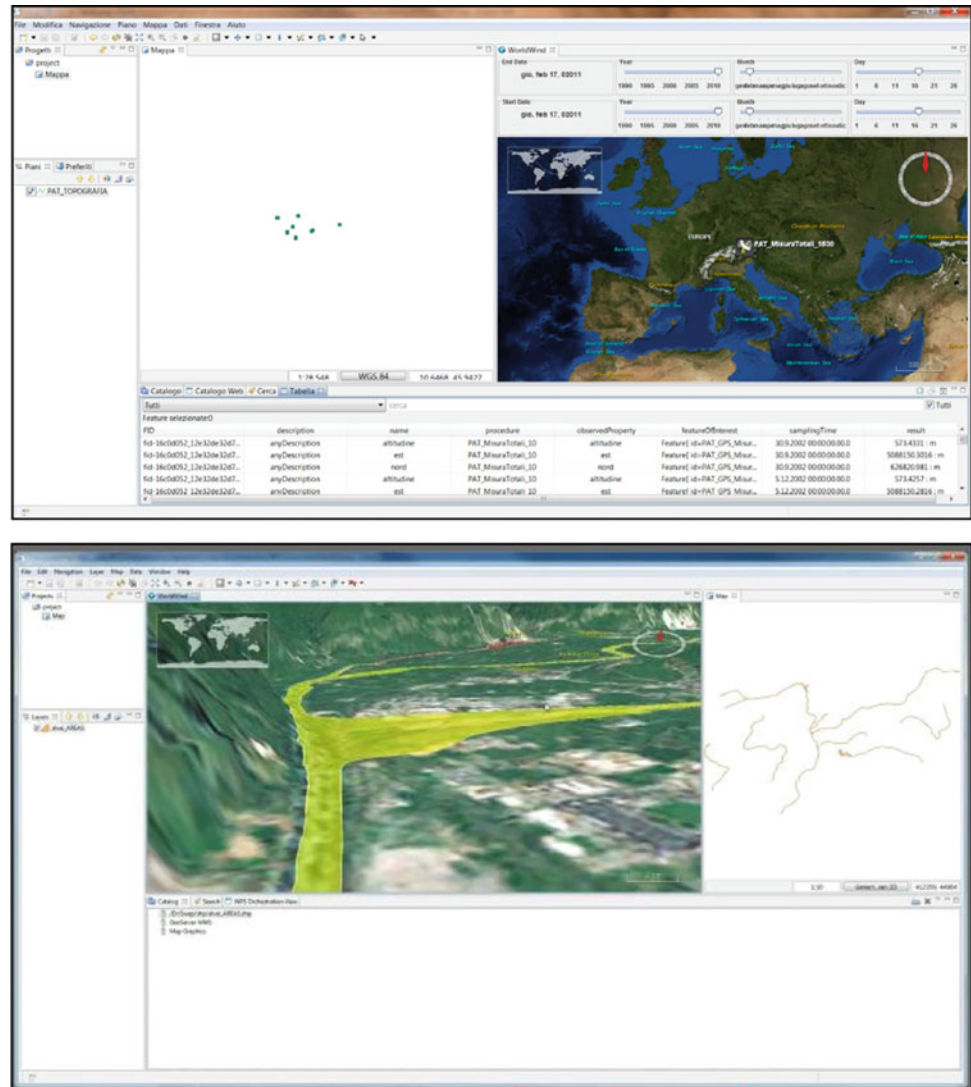
At the bottom of the page a panel providing logging functionalities is provided. On one of the sides of the interface it the user can access the resources available to the system. These include available data and services, table of content, access to metadata information through tables etc.

A further section will be devoted to service orchestration. As illustrated in Fig. 2, this approach allows different graphical components to be plugged together. Each service can be rendered as a graphical component, formatted according to the type of service (e.g. WPS, WFS etc.), to the input required as well as to the output provided.

Most notably the operator can access processing functionality in a graphical manner by connecting server-side processing units at the client side. In fact the user is able to connect graphically compatible input and output which will be snapped by the system automatically (if compatible data-wise), whenever the user drags them close to one another. This way it is possible to create complex service chains in a very user friendly manner without the user being forced to be aware of the underlying infrastructure. The user can then run the corresponding processing sequence, while the orchestration components take care of all the overhead and underlying communication.

Finally the remaining part of the interface is devoted to the different software components responsible for visualizing different data patterns.

Fig. 2 Two images of the client. As visible from the screenshots the client is composed of many panels to ensure access to various types of data, including a 3D window which can be used to interactively navigate the data repositories



Conclusions

BRISEIDE is deploying several operational pilots addressing civil protection scenarios and environmental risk management, including landslide risk, whereby operators can access processing services through an interactive web-based 3D client capable to allow management, authoring, interaction, filtering of existing data through orchestration of web processing services.

The project mobilizes a value-chain of stakeholders to validate the pilots from a technical, organizational and legal standpoint. Most relevantly the services deployed in the context of BRISEIDE will be used for 12 months, starting from the end of summer 2011, by operators at

ISPRA the Italian National Institute for the Protection and Environmental Research, within operational scenarios to better plan and coordinate response to emergencies caused by landslides.

Acknowledgments The work described within this paper has been carried on in the context of the project BRISEIDE, which is partially funded under the ICT Policy Support Programme (ICT PSP) as part of the Competitiveness and Innovation Framework Programme of the EC (http://ec.europa.eu/ict_psp). This publication reflects the views only of the author, and the European Commission cannot be held responsible for any use which may be made of the information contained therein. The authors wish to thank the L. Guerrieri, D. Spizzichino, A. Trigila, C. Iadanza, C. Margottini, D. Fiorenza, E. Vittori, G. Delmonaco from ISPRA the Italian National Institute for the Protection and Environmental Research, for their support to the activities described within this paper.

References

- Ambrosanio M, Ioannilli M, Paregiani A (2009) A new approach to risk assessment from the civil protection perspective. In: Scarlatti F, Rabino G (eds) *Advances in models and methods for planning*. Pitagora Editrice, Bologna, pp 201–210
- Brenning A. (2005) Spatial prediction models for landslide hazards: review, comparison and evaluation. *Nat Hazard Earth Syst Sci* 5:853–862, 2005 SRef-ID: 1684-9981/nhess/2005-5-853
- Dai FC, Lee CF (2002) Landslide characteristics and slope instability modeling using GIS, Lantau Island, Hong Kong. *Geomorphology* 42:213–228
- Peuquet DJ, Duan N (1995) An event-based spatiotemporal data model (ESTDM) for temporal analysis of geographical data. *Int J Geogr Inf Sci* 9(1):7–24
- Xie M, Qiu C, Liu X (2009) GIS-based 3D spatial-temporal assessment of landslide hazard. *Geophys Res Abstr* 11:EGU2009-13511



Lahar, Floods and Debris Flows Resulting from the 2010 Eruption of Eyjafjallajökull: Observations, Mapping, and Modelling

Esther H. Jensen, Jon Kr. Helgason, Sigurjón Einarsson, Gudrun Sverrisdóttir, Armann Höskuldsson, and Björn Oddsson

Abstract

Historic, post-eruptive debris flows of remobilised volcanic ash are rare in Iceland, being restricted to explosive eruptions. Volcanic ash slurry from the southern slopes of the ice-capped Eyjafjallajökull volcano on 19 May 2010 is the first lahar observed in Iceland since the 1947 Hekla eruption. This study focuses on the volume of sediment transported, the size and hydrological behavior of watersheds, and the resulting erosion. The analysis is based on: (1) direct measurements of the 19 May lahar; (2) direct measurements of ash fallout; (3) aerial and ground-based imagery; (4) topographic data from an airborne LIDAR survey; (5) airborne synthetic-aperture radar; and (6) precipitation data. The volume of the lahar in the Svaðbælisá channel was estimated at 200,000 m³. This flow originated from crown and flank failures, similar to slab avalanches, with water-saturated, fine-grained ash as the slip surface. Several ash-laden floods occurred in Svaðbælisá and neighboring channels during the summer of 2010. None, however, were as saturated as the 19 May lahar. An increased number of small debris flows were also recorded some blocking roads to farms. Precipitation during the summer of 2010 was not higher than average and therefore does not explain this increased erosion. Large quantities of volcanic ash mantle the lower slopes of the ice-cap. Ash in the ablation zone is expected to be transferred down-slope in the next few years inducing the erosion to the root of the mountain endangering homes and infrastructure. Fieldwork during the summer of 2010 has resulted in a map showing the volume of ash above and below the ablation zone of the main catchments and recorded erosion events. This data was used to assess the hazard and the need for immediate actions.

Keywords

Volcanic eruption • Lahar • Debris flows • Floods • Ash volume • LIDAR • Radar imagery

E.H. Jensen (✉) • J.K. Helgason
Icelandic Meteorological Office, Bústaðavegur 9,150, Reykjavík,
Iceland
e-mail: esther@vedur.is

S. Einarsson
Soil Conservation Service of Iceland, 851 Hella, Iceland

G. Sverrisdóttir • A. Höskuldsson • B. Oddsson
Institute of Earth Sciences, University of Iceland, 101 Reykjavík,
Iceland

Introduction

Post-eruptive debris flows of remobilised volcanic ash are rare in Iceland in historic time, being restricted to explosive eruptions. Slurry of volcanic ash from the southern slopes of the ice-capped Eyjafjallajökull volcano on 19 May 2010 is the first lahar observed in Iceland since the 1947 Hekla eruption. The eruption in Eyjafjallajökull lasted about 40 days resulting in ash covered hillsides. Problems with increased flooding and debris flows evoke the need for thorough analyses of the situation.

Methods

The analyses aimed at estimating the possibilities of lahars and increased landslide danger. It was based on:

- Direct measurements of ash fallout; Distribution map of ash fallout was made from ground measurements during the summer 2010. Volume calculations were made using ArcGIS-Spatial Analyst based on catchment delineation made with ArcHydro tools.
- Direct measurements of the 19 May lahar; Field survey made shortly after the flood.
- Aerial and ground-based imagery; High resolution aerial photographs from Samsýn Ehf., SPOT5 satellite images and photos taken during field trips.
- Topographic data from an airborne LIDAR survey; A high resolution digital elevation model.
- Airborne synthetic-aperture radar; Icelandic coast guard aircraft TF-Sif (Dash8) equipped with a Side looking radar (SLAR). Images were taken during the eruption.
- Precipitation data; Two rain gauges to the south and west of the volcano where mainly used for analyzing the rain-fall “threshold”.

The south side of the volcano an inhabited area and therefore the focus in this study was only there.

Ash Distribution

An explosive eruption in Eyjafjallajökull 2010 started on 14 April. On 17 April the explosive activity was intense and extremely fine ash settled in a large quantity on the south flanks of the volcano, partly by base surges. The ashfall continued for a month in varying wind directions, but far the most accumulation of tephra was on the south and east flanks of the volcano.

An estimated 25 mi. m³ of lava and 140 million m³ of ash was expected to have broken out in the Eyjafjallajökull eruption. The thickest ash fell on the glacier by the crater, up to several tens of meters thick. Ash distribution map was used in order to estimate the thickness of the tephra in each river basin. Basins were divided into three categories; areas above and below the equilibrium line and the area below the terminus. On the south side the largest river basins are Kaldaklifsá (37 km²), Skógaá (36 km²), Íra (20 km²), Laugará (18 km²), Miðskálaá (18 km²), Holtsá (18 km²) and Svaðbælisá (15 km²), all of the southern side of the glacier. Fig. 1 and Table 1 show the distribution and volume of tephra in the catchments.

According to volume calculations of tephra over one third of the approximately 140 mi. m³ of ash that submerged during the eruption fell into river basins on the glacier Eyjafjallajökull or about 54 million. m³. About 70 % of the

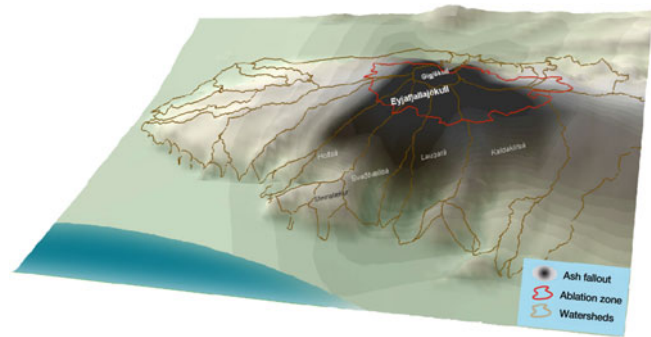


Fig. 1 Ash fallout, ablation zone and watershed of Eyjafjallajökull

ash, or about 38 mi. m³, fell above the equilibrium line of the glacier. The majority of the content, or nearly 70 % fell within the catchment area of Gígjökull, or about 26 mi. m³, mostly around the crater. Below the equilibrium line fell more than 16 mi. m³, or about 30 % of the ash that fell on the glacier and its foot hills. Looking specifically at the river basin where lahar, debris flow and flood have been frequent after the eruption and influencing the communities and infrastructure south of the glacier, shows that about 8 mi. m³, or 20 % of tephra that fell above the equilibrium line, fell in the river Holtsá, Svaðbælisá, Laugará and Kaldaklifsá. More than 3 mi. m³, or about 70 % of the material that fell below the equilibrium line fell within these catchment areas and more than 5 mi. m³, or 50 % of the material that fell on the foot hills of the mountain, landed within these catchments and the catchment of Lambafellsá (a subcatchment of Svaðbælisá) (Table 1).

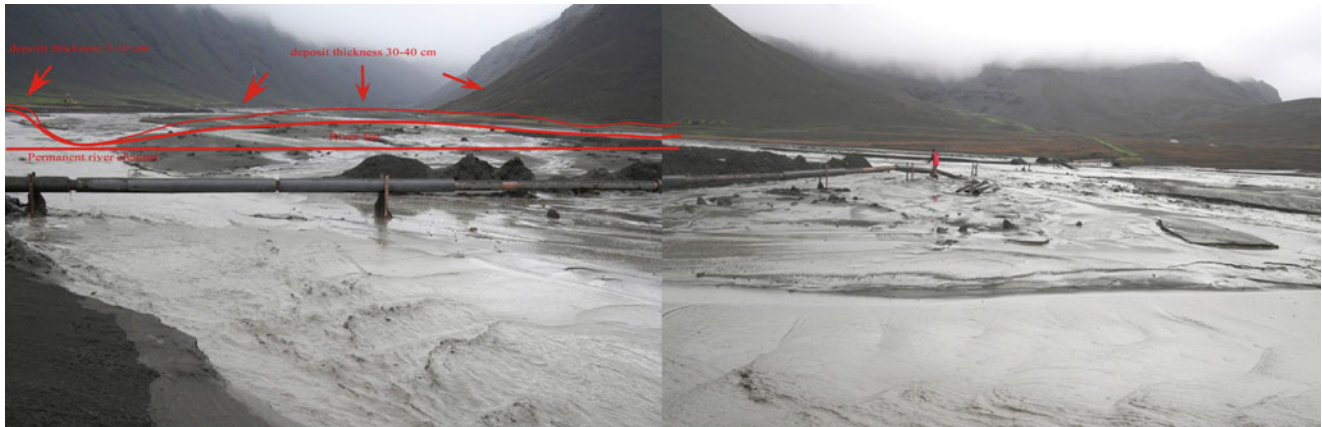
Direct Measurements of the 19 May Lahar

The night before May 19th, the first considerable rain for weeks occurred in the area south of the volcano. The rain was moderate in the inhabited area, but was presumably intense at higher elevation. All rivers draining the southern slopes of the glacier were overflowed by muddy water. In Svaðbælisá, a braided river, which drained a jökulhlaup in the beginning of the eruption, the flow was more concentrated or similar to lahar debris flow. The flow occurred in the morning and was described to have the consistency of wet cement. It reached peak discharge within an hour and was soon diluted by the river and several tributary streams. Fig. 2 is taken after the flow had receded and diluted to muddy stream flow. The photo is overlain by a schematic drawing of the lahar deposit.

The lahar on May 19. (Fig. 2) is the first lahar observed and studied by Icelandic scientists since Guðmundur Kjartanson studied a lahar in the Hekla eruption in 1947 (Guðmundur Kjartansson 1951). It was first observed by Olafur Eggertsson, a farmer in Porvaldseyri, in the river

Table 1 Volume of ash in several catchments

River basin/volume of tephra	Above abl.zone (mi. m ³)	Below abl.zone (mi. m ³)	On foot slopes (mi. m ³)	Total volume rate (%)
Kaldaklifsá	2.5	1.1	1.3	8.7
Laugará	0.8	0.6	0.3	0.6
Holtsá	1.5	0.7	1.4	6.3
Svaðbælisá	2.9	1.0	1.5	9.6
Steinalækur	0	0	0.1	0.2

**Fig. 2** Is taken after the flow had receded and diluted to muddy stream flow. The photo is overlain by a schematic drawing of the lahar deposit

course of Svaðbælisá at 09:00 am reaching the flood peak about an hour later. During the flow waves were seen in the river every 1–2 min, but the measurements and observations on lahars show that they are noticeably unstable nature and flow in pulses (Iversen 1997). During the event river constantly changed its course. Large quantities of debris were in the course of the river as a result of the glacier outburst mentioned earlier. The lahar filled the channel of Svaðbælisá and overflowed a long section of the river bank and deposited an average 30 cm thick layer in the upper 2.5 km of its lowland course. The layer was greyish, rather dense and dull, and there was no distinct layering.

During the mapping of the lahar it was difficult to distinguish between air-borne volcanic ash, a substance that came down in the jökulhlaup 14 April of similar properties and appearance tephra. Mapping revealed that about 125 thousand m³ of sludge was deposited in the channel of Svaðbælisá but it may have carried the same amount or more to the sea.

Cumulated rainfall the day prior to the flow was nearly 20 mm in Sámstaðir and the peak in the precipitation intensity was 8 h before the flood. The station does give an inadequate picture of the situation on the glacier whereas it is a few km west of it and the rain storm was a SE creating a rain shadow at the location of the rain gauge. It was not possible to use the facilities closer to the volcano since ash filled the rain gauge and distorted the measurement results.

Airborne Synthetic-Aperture Radar

The origin of the flow was first observed on a radar image taken by the Icelandic coast guard aircraft TF-Sif, on May 19th. TF-SIF is a Dash8 equipped with a Side looking radar (SLAR). The source flank of the lahar was roughly estimate to be 5 km² and a thickness of tephra that was mobilized was probably about 50 cm, or at least several tens of cm, in most part of the area. It is likely that the size of the mobile flank was in the range of millions or even several million m³. A large proportion of this ash piled up further down the glacier and a minority of the material reached all the way into the river course and down to the lowlands. This is based on the measurements of the volume of sediment deposited in the channel of Svaðbælisá and rough assessment of the probable sediment transport into the sea.

The radar image implies the source of the flood on the glacier above the heath Svaðbælisheiði in over 1,200 m above sea level, to the west of the ice channel on 14 April. (see Fig. 3).

Tephra on the Glacier

The radar images encouraged people to go up on the glacier and observe the source. During a field trip on May 25 to 26. the scrap of the lahar was measured to about 50 cm in a 25° inclination and height of the scrap was similar in other areas



Fig. 3 The image shows several sliding areas on the south slopes of the glacier. The *red lines* show contours of these areas, but the *blue* one delineates the area later verified to have fed the Svaðbælisá lahar flow

observed. The pile contained four different layers: the top layer was beaten wind shell (~4 cm thick), layer two was rough granular, and also contained a high permeability (~20–25 cm thick). Layer 3 (~16 cm thick) was fine-grained, completely saturated with water and liquefied during the smallest agitation. The fourth and bottom layer (~10 cm thick) was slightly tougher than layer 3, but fine grained anyway, but little or no water saturated. This stratification was seen on the whole southern part of the glacier in the catchments of Holtsá, Svaðbælisá and Kaldaklifsá (the river Lambafellsá does not enter the glacier and is not involved here) (Helgason and Oddsson 2010).

Precipitation and stream erosion has washed ash, to a large extent, of vast areas on the glacier's ablation area. There the glacier has deep crevices and channels and is difficult to pass. In other areas the ash was so thick that it insulated the snow and prevented melting during the summer resulting in less stream erosion. There thick layers of ash cover the winter snow of 2010. This ash is partly undisturbed dense fine layers that water seeps through. These layers can act as slip surface triggering lahars similar to the one that occurred on May 19th 2010, however, the risk of such flooding is probably much lower than during the summer of 2010.

Aerial and Ground Based Imagery

In the southern part of the glacier extensive evidence of stream erosion, on the tephra layers was observed during the field trip. Aerial photographs of Samsýn taken in July 2010 (Fig. 5e) cast a further light on the status of the tephra in the slopes of the glacier. Major changes had occurred between May and July. The radar images taken in mid-May were a few traces of tephra slab avalanches were

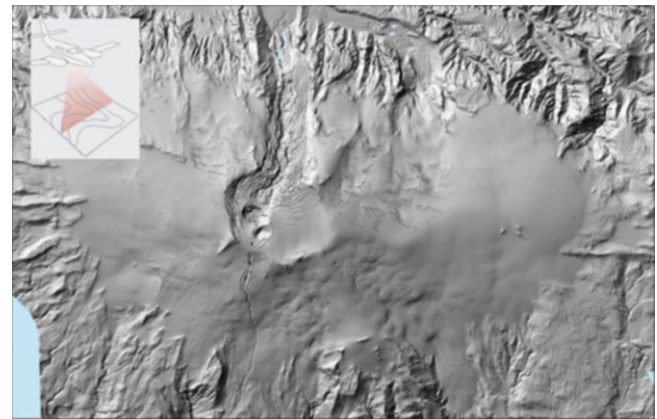


Fig. 4 High resolution DEM derived from LiDAR measurements

observed and the aforementioned air photos taken in July revealed traces of the many additional small slab avalanches within the catchments of Svaðbælisá Holtsá.

Evidence of the lahar and mud flows can also be seen clearly in digital elevation model made with a laser measurement (LiDAR) from an airplane in August 2010 (Fig. 4). Sheet wash erosion is a common landform on the slopes of volcanoes after eruptions fine grained ash forming of impermeable layers in the pile or on the surface of the tephra stratum (Manville et al. 2000). This was the case close to the bottom of the pile in the southern Eyjafjallajökull (referred to as layer 3 above).

During the field expedition in May 2010 it was also found that many channels had formed and material had accumulated along them, forming levee's, similar to what happens during debris flows (Selby 1993). These channels were mostly rather narrow, or an average of 4 m wide, but grew moving further down. A closer examination of air photos showed that the channels formed two patterns.

East of the gorge that formed in a glacial outburst on 14 April. (Figs. 4 and 5a, b) are many small channels could be seen that were merged into larger channels lower down the slopes forming a dendritic pattern similar to braided rivers (Fig. 4). West of the canyon where the flank ruptured the circuits are larger and denser, lying parallel to each other and forming a parallel pattern. This type of channels has been observed where ash slab avalanches have occurred (Manville et al. 2000). It is expected that these channels had formed from water erosion, but as described by Austin (1984) on erosion after the eruption of Mt. Saint Helens in 1980, channels of this type can also occur when the instability of volcanic ash pile causes a chain reaction and collapse within the stack and a retrogressive erosion occurs.

Density and pattern of channels is determined by how much the underlying deficit, namely the density of channels becomes greater as the deficit is greater and the slopes are longer (Tamio Chine 1986). The formation of channels will be influenced by roughness of the tephra, but commonly this

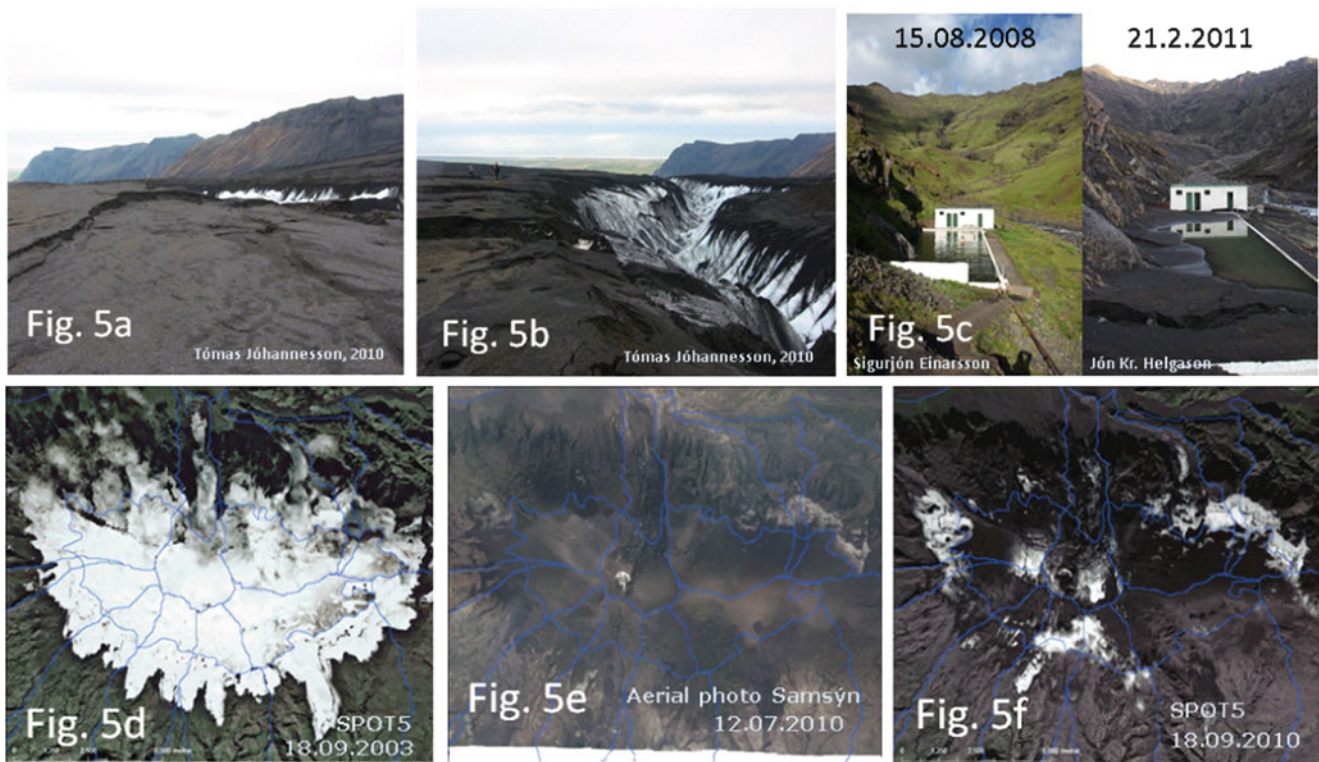


Fig. 5 Aerial and ground based imagery

pattern occurs where tephra grain size is similar to sand. Channels of this nature are usually formed a few days after the ash fall (Manville et al. 2000). The SPOT satellite image taken on 16 September 2010 (Fig. 5f) shows the significant changes had occurred from July (Fig. 5e) to September despite the unusually low rainfall during the summer. A satellite image from 2003 was used for comparison (Fig. 5d). One can see that the drainage channels at the glacier had reached in some places up to 10 m wide and eroded into glacial ice. Commonly, the channels reduce as they become larger and the size is determined partly by the number of precipitation days (Selby 1993; Horton 1945). SPOT image shows that much material was washed from the bottom of the glacier below the current equilibrium line to the west, northeast and south.

Results

It is clear that large amount of material is still on the mountain and the foothills. Photos taken before and after the eruption tell more than thousand words (Fig. 5c). Erosion, transport and accumulation of tephra during extreme precipitation as well as ordinary precipitation events will transport the ash steadily down to the lowlands. It is difficult to estimate how much material has washed down and deposited in the channel controls, as well as part of the material has

blown off or washed out to sea. Something in the range of 400,000 m³ has been bulldozed out of river channels of Svaðbælisá and Holtsá. Excavation by contractors in the area is about 4 % of the tephra that fell below the ablation zone the aforementioned rivers.

The next years ash on the glacier's ablation areas will be eroded relatively quickly by streams. As mentioned above, there are about 16 mi. m³ of material on the south side and about 9 mi. m³ of which are within the ablation area of the catchments Holtsá, Svaðbælisá, Laugará and Kaldaklifsá.

The thickest ash layers are high up on the glacier and are covered with snow. Ashes that fell above the equilibrium line about 1,200 m.a.s.l. will submerge into the glacial ice. It passes down to the ablation zone by moving ice over a long period of time, and when it arrives there it will be eroded by melt water. This process takes decades. The volume of this tephra is about 38 mi. m³ and it is estimated that about 8 mi. m³ thereof have fallen in the drainage basin of Holtsá, Svaðbælisá, Laugará and Kaldaklifsá.

The Lahar Hazard

There less danger of lahar in winter when the ash layers are frozen. The hazard has also decreased due to channel forming in the ash pile disturbing the layering. Historical

sources indicate that mud flow hazard can last up from several months to several years, or until the ash on the surface runs short (Manville et al. 2009).

The Landslide Hazard

The Meteorological Office has monitored the area since the eruption ended and recorded ten landslides in the vicinity of the settlement. Natural Museum (NM) and the Meteorological Office (IMO) run a landslides database in Iceland. Information about landslides have either been acquired from books, from individuals having local knowledge or people with direct observations. A report by Saemundsson (1997) traces the history of landslides and rock falling under Eyjafjöll (foot slopes of Eyjafjallajökull) during the period 1925–1997. There are 16 recorded landslides, mudslides and falling rocks in that period. After the eruption in 2010, 10 events were recorded so clearly, mass movements and stream erosion are more frequent after the ashes deposited on the mountain (E.H. Jensen 2010a, b; Jensen et al. 2010).

Conclusions

The study shows that satellite and radar images can be of great help in estimating the situation on a mountain after a volcanic eruption. Radar images are taken during the event area especially valuable in casting a light on the events. High resolution DEM made with LiDAR technology can reduce the days needed for fieldwork and is very important in Iceland where the field work season is very short.

Acknowledgments We would like to thank Ingibjörg Jónsdóttir and Rósa Ólafsdóttir at the University of Iceland and Tómas Jóhannesson at the Icelandic Meteorological Office as well as the Icelandic Coast Guard for use of their data.

References

- Austin SA (1984) Rapid erosion at Mount St. Helens. *Origins* 11(2):90–98
- Chinen T (1986) Surface erosion associated with tephra deposition on Mt. Usu and other volcanoes environmental science. *Hokkaido J Grad Sch Environ Sci, Hokkaido Univ Sapporo* 9(1):137–149
- Helgason JK, Oddsson B (2010) Mudflow hazard in the south sides of Eyjafjallajökull. Icelandic Meteorological Office, Memo: JKH/BO-2010-01, in Icelandic
- Horton RE (1945) Erosional development of streams and their drainage basin; hydrophysical approach to quantitative morphology. *Bull Geol Soc Am* 56:275–370
- Iversen RM (1997) The physics of debris flows. *Rev Geophys* 35(3):245–296
- Jensen EH (2010a) A debris flow by Steinar IV in Eyjafjöll, Aug 7. 2010. Icelandic Meteorological Office, Memo dated 19.08.2010, in Icelandic
- Jensen EH (2010b) A debris flow east of Steinar IV in Eyjafjöll Sept 25. 2010. Icelandic Meteorological Office, Memo dated. 20.11.2010, in Icelandic
- Jensen EH, Brynjólfsson S, Sverrisdóttir G, (2010) Mudflow in Steinalækur July 12. 2010. Icelandic Meteorological Office and Institute of Earth Science, University of Iceland, Memo dated 20.7.2010, in Icelandic
- Kjartansson G (1951). Water floods and mud flows. The eruption of Hekla 1947–1948. II. 4. *Soc. Sci. Isl.* 51pp. Horton, RE (1945) Erosional development of streams and their drainage basin; hydrophysical approach to quantitative morphology. *Bull Geol Soc Am* 56:275–370
- Manville V, Hodgson KA, Houghton BF, Keys JRH, White JDL (2000) Tephra, snow and water: complex sedimentary responses at an active snow-capped stratovolcano, Ruapehu, New Zealand. *Bull Volcanol* 62:278–293
- Manville V, Németh K, Kano K (2009) Source to sink: a review of three decades of progress in the understanding of volcanoclastic processes, deposits and hazards. *Sediment Geol* 220:136–161
- Sæmundsson Th (1997) Rockfall from Steinafjall eastern Eyjafjöll on September 12. 1997. Icelandic Meteorological Office, report 97029
- Selby MJ (1993) *Hillslope materials and processes*, 2nd edn. Oxford University Press, New York